

Mechanisms and Machine Science 24

Paulo Flores

Fernando Viadero *Editors*

New Trends in Mechanism and Machine Science

From Fundamentals to Industrial
Applications

 Springer

Mechanisms and Machine Science

Volume 24

Series editor

Marco Ceccarelli, Cassino, Italy

More information about this series at <http://www.springer.com/series/8779>

Paulo Flores · Fernando Viadero
Editors

New Trends in Mechanism and Machine Science

From Fundamentals to Industrial
Applications

 Springer

Editors

Paulo Flores
Department of Mechanical Engineering
University of Minho
Guimarães
Portugal

Fernando Viadero
Department of Structural and Mechanical
Engineering
University of Cantabria
Santander
Spain

ISSN 2211-0984

ISBN 978-3-319-09410-6

DOI 10.1007/978-3-319-09411-3

ISSN 2211-0992 (electronic)

ISBN 978-3-319-09411-3 (eBook)

Library of Congress Control Number: 2014946391

Springer Cham Heidelberg New York Dordrecht London

© Springer International Publishing Switzerland 2015

This work is subject to copyright. All rights are reserved by the Publisher, whether the whole or part of the material is concerned, specifically the rights of translation, reprinting, reuse of illustrations, recitation, broadcasting, reproduction on microfilms or in any other physical way, and transmission or information storage and retrieval, electronic adaptation, computer software, or by similar or dissimilar methodology now known or hereafter developed. Exempted from this legal reservation are brief excerpts in connection with reviews or scholarly analysis or material supplied specifically for the purpose of being entered and executed on a computer system, for exclusive use by the purchaser of the work. Duplication of this publication or parts thereof is permitted only under the provisions of the Copyright Law of the Publisher's location, in its current version, and permission for use must always be obtained from Springer. Permissions for use may be obtained through RightsLink at the Copyright Clearance Center. Violations are liable to prosecution under the respective Copyright Law. The use of general descriptive names, registered names, trademarks, service marks, etc. in this publication does not imply, even in the absence of a specific statement, that such names are exempt from the relevant protective laws and regulations and therefore free for general use.

While the advice and information in this book are believed to be true and accurate at the date of publication, neither the authors nor the editors nor the publisher can accept any legal responsibility for any errors or omissions that may be made. The publisher makes no warranty, express or implied, with respect to the material contained herein.

Printed on acid-free paper

Springer is part of Springer Science+Business Media (www.springer.com)

Preface

EUCOMES 2014 is the fifth event in a series that was started in 2006, under the Patronage of IFToMM, International Federation for the Promotion of Mechanism and Machine Science. The aim of the conference is to bring together European researchers, industry professionals, and students from the broad range of disciplines referring to Mechanism Science, in an intimate, collegial, and stimulating environment.

The EUCOMES conference began in February 2006 in Obergurgl (Austria), and has continued subsequently in Cassino (Italy) in September 2008, Cluj-Napoca (Romania) in September 2010, and Santander (Spain) in September 2012. The 2014 edition is organized by the Center for Mechanical and Materials Technologies (CT2M) and the Department of Mechanical Engineering (DEM) of the Engineering School of the University of Minho in Guimarães, Portugal, from 16 to 19 September 2014.

This book compiles the most recent research results in mechanism science, intended to reinforce and improve mechanical systems in a variety of applications in daily life and industry. This book is published under the Machine and Mechanism Science series and addresses issues related to: Theoretical kinematics, Computational kinematics, Mechanism design, Experimental mechanics, Mechanics of robots, Dynamics of machinery, Dynamics of multibody systems, Control issues of mechanical systems, Mechanisms for biomechanics, Novel designs, Mechanical transmissions, Linkages and manipulators, Micromechanisms, Teaching methods, History of mechanism science, and Industrial and nonindustrial applications.

EUCOMES 2014 received more than one hundred submissions, and after a rigorous review process by at least two reviewers for each paper, 100 papers were accepted for oral presentation at the conference and are included in this book.

We express our grateful thanks to IFToMM, Portuguese Association of Theoretical, Applied and Computational Mechanics (APMTAC), the Department of Mechanical Engineering of the University of Minho, the members of the International Scientific Committee for their cooperation: Prof. Bukhard Corves (Germany), Prof. Doina Pisla (Romania), Prof. Fernando Viadero (Spain), Prof. Jean-Pierre Merlet (France), Prof. Manfred Husty (Austria), Prof. Marco Ceccarelli (Italy),

Prof. Paulo Flores (Portugal), and Prof. Teresa Zielinska (Poland), the members of the Award Committee and the members of the Honorary Committee.

We also want to express our gratitude to all the authors for their interest in participating in EUCOMES 2014 and for writing the manuscripts in a timely manner, allowing this conference to be a reality in a short period of time.

We thank all anonymous and volunteer reviewers for their outstanding work, which allowed the Conference Springer Book to be published as scheduled.

We thank the University of Minho for hosting the EUCOMES 2014 conference and we express our deepest gratitude to The Local Organizing Committee: Eurico Seabra, João Mendonça Silva, José Machado, Luís Ferreira da Silva, Mário Lima, Nuno Peixinho, Paulo Flores (Chairman), Pedro Souto, and Sara Cortez.

Guimarães, June 2014
Santander

Paulo Flores
Fernando Viadero

Contents

Part I Theoretical Kinematics

Dimensional Synthesis of Six-Bar Linkages with Incomplete Data Set	3
Shaoping Bai	
Mathematical Modelling and Simulation for Beaded Pad Automatic Weaving Trajectory	13
Jianye Yan, Ligang Yao, Dongliang Lin and Zhijun Liu	
Graphical User Interface for the Singularity Analysis of Lower-Mobility Parallel Manipulators	21
Stéphane Caro, Latifah Nurahmi and Philippe Wenger	
On the Redundancy of Cable-Driven Parallel Robots	31
J.-P. Merlet	

Part II Computational Kinematics

On the Resolution of Forward Kinematic Problem Using CAD Graphical Techniques: Application on Planar Parallel Robotic Manipulators	43
K.A. Arrouk, B.C. Bouzgarrou and G. Gogu	
Introducing Distance Restrictions in the Deformed Position Problem	53
I. Fernández de Bustos, V. García Marina, M. Abásolo and R. Avilés	
On Generalized Euler Angles	61
Aleix Rull and Federico Thomas	

Guaranteed Detection of the Singularities of 3R Robotic Manipulators	69
Romain Benoit, Nicolas Delanoue, Sébastien Lagrange and Philippe Wenger	
Workspace Analysis for Evaluating Laparoscopic Instruments	81
J.-H. Borchard, F. Dierßen, J. Kotlarski, L.A. Kahrs and T. Ortmaier	
A Novel, Loop-Based Approach for Rigidity Detection for Systems with Multiple Spherical–Spherical Bars: The “Double-Banana” Case	91
F. Simroth, H.F. Ding and A. Kecskeméthy	
Planar Four-Link Mechanism Analysis for Application in 3D Printing Machines	99
A. Kłodowski	
 Part III Mechanism Design	
Path Generating Belt Mechanisms as Kinematic Chains for Mechatronic Applications	111
E.-C. Lovasz, D. Perju, K.-H. Modler, C.M. Gruescu, D. Mărgineanu, C.E. Moldovan and C. Pop	
Synthesis of a Mechanism for Human Gait Rehabilitation: An Introductory Approach	121
Pedro Alves, Francisco Cruz, Luís F. Silva and Paulo Flores	
A Form-Closed Cam-Follower Mechanism for a Breath Simulator Machine	129
R.F. Oliveira, P. Flores, S.F. Teixeira, H.M.C. Marques and J.C. Teixeira	
Dimensional Synthesis with Mechanism Processing Strategy	139
M. Hüsing, R. Braune and B. Corves	
Dynamic Modelling of a Four Legged Robot.	147
I. Geonea, A. Ungureanu, N. Dumitru and L. Racilă	
Lifting Mechanism for Payload Transport by Collaborative Mobile Robots.	157
B. Hichri, J.-C. Fauroux, L. Adouane, I. Doroftei and Y. Mezouar	

Kinematic Design of a Reconfigurable Deployable Canopy	167
G. Kiper, F. Gürcü, K. Korkmaz and E. Söylemez	
Function Generation Synthesis with a 2-DoF Overconstrained Double-Spherical 7R Mechanism Using the Method of Decomposition and Least Squares Approximation.	175
G. Kiper and B. Bağdadioğlu	
Designing Cam Mechanisms Using CAx	185
J. Ondrášek	
Kinematics Analysis and Verification on the Novel Reconfigurable Ankle Rehabilitation Robot Based on Parallel Mechanism.	195
Shilong Zeng, Ligang Yao, Xiaoning Guo, Hengli Wang and Pengju Sui	
Finite Element Modeling and Analysis of an Isoglide-Type Parallel Manipulator to Determine Its Rigidity/Stiffness.	203
A. Kozyrev and V. Glazunov	
Modular Cooperative Mobile Robots for Ventral Long Payload Transport and Obstacle Crossing	211
M. Krid, J.C. Fauroux and B.C. Bouzgarrou	
Hypo-Cycloidal Crank Mechanism to Produce an Over-Expanded Cycle Engine	221
J. Pinto, T. Costa, J. Martins and F.P. Brito	
 Part IV Experimental Mechanics	
Influence of the Mass of the Weight on the Dynamic Response of the Laboratory Fibre-Driven Mechanical System	233
P. Polach and M. Hajžman	
On the Experimental Intradiscal Pressure Measurement Techniques: A Review	243
A. Araújo, N. Peixinho, A. Pinho and J.C.P. Claro	
Geometry and Material Strategies for Improved Management of Crash Energy Absorption	251
N. Peixinho	

An In Vitro Experimental Evaluation of the Displacement Field in an Intracranial Aneurysm Model.	261
Diana Pinho, David Bento, João Ribeiro, Rui Lima and Mário Vaz	
Experiments on the Edge of Chaos of a Planar Closed Chain Underactuated Mechanism.	269
J. Xie, H. Zhao, Z.-H. Liu and Y. Chen	
Systematic and Rapid Construction of Test Beds for Planar Mechanism	277
H. Mencek and R. Soylu	
Development of Impact Loading Equipment for Testing of FRP Strips as Reinforcement of Masonry Bricks.	287
P. Correia and N. Peixinho	
 Part V Mechanics of Robots	
Design of a Driving Module for a Hybrid Locomotion Robot.	299
J.J. Castillo, J.A. Cabrera, M. Jaimez, F. Vidal and A. Simón	
Analysis of Joint Clearance Effects on Dynamics of Six DOF Robot Manipulators	307
S. Erkaya	
Investigating the Effect of Cable Force on Winch Winding Accuracy for Cable-Driven Parallel Robots.	315
Valentin Schmidt, Alexander Mall and Andreas Pott	
Solving the Dynamic Equations of a 3-PRS Parallel Manipulator.	325
M. Díaz-Rodríguez, R. Bautista-Quintero and J.A. Carretero	
 Part VI Dynamics of Machinery	
Optimization of Textile Machines in Order to Increase Productivity	337
B. Corves, M. Hüsing, M. Schumacher and F. Schwarzfischer	
Motion Equation of Linkages with Changeable Close Loop.	345
E. Gebel	

Elastodynamic Analysis of the Sucker Rod Pumping System Mechanism 355
 N. Dumitru, N. Craciunoiu, R. Malciu and N. Ploscaru

Dimensioning the NC: Axes of a Radial Cam Grinding Machine 365
 V. Crhák, P. Jirásko and M. Václavík

Efficiency Analysis of Shifted Spur Gear Transmissions. 373
 A. Diez-Ibarbia, A. Fernández del Rincón, M. Iglesias, A. De Juan, P. García and F. Viadero

Part VII Dynamics of Multi-body Systems

A New Approach to Eliminate the Constraints Violation at the Position and Velocity Levels in Constrained Mechanical Multibody Systems 385
 P. Flores

Vehicle Dynamic Simulation Using Robotic Techniques and Taking into Account a Tyre Model 395
 B. Menkouz and M. Haddad

An Advanced 3D Multi-body System Model for the Human Lumbar Spine 405
 S. Sousa and J.C.P. Claro

Energy-Consistent Integration Scheme for Multi-body Systems with Dissipation 413
 S. Conde Martín and J.C. García Orden

Multi-objective Optimization of Mechanisms with Clearances in Revolute Joints 423
 Z. Zhang, L. Xu, Y.Y. Tay, P. Flores and H. Lankarani

Biomechanical Experimental Data Curation: An Example for Main Lumbar Spine Ligaments Characterization for a MBS Spine Model 435
 C. Lourenço and J.C.P. Claro

A Three-Dimensional Multibody Model of the Human Ankle-Foot Complex 445
 T.M. Malaquias, S.B. Gonçalves and M. Tavares da Silva

Inverse Dynamics of 2-DOF Parallel Mechanism Used for Orientation	455
T. Itul, B. Gherman, D. Cocorean and D. Pislă	
Wear Prediction of Ceramic-on-Ceramic Artificial Hip Joints	463
E. Askari, P. Flores, D. Dabirrahmani and R. Appleyard	
Techniques for Geometrical Detection of Contact Within Multibody Systems	471
M. Machado, P. Flores and J. Ambrósio	
On the Equivalence Between Forward and Inverse Dynamic Analysis of Human Motion Tasks.	479
C. Quental, J. Folgado, J. Ambrósio and J. Monteiro	
Railway Vehicle Modelling for the Vehicle-Track Interaction Compatibility Analysis.	487
H. Magalhães, J. Ambrósio and J. Pombo	
Validation of an Enhanced Cylindrical Contact Force Model Using Numerical and Analytical Approaches.	497
C. Pereira, A. Ramalho and J. Ambrosio	
Human Gait Analyses Using Multibody Systems Formulation: Normal and Pathological Scenarios	505
P. Moreira, J. Peixoto, U. Lúgrís, J. Cuadrado, P. Flores and P. Souto	
Numerical Simulation of a Granular Material Damper	515
T. Koga, T. Sato, A. Weller and K. Ono	
Wagon Multibody Model and Its Real-Time Application.	523
M. Spiryagin, S.S.N. Ahmad, C. Cole, Y.Q. Sun and Tim McSweeney	
Part VIII Control Issues of Mechanical Systems	
Experimental Validation of the Mechatronic Model of a Parallel Manipulator	535
O. Altuzarra, F.J. Campa, C. Roldan-Paraponiaris and Ch. Pinto	
Preferable Operation Modes of a Wind Turbine with a Differential Planetary Gearbox.	545
M. Dosaev, A. Holub and L. Klimina	

Hybrid Position/Force Control of a Cable-Driven Parallel Robot with Experimental Evaluation 553
 Werner Kraus, Philipp Miermeister, Valentin Schmidt and Andreas Pott

The Control System of a Parallel Robot for Brachytherapy 563
 C. Vaida, D. Pislă, A. Szilaghyi, F. Covaciu, D. Cocorean and N. Plitea

Ambient Assisted Living Platform for Remote Monitoring of Bedridden People 573
 F. Pereira, C. Barros, V. Carvalho, J. Machado, C.P. Leão, F. Soares, K. Bezerra and D. Matos

Part IX Mechanisms for Biomechanics

Design and Simulation of Humanoid Spine 585
 Daniele Cafolla and Ceccarelli Marco

Feet Compliance in Two Legged Locomotion 595
 Magdalena Zurawska and Teresa Zielinska

Lab Experiences with LARM Clutched Arm for Assisting Disabled People 603
 C. Copilusi, M. Kaur and M. Ceccarelli

Design and Simulation of Walking Operation of a Cassino Biped Locomotor 613
 Mingfeng Wang and Marco Ceccarelli

Pneumatic Video Tactile Sensor for Laparoscopic Surgery 623
 M. Dosaev, I. Goryacheva, F.-C. Su, C.-H. Yeh, M.-S. Ju, M. Gubenko, A. Lyubicheva, A. Morozov and Yu Selyutskiy

Design of a New Medical Device for Aiding Clinical Diagnosis of Patellofemoral Disorders 633
 A. Leal, R. Pereira, H. Pereira, P. Flores, F.S. Silva and J. Espregueira-Mendes

Lab Experiences with a Linkage Exoskeleton for Walking Assistance 643
 I. Silva, M. Ceccarelli, C. Copilusi and P. Flores

Characterization and Analysis of Data in Autistic Walk Pressure 651
 L. Souza, S. Rosa, M. Carvalho and T. Torquato

Physiological-Like Testing of the Dislocation Stability of Artificial Hip Joints	659
S. Herrmann, M. Kähler, R. Grawe, D. Kluess, C. Woernle and R. Bader	
Experimental Bench Used to Test Human Elbow Endoprosthesis	669
D. Tarnita, D. Popa, C. Boborelu, N. Dumitru, D. Calafeteanu and D.N. Tarnita	
A Dynamic Intramedullary Implant for Bone Fracture Repair	679
A. Dowd, B.J. Mac Donald, R. Lostado, W.T. McCartney and D. Comiskey	
A Computational Benchmark for 2D Gait Analysis Problems	689
R. Pàmies-Vilà, J.M. Font-Llagunes, U. Lugrís, F.J. Alonso and J. Cuadrado	
Development and Early Results of a New Concept of an Orthopedic Footwear Stirrup	699
J. Peixoto, B. Moura, P. Moreira, A.P. Souto and P. Flores	
Dynamic Analysis of an Exoskeleton New Ankle Joint Mechanism	709
N. Dumitru, C. Copilusi, I. Geonea, D. Tarnita and I. Dumitrache	
Part X Novel Designs	
Analysing of Flying Conditions of Aircrafts Using Artificial Neural Networks	721
Ş. Yıldırım and S. Erkaya	
Digital-Based Engineering Tools for Tailored Design of Medical Implants	733
R. Neto, T. Marques, M. Marta, N. Leal, M. Couto and M. Machado	
Synthesis of PR/RP-Chain Based Compliant Mechanisms: Design of Applications Exploiting Fibre Reinforced Material Characteristics	743
U. Hanke, E.-C. Lovasz, M. Zichner, N. Modler, A. Comsa and K.-H. Modler	
Computer and Physical Simulation of Space Mirror Deployment	753
V.I. Bujakas	

Permeability Evaluation of Flow Behaviors Within Perfusion Bioreactors 761
 D. Freitas, H.A. Almeida and P.J. Bártolo

Part XI Mechanical Transmissions

Load Sharing and Contact Stress Calculation of High Contact Ratio Internal Spur Gears 771
 M. Pleguezuelos, J.I. Pedrero and M.B. Sánchez

Calculation of Load Capacity of Cylindrical Gears: Review of Different Approaches and Calculation Tools 779
 S.M.O. Tavares and P.M.S.T. de Castro

Load Distribution in Spur Gears Including the Effects of Friction 789
 Pedro M.T. Marques, Ramiro C. Martins and Jorge H.O. Seabra

Influence of Gear Loss Factor on the Power Loss Prediction 799
 Carlos M.C.G. Fernandes, Pedro M. T. Marques, Ramiro C. Martins and Jorge H. O. Seabra

Hydraulic Hose as an Instability Reducer for a Flexible Shaft Composed by Universal Joints 807
 V.H. Carneiro and J. Meireles

Propulsion Architectures Using Mechanical Energy Storage 817
 Madhusudan Raghavan

Part XII Linkages and Manipulators

Closed-Chain Principal Vector Linkages 829
 V. van der Wijk

Design of a Low-Cost Manipulator Arm for Industrial Fields 839
 E. Soriano, H. Rubio, C. Castejón and J.C. García-Prada

Part XIII Micro-Mechanisms

A New Pseudo-Rigid-Body Model of Compliant Mechanisms Considering Axial Deflection of Flexural Beams 851
 Yue-Qing Yu, Peng Zhou and Qi-Ping Xu

An Internal Gyroscopic Micro-Mechanism for Development of Lateral Deviation of a Projectile. 859
 C.M. Umstead, Y.Y. Tay and H.M. Lankarani

An Approach to the Characterization of Flexure Hinges for the Purpose of Optimizing the Design of a Micromanipulator 869
 D. Schoenen, I. Ivanov and B. Corves

Part XIV Teaching Methods

Machine and Mechanism Design at UMinho: Research-Teaching Interaction 881
 M. Lima, E. Seabra and L.F. Silva

Computer Aided, Task-Based Kinematic Design of Linkages: A New Lecture for Engineering Students 891
 K. Abdul-Sater, T.C. Lueth and F. Irlinger

Part XV History of Mechanism Science

A.N. Krylov: The Pioneer of Photographic Non-invasive Measurement Methods in Russian Science 903
 Andrei Vukolov and Alexander Golovin

Animation of Historical Patents 913
 U. Döring, C. Brandt-Salloum, V. Henkel and T. Brix

Part XVI Industrial and Non-industrial Applications

Dynamic Modeling and Analysis of an Industrial Cutting File Machine 923
 E. Seabra, Luís F. Silva and P. Flores

An Overview of Industrial Communication Networks 933
 M. Silva, F. Pereira, F. Soares, C.P. Leão, J. Machado and V. Carvalho

Rapid Development of Control Algorithms and Interfaces for Remote Monitoring of Robotic Arm Through Internet of Things (IoT) 941
 M. Murar and S. Brad

Numerical Simulation of Impact Loading on Open-Cell Aluminum Foams 949
P. Moreira, J.P. Mendonça and N. Peixinho

Combining the Finite Element Method and Response Surface Methodology for Adjustment of Contact Stress Ratios in Tapered Roller Bearings 957
R. Lostado, R. Escibano, R. Fernandez Martinez and B.J. Mac Donald

Author Index 965

Part I
Theoretical Kinematics

Dimensional Synthesis of Six-Bar Linkages with Incomplete Data Set

Shaoping Bai

Abstract The paper deals with the synthesis problem of six-bar linkage for motion guidance with a finite set of prescribed poses. Compared with four-bar linkage which admits exact solutions for five separated poses, the six-bar linkages in general admit infinitive many solutions for the same number of poses, due to the fact that the motion-guidance in the case of six-bar linkage provides incomplete data for linkage synthesis. In this paper, the problem of six-bar linkage synthesis is revisited addressing the problem with incomplete data and its implication in design flexibility. A new method is developed to incorporate with incomplete set of data. A design example is included to demonstrate the application of the method.

Keywords Burmester problem • Six-bar linkage • Rigid-body guidance • Exact dimensional synthesis • Synthesis with incomplete data set

1 Introduction

Rigid-body motion guidance, or the Burmester problem, deals with the finding of geometric parameters of linkages, classically, the four-bar linkage, for a prescribed set of finitely separated poses.¹ The problem begins with a set of locations, or poses, for the floating link. For four-bar linkage, the synthesis is conducted for cranks. The design of one crank is to find a dyad being given by a pair of points, the *circlepoint* in the floating link and the *centrepoint* in the grounded link. Two cranks designed form the desired four-bar linkage.

¹ “Are there any points in a rigid body whose corresponding positions lies on a circle of the fixed plane for the four arbitrarily prescribed positions?” [1].

S. Bai (✉)

Department of Mechanical and Manufacturing Engineering, Aalborg University,
Aalborg, Denmark
e-mail: shb@m-tech.aau.dk

The Burmester problem has been extensively studied for the case of four-bar linkages. Bottema and Roth [2], McCarthy [3] and Hunt [4] solved the problem by intersecting two centrepoint curves of two four-pose problems for two subsets of four poses out of the given five-pose set, to obtain the centers. Modler [5] investigated various special cases. Al-Widyan and Angeles [6] developed a robust algorithm to synthesize four-bar linkages, in which circlepoints and centrepoints were found through the intersections of the four possible contours of the four-pose problems. The Burmester theory was also generalized for spherical and spatial four-bar linkages [7, 8].

While the major literatures are related to the four-bar linkages, there are very few works reported for six-bar linkages. A method of six-bar linkage synthesis was developed by Soh and McCarthy, where they considered the linkages as constrained 3R chains [9]. An optimum synthesis method for six-bar linkages using differential evolution was reported in [10]. Dimensional synthesis of six-bar linkages was studied for a symmetrical Watt's mechanism in [11]. Compared with four-bar linkages, the six-bar linkages in general have a large flexibility in synthesis. The flexibility is due to the fact that the synthesis with prescribed poses, namely, five poses, lead to a mixture of motion-guidance and path generation problems, the latter having incomplete data set to be a determined case. While a set of incomplete pose data allows designers to define some link dimensions as additional constraints in addition to the prescribed poses, it brings new problem to deal with the flexibility in synthesis. Novel methods are required to handle the synthesis of six-bar linkage.

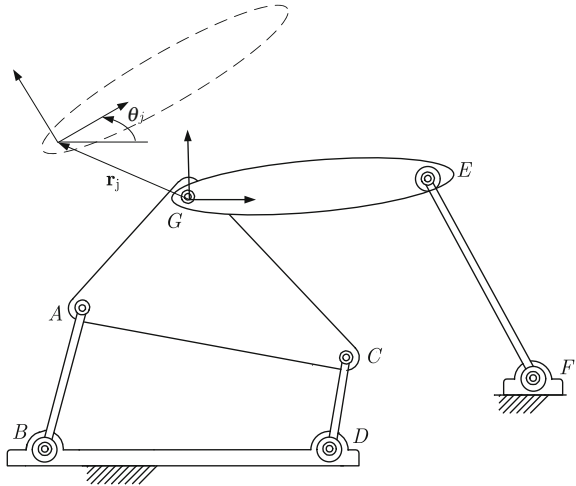
In this paper, the Burmester problem is re-visited with extension to six-bar linkages. The problem of dimensional synthesis with incomplete data is addressed and its implication in design flexibility is discussed. A new method is developed to incorporate with incomplete set of data and demonstrated with a design example.

2 Problem Formulation

We extend the classic Burmester problem from the four-bar linkage to the six-bar linkage. The Burmester problem reads: A rigid body, as shown in Fig. 1, is to be guided through a discrete set of m poses, given by $\{\mathbf{r}_j, \theta_j\}_0^m$, where \mathbf{r}_j is the position vector of a landmark point G of the body at the j th pose and θ_j is the corresponding angle of a line of the body. The problem consists in finding the joint centers A_0 and B , aka the circlepoint and the centrepoint, that define the BA_0 dyad. Dyads DC_0 and FE_0 are determined likewise.

The problem at hand is to find the three revolute-revolute (RR) dyads to construct a six-bar linkage able to visit the prescribed poses. The linkage in Fig. 1 is the type of Stephenson-III mechanism, which is the linkage addressed in this work. In the balance of this paper, we will develop a general synthesis method for five poses, applicable to problems admitting both RR and PR (prismatic-revolute) dyads.

Fig. 1 A six-bar linkage with revolute-revolute (RR) dyads only

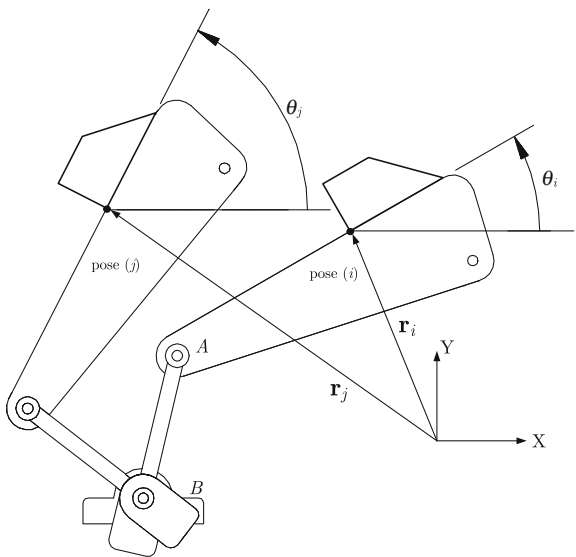


3 Synthesis with Burmester Theory

In applying the Burmester theory, the reference coordinate system is established with the origin at point G_0 . The moving coordinate system is attached to the floating rigid body, with the origin located at G_j .

Without loss of generality, we start the synthesis with a general four-bar linkage, as shown in Fig. 2. Under the usual rigid-body assumption, the synthesis equation is readily derived:

Fig. 2 Two finitely-separated poses of a rigid body carried by the coupler link of a four-bar linkage



$$\| \underbrace{(\mathbf{r}_j - \mathbf{b}) + \mathbf{Q}_j \mathbf{a}_0}_{\mathbf{a}_j - \mathbf{b}} \|^2 = \|\mathbf{a}_0 - \mathbf{b}\|^2, \quad \text{for } j = 1, \dots, m \quad (1)$$

where \mathbf{a}_0 and \mathbf{b} are position vectors of points A_0 and B , the design parameters of the linkage. \mathbf{Q}_j denotes the rotation matrix carrying the guided body from pose 0 to pose j by an angle $\phi_j = \theta_j - \theta_0$.

Equation (1) is the vector form of the Burmester theory, which implies that the trajectory of point A is a circle of radius $r = \|\mathbf{a}_0 - \mathbf{b}\|$, centered at point B .

Upon expansion of Eq. (1) and simplification, we obtain

$$\mathbf{b}^T (1 - \mathbf{Q}_j) \mathbf{a}_0 + \mathbf{r}_j^T \mathbf{Q}_j \mathbf{a}_0 - \mathbf{r}_j^T \mathbf{b} + \frac{\mathbf{r}_j^T \mathbf{r}_j}{2} = 0, \quad j = 1, \dots, m \quad (2)$$

which are the *synthesis equations* that can be used to compute the design parameters. The equation contains four variables, which are the coordinates of points A and B . The dyad admits exact solutions for at most five poses ($m = 4$), a well-known result.

Likewise, the synthesis equations for RR dyad C_0D are

$$\mathbf{d}^T (1 - \mathbf{Q}_j) \mathbf{c}_0 + \mathbf{r}_j^T \mathbf{Q}_j \mathbf{c}_0 - \mathbf{r}_j^T \mathbf{d} + \frac{1}{2} \mathbf{r}_j^T \mathbf{r}_j = 0, \quad j = 1, \dots, m \quad (3)$$

3.1 Synthesis Equation for PR Dyads

To accommodate both PR and RR dyads, we define

$$\mathbf{b} \equiv \frac{\beta}{w}, \quad w = 1 \quad \text{or} \quad 0 \quad (4)$$

A PR dyad can be regarded a case with $w = 0$, i.e., \mathbf{b} corresponding to a point at infinity. Moreover, we define $\|\beta\| = 1$, in that a point at infinity has only a “direction,” but not a position.

Upon substitution of Eq. (4) into Eq. (2), and simplifying, we obtain

$$[(1 - \mathbf{Q}_j) \mathbf{a}_0 - \mathbf{r}_j]^T \beta = 0, \quad j = 1, \dots, m \quad (5)$$

3.2 Elimination of Motion Variables

The orientation angle ϕ_j is a motion variable which is not the interest of designers. It could be eliminated as presented below.

We develop below all terms of Eq. (2) by writing \mathbf{Q}_j in the form $\mathbf{Q}_j = \mathbf{c}_j \mathbf{1} + s_j \mathbf{E}$, in which $\mathbf{1}$ is the 2×2 identity matrix, while $s_j \equiv \sin \phi_j$ and $c_j \equiv \cos \phi_j$. Hence,

$$\begin{aligned}\mathbf{b}^T(1 - \mathbf{Q}_j)\mathbf{a}_0 &= \mathbf{b}^T(1 - c_j\mathbf{1} - s_j\mathbf{E})\mathbf{a}_0 \\ &= \mathbf{b}^T\mathbf{a}_0 - c_j\mathbf{b}^T\mathbf{a}_0 - s_j\mathbf{b}^T\mathbf{E}\mathbf{a}_0\end{aligned}\quad (6a)$$

$$\begin{aligned}\mathbf{r}_j^T\mathbf{Q}_j\mathbf{a}_0 &= \mathbf{r}_j^T(c_j\mathbf{1} + s_j\mathbf{E})\mathbf{a}_0 \\ &= c_j\mathbf{r}_j^T\mathbf{a}_0 + s_j\mathbf{r}_j^T\mathbf{E}\mathbf{a}_0\end{aligned}\quad (6b)$$

Equation (2) can be written for dyad A_0B in a short form as

$$A_1c_j + B_1s_j + C_1 = 0 \quad (7a)$$

with all coefficients being

$$A_1 = \mathbf{r}_j^T\mathbf{a}_0 - \mathbf{b}^T\mathbf{a}_0 \quad (7b)$$

$$B_1 = \mathbf{r}_j^T\mathbf{E}\mathbf{a}_0 - \mathbf{b}^T\mathbf{E}\mathbf{a}_0 \quad (7c)$$

$$C_1 = \mathbf{b}^T\mathbf{a}_0 - \mathbf{r}_j^T\mathbf{b} + \mathbf{r}_j^T\mathbf{r}_j/2 \quad (7d)$$

Likewise, the synthesis equation for dyad C_0D leads to

$$A_2c_j + B_2s_j + C_2 = 0 \quad (8a)$$

with

$$A_2 = \mathbf{r}_j^T\mathbf{c}_0 - \mathbf{d}^T\mathbf{c}_0 \quad (8b)$$

$$B_2 = \mathbf{r}_j^T\mathbf{E}\mathbf{c}_0 - \mathbf{d}^T\mathbf{E}\mathbf{c}_0 \quad (8c)$$

$$C_2 = \mathbf{d}^T\mathbf{c}_0 - \mathbf{r}_j^T\mathbf{d} + \mathbf{r}_j^T\mathbf{r}_j/2 \quad (8d)$$

Equations (7a) and (8a) yield

$$c_j = \frac{B_1C_2 - C_1B_2}{A_1B_2 - A_2B_1}; \quad s_j = -\frac{A_1C_2 - A_2C_1}{A_1B_2 - A_2B_1} \quad (9)$$

Finally, substituting the solutions of c_j and s_j into $s_j^2 + c_j^2 = 1$ yields

$$\begin{aligned}A_1^2C_2^2 - 2A_1C_2A_2C_1 + A_2^2C_1^2 + B_1C_2A_1B_2 - B_1^2C_2A_2 - C_1B_2^2A_1 \\ + C_1B_2A_2B_1 - A_1^2B_2^2 + 2A_1B_2A_2B_1 - A_2^2B_1^2 = 0\end{aligned}\quad (10)$$

which is the equation for the four-bar linkage applicable to pose j . It is seen that the equations are dependent only to the displacements, but not to the orientations. In this light, it is obvious that the problem for the dyads is converted to path

generation, rather than motion guidance. On the other hand, the synthesis of dyad E_0F is still a problem of rigid-body guidance.

3.3 Flexibility of Design with Incomplete Sets

Based on the formulated equation of synthesis, the problem is decomposed into two subproblems, one rigid-body motion guidance, and the other path generation. The two subproblems admit different solutions:

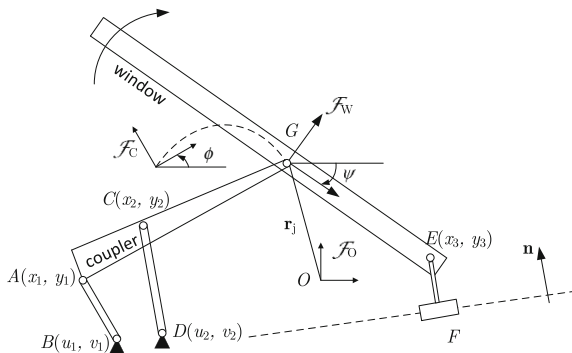
- The solution for RR dyad E_0F pertains to the motion guidance problem. It admits exact solutions for maximum 5 prescribed poses, i.e., $m = 4$, a well-known results.
- The path generation of the four-bar linkage BA_0C_0D , on the other hand, admits exact solutions for maximum 9 prescribed positions.

For the problem at hand, it is not possible to provide prescribed data separately for the two subproblems. When five poses are predefined, it is known that finite exact solutions exist for motion guidance, but infinitively many solutions for path generations. The problem of six-bar linkage synthesis thus admits infinitely many solutions for the five-pose synthesis.

In the six-bar synthesis with five poses, the dyads C_0D and A_0B have only position constraints, while the orientation angles are motion variables, which are dependent on the link dimensions. In this light, the two dyads are subject to constraints of incomplete data sets. The incomplete data implies flexibility to define a few design parameters by designers, while exact solutions are still possible. Different selections of design parameters can be applicable to getting solutions. Some possibilities include:

- Select and define one of the two RR dyads, either A_0B or C_0D . In this case, we have a known 3R kinematic chain. The problem requires only to find the other RR dyads, together with the chain E_0F . This is the case of synthesis with constraints of 3R chain, which was reported by Soh and McCarthy [9].
- Select and define two grounding points, i.e., centrepoints, B and D . The problem becomes to find two circlepoints A_0 and C_0 , together with the dyad E_0F .
- Specify any four coordinates for the four points A_0, B, C_0 and D .

There are other possibility of selection to be explored. Note that the selection might lead to no-solution situation. Thus how to specify robustly additional conditions (constraints) will be a challenging problem to study.

Fig. 3 The six-bar linkage**Table 1** Five poses for the example

j	\mathbf{r}_j [cm]	ψ_j
0	$[0 \ 0]^T$	0
1	$[-2.89 \ 23.12]^T$	-45°
2	$[11.46 \ 33.74]^T$	-67°
3	$[2.34 \ 30.05]^T$	-90°
4	$[0.29 \ 3.0]^T$	-150°

4 A Design Example

We provide an example to illustrate the foregoing synthesis procedure. This example is related to the motion guidance of window opening by a six-bar linkage, as demonstrated in Fig. 3. The window has a pivoting joint in the middle, while one of its end is connected to a linear guide through a prismatic joint. The linkage thus includes both RR and PR dyads. The poses to be visited are listed in Table 1.

Prior to embarking on the numerical solution of the synthesis equations, we normalize the equations to render them dimensionless, thereby avoiding loss of precision. All displacements are normalized through characteristic length

$$\lambda = \sqrt{\frac{1}{m} \sum_{j=1}^m \mathbf{r}_j \cdot \mathbf{r}_j} \quad (11)$$

Refer to Fig. 3, a fixed coordinate system \mathcal{F}_O is established, for which $\mathbf{r}_0 = 0$ and $\phi_0 = 0$. Two moving frames \mathcal{F}_C and \mathcal{F}_W are attached to the coupler link and the window, respectively. Their origins are coincident at point G .

Table 2 Solutions for the example

Points	Coordinates [cm]	Points	Coordinates [cm]	Points	Coordinates [cm]
B	$[-25, 0]^*$	A_0	$[-35., -1.12]$	E	$[36.032, 4.67]$
D	$[-20, 0]^*$	C_0	$[-30.57, -3.54]$	\mathbf{n}	$[-.344, .938]^T$

* User-specified parameters

Two rotation matrices for frames \mathcal{F}_C and \mathcal{F}_W are defined

$$\mathbf{R}_j = \begin{bmatrix} \cos \phi_j & -\sin \phi_j \\ \sin \phi_j & \cos \phi_j \end{bmatrix}; \quad \mathbf{Q}_j = \begin{bmatrix} \cos \psi_j & -\sin \psi_j \\ \sin \psi_j & \cos \psi_j \end{bmatrix}, \quad j = 1, \dots, m \quad (12)$$

where $m = 4$ is the number of poses in this problem.

The synthesis equation for dyad E_0F is

$$(\mathbf{r}_j - (1 - \mathbf{Q}_j)\mathbf{e}_0)^T \mathbf{n} = 0 \quad j = 1, \dots, m \quad (13)$$

where n is the direction vector normal to the guiding slot.

Equations (2), (3) and (13) compose the system of synthesis equations for this six-bar linkage.

We specify two centrepoints, namely, B and D . The other points and the normal vector of the guiding slot are found as listed in Table 2. The synthesis error in this example is found as 2.773×10^{-6} .

5 Conclusions and Discussion

The synthesis of six-bar linkage is studied by resorting to the Burmester theory. The synthesis equations are formulated for a Stephenson mechanism by extending synthesis equations of four-bar linkage to the six-bar. The equations reveal that the six-bar linkage synthesis with five poses is essentially a problem with incomplete data set—a determined dyad synthesis for motion guidance, combining with an underdetermined four-bar linkage for path generation. The synthesis of six-bar linkage is thus generally in need to incorporate with incompleteness of pose data. The synthesis strategy is discussed. An example is included to demonstrate the application of the developed method.

The paper deals with linkage synthesis with incomplete data for the case of six-bar linkages. As a matter of fact, the synthesis with incomplete data can also be found in other cases, where non-symmetric kinematic chains exist. For example, the synthesis of spatial RCCC linkage is involved with incomplete data set too, as RC and CC dyads admit exact solutions for different number of poses. The synthesis with incomplete data stands for a special type of problem and requires more attentions.

Given the incompleteness of data, additional conditions can be provided to obtain solutions, which implies a great flexibility in design to choose freely some design parameters. The selection of parameters with consideration of robustness is an interesting problem for future study.

Acknowledgments The author acknowledges the industrial support from Peder Nielsen Beslagfabrik A/S and collaboration with Mr. Skjold Rune Mortensen.

References

1. Burmester L (1888) Lehrbuch der Kinematik. Arthur Felix Verlag, Leipzig
2. Bottema O, Roth B (1979) Theoretical kinematics. North-Holland Pub. Co., New York
3. McCarthy JM, Soh GS (2011) Geometric design of linkages. Springer, New York
4. Hunt KH (1978) Kinematic geometry of mechanisms. Oxford University Press, New York
5. Modler KH (1972) Beitrag zur theorie der burmesterschen mittelpunktkurve, –teil 1. Maschinenbautechnik 21(3):98–102
6. Al-Widyan K, Angeles J, Cervantes-Sánchez JJ (2002) A numerical robust algorithm to solve the five-pose Burmester problem. In: Proceedings of DETC2002, Montreal, #MECH-34270
7. Angeles J, Bai S (2010) A robust solution of the spherical Burmester problem. In: Proceedings of DETC2010, Montreal, #MECH-28189
8. Bai S, Angeles J (2012) A robust solution of the spatial Burmester problem. ASME J Mech Robot 4(3):031003.1–031003.10
9. Soh GS, McCarthy JM (2008) The synthesis of six-bar linkages as constrained planar 3R chains. Mech Mach Theory 43(2):160–170
10. Shiakolas PS, Koladiya D, Kebrle J (2005) On the optimum synthesis of six-bar linkages using differential evolution and the geometric centroid of precision positions technique. Mech Mach Theory 40(3):319–335
11. Todorov TS (1997) Synthesis of Watt’s six-link mechanism for manipulation action in relative space. Mech Mach Theory 32(5):559–568

Mathematical Modelling and Simulation for Beaded Pad Automatic Weaving Trajectory

Jianye Yan, Ligang Yao, Dongliang Lin and Zhijun Liu

Abstract Beaded pads utilized as cooling mat and handicraft are popular. Nowadays, all the beaded pads are hand-woven. This paper proposes a beaded pad automatic weaving method to solve the hand-woven problems of inefficiency, poor consistency and higher cost. The single-line direct-threading automatic weaving method is proposed on the basis of the investigation of the hand-woven process. Further, the beaded pad automatic weaving trajectory mathematical modelling and simulation for the proposed single-line direct-threading weaving method is presented.

Keywords Beaded pad · Motion trajectory · Upward-string · Downward-string

1 Introduction

The beaded pad shown in Fig. 1 is a cushion which connects the beads in turn vertically or horizontally. The pad unit consists of four beads (0–3) and a single-line. The constraints between the beads and the single-line make the beaded pad's structure tight and stable. The pad can keep the seat clean and cool in summer.

Although this kind of the beaded pad favored by the majority of consumers, the pad sold in the market is hand-woven so far. There are still no automatic weaving machines for weaving this kind beaded pad, and even the corresponding weaving trajectory analysis and simulation. There are other kinds pads which are woven with a tool [1–3] based on the wrap/weft weaving method, unfortunately these pads have compact integral structure and poor air permeability. Another kind of pads are made by using lockstitch weaving method [4–6] under the lockstitch machine's stitch and their structures are instability and easy to damage because of the knot in

J. Yan (✉) · L. Yao · D. Lin · Z. Liu

School of Mechanical Engineering and Automation, Fuzhou University, Fuzhou, China
e-mail: yanjianye0728@163.com

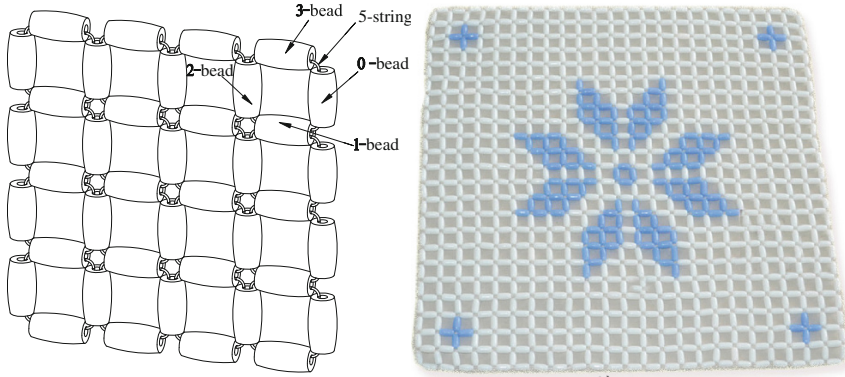


Fig. 1 3-D model and physical map of the beaded pad

the cord inside the bead hole. The proposed mongline right angle loop [7] and right angle weaving method [8–10] are merely applicable to hand-woven, due to too many turns of the needle weaving.

2 Single-Line Direct-Threading Automatic Weaving Method

Currently, the beaded pad is woven with method of single-line by hand, which is tedious and inefficient. The human weaving process, shown in Fig. 2, is carried out by stringing four beads (0–3) at the two ends of the single-line and then piercing one string ends through bead 3 to get a four-beads unit. The other units could be weaved in the same way. The two ends of the single string are defined as the

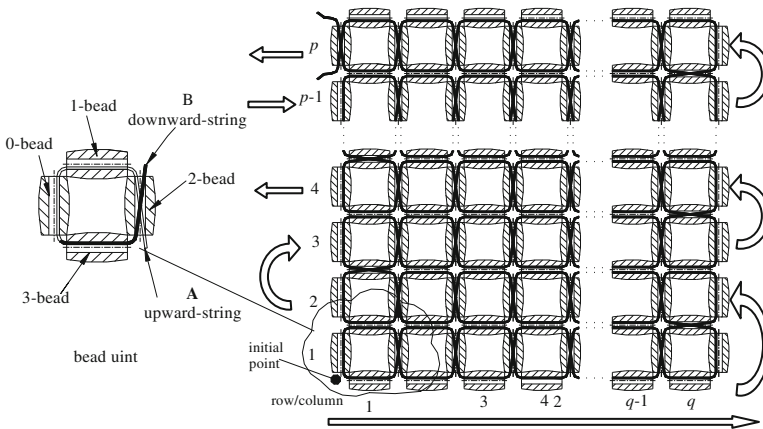


Fig. 2 Beaded pad weaving process

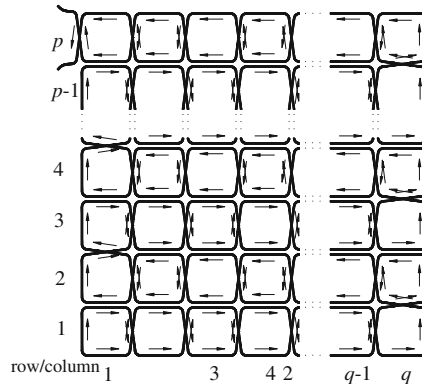


Fig. 3 String g's motion trajectory

downward-string and upward-string [11]. So the weaving trajectory is the movement routes for upward-string and downward-string. The string end whose first step moves upwards/rightwards is defined as upward-string A/downward-string B. A list of pad units connected by a string in the horizontal and vertical direction is called the row and column. The unit numbers in Fig. 2 are termed as row and column respectively. Therefore, the pad is denoted as $LD_{p \times q}$.

According to above mentioned weaving method, the trajectory of the upward-string and downward-string for the $LD_{p \times q}$ pad can be illustrated in Fig. 3 without displaying the beads. The arrows show upward-string and downward-string's movement direction in the process of weaving and the string initial point is located in the lower left corner.

On the basis of the human weaving method and weaving trajectory, the single-line direct-threading automatic weaving method [12] is proposed and shown in Fig. 4. It simplifies the hand-weaving process and avoids the two ends of the string's alternate threading motion. It's easy to be implemented on the machine. The automatic weaving process can be described in the follows. First, thread all needed beads on the upward-string, at this position the upward-string is in a state of straight line. Then, thread a bead on the downward-string B and pierce the downward-string B through the second bead's hole to form a bead unit. The machine can weave single-row pad by repeating the process for downward-string B. The upward-string needs to pierce the bead to complete the weaving process when

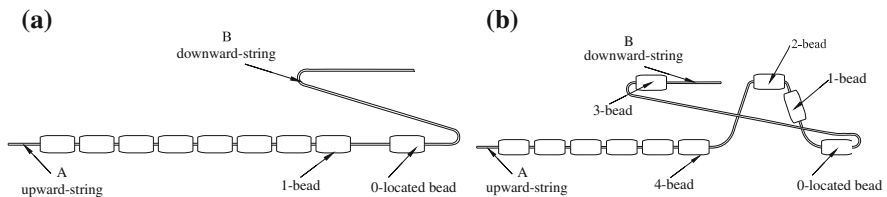
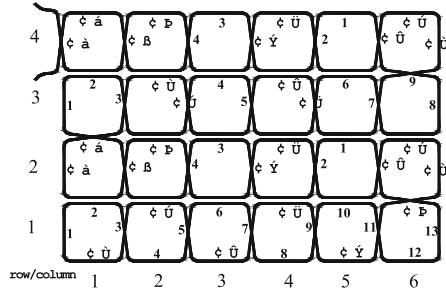


Fig. 4 The weaving process of single-line direct-threading weaving method

Fig. 5 Numbering the beads



it weaves the second-row according to Fig. 2. It has the similar threading movement between the upward-string and downward-string. As long as it controls the woven-bead number, the threading trajectory and when the string passing through the bead, the beaded pad weaved with the above method achieves the same goals that weaved with the method of single-line by hand.

Based on the above weaving method, the number of beads which are pierced on the upward-string is $2q + 1$. While weaving the first row, it needs to thread an additional bead on the downward-string by controlling its movement in weaving a bead unit, so the number of beads pierced on the downward-string is q . The upward-string and downward-string, with the constraints of the first row unit, need to pierce the beads alternately and accomplish the same threading movement, when the machine weaves the next row unit. According to the method and the law of upward-string and downward-string’s movement route, the upward-string strings a bead and the downward-string strings another bead. Then the upward-string and downward-string pierce the common bead so as to complete a bead unit. The process of numbering the beads for the beaded pad is shown in Fig. 5. The number of the beads which are on the upward-string and downward-string is shown in Fig. 5. It presents the situation where the row p is 4 and the column q is 6.

3 Mathematical Modeling for the Weaving Trajectory

In order to describe the threading process, it needs to analyze the law of string’s movement route. The paper respectively extracts the motion trajectory of upward-string and downward-string in Fig. 6.

It is obvious that the motion trajectories of string in the odd/even row are the same, shown in Fig. 6. That is, weaving trajectory has a period in two rows. The string has the same movement direction every four steps (one arrow stands for one step) in every row, except the last column of the odd row for the downward-string. Therefore, it considers that the string’s period of motion is four steps every rows, every four steps has a fixed cycle. So, the downward-string’s motion trajectory has a periodical characteristic. It only needs to describe one period of the motion as describe the threading process. Similarly, the downward-string’s motion trajectory has the same law.

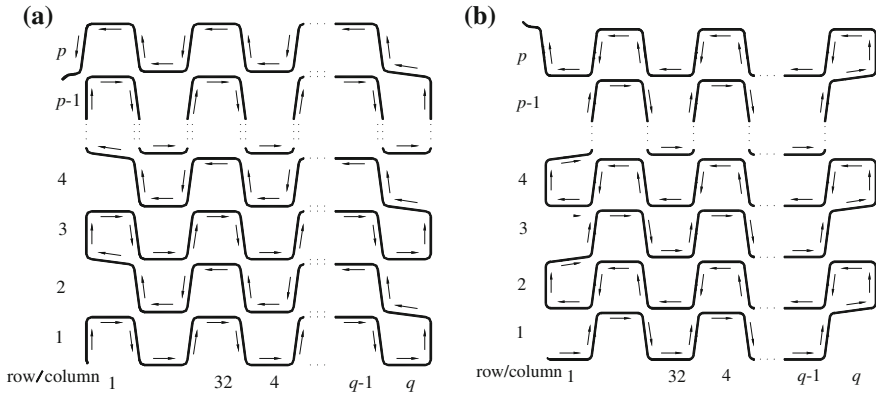


Fig. 6 a Upward-string's motion trajectory. b Downward-string's motion trajectory

In order to describe the law of motion path of upward-string and downward-string with mathematical method, it needs to simplify the trajectory of string. The string's terminal must be linear motion and pierce through the centre axis of the beads hole, regardless of the position of the string, and the steering angle must be rectangular. The steps of upward-string make the following stipulations: number the steps form 1 in each row, count from left to right (right to left) for the odd (even) row, and start to count form the first horizontal direction of each row. The number of steps in each row is $2q$ after processing. Because the downward-string's motion trajectory has the same law as the upward-string's, this paper only gives the mathematic expression of downward-string.

After simplification, the motion trajectory of i and $i + 1$ row for the downward-string is shown in Fig. 7. where i and $i + 1$ are odd, the solid line and double dash dot line represent i and $i + 1$ row of the downward-string respectively, the number beside the arrow is step number n_1 . The relation between step and column number can be deduced from the picture.

The coordinate system is established in Fig. 8. Where the origin of coordinates is the initial point of the first step of the first row in the downward-string and i is odd. The end of each step is the starting point of the next step in the figure and the movement of step can be obtained according to the coordinates of the end of each

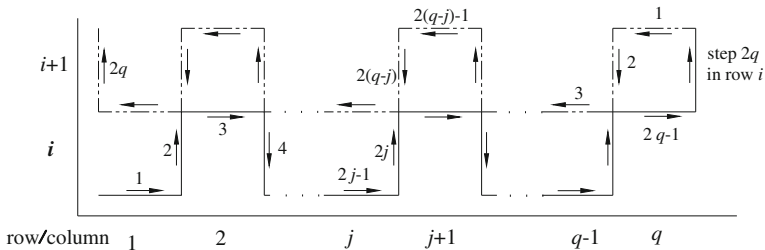


Fig. 7 Relations among motion trajectory, step and row/column number

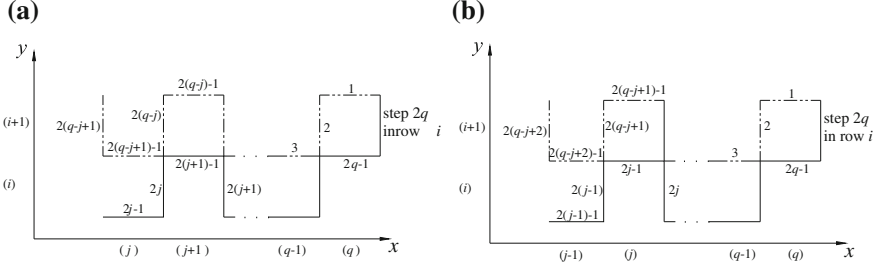


Fig. 8 Coordinate representation for the downward-string's motion trajectory **a** column j is odd, **b** column j is even

step. The mathematical expressions of destination coordinates of downward-string can be obtained, if the step-length L (L is the bead length), the step number n_1 , row i and column j is given.

The destination coordinates (x, y) of each step at odd rows i of downward-string.

$$\text{For } n_1 = 2j - 1, \begin{cases} x = j \times L \\ y = (i - 1) \times L \end{cases} \quad (1)$$

$$\text{For } n_1 = 2j, \begin{cases} x = j \times L \\ y = i \times L \end{cases} \quad (2)$$

Where j is odd column, as shown in Fig. 8a.

$$\text{For } n_1 = 2j - 1, \begin{cases} x = j \times L \\ y = i \times L \end{cases} \quad (3)$$

$$\text{For } n_1 = 2j, \begin{cases} (1) \text{ if } j < p, \begin{cases} x = j \times L \\ y = (i + 1) \times L \end{cases} \\ (2) \text{ if } j = p, \begin{cases} x = j \times L \\ y = (i + 1) \times L \end{cases} \end{cases} \quad (4)$$

Where j is even column, as shown in Fig. 8b.

The destination coordinates (x, y) of each step at even rows $i + 1$ for downward-string and each step for upward-string can be obtained with the same method.

4 Simulations of the Weaving Trajectory

The program flow diagram of string's motion trajectory can be obtained according to the relations among string's motion trajectory, step and row and column number. Define the basic parameters as below: $p = 6$ and $q = 6$, which is given a beaded pad of $LD_{6 \times 6}$, and set the step length $L = 10$. The motion trajectories of upward-

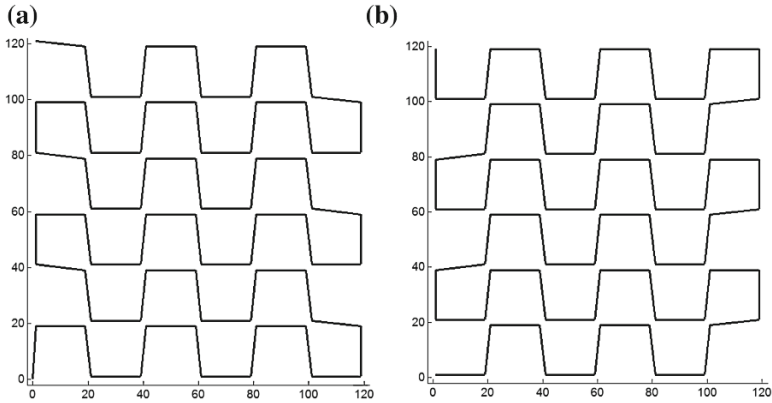


Fig. 9 Simulation result of the motion trajectory **a** uplink's motion trajectory, **b** downlink's motion trajectory

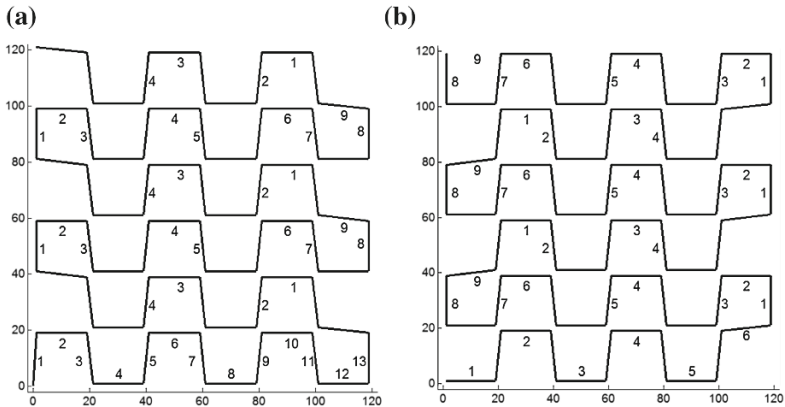


Fig. 10 Numbers of the bead pad **a** numbers for uplink **b** numbers for downlink

string and downward-string in weaving process are solved by computer using the program. The result is shown in Fig. 9. The process of numbering the beads of the beaded pad can be simulated, and the result is shown in Fig. 10. The number of each bead shown in Fig. 10 is one-to-one correspondence to the number shown in Fig. 5.

The motion trajectory shown in Fig. 9 is the simulation result of upward-string and downward-string motion trajectory of beaded pad weaving process shown in Fig. 6. The movement direction of the string can reference Fig. 6, and the initial point is located in the lower left corner.

5 Conclusions

This paper proposed a single-line direct-threading automatic weaving method for beaded pads and classified the motion as the synthesis of upward-string and downward-string. The weaving trajectory has the same period in two rows except the last column of the odd row for the downward-string. The proposed mathematical modelling and simulation methods can illustrate the automatic weaving trajectory directly and correctly.

Acknowledgments The authors wish to thank Natural Science Foundation of China (Grant No. 51275092) for funding the researches.

References

1. Hirai Y (2008) Woven bead fabric and weaving method. Japan patent, JP2008007866A
2. D'Estais M, Cairon O (2004) Bead-weaving system. U.S. patent, US20040069363A1
3. Ogura H (1996) Bead-weaving machine with curved needle. Japan patent, JPH0860490A
4. Zhu T (2001) Bead-braided product and its braiding method. China patent, CN1309032A
5. Zhu T (2001) Device for weaving beads with holes. China patent, CN2458173Y
6. Zhu T (2003) Eye-hole pearl stuff and weaving method. China patent, CN1412011A
7. Gao J (2008) Plane bead weaving handicraft. China patent, CN201172353Y
8. Prussing C (2004) Beading with right angle weave. Interweave Press, UK
9. Fisher GL, Mellor B (2012) Using tiling theory to generate angle weaves with beads. *J Math Arts* 6(4):141–158
10. http://www.skunkhillstudio.com/projects/right_angle_weave/right_angle_weave.shtml
11. Yao L et al (2011) Method for describing upward-string and downward-string weaving movement rule of bead cool cushion. China patent, CN102206893A
12. Yao L et al (2012) Single-line direct-threading weaving method of bead stringed cooling mat. China patent, CN102587029A

Graphical User Interface for the Singularity Analysis of Lower-Mobility Parallel Manipulators

Stéphane Caro, Latifah Nurahmi and Philippe Wenger

Abstract In this paper, a new graphical user interface is developed for the singularity analysis of lower-mobility parallel manipulators. The algorithm used for this tool is based upon the Grassmann-Cayley Algebra in addition to the concept of wrench graph to provide a simplified expression of the superbracket decomposition. Then, using the appropriate geometric incidences, the superbracket expression will be transformed into a geometric statement characterizing the singularity conditions of the manipulators. In this graphical user interface, useful options are introduced to better guide the user in the formulation of the superbracket and the interpretation of the singularities.

Keywords Singularity · Parallel manipulators · Grassmann-Cayley algebra · Graphical-user interface

1 Introduction

A graphical user interface called *SINGULAB* was developed by Ben-Horin et al. in [2] as an automatic tool for the singularity analysis, geometric interpretation and visualization of singularities of some classes of parallel robots. This interface is based on Grassmann-Cayley Algebra (GCA) and can be used to analyse 6-degree-of-freedom (*dof*) Parallel Manipulators (PMs) and more precisely Gough-Stewart Platforms (GSPs). Nevertheless, this interface cannot be used to analyse the singularities of lower-mobility PMs for the following reasons:

S. Caro (✉) · L. Nurahmi · P. Wenger
CNRS, Institut de Recherche en Communications et Cybernétique de Nantes, Nantes, France
e-mail: stephane.caro@irccyn.ec-nantes.fr

L. Nurahmi
e-mail: latifah.nurahmi@irccyn.ec-nantes.fr

P. Wenger
e-mail: philippe.wenger@irccyn.ec-nantes.fr

1. SINGULAB does not consider points at infinity in the superbrackets which lets the user simplify and operate manually with monomials and brackets containing points at infinity.
2. For lower-mobility PMs the choice of two points on a Plücker line of the extended Jacobian matrix J_E is not as simple as for GSPs. Indeed, in many cases there are several (more than two) points likely to be selected on a given line of J_E and their choice for the superbracket expression is not straightforward.
3. SINGULAB does not vanish a bracket with three aligned points or with four coplanar distinct points.

As a consequence, we have developed a graphical user interface to analyse a large range of lower-mobility PMs and to help the user well formulate the superbracket and interpret the singularities. This tool considers the points at infinity which were used for the first time in a superbracket by Kanaan et al. in [3], in addition to the concept of wrench graph developed by Amine et al. in [1]. The wrench graph illustrates the wrenches acting on the PMs in the projective space.

2 The 3-Dimensional Projective Space

The 3-dimensional projective space \mathbb{P}^3 is characterized by the affine space \mathbb{R}^3 and the plane at infinity Ω_∞ . In the projective space \mathbb{P}^3 , a finite point is represented by four homogeneous coordinates $a = (a_1, a_2, a_3, 1)^T$, while a finite line is represented by six Plücker coordinates $F = (s; r \times s)$.

Let underline points denote points at infinity. This notation is used in the text, while points at infinity are denoted with capital letters in the interface. Any finite line has a unique point at infinity $\underline{c} = (s; 0)$. This point only depends on the line direction \mathbf{s} . Any pair of parallel finite lines along \mathbf{s} intersects at one common point at infinity \underline{c} . All parallel finite planes intersect each other at one common line at infinity, namely, $M = (0_{3 \times 1}; m)$. This line passes through the point at infinity of any finite line orthogonal to \mathbf{m} . Two lines at infinity intersect at a unique point at infinity.

3 Grassmann-Cayley Algebra

The GCA was developed by Herman Grassmann and Arthur Cayley as a calculus for linear varieties. This geometric algebra expresses a synthetic geometric condition by expanding two main operators, namely *join* “ \vee ” and *meet* “ \wedge ” operators and typically provides brackets which are determinants of four homogeneous coordinates. It provides a translation of synthetic geometric conditions into invariant (coordinate-free) algebraic expressions.

The basic elements of GCA are termed *extensors*, which are symbolically denoted by Plücker coordinate vectors. The extensors are vectors that represent

geometric entities without making reference to any coordinate system. they are characterized by their *Step* 1, 2, and 3 that correspond to point, line and plane respectively.

3.1 Superbracket Decomposition

The rows of the extended Jacobian matrix \mathbf{J}_E (\mathbf{J}_E was further explained in [1]) are composed of six wrenches corresponding to six Plücker vectors. Those six wrenches are either actuation wrenches or constraint wrenches. The determinant of \mathbf{J}_E corresponds to the superjoin of the six associated Plücker vectors, named superbracket. Consequently, a singularity occurs when the superbracket is equal to zero, namely, the six Plücker vectors are dependent.

The superbracket is an expression involving 12 points selected on the governing lines and can be developed into a linear combination of 24 bracket monomials, each bracket monomial being the product of three brackets of four projective points:

$$S = [ab,cd,ef,gh,ij,kl] = \sum_{i=1}^{24} y_i \quad (1)$$

y_i is the bracket monomial and it is given in [1–3]. Usually the selection of the twelve points must lead to the simplest expression of the superbracket decomposition.

The bracket of four projective points is defined as the determinant of the matrix whose columns are the homogeneous coordinates of these points. This bracket is null if and only if all points are coplanar. Hence, the bracket of any four points at infinity is null. In the same vein, a bracket containing three aligned points is null.

4 A Graphical User Interface for the Singularity Analysis of Lower-Mobility Parallel Manipulators

In what follows, we explain the steps provided in this new graphical user interface, shown Fig. 1.

4.1 Superbracket Expression

To make the difference between points at infinity and finite points in the interface, we use capital letters for points at infinity while lower-case letters stand for finite points.

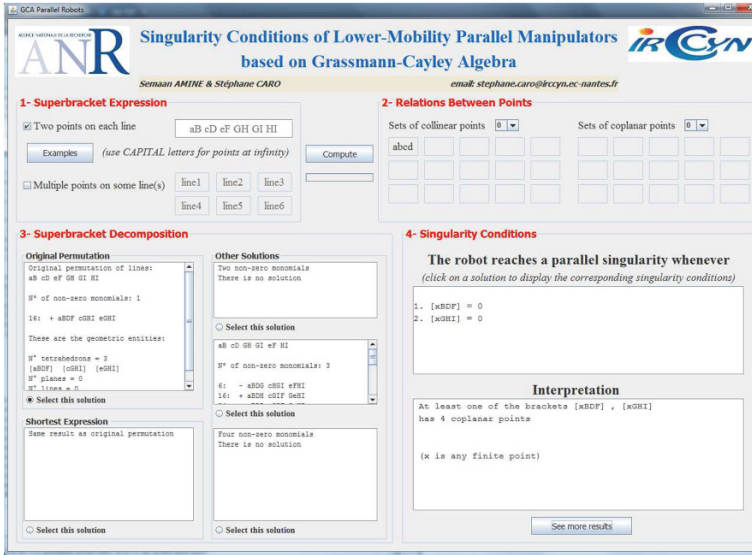


Fig. 1 Graphical user interface for the singularity analysis of the 3-UPU PM

A superbracket expression is formulated with twelve points selected on six Plücker lines corresponding to the governing lines of a given PM. However, for lower-mobility PMs the selection of two points on a constraint or an actuation wrench of a given leg is not trivial. In most cases, more than two points are likely to be selected on a given wrench and the most appropriate choice is not necessarily obvious. Thus, the user has two possibilities to provide information about the six governing lines:

1. To enter two points on each governing line.
2. To enter multiple points on each governing line. This option is useful when there are some geometric relations between points on different governing lines. Thus, when the choice of two points on each line is not trivial, this option can be used to express all possible superbrackets (selections of two points among the possible points on each line) and to return the most convenient expression(s).

4.2 Relations Between Points

The next step before expanding the 24 monomials of the superbracket expression is to provide the interface a set of vanishing rules in order to return uniquely the non-zero monomials.

Accordingly, the first two properties to implement in the superbracket decomposition are:

1. To vanish any monomial in which at least one bracket has two identical points among its four points.
2. To vanish any monomial in which at least one bracket has four capital letters (points at infinity).

To increase the efficiency of the simplification in the superbracket decomposition, we add an option to enter, if necessary, some sets of collinear and/or coplanar points. In that case, these sets will be taken into consideration automatically by the interface when decomposing the superbracket to vanish some additional monomials instead of doing it manually.

4.3 Superbracket Decomposition

An important property to highlight here is that a superbracket decomposition depends on the order of the entered lines in the superbracket. This is due to the expression of the 24 monomials. Let us consider for example the two superbrackets $S_1 = [ab,ac,ef,gh,ij,kl]$ and $S_2 = [ab,ef,ac,gh,ij,kl]$. If we compare the decomposition of these two superbrackets based on the form of Eq. (1), we can easily notice that the number of brackets in the decomposition of S_1 in which point a is repeated is greater than the number obtained with the decomposition of S_2 . Thus, different permutations of the lines of the superbracket may lead to different numbers of non-zero monomials.

On the other hand, it should be noted that the geometric interpretation of the singularity condition depends on the permutation of the six superbracket lines, i.e., a different permutation of the same six lines may lead to another geometric incidence and thus, to other geometric interpretations of singularities. Moreover, some permutations do not lead to a geometric interpretation. Thus, the superbracket decomposition in the interface provides three options to the user:

1. Original permutation: this option expresses the non-zero monomials corresponding to the original permutation of lines, namely, to the order of lines as they were entered in step 1. In case multiple points are entered on the six lines, the original permutation takes the first entered two points on each line.
2. Shortest expression: this option will decompose the superbrackets obtained from all the possible permutations of the six lines and will return a permutation providing the minimum number of non-zero monomials and expand these monomials. In case multiple points are selected on the six lines, this option will first make all the possible choices of two points on each line and then develop all possible permutations for each choice to return finally one of the permutations that provides the minimum number of non-zero monomials and expand these monomials.
3. Other solutions: this option operates similarly to the previous one to provide, if any, a permutation with 2, 3 or 4 non-zero monomials.

4.4 Interchangeable Points and Geometric Entities

The next step is to explore the obtained superbracket decomposition, consisting of non-zero monomials, in order to find automatically the geometric entities involved in the singularity condition. These entities can be lines, planes or tetrahedra.

First, we assume that if a point appears more than once in each monomial, then each appearance will belong to a different geometric entity. Each monomial has three brackets, each bracket containing four points, thus 12 points are part of geometric entities that have to be identified. From the definition of the *meet* operator, to obtain a monomial of brackets of four points, the involved geometric entities may be 2- or 3-extensors (lines or planes). Otherwise, a meet including a 4-extensor (tetrahedron) and another entity would lead to a bracket containing five points. Moreover, a monomial composed of brackets of four points may result from a bracket containing a tetrahedron and two other brackets resulting from a meet of lines and planes. Accordingly, when the main entities that we are looking for are lines, planes and tetrahedra, the following groups can be found:

1. three tetrahedra;
2. two tetrahedra and two lines;
3. one tetrahedron and four lines;
4. one tetrahedron, two planes and one line;
5. four planes;
6. two planes and three lines;
7. six lines.

The searching procedure for the geometric entities was detailed in [2]. It is applied in our interface to highlight the geometric entities involved in the geometric singularity conditions. However, not all of the seven groups enumerated above can be associated with a geometric interpretation of the singularities. This will depend on the geometric incidence that can be identified in each case. Therefore, the interface provides many possible solutions to the user so that they can select the (one of the) solution(s) that provide(s) geometric interpretation(s) of the singularities.

For instance, some geometric entities are explained as follows:

1. Three tetrahedra. In such a case, the superbracket decomposition takes the form: $S = [abcd][efgh][ijkl]$ and the corresponding singularity condition is that at least one of the three tetrahedra (brackets) vanishes, i.e., consists of four coplanar points.
2. One tetrahedron, two planes and one line. In such a case, the superbracket decomposition takes the form: $S = [abcd]([efg\overset{\cdot}{h}][\overset{\cdot}{i}jkl])$ and the singularity conditions are:
 - (a) Points a, b, c and d are coplanar.
 - (b) Line hi intersects with the intersection line of planes efg and jkl.

3. Four planes. In such a case, the superbracket decomposition takes the form:

$S = [abc \overset{\cdot}{d}][efg \overset{\cdot}{h}][\overset{\cdot}{i} jkl]$ and the singularity condition is that the four planes abc , efg , $ijkl$ and dhi intersect at least at one common point.

4. Two planes and three lines. For example let us consider the superbracket decomposition

$$S = [abdi][akle][jfeh] - [abdj][akle][ifeh] - [abdk][aije][lfeh] + [abd1][aije][kfeh] \quad (2)$$

The geometric entities are two planes: abd and feh and three lines: ak , le and ij . To highlight the singularity conditions corresponding to this case, let us rewrite it as follows:

$$S = [akle]([abd \overset{\cdot}{i}][\overset{\cdot}{j} feh]) - [aije]([abd \overset{\cdot}{k}][\overset{\cdot}{l} feh]) \quad (3)$$

From [1], we know that:

$$\begin{aligned} ([abd \overset{\cdot}{i}][\overset{\cdot}{j} feh]) &= abd \wedge feh \wedge ij \\ \text{and} \\ ([abd \overset{\cdot}{k}][\overset{\cdot}{l} feh]) &= abd \wedge feh \wedge kl \end{aligned}$$

Now if we let mn be the intersection line of planes abd and feh , then:

$$\begin{aligned} abd \wedge feh \wedge ij &= [mni j] \\ \text{and} \\ abd \wedge feh \wedge kl &= [mnkl] \end{aligned}$$

Finally, the superbracket S of Eqs. (2) and (3) becomes:

$$S = [akle][mni j] - [aije][mnkl] \quad (4)$$

Thus, the singularity condition corresponding to this group of geometric entities, namely, two planes abd and feh and three lines ak , le and ij , is that the product of the volume of two tetrahedra $[akle]$ and $[mni j]$ is equal to the product of the volume of two tetrahedra $[aije]$ and $[mnkl]$ where mn is the intersection line of planes abd and feh .

An alternative notation for sum over shuffles is *dotted* notation. The dots are simply placed over the shuffled vectors, with the summation and sign implicit, as explained in [4].

4.5 Singularity Conditions

The last stage in the interface is to enumerate the singularity conditions of the PMs under study. Since several solutions are provided by the interface, the user can select the solution, in which he/she wants to visualize the geometric interpretation, namely, the original permutation, the shortest expression, a superbracket with two (respectively with three, or with four) non-zero monomials. It is noteworthy that the properties related to points at infinity are considered in the results provided by the interface.

An additional option is provided with the button “*see more results*”. Accordingly, by pressing on this button, another window is opened, which enumerates all the superbracket permutations providing $n \leq 4$ non-zero monomials as well as the geometric singularity condition, if there is any, associated with each permutation. Moreover, a “*hints*” button is also introduced in this window to indicate, when the interface cannot find a geometrical interpretation, some useful substitutions that can be made manually in order to obtain further simplifications of the superbracket decomposition.

5 Applications

In this section, the proposed graphical user interface is used to analyse the singularity conditions of the 3-UPU PM, shown in Fig. 2. The 3-UPU PM is a 3-*dof* PM proposed by Tsai [5] and is composed of three identical UPU legs. Each leg consists of one universal joint attached to the base, one actuated prismatic joint and one universal joint attached to the moving platform. Each leg applies one constraint

Fig. 2 The 3-UPU PM

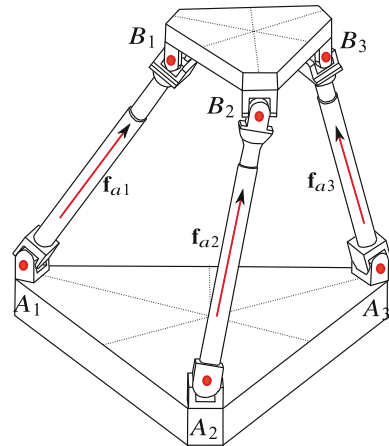
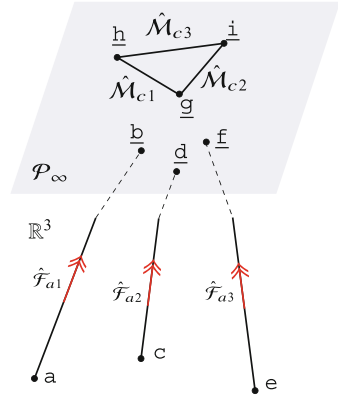


Fig. 3 Wrench graph of 3-UPU



moment perpendicular to the axes of both universal joints and one actuation force that intersects points A_i and B_i ($i = 1, 2, 3$).

In a non-singular configuration, the constraint wrench system of such a PM is spanned by three moments. Let n_i be direction perpendicular to the axes of both universal joints in each leg, thus $\hat{M}_{ci} = (0_{3 \times 1}, n_i)$ be such three moments. We may formulate $\hat{M}_{c1} = \underline{g}\underline{h}$, $\hat{M}_{c2} = \underline{g}\underline{i}$ and $\hat{M}_{c3} = \underline{h}\underline{i}$. In turn, the actuation wrench system of such a PM is give by $\hat{F}_{ai} = (f_{ai}, r_{Bi} \times f_{ai})$. f_{ai} is unit vector along the leg i and r_{Bi} is a position vector of point B_i . These forces can be expressed as: $\hat{F}_{a1} = \underline{a}\underline{b}$, $\hat{F}_{a2} = \underline{c}\underline{d}$ and $\hat{F}_{a3} = \underline{e}\underline{f}$. The wrench graph of the 3-UPU PM is shown in Fig. 3 as studied in [3]. The extended Jacobian matrix \mathbf{J}_E of this manipulator is expressed as: $J_E = [\hat{F}_{a1}, \hat{F}_{a2}, \hat{F}_{a3}, \hat{M}_{c1}, \hat{M}_{c2}, \hat{M}_{c3}]$.

From the expression of the extended Jacobian matrix, the superbracket expression can be formulated as $S = [\underline{a}\underline{b}, \underline{c}\underline{d}, \underline{e}\underline{f}, \underline{g}\underline{h}, \underline{g}\underline{i}, \underline{h}\underline{i}]$. This expression is entered into the proposed graphical user interface as an input. The results are shown in Fig. 1 in which the singularities fall into two main cases: $[\underline{g}\underline{h}\underline{i}] = 0$ and $[\underline{b}\underline{d}\underline{f}] = 0$. The first condition corresponds to the constraint singularities when the limbs lose their ability to constraint the motion. Whereas the second condition corresponds to the actuation singularities when the limbs of the manipulator cannot control the translational motion of the moving platform.

6 Conclusions

A new graphical user interface was introduced in this paper that allows the user to analyse automatically the singularities of the lower-mobility PMs. This interface was developed based upon the GCA in addition to the wrench graph. The rules for the formulation of the superbracket of a lower-mobility PM were introduced. Then, some rules for the simplification of the superbracket decomposition and some

bracket properties related to the existence of points at infinity were presented. Furthermore, this interface applies the rules of simplification of the superbracket decomposition and provides geometric conditions for the parallel singularities of the PM under study.

References

1. Amine S, Caro S, Wenger P, Kanaan D (2012) Singularity analysis of the H4 robot using Grassmann-Cayley Algebra. *Robotica* 30(7):1109–1118
2. Ben-horin P, Shoham M, Caro S, Chablat D, Wenger P (2008) SINGULAB-graphical user interface for the singularity analysis of parallel robots based on Grassmann-Cayley Algebra. In: (ed) *Advances in robot kinematics: analysis and design*, Springer, Netherlands, pp 49–58
3. Kanaan D, Wenger P, Caro S, Chablat D (2009) Singularity analysis of lower-mobility parallel manipulators using Grassmann-Cayley algebra. *IEEE Trans Robot* 25:995–1004
4. White NL (1991) Multilinear Cayley factorization. *J Symbolic Comput* 11:421–438
5. Tsai LW (1996) Kinematics of a three-DOF platform with three extensible limbs. In: Lenarcic J, Parenti-Castelli V (eds) *Recent advances in robot kinematics*, pp 401–410

On the Redundancy of Cable-Driven Parallel Robots

J.-P. Merlet

Abstract This paper addresses the concept of redundancy for cable-driven parallel robot (CDPR). We show that although CDPR may be considered as kinematically redundant, they constitute a special class for which the self-motion manifold is 0-dimensional and that they are not statically redundant (i.e. the tension distribution cannot be changed continuously while keeping the platform at a given pose). A direct consequence is that a CDPR with more than 6 cables is always in a configuration where at most 6 cables are simultaneously under tension. However for a given pose there may be several set of 6 cables that are valid, which allow us to define the concept of *weak statical redundancy*. We show how the possible valid configuration(s) may be determined on a trajectory. All these concepts are illustrated on a real robot.

Keywords Cable-driven parallel robots · Kinematics · Redundancy

1 Introduction

Cable-driven parallel robot (CDPR) have the mechanical structure of the Gough platform with *UPS* rigid legs except that the *UPS* rigid structure is substituted by a cable whose length may be controlled. In practice we may assume that the output of the coiling system for cable i is a single point A_i while the cable is connected at point B_i on the platform (Fig. 1). The flexibility of the cable at A_i , B_i allows to consider that we have a U and S joint at these points. We denote by d_i the distance $\|A_i B_i\|$ and by l_i the length of the cable between the coiling system and B_i . The length l_i may be written as $l_i = a_i + \rho_i$ where a_i is a constant length corresponding to the amount of cable between the coiling system and A_i and ρ_i is the cable length between A_i , B_i . In this paper we will assume that the weight of the cable is neg-

J.-P. Merlet (✉)
INRIA Sophia-Antipolis, Sophia Antipolis Cedex, France
e-mail: Jean-Pierre.Merlet@inria.fr

ligible so that there is no sagging. If cable i is under tension, then it exerts a force \mathbf{f}_i on the platform such that

$$\mathbf{f}_i = -\frac{\mathbf{A}_i \mathbf{B}_i}{\rho_i} \tau_i \quad (1)$$

where τ_i is the positive tension in the cable. As a cable cannot exert a pushing force, if the cable is not under tension then \mathbf{f}_i is 0. Consider a CDPR with n cables and let τ denotes the set of f_i which are not 0 while \mathcal{F} will be the external wrench applied on the platform with the torques applied around a point C . The mechanical equilibrium imposes

$$\mathcal{F} = \mathbf{J}^{-\mathbf{T}}(\mathbf{X})\tau \quad (2)$$

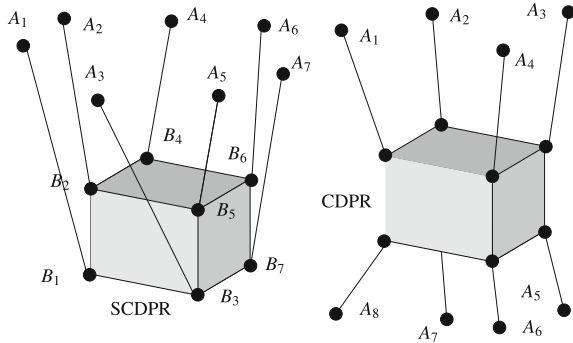
where $\mathbf{J}^{-\mathbf{T}}$ is the transpose of the inverse kinematic jacobian matrix of the robot whose j -th column is $((\mathbf{A}_j \mathbf{B}_j / \rho_j \mathbf{C} \mathbf{B}_j \times \mathbf{A}_j \mathbf{B}_j / \rho_j))$. This matrix is dependent upon the pose \mathbf{X} of the platform. A CDPR will be called *pure force submitted* (PFS) if the wrench \mathcal{F} at its center of mass G is reduced to a force while the torque components are 0. A pose will be called *suspended* if

1. the robot is PFS and the platform is only submitted to a force g composed of the gravity force and of small non vertical disturbances
2. at this pose we have $\mathbf{g} \cdot \mathbf{A}_i \mathbf{B}_i > 0$ for all i such that cable i is under tension

A CDPR will be called *suspended* (SCDPR) if all poses of its workspace are suspended. Hence the cables of a SCDPR cannot exert a downward force and the mechanical equilibrium of the robot relies on the gravity force.

A CDPR with a platform having m dof is also called *fully constrained* if all the dof can be controlled. A well known result is that a fully constrained robot must have at least $m + 1$ cables, except in the case of a SCDPR where only m are required. However a strong argument for designing CDPR with more than the strict minimum of cables (and hence usually called *redundant* CDPR) is that additional cables, if appropriately located, may drastically increase the size of the workspace of the robot. Hence several authors have addressed the problem of calculating the reachable workspace with positive tensions in the cables [1, 4, 5, 7, 11, 13, 15, 16]. Another reason to have more cables is to be able to change the distribution of the cable tensions. Numerous works have addressed the problem of computing an appropriate set of cable tensions, for a given platform pose, see [2, 3, 10, 12, 14] to name a few. In this paper we will consider CDPR with more than 6 cables and examine the notion of redundancy of such a robot.

Fig. 1 Cable driven parallel robots: on the *left* the suspended version



2 Redundancy of CDPR

In this paper we assume that the cables of a CDPR are not elastic (elasticity of the cables induce other difficulties that has been partly addressed in [8]). The concepts of redundancy of parallel robots has been properly addressed recently by Müller [9] but needs to be refined for CDPRs. Let \mathbf{q} be the set of the n joint variables of the robot and let us define the loop closure constraints by $\mathbf{h}(\mathbf{q}) = 0$. Time differentiating this equation leads to $\mathbf{J}(\mathbf{q})\dot{\mathbf{q}} = 0$ where \mathbf{J} is the constraint jacobian. The local dof of the robot is defined as $n - \text{rank}(\mathbf{J})$ while the maximal value of this quantity over a given workspace W is referred as the *global dof* δ . The robot will be denoted *kinematically redundant* if $\delta > \text{Dim}(W)$ while the *degree of kinematic redundancy* is defined as $\delta - \text{Dim}(W)$. The *self-motion* of a kinematically redundant robot is defined as the set of joint variables that may be obtained for a fixed pose of the end-effector. The dimension of this manifold may be equal to the degree of kinematic redundancy (e.g. for a 7R serial robot) but this is not always the case. For example for a 6 dof CDPR with $m > 6$ cables at a given pose the joint variables ρ have fixed values: hence although the degree of kinematic redundancy is $m - 6 > 0$ the self-motion manifold is zero-dimensional. Hence we may refine the concept of kinematics redundancy by asserting that a robot is kinematically redundant iff the dimension of its self-motion manifold is not equal to 0: with that definition **CDPR are not kinematically redundant**.

Now let's look at the actuation scheme and define m as the number of actuated joint variables, under the assumption that the CDPR have at least 7 cables (or 6 for SCDPR). The *degree of redundancy of the actuation* is defined as $m - \delta$ and a parallel robot is called *redundantly actuated* if $m - \delta > 0$. With that definition a CDPR with at least 8 cables (7 for SCDPR) is redundantly actuated. But we have to determine if this redundancy can be used to change the distribution of the tension in the cables while maintaining the pose of the platform: in other words we have to examine if actuation redundancy implies *statical redundancy*.

We must first note that a cable coiling mechanism is a single input- single output system (SISO) which implies that, for example, we may control the length of the

cable or its tension but not both. As for preserving the pose of the platform we have to control the lengths of the cables we consequently cannot change their tensions.

Another point in that direction is to look at the mechanical equilibrium condition (2) which is used as the basic equation for workspace and tension distribution algorithm. There is a constraint for using this equation that is seldom mentioned: they are valid only if $\rho_j = \|\mathbf{A}_j \mathbf{B}_j\|$. Even if we assume that we have an exact measurement of ρ_j managing the distribution of all cable tensions implies that the CDPR controller is able to satisfy the constraint $\rho_j = \|\mathbf{A}_j \mathbf{B}_j\|$ **at any time**. Such an assumption is unrealistic (especially with the discrete time controller that is used) and with the unavoidable uncertainties in the measurements and control. In reality a CDPR at each time will have at most six cables under tension, while the other cables will be such that $\rho_j > \|\mathbf{A}_j \mathbf{B}_j\|$ and consequently are slack. This allows us to claim that **redundantly actuated CDPR are not statically redundant**.

We define the *cable configuration* of a CDPR at a given pose as the set of cable number that are under tension at this pose. A *m cable configuration* is a cable configuration with m cables under tension, the others being slack. We consider CDPR with non elastic cables with $m > 7$ cables ($m > 6$ for SCDPR). In that case the number of cables under tension is at most 6. But for a given pose the number of cables sextuplets such that the cable tension are positive and satisfy the mechanical equilibrium condition (2) may not be unique. If this is the case let us define m_6 as the number of valid cables sextuplets. For each of them we may calculate the cables tensions by solving (2) which is a set of 6 linear equations in the 6 unknown cable tensions. These tensions will differ for each of the m_6 cable configurations. Hence a pose will be called **weakly statically redundant** if $m_6 > 1$: at such a pose we may adjust the cable tension distribution by selecting one of the cable configuration in the set of m_6 cable configurations. In practice this means that the cables that are not part of the selected cable configuration should be made slack by setting their control variable ρ_j to a value that is significantly larger than $\|\mathbf{A}_j \mathbf{B}_j\|$ for this pose. We will illustrate these concepts on an example.

We consider the large scale robot developed by LIRMM and Tecnia as part of the ANR project Cogiro [6] This robot is a SCDPR with 8 cables whose A_i coordinates are given in the following Table 1 will all dimensions in meters.

The platform pose is defined by the coordinates x_g, y_g, z_g of its center of mass in a given reference frame. The orientation is defined by the three Euler's angles ψ, θ, ϕ . We consider a circular trajectory for this robot defined by

$$x_g = \cos(\lambda\pi)y_g = \sin(\lambda\pi)z_g = 2\psi = \theta = \phi = 0$$

where λ is a parameter in the range $[0, 1]$. As mentioned previously although this CDPR has 8 cables only 6 of them at most will be in tension simultaneously. Our purpose is to determine what are the cable configurations that satisfy the constraint (2) on the trajectory. For that purpose we will consider all combinations of 6 cables among the possible 8. It is then relatively easy to determine on which part of the trajectory a given set of 6 cables allows to satisfy the constraints.

Table 1 A_i coordinates

x	y	z	x	y	z
-7.175	-5.244	5.462	-7.316	-5.1	5.47
-7.3	5.2	5.476	-7.161	5.3	5.485
7.182	5.3	5.488	7.323	5.2	5.499
7.3	-5.1	5.489	7.161	-5.27	5.497

Figure 2 shows the result for all the trajectory. The analysis of these curves shows that there is not a single 6 cables configuration that remain valid on all the trajectory. Furthermore at any pose on the trajectory there are at least 3 valid cable configurations and up to 7 configurations. A possible strategy to perform this trajectory while minimizing the number of configuration changes will be to start with $\lambda = 0$ under configuration 345678 until λ reaches the value 0.39239, switch to configuration 123456 at this pose until λ is 0.589, move to configuration 123478 at this point until λ is 0.9043 and then move again to configuration 345678 until $\lambda = 1$.

The circular trajectory has been tested by LIRMM on the robot without taking into account the cable configurations. An analysis of the measured motor torques (which does not exactly reflect the cable tensions but give a rough idea) have shown that indeed the robot switches between 6 cables configurations during its motion at time that are compatible with our calculation.

This trajectory is hence weakly statically redundant and we may use this property to manage the tension distribution. For example for $\lambda = 0$ there are 4 valid cable configurations with $\|\tau\|_\infty$ and $\|\tau\|_2$ for a mass of 1 N: 125678 (0.78425, 1.48345), 145678 (0.81685, 1.51699), 235678 (0.76469, 1.4422), 345678 (0.76623, 1.4639).

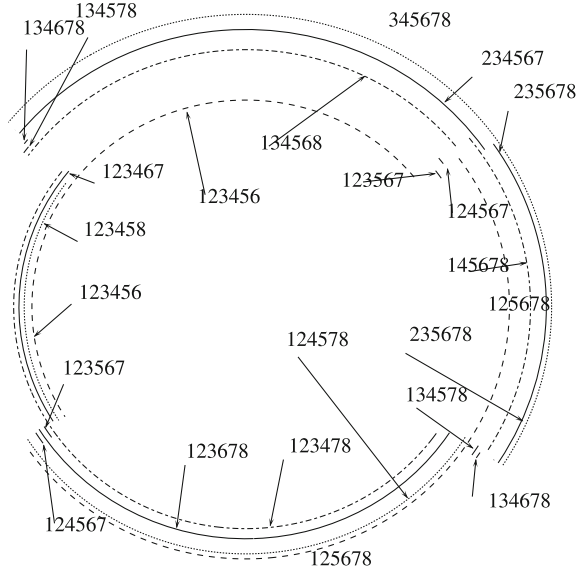
3 Cable Configuration and Uncertainties

Up to now we have examined the cable configuration at a given pose but we have also to consider that the pose is obtained from the uncertain cable lengths measurements. Hence to reach a nominal pose \mathbf{X}_0 we apply as control ρ_0 but the real lengths of the j -th cable lies in the range $[\rho_0^j - \Delta\rho, \rho_0^j + \Delta\rho]$ where $\Delta\rho$ represents the limits of the control and measurement errors. The problem we want to solve may be stated as follows:

Problem: determine all possible valid 6-cables configurations for all values of the ρ 's in their ranges

An assumption is made in our algorithm: the actual pose of the platform is close to \mathbf{X}_0 , i.e. the platform has not moved close to another solution \mathbf{X}_1 of the forward kinematic problem $\rho_0 = \mathbf{f}(\mathbf{X})$. This is a weak assumption as we are able to calculate all the forward kinematics solutions and therefore the full set of valid cable

Fig. 2 The possible cable configuration on the circular trajectory. The *arcs* have been translated to show the valid cable configuration



configurations. We will call *dominant cables* the one under tension in a given cable configuration.

As the ρ 's have interval values we consider solving this problem with interval analysis. Under that assumption the mechanical equilibrium constraints become a interval linear system $\mathcal{F}\Theta = A\tau$ for which there are methods that allows one to determine if this system admits only positive solutions in τ or has at least one of the τ that is always negative or maybe either positive or negative according to the real values of the ρ 's. In the same manner interval analysis allows to determine if for given ranges for the ρ 's constraints such as $\|A_j B_j\| < \rho_j$ is always valid, is always violated or may be valid for some some ρ_j and violated for some others.

For a given cable configuration with n cables under tension the unknowns are the pose parameters, the real values of the ρ of the CDPR with $m \geq 6$ cables and the n tensions. With the minimal representation of a pose we end up with $6 + m + n$ unknowns. If $n = 6$ the constraints we have can be decomposed into three sets

- a system of 6 equations composed of the 6 kinematic equations in the pose parameters and the 6 ρ
- the 6 Eq. (2) that is easily solvable as soon as the pose is known
- a set of $m - 6$ inequalities $\rho_j > \|A_j B_j\|$

Note that all the unknowns may be bounded as we have assumed that the pose remains close to the nominal pose \mathbf{X}_0 so that all solutions shall lie within a set of ranges \mathcal{I}_0 . The interval analysis algorithm we are using is a classical branch and bound algorithm whose principle has been explained in several papers. It basically consider a list \mathcal{L} of possible set of intervals for the unknowns, called a *box*, that is initialized with \mathcal{I}_0 .

For each box in \mathcal{L} we start the algorithm by fixing the pose parameters to the mid-points of their intervals. For this pose we have a unique value for the cable lengths and we check if the lengths of the dominating cables all lie in the ρ ranges and for the non dominating cables k that we have a value ρ_k^l in the ρ_k ranges such that $\rho_k^l > \|\mathbf{A}_k \mathbf{B}_k\|$. If the cable lengths satisfy these properties we then check the positiveness of the τ of the dominating cables by solving the linear system (2). If this is the case the current cable configuration is valid and the algorithm completes.

If this test fails the algorithm checks if at least one of the constraints is always violated, in which case the box is eliminated from \mathcal{L} . If this cannot be asserted the box is bisected (i.e. one unknown is selected and its range is bisected into two ranges) and the 2 boxes resulting from this bisection are placed at the end of \mathcal{L} and the algorithm moves to the next box in \mathcal{L} .

This algorithm is guaranteed to complete because of the bisection process except in 2 cases: there is a singularity around \mathbf{X}_0 or a box is reduced to a single point and the numerical round-off errors do not enable to assert the constraints. In both cases we perform a local analysis that is not described here for lack of space.

We have implemented the algorithm described in the previous section to determine all 6-cables configurations. We use as test an analysis of the possible cable configurations for the pose obtained for $\lambda = 0$ of the circular trajectory for the robot presented in Sect. 2. At this pose if we have no uncertainty on the cable lengths, then we have 4 possible cable configurations: 125678, 145678, 235678, 345678. If we have an uncertainty of ± 3 cm on the ρ measurement the cable configuration 124578 becomes possible. The 5 cable configuration are determined in a computation time of 43 mn. If we extend $\Delta\rho$ to ± 4 cm, then the cable configuration 123678 becomes also possible and it takes about 3 h to determine all cable configurations. For a $\Delta\rho$ of 1 cm the maximal deviation of the platform pose $\|\mathbf{X} - \mathbf{X}_0\|$ is 0.019307+ [0, 0001] meter for the Euclidean distance and the maximal absolute deviation for each components of C are 0.008064, 0.007066, 0.011388 meters with an error in the range [0, 0.0001].

4 Conclusions

This first major contribution of this paper is to clarify the concept of redundancy for CDPR. Having more cables than strictly necessary to control the 6 dof of the platform has a large influence on the robot workspace but the redundancy level is much weaker than is usually believed: the kinematics redundancy and static redundancy manifolds are 0 dimensional (meaning that the cable tensions cannot be continuously controlled). Hence it is unclear if a cable tension control scheme will really improve the tensions distribution while certainly will leads to poor positioning accuracy. On the other hand position and velocity control are much less sensitive to parameters errors, which explain the surprisingly good performances of CDPR prototypes. Note that the concept of cable configurations with 6 cables under

tension while the other one are slack has been observed experimentally on a 8 cables CDPR.

The performances of CDPR may possibly be improved by using a cable configuration planning algorithm that will

- select the best set of 6 dominating cables among the possible cable configurations. For example the best set may be the one leading to the lowest positioning errors for given bound of the ρ measurement errors or the one satisfying an optimality criterion for the cable tensions
- deliberately let the non dominating cables become slack.

This strategy of voluntary letting cables become slack is clearly counter-intuitive and has to be confirmed experimentally but may be the best one for CDPR.

To conclude we have examined cable configuration having 6 dominant cables at a given pose but we have already extended the cable configuration research to less than 6 dominant cables and to a trajectory. This result will be presented in another paper.

This research has received partial funding from the European Community's Seventh Framework Program under grant agreement NMP2-SL-2011-285404 (CABLEBOT).

References

1. Aref M, Taghirad H (2008) Geometrical workspace analysis of a cable-driven redundant parallel manipulator: KNTU CDRPM. In: IEEE International Conference on Intelligent Robots and Systems (IROS). Nice, France, pp 1958–1963, 22–26 Sept 2008
2. Bedoustani Y, Taghirad H (2010) Iterative-analytic redundancy resolution scheme for a cable-driven redundant parallel manipulator. In: IEEE/ASME international conference on advanced intelligent mechatronics. Montréal, 6–9 July 2010
3. Bruckman T et al (2008) Parallel manipulators, new developments, chap. Wire robot part I, kinematics, analysis and design. ITECH, pp 109–132, Apr 2008
4. Diao X, Ma O (2008) Workspace determination of general 6-dof cable manipulators. *Adv Robot* 22(2–3):261–278
5. Gouttefarde M, Daney D, Merlet JP (2011) Interval-analysis based determination of the wrench-feasible workspace of parallel cable-driven robots. *IEEE Trans Robot* 27(1):1–13, Feb 2011. URL <http://hal.inria.fr/lirmm-00573491/en>
6. Gouttefarde M et al (2012) Simplified static analysis of large-dimension parallel cable-driven robots. In: IEEE international conference on robotics and automation. Saint Paul, pp 2299–2305, 14–18 May 2012)
7. Lim W et al (2011) A generic force closure algorithm for cable-driven parallel manipulators. *Mech Mach Theory* 46(9):1265–1275
8. Merlet JP Managing the redundancy of N-1 wire-driven parallel robots. In: ARK. Innsbruck, pp 405–412, 25–28 June 2012. URL <http://www-sop.inria.fr/coprin/PDF/ark2012.pdf>
9. Müller A (2013) On the terminology and geometric aspects of redundant parallel manipulators. *Robotica* 31(1):137–147
10. Pott A, Bruckmann T, Mikelsons L (2009) Closed-form force distribution for parallel wire robots. In: Computational kinematics. Duisburg, pp 25–34, 6–8 May 2009

11. Riechel A, Ebert-Uphoff I (2004) Force-feasible workspace analysis for underconstrained point-mass cable robots. In: IEEE international conference on robotics and automation. New Orleans, pp 4956–4962, 28–30 Apr 2004
12. Roberts R, Graham T, Lippit T (1998) On the inverse kinematics, statics and fault tolerance of cable-suspended robots. *J Robot Syst* 15(10):581–597
13. Stump E, Kumar V (2006) Workspaces of cable-actuated parallel manipulators. *ASME J Mech Design* 128(1):159–167
14. Taghirad H, Bedoustani Y (2011) An analytic-iterative redundancy resolution scheme for cable-driven redundant parallel manipulator. *IEEE Trans Robot* 27(6):670–676
15. Tavolieri C, Ceccarelli M, Merlet JP (2008) A workspace analysis of a fully constrained cable-based parallel manipulator by using interval analysis. In: Musme. San Juan, Argentina, 8–12 Apr 2008
16. Verhoeven R (2004) Analysis of the workspace of tendon-based Stewart platforms. PhD thesis, University of Duisburg-Essen, Duisburg

Part II
Computational Kinematics

On the Resolution of Forward Kinematic Problem Using CAD Graphical Techniques: Application on Planar Parallel Robotic Manipulators

K.A. Arrouk, B.C. Bouzgarrou and G. Gogu

Abstract The existence of singularity-free trajectories joining different assembly modes of a parallel robotic manipulator is a crucial property that permits to have a large effective workspace. The investigation of such a characteristic requires considering the forward kinematics problem. In this paper, an original method for forward kinematics resolution and singularity-free trajectory planning between different assembly modes is presented. The proposed method is based on a pure geometric approach and exploits the CAD environments utilities for geometric entity manipulations such as Boolean operations. The developments presented herein are mainly performed on 3-RPR planar parallel robot (PPR) and can be extended to several 3-DOF PPRs providing some adaptations.

Keywords Forward kinematic problem (FKP) · Computer-aided design (CAD) techniques · Planar parallel robot (PPRs) · Singularity-free trajectory planning · Coupler curves · NURBS surfaces

1 Introduction and State of the Art

The resolution of the forward kinematic problem (FKP) remains an outstanding and complex task for robots having parallel structure. We can state the FKP of a parallel robot (PR) as follows: determining the pose coordinates of the end-effector characteristic point (EECP) fixed on the mobile platform for given values of the actuated joints variables. It is well known that the inverse kinematic problem (IKP) of

K.A. Arrouk (✉) · B.C. Bouzgarrou · G. Gogu
Clermont Université, Pascal Institute, UMR 6602 CNRS/UBP/IFMA, BP10448,
F63000 Clermont-Ferrand, France
e-mail: khaled.arrouk@ifma.fr

B.C. Bouzgarrou
e-mail: belhassen-chedli.bouzgarrou@ifma.fr

G. Gogu
e-mail: grigore.gogu@ifma.fr

these mechanisms is, in general, much easier to resolve than the forward one. As a matter of fact, IKP of PRs can be resolved using formulations developed for serial robots. FKP formulation leads to a set of non-linear equations with multiple solutions. That is to say, parallel robot has several ways of assembling for specified motorized joints variables. Even though PPRs have only 3-DOF, and despite the apparently simple architecture of these mechanisms; no closed form solution can be established for its FKP. Many research papers carried out in the area of PPRs has been focused on this challenging problem referred as resolving the FKP [3, 4]. Research in this domain has mainly focused on the transformation of the FKP into a high order univariate polynomial. In what follows, we present a concise overview of the approaches used to resolve FKP only for PPRs. Numerical and algebraic methods have been proposed to solve FKP of 3-RPR. In [3, 8] authors have independently shown that the FKP of this mechanism can be reduced to the solution of a characteristic polynomial of degree 6. The formulation due to [3] has then become the standard one [9]. In this approach, the key idea aims to find an equation which depends only on the orientation angle of the mobile platform, by eliminating all other variables from the system of equations. Finally, a tangent-half-angle substitution is performed to translate sine and cosine functions of β , which designates the orientation angle of the moving platform, into rational polynomial expressions in variable $T = \tan(\beta/2)$. Husty [5] has used the technique of *kinematic mapping* to resolve the FKP for 3-RPR. In this work, he formulated a mathematical equation by considering the displacements of EECp in the four-dimensional homogeneous space. Hayes and Chen in [4] have presented a geometric and algebraic tool which consists in developing a set of constraint equations that can be used to solve the inverse and forward geometric problems of all possible three-legged planar platforms possessing 3-DOF. Rojas and Thomas have suggested a numerical approach to find the FKP solutions of 3-RPR which avoids all problems related to other approaches, and have shown how the univariate polynomials of all fully PPRs can be derived directly from that of the 3-RPR robot by formulating these polynomials in terms of distances [9] and oriented areas [10]. The polynomial thus obtained is achieved straightforwardly avoiding both variable eliminations and tangent-half-angle substitutions. In [7] authors have proposed a 2D graphical method for the kinematic synthesis of different examples of four-bar linkages using CAD software. Kilit in [6], has proposed a geometric approach for FKP analysis based on 22 steps for 3-RRR. Readers can refer to our previous work [1], where an extensive bibliographic study of FKP resolution issue has been performed.

2 Classical Graphical Interpretation of the FKP: General 3-RPR-Type PPRM Case Study

The choice of the 3-RPR PPM is motivated by its practical interest, mechanical simplicity, and rich mathematical properties [9]. In these notations, \underline{P} stands for the actuated prismatic joint and R for passive revolute joint. This manipulator has 3-

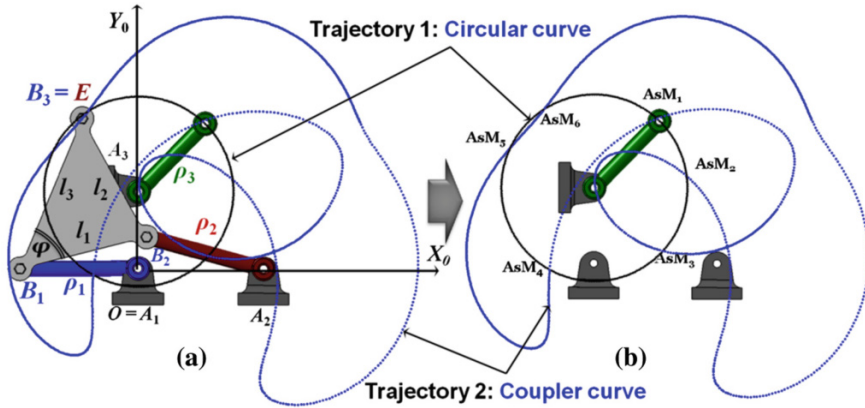


Fig. 1 Graphical resolution interpretation of the FKP for 3-RPR-type PPR

DOF. It is composed by a mobile platform and a fixed base connected by three kinematic chains called limbs. Each limb is composed by an actuated prismatic joint and two passive revolute joints at its two extremities. In this study, the rotary motion of passive revolute joints are assumed unlimited. We denote by A_i ($i = 1, 2, 3$) the center of the i th revolute passive joint attached to the fixed base. With a view to simplification, the origin of the fixed coordinate system R_0 (O_0, X_0, Y_0, Z_0) is attached to point A_1 as depicted in the Fig. 1. Similarly, we denote by B_i ($i = 1, 2, 3$) the center of i th revolute passive joint attached to the mobile platform. The planar coordinates of A_i in R_0 (O_0, X_0, Y_0, Z_0) are denoted by (c_i, d_i) . The planar coordinates of B_i in R_E (O_E, X_E, Y_E, Z_E) are denoted by (x_{bi}, y_{bi}) . We denote by E the end-effector characteristic point (EECP) attached to the mobile platform. Its planar coordinates in R_0 (O_0, X_0, Y_0, Z_0) are given by (x_E, y_E) . The orientation of the mobile platform around the axis O_0Z_0 is defined by angle β . The operational variables, giving the position and the orientation of the mobile platform relative to the base, are x_E, y_E and β .

A deep understanding of the FKP is an essential step in developing resolution methods. In this paragraph, the classical geometric interpretation of such a problem is presented.

For 3-RPR mechanism, the actuated joint variables are fixed: the length of the three legs A_1B_1, A_2B_2 and A_3B_3 are respectively fixed to ρ_1, ρ_2 and ρ_3 . If the leg A_3B_3 is disconnected from the rest of the mechanism, see Fig. 1a, it can be observed that B_3 , belonging to the mobile platform, describes a coupler curve of the four-bar mechanism ($A_1B_1B_2A_2$) which is a six-degree algebraic curve. Besides, the extremity B_3 belonging to the disconnected leg A_3B_3 describes a circular curve of radius ρ_3 and centered in A_3 . The points of intersection between the coupler and the circular curves correspond to the possible locations of B_3 for which the 3-RPR mechanism can be assembled. Therefore, the number of intersection points corresponds to the number of FKP solutions of a 3-RPR manipulator.

In Fig. 1, the six assembly-modes of 3-RPR-type PPR are graphically determined. It must be noted that, if we modify the ρ_3 value, the number of intersecting points may be 0, 2, 4 or 6, which corresponds to the number of assembly-modes for this type of manipulator. For this mechanism, it has been confirmed, by using Bézout's circularity theorem, that the number of FKP solutions is equal to 12, where 6 of them are imaginary [11]. Consequently, there are at most 6 possible solutions of the FKP for the 3-RPR manipulator associated to the different assembly modes.

The mechanism geometric parameters for the example illustrated in Fig. 1 are: $\rho_1 = 14.98$, $\rho_2 = 15.38$, $\rho_3 = 12$, $c_2 = 15.91$, $c_3 = d_2 = 0$, $d_3 = 10$, $l_1 = 17.04$, $l_2 = 16.54$, $l_3 = 20.84$, $\varphi = 50.1$ deg.

3 Proposed Approach for FKP Resolution

The key idea of our method is to consider each limb of a PPR as a serial chain isolated from the rest of the mechanism and having the mobile platform as effector. When actuated joint variables of planar 3-DOF robot are fixed, the EECP describes a 2D region embedded in the 3D operational space (x, y, β) . The intersection of these regions gives a set of finite number of points corresponding to the solutions of the FKP associated with the various assembly-modes of the robot.

3.1 CAD-Graphical Technique for FKP Resolution

The proposed CAD graphical technique has been implemented in CATIA[®] CAD software, it consists of four major steps which will be illustrated for 3-RPR-type PPR: **Step 1: Construction of the feasible curves (regions) by the extremity of each limb when the actuated joint variables are fixed.** This step consists, for a given orientation of the mobile platform, in constructing the 2D curve achievable by the vertex of each limb isolated from the rest of the mechanism, when the actuated joint variables are fixed. For the 3-RPR manipulator, these regions are circular for fixed prismatic joint strokes, Fig. 2a. These circular regions are centered in the first revolute passive joints defined by points A_1 , A_2 and A_3 , and have as radii the joint variables ρ_1 , ρ_2 and ρ_3 . **Step 2: Construction of generic helical trajectories.** In this step, the helical curve represents the orientation change of the vector $\mathbf{B}_i\mathbf{E}$ when the orientation angle β of the mobile platform varies from 0 to 2π ; see Fig. 2a. The axis of each helical curve is normal to the plane containing the circular region determined in Step 1. The radius of the i th helix is equal to $\|\mathbf{B}_i\mathbf{E}\|$, and the height of the helix is 2π rad for $\beta = 2\pi$, as depicted in Fig. 2b. For each limb, a generic helical trajectory is created independently. **Step 3: Generation of the swept surface reachable by the EECP associated to each limb for all orientations of the mobile platform.** In order to generate continuously the whole surface produced by each

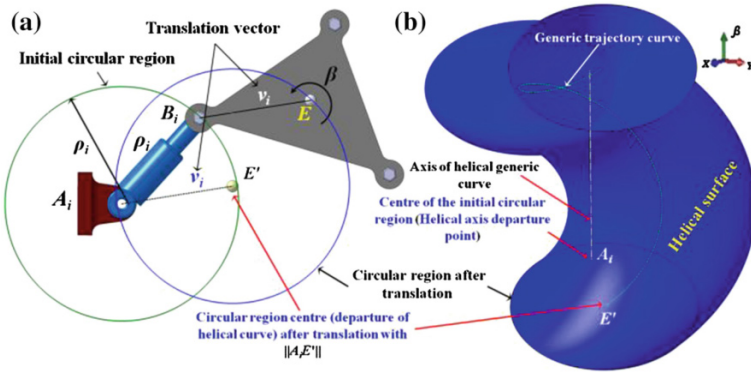


Fig. 2 Procedure for construction of a swept surface for one limb of 3-RPR-type PPR

limb corresponding to different values of the orientation angle of the mobile platform, a sweep operation is applied.

This operation consists in sweeping the region created in Step 1, for a given orientation of the platform and after performing a translation on it by vector $B_i E$ ($i = 1, 2, 3$) along the helical generic trajectory which is set up in Step 2, as shown in Fig. 2b. It is applied by iteration to all vertex regions reached by three kinematic chains of the manipulator, Fig. 3a. **Step 4: Determination of the common points** (x_E, y_E, β) associated to the different assembly-modes for the PPR. Once we have modeled all surfaces feasible by the chosen EECF associated to the different limbs on the moving platform, we determine all points associated to the different assembly-modes by using intersection operations (Fig. 3c). This can be formulated:

$$\{(x_i, y_i, \beta_i), i = 1 \dots N_m\} = S_{screw1}(\rho_1) \cap S_{screw2}(\rho_2) \cap S_{screw3}(\rho_3) \quad (1)$$

Note 1: The surfaces created in Step 3 will be named “helical surfaces” or “screw surfaces”, or “twisted columns”. It is noteworthy that the position of the EECF influences the construction parameters of the surfaces generated; in other

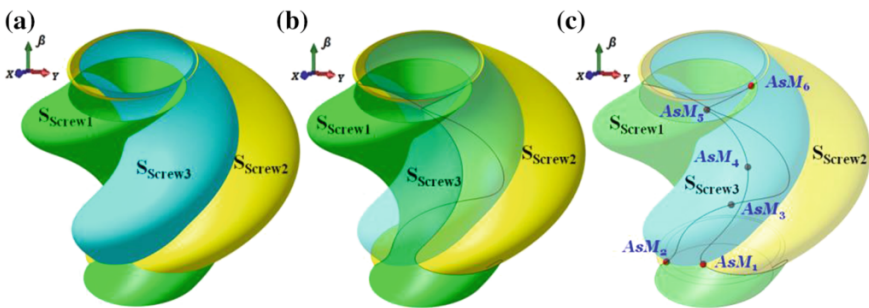


Fig. 3 Screw surfaces (twisted columns) attainable by the point E associated to each limb

words, if point E is fixed on the center of the second revolute joint represented by points B_i with $(i = 1, 2, 3)$, in the center of B_1 for example, the helical surface produced by this limb A_1B_1 degenerates into a cylindrical one. The radius of the helical trajectory for this limb will tend to zero, that means: $\|B_1E\| = 0$. The height of the cylindrical surface represents the amplitude of the orientation of the moving platform.

Note 2: Through the proposed developments, we can state that a classical 2D coupler curve of a four-bar linkage, in XY plane, is nothing but the orthogonal projection along β direction of 3D curve resulting from the intersection of two 3D screw surfaces, constructed according to the above described CAD graphical procedure. This mathematical result can be proven in another framework.

3.2 Numerical Examples

In this subsection, a numerical example is presented in order to illustrate the effectiveness of the proposed CAD graphical approach. The accuracy of the FKP resolution based on this approach can be verified by applying the inverse kinematic model (IKM) to the set of P_{Ass-M} points. Afterwards, the results obtained are compared to the target values of the joint variables ρ_1 , ρ_2 , and ρ_3 . We consider herein two PPRs of type 3-RPR, the **first** robot has the geometric design parameters that has been studied in several papers [1–3, 12]. These parameters are depicted in Sect. 2 of this paper with $\rho_1 = 16.5$, $\rho_2 = 18.5$, and $\rho_3 = 17$. The **second** robot have the following geometric design parameters $c_2 = 20$, $d_2 = 0$, $c_3 = 40$, $d_3 = 0$, $l_1 = l_2 = l_3 = 52$, with $\rho_1 = 50$, $\rho_2 = 40$, $\rho_3 = 35$, this robot is proposed in [1].

If we apply our CAD graphical technique to these manipulators, we obtain a set of **6** Cartesian coordinates for (**Robot 1**), and **4** Cartesian coordinates for (**Robot 2**) associated to the assembly-modes. The CAD procedure is completely illustrated in Fig. 4. A 3D representation of these configurations is given. In order to highlight the orientation of the mobile platform for these two 3-RPR-type PPR, their postures have been drawn in 3D representation, Fig. 4. We have considered in these cases study that the EECF is located in the center B_1 of second revolute passive joint of first limb for both robots, see Fig. 1. To verify the accuracy of our proposed

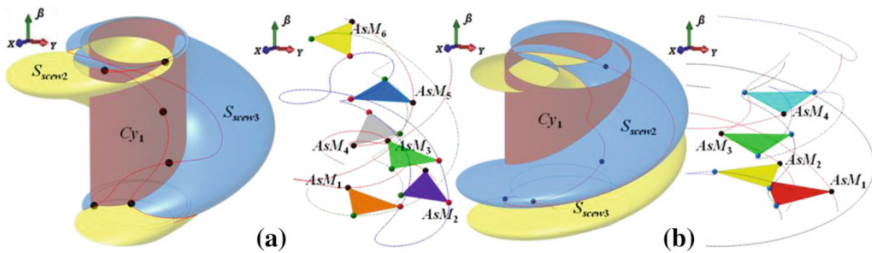


Fig. 4 Resolution of FKP for robot 1 (a), and robot 2 (b) using our CAD approach

Table 1 Solutions of FKP obtained by CAD approach and the images in joint space (IKM)

N°	x_E (mm)	y_E (mm)	β (rad)		ρ_1	ρ_2	ρ_3
Robot 1	16.43690762	1.441550565	0.89319419	Images for Robot 1	16.5	18.4999	16.9999
	-15.25884275	6.27835313	0.28542219		16.5	18.5003	17.0002
	0.837636385	16.47872463	4.50990038		16.5	18.5004	16.9997
	16.07422689	3.724141484	2.79382613		16.5	18.4999	17.0000
	-3.070707045	-16.21174754	6.15543095		16.5	18.5	16.9996
	-13.40890612	-9.615156618	0.86015029		16.5	18.5	17.0001
Robot 2	-34.4082	36.2777	5.0369	Images for Robot 2	50	39.9984	35.0006
	-1.96401	-49.9614	0.3886		50	39.9982	35.0009
	46.1282	19.2921	2.9002		50	39.9998	35
	36.6896	-33.9686	1.1569		50	40	34.9992

CAD technique, we compare the obtained results with the target values. So, we calculate the image in the joint space of each obtained pose, associated to the assembly-modes, by using the IKM. The resulted poses are indicated in Table 1.

Note 3: The target values for **Robot 1** are ρ_i (16.5, 18.5, 17), and for **Robot 2** ρ_i (50, 40, 35). Due to the fact that CAD software uses Spline curves and NURBS surfaces, a very small deviation between the exact solutions and those obtained by our proposed CAD graphical approach can be observed

4 Singularity-Free Paths Connecting Assembly Modes

The generation of singularity-free trajectories connecting different assembly modes is very important to extend the effective workspace of the robot. In our study, the interferences which can occur between different mechanism parts are neglected. Figure 5 shows clearly that parallel singularity surface divides 3D total workspace into two adjacent regions [1, 2], so called aspects. In fact, the concrete representation and superposition of CAD models of singularity-free zones within the 3D total operational workspace, CAD model corresponding to parallel singularity surface, and FKP solutions in the same graph allows robot designers to identify effectively the solutions of FKP associated with different assembly modes, which belong to different singularity-free regions within workspace.

The last result gives designers all the possibilities to cope with problems related to the generation of singularity-free trajectories. Our CAD approach offers the potential to connect, two different solutions of FKP without the need to encircle a cuspidal point in the joint workspace [12] for the 3-RPR-type PPR where three solutions of FKP coalesce. For more details on the techniques used to determine the CAD model of 3D total workspace, parallel singularity surface, and singularity-free

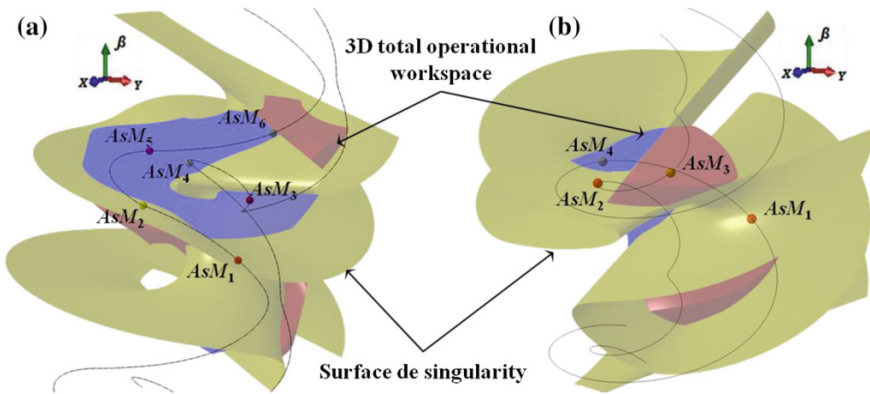


Fig. 5 Superimposing in the same graph the 3D workspace CAD model, parallel singularity surface and solutions of FKP for robot 1 (a) and robot 2 (b)

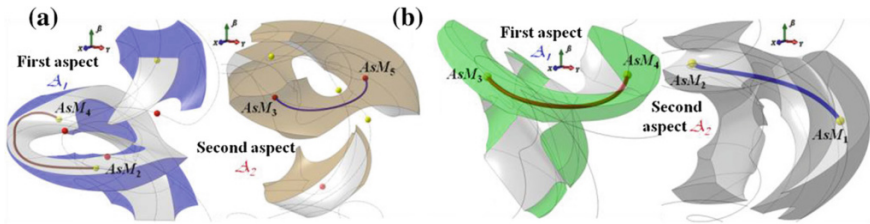


Fig. 6 Singularity-free trajectories connecting assembly modes: Robot 1 (a), Robot 2 (b)

regions for different architectures of PPRs readers can refer to our works [1, 2]. Figure 6 shows CAD model for planning singularity-free trajectories for both 3-RPR-types PPR described previously which connect different assembly modes.

5 Conclusions

A new graphical technique using CAD tools for FKP resolution of PPRs is presented. 3-RPR manipulator has been taken as an example of application; but our approach can be used for all PPRs. This method offers a better understanding of the assembly modes and the singularity-free trajectories within 3D workspace. In fact, designers don't need to develop analytic expressions neither for 3D workspace nor for FKP resolution. Indeed, our work opens the door widely to go very far in the use of geometric approaches to analyze, design and optimize PRs.

Acknowledgments This work is supported financially by the Excellence Laboratory "LabEX" IMobS3 of Clermont-Ferrand, and the Research National Agency.

References

1. Arrouk KA (2012) Techniques de Conception Assistées par Ordinateur (CAO) pour la caractérisation de l'espace de travail de robots manipulateurs parallèles. Ph.D. Thesis, University Blaise PASCAL-Clermont II, Institut PASCAL
2. Arrouk KA et al (2012) CAD based geometric procedures for workspace and singularity determination of the 3-RPR parallel manipulator. In: Gogu G, Maniu I, Lovasz E-C, Fauroux J-C, Ciupe V (eds), Mechanisms, mechanical transmissions and robotics, pp 131–140, Trans Tech Publications, ISBN 978-3-03785-395-5
3. Gosselin C et al (1992) Polynomial solutions to the direct kinematic problem of planar 3-DOF parallel manipulators. Mech Mach Theor 27(2):107–119
4. Hayes MJD et al (2004) Kinematic analysis of general planar parallel manipulators. ASME J Mech Des 126(5):866–874
5. Husty ML (1995) Kinematic mapping of planar three-legged platforms. In: Proceedings of 15th Canadian congress of applied mechanics CANSAM, Victoria, Br. Columbia, Canada, vol 2, pp 876–877

6. Kilit O (2010) A new geometric algorithm for direct position analysis of planar 3-RRR manipulator. In: Proceedings of international symposium of mechanism and machine science IFToMM, Turkey, pp 396–402
7. Kinzel EC et al (2006) Kinematic synthesis for finitely separated positions using geometric constraint programming. *ASME J Mech Des* 128(5):1070–1079
8. Pennock GR, Kassner DJ (1992) Kinematic analysis of a planar eight-bar linkage: application to a platform type robot. *ASME J Mech Des* 114(1):87–95
9. Rojas N, Thomas F (2011) The forward kinematics of 3-RPR planar robots: a review and a distance-based formulation. *IEEE Trans Rob* 27(1):143–150
10. Rojas N, Thomas F (2013) The univariate closure conditions of all fully parallel planar robots derived from a single polynomial. *IEEE Trans Rob* 29(3):758–765
11. Tancredi L, Teillaud M (1999) Application de la géométrie synthétique au problème de modélisation géométrique directe des robots parallèles. *Mech Mach Theor* 34:255–269
12. Zein M et al (2008) Non-singular assembly mode changing motions for 3-RPR parallel manipulators. *Mech Mach Theory* 43(4):480–490

Introducing Distance Restrictions in the Deformed Position Problem

I. Fernández de Bustos, V. García Marina, M. Abásolo and R. Avilés

Abstract The deformed position problem is the basis for methods dealing both with synthesis and analysis of mechanisms. This paper analyzes how nonlinear restrictions can be introduced into the method so that it can be used to represent restrictions in the distance between two arbitrary points in the mechanism. The applications of this algorithm range from designing grippers to defining the required behavior of discrete elements such as springs or dampers. In order to introduce these restrictions, the original method has undergone heavy modifications to include simple Karush-Kuhn-Tucker systems along with saddle-point avoidance and under determined Hessian matrices. Two possible variants of the method were studied. Numerical results of the method have been included to demonstrate the efficiency of the alternatives offered by the method.

Keywords Optimization · Mechanism synthesis and analysis · Karush-Kuhn-Tucker systems · Nonlinear restrictions

1 Introduction

The deformed position problem has shown itself to be highly versatile when used in the analysis and synthesis of mechanisms, having been successfully employed to solve position problems, mechanism synthesis [1] and even path-planning problems [2]. As in any other optimization problem, the versatility is much increased by the means of restrictions implemented to allow boundary conditions and requirements to be introduced.

Many different restrictions can be readily introduced by including linear constraints, but some features can only be implemented by means of nonlinear restrictions. Although the inclusion of nonlinear restrictions in the deformed

I.F. de Bustos (✉) · V.G. Marina · M. Abásolo · R. Avilés
University of the Basque Country, Bilbao, Spain
e-mail: impfedei@ehu.es

position problem is not new [2], no proper study has yet been conducted on alternative ways of introducing them and solving the resultant system. The efficient introduction of such restrictions is a prerequisite to approaching the synthesis of mechanisms with these kinds of restrictions.

2 The Deformed Position Problem

The deformed position problem is defined in the following form. First, we define the mechanism as being composed of deformable, linear elastic elements. Then, restrictions are derived from the mechanism topology (fixed points and similar boundary conditions). Finally, other boundary conditions derived from the problem to be solved (input values, for example), are introduced. Most of these restrictions are linear, but if the aim is to simulate the input by means of a linear actuator, in the general case a nonlinear constraint must be introduced, which is the point of this work.

In its simplest form of the method, a mechanism can be defined as consisting of truss elements. In this case the error function can be written as in Eq. (1):

$$f_p(\{x\}) = \sum_{i=1}^b (l_i(\{x\}) - L_i)^2, \quad (1)$$

where L_i is the undeformed length of truss i ; $l_i(\{x\})$ is the deformed length of the truss, as defined for the coordinates of the joints to be optimized, $\{x\}$; and b is the number of trusses in the mechanism. We can safely say that this is a finite element approach, in which the finite elements represent the solid–rigid elements of the mechanism. In the case of elements including more joints, it might well be necessary to include other kinds of elements having angular dimensions. From now on, we will use the simplest form of the objective function, Eq. (1), but keeping in mind the fact that the algorithms presented here are of general use.

With this in mind, we can define the deformed position problem as the problem of obtaining the coordinates $\{x\}$ that minimize Eq. (1), subject to the linear restrictions defined by the fixed element and/or input elements and any nonlinear restriction defined by input elements. One of these possible nonlinear restrictions is the point-to-point distance requirement which was the subject of this study.

3 Introducing Point-to-Point Distance Restrictions

A point-to-point distance requirement in a precision point is the desired distance from a point of an element in the mechanism to some point of a different element. This requirement, although it may seem to be of little interest, is in fact of great

relevance to the design of many mechanisms, ranging from motorcycle suspensions to grippers. If we denote (x_a, y_a) as the coordinates of the first point and (x_b, y_b) as the coordinates of the second point, the most straightforward method of representing the requirement is Eq. (2), where D_i is the required distance for the i restriction:

$$r_i(\{x\}) = \sqrt{(x_{bi} - x_{ai})^2 + (y_{bi} - y_{ai})^2} - D_i = 0. \quad (2)$$

But also of interest is the alternative, expressed by Eq. (3):

$$\bar{r}_i(\{x\}) = (x_{bi} - x_{ai})^2 + (y_{bi} - y_{ai})^2 - D_i^2 = 0. \quad (3)$$

The interest in this formulation resides in the fact that its derivatives are easier to obtain, but convergence should be checked.

In previous works, Eq. (2) has been successfully used to solve, for example, the path-planning problem. But this is not a general case, due to the fact that it is a successive position problem; thus we always have a good starting guess for that optimization problem, which avoids problems derived from saddle points.

The most straightforward method of solving the problem is to use Lagrange multipliers. To implement them, our expanded error function takes the form:

$$F(\{x\}) = f_p(\{x\}) + \sum_{t=1}^r \lambda_t r_t(\{x\}). \quad (4)$$

Or, using Eq. (3), the alternative expanded error function:

$$F(\{x\}) = f_p(\{x\}) + \sum_{t=1}^r \lambda_t \bar{r}_t(\{x\}), \quad (5)$$

where λ_t is the Lagrange multiplier for restriction t .

4 Optimization Process

The minimization of Eq. (5) by sequential programming using the Newtonian method for multiple variables requires the first and second derivatives of Eqs. (4) and (5) with respect to the variables $\{x\}$ and with respect to the Lagrange multiplier $\{\lambda\}$. It is easy to obtain, for the first formulation:

$$\frac{\partial r_i(\{x\})}{\partial \{x\}} = \{g_i(\{x\})\} = \frac{1}{d_i(\{x\})} \begin{Bmatrix} -(x_{bi} - x_{ai}) \\ -(y_{bi} - y_{ai}) \\ (x_{bi} - x_{ai}) \\ (y_{bi} - y_{ai}) \end{Bmatrix}, \quad (6)$$

where $d_i(\{x\})$ is the value of the distance among the points as defined by the coordinates. For the second formulation:

$$\frac{\partial \bar{r}_i(\{x\})}{\partial \{x\}} = \{\bar{g}_i(\{x\})\} = 2 \begin{Bmatrix} -(x_{bi} - x_{ai}) \\ -(y_{bi} - y_{ai}) \\ (x_{bi} - x_{ai}) \\ (y_{bi} - y_{ai}) \end{Bmatrix}. \quad (7)$$

The second derivative for the first formulation:

$$\frac{\partial^2 r_i(\{x\})}{(\partial \{x\})^2} = [h_i(\{x\})] = \frac{1}{d_i(\{x\})} \begin{bmatrix} 1 - l_{xi}^2 & -l_{xi}l_{yi} & -1 + l_{xi}^2 & l_{xi}l_{yi} \\ -l_{xi}l_{yi} & 1 - l_{yi}^2 & l_{xi}l_{yi} & -1 + l_{yi}^2 \\ -1 + l_{xi}^2 & l_{xi}l_{yi} & 1 - l_{xi}^2 & -l_{xi}l_{yi} \\ l_{xi}l_{yi} & -1 + l_{yi}^2 & -l_{xi}l_{yi} & 1 - l_{yi}^2 \end{bmatrix}, \quad (8)$$

where $l_{xi} = \frac{x_{bi} - x_{ai}}{d_i(\{x\})}$, and $l_{yi} = \frac{y_{bi} - y_{ai}}{d_i(\{x\})}$. For the second formulation:

$$\frac{\partial^2 r_i(\{x\})}{(\partial \{x\})^2} = [\bar{h}(\{x\})] = \begin{bmatrix} 2 & 0 & -2 & 0 \\ 0 & 2 & 0 & -2 \\ -2 & 0 & 2 & 0 \\ 0 & -2 & 0 & 2 \end{bmatrix}. \quad (9)$$

The resultant Karush-Kuhn-Tucker system:

$$\begin{bmatrix} [H_L(\{x\})] & [E^T(\{x\})] \\ [E(\{x\})] & [0] \end{bmatrix} \begin{Bmatrix} \Delta \{x\} \\ \Delta \{\lambda\} \end{Bmatrix} = - \begin{Bmatrix} \{G_L\} \\ \{R\} \end{Bmatrix}, \quad (10)$$

being $[H_L] = [H] + [H_r]$, where $[H]$ is the Hessian matrix of the original function and $[H_r] = \sum_{i=1}^r [h_r(\{x\})]$, and $\{G_L\} = \{G\} + \{G_r\}$, where $\{G\}$ is the gradient of the

original function and

$\{G_r\} = \sum_{i=1}^r \lambda_r \{g_r(\{x\})\}$, $[E] = [\{g_1(\{x\})\} \quad \{g_2(\{x\})\} \quad \dots \quad \{g_r(\{x\})\}]^T$ and

$$\{R\} = \begin{Bmatrix} r_1(\{x\}) \\ \dots \\ r_r(\{x\}) \end{Bmatrix}.$$

The second formulation leads to similar equations.

In order to solve this system, we decided to use the null-subspace method (see [3]), mainly because we wanted to obtain a result which separated the part of the increment of the coordinates required to verify the restrictions from the rest of it. This allowed us to scale the increment that was not needed to verify the restrictions. In order to do so, we separated the original system in:

$$[H^L]\Delta\{x\} + [E]^T\Delta\{\lambda\} = -\{G^L\} \quad (11)$$

and:

$$[E]\Delta\{x\} = -\{R\} \quad (12)$$

The null-subspace method introduces the expression:

$$\Delta\{x\} = \Delta\{x_p\} + [N_e]\Delta\{y\}, \quad (13)$$

where $[N_e]$ is the null subspace of $[E]$ and $\Delta\{x_p\}$ is a particular solution of Eq. (12). In order to obtain $[N_e]$ and $\Delta\{x_p\}$, we resorted to the Golub-Reinsch [4] algorithm for the SVD factorization. The SVD factorization has the advantage that we obtain the less norm solution for $\Delta\{x_p\}$. This is important in order to make the correction of the solution required to verify the restrictions as small as possible. An alternative which is currently under investigation is tridiagonalization to obtain this solution rapidly, yet keeping the numerical error as small as possible.

Introducing Eq. (13) into Eq. (11), we obtain:

$$[H]^L[N_e]\Delta\{y\} + [E]^T\Delta\{\gamma\} = -\{G\} - [H]^L\Delta\{x_p\}. \quad (14)$$

Pre-multiplying by $[N_e]^T$, we obtain a symmetrical system:

$$[N_e]^T[H]^L[N_e]\Delta\{y\} = -[N_e]^T\{G\} - [N_e]^T[H]^L\Delta\{x_p\}. \quad (15)$$

We must remember that $[N_e]$ is the null subspace of $[E]$ and, thus, $[N_e][E] = 0$. Taking into account the Karush-Kuhn-Tucker conditions, we can use Eq. (15) to implement saddle point and undesired extrema avoidance. In order to do so, modified factorization systems can be used, but these lead to a lack of control on the resolution.

An alternative is to perform diagonalization of the system, which can be done utilising SVD [4], Bunch-Kaufmann [4], Bunch-Parlett [4] or the factorization presented in [5]. The authors opted for the latter, since it represents a good compromise between computational cost and accuracy. The advantage of this approach is that the optimization is decoupled to arrive at a set of independent optimizations comprising one variable each, rather than a system of coupled optimization equations. Obviously, this decoupling is only valid for the order two approximation of the error function in the current iteration, but it is obtained for each iteration at negligible cost. This decoupling allows each of the decoupled variables to be tackled independently, and the result can be modified accordingly if it means a non-desired extrema (maximization in this case) or a inflexion point (Fig. 1).

In this study the increment in the event of saddle point or inflexion point was simply fixed in the correct direction given by the gradient.

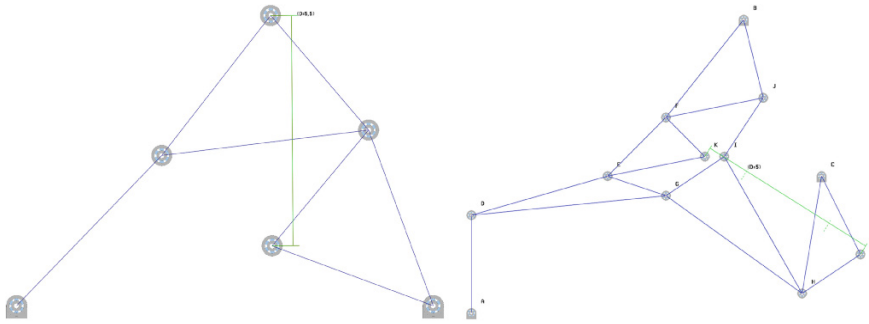


Fig. 1 Topologies for the simple and complex test mechanisms with the placement of the point-to-point restriction

5 Experimentation

A set of simple problems was designed to test the efficiency of both alternatives. These can be divided into simple and complex, ‘far’ and ‘successive’, and ‘deformed’ and ‘undeformed’ problems. A problem is ‘far’ when the starting guess is far from the solution to be obtained, and ‘successive’ whenever the starting guess is close to the solution. A problem is ‘deformed’ whenever there is no undeformed solution verifying the requisites, and ‘undeformed’ when there is a solution that could be achieved by the mechanism without deformation.

Here we will show the results for only two representative configurations, due to space limitations. Note that not only is the convergence in deformation energy of interest, but also the verification of the nonlinear restriction.

In most examples, the linear formulation led to an extremely fast reduction of the error in the restriction, which would usually translate into a marginally more rapid convergence, but most of the time the difference was unnoticeable, as in Fig. 2

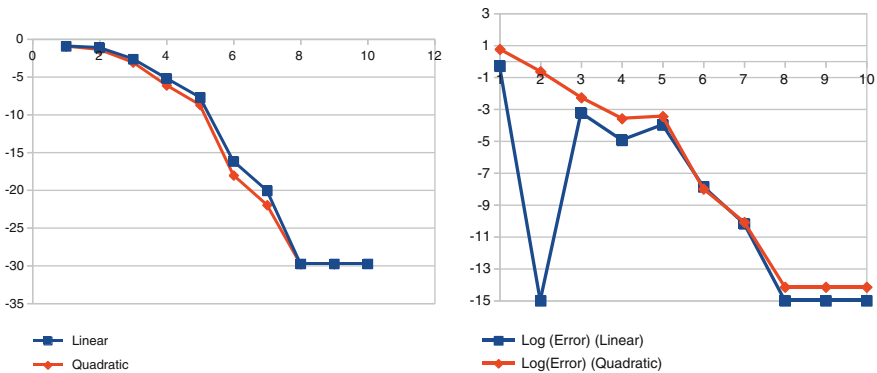


Fig. 2 Evolution of the deformation energy and the linear restriction error for the simple mechanism, successive problem, undeformed case

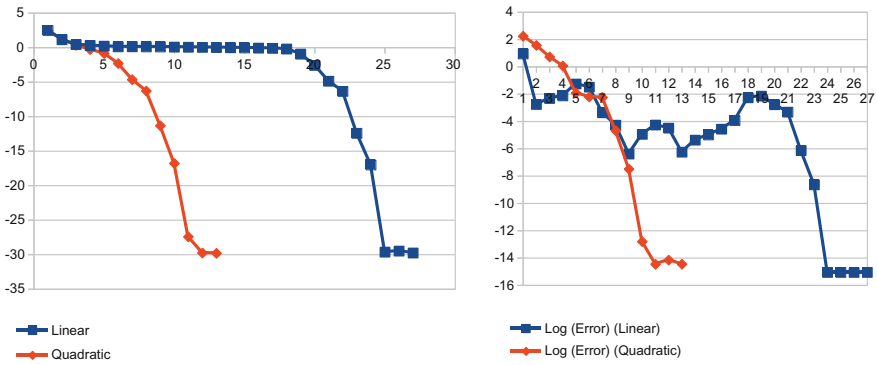


Fig. 3 Evolution of the deformation energy and the linear restriction error for the simple mechanism, far guess, undeformed case

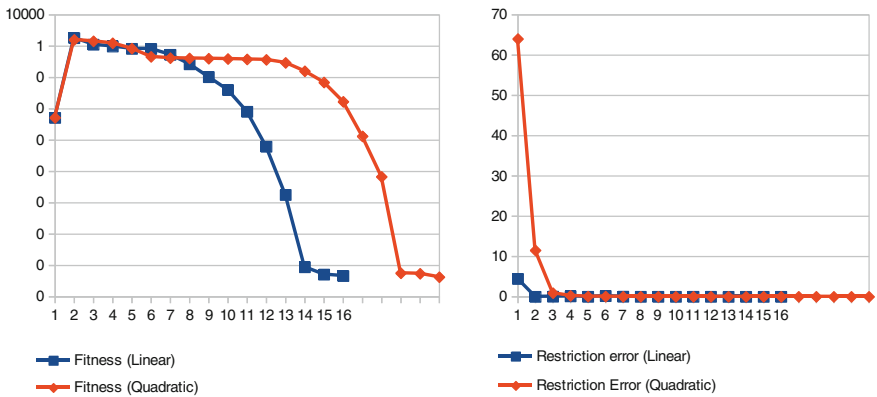


Fig. 4 Evolution of the deformation energy and the linear restriction error for the complex mechanism, far guess, undeformed case

(although this was not always the case, as we will see in Fig. 4). It is important to point out that this aggressive behavior sometimes leads to an oscillation in the restriction that leads to delayed convergence, as can be seen in Fig. 3.

The complex mechanism only showed an increment in computational cost, but with similar behavior.

6 Conclusions and Future Work

The behaviors of two formulations for introducing nonlinear distance restrictions in the deformed position problem were studied. Both methods seemed to perform without major problems, but one was simpler to implement and the other usually achieved better convergence.

The next task to be performed is to take advantage of these implementations to approach the synthesis of mechanisms with fixed length restrictions and other point-to-point constraints. It is also of interest to use a similar quadratic form to approach the deformation problem itself, and it is also important to develop other nonlinear restrictions such as angular requisites.

Acknowledgments The authors wish to thank the Spanish Ministry of Science and Innovation for their support of this research (DPI grant).

References

1. Avilés R, Vallejo J, Aguirrebeitia J, Fernández de Bustos I, Ajuria J (2010) Optimization of linkages for generalized rigid-body guidance synthesis based on finite element models. *Finite Elem Anal Des* 46(9):721–731
2. Agirrebeitia J, Avilés R, Fernández de Bustos I, Ajuria G (2008) A new APF strategy for path planning in environments with obstacles. *Mech Mach Theor* 40:645–658
3. Nocedal J, Wright S (2006) Numerical optimization. Springer Series in Operations Research and Financial Engineering, 2nd (ed)
4. Golub GH, van Loan CF (1989) Matrix computations Johns Hopkins studies in the mathematical sciences, 3rd edn. Johns Hopkins University Press, Baltimore
5. Fernández de Bustos I, Aguirrebeitia J, Ajuria G, García Marina V (2013) Rotation schemes for full pivoting factorization of indefinite symmetric matrices. *Congr Numer Meth Eng* 2013. Bilbao, 25–28 June

On Generalized Euler Angles

Aleix Rull and Federico Thomas

Abstract This paper first explores the generalization of Euler angles to the case in which the rotation axes are not necessarily members of an orthonormal triad, and presents a concise solution to their computation that relies on the calculation of standard Euler angles. Then, this generalization is taken one step further by introducing translations, that is, by defining generalized Euler angles about screw axes using a variation of the principle of transference that avoids the use of dual numbers. As an example, the obtained formulation is applied to solve the inverse kinematics of a 3C manipulator.

Keywords Euler angles · Generalized Euler angles · Dual Euler angles · 3C Manipulator

1 Introduction

Decomposing a rotation into three partial rotations about prescribed axes is considered an important problem in the parametrization of the three-dimensional rotation group [1] with applications to motion planning and inverse kinematics. For example, the inverse kinematics of a wrist-partitioned manipulator requires the decomposition of a given finite rotation of the end-effector into three successive finite rotations about prescribed joint axes. When these three axes are selected from an orthogonal basis, the rotation angles are the well-known Euler angles. The case in which the three axes are not necessarily orthogonal was first treated by Davenport in [2]. He considered the case in which the first and the third axes were orthogonal to the second, but the angle between the first and third was arbitrary. In

A. Rull (✉) · F. Thomas
Institut de Robòtica i Informàtica Industrial (CSIC-UPC), Barcelona, Spain
e-mail: arull@iri.upc.edu

F. Thomas
e-mail: fthomas@iri.upc.edu

1978, Dimentberg took the problem in all its generality and reduced it to three quadratic equations each relating the tangent of the half input angle with the tangents of the half rotations angles [3]. In 1992, Wohlhart obtained a similar expression for the first rotation angle and two linear equations relating the tangents of the first angle and each of the other two angles, thus improving Dimentberg's formulation [4]. The main problem of these two formulations is their discontinuity at $\pm\pi$. In 2003, Wittenburg and Lilov [5], and Shuster and Markley [6], independently gave a successful solution to the problem that avoids this formulation singularity. More recently, in 2011, Mladenova and Mladenov solved the problem using a vector-like parametrization of the rotation group [7], and in 2012 Piovan a Bullo presented a solution based on a coordinate-free formulation [8].

Another generalization of Euler angles consists in introducing translations, that is, in defining Euler angles about screw axes [9]. This leads to the concept of dual Euler angles which has successfully been used in several biomechanical applications [10, 11]. A dual angle, say $\hat{\phi}$, is defined as a dual number of the form $\phi + \epsilon d$, with $\epsilon^2 = 0$, so that ϕ is the rotation about and d the slide along a given axis. Dual numbers were introduced in the 19th century by Clifford, and their application to rigid body kinematics was subsequently generalized by Kotelnikov and Study in their *principle of transference*. This principle essentially states that, if dual angles replace real ones, then all equations obtained for spherical problems are also valid for spatial ones [12]. Therefore, general coordinate transformations can be expressed as a sequence of rotations through three dual Euler angles.

This paper deals with the problem of computing dual Euler angles for the case in which the three rotation axes are not mutually orthogonal, thus giving a unified treatment of the two generalizations of Euler angles available in the kinematics literature. It is interesting to observe that this problem was implicitly solved by Pennock and Vierstra in [15] when calculating the inverse kinematics of the general 3C manipulator [15]. Curiously enough, this connection remained unnoticed in all subsequent works dealing with generalizations of Euler angles. One of the purposes of this paper is to highlight this connection and to provide a more concise and readable formulation to that given in [15].

The rest of this paper is organized as follows. In Sect. 2, by relying on the computation of standard Euler angles, a concise way to compute generalized Euler angles is presented. Next, in Sect. 3, this result is extended to dual angles using an alternative formulation of the principle of transference that makes no explicit use of dual numbers. The derived equations are then used, in Sect. 4, to solve the inverse kinematics of a 3C manipulator. Finally, conclusions are drawn in Sect. 5.

2 Computing Sets of Generalized Euler Angles

The problem of decomposing a rotation about an axis \mathbf{n} by an angle ϕ into three successive rotations about three axes \mathbf{n}_1 , \mathbf{n}_2 , and \mathbf{n}_3 by angles α_1 , α_2 , and α_3 , respectively, can be algebraically expressed as:

$$\mathbf{R}_n(\phi) = \mathbf{R}_{\mathbf{n}_1}(\alpha_1)\mathbf{R}_{\mathbf{n}_2}(\alpha_2)\mathbf{R}_{\mathbf{n}_3}(\alpha_3). \quad (1)$$

Expressing the rotations about \mathbf{n}_1 , \mathbf{n}_2 , and \mathbf{n}_3 in terms of rotations about the z -axis, we have:

$$\mathbf{C}_1\mathbf{R}_z(\alpha_1)\mathbf{C}_1^T\mathbf{C}_2\mathbf{R}_z(\alpha_2)\mathbf{C}_2^T\mathbf{C}_3\mathbf{R}_z(\alpha_3)\mathbf{C}_3^T = \mathbf{R}_n(\phi),$$

where \mathbf{C}_i , $i = 1, 2, 3$, is a rotation matrix that rotates the reference frame so that the rotated z -axis coincides with \mathbf{n}_i . Rearranging terms, this can be rewritten as:

$$\mathbf{C}_3^T\mathbf{R}_n^T(\phi)\mathbf{C}_1\mathbf{R}_z(\alpha_1)\mathbf{C}_1^T\mathbf{C}_2\mathbf{R}_z(\alpha_2)\mathbf{C}_2^T\mathbf{C}_3\mathbf{R}_z(\alpha_3) = \mathbf{I}.$$

Then, computing the products of all constant matrices, we obtain:

$$\mathbf{A}_1\mathbf{R}_z(\alpha_1)\mathbf{A}_2\mathbf{R}_z(\alpha_2)\mathbf{A}_3\mathbf{R}_z(\alpha_3) = \mathbf{I}.$$

Now, after computing a set of valid ZYZ Euler angles for \mathbf{A}_i , $i = 1, 2, 3$, we have:

$$\begin{aligned} \mathbf{R}_z(\beta_1)\mathbf{R}_x(\gamma_1)\mathbf{R}_z(\delta_1)\mathbf{R}_z(\alpha_1)\mathbf{R}_z(\beta_2)\mathbf{R}_x(\gamma_2)\mathbf{R}_z(\delta_2)\mathbf{R}_z(\alpha_2) \\ \mathbf{R}_z(\beta_3)\mathbf{R}_x(\gamma_3)\mathbf{R}_z(\delta_3)\mathbf{R}_z(\alpha_3) = \mathbf{I}. \end{aligned}$$

Hence, by collapsing the sequences of rotations about the same axis into a single rotation, we conclude that:

$$\mathbf{R}_x(\gamma_1)\mathbf{R}_z(\theta_1)\mathbf{R}_x(\gamma_2)\mathbf{R}_z(\theta_2)\mathbf{R}_x(\gamma_3)\mathbf{R}_z(\theta_3) = \mathbf{I}, \quad (2)$$

where $\theta_1 = \delta_1 + \alpha_1 + \beta_2$, $\theta_2 = \delta_2 + \alpha_2 + \beta_3$, and $\theta_3 = \delta_3 + \alpha_3 + \beta_1$.

Observe that Eq. (2) can be seen as the closure condition of the spherical triangle depicted in Fig. 1 [13]. Then, the analogues of the law of cosines for the angles θ_1 , θ_2 and θ_3 of this spherical triangle allow us to write:

$$g_1(\gamma_1, \gamma_2, \gamma_3, \theta_1) = \cos \gamma_1 \cos \gamma_2 - \cos \gamma_3 - \sin \gamma_1 \sin \gamma_2 \cos \theta_1 = 0, \quad (3)$$

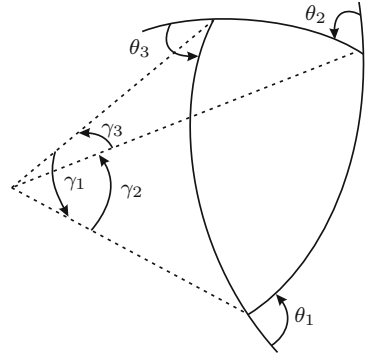
$$g_2(\gamma_1, \gamma_2, \gamma_3, \theta_2) = \cos \gamma_3 \cos \gamma_2 - \cos \gamma_1 - \sin \gamma_3 \sin \gamma_2 \cos \theta_2 = 0, \quad (4)$$

$$g_3(\gamma_1, \gamma_2, \gamma_3, \theta_3) = \cos \gamma_3 \cos \gamma_1 - \cos \gamma_2 - \sin \gamma_3 \sin \gamma_1 \cos \theta_3 = 0. \quad (5)$$

Finally,

$$\begin{aligned} \theta_1 &= \pm \arccos\left(\frac{\cos \gamma_1 \cos \gamma_2 - \cos \gamma_3}{\sin \gamma_1 \sin \gamma_2}\right), \\ \theta_2 &= \pm \arccos\left(\frac{\cos \gamma_3 \cos \gamma_2 - \cos \gamma_1}{\sin \gamma_3 \sin \gamma_2}\right), \\ \theta_3 &= \pm \arccos\left(\frac{\cos \gamma_3 \cos \gamma_1 - \cos \gamma_2}{\sin \gamma_3 \sin \gamma_1}\right). \end{aligned}$$

Fig. 1 Spherical triangle associated with matrix Eq. (2)



If we take one solution for any of these three angles, the solution for the other two becomes unique. Thus, we have two sets of solutions. To avoid checking the eight combinations of signs to obtain the two right combinations, we can express, for example, θ_2 and θ_3 in terms of θ_1 . To this end, applying the law of sines to the spherical triangle in Fig. 1, we have:

$$\sin \theta_2 = \frac{\sin \gamma_1}{\sin \gamma_3} \sin \theta_1,$$

$$\sin \theta_3 = \frac{\sin \gamma_2}{\sin \gamma_3} \sin \theta_1.$$

Therefore,

$$\theta_2 = a \tan 2 \left(\frac{\sin \gamma_1}{\sin \gamma_3} \sin \theta_1, \frac{\cos \gamma_3 \cos \gamma_2 - \cos \gamma_1}{\sin \gamma_3 \sin \gamma_2} \right),$$

$$\theta_3 = a \tan 2 \left(\frac{\sin \gamma_2}{\sin \gamma_3} \sin \theta_1, \frac{\cos \gamma_3 \cos \gamma_1 - \cos \gamma_2}{\sin \gamma_3 \sin \gamma_1} \right).$$

As an example, consider the problem solved in [4] and [7] (note that the latter reference contains several typos in the provided numerical values). In this particular case, $\mathbf{n}_1 = (\cos 80^\circ \cos 45^\circ, \cos 80^\circ \sin 45^\circ, \sin 80^\circ)$, $\mathbf{n}_2 = (\sin 60^\circ, \cos 60^\circ, 0)$, $\mathbf{n}_3 = (1, 0, 0)$, $\mathbf{n} = (\cos 50^\circ \cos 25^\circ, \cos 50^\circ \sin 25^\circ, \sin 50^\circ)$, and $\phi = 60^\circ$. Using the procedure given above, we obtain

$$\begin{aligned} \delta_1 &= 90^\circ, & \beta_2 &= 143.03^\circ, & \theta_1 &= \pm 93.24^\circ, \\ \delta_2 &= -27.39^\circ, & \beta_3 &= -60^\circ, & \theta_2 &= \pm 91.88^\circ, \\ \delta_3 &= 132.01^\circ, & \beta_1 &= 29.78^\circ, & \theta_3 &= \pm 149.58^\circ. \end{aligned}$$

The resulting two sets of solutions are $\{\alpha_1 = 33.73^\circ, \alpha_2 = -4.50^\circ, \alpha_3 = 48.63^\circ\}$ and $\{\alpha_1 = -139.79^\circ, \alpha_2 = 179.27^\circ, \alpha_3 = -12.21^\circ\}$, which coincide with those given in [4] and [7].

3 Applying the Principle of Transference

All the presentations of the principle of transference invariably resort to the algebraic structure of dual numbers, but for our purposes it is better to avoid it to derive a more easily implementable formulation. To this end, let us suppose that a loop closure conditions in a spherical mechanism can be expressed as:

$$g_1(\xi_1, \dots, \xi_n) = 0, \dots, g_m(\xi_1, \dots, \xi_n) = 0,$$

where $\xi_i, i = 1, \dots, n$ represent rotations about the axes $\mathbf{n}_1, \mathbf{n}_2, \dots, \mathbf{n}_n$, respectively. Then, if we do not only rotate but, at the same time, we also translate along the directions defined by these axes the quantities d_1, d_2, \dots, d_n , respectively, these translations cannot be assigned independently, they must satisfy the following n relationships:

$$\sum_{i=1}^n d_i \frac{\partial g_1}{\partial \xi_i} = 0, \dots, \sum_{i=1}^n d_i \frac{\partial g_m}{\partial \xi_i} = 0,$$

where the sign of d_i is imposed by the sign of ξ_i according to the right hand rule (see [14] for details).

Now, if we apply the principle of transference, as stated above, to (3), (4), and (5), we obtain:

$$(\mathbf{a}_1 \quad \mathbf{a}_2 \quad \mathbf{a}_3) \begin{pmatrix} d_{\gamma_1} \\ d_{\gamma_2} \\ d_{\gamma_3} \end{pmatrix} + (\mathbf{b}_1 \quad \mathbf{b}_2 \quad \mathbf{d}_3) \begin{pmatrix} d_{\theta_1} \\ d_{\theta_2} \\ d_{\theta_3} \end{pmatrix} = 0, \quad (6)$$

where $d_{\gamma_1}, d_{\gamma_2}, d_{\gamma_3}, d_{\theta_1}, d_{\theta_2}$, and d_{θ_3} correspond to translations along the axes associated with the rotation angles $\gamma_1, \gamma_2, \gamma_3, \theta_1, \theta_2$, and θ_3 , respectively, and

$$\begin{aligned} \mathbf{a}_1 &= \begin{pmatrix} -\sin \gamma_1 \cos \gamma_2 - \cos \gamma_1 \sin \gamma_2 \cos \theta_1 \\ \sin \gamma_1 \\ -\cos \gamma_3 \sin \gamma_1 - \sin \gamma_3 \cos \gamma_1 \cos \theta_3 \end{pmatrix}, \mathbf{b}_1 = \begin{pmatrix} \sin \gamma_1 \sin \gamma_2 \sin \theta_1 \\ 0 \\ 0 \end{pmatrix}, \\ \mathbf{a}_2 &= \begin{pmatrix} -\cos \gamma_1 \sin \gamma_2 - \sin \gamma_1 \cos \gamma_2 \cos \theta_1 \\ -\cos \gamma_3 \sin \gamma_2 - \sin \gamma_3 \cos \gamma_2 \cos \theta_2 \\ \sin \gamma_2 \end{pmatrix}, \mathbf{b}_2 = \begin{pmatrix} 0 \\ \sin \gamma_3 \sin \gamma_2 \sin \theta_2 \\ 0 \end{pmatrix}, \\ \mathbf{a}_3 &= \begin{pmatrix} \sin \gamma_3 \\ -\sin \gamma_3 \cos \gamma_2 - \cos \gamma_3 \sin \gamma_2 \cos \theta_2 \\ -\sin \gamma_3 \cos \gamma_2 - \cos \gamma_3 \sin \gamma_1 \cos \theta_3 \end{pmatrix}, \mathbf{b}_3 = \begin{pmatrix} 0 \\ 0 \\ \sin \gamma_3 \sin \gamma_1 \sin \theta_1 \end{pmatrix}. \end{aligned}$$

In the next section, these formulas are used to solve the inverse kinematics of a 3C manipulator.

4 Example: Inverse Kinematics of the 3C Manipulator

Clearly, calculating the inverse kinematics of an oblique spherical wrist¹ is equivalent to solving (1) for α_1 , α_2 , and α_3 . As a generalization, it can be observed that calculating the inverse kinematics of serial manipulator with three cylindrical joints can be reduced to solve the same set of equations to obtain the revolute joint angles, and the system of equations in (6) to obtain the prismatic joint displacements.

The inverse kinematics of a general 3C manipulator was solved for the first time in [15]. Since then, this has remained the standard reference for this kind of robot. To exemplify the equivalence between calculating the inverse kinematics of 3C manipulators and calculating generalized dual Euler angles, let us considered the 3C manipulator shown in Fig. 2. Solving its inverse kinematics reduces to solve the matrix equation

$$\begin{aligned} \mathbf{T}_z(d_1)\mathbf{R}_z(\theta_1)\mathbf{R}_x(-30^\circ)\mathbf{T}_x(35)\mathbf{T}_z(d_2)\mathbf{R}_z(\theta_2)\mathbf{R}_x(70^\circ) \\ \mathbf{T}_z(d_3)\mathbf{R}_z(\theta_3)\mathbf{T}_z(50)\mathbf{T}_x(30) = \mathbf{E}, \end{aligned} \quad (7)$$

where \mathbf{E} represents the location of its end-effector. If we set

$$\mathbf{E} = \begin{pmatrix} 0 & 0 & -1 & -115 \\ 0 & 1 & 0 & 25 \\ 1 & 0 & 0 & 85 \\ 0 & 0 & 0 & 1 \end{pmatrix}, \quad (8)$$

and calculate the ZZX dual Euler angles of $\mathbf{E}\mathbf{T}_x(-30)\mathbf{T}_z(-50)$, (7) can be rewritten as:

$$\begin{aligned} \mathbf{T}_z(d_1)\mathbf{R}_z(\theta_1)\mathbf{R}_x(-30^\circ)\mathbf{T}_x(35)\mathbf{T}_z(d_2)\mathbf{R}_z(\theta_2)\mathbf{R}_x(70^\circ)\mathbf{T}_z(d_3)\mathbf{R}_z(\theta_3) \\ = \mathbf{R}_z(-90^\circ)\mathbf{T}_z(55)\mathbf{R}_x(90^\circ)\mathbf{T}_x(-25)\mathbf{R}_z(90^\circ)\mathbf{T}_z(65). \end{aligned} \quad (9)$$

After rearranging terms, we finally obtain:

$$\begin{aligned} \mathbf{R}_x(-90^\circ)\mathbf{T}_x(25)\mathbf{R}_z(\theta_1 + 90^\circ)\mathbf{T}_z(d_1 - 55)\mathbf{R}_x(-30^\circ)\mathbf{T}_x(35) \\ \mathbf{R}_z(\theta_2)\mathbf{T}_z(d_2)\mathbf{R}_x(70^\circ)\mathbf{R}_z(\theta_3 - 90^\circ)\mathbf{T}_z(d_3 - 65) = \mathbf{I}. \end{aligned} \quad (10)$$

After dropping translations and proceeding as explained in Sect. 2, the following two sets of revolute joint angles are obtained: $\{\theta_1 = 43.16^\circ, \theta_2 = -129.08^\circ, \theta_3 = 67.16^\circ\}$, and $\{\theta_1 = -223.16^\circ, \theta_2 = 129.08^\circ, \theta_3 = 112.84^\circ\}$. Then, substituting these results in (6), and solving the resulting linear system in d_1 , d_2 and d_3 , we obtain the following sets of translations for the prismatic joints: $\{d_1 = 52.49, d_2 = 2.9, d_3 = 89.54\}$, and $\{d_1 = 57.51, d_2 = -2.9, d_3 = 40.46\}$, respectively. In Fig. 3, the robot is represented in both configurations.

¹ A spherical wrist is said to be simple if $\mathbf{n}_1 \perp \mathbf{n}_2$ and $\mathbf{n}_2 \perp \mathbf{n}_3$ or oblique, otherwise.

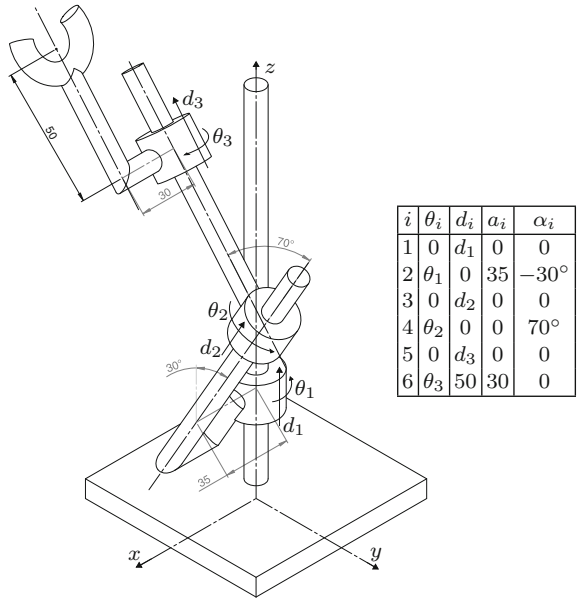


Fig. 2 A 3C manipulator and its DH-parameters

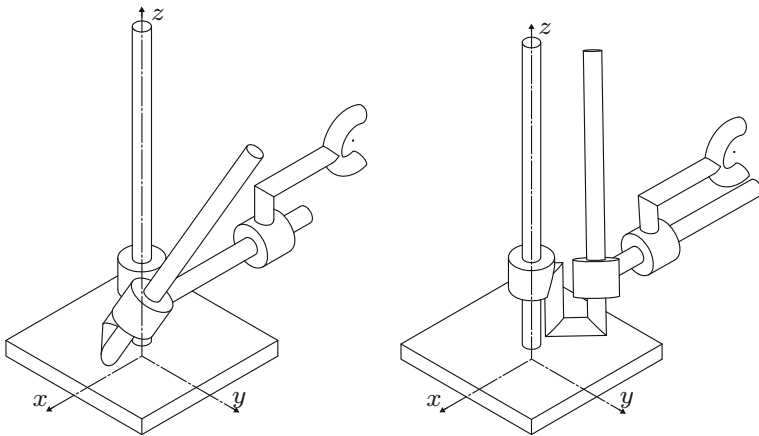


Fig. 3 The two inverse kinematics solutions of the analyzed manipulator for a particular location of its end-effector (see text for details)

5 Conclusions

We have presented an alternative simple procedure to calculate sets of generalized Euler angles. Next, this procedure has been extended from spherical to spatial kinematics using a variation of the principle of transference that does not rely on the use of dual angles. The arising equations have been shown to be equivalent to those resulting from solving the inverse kinematics of the general 3C robot, a problem already solved using dual orthogonal matrices by Pennock and Vierstra in [15]. Probably due to the fact that, in the example presented by these authors, the axes of the cylindrical joints are orthogonal, their work has been overlooked in recent papers dealing with generalizations of Euler angles.

References

1. Stuelpnagel J (1964) On the parametrization of the three-dimensional rotation group. *SIAM Rev* 6(4):422–430
2. Davenport PB (1973) Rotations about nonorthogonal axes. *AIAA J* 11(6):853–857
3. Dimentberg FM (1978) Theory of screws and its applications. Nauka, Moscow
4. Wohlhart K (1992) Decomposition of a finite rotation into three consecutive rotations about given axis. In: Proceedings of the 6th international Conference on the theory of machines and mechanisms, Lieberec, Czechoslovakia, pp 325–332
5. Wittenburg J, Lilov L (2003) Decomposition of a finite rotation into three rotations about given axes. *Multibody Sys Dyn* 9(4):353–375
6. Shuster MD, Markley FL (2003) Generalization of the euler angles. *J Astron Sci* 51(2): 123–132
7. Mladenova CD, Mladenov IM (2011) Vector decomposition of finite rotations. *Rep Math Phys* 69(1):107–117
8. Piovan G, Bullo F (2012) On coordinate-free rotation decomposition: Euler angles about arbitrary axes. *IEEE Trans Rob* 28(3):728–733
9. Baker JE, Parkin IA (1998) On compounding three successive finite displacement screws, *Advances in Robot Kinematics: Analysis and Control*, pp 337–342, Springer
10. Ying N, Kim W (2002) Use of dual Euler angles to quantify the three-dimensional joint motion and its application to the ankle joint complex. *J Biomech* 35(12):1647–1657
11. Teua KK, Kimb W, Fussa FK, Tanc J (2006) The analysis of golf swing as a kinematic chain using dual Euler angle algorithm. *J Biomech* 39(7):1227–1238
12. Rico-Martnez JM, Duffy J (1993) The principle of transference: history, statement and proof. *Mech Mach Theory* 28(1):165–177
13. Duffy J, Rooney J (1975) A foundation for a unified theory of analysis of spatial mechanisms. *J Eng Ind Trans ASME* 97(4):1159–1164
14. Thomas, F.: On the n-bar mechanism, or how to find global solutions to redundant single loop spatial kinematic chains. In: Proceedings of the 1992 IEEE International Conference on Robotics and Automation, I, 403-408 (1992)
15. Pennock GR, Vierstra BC (1990) The inverse kinematics of a three-cylindric robot. *Int J Robot Res* 9(4):75–85

Guaranteed Detection of the Singularities of 3R Robotic Manipulators

Romain Benoit, Nicolas Delanoue, Sébastien Lagrange
and Philippe Wenger

Abstract The design of new manipulators requires the knowledge of their kinematic behaviour. Important kinematic properties can be characterized by the determination of certain points of interest. Important points of interest are cusps and nodes, which are special singular points responsible for the non-singular posture changing ability and for the existence of voids in the workspace, respectively. In practice, numerical errors should be properly tackled when calculating these points. This paper proposes an interval analysis based approach for the design of a numerical algorithm that finds enclosures of points of interest in the workspace and joint space of the studied robot. The algorithm is applied on 3R manipulators with mutually orthogonal joint axes.

Keywords Interval analysis · Singular points · 3R Robot · Cusp · Node

1 Introduction

Algorithms and methods described in this article are applied to the study of a family of robotic manipulators: *3 revolute-jointed manipulators with mutually orthogonal joint axes*. Those manipulators are first studied because they can be regarded as the

R. Benoit (✉) · N. Delanoue · S. Lagrange
LARIS, 62 avenue Notre Dame du Lac, 49000 Angers, France
e-mail: romain.benoit@etud.univ-angers.fr

N. Delanoue
e-mail: nicolas.delanoue@univ-angers.fr

S. Lagrange
e-mail: sebastien.lagrange@univ-angers.fr

P. Wenger
Institut de Recherche en Communications et Cybernétique de Nantes, 1 rue la Noë, 44321
Nantes cedex 03, France
e-mail: philippe.wenger@ircsyn.ec-nantes.fr

positioning structure of a 6R manipulator with a spherical wrist. A main point is that they can be *cuspidal*, which means that they can change their posture without having to meet a singularity, as detailed in [1] and [10]. It may or may not be the desired behaviour. A cuspidal robot has at least one cusp in a planar cross section of its workspace. On the other hand, the existence of nodes in this section is intimately related to the existence of voids in the robot workspace. Thus, cusps and nodes are important points of interest [5]. A classification based on the number of such points can be established [1, 4].

The main point of the algorithm and methods we are detailing here is to use Interval Analysis to enclose, in a guaranteed way, the cusps and nodes in the generator plane section of the manipulator workspace. To find these points, we use two systems of equations, whose roots are joint space points yielding the cusps and nodes. To enclose the roots of those systems of equations, the *Interval Newton* method is used.

We will verify that, for manipulators with no internal motion, and with some imprecision in their geometric parameters, it is possible to find their cusp and node points, with the formerly introduced algorithms.

Complete studies of manipulator families, as done in [1], allow one to choose a manipulator within a large range of geometric parameters, when a precise behaviour is needed. Alternatively, algorithms presented in this article make it possible to study manipulators with geometric parameters between chosen bounds. It makes them a first step in guaranteeing the behaviour of a manipulator, given its geometric parameters, and the precision affordable for building the actual manipulator.

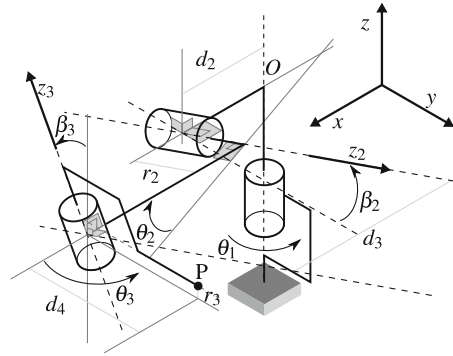
2 Studied Manipulators

The studied manipulators have three unlimited revolute joints. Thus, it is sufficient to restrict the analysis to their last two joints. Since the workspace is symmetric about the first joint axis, it is enough to restrict its analysis to a planar half cross-section in the plane defined by $(\sqrt{x^2 + y^2}, z)$, that we will identify to $(x^2 + y^2, z)$ for computational purposes.

Figure 1 shows the studied manipulator and its geometric parameters. Note that, for a matter of convenience in our algorithms, angles β_i have been used instead of the standard α_i , where $\beta_i = \pi/2 - \alpha_i$

We will first consider the same manipulators as in [1] that is, *manipulators with orthogonal rotations and no offset along their last joint*. With conventions chosen in Fig. 1, these manipulators are defined by $\beta_2 = \beta_3 = r_3 = 0$. We will show that our methodology is able to provide the same results as in [1]. Furthermore, our approach can also be used for manipulators with an offset along their last joint and always returns an exact enclosure of the searched singular joint space points.

Fig. 1 Kinematic diagram of a general 3R manipulator with $\theta_1 = 0$



3 Application of Interval Analysis

3.1 Interval Analysis

Interval analysis is a computing method, that operates on intervals instead of operating on values. The point of this is mainly for numerical computation because it allows one to enclose values in intervals, whose bounds can be *exactly* stored by a computer. With this computing method, thus, values are guaranteed to be between bounds (see [6, 8]). *Interval analysis is a simultaneous computation of numbers and errors.*

In this article, domains will be vectors of intervals. The notion of interval can be extended by Cartesian product, so Interval analysis can be extended to domains by the use of inclusion maps.

Definition 3.1.1 (*Inclusion map*)

Let f be a map. An inclusion map of f is a function $[f]$ that associates to a domain D , a domain $[f](D)$ such that $f(D) \subset [f](D)$. Note that $(x \in D \Rightarrow f(x) \in [f](D))$.

In practice, the inclusion map $[f]$ of f is chosen to minimize the domains $[f](D)$ with respect to inclusion.

This computing method is useful for its usability when a limited set of values can be exactly represented, as for numerical computations. *In this case, a point P is represented by the smallest domain D containing P and $f(P)$ is represented by $[f](D)$, the smallest domain in the image space containing $f(D)$.*

3.2 Interval Analysis in Robotics

Interval analysis is a tool that can be used for many applications in Robotics (see [7]) such as computing the kinematics of manipulators, including parallel ones.

Indeed, the Interval Analysis properties seen in Sect. 3.1 allow one to search interest points, without any round-off error (see [7] again).

One of the robotic applications of Interval Analysis is *singularity analysis*, that is, finding singular points of the kinematic map of a manipulator. To find those singular points, a general scheme is used, which consists of a subdivision and shrinking process on the domain of study. The main idea is that the searched points are defined as roots of an equation. Then, any domain whose image by the map associated with the equation does not contain 0, does not contain any searched point. If a domain may contain a root, then an operator is used to shrink the domain to smaller ones containing the roots in the initial domain. Ultimately, when the domain cannot be reduced this way, it is cut into several sub-domains that are studied again. An instance of this scheme, to enclose the singular points of manipulators, can be found in [3] and [2]. What makes the general scheme synergistic with Interval Analysis, is that they both operate on domains and have the purpose to enclose computed values.

Several methods, using Interval Analysis or not, exist to enclose the singular points of a manipulator. But, *it is also necessary to verify the nature of those singular points*. For instance, suppose you succeeded in finding the enclosure of the singular set in the workspace as in Fig. 2a. The real singular set can be either as in Fig. 2b or c. To conclude on the behaviour of the manipulator, it is necessary to verify if the two curves intersect or not.

In this paper, we propose an algorithm to enclose *specific singular points* that define the behaviour of a manipulator, using Interval analysis. Accordingly, next subsection proposes a method to enclose numerically roots from a system of equations, through Interval Analysis: *The Interval Newton method*.

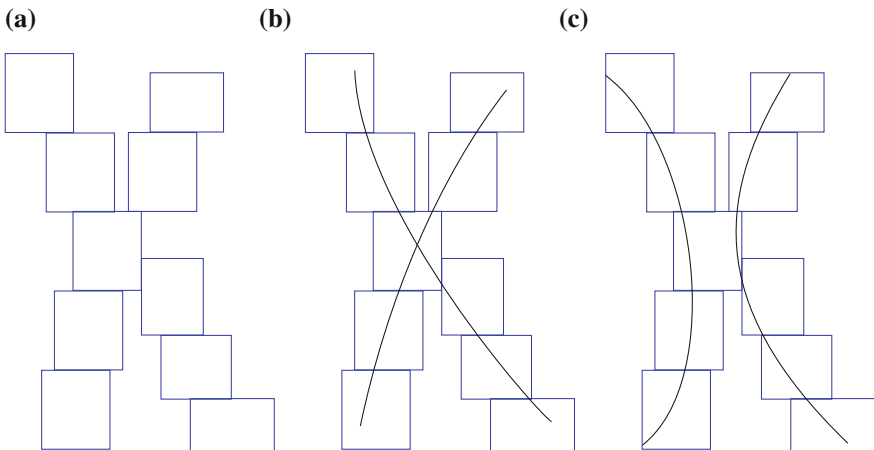


Fig. 2 Example uncertainty of singular set crossing. **a** Example enclosure of a singular set in the workspace, **b** instance of crossing enclosed singular set, **c** instance of non-crossing enclosed singular set

3.3 The Interval Newton Algorithm

Given a square system of equations described by $f=0$, we can define an operator over domains. This Interval Newton operator N_f associated to the map f is defined by:

$$N_f: D \mapsto x - ((df(D))^{-1} \times f(x)), \text{ where } D \text{ is adomain and } x \in D \quad (1)$$

$df(D)$ is the matrix of intervals enclosing all the matrices associated to the linear map of the differential of f at a point in D and $(\cdot)^{-1}$ is the operator of matrix inversion. The main point is that the topological relation between D and $N_f(D)$ depends on the presence of a root in D :

1. if $N_f(D) \subset D$ then $\exists!x \in D$ such as $f(x) = 0$ and $x \in N_f(D)$,
2. if $N_f(D) \cap D = \emptyset$ then $\exists / x \in D$ such as $f(x) = 0$,
3. if $N_f(D) \cap D \neq \emptyset$ then (if $\exists x \in D$ such as $f(x) = 0$ then $x \in N_f(D) \cap D$).

The Interval Newton method applied with f is defined (see [9]) as being the Algorithm 1

Algorithm 1 Interval Newton Algorithm

Require: A list “domains-of-study” of domains $(D_j)_{j \in J}$ and a real number “precision”, $\varepsilon > 0$

return Two lists of vectors of intervals : “roots” and “indeterminate”

Core of the algorithm {The algorithm computes the Interval Newton operator, associated with the studied map, on the domains in “domain-of-study”, and adds the ones that check the inclusion of condition 1. to “roots”, while cutting the domains for which the presence of a root is unclear (condition 3.) and adding back the defined domains to “domains-of-study” (as long as their sizes are not smaller than ε).}

Remark 3.3.1 (Interval Newton Algorithm with no indeterminate)

The Interval Newton algorithm is able to find the roots of a square system of equations if the Jacobian matrix associated with it is invertible for the roots of the studied system, implying that the Interval Newton method can only find isolated roots.

The Interval Newton method can also fail if the chosen precision is not small enough. For instance it can allow a studied domain with a size smaller than the precision to contains several roots. One then has to choose a smaller precision, such as no domain can contain several roots.

4 Finding Cusps and Nodes

4.1 Notations and Definitions

- JS refers to the joint space formed by couples (θ_2, θ_3) ,
- SWS refers to a plane section of the workspace, containing the first rotation axis of the robotic manipulator and described by couples $(\rho = x^2 + y^2, z)$,

- $f: JS = \mathbb{R}^2 \mapsto \mathbb{R}^2 = SWS$ is the kinematic map of the robotic manipulator,
- $f_1, f_2: JS = \mathbb{R}^2 \mapsto \mathbb{R}$ are the components of f . Their expressions are, with $\beta_2 = \beta_3 = 0$:
 - $f_1(\theta_1, \theta_2) = (\cos(\theta_1)(d_4 \cos(\theta_2) + d_3) + d_2 - r_3 \sin(\theta_1))^2 + (d_4 \sin(\theta_2) + r_2)^2$,
 - $f_2(\theta_1, \theta_2) = \sin(\theta_1)(d_4 \cos(\theta_2) + d_3) + r_3 \cos(\theta_1)$,
- df refers to the differential of f and Df refers to the Jacobian matrix of f (the matrix associated to df).
- An internal motion occurs when the end tip point P reaches a joint axis. In this case, the inverse kinematics admits a continuum of solutions, which forms a line in the joint space.
- The joint space singular points are the points such as $\det(Df) = 0$.
- The workspace singular points are the images through f of the joint space singular points.
- Cusps points and nodes points in the workspace are singular points satisfying some additional properties: a cusp admits three equal inverse kinematic solutions and a node admits two distinct pairs of equal inverse kinematic solutions.
- Cusps and nodes in the joint space are the sets of the inverse kinematic solutions of the cusp points and node points in the workspace, respectively.
- S_j is the singular set in the joint space.
- $\Delta E = \{(a, a) | a \in E\}$

4.2 Applying the Interval Newton Algorithm

4.2.1 Application to the Cusps

Geometric considerations: We consider that a joint cusp point, C , is a point for which the orthogonal of $\text{Ker}(df(C))$ is collinear with the gradient of the singular curve, defined by $\det(Df) = 0$. It is worth noting that in \mathbb{R}^2 , being collinear with a vector $v = (v_1; v_2) \neq 0$ is the same as being orthogonal to the vector $w = (-v_2; v_1) \neq 0$. Also, if $Df(P) \neq 0$, the rows of Df are a base of the orthogonal of $\text{Ker}(df(P))$ and as long as $Df(P)$ is invertible, the orthogonal of $\text{Ker}(df(P))$ is of dimension 2 and thus it cannot be collinear with $\text{grad}(\det(Df))(P)$. Putting all of this together, we can conclude that if $\text{grad}(\det(Df))(P)$ is not the null vector and $Df(P)$ is not the null matrix, then P is a cusp point if :

$$\begin{cases} \frac{\partial f_1}{\partial \theta_1}(P) \cdot \left(-\frac{\partial \det(df)}{\partial \theta_2}(P)\right) + \frac{\partial f_1}{\partial \theta_2}(P) \cdot \frac{\partial \det(df)}{\partial \theta_1}(P) = 0 \\ \frac{\partial f_2}{\partial \theta_1}(P) \cdot \left(-\frac{\partial \det(df)}{\partial \theta_2}(P)\right) + \frac{\partial f_2}{\partial \theta_2}(P) \cdot \frac{\partial \det(df)}{\partial \theta_1}(P) = 0 \end{cases} \quad (2)$$

Specificities for the algorithm: System (2) is square, which allows one to use the Interval Newton Method to find its isolated roots. The roots of system (2) that we

are searching are singular points. Then, we will apply the Interval Newton Method only if a studied domain contains a singular point, that is, if $\det(Df)$ may be null on the domain. The final point is that $\text{grad}(\det(Df))(P)$ and $Df(P)$ must not be null for the searched roots P , in order to detect those. Then, we will always verify that the components of $\text{grad}(\det(Df))$ and $Df(P)$ are not null on the domains that should contain a cusp-root. If it is not the case on one of the isolated domain, it will be cut into pieces that will be studied again.

4.2.2 Application to the Nodes

Geometric considerations: Node points are much simpler than cusp points for transcription in roots of a map. Indeed, we are searching for couples $(x_1, x_2) \in \mathbb{R}^2 \times \mathbb{R}^2 - \Delta\mathbb{R}^2$, satisfying :

$$\begin{cases} f(x_1) = f(x_2) \\ \det(Df(x_1)) = 0 \\ \det(Df(x_2)) = 0 \end{cases} \quad (3)$$

Specificities for the algorithm: To apply the Interval Newton method to the system (3), this system needs to be a square one, which is the case here, with 4 joint variables and four equations. We search the roots in $JS \times JS \subset \mathbb{R}^2 \times \mathbb{R}^2$ while avoiding the roots in $\Delta JS \subset \Delta\mathbb{R}^2$, because on this last subset, the Jacobian matrix associated with the system (3) is not invertible while having roots and the Interval Newton method fails.

Instead of applying the time consuming process of verifying that a studied domain does not intersect ΔJS and verifying the injectivity of f , restricted to a subset of S_j each time the intersection occurs, one can build a covering of S_j verifying a well chosen property. Indeed, if the covering is done so that any intersecting domains admit a hull on which f , restricted to S_j , is injective, then, it suffices to apply Interval Newton algorithm with system (3) to couples of disjoint domains, in this last covering.

Note that *the covering, built along with the process, is a guaranteed covering of the singular set.*

5 Performances of the Algorithms

Implementing and Running the Cusp and Node Algorithms

All results in this section are valid for any value, or interval of values, of r_3 . To implement, in C++, the algorithms defined in Sect. 4.2, for 3 revolute-jointed manipulators with mutually orthogonal joint axes, we calculated the formal

expression of the derivatives and matrix derived from f , needed in the algorithms. The algorithms evaluate the needed expression on the required domains, replacing the standard functions and operators by corresponding inclusion maps.¹

The application to more general 3 revolute-jointed manipulators, with $\beta_2 \neq 0$ or $\beta_3 \neq 0$, can be done by calculating their kinematic map. But, as the formal expressions increase in length, the running time of the algorithm may increase and the precision needed to enclose the interest points may need to be higher.

In the implemented algorithms, the initial domain of study for (θ_2, θ_3) can be defined using any domain or list of domains, in \mathbb{R}^2 . The domain of geometric parameters can also be chosen. Our algorithms are currently being improved to contain a procedure enclosing the usable joint space, given a simple volumetric model of the manipulator.

Table 1 shows results returned by the algorithms² applied to examples of classes of studied parameters³ for 3 revolute-jointed manipulators, with orthogonal axes and with an initial domain of study for (θ_2, θ_3) of $[-3.1415, 3.1415] \times [-3.1415, 3.1415]$ close to the $[-\pi, \pi] \times [-\pi, \pi]$ full range for the joint angles.

The cusp enclosing Algorithm

Manipulator inducing no indeterminate (cases a, b, d and e of Table 1): The algorithm has been applied to every example of geometric parameters sets in [1]. When the manipulator does not have an internal motion, for a moderate precision, the algorithm needs little time to find the rigorous enclosures of the cusps, and does not return any indeterminate domain.

Manipulator inducing indeterminate (case f of Table 1): When the algorithm is applied to a robot that has internal motions, it finds the cusps outside the internal motions, with the same running time as before. The algorithm then has to run for some time until it encloses the lines associated with the internal motions with domains whose size is the chosen precision. The running time is then dependant of the chosen precision.

The nodes enclosing Algorithm

On domains where there is no cusps and no internal motion lines (case d of Table 1) the nodes enclosing algorithm concludes after a running time close to the one needed for the cusp enclosing algorithm with no internal motion. However, when the domain includes a cusp (cases a, b and e of Table 1) the running time of the algorithm increases quite significantly, because, near cusps, f restricted to S_j , is injective only on small domains. In the same way, the Interval Newton method can conclude, only on small domains when the hull domain of its two components is close to a cusp point.

¹ The library used to handle intervals and operate on them is “Filib++”.

² Running time is given for a computer with a 64 bits operating system and an Intel® Core™ i7 CPU.

³ Notation: [n] is used for non computer storable parameter replaced by the smallest interval containing it.

Table 1 Some studied cases of robotic manipulators and algorithms performances on them

Characteristics	Geometric parameters						Properties of manipulator					
	d_2	d_3	d_4	r_2	r_3	Nodes	Internal motion	Cusps	Nodes			
Designation	d_2	d_3	d_4	r_2	r_3	Nodes	Internal motion	Cusps	Nodes			
<i>a</i>	1	2	1.5	1	0	No	No	4	0			
<i>b</i>	1	2	1.5	1	0.5	No	No	4	0			
<i>c</i>	[1, 1.001]	[2, 2.001]	[1.5, 1.501]	[1, 1.001]	0	NA	NA	4	NA			
<i>d</i>	1	[0.7]	[0.3]	[0.2]	0	No	No	0	0			
<i>e</i>	1	1.5	[0.7]	0.5	0	No	No	4	2			
<i>f</i>	1	0.5	[1.3]	[0.2]	0	Yes	Yes	0	2			
	Cusp algorithm						Node algorithm					
Designation	Precision	Cusps	Indeterminate	Time	Precision	Nodes	Indeterminate	Time				
<i>a</i>	10^{-4}	4	No	32 s	2.5×10^{-10}	0	No	10 h				
<i>b</i>	10^{-4}	4	No	46 s	2.5×10^{-10}	0	No	18 h				
<i>c</i>	10^{-4}	4	No	35 s	2.5×10^{-10}	N/A	Yes	N/A				
<i>d</i>	10^{-4}	0	No	12 s	2.5×10^{-10}	0	No	52 s				
<i>e</i>	10^{-4}	4	No	52 s	2.5×10^{-10}	2	No	35 h				
<i>f</i>	10^{-2}	0	Yes	12 min	10^{-2}	2	Yes	42 s				
<i>f</i>	10^{-3}	0	Yes	90 min	10^{-3}	2	Yes	41 s				

Application with domains of geometric parameters

Our algorithms have been implemented to handle intervals of geometric parameters, so to use intervals of parameters (as for case *b* of Table 1) it is only needed to define a domain of geometric parameters which is not restricted to a point.

If the algorithms find a solution domain, then, *for any set of geometric parameter in the defined domain of parameters*, there is a single interest point in the solution domain. There will be no interest point in any domain that is neither a solution domain nor an indeterminate domain *for any set of geometric parameter, in the defined domain of parameters*. Ultimately, it can exist interest points, for any set of geometric parameter in the defined domain of parameters, only in solution domains and in indeterminate domains. For a manipulator with an internal motion, the algorithms return, at least, enclosures for a subset of the interest point and a covering of the research space that can contain interest points.

6 Conclusion

The main interest of the proposed method is that it can be used to find any isolated point of interest for the evaluation of the behaviour of any manipulator, provided it can be defined by a root of a square system of equations. Then, this methodology constitutes a possible way of describing a robotic manipulator singular set, allowing for the guaranteed detection of isolated specific singular points of interest.

It is to be noted that most of the running time of the algorithm is used to treat domains where the Interval Newton algorithm fails to conclude. To increase the performance of the algorithm, alternate methods for splitting and localized tests need to be used and are searched.

As for a lot of Interval Analysis algorithms, our algorithm can be time consuming when dealing with complicated kinematic functions or high dimension domains of study, especially for the nodes enclosing algorithm, due to the doubled dimension of the domain of study, although attenuated by a pre-subdividing in the joint space. However, provided that the algorithm runs for the time needed with a sufficient precision, it is able to find enclosures for the searched points without errors, or at least a subset of those enclosures and a covering of the searched points.

References

1. Baili M, Wenger P, Chablat D (2004) A classification of 3R orthogonal manipulators by the topology of their workspace. IEEE international conference on robotics and automation, pp 1933–1938
2. Bohigas O, Manubens M, Ros L (2013) Singularities of non-redundant manipulators: a short account and a method for their computation in the planar case. Mech Mach Theory 68:1–17
3. Bohigas O, Zlatanov D, Ros L, Manubens M, Porta JM (2012) Numerical computation of manipulator singularities. In: Robot Autom (ICRA), 2012 IEEE international conference on, pp 1351–1358. IEEE

4. Corvez S, Rouillier F (2004) Automated deduction in geometry, lecture notes in computer science. In: Chapter using computer algebra tools to classify serial manipulators, vol 2930. Springer, Berlin, pp 31–43
5. Husty M, Ottaviano E, Ceccarelli M (2008) Advances in robot kinematics, analysis and design. In: Chapter a geometrical characterization of workspace singularities in 3R manipulators. Springer, pp 411–418
6. Jaulin L, Kieffer M, Didrit O, Walter E (2001) Applied interval analysis with examples in parameter and state estimation. Springer-Verlag, Robust Control and Robotics
7. Merlet JP (2011) Interval analysis and robotics. In: Robotics Research. Springer, pp 147–156
8. Moore RE (1996) Interval Analysis. Prentice-Hall, Englewood Cliffs
9. Neumaier A (1990) Interval methods for systems of equations, encyclopedia of mathematics and its applications, vol 37. Cambridge University Press, Cambridge
10. Wenger P (2007) Cuspidal and noncuspidal robot manipulators. *Robotica* 25, pp 677–689. doi:10.1017/S0263574707003761. URL http://journals.cambridge.org/article_S0263574707003761

Workspace Analysis for Evaluating Laparoscopic Instruments

J.-H. Borchard, F. Dierßen, J. Kotlarski, L.A. Kahrs and T. Ortmaier

Abstract Laparo-endoscopic surgery is the treatment of choice in a variety of intra-abdominal interventions, leading to lower infection risk, shorter recovery time, and smaller scars. This paper presents a method for quantifying workspaces of instruments in laparoscopic surgery. In contrast to most existing approaches, the proposed performance criterion combines the executable positions and orientations of the instrument's functional end. Together with both, an intervention specific workspace and consideration of collisions between instruments, the introduced criterion is suitable to evaluate and compare laparoscopic instruments and systems quantitatively. A three-dimensional, color-scale visualization of the criterion helps analyzing laparoscopic instruments or systems. The presented methods are evaluated with instruments of the da Vinci Surgical System by Intuitive Surgical, Inc. While evaluating the presented performance criterion, the workspace dependency of EndoWrist instruments under influence of different distances of trocar points is demonstrated and quantified.

Keywords Kinematic evaluation · Workspace · Medical devices · Laparoscopic surgery

1 Introduction

Laparo-endoscopic surgery is the treatment of choice in a variety of intra-abdominal interventions, leading to lower infection risk, shorter recovery time, and smaller scars. Typically, an endoscope and two laparoscopic instruments for tissue manipulation or suturing are inserted through trocars. Common laparoscopic instruments provide four degrees of freedom (DoF) only. Therefore, the complexity of interventions is limited. New surgical instruments are available or in develop-

J.-H. Borchard (✉) · F. Dierßen · J. Kotlarski · L.A. Kahrs · T. Ortmaier
Institute of Mechatronic Systems, Leibniz Universität Hannover, Hanover, Germany
e-mail: jan-hinnerk.borchard@imes.uni-hannover.de

© Springer International Publishing Switzerland 2015
P. Flores and F. Viadero (eds.), *New Trends in Mechanism and Machine Science*,
Mechanisms and Machine Science 24, DOI 10.1007/978-3-319-09411-3_9

ment, providing additional joints at the instrument tip to support six DoF for manipulation. One of those instruments is already in use in many clinics, the Endo Wrist of the da Vinci Surgical System by Intuitive Surgical Inc. [1].

Recently, different approaches to further reduce invasiveness have been developed, e.g. laparo-endoscopic single-site surgery (LESS) [2, 3]. In LESS, typically a scope and laparoscopic instruments are inserted through one incision, leading to an almost unremarkable scar if the cut is positioned in the umbilicus. For instance, Intuitive Surgical developed the VESPA instruments for use in LESS [4]. Petroni et al. [5] and Ding et al. [6] present the SPRINT and the IREP Robot for LESS two intracorporeal arms with six DoF.

For evaluating such systems quantitatively, only few approaches are published so far. For instance, Deutschmann et al. [7] use a performance number for evaluating laparoscopic instruments according to the feasibility of desired trajectories. Other authors presented the reachable workspaces of the EndoWrist, the SPRINT, and the IREP system [5, 8, 9]. The aforementioned approaches define the reachable workspace as positions of the end-effector (EE) which can be reached with at least one orientation. This workspace offers an easily comprehensible visualization, but while comparing reachable workspaces of different systems, the following questions remain open:

- How many different orientations are possible while accessing specific positions with a manipulator?
- How affect collisions of instruments the reachable workspace?
- How can a performance number be defined to compare instruments or overall LESS systems in terms of workspace suitability for specific interventions?

This kind of evaluation and comparison is a precondition for systematic development and determination of optimal designs and kinematics. This paper is driven by the following hypotheses:

- Interventions have specific desired workspaces and those are independent from laparoscopic instruments and systems.
- Information about executable workspace is helpful for benchmarking laparoscopic instruments or systems.
- The number of executable poses (position and orientation) in comparison to the number of overall possible poses of a workspace acts as performance criteria for evaluation and quantification of laparoscopic instruments or systems.
- 3D visualization of performance numbers helps comparing laparoscopic instruments or systems.

In a previous work we presented methods for defining a desired workspace and modeling of the kinematics and shape of laparoscopic systems [10]. Based on these methods, this paper presents a performance number, the percentage of executable six dimensional poses, for evaluating and quantifying the executable workspaces of developed systems. It combines the ability of an EE to reach desired positions and orientations. Hence, this performance number is convenient to be used in optimization approaches or to compare different systems. Furthermore, the performance

number is visualized in the three dimensional space. Therefore, existing approaches of non medical systems [11, 12] are adapted.

To demonstrate the significance of the proposed methods simulation results are presented. For that, EndoWrist instruments of the da Vinci Surgical System are modeled. Furthermore, the dependency of the workspace of the EndoWrist instruments on the distances between the trocar points are analyzed. Thereby, the influence of collisions to the executable workspace, i.e. executable positions and orientations, of these instruments is quantified.

2 Material and Methods

2.1 Workspaces and Performance Number

Here, two different workspaces are considered to evaluate laparoscopic equipment quantitatively. The desired workspace $\mathbf{W}_{\text{target}}$, adapted to the intended intervention, contains a number of n_{target} target poses $\mathbf{p}_{\text{target},i}$ a manipulator should be able to reach:

$$\mathbf{W}_{\text{target}} = \{\mathbf{p}_{\text{target},i} | i \in \{1, \dots, n_{\text{target}}\}\}. \quad (1)$$

The executable workspace $\mathbf{W}_{\text{exe},A}$ contains all target poses $\mathbf{p}_{\text{target},i}$ inside the desired workspace $\mathbf{W}_{\text{target}}$ an instrument A is able to reach:

$$\mathbf{W}_{\text{exe},A} = \{\mathbf{W}_{\text{target}} | f_{\text{sys},A}(\mathbf{p}_{\text{target},i})\}. \quad (2)$$

The function $f_{\text{sys},A}(\mathbf{p}_{\text{target},i})$ depends on the kinematics model, the shape model, and the configuration, i.e. pose of instrument B and laparoscope, of the studied system. It returns one, if a target pose $\mathbf{p}_{\text{target},i}$ is executable by instrument A and zero if not. A target pose $\mathbf{p}_{\text{target},i}$ is executable by instrument A, if its inverse kinematics has a solution for $\mathbf{p}_{\text{target},i}$ and no collisions with instrument B or laparoscope are identified. The performance number

$$p_{\text{pose,c}} = \frac{|\mathbf{W}_{\text{exe},A}|}{|\mathbf{W}_{\text{target}}|} 100 \% \quad (3)$$

rates the system by calculating how much percent of the poses inside the desired workspace are executable.

2.2 Evaluated Medical Equipment and Parameters

To execute a specific six dimensional pose $p_{\text{target},i}$ an instrument needs at least six DoF. The classic manual laparoscopic instruments do not achieve this requirement. They have, besides the functional DoF of the forceps, only three rotational and one translational DoF at the trocar point. The da Vinci Surgical System by Intuitive Surgical Inc. is widespread in use and overcomes this limitation [1]. Its instruments have two additional DoF at the instrument's tip (see Fig. 1). With these wrist joints the instruments provide six DoF.

The values of the EndoWrist's kinematics and shape are manually measured. The modeling is adapted from a previous publication [10].

The rotatory joints $q_{ew,1}$, $q_{ew,2}$, and $q_{ew,3}$ as well as the prismatic joint $q_{ew,4}$ are located at the trocar point. The joints $q_{ew,1}$ and $q_{ew,2}$ represent the pivoting of the instrument's shaft under elastic deformation of the abdominal wall. They are limited to $-90^\circ \leq q_{ew,1} \leq 90^\circ$ and $-90^\circ \leq q_{ew,2} \leq 90^\circ$. The joint $q_{ew,3}$ allows for a rotation of the instruments shaft and is expected to be unlimited. With joint $q_{ew,4}$ the linear movement of the shaft into the abdomen is modeled. The limits $8 \text{ mm} \leq q_{ew,4} \leq 367 \text{ mm}$ ensure the shaft to completely stay inside the trocar. The full length of the shaft $l_{ew,1} = 375 \text{ mm}$ is used to represent the shaft's shape for the collision monitoring only. The first wrist joint between the shaft and the wrist link $l_{ew,2} = 9.3 \text{ mm}$ is limited to $-85^\circ \leq q_{ew,5} \leq 85^\circ$ by design. The second wrist joint is limited to $-105^\circ \leq q_{ew,6} \leq 105^\circ$. The grasper is modeled as a rigid link $l_{ew,3} = 17 \text{ mm}$ without representing the grasping movement, which is neglected in this paper. For collision monitoring the diameter of all links are considered with $d_{ew} = 8 \text{ mm}$.

Additionally the kinematics and shape of the da Vinci Si HD by Intuitive Surgical Inc. is modeled in the same way as the EndoWrist instruments. Differences are the limits of the linear movement of the shaft into the abdomen $8 \text{ mm} \leq q_{sc,4} \leq 379 \text{ mm}$ and the full length of the shaft $l_{sc} = 387 \text{ mm}$. Furthermore, the scope has no wrist joints but an angled view axis about $\varphi_{sc} = 30^\circ$. For the collision monitoring the diameter of the shaft is considered with $d_{sc} = 12 \text{ mm}$.

The instruments' bases with the driving pulleys of the instrument as well as the robotic arms of the Da Vinci Surgical System are not modeled. Therefore, their kinematic limitations and the collisions among themselves are not represented. On the one hand, this leads to larger workspaces than the real Da Vinci Surgical System is able to execute. On the other hand, this simplification focus the problem of instrument clashing, making the results more general and independent of the system used outside the patient.

2.3 Simulation Setup and Visualization

The EndoWrist instruments were used for LESS [13, 14], but surgeons complained about a smaller workspace and more self collisions with respect to conventional use of the system. These effects will be evaluated quantitatively in this

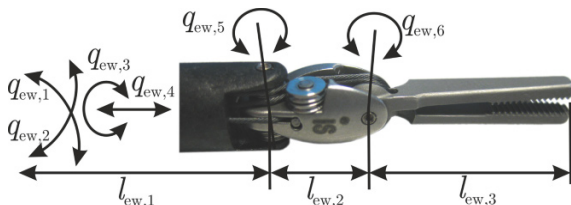


Fig. 1 Kinematik of EndoWrist long forceps, Intuitive Surgical Inc., Sunnyvale, USA

paper. Therefore, in a sequence of several simulation settings the influence of trocar distance d_t to the executable poses $p_{\text{pose},c}$ is analyzed. The simulation is simplified in a way that the trocars are positioned as corners of an equilateral triangle with origin in the center of mass (compare Fig. 2). For each simulation different trocar distances $12 \text{ mm} \leq d_t \leq 250 \text{ mm}$ are defined. Figure 2 shows the simulated situation: left trocar (compare Fig. 2b) is equipped with EndoWrist (instrument B), upper trocar with a da Vinci Si HD, and right trocar with EndoWrist (instrument A, not shown). For all trocar distances d_t the EE of instrument B has the same position $p_{\text{ee},B} = (200 \text{ mm}, 0, 0,)^T$ and is not rotated referring to the coordinate frame of origin $(CF)_0$. The view axis of the endoscope is always directed to the EE position of instrument B $p_{\text{ee},B}$ with a distance of $d_{\text{sc},\text{ee},B} = 70 \text{ mm}$. Its revolute joint is fixed and set to $q_{\text{sc},3} = 0^\circ$, so that the view comes always from the upper site.

The desired workspace shall satisfy the needs of the desired intervention. Here, a cholecystectomy is chosen [15, 16]. The position and size of the gallbladder leads to a spherical desired workspace with radius $r_{\text{ws}} = 100 \text{ mm}$ and distance of $d_{\text{ws}} = 200 \text{ mm}$ between sphere center and abdominal wall. That leads to the coordinates of the sphere center $p_{\text{ws}} = (d_{\text{ws}}, 0, 0,)^T = p_{\text{ee},B}$. Target positions are defined inside the volume with $d_p = 15 \text{ mm}$ mesh and additionally on the surface of the volume. At each target position 6^3 target orientations are defined. Altogether, this leads to $n_{\text{target}} = 4.5 \cdot 10^5$ target poses $p_{\text{target},i}$.

To get an easy interpretable visualization of the executable workspace $W_{\text{exe},A}$, a volume is estimated. As result, the shape as well as the volume of the executable workspace are approximated and visualized. Additionally, the proportion of executable orientations at each position is visualized in a color scale.

3 Results

To point out the influence of the trocar distance d_t on the percentage of executable poses $p_{\text{pose},c}$ of an EndoWrist, several simulations with a setup defined in Sect. 2.3 are performed. Figure 3 shows the results of two different trocar distances. It can be noticed, that the number of executable orientations at each position is limited to approximated 60 %. This result is caused by the limits of the wrist joints $q_{\text{ew},5}$ and

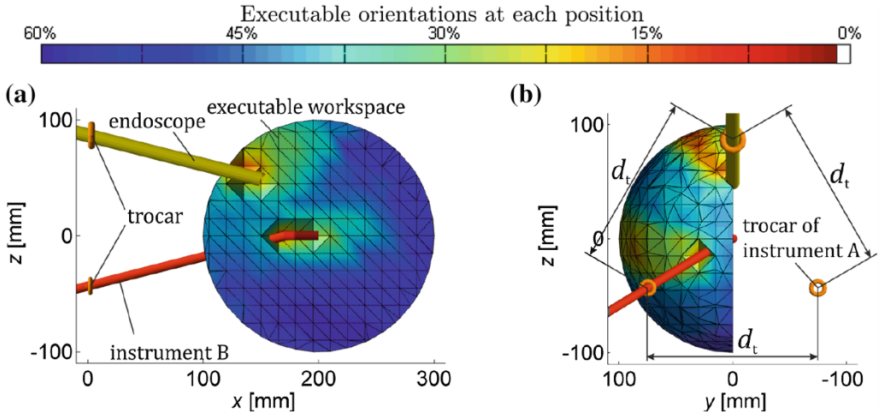


Fig. 2 Clipped executable workspace of instrument A (not shown) in a sectional view with a trocar distance $d_t = 150$ mm and a number of executable poses of $p_{pose,c} = 42.4\%$. **a** Side view. **b** Front view

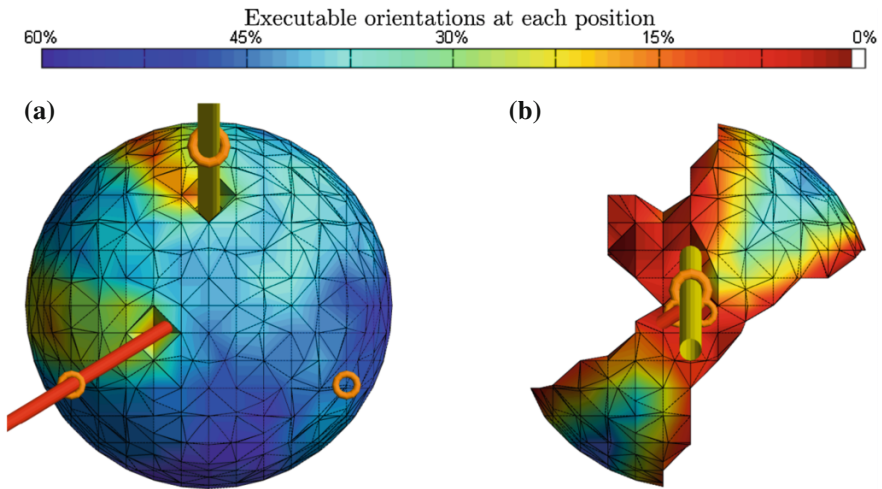


Fig. 3 Executable poses $p_{pose,c}$ of instrument A (not shown) inside of the desired workspace for different trocar distances d_t in a front view. **a** $d_t = 150$ mm; $p_{pose,c} = 42.4\%$. **b** $d_t = 14$ mm; $p_{pose,c} = 10.2\%$

$q_{ew,6}$ of instrument A. These joints inside the patient are, in addition to the joint $q_{ew,3}$ outside the patient, primarily responsible to orientate the EE. The limits of the joints $q_{ew,5}$ and $q_{ew,6}$ lead to the confinement that the EE of the EndoWrist instrument can not be angled towards its trocar point.

The number of executable orientations of instrument A is not equal at each position. This effect is caused by collisions with the instrument B and the scope, respectively. The collisions affect the executable workspace less when using bigger

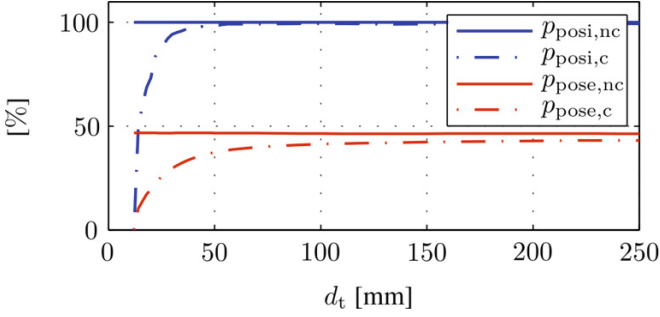


Fig. 4 Rate of executable positions not limited $p_{\text{posi,nc}}$ and limited due to collisions $p_{\text{posi,c}}$ and rate of executable poses not limited $p_{\text{pose,nc}}$ and limited due to collisions $p_{\text{pose,c}}$ of an EndoWrist Instrument with respect to the trocar distance d_t

trocar distances d_t . For example, in Fig. 3a a trocar distance of $d_t = 150$ mm is assumed. Here, the collisions affect only small areas behind the instrument B and the scope, leading to $p_{\text{pose,c}} = 42.4\%$. The influence of collisions increases when the trocar distances decreases. If the trocar distance is reduced to $d_t = 14$ mm (see Fig. 3b) some positions inside the desired volume are not executable in any orientation. The number of executable poses decreases to $p_{\text{pose,c}} = 10.2\%$.

Figure 4 gives an overview of the percentage of executable poses $p_{\text{pose,c}}$ of the instrument A with respect to the trocar distances d_t . Useful for comparison, the rate of executable positions $p_{\text{posi,c}}$ is added. Therefore, all positions inside the desired volume are considered, which are executable in at least one orientation. Additionally, the rate of executable poses and positions are calculated without considering the limitations due to collisions ($p_{\text{pose,nc}}$ and $p_{\text{posi,nc}}$).

With the last-mentioned disregard of collision detection, the executable positions $p_{\text{posi,nc}}$ and the executable poses $p_{\text{pose,nc}}$ do not give sensitive results for different surgical settings, e.g. different trocar distances d_t . Hence, self collisions have to be considered. In this case the number of executable positions $p_{\text{posi,c}}$ and the number of executable poses $p_{\text{pose,c}}$ increase while increasing the trocar distances d_t .

When the number of executable positions $p_{\text{posi,c}}$ has a almost constant value for trocar distances $d_t \leq 80$ mm, the number of executable poses $p_{\text{pose,c}}$ is still sensitive. Furthermore, the number of executable positions $p_{\text{posi,c}}$ does not indicate the systems ability of executing different orientations, being essential for performing complex tasks. The results show, the performance number $p_{\text{pose,c}}$ is sensitive enough for evaluating, comparing and optimizing laparoscopic instruments. The examined simulation shows, the executable workspace decreases dramatically while using trocar distances $d_t \leq 60$ mm. Especially in LESS the instruments have a very low distance to each other. The EndoWrist instruments seem to have some limitations for use in that settings.

4 Conclusion and Future Work

This paper introduced appropriate methods and a criterion to quantitatively rate and compare systems for laparoscopic surgery. For that purpose, a performance number, the percentage of executable poses is introduced. The proposed criterion combines the ability of an EE to reach desired positions and orientations. This performance number is convenient to be used in optimization approaches and to compare different systems. In comparison to most existing approaches, collisions are considered within the workspace analysis leading to practical results. The results show the significance of the performance number, i.e. the percentage of executable poses. Furthermore, the presented approaches are easy to adapt and transferable to different laparoscopic systems. This is the precondition for the final aim of the authors, to automatically synthesize intervention optimal kinematics for LESS equipment.

In addition, the visualization methods result in meaningful figures. Here, the number of executable positions inside the desired workspace is presented as a volume and the executable orientations are visualized in a color scale.

References

1. Guthart GS, Salisbury JK (2000) The Intuitive™ telesurgery system: overview and application. In: Proceedings of the IEEE international conference on robotics and automation. pp. 618–621, San Francisco, CA. ISBN: 0-7803-5886-4
2. Ahmed K, Wang TT, Patel VM, Nagpal K, Clark J, Ali M, Deeba S, Ashrafian H, Darzi A, Athanasiou T, Paraskeva P (2011) The role of single-incision laparoscopic surgery in abdominal and pelvic surgery: a systematic review. *Surg Endosc* 25(2):378–396
3. Rao PP, Rao PP, Bhagwat S (2011) Single-incision laparoscopic surgery—current status and controversies. *J Minim Access Surg* 7(1):6
4. Escobar PF, Haber GP, Kaouk J, Kroh M, Chalikonda S, Falcone T (2011) Single-port surgery: laboratory experience with the daVinci single-site platform. *J Soc Laparoendosc Surg* 15(2):136
5. Petroni G, Niccolini M, Menciassiz A, Dario P, Cuschieri A (2013) A novel intracorporeal assembling robotic system for single-port laparoscopic surgery. *Surg Endosc* 27(2):665–670
6. Ding J, Goldman R, Xu K, Allen P, Fowler D, Simaan N (2013) Design and coordination kinematics of an insertable robotic effectors platform for single-port access surgery. In: Proceedings of the IEEE/ASME transactions on mechatronics
7. Deutschmann B, Konietschke R, Albu-Schauffer A (2013) Task-specific evaluation of kinematic designs for instruments in minimally invasive robotic surgery. In: 2013 IEEE/RSJ international conference on intelligent robots and systems (IROS)
8. Clinical Advantages of the da Vinci S and da Vinci Si Systems Compared to the Standard da Vinci System. Intuitive Surgical Inc. (2009)
9. Xu K, Goldman RE, Ding J, Allen PK, Fowler DL, Simaan N (2009) System design of an insertable robotic effector platform for single port access (SPA) surgery. In: Proceedings of the IEEE/RSJ international conference on intelligent robots and systems (IROS)
10. Borchard JH, Kotlarski J, Ortmaier T (2013) Workspace comparison of cooperating instruments in laparo-endoscopic single-site surgery. In: Proceedings of the IEEE/ASME international conference on advanced intelligent mechatronics (AIM)

11. Pettitt JD, Miller K (2003) Sixdimensional visualisation of end-effector pose using colour spaces. In: Proceedings of the Australian conference on robotics and automation
12. Zacharias F (2012) Knowledge representations for planning manipulation tasks. Springer, Berlin
13. Ragupathi M, Ramos-Valadez DI, Pedraza R, Haas EM (2010) Robotic assisted single incision laparoscopic partial cecectomy. *Int J Med Rob Comput Assis Surg* 6(3):362–367
14. White MA, Haber GP, Kaouk JH (2010) Robotic single-site surgery. *Curr Opin Urol* 20(1):86–91
15. Kishk SM, Darweesh RM, Dodds WJ, Lawson TL, Stewart ET, Kern MK, Hassanein EH (1987) Sonographic evaluation of resting gallbladder volume and postprandial emptying in patients with gallstones. *AJR Am J Roentgenol* 148(5):875–879
16. Ko SY, Kim J, Lee WJ, Kwon DS (2007) Compact laparoscopic assistant robot using a bending mechanism. *Adv Robot* 21(5–6):689–709

A Novel, Loop-Based Approach for Rigidity Detection for Systems with Multiple Spherical–Spherical Bars: The “Double-Banana” Case

F. Simroth, H.F. Ding and A. Kecskeméthy

Abstract Rigidity detection is a very important tool for structural synthesis of mechanisms and the processing of CAD-generated models, as it helps to unveil possible sources of inconsistency in Grübler’s count of degrees of freedom (DOF) and thus to generate consistent kinematical models of complex mechanisms. This paper proposes a loop-based rigidity detection algorithm that is able to detect rigidity/mobility for special cases including multiple spherical–spherical pairs, such as the famous “double-banana” mechanism. To this end, the algorithm tracks “isolated” DOFs which are split into “fully isolated” and “transmitted isolated” DOFs. Using the independent loops as the basic building blocks, the kinematical network and its reduced loop connection graph are obtained, from which rigid sub-systems and the inherent “global” isolated rotational DOFs are recognized. The procedure is explained for the “double-banana” mechanism but is easily extended to other mechanisms.

Keywords Rigidity detection · “Double-banana” mechanism · Kinematical network · Multiple spherical joint

1 Introduction and Problem Statement

Rigidity detection has attracted researchers in the field of robotics and mechanisms since many decades as it is a necessary component in the process for automatic synthesis of mechanisms as well as the processing of CAD-generated models. The

F. Simroth (✉) · A. Kecskeméthy
University of Duisburg-Essen, Duisburg, Germany
e-mail: florian.simroth@uni-due.de

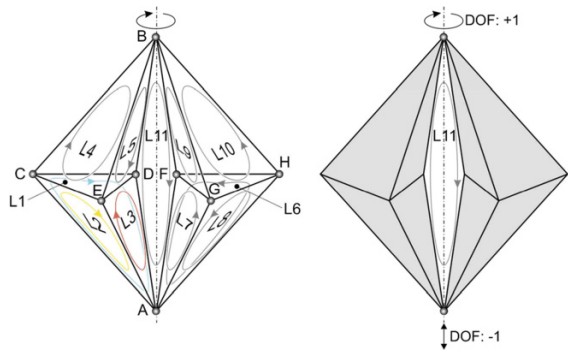
A. Kecskeméthy
e-mail: andres.kecsekemethy@uni-due.de

H.F. Ding
Yanshan University, Qinhuangdao, China
e-mail: dhf@ysu.edu.cn

problem is to identify (1) whether a mechanism contains substructures with negative DOF and if so, detect (2) the parts forming the rigid substructures, such that their negative degrees of freedom (DOF)s do not illicitly cancel out positive DOFs in other parts of the structure. Based on Laman’s theorem [1], many algorithms were proposed to detect the rigidity for both planar and simple spatial mechanisms. Hwang and Hwang [2] presented an algorithm for the detection of rigid sub-chains based on a loop-decreasing method which is limited to the detection of rigid planar kinematic chains. Lee and Yoon [3] proposed a method that involves deleting binary chains in turn to simplify the chain for rigid sub-chain detection. But the computer-aided implementation of this method has not been accomplished yet. For the first time Tuttle [4] obtained basic rigid chains with 7 or fewer links, and then attempted according to these rigid chains to identify rigid sub-chains in systems with more links. But with increasing complexity, this method can hardly be applied to mechanisms with more than 10 links. Moukarzel [5] adopted the description of a system as a collection of rigid bodies connected by bars to improve efficiency of rigidity detection. The algorithm for detecting the rigid structure in planetary gear trains is proposed by Hsu and Wu [6] while this algorithm is limited to a planar graph. Recently, a theorem based on an independent loop set is presented by Ding [7], where by three operations of loops rigidity of planar mechanisms can be detected. Xia, Ding and Kecskemethy [8] presented a loop-based method for identifying rigid subsystems based on a kinematical network.

Although many rigidity detection algorithms have been thus provided, an automatic rigidity detection algorithm for systems involving isolated DOFs, such as the famous “double-banana”, shown in Fig. 1, seems not to have been reported so far. The “double banana” consists of 18 rods connected at 8 nodes which can be interpreted as (multiple) spherical joints. If we give to each node 3 DOFs and subtract one constraint per bar, then the Grübler count gives $DOF = 0$, thus suggesting that the structure is rigid. However, one can clearly “see” that the double banana structure consists of two rigid bipyramids, one at the left and one at the right, which are coupled together by two spherical joints (A and B). Thus there is an “implied edge” [9] between A and B about which the two halves can rotate with respect to each other, while the longitudinal direction along this edge is overconstrained with $DOF = -1$.

Fig. 1 The “double banana” mechanism



Another famous test equation for rigidity is Maxwell's rule [10] proposed in 1864, which states that a statically and kinematically determined framework with b bars and j joints follows the equation

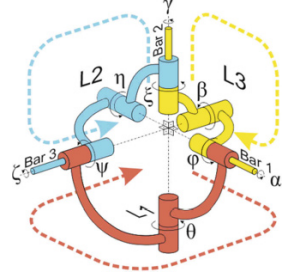
$$b = 3j - 6 \quad (1)$$

It is obvious that a bipyramid (single banana), with 9 bars and 5 joints (correctly) satisfies the condition of the Maxwell's rule. However, also the "double-banana" structure obeys the Maxwell's rule, although it is obviously not rigid. Thus, this structure is a classical (non-trivial) example of a mechanism satisfying Maxwell's rule of a statically and kinematically determined framework, but which is nevertheless generically able to move, and which has thus attracted considerable attention in the literature: Fowler [11] analyzed the symmetry of the structure, and presented the result of the symmetry of multiple banana mechanisms; Cheng and Sitharam [9] studied the rigidity of the 3D structure with the "double-banana" as an example; and Rojas [12] proposed the position analysis based on the closure condition of the "double-banana".

The cause for the double-banana paradox is that there exist in the mechanism "isolated" DOFs (at the outset a total of 18 "isolated"—i.e. immaterial—DOFs as rotations of the bars about their axis) which create an own level of transmission kinematics, which in some parts become overconstrained, while in others remain as "free". An algorithm for identifying mobility/rigidity must thus be able to track these isolated DOFs in order to detect where they are overconstrained and where they can spin freely.

We propose in this paper a novel procedure for tracking such isolated DOFs by viewing the structure not as an assembly of bars and joints, but as a system of interconnected kinematical loops, called the "kinematical network" [13]. The interconnected kinematical loops are chosen as a set of "smallest" independent loops, termed a minimal cycle basis, in which the sum of numbers of relative joint variables within each loop over all loops is smallest. While the number n_L of independent loops is unique and is given by $n_L = n_G - n_B + 1$, where n_G is the number of proper (binary) joints and n_B is the number of bodies, the choice of the independent loops is not unique. In the present case we choose the 11 independent loops shown in Fig. 1. Note that, apart from loop L11, which is quadrilateral, all loops are triangles, each "corner" being embodied by a spherical joint. At the beginning, each loop is regarded as an independent transmission element, i.e., all relative motions within a loop are regarded as independent. When several loops are incident to one joint, kinematical balance equations may arise between the relative internal loop variables, stating e.g. for spherical joints that the product of rotation matrices of the relative rotations defined within each incident loop at the spherical joint yields unity (=3 dependencies). As shown in [13], the number of kinematical balance conditions at each joint is equal to $n_C = n_L - n_B + 1$, where n_L is the number of incident loops and n_B is the number of incident bodies at the joint. Clearly, for the loop basis of Fig. 1, the loop coupling condition gives one spherical coupling condition at joints E, G, D and F and two spherical coupling conditions at joint A.

Fig. 2 Loop coupling conditions at a multiple spherical joint



2 Coupling Conditions and Kinematical Network

When multiple loops coincide at one spherical joint, one can always decompose the relative rotations within a loop into two terminal rotations about the connecting bars, and one intermediate rotation about some arbitrary axis, which should however be warranted never to become parallel to one of the rods over the complete motion. Figure 2 shows such a decomposition for the three loops L1, L2 and L3 of the left banana coinciding at spherical joint A in Fig. 1. For each bar, one can register exactly one rotation about this bar as fully isolated, as it does not have any influence on the internal and external kinematics of the loops. In the example of Fig. 2, these are rotations α and γ about bars 1 and 2 within loop L3, and rotation ζ about bar 3 within loop L2, respectively, which are arbitrary and “invisible” and which have thus been “welded” with the joint sleeve for better traceability. The further loops incident to this joint introduce additional, superposed bar rotations which although isolated within the corresponding loop transmit to the other neighboring loops. In the example of Fig. 2, the superposed locally isolated rotation ξ of loop L2 transmits to the intermediate rotation θ of loop L1, and thus is clearly a “transmitted” isolated DOF. Moreover, the two locally isolated DOFs ψ and ϕ of loop L1 are a function of the relative rotations \underline{R}_2 (ξ, η, ζ) and \underline{R}_3 (α, β, γ) of loops L2 and L3 according to the kinematical spherical closure condition

$$\underline{R}_1(\phi, \theta, \psi) = \underline{R}_2(\xi, \eta, \zeta) * \underline{R}_3(\alpha, \beta, \gamma). \quad (2)$$

Assuming for example Euler (z - x - z) angles decomposition, the dependent rotation \underline{R}_1 (ϕ, θ, ψ) can be resolved in terms of the three unknown angles ϕ, θ , and ψ as a function of the 2×3 “inputs” of the coupling condition α, β, γ and ξ, η, ζ .

Using the coupling conditions described in Sect. 1, one obtains for the double-banana example of Fig. 1 the kinematical network shown in Fig. 3. In this kinematical network, the following peculiarities can be observed:

- (1) Each of the loops L1, ..., L10 display 3 local DOFs, which are the three isolated DOFs about the three bars; likewise, loop L11, which comprises four spherical joints, displays 6 local DOFs.

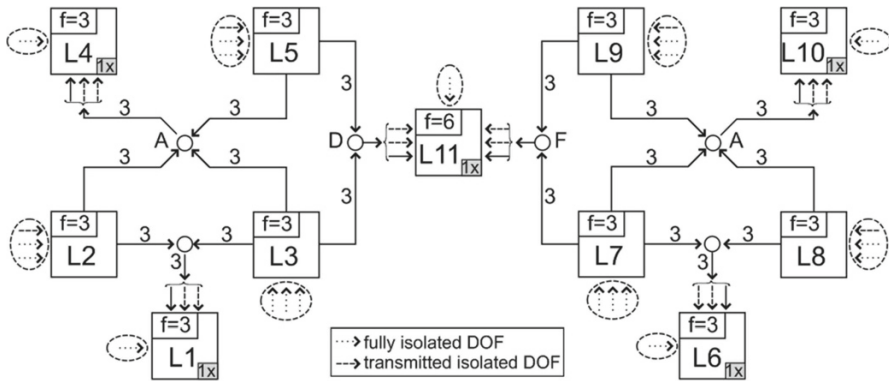


Fig. 3 The kinematical network of the “double-banana” mechanism

- (2) At each coupling joint, three coupling equations according to Eq. (2) are produced. Two of these coupling conditions go into isolated DOFs, while one propagates into a transmission angle, which is the opening angle of the intermediate joint of the z-x-z decomposition.
- (3) By the sink method, one can start the orientation of the edges by choosing candidates for a sink. These are loops for which the number of existing connection edges is less or equal than the local DOF of the loop. For the example at hand, the sink loops are L1, L4, L6, L10 and L11. However, for each of these loops, the “intermediate” coupling angle (θ in the case of loop L1) actually transmits into the loop kinematics and is subject to a constant condition there (due to the triangle condition it follows $\theta = \text{const.}$). Thus the sink loop actually introduces an implicit equation (marked “1x” in a gray box within the loop) which must be fulfilled by the transmitted DOFs entering the loop. On the other hand, each sink loop features an additional fully isolated DOF, which is about the third edge that is not shared with any other loop. Note that in the kinematical network of Fig. 3, and for all figures below, we will use dotted lines for fully isolated DOFs and dashed lines for transmitted isolated DOFs, respectively.
- (4) After having determined all sinks, the remaining loops are completed by feeding enough inputs to each loop such that the local loop DOF count is obeyed. Here, it is important that exactly (only) *one* fully isolated DOF is registered for each bar; thus if already registered by another loop the local isolated DOF of a loop becomes a “transmitted” isolated DOF. In the example of Fig. 3, we registered all three isolated DOFs of loop L3 as fully isolated; thus in loop L2 we can only register two isolated DOFs as fully isolated, while the third (about the common bar with L3) must be chosen as a transmitted isolated DOF. Moreover, after receiving its inputs at joints D and F, loop L11 detects a fully isolated DOF about the axis connecting joints A and B (as the distance between the two centers of the spherical joints is invariant under the

six joint variables contained in joints A and B), which is registered as an additional fully isolated DOF operating on this loop.

- (5) The fully isolated DOFs can be applied irrespectively of the rest of the structure, thus from Fig. 3 one can see that there are in total 19 fully isolated DOFs, 18 representing the spins of the bars, and one in loop L11 representing the spinning rotation between the two bananas about the implied axis A-B. Thus the kinematical network already is able to detect that, apart from the 18 isolated bar spins, loop L11 features an additional DOF that is not cancelled by the rest of the structure. However, it remains to detect which parts of the structure are rigid or over-rigid. This is done in the next section.

3 Loop Connection Graph and Rigidity Detection

As described in [8], a kinematical network can be transformed into a “loop connection graph” describing the level of dependency of the individual loops and possible implicit conditions. We show here the loops as boxes and implicit conditions as gray disks, with the number n of implicit equations denoted by “ n x” within the disk, and the indices i, j, \dots of loops L_i, L_j, \dots embracing these implicit conditions in braces besides the disk. The connections between loops and circles are represented by weighted edges, where the weight represents the number of joint variables transferred through this edge. External inputs are depicted by edges from the source “S” to the corresponding loop, while the level of dependency is expressed by the distance (in rows) from the source to the node, as shown in Fig. 4.

According to [8], rigidity detection can be performed on this acyclic graph by evaluating directed ‘cuts’ such that the source is on one side, the sink(s) is on the other, and all edges through which the cut passes are directed from the ‘upstream’ to the ‘downstream’ side. Such cuts can be easily determined using state-of-art graph-theoretic methods [14]. The sum of weights of the cut edges is termed the *weight* of the cut, while the sum of implicit equations in the downstream side of the cut is termed the *absorbing degree* of the cut. The DoF of the cut is equal to its weight minus its absorbing degree. This DoF is equal to the DoF of the nodes on the downstream side of the cut. Whenever the DoF of the cut is less or equal to zero, the

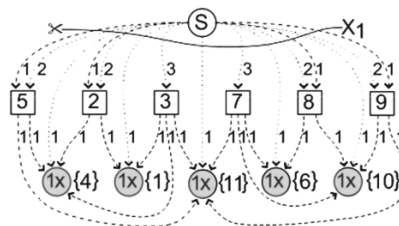


Fig. 4 The loop connection graph of Fig. 3

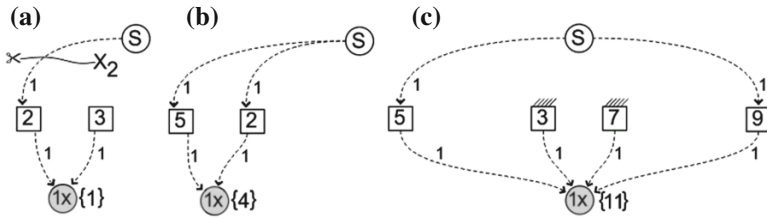


Fig. 5 Pruned graphs for each of the four special shared joints. a, b, c

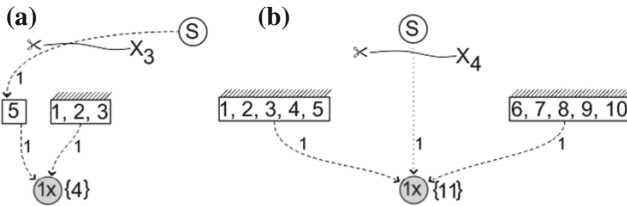


Fig. 6 Minimal cuts and resulting DOFs for each substructure. a, b

downstream subsystem will represent a rigid or an overconstrained subsystem. The cut with the minimal DoF will determine the most overconstrained substructure. Clearly, the cut X_1 in Fig. 4 displays a weight of 4, and an absorbing degree of 5, thus the whole structure is over-rigid with $DOF = -1$. However, as there is additionally a fully isolated DOF entering loop L11, this over-rigid structure also features one proper DOF. Thus the structure is further analyzed to detect the rigid subsystems involved in the structure.

Since the isolated degrees need not be taken into account for rigidity detection, only the transmitted isolated DOFs (dashed lines) are now of interest. In order to simplify the search for adequate cuts, the loop connection graph is decomposed in “pruned” subgraphs for each sink, each being the sub-graph obtained when removing all nodes that are not on any path from the sink to the source (Fig. 5). Clearly, only one such pruned sub-graph has a cut with non-positive DOF (X_2 in Fig. 5a). Thus the subsystem $\{L_1, L_2, L_3\}$ can be replaced by a rigid body. Restarting the algorithm with these loops replaced by a rigid body gives Fig. 6a, which again displays a cut X_3 with $DOF = 0$, hence the subsystem $\{L_1, L_2, L_3, L_4, L_5\}$ is again rigid. Replacing this again by a rigid body and carrying out the analogous steps for the right half of the double banana graph gives the pruned graph of Fig. 6b. This graph has now a cut X_4 with transmitted weight zero (not counting the fully isolated DOF of loop L11) and an absorbing degree of 1, hence the cut has $DOF = -1$. Thus the algorithm detects both halves of the double banana as rigid, and also detects that their assembly into loop L11 features one fully isolated DOF (the spin rotation about the implied edge A–B) and one overconstrained direction with $DOF = -1$ (the longitudinal direction of edge A–B).

4 Conclusions

Based on the concept of the kinematical network, the present method is able to detect mobility and rigidity for systems featuring spherical–spherical pairs, such as the double banana case. The method consists in viewing the mechanism as an assembly of coupled independent kinematical loops instead of regarding it as a system of coupled bodies and joints (or of bars and nodes). Due to this, it is possible to track isolated degrees of freedom separately from transmitted joint angles, and by this to dissect rigid subsystems and superimposed local mobility. We believe that the method can be extended to more complex systems involving spherical–spherical connections, such as the nucleation-free examples presented in [9]. In this setting, it is interesting to note that there may exist bi-directed (acausal) connections between pairs of nodes for transmitted and isolated DOFs, respectively.

References

1. Laman G (1970) On graphs and rigidity of plane skeletal structures. *J Eng Math* 4(4):331–340
2. Hwang WM, Hwang YW (1991) An algorithm for the detection of degenerate kinematic chains. *Math Comput Modell* 15:9–15
3. Lee HJ, Yoon YS (1992) Detection of rigid structure in enumerating basic kinematic chain by sequential removal of binary link string. *JSME Int J Ser 3 Vib Control Eng Eng Ind* 35:647–651
4. Tuttle ER (1996) Generation of planar kinematic chains. *Mech Mach Theory* 31:729–748
5. Moukarzel C (1996) An efficient algorithm for testing the generic rigidity of graphs in the plane. *J Phys A: Math Gen* 29(24):8079–8098
6. Hsu CH, Wu YC (1997) Automatic detection of embedded structure in planetary gear trains. *J Mech Des* 119:315–318
7. Ding H, Huang Z, Mu D (2008) Computer-aided structure decomposition theory of kinematic chains and its applications. *Mech Mach Theory* 43:1596–1609
8. Xia S, Ding H, Kecskemethy A (2002) A loop-based approach for rigid subchain identification in general mechanisms. In: *Latest Advances in Robot Kinematics*, pp 19–26
9. Cheng J, Sitharam M, Streinu I (2009) Nucleation-free 3d rigidity. In *Proceedings of the 21st Canadian conference on computational geometry (CCCG2009)*, pp 71–74
10. Maxwell JC (1864) On reciprocal gures and diagrams of forces. *Philos Mag* 4(27):250–261
11. Fowler PW, Guest SD (2002) Symmetry analysis of the double banana and related indeterminate structures. In Drew HR, Pellegrino S (eds) *New approaches to structural mechanics, shells and biological structures*, pp 91–100
12. Rojas N, Thomas F (2013) The closure condition of the double banana and its application to robot position analysis. In: *IEEE international conference on robotics and automation (ICRA) Karlsruhe, Germany*, pp 6–10
13. Kecskemethy A (1993) On closed form solutions of multiple-loop mechanisms. In: Angeles J, Hommel GE, Kovacs PE (eds.) *Computational kinematics*, pp 263–274
14. Abel U, Bicker R (1982) Determination of all minimal cut-sets between a vertex pair in an undirected graph. *IEEE Trans Reliab R-31(2):167–171*

Planar Four-Link Mechanism Analysis for Application in 3D Printing Machines

A. Klodowski

Abstract The aim of the paper is to present planar pantograph mechanism analysis that can be used to aid design of new mechanics for desktop 3D printers. Matlab code for inverse and forward kinematics was developed and equations are presented in this study. Theoretical accuracy of the proposed design indicate that the proposed mechanism could provide similar accuracy to 3D printers based on linear Cartesian systems, at the same time reducing complexity of the mechanics, with slight increase in the complexity of the controller software.

Keywords Parallel mechanics · Inverse kinematics · Forward kinematics

1 Introduction

Rapid development in the 3D printing is mostly focused on developing new materials and improved polymer deposition processes [1]. Fused filament fabrication seems to dominate the current market, especially in the low-price community developed 3D printing machines [2]. Cartesian kinematics, due to the simplicity of the control is dominating current solutions—30 out of 35 solutions for RepRap printers [3] are based on Cartesian kinematics. Delta robots [4] (3 constructions on RepRap page¹) or kinematics based on cylindrical coordinates (1 construction on RepRap page) have also been employed in several projects but so far did not beat the popularity of the linear stages of motion. There is also one prototype that utilizes solution under development that represents same concept as proposed in this article.

¹ http://reprap.org/wiki/RepRap_Options.

A. Klodowski (✉)
Lappeenranta University of Technology, Lappeenranta, Finland
e-mail: adam.klodowski@lut.fi

Small number of non-Cartesian mechanics indicate opening for the development in the mechanical aspects of the 3D printer's design. This paper represents feasibility study, where applicability of the planar parallel robotics kinematics for the horizontal motion of the 3D printing nozzle is verified using forward kinematic model. To ease implementation of the control, also inverse kinematic model for the mechanism is developed. Finally discussion presenting optimal table size 3D printer mechanism is presented with remarks concerning accuracy and controllability of the system.

2 Materials and Methods

Forward and inverse kinematic model for the four-link mechanism is derived and implemented in Matlab. The mechanism model is parametric, and the mechanism is assumed to be symmetric. Lengths of first stage arms are thus equal and denoted by L_1 , and the lengths of second stage arms are equal and denoted by L_2 . Distance between the first-stage arm bearing and the coordinate system origin is denoted d . Coordinate frame used for model development is fixed at the middle between first-stage arm bearings. Illustration of the mechanism is presented in Fig. 1. Rotational joints are characteristic points of the mechanism and are marked as P_1 , P_2 , and P_3 in the derivations as indicated in Fig. 1b. Presented mechanism has two degrees of freedom. Printing nozzle is located at point P_3 , while rotary actuators at the origins of the first-stage arms.

2.1 Forward Kinematics

Independent parameters of the mechanism are angles α_1 and α_2 . Position of the point P_3 on the x-y plane is the dependent variable. Positive direction of angles α_1 and α_2 are indicated by the arrows in Fig. 1b. Origin of the coordinate system is marked with blue arrows in Fig. 1a, b. Position of the point P_3 depends on the angles α_1 and α_2 , as well as on the length of the arms and distance between origins of the first-stage arms. Position of point P_1 can be derived using the following equation.

$$P_1 = \begin{bmatrix} d + L_1 \cos(\alpha_1) \\ L_1 \sin(\alpha_1) \end{bmatrix} \quad (1)$$

Similarly, position of the point P_2 can be derived using Eq. (2).

$$P_2 = \begin{bmatrix} -d - L_1 \cos(\alpha_2) \\ -L_1 \sin(\alpha_2) \end{bmatrix} \quad (2)$$

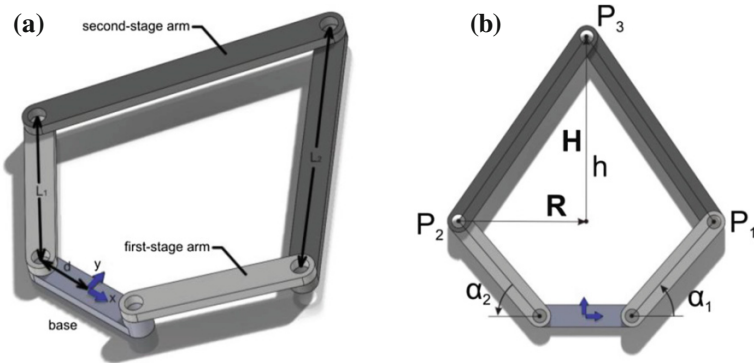


Fig. 1 Model of the 4-link mechanism. **a** Isometric view. **b** Top view with basic parameters

It can be noticed, that points $P_1, P_2,$ and P_3 create an isosceles triangle. The middle point at the base of this triangle can be found using vector, \mathbf{R} , lying on the line between points P_2 and P_1 , and having the magnitude of the half of the P_2 to P_1 distance.

$$\mathbf{R} = \frac{P_1 - P_2}{2} \tag{3}$$

Let's denote the height of this triangle as h , then h can be computed using the following equation.

$$h = \sqrt{L_2^2 - \frac{(P_{1x} - P_{2x})^2}{4} - \frac{(P_{1y} - P_{2y})^2}{4}} \tag{4}$$

where indexes x and y indicate corresponding coordinates of the points P_1 and P_2 . Height of the triangle can also be represented by a vector, \mathbf{H} , pointing from the center of the triangle's base to the tip. Because vector \mathbf{H} is perpendicular to the vector \mathbf{R} , 90° counterclockwise rotation of vector \mathbf{R} will yield direction of vector \mathbf{H} . Therefore vector \mathbf{R} , can be derived as follows.

$$\mathbf{H} = \begin{bmatrix} 0 & 1 \\ -1 & 0 \end{bmatrix} \mathbf{R} \frac{h}{|\mathbf{R}|} \tag{5}$$

In Eq. 5, $|\mathbf{R}|$ is the length of vector \mathbf{R} , and $\begin{bmatrix} 0 & 1 \\ -1 & 0 \end{bmatrix}$ represent rotation matrix for counterclockwise 90° rotation. Using vector sum, point P_3 can be found.

$$P_3 = P_1 - \mathbf{R} + \mathbf{H} \tag{6}$$

2.2 Inverse Kinematics

In inverse kinematics, the location of point P_3 is the independent variable, while orientations of first-stage links, α_1 and α_2 , are the dependent variables. Points P_1 , P_3 , P_0 form a triangle. Let's consider edge $P_3 - P_0$ as the base of the triangle and denote its length by a . Then the height of this triangle can be denoted as h_1 , and the fragment of the base between point P_0 and the height is referred as a_1 as indicated in Fig. 3. Point P_0 can be defined as follows.

$$P_0 = \begin{bmatrix} d \\ 0 \end{bmatrix} \quad (7)$$

Length of the base, a , can be formulated as in the Eq. 8.

$$a = \sqrt{(P_{3x} - P_{0x})^2 + (P_{3y} - P_{0y})^2} \quad (8)$$

Length of the part of the base, a_1 can be computed then as follows.

$$a_1 = L_1 \frac{(L_1^2 + a^2 - L_2^2)}{2L_1 a} \quad (9)$$

Height of this triangle, h_1 , can be computed using Pythagoras's theorem as shown in Eq. 10.

$$h_1 = \sqrt{L_1^2 - a_1^2} \quad (10)$$

Vector \mathbf{R}_1 from Fig. 2 can be formulated as follows.

$$\mathbf{R}_1 = (P_3 - P_0) \frac{a_1}{a} \quad (11)$$

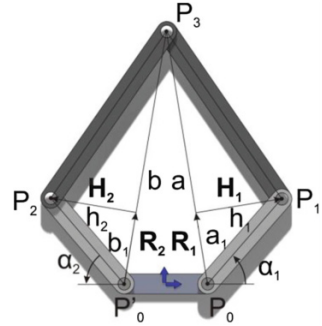
Vector \mathbf{H}_1 , that has magnitude h_1 and lies on the height of the triangle, it can be computed as a 90° clockwise rotation of vector \mathbf{R}_1 normalized to the magnitude h_1 .

$$\mathbf{H}_1 = \begin{bmatrix} 0 & -1 \\ 1 & 0 \end{bmatrix} \mathbf{R}_1 \frac{h_1}{a_1} \quad (12)$$

Point P_1 can then be found using vector sum of vectors \mathbf{H}_1 and \mathbf{R}_1 .

$$P_1 = P_0 + \mathbf{R}_1 + \mathbf{H}_1 \quad (13)$$

Fig. 2 Parameters of the inverse kinematics model



Knowing location of point P_1 , the orientation of the right first-stage link, α_1 , can be found using Eq. 14.

$$\alpha_1 = \text{asin}\left(\frac{P_{1y} - P_{0y}}{L_1}\right) \tag{14}$$

Due to the assumption that α_1 is in the range $\pm 90^\circ$, the asin function is deterministic. Location of point P_2 , required to determine α_2 can be derived in analogical way. Point P_0' is symmetrically located to point P_0 with respect to the y axis of the coordinate system.

$$P'_0 = \begin{bmatrix} -d \\ 0 \end{bmatrix} \tag{15}$$

The length of base b of triangle P_2, P_0, P_3 has to be determined.

$$b = \sqrt{(P_{3x} - P'_{0x})^2 + (P_{3y} - P'_{0y})^2} \tag{16}$$

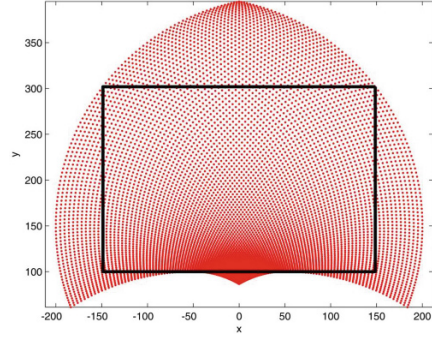
Length of the part of the base, b_1 , between point P_0' and the height can be computed then as follows.

$$b_1 = L_1 \frac{(L_1^2 + b^2 - L_2^2)}{2L_1 b} \tag{17}$$

Height of this triangle, h_2 , can be computed using Pythagoras's theorem as shown in Eq. 18.

$$h_2 = \sqrt{L_1^2 - b_1^2} \tag{18}$$

Fig. 3 Usable workspace of the optimized mechanism with maximum rectangle area section highlighted



Vector \mathbf{R}_2 from Fig. 3 can be formulated as follows.

$$\mathbf{R}_2 = (P_3 - P'_0) \frac{b_1}{b} \quad (19)$$

Vector \mathbf{H}_2 , that has length h_2 and lies on the height of the triangle, can be computed as a 90° counterclockwise rotation of vector \mathbf{R}_2 with the magnitude h_1 .

$$\mathbf{H}_2 = \begin{bmatrix} 0 & 1 \\ -1 & 0 \end{bmatrix} \mathbf{R}_2 \frac{h_2}{b_1} \quad (20)$$

Point P_2 can then be found using vector sum of vectors \mathbf{H}_2 and \mathbf{R}_2 .

$$P_2 = P'_0 + \mathbf{R}_2 + \mathbf{H}_2 \quad (21)$$

Knowing location of point P_2 orientation of the left first-stage link, α_2 , can be found using Eq. 22.

$$\alpha_2 = \text{asin}\left(\frac{P_{2y} - P'_{0y}}{L_1}\right) \quad (22)$$

3 Discussion

Using the forward kinematic model, printing space can be obtained for different mechanism parameters. Moreover, theoretical accuracy of positioning can be studied when the accuracy of orientation measurement is known. Build area in horizontal plane of common desktop 3D printers varies between 180×180 up to 200×252 mm. Therefore, as an optimization objective build area of 200×200 was assumed. Distance between first-stage arms was assumed 100 mm to accommodate space for motors and optionally the transmission. Maximizing workspace is

achieved by allowing -90 to 90° motion for each of the first-stage arms. If first-stage arms' length and distance between rotation axes of the first-stage links are considered as independent variables, the second stage arms' length can be computed. When both first-stage arms are at zero degrees position (pointing outwards), the condition for minimum second-stage links can be determined.

$$L_{2min} > L_1 + d \quad (23)$$

To avoid instability point at the $L_2 = L_1 + d$, the length of the secondary arms is assumed 50 mm larger than the sum on the right-hand side of the Eq. 23. Integer linear programming optimization was used for the mechanism parameters estimation [5]. Optimization target function was maximization of the rectangular area that can be fitted within the achievable print area. Additional condition was achieving rectangular print area of at least 200×200 mm. The results of the optimization was $L_1 = 150$ mm, and $L_2 = 250$ mm, yielding maximum rectangular printing area of 297×201 mm. The achievable printing range is indicated in Fig. 4.

The plot presented in Fig. 4 is the result from forward dynamics kinematics run with 1.8° step size for α_1 and α_2 parameters varied between -90 and 90° . It can be seen, that the position accuracy is distributed relatively uniform. Only in the extreme positions of the end effector along the y axis for x coordinate close to zero, the positioning accuracy is increased. Those zones can be used for printing small details, which require higher precision.

RepRap 3D printers as well as many commercial designs use most commonly Nema 17 stepper motors, which can offer 1.8° or 0.9° step resolution [3]. With direct drive setup this would result in positioning accuracy in the least accurate region within ± 3.81 , and ± 2.95 for x and y directions respectively for 1.8° motor step size. This is insufficient for quality 3D printing operation. To increase the accuracy, either micro stepping control can be used, which with good controller can achieve 1/16 of the step resolution, yielding ± 0.15 , and ± 0.2 mm positioning accuracy. However, to reach sufficient resolution close to ± 0.01 mm achievable in Cartesian systems, transmission is required. To provide smooth motion and avoid backlash, toothed belt drive would be preferred in this application. Provided 1:8 transmission ratio is used with micro stepping controller capable of dividing step to 16 parts, the accuracy would reach ± 0.015 and ± 0.025 mm for the x and y directions respectively. Theoretically further refinement of the accuracy could be obtained with even more advance stepper motor controller, capable of higher step division, practically however, reduction of the torque of the motor positioned in between steps would result much lower than the theoretically computed accuracy [6]. However, smoother motion between steps would be achieved.

In many desktop 3D printers rotary to linear motion is transmitted using belt drive. Usually systems use pulley diameter around 20 mm. In the new design gear ratio of 1:8 is assumed. Using those assumptions comparison of rotary velocities of motors in Cartesian and new design can be made. Due to the fact that deposition of material is most accurate when the tool moves at constant velocity, thus constant 100 mm/s velocity condition will be used in all the test cases. Five test cases

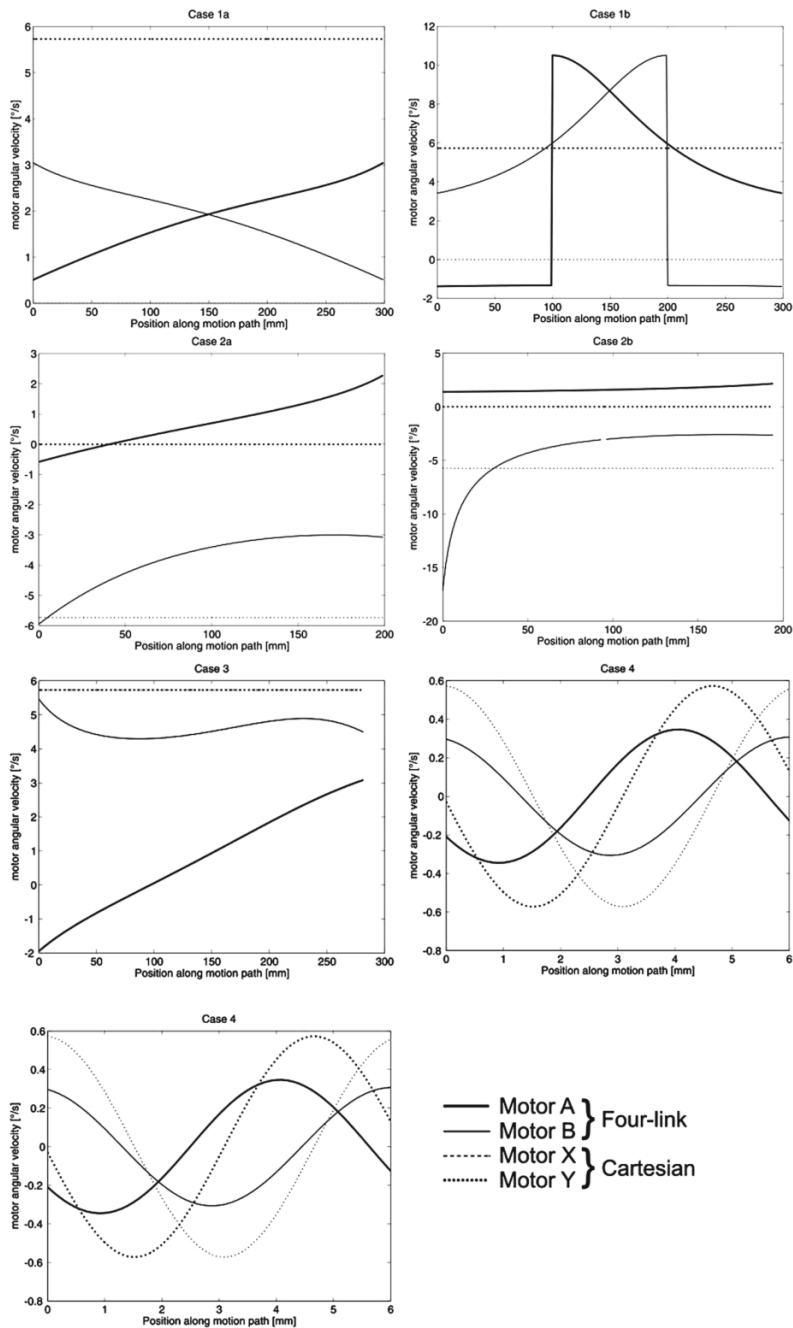


Fig. 4 Motor angular velocity profiles versus position along motion path

representing typical moves of the printing nozzle will be shown to compare velocity profiles of x-y motion stages motors in Cartesian and in the new solution.

Case 1 is straight line along printer's x axis (a) at the upper edge of the rectangular print area and (b) at the lower edge. Case 2 is straight line along y axis (a) at the edge of the print area, (b) above rotary joint in the base ($x = 50$). Case 3 is a diagonal line at 45° with respect to the x axis. Case 4 is small circle of 2 mm diameter placed in a corner of printer's work area. Finally, case 5 is a large circle, 190 mm in diameter, placed in a corner of printer's work area.

Inverse kinematic model allows for estimation of motors angular positions at each single motion stage. Discrete derivative can be then computed to solve motors angular velocity profiles during the motion (see Fig. 4). In all the cases, printing head velocity is a non-linear function of motor velocities in the four-link mechanism. However, to maintain the same printing head velocity as in the Cartesian system, the maximum motor velocity will be lower in the new system for all of the presented cases except 1b and 2b. Case 2b can be used to determine maximum printing speed achievable by the system, while case 1b can be used to determine the lowest y coordinate that should be practically reached by the system during printing. For Cartesian system location of a feature does not influence the velocity profile of the motors, however in the four-link mechanism it is not the case.

4 Conclusions

Based on the simulation of the presented mechanism, it is concluded that this mechanism could be used for 3D printer planar motion of the printing head providing comparable accuracy to traditional Cartesian system based on linear motion. With the slight increase of control algorithm complexity, great simplification of the mechanics is achieved and multi arm, multi nozzle setups could be created using this concept to parallelize the printing process. Replacing linear stages of motion allows reducing the weight of moving parts, therefore higher speed of printing can be expected. In addition ball-bearings are maintenance-free in comparison to linear bearing which require scheduled lubrication and cleaning.

Further work on the prototype will be concluded to verify practical feasibility of the proposed solution, and to study the control.

References

1. Kłodowski A, Eskelinen H, Semken S (2014) Leakage-proof nozzle design for RepRap community 3D printer. *Robotica FirstView*:1–26
2. Fonda C (2013) A practical guide to your first 3D print. In: *Low-cost 3D printing for science, education and sustainable development*, 1st edn. ICTP—The Abdus Salam International Centre for Theoretical Physics 2013 ICTP Science Dissemination Unit, pp 25–60

3. Jones R, Haufe P, Sells E, Iravani P, Olliver V, Palmer C, Bowyer A (2011) RepRap—the replicating rapid prototyper. *Robotica* 29:177–191
4. Pierrot F, Reynaud C, Fournier A (1990) DELTA: a simple and efficient parallel robot. *Robotica* 8(1):105–109
5. Lenstra HW Jr (1983) Integer programming with a fixed number of variables. *Math Oper Res* 8(4):538–548
6. McGuinness J (1994) Advantages of five phase motors in microstepping drive. In: IEE colloquium on stepper motors and their control, pp 1–1

Part III
Mechanism Design

Path Generating Belt Mechanisms as Kinematic Chains for Mechatronic Applications

E.-C. Lovasz, D. Perju, K.-H. Modler, C.M. Gruescu, D. Mărgineanu, C.E. Moldovan and C. Pop

Abstract The paper deals with a special type of planar belt mechanism with two degrees of freedom. Belt mechanisms achieve in principle any movement task, precisely, in a defined range, by using a belt as a flexible and inextensible element and at least one profiled wheel (non-circular wheel), on which the belt is enveloped or developed. In order to use belt mechanisms in mechatronic applications, the increasing of the degree of freedom and the use of simple circular wheel are required. The control of the actuator's movement makes theoretically possible the generation of any movement task in the wheel's plane.

Keywords Belt mechanism · Mechatronic system · Flexible element · Kinematic analysis

E.-C. Lovasz (✉) · D. Perju · C.M. Gruescu · D. Mărgineanu · C.E. Moldovan · C. Pop
Politehnica University of Timișoara, Timișoara, Romania
e-mail: erwin.lovasz@upt.ro

D. Perju
e-mail: dan.perju@upt.ro

C.M. Gruescu
e-mail: corina.gruescu@upt.ro

D. Mărgineanu
e-mail: dan.margineanu@upt.ro

C.E. Moldovan
e-mail: cristian.moldovan@upt.ro

C. Pop
e-mail: cristian.pop@upt.ro

K.-H. Modler
Technische Universität Dresden, Dresden, Germany
e-mail: karl-heinz.modler@tu-dresden.de

1 Introduction

Belt mechanisms, in comparison with linkages, are suitable for generating non-linear transmission functions or special paths, as they use links with variable length. The variable length link consists of a belt as a flexible and inextensible element enveloped or developed on at least one profiled wheel (non-circular wheel). Belt mechanism allows theoretically the reproducing of any transmission function (between input-output parameters), with a theoretically absolute accuracy in a defined range of the input parameters, given by manufacturing conditions and with a minimum number of elements, i.e. four.

Hain [1] began with the study of the belt mechanisms as periodical mechanisms. The study was continued by Dizioglu in [2] with an analytical dynamic analysis of belt mechanisms used in weaving looms. In [3] Hain deals with the grapho-analytical synthesis of the belt mechanism with 4 elements. Bayer, by means of using the Euler relationships, presents in [4] a grapho-analytical analysis method for computing the kinematic parameters of the belt mechanism. The development of the computation capacities allowed the development of analytical methods for analysis and synthesis of belt mechanisms. Thus, an analytical method using the tangent condition between the belt and non-circular wheel(s) and the preservation of the total length of the belt (free and enveloped length) is presented in [5, 6, 9]. Papers [7, 8] and [9] present an analytical method using the relationship between the evolute and involute considering the inverse movement. The analytical methods were developed for path generating [6, 9] and function generating [7, 8] belt mechanisms respectively.

Authors of [10–12] developed analysis methods for belt mechanisms with circular wheels, which are centric or eccentric jointed. Ebert modeled the belt mechanisms and then computed the dynamic behavior [13, 14].

In order to integrate the belt mechanism in mechatronic systems it is necessary to adjust the variable link lengths to the various movement tasks. For this requirement, it is necessary to increase the degree of freedom of the mechanisms and to use a simple circular wheel instead of a particular non-circular wheel. Theoretically, any movement task is possible to generate through the control of the actuator's movement.

2 Structural Synthesis of the 5-Link Belt Mechanism

The 5-link belt mechanisms are planar mechanisms, which contain a centrode kinematic pair, accomplished by enveloping or developing of a belt on a profiled or circular wheel. The belt is considered flexible, inextensible and permanently tensile loaded, in order to be assimilated to instantaneous rigid links. For the structural synthesis, the other kinematic pairs are chosen with one degree of freedom $f = 1$: revolute or prismatic pair.

The condition to have a constrained motion is:

$$2 \cdot e_1 - 3 \cdot n + 3 + F = 0, \quad (1)$$

where:

e_1 The number of the kinematic pairs with $f = 1$,

n The number of elements

The condition (1) is satisfied for $e_1 = 5$, $n = 5$ and the degree of freedom (DOF) $F = 2$. That means the two driving movements (inputs) must be correlated and controlled according with the imposed kinematic task. The systematic development of the mechanism structure considered the 4 possible kinematic chains and the Reuleaux structural method, which considers an element of the kinematic chain as frame, two other elements as driving and one as driven elements. The structural synthesis of the 5-link belt mechanism structures is shown in Fig. 1, where R means revolute kinematic pair, P—prismatic kinematic pair and C—centrode kinematic pair. The notation of the developed structures comprises the sequence of the joints type and the frame element of the chain in brackets.

The choice for useful structures of 5-link belt mechanisms needs some boundary conditions: all driving elements should be jointed to the frame and one of them should be the circular wheel.

3 Kinematic Analysis of the 5-Link Belt Mechanisms as Path Generating Ones

The 5-link belt mechanism of type RRRCR(e) considers the profiled wheel as circular wheel and the frame length equal to zero (see Fig. 2). The simple manufacturing of the circular wheel allows a continuous adjustment, which recommends this mechanism structure for the use in mechatronic applications. The permanent tensile load of the belt can be realized by means of a compression spring between the 2 rigid links or a belt, manufactured of composite material with axial rigidity. The link 2 and the circular wheel 5 are driving elements.

The movement task of the 5-link belt mechanism as path generating mechanism is the exact tracing of a given curve:

$$K = x(t) + i \cdot y(t), \quad (2)$$

with the parameter $t \in [0, 1]$.

With the notations in Fig. 2, the same coupler point K can be described by the relationship in complex numbers:

$$K = l_2 \cdot e^{i \cdot \varphi(t)} + l_5 \cdot e^{i(\alpha + \vartheta(t))}. \quad (3)$$

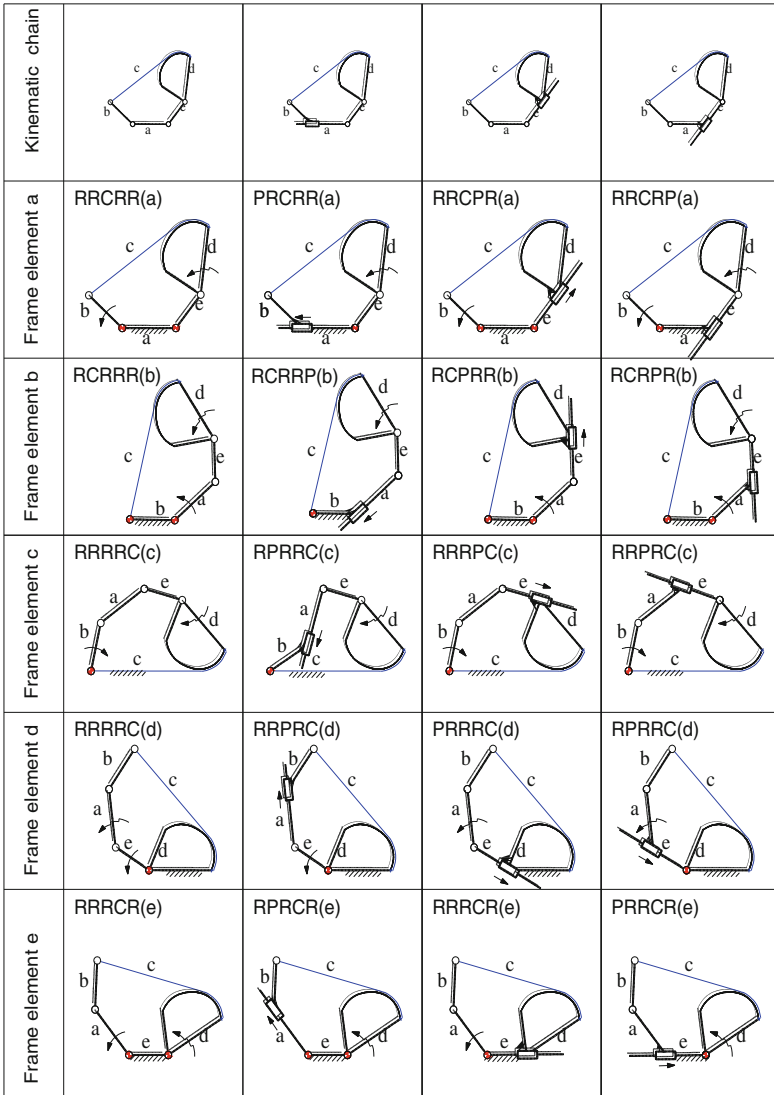
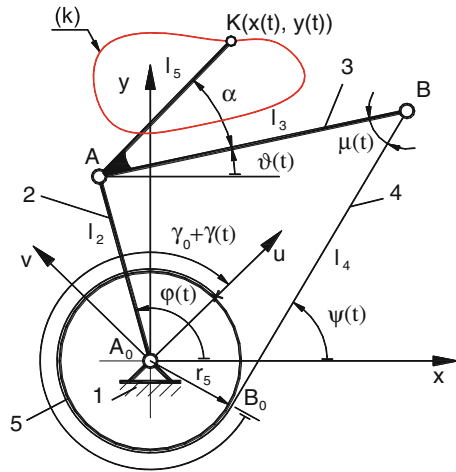


Fig. 1 Structural synthesis of the 5-link belt mechanisms

Fig. 2 5-link belt mechanism for generating of a circular path



By equalizing Eqs. (2) and (3) and eliminating the exponent $\alpha + \vartheta(t)$ results:

$$\varphi(t) = 2 \cdot \arctan \frac{B(t) \pm \sqrt{A^2(t) + B^2(t) - C^2(t)}}{A(t) - C(t)}, \quad (4)$$

where:

$$A(t) = 2 \cdot l_2 \cdot x(t) \quad B(t) = 2 \cdot l_2 \cdot y(t) \quad C(t) = l_5^2 - x^2(t) - y^2(t) - l_2^2. \quad (5)$$

Through multiplication of relationship (3) with its complex conjugate relationship:

$$\bar{K} = l_2 \cdot e^{-i \cdot \varphi(t)} + l_5 \cdot e^{-i(\alpha + \vartheta(t))}. \quad (6)$$

the positional angle of the coupler 3 results:

$$\vartheta(t) = \varphi(t) - \alpha + \arccos \left(\frac{x^2(t) + y^2(t) - l_2^2 - l_5^2}{2 \cdot l_2 \cdot l_5} \right). \quad (7)$$

The joint B of the belt mechanism RRRCR(e) can be described with two polygonal loops in the fixed axes system xCy:

$$B = l_2 \cdot e^{i \cdot \varphi(t)} + l_3 \cdot e^{i \cdot \vartheta(t)}, \quad (8)$$

$$B = (l_4(t) - i \cdot r_5) \cdot e^{i \cdot \psi(t)}, \quad (9)$$

where the developed length of the belt l_4 is:

$$l_4(t) = l - [\gamma_0 + \gamma(t)] \cdot r_5, \quad (10)$$

with l —the total length of the belt, r_5 —the radius of the circular wheel and γ_0 —the initial wrapped belt angle for $t = 0$.

The relationships (8) and (9) allow the calculus of the angle $\gamma(t)$ of the belt in the mobile system of the wheel and the calculus of the drive angle $\psi(t)$ of the wheel. These angles are:

$$\gamma(t) = \frac{l - \sqrt{l_2^2 + l_3^2 - r_5^2 + 2 \cdot l_2 \cdot l_3 \cos(\varphi(t) - \vartheta(t))}}{r_5} - \gamma_0, \quad (11)$$

$$\psi(t) = 2 \arctan \frac{r_5 \mp \sqrt{r_5^2 + l_4(t)^2 - (l_2 \cos \varphi(t) + l_3 \cos \vartheta(t))^2}}{l_4(t) + l_2 \cos \varphi(t) + l_3 \cos \vartheta(t)}. \quad (12)$$

According with the relationships (4) and (12), which allow the computation of the parameterized drive angles $\varphi(t)$ and $\psi(t)$, it is feasible to generate different imposed curves (2) with the 5-link belt mechanism. The ranges of the movement tasks depend on the workspace of the coupler point. The kinematic parameters will be computed according to the geometrical parameters depending on time.

4 Example Problems for Generating Different Paths

The example problems consider that the belt mechanism RRRCR(e) should generate different paths as circular curve and a path as straight line. In both cases, it is preferable to express their equations in a parametric form, which is more recommended for control of the drives.

The path as circular curve is given through the equations:

$$x(t) = a_0 + R \cdot \cos 2\pi \cdot (t_0 + t), \quad y(t) = b_0 + R \cdot \sin 2\pi \cdot (t_0 + t), \quad (13)$$

and as straight line through the equations:

$$x(t) = a_1 + (a_2 - a_1) \cdot t, \quad y(t) = b_1 + (b_2 - b_1) \cdot t, \quad (14)$$

with the parameter $t \in [0, 1]$ and the initial parameter of the path t_0 . This will be computed according with the initial drive angle ($t_0 \rightarrow \varphi_{\min}$).

The chosen geometrical parameters of the belt mechanism RRRCR(e) are given in Table 1.

Table 1 Geometrical parameters of the belt mechanisms

Frame length	$l_1 = 0$ mm	Coupler length	$l_3 = 70$ mm	Belt length	$l = 256.8$ mm
Crank length	$l_2 = 50$ mm	Coupler length	$l_5 = 30$ mm	Wheel radius	$r_5 = 30$ mm
		Coupler angle	$\alpha^\circ = 120^\circ$		

The path should belong to the workspace of the coupler point. The workspace of the coupler points $(x_K(t), y_K(t))$ is defined as a concentric range between the boundary circles:

$$l_2 - l_5 < \sqrt{x_K(t)^2 + y_K(t)^2} < l_2 + l_5. \tag{15}$$

Through the correlation between the drive angle φ and the circle path parameter, t , it results that the driving element 2 should perform a swing movement. In order to avoid the singularities, it is necessary to have the transmission angle always positive and $\mu(t) > \mu_{\min}$, where:

$$\mu(t) = \psi(t) - \vartheta(t). \tag{16}$$

In Figs. 3, 4 and 5 are shown the 5-link belt mechanisms in two extreme positions with the corresponding drive angles $\varphi(t)$ and $\gamma(t)$, the transmission angle $\mu(t)$ and the belt angle $\psi(t)$ in the reference system for three different movement tasks. Table 2 gives the chosen parameters for the paths from Figs. 3, 4 and 5.

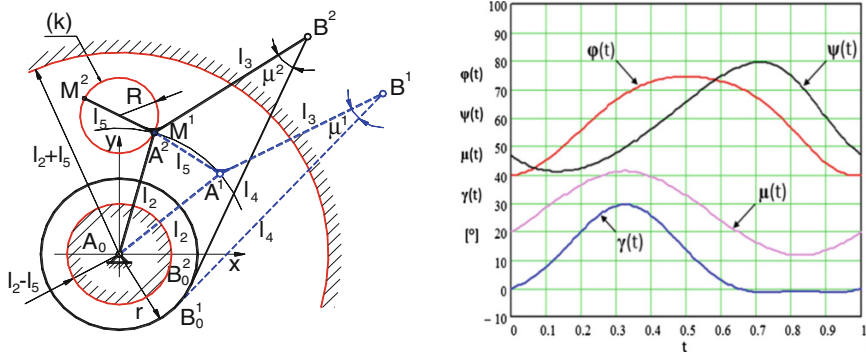


Fig. 3 Examples of 5-link belt mechanism for generating of a circular path (circle 1)

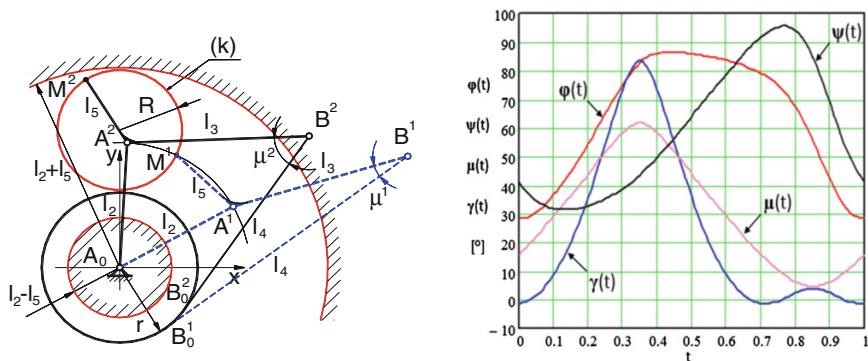


Fig. 4 Examples of 5-link belt mechanism for generating of a circular path (circle 2)

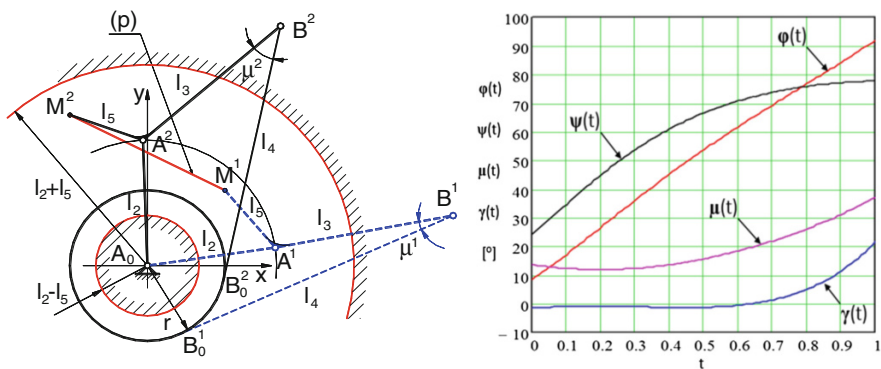


Fig. 5 Examples of 5-link belt mechanism for generating of a circular path (straight line)

Table 2 Path's geometrical parameters

Circle 1	$a_0 = 0$ mm	$b_0 = 55$ mm	$R = 15$ mm	
Circle 2	$a_0 = 0$ mm	$b_0 = 55$ mm	$R = 24$ mm	
Straight line	$a_1 = 30$ mm	$a_2 = -30$ mm	$b_1 = 30$ mm	$b_2 = 60$ mm

5 Conclusions

The 5-link belt mechanism is a special type of planar belt mechanism with two degrees of freedom, which achieves any movement task precisely in a defined range, through using a belt as a flexible and inextensible element and at least one particular profiled wheel as circular wheel. The presented examples, calculated using MathCAD demonstrate that through the control of the actuators (driving elements) is possible to generate theoretically any paths in the wheel's plane.

The 5-link belt mechanism is smaller in size and allows larger workspace in comparison with the similar 5-bar linkage, having the same link lengths.

This characteristic recommends the 5-link belt mechanism for use in mechatronic applications, such as kinematic chains of mobile robots, planar manipulators, etc. The authors intend to develop an optimal synthesis of the 5-link belt mechanism in order to optimize the control of the actuators and to use it in mechatronic applications.

References

1. Hain K (1953) Periodische Bandgetriebe. VDI-Zeitschrift 95(6):192–196
2. Dizioglu B (1956) Zur Dynamik des einfachen Bandgetriebes mit Anwendung auf die Synthese der Schlagmechanismen der Webstühle. VDI-Berichte 12:55–62
3. Hain K (1957) Einfache Bandgetriebe, VDI-461. VDI Verlag, Düsseldorf
4. Beyer R, Goodman TP (1958) Beschleunigungsermittlung in Bandgetrieben und Zahnstangen - Kurbelgetrieben. Konstruktion 10(1):10–16
5. Luck K, Modler K-H (1992) Burmester-theory for band-mechanisms. Mech Des Synth ASME 46:55–59
6. Wadewitz C (1997) Ein Beitrag zur Analyse und Synthese von einfachen viergliedrigen Bandgetrieben. PhD thesis, Dresden
7. Modler K-H, Lovasz E-C (1997) Viergliedrige Bandgetriebe als Übertragungsgetriebe. In: Proceedings of SYROM'97, Bucuresti, 1, pp 209–216
8. Lovasz E-C (1998) Synthese der Übertragungsgetriebe mit Anwendungen in der Feinmechanik. PhD thesis, Dresden/Timişoara
9. Modler K-H, Wadewitz C, Lovasz E-C (1998) Viergliedrige Bandgetriebe und ihre Anwendungen, VDI-1423, Kassel, VDI Verlag, pp 289–308
10. Modler K-H, Lovasz E-C (2000) Verstellmöglichkeiten in Bandgetriebe. In: Proceedings of MTM 2000, Timişoara, 1, pp 179–184
11. Moldovan CE (2011) Contribuţii la analiza şi sinteza mecanismelor având cuple cinematice de tip centroidal. PhD thesis, Timişoara
12. Perju D, Lovasz E-C, Modler K-H, Moldovan CE, Carabaş I (2012) Kinematic analysis of a belt mechanism with a circular eccentric output element. In: Proceedings of MMT and Robotics, Clermont-Ferrand, France, pp 183–188
13. Ebert F, Berger M, Heinrich S (2011) Ganzheitliche Systemsimulation komplexer Antriebssysteme mit nichtlinearer Charakteristik. In: Proceedings of 9. Kolloquium Getriebetechnik, Chemnitz, pp 395–418
14. Ebert F, Berger M (2012) Band mechanism with nonlinear gear ratio for gravity force balance: design and analysis in total system network. Adv Mech Des Mech Mach Sci 8:21–26

Synthesis of a Mechanism for Human Gait Rehabilitation: An Introductory Approach

Pedro Alves, Francisco Cruz, Luís F. Silva and Paulo Flores

Abstract The traditional concept of physical rehabilitation focused on maximizing the remaining body functions in a way that patients used them in a compensatory fashion. Recently, it has been observed that the repetition of task oriented motions proved to improve muscular strength and movement coordination in patients with neurologic or orthopedic impairments. Traditional physiotherapy is laborious and expensive, and may present undesired variability in the movement cycles between sessions. The use of robotic and mechanical devices allows for greater repeatability in movements. It also decreases the number of required therapists as the degree of exhaustion allowing to increase the sessions time and number. This paper intends to present the methodology to build a gait rehabilitation device of low cost, complexity and high adaptability, based on a four bar linkage.

Keywords Gait rehabilitation · Mechanism design · Four bar linkage · Biomechanics

1 Introduction

Human Gait (HG) is an apparently natural, fluid and flexible action; however this highly complex action requires the integration of locomotion and motor control mechanisms with the musculoskeletal function. It relates the interaction of muscle

P. Alves (✉) · F. Cruz · L.F. Silva · P. Flores
University of Minho, Braga, Portugal
e-mail: pedro.orlando.alves@gmail.com

F. Cruz
e-mail: a58843@alunos.uminho.pt

L.F. Silva
e-mail: lffsilva@dem.uminho.pt

P. Flores
e-mail: pflores@dem.uminho.pt

forces, the movement of several body joints and the action of external forces. HG is a particular form of animal locomotion, for it is bipedal and reveals itself to be highly efficient and functional. To achieve healthy HG it is required the integration of the central nervous system with several sensorial stimuli in order to control the different components which act on the skeletal system with different degrees of freedom. People who suffer from any sort of gait impairment experience a great decrease in its quality of life. These impairments are often the result of injuries, neurological and musculoskeletal pathologies. In the latter cases, which include Parkinson's disease, strokes, spinal cord injury or neuromuscular diseases, have been reported to alter HG patterns in specific sorts [1].

Traditional HG rehabilitation strategies in irreversible strength deficit as well as in motor control and balance failure presuppose a compensatory perspective, this meaning, instead of correcting the impairment it embraces and enables it. In order to achieve a given objective, the patient learns to compensate his disability through alternative means or to alter the task/living environment. A more recent rehabilitation approach considers the introduction of repetitive locomotive training as soon as the patient is able to perform simple gait cycles. This approach as shown positive results in patients suffering from neurological conditions such as Parkinson's disease; spinal cord injuries, stroke and recovery from arthroscopy surgery. Following this approach, several mechanical and robotic devices were developed such as the Hocoma's Lokomat. Although the trajectory performed by the subject's ankle is not exactly planar, these devices acted to manipulate his limb's trajectory in the sagittal plane with successful results [2].

Traditional physiotherapy requires at least three therapists to perform lower limbs movement cycle, has low reproducibility in the gestures performed in different sessions and presents itself as laborious, tiring and expensive. Mechanical and robotic devices decrease each sessions required number of therapists to one, have high movement cycle reproducibility and allow a greater number of gait cycles performed as for longer rehabilitation sessions. However available devices are costly, making them only available to large rehabilitation centers.

Projects have recently been developed in order to develop linkages that simulate human walking, using the Chebyshev mechanism or 8 bar linkages [3, 4]. However, the four bar linkage is one of the most common, simple and versatile mechanisms. It presents different geometrical relations between its components, as it does between its input/output movements. These are characteristics that endorse the four bar linkages popularity. It is often found in several biomedical applications such as lower limb rehabilitation devices [1]. This work presents the design of a simple, cost effective and highly adaptable device for human gait rehabilitation. It intends to establish a method for the synthesis of a four bar linkage, which can be used to generate a gait pattern on the sagittal plane, with the final objective of patient rehabilitation.

2 Human Gait

Walking is one of the most common of the human motions and although man does not have the ability to walk since birth, once learnt it becomes practically sub-conscious. Most people follow the same basic walking pattern, however several features of the musculoskeletal structure, such as limb lengths, body mass and shape or stride length, influence their individual movement. HGs research literature focus itself in the study and interrelation of gait parameters, some of which referred in Table 1, and on the gait cycle using a kinetic, kinematic and energetic approach. These provide valuable information that allows greater understanding of healthy and pathological gait. However, they may be only comparable with well-defined gait conditions and variables such as age, gender and weight.

A common view is that walking is a dynamical process where the body centre of mass (BCOM) is periodically brought further forward than the limit of static stability, causing the body to fall forward, and then, by placing a foot forward in time, an actual fall is prevented. In healthy HG, the pathway of the BCOM is a smooth, regular curve that moves up and down in the vertical plane with an average rise and fall of about 4 cm. The low point is reached when both feet are on the ground; the high point occurs at midstance. The BCOM is also displaced laterally in the horizontal plane during locomotion, with a total side-to-side distance traveled of about 5 cm. The motion is toward the weight-bearing limb and reaches its lateral limits in mid-stance. The combined vertical and horizontal motions of the COM of the body describe a double sinusoidal curve [5]. These movements, which occur in planes closer to the coronal and transverse planes of the body, have greater individual variations which result on a distinct individual way of walking.

HG uses gravity as main driving force, which is very economic muscular energy wise. Lettre and Contini [6] have described human and animal locomotion by having three distinct stages: development stage (from rest to constant velocity), rhythmic stage (constant average velocity), and decay stage (back to rest). The term “free speed of walking” relates to the rhythmic stage and is an important reference because most will adopt a walking speed that consumes the less energy and its patterns of movements are remarkably consistent between individuals [7]. This is a useful concept for diagnosing individuals before and after treatment.

A complete gait cycle is defined as the movement from one foot strike to the successive foot strike on the same side. Descriptions of walking are normally

Table 1 Gait variables and descriptors

Variable	Descriptors
Temporal-spatial	Velocity; cadence; stance duration; step length; stride length
Kinematic	Trunk flexion; trunk lateral flexion; anterior pelvic tilt; pelvic obliquity; pelvic rotation; hip extension, hip adduction; knee flexion initial contact; knee flexion mid-stance; ankle flexion initial contact; lateral COM displacement
Kinetic	Push-off terminal stance
Energetic	Oxygen cost; oxygen consumption

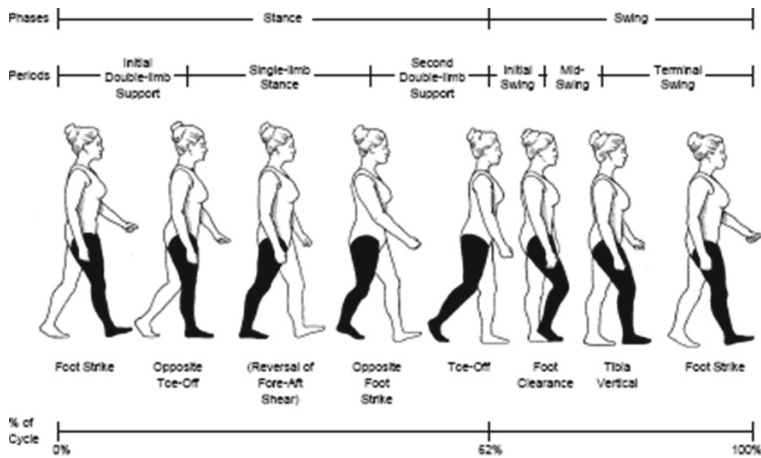


Fig. 1 Phases and periods of the gait cycle (adapted from [10])

confined to a single cycle, with the assumption that successive cycles are similar. Two key events delineate and limit the gait cycle: foot strike and foot-off. Since there are two extremities, there are four events: foot strike, opposite foot-off, opposite foot strike, and foot-off. The entire cycle repeats itself with the second foot strike (see Fig. 1). These four basic events define two gait phases: stance and swing. It is common to describe the cycle in terms of percentage thus allowing normalization of the data for multiple subjects. Therefore, initial foot strike is designated as 0 % and the successive same foot strike as 100 %. In normal subjects, the opposite limb repeats the same sequence of events, but is 180° out of phase. In normal gait there is a natural symmetry between the left and right sides, but in pathological gait an asymmetrical pattern very often exists [8].

The stance phase comprises the period between foot strike and ipsilateral foot-off (62 %). It is the percentage of the gait cycle when the reference foot is in contact with the ground and is commonly divided into three periods [8]: (i) *Initial double limb support* (foot strike to opposite foot-off) when both feet are in contact with the ground. It is characterized by a very rapid loading onto the forward limb with shock absorption and slowing of the body's frontal momentum; (ii) *Single limb support* (opposite foot-off to opposite foot strike) when the left foot is swinging through and only the right foot is in ground contact. The opposite leg is in swing, and the weight-bearing limb is in single limb stance. Forward shear reverses to aft shear, the center of mass falls, and forward and vertical velocity increase; (iii) *Second double limb support* (opposite foot strike to foot-off) when both feet are again in ground contact. As weight is transferred rapidly to the forward limb, the trailing limb is in preparation to swing forward in front of the body.

The swing phase starts with a foot off, ends at second ipsilateral foot strike, and can be subdivided into three periods [8]: (i) *Initial swing* (foot-off to foot clearance), begins as the foot leaves the ground and the subject activates the hip flexor muscles to accelerate the leg forward; (ii) *Midswing* (foot clearance to tibia vertical), occurs when

the foot passes directly beneath the body, coincidental with midstance for the other foot; (iii) *Terminal swing* (tibia vertical to foot strike), describes the action of the muscles as they slow the leg and stabilize the foot in preparation for the next heel strike.

3 Ankle Trajectories

The intended device should be able to manipulate the subjects ankle into perform a trajectory that mimics that of a healthy way of walking. The used gait parameters are available on an online database [9]. The acquired data corresponds to joint angles and is used to order to calculate the vertical and horizontal ankle displacement, the desired movement pattern. These angles are commonly used because they are more scalable and may be normalized to a full gait cycle. Figure 2 represents the proposed kinematic model of the hip and knee and correspondent joint angles one may use to obtain the ankles trajectory.

Equation (1) is considered here to determine the ankles trajectory, where x_i and y_i represent the ankles Cartesian coordinates in a given instant of the gait cycle, x_H and y_H correspond to the hip reference position, L_1 and L_2 are the length of the anatomic segment between the hip joint-knee joint and knee joint-ankle joint, respectively, and are calculated as a function of the subjects height (H) through Eqs. (2) and (3). Finally, θ_H and θ_K are the angles represented in Fig. 2.

$$i (1, \dots, n) = \begin{cases} x_i = x_H + L_1 \times \sin \theta_{H,i} + L_2 \times \sin(\theta_{H,i} - \theta_{K,i}) \\ y_i = y_H + L_1 \times \cos \theta_{H,i} - L_2 \times \cos(\theta_{H,i} - \theta_{K,i}) \end{cases} \quad (1)$$

$$L_1 = 0.245H \quad (2)$$

$$L_2 = 0.246H \quad (3)$$

Thus, the resulting ankle trajectory is represented in Fig. 3, which is the objective of the mechanism synthesis of the four bar linkage considered in this study.

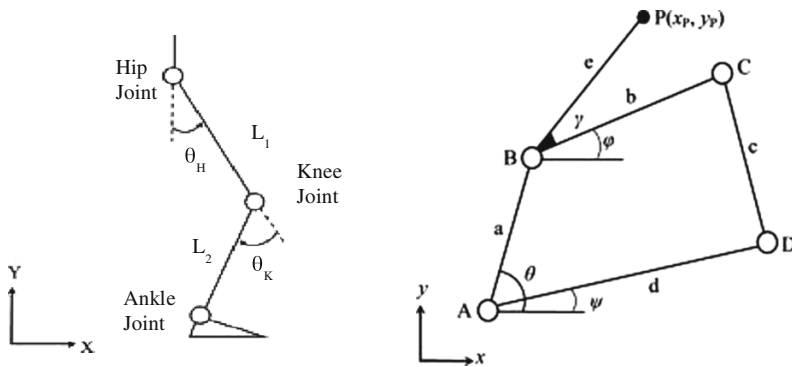
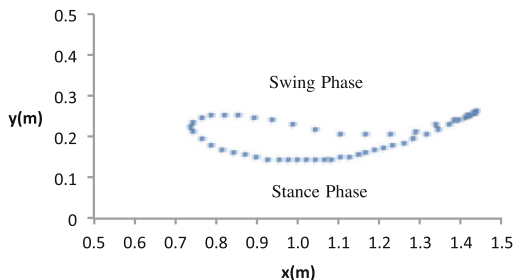


Fig. 2 Adopted leg kinematic model (left) and representation of a four bar linkage (right)

Fig. 3 Ankle trajectory in the sagittal plane



4 Kinematic Synthesis of the Mechanism

The selected mechanism to develop the present project is the well-known four bar linkage due to its versatility and simplicity. An example of a four bar linkage is represented in Fig. 2. After determining the desired trajectory one must find the parameters that allow for the development of the four bar linkage that ensures the replication of the required trajectory. These parameters are the coordinates of the reference point A , lengths of the links (a , b , c , d), angle ψ , and the couplers length and angle (e and γ), as it is illustrated in Fig. 2.

Hrones and Nelson [10] present a comprehensive atlas that contains several coupler curves and comparing the desired curve with the ones available in this reference work. Thus, one may find tabled values for the linkage parameters. In the present work, the considered reference values were as follows: $a = 1$; $b = 2.5$, $c = 2$, $d = 3$, $e = 2.8$ and $\gamma = 10^\circ$, $\psi = 0^\circ$, which permit the representation of the curve plotted in Fig. 4. As the values presented by this book represent the relative dimensions of the bars, the values above presented are dimensionless. The Interactive Four-Bar Coupler Curve Plotting [11] allows for the performing a quick verification of these results. Although the shape of the curve is similar, the orientation and size of this curve should resemble the most to the experimental results, demanding for an optimization procedure.

Equations (4)–(6) are utilized to calculate the couplers point P (see Fig. 4) that describes the desired trajectory and to adjust the linkage size and orientation.

$$x_p = x_a + a \cos \theta + e \cos(\varphi - \gamma) \quad (4)$$

$$y_p = y_a + a \sin \theta + e \sin(\varphi - \gamma) \quad (5)$$

$$2ab \cos(\varphi - \theta) - 2bd \cos \gamma - 2ad \cos \theta + a^2 + b^2 + d^2 - c^2 = 0 \quad (6)$$

In order to better adjust the initial and desired coupler curves, a factor of 0.7 relatively to the size of the links is calculated, thus reaching the values for each link length as follows $a = 0.70$; $b = 1.75$; $c = 1.40$; $d = 2.10$; and $e = 1.96$. Finally, the new orientation angle (ψ) found is equal to 25.40° . Since the movement of the ankle

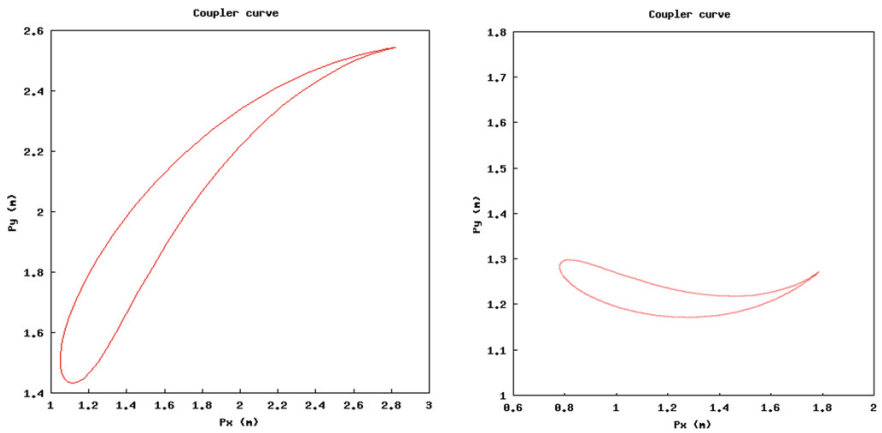


Fig. 4 Initial (*left*) and obtained trajectory (*right*) of the four bar linkage

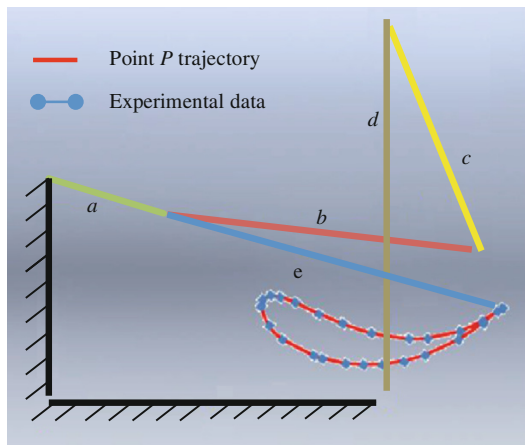
must be fluid and continuous, the mechanism must allow for such a behavior. Therefore, one must verify if the Grashof criterion is fulfilled, as follows in Eq. 7:

$$C_d + C_a < C_b + C_c \tag{7}$$

For the parameters previously found, we have that $2.8 < 3.15$, and the Grashof criteria is satisfied, guarantying the intended continuous movement of the linkage.

Figure 5 represents a generic position of the resulting four bar mechanism under analysis, in which the red line is the trajectory performed by the linkage and the dots are the experimental data are plotted. It can be observed the good correlation between the two.

Fig. 5 Representation of the solution for the designed linkage and trajectory. Symbols *a–e* represent the four bar links



5 Concluding Remarks

In this work, a procedure to deal with a synthesis a mechanism for human gait rehabilitation has been presented. The synthesis method allows for the design of a four bar linkage which replicates the trajectory of the human ankle in a continuous manner. Although this methodology ensures a possible solution for this problem this is not an optimal solution. Thus, future work includes an optimal solution through the minimization of the deviation between the actual ankle trajectory, and the trajectory of the linkage via computational and numerical techniques. Then, a 3D computational model will be considered to help the fabrication of a physical prototype. Finally, it must be said that, the final goal is the development of prototype with view to clinical testing. The devices features should include haptic and passive characteristics as well as be of easy maintenance, and grant easy access and use to patient and therapist.

References

1. Ball SJ, Brown IE, Scott SH (2007) A planar 3DOF robotic exoskeleton for rehabilitation and assessment Engineering in Medicine and Biology Society. EMBS 2007. In: 29th annual international conference of the IEEE 22–26, pp 4024–4027
2. Jezernik S, Colombo G, Keller T, Frueh H, Morari M (2003) Robotic orthosis lokomat: a rehabilitation and research tool. *Neuromodulation* 6(2):108–115
3. Araidah O et al (2011) Conceptual design of a single DOF human-like eight bar leg mechanism. *Jordan J Mechan Indus Eng* 5(4):285–289
4. Copilusi M, Ceccarelli N, Dumitru G (2013) Carbone, design and simulation of a leg exoskeleton linkage for a human rehabilitation system. In: The 11th IFToMM international symposium on science of mechanisms and machines (SYROM'13 Brasov), Springer, Dordrecht, pp 117–125
5. Chambers HG, Sutherland DH (2002) A practical guide to gait analysis. *J Am Acad Orthop Surg* 10:222–231
6. Lettre C, Contini R, (1967) Accelerographic analysis of pathological gait. New York University School of Engineering and Science Technical Report 1368-01
7. Sutherland DH (2007) The evolution of clinical gait analysis part III—kinetics and energy assessment. *Gait Posture* 21:447–461
8. Sutherland DH, Kaufman KR, Moitza JR (2006) Kinematics of normal human walking. In: Rose J, Gamble JG (eds) *Human walking*, 3rd edn. Williams and Wilkins, Baltimore, pp 34–51
9. CGA Normative Gait Database. <http://www.clinicalgaitanalysis.com/data/>. Assessed on 03 Mar 2014
10. Hrones JA, Nelson GL (1951) Analysis of the four-bar linkage: its application to the synthesis of mechanisms. Technology Press of the Massachusetts Institute of Technology, and Wiley, New York
11. Interactive Four-Bar Coupler Curve Plotting. <http://www.softintegration.com/>. Assessed on 03 Mar 2014

A Form-Closed Cam-Follower Mechanism for a Breath Simulator Machine

R.F. Oliveira, P. Flores, S.F. Teixeira, H.M.C. Marques
and J.C. Teixeira

Abstract The worldwide incidence of asthma yields 250,000 deaths annually, being almost all of these deaths avoidable. The inhalation therapy is the preferable route to deliver bronchodilator/anti-inflammatory drugs to the patient lungs. Within this route of treatment, pressurized Metered Dose Inhalers (pMDI's) are the cornerstone devices. When coupled with a Valved Holding Chamber (VHC), its efficiency increases and the limitations almost vanish. The VHC devices efficiency is something of interest to measure. For that, it is necessary an experimental setup that evaluates the amount of drug delivered by the device. This setup shall replicate a human breath waveform as input, therefore a breath simulator machine was build. The report herein describes the project process of the form-closed cam-follower mechanism necessary to replicate the waveform. The design and dimensional constrains are input in the cam design, leading to a piston diameter of 63.0 mm and a cam base diameter of 250.0 mm. A performance analysis to the pressure angle, curvature radius and backlash impact force, is reported. It can be concluded that a larger diameter would improve the performance results substantially.

Keywords Form-closed · Cam-follower mechanism · Breath simulator · Synthesis

R.F. Oliveira (✉) · P. Flores · J.C. Teixeira
CT2M R&D Center, University of Minho, Braga, Portugal
e-mail: ricardo.falcao.oliveira@gmail.com

P. Flores
e-mail: pflores@dem.uminho.pt

J.C. Teixeira
e-mail: jt@dem.uminho.pt

S.F. Teixeira
CGIT R&D Center, University of Minho, Braga, Portugal
e-mail: st@dps.uminho.pt

H.M.C. Marques
iMed.UL R&D Center, University of Lisbon, Lisbon, Portugal
e-mail: hcmarques@ff.ul.pt

1 Introduction

Human airways diseases, such as asthma, are worldwide spread and its incidence is growing [5]. The inhalation therapy is the preferred route for delivery of medicine, though the use of specific devices such as: the nebulizers, Dry Powder Inhalers or pressurized Metered Dose Inhalers (pMDI).

According to asthma guidelines for treatment of acute persistent asthma in children, it is advisable to use a pMDI with a spacer attached [4, 8, 11]. The spacers, mainly the Valved Holding Chamber (VHC) attached to the pMDI, are the cheapest and most efficient way to treat asthma in children.

The VHC main feature is the one-way valve, so that the patient cannot exhale to its interior, and can only inhale the pMDI plume uncoordinatedly with its activation. This characteristic makes this device only likely to be correctly evaluated by an unsteady flow experimental setup. The Canadian normative for VHC assessment states that several conditions shall be followed to evaluate the performance of a VHC [1]. The same methodology was followed and analyzed by Mitchell and Dolovich [6, 7]. With that characteristic in mind, an experimental setup was projected to evaluate the Aerodynamic particle size distribution of the active pharmaceutical ingredient delivered by the VHC. It was based in a configuration proposed by Foss and Keppel in 1999 [3]. An essential component in this setup is the breath simulator machine. This device is the main focus of this report; herein will be described the project of the breath simulator machine by means of a form-closed cam-follower mechanism connected to a pneumatic cylinder.

2 Breath Simulator Machine

This machine has the purpose of replicating a human breath wave by means of a mechanical system. The system is composed of the spin motor, two worm reducers coupled in tandem, one form-closed cam-follower mechanism and a pneumatic cylinder. The spin motor rotational movement will actuate a cam, which transforms its movement to a non-linear translational follower's displacement. This latest is connected to the pneumatic cylinder. A schematic can be found elsewhere [10].

The cam-follower mechanism is fully dependent on the breath wave that is intended to be replicated. It is also limited by the pneumatic cylinder piston cross section area and the angular velocity of the cam.

2.1 Breath Profile

As the holding chamber use is intended for children and elder without the capacity for breathing-actuation coordination, the breathing cycle used is based in data for asthmatic children around 7 years old. According to the Canadian normative for

holding chamber testing, a good simplified approach for the shape of the respiratory cycle (flow vs. time) is a sine function [1]. For a correct definition of the sinusoidal wave, it is of utmost importance to obtain the suitable experimental data of breathing: frequency (breaths per minute—BPM), duty cycle (ratio of inspiration time per total cycle time) and tidal volume of inhaled air. Detailed information on the breath parameters sources can be found elsewhere [10]. Although there is some spread with the experimental evidence, the following values were assumed to be the most adequate: frequency of 30 BPM, duty cycle of 0.33 and tidal volume of 150 mL. The breathing cycle used is represented somewhere else [10].

The amplitude of the inspiratory sinus (≈ 21 L/min) was obtained by fitting the integral of a sine function to the tidal volume. The same procedure was applied for the exhalation phase. A pause of 4 s between the phases was added, to allow for the sedimentation of drug particles inside the lungs. This delay is recommended to improve efficacy in drug delivery. After the exhalation phase, a 2 s pause was added, which is proposed by Mitchell and Dolovich, as well as, by the Canadian normative for VHC testing [1, 6]. This delay is intended to simulate the poor coordination of an asthmatic patient using a VHC.

2.2 Cam Profile Calculations

Based in the profile previously defined, the piston shall move accordingly to reproduce the flow rate as described. In the present case the time dependent flow rate of the respiratory cycle was obtained by the use of a cam/cylinder combination. This design is robust and can provide accurate flow profiles at a low construction cost. Once the internal diameter of the cylinder, D_p , is assumed, the corresponding circular area is calculated. Dividing the sine function by the value of the piston cross section area, the piston linear velocity is obtained. By differentiating the velocity function, the acceleration is obtained, and sequentially, the jerk can be obtained. By integrating the velocity, the displacement function is obtained. The four functions are shown in Fig. 1, and they are essential to the definition of the follower path in the cam, as well as, the performance analysis.

Using the profiles for the piston movement and the proper equations for form-closed cam-follower calculation, the profile is obtained by the approximation of a curve tangent to the position of the follower. Equation (1) is used for the calculation of the follower movement, as [2, 9]:

$$F(x, y, \theta) = (x - x_c)^2 + (y - y_c)^2 - R_r^2 = 0 \quad (1)$$

where R_r is the radius of the contact roller (i.e. 19.0 mm) and (x_c, y_c) are the roller center coordinates, given by Eqs. (2) and (3) [2, 9]:

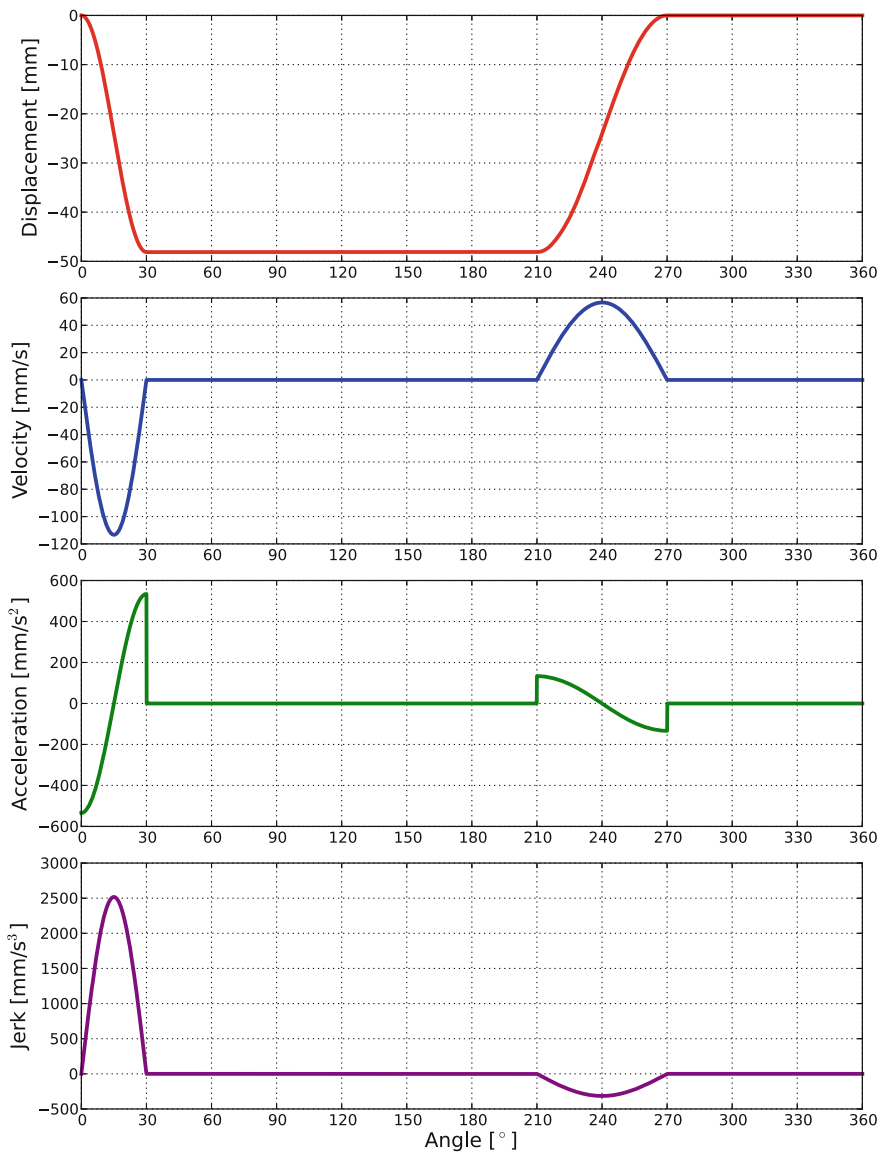


Fig. 1 Follower profiles calculated: displacement, velocity, acceleration, and jerk

$$x_c = -(R_b + R_r + s) \cdot \sin \theta \quad (2)$$

$$y_c = (R_b + R_r + s) \cdot \cos \theta \quad (3)$$

In these equations R_b is the base radius of the cam, s is the displacement (see Fig. 1). Differentiating Eq. (1) with respect to θ , Eq. (4) is obtained [2, 9]:

$$\frac{\partial F}{\partial \theta} = -2(x - x_c) \frac{dx_c}{d\theta} - 2(y - y_c) \frac{dy_c}{d\theta} = 0 \quad (4)$$

The derivatives of Eqs. (2) and (3) with respect to θ are given by Eqs. (5) and (6) [2, 9]:

$$\frac{dx_c}{d\theta} = -(R_b + R_r + s) \cos \theta - \frac{ds}{d\theta} \sin \theta \quad (5)$$

$$\frac{dy_c}{d\theta} = -(R_b + R_r + s) \sin \theta - \frac{ds}{d\theta} \cos \theta \quad (6)$$

where $ds/d\theta$ represents the velocity of the follower (see Fig. 1). Solving, simultaneously, Eqs. (1) and (4), Eqs. (7) and (8) for cam profiles coordinates, are obtained [2, 9]:

$$x = x_c \pm R_r \left(\frac{dy_c}{d\theta} \right) \left[\left(\frac{dx_c}{d\theta} \right)^2 + \left(\frac{dy_c}{d\theta} \right)^2 \right]^{-\frac{1}{2}} \quad (7)$$

$$y = y_c \mp R_r \left(\frac{dx_c}{d\theta} \right) \left[\left(\frac{dx_c}{d\theta} \right)^2 + \left(\frac{dy_c}{d\theta} \right)^2 \right]^{-\frac{1}{2}} \quad (8)$$

Equations (7) and (8) represent the inner and outer profiles for the cam, as shown in Fig. 2a. The pressure angle value was obtained accordingly to Eq. (9) [2]:

$$\phi = \tan^{-1} \frac{y' - e}{\sqrt{(R_b + R_r)^2 - e^2 + y}} \quad (9)$$

where e is the misalignment between the roller and the cam center. In the calculation of the curvature radius, one can calculate it through Eq. (10) [2]:

$$\rho = \frac{\left[\left(\frac{dx}{d\theta} \right)^2 + \left(\frac{dy}{d\theta} \right)^2 \right]^{\frac{3}{2}}}{\frac{dx}{d\theta} \frac{d^2y}{d\theta^2} - \frac{dy}{d\theta} \frac{d^2x}{d\theta^2}} \quad (10)$$

The backlash impact force is found by Eq. (11), considering the backlash (i.e. $y_{tol} = 0.05$ mm), the system stiffness (i.e. $k = 1.3E11$ N/m) and the system equivalent mass (i.e. $m = 0.48$ kg) [9]:

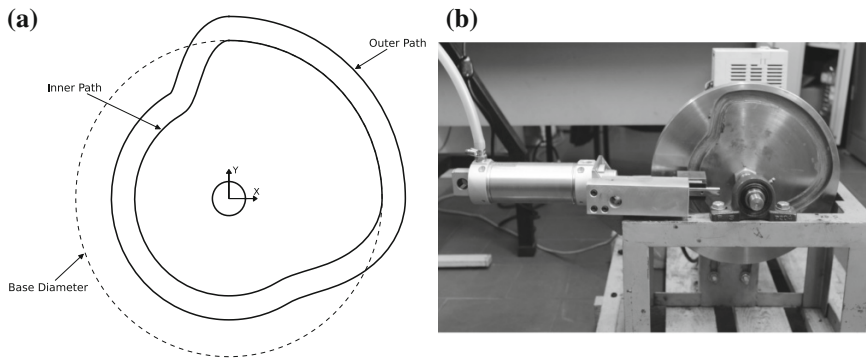


Fig. 2 a Cam profiles. b Photograph of the breath simulator machine

$$F_c \cong \left[\frac{1}{2} \left(\frac{d^3 y}{d\theta^3} \right)^{\frac{1}{3}} \cdot (6 \cdot y_{tol})^{\frac{2}{3}} \right] \sqrt{m \cdot k} \quad (11)$$

All these calculations have been programmed using Python language and a script was obtained. Several dimensional configurations for the base diameter and piston diameter were assessed. Also, several constrains were introduced, such as:

- cylinder feasible diameters could not be outside the manufacturer range;
- the maximum feasible displacement could not be outside the cylinder manufacturer range;
- cam outer profile could not be located at less than 6.0 mm to the maximum disk diameter (i.e. 310.0 mm);
- cam inner profile could not be located at less than 5.0 mm to the disk bore diameter (i.e. 27.0 mm).

Within such constrains, several possible combinations were obtained. Amongst all the feasible solutions, the one presenting the lower value for pressure angle was selected (i.e. Base diameter: 250.0 mm and Piston diameter: 63.0 mm with a maximum pressure angle of 46.4°). Figure 2a shows the calculated path profiles for the chosen cam dimensions.

The cam disk was manufactured by CNC milling of alloyed steel (UNE F-5303) with a surface hardening nitriding process, to provide extra wear resistance. The disk has an outer diameter of 310.0 mm and an inner bore of 27.0 mm, with a thickness of 22.0 mm and a track depth of 10.0 mm. In Fig. 2b, it is possible to observe the system after manufactured and assembled.

3 Performance Analysis

Figure 3 shows the performance analysis by focusing in the pressure angle, curvature radius and backlash impact force. The pressure angle value is maximum (i.e. 46.4°) at 17° , a second smaller peak (i.e. 27.7°) is found at the position 235.7° ; these values are within an acceptable range. Regarding the curvature radius, it can be observed the existence of some peaks, coming in from points where sharp corners are present. This could be mitigated by increasing the cylinder piston diameter (or largely increase the base diameter). The backlash impact force is calculated based in a backlash between the roller and the cam track walls and the jerk, the last can only be reduced by increasing the cylinder piston diameter.

The geometric parameters chosen are the best within the constraints imposed by the support structure, spin-motor torque and commercially available pneumatic

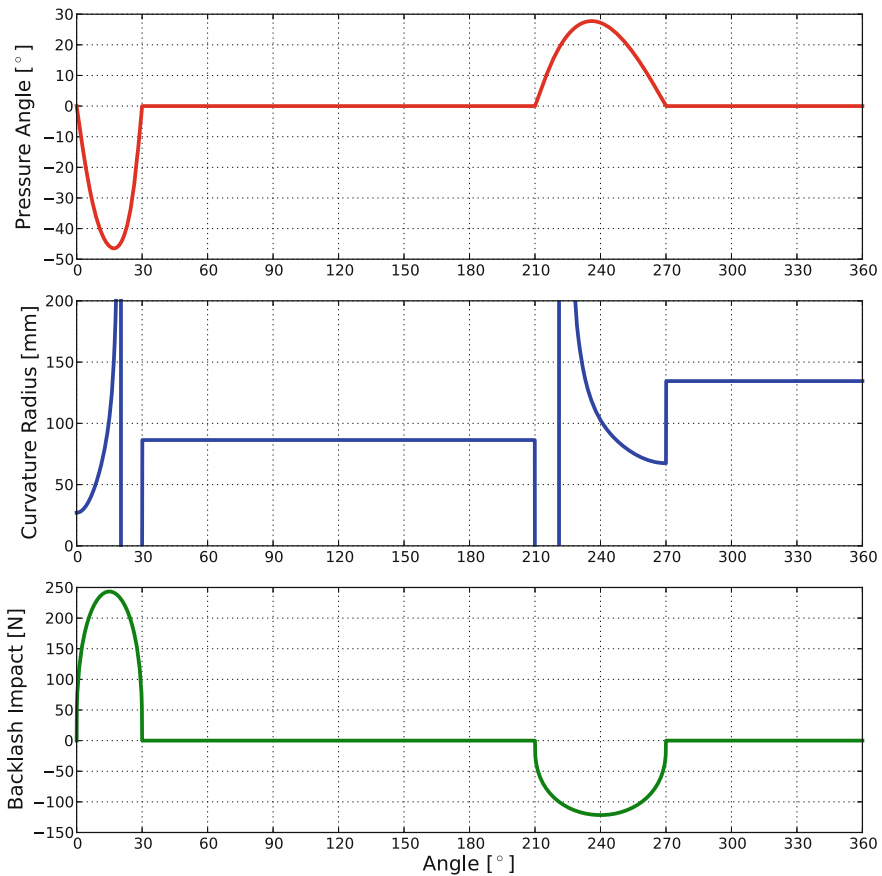


Fig. 3 Performance profiles: pressure angle, curvature and backlash impact

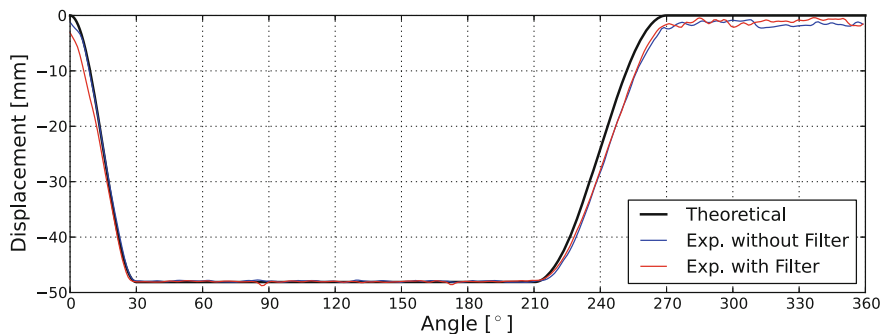


Fig. 4 Displacement profiles: theoretical, experimental with and without filter

cylinders in the market. Although, no experimental validation results are presented, the system is working without jamming.

Using a Linear Variable Differential Transformer (LVDT), the displacement was measured for two scenarios, with and without paper filter (i.e. the tool with is applied to the output of the breath machine for drug particle retention). Figure 4 depicts the experimental results, as well as the theoretical displacement profile presented previously (see Fig. 1). The results show a good agreement between the experimental and theoretical data, although the critical points are found at locations of high displacement variations. Some oscillations are present in the dwelling phases, that may rise due to the existence of backlash between the roller and the cam walls. Also it is noticed no significant influent of the pressure drop induced by the paper filter on the outcomes.

4 Conclusions

This project reports the design and development of a form-closed cam-follower mechanism, with the objective of replicating a human breath waveform. The project was successfully completed, even constrained by the space and material limitations.

The present geometric constrains lead the system to some kinematic singularities in the curvature radius profile. Some undercutting problems risen from the geometric limitations of cylinder piston size. Although, the small angular velocity of the system mitigates these kinematic imperfections. Experimental results from the LVDT show an acceptable fit with the theoretical profile.

Acknowledgments The first author would like to express his gratitude to the Portuguese Foundation for Science and Technology (FCT) through the PhD grant SFRH/BD/76458/2011. This work was financed by National Funds-Portuguese Foundation for Science and Technology, under Strategic Project PEst-C/EME/UI4077/2011 and PEst-OE/EME/UI0252/2011.

The authors are also grateful for the help of Dr. Eurico Seabra from the University of Minho with the data acquisition from the LVDT.

References

1. CAN/CSA-Z264.1-02(R2008) (2008) Spacers and holding chambers for use with metered-dose inhalers. Canadian Standards Association, Toronto
2. Flores P (2009) Projecto de mecanismos Came-Seguidor. Publindústria, Porto
3. Foss SA, Keppel JW (1999) In vitro testing of MDI spacers: a technique for measuring respirable dose output with actuation in-phase or out-of-phase with inhalation. *Respir Care* 44 (12):1474–1485
4. Global Initiative for Asthma (2012) Global strategy for asthma management and prevention. Technical report, GINA. <http://www.ginasthma.org>
5. Masoli M, Fabian D, Holt S, Beasley R (2004) The global burden of asthma: executive summary of the GINA Dissemination Committee report. *Allergy* 59(5):469–478
6. Mitchell JP, Dolovich MB (2012) Clinically relevant test methods to establish in vitro equivalence for spacers and valved holding chambers used with pressurized metered dose inhalers (pMDIs). *J Aerosol Med Pulm Drug Deliv* 25(4):217–242
7. Mitchell JP, Nagel MW (2004) Particle Size Analysis of Aerosols from Medicinal Inhalers. *KONA Powder Part J* 22:32–65
8. National Heart Lung and Blood Institute (2007) Expert Panel Report 3: guidelines for the diagnosis and management of asthma. Technical report, National Heart Lung and Blood Institute (NHLBI), Bethesda
9. Norton RL (2002) Cam design and manufacturing handbook. Industrial Press, New York
10. Oliveira RF, Teixeira JC, Marques HMC, Teixeira SFCF (2013) An experimental setup for API assessment of a valved holding chamber device. In: Proceedings ASME 2013 international mechanical engineering congress and exposition—IMECE2013, p 8. ASME, San Diego
11. Scottish Intercollegiate Guidelines Network, British Thoracic Society (2011) British guideline on the management of asthma: a national clinical guideline. Technical report, BTS and SIGN, UK

Dimensional Synthesis with Mechanism Processing Strategy

M. Hüsing, R. Braune and B. Corves

Abstract The dimensional synthesis of mechanisms is an important part within the process of mechanism design. In practice it is essential to possess a tool for the synthesis that solves the problem perfectly. This means that not the solution of the problem should adapt to the synthesis tool but the synthesis tool must adapt to the specific task. This, the co-author R. Braune realized at an early stage. He conceived a mechanism processing strategy and implemented this strategy into the tool GENESYS. With GENESYS the user is able to set up an individual and tailor made workflow adapted to the mechanism design problem. The mechanism processing strategy will be presented using the dimensional synthesis of straight line displacement.

Keywords Mechanism Processing Strategy · Dimensional synthesis · Precision positions · Coupler-curve synthesis · Straight line displacement

1 Introduction

When designing complex mechanisms, there is generally a relatively large number of free dimensional parameters. In the scope of dimensional synthesis, these parameters must be defined in such a way that, on the one hand, the primary kinematic/functional task is solved in the best possible way while, on the other hand, sufficiently meeting an abundance of additional requirements with respect to

M. Hüsing (✉) · B. Corves
RWTH Aachen University, Aachen, Germany
e-mail: huesing@igm.rwth-aachen.de

B. Corves
e-mail: corves@igm.rwth-aachen.de

R. Braune
Leibniz Universität Hannover, Hannover, Germany
e-mail: r.braune@gmx.com

the general properties of the mechanism. At the Department of Mechanism Theory and Dynamics of Machines at RWTH Aachen University, approaches have been presented that use geometry programs such as CINDERELLA or GeoGebra [1, 2]. The mechanism design software GECKO was developed at this department [3].

This study will describe an alternative possibility for executing mechanism design. This method was developed at Leibniz University of Hannover by co-author Braune and his team [3–5]. We refer to this method as “Mechanism Processing Strategy” (MPS). The method is based on the idea of interactively generating a task-specific processing workflow from a collection of general dimensioning modules. This workflow can be run through gradually and repeatedly. This procedure is highly practical for design engineers, as they typically execute their designs gradually and iteratively. This processing workflow is integrated into the software tool GENESYS.

As an application example to illustrate MPS, we will look at the design of a mechanism for creating a straight line displacement. This example will show that the method of the dimensional synthesis of precision positions has particular importance in the dimensioning of the elements of a mechanism. This is because the method allows the number of free design/kinematic parameters to be reduced by specifying functional constraints.

Until now, the term “Mechanism Processing Strategy” has only appeared in print in the German language [3–6]. One goal of this study is to establish this concept internationally.

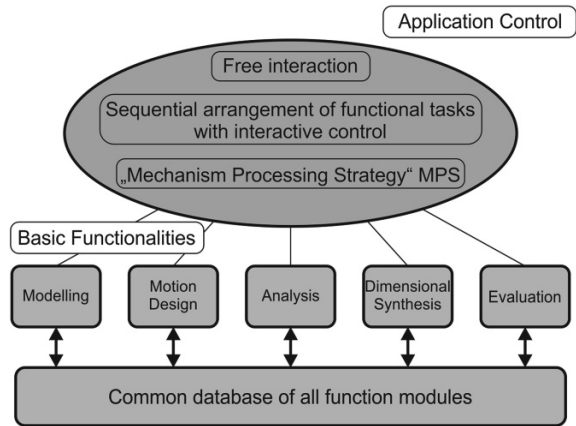
2 The Software Tool GENESYS

The program system GENESYS was developed with the objective, on the one hand, of covering all areas of mechanism development in a continuously computer-integrated way and, on the other, of being used effectively both while retaining its flexibility and universality when applied to problem-specific, predefined workflows. This objective is reached through the provision of three elements: basic functionality, database and application control (Fig. 1).

The basic functionality comprises five areas:

- **Modelling** (definition of mechanism types and structural building/topology): In this module, the mechanism type is defined or selected.
- **Motion design**: To design cam mechanisms and motion control systems, motion design is supported on the basis of the interactive variation of interlinked polynomial sections.
- **Analysis**: The analysis functionality includes kinematic analysis (determination of the motion of all links by given drive motion) and kinetostatic analysis (determination of joint and drive forces and moments for given loads).
- **Dimensional synthesis modules**: To determine suitable dimensions for mechanisms, suitable modules of dimensional synthesis are implemented.

Fig. 1 Elements and concept of use of the program system GENESYS



- Evaluation:** By experience ideally an evaluation of mechanism design should be based on kinematic/functional tasks but also on additional requirements with respect to the general properties of the mechanism. For this, powerful possibilities of diagrams are provided.

The common database for all functional modules contains non-redundant data about the mechanisms as well as all input and output files of the functional modules.

The special, even unique feature of GENESYS is its provision of sequential arrangement of functional tasks with interactive control. This concept-based procedure for designing mechanisms is the core of Mechanism Processing Strategy (MPS).

3 Mechanism Processing Strategy

The best strategy is hardly of any use today without the availability of suitable software tools and methods. Today, an abundance of methods have been developed for determining mechanisms for pre-defined motion tasks. Optimisations play a major role in this. Procedures, e.g. based on mathematical homotopy, have also been recommended by the present authors [3]. However, it is essential that the optimisation procedure does not excessively limit the design of mechanisms, for what good does it do for designers if they find a mechanism for the required motion tasks, but the installation space is violated or the transmission properties are not satisfied, etc. The design of a mechanism must be a gradual, clear process for the designer. Moreover, the designer must have constant control over the design process. GENESYS solves the apparent conflict of goals between the universality of a design program and the individual solution of a specific design problem by granting the option of creating a processing list for a mechanism-related problem and thus a specific processing workflow based on methods from the processing kit.

In GENESYS, required individual functions from the different functional areas, i.e. modelling, analysis and dimensional synthesis can be combined in any logic sequence by the user by means of interactive control. Also, it organises the transfer of data from one functional call to the other. Moreover, when executing a repeated run, one has the option of only re-entering input values that should actually be changed, with the option of skipping input positions for input values that are not to be changed for that run.

For this purpose, the program system GENESYS has a “processing kit” that offers a coordinated selection of individual functions typically required in processing strategies. This can be used to compile a problem-specific “processing list” depending on the task on a purely interactive basis—i.e. by means of menu calls alone and without any programming. When first creating such a processing list, each step “learns” which data it must take from the current state of the model database currently being processed, which data must be re-entered by the user, how these data should be processed and which data ultimately should be written back to the database of the processed mechanism as the result of the respective step. In a so-created processing list, the user can then “navigate” at will, i.e. jump back to an earlier processing step, change an input value for that step and then jump forward again to any desired position of the processing list. The intermediate steps that are skipped over in this way are then automatically processed by the system without any further inputs and the state of the model is adapted to the altered input value. Figure 2 shows a typical screen view of GENESYS with a specific processing list, in this case with the integration of precision position synthesis. However, processing lists can also provide valuable assistance for pure dimensional variations with no precision position synthesis. Details about the concept of GENESYS, the processing strategy and the elements of the processing kit have been discussed in detail and published in [3, 6].

In particular, the demand for an individually adjustable design strategy for a mechanism renders the functional elements of the precision position synthesis in the processing kit indispensable. This is because the precision position synthesis ideally reduces the number of free parameters of a mechanism to satisfy the motion task. Only this way can specific mechanism parameters be allocated to the solution of a motion task in a targeted way. In the selection of precision positions, the designer has an ideal influence on the solution-finding process.

The processing kit includes different dimensioning modules for precision position synthesis. One dimensioning model, which is to be applied later, is the three-link-group (TLG). The TLG corresponds to the generalised view of BURMESTER: For two link planes E_1 and E_2 , sets of positions assigned to each other are given relative to a reference system E_0 . What we are looking for point pairs which are assigned to each other, i.e. G_1 in E_1 and G_2 in E_2 , which exhibit a constant distance to all pre-defined link positions, whose homologous positions are located relative to the other respective link plane and therefore on a circle. G_1 and G_2 can then be designed as revolute joints connected by a coupling link. The derivation of the required systems of equations is described in detail e.g. in [3].

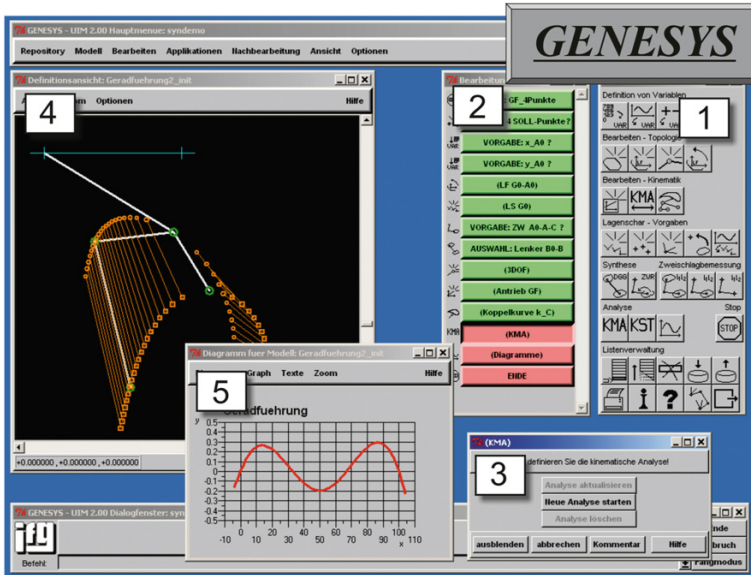


Fig. 2 Screenshot: developing and applying a processing list: (1) processing kit, (2) processing list, (3) dialogue windows for the current process step, (4) view of the current state with synthesis results and their choice, (5) diagram for evaluation

4 Dimensional Synthesis of Straight Line Displacement

A practical design of a mechanism is best suited for introducing and explaining Mechanism Processing Strategy. In the example presented here, a four-link linear guide mechanism is to be determined with an especially good linear guide over a range of $l_g = 100$ (Fig. 3a).

It stands to reason that the extended linear guide can be reached by specifying a number of target positions C_i for point C of link 2 on the target line. To calculate possible guide links A_oA and B_oB , however, complete position specifications for link 2 are required. Thus the specification of a target angle β_i is also required for every target point C_i . However, these position angles are not directly specified by the task. It would be difficult to make any sensible specifications without additional reference points. The danger would certainly exist of unintentionally producing bad solutions through unfavourable specifications. A clearer option is to specify a two-link assembly B_oBC by specifying the frame joint B_o and its link lengths B_oB and BC . If the two-link assembly with its link point C is guided to target positions C_i and one of the two possible two-link assembly positions is selected, “natural” link positions are the result for plane 2 relative to the frame. The dimensioning module three-link group (TLG) can then be used to calculate the link length A_oA of link 1 as a connection link between frame 4 and link 2.

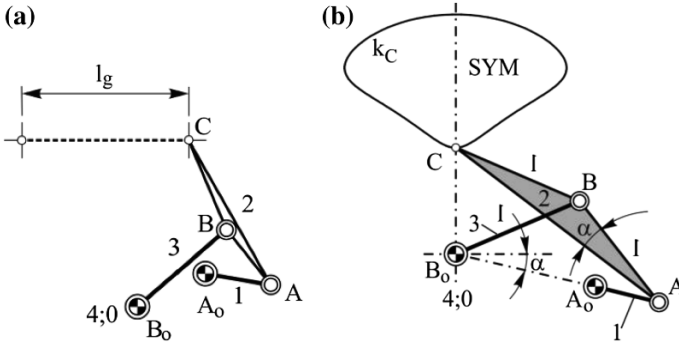


Fig. 3 Four bar linkage (not scaled): **a** Generation of a straight line displacement with a general four bar linkage. **b** Special four bar linkage with a symmetric coupler-curve

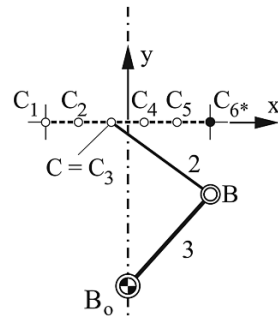
What is especially interesting and promising is the use of four-link mechanisms with a symmetrical coupler-curve (Fig. 3b). It is a known fact that such four-link mechanisms create a symmetrical coupler-curve if the joint point distances $B_0B = AB = BC$ are equal [7–10]. The direction of the axis of symmetry SYM results as marked from angle α in the coupler triangle BAC. As is known, such mechanisms can also generate especially good linear guides. This is why this mechanism type is used for the precision position synthesis.

Five precision points are to be specified (Fig. 4). Because of the symmetrical coupler-curve the points C_4 and C_5 must be symmetric to the points C_3 and C_2 . That means that $x_{C_4} = -x_{C_3}$ and $x_{C_5} = -x_{C_2}$. As a symmetrical coupler-curve is created, a sixth point C_{6^*} with $x_{C_{6^*}} = -x_{C_1}$ is fulfilled automatically.

The processing list is put together as follows:

- Consecutive specification of coordinate values C_1 – C_5
- Specification of y_{B_0}
- Specification of guide $B_0B = AB = BC$
- Generation of point and position set for later synthesis
- Selection of link 1 according to precision position synthesis using TLG
- Selection of drive link of coupler-curve
- Kinematic analysis and display of results

Fig. 4 Five coupler points C_1, C_2, C_3, C_4 and C_5 are given



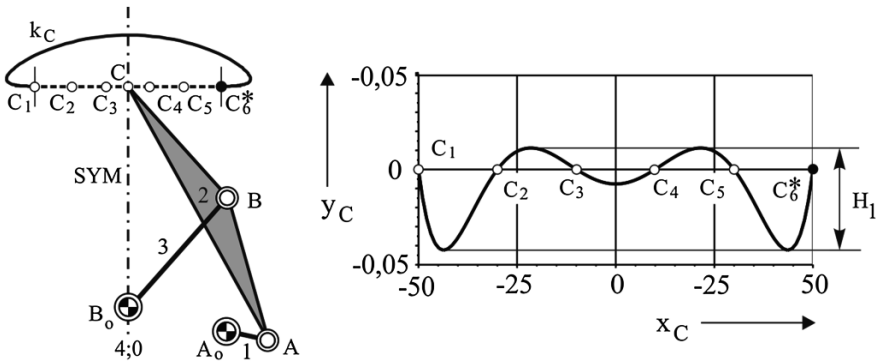


Fig. 5 Result of first dimensional synthesis (mechanism: drawn to scale)

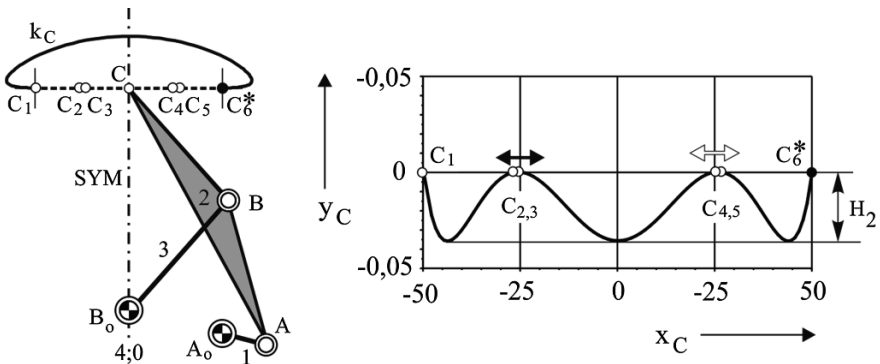


Fig. 6 Result of final dimensional synthesis (mechanism: drawn to scale)

The result presented in Fig. 5 shows an initial synthesis with the linear guide tolerance band $H_1 = 0.054$. Now it is very easy to change the points to be specified C_1 – C_5 . The list is then processed automatically after each change.

Finally, a result as shown in Fig. 6 can be generated. However, the linear guide tolerance band $H_2 = 0.036$ could be clearly reduced in this result compared to H_1 (more than 30 %).

5 Conclusions

In this study, the Mechanism Processing Strategy within the program GENESYS was introduced using the example of the creation of a linear guide mechanism as a suitable method for executing the design of a mechanism. In the process, it was shown that the use of the precision position synthesis is an ideal procedure, which in the case presented here is certainly far superior as a method to pure parameter variation by means of “blind” trial and error. However, especially with multi-loop mechanisms, the most

important requirement is that clearly defined kinematic/functional tasks can be allocated to individual link groups in the overall mechanism, tasks which can be accurately grasped by means of a limited number of precision points.

The success of the mechanism design depends on the processing workflow developed by the user. Therefore, in order for the conventional precision point synthesis to be applied practically, a profound understanding of kinematics is certainly required of the user.

References

1. Corves B, Riedel M, Hüsing M (2011) Descriptive and intuitive mechanism design and synthesis using geometry-based computer-aided methods. In: 3th world congress in mechanism and machine science, Guanajuato, México, 19–25 June—International Federation for the Promotion of Mechanism and Machine Science
2. Kurtenbach S, Prause I, Weigel C, Corves B (2013) Comparison of geometry software for the synthesis and analysis in mechanism theory In: Mechanisms and machine science 19, new trends in educational activity in the field of mechanism and machine theory, Leganés, Spain. Springer, Berlin. ISBN: 978-3-319-01835-5, pp 193–202
3. Wohlenberg P (2001) Auslegung von Koppelgetrieben mit wiederholtem Durchlauf interaktiv erstellter Bearbeitungsstrategien. (Design of mechanisms with repeated run interactively generated mechanism processing strategies) Fortschritt-Berichte VDI, Reihe 1, Nr. 337. VDI Verlag, Düsseldorf
4. Braune R (1996) Das Projekt GENESYS—Zielsetzung und Realisierungsstand eines neuen umfassenden Software-Systems für die Entwicklung ungleichmäßig übersetzender Getriebe. (The Project GENESYS—Objectives and implementation state of a new comprehensive software system for the development of mechanisms) VDI-Berichte 1281, pp 17–45
5. Breitfeld C (1995) GENESYS—Architektur und Kernrealisierung eines Softwaresystems zur Entwicklung ungleichmäßig übersetzender Getriebe. (GENESYS—Architecture and core implementation of a software system for design of mechanisms) Fortschritt-Berichte VDI, Reihe 1, Nr. 257. VDI-Verlag, Düsseldorf
6. Braune R (2001) Das Konzept “Bearbeitungsstrategie”—Bemerkungen zu einem klassischen Ansatz für die Auslegung von komplexen Koppelgetrieben in einer neuen rechnergestützten Entwicklungsumgebung. (The concept, mechanism processing strategy—remarks on a classical approach for the design of complex mechanisms in a new computer-based development environment) Vortrag zum Fachkolloquium Getriebetechnik, Dresden 2001. Wiss. Z. TU Dresden 50, Heft 3, pp 43–52
7. Meyer zur Capellen W, Rischen K-A (1962) Symmetrische Koppelkurven und ihre Anwendungen. (*Symmetric coupler-curves and there applications*) Forschungsbericht Nr. 1066 des Landes NRW, GER 1962
8. Lonij G, Hüsing M, Choi S-W, Corves B (2008) Development of a spherical linkage mechanism with the aid of the dynamic spatial geometry program “GECKO” In: 2-nd European conference on mechanism science EUCOMES, Cassino, 17–20 Sept 2008
9. Stolle G, Corves B, Hüsing M (2004) Dimensional synthesis of 6- and 8-bar planar mechanisms using centerpoint search and polynomial continuation method in automotive engineering. In: Proceedings of the 11th world congress in mechanism and machine science, vol 3, 1–4 Apr 2004, China Machine Press, Tianjin
10. Uicker JJ, Pennock GR, Shigley JE (2011) Theory of machines and mechanisms, 4th edn. Oxford University Press, Oxford, ISBN: 978-0-19-977781-5

Dynamic Modelling of a Four Legged Robot

I. Geonea, A. Ungureanu, N. Dumitru and L. Racilă

Abstract In this paper we present the kinematic model of a mechanism, which represent the legs of a four legged robot. The anterior legs and posterior are realized as plane mechanisms, with articulated bars. Each anterior leg has a complex structure, with four closed loops, mean while each posterior leg has only three closed loops. Each mechanism is actuated by an electric motor. The geometric and kinematic modelling of the anterior leg mechanism is achieved by means of some vectorial and scalar equations. Also, the dynamic simulation is achieved during walking, by means of ADAMS software.

Keywords Mobile robot · Biomechanism · Kinematics · Dynamics

1 Introduction

In case of four legged mammals, the structure of anterior and posterior legs is very similarly with the structure of most majorities of actual four legs quadrupeds [1–3]. To some quadrupeds, the anterior legs are short that those posterior. To remark, that at quadrupeds, the anterior legs have the degree of mobility larger than the posterior. Legged walking robots such as biped robots, quadrupeds, hexapods and eight-legged robots have attracted great interests in the past decades. Legged locomotion has a lot of advantages as compared with wheeled locomotion. It is

I. Geonea (✉) · A. Ungureanu · N. Dumitru · L. Racilă
University of Craiova, Craiova, Romania
e-mail: igeonea@yahoo.com

A. Ungureanu
e-mail: ca_ungureanu@yahoo.com

N. Dumitru
e-mail: nicolae_dtru@yahoo.com

L. Racilă
e-mail: racila_laurentiu@yahoo.com

versatile and flexible when it operates in rough terrain or in unstructured environments [1, 4].

Leg mechanisms with a limited number of degrees of freedom (DOF) are widely used in legged walking robots for the purpose of reducing the number of motors and simplifying the control algorithms [4, 5]. At LARM: Laboratory of Robotics and Mechatronics in Cassino, reduced DOF leg mechanisms have been implemented in several prototypes like one-DOF biped robot [4, 5], and a rickshaw walking robot [6]. A one-DOF biped robot has been able to perform a biped walking gait in a lab test [7].

In this paper is presented the design problem for a new quadruped walking robot by looking at solutions in dog’s locomotors system. Thus, a mechanism design is proposed as to be implemented for a novel quadruped—like walking robot.

2 Mechanism Structural and Kinematics Analysis

The kinematics scheme of the quadruped biomechanism is achieved in vertical longitudinal plane (Fig. 1), in which are represented the plane articulated mechanisms of those two legs, from rear (Fig. 1a) and front (Fig. 1b). The booth mechanisms are articulated in the upper side to a horizontal link, which represent the body of the physically modeled robot. The joints D and F of each mechanism to the upper mobile platform (Fig. 1) are considered as basis joints, by this reason this platform has been noted with 0. Each of those two mechanisms (rear and front), has a first kinematic chain, the four bar mechanism ABCD, which is composed by the links 0, 1, 2 and 3. The others kinematical chains of each mechanism are the four bar articulated mechanisms DEFG, HIGJ, with the links 0, 3, 4, 5, and 4, 5, 6, 7, as can be seen in Fig. 1.

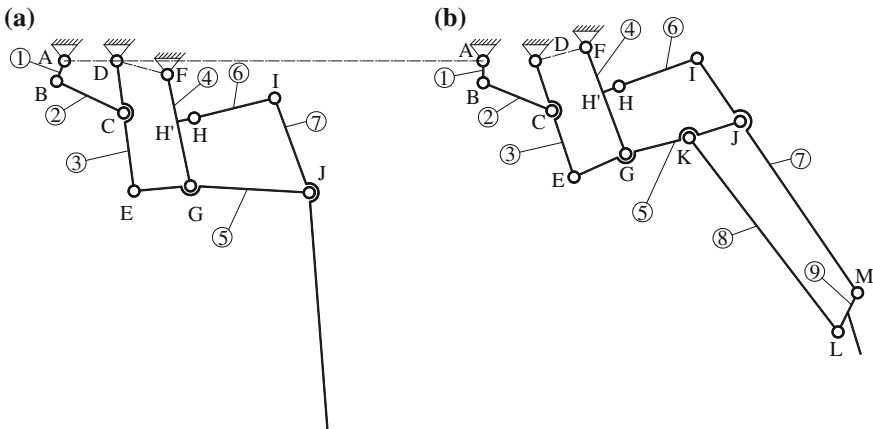


Fig. 1 Kinematical scheme of the mechanism from posterior legs (a) and anterior (b)

The mechanism of the front leg contain in his structure another kinematic chain KJLM, composed by the links 5, 7, 8 and 9.

The mobility of each from those two plane mechanisms is calculated with the Dobrovolski formula:

$$M_{bf} = (6 - f)n - \sum_{k=f+1}^5 (k - f)C_k \quad (1)$$

This for $f = 3$ (plane mechanisms) becomes the Grübler-Cebâşev relation:

$$M_{b3} = 3n - \sum_{k=f+1}^5 (k - 3)C_k = 3n - 2C_5 - C_4 \quad (2)$$

where the class of the kinematic joint reveals the imposed restrictions ($k = 5, k = 4$).

Also, the mechanism degree of mobility, can be calculated with the general formula, of Păun Antonescu [8, 9]:

$$M_b = \sum_{m=1}^5 mC_m - \sum_{r=2}^6 rN_r \quad (3)$$

where is emphasized the kinematics joints mobility: $m = 6 - k$ and the class of each independent closed loop: $r = 6 - f$. For plane mechanism the relation (3), can be writhed as:

$$M_b = \sum_{m=1}^2 mC_m - 3N_3 = C_1 + 2C_2 - 3N_3 \quad (4)$$

To calculate the mobility of those two mechanisms (Fig. 1a, b) we use the relations 2 or 4:

a)

$$\begin{aligned} M_{b3} &= 3n - 2C_5 - C_4 = 3 \times 7 - 2 \times 10 - 0 = 1; \\ M_b &= C_1 + 2C_2 - 3N_3 = 10 + 2 \cdot 0 - 3 \cdot 3 = 1. \end{aligned}$$

b)

$$\begin{aligned} M_{b3} &= 3n - 2C_5 - C_4 = 3 \times 9 - 2 \times 13 - 0 = 1; \\ M_b &= C_1 + 2C_2 - 3N_3 = 13 + 2 \times 0 - 3 \times 4 = 1. \end{aligned}$$

The characteristics dimensions of those two mechanisms are (Fig. 1 a, b):

a)

$$l_{AB} = 5; \quad l_{BC} = 17; \quad l_{DC} = 12; \quad l_{CE} = 18; \quad l_{FH'} = 11; \quad l_{HH'} = 4; \quad l_{H'G} = 15; \\ l_{EG} = 13; \quad l_{GH} = 15.52; \quad l_{HI} = 19; l_{GJ} = 27.29; \quad l_{IJ} = 17.5; \quad l_{JM} = 54;$$

b)

$$l_{AB} = 5; \quad l_{BC} = 17; \quad l_{DC} = 12; \quad l_{CE} = 18; \quad l_{FH'} = 11; \quad l_{HH'} = 4; \quad l_{H'G} = 15; \quad l_{EG} = 13; \\ l_{GH} = 15.52; \quad l_{HI} = 19; l_{GJ} = 27.29; \quad l_{IJ} = 17.5; \quad l_{JM} = 47.5; \quad l_{KL} = 56; \quad l_{LM} = 10;$$

In the topological structure of each mechanism we identify the link 1, as motor, and three or four dyadic kinematics chains.

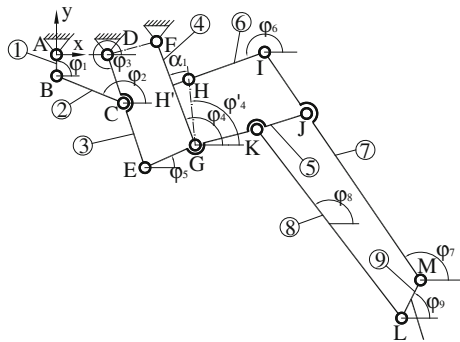
The mechanism has four independent contours (Fig. 2) first is the four bar mechanism ABCD, which is composed by the links 0, 1, 2, 3. The second kinematical chain of each mechanism is the four bar articulated mechanism DEFG, with the links 0, 3, 4 and 5 as can be seen in Fig. 2.

The third and four kinematics chain are HIGJ and KJLM, composed by the links 4, 5, 6, 7 and 5, 7, 8, 9. The assumption made for the kinematic modelling is that the leg mechanism operates on a supporting stand.

We choose a coordinate system with the origin in the fixed joint A, having the axis Ax and Ay orientated from right to left, respectively from upper to bottom. For each side of those four closed independent contours we choose conveniently senses, for that the positioning angles (measured in trigonometric sense) to be most small (Fig. 2).

We write the closing vectorial equation for the contours, the purpose being to establish the variations of angles φ_i , considering an uniform angular speed of the motor element: $\omega_1 = d\varphi_1/dt = 1.2 \text{ rad/s}$. The variation of angles $\varphi_i, i = 1 \dots 9$, are determined by solving some equations under the form:

Fig. 2 Kinematical scheme of the anterior leg mechanism



$$\varphi_i = 2 \arctg \left(\frac{A_i \pm \sqrt{A_i^2 + B_i^2 - C_i^2}}{B_i - C_i} \right), \quad (5)$$

The expression of variable coefficients is calculated with relations under the form:

$$\begin{aligned} A_2(\varphi_2, \varphi_3) &= 2b_1 l_{BC}; & B_2(\varphi_2, \varphi_3) &= 2a_1 l_{BC}; & A_3(\varphi_2, \varphi_3) &= -2b_1 l_{DC}; & B_3(\varphi_2, \varphi_3) &= -2a_1 l_{DC}; \\ C_2(\varphi_2, \varphi_3) &= l_{DC}^2 - a_1^2 - b_1^2 - l_{BC}^2; & C_3(\varphi_2, \varphi_3) &= l_{BC}^2 - a_1^2 - b_1^2 - l_{DC}^2; \\ a_1 &= (x_D - x_B), & b_1 &= (y_D - y_B) \end{aligned} \quad (6)$$

$$\begin{aligned} A_4(\varphi_3, \varphi_4, \varphi_5) &= 2b_2 l_{FG}; & B_4(\varphi_3, \varphi_4, \varphi_5) &= 2a_2 l_{FG}; \\ A_5(\varphi_3, \varphi_4, \varphi_5) &= 2b_2 l_{GE}; & B_5(\varphi_3, \varphi_4, \varphi_6) &= 2a_2 l_{GE}; \\ C_4(\varphi_3, \varphi_4, \varphi_6) &= l_{GE}^2 - a_2^2 - b_2^2 - l_{FG}^2; & C_5(\varphi_3, \varphi_4, \varphi_6) &= l_{FG}^2 - a_2^2 - b_2^2 - l_{GE}^2; \\ a_2(\varphi_3) &= (x_F - x_D) + l_{DE} \cos \varphi_3; & b_2(\varphi_3) &= (y_F - y_D) + l_{DE} \sin \varphi_3 \end{aligned} \quad (7)$$

$$\begin{aligned} A_6(\varphi_6, \varphi_7) &= 2b_3 l_{IH}; & B_6(\varphi_6, \varphi_7) &= 2a_3 l_{IH}; & C_6(\varphi_6, \varphi_7) &= l_{IJ}^2 - a_3^2 - b_3^2 - l_{IH}^2; \\ A_7(\varphi_6, \varphi_7) &= -2b_3 l_{IJ}; & B_7(\varphi_6, \varphi_7) &= 2a_2 l_{IJ}; & C_7(\varphi_6, \varphi_7) &= l_{IH}^2 - a_3^2 - b_3^2 - l_{IJ}^2; \\ a_3(\varphi_4, \varphi_5) &= l_{JG} \cdot \cos \varphi_5 - l_{HG} \cos \varphi_4'; & b_3(\varphi_4, \varphi_5) &= l_{JG} \cdot \sin \varphi_5 - l_{HG} \sin \varphi_4'; \end{aligned} \quad (8)$$

$$\begin{aligned} A_8(\varphi_8, \varphi_9) &= 2b_4 l_{KL}; & B_8(\varphi_8, \varphi_9) &= 2a_4 l_{KL}; & C_8(\varphi_8, \varphi_9) &= l_{ML}^2 - a_4^2 - b_4^2 - l_{KL}^2; \\ A_9(\varphi_8, \varphi_9) &= -2b_4 l_{ML}; & B_9(\varphi_8, \varphi_9) &= -2a_4 l_{ML}; & C_9(\varphi_8, \varphi_9) &= l_{KL}^2 - a_4^2 - b_4^2 - l_{ML}^2; \\ a_4(\varphi_5, \varphi_7) &= l_{JM} \cdot \cos \varphi_7 - l_{JK} \cos \varphi_5; & b_3(\varphi_5, \varphi_7) &= l_{JM} \cdot \sin \varphi_7 - l_{JK} \sin \varphi_5; \end{aligned} \quad (9)$$

Solving the equations which describe the kinematic model, in Maple software package, we represent the law of variation of mechanism angles of motion, in Fig. 3.

3 Dynamic Modelling of the Robot

Dynamic simulation has been computed through a suitable Adams modelling, during the walking activity, on the ground, taking into account the ground contact, and the joints friction. To achieve this purpose it is developed an assembly model with the four legs of the walking robot, each leg being positioned in a suitable position, corresponding to the walking phases.

To simulate the mechanism in Adams environment, there is modelled as a 3D structure, on which the kinematics links are defined as shape, geometry and material

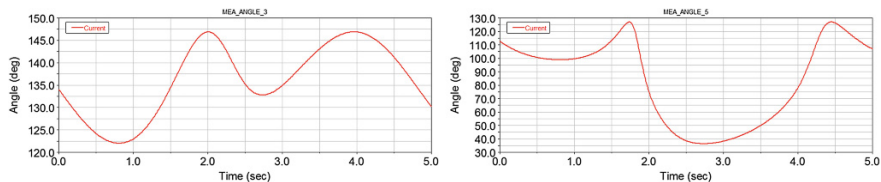


Fig. 3 Computed plot of the angle φ_6 variation and φ_9 variation

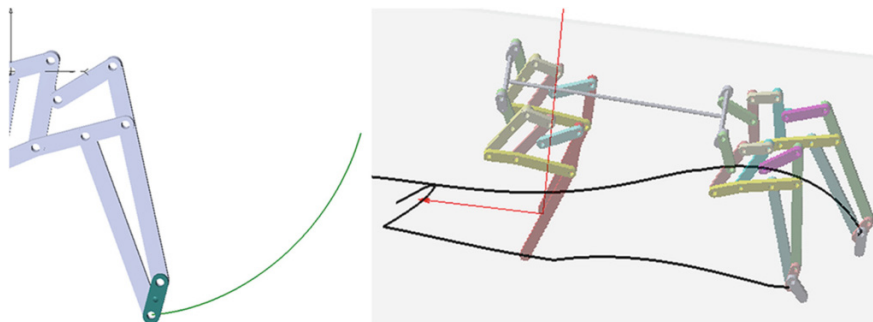


Fig. 4 Computed path of the front legs ankle trajectory, standing and walking

property. They are defined the kinematical joints of the mechanism with corresponding constraints and mobility's, we define the local and global coordinates systems upon we calculate the mechanism kinematical parameters. We define the motor element and eventually loads (forces or moments which act upon the kinematical links) upon we process the kinematical analysis. For this step the mechanism is considered fixed to basis joints on an operating stand. The motion of motor is considered uniform, by 1.2 rad/s, (Fig. 2). In Fig. 4, is presented the trajectory described by the leg, when she operates on a supporting stand. From figure is also observed the initial position of the mechanism and the final position of the mechanism, corresponding to one step of the dog robot. The trajectory was obtained with MSC.Adams software, by tracking the motion of point L. The CAD model of the robot is imported into Adams data basis, and trough a suitable modelling in achieved the dynamic modelling, when the robot is walking on ground. For the rotation joints are defined the friction from the pin hole joint, the ground contact model. Simulation parameters of the leg mechanisms considered for dynamic analysis are indicated in Table 1.

For each crank of those four leg mechanism is defined the motor motion. It is observed that the cranks are positioned at 180° for the opposite legs, for a suitable walking phase.

Considering the body weight of the robot by 20 kg and the angular speed of actuation motor by 1.2 rad/s, there are computed in Adams dynamic simulation the

Table 1 Simulation parameters for dynamic analysis

Pin hole joints	Bushing parameters	Ground contact
$\mu_{\text{static}} = 0.3$	<i>Translational properties</i>	Normal force: impact
$\mu_{\text{dynamic}} = 0.1$	Stiffness: 1.2×10^{-3} N/mm	Static friction coefficient: 0.4
	Damping: 1.2 N s/mm	Dynamic friction coefficient: 0.3
Pin radius: 6 mm	<i>Rotational properties</i>	Stiffness: 1×10^4 N/mm
Friction effect: stiction	Stiffness: 0.2 N mm/deg	Force exponent: 1.4
	Damping: 3 N mm s/deg	Penetration depth: 0.1
	Preload: 10 N mm	Damping: 80 N s/mm

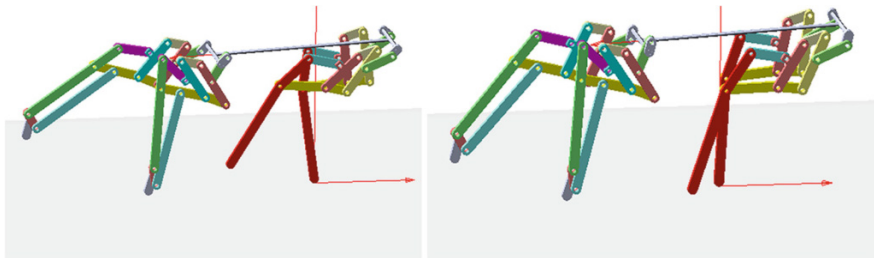


Fig. 5 Sequences from the walking activity

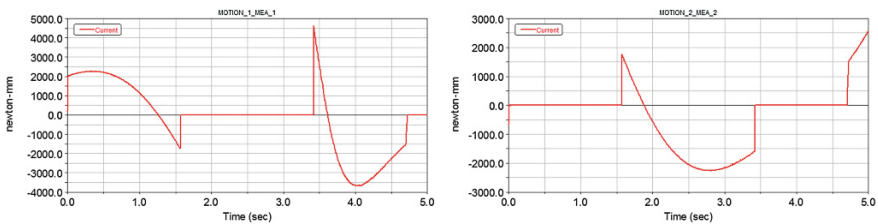


Fig. 6 Computed torque motor variation for the right, and left posterior leg, during walking

motion trajectories of ankle joints, when the model walks on ground. In Fig. 4 is presented the Adams computed path described by ankle joints.

Sequences from the walking activity of the robot model, obtained in Adams are presented in Fig. 5. Stepping sequences during walking on ground, demonstrate the viability of the solution implemented for legs mechanism.

From dynamic simulation is obtained the resistant torque at the shaft which actuates those four legs cranks. From the variation of resistant motor, presented in Fig. 6, it's depicted the conclusion that the maximum value is by 4 Nm, that being useful for the choice of an actuation electric motor for the experimental prototype (Fig. 7).

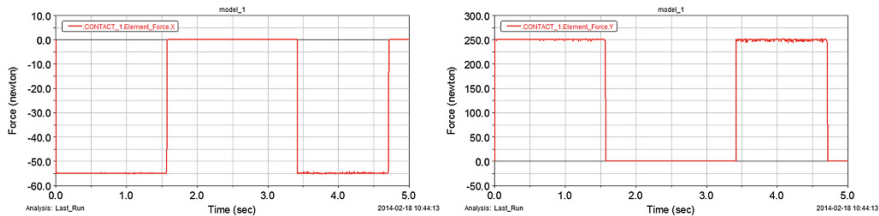


Fig. 7 Computed contact force upon x and y axis, for the posterior right leg

4 Conclusions

In this paper a kinematics and dynamic simulation of a one DOF robot leg mechanism is carried out, in order to characterize the mechanism performance. They are two different structures, for the legs, one for the anterior leg, and another one for the posterior legs. Each leg is actuated by a single motor element. Kinematics equations of the proposed leg mechanism are formulated for a situation when the leg operates on a supporting stand and solved in Maple computational algorithm. In Adams software is simulated the walking activity taking into account the ground contact with the leg. There are obtained the paths for trajectories when leg operates on a supporting stand and walking on ground. Simulation results show suitable performance of the proposed leg mechanism structure. The novelty of the design structure represents the fact that for each mechanism is needed only one motor, which has a constant angular rotation, so is no needed a complex command and control algorithm.

Acknowledgment This work was partially supported by the grant number 45C/2014, awarded in the internal grant competition of the University of Craiova.

References

1. Hiller M, Germann D, Morgado de Gois JA (2004) Design and control of a quadruped robot walking in unstructured terrain. In: Proceedings of the 2004 IEEE international conference on control applications, vol. 2, pp 916–921, Taipei
2. Inagaki K (2007) Reduced DOF type walking robot based on closed link mechanism. In: Habib MK (ed) Bioinspiration and robotics: walking and climbing robots. ISBN 978-3-902613-15-8, pp 544, I-Tech, Vienna, Austria, EU
3. Liu J, Tan M, Zhao XG (2007) Legged robots—an overview. *Trans Inst Measur Control* 29 (2):185–202
4. Tavolieri C, Ottaviano E, Ceccarelli M, Nardelli A, A design of a new leg-wheel walking robot. In: Proceedings of the 15 th mediterranean conference of automation and control & automation, Athens, 27–29 July 2007
5. Ceccarelli M, Carbone G, Ottaviano E, Lanni C (2009) Leg designs for walking machines at LARM in Cassino, ASI workshop on Robotics for moon exploration, Rome

6. Hun-ok L, Atsuo T (2006) Mechanism and control of anthropomorphic biped robots, mobile robots, moving intelligence, ISBN: 3-86611-284-X, Edited by Jonas Buchli, p 576, ARS/pIV, Germany
7. Ogura Y, Aikawa H, Lim H-O, Takanishi A (2004) Development of a human-like walking robot having two 7-DOF Legs and a 2-DOF Waist. In: Proceedings of the 2004 IEEE international conference on robotics & automation, New Orleans
8. Antonescu P (2005) Mechanism and machine science. Printech Publishing House, Bucharest
9. Micu C, Geonea I, Buzea (2010) Kinematic modeling and simulation of quadruped biomechanism, ICOME 2010—27th–30th of April 2010, Craiova, Romania

Lifting Mechanism for Payload Transport by Collaborative Mobile Robots

B. Hichri, J.-C. Fauroux, L. Adouane, I. Doroftei and Y. Mezouar

Abstract This paper reviews lifting mechanisms and provides a description of a new lifting system that could be fixed on a mobile robot frame. The resulting collaborative mobile robots would be able to transport an object of any shape by lifting it above their transporting platform using the proposed system while keeping a stable formation in order to successfully achieve the task.

Keywords Lifting mechanisms · Collaborative mobile robots · Object manipulation · Transport

1 Introduction

Many industrial tasks (vehicle and construction machine, product manufacturing...) and commercial activities (freight charging, parcel transport) require automated load lifting systems. Industries for which we are interested to develop a robotic system for material lifting and transport are one of the sectors where modern innovative technologies allow to gain better adaptability and productivity.

B. Hichri (✉) · J.-C. Fauroux · L. Adouane · Y. Mezouar
Institut Pascal, Clermont-Ferrand, France
e-mail: bassem.hichri@ifma.fr

J.-C. Fauroux
e-mail: jean-christophe.fauroux@ifma.fr

L. Adouane
e-mail: lounis.adouane@univ-bpclermont.fr

Y. Mezouar
e-mail: youcef.mezouar@univ-bpclermont.fr

I. Doroftei
Gheorghe Asachi Technical University of Iași, Iași, Romania
e-mail: idorofte@mail.tuiasi.ro

Our goal in the C³Bots project (Collaborative Cross and Carry Mobile Robots) is to design several mobile robots with a simple mechanical architecture, called m-bots, that will be able to autonomously co-manipulate and transport objects of any shape by connecting together. The resulting poly-robot system, called p-bot, will be able to solve the so-called removal-man-task [13] to transport any object on the top platform of m-bots (dorsal transport). Reconfiguring the p-bot by adjusting the number of m-bots allows to manipulate heavy objects with any shape, particularly if they are wider than a single m-bot. This particular variant of the C³Bots project will be called C³Bots DGP (Dorsal General Payload transport).

Until now some industrials and constructions still use dedicated equipments that request a long time to be installed. In some cases, manipulated parts are lifted manually to a required altitude. Manual Material Handling (MMH) [15, 21, 22] uses different techniques for object lifting in a safe and efficient way but can cause Repetitive Strain Injuries (RSI).

Diverse mechanisms and technologies are used for objects lifting and transportation. Some transport solutions require heavy infrastructure such as Automated Guided Vehicles (AGV) (e.g. ground landmarks, guiding rails) or specific stacking racks for storage as for Automated Storage and Retrieval System (ASRS). Human assistance could also be needed to put the object on the transporting platform (e.g. scissor [5]). Forklifts [24] use forks to lift and transport the object but they require the positioning of the object on a pallet. Grabbing systems limit the manipulated payload size and shape. According to the previous mentioned systems, one can conclude that for a better stability, an object should be better transported on the robot body [3, 4] or as close as possible to the robot body, to keep the gravity center above the polygon of support and ensure a bigger stability margin.

There are many patented mechanisms for lifting applications with various structures and architectures. In [10], a lifting mechanism for an articulated bed is described. It is based on two parallel arms, hinged to the chassis and the bed plane, which forms an articulated parallelogram with one extendable arm through two segments and equilibrating elastic means. Herrera [11] presents another articulated lifting mechanism comprising a set of arms forming the sides of two rhomboid polygons to lift objects in a vertical direction parallel to the chassis. In [20], the well known lifting jack mechanism, used to lift a vehicle, is presented. Another innovative design [9] is used for a vehicle lifting mechanism using a Y shaped chassis based on a lever, a hydraulic actuator and an articulated support arm. Other example for object lifting and transport is the hand-truck with an innovative design using wheels and a vertical lifter sub assembly [19]. Eppert [7] presents a monitoring payload system for a load lifting vehicle based on a lifting arm and hydraulic actuators. In [8] a lifting mechanism that could be mounted on the rear of truck is described. A mechanism for patient lifting and transport is designed in [23]. Charlec [5] presents a lifting system for metallic parts in construction sites based on a scissor linkage system with metallic bars and a mechanism ensuring the lift up and down movement.

Many robotic systems used for objects manipulation and transportation can be found in literature: [1, 3, 6, 14, 16–18, 25]. The proposed design in this paper is

characterized by: the simplicity of mechanical architecture comparing to the systems presented in [3, 25]; the use of a modular swarm of elementary robots [2, 17]; the adaptability to objects of any shape and mass and the ability to provide a fully autonomous system, without human mediation, contrary for example to robotic system proposed in [1, 14].

This overview about lifting mechanisms and manipulation strategies allows to design an innovative robotic system equipped with a lifting mechanism dedicated to payload co-manipulation and transportation. This paper is organized as follows. In Sect. 2 the specification of C³ Bots project is briefly presented. Section 3 details the developed lifting mechanism structure, provides the dimension analysis and presents the first prototype. Finally, Sect. 4 presents the conclusion and future works.

2 C³Bots Paradigm

2.1 Specification

The C³Bots project aims to design identical m-bots equipped with a manipulator. Together they will be able to lift, co-manipulate and transport a payload which has to be laid on the top platform of each m-bot. Consequently, in addition to an end-effector, the m-bot manipulator has to include a lifting mechanism. For simplicity reasons, the end-effector is considered here to be a rigid contact plate in order to fit variable payload contact surfaces. This paper will focus exclusively on the architecture of the lifting mechanism that has to comply with the following requirements R_i : R_1 -payload is lifted by several m-bots with unknown number and pose; R_2 -collision-free payload trajectory from the ground to the top of robot platform with constant orientation; R_3 -mountable mechanism on each m-bot; R_4 -a free steering mobility for each m-bot during payload transport. According to this set of requirements, the global co-manipulation methodology will be described and a suitable kinematic structure will be deduced.

2.2 Co-manipulation Method

The proposed co-manipulation and prehension methodology was described in [12]. Figure 1 presents different steps from object detection phase to transport phase. First, m-bots have to locate the object and surround it using distance sensors and turn on themselves so the end-effector faces the object (Fig. 1a). In a second phase, the m-bots collectively hold the object between their end-effectors and exert a collective pressure to hold it using wheel propulsion (Fig. 1b). Submitted to collective pressure and to the proposed co-lifting manipulation, the object is elevated and laid on the m-bots top platform (Fig. 1c). Finally, locomotion and transport is performed where m-bot number m must have a specific steering angle θ_m to ensure a unique Instantaneous Center of Rotation (ICR) of the p-bot (Fig. 1d).

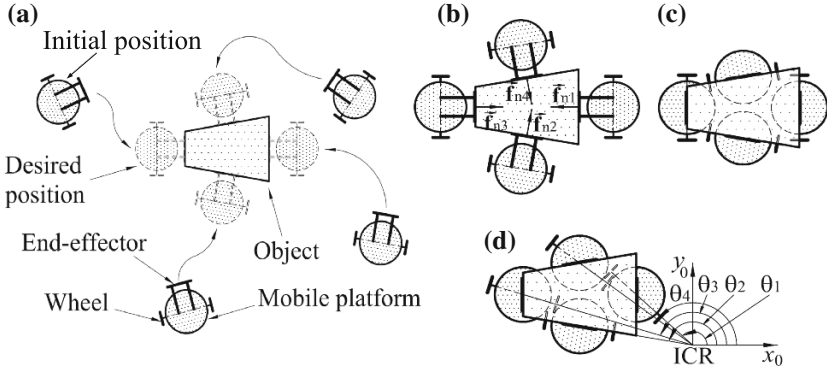


Fig. 1 Co-manipulation method: **a** Target reaching; **b** Object holding; **c** Object set on robot bodies; **d** Object transport: a unique Instantaneous Center of Rotation (ICR) requires different steering angles θ_m

2.3 Pre-dimensioning the Lifting Capacity

A m-bot # m , with a mass M , could apply on the payload a pushing force $f_{m,p,n}$, which generates a lifting force $f_{m,p,t}$, (Fig. 2) counting on wheel propulsion. The contact point $C_{m,g}$ (wheel/ground) is characterized by a friction coefficient μ_g . The maximal lifting force for the m-bot # m can be written as:

$$f_{m,p,t} = \mu_p f_{m,p,n} = \mu_p f_{m,g,t} = \mu_p (\mu_g f_{m,g,n}) = \mu_p (\mu_g M g) \quad (1)$$

$$\text{The maximal total lifting force is } f_{p,t} = \sum_{m=1}^{m_{\max}} f_{m,p,t} = m_{\max} \mu_p (\mu_g M g) \quad (2)$$

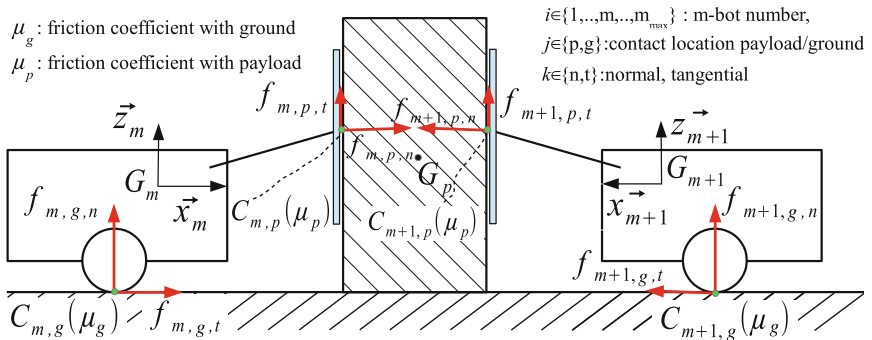


Fig. 2 Payload lifting by two m-bots

With the simplifying assumption $\mu_g = \mu_p = 0.5 \Rightarrow f_{p,t} = \frac{Mm_{max}g}{4}$. One can conclude that to increase the p-bot lifting capacity $f_{p,t}$, the total number m_{max} of m-bots, their mass M or the friction coefficients μ_g and μ_p have to be increased.

3 Designing a Lifting Mechanism

3.1 Structural Synthesis

The various requirements R_i will influence directly the kinematics structure. R_3 and R_4 can be satisfied by supporting the lifting mechanism on a turret. As a consequence, a revolute joint with z axis will support the mechanism (Fig. 1b, c). R_1 defines the initial and final poses P_1 and P_2 of the lower point P of the end-effector that holds the object (Fig. 4). The latter will keep its orientation constant during the lifting motion. The trajectory must start with a vertical lifting motion ($+z_m$) and finishes with a backward horizontal motion ($-x_m$) towards the m-bot platform (Fig. 3a). R_2 implies not to start the horizontal motion too early in order to avoid collision with the m-bot platform. Different trajectories are allowed (Fig. 3a) among which the square and the circular motions are the most obvious. A square trajectory could be achieved using two orthogonal prismatic joints (Fig. 3b) and two actuators. A circular trajectory would lead to a simpler solution using only one actuated revolute joint. However, to keep the payload orientation along the circular trajectory, a parallelogram mechanism is preferred (Fig. 3c) while keeping the control

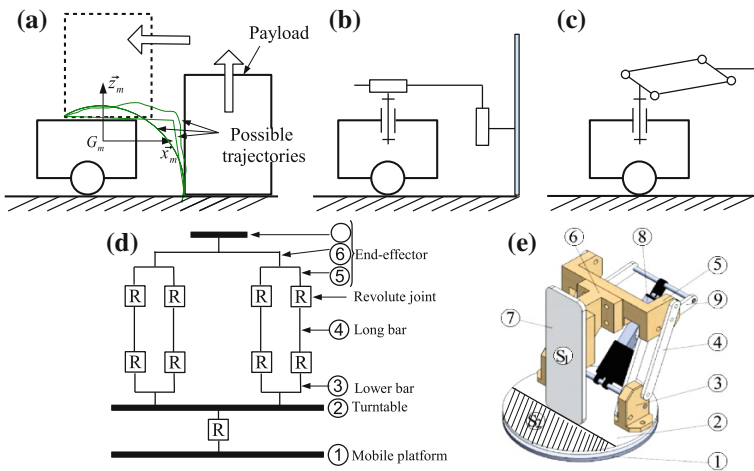


Fig. 3 Elementary lifting systems: **a** Payload initial and final position; **b** 2 DOF solution; **c** 1 DOF solution based on parallelogram mechanism; **d** Binding graph; **e** 3D CAD view

simplicity with a single actuator. The proposed mechanism will be fixed on the top of a unicycle mobile platform.

3.2 Structural Analysis

The proposed lifting mechanism is described in Fig. 3. Part 1 is a base to be fixed on the mobile platform. Part 2 is a turntable connected to 1 via a revolute joint (z_m axis) which allows the robot frame to steer freely when the payload lays on surface S_2 on the top of 2. Two identical parallelogram mechanisms are mounted on 2. Each one is composed of a lower bar 3, two long bars 4 and an end-effector support 5, 6, 7. The end-effector is a plate using the contact surface S_1 to hold the object in collaboration with the other m-bots. A linear actuator 8 is used to ensure object lifting and to control the parallelogram mechanism via an additional lever 9. The actuator allows to maintain the pressure force on the payload.

3.3 Dimensional Synthesis

P_1 and P_2 represents respectively the initial and final positions of lower point of the end-effector P . Two clearance parameters δ_1 and δ_2 are imposed to avoid collision between P and the robot platform during payload lifting at position P_3 . Constant and variable parameters are expressed in Fig. 4. Constants are: h -the mobile platform height, l -the distance between P_2 and the front of the robot, clearances δ_1 and δ_2 , α_1 -the initial angle for the parallelogram mechanism. The synthesis consists in determining the radius of the trajectory $r = l_{AB} = l_{CD}$, then calculating the distance L_1 and finally deducing the positions of A and B :

$$r = l_{AB} = \frac{-m + \sqrt{m^2 - 4np}}{2p} \quad \text{with} \quad m = -4\{[(l + \delta_1)^2 + \delta_2^2](\delta_2 + 2h \sin \alpha)\}; \quad (3)$$

$$\begin{aligned} n &= 4[(l + \delta_1)^2 \cos^2 \alpha - \delta_2^2 \sin^2 \alpha]; \\ p &= -[(l + \delta_1)^2 + \delta_2^2][(l + \delta_1)^2 + \delta_2^2 + 4h(\delta_2 + h)] \\ L_1 &= \frac{(l + \delta_1)^2 + \delta_2^2 + 2\delta_2(h + r \sin \alpha_1)}{2(l + \delta_1)} + r \cos \alpha_1 \end{aligned} \quad (4)$$

$$c = L_1 - r \cos \alpha_1 \quad (5)$$

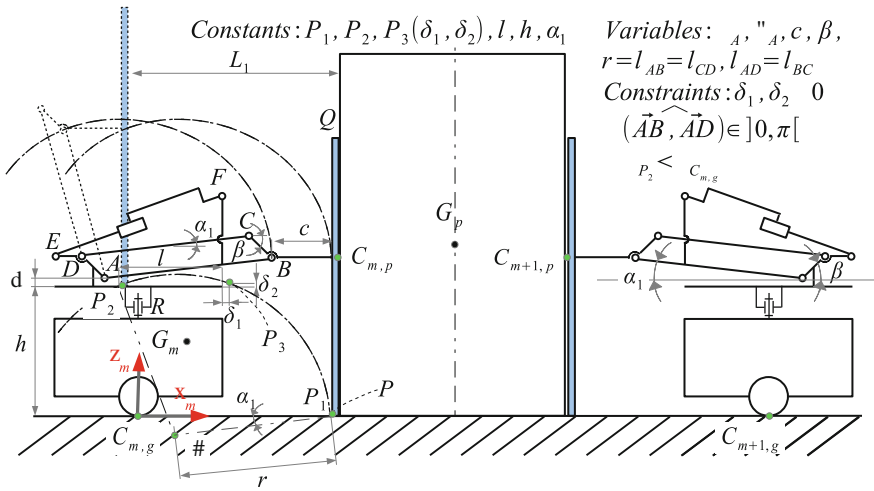


Fig. 4 Dimension synthesis

Now the position of A can be written as:

$$x_A = x_B - r \cos \alpha_1 = x_{P_1} - c - r \cos \alpha_1; \quad z_A = r \sin \alpha_1 + h + d \quad (6)$$

The angle β is chosen so that the parallelogram $ABCD$ remains as far as possible from the singular flat configuration in the extreme positions P_1 and P_2 . Length l_{AD} is not constrained.

3.4 First Prototype

Figure 5a presents the designed m-bot with the lifting mechanism in a prehension position. Figure 5b illustrates the 3D model for a group of four robots. Two prototypes based on Khepera platform have been realized to validate the manipulation strategy. Each m-bot weighs 1.4 kg. Figure 5c presents two antagonist robots

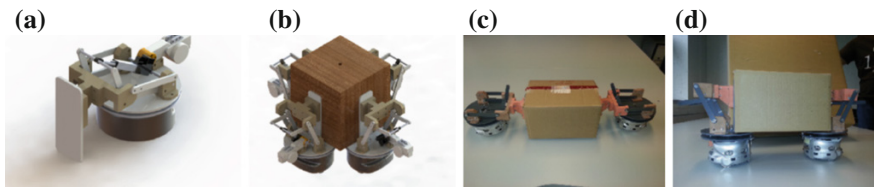


Fig. 5 Model and first prototype based on Khepera platform: **a** First prototype design; **b** Four robots manipulating a box; **c** Box prehension by two robots; **d** Box transport by two robots

manipulating a box ($200 \times 300 \times 200$ mm) and lifting it on their bodies. The m-bots keep their end-effectors down and hold the payload in between. Then they lift it up and put it on top of their bodies to be transported (Fig. 5d).

4 Conclusion and Future Work

This paper has presented the paradigm of C³Bots which aims to co-manipulate and transport a common payload by collaboration between several similar m-bots. Each m-bot is mainly made of two parts: a mobile platform and a manipulation mechanism. A first design of a lifting mechanism to be fixed on the mobile platform has been presented. The developed p-bot is modular and can gather a variable number of m-bots to manipulate an object of a general shape. The m-bot was built from a single-axle robot (Khepera platform). A specific manipulation arm was attached to a vertical actuated and reversible revolute joint to let the m-bot turn freely on itself when the payload is supported by the m-bots. The resulting p-bot is thus allowed to manoeuvre (translation along any direction and rotation around any point in the ground plane). This preliminary design allows object manipulation without considering obstacle climbing which will be the goal of a second part of the project. For future work, experiments are under process for evaluating the transport efficiency with the p-bot. Stability will also have to be evaluated and optimized during prehension, lifting and transport phases while taking into account objects shapes and weights.

Acknowledgments LABEX IMobS3 Innovative Mobility: Smart and Sustainable Solutions, the French National Centre for Scientific Research (CNRS), Auvergne Regional Council and the European funds of regional development (FEDER) are gratefully acknowledged.

References

1. Abou-Samah M, Krovi V (2002) Optimal configuration selection for a cooperating system of mobile manipulators. In: ASME 2002 International Design Engineering Technical Conferences, Montreal
2. Adouane L, Le-Fort-Piat N (2004) Emergence of group intelligence from minimalist control of mobile mini-robots. In: 35th international symposium on robotics ISR
3. Aiyama Y et al (1999) Cooperative transportation by two four legged robots with implicit communication. *Robot Auton Syst* 29(1):13–19
4. Bay JS (1995) Design of the army-ant cooperative lifting robot. *IEEE Robot Autom Mag* 1 (36):43
5. Charlec JP (2013) Elevateur pour mise en place des équipements de chantier. French patent FR2987613A1
6. Dorigo M et al (2013) Swarmanoid: a novel concept for the study of heterogeneous robotic swarms. *IEEE Robot Autom Mag* 20(4):60–71
7. Eppert DA (2012) Load measuring, fleet asset tracking and data management system for load lifting vehicles. Patent WO2012155265A1

8. Fletcher SG, Agg D (2013) Lift for a vehicle. EU patent EP2631117 A1
9. Galla TJ (2013) Lifting mechanism with lift stand accommodation. US patent US2013248786A1
10. Gianfranco G (2009) Lifting mechanism for articulated bed. EU patent EP2108288A1
11. Herrera SF (2011) Lifting mechanism for a storage bed base. EU patent EP2462842A1
12. Hichri B, Fauroux J-C, Adouane L, Mezouar Y, Doroftei I (2014) Design of collaborative cross and carry mobile robots C3Bots. *Adv Mater Res* 837:588–593
13. Hirata Y, Kosuge K, Asama H, Kaetsu H, Kawabata K (2002) Transportation of an object by multiple distributed robot helpers in cooperation with a human. *Trans Jpn Soc Mech Eng* 68 (668):1207–1214
14. Hiroaki Y et al (2011) Control of a five-axle, three-steering coupled-vehicle system and its experimental verification. In: *Preprints of the 18th IFAC world congress, Milano*, pp 12976–12984
15. Hsiang SM et al (1997) Low back pain (LBP) and lifting technique—a review. *Int J Indus Ergonomics* 19(1):5974
16. Ijspeert AJ et al (2001) Collaboration through the exploitation of local interactions in autonomous collective robotics: the stick pulling experiment. *Auton Robot* 11(2):149–171
17. Kernbach S et al (2008) Symbiotic robot organisms: REPLICATOR and SYMBRION projects. In: *Proceedings of the 8th workshop on performance metrics for intelligent systems, New York, USA*, pp 62–69
18. Khatib O et al (1999) Robots in human environments: basic autonomous capabilities. *Int J Robot Res* 18(7):684–696
19. Kunkel SH, Leatherman JM (2011) Multi dimensional lifting hand truck. US patent US2011052356A1
20. Pino NG (1997) A screw and pentograph lifting jack, particularly for a motor vehicle. EU patent EP0771757A2
21. Plamondon A et al (2014) Lifting strategies of expert and novice workers during a repetitive palletizing task. *Appl Ergonomics* 45(3):471–481
22. Rabinowitz D et al (1998) Lifting technique and abdominal belt usage: a biomechanical, physiological and subjective investigation. *Saf Sci* 28(3):155–164
23. Van Oirschot F (2013) Patient lifting device. US patent US2013269103A1
24. Wang JY et al (2010) Innovative design of the lifting mechanisms for forklift trucks. *Mech Mach Theor* 45(12):1892–1896
25. Wilcox BH et al (2007) Athlete: a cargo handling and manipulation robot for the moon. *J Field Robot* 24(5):421–434

Kinematic Design of a Reconfigurable Deployable Canopy

G. Kiper, F. Gürcü, K. Korkmaz and E. Söylemez

Abstract A reconfigurable and deployable mechanism is proposed for a canopy which can also be used as a tent or a semi-open structure. The proposed single degree-of-freedom mechanism has four assembly modes. The conditions for deployment and reconfiguration of the mechanism are derived. These conditions impose three equality and two inequality constraints on the 11 design parameters of the mechanism. A virtual model of the mechanism is constructed in Excel for design and simulation purposes. A computational case study is presented.

Keywords Kinetic architecture · Deployable structures · Canopy design · Reconfigurable mechanisms

1 Introduction

The term “reconfigurable” is used for several different meanings in the literature. Some authors use reconfigurable structure to describe movable systems which can attain different stable forms, like a chair which can transform into a ladder [1]. In this context, reconfigurable may be used interchangeably with transformable. In this study, what we mean by reconfiguration is assembly mode change for a mechanism.

G. Kiper (✉) · K. Korkmaz
İzmir Institute of Technology, İzmir, Turkey
e-mail: gokhankiper@iyte.edu.tr

K. Korkmaz
e-mail: koraykorkmaz@iyte.edu.tr

F. Gürcü
Erciyes University, Kayseri, Turkey
e-mail: fulyagurcu@erciyes.edu.tr

E. Söylemez
Middle East Technical University, Ankara, Turkey
e-mail: eres@metu.edu.tr

Also the word configuration is used for different concepts in various studies. In most mechanism science textbooks configuration is used as equivalent to assembly mode (Ex. [2]). Mason [3] defines a configuration of a system as the location of every point in the system, so that he can define the configuration space as a metric space comprising all configurations of a given system. On the other hand, Kuo et al. [4] use the configuration definition of Merriam-Webster Dictionary as “relative arrangement of parts or elements”. According to this last definition, a Scotch-Yoke mechanism and a double slider mechanism with orthogonal slider axes have the same configuration [4]. In this study we use configuration interchangeably with assembly mode.

In most applications reconfiguration is undesirable, because it causes uncontrolled motion of a mechanism. However, recently some designs make use of reconfiguration in order for the mechanism to adapt to different tasks or service conditions. Even an ASME/IFTOMM conference series is started about reconfigurable mechanisms and robots [5]. In MecArt—Kinetic Designs in Architecture group [6] in Iztech we recently started working on reconfigurable designs and the first design concept is presented as a reconfigurable deployable canopy design [7]. To our knowledge this is the first and only reconfigurable single degree-of-freedom design in kinetic architecture. The design is not only reconfigurable, but also deployable, so that the mechanism has a compact state (Fig. 1a). The mechanism may be reconfigured to be used as a canopy (Fig. 1b) or a tent (Fig. 1c) or in a semi-open hybrid form (Fig. 1d). The planar mechanism demonstrated in Fig. 1 is used as a module and several such planar modules can be combined with parallelogram loops in order to obtain spatial assemblies (Fig. 2). In [7] we presented the initial design with parallelogram loops. In this study we investigate alternate designs with general link dimensions.

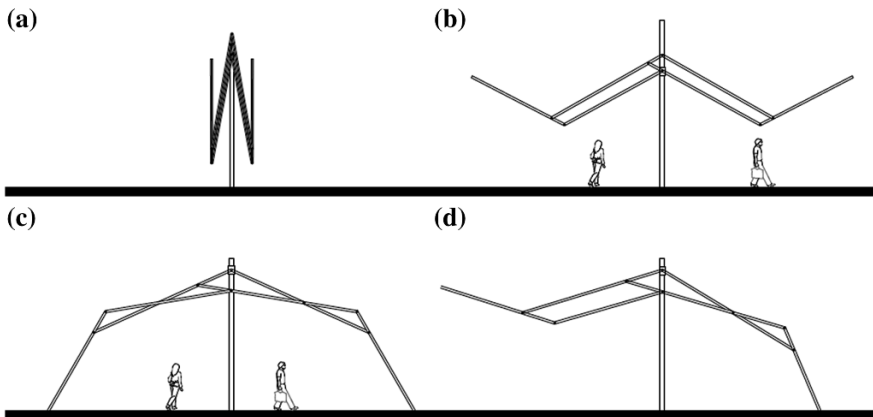


Fig. 1 Planar mechanism module in **a** compact form, **b** fully open (canopy) form, **c** fully closed (tent) form and **d** semi-open form

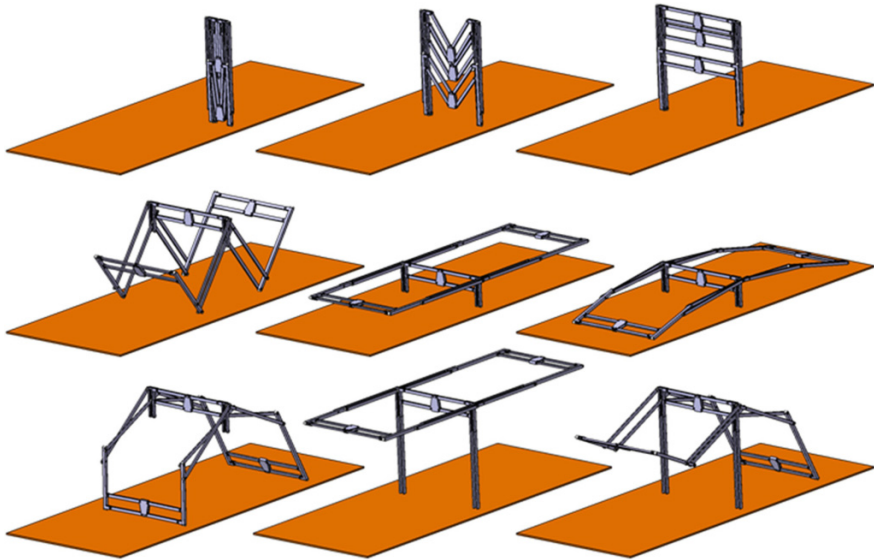


Fig. 2 The spatial assembly

2 Kinematic Model of the Mechanism

The kinematic diagram of the planar mechanism is illustrated in Fig. 1. The reconfigurable mechanism comprises two four-bar loops and a slider-crank loop (Fig. 3). It has single degree-of-freedom with 8 links and 7 joints (The slider at joint D is not shown in Fig. 3). The design parameters of the mechanism are defined as $|A_0D_0| = a_1$, $|AD| = a_2$, $|DE| = b_2$, $|AA_0| = a_3$, $|AB| = b_3$, $|BC| = a_4$, $|BG| = b_4$, $|DC| = a_5$, $|EF| = a_6$, $|FH| = b_6$ and $|A_0F| = a_7$. The variable joint parameters are θ_{12} , θ_{13} , $|A_0D| = s_{18}$, θ_{14} , θ_{15} , θ_{16} and θ_{17} .

A parametric model of this mechanism is constructed in Microsoft Excel[®] environment. See [8] for use of Excel[®] in mechanism applications. Figure 4 illustrates the design of the reconfigurable mechanism with Microsoft Excel[®]. First of all, link length parameters a_1 , a_2 , b_2 , a_3 , b_3 , a_4 , b_4 , a_5 , a_6 , a_7 are specified. Variable joint parameters θ_{12} , θ_{13} , s_{18} , θ_{14} , θ_{15} , θ_{16} , θ_{17} are determined in row 17 using the Visual Basic macro functions explained in [9]. The joint coordinates are evaluated in columns E and F. The input angle θ_{12} can be varied using the associated spin button and the graph of the mechanism can be animated.

Two configuration variables are defined in cells B20 and B21 for the two loops of the mechanism. These variables take the value 1 for the open configuration and -1 for the cross configuration of the four bar loops ABCD and A_0AEF . Also the clear span width (the distance between end points G and H when they are collinear on the ground in the fully closed form of the mechanism) is monitored in cell B23.

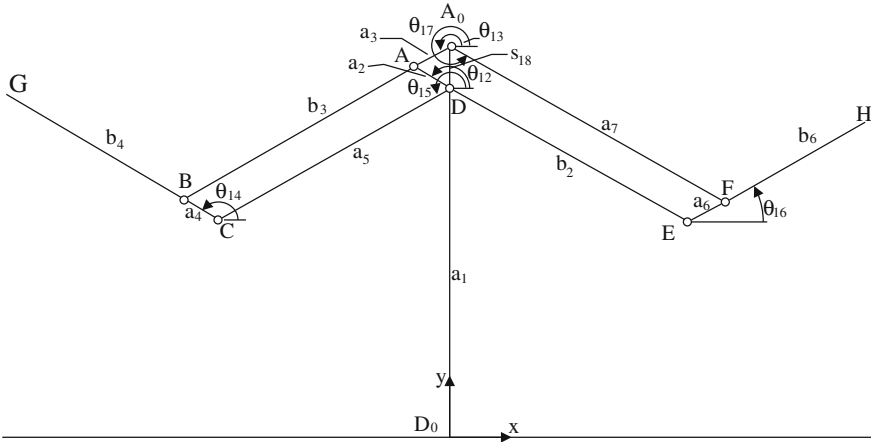


Fig. 3 Kinematic diagram of the mechanism

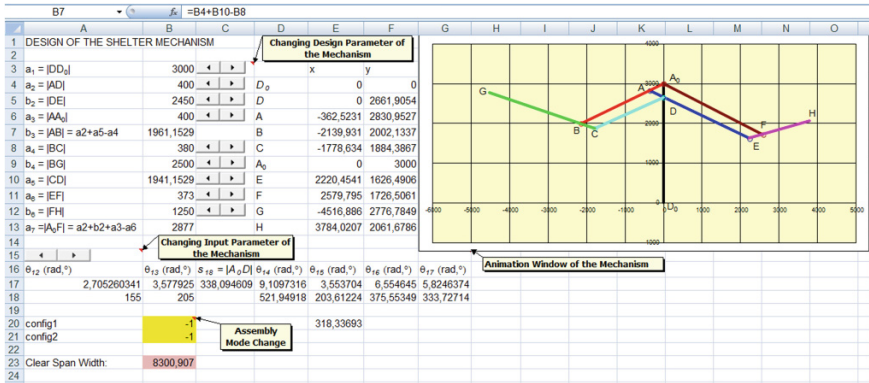


Fig. 4 Design of the reconfigurable mechanism with Microsoft Excel®

3 Determining the Link Length Dimensions

The crucial part of the overall design process of reconfigurable deployable shelter is its geometric design. In order to have a fully compact configuration, the mechanism must obey a general deployability condition [10]. The deployability condition is that all of the joints of the mechanism are collinear in the folded configuration. The deployability conditions for the two four bar loops ABCD and A₀AEF are as follows:

$$\text{For loop ABCD: } a_2 + a_5 = a_4 + b_3 \tag{1}$$

$$\text{For loop A}_0\text{AEF: } a_3 + (a_2 + b_2) = a_6 + a_7 \tag{2}$$

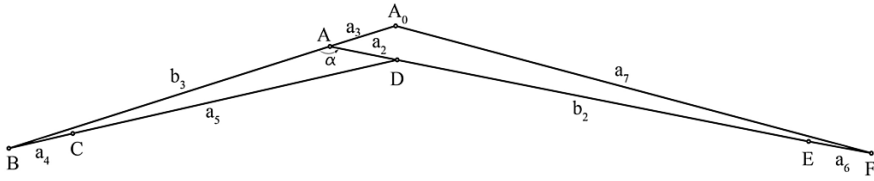


Fig. 5 The four-bar loops in dead center position

There are also some inequality constraints as design requirements. The main design requirement is reconfigurability. Reconfiguration is obtained through the dead center positions when links DC and CB are collinear for loop ABCD and AE and EF are collinear for loop A_0AEF . In order to have this collinearity, the following reconfigurability conditions should be satisfied:

$$\text{For loop ABCD: } a_4 + a_5 \leq b_3 + a_2 \quad (3)$$

$$\text{For loop } A_0AEF: a_2 + b_2 + a_6 \leq a_7 + a_3 \quad (4)$$

Combining the reconfigurability conditions (3) and (4) with the deployability conditions (1) and (2):

$$a_4 \leq a_2 \quad (5)$$

$$a_6 \leq a_3 \quad (6)$$

Reconfigurations of the two loops have to occur simultaneously, because if one of the loops reaches the dead center position before the other one, this other loop does not reach its dead center position. When the two loops simultaneously reach their dead center positions, the loops are instantaneously positioned as in Fig. 5.

Writing cosine theorem for triangles ABD and A_0AF in Fig. 5:

$$(a_4 + a_5)^2 = a_2^2 + b_3^2 - 2a_2b_3 \cos \alpha \Rightarrow \cos \alpha = \frac{a_2^2 + b_3^2 - (a_4 + a_5)^2}{2a_2b_3} \quad (7)$$

$$\begin{aligned} a_7^2 &= a_3^2 + (a_2 + b_2 + a_6)^2 - 2a_3(a_2 + b_2 + a_6) \cos(\pi - \alpha) \\ \Rightarrow \cos \alpha &= \frac{a_7^2 - a_3^2 - (a_2 + b_2 + a_6)^2}{2a_3(a_2 + b_2 + a_6)} \end{aligned} \quad (8)$$

Combining Eqs. (7) and (8):

$$\frac{a_2^2 + b_3^2 - (a_4 + a_5)^2}{a_2b_3} = \frac{a_7^2 - a_3^2 - (a_2 + b_2 + a_6)^2}{a_3(a_2 + b_2 + a_6)} \quad (9)$$

Equation (9) shall be called the simultaneous reconfiguration condition. Equation (9) imposes another restriction on the design parameters. In total there are two equality and three inequality constraints on the 11 design parameters. Due to the equality constraints, 8 of the 11 parameters can be selected freely. Here is a description of the design procedure: The dimension a_1 is the height of the reconfigurable shelter and can be selected freely according to the design requirements. There are five relationships among the link length $a_2, b_2, a_3, b_3, a_4, a_5, a_6$ and a_7 of the two four-bar loops: deployability conditions (1) and (2), reconfigurability conditions (3) and (4), and the simultaneous reconfiguration condition (9). Due to the three equality constraints, among the 8 parameters defined above 5 of them can be selected independently. It is rational that a_2, a_3, a_4, a_6 are should be independent parameters to satisfy the inequality constraints (5) and (6). The remaining independent parameter can be selected among b_2, b_3, a_5 or a_7 . For instance, let b_2 be selected as an independent parameter. From the deployability conditions two out of b_3, a_5 or a_7 are dependent on the others. Let b_3 and a_7 be dependent. So from (1) and (2)

$$b_3 = a_2 + a_5 - a_4 \quad (10)$$

$$a_7 = (a_2 + b_2) + a_3 - a_6 \quad (11)$$

a_5 should be solved from the simultaneous reconfiguration condition (9). Manipulating Eq. (9):

$$a_3(a_2 + b_2 + a_6) \left[a_2^2 + b_3^2 - (a_4 + a_5)^2 \right] = a_2 b_3 \left[a_7^2 - a_3^2 - (a_2 + b_2 + a_6)^2 \right] \quad (12)$$

Substituting (10) and (11) in (12), expanding and simplifying:

$$\begin{aligned} a_3(a_2 + b_2 + a_6) [a_2(a_2 - a_4) + (a_2 - 2a_4)a_5] \\ = a_2(a_2 - a_4 + a_5) [(a_2 + b_2)(a_3 - 2a_6) - a_3a_6] \end{aligned} \quad (13)$$

Solving for a_5 from (13):

$$a_5 = \frac{a_2 a_6 (a_2 - a_4) (a_2 + b_2 + a_3)}{a_3 a_4 (a_2 + b_2 + a_6) - a_2 a_6 (a_2 + b_2 + a_3)} \quad (14)$$

The remaining link lengths b_4 and b_6 are subject to two conditions: In fully closed configuration, points G and H must be in line with D_0 and distance between G and H should be equal to the required clear span width. These requirements are satisfied by changing b_4 and b_6 in Excel using the associated spin buttons.

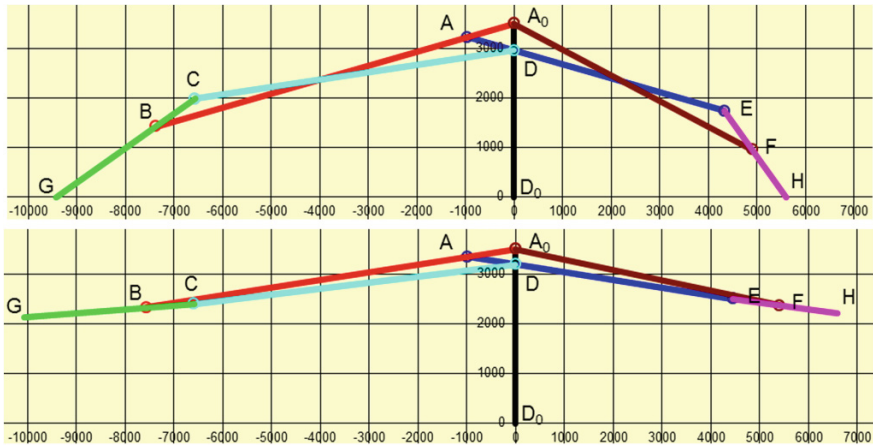


Fig. 6 Fully closed form of case study

4 Case Study

Consider a canopy design with a desired height 3.5 m and desired clear span width 15 m. A proper set of link length dimensions according to the formulations in Sect. 3 are determined as: $a_2 = 1$ m, $b_2 = 4.5$ m, $a_3 = 1$ m, $b_3 = 6.663$ m (from Eq. (10)) $a_4 = 0.98$ m, $b_4 = 2.5$ m, $a_5 = 6.643$ m (from Eq. (14)), $a_6 = 0.973$ m, $b_6 = 1.18$ m and $a_7 = 5.527$ m (from Eq. (11)). The span width is 15.032 m. The fully closed and fully open forms of the designed mechanism are illustrated in Fig. 6.

5 Conclusions

For the first time a reconfigurable single degree-of-freedom mechanism is proposed for an architectural application in this study. The 8-link mechanism is to be used as a deployable canopy which can transform into a tent or a semi-open form. The deployability, reconfigurability and simultaneous reconfiguration conditions for the mechanism are derived such that among 11 design parameters, 8 of them can be selected freely. In further studies we plan to devise means for obtaining reconfiguration of the mechanism manually or automatically.

References

1. Weaver JM, Wood KL, Jensen D (2008) Transformation facilitators—a quantitative analysis of reconfigurable products and their characteristics. In: Proceedings of the ASME 2008 international design engineering technical conferences & computers and information in engineering conference IDETC/CIE 2008, Brooklyn, NY, DETC2008-49891
2. Söylemez E (2009a) Mechanisms, 4th edn. METU Press, Ankara, Turkey
3. Söylemez E (2009b) Appendix 2: function routines for simple mechanisms and basic trigonometry. In: Mechanisms, 4th edn METU Press (2009b). Available via METU OpenCourseWare. http://ocw.metu.edu.tr/pluginfile.php/3961/mod_resource/content/12/appendices/ek2.htm
4. Mason MT (2001) Mechanics of robotic manipulation (series: intelligent robots and autonomous agents). MIT Press, Cambridge, p 11
5. Kuo C-H, Dai JS, Yan HS (2009) Reconfiguration principles and strategies for reconfigurable mechanisms. In: Dai JS, Zoppi M, Kong X (eds) ASME/IFTOMM international conference on reconfigurable mechanisms and robots REMAR 2009, pp 1–7
6. Dai JS, Zoppi M, Kong X (eds) (2009) ASME/IFTOMM international conference on reconfigurable mechanisms and robots REMAR 2009. Available via IEEEExplore® digital library. <http://ieeexplore.ieee.org/xpl/mostRecentIssue.jsp?punumber=5167202>
7. Korkmaz K (2014) Mec-art—kinetic designs in architecture. <http://mecart.iyte.edu.tr>. Last accessed: 06 Mar 2014
8. Gürcü F, Korkmaz K, Kiper G (2014) Design of a reconfigurable deployable structure. In: Proceedings of the first conference transformables 2013. Seville, pp 145–149
9. Söylemez E (2008) Using computer spreadsheets in teaching mechanisms. In: Proceedings of EUCOMES 08. Springer, pp 45–53
10. Maden F, Korkmaz K, Akgün Y (2011) A review of planar scissor structural mechanisms: geometric principles and design methods. *Archit Sci Rev* 54:246–257

Function Generation Synthesis with a 2-DoF Overconstrained Double-Spherical 7R Mechanism Using the Method of Decomposition and Least Squares Approximation

G. Kiper and B. Bağdadioglu

Abstract This study addresses the approximate function generation synthesis with an overconstrained two degrees-of-freedom double spherical 7R mechanism using least squares approximation with equal spacing of the design points on the input domain. The 7R mechanism is constructed by combining a spherical 5R mechanism with a spherical 4R mechanism with distant centers and a common moving link and then removing the common link. This construction allows the analysis and synthesis of the resulting single-loop mechanism by decomposing it into fictitious 5R and 4R loops. The two inputs to the mechanism are provided in the 5R loop and the output is in the 4R loop. The fictitious output of the 5R loop is an input to the 4R loop this intermediate variable is used to also decompose the function to be generated. This decomposition provides the designer extra freedom in synthesis and enables decreasing the error of approximation. A case study is presented at the end of the study where the 7R design is compared with an equivalent spherical 5R mechanism; hence the advantage of the 7R mechanism is demonstrated.

Keywords Multi-input function generation • Overconstrained mechanism • Method of decomposition • Least squares approximation

1 Introduction

Due to constructional simplicity, low cost, ease of use and stiffness capabilities, kinematically deficient manipulators are becoming popular ([1] and as an example see [2]). Some researchers use the deficient term as a substitute to under-actuated,

G. Kiper (✉) · B. Bağdadioglu
İzmir Institute of Technology, İzmir, Turkey
e-mail: gokhankiper@iyte.edu.tr

B. Bağdadioglu
e-mail: barisbagdadioglu@iyte.edu.tr

however what we mean by a deficient manipulator is a manipulator with less degrees-of-freedom (dof) than the task-space dimension. Although analytical synthesis methods for single dof mechanisms are widely studied [3, 4], mostly optimization methods are utilized for determining link length dimensions of multi-dof mechanisms (ex. see [5]). An exceptional study is analytical motion synthesis of a 3-RPS manipulator [6].

We have recently presented several studies on synthesis of 2-dof spherical and planar 5R mechanisms [7–9] as a case study of approximate analytical synthesis of multi-dof mechanisms. Specifically in [7] the function synthesis problem for a spherical 5R mechanism is addressed, where one of the fixed joints is an input, the mid-joint is the second input and the remaining fixed joint is the output. The reason of choosing the mid-joint as an input instead of a joint adjacent to a fixed joint is that this selection leads to linear set of equations. We make use of such a spherical 5R loop in this study, as well.

Another tool to enhance the stiffness of a manipulator is overconstraint. Huang et al. [1] note that most of the lower-mobility (deficient) parallel manipulators are overconstrained mechanisms. Recently we worked on the Bennett 6R mechanisms [10, 11]. The Bennett 6R mechanisms are the single-loop double-planar, double-spherical and plano-spherical linkages, which are respectively obtained by combining two planar slider-crank mechanisms with intersecting planes, two spherical four bar linkages with distinct centers and a planar four-bar and a spherical four-bar mechanisms, all with a common moving link connected to the common fixed link, and then removing the redundant joint connecting the two common links [12]. The removed joint is called a passive joint. Since the dof of these mechanisms according to Grübler-Kutzbach mobility formula is equal to zero despite the single dof mobility of the mechanisms, the mechanisms are overconstrained with general constraint one [13]. In [10] we derived the input-output equations of the Bennett 6R mechanisms and in [11] we worked out the function synthesis of these linkages making use of the method of decomposition [14]. The method of decomposition is based on the fact that the above-mentioned single loop 6R mechanisms may be decomposed into two imaginary loops. By taking the input and output joints as the fixed joints, the I/O equations for each imaginary loop are obtained. The passive joint is output for the first loop and input for the second loop. Besides being overconstrained, these linkages prove themselves useful in synthesis thanks to the large number of construction parameters (link lengths) [11].

In this study we combine a 2-dof 5R spherical mechanism with a single-dof 4R spherical mechanism with a common moving link and remove the redundant common joint to obtain a single-loop 2-dof overconstrained 7R spherical mechanism. We address the problem of function synthesis of this mechanism for approximate generation of a continuous function with two inputs and single output. For the synthesis method we use the least squares approximation method instead of the Chebyshev method used in [7].

$$c_3c_4 + s_3s_4c\phi = c\beta \quad (2)$$

On the other hand the scalar product of \bar{C} and \bar{E} from Eq. (1) yields

$$\bar{C} \cdot \bar{E} = c\beta \Rightarrow c_1c_2c_5 - s_1s_2c_5c\theta - s_1c_2s_5c\psi - c_1s_2s_5c\theta c\psi + s_2s\theta s_5s\psi = c\beta \quad (3)$$

Combining Eqs. (2)–(3) and rearranging

$$c_1c_2c_5 - c_3c_4 - s_3s_4c\phi - s_1s_2c_5c\theta + s_2s_5s\theta s\psi - c_1s_2s_5c\theta c\psi - s_1c_2s_5c\psi = 0 \quad (4)$$

Equation (4) can be written in the following polynomial form

$$\sum_{j=1}^m P_j f_j(\mathbf{x}) - F(\mathbf{x}) = 0 \quad (5)$$

where $m = 5$, $\mathbf{x} = \{\theta, \phi, \psi\}$ and

$$P_1 = \frac{c_1c_2c_5 - c_3c_4}{s_1c_2s_5}, P_2 = \frac{s_3s_4}{s_1c_2s_5}, P_3 = \frac{t_2}{t_5}, P_4 = \frac{t_2}{s_1}, P_5 = \frac{t_2}{t_1}$$

$$f_1(\mathbf{x}) = 1, f_2(\mathbf{x}) = -c\phi, f_3(\mathbf{x}) = -c\theta, f_4(\mathbf{x}) = s\theta s\psi, f_5(\mathbf{x}) = -c\theta c\psi \text{ and } F(\mathbf{x}) = c\psi \quad (6)$$

for $t_k = \tan \alpha_k$. P_j are determined using least squares approximation as explained in Sect. 3. After P_j are determined, the construction parameters of the mechanism are determined from Eq. (6) as

$$\alpha_1 = \pm \cos^{-1} \frac{P_5}{P_4}, \alpha_2 = \tan^{-1}(P_4 s_1), \alpha_5 = \tan^{-1} \frac{t_2}{P_3}, \alpha_3 = \frac{A \pm B}{2}, \alpha_4 = \frac{A \mp B}{2} \quad (7)$$

where $A = \cos^{-1}[c_2(c_1c_5 - (P_1 + P_2)s_1s_5)]$, $B = \cos^{-1}[c_2(c_1c_5 - (P_1 - P_2)s_1s_5)]$. Notice from Fig. 1 and Eq. (2) that interchanging α_3 and α_4 does not affect the I/O relationship. For the spherical 4-bar AFGH, the coordinates of joints F and G are

$$\bar{F} = X(-\psi)Z(\alpha_6) \begin{bmatrix} -1 \\ 0 \\ 0 \end{bmatrix} = \begin{bmatrix} -c_6 \\ -s_6c\psi \\ s_6s\psi \end{bmatrix},$$

$$\bar{G} = Z(\alpha_9)X(-\eta)Z(\alpha_8) \begin{bmatrix} -1 \\ 0 \\ 0 \end{bmatrix} = - \begin{bmatrix} c_8c_9 - s_8s_9c\eta \\ c_8c_9 + s_8s_9c\eta \\ -s_8s\eta \end{bmatrix} \quad (8)$$

Evaluating the scalar product of \bar{F} and \bar{G} and manipulating:

$$c_6c_8c_9 - c_7 + s_6c_8s_9c\psi + s_6s_8c_9c\eta c\psi + s_6s_8s_9\eta s\psi - c_6s_8s_9c\eta = 0 \quad (9)$$

Equation (9) can be written in polynomial form of Eq. (5), but $m = 4$, $\mathbf{x} = \{\psi, \eta\}$ and

$$P_1 = \frac{c_6c_8c_9 - c_7}{c_6s_8s_9}, P_2 = \frac{t_6}{t_8}, P_3 = \frac{t_6}{t_9}, P_4 = \frac{t_6}{s_9}, \quad (10)$$

$$f_1(\mathbf{x}) = 1, f_2(\mathbf{x}) = c\psi, f_3(\mathbf{x}) = c\eta c\psi, f_4(\mathbf{x}) = s\eta s\psi \text{ and } F(\mathbf{x}) = c\eta$$

After P_j are determined as explained in Sect. 3, the construction parameters are determined from Eq. (10) as

$$\begin{aligned} \alpha_9 &= \pm \cos^{-1} \frac{P_3}{P_4}, \alpha_6 = \tan^{-1}(P_4s_9), \alpha_8 = \tan^{-1} \frac{t_6}{P_2}, \\ \alpha_7 &= \pm \cos^{-1}(c_6c_8c_9 - c_6s_8s_9P_1) \end{aligned} \quad (11)$$

3 Function Generation Synthesis

Let the function to be generated be $z = f(x, y)$ for $x_{\min} \leq x \leq x_{\max}$ and $y_{\min} \leq y \leq y_{\max}$. The independent variables x and y should be related to the mechanism inputs θ and ϕ and the dependent variable z should be related to the mechanism output η . Via method of decomposition the intermediate joint angle ψ should be related to an intermediate variable w such that $w = g(x, y)$ and $z = h(w) = f(x, y)$. θ , ϕ , ψ and η can be chosen in arbitrary ranges $\theta_{\min} \leq \theta \leq \theta_{\max}$, $\phi_{\min} \leq \phi \leq \phi_{\max}$, $\psi_{\min} \leq \psi \leq \psi_{\max}$, $\eta_{\min} \leq \eta \leq \eta_{\max}$. We shall linearly relate x , y , w and z to θ , ϕ , ψ and η as

$$\begin{aligned} \frac{x - x_{\min}}{x_{\max} - x_{\min}} &= \frac{\theta - \theta_{\min}}{\theta_{\max} - \theta_{\min}}, \frac{y - y_{\min}}{y_{\max} - y_{\min}} = \frac{\phi - \phi_{\min}}{\phi_{\max} - \phi_{\min}}, \\ \frac{w - w_{\min}}{w_{\max} - w_{\min}} &= \frac{\psi - \psi_{\min}}{\psi_{\max} - \psi_{\min}} \text{ and } \frac{z - z_{\min}}{z_{\max} - z_{\min}} = \frac{\eta - \eta_{\min}}{\eta_{\max} - \eta_{\min}} \end{aligned} \quad (12)$$

Then desired ψ and η values for given inputs θ and ϕ are found as follows:

$$\begin{aligned} \theta &= \frac{\theta_{\max} - \theta_{\min}}{x_{\max} - x_{\min}}(x - x_{\min}) + \theta_{\min}, \phi = \frac{\phi_{\max} - \phi_{\min}}{\phi_{\max} - \phi_{\min}}(y - y_{\min}) + \phi_{\min}, \\ \psi &= \frac{\psi_{\max} - \psi_{\min}}{w_{\max} - w_{\min}}(g(x, y) - w_{\min}) \text{ and } \eta = \frac{\eta_{\max} - \eta_{\min}}{z_{\max} - z_{\min}}(f(x) - z_{\min}) + \eta_{\min} \end{aligned} \quad (13)$$

and conversely

$$\begin{aligned} x &= \frac{\theta - \theta_{\min}}{\theta_{\max} - \theta_{\min}} (x_{\max} - x_{\min}) + x_{\min}, \quad y = \frac{\phi - \phi_{\min}}{\phi_{\max} - \phi_{\min}} (y_{\max} - y_{\min}) + y_{\min}, \\ w &= \frac{\psi - \psi_{\min}}{\psi_{\max} - \psi_{\min}} (w_{\max} - w_{\min}) + w_{\min} \quad \text{and} \quad z = \frac{\eta - \eta_{\min}}{\eta_{\max} - \eta_{\min}} (z_{\max} - z_{\min}) + z_{\min} \end{aligned} \quad (14)$$

Equation (13) is used for determining the design points θ_i , ϕ_i , ψ_i and η_i from x_i , y_i , $w_i = g(x_i, y_i)$ and $z_i = f(x_i, y_i)$. Selection of x_i and y_i may be done with equal spacing, Chebyshev spacing, or any other type of spacing.

In least squares approximation the number of design points, n , should be more than the number of construction parameters m ($=5$ for the 5-bar and 4 for the 4-bar mechanism) and the aim is to minimize the square sum of the errors at the design points \mathbf{x}_i for $i = 1, \dots, n$. Due to the generation error, Eq. (5) is not exactly satisfied, but there is an error δ_i . In order to find the minimum of the square sum we differentiate the square sum with respect to coefficients P_j and equate to zero:

$$\frac{d}{dP_j} \left\{ \sum_{i=1}^n \left[\sum_{j=1}^m P_j f_j(\mathbf{x}_i) - F(\mathbf{x}_i) \right]^2 \right\} = 0 \quad \text{for } j = 1, \dots, m \quad (15)$$

Equations (15) are linear in P_j , hence P_j can be determined uniquely. However there are some restrictions on P_j in order to obtain a mechanism. For instance, from Eq. (7) we see that $|P_5| \leq |P_4|$ in order to be able to compute \cos^{-1} .

The maximum percentage error is defined as

$$\%|E|_{\max} = \max \left(\left| \frac{z_{\text{desired}} - z_{\text{generated}}}{z_{\text{desired}}} \right| \times 100 \right) \quad (16)$$

During the computations $\%|E|_{\max}$ is monitored and the freely chosen parameters that are associated with selection of the intermediate function w and the limits of the input/output joint variables are tuned in order to minimize the maximum error.

4 Case Study

As an example consider the function $z = x^{0.6}y^{0.2}$ for $5 \leq x \leq 10$ and $14 \leq y \leq 17$. We defined the intermediate variable as $w = x^a y^b$ such that $z = w^c$, where c can be chosen freely, $a = 0.6/c$ and $b = 0.2/c$. We employed 25 design points as equally spaced 5 by 5 grid for the inputs x and y . The limits of the inputs θ and ϕ , the passive joint variable ψ and the output η of the mechanism are also free to choose. Therefore, there are 9 free parameters in this synthesis problem. After several trials

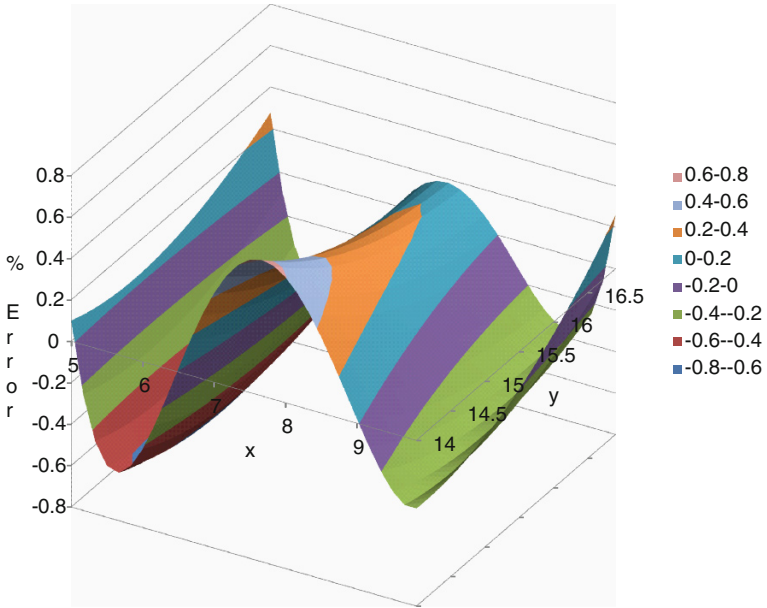


Fig. 2 Percentage error variation for generation of $z = x^{0.6}y^{0.2}$

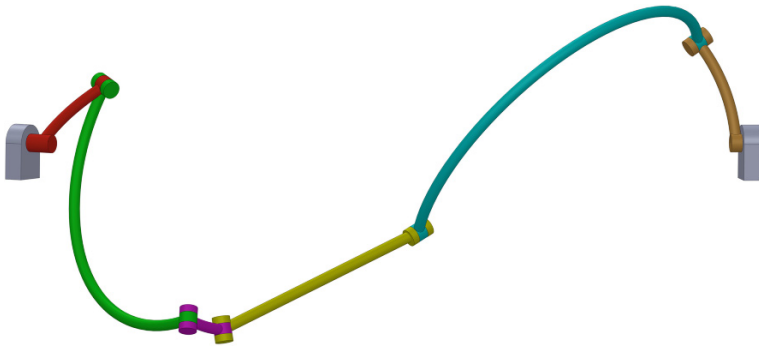


Fig. 3 CAD model of the designed 7R mechanism

on the free parameters, a solution with relatively low error is determined for $c = 0.9$, $145^\circ \leq \theta \leq 300^\circ$, $100^\circ \geq \phi \geq 80^\circ$, $105^\circ \leq \psi \leq 185^\circ$ and $250^\circ \geq \eta \geq 185^\circ$. The maximum percentage error is found as 0.656 %. The maximum percentage error can be further decreased; however the link length ratios get worse. Percentage error variation is depicted in Fig. 2. For comparison we also worked out the synthesis with a spherical 5R mechanism for the same function and maximum percentage error is found as 0.834 %.

The construction parameters of the designed 7R mechanism are $\alpha_1 = 126.13^\circ$, $\alpha_2 = 31.61^\circ$, $\alpha_3 = 127.69^\circ$, $\alpha_4 = 17.89^\circ$, $\alpha_5 = 86.65^\circ$, $\alpha_6 = 28.47^\circ$, $\alpha_7 = 171.52^\circ$, $\alpha_8 = 35.52^\circ$ and $\alpha_9 = 166.74^\circ$. It is verified that the mechanism successfully generates the desired function by means of a CAD model which is given in Fig. 3.

5 Conclusions

This study focuses on formulation of function generation synthesis of an over-constrained 2-dof 7R mechanism using least squares approximation and making use of method of decomposition. The inputs of the mechanism are chosen such that the resulting synthesis equations are linear. Several case studies are performed and one of them is presented. The case study shows that the maximum error may be decreased by use of a 7R mechanism instead of a spherical 5R mechanism. Future studies involve applying other approximation methods for the 7R mechanism and comparing the results.

Acknowledgments The authors thank Prof. Rasim Alizade for his guidance.

References

1. Huang Z, Li Q, Ding H (2013) Theory of parallel mechanisms (series: mechanisms and science). Springer
2. Vaida C et al. (2014) Structural analysis and synthesis of parallel robots for brachytherapy. In: New trends in medical and service robots. Springer
3. Sandor GN, Erdman AG (1984) Advanced Mechanism design: analysis and synthesis, vol 2. Prentice Hall, NJ
4. McCarthy JM, Soh GS (2011) Geometric design of linkages, 2nd edn. Springer, Berlin
5. Alizade RI, Rao AVM, Sandor GN (1975) Optimum synthesis of two-degree-of-freedom planar and spatial function generating mechanisms using the penalty function approach. J Eng Ind 97:629–634
6. Kim Tsai (2003) Kinematic synthesis of a spatial 3-RPS parallel manipulator. J Mech Des 125:92–97
7. Kiper G, Bilginçan T, Dede MİC (2013) Function generation synthesis of planar 5R mechanism. Prob Mech 51:28–31
8. Kiper G, Bağdadioğlu, B. and Bilginçan, T (2014a) Function synthesis of the planar 5R mechanism using least square approximation. Accepted for presentation in the 14th international symposium on advances in robot kinematics
9. Kiper G, Bilginçan T (2014b) Function generation synthesis of spherical 5R mechanism. To appear in mechanism and machine theory
10. Alizade RI, Kiper G, Dede MİC, Uzunoglu E (2013) Derivation of input–output relationship for the Bennett 6R linkages based on the method of decomposition. In: New advances in mechanisms, transmissions and applications—proceedings of the second conference metrapp (series: mechanisms and machine science). Springer, Berlin
11. Alizade RI, Kiper G, Bağdadioğlu B, Dede MİC (2014) Function synthesis of Bennett 6R mechanisms using Chebyshev approximation. To appear in mechanism and machine theory

12. Bennett GT (1905) The parallel motion of Sarrus and some allied mechanisms. *Philos Mag* 9:803–810 (6th series)
13. Alizade RI, Selvi Ö, Gezgin E (2010) Structural synthesis of parallel manipulators with general constraint one. *Mech Mach Theory* 45:1–14
14. Alizade RI, Aydazade KP, Novruzbekov IG (1980) Analysis and synthesis of planar mechanisms by using decomposition method. *J Mech Mach Acad Sci USSR* 57:26–32

Designing Cam Mechanisms Using CAx

J. Ondrášek

Abstract Very important mechanical objects are cam mechanisms whereas their dynamic properties affect the overall behavior of the given mechanical system. For this reason it is necessary to create a mathematical model of those objects whose main objective is to determine the time course of the dynamic behavior of the system. When creating mathematical models of combined cam mechanisms, there are used options and features of NX I-DEAS, MSC.ADAMS and MSC.EASY5 expert systems. This approach is shown in the design of the wire feeder drive of the nail making machine. The drive is designed by a cam mechanism with a radial conjugate cams and an oscillating roller follower. The aim of the analysis was to determine the characteristic dimensions of the cam mechanism.

Keywords Cam mechanism · Displacement law · Linkage · Hertz pressure · Dynamic analysis

1 Introduction

Cam mechanisms can implement the required working movements very accurately with a small number of links located in a relatively small space. Thus, they still are used in the construction of varied machinery. They are mainly machine tools, printing, textile, metal forming machines, etc. Increasing requirements on the performance of the mentioned machines demand appropriate processes for the design of cam mechanisms. With the development of numerical mathematics and informatics, numerical methods have begun to be applied in the design of cam mechanisms. At present it is possible user-oriented subroutines to implement into commercially available expert systems. In the case of combined cam mechanisms, these subroutines describe mathematic models of displacements and kinematic quantities of cam mechanisms and transforming linkages. The set of these

J. Ondrášek (✉)
VÚTS Liberec, Liberec, Czech Republic
e-mail: jiri.ondrasek@vuts.cz

subroutines may be used for kinematic analysis and synthesis of cam mechanisms. They may be applied also to the dimensional optimization of the mechanism regarding e.g. the value of the minimal radius of curvature of the cam profile or the maximum pressure angle. They may be used to solve the dynamics of combined cam mechanisms with rigid or flexible bodies.

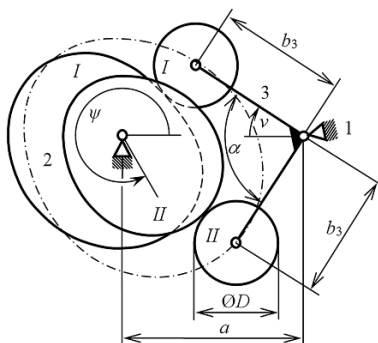
This approach is shown in the design of the wire feeder drive of the nail making machine. The drive is designed by a cam mechanism. The resulting mathematical model was defined by the algorithms of the expert system MSC.ADAMS with the assistance of user subroutines, created in the programming environment of MSC.EASY5. The numerical solution of motion equations was carried out in MSC.ADAMS. NX I-DEAS was used to the quantification of geometrically-mass parameters of bodies of the analyzed mechanical system. Individual bodies and kinematic joints, eventual deformation field of flexible bodies, may be further defined in NX I-DEAS. The aim of the analysis was to determine the characteristic dimensions of the cam mechanism.

2 Combined Cam Mechanisms

This section gives only basic information on how to solve tasks of combined cam mechanisms. Detailed knowledge of this issue may be found in [1].

The general cam mechanism is typically referred to a three-link mechanism with one degree of freedom, which includes at least one cam connected to the driven link with at least one general kinematic pair. The shape of a cam contour is usually determined by the synthesis which is based on the knowledge of the displacement law of the given cam mechanism and its dimensional parameters. The algorithms of solving of the mathematical models of general cam mechanisms include relevant subroutines. They are integrated into the user library of the MSC.EASY5 system and that are identified by block *C* for other needs. Schematic representation of a cam mechanism with a radial conjugate cams and an oscillating roller follower is shown in Fig. 1.

Fig. 1 General cam mechanism



As a combined cam mechanism it is generally called a mechanical system usually with one degree of freedom which includes at least one general cam mechanism. The system may further include gearing and linkages with not only a constant, but also a generally variable gear ratio. To the driving link of a combined cam mechanism it is assigned variable τ . The position of the driven link is indicated with the variable w . For a driven link it is usually regarded as a working link or the body whose values are the result of the solution. The position of the cam relative to the frame of the cam mechanism is determined with an angular variable ψ and the position of the follower is indicated with the generalized variable v .

Displacement laws $w(\tau)$ of combined cam mechanisms with rotating cams are periodical functions with a period of 2π . The period 2π may be divided into motion and dwell intervals. Displacements on each motion interval may be different in a maximum total rise W and an expression of the normalized form $\eta = \eta(\xi)$ [1]. The variables ξ , η of each motion interval are in linear correlation with the original variables τ , w and can be expressed as [1]:

$$\xi = (\tau - \tau_0)/T, \quad \eta = (w(\tau) - w_0)/W. \quad (1)$$

The initial point of displacement on the motion interval is defined by the coordinates τ_0 , w_0 . The interval length of the independent variable τ is given by the magnitude T . The user library of the displacement laws was developed in the MSC.EASY5 expert system.

The input of the relevant linkage is an ordered triple of variables $\mathbf{q}_{2k} = (q_{2k}, \dot{q}_{2k}, \ddot{q}_{2k})$ expressing motion of the input link of a mechanical system. The output is then a triple of variables $\mathbf{q}_{4k} = (q_{4k}, \dot{q}_{4k}, \ddot{q}_{4k})$, which represents the motion of the output link of the same system. Index k denotes the numerical indication of the relevant linkage. The general equation of the linkage may be defined as an implicit function:

$$F_k(q_{2k}, q_{4k}) = 0, \quad q_{2k} = q_{2k}(t), \quad q_{4k} = q_{4k}(t). \quad (2)$$

By differentiating the Eq. (2) in time a relation may be obtained between velocity and acceleration [1]. The individual linkage can be placed into so-called *chains* when the outputs of the given mechanism are also the inputs of the following mechanism. In the programming environment of the MSC.EASY5 system, the algorithms of solving of the mathematical models of the linkages are created by relevant subroutines that are marked with transformation blocks T_k .

The procedure of calculating a combined cam mechanism is shown through a block diagram, which is formed from transform blocks T_k and transform block C , see Fig. 2. From the view of the structure of a block diagram, it is advisable to divide the transform blocks into 3 groups, which are identified by the term *chain*:

- The input *chain IC* connects the input of the system with the input of block C ,
- The output *chain OC* connects the output of block C with the output of the system,
- The parallel *chain PC* consists of blocks that do not belong to previous chains.

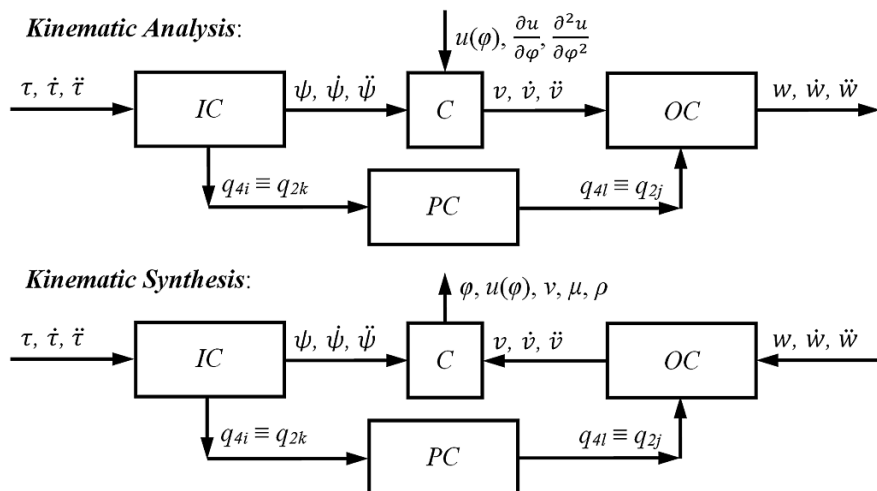


Fig. 2 Block diagrams of a computation of a combined cam mechanism

Indexes i, j, k, l denote i th, j th, k th, l th the linkage of the relevant chain.

The calculation of the positional and kinematic quantities of any link of a combined cam mechanism is designed as kinematic analysis, see the block diagram in Fig. 2. The input data is typical data on a mechanism, the procedure of computation of its chains, displacement function $\tau = \tau(t)$ of the driving link and the shape of the cam theoretical profile $u(\varphi)$. The output of the solution is the displacement of the selected link of the mechanical system w, \dot{w}, \ddot{w} . As a kinematic synthesis of a combined cam mechanism is designed the computation of polar coordinates φ, u of a radial cam or cylindrical coordinates φ, x, y of an axial cam. Furthermore, via synthesis, normal angle ν , pressure angle μ and radius of curvature of cam profile ρ are set. The input data of the task include data on a mechanical system, the calculation procedure of its chains, displacement function of driving link $\tau = \tau(t)$ and driven link of the system $w = w(t)$.

3 Feeder

The subject of the development work has been the design of a feeder drive where its basic kinematic scheme and the geometrically-mass characteristics of the individual bodies were specified. The feeder itself consists of a crank mechanism and a four-bar linkage, which are defined as implicit functions [1]:

$$L_c(\sigma_5, w) = l_6^2 + 2p_5(b_{5,7} \cos \sigma_5 + w \sin \sigma_5) - (b_{5,7}^2 + w^2 + p_5^2) = 0,$$

$$L_f(\sigma_3, \vartheta_5) = l_4^2 - b_{3,5}^2 - p_3^2 - q_5^2 + 2p_3q_5 \cos(\sigma_3 - \vartheta_5) + 2b_{3,5}(p_3 \cos \sigma_3 - q_5 \cos \vartheta_5) = 0. \tag{3}$$

The links of the crank mechanism are driver 7—working link, connecting rod 6 and crank 5, which is also a body of the four-bar linkage. The remaining links of the four-bar linkage are pitman 4 and rocker 3, see Fig. 3.

The drive is implemented with a cam mechanism with a radial conjugate cams and an oscillating roller follower. The aim of the optimization calculations was to determine the characteristic dimensions of the cam mechanism, i.e.:

- Arm length b_3 of rocker 3,
- Distance a of rotary axes of double cam 2 and rocker 3,
- Angle α between the arms of rocker 3,

and a shape of the radial double cam. Furthermore, the length of motion and dwell intervals had to be respected, see Table 1.

The dynamic properties and behavior of the feeder drive were assessed on the basis of a displacement law whose motion intervals are described by a polynomial of the fifth degree [1]:

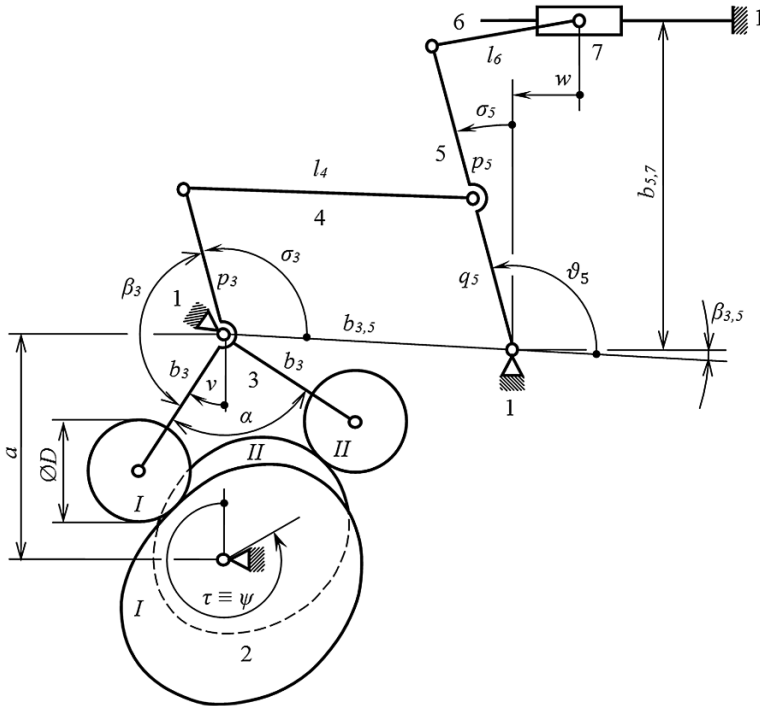


Fig. 3 Kinematic scheme of the constrained mechanical system of the feeder

Table 1 Boundary points of displacement law

Boundary point	1st	2nd	3rd	4th	5th
$\tau \equiv \psi$ [°]	0	130	165	325	360
W_{max} [mm]	0	100	100	0	0

$$\eta(\xi) = 0.125\xi \left[15 - 10(2\xi)^2 + 3(2\xi)^4 \right]. \tag{4}$$

The displacement law of the cam mechanism of the feeder is a functional expression of the displacement of driver 7 on the movement of cam 2, i.e. $w = f(\tau)$.

The resulting mathematical model of the combined cam mechanism of the feeder was created on the basis of the optimization processes of the synthesis of the drive cam mechanism in such way to achieve the greatest possible number of working cycles at the expected working frequency $n_n = 1,200$ rev/min and maximum working displacement $W_{max} = 100$ mm of driver 7. The own synthesis was carried out in the environment of expert systems NX I-DEAS, MSC.ADAMS and MSC.EASY5. Figure 4 shows the block diagram of the computation of the mathematical model, which was created in the MSC.EASY5 system environment. Each icon represents the relevant computing object, such as displacement laws, general cam mechanisms, linkages, etc. The first icon symbolizes the interconnection of systems MSC.ADAMS and MSC.EASY5. The mechanical system contains only the output chain OC, thus $\tau = \psi$. The non-uniform motion of cam 2 τ and normal reaction of general kinematic pairs N_I, N_{II} were computed by MSC.ADAMS. The cam profiles radii of curvature ρ_I, ρ_{II} and Hertz's pressures $p_{H,I}, p_{H,II}$ were computed by MSC.EASY5.

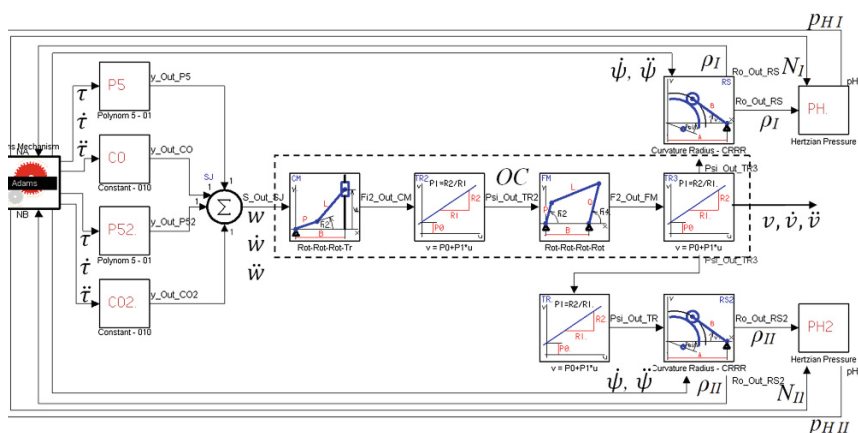


Fig. 4 Block diagram of the task of synthesis

3.1 A Sample of the Results of Dynamic Analyses

The proposed characteristic dimensions of the cam mechanism of the feeder drive that have emerged on the basis of the dynamic analyses of the composed cam mechanism take the following values:

- $a = 150$ mm distance of the rotary axes of cam shaft 2 and rocker 3,
- $b_3 = 96$ mm arm lengths of rocker 3,
- $\alpha = 100^\circ$ angle between the arms of rocker 3,
- $D = 80$ mm diameter of rollers.

In the operation of cam mechanisms, fatigue damage of the contact surfaces of a cam and a follower may appear. This damage is in the form of pitting that develops from cracks on the surface of the active area. This type of damage is due to contact stress described by Hertz's theory. The contact of the roller with the cam occurs in the contact surface of length l whereas in its length, a transfer of normal reaction N occurs in the general kinematic pair. Normal reaction N will cause a deformation of both bodies and induce contact pressure p . Maximum pressure value p is called Hertz's pressure, which can be determined from the relationship derived from the contact theory of cylindrical bodies with parallel axes [1, 2]:

$$p_H = \sqrt{\frac{N(|\rho| + \text{sign}(\rho)R_k)}{\pi(\delta_1 + \delta_2)lR_k|\rho|}}, \quad \delta_{1,2} = \frac{1 - \nu_{1,2}^2}{E_{1,2}}. \quad (5)$$

R_k denotes the roller diameter and ρ the radius of curvature of the active surface of the cam. Quantities $\delta_{1,2}$ characterize the elasticity of the material of the bodies in contact. Constants $\nu_{1,2}$ represent Poisson's ratio and $E_{1,2}$ Young's modulus of elasticity in tension. The value of the Hertz's pressure depends on the grade of steel from which a cam is produced and on the heat or chemo-thermal treatment of the surface layer of cams. Figure 5 shows a possible course of Hertz's pressures in the

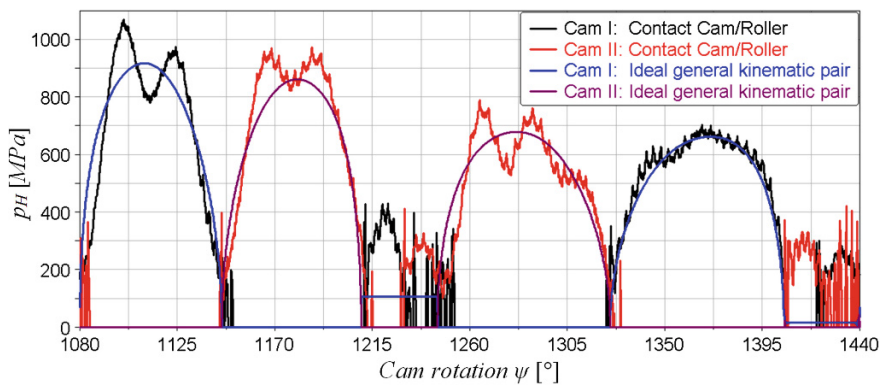


Fig. 5 Hertz's pressure in the cam mechanism

Table 2 Rating life of the bearings of the rollers

Cam roller NUKR80	p	C_w [N]	R_{ekv} [N]	L_{10} 10^6 [cycles]
I	10/3	67,000	13,000	240
II	10/3	67,000	12,000	310

cam mechanism of the feeder drive at the operating frequency $n_n = 1,200$ rev/min. From their curves it is evident that the value of Hertz's pressure within the machine working cycle does not exceed the size limit.

In terms of the dynamic behavior of the analyzed mechanic system, rating life L_{10} of the bearing of the cam mechanism rollers was assessed that result from the relationship [3]:

$$L_{10} = (C_w/R_{ekv})^p \cdot 10^6 \quad [\text{cycles}]. \quad (6)$$

In expression (6), C_w stands for the basic dynamic load rating of the bearing and R_{ekv} for equivalent load, which is determined on the basis of reaction forces in the respective bearing. The parameter of the bearing p achieves those values:

- $p = 3$: for bearings with point contact,
- $p = 10/3$: for bearings with line contact.

For the machine working speed $n_n = 1,200$ rev/min and the working displacement of the driver $W_{max} = 100$ mm, it results the rating life of the bearings of the cam mechanism rollers according to Table 2.

4 Conclusions

User libraries of procedures and functions have been created that contain the algorithms of solving combined cam mechanisms. They are used for an efficient creation of mathematical models of those mechanical systems. During this activity, a cooperation of systems NX I-DEAS, MSC.ADAMS and MSC.EASY5 was used.

This approach of designing a cam mechanism was applied in the synthesis of the feeder drive. The dynamic properties and behavior of the feeder drive were assessed on the basis of a displacement law whose motion intervals are described in a polynomial of the fifth degree. In computational analyses, the cam mechanism itself was being loaded with the inertia effects of the feeder mechanism and with working force. The relevant working force is induced with motion and deformation effects of a wire that enters into the machine working operation. Based on the computational simulations, the rollers of the cam mechanism appear to be critical nodes of the designed mechanism in terms of durability. Rollers whose bearings will reach rating life L_{10} were chosen in an order of 1×10^8 cycles at least.

Acknowledgments This paper was created within the work on the FR-TI4/801—Project supported by the Ministry of Industry and Trade.

References

1. Koloc Z, Václavík M (1993) Cam mechanisms. Elsevier, Amsterdam. ISBN 0-444-98664-2
2. Johnson KL (1985) Contact mechanics. Cambridge University Press, Cambridge. ISBN 0 521 34796 3
3. Pešík L (2008) Části strojů, Technická univerzita v Liberci, ISBN 978-80-7372-319-4—in Czech (Parts of machines)

Kinematics Analysis and Verification on the Novel Reconfigurable Ankle Rehabilitation Robot Based on Parallel Mechanism

Shilong Zeng, Ligang Yao, Xiaoning Guo, Hengli Wang and Pengju Sui

Abstract This paper proposes a novel reconfigurable ankle rehabilitation robot based on parallel mechanism. The proposed robot is composed of the linear actuators, reconfigurable mechanism, connecting rods, rockers and the moving platform. Then, the kinematic characteristics analysis for the proposed robot is given. The function relationships between the moving platform and the actuators are obtained. Furthermore, the verification for this novel reconfigurable robot is completed by wireless movement capture instrument, and the results show that the prototype ankle rehabilitation robot can meet the motion needed for the ankle rehabilitation.

Keywords Ankle rehabilitation robot · Reconfigurable mechanism · Kinematics · Motion trajectory

1 Introduction

In the field of rehabilitation robotics research, the development of the ankle rehabilitation robot is a hotspot [6]. Currently, medical experts consider that the movements of the human ankle can be summarized as the rotations around spatial joint axes [3, 13]. In order to realize the rehabilitation, it's vital to completely imitate the movements of the ankle around these spatial joint axes with medical rehabilitation robot. Consequently, Cartesian coordinate system and spatial three axes rotation model are chosen to design the robot mechanism. The imitating movements of the ankle are broken down into the rotation model rotating around three vertical axes, which are inversion/eversion, plantar flexion/dorsiflexion and adduction/abduction [1]. For most people, the angle range of inversion rotation varies from 35 to 40° and the eversion rotational angle is 0–25°, the angle of

S. Zeng (✉) · L. Yao · X. Guo · H. Wang · P. Sui
School of Mechanical Engineering and Automation, Fuzhou University, Fuzhou, China
e-mail: zengsl@hotmail.com

plantar-flexion rotation is $5\text{--}50^\circ$ and the dorsiflexion rotational angle is from 20 to 25° . To the angle range of the adduction and the abduction rotation, it is $25\text{--}30^\circ$ [7]. Many rehabilitation devices based on the 3-axes model parallel mechanism were proposed. The typical 3-axes ankle rehabilitation robots were developed based on the mechanisms including the 3-SPS/S, 2-RRR/UPRR, 3UPS/U, and the 3PUP type [4, 8, 9, 14, 16].

The researches on these mechanisms had provided the basis for the ankle rehabilitation robot development. However, there are some disadvantages of incontinent adjustment and control. It is shown that in the rehabilitating process, the rotation angle of rehabilitation robotics needs be adjusted according to the movement of the ankle and the patients' condition. Because of reconfigurable mechanism adapt to different requirements and various environments [2, 3, 17, 18], and it can be utilized to regulate the rotation angle of ankle rehabilitation robot. Furthermore, the ankle rehabilitation device should establish a suitable ankle motion mode, a proper mechanism, correct driving scheme and control system [10–12, 15]. To overcome the above mentioned deficiencies, this paper proposes a novel reconfigurable ankle rehabilitation robot based on the parallel mechanism. The research carried out on the mechanism construction, the reconfigurability, the kinematics characteristics analysis and the verification for this novel reconfigurable ankle rehabilitation robot will be discussed.

2 The Novel Ankle Rehabilitation Robot with Reconfigurable Mechanism

In order to guarantee high stiffness and excellent supporting capability, the proposed reconfigurable ankle rehabilitation robot is based on a parallel mechanism, as shown in Fig. 1. This parallel mechanism is made up by a moving platform, a fixed platform (with a support bar) and three sub-branch mechanisms. One of the sub-branch mechanisms is composed of a linear actuator 1 and 2, a rocker 3 and a connecting rod 4. The linear actuator is selected as a power source for linear drive mechanism. Reciprocal motion of linear actuator pushes rocker 3. Through the swing of rocker 3, the rod 4 drives the end slider 5 which is connected with the moving platform.

The moving platform is driven by the three sub-branch mechanisms and can rotate around the support bar. Consequently, it can simulate the three axes ankle rehabilitation movement effectively. Because of the individual differences and different needs of ankle rehabilitation for different people, the adjustability is indispensable required. Therefore, the reconfigurable mechanism composed by three liner actuators and a base platform, shown in Fig. 2, is proposed in the lower part of the robot. The reconfigurable mechanism can improve the workability of the moving platform.

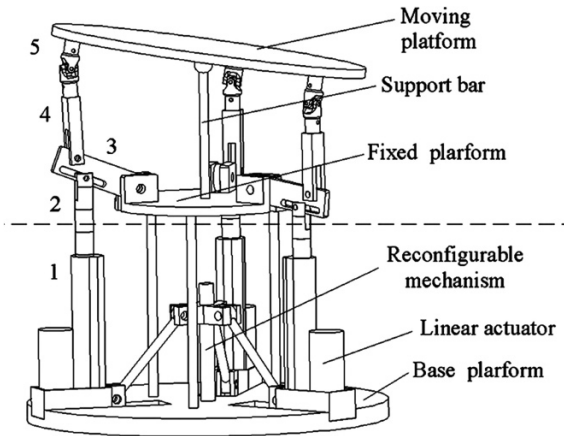


Fig. 1 Diagram of ankle rehabilitation robot

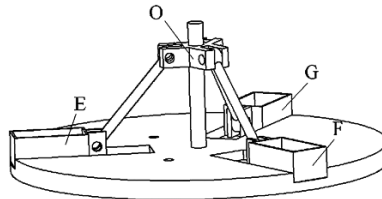


Fig. 2 Reconfigurable mechanism

As it is commonly known, the reconfigurable mechanism is a type of mechanism whose structural dimension, joint position and other parameters can be adjusted under the additional adjusting means. To realize the reconfigurability in ankle rehabilitating, the following functions need to be implemented:

- (1) The motion range of the moving platform can be adjusted.
- (2) The mechanism rejects quick return.
- (3) Range adjustment can be easily adjusted and controlled.

The sub-branch mechanism is designated as the slider-crank mechanism for its excellent anti-quick-return characteristic. The output of moving platform is directly depending on the rocker inputs. The linear actuator 2 pushes the rocker 3 rotating around the fixed platform joint. The position of the joint between the actuator 2 and the rocker 3 can be adjusted: the connection position on the rocker 3 and stroke of line actuator change the swing angle of rocker 3. In order to adjust the position of three actuators synchronously, the robot reconfigurable mechanism uses the three double slider mechanisms shown in Fig. 2 and the synchronous movements of actuator sliders *E*, *F* and *G* are carried out by the vertical movement of slider *O*.

3 Kinematic Characteristics Analysis

Obviously, the novel parallel mechanism combines two parts, the upper part as the rehabilitation mechanism and the low part as the reconfigurable mechanism. The rehabilitation mechanism can achieve the ankle rehabilitation rotation around three axes, and the reconfigurable mechanism has adjusting ability. To determine the characteristics of the robot, the followings will discuss the kinematic characteristics analysis for the upper part robot by building coordinate transformation matrix to solve the inverse solution of rehabilitation mechanism.

3.1 Coordinate Transformation for the Rehabilitation Mechanism

The coordinate transformation is kinematics analysis foundation. According to the Fig. 1, a fixed coordinate S - XYZ on the fixed platform and a moving coordinate S' - uvw connecting with the moving platform are established, as shown in Fig. 3. Where in Fig. 3, A_i ($i = 1, 2, 3$) and a_i ($i = 1, 2, 3$) are revolution joints. The distance between A_i and S is R_A . R_a represents the distance between point a_i and the point S' . The rocker length is $|A_i B_i| = r$, and the rod length is $|B_i a_i| = l$. In the initial position, the moving platform is parallel to the fixed platform. From the point S to point S' , the distance is t . There is a geometric relation, given by

$$l^2 = (R_A + r - R_a)^2 + t^2 \tag{1}$$

The moving platform of the mechanism has 3° of freedom, respectively around X axis, Y axis and Z axis of rotation. So we can consider that the matrix transformation follows the following steps. Firstly, the moving coordinate S' - uvw ,

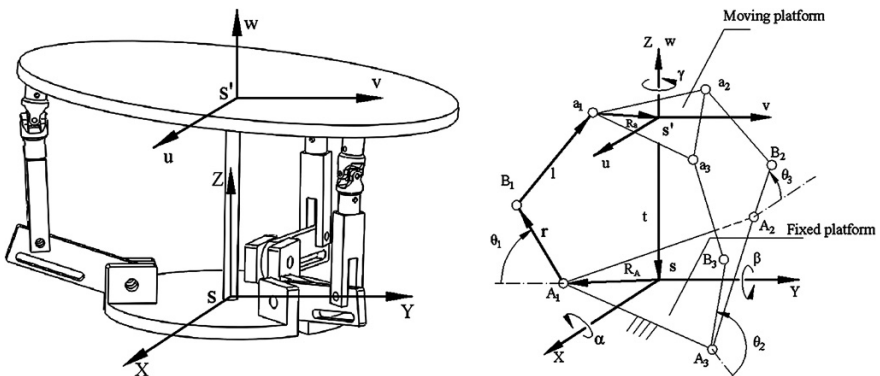


Fig. 3 Coordinate system on the rehabilitation mechanism

rotates the angle α around the X axis, then rotates angle β around the Y axis, and finally rotates angle γ around the Z axis. Therefore, the matrix transformation can be represented as T , given by

$$T = \begin{bmatrix} c\beta c\gamma & s\alpha s\beta c\gamma - s\gamma c\alpha & c\alpha s\beta c\gamma + s\alpha s\gamma \\ s\gamma c\beta & s\alpha s\beta s\gamma + c\alpha c\gamma & c\alpha s\beta s\gamma - s\alpha c\gamma \\ -s\beta & c\beta s\alpha & c\beta c\alpha \end{bmatrix} \quad (2)$$

In the all formulas of this paper, s represents sin function, and c represents cos function.

3.2 Inverse Solution of the Rehabilitation Mechanism

When choosing the design parameters for ankle rehabilitation, the values of rotation angle of the moving platform can be determined by the angle of patient's motion. In the introduction, the rotation angle of the ankle is known, so the output angle of the robot (α , β , γ) has been determined to simulate the ankle rehabilitation movement, in which α is related to the angle of dorsiflexion/plantarflexion, β is related to the angle of inversion/eversion, and γ is related to the angle of adduction/abduction. In the rehabilitation mechanism, we can find the rotation of rockers is important to the rotation angles (α , β , γ). Consequently, the process of solving inverse solution is to find the input rotation angles of three rockers $q = (\theta_1, \theta_2, \theta_3)$, as shown in Fig. 3.

Again in Fig. 3, the coordinate matrix of the point a_i ($i = 1, 2, 3$) is M'_a in the moving coordinate system $S'-uvw$. The point a_i ($i = 1, 2, 3$) in the fixed coordinate S -XYZ can be obtained by the coordinate transformation. The coordinates of the matrix M_a represents the point a_i ($i = 1, 2, 3$) coordinate in the fixed coordinate S -XYZ, then:

$$M_a = TM'_a \quad (3)$$

The coordinates of the point B_i ($i = 1, 2, 3$) in the fixed coordinates S -XYZ is given by

$$B_1 = [A_{1x} - r \cdot c\theta_1 \quad 0 \quad A_{1z} + r \cdot s\theta_1]^T \quad (4)$$

$$B_2 = \left[A_{2x} + \frac{\sqrt{3}}{2} r \cdot c\theta_2 \quad A_{2y} - \frac{1}{2} r \cdot c\theta_2 \quad A_{2z} + r \cdot s\theta_2 \right]^T \quad (5)$$

$$B_3 = \left[A_{3x} + \frac{\sqrt{3}}{2} r \cdot c\theta_3 \quad A_{3y} + \frac{1}{2} r \cdot c\theta_3 \quad A_{3z} + r \cdot s\theta_3 \right]^T \quad (6)$$

By the geometric relationship given by Eq. (1), we can obtain:

$$l^2 = (B_{ix} - a_{ix})^2 + (B_{iy} - a_{iy})^2 + (B_{iz} - a_{iz})^2 (i = 1, 2, 3) \quad (7)$$

Substituting (α, β, γ) to solve equation group Eq. (7), we can obtain input solution of rockers $q = (\theta_1, \theta_2, \theta_3)$. It is easy to find that matrix method for the parallel mechanism is concise and convenient. With the solution of the inverse method, the rotation angle of moving platform can be achieved to compute the input of rockers.

4 Verification Rotation Angle of the Moving Platform

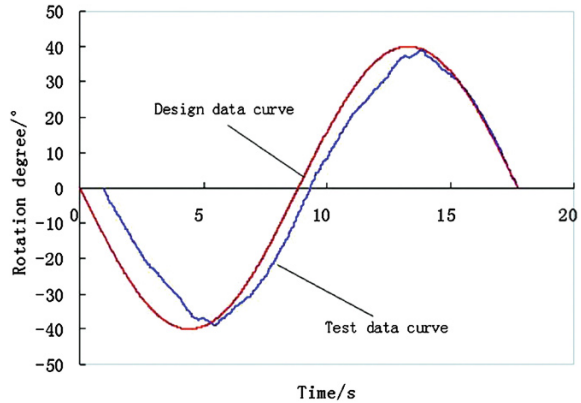
The robot prototype is developed to verify the rehabilitation characteristics. The robot is shown in Fig. 4. The plantar-flexion rotation angle is relatively larger than the others, and for this reason the plantar-flexion rotation of the robot was used for this verification. The plantar-flexion rotation angle is determined as 40° , then we designate the moving platform to do plantar-flexion rotation according to the rule of sin function in one period, as shown Fig. 5. A wireless motion capture instrument was used to test the plantar-flexion rotation angle of experimental prototype, as shown in Fig. 4. The wireless motion capture system is an advanced trajectory capture instrument and has high-speed data process ability. It can measure the spatial position information and direction information through the measuring block Marker [5]. In the testing, the block Marker was placed on the center of the moving platform. The instrument was opened to acquire the motion data of the moving platform through recording Marker's trajectory. The prototype utilizes a micro-controller to control.

In order to test the reliability of the design and manufacture of the prototype, test results are compared with the design angle of ankle rehabilitation. The obtained test data was compared with design data for rehabilitation, as shown in Fig. 5. The test data waveform is a sine wave-shaped, which is stable and continuous in the

Fig. 4 Measurement sensor marker placed on the center of the moving platform



Fig. 5 Rehabilitation exercise test data curve and design data curve



direction of rotation. Because of manufacture error, the test data curve presents a little delay compared with the design data curve. The delay of the robot is influenced by the connection of components, which will be reduced by improving the manufacturing precision. The tested plantar-flexion angle of rotation meets what is needed for a normal persons' ankle rehabilitation, and its value can still be changed by the reconfigurable mechanism.

5 Conclusions

The reconfigurable ankle rehabilitation robot, according to the principles of the reconfigurable, is proposed to solve the problem that the same type of ankle rehabilitation devices presents to carry out a flexible adjustment. The robot has two parts, in which the rehabilitation mechanism can realize ankle rehabilitation rotation, and the reconfigurable mechanism can adjust the angle rotation of rehabilitation mechanism. Based on the kinematic characteristics analysis and the experiment test, the results show that the prototype can help patients for ankle rehabilitation. In future, to observe the real effect on human which is worked by the robot, a virtual rehabilitation mannequin experiment will be discussed.

Acknowledgments The authors wish to thank Natural Science Foundation of China (Grant No. 51275092) for funding the researches.

References

1. Dai JS, Zhao TS, Christopher N (2004) Sprained ankle physiotherapy based mechanism synthesis and stiffness analysis of a robotic rehabilitation device. *Auton Robots* 16:207–218
2. Ding XL, Ynag Y (2010) Reconfiguration theory of mechanism from a traditional artifact. *J Mech Des* 132:114501

3. Dai JS, Zoppi M, Kong XW (2012) *Advances in reconfigurable mechanisms and Robots I*. Springer, London/Heidelberg, pp v–viii
4. Gironi M, Burdea G, Bouzit M, Popescu V (2001) A Stewart platform-based system for ankle telerehabilitation. *Auton Robots* 10:203–212
5. http://polhemus.com/?page=Motion_Liberty_Latus
6. Pan LQ, Shen XD (2010) Robotics technology in the instrumentation of traditional Chinese medicine treatment. *Technol Appl Robots* 10:28–30
7. Parenteau CS, Viano DC, Petit PY (1998) Biomechanical properties of human cadaveric ankle subtalar-joints in quasi-static loading. *J Biomech Eng* 120:105–111
8. Saglia JA, Tsagarakis NG, Dai JS et al (2009) A high performance 2-dof over-actuated parallel mechanism for ankle rehabilitation. In: *IEEE international conference on robotics and automation*, Kobe, international conference center, pp 2180–2186
9. Saglia JA, Tsagarakis NG, Dai JS, Caldwell DG (2012) Control strategies for patient-assisted training using the ankle rehabilitation Robot. *IEEE/ASME Trans Mechatron* 99:1–9
10. Sui PJ, Yao LG, Lin ZF, Yan HY, Dai JS (2009) Analysis and synthesis of ankle motion and rehabilitation Robots. In: *Proceedings of the 2009 IEEE international conference on robotics and biomimetics*, Guilin, pp 2533–2538
11. Sui PJ, Yao LG, Lin ZF, Yan HY, Dai JS (2010) Kinematics analysis of a novel ankle rehabilitation robotics. In: *International conference and course on orthopaedic biomechanics clinical applications and surgery*, West London, pp S70
12. Sui PJ, Yao LG, Dai JS, Wang HL (2011) Development and key issues of the ankle rehabilitation robots. In: *13th world congress in mechanism and machine science*, Guanajuato, pp A12–416
13. Yu DS (1993) *Manual of rehabilitation medicine*. Huaxia Publishing House, Beijing, pp 55–57
14. Yoo JW, Ryu J (2005) A novel reconfigurable ankle/foot rehabilitation robot. In: *IEEE international conference on robotics and automation*, Barcelona, international conference center, pp 2290–2295
15. Yao LG, Lin ZF, Yan HY, Wei GW, Dai JS (2008) Mechatronics integrated system for ankle rehabilitation and foot massage. In: *Proceedings of the 11th mechatronics forum biennial international conference*, Ireland, pp 305–310
16. Zhao TS, Yu HB, Dai JS (2005) Ankle rehabilitation robot based on 3-rss/s parallel mechanism. *J Yanshan Univ* 29:471–475
17. Zhang KT, Dai JS, Fang YF (2012) Constraint analysis and bifurcated motion of the 3PUP parallel mechanism. *Mech Mach Theory* 49:256–269
18. Zhang KT, Dai JS, Fang YF (2013) Geometric constraint and mobility variation of two 3SvPSv metamorphic parallel mechanisms. *J Mech Des* 35:1–8

Finite Element Modeling and Analysis of an Isoglide-Type Parallel Manipulator to Determine Its Rigidity/Stiffness

A. Kozyrev and V. Glazunov

Abstract Currently, in many industrial factories, in medical devices, in training aircraft, space and tank simulators and in other areas the robots based on the parallel manipulators are widely used or planned for the implementation. According this, the problem of choosing the particular manipulator, which is able to provide the best desired characteristics is rather acute because of the wide variety of specific designs. One of the main characteristics of manipulators of conventional structure and parallel structure is their stiffness under the different variants of loading by the external force. The aim of this work is to analyse the stiffness parameters of the three-dimensional model of the parallel manipulator of the Isoglide type, to identify weaknesses and to make proposals for the improvements of the manipulator in order to increase rigidity if it is necessary.

Keywords FEA · Parallel manipulator · Stiffness · Stress

1 Introduction

The modern method of stress analysis is the finite element method (FEM). By using computer technologies, which are capable to handle complex models, the results of the FEM-analysis can be obtained of a very high quality and reliability. Most often, the finite element method is used to analyze the stresses and deformations of individual parts under the loading, but in this work, the FEM-analysis was applied to research the stiffness characteristics of the assembled manipulator in different positions.

A. Kozyrev (✉) · V. Glazunov
Institute of Machines Science, (A.A. Blagonravov of the Russian
Academy of Sciences), Moscow, Russia
e-mail: lexxko@yandex.ru

V. Glazunov
e-mail: vaglzv@mail.ru

The Isoglide is a spatial parallel manipulator with three independent translational degrees of freedom. The Isoglide family of robots has been investigated by Grigore Gogu and his team at the French Institute of Advanced Mechanics [1]. A study of stiffness of the Isoglide manipulators has been performed by Rany Rizk in his PHD. [7]. However, the manipulators with additional kinematical chains [3] weren't considered.

The manipulator having independent degrees of freedom has both advantages and disadvantages [2, 4, 5, 6, 8]. The advantages include:

- simple control system, due to the fact that the movement of the endpoint along any axis is equal to the displacement of the corresponding drive;
- simple parts of the manipulator (there is no need to use complex-shaped parts);
- the manipulator is easy to assemble.

The main disadvantage is that only one of the three kinematical chains carries the external load applied to the endpoint if it is directed along one of the main axes (parallel to the direction of one of the drives) and if mechanism deformation is insignificant. Thereby, the increased rigidity, which is a significant advantage of the parallel manipulators over the ordinary manipulators, is lost.

In this paper, we analyzed the stiffness parameters of the parallel manipulator of the Isoglide type with different variants of the load applied on the endpoint by using the finite element method. The study was carried out by using the Autodesk Inventor.

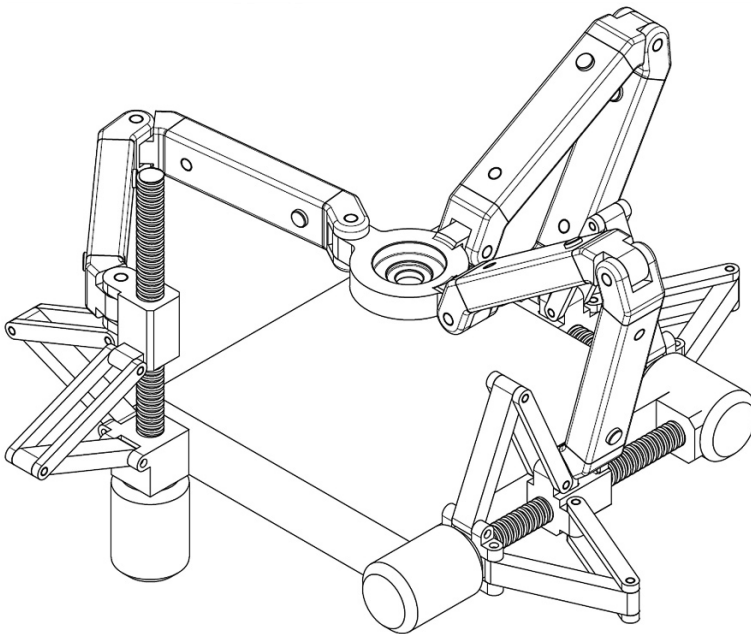


Fig. 1 The Isoglide manipulator

Moving range of each drive of the model is 280 mm, and all the kinematical chains are the same. Each of the three kinematical chains consists of two identical links of length 300 mm. In order to get rid of the need for linear actuators (which must be very precise and thus quite expensive to ensure reasonable kinematical accuracy of the manipulator) two additional kinematical chains were added [3] to prevent rotation of the actuator’s slider around the screw and to decrease the load on the screw (Fig. 1). FE-models use tetrahedron elements of first and second order. Average element size is 0.100 (as a fraction of bounding box length), minimum element size is 0.200 (as a fraction of average size), and grading factor is 1.5. Maximum turn angle is 60.00°. The boundary conditions are shown on the Figures.

2 Selection the Type of a Cross-Section of Links

The first point of the analysis is to determine what forces have a greater effect on the strain at the origin of each kinematical chain, is it a torque or a bending force. To investigate this question two simplified three-dimensional models of the individual kinematical chains were built.

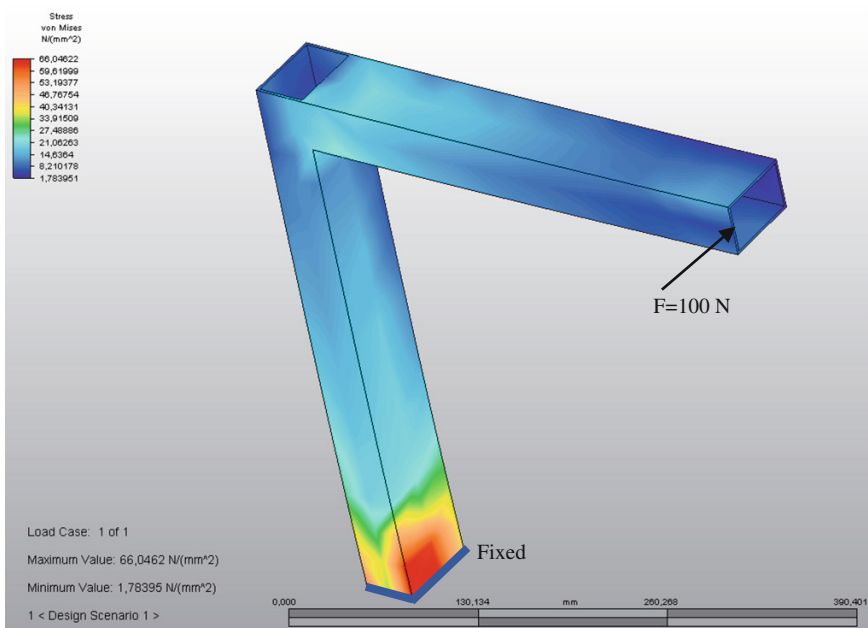


Fig. 2 Stress diagram of the simplified model of the kinematical chain with the link having rectangular cross-section

In one of them, both links of the kinematical chain are made of rectangular tubes, what implies a better stiffness in the case of the bending force dominating over the torque.

In another model, the first element is made of a circular tube with the same wall thickness and with similar geometric parameters, what implies a better stiffness of the kinematical chain in case of the torque dominating over the bending force.

Each of the two simplified models was tested by the application of the same load on the endpoint. FEM was used because it is analysis that is more versatile and it can be extended to explore objects that are more complex. The simulation results are shown on Figs. 2 and 3.

As it is evident on the diagrams, a model comprising the two tubes with a rectangular cross-section has a significantly greater stiffness in comparison with the model in which the first link is made of a circular tube. This means that the dominant force factor in the origin of the kinematical chain is not a torque but the bending force. Accordingly, to build the complete model of the manipulator, the tube links having a rectangular cross-section were used, because they has stiffness much greater under the typical load than link with circular cross-section.

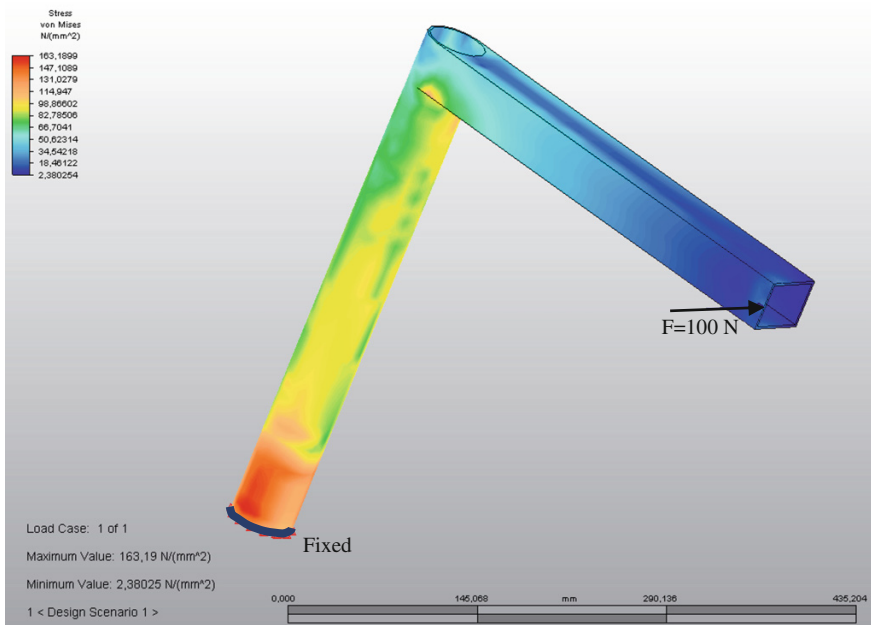


Fig. 3 Stress diagram of the simplified model of the kinematical chain with the link having *round cross-section*

3 Applying the Load to the Endpoint of the Manipulator

The next research problem is to check the stiffness of the whole manipulator in different positions and in different variants of loading. According to Sect. 2 conclusions, links having a rectangular cross-section were used to build the robot. In this work, the vertical load and the mixed load on the endpoint were considered, because such loads are the most typical. Mixed load means that the applied external

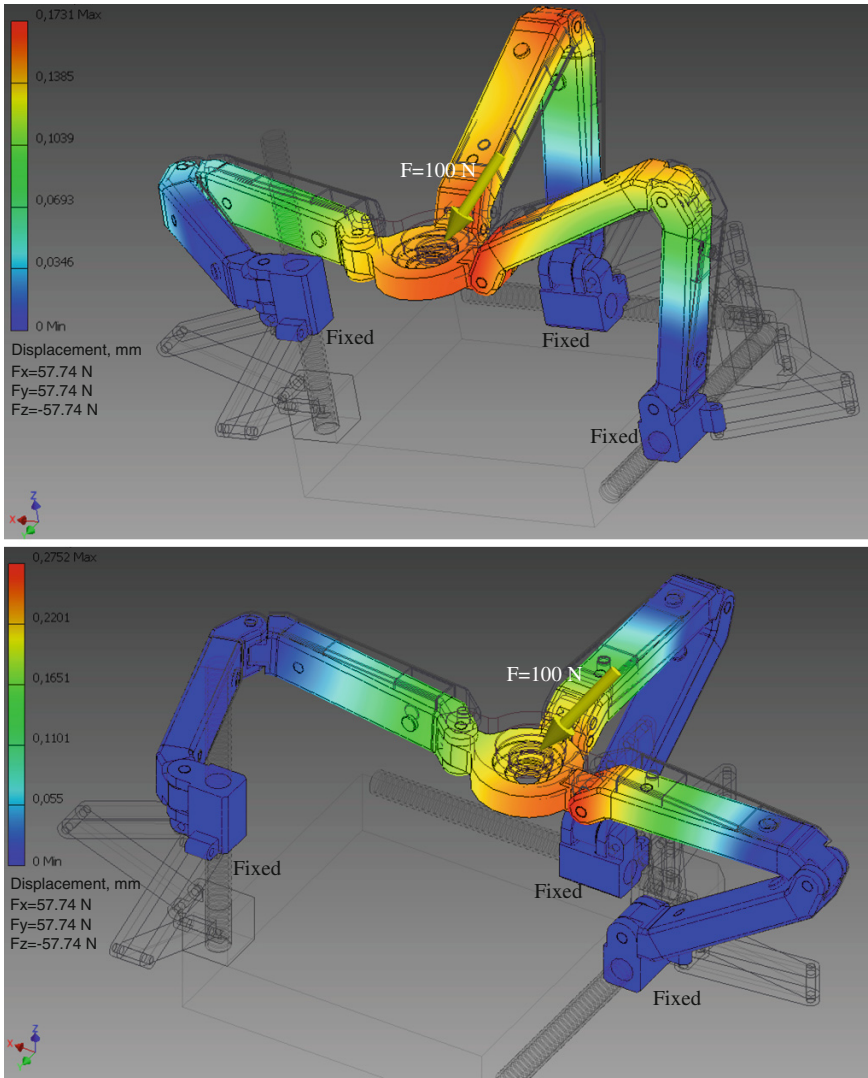


Fig. 4 Displacement diagrams of the manipulator (two positions) under the mixed spatial force

force is a spatial vector and it has all three non-zero coordinates. Since all kinematical chains are the same, there is no need to check the manipulator by applying each of the axial force to the endpoint, because the results are almost identical to the case when the force is vertical.

Figure 4 shows the results of the experiment (displacement diagram) when the spatial external force of is applied to the endpoint of the manipulator. As can be seen, the load is distributed to the all three kinematical chains; therefore, the

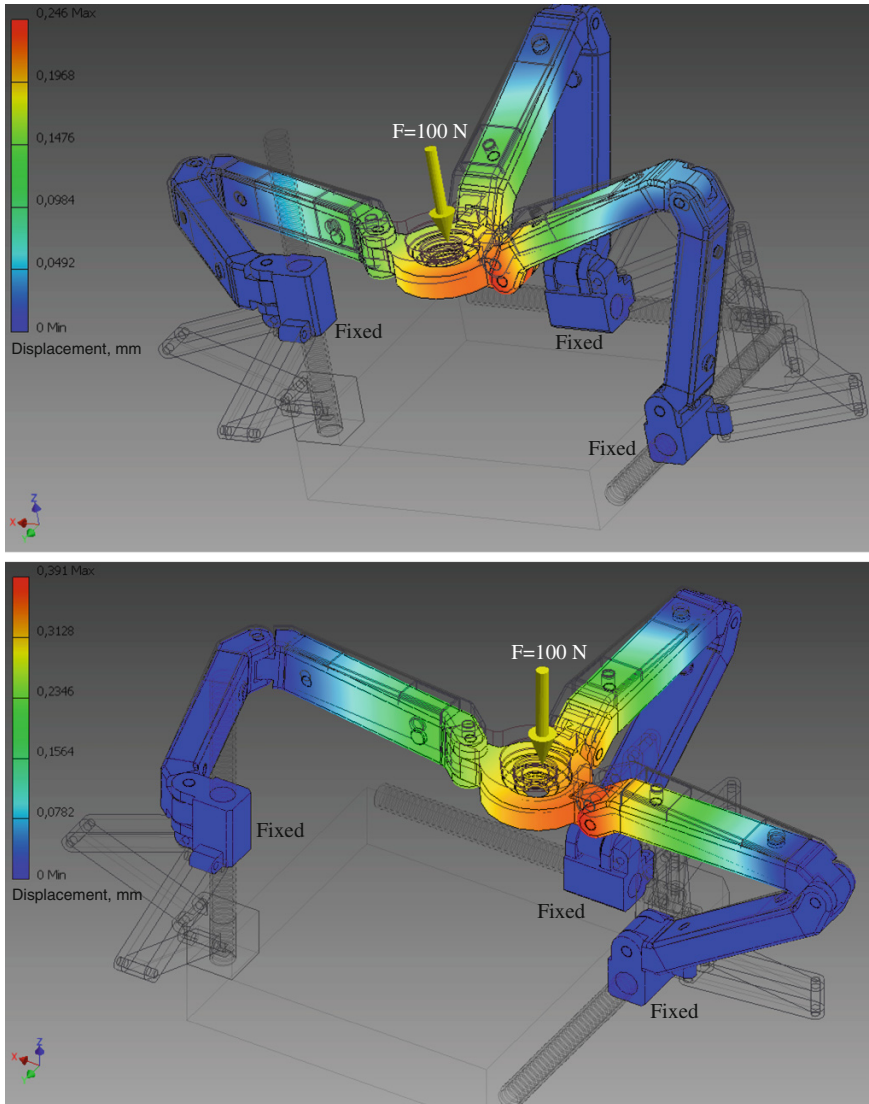


Fig. 5 Displacement diagrams of the manipulator (two positions) under the vertical force

displacement is not significant. In such case of the external force application, the manipulator shows the increased stiffness (this is reflected in less deformation) what is one of the main advantages of the parallel structure over the serial structure.

Figure 5 shows the results of the experiment when the vertical external force is applied to the endpoint of the manipulator. As can be seen, the load affects mainly the kinematic chain, which is placed horizontally and attached to the vertical actuator. In such case of an external force application, the manipulator does not provide increased rigidity and the displacement of the endpoint is significantly larger. The fact that the small part of the load is still distributed to the other two kinematical chains is the result of the manipulator's deformation and changed geometric parameters. However, only one kinematic chain takes the main part of the load.

4 Ways to Increase the Stiffness of the Manipulator

As expected, when applying axial forces directed along the main axes, the parallel manipulator of the Isoglide type shows mediocre stiffness characteristics. In order to increase the stiffness of the manipulator when the load is axial there are at least two solutions exist:

- Duplicating each kinematic chain with a similar one. Therefore, if the external force is axial there are always two kinematic chains involved, and the stiffness of the manipulator is increased significantly. It should be noted also, that the stiffness under the axial load in this case is expected to be much more stable and the influence of the total length of the kinematic chain is expected to be significantly less. However, this decision will complicate a lot the design.
- Getting rid of the isomorphism, for example by changing angles between actuators. In this case, the load is distributed between at least two kinematic chains. However, this option entails a complication of the control system associated with the appearance of the dependence between degrees of freedom of the endpoint.

However, these suggestions should be justified experimentally.

5 Conclusions

In this paper we considered the 3D model of the parallel manipulator of the Isoglide type with three translational degrees of freedom. For this model, experiments were carried out, aimed at identifying the qualitative characteristics of the stiffness including identifying deformations of the mechanism under the loads.

As a result, the tubular link with rectangular cross-section has been selected of the two variants of links having different cross-sections.

Also, as a result of experiments the assumptions about decreased stiffness parameters of the manipulator when external forces applied along the principal axes (parallel to the direction of the drives) were confirmed.

It was also proposed two ways to increase the overall stiffness of the manipulator under axial loads: to duplicate each of the three kinematic chains and to get rid of the isomorphism of the mechanism by changing the angles between the drives so that they were not perpendicular to each other, but these suggestions should be justified with experiments.

References

1. Bouzgarrou B-C, Fauroux J-C, Gogu G, Heerah Y (2004) Rigidity analysis of T3R1 parallel robot with uncoupled kinematics. In: Proceedings 35th international symposium on robotics (confÉrence ISR'04), March 23–26, 2004, Pari—Nord Villepinte/France 6 p, CD-ROM file
2. Ceccarelli M (2004) Fundamentals of mechanics of robotic manipulations. Kluwer Academic Publishers, Berlin
3. Ganiev RF, Kasilov VP, Glazunov VA, Kovalev VE, Levin SV, Shaljukhin KA (2013) Patent of the Russian Federation 133045 spatial mechanism having self-stabilizing kinematical chains. 2013
4. Glazunov VA (1995) Principles of the construction and analysis of spatial parallel structure mechanisms. *J Mach Manuf Reliab* 1:10–15
5. Glazunov VA, Koliskor AS, Krainev AF (1991) Spatial parallel mechanisms. Nauka, Moscow, p 95 in Russian
6. Glazunov VA, Kovalev VE, Levin SV, Sukhorukov RY, Shaljukhin KA (2013) Patent of the Russian Federation 2478464 Modular robotic technologic machine, 2013
7. Rizk R (2012) Study of the accuracy and stiffness of parallel robots with decoupled motion. PHD, <http://tel.archives-ouvertes.fr/tel-00698903>
8. Tsai L-W (1999) Robot analysis: the mechanics of serial and parallel manipulators. Wiley, New Jersey

Modular Cooperative Mobile Robots for Ventral Long Payload Transport and Obstacle Crossing

M. Krid, J.C. Fauroux and B.C. Bouzgarrou

Abstract In this paper, a new architecture for cooperative all-terrain mobile robots is introduced. It consists in a poly-robot system called C^3 Bots AT/VLP robot. It is formed by the association of two or more identical mono-robots with simple kinematics that makes a poly-robot system while using the payload as a connecting frame. The mono-robots are able to co-manipulate long objects whatever their length and mass and to transport them in unstructured environments. Each mono-robot has a manipulator with up to four degrees of freedom that can catch the payload on the ground and lift it for a ventral transportation mode. The paper presents several kinematics and an obstacle crossing process in eighteen stages that guarantee permanent stability of the poly-robot thanks to motions of the mono-robots with respect to the payload.

Keywords Cooperative mobile robots · Long payload ventral transportation mode · Obstacle crossing

1 Introduction

It is very important to have a transport robot at disposal in many situations such as work in a dangerous environment (nuclear power station) or delicate transport (transport of injured people on stretchers). In this case, robot must be able to manipulate and transport different forms of objects [1], to manoeuvre on irregular

M. Krid (✉) · J.C. Fauroux · B.C. Bouzgarrou
Institut Pascal UMR 6602 UBP/CNRS, Campus Universitaire des C  zeaux/Les
C  zeaux CS 20265, 63175 Aubiere Cedex, France
e-mail: Mohamed.Krid@ifma.fr

J.C. Fauroux
e-mail: jean-christophe.fauroux@ifma.fr

B.C. Bouzgarrou
e-mail: belhassen-chedli.bouzgarrou@ifma.fr

grounds and to cross obstacles [2]. The all terrain mobile robots were developed for planetary or dangerous area exploration. They have different architectures [3, 4] and locomotion modes [5, 6] but the same purposes: They must be able to roll on irregular or unstructured environment and to guarantee a minimum stability during a mission. In the literature, cooperative mobile robots for transport are often complex. They use many actuated joints and a sophisticated control system. The simpler ones must comply with many constraints on the payload and the environment such as Army Ant cooperative lifting robots [3]. In this paper, we present the synthesis of the cooperative $C^3Bots AT/VLP$ (All-Terrain/Ventral Long Payload) mobile robot. Section 2 describes the resulting poly-robot, associating two or more identical mono-robots that connect directly to the payload for transporting it. Section 3 describe the kinematics of the mono-robot, particularly the required degrees of freedom for the ventral manipulator. In Sect. 4, the mobilities are combined to present an obstacle-crossing process in eighteen stages with only two mono-robots, where stability is achieved by motions of the mono-robots with respect to the payload.

2 $C^3Bots AT/VLP$ General Architecture

The concept presented in this work is based on the *OpenWHEEL i3R* platform [6]. *OpenWHEEL i3R* contains two axles linked with a serial inter-axial mechanism using three simple revolute joints (one active central joint for warping and two passive joints for steering). Each axle contains two actuated wheels [6]. *OpenWHEEL i3R* has an original climbing process based on a serpentine movement and divided into nineteen stages. Each stage is produced by a movement of a joint or by a wheel contact being removed or regained. For the new $C^3Bots AT/VLP$ robot, it was decided to design a new platform suitable for the ventral transport of long payloads and partially inspiring from *OpenWHEEL i3R* for stable obstacle crossing. C^3Bots is original by the concept of combining several identical mono-robots with simple kinematics that make a poly-robot system using the payload as a connecting frame. $C^3Bots AT/VLP$ focuses particularly on the transport of long payloads. The stability of the platform is a necessary condition to perform the climbing process.

Previous works [7, 8] showed that decreasing the wheelbase with respect to the track width increased the stability (Figs. 1 and 2) on three wheels during stages 4–8–13–17 of the climbing process presented in [8]. We also noticed that increasing the wheelbase reduced pitch variation when crossing an obstacle of a given height. Finally, crossing a high obstacle required to bring frontward the center of mass with respect to the contact points in order to equilibrate the crossing capacities of front and rear axles [9]. From these three remarks raised the necessity of a longitudinal translation mobility of the centre of mass with respect to the wheels (requirement R1). A second idea concerns the use of collaborative robots and led us to separate the initial *OpenWHEEL i3R* robot into two single axle mono-robots (requirement R2). By combining requirements R1 and R2 was born the $C^3Bots AT/VLP$

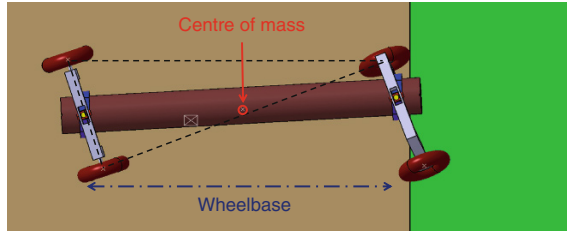


Fig. 1 Unstable configuration due to the *centre of mass* on the edge of the lifting polygon of support of *three contact points*

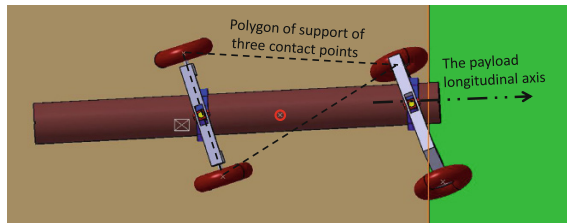


Fig. 2 Improvement of the stability thanks to the translation of the rear mono-robot along the payload

(All-Terrain/Ventral Long Payload) robot concept using several single axle mono-robots able to catch the payload, translate along the payload longitudinal axis to change the wheelbase length and to rotate around their longitudinal axis to warp the poly-robot and elevate one wheel with respect to the others.

C³Bots AT/VLP must be able to transport long payloads. To overcome the constraints related to the length of the transported payload, two or more cooperative mono-robots are used. The mono-robots are initially independent entities. Then, they connect to the payload, that becomes part of the resulting platform, called poly-robot (Fig. 3). It should be note that some trucks dedicated to long payload transport also use the payload as a structural part [10]. The mono-robot cannot climb obstacles with its simple kinematic structure. But the poly-robot version can perform such an operation because the additional mobilities in the connecting chains can be used to generate relative motions between the mono-robot and the payload. In the next section, we present the mono-robot kinematic and poly-robot architecture.

3 Required Mobilities and Proposed Kinematics

The mono-robot includes an axle, a positioning mechanism and a gripping mechanism (Figs. 4 and 5). The mono-robot, denoted MR_a , includes two wheels W_{a1} and W_{a2} motorized independently with two motors (with index “a” equals to “1” for front axle and “2” for rear axle, “1” for right wheel and “2” for left wheel). To be able to manipulate the object, the robot is equipped with a gripper mounted at the

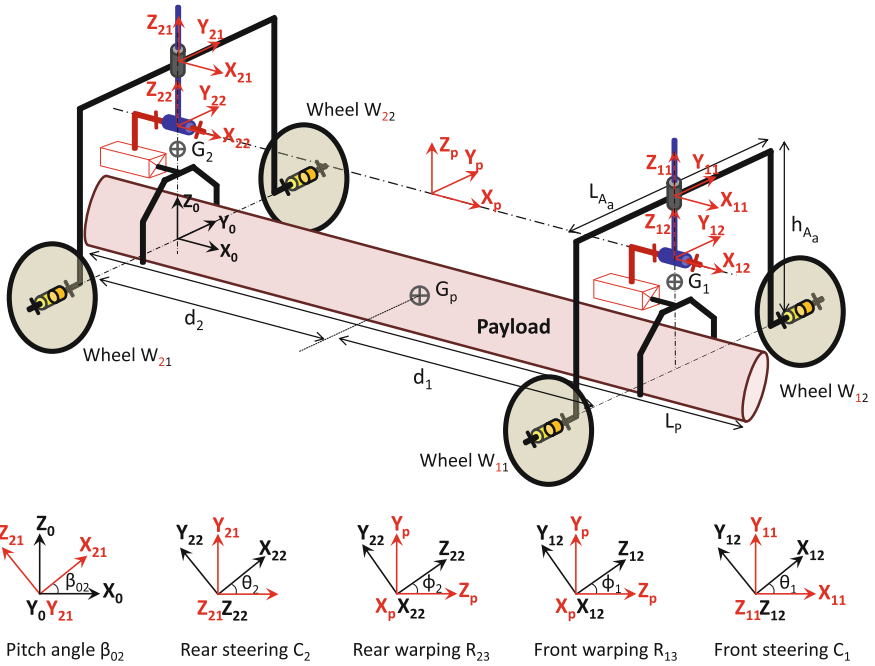


Fig. 3 Relative position of each frame and the associated angles

Fig. 4 Kinematic graph of a mono-robot MR_a

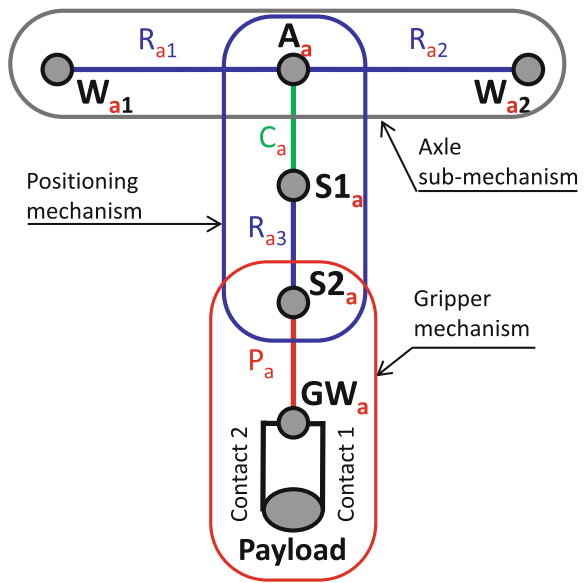
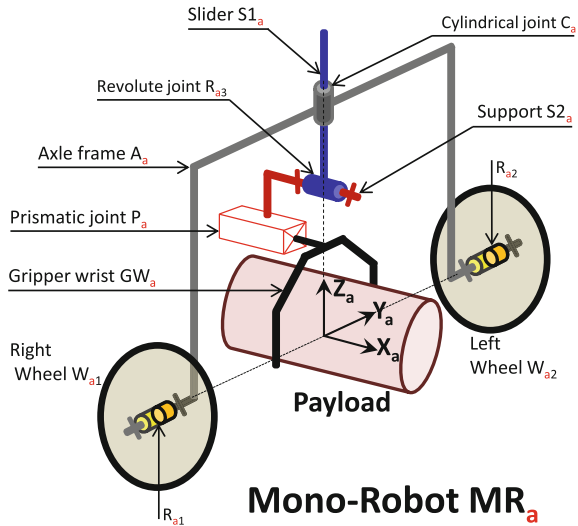


Fig. 5 Kinematic diagram of a mono-robot MR_a



bottom of the chassis. The originality of the concept lays on the kinematic chain of the positioning mechanism. The axle frame (A_a) can freely steer around the cylindrical joint C_a with respect to slider ($S1_a$). The remaining vertical motorized translation T_{za} of C_a allows controlling the altitude of the gripper and consequently of the payload. The roll motion R_{xa} between the slider body ($S1_a$) and the support body ($S2_a$) is ensured by the revolute motorized joint (R_{a3}) which is compulsory to reproduce warping motion of one axle roughly around the longitudinal axis of the payload, as the original *OpenWHEEL i3R* did. During solo locomotion configuration, the mono-robot can transport small payload on flat ground. Stability can be obtained by several solution: active pitch control in the same way as [11] or adding a retractable arm with a passive caster wheel.

The connection between the mono-robots is ensured by the transported payload as shown in Fig. 3. The co-manipulation of the payload by the two mono-robots allows obstacle crossing. The poly-robot combines the mobilities of the mono-robots. It can control the passive rotation R_{za} of the cylindrical joint (C_a) on each mono-robot by the difference of angular velocities of the two wheels of each axle. The redundant revolute joints R_{13} (front) and R_{23} (rear) give a warping degree of freedom to the poly-robot. When joints R_{a3} are actuated (either R_{13} or R_{23}), a warping motion is generated of one mono-robot around the joint R_{a3} axis with respect to the other mono-robot. This movement allows to lift the exploration wheel off the ground. We have therefore a new configuration of the system with only 3 wheel-ground contacts. Finally, prismatic joint P_a between gripper GW_a and support $S2_a$ in each mono-robot allows translating the mono-robot along the payload axis. Several equivalent serial kinematic chains are presented in Fig. 6 and can be used for a real implementation. As a conclusion, the implementation shown in Fig. 3 provides the four mobilities required on each mono-robot for stable payload transport and obstacle of the poly-robot:

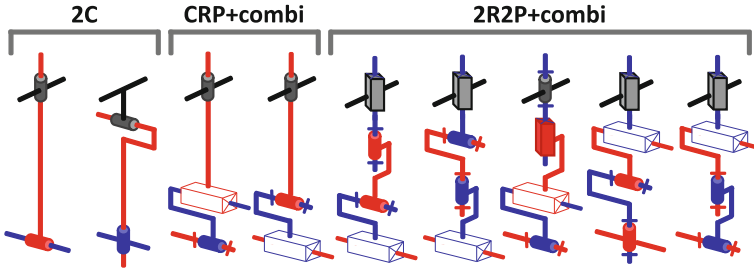


Fig. 6 Selection of equivalent joint combinations for producing the four required mobilities (T_{xa} , T_{za} , R_{xa} , R_{za}) between axle and gripper

- a rotation R_{xa} for wheel elevation on obstacles (R_{a3}).
- a rotation R_{za} for steering and stabilization on 3 wheels configuration (C_a).
- a translation T_{xa} for on improved stabilization with a long payload (P_a).
- a translation T_{za} for payload elevation (C_a).

4 Locomotion Modes for Obstacle Crossing

In this section, two locomotion modes are described for obstacle crossing. We are interested in the case where two axles or more are used. First, the warping mode inspired by *OpenWHEEL i3R* is developed for two axles. Then, we describe the 2D crossing modes with three axles and more.

4.1 Two Axles Warping Mode Inspired by *OpenWHEEL i3R*

The climbing process of the C^3 Bots AT/VLP platform is an original process based on a ‘serpentine’ movement. It is divided into eighteen manoeuvres within four phases (Fig. 7). Each manoeuvre is achieved by the motion of a single joint or by a change in the contacts of wheels on the ground. We define a phase P as a series of manoeuvres M that conducts to crossing a wheel W_{as} . Thereby, there are four phases in the process along with some intermediate manoeuvres to rearrange the body of the robot. The phases are given representative names depending on the lifted wheel to lift during the phase. For example, $PW_{12}M_{02}$ is the second manoeuvre M_{02} of the phase referring to lifting the front left wheel W_{12} .

The climbing process starts by approaching the obstacle. We suppose that the first axle of the poly-robot is brought parallel to the obstacle and that the axle frames (A_1) and (A_2) are perpendicular to the payload axis. The mono-robots are in the extremity of the payload before starting the climbing process. The first phase consists in stepping over the obstacle with wheel W_{11} .

The first manoeuvre $PW_{11}M_{01}$ is made to find the optimal position of rear axle in order to prepare the lift-off of the exploring wheel with a maximum stability

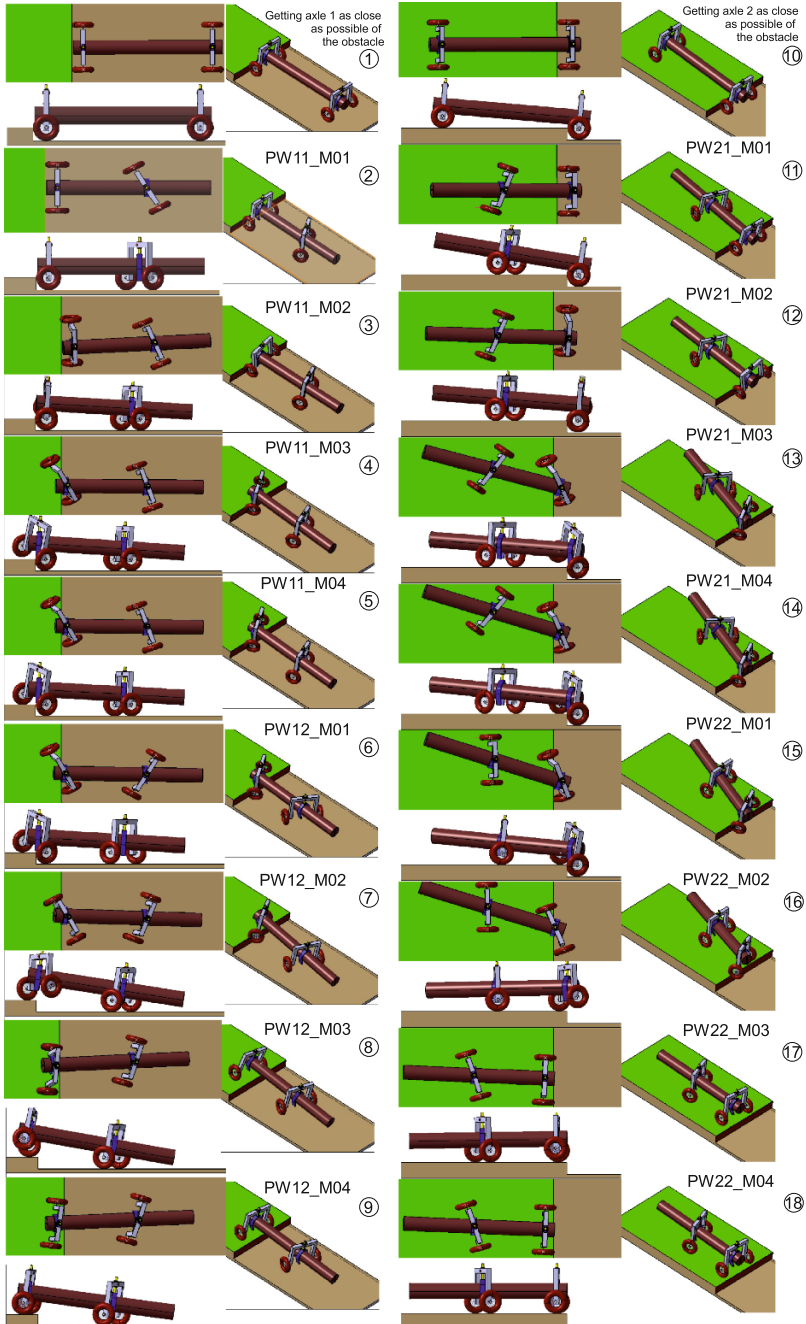


Fig. 7 Climbing sequence of the poly-robot with only two axles

margin. In this manoeuvre we have to find two parameters: the distance between the mono-robots and the steering angle of the rear axle. Stability analysis and optimization of these parameters will be presented in a future work. Warping the front mono-robot lift-off the exploring wheel at manoeuvre $PW_{11}M_{02}$. At manoeuvre $PW_{11}M_{03}$, the rear wheels are actuated while the wheel W_{12} is locked. The exploring wheel passes over the obstacle by a steering motion of the front axle. Finally, the first phase is achieved by putting down the exploring wheel W_{11} at manoeuvre $PW_{11}M_{04}$. The same is done for W_{12} crossing in the phase PW_{12} , which starts at $PW_{12}M_{01}$ by finding the optimal position of the rear mono-robot and finishes by putting down the wheel on the obstacle at $PW_{12}M_{04}$. After finishing the two first phases, the front axle of the robot is on the obstacle. This time, the exploring wheel will be one from the rear axle (wheel W_{21} or W_{22}). So the first manoeuvre $PW_{21}M_{01}$ consists to bring forward the rear axle to the obstacle and to find the optimal position of front axle. After warping the rear mono-robot in the manoeuvre $PW_{21}M_{02}$, the front axle moves forward to bring the exploring wheel over the obstacle (manoeuvre $PW_{21}M_{03}$) and puts down the exploring wheel in the last manoeuvre $PW_{21}M_{04}$ of the third phase. The same is done for the last wheel W_{22} . The phase PW_{22} starts by finding the optimal steering position of the front mono-robot at manoeuvre $PW_{22}M_{01}$ and finishes by putting the wheel on the obstacle after manoeuvre $PW_{22}M_{04}$. Finally, the poly-robot rearranges the positions of the rear and front axles to find its standard configuration.

4.2 Three Axles and More 2D Crossing Modes

The climbing process with three axles and more is very simple compared to the two axles configuration, because during the climbing process, the poly-robot has always two axles or more on the ground and one axle only is lifting off to climb obstacle. With three axles A_1, A_2, A_3 , the climbing process starts by approaching the obstacle and moving forward A_2 to have the centre of mass of the payload between A_2 and A_3 . After that, axle A_1 is raised. Then A_2 and A_3 are actuated to bring A_1 over the step. The axle A_1 is then put down on the step. The same is done for axles A_2 and A_3 . Viewing different possible configurations for the robot, we can say as a general conclusion that the three axles (and more) configuration allows an easy obstacle crossing 2D mode at the price of high number of axles. For the final configuration, we recommend to use two mono-robot and the warping mode described in (4.1) as it requires a minimal number of mono-robot.

5 Conclusion and Future Work

In this paper, we proposed a new concept of cooperative mobile robots to deal with the problem of long object transportation in unstructured environment whatever the payload length. The proposed $C^3Bots AT/VLP$ robot is formed by the association of

two or more mono-robots with simple kinematics forming a poly-robot system. Using such a modular poly-robot provides interesting advantages such as easy adaptation to the task, fast maintenance by simple replacement of defective mono-robots and standardization of the mechatronics architecture and associated control. Moreover, the proposed poly-robot has crossing obstacle capabilities and can use a climbing mode inspired from the *OpenWHEEL i3R* mobile robot. As a perspective for this work, the optimization of the process for all the steps will be considered as well as the evaluation of the dynamic stability for critical configurations of the robots. This must be done to ensure a smooth transition between the steps of the process. By ensuring the stability of the payload and its position control, *C³Bots AT/VLP* can transport sensitive payloads such as victims and hazardous equipments that must be maintained in a well-defined position.

Acknowledgments LABEX IMobS³ Innovative Mobility: Smart and Sustainable Solutions, the French National Centre for Scientific Research (CNRS), Auvergne Regional Council and the European funds of regional development (FEDER) are gratefully acknowledged.

This work has been sponsored by the French government research program “Investissements d’avenir” through the RobotEx Equipment of Excellence (ANR-10-EQPX-44), by the European Union through the program Regional competitiveness and employment 2007–2013 (ERDF Auvergne Region), by French Institute for Advanced Mechanics and by the Auvergne Region.

References

1. Holland CM, Oulman PB, Marmaras C (2013) Remote controlled load transport system, Pub No.: US 2013/0017047 A1
2. Kim D et al (2012) Optimal design and kinetic analysis of a stair-climbing mobile robot with rocker-bogie mechanism. *Mech Mach Theor* 50:90–108
3. Bay J (1995) Design of the army-ant cooperative lifting robot. *Robot Autom Mag* 2(1):36–43 IEEE
4. Trebi-Ollennu A et al (2002) Mars rover pair cooperatively transporting a long payload. In: *Proceedings on robotics and automation ICRA '02 vol 3*, pp 3136–3141
5. Michaud F et al: Co-design of AZIMUT, a multi-modal robotic platform. In: *proceedings ASME 2003 design engineering technical conference and computers and information*. In engineering conference, pp 46–50
6. Fauroux J et al (2006) A new principle for climbing wheeled robots: serpentine climbing with the open wheel platform. In: *Proceedings intelligent robot and systems, IROS' 2006, Beijing*
7. Chebab ZE (2010) Optimization of a climbing process. Master’s thesis, UPMC, Paris VI
8. Fauroux J et al Improving obstacle climbing with the hybrid mobile robot openwheel i3R. In: *Proceedings 12th international conference on climbing and walking Robots, CLAWAR'09, Istanbul*
9. Fauroux J et al (2010) OpenWHEEL i3R-A new architecture for clearance performance. In: *Proceedings of ROBOTICS 2010. international symposium, September 3–4 2010, Clermont-Ferrand, France*
10. Wobben, A.: Transport vehicle for oversized loads. EP1465789 B1 (Apr 16, 2008)
11. <http://www.segway.com>

Hypo-Cycloidal Crank Mechanism to Produce an Over-Expanded Cycle Engine

J. Pinto, T. Costa, J. Martins and F.P. Brito

Abstract In order to achieve a low consumption engine, to participate with a prototype in the Eco-Marathon Shell contest, a single-cylinder engine was designed and manufactured. This engine has the particularity of operating under the Miller Cycle (over expanded). For that purpose a special crankshaft system was designed, using a planetary hypo-cycloidal crank mechanism. With this strategy, a variable stroke engine was achieved, with an expansion stroke that is longer than the compression stroke, thus providing the over-expansion feature that increases cycle efficiency without loss in power density. This paper details the steps of the design and thermodynamic analysis of this engine, with special emphasis on the crankshaft system.

Keywords Engine · Miller cycle · Hypo-cycloidal crank mechanism · Low fuel consumption · Efficiency engines

1 Introduction

Nowadays the concerns with environmental problems and the low reserves of petroleum are leading the manufacturers to build less polluting and less consuming engines. The stringent goals for emission reductions and energy efficiency increase proposed by global policies, namely in Europe [1], are pushing the automotive

J. Pinto (✉) · T. Costa · J. Martins · F.P. Brito
University of Minho, Braga, Portugal
e-mail: jorgepinto.gt3@gmail.com

T. Costa
e-mail: zm10tro@hotmail.com

J. Martins
e-mail: jmartins@dem.uminho.pt

F.P. Brito
e-mail: francisco@dem.uminho.pt

Fig. 1 EconomicUM prototype car



industry towards intense research and development in these fields as never seen before in the automotive history [2]. In this framework, the Academia's internal combustion engine research and training has naturally gained a strong focus on these subjects. The formation of College teams participating in vehicle efficiency-related contests such as the Shell Eco-Marathon super-mileage contest has shown to be a good opportunity to promote applied research in this field with highly motivated students and researchers.

With the purpose of participating in the Shell Eco-marathon contest, in which the objective is to achieve the lowest possible consumption, the Department of Mechanical engineering of the University of Minho has made remarkable efforts in the past years to achieve the best possible results with its prototype car *EconomicUM* (Fig. 1). The current record was set in 2009, in Rockingham, England with the mark of 1,565 km/L, with a heavily modified engine based on a four stroke *Honda Today* motorcycle 49 cc engine.

Previous studies have shown that one of the cycles that can theoretically achieve better efficiency is the Miller cycle with variable compression ratio [3, 4]. With the objective of further improving the results already achieved, a new engine using the Miller cycle has been designed and manufactured.

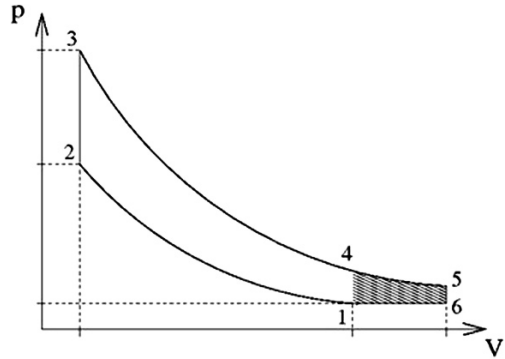
The over-expansion was obtained through the use of a special crankshaft based on a planetary hypo-cycloidal crank mechanism.

2 Miller Cycle

The majority of the engines used in automobile industry are based on the Otto cycle. When the exhaust valve of this kind of engines opens, there is still a fair amount of energy in the cylinder, in the form of pressure and temperature (enthalpy) of the exhaust gases that is lost through the exhaust blow-out [5–7].

With an over-expanded cycle engine, in which the expansion stroke is longer than the admission stroke, it is possible to significantly reduce this energy waste, enhancing the efficiency of the engine [6]. This over-expansion concept was patented by Ralph Miller, an American engineer, in the 1940s, but the concept was proposed earlier by Atkinson. Previous work by the group has shown the potential of this strategy, especially when combined with optimized compression ratios [3, 4,

Fig. 2 Miller theoretical cycle



8–10], with a Patent having been issued [11]. The over-expansion was achieved with a Late Intake Valve Closure (LIVC) strategy, in which the effective admission and compression strokes are reduced while keeping unaltered the expansion (and exhaust) stroke. This strategy is highly attractive in terms of simplicity. Its main disadvantage is that this reduction of the compression stroke induces a proportional reduction in engine power. An alternative would be to increase the expansion stroke instead of decreasing the compression stroke. This is only possible by having physically different compression and expansion strokes [12]. This was the approach chosen for the present work.

In the Pressure-Temperature diagram presented on Fig. 2 it is possible to observe the efficiency gain of the theoretical Miller Cycle in relation to the more usual Otto cycle [4]. This gain can be quantified by the grey area represented by the points 4,5,6,1. In fact, these P–V diagram areas represent work ($\int P dV$).

In order to implement this variable stroke cycle it was necessary to develop and study a hypo-cycloidal system for the crankshaft, which would provide the length of the intended strokes, and also the required relation between admission and expansion.

3 Hypo-Cycloidal Crank Mechanism

The intended engine size was set between 45 and 50 cc based on the admission stroke, with a 39 mm diameter piston. The expansion stroke should be approximately two times the length of the admission stroke, in order to optimize the efficiency of the cycle, as found in previous studies by the group [4].

This system consists of an internal/hypo-cycloidal gear set in which two crankshafts have been included. The main crankshaft is responsible for the main alternative movement of the piston (the base stroke), while the additional one is responsible for the variation of the base stroke between admission and expansion. A fixed annular gear with internal teeth and a smaller interior spur gear operating within the latter were used for the hypo-cycloidal crank mechanism. To obtain our aim for an expansion/compression ratio of 2:1 the required gear ratio is 2:3. This is

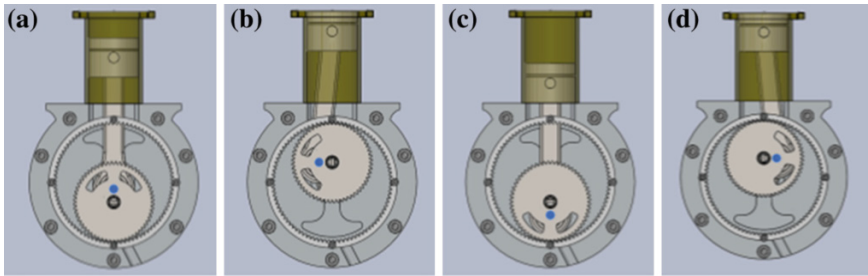


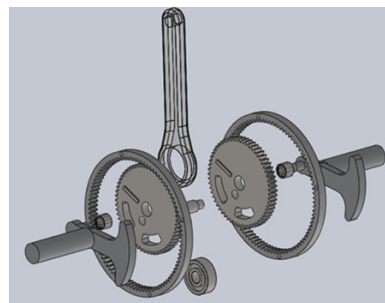
Fig. 3 Hypo-cycloidal crank mechanism: **a** admission (short stroke); **b** compression (short stroke); **c** expansion (long stroke); **d** exhaust (long stroke)

necessary so that the small crank completes a quarter of a revolution for each stroke, with each stroke corresponding to half of a revolution of the main crank, as depicted in Fig. 3. A unitary module was defined for the internal gear set, enabling a good compromise between gear precision, sliding friction and resistance for the desired application. After studying the dimensions and the desired piston stroke, a large annular gear with 90 inner teeth, and an inner spur gear with 60 teeth were chosen. As the module is one, their pitch diameters, in millimetres, correspond to their number of teeth.

Figure 3 is a schematic view of the hypo-cycloidal crank mechanism. The blue dot marks the location where the shaft of the connecting rod connects eccentrically to the inner spur gear. As it may be seen, the difference between the two bottom dead centres (corresponding to the lowest position achieved by the piston in the stroke) is given by twice the distance from the centre of the connecting rod bearing (eccentric hole in the inner spur gear, in blue) to the centre of the main crankshaft bearing. In this case, the distance between centres is 10 mm, leading to an expansion stroke that is 20 mm longer than the admission stroke. The top dead centre location does not change from the admission to the expansion stroke as the hole of the connecting rod shaft is either to the left or to the right of the centre of the main crankshaft bearing.

The crankshaft design (Fig. 4) was made as compact as possible, in order to reduce torsion forces, and to get a small crankcase to minimize weight.

Fig. 4 Exploded view of the crankshaft



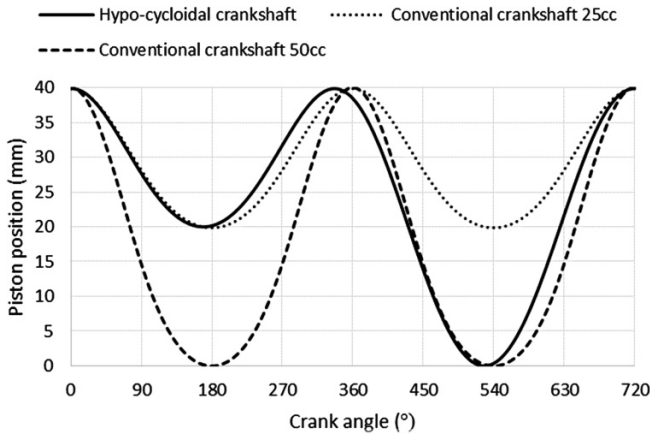


Fig. 5 Piston position versus crank angle

The position of the piston inside the cylinder during two revolutions of the crankshaft, obtained analytically, is shown in Fig. 5, completing the four strokes of the engine. The zero in Fig. 5 corresponds to the (upper) bottom dead centre, the beginning of the intake stroke.

With this planetary hypo-cycloidal crank mechanism it was possible to achieve the required specifications for this engine, as it can be seen in Table 1.

The use of a planetary epi-cycloidal system for the crankshaft was also assessed, but, in this case, the system would present some drawbacks. It would result in a more complex system to manufacture, and it would have the disadvantage, in comparison with the hypo-cycloidal system, of displaying a significantly more oblique angle of the connecting rod during the power stroke. This would lead to higher lateral forces in the piston and consequently a higher friction with the cylinder wall.

As shown in Fig. 6, using the hypo-cycloidal crank mechanism the connecting rod stays nearly vertical during the whole power stroke. This happens due to the combination of the motion of the two crankpins. During expansion it can be seen that when the main crankpin is located to the left, the secondary crankpin will be located to the right, and vice versa. This will reduce the total offset of the piston connecting rod crankpin from the axis of the cylinder when compared with an epicycloidal or even a conventional crank mechanism.

Table 1
Engine specifications

Largest stroke	39.50 mm
Smaller stroke	19.50 mm
Displacement (expansion)	47.18 cm ³
Displacement (admission)	23.24 cm ³
Expansion/admission ratio	2.03

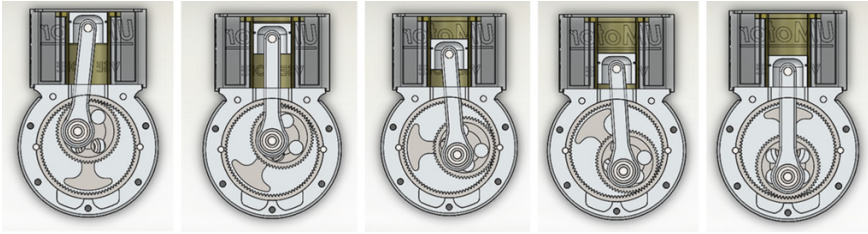


Fig. 6 Verticality of connecting rod during power stroke

This design reduces friction between piston skirt and cylinder as explained by Badami and Andriano [13].

4 Engine Thermodynamic Model

Engine modelling enables the design and improvement of the engine in a faster and cheaper way than going for a real engine development and manufacture. Internal combustion engine models can be of single or multiple zones (in the first, all the mass inside the engine is considered to have a uniform pressure, temperature and chemical constitution). In these models the combustion chamber geometry is not taken into consideration, nor the gradients in temperature and composition distribution. Fluid flow effects are not considered as depending on space but have rather a bulk treatment described by coefficients. These types of models are used to predict pressure variation in the cylinder, considering a certain correlation for combustion rate, and evaluate the engine performance, using several parameters. The work herein developed aims at the evaluation of engine performance (through specific fuel consumption and power) avoiding the large efforts in computational resources, programming and running time. Hence, a single zone model was adopted, this being considered as sufficient to satisfactorily reach the intended objectives, which are the validation of the present design as a means of achieving top engine efficiency.

In order to obtain results which may confirm the theoretical efficiency improvement of the Miller cycle, a model which was previously built by the team in Matlab-Simulink has been used [14]. It is suitable for single cylinder four-stroke engine, and includes instantaneous volume, pressure and temperature calculations, chemical species characteristics, mass exchange, combustion, heat transfer, and friction.

Table 2 Engine cycle simulated

	Crankshaft	Engine cycle	Intake pressure (bar)	Intake DISP	Expansion DISP	Geometric CR	Trapped CR
1	Conventional	Otto	0.5	50 cc	50 cc	11:1	11:1
2		Miller	1.0	25 cc ^a	50 cc	22:1	11:1
3		Otto	1.0	25 cc	25 cc	11:1	11:1
4	Hypo-cycloidal	Miller	1.0	25 cc	50 cc	22:1	11:1

^a Trapped displacement. The engine is a 50 cc engine but it admits only 25 cc

4.1 Model Results

Using the numerical model described above, seven engine cycles were simulated with different geometric characteristics and different working cycles (Table 2). The displacement values are approximate.

The simulated cycles characterize four different ways of performing the 4-stroke spark ignition cycle, with an expansion displacement of 50 cc (with one exception) and working at similar load. All engine cycles intake the same amount of air during the intake stroke, therefore the same amount of fuel is used.

Engine #2 and #4 work as Miller cycle, the first one done by LIVC (using a conventional crankshaft) and the latter done by the special crankshaft mechanism. Two engines working under the Otto cycle were also simulated, one working at half load but with the same intake and expansion displacement of 50 cc (#1), and a second working at full load Wide Open Throttle (WOT) but with just half of the admission displacement (#3). In all cases it is considered that the intake mixture is stoichiometric.

The resulting p-V diagrams of the engine cycles can be seen in Fig. 7.

Despite of the efficiency improvement (Table 3), the engine cycle #2 has almost the same torque (or power) output compared to the same engine performing the Otto cycle at half load (#1). This disadvantage does not appear when the hypo-cycloidal crank mechanism is used (#4), as it produces more power than the engine using the traditional crankshaft with the same intake displacement at full load (#3). Additionally it shows a cycle efficiency improvement of 23 % (from 30 to 37 %).

Overall the Otto cycled engine got an improvement of 37 % (from 27 to 37 %) when compared hypo-cycloidal Miller engine.

The thermal efficiencies (η) and torque at 3,000 rpm obtained with this simulation are presented in Table 3.

As expected, the engine using the hypo-cycloidal crank mechanism to implement the Miller cycle (#4) shows the highest efficiency. The lowest efficiency, attained by the Otto cycle at half load (#1) was also expected, as the pumping losses (intake at lower pressure than exhaust) reduce the net work for the same heat of combustion.

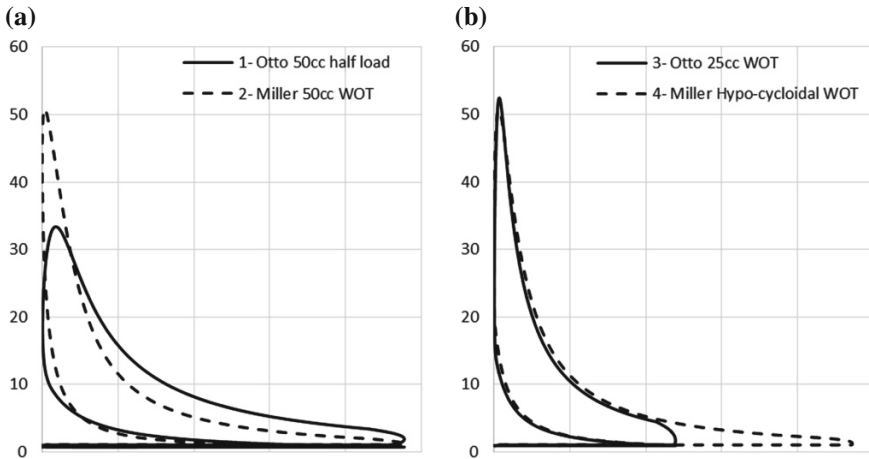


Fig. 7 P-V diagrams for the 4 engine cycles simulated

Table 3 Efficiency results of the 4 different engine concepts

	Crankshaft	Engine cycle	Load (%)	η	Torque (Nm)
1	Conventional	Otto 50 cc	50	27	1.20
2		Miller 50 cc	100	35	1.27
3		Otto 25 cc	100	30	1.01
4	Hypo-cycloidal	Miller	100	37	1.44

5 Conclusions

The present paper describes the development of a small high efficiency engine used for a super-mileage contest, including a thermodynamic simulation of the engine behaviour.

The proposed design, based on a hypo-cycloidal crank mechanism, successfully implements a variable stroke cycle with an expansion stroke that is larger than the compression stroke. With this strategy the over-expanded (Miller) cycle, a cycle that has been proven to display very high efficiencies, can be implemented.

The use of a planetary epicycloid system for the crankshaft was also assessed, but, not only such system would be more complex to manufacture but it would also induce higher friction at the cylinder walls due to a less vertical connecting rod during the power stroke.

This design does not have the disadvantages (namely low power density) that are typical of constant stroke atmospheric Miller engines based on intake valve timing adjustments (EIVC, LIVC). The numerical simulations predicted a 37 % improvement in engine efficiency relatively to the Otto Cycle engine working at part load for the same amount of injected fuel.

The present engine is at an advanced status of development but it has still not been finished and tested. Only then will its deployment in the Economic UM prototype be considered.

References

1. European Commission, EU Climate and Energy Package (2010) http://ec.europa.eu/clima/documentation/package/docs/climate_package_en.pdf
2. Jost K (2010) Upfront (editorial): green innovations. *Automot Eng Int*, 118-3, p. 4
3. Ribeiro B, Martins J (2007) Desenvolvimento do Conceito de Motor Sobre-Expandido— análise teórica, numérica e experimental”, 8º Congresso Iberoamericano De Engenharia Mecânica (CIBIM 8), Cuzco, October 23–25, 2007
4. Ribeiro B, Martins J (2007) “Direct comparison of an engine working under Otto, Miller and Diesel cycles: thermodynamic analysis and real engine performance. SAE technical paper series, n 2007-01-0261, 2007
5. Heywood J (1988) *International combustion engine fundamentals*. McGraw Hill, New York
6. Martins J (2013) *Motores de Combustão International 4th edition, revised and extended*. (ISBN: 978-989-723-033-2) Publindustria, Porto, 2013
7. Kutlar OA, Arslan H, Calik AT (2005) Methods to improve efficiency of four stroke, spark ignition engines at part load. *Energy Convers Manag* 46(2005):3202–3220
8. Martins J, Uzuneanu K, Ribeiro B, Jasansky O (2004) Thermodynamic analysis of an over-expanded engine”, SAE 2004-01-0617, 2004
9. Ribeiro B, Martins J, Nunes A (2007) Generation of entropy in spark ignition engines. *Int J Thermodyn* 10(2):53–60 ISSN 1301-9724
10. Martins J, Ribeiro B, Ion I (2009) Thermodynamic analysis of spark ignition (SI) engines using the entropy generation minimisation method. *Int J Energy* 6(1):93–110
11. Martins J, Ribeiro B (2008) Motor com Ciclo Sobre-Expandido com Taxa de Compressão Efectiva Constante. Patente Nacional n103363, concedida a 11 de Abril de 2008 (Boletim da Propriedade Industrial no. 73/2008 de 11 de Abril de 2008)
12. Takita Y, Kono S, Naoi A (2011) Study of methods to enhance energy utilization efficiency of micro combined heat and power generation unit-equipped with an extended expansion linkage engine and reduction of waste energy,” SAE Technical Paper 2011-32-0574, 2011
13. Badami M, Andriano M, (1998) Design, construction and testing of hypocycloid machines. SAE technical paper 980120, doi:[10.4271/980120](https://doi.org/10.4271/980120)
14. Ribeiro B, Martins J, Kothari N (2006) Otto and VCR miller engine performance during the European driving cycle”, SAE technical paper series, n 2006-01-0440, 2006

Part IV
Experimental Mechanics

Influence of the Mass of the Weight on the Dynamic Response of the Laboratory Fibre-Driven Mechanical System

P. Polach and M. Hajžman

Abstract Experimental measurements focused on the investigation of a fibre behaviour are performed on an assembled weigh-fibre-pulley-drive mechanical system. The fibre is driven with one drive and it is led over a pulley. On its other end there is a prism-shaped steel weight, which moves in a prismatic linkage on an inclined plane. An extra mass can be added to the weight. Drive exciting signals can be of a rectangular, a trapezoidal and a quasi-sinusoidal shape and there is a possibility of variation of a signal rate. Time histories of the weight position and of the force acting in the fibre are measured. The same system is numerically investigated by means of a multibody model. The influence of the mass of the weight on the coincidence of results of experimental measurements and simulations is evaluated. The simulations aim is to create a phenomenological model of a fibre, which will be utilizable in fibre modeling in the case of more complicated mechanical or mechatronic systems.

Keywords Fibre · Mechanical system · Dynamic response · Phenomenological model · Experiment

1 Introduction

The replacement of the chosen rigid elements of manipulators or mechanisms by fibres or cables [1] is advantageous due to the achievement of a lower moving inertia, which can lead to a higher machine speed, and lower production costs. Drawbacks of using the flexible elements like that can be associated with the fact that cables should only be in tension (e.g. [4]) in the course of a motion.

P. Polach (✉) · M. Hajžman
Research and Testing Institute Plzeň, Plzeň, Czech Republic
e-mail: polach@vzuplzen.cz

M. Hajžman
e-mail: hajzman@vzuplzen.cz

Experimental measurements focused on the investigation of the fibre behaviour were performed on an assembled weigh-fibre-pulley-drive system [8–10, 12]. A fibre is driven with one drive, is led over a pulley and on its other ends there is a prism-shaped steel weight, which moves on an inclined plane. The position of the weight can be symmetric or asymmetric with respect to the plane of drive-pulley symmetry (in the presented case a symmetric position is considered—see Fig. 1). It is possible to add an extra mass to the weight (in the presented case an added mass is considered). The same system is numerically investigated using a multibody model created in the **Alaska** simulation tool [6]. The influence of the model parameters on the coincidence of the results of experimental measurements and the simulations results is evaluated. The simulation aim is to create a phenomenological model of the fibre that will be utilizable in fibre modeling in the case of more complicated mechanical or mechatronic systems.

The first pieces of knowledge concerning the phenomenological model of a simple fibre-mass system (the system consists of a moving weight coupled with a frame by a fibre) creation are given in [7]. The paper continues investigating the weight-fibre-pulley-drive system given in [9] and [12], where the position of the weight was symmetric with respect to the plane of the drive-pulley symmetry, and in [8] and [10], where the position of the weight was asymmetric and the weight was without the added mass. Pieces of knowledge given in [12] are elaborated in more detail in this paper.

2 Experimental Stand

Experimental measurements focused on the investigation of the fibre behaviour are performed on an assembled weigh-fibre-pulley-drive mechanical system (see Fig. 1). A carbon fibre with a silicone coating (see e.g. [11]) is driven with one drive and is led over a pulley. The fibre length is 1.82 m (fibre weight is 4.95 g), the pulley diameter is 80 mm. The weight position can be symmetric [9, 12] or asymmetric [8, 10] with respect to the vertical plane of the drive-pulley symmetry (as it has been already mentioned symmetric position is considered in this paper). The fibre is attached to a force gauge at the drive end. At the other end of the fibre there is a prism-shaped steel weight (weight 3.096 kg), which moves in a prismatic linkage on an inclined plane. It is possible to add an extra mass (of the weight of 5.035 kg) to the weight (as it has been already mentioned the added mass is considered in this paper). The angle of inclination of the inclined plane could be changed (in this case the angle is $\alpha = 30^\circ$ and the pulley-fibre angle is $\varphi = 150^\circ$). Drive exciting signals can be of a rectangular, a trapezoidal and a quasi-sinusoidal shape and there is a possibility of variation of a signal rate [11]. The size of the drive displacements amplitudes is up to 90 mm. Time histories of the weight position u (in direction of the inclined plane; measured by means of a dial gauge), of the drive position x (in vertical direction) and of the force acting in the fibre (measured on a force gauge at drive) were recorded using the sample rate of 2 kHz.

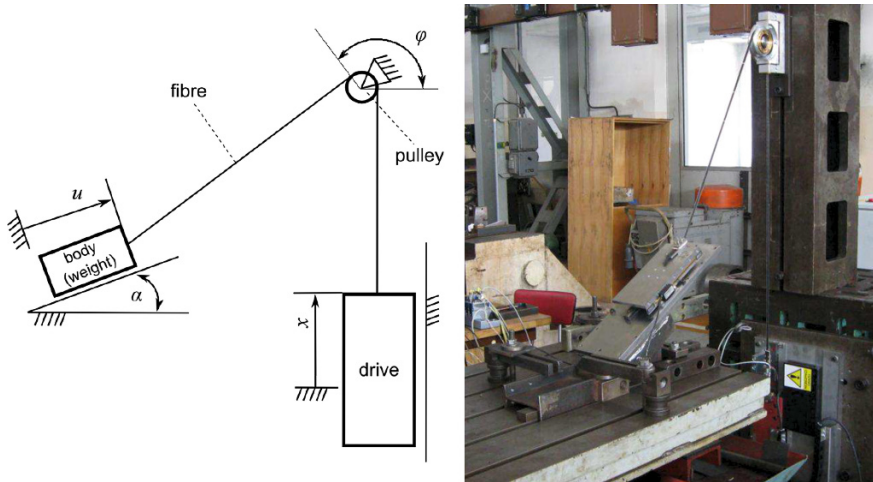


Fig. 1 Scheme and a real weight-fibre-pulley-drive mechanical system

3 Possibilities of the Fibre Modeling

The fibre (cable, wire etc.) modeling should be based on considering the fibre flexibility and suitable approaches can be based on the flexible multibody dynamics (see e.g. [3, 15]). Studied problems are characterized by a general large motion of interconnected rigid and flexible bodies with the possible presence of various nonlinear forces and torques. There are many approaches to the modeling of flexible bodies in the framework of multibody systems [5]. Comprehensive reviews of these approaches can be found e.g. in [15, 16]. Further development together with other multibody dynamics trends was introduced in [14].

The simplest way how to incorporate fibres in equations of motion of a mechanism is a force representation of the fibre (e.g. [2]). It is assumed that the mass of fibres is low to such an extent comparing to the other moving parts that the inertia of fibres is negligible with respect to the other parts. The fibre is represented by the force dependent on the fibre deformation and its stiffness and damping properties. This way of the fibre modeling is considered in this phase of investigation of the weight-fibre-pulley-drive system. The fibre model is considered to be phenomenological and it is modeled by the forces which comprise e.g. influences of fibre transversal vibration, “jumping” from pulley etc. The weight (with added mass), the pulley and the drive are considered to be rigid bodies [10]. The number of degrees of freedom in kinematic joints is 5. A planar joint between the weight and the base (prismatic linkage), a revolute joint between the pulley and the base and a prismatic joint between the drive and the base (the movement of the drive is kinematically prescribed) are considered. Behaviour of this nonlinear system is investigated using the **Alaska** simulation tool [6].

4 Simulation and Experimental Results

As it has already been stated the simulations aim was to create a phenomenological model of a fibre. When looking for compliance of the results of experimental measurement with the simulation results influences of three system parameters are considered. The parameters are the fibre stiffness, the fibre damping coefficient and the friction force acting between the weight and the prismatic linkage.

The investigation of the (carbon) fibre properties eliminating the influence of the drive and of the pulley was an intermediate stage before the measurement on the stand [7]. When looking for the fibre model [7] that would ensure the similarity of time histories of the weight displacement and time histories of the dynamic force acting in the fibre as high as possible fibre stiffness and fibre damping coefficient were considered to be constant in this phase of the fibre behaviour research. The friction force course (in dependence on the weight velocity) was considered non-linear (e.g. [13]). A general phenomenological model of the fibre was not determined, but general influences of individual parameters on the system behaviour, which are usable for all systems containing fibre-mass subsystem(s), were assessed. A suitable fibre model, but only in dependence on the definite simulated test situation, was determined.

“Starting” values for the phenomenological model creating are, identically with [7], fibre stiffness measured on a tensile testing machine [11] (94×10^3 N/m) and fibre damping coefficient derived on the basis of experience (46.9 N \times s/m). The “starting” friction force between the weight and the prismatic linkage is considered to be zero [9]. Final values were calculated on the basis of the final values determined in [9] and are the same as in [8–10, 12] (stiffness = 34×10^3 N/m, damping coefficient = 27.5 N s/m). The friction force course determined at investigating the weight-fibre mechanical system [7] with the angle of inclination of the inclined plane $\alpha = 30^\circ$ was applied in the model of the weight-fibre-pulley-drive mechanical system [8–10, 12].

Results of experimental measurements and simulations of four tested situations are presented (altogether eight situations were tested; see Figs. 2, 3, 4, 5 and 6). Two tested situations at a “quicker” drive motion (situations 10 and 11) and two situations at a “slower” drive motion (situations 9 and 14) are presented in this paper (see time histories of drive motion in Figs. 2a, 3a, 4b and 6b). Frequencies of drive motion (i.e. the input signal frequencies) higher than 1 Hz are designated as “quicker” drive motions, frequencies of drive motion lower than 1 Hz are designated as “slower” drive motions.

The influence of the fibre stiffness, the fibre damping coefficient and the friction force acting between the weight and the prismatic linkage on time histories of the weight displacement and also on time histories of the dynamic force acting in the fibre was evaluated partly visually and partly on the basis of the value of the correlation coefficient [8–10] between the records of the experimental measurements and the simulation results.

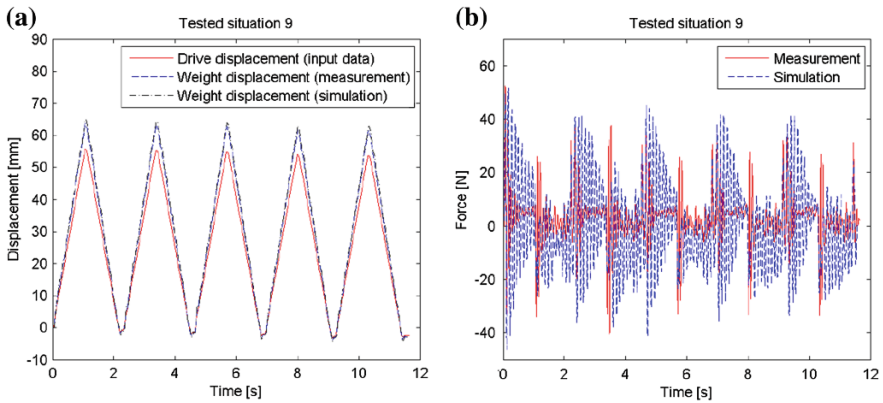


Fig. 2 Time histories at “quicker” tested situation 10. **a** Weight displacement. **b** Dynamic force acting in a fibre

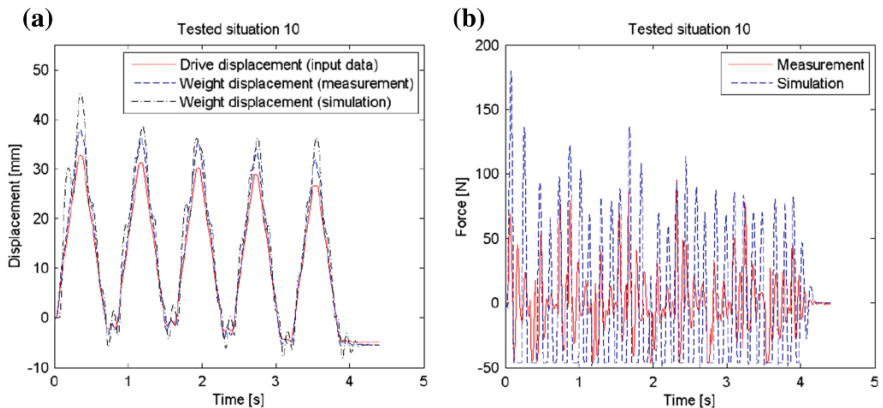


Fig. 3 Time histories at “slower” tested situation 9. **a** Weight displacement. **b** Dynamic force acting in a fibre

Time histories of the weight displacement recorded at the experimental measurements and computed at the computer simulations at “slower” tested situations (9 and 14) are approximately identical (see Figs. 3a and 6b).

At simulating the experimental measurements at the “slower” drive motion the monitored time histories of the weight displacement are identical independently of the fibre stiffness, the fibre damping coefficient and the friction force (between the weight and the prismatic linkage). At the “quicker” tested situations (10 and 11) the measured and computed time histories of the weight displacement are of the same character (see Figs. 2a and 4b). At simulating the experimental measurements at the “quicker” drive motion the local extremes of the monitored time histories of the weight displacement are dependent on all the phenomenological model parameters (i.e. on the fibre stiffness, the fibre damping coefficient and the friction force). All

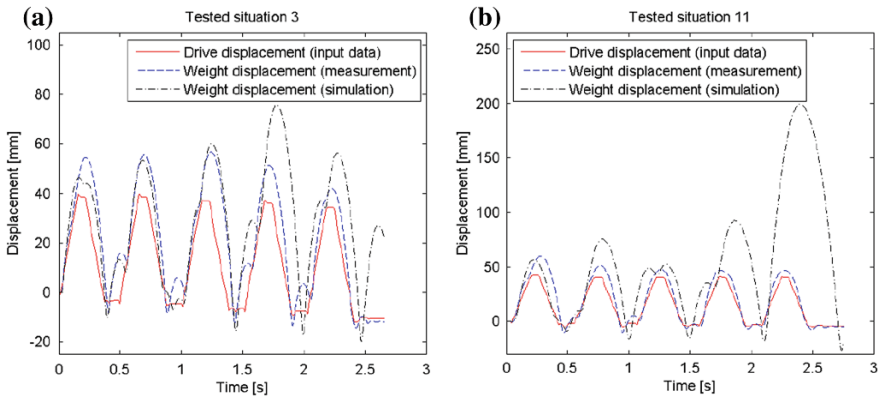


Fig. 4 Time histories of the weight displacement at “quicker” tested situations, influence of the mass of the weight. **a** Situation 3 (weight without added mass—taken from [12]). **b** Situation 11 (weight with added mass—taken from [12])

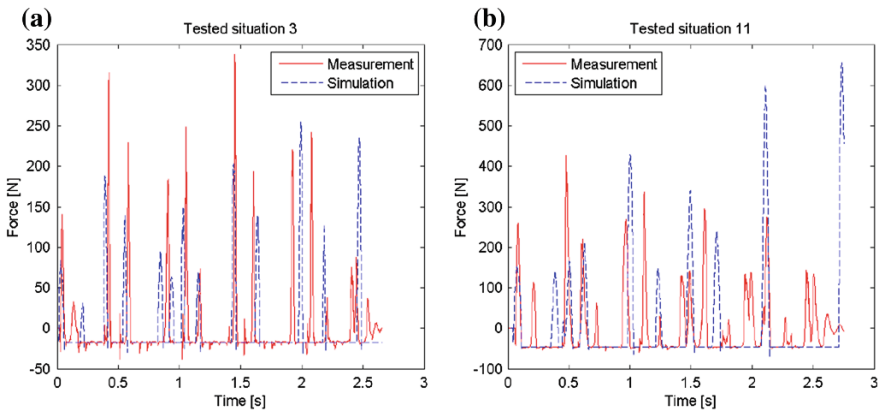


Fig. 5 Time histories of the dynamic force acting in a fibre at “quicker” tested situations, influence of the mass of the weight. **a** Situation 3 (weight without added mass—mentioned in [9]). **b** Situation 11 (weight with added mass)

findings given in this paragraph correspond to the results obtained in previous investigation of the weight-fibre-pulley-drive [8–10, 12].

When changing the computational model parameters the time histories of the dynamic force acting in the fibre are different (more or less) but their character remains the same (the same finding as in [8–10] again) at all the simulations. From Figs. 2b, 3b and 5b it is evident that the time histories of the dynamic force acting in the fibre are not suitable for searching for the parameters of the fibre phenomenological model. It follows from the fact that the phenomenological model of the fibre is to cover e.g. influences of the fibre transversal vibration, “jumping” from pulley etc. As the phenomena are not included physically (but by the change in the

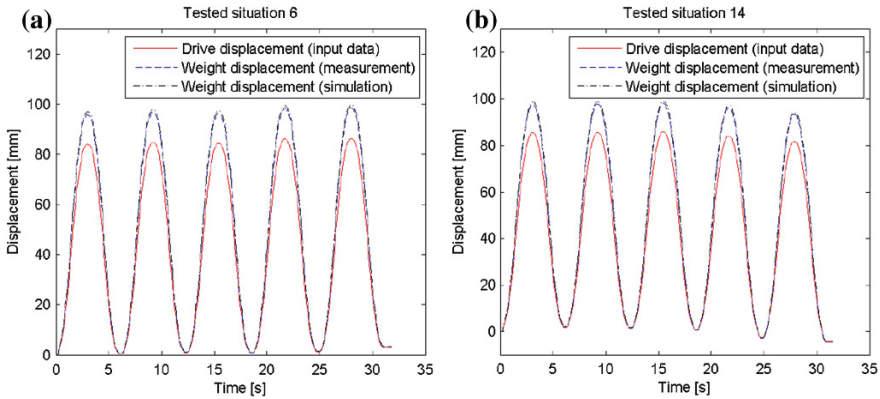


Fig. 6 Time histories of the weight displacement at “slower” tested situations, influence of the mass of the weight. **a** Situation 6 (weight without added mass—mentioned in [9]). **b** Situation 14 (weight with added mass)

introduced model parameters), it is evident, that it is not possible to expect the introduced time histories of dynamic force acting in fibre to be of the same course.

As to the influence of the mass added to the weight on the experimental measurements and computer simulations results, a higher mass is reflected in higher magnitudes of time histories of the weight displacement at the “quicker” situations (see Fig. 4). At the “slower” situations a higher mass of the weight influences the magnitudes of time histories of the weight displacement only slightly (see Fig. 6). The mass added to the weight is reflected in higher magnitudes of dynamic forces acting in the fibre independently of the input signal rate. The higher the mass of the weight the higher the influence of the input signal rate (see Figs. 4 and 5).

From the obtained results it is evident that parameters of the fibre phenomenological model must be, in addition, considered dependent on the speed of the weight motion (i.e. simultaneously on the input signal rate).

To search for the parameters of the fibre phenomenological model it would be useful to perform more experimental measurements with the “quicker” drive motion. In reality the “quicker” drive motion is limited on the one hand by limited amplitudes of the drive displacements and limited drive speed and on the other hand by the danger of the weight “flinging out” of the prismatic linkage.

5 Conclusions

The approach to the fibre modeling based on the force representations was utilised for the investigation of the motion of the weight in the weigh-fibre-pulley-drive mechanical system. The simulation aim is to create a phenomenological model of the fibre that will be utilizable in fibre modeling in the case of more complicated mechanical or mechatronic systems. The created phenomenological model is

assumed to be dependent on the fibre stiffness, on the fibre damping coefficient and on the friction force acting between the weight and the prismatic linkage in which the weight moves.

The fibre phenomenological model development will continue. From the obtained results it is evident that the parameters of the fibre phenomenological model must be, in addition, considered dependent on the speed of the weight motion. The question is if it is possible to create the phenomenological model like that.

Acknowledgments The paper has originated in the framework of solving No. P101/11/1627 project of the Czech Science Foundation and institutional support provided by the Ministry of Industry and Trade of the Czech Republic.

References

1. Chan EHM (2005) Design and implementation of a high-speed cable-based parallel manipulator. Ph.D. thesis, University of Waterloo, Waterloo
2. Diao X, Ma O (2009) Vibration analysis of cable-driven parallel manipulators. *Multibody Sys Dyn* 21:347–360
3. Gerstmayr J, Sugiyama H, Mikkola A (2012) Developments and future outlook of the absolute nodal coordinate formulation. In: *Proceedings of the 2nd joint international conference on multibody system dynamics*, Stuttgart, USB flash drive
4. Gosselin C, Grenier M (2011) On the determination of the force distribution in overconstrained cable-driven parallel mechanisms. *Meccanica* 46:3–15
5. Hajžman M, Polach P (2008) Modelling of flexible bodies in the framework of multibody systems. In: *Proceedings of the 6th international conference dynamics of rigid and deformable bodies 2008*, Ústí nad Labem, pp 33–42
6. Maißer P et al (1998) *Alaska*, user manual, version 2.3. Institute of Mechatronics, Chemnitz
7. Polach P, Hajžman M, Václavík J (2013) Experimental and computational investigation of a simple fibre-mass system. In: *Proceedings of the 19th international conference engineering mechanics*, Svratka, pp 443–452
8. Polach P, Hajžman M, Václavík J, Červená O (2014) Dynamics of the weight-fibre-pulley-drive mechanical system: influence of mass of weight at system asymmetry. In: *Proceedings of National Colloquium with international participation dynamics of machines*, Prague, pp 115–124
9. Polach P, Hajžman M, Václavík J, Šika Z, Svatoš P (2013) Model parameters influence of a simple mechanical system with fibre and pulley with respect to experimental measurements. In: *Proceedings of ECCOMAS thematic conference multibody dynamics*, Zagreb, CD-ROM, pp 473–482
10. Polach P, Hajžman M, Václavík J, Šika Z, Valášek M (2013) Experimental and computational investigation of a simple mechanical system with fibre and pulley. In: *Proceedings of 12th conference on dynamical systems—theory and applications, dynamical systems—applications*, Łódź, pp 717–728
11. Polach P, Václavík J, Hajžman M (2012) Load of fibres driving an inverted pendulum system. In: *Proceedings of 50th annual international conference on experimental stress analysis*, Tábor, pp 337–344
12. Polach P, Václavík J, Hajžman M, Šika Z, Valášek M (2013) Influence of the mass of the weight on the dynamic response of the simple mechanical system with fibre. In: *Proceedings of 29th conference with international participation computational mechanics*, Špičák, pp 97–98
13. Půst L, Pešek L, Radolfová A (2011) Various types of dry friction characteristics for vibration damping. *Eng Mech* 18:203–224

14. Schiehlen W (2007) Research trends in multibody system dynamics. *Multibody Sys Dyn* 18:3–13
15. Shabana AA (1997) Flexible multibody dynamics: review of past and recent developments. *Multibody Sys Dyn* 1:189–222
16. Wasfy TM, Noor AK (2003) Computational strategies for flexible multibody systems. *Appl Mech Rev* 56:553–613

On the Experimental Intradiscal Pressure Measurement Techniques: A Review

A. Araújo, N. Peixinho, A. Pinho and J.C.P. Claro

Abstract The intradiscal pressure has been essential for prevent the spinal complaints by forming a basis for clinical advice to promote the correct sitting postures. As a consequence, it is evident the need of an accurate method for measure the intradiscal pressure, to better understand the disc response to hydrostatic pressure fluctuations. Numerous reviews regarding disc mechanics are available, including intradiscal pressure benchmarks; however, an analysis on the techniques of intradiscal pressure measurement is needed. Therefore, this review will remain focused on the methodologies adopted for measure the intradiscal pressure in several conditions: for different daily activities, under external loads and for values where occurs annulus fibrosus disruption. The importance of the intradiscal pressure on disc function will be discussed as well as the some guidelines for design new measurement techniques will be defined.

Keywords Intervertebral disc · Intradiscal pressure

1 Introduction

The intervertebral disc (IVD) is a fibrocartilage structure located between two vertebral bodies, which is surrounded by ligaments and muscles [21]. This intricate organization is comprised by a peripheral angle-ply laminate ring, the annulus

A. Araújo (✉) · N. Peixinho · A. Pinho · J.C.P. Claro
University of Minho, Braga, Portugal
e-mail: angeloaraujo@dem.uminho.pt

N. Peixinho
e-mail: peixinho@dem.uminho.pt

A. Pinho
e-mail: acmpinho@dem.uminho.pt

J.C.P. Claro
e-mail: jcclaro@dem.uminho.pt

fibrosus (AF) with a gelatinous nucleus in its center (NP), and it is limited above and beyond by the cartilaginous endplates (CEP) [13] (Fig. 1).

The IVD plays an important role at spinal level: it is responsible for the spine motion, helping the spine on the weight support and load transfer from head and upper torso to the pelvis [14, 26]. The IVD is specially designed to perform these functions, since the mechanical response of disc to loading is time-dependent [23]: while the short time response is governed by viscoelastic phenomena [2, 6], the long term response is guided by poroelastic and osmotic events [19, 23].

Moreover, in opposition to the AF generally considered as a fibrous solid [1], the NP presents an high water content, revealing a fluid-like behavior [1]. Thus, a healthy NP is capable of sustain stress gradients due to hydrostatic pressure exhibited by NP, normally known as intradiscal pressure (IDP) [3] (Fig. 1).

The IDP varies with body posture and the direct compressive force applied on IVD [18]. In this review, the importance of the IDP on IVD function will be discussed and the criteria for design new IDP measurement techniques will be defined. Subsequent sections describe the previous methodologies developed to determine the IDP in physiological and in failure cases. Finally, it will conclude with some main points about the development of new IDP measurement techniques.

2 The IDP Importance for Disc Function Evaluation and Properties Determination

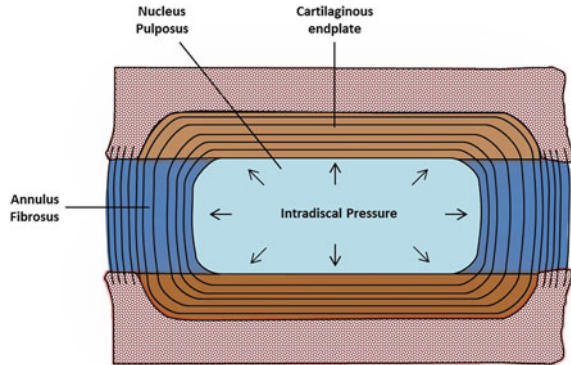
The internal disc pressure or intradiscal pressure (IDP) can be defined as the hydrostatic pressure presented by the NP of an healthy IVD [3]. The IDP plays a key role on the IVD's ability to withstand the physiological loads [22], being an important parameter to understand the spinal on the disc degeneration.

The IDP data has been essential for prevent the spinal complaints by forming a basis for clinical advice to promote the correct sitting postures [3]. The measurements of IDP help to clarify the effect of the external loads on the IVD behavior [3] and to recognize the mechanism of IDP drop in disc degeneration. In addition, these data is the basis for physiotherapy and rehabilitation programs [27].

At a biomechanical point of view, the IDP is highly influenced by the axial spinal load [17]. According to this, an increase on the compressive load applied to healthy discs is converted into IDP [18]. Since the NP can be considered as incompressible, the AF bulges outward due to the stretch of annular [24], which, together with osmotic phenomenon, promotes a loss on both disc height and volume.

The importance of IDP is reinforced due to difficult on the assessment of the disc strengthen properties. For example, a simple compressive overloading does not induce damage on the disc structure. Previous studies showed that before occurring any disc disruption, the compressive overloading promotes the vertebral endplate damage and collapse [18]. These phenomena could be explained at a cellular level

Fig. 1 The IVD and its compounds. The intradiscal pressure (*IDP*) exerted by the NP is omnidirectional and varies with applied load



by the influence of the IDP on the chondroid tissues, characteristic of the IVD [1]. On the one hand, the IDP or gradient pressures could induce the internal disruption on these tissues, causing a progressive structural failure typical on disc degeneration [1]. On the other hand, the stresses and pressures oscillation also affects the cell metabolism, where the IDP levels influences the matrix synthesis¹. In sum, it is evident the need of an efficient method for measure the IDP, in order to better understand the mechanical behavior of IVD.

3 On the IDP Measurement: A Methodology Review

The measurement of the IDP is a subject of intense research. Numerous authors have developed experimental methods to determine the relationship between the IDP and the disc mechanics: some authors were focused on the association between the IDP and the external load applied or posture adopted; others were more centered on the calculation of IDP value that leads to AF disruption. Next subsections will describe with more detail the studies performed under these subjects.

3.1 Relationship Between IDP and External Loading

Previous studies investigated the relationship between external loads applied and IDP on lumbar [5, 8, 10, 12, 17, 19, 27] or cervical [4, 7, 16] IVDs.

The methodologies developed for measure the IDP were diverse (Table 1).

The first approaches were performed on the 1960s and 1970s [10, 11, 15] on in vivo situation, alerting for the importance of IDP on the spinal biomechanics [3]. A pressure transducer using elastic polyethylene tubing threaded over the side near

¹ Interdiscal pressure (IDP)

Table 1 Previous studies reporting the IDP according to the type of load/posture adopted

Author	Year	Transducer type	IDP evaluation	Mean IDP (MPa)
<i>Lumbar spine</i>				
Nachemson	1964/ 1965	Liquid-filled	Relaxed standing	0.70
			Relaxed sitting	1.13
Nachemson and Elfstrom	1970	Piezoresistive	Relaxed standing	0.72
			Relaxed sitting	1.00
Schultz	1982	Piezoresistive	2,400 N axial load	1.60
Sato	1999	Piezoresistive	Relaxed standing	0.53
			Relaxed sitting	0.63
Wilke	1999	Piezoresistive	Relaxed standing	0.50
			Relaxed sitting	0.46
			Lifting a 20-kg weight with round flexed back	2.30
Heuer	2007	Laser scanning	500 N axial load	0.49
Dennison	2008	Fiber bragg gratings	800 N axial load ^a	2.40–3.50
<i>Cervical spine</i>				
Hattori	1981	Piezoresistive	53 N axial load	0.31
			75 N axial load	0.45
			100 N axial load	0.59
			155 N axial load	0.91
Pospiech	1999	Piezoresistive	<i>Muscular inactivation</i> • Flexion/extension	0.23–0.32
			<i>Muscular activation</i> • Flexion/extension	0.36–0.64
Cripton	2001	Piezoresistive	~1,000 N axial load	3.5

^a MegaPascal.

of a tip from hollow liquid-filled needle, connected with an electromanometer, was used in healthy discs for IDP determination. The data showed that a healthy NP could behave hydrostatically and the IDP is dependent on the posture. Even though the interesting findings, this pioneer approach presents a couple of limitations. First, the polyethylene membrane does not present enough sensitivity for dynamic pressure measurements. Second, the fluid-filled needle is not prepared to bend more than 20° [10].

The evolution of the transducer technology and its increased accuracy leads to a decrease on the IDP measurement (a reduction of 25 and 33 %) [3], due to the replacement of liquid-filled sensors by the piezoresistive ones, as well as the set of calibration to body temperature rather than room temperature [3].

The initial approach using was developed by Nachemson [12], using a piezo-resistive semiconductor strain gauge imbedded in a rigid resin into a tip of a 0.8 mm

diameter transducer needle [3]. This sensor allows bending until 40° without affecting the IDP measurement [3], increasing the IDP measurement accuracy.

In early 80s, Schultz et al. [20] tried to validate a biomechanical model lumbar spine by monitoring IDP and myoelectric signals, using a piezoresistive transducer for IDP measurement. This study pointed to 1.6 MPa of mean IDP, for a compressive load as much as 2.4 kN. The main finding of this study was that overloading could be a promoter of low back disorders.

In end of the 90s, two important studies were published: Sato et al. [17] developed a new approach using a piezoresistive sensor to determine the IDP in vivo young patients (25 ± 2 y.o.). The innovative principle of this method is the sensor positioning: the sensing diaphragm was mounted laterally on the transducer needle (1.2-mm diameter); Wilke et al. [27], studied the IDP in vivo, in one volunteer performing various daily life activities. To measure the IDP, a piezoelectric pressure transducer, with 1.5 mm diameter and 7 mm length, was implanted in the NP of a healthy L4–L5 disc. However, in this case, the IDP was record with a telemetrically, avoiding the problem of having a needle in situ. These studies reported similar IDP for standing position and reinforced the idea that in vivo IDP varied according to the adopted position of the body and the compressive force applied.

Although the accuracy of piezoelectric sensors, they are not able to characterize pressure profiles within disc [5]. With the advances on the sensor technology, new sensors were adapted for IDP measurement. Dennison et al. [5] used small diameter (125 μm) Fiber-Bragg grating, which consist on an optical fiber with a Bragg grating inscribed into a fiber core. These sensors present a biocompatibility, mechanical compliance and insusceptibility to electromagnetic interference. The results reported a linear response of disc pressure to compressive loads.

The IVD bulging was also adopted as an indirect parameter of the internal stress measurement of the disc. Heuer et al. [8] quantified the IDP ex vivo using a non-contact laser scanning method, which measure a 3D contour. The test consists on the application of 15 min of a 500 N static compression. This work showed that these loads results on an IDP of 0.49 MPa (range: 0.36–0.53 MPa), decreasing linearly to 0.48 MPa (0.36–0.52 MPa) when discs were constantly compressed.

In contrast to the extensive experimental work on lumbar IDP, the data related to cervical pressure is extremely scarce. The measurements on the cervical are challenging due to small size and anatomy of cervical IVDs.

Hattori et al. [7] was the first study recording the cervical IDP in vivo. A needle-based pressure transducer was used to measure IDP, during common neck movements. The results found no differences between cervical IVDs, detecting the values of 0.31 and 0.91 MPa for 53 and 155 N of axial load, respectively.

Later, Pospiech et al. [16] studied the IDP of cervical spine in vivo under simulated muscular forces in intact spines as well as in fused specimens. The IDP was measured using a pressure transducer mounted on a 1.3 mm-diameter needle. The results showed significant increase in IDP when the musculature was activated and a marked increase in IDP in both segments adjacent to fusion IVDs.

Although the importance of these findings, the cervical IDP measurement presents more difficult, since they cervical annular fibers could disrupt with the needle-

tip insertion, due to its rigidity and its large diameter (over 1 mm) [4]. To minimizing the AF disruption and reduce the distortion of the IDP signals or specimen kinematic behavior, Cripton et al. [4] tested *ex vivo* the cervical IDP response to external loads, using with a 0.26 mm diameter flexible electric wires passing through AF. They found a maximum of 3.5 MPa for cervical IDP, with 1,000 N load, while in lumbar for the same load, it is common an IDP of 1 MPa.

3.2 The Annular Failure Strength Due to Inflation Method Pressurization

Despite the panoply of mechanical testing found on literature intending to clarify the contribution of loads to annular tear or disruption, the effect of the IDP fluctuation on the AF injury remains largely unknown. The measurement of the IDP value that leads to AF disruption is a subject of extreme interest, not only to understand the mechanisms of IVD failure but also for IVD replacement designing, since it should withstand the daily routine activities without collapsing.

Some studies determined the maximum value of IDP that annular fibers support before failure [9, 18, 25]. The Table 2 reports the failure IDP in previous studies.

Schechtman et al. (2005) investigated the intrinsic failure strength of the intact bovine caudal disc under a simple mode of inflation, using a hydraulic actuator. They injected a colored hydrogel, under monitored pressure, into the NP. It was found a mean hydrostatic failure pressure of 18 ± 3 MPa. This method allowed understanding the alterations of the intrinsic disc strength associated with prior loading history or degeneration. However, it does not give information about the microstructural behavior of inner annular fibers after the inflation.

Later, Veres et al. [25] used the same technique performed by Schechtman et al. (2005) to investigate the role of high IDP on annular fibers disruption in ovine lumbar IVDs. This team included the analysis of the AF damage after pressure insertion by a microstructural investigation. The main findings showed that posterior annular region is more susceptible to disruption than the other disc regions, due to its inability to distribute hydrostatic pressures circumferentially.

In terms of cervical spine, Menkowitz et al. [9] documented a mean intradiscal rupture pressure of 0.28 MPa (range 0.1–1.18 MPa), using a 25G needle for the insertion of a contrast dye with IDP monitoring during time. This study showed that in cervical spine the injury could be induced at lower pressures.

Table 2 Previous studies reporting failure pressure data several IVD models

Author	Year	Models	Mean failure pressure (MPa)
Schetchman	2006	Lumbar bovine	18 ± 3
Veres	2010	Lumbar ovine	14.1 ± 3.9
Menkowitz	2005	Cervical human spine	0.28 (min–máx: 0.1–1.18)

4 The Criteria for a New Method for Intradiscal Measurement

Current work aimed to define a criterion for design new IDP measurement techniques. According with this, the importance of the IDP on intervertebral disc function was discussed as well as previous studies on this field were analyzed.

Previous methodologies helps to generate valuable data, useful for a pre-clinically evaluation of disc injuries. However, some difficulties are noticed on the experimental determination of IDP: the direct measurements of IDP through in vivo studies could damage the IVD [27]. Thus, the technique for in vivo IDP measurement should be non-invasive, since the IVD should keep its complete functions after the IDP monitoring. New techniques must be also accurate, as the IDP magnitude is low and highly sensitive to movements or load application.

In terms of AF failure, more studies should be performed to fully understand the rupture mechanism. Previous studies did not follow-up how the failure occurs: they only assessed the IVD structure after the rupture. Therefore, it is desirable an approach that assesses the disc behavior during the inflation.

With the advance of imaging techniques, the assessment of inner IVD pressure is possible, representing a non-invasive approach that could be better explored. For instance, coupling an inflation method with a microstructural assessment real time could bring a new light on poorly understood mechanism of IVD failure. New techniques must also allow the measurement of IDP on NP substitutes, in order to study its hydrostatic response.

Concluding, notwithstanding the great efforts performed for experimental IDP measurements, new approaches and techniques are needed to better understand the IDP influence on disc behavior.

Acknowledgments This work was funded by the project “NP Mimetic—Biomimetic Nano-Fibre Based Nucleus Pulposus Regeneration for the Treatment off Degenerative Disc Disease”, financed by the European Commission under FP7 (grant NMP-2009-SMALL-3-CP-FP 246351).

References

1. Adams MA, Dolan P, McNally DS (2009) The internal mechanical functioning of intervertebral discs and articular cartilage, and its relevance to matrix biology. *Stress Int J Biol Stress* 28:384–389
2. Campana S, Charpail E, de Guise JA, Rillardon L, Skalli W, Mitton D (2011) Relationships between viscoelastic properties of lumbar intervertebral disc and degeneration grade assessed by MRI. *J Mech Behav Biomed Mater* 4(4):593–599
3. Claus A, Hides J, Moseley GL, Hodges P (2008) Sitting versus standing: does the intradiscal pressure cause disc degeneration or low back pain? *J Electromyogr Kinesiol* 18(4):550–558
4. Cripton PA, Dumas GA, Nolte LP (2001) A minimally disruptive technique for measuring intervertebral disc pressure in vitro: application to the cervical spine. *J Biomech* 34(4):545–549

5. Dennison CR, Wild PM, Byrnes PWG et al (2008) Ex vivo measurement of lumbar intervertebral disc pressure using fibre-Bragg gratings. *J Biomech* 41(1):221–225
6. Ellingson AM, Nuckley DJ (2012) Intervertebral disc viscoelastic parameters and residual mechanics spatially quantified using a hybrid confined/in situ indentation method. *J Biomech* 45(3):491–496
7. Hattori S, Oda H, Kawai SU-S (1981) Cervical intradiscal pressure in movements and traction of the cervical spine. *Z Orthop* 19:568–569
8. Heuer F, Schmitt H, Schmidt H, Claes L, Wilke H-J (2007) Creep associated changes in intervertebral disc bulging obtained with a laser scanning device. *Clin Biomech* 22 (7):737–744
9. Menkowitz M, Stieber JR, Wenokor C, Cohen JD, Donald GD, Cresanti-Dakinis C (2005) Intradiscal pressure monitoring in the cervical spine. *Pain Physician* 8(2):163–166
10. Nachemson A, Elfström G (1970) Intravital dynamic pressure measurements in lumbar discs. A study of common movements, maneuvers and exercises. *Scand J Rehabil Med Suppl* 1:1–40
11. Nachemson A (1965) The effect of forward leaning on lumbar intradiscal pressure. *Acta Orthop Scand* 35:314–328
12. Nachemson A (1963) The influence of spinal movements on the lumbar intradiscal pressure and on the tensile stresses in the annulus fibrosus. *Acta Orthop Scand* 33:183–207
13. Nerurkar NL, Elliott DM, Mauck RL (2010) Mechanical design criteria for intervertebral disc tissue engineering. *J Biomech* 43:1017–1030
14. Niosi CA, Oxland TR (2004) Degenerative mechanics of the lumbar spine. *Spine J* 4(6 Suppl):202S–208S
15. Okushima H (1970) Study on hydrodynamic pressure of lumbar intervertebral disc. *Nihon Geka Hokan* 39(1):45–57
16. Pospiech J, Stolke D, Wilke HJ, Claes LE (1999) Intradiscal pressure recordings in the cervical spine. *Neurosurgery* 44(2):379–385
17. Sato K, Kikuchi S, Yonezawa T (1999) In vivo intradiscal pressure measurement in healthy individuals and in patients with ongoing back problems. *Spine* 24(23):2468–2474 (Phila Pa 1976)
18. Schechtman H, Robertson PA, Broom ND (2006) Failure strength of the bovine caudal disc under internal hydrostatic pressure. *J Biomech* 39(8):1401–1409
19. Schroeder Y, Wilson W, Huyghe JM, Baaijens FPT (2006) Osmoviscoelastic finite element model of the intervertebral disc. *Eur Spine J Suppl* 3:S361–S371
20. Schultz A, Andersson G, Ortengren R, Haderspeck K, Nachemson A (1982) Loads on the lumbar spine. Validation of a biomechanical analysis by measurements of intradiscal pressures and myoelectric signals. *J Bone Joint Surg Am* 64(5):713–720
21. Silva-Correia J, Correia SI, Oliveira JM, Reis RL (2013) Tissue engineering strategies applied in the regeneration of the human intervertebral disk. *Biotechnol Adv* 31(8):1514–1531
22. Steffen T, Baramki HG, Rubin R, Antoniou J, Aebi M (1998) Lumbar intradiscal pressure measured in the anterior and posterolateral annular regions during asymmetrical loading. *Clin Biomech* 13(7):495–505 (Bristol, Avon)
23. Stokes IF, Laible JP, Gardner-Morse MG, Costi JJ, Iatridis JC (2011) Refinement of elastic, poroelastic, and osmotic tissue properties of intervertebral disks to analyze behavior in compression. *Ann Biomed Eng* 39(1):122–131
24. Van der Veen AJ, Mullender MG, Kingma I, van Dieen JH, Van JH, Smit TH (2008) Contribution of vertebral bodies, endplates, and intervertebral discs to the compression creep of spinal motion segments. *J Biomech* 41(6):1260–1268
25. Veres SP, Robertson PA, Broom ND (2010) The influence of torsion on disc herniation when combined with flexion. *Eur Spine J* 19(9):1468–1478
26. White AA, Panjabi MM (1990) *Clinical biomechanics of the spine*. Lippincott Williams & Wilkins, Philadelphia
27. Wilke HJ, Neef P, Caimi M, Hoogland T, Claes LE (1999) New in vivo measurements of pressures in the intervertebral disc in daily life. *Spine* 24(8):755–762

Geometry and Material Strategies for Improved Management of Crash Energy Absorption

N. Peixinho

Abstract This study presents alternative approaches for the improvement of crash energy absorption in representative automobile crashworthy structures. One such approach is the use of configurable crush initiators introduced through localized heating in tubular structures. The main objective is to improve the ability to absorb impact energy in a progressive and controlled manner by a local modification of material properties. In this manner, associated with the softening of the aluminium alloy, the deformation can be introduced precisely, forcing the tubular structure to deform in a mode of high energy absorption and reducing the maximum load in a controlled manner. An alternative approach for controllable energy absorption consists in the internal pressurization of structures in the framework of a crash-adaptive response. Within this strategy, the effect of internal pressurization of tubular structures in a crashworthiness application is investigated. The concept of internal pressurization can be implemented as a crash-adaptive structure therefore allowing different responses according to the intensity of shock.

Keywords Impact loading · Crashworthiness · Numerical simulation · Experimental validation

1 Introduction

The requisites for improvements in fuel usage while maintaining or improving structural response in the automotive industry have contributed to new developments seeking weight reduction. Crashworthiness response is an important requisite for automotive structures that has driven diverse design and materials/manufacturing developments.

N. Peixinho (✉)
University of Minho, Braga, Portugal
e-mail: peixinho@dem.uminho.pt

The objectives of obtaining controlled and reproducible crush response of tubular structures intended for crashworthy parts have led to various trigger or crush initiators applications. Zhang and co-authors [1] proposed a concept wherein by installing a buckling initiator near the impact end which is composed of a pre-hit column and pulling strips, the initial peak force of the square tube could be greatly reduced (aprox. 30 %) while the deformation mode and energy absorption were retained. Marsolek [2] used non-axisymmetric folding patterns for an improved control of absorption of kinetic crash energy. The trigger geometry mechanism was optimized for different loads allowing for significantly reduced peak load [2].

The concept of using thermal modification of an aluminium alloy in localized areas can provide a larger global deformation of a part and higher energy absorption before failure. This advantageous use of aluminium is possible by applying “local material design”, which in the present context is defined as controlled manipulation of material properties like strength, work hardening and ductility by means of non-homogenous heating [3]. In particular, the buckling of crash boxes during a crash situation may be controlled by deliberately imposing local soft zones (i.e. thermally induced triggers) [4].

Another strategy for improvement of crash energy absorption is the concept of crash-adaptive structures. Crash adaptive safety applications are introduced at passenger cars up to now mainly for interior, restraint and seat applications. Having sensor information available one has the ability to prepare vehicle structures in advance of an impact and obtain a controlled crash response resulting on a tailored crash pulse. Having crash performance and packaging aspects in mind, one technical solution that appears as an attractive approach to create overall benefits is the use of pressurized structures. Two alternatives can be used [5, 6]: one where initial structural shape of the crashworthy components remains unchanged during pressurization, therefore, pressure has to be adjusted carefully; alternatively, the implementation can be performed in a way that the structure expands from a small cross-section to a larger one when being pressurized. This effect can provide great benefits, such as packaging benefits or extending the crash length.

This study presents experimental and numerical simulation results from recent work on two strategies for management of crash energy absorption [4, 7], here referred as thermal trigger approach and internal pressurization approach.

2 Methods and Results

2.1 Thermal Triggers in Aluminium Tubular Structures

Test specimens and tubular structures were manufactured from an aluminium alloy 6061-T5. The microstructure of the studied alloy can be modified as function of temperature and heating cycle applied. The most significant changes in the microstructure of the alloy occur for temperatures between 250 and 550 °C where a decrease in hardness arises, associated to the over ageing and dissolution effect of

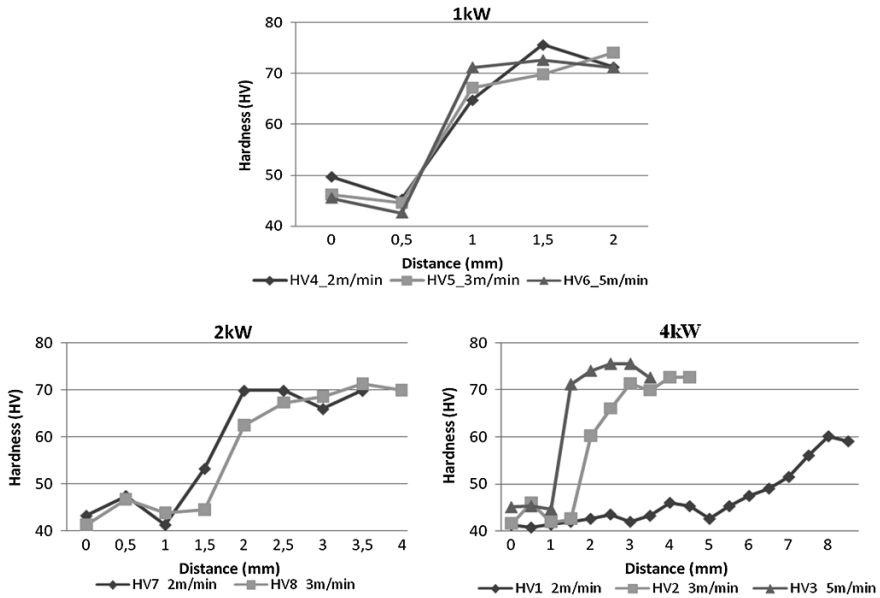


Fig. 1 Hardness results for laser heat treatment versus distance to the HAZ zone

copper rich precipitates due to the imposed thermal cycle. The choice of the appropriated heating cycle parameters is of major importance for the purpose of alloy softening.

For carrying out a local heat treatment a CO₂ laser welding machine was used (Trumpf—4,000 W). The density of energy could be regulated from laser power and feed rate thus changing the heat affected zone. The laser local heat treatment was used with a combination of different feed rates (2, 3 and 5 m/min) and power input (1, 2 and 4 kW). The hardness results are presented in Fig. 1. The different graphs present hardness values versus distance from laser path in order to evaluate the hardness in the Heat Affected Zone (HAZ). The results show similar values in the HAZ for power inputs of 1 and 2 kW. At 4 kW and with a feed rate of 2 m/min there is a significant increase of the HAZ. Therefore, both local hardness and affected area can be tailored for trigger application.

The structure considered in this study is a tubular column, of aluminium alloy 6061-T5, with a square cross-section. The dimension of the cross-section is 75 × 75 mm with a wall thickness of 1.5 mm and a length of 300 mm.

Experimental quasi-static tests were performed in a Shimadzu AG-250 KNG hydraulic machine that has a capacity of 250 kN, operated with a constant rate of 10 mm/min and a maximum displacement of 150 mm. Load-displacement curves, maximum and mean crushing load, total energy absorbed and maximum displacement were evaluated in the experimental tests.

The type of triggers used is illustrated in Fig. 2 and its characteristics presented in Table 1. The triggers described are arranged in the faces of the tubular structure

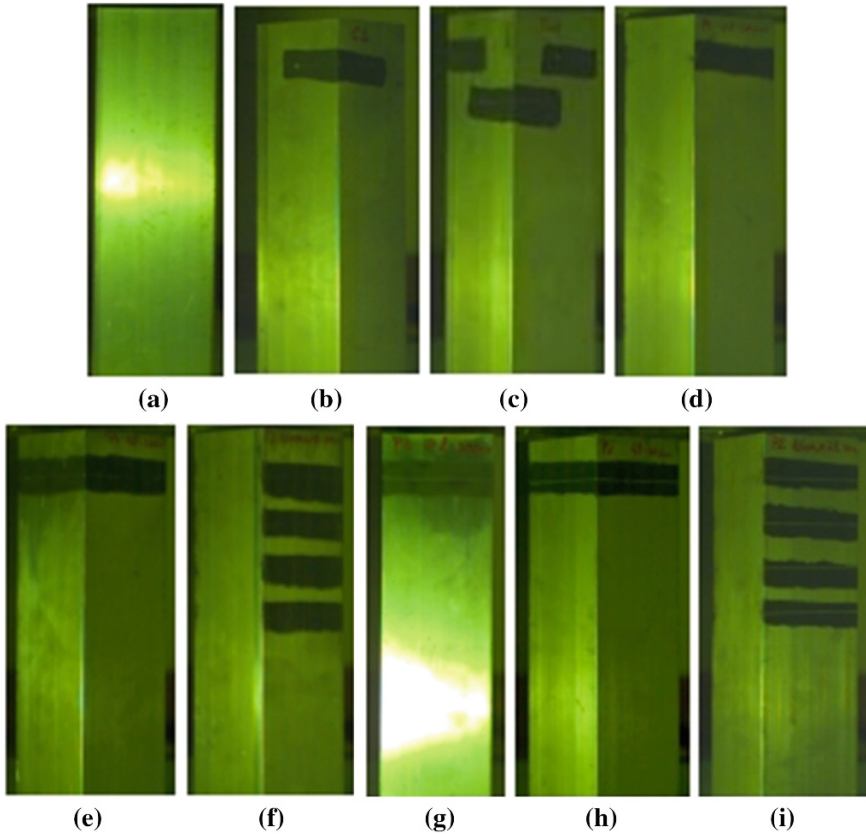


Fig. 2 Type of trigger used as referenced in Table 1

at a distance of 30 mm from the top and spaced of 30 mm from each other if more than one trigger is used (for example, two triggers refer to two laser paths in a tube face). The choice of laser heat treatment parameters is also presented in Table 1 and is based on the results from Fig. 1, seeking to evaluate the best parameters for local heat-treatment.

Results for maximum load (P_{max}), total absorbed energy (E_a), mean load (P_m) and final displacement (δ_f) for each of the quasi-static tests are presented in Table 2 while load-displacement curves of selected test results are presented in Fig. 3.

For the quasi-static tests, it is possible to observe that the geometry 4l-p1 has the lowest peak force, followed by geometry c1. These two geometries of HAZ triggers were manufactured with the same parameters (p1), being possible to observe that the geometries with parameters p1 have a lower maximum peak force than the geometries with parameters p2. The geometry 4laser-p2 has a higher maximum peak of force, which was attributed to the influence of plastic fold initiation that started in the third line of the HAZ trigger.

Table 1 Trigger characteristics

Sample ref.	(a)	(b)	(c)	(d)	(e)	(f)	(g)	(h)	(i)
	w.t.	c1	c2	2l-p1	4l-p1	4laser-p1	2l-p2	4l-p2	4laser-p2
Trigger type	Without trigger	Complex trigger in two faces	Two complex triggers in two faces	One trigger in two opposite faces	One trigger in four faces	Four triggers in two opposite faces	One trigger in two opposite faces	One trigger in four faces	Four triggers in two opposite faces
HAZ parameters P (kW)/V (m/min.)	-	2/2	2/2	2/2	2/2	2/2	4/3	4/3	4/3

Table 2 Characteristic values for experimental quasi-static compression tests

	w. t.	c1	c2	2l-p1	4l-p1	4laser-p1	2l-p2	4l-p2	4laser-p2
	(a)	(b)	(c)	(d)	(e)	(f)	(g)	(h)	(i)
P_{max} (kN)	48.5	39.4	42.9	38.9	34.0	43.1	43.1	42.0	52.0
E_a (kJ)	2.4	2.3	2.8	2.3	2.3	2.6	2.3	2.3	2.8
P_m (kN)	15.9	15.3	18.4	15.4	15.1	17.2	15.2	15.2	19.0
δ_f (mm)	150	150	150	150	150	150	150	150	150

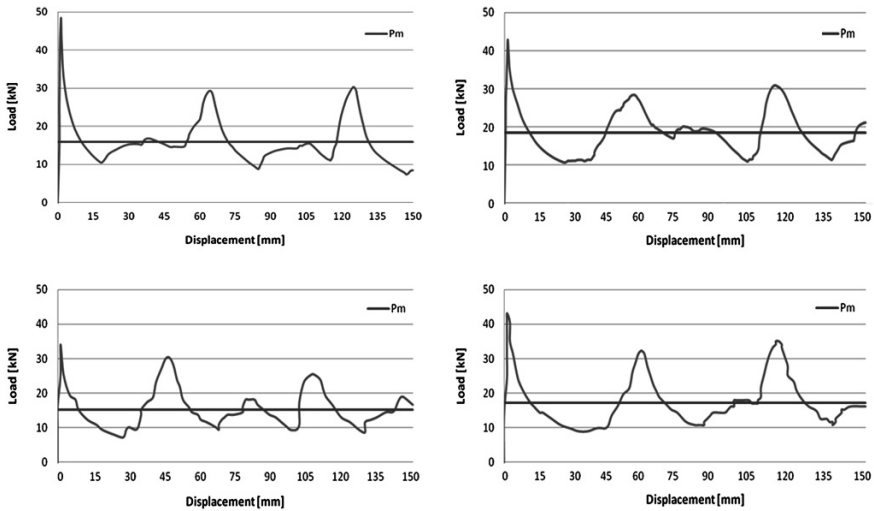


Fig. 3 Load-displacement curves of the samples, w.t.; c2; 4l-p1; 4laser-p1

2.2 Internal Pressurization of Tubular Structures

A numerical study was conducted on the impact behavior of a thin-walled tubular structure, representative of a front crash box of an automobile. This structure has circular cross section and the concept of internal pressurization was implemented in order to evaluate crash performance (Fig. 4). The impact mass (m) was set numerically as moving rigid wall with 76 kg. The material used to simulate the component is an austenitic stainless steel (Nirosta H400) due to its excellent mechanical properties suitable for use in structures designed for crashworthiness [8]. The simulations are performed in LS-DYNA software.

The finite element model is presented in Fig. 5. The model includes triggers to initiate the deformation on a prescribed position and therefore obtain a more controlled crushing process. The tubular structure is assumed to deform under the following constraint conditions: one end is fixed, with all degrees of freedom constrained in the distal surface nodes, and the other is impacted by a rigid wall travelling with initial impact velocity v . The model was constructed using 4 node

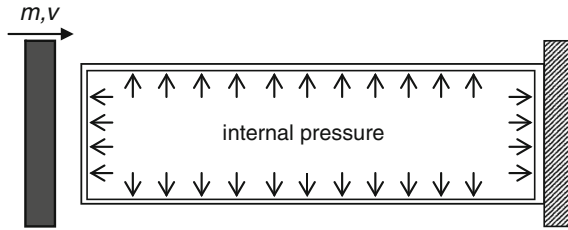


Fig. 4 Concept of pressurized cylindrical tubular structure

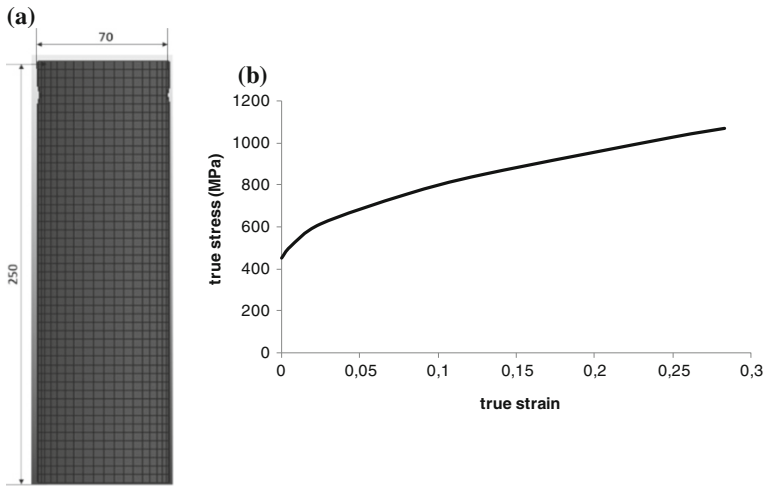


Fig. 5 Numerical model. **a** Mesh geometry [7]. **b** Material curve for H400 [8]

quadrilateral Belytschko-Tsay shell elements with 5 through-thickness Gauss points. An average element size of 5 mm was used. Geometric imperfections were introduced in the form of nodes displaced 0.5 mm out of plane in sympathy with the expected mode of collapse in order to trigger the analysis. Material model number 24 (Mat_Linear_Isotropic_Plasticity) from the LS-DYNA model library was used with the true stress-strain curve presented in Fig. 5b [8]. The strain-rate dependence was included through the Cowper-Symonds coefficients D and p , as described in [8]. The contact between the mass (rigid wall) and the specimen was modelled using a Contact_automatic_nodes_to_surface interface with a friction coefficient of 1.0 to prevent any sliding between specimen and wall. To account for the contact between the lobes during deformation a Contact_automatic_single_surface algorithm with friction coefficient equal to 0.1 was specified.

The internal pressure was applied using the keyword load and option SHELL_SET to apply pressure to the internal shell surface within the prescribed duration time of the test, corresponding to a constant pressure application.

Table 3 Results for internal pressurization analysis

Test name	δ_f (mm)	E_a (kJ)	P_m (kN)	P_m improv. (%)	(%)
1.14_10014_0.0	54	3.9	72.4	–	64.8
1.14_10014_2.0	46	3.7	82.0	13.3	73.5
1.14_17777_0.0	159	12.1	76.0	–	68.1
1.14_17777_2.0	131	11.9	90.7	19.33	81.3

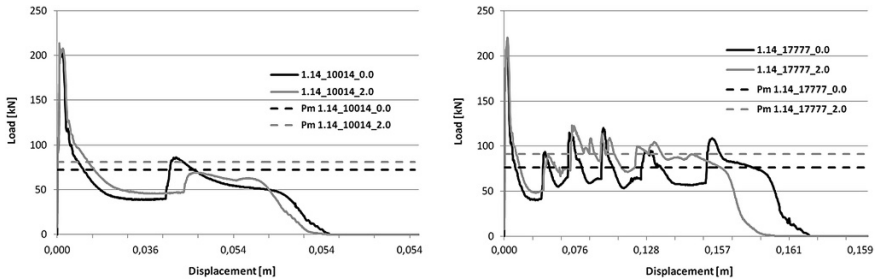


Fig. 6 Load versus displacement curves for internal pressurization analysis

For the validation of the internal pressurization concept a value of 20 bar was analyzed, which was considered relevant from airbag inflation industrial practice. The nomenclature used is the following: *Test Name = Thickness_Impact Speed (mm/s)_Additional Inside Pressure (Pa)*. Results can be observed in Table 3, where δ_f is the total displacement, E_a is the energy absorbed, P_m is the mean crushing force, and is the efficiency of the structure for crashworthiness purposes [7]. It is also presented the percentage improvement of P_m .

Considering the simulations conducted at the same impact velocity, it is observed that the total displacement was reduced with the introduction of internal pressure while the mean load and the efficiency of the structure also increased. Figure 6 illustrates the load vs displacement curves for these initial tests as well as the mean crushing forces associated.

From the results presented in Table 3 and Fig. 6 it transpires that it is possible to improve crash performance recurring to internal pressurization of tubular structures. Such improvement is quantified in the improvements observed in the structural efficiency and in the increase of average mean crushing load.

3 Conclusions

This paper presented two alternative approaches to management of crash energy absorption in representative structures of automobile crash absorption systems. One such approach is the use of configurable crush initiators introduced through

localized heating in tubular structures. Other methodology relies on internal pressurization of structures potentially allowing for the implementation of crash-adaptive response.

Experimental results of heat-treatment of aluminum alloys with the purpose of inducing local modification of material properties were presented. This effect was achieved using laser heat-treatment, being verified that it is possible to change the local hardness in a controlled way, through the choice of laser power and feed rate.

The quasi-static tests presented demonstrated the possibility to reduce the maximum crushing force for almost all tested cases. For the tests performed in trigger geometries p2 and 4laser-p1 an increase of mean crushing force was achieved. This reveals that it is possible to obtain HAZ parameters and trigger geometries that are according to the objectives, therefore the concept of using thermal modification of an aluminium alloy in localized areas for triggering and crush response appears as possible and effective in the experimental work presented.

Regarding the internal pressurization concept a numerical study was performed on the simulation of a tubular structure with circular section, which fits in the type of structure for crashworthiness application. The purpose was to study the influence of pressurization inside the structure. Based on the obtained results it can be concluded that it is possible to increase the impact resistance of the structure with the introduction of internal pressurization which would benefit from its use in crashworthiness applications. The deformation decreased with increased internal pressure, and the average load increased. Therefore the structure efficiency increased with the introduction of internal pressure.

The results obtained with numerical simulations show good indications for the validity of an adaptive crashworthiness concept wherein tube pressurization could act as enhancement of energy absorption properties. Such final validation is dependent on experimental results, while implementation of a pressurization scheme and deployment parameters could be better described with a coupled fluid-structure numerical model. The technological implementation should be analyzed considering other factors, such as, pressure build-up and matching with design crash pulse, assembly procedures and cost.

References

1. Zhang XW, Su H, Yu TX (2009) Energy absorption of an axially crushed square tube with a buckling initiator. *Int J Impact Eng* 36(3):402–417
2. Marsolek J, Reimerdes H-G (2004) Energy absorption of metallic cylindrical shells with induced non-axisymmetric folding patterns. *Int J Impact Eng* 30:1209–1223
3. Bjørneklett BI, Myhr OR (2003) Materials design and thermally induced triggers in crash management. In: Proceedings of IBEC conference
4. Peixinho N, Soares D, Vilarinho C, Pereira P, Dimas D (2012) Experimental study of impact energy absorption in aluminium square tubes with thermal triggers. *Mater Res* 15(2):323–332
5. Nohr M, Blume K (2004) Crash adaptive vehicle structures and components. DAIMLER report, Sindelfingen

6. Fäult S, Hedin J, Larsson J, Oliveira N, Carlsson B (2011) Inflatable side impact beams in martensitic steel. SAE International technical papers
7. Noversa M, Peixinho N (2013) Numerical simulation of impact behaviour of structures with internal pressurization for crash-adaptive concept. Eng Trans 61(3):185–196
8. Durães M, Peixinho N (2008) Dynamic material properties of stainless steel and multiphase high strength steels. Mater Sci Forum 587–588:941–945

An In Vitro Experimental Evaluation of the Displacement Field in an Intracranial Aneurysm Model

Diana Pinho, David Bento, João Ribeiro, Rui Lima and Mário Vaz

Abstract The purpose of this paper is to develop a system able to study experimentally the displacement field of an in vitro intracranial aneurysm. Origin and growth of aneurysms is the result of a complex interaction between biological processes in the arterial wall and the involved hemodynamic phenomena's. Once the aneurysm forms, the repetitive pressure and shear stresses exerted by the blood flow on the debilitated arterial wall can cause a gradual expansion. One promising method to evaluate and measure this expansion is to use optical field experimental techniques, such as interferometry. In this work the Electronic Speckle Pattern Interferometry was used to evaluate the deformation occurred on an intracranial aneurysm model fabricated in polydimensiloxane (PDMS) by using a 3D printer combined with a soft lithography technique.

Keywords Aneurysms · Displacement field · Electronic speckle pattern interferometry · 3D printer · In Vitro models

D. Pinho (✉) · D. Bento · J. Ribeiro
Polytechnic Institute of Bragança, University of Porto, Porto, Portugal
e-mail: diana@ipb.pt

D. Bento
e-mail: davidbento@ipb.pt

J. Ribeiro
e-mail: jribeiro@ipb.pt

R. Lima
Polytechnic Institute of Bragança/CEFT, FEUP, University of Porto, Porto, Portugal
e-mail: ruimec@ipb.pt

M. Vaz
University of Porto, Porto, Portugal
e-mail: gmavaz@fe.up.pt

1 Introduction

A cerebral aneurysm or intracranial aneurysm (IA) is a weak bulging spot on the wall of a brain artery very much like a thin balloon or weak spot on an inner tube. Over time, the blood flow by applying pressure against the thinned wall of the vessel artery leads to the appearance of aneurysms. This pressure may promote the rupture of the aneurysm and consequently the blood tends to flow to the surroundings outside the artery. It is worth mentioning that the rupture of a brain aneurysm most often requires advanced surgical treatment [1].

It is well known that blood flow behaviour in microcirculation depends on several combined effects such as cell deformability, flow shear rates and geometry of the microvessel, although still no consensus about the reasons for creation and rupture of aneurysms. Hence, a better understanding of the relationship between the pathophysiological aspects of an aneurysm and its arterial geometry or local hemodynamics is critical to better understand aneurysm growth, predict the risk of regrowth after treatment, and improve endovascular treatments. In order to investigate the hemodynamics in blood arteries, some mathematical and experimental studies have been performed over the years. Nonetheless, *in vitro* experiments have been conducted only for flows in simple geometries such as straight bifurcation using glass pipes or acrylic pipes [2], glass capillaries [3, 4] and more recently in polydimethylsiloxane (PDMS) microchannels [5–8].

A promising approach to understand the mechanical behavior of aneurysms is the global measurement of deformation using experimental field optical techniques. These optical techniques provide the accurate measurement of displacement and strain fields of the global deformation occurred on the aneurysm. The experimental field optical techniques can be classified in interferometric, photoelastic and Digital Image Correlation (DIC) [9]. The interferometric techniques are based on the interferometry phenomenon of light and use of a coherent light (laser), and the most common are the holography, the Moiré Interferometry and the Speckle methods [10]. The photoelastic methods use the optical properties (birefringence) of certain materials where when a ray of light passing through these materials experiences two refractive indices [11]. The DIC technique is based on the comparison of two images acquired at different states, i. e., before and after the deformation. By using this technique the object is illuminated by a non coherent light and the intensity patterns result of the surface texture [12]. In this work we have decided to measure the aneurysm deformation by using ESPI mainly because this technique enables a rapid and accurate determination of out-of-plane displacement field which is a predominant component of the displacement occurred in current study.

Recently, several numerical hemodynamics studies have been reported [2, 13] in order to better understand the creation and rupture of a cerebral aneurysm. Other studies have used a soft lithography method to manufacture in PDMS carotid arteries having an aneurysm with a thick wall [14, 15]. However, experimental analysis of *in vitro* cerebral aneurysms with geometries close to *in vivo* ones has not

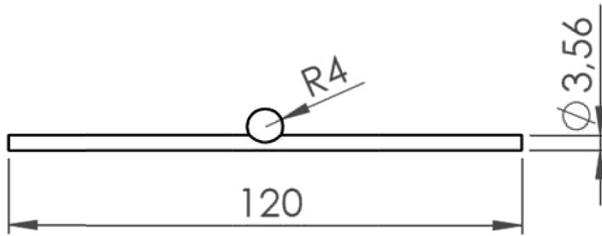


Fig. 1 Geometry and dimensions (mm), of the aneurysm model

been reported yet. This is mainly because it is extremely difficult to fabricate three-dimensional geometry models with thin walls.

The objective of this paper is to develop a realistic three-dimensional system able to obtain measurements of the expansion and pressure around the wall of an intracranial aneurysm. The experimental measurements are made using a Speckle method, more precisely an Electronic Speckle Pattern Interferometry (ESPI). This method uses a surface roughness illuminated by a laser beam, which generates a pattern that could be used to measure an out-of-plane displacement field. The aneurysm model was fabricated in PDMS by using Acrylonitrile Butadiene Styrene (ABS) molds manufactured with a 3D printer.

2 Materials and Methods

2.1 Geometric Parameters

The geometry and dimensions of the aneurysm model were based in clinical data for a common saccular intracranial aneurysm [16] and drawn in the Solidworks[®] CAD software. This geometry was used to produce the aneurysm model in PDMS for the experimental tests. In Fig. 1 it is represented the geometry and dimensions of the used aneurysm model.

2.2 Fabrication of the Aneurysm Model

The model of aneurysm has been produced in PDMS. This material is biocompatible and its elastic behavior is similar to the arteries [17]. To obtain the aneurysm model seen in Fig. 2e it was necessary to develop and elaborate a special mould with the same geometry and dimensions of the model. The mould was fabricated in ABS material using a Solidoodle[®] 3D Printer. In Fig. 2a it is possible to observe the mould and core used to obtain the PDMS aneurysm model and a detail of the 3D printer used for this study. The moulds and cores obtained from the 3D Printer were

firstly subjected to a surface treatment to decrease the superficial roughness with acetone vapor (Fig. 2b). Before pouring the PDMS into the mould cavity, was made the assembly of the mould with the core (see detail of Fig. 2b). The used PDMS was Sylgard 184, Dow Corning Corporation product, which is a silicone elastomer kit. The kit contains two chemicals: base (part A) and curing agent (part B), that was mixed in 10:1 mass ratio and poured onto master mold in a Petri dish (see Fig. 2c). The PDMS was cured at room temperature in order to completely release the bubbles formed during the plinth of the PDMS and by the contact with the material of the mould and core. After a complete cure (42 h) of the PDMS the materials were

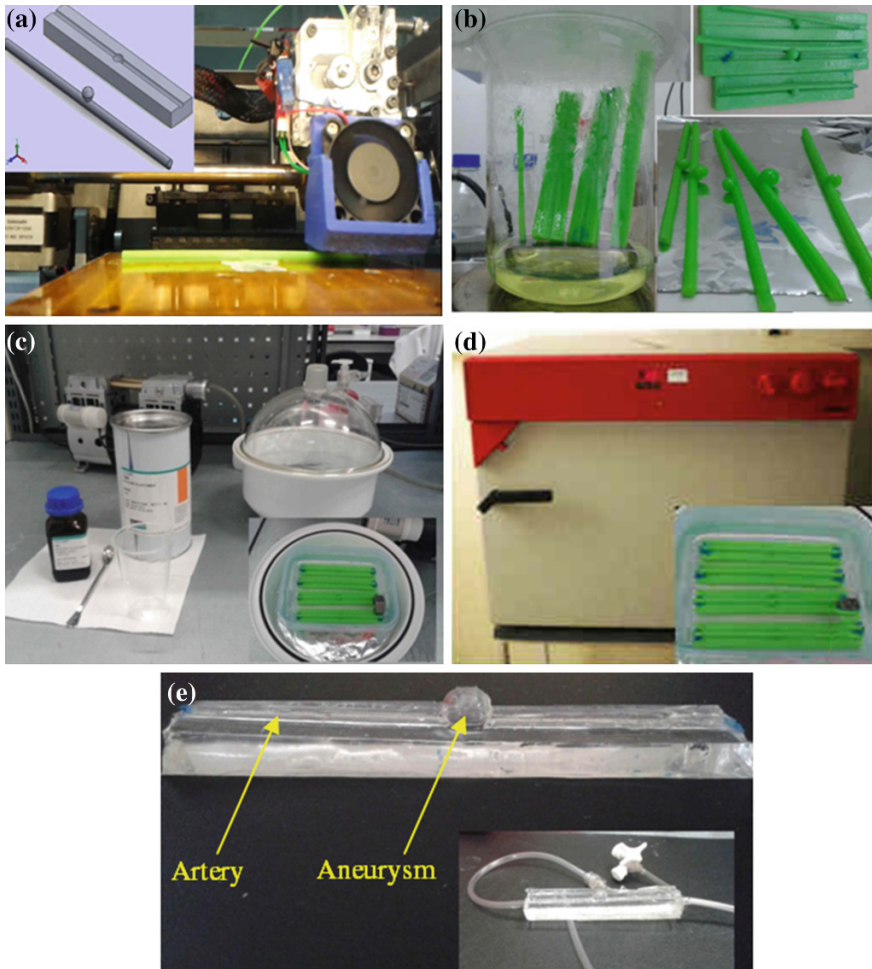


Fig. 2 Main steps of the fabrication procedure: **a** printing the geometries in ABS by means a 3D printer; **b** surface treatment with acetone vapors; **c** deposition of the polymer PDMS over the molds to obtain the channel; **d** curing the polymer at room temperature for 42 h and more at 80 °C for 30 min; **f** three-dimensional PDMS channel with the input/output connections

placed into the oven at 80 °C for 30 min (Fig. 2d). Finally, after the molds have cooled down, they were cut and taken off from the petri dish where the inlet and outlet holes were made.

2.3 Experimental Set-up

The experimental method used to obtain the measurement of displacement field on the PDMS aneurysm model was the ESPI. In this analysis the deformation occurred mainly on out-of-plane direction as the implemented ESPI set-up allows the measurement in this direction. To achieve this step, the experimental setup was coupled with an accurate image processing tool and designed to cancel rigid body motion only obtaining the above mentioned. The optical set-up used to measure out-of-plane displacement fields with ESPI are schematically represented in Fig. 3. In this case, the laser beam is splitted in two, one being the object beam and used to illuminate the object and the other being the reference beam. This combination generates a sensibility vector normal to the object surface. The mirror mounted on a piezoelectric transducer is used to implement the phase stepping technique, which in combination with image processing algorithms allows the calculation of the spatial phase distribution. The light source used was a 2 W laser from COHERENT (Verdi) with a radiation wave length of 514 nm.

To calculate the displacement field eight images were recorded at different phase shift, being half of them taken before and the remaining after the injection of the glycerin.

The PDMS aneurysm model was fixed on the optical table and was pumped glycerin by means of a syringe pump with a flow rate of 250 $\mu\text{l}/\text{min}$. Figure 4 shows the aneurysm model placed in the out-of-plane displacement set-up.

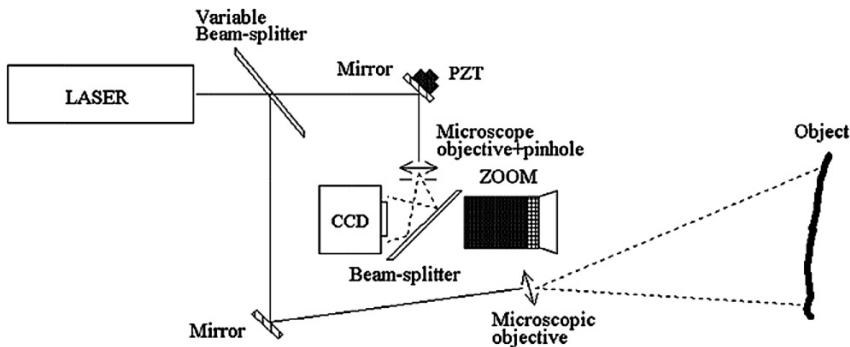


Fig. 3 ESPI set-up to measure out-of-plane displacement fields [18]

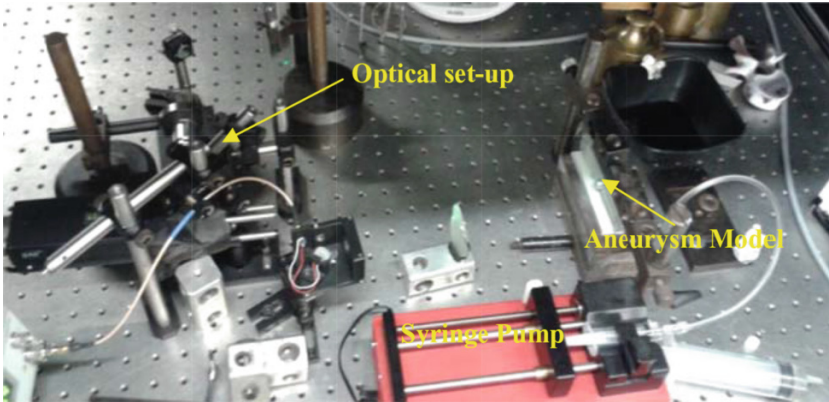


Fig. 4 PDMS aneurysm model in an out-of-plane displacement set-up

3 Results and Discussion

Using the ESPI the displacement field is calculated by subtracting the speckle phase maps obtained before and after the fluid flow. The discontinuities in Fig. 5a are due to the phase calculation algorithm and can be removed by phase unwrapping. Different solutions are available for this purpose according to the data spatial noise [19]. The results presentation could be improved using a pseudo color presentation where the displacement intensity is codified according to a color, see Fig. 5b.

A more understandable way to present the information is by showing a three-dimensional representation of displacement field. Figure 6 represents the displacement field measured with ESPI. Analyzing the obtained preliminary results it is observe that the maximum displacement has occurred on the aneurysm region and on the inlet of the artery. This phenomenon could be explained by two possible reasons: the pressure is higher in both aneurysm region and artery inlet; the wall thickness in the regions of the highest displacements could be lower than the other regions of the model.

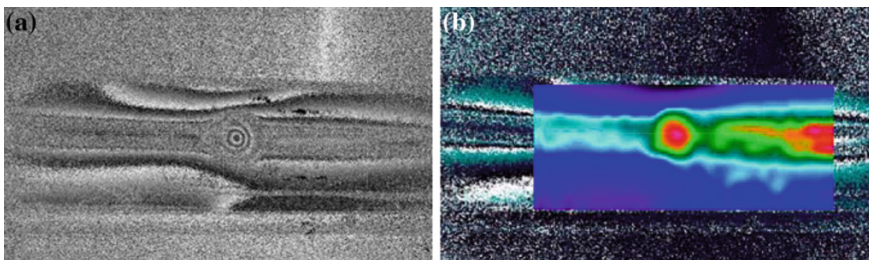
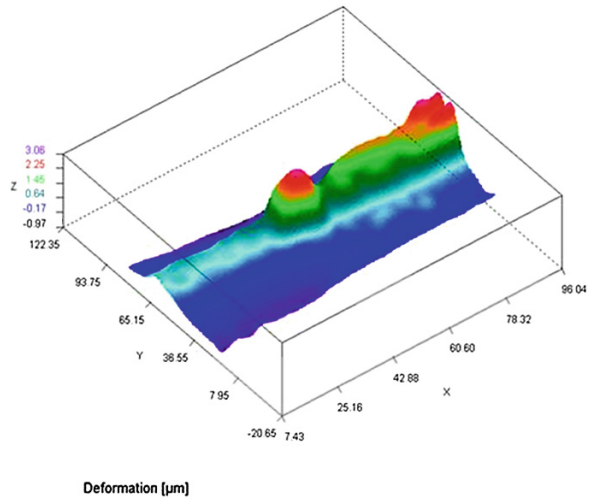


Fig. 5 **a** Phase map and **b** Unwrapped phase map of displacement field. The flow direction is from *right* (inlet) to *left* (outlet)

Fig. 6 Out-of-plane displacement field measured on PDMS aneurysm model with ESPI



4 Conclusions

The fabrication methodology used to obtain an aneurysm model has allowed to achieve an in vitro model with a geometry and dimensions very similar to a realistic in vivo aneurysm. However, the demolding process was extremely laborious and consequently some parameters like wall thickness and superficial roughness were difficult to control. The roughness of the moulds and cores can influence the velocity and pressure inside the model however the tested surface treatment with acetone vapors may be a good solution to eliminate this influence.

The optical technique of ESPI proved to be well adapted for displacement field measurement on PDMS materials. The results show that this technique correlates well in the displacements when high spatial resolution is used, allowing extracting the information for the applied deformation. A study to compare in more detail the present experimental results with numerical simulations is currently under way.

In the near future we intend to optimize the fabrication process by using others materials to produce the moulds and cores. Regarding the displacement field measurements we plan to obtain more accurate results and out-of-plane measurements by using other techniques such as Digital Image Correlation. Experiments at different and higher flow rates are also one of the futures goals.

Acknowledgments The authors acknowledge the financial support provided by PTDC/SAU-ENB/116929/2010, EXPL/EMS-SIS/2215/2013, scholarship SFRH/BD/91192/2012 and scholarship SFRH/BD/89077/2012 from FCT (Science and Technology Foundation), COMPETE, QREN and European Union (FEDER).

References

1. Bessa K et al (2012) Biomechanical factors analysis in aneurysm. In: Fluid dynamics, computational modeling and applications, Dr. L Hector Juarez (ed) ISBN: 978-953-51-0052-2, InTech (2012). Available in: <http://www.intechopen.com/books/fluid-dynamics-computational-modeling-and-applications/biomechanical-factors-analysis-in-aneurysm>
2. Oshima M et al (2001) Finite element simulation of blood flow in the cerebral artery. *Comput Meth Appl Mech Eng* 191:661–671
3. Lima R et al (2008) Radial dispersion of red blood cells in blood flowing through glass capillaries: role of hematocrit and geometry. *J Biomech* 41:2188–2196
4. Lima R et al (2009) Measurement of individual red blood cell motions under high hematocrit conditions using a confocal micro-PTV system. *Ann Biomed Eng* 37:1546–1559
5. Lima R et al (2009) Axisymmetric PDMS microchannels for in vitro haemodynamics studies. *Biofabrication* 1:035005
6. Pinho D et al (2013) A microfluidic device for partial cell separation and deformability assessment. *Biochip J* 7(4):367–374
7. Faustino V et al (2014) Extensional flow-based microfluidic device: deformability assessment of red blood cells in contact with tumor cells. *Biochip J* 8(1):42–47
8. Leble V et al (2011) Asymmetry of red blood cell motions in a microchannel with a diverging and converging bifurcation. *Biomicrofluidics* 5:044120
9. Gåsvik KJ (2002) *Optical metrology*. John Wiley & Sons Ltd, New York
10. Cloud G (1998) *Optical methods of engineering analysis*. Cambridge University Press, Cambridge
11. Otani Y (2009) *Handbook of optical metrology principles and applications*. Taylor & Francis Group, London
12. Sutton M et al (2009) *Image correlation for shape, motion and deformation measurements*. Springer, Berlin
13. Chatziprodromou I et al (2007) Haemodynamics and wall remodelling of a growing cerebral aneurysm: a computational model. *J Biomech* 40:412–426
14. Vania F et al (2010) Rapid prototyping of 3D anatomical models to hemodynamic studies. In: 3rd international conference on biomedical electronics and devices. Valencia. pp 246–250. ISBN 978-989-674-017-7
15. Queijo L, Lima R (2010) PDMS anatomical realistic models for hemodynamic studies using rapid prototyping technology. In: Lim T, Goh JCH (eds) WCB 2010, IFMBE proceedings 31, pp 434–437
16. Parlea L et al (1999) An Analysis of the geometry of saccular intracranial aneurysms. *AJNR Am J Neuroradiol* 20:1079–1089
17. Khanafer K et al (2009) Effects of strain rate, mixing ratio, and stress–strain definition on the mechanical behavior of the polydimethylsiloxane (PDMS) material as related to its biological applications. *Biomed Microdevices* 11:503–508
18. Ribeiro J et al (2013) Assessment of the displacement field along a surface crack in a flat plate using optical techniques. experimental techniques. In press (2013)
19. Creath K, Schmit J (1996) N-point spatial phase-measurement techniques for nondestructive testing. *Opt Lasers Eng* 24:365–379

Experiments on the Edge of Chaos of a Planar Closed Chain Underactuated Mechanism

J. Xie, H. Zhao, Z.-H. Liu and Y. Chen

Abstract Experiment investigation of planar five-bar underactuated mechanism is carried out. The focus is on chaotic motion and the edge of chaos, at which the motion of the mechanism changes from period to chaos. The angular velocity of active joint is taken as the controlling parameter, i.e. the input angular velocity. Eighty seven values of input angular velocity ranging from 0.57 to 49.78 rpm are set to experiments. The displacements of the slider connected with frame are measured. Based on the data acquired, chaotic motion is identified by means of phase portrait, Poincaré mapping and Lyapunov exponent. The results of experiments show that the motion of mechanism undergoes from periodic motion to chaotic motion with the increasing of the input angular velocity. The edge of chaos is not a value of input angular velocity, but a range of input angular velocities. And at the edge of chaos, the periodic motion coexists with chaotic motion, and the motion of the mechanism alternates between the two states of motion.

Keywords Closed train underactuated mechanism · Chaos · Edge of chaos · Experiment

J. Xie (✉) · H. Zhao · Z.-H. Liu · Y. Chen
Southwest Jiaotong University, Jiaotong, People's Republic of China
e-mail: xj_6302@263.net

H. Zhao
e-mail: neil86@163.com

Z.-H. Liu
e-mail: zhhlui@home.swjtu.edu.cn

Y. Chen
e-mail: cykine163@163.com

1 Introduction

Chaotic motion of mechanism has recently attracted growing attention in the field of mechanism analysis and design. In 1992 Senevirratne and Earles observed that the performance of a mechanism with clearance would be chaos in some range of system parameters [25]. Since then, many mechanisms have been found to have the potential of chaotic motion. They are linkages [4, 6, 9, 12], cams [2, 3], gears [5, 7, 8, 10, 11, 28], gear trains [15, 18], and so on.

Referring to the question what factors cause these mechanisms exhibit chaotic motion, Moon provided the answers in [20], it is because the mechanisms consist of some nonlinear elements, for examples, nonlinear elastic or spring elements, nonlinear damping, such as stick-slip friction, backlash, play, or bilinear springs.

Underactuated mechanism is another class of mechanism to exhibit chaotic motion. An underactuated mechanism is a mechanism with less controlling inputs than its degrees of freedom, which can arise from either the absence or failure of some actuators, or due to avoiding use of some available actuators, or for the sake of reducing weight, cost or energy consumption while maintaining an adequate degree of dexterity. An underactuated mechanism can be referred as a dynamic system with second-order nonholonomic constraints.

Nowadays, chaotic phenomena and controlling chaos of open chain underactuated mechanism, especially the underactuated robots, have been investigated extensively [1, 13, 14, 17, 19, 21, 23, 26, 27], however, to a much lesser degree with closed chain underactuated mechanism. To the best of our knowledge, Li presented a study of chaotic motion of a planar closed chain mechanism, which is composed of five links and six lower kinematic pairs with only one actuator [16].

The aim of this paper is multiple. Firstly, the mechanism studied in this paper is a planar five-bar linkage with two degrees of freedom and only one joint is actuated. The controlling input parameter at the active joint is the angular velocity of the actuator instead of the generalized force adopted in aforementioned investigations. Secondly, both the theoretical analysis and simulations show that this five-bar underactuated mechanism can exhibit chaotic motion under some angular velocities of input [22]. To confirm this conclusion, experiment is needed. Finally, in order to find out the conditions of chaos arising and lay down the foundations for controlling chaos, this paper is focused on the edge of chaos at which the motion of the mechanism changes from period to chaos. In one word, the motivation of this study is to put forward the study of chaos arising from a closed train mechanism.

The remaining parts of this paper are organized as follows. In Sect. 2, the experimental conditions are presented together with the method of numerical treatment, then the results of experiment are presented in Sect. 3, some discussions and conclusive remarks are offered in Sect. 4.

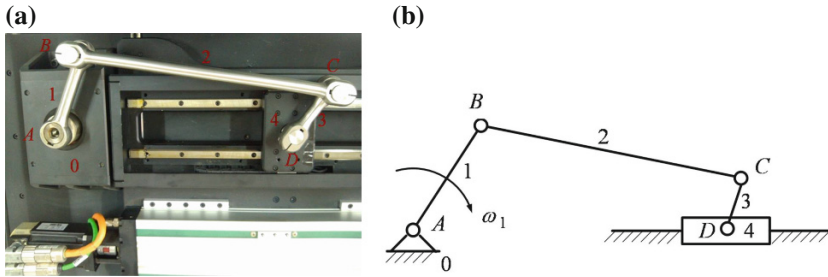


Fig. 1 Five-bar underactuated mechanism. **a** Test bed **b** schematic diagram

2 Experimental Setup and Data Treatments

2.1 Five-Bar Underactuated Mechanism

The mechanism test bed and its schematic diagram are shown in Fig. 1. In order to eliminate the effect of gravity, we set the mechanism in the horizontal plane.

The mechanism consists of four revolute joints, denoted by A, B, C, D respectively, and one prismatic joint, denoted by slider D . The frame is denoted by 0 , and the links AB, BC, CD and slider D are denoted by $1, 2, 3, 4$ respectively.

The mechanism possesses 2° of freedom. The motion of mechanism is predictable only when there are two joints actuated independently. When only the joint A actuated, a case studied here, the mechanism is an underactuated mechanism.

2.2 Hardware and Software for Measurement and Controlling

Link 1 is connected with the output axis of a synchronous servo motor. Programmable logic controller (PLC) is employed to control all of the devices of the experiment. The schematic of the hardware and software system is shown in Fig. 2.

TwinCAT System manager/PLC Controller/Scope View are the user interfaces implemented in the industrial PC (IPC). One can input the desired angular velocity of Link 1 through TwinCAT PLC Controller, and then the run-command is sent to the motion controller for execution. The IPC converts the commands into command signals to move the servo motor; at the same time the controller monitors the system to prevent any changes on the angular velocity of Link1. The linear encoder measures the displacements of Link 4, and sends the data to IPC for processing. Once the controller ends the experiment, the curve of the displacements of Link 4 with respect to time will be displayed on the screen of IPC, and the data can also be exported for further analysis through TwinCAT Scope View.

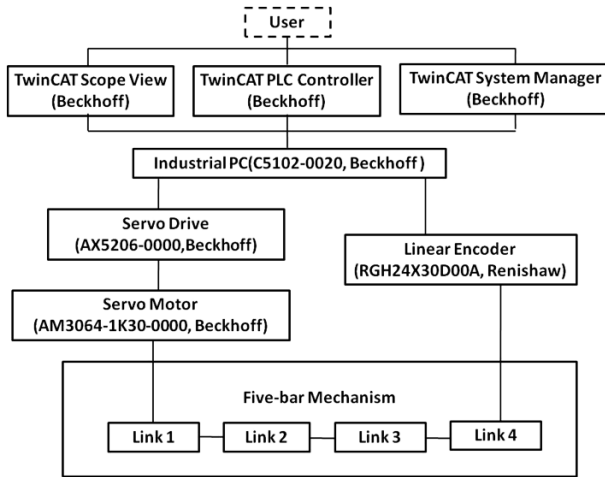


Fig. 2 The hardware and software for measurement and controlling

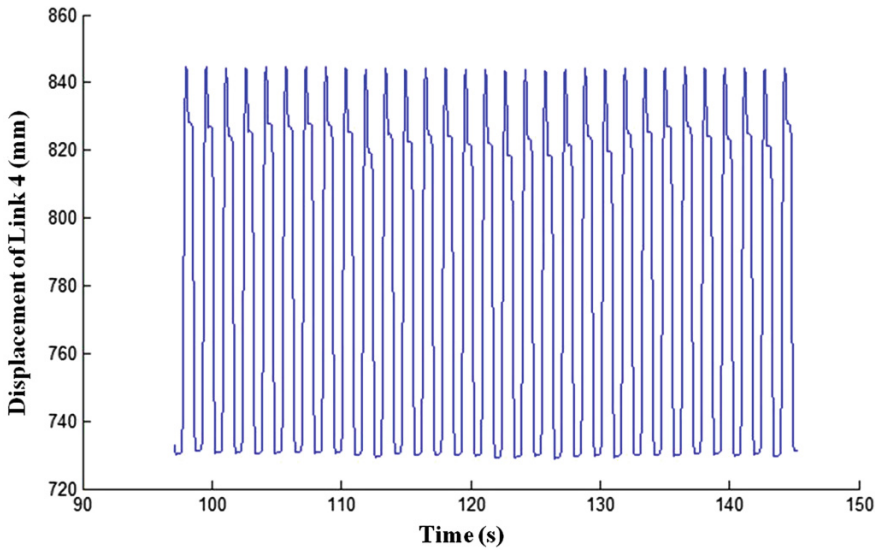


Fig. 3 The displacement of Link 4 with respect to time ($n_1 = 40$ rpm)

Figure 3 shows the displacements of Link 4 with respect to time when the input angular velocity, n_1 , is 40 rpm.

2.3 Numerical Treatments

After the data acquisition, the data for the first 60 s plus should be omitted, as shown in Fig. 3, because we concern mostly the steady phase, not the starting phase.

The data acquired may involve noise induced by the weak shake of the experiment bed, the electromagnetic wave emitted by the electric devices, and stains on the linear encoder. The noise should be filtered since it possibly has impact on the identification of chaotic motion. The method known as median-Gaussian filtering [29] is employed in this paper.

In order to identify chaotic motion by the data acquired, in this paper, we carry out the following checking program.

We start with looking at the time response of the mechanism, which is indicated by the displacement of Link 4 versus time, as shown in Fig. 3. Obviously the motion of Link 4 is disorganized and erratic.

Then we look at the phase diagrams. By means of the numerical differentiation, we are able to find out the velocity of Link 4 and plot the phase portrait, shown in Fig. 4a, from which it can be seen that the trajectory of Link 4 in phase plane never stabilizes within a bounded regime.

In nonlinear dynamical system, it is named as an attractor if the trajectory occupies certain zones in the bounded phase space, and goes and stays there forever. However, there are many kinds of attractors, for examples, periodic attractor, chaotic attractor and so on. The best way to identify the type for an attractor is using the Poincaré section [24, 30]. In Fig. 4b, we plot the Poincaré mapping. As shown in Fig. 4b, attractor shows some type of organization but with relatively complex geometry, and it is made up by an infinite number of points, and more they have distinctive fine structure. This is the most important characteristic of chaotic attractor. According to this rule, we conclude intuitively that the motion of Link 4 is chaotic.

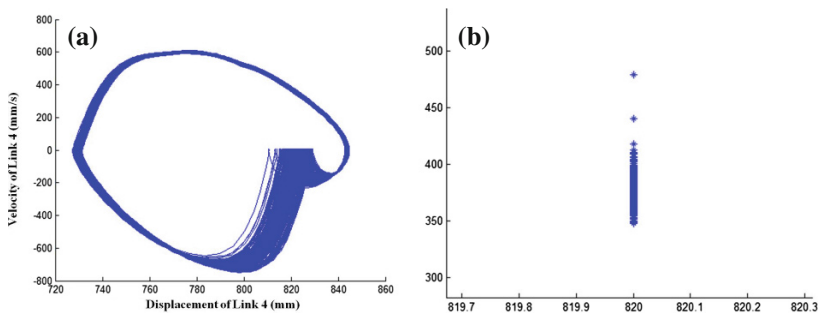


Fig. 4 Phase portrait and Poincaré mapping of Link 4. **a** Phase portrait **b** Poincaré mapping

Finally, to confirm this conclusion, we check the Lyapunov exponent which capsules the average rate of convergence or divergence of two neighboring trajectories in phase space. Since chaos means that the trajectory of a dynamic system is sensitively dependent upon the initial conditions, then a positive Lyapunov exponent defines chaos. Using the toolbox in MATLAB[®], Lyapunov exponent, 0.0402, can be obtained.

Based on the checks above, we are certain that the motion of Link 4 is chaotic when the input angular velocity, n_1 , is 40 rpm.

3 Results

For unification, all the kinematic pairs, A, B, C, D , are on the horizontal line at the beginning of the experiment. Link 1 rotates at the clockwise direction. The duration of data acquisition is 600 s when the mechanism is in steady working phase.

We set the input angular velocity, i.e. the angular velocity of Link 1, with different values ranging from 0.57 to 49.78 rpm with step 0.57 rpm. Totally, there are 87 input angular velocities. Based on the data acquired in experiment for each input angular velocity, the state of motion is identified with the checking program described in Sect. 2.3. If the motion is periodic, we index the input angular velocity with number -0.5 , and if the motion is chaotic, with 0.5 . In this way, all the states of motion respecting to the 87 input angular velocities are depicted in Fig. 5.

It can be seen that at a low input angular velocity, say lower than 9.15 rpm, the motion of the mechanism is periodic, and at a high input angular velocity, higher than 15.44 rpm, the motion is chaotic. When the input angular velocity is higher than 9.15 rpm and lower than 15.44 rpm, i.e. in the interval indicated by b and c in Fig. 5, the motion of mechanism may be periodic or chaotic. In other word, in the

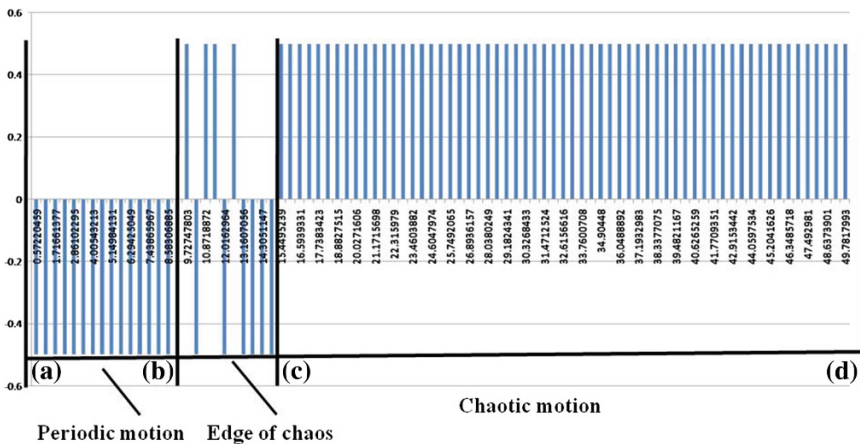


Fig. 5 States of motion respecting to the 87 input angular velocities

interval (b, c), periodic motion coexists with chaotic motion. The interval (b, c) is as a demarcation between periodic motion and chaotic motion; we name it as the edge of chaos.

4 Conclusions

In this paper, we study the chaotic motion of planar five-bar underactuated mechanism through experiment.

The angular velocity of Link 1 is regarded as the parameter of input, and the results show that the state of motion of the mechanism is depended on it evidently.

When the input angular velocity is lower than 9.15 rpm, the motion of the mechanism will be periodic; when input angular velocity is between 9.15 and 15.44 rpm, the motion of the mechanism alternates periodic and chaotic; and when input angular velocity is higher than 15.44 rpm, the motion of the mechanism will be permanently chaotic.

It is worth to notice that the edge of chaos of this underactuated mechanism is not a value of input angular velocity, but a range of input angular velocity, say from 9.15 to 15.44 rpm. At the edge of chaos, the periodic motion coexists with chaotic motion. The study of the edge of chaos may allow us to understand something about the arising of chaos, and find efficient measures to control chaos.

In the five-bar underactuated mechanism, there are four passive joints. They are revolute joints *B*, *C*, *D* and prismatic joint *D*. Exactly speaking, the chaotic motion studied here is referred to the motion at prismatic joint *D*, i.e. the relative motion between the Link 4 and the frame 0. Whether or not the relative motions between the two links at other passive joints are also chaotic at the same time has not been verified, and maybe there exists periodic relative motion at other passive joints. This question is interesting, and further works will lead to new findings.

Acknowledgment The authors would like to acknowledge the financial support of NSFC (National Natural Science Foundation of China) under the grant No. 51175437

References

1. Alvarez-Gallegos J, Gonzalez-Hernandez HG (1997) Analysis of the dynamics of an underactuated robot: the forced pendubot. In: Proceedings of the 36th IEEE conference on decision and control, San Diego, CA, USA, pp 1494—1499
2. Alzate R, Di Bernardo M et al (2009) Experimental and numerical investigation of coexistence, novel bifurcations, and chaos in a cam-follower system. *SIAM J Appl Dyn Syst* 8 (2):592—623
3. Alzate R, Piironen PT, Di Bernardo M (2012) From complete to incomplete chattering: a novel route to chaos in impacting cam-follower systems. *Int J Bifurcat Chao Appl Sci Eng* 22 (5):1250102
4. Belato D, Weber HI et al (2001) Chaotic vibrations of a nonideal electro-mechanical system. *Int J Solids Struct* 38(10—13):1699—1706

5. Chang-Jian C-W (2013) Gear dynamics analysis with turbulent journal bearings under quadratic damping and nonlinear suspension—bifurcation and Chaos. *J Comput Nonlin Dyn* 8 (1):011013-1—011013-10
6. Chang Z, Zhang C et al (2001) Bifurcation and chaos in linkage with a clearance. *J Mech Strength* 23(1):77—79
7. Cui Y, Liu Z et al (2010) Bifurcation and chaos of gear transmission system with clearance subjected to internal and external excitation. *J Mech Eng* 46(11):129—136
8. De Souza SLT, Caldas IL (2001) Basins of attraction and transient chaos in a gear-rattling model. *J Vib Control* 7(6):849—862
9. Farahanehi F, Shew SW (1994) Chaotic and periodic dynamics of slider-crank mechanism with slider clearance. *J Sound Vib* 177(3):307—324
10. Farshidianfar A, Saghafi A (2013) Global bifurcation and chaos analysis in nonlinear vibration of spur gear systems. *Nonlin Dyn*, pp 1-24
11. Gao Z, Shen Y et al (2005) Research on period-doubling bifurcation and chaos hierarchy in gear system. *Chinese J Mech Eng* 41(4):44—48
12. Ge Z-M, Lee C-I (2003) Non-linear dynamics and control of chaos for a rotational machine with a hexagonal centrifugal governor with a spring. *J Sound Vib* 262:845—864
13. Gonzalez-Hernandez HG, Alvarez J, Alvarez-Gallegos J (2004) Experimental analysis and control of a chaotic pendubot. *Int J Robot Res* 23(9):891—901
14. Lankalapalli S, Ghosal A (1997) Chaos in robot control equations. *Int J Bifurcat Chaos* 7 (3):707—720
15. Li S, Wu Q et al (2014) Bifurcation and chaos analysis of multistage planetary gear train. *Nonlin Dyn* 75(1—2):217—233
16. Li Z (1995) Chaotic vibration sieve. *Mech Mach Theory* 30(4):613—618
17. Liu Z-H, Li L (2004) Chaotic self-motion of flexible redundant robots. *China Mech Eng* 15 (13):1186—1189
18. Ma H, Xue D (2013) Bifurcation and chaos of planetary reverse system to external excitation. *China Mech Eng* 24(23):3129—3133
19. Mejia OP, Gallegos JA (2004) Chaos suppression of an underactuated manipulator: experimental results. *Latin America Trans, IEEE (Revista IEEE America Latina)* 2(1):19—24
20. Moon FC (1987) Chaotic vibrations an introduction for applied scientists and engineers. John Wiley & Sons Inc, New York
21. Nakamura Y, Suzuki T, Koinuma M (1997) Nonlinear behavior and control of a nonholonomic free-joint manipulator. *IEEE Trans Robot Autom* 13(6):853—862
22. Qin Y-Z (2011) Research on chaos and its control of planar closed chain underactuated mechanism. In: MS thesis, southwest Jiaotong University, Chengdu, P. R. China
23. Ravishankar AS, Ghosal A (1999) Nonlinear dynamics and chaotic motions in feedback-controlled two- and three-degree-of-freedom robots. *Int J Robot Res* 18(1):93—108
24. Robinson RC (2005) An Introduction to dynamical system: continuous and discrete. Pearson Education Inc, NY
25. Seneviratne LD, Earles SWE (1992) Chaotic behavior exhibited during contact loss in a clearance joint of a four-bar mechanism. *Mech Mach Theory* 27:307—321
26. Vakakis AF, Burdick JW, Caughey TK (1991) An interesting strange attractor in the dynamics of a hopping robot. *Int J Robot Res* 10(6):606—618
27. Varghese M, Fuchs A, Mukundan R (1991) Characterization of chaos in the zero dynamics of kinematically redundant robots. In: Proceedings of the 1991 American control conference, Boston, MA, USA, pp 225—230
28. Wang S, Shen Y et al (2002) Chaos and bifurcation analysis of a spur gear pair with combined friction and clearance. *Chinese J Mech Eng* 38(9):8—11
29. Wei Z-P, Wang J et al (2012) A median-Gaussian filtering framework for Moiré pattern noise removal from X-ray microscopy image. *Micron* 43:170—176
30. Williams GP (1997) Chaos theory tamed. Joseph Henry Press

Systematic and Rapid Construction of Test Beds for Planar Mechanism

H. Mencek and R. Soylu

Abstract In this study, a systematic approach, for constructing planar mechanisms by utilizing a robotic kit, is proposed. Various models for revolute and prismatic joints and various models to be used as links are suggested. The actual performances of the prototype mechanisms may be experimentally assessed by taking three basic measurements regarding the actuator voltage, actuator current and the rotational displacement of the input link. Slider crank, double slider and four bar mechanism prototypes are constructed as example planar mechanisms. In addition, the electrical power consumption of a slider crank mechanism is obtained experimentally. This consumption is compared with the power consumption obtained via a mathematical model of the mechanism.

Keywords Dynamic performance · Planar mechanisms · Construction of mechanisms · Robotic kit · Test bed

1 Introduction

Dynamic characteristic of a mechanism affects the energy consumption of the mechanism, the operating noise/vibration levels and the lives of the bearings and connection elements that connect the mechanism to the ground. Hence, it is important to optimize these behaviours. There are numerous methods that are proposed to improve the dynamic characteristics of mechanisms (see [1] for a comprehensive survey of the available methods). These methods are used in order to compensate for the gravitational forces and/or to minimize the fluctuations of shaking forces, shaking moments and actuator torques. Some of these methods

H. Mencek (✉) · R. Soylu
Department of Mechanical Engineering, Middle East Technical University, Ankara, Turkey
e-mail: hmencek@gmail.com

R. Soylu
e-mail: soylu@metu.edu.tr

involve, for instance, addition of springs, addition of counterweights and connection of auxiliary linkages. In an ongoing project funded by The Scientific and Technological Research Council of Turkey (TUBITAK), the authors are investigating the means of improving the dynamic performances of mechanisms by utilizing adjustable mechanisms, and/or efficient, mechanical force and torque generators, which are to be patented. Adjustable mechanisms can be defined as mechanisms where, the kinematic dimensions and the inertial parameters of the links may be changed as desired [3]. In the aforementioned project, both theoretical and experimental approaches are being employed. Typical planar mechanisms, with different topologies, have been modelled on the computer and alternative designs have been developed to improve their dynamic performances. For the designs that are found to be theoretically successful, prototypes will be produced so that the dynamic performances of the mechanisms are measured experimentally.

It is well known that, construction of test set-ups may require extensive amounts of time and effort. Therefore, in order to construct numerous different mechanisms with desired kinematic and dynamic characteristics in an efficient manner, one needs special components that are compatible with each other so that they may easily be connected together. For this purpose, it is possible to utilize one of the educational robotic kits available in the market. Lego Mindstorm [2] and VEX Robotic Design System [4] are two of the most comprehensive kits available. These robotic kits contain various structural and connection elements together with compatible actuators, sensors, programmable micro-controllers and power accessories.

Planar mechanisms constructed by means of a robotic kit may be utilized for different purposes. One possibility is to use the prototype mechanism as the scaled-down model of a larger mechanism which is actually in use. Using dimensional analysis, the experiments performed on the scaled-down mechanism may be utilized to predict the results of difficult and/or expensive experiments to be performed on the actual mechanism. It is also possible to use such prototypes for verifying, experimentally, the validity of suggested friction models for different joints. Such prototypes can also be very useful for educational purposes.

In this study, a systematic approach, to construct planar mechanisms by utilizing the VEX robotic design system, is proposed. Slider-crank, four bar and double slider mechanisms are presented as examples. Various measurements are taken from a prototype slider crank mechanism. The validity of these measurements are checked by using a mathematical model of the prototype.

2 VEX Robotic Design System

VEX robotic design system is a robotic construction kit developed by Innovative First International company. The VEX robotic design system includes various structural parts (made of steel or aluminum) and connection elements. There are additional components for the construction of gear pairs, revolute and prismatic

joints. Structural parts have many square shaped holes which allow construction of different designs by using bolt and nut pairs. In addition, DC and servo motors, optical shaft encoders, bump switches, potentiometers, gyroscopes, accelerometers, micro-controllers and battery units are also included in the robotic kit. Micro-controllers are programmable via the RobotC and EasyC compilers for user controlled or autonomous operations.

3 Construction of Planar Mechanisms

During the construction of planar mechanisms, one should consider the following three physical limitations.

1. Links must be on the same plane (or, on parallel planes) throughout the motion.
2. There cannot be any collisions between any two elements (such as links, shafts, connection elements, etc.) of the mechanism throughout the motion.
3. For a planar mechanism the links of which lie on planes parallel to the x-y plane, the out-of-plane forces and moments (i.e., forces along the z axis and moments about the x and y axes) must not be extensive, so that they do not lead to large frictional forces which may 'lock' the mechanism.

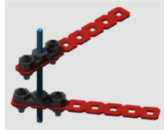
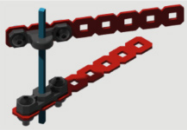



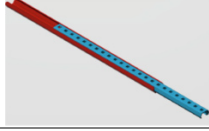
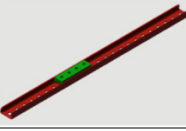
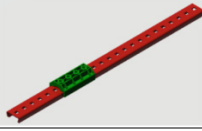
In order to satisfy these physical limitations, one may take various precautions. For example, gravitational effects may disturb the parallelism of the links violating limitation (1). Furthermore, in order to satisfy limitation (2), one needs to increase the distance between the links along the z axis. However, an increase along the z axis leads to a violation of limitation (3) due to the increasing out-of-plane forces and moments. In order to completely balance the out-of-plane forces and moments of a planar mechanism, one may use a common symmetry plane (for all links) parallel to the x-y plane. This construction approach requires symmetrical link and joint models which are discussed in the following sections.

CAD models for the basic revolute and prismatic joints that are suggested in this study are presented in Table 1. Note that, the CAD models of the individual components are already available in [4]. A simple notation is utilized to label the models for future reference. For example, BRJ2 indicates the basic revolute joint type 2 model, whereas BPJ3 indicates the basic prismatic joint type 3 model. Note that, the input link of the mechanisms need to be actuated via the so-called driven revolute joints (DRJ).

The symmetrical revolute joint models that are designed to construct a mechanism with a common symmetry plane are shown in Fig. 1. Here, the SRJ3 joint model is designed to allow the motion of another link through the axis of rotation of the revolute joint.

In some cases, it is possible to tolerate the out-of-plane forces and moments, up to a limit, by using the revolute joint model (URJ) shown in Fig. 2.

Table 1 Basic joint models

Category	Type 1	Type 2	Type 3
Basic Revolute Joints (BRJ)			
Driven Revolute Joints (DRJ)			
Basic Prismatic Joints (BPJ)			

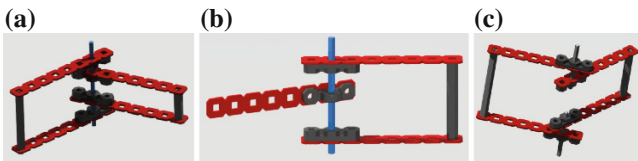



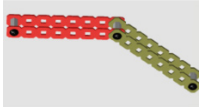

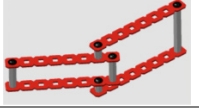
Fig. 1 Symmetrical Revolute Joint Models (SRJ)



Fig. 2 Unsymmetrical Revolute Joint Design (URJ)

The VEX design system allows one to construct mechanisms, efficiently, with different kinematic dimensions using standard structural parts. In order to construct mechanisms with a common symmetry plane, one may utilize the symmetrical link models shown in Table 2. Here, the Fixed Width Link (FWL) and Varying Width Link (VWL) models are obtained by rigidly connecting the same basic link types in parallel. Furthermore, for the FWL2 and VWL2 models, it is possible to adjust the relative angle between the components at a fixed value.

Table 2 Symmetrical Link Models

Category	Type 1	Type 2
Fixed Width Links (FWL)		
Varying Width Links (VWL)		

4 Performance Evaluation

Performance evaluation of the constructed mechanisms may be realized in two steps. In the first step, the actual performance of the mechanism is experimentally assessed by taking three basic measurements regarding the actuator voltage, actuator current and the input link rotational displacement. A data acquisition system consisting of NI-cDAQ USB chassis, NI9229, NI9239, Labview Software and a current transducer (CR Magnetics—CR5211) are utilized in order to measure the voltage and the current. In addition, the rotational displacement of the input link is obtained via the quadrature encoder of the VEX design system.

In order to drive the mechanisms, a DC motor (motor 269 of the VEX design system) with a free speed of 100 rpm, stall torque of 0.98 N.m, free current of 0.18 A and a stall current of 2.6 A is used [4]. These specifications and the efficiency curve of the motor are given for an input voltage of 7.2 V by stating that the actual motor specifications are within 20 % of these values.

In the second step, the performance of the mechanism is obtained by using the mathematical model of the prototype. This model is based upon the equations of the DC motor model and the equation of motion of the prototype mechanism which is derived and coded using MATHEMATICA. The kinematic and inertial parameters of the constructed mechanisms are obtained using the available CAD models and the material properties of the VEX design system components.

One may utilize the following set of equations to simulate the dynamic behaviour of the prototype mechanism and the connected DC motor.

$$V_i(t) = L\dot{I}(t) + RI(t) + k_v\dot{\theta}(t) \tag{1}$$

$$J_m\ddot{\theta}(t) = k_t I(t) - b_m\dot{\theta}(t) - T_A\left(\theta(t), \dot{\theta}(t), \ddot{\theta}(t)\right) \tag{2}$$

here, L is the inductance, R is the electrical resistance, k_v is the speed constant, k_t is the torque constant, J_m is the moment of inertia of the DC motor reduced to the output shaft and b_m is the coefficient of viscous friction associated with the output shaft of the motor. Furthermore, $V_i(t)$ is the input voltage, $I(t)$ is the current drawn

by the motor, T_A is the actuator torque to be provided to the prototype mechanism driven by the motor and $\theta(t)$ is the angular position of the output shaft, which is equal to the angular position of the input link of the mechanism. Note that the actuator torque, T_A , is determined from the equation of motion of the mechanism. Hence, for a given input voltage $V_i(t)$, one may obtain the response of the mechanism by solving Eqs. (1) and (2) for $I(t)$ and $\theta(t)$.

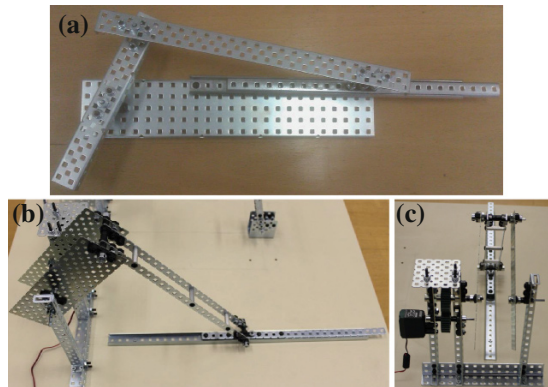
In order to form the mathematical model, it is clear that the parameters of the DC motor model, i.e., the elements of the vector $\mathbf{P} = [L, R, k_v, J_m, k_t, b_m]$, must be determined accurately. In this study, these six parameters are estimated by minimizing an objective function based upon the errors $e_i(t)$ and $e_\theta(t)$, which are associated with $I(t)$ and $\theta(t)$. Here, $e_i(t) = I_m(t) - I_s(t)$ and $e_\theta(t) = \theta_m(t) - \theta_s(t)$ where ‘m’ and ‘s’ refer to the ‘measured’ and ‘simulated’ values, respectively. Note that, the initial values of the estimated parameters are obtained from the given motor specifications.

5 Examples

5.1 Constructed Mechanisms

The first constructed mechanism is the slider-crank mechanism (SCM-P1) shown in Fig. 3a. In this mechanism, the DRJ1, BRJ1 and BPJ1 joint models are utilized. Tests indicate that the SCM-P1 model cannot satisfy limitations (1) and (3). Hence, the symmetrical slider crank mechanism (SCM-P2) shown in Fig. 3b, c has been designed to satisfy all physical limitations. SCM-P2 utilizes the symmetrical joint models, SRJ1, SRJ2, SRJ3 and BPJ1. Note that, due to the full rotation of the crank, the coupler link interferes with the revolute joint between the base and the crank.

Fig. 3 Slider crank mechanism prototypes: **a** First slider crank mechanism model (SCM-P1), **b** Side view of the symmetrical slider crank mechanism (SCM-P2), **c** View showing the common symmetry plane of the SCM-P2



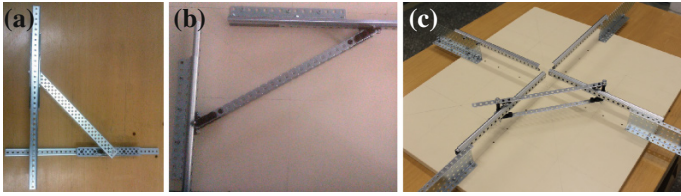


Fig. 4 Double slider mechanisms: **a** DSM-P1, **b** DSM-P2, **c** DSM-P3

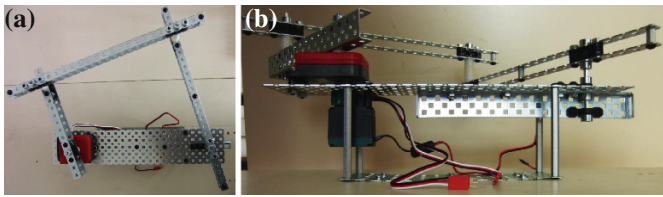


Fig. 5 Four bar mechanism prototype (FBM-P1): **a** *Top view* of the model, **b** *Side view* of the model

Hence, in order to prevent collision of the coupler link with the joint shaft, the SRJ3 model is used for the revolute joint which connects the crank to the base.

Three types of double slider mechanisms that have been constructed are shown in Fig. 4. Here, the DSM-P1 model suffers from the out-of-plane forces and moments. The DSM-P2 model has a common symmetry plane to balance the out-of-plane forces and moments. However, its coupler link, which will be used as the driving link, cannot perform a 360° rotation. Hence, considering the problems associated with the previous models, The DSM-P3 model is designed to successfully satisfy all physical limitations.

Two different four bar mechanisms that have been constructed using the VEX design system are shown in Fig. 5. Both mechanisms are of the crank-rocker type and they operate successfully without violating the aforementioned physical limitations.

5.2 Results for the Slider Crank Mechanism Prototype (SCM-P2)

In this section, experimental measurements realized on the SCM-P2 model are discussed. The mechanism operates on the x-y plane, whereas, gravity acts along the y axis. The DC motor driving the mechanism has been connected to a 7.2 V power supply. Supplied voltage, current drawn by the motor and the angular position of the

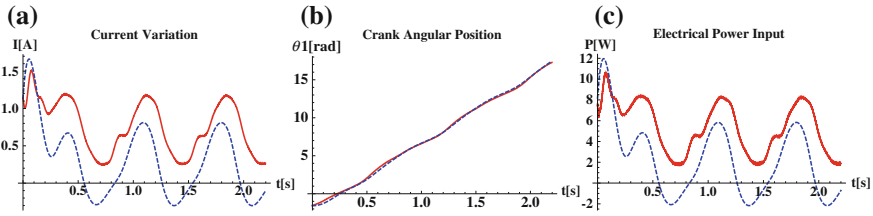


Fig. 6 Experimental measurements (*solid line*) and the simulation results obtained from the mathematical model (*dashed line*) for SCM-P2 model: **a** Current drawn by the motor, **b** Angular position of the crank, **c** Electrical power consumption

crank link have been measured. Measurements related to the drawn current, the angular position of the crank and the electrical power consumption for the SCM-P2 model are shown in Fig. 6. Note that, the experimental measurements have been synchronized such that the starting time of motion has been taken as $t = 0$. Hence, the initial condition for the current has been obtained as $I(0) = 1.137$ A.

The simulated values for $I(t)$, $\theta(t)$ and the electrical power, on the other hand, are obtained by solving $I(t)$ and $\theta(t)$ from Eqs. (1) and (2) subject to the same experimental input voltage (i.e., $V_i(t) = 7.2$ V) and the same experimental initial conditions (i.e., $I(0) = 1.137$ A, $\theta(0) = -90$ deg and $\dot{\theta}(0) = 0$).

The results obtained by using the mathematical model given by Eqs. (1) and (2) are also shown in Fig. 6. Here, the main reason for the differences between the experimental measurements and the simulation results is the lack of a friction model for the revolute and prismatic joints in the developed equation of motion. Hence, the current and power requirements simulated by the model are less than the measured values which includes frictional effects as well.

6 Conclusions

In this study, a systematic approach, to construct planar mechanisms by means of a robotic kit, has been proposed. Various revolute and prismatic joint construction models and various link models have been suggested. Some of the proposed models are designed to overcome the negative effects of the out-of-plane forces and moments. Slider-crank, double slider and four bar mechanisms are constructed as examples. Furthermore, the actual and simulated power consumptions of a slider crank mechanism are presented briefly in order to illustrate a possible application as a test bed. The authors acknowledge the financial support of The Scientific and Technological Research Council of Turkey (TUBITAK) to this study through the 112M110 research project.

Acknowledgments The authors acknowledge the financial support of The Scientific and Technological Research Council of Turkey (TUBITAK) to this study through the 112M110 research project.

References

1. Arakelian VH, Smith MR (2005) Shaking force and shaking moment balancing of mechanisms: a historical review with new examples. *J Mech Des* 127(2):334–339
2. Lego Mindstorm. <http://www.lego.com/en-us/mindstorms>. Accessed 21 Feb 2014
3. Mencek H, Soylu R (2013) Improvement of the dynamic performances of mechanisms via a two-degree-of-freedom adjustment system. In: Proceedings of the 16th national symposium on machine theory, Erzurum, Turkey, 182–191
4. VEX Robotics. <http://www.vexrobotics.com>. Accessed 21 Feb 2014

Development of Impact Loading Equipment for Testing of FRP Strips as Reinforcement of Masonry Bricks

P. Correia and N. Peixinho

Abstract The preservation of a cultural heritage has been, in nowadays, one important research topic. Some new techniques and materials have been studied. The use of Fibre Reinforced Polymer (FRP) is one of them. The static material properties of these materials when used in brick masonry are regularly studied. The dynamic studies are, however, almost non-existent. The development of a device capable to test dynamically the specimens already used in static tests is presented in this paper. It is described the construction of a drop weight tower to test FRP strips glued to brick masonry.

Keywords Impact loading machine · FRP · Pull-out · Drop tower development

1 Introduction

The preservation of cultural heritage buildings is considered a major issue in the cultural life of modern societies. However, this task requires the establishment of proper methodologies, able to tackle simultaneously their considerable architectural and cultural value and their structural safety [1]. An important topic in current research is the development of efficient and cost effective strengthening techniques, able to reestablish the performance of cultural heritage buildings and to prevent their brittle failure, particularly under earthquake loading but also damage resulting from terrorist activities.

The use of fiber reinforced polymer (FRP), materials has been an option, due to the various advantages of the use of composite materials: low density, immunity to corrosion, high tensile strength as well as flexibility and ease of implementation make these materials attractive.

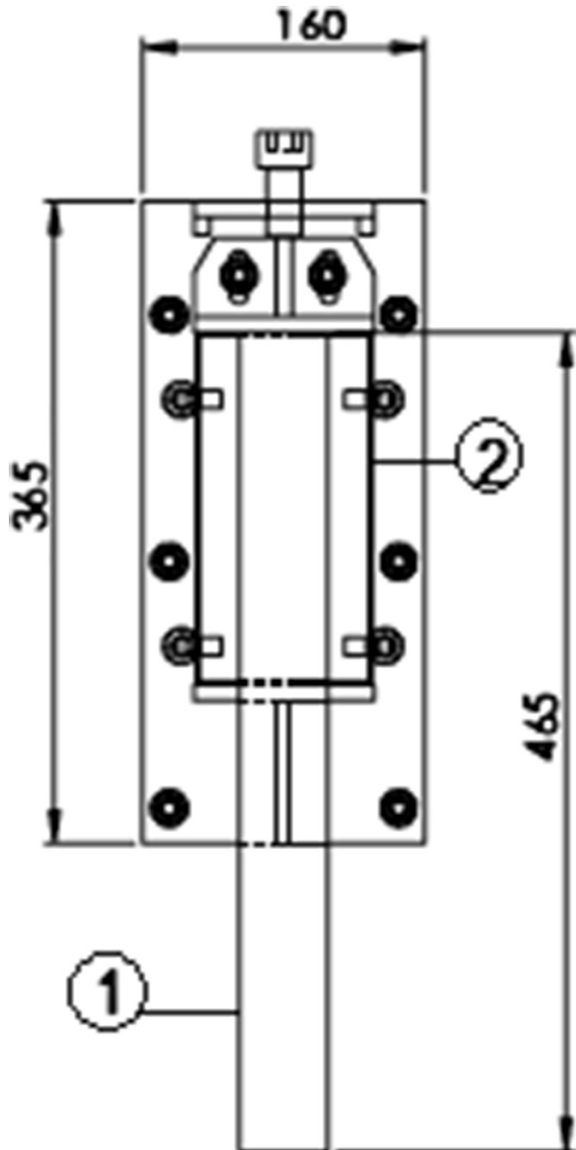
P. Correia (✉) · N. Peixinho
University of Minho, Minho, Portugal
e-mail: pedrocorreia@dem.uminho.pt

N. Peixinho
e-mail: peixinho@dem.uminho.pt

Since these are novel materials, and in particular their use as composites for buildings, their study and characterization is very recent. At the static level studies have been developed [1–4], however, for dynamic loading few studies have been developed.

Apparently the quality of the bond between the ceramic material and the FRP is what defines the maximum applicable load. The aim of the study was to develop a device which enables the dynamic test (impact) in tensile pull-out of these

Fig. 1 Specimen and fixing structure: 1 is the FRP and 2 the Brick



materials. The requisite for using the same type of specimens in static and dynamic tests should be important, allowing this way to better compare test values. In Fig. 1 we can observe the specimens, where (1) is the FRP strip and (2) is the brick masonry.

2 Architecture and Design of the Apparatus

The developed equipment is based on a drop-weight tower specifically designed for dynamic tests in FRP-Brick assembly. It is required a rigid drop tower to ensure a free falling mass to impact the specimens. The stability of the apparatus is due to its simple design, a solid base plate, and almost frictionless sliding guides that allow performing impact tests.

The first step to design the apparatus was to define the velocity and the energy. From such definition general guidelines for the equipment could be implemented in the detail design. Instrumentation requirements, for load cell measurement, are also important for the definition of specimen fixture and stiffness of base plate and specimen//fixture/load cell system.

2.1 Initial Parameters

The tests will be based on the composite type of specimen used in the static tests performed at the CFRP/GFRP-ceramic. In this way it is possible to compare the dynamic tests with static loading. On the other hand it is necessary that the equipment has enough energy and strength to break the impacted specimen.

Static tests indicate values of 10 kN, and less than 1 mm displacement [2]. Thus, considering the falling energy equal to the work of deformation:

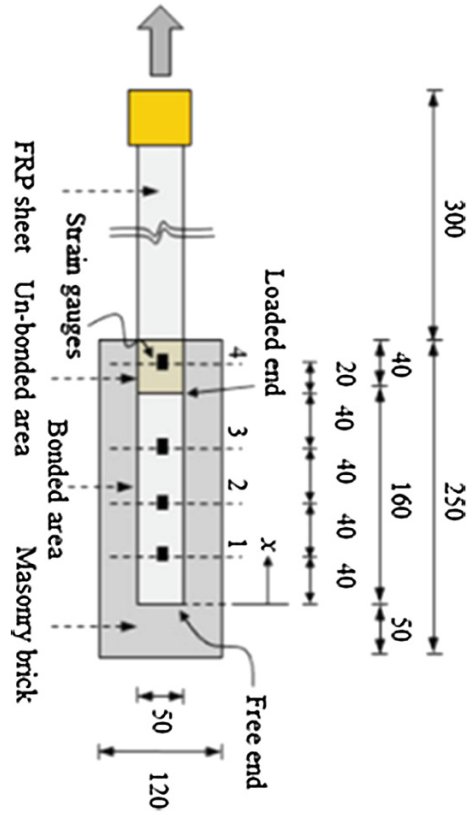
$$E = \omega \tag{1}$$

$$\omega = F \times \Delta r = 10J \tag{2}$$

Thus, observing the Eq. 2 the energy required to deform will be statically 10 J. In view of the specimen shown in Fig. 2, and considering the impact velocity that would be the same than deform the specimen (which is a lower bound approximation) one can calculate the speed of impact required to achieve a nominal strain rate, represented by Eq. 3.

$$\dot{\varepsilon} = \frac{\varepsilon}{\Delta t} = \frac{dl}{dtl} = \frac{v}{l} \tag{3}$$

Fig. 2 Static specimen sketch



The impact velocity calculated for the limits of shear rate is shown in Table 1. Observing the values shown in Table 1, these were taken as extremes for the equipment design, but that served as the basis for the apparatus’s idealization.

2.2 Design

The machine design was realized taking into account the initial parameters and the fact that the specimen’s design should be the same than the static test. In Fig. 3 it is observed a 3D model of the test machine. In order to guarantee the pull-out at high

Table 1 Velocity calculations and strain rate

Strain rate (s - 1)	l (m)	v (m/s)
1	0.16	0.16
200	0.16	32

velocity using the same type of specimens and a drop weight tower it was necessary to develop a gripping structure for the specimen, as presented in Fig. 3.

The specimens grip is supported by a W157X37.1 standard profile that is welded to a plate with thickness of 10 mm and fixed to the machine base with M20 bolts.

Fig. 3 3D model

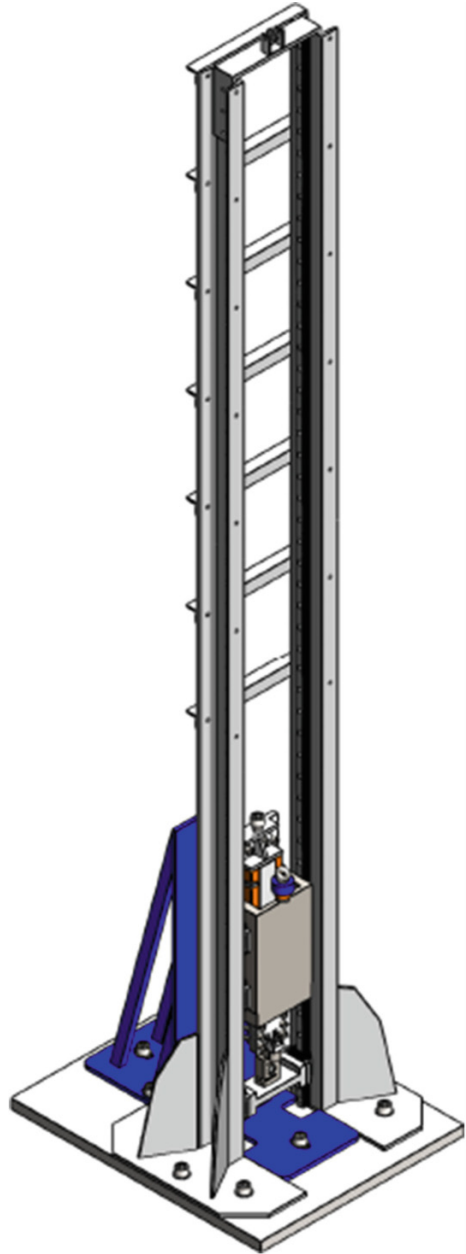
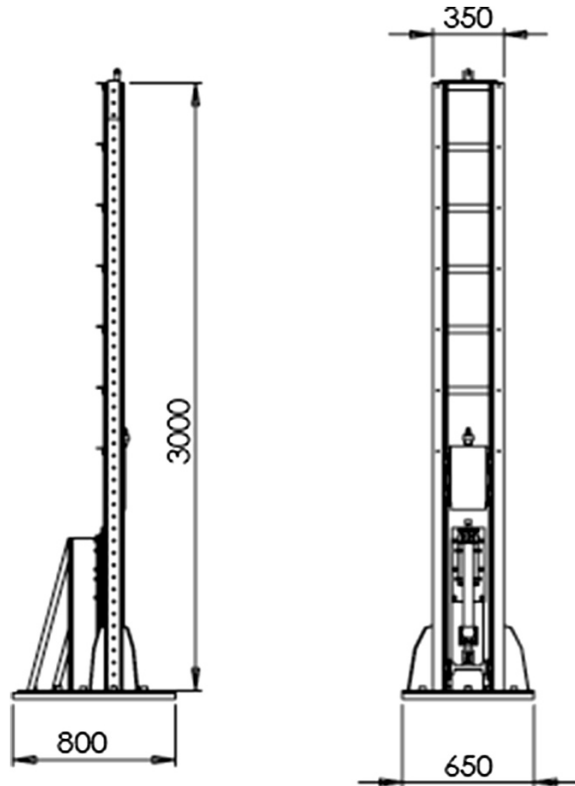


Fig. 4 General machine dimensions (mm)



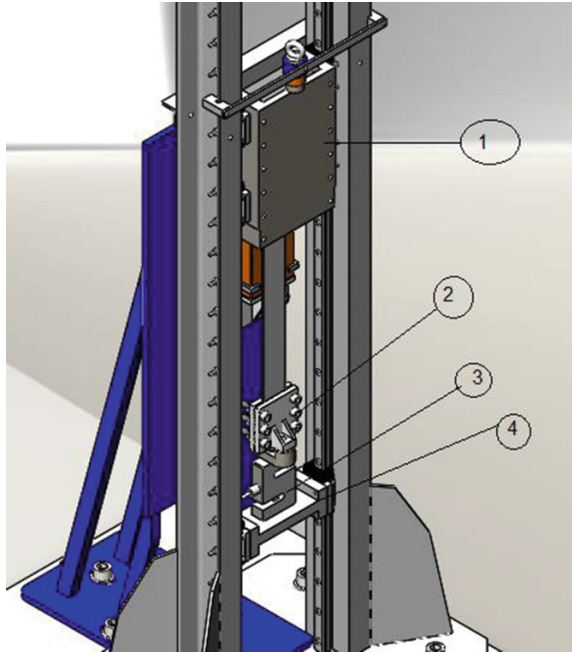
One of the most important aspects in a drop weight tower for impact testing is their stability and non-vibrations capacity. In order to minimize energy losses and vibration the base of the structure should be rigid and adequately fixed at the ground. The base dimensions for the base plate are 800×650 mm with 30 mm of thickness. The material is a Steel S235 JR. Another important aspect is the distance between the impactor guides. This value should be the smallest as possible. In Fig. 4 its dimensions are presented.

The impactor guide lines are a very important part in the equipment. In this case *HIWIN HG25* guide lines were used, supported by a U 150 standard profile, welded at a base and fixed at the machine principal base

Quantitative information as force is measured by a VETEK VZ101BH load cell. This is connected by moorings at the fiber specimen and connected at specially designed part that is intended to support the impact from the impactor.

The impactor (1), observed in Fig. 5, with mass of 15 kg, is dropped, releasing the electroiman from AC MAGNETS, and impacts the transfer component (4). The load cell (3) connects the clamps (2), at the specimen and transmits the load. The impactor design considered in addition the possibility to further increase the drop mass.

Fig. 5 Details from impact system and force measurement



3 Apparatus Assembly and Installation

During assembly, care was taken with the parallelism between the guide lines and the correct alignment was taken in account. All parts were welding fixed in the base to avoid warping or at least minimized. In Fig. 6 one such example is observed.

Fig. 6 Welding detail for the column tower reinforcement

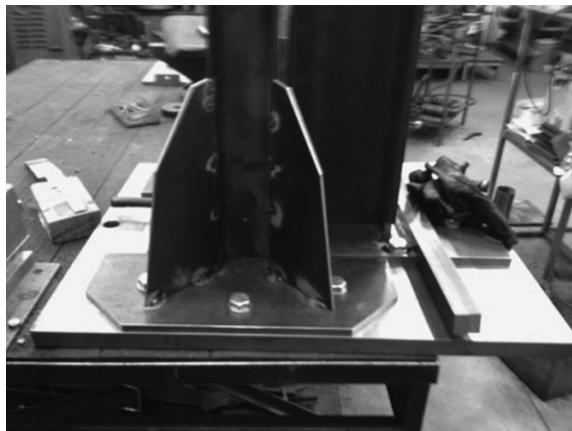


Fig. 7 Machine installation



The installation of the test machine can be observed in Fig. 7. Some preliminary tests were performed allowing to verify that the operating principle is working and that the test specimens are fractured at the selected impact energy.

4 Conclusions

This paper presented the development of a device capable to test dynamically FRP reinforced brick specimens. The equipment design was fulfilling of the initial requisites, being now possible to test the specimens dynamically. Design and construction details of the novel equipment were presented being highlighted its robustness and versatility for different impact energies. In addition the equipment allows for impact testing of different strip reinforcements, within fixture dimensions limits. Preliminary validation tests allowed to verify the capacity for reproducible tests at impact loading with fracture of the bonded connection of the strip-brick specimen. Further validation tests are required for the analysis of load-time readings and comparison with static results.

Acknowledgments The support of FCT project PTDC/ECM/120118/2010: “Redução da vulnerabilidade de edifícios da herança cultural a explosões—CH-SECURE” is acknowledged.

References

1. Oliveira DV, Basilio I, Lourenço PB (2011) Experimental bond behavior of FRP sheets glued on brick masonry. *J Compos Constr* © ASCE/January/February 2011 15:32–41
2. Ghiassi B, Marcari G, Oliveira DV, Lourenço PB (2012) Numerical analysis of bond behavior between masonry bricks and composite materials. *Eng Struct* 43:210–220
3. Grande E, Imbimbo M, Sacco E (2011) Bond behaviour of CFRP laminates glued on clay bricks: experimental and numerical study. *Composites: Part B* 42:330–340
4. Mazzotti C, Savoia M, Ferracuti B (2009) A new single-shear set-up for stable debonding of FRP-concrete joints. *Constr Build Mater* 23:1529–1537

Part V
Mechanics of Robots

Design of a Driving Module for a Hybrid Locomotion Robot

J.J. Castillo, J.A. Cabrera, M. Jaimez, F. Vidal and A. Simón

Abstract One of the challenges in today's mobile robotics is the design of high mobility and maneuverability robots. In this work we present the design and construction of a new concept of a locomotion system for mobile robots. It consists of a hybrid leg-wheel module that can be attached to the main body of a robot in a similar way to a conventional wheel. The mechanical configuration of the driving module is described, emphasizing the characteristics which make it different from other hybrid locomotion systems. A dynamic model that simulates the movement of the module was developed to analyze its behavior and to test different control algorithms that were subsequently implemented on the real module. Finally, we have carried out a series of simple experiments that demonstrate the correct operation of the module on flat ground without obstacles.

Keywords Hybrid locomotion · Robotics · Mechanical design · Dynamic model · Control

J.J. Castillo (✉) · J.A. Cabrera · M. Jaimez · F. Vidal · A. Simón
University of Málaga, Málaga, Spain
e-mail: juancas@uma.es

J.A. Cabrera
e-mail: jcabrera@uma.es

M. Jaimez
e-mail: mjaimezt_mjt@hotmail.com

F. Vidal
e-mail: fvidal@uma.es

A. Simón
e-mail: mata@uma.es

1 Introduction

The amount of terrains or surfaces on which a robot can operate is very high, especially in reconnaissance, exploration and rescue. Nowadays there is not a dominant solution, but rather a wide range of geometric configurations and locomotion systems that solve the mobility demands for specific environments [3, 9, 10]. Originally wheel locomotion systems were used because they had great advantages over other configurations, such as high energy efficiency and high speeds. However, its ability to move over uneven terrains or areas with a high density of obstacles is very limited [13]. As an alternative, robots with legs or “feet” that try to emulate the mechanics of animal movement arose. Its ability to overcome obstacles or operate in heterogeneous environments is clearly superior but they require greater mechanical complexity and a greater number of actuators, its energy efficiency being lower.

The third traditional solution is tracked robots. These robots use continuous or caterpillar tracks instead of wheels. They move reasonably well on rough or compact terrains. Among its disadvantages, we could indicate that its energy consumption is high and that they can only overcome obstacles not bigger than the height of their chains.

Recently, other configurations that cannot be included in any of the categories above are emerging. One of these new approaches is spherical robots for example [6]. However, most new mechanical configurations are hybrid solutions that mix some of the main characteristics of the previously mentioned locomotion systems. One of the most common hybrid configurations is the one in which wheels are placed at the ends of movable articulations or mechanisms [1, 12, 14]. Other solutions include mechanisms which allow robot limbs to be reconfigured. Therefore, they can take the form of wheels or leg as required, resulting in a wide range of movement patterns [7, 8, 11]. Some hybrid locomotion systems for robots make use of rolling elements similar to wheels but with very different geometries [4, 5].

In this paper, we describe a new traction module for a hybrid locomotive system in which the movement of the robot is achieved by varying the length of the supporting legs. Section 2 is focused on the mechanical design of the module. Electrical and electronic drive and control elements are detailed in Sect. 3. The fourth section is dedicated to describe the model of the hybrid module. Experimental results are included in Sect. 5. Finally, conclusions are summarized in Sect. 6.

2 Mechanical Design

The new driving module that has been developed arises from the study of the advantages and disadvantages of a hybrid system described as “pseudo-spherical” with adjustable foot length [2]. Thanks to its geometry, this robot has the ability to

move over almost any terrain. Its speed would only be limited by the speed of its actuators and the efficiency of the programmed dynamic control. However, several drawbacks appear that make it difficult to implement and build a real robot based on this configuration. Some of them are that it needs an actuator for each movable foot, a very difficult dynamic control, the complexity of the design of the central part of the robot and there is not a fixed or, at least, stable orientation part of the robot where sensors such as cameras, lasers, ... could be attached. Ichikawa and his co-workers [5] have developed a robot known as ‘IMPASS’. It consists of modules which incorporate sliding legs. Its main drawback is that it needs a heavy robot body to move, since the rotation of the legs is produced with a motor placed in the robot body.

In the new design we changed to a cylindrical geometry instead of a spherical one. Thus, the feet move in a direction perpendicular to the axis of the cylinder and are placed successively along it to be non-coplanar. This structure is not a robot itself, but a driving module that can be attached to a robotic body with a shaft. The advantages of this design compared to the spherical geometry are the reduction in the number of actuators, simplicity in design, easier controllability and the possibility of attaching it to a robotic body where other devices could be installed, such as: batteries, cameras, lasers, etc. In Fig. 1, examples of robotic structures that may use this module are shown.

The CAD model of the developed module and a photograph of the manufactured module can be seen in Fig. 2. The central part of the module is composed of two aluminum plates connected by thermoplastic blocks at their periphery. The Motors and all the mechanical transmission elements are placed in the space between both plates (Fig. 3). Motion is transmitted to the rack engraved in the leg with gears.

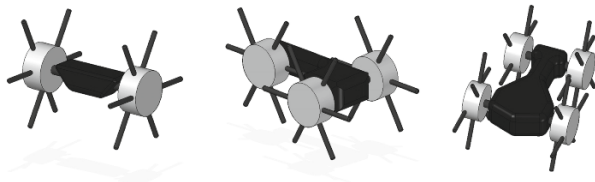


Fig. 1 Different robot configurations with sliding legs modules

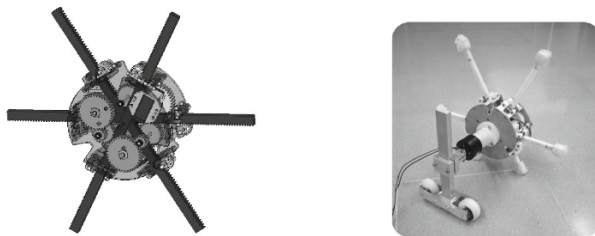


Fig. 2 CAD view of the driving module. Module photograph

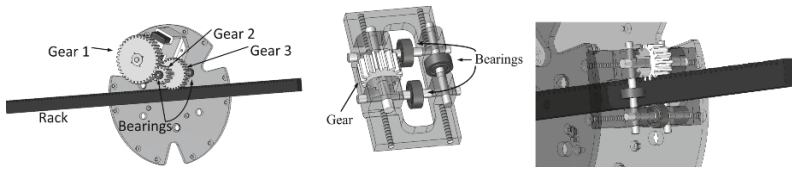


Fig. 3 Parts designed to allow the movement of the rack

Parts have been designed to allow the movement of the legs inside the module. They are composed of 3 bearings and a gear to facilitate the movement of the rack on its 4 sides (Fig. 3). These pieces are also used to connect the two metal plates. Thus, these parts not only fulfill a structural function but also serve to guide the racks. One of the plates incorporates a shaft to join the module with the robot body. This shaft neither interferes with the relative rotation of the module nor transmits motion from the module to the robot. It includes a sensor to measure the angular rotation of the module.

3 Electronics and Sensing

In this section, the electronic components as well as the sensors installed on the module are described. The robot has three servomotors which have a maximum torque of 1.6 N·m and a maximum speed of 5.82 rad/s. The motor speeds are regulated using PWM signals. There are six contact sensors (one sensor at each extreme of the legs) to detect whether the corresponding leg is contacting the ground or an obstacle or not. For this purpose, a graphite-based sensor, specifically designed for this application, has been employed. It consists of a sensing surface which is covered with a small piece of fabric. The resistance of the sensor is normally very high but decreases to about 900 Ω when the leg contacts an object or the ground.

As a necessary tool for the kinematic control of the module, an angular sensor is used to measure the angle between the main body of the robot and the module. Finally, all the components are powered with an external battery. A slip ring allows the transmission of power from the stationary shaft to the rotating structure. The control of the robot is carried out using an Arduino Uno Board. The Arduino Uno Board is also used to acquire the data from the sensors installed on the module. The programming of the module was carried out using the software provided by Arduino. Besides this, we have created a program in LabVIEW™ that communicates with the Arduino and that also serves as an interface with the user.

4 Module Modeling

The equations which model module behavior, together with some 2-D simulations are included in this section. The model was made with SimMechanics™, which is a toolbox by Matlab®/Simulink® that provides a multibody simulation environment for 3D mechanical systems. The forward and vertical movements have been modelled, assuming that the robot is moving on a level, flat and smooth surface.

Three elements are essential when modeling the behavior of the robot: the servomotors, the contact with the surface and legs movement. The first main components are the servomotors. The force exerted by the servomotors on the leg has been modeled as a function of the maximum torque of the motors, the supply voltage and the position error of the foot. Thus, the power supplied is linear with the position error of the leg until the error reaches its critical value. Beyond this point the power is saturated at its maximum value.

Ground contact is modeled considering friction and ground deformation. An elastic constant, to reproduce surface elasticity, and a dissipation constant, which multiplies the ‘penetration’ rate of the leg on the ground in the vertical direction to take into account the energy loss due to friction or ground deformation, are used.

The position of the ends of the legs is defined by the angular reference of the module and the desired height, (H_{ref}), during operation (Fig. 4).

When one foot is in the contact phase, i.e., when its angular position is between ‘ α ’ and ‘ β ’, the radial position of the leg is given by Eq. (1):

$$r_i^{ref} = \text{sign}(\sin(-\theta_i)) \left(\left| \frac{H_{ref}}{\sin(-\theta_i)} \right| - \frac{l}{2} \right) \tag{1}$$

where r_i^{ref} is the radial position of the ‘i’ leg and ‘l’ is the length of the leg. Sign function and absolute values are used to make this expression valid for both ends of the rack. The movement of the leg when its ends are not in contact with the ground is, in principle, free of any restrictions. A possible solution is to impose a smooth transition between the end of the contact of one leg and the beginning of the contact of the opposite one, which is guaranteed by the following Eq. (2):

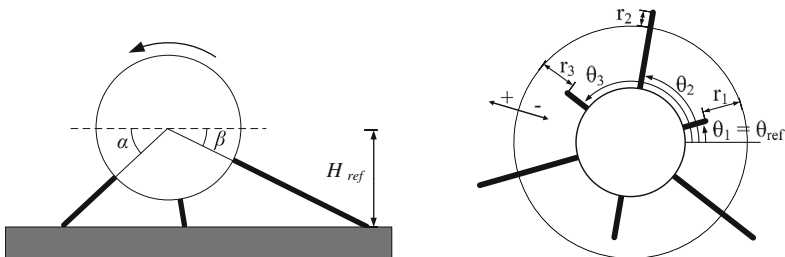


Fig. 4 Geometric parameters related to the control of the feet

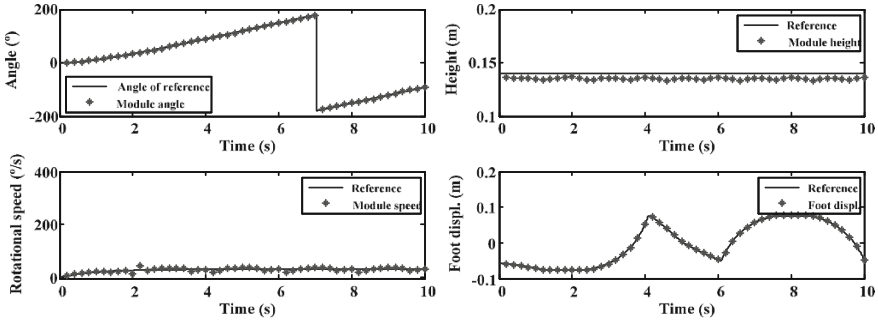


Fig. 5 30°/s Simulation. Angle, height, rotational speed and foot displacement

$$r_i^{ref} = - \left(\left| \frac{H_{ref}}{\sin(\beta)} \right| - \frac{l}{2} \right) \frac{\sin(\theta_i)}{\sin(\beta)} \quad (2)$$

Once the horizontal position is reached, the other end of the rack defines the movement of the leg. During this phase, the foot moves from its equilibrium position toward the position which makes it contact the ground, i.e., when its angle reaches the value ‘ α ’. Leg displacement is described by Eq. (3):

$$r_i^{ref} = - \left(\left| \frac{H_{ref}}{\sin(\alpha)} \right| - \frac{l}{2} \right) \frac{\sin(\theta_i)}{\sin(\alpha)} \quad (3)$$

Finally, Figs. 5 and 6 show results obtained from two simulations. Both tests start with the module in stationary position and with one of its legs in a horizontal position. Then the module is accelerated to reach the desired rotational speed (30 and 90°/s respectively). The discontinuities that can be seen in the top-left plot are due to the fact that the angle values are plotted between -180° and $+180^\circ$.

In both tests the height of the robot is quite close to the reference height. The error in height is not greater than 5 mm at any moment. The differences that appear in the rotational speed occur when the servomotors have to generate high torque

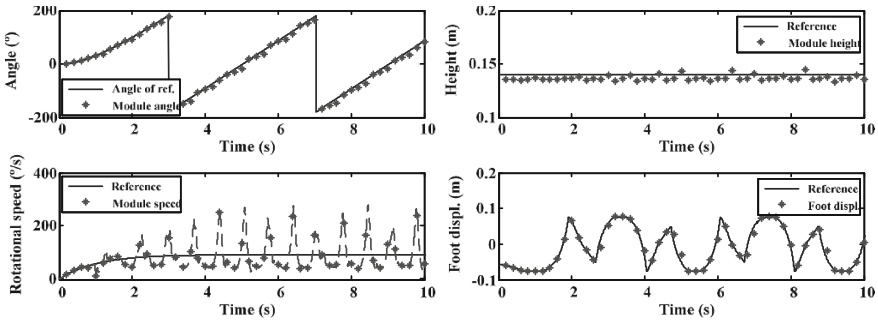


Fig. 6 90°/s Simulation. Angle, height, rotational speed and foot displacement

values. Moreover, the foot displacement matches with the reference quite well. The maximum error at the higher speed ($90^\circ/s$) was below 5 mm. The desired rotational speed is achieved in less than $\frac{1}{4}$ and $\frac{1}{2}$ rotations respectively.

It can be seen that, in general, the module follows the reference although there are peaks in the speed just when one foot passes the vertical position. This phase of the movement is the most delicate stage to perform a continuous movement because is when triple contact occurs, making it difficult to move the three feet symmetrically and homogeneously. In spite of that, the module always follows the angular reference and the movement is smooth.

5 Experimental Results

In this section, experimental results obtained with the real module are detailed. Two tests with the same reference speeds that we used in simulations (30 and $90^\circ/s$) are included. Control parameters are the same as those used in the previous simulations, i.e., $H_{ref} = 0.14$ m, $\alpha = 32^\circ$ and $\beta = 28.5^\circ$. The reference and the measured angular position of the module are included in the upper plots of Fig. 7, while the lower graphs show the angle errors. The initial conditions of the experiments are similar to the ones used in the simulations. We assume that the module starts from a still position, with one of the feet in a horizontal position. The speed increases and decreases progressively at the beginning and at the end of the test.

We can see how the module faithfully follows the reference. The maximum angle errors are smaller than 9° and 20° respectively. The stepped shape of the error function is due to the resolution of the analog input of the Arduino board (10 bits). It can be observed that errors increase with increasing references since the movement of the module becomes sharper and less smooth when moving faster. Finally, we want to remark that the experimental results are very similar to those obtained in simulations, which makes us think that the model, despite its simplifications, accurately reproduces the 2D dynamics of the driving module.

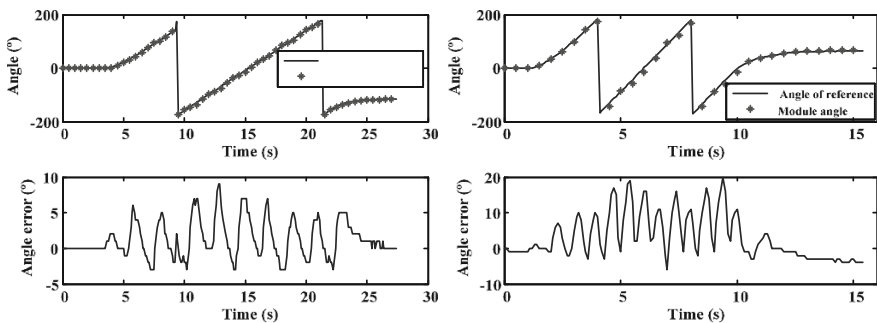


Fig. 7 Experimental tests. $\omega_{ref} = 30^\circ/s$ (left) y $\omega_{ref} = 90^\circ/s$ (right)

6 Conclusion

A new concept of a locomotion system for mobile robots has been proposed, designed and built in this work. We have programmed a dynamic model of the module in SimMechanics™. Simulations show that the model accurately reproduces the movement of the module, being a very useful tool to test different control algorithms that can be implemented on the real robot. A control algorithm has been programmed making use of the results obtained with the model. Finally, we have carried out a series of simple tests that demonstrate the correct operation of the module when moving on a flat, smooth surface without obstacles.

References

1. Adachi H et al (1999) Mechanism and control of a leg-wheel hybrid mobile robot. In: IEEE/RSJ international conference on intelligent robots and systems, vol 3, pp 1792–1997
2. Gheorghie V et al (2008) Design of a rolling robot with telescopic legs able to displace itself on irregular surfaces. *Rom Rev Precis Mech Opt Mechatron* 18(34):139–144
3. Hardarson F (1998) Locomotion for difficult terrain Technical report. Department of Machine Design, Royal Institute of Technology, Stockholm (TRITA-MMK)
4. Hong D, Laney D (2006) Preliminary design and kinematic analysis of a mobility platform with two actuated spoke wheels. In: US Korea conference on science, technology and entrepreneurship
5. Ichikawa Y, Ozaki N, Sadakane K (1983) A hybrid locomotion vehicle for nuclear power plants. *IEEE Trans Syst Man Cybern* 13(6):1089–1093
6. Jaimez M, Castillo JJ, Cabrera JA (2012) Design and modelling of Omnibola©, a spherical mobile robot. *Mech Based Des Struct Mach Int J* 40(4):383–399
7. Rohmer E et al (2008) Action planner of hybrid leg-wheel robots for lunar and planetary exploration. IEEE/RSJ international conference on intelligent robots and systems, pp 3902–3907
8. Schroer RT et al (2004) Comparing cockroach and whegs robot body motions. In: IEEE international conference on robotics and automation, vol 4, 3288–3293
9. Seeni A et al (2008) Robot mobility concepts for extraterrestrial surface exploration. *IEEE Aero-space Conference* pp 1–14
10. Siegwart R, Nourbakhsh IR (2004) Introduction to autonomous mobile robots. The MIT Press, Cambridge
11. Tadakuma K et al (2010) Mechanical design of the wheel-leg hybrid mobile robot to realize a large wheel diameter. In: IEEE/RSJ international conference on intelligent robots and systems, pp 3358–3365
12. Takahashi M, Yoneda K, Hirose S (2006) Rough terrain locomotion of a leg—wheel hybrid quadruped robot. In: IEEE international conference on robotics and automation, pp 1090–1095
13. Wong JY, Huang W (2006) Weels versus tracks—a fundamental evaluation from the traction perspective. *J Terramech* 43(1):27–42
14. Yuk N-S, Kwon D-S (2008) Realization of expressive body motion using leg-wheel mobile robot: Kamero. In: International conference on control, automation and systems, pp 2350–2355

Analysis of Joint Clearance Effects on Dynamics of Six DOF Robot Manipulators

S. Erkaya

Abstract Clearance as a real joint characteristic leads to deviation from desired trajectory in robotic systems. This phenomenon leads to deviations from desired kinematic and dynamic performances of the robots. This study investigates the effects of joint clearance on a robot having six degree-of-freedom (DOF). For the case of different clearance sizes, theoretical analysis is carried out to investigate the kinematic and dynamic characteristics of the robot manipulator with joint clearance. For the case of two different clearance sizes, the results show that the joint clearance causes to degradation in system performance. Even if the clearance size is small, it has an important role on joint forces.

Keywords Joint clearance · Contact force · Robot manipulator

1 Introduction

With the development of the manufacturing technology, robots are used in industrial applications where high accuracy, repeatability and stability of operations are required. Robot systems in welding processes not only improve production efficiency and working condition but also realize welding automation of small-scale production process. An intelligent fuzzy-logic controller for the seam tracking of an arc welding robot having perfect joint, that is, there is no clearance was presented [1]. The designed controller was used to operate in the uncertain environment of weld seam tracking. Also, dynamic modeling, simulation and control of a manipulator with flexible links and perfect joints were investigated [2]. For the case of joint clearance, a methodology for analyzing the location of the discontinuities in a 5R parallel mechanism was presented. In this study, trajectory analysis at different cycle periods proved that how inertial loads can affect the location of the discontinuities.

S. Erkaya (✉)
Erciyes University, Kayseri, Turkey
e-mail: serkaya@erciyes.edu.tr

The singularity analysis and modeling of the effects of the joint clearance for a 3-UPU parallel robot was studied to predict easily the pose error for a given external load, a nominal pose and the structural parameters [3]. The optimal allocation of joint tolerances with consideration of the positional and directional errors of the robot end effector and the manufacturing cost were investigated by using interval analysis [4]. A probability density function was introduced to literature for achieving the desired position repeatability in a robot manipulator with joint clearance [5]. A novel method was presented based on trajectory planning to avoid the detachment of joint elements of a manipulator with clearances [6]. Dynamics of a space robot manipulator with joint clearance were investigated by considering the nonlinear equivalent spring-damper model in joint clearance [7]. Also, the friction effect was considered using the Coulomb friction model. The effects of joint clearances on kinematics and dynamics of planar and spatial mechanisms with rigid and elastic links were studied extensively [8–14]. Different clearance sizes and joint types were analyzed. Dry contact including friction and lubrication effects between journal and bearing parts were considered for a lot of case studies. It was proposed a methodology to quantify the wear phenomenon in clearance joints. In addition to effects of joint clearance on kinematics and dynamics of planar mechanisms, optimum design applications to decrease the undesired effects of clearance were also introduced and studied extensively [15–19].

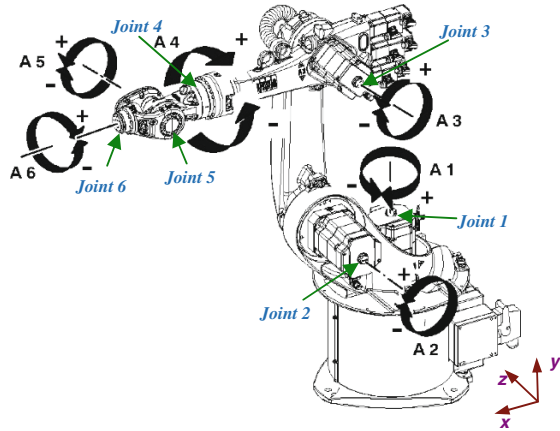
This study investigates the effects of joint clearance on a welding robot manipulator to obtain the exact kinematic and dynamic outputs of the system.

2 Equation of Robot Manipulator Having Joint with Clearance

A six-axis industrial robot was considered for the theoretical analysis. Main applications of this robot are welding, handling, assembly etc. Robot manipulator has six degrees of freedom while all joints are perfect as shown in Fig. 1.

The existence of clearances in the joints of mechanical systems is inevitable due to the assembly, manufacturing errors and wear. A reasonable clearance for the joints at link connections of mechanical system is necessary to allow the relative motion of the connected links. Artificial clearance was constituted to investigate the effects of joint clearance on robot manipulator. Dynamic model of robot manipulator must be constituted considering the joint clearance. Because, joint clearance can cause different motion characteristics in a joint during the robot motion (such as free-flight, impact or continuous contact modes). So, robot manipulator system having joint with clearance is a variable topology system. For the case of free-flight mode phase (no contact between journal and bearing), dynamic equation for the robot manipulator is given as follow,

Fig. 1 Schematic representation of joint motion for robot manipulator



$$\mathbf{M}(q(t)) \ddot{\mathbf{q}}(t) + \mathbf{C}(q(t), \dot{\mathbf{q}}(t)) \dot{\mathbf{q}}(t) + \mathbf{Q}(\dot{\mathbf{q}}(t)) + \mathbf{G}(q(t)) = \mathbf{F}(t) \quad (1)$$

where \mathbf{q} denotes the generalized coordinate column matrix. $\mathbf{M}(q(t))$ is then $n \times n$ symmetric inertia matrix of the robot manipulator. $\mathbf{C}(q(t), \dot{\mathbf{q}}(t))$ represents the $n \times 1$ vector of centrifugal and coriolis terms. $\mathbf{Q}(\dot{\mathbf{q}}(t))$ is the $n \times n$ friction term, which comprises the viscous and dynamic frictions. $\mathbf{G}(q(t))$ denotes the vector of gravity term and $\mathbf{F}(t)$ is the generalized force matrix. In case of impact or continuous contact mode phases, contact force takes places between journal and bearing in the joint. So, dynamic equation is outlined as,

$$\mathbf{M}(q(t)) \ddot{\mathbf{q}}(t) + \mathbf{C}(q(t), \dot{\mathbf{q}}(t)) \dot{\mathbf{q}}(t) + \mathbf{Q}(\dot{\mathbf{q}}(t)) + \mathbf{G}(q(t)) = \mathbf{F}(t) + \mathbf{F}_C(\delta, \dot{\delta}) \quad (2)$$

where $\mathbf{F}_C(\delta, \dot{\delta})$ is the contact force which contains normal and tangential components.

$$\mathbf{F}_C = \mathbf{F}_N + \mathbf{F}_T \quad \text{if } \delta \geq 0 \quad (3)$$

where \mathbf{F}_N and \mathbf{F}_T are normal and tangential force components, respectively. When the journal reaches the bearing wall, that is, the magnitude of the clearance vector is greater than radial clearance, an impact takes place and the penetration depth is given by $\delta = e - c > 0$. e is the magnitude of the clearance vector between the bearing and journal centers, and c is the radial clearance. The magnitude of the clearance vector is expressed as $|e| = (\mathbf{e}_x^2 + \mathbf{e}_y^2)^{1/2}$. \mathbf{e}_x and \mathbf{e}_y represent the relative displacements of the journal inside the bearing for X and Y directions, respectively. These relative displacements can be obtained from the global position vectors of the bearing and journal centers (Fig. 2). Q_i and Q_j denote the contact points on the bearing and journal, respectively. The global position of these points is expressed by

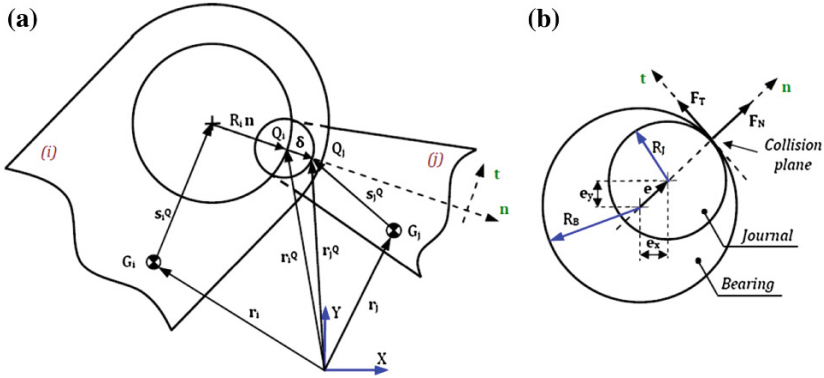


Fig. 2 **a** Representation of a revolute joint with clearance, **b** Normal and tangential forces between the journal and bearing as a result of an impact

$$\mathbf{r}_k^O = \mathbf{r}_k + \mathbf{s}_k^O + R_k \mathbf{n} \quad (k = i, j) \tag{4}$$

where \mathbf{r}_i and \mathbf{r}_j are the global positions of the mass centers for i th and j th bodies, respectively. \mathbf{s}_i^O and \mathbf{s}_j^O denote the positions of the journal and bearing centers relative to the mass centers of i th and j th bodies, respectively. R_i and R_j are the bearing and journal radius, respectively. \mathbf{n} is the unit vector normal to the collision plane and can be defined as $\mathbf{n} = \mathbf{e}/|\mathbf{e}|$.

The velocity of the contact points Q_i and Q_j can be derived by using Eq. (4)

$$\dot{\mathbf{r}}_k^O = \dot{\mathbf{r}}_k + \dot{\mathbf{s}}_k^O + R_k \dot{\mathbf{n}} \quad (k = i, j) \tag{5}$$

Also, the relative contact velocity can be defined as

$$\dot{\delta} = (\dot{\mathbf{r}}_j - \dot{\mathbf{r}}_i) + (\dot{\mathbf{s}}_j^O - \dot{\mathbf{s}}_i^O) + (R_j - R_i) \dot{\mathbf{n}} \tag{6}$$

The normal contact force in collision plane is outlined as

$$\mathbf{F}_N = K\delta^{(3/2)} + D\dot{\delta} \tag{7}$$

where the first term represents the elastic force component and the second term explains the energy dissipation. K is the generalized stiffness parameter, D is the hysteresis damping coefficient. The stiffness parameter K is given by

$$K = \{4/3(h_i + h_j)\} \{R_i R_j / R_i + R_j\}^{1/2} \tag{8}$$

Table 1 Geometric, mass and inertia properties of robot manipulator

Robot arms	Length (mm)	Mass (kg)	Inertia characteristics (kgm ²)		
			J _{xx}	J _{yy}	J _{zz}
Arm 1	680	37.04	1.63	0.16	1.627
Arm 2	402	43.51	0.33	1.41	1.362
Arm 3	268	7.87	1.82×10^{-2}	6.46×10^{-2}	5.89×10^{-2}
Arm 4	115	8.08	2.08×10^{-3}	4.89×10^{-3}	4.85×10^{-3}

where the material parameters h_k are expressed as

$$h_k = (1 - \nu_k^2) / E_k \quad (k = i, j) \tag{9}$$

ν_k and E_k are the Poisson’s coefficient and the Young’s modulus associated with each body, respectively. The hysteresis damping coefficient is given as;

$$D = \left(3(1 - \zeta^2) K \delta^{3/2} \right) / 4v_0 \tag{10}$$

where ζ is the restitution coefficient and v_0 is the initial impact velocity. Friction forces act when contacting bodies tend to slide relative to each other. These forces are tangential to the surfaces of contact and are opposite to the sliding velocity. Friction force model is expressed as

$$\mathbf{F}_T = -\mu_d \mathbf{F}_N \text{sgn}(\mathbf{V}_T) \tag{11}$$

where μ_d is the friction coefficient and \mathbf{V}_T is the sliding velocity. $\text{sgn}(\mathbf{V}_T)$ is the sign function of the relative sliding velocity between contact points. Geometric, mass and inertial characteristics of robot manipulator are outlined in Table 1.

3 Results

In this study, robot manipulator has six degrees of freedom while all joints are realized as perfect. All links in robot manipulator were assumed as rigid. For the case of clearance analysis, joint 5 was considered as imperfect and clearance sizes were adjusted as 0.2 and 0.5 mm. In the case of perfect and imperfect joint approaches, all simulations were performed in a Pentium Core 2 Quad Q6600 computer. Used parameters in dynamic simulation of welding robot manipulator having joint clearance are given in Table 2.

It is obvious from the simulations that much more computation time is necessary in the case of imperfect joint approach. Contact force components in Joint 5 are given in Fig. 3.

Table 2 Simulation parameters of robot manipulator

Description	Value
Friction coefficient	0.03
Restitution coefficient	0.46
Poisson's coefficient	0.33
Young's modulus	71.7 GPa
Integration step size	1×10^{-4} s
Integration tolerance	1×10^{-5}

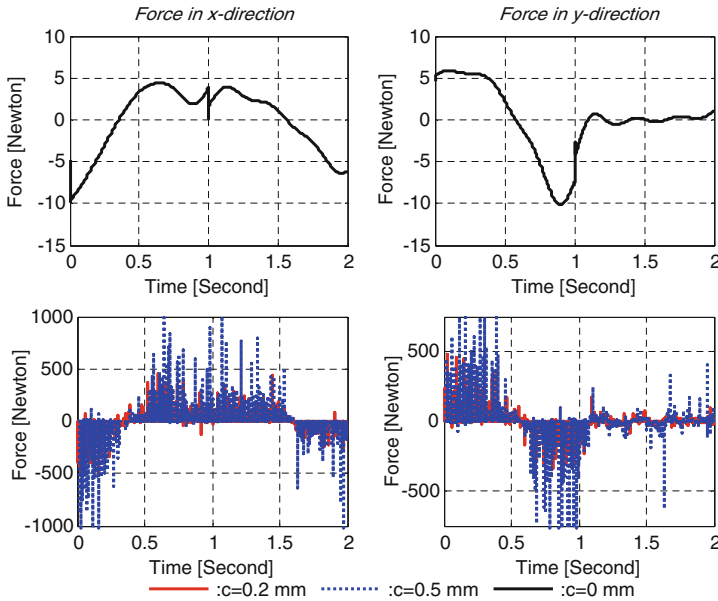


Fig. 3 Force components of Joint 5

As outlined in Fig. 3, the existence of joint clearance causes impulse type contact forces. These forces take place during a small time interval. When the clearance size is increased, there is also an increasing in amplitude of the contact force. This force characteristic not only decreases the performance of welding robot manipulator, but also leads to degradation of its vibration and noise quality. Joint forces of the other arm connections are given in Fig. 4. As seen from this figure, the whole system dynamics is naturally affected from the clearance joint. The impulsive force within the joint with clearance leads to the degradation of the overall system performance. Also, clearance size has an important effect on the system response. Dynamic characteristics of the robot manipulator are obviously different for the case of different clearance sizes. The lower size of clearance leads to small impulsive force having high-frequency character. The bigger size of clearance causes to higher amplitudes of joint forces.

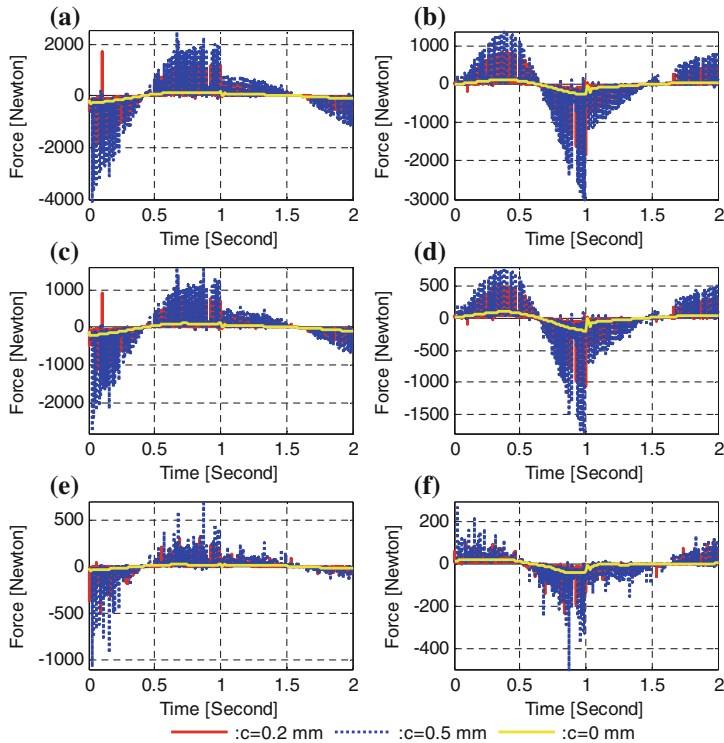


Fig. 4 Force components of 2nd, 3rd and 4th joints: **a** x-direction of Joint 2, **b** y-direction of Joint 2, **c** x-direction of Joint 3, **d** y-direction of Joint 3, **e** x-direction of Joint 4, **f** y-direction of Joint 4

4 Conclusion

The aim of this study was focused on investigation of joint clearance effects on a welding robot manipulator. The robot manipulator has six degrees of freedom while all joints are perfect. In the current study, Joint 5 was considered as imperfect to show the effects of joint clearance on system. The existence of joint clearance has clear effects on system kinematics and causes to impulse type contact force which has high frequency and amplitude. From the evaluation of the proposed results, it is concluded that higher size of joint clearance causes to increases in amplitudes of accelerations and joint forces. Also, lower size of joint clearance leads to higher frequencies at the kinematic and dynamic responses of the system. Discontinuities can appear on the actual trajectory of weld seam due to the different motion types between journal and bearing in a joint with clearance. These phenomena are reasons for degradation of penetration depth and weld seam. Kinematic and dynamic analyses having joint with clearance can be considered as the basis of the motion accuracy analysis of the robot manipulator system even if the clearance size is small.

References

1. Xiangdong G, Yamamoto M, Mohri A (1997) Application of fuzzy logic controller in the seam tracking of arc-welding robot. In: 23rd international conference on industrial electronics, control and instrumentation vol 3, pp 1367–1372
2. Subudhi B, Morris AS (2002) Dynamic modeling, simulation and control of a manipulator with flexible links and joints. *Robot Auton Syst* 41:257–270
3. Chebbi AH, Affi Z, Romdhane L (2009) Prediction of the pose errors produced by joints clearance for a 3-UPU parallel robot. *Mech Mach Theor* 44:1768–1783
4. Wu W, Rao SS (2007) Uncertainty analysis and allocation of joint tolerances in robot manipulators based on interval analysis. *Reliab Eng Syst Saf* 92:54–64
5. Zhu J, Ting KL (2000) Uncertainty analysis of planar and spatial robots with joint clearances. *Mech Mach Theor* 35:1239–1256
6. Bu W, Liu Z, Tan J, Gao S (2010) Detachment avoidance of joint elements of a robotic manipulator with clearances based on trajectory planning. *Mech Mach Theor* 45:925–940
7. Zhao Y, Bai ZF (2011) Dynamics analysis of space robot manipulator with joint clearance. *Acta Astro* 68:1147–1155
8. Flores P, Ambrosio J, Claro HCP, Lankarani HM, Koshy CS (2006) A study on dynamics of mechanical systems including joints with clearance and lubrication. *Mech Mach Theor* 41:247–261
9. Flores P (2009) Modeling and simulation of wear in revolute clearance joints in multibody systems. *Mech Mach Theor* 44:1211–1222
10. Flores P, Ambrosio J, Claro JCP, Lankarani HM (2006) Influence of the contact—impact force model on the dynamic response of multi-body systems. *Proc Inst Mech Eng, Part-K J Multibody Dyn* 220:21–34
11. Tian Q, Liu C, Machado M, Flores P (2011) A new model for dry and lubricated cylindrical joints with clearance in spatial flexible multibody systems. *Nonlinear Dyn* 64:25–47
12. Flores P, Koshy CS, Lankarani NM, Ambrosio J, Claro JCP (2011) Numerical and experimental investigation on multibody systems with revolute clearance joints. *Nonlinear Dyn* 65:383–398
13. Flores P (2010) A parametric study on the dynamic response of planar multibody systems with multiple clearance joints. *Nonlinear Dyn* 61:633–653
14. Flores P, Ambrósio J (2010) On the contact detection for contact-impact analysis in multibody systems. *Multibody SysDyn* 24:103–122
15. Erkaya S, Uzmay I (2008) A neural-genetic (NN-GA) approach for optimising mechanisms having joints with clearance. *Multibody SysDyn* 20:69–83
16. Erkaya S, Uzmay I (2009) Investigation on effect of joint clearance on dynamics of four-bar mechanism. *Nonlinear Dyn* 58:179–198
17. Erkaya S, Uzmay İ (2009) Determining link parameters using genetic algorithm in mechanisms with joint clearance. *Mech Mach Theor* 44:222–234
18. Erkaya S, Uzmay İ (2009) Optimization of transmission angle for slider-crank mechanism with joint clearances. *Struct Multidiscip Optim* 37:493–508
19. Erkaya S, Uzmay İ (2010) Experimental investigation of joint clearance effects on the dynamics of a slider-crank mechanism. *Multibody SysDyn* 24:81–102

Investigating the Effect of Cable Force on Winch Winding Accuracy for Cable-Driven Parallel Robots

Valentin Schmidt, Alexander Mall and Andreas Pott

Abstract This paper focuses on the winch winding properties of typical driving mechanisms of cable-driven parallel robots. While cable properties have already been studied, the accuracy of winding mechanisms to control cable robots and the interaction with cable properties has yet to be investigated. To initiate this, some properties believed to affect the winding accuracy are outlined. It was found that cable force can have a significant effect not only because of finite stiffness, but due to ovalisation and elongation effects of the rope. An experimental test on ovalisation showed significant deviations from a standard approximation to evaluate transmission accuracy. This effect can change the accuracy of winding mechanisms by 0.3–1.2 %. Thus when investigating cable-robot accuracy the winch winding properties cannot be ignored.

Keywords Cable-driven parallel robots · Winch · Winding properties · Ovalisation

1 Introduction

Cable-driven parallel robots are a subclass of robots where a platform is positioned through the active control of cable lengths. These robots were introduced around 30 years ago [1], and have been subject to research throughout these years. Several prototypes have been developed [7, 8] mainly for research use.

One critical aspect for this type of robot is the accuracy of such a system. Many factors have been already investigated, from the geometrical influence of pulley

V. Schmidt (✉) · A. Mall · A. Pott
Fraunhofer IPA, Stuttgart, Germany
e-mail: valentin.schmidt@ipa.Fraunhofer.de

A. Mall
e-mail: alexander.mall@ipa.Fraunhofer.de

A. Pott
e-mail: andreas.pott@ipa.Fraunhofer.de

systems [10] to cable mass and elongation [9]. It was observed that many of the factors affecting the accuracy are actually within equal orders of magnitude, thus making the isolation and elimination of inaccuracies challenging. In this paper we will discuss a further impact on the accuracy of the robot which is the accuracy of the drive system itself.

Understanding the winch winding accuracy is important as this gives us the relationship between the drum angle and the cable length. In many cases cable robots operate without any additional sensor to estimate the pose. This pose is simply calculated from the cable lengths, which in turn are estimated through the drive train. Since many motors already include very accurate position monitoring this is a sensible choice. However, it is crucial to know the transmission behavior of the winch as the cable length (and therefore position) is measured indirectly in the motor encoder.

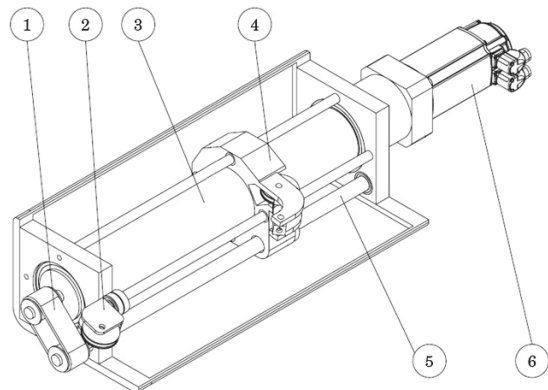
The winch winding mechanism was already investigated by Merlet [5], who found that linear actuators (effectively an active block and tackle) had good accuracy results, especially over the traditional multi-winding winch. In this paper the focus is on a single-winding winch which also has high accuracy due to precise control over the cable placement on the drum.

The mechanism to achieve single-winding under scrutiny for this analysis is the winch concept shown in Fig. 1. This concept was produced into a series of winches for cable robot applications at the Fraunhofer IPA which will be referred to as the IPAnema winch [8]. Here a spoolguide ensures that the cable is precisely placed in a helical groove on the drum. This leads to a more complicated winch design, but aids in reducing the cable-wear and increases the accuracy of winding.

2 Properties Affecting Winding Accuracy

The factors which affect the winding accuracy are not limited to this type of winch. In fact even linearly actuated winches are affected by all of these characteristics despite having a radically different design. Unfortunately some of these factors will have interdependencies which go beyond the scope of this paper.

Fig. 1 Single winding winch concept: 1 spoolguide transmission, 2 final pulley, 3 drum, 4 spoolguide, 5 spindle, 6 servo motor



While all of these physical phenomena are relevant only an estimate can be made on their final impact on winding accuracy when winding under different cable tension forces.

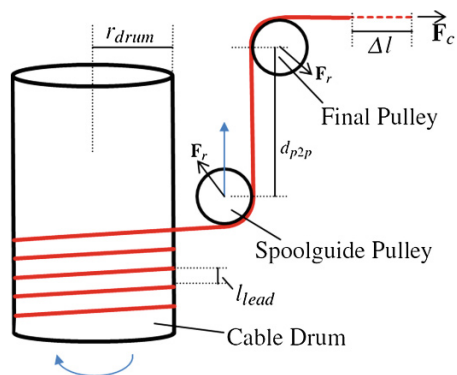
2.1 Physical Winch Properties

Manufacturing accuracy is an evident factor affecting the positioning accuracy of the cable winch as a whole. These can take very many forms. For the example winch with single winding, this would be the helix formed by the groove in the drum, the positioning of the pulleys in the spoolguide and the final pulley, poor transmission ratios for the spoolguide and many more. Due to modern manufacturing techniques these are regarded as having very little impact. For example using simple geometry we can discern that a positioning inaccuracy of the spoolguide pulley of 0.1 mm has very little effect <0.1 mm on the absolute length, as the cable spans a much longer distance (even internally in the winch) than any mechanical error we can expect. This is relevant for any finite stiffness in the winch system, which will then be affected by the change in cable tensions. The cable force causes resultant forces as depicted in the schematic diagram of Fig. 2 as F_r on the pulleys and also on the drum and peripheral winch components. However these inaccuracies are in the same order of magnitude as manufacturing inaccuracies. In the case of the IPAnema winch these can be neglected.

2.2 Drive Train Accuracy

Motor accuracy can have a significant impact. In this case there is a finite accuracy on the rotation angle of the motor. Clearly this also exists for linear motors. Depending on the type of motor this accuracy can be chosen very deliberately. In

Fig. 2 Schematic diagram of IPAnema winch cable leading



the case of the IPAnema winch the motor accuracy is extremely high due to the use of servomotors. The system accuracy of these as stated by the manufacturer is ± 20 angular seconds¹ [2] which is equivalent to $\pm 97.0 \times 10^{-6}$ radians. Positional accuracy is further increased through a gear ratio of $i = 12$. Thus for the experimental setup this factor will be ignored as these are in a similar order of magnitude as the manufacturing inaccuracies.

It can be seen on Fig. 2 that the length change of the spoolguide d_{p2p} will cause an additional linear length change as it ensures straight unwinding moving with the lead rise of the helix on the drum l_{lead} . This distance is adjusted by transmission ratio T_{spl} whose sign depends on whether the final pulley in Fig. 2 is positioned on the top or bottom. Thus we can approximate relationship of motor angle $\Delta\theta$ in radians to cable length change Δl from

$$\Delta l = \left(\sqrt{\left(r_{drum} + \frac{d}{2} \right)^2 + \left(\frac{l_{lead}}{2\pi} \right)^2} + T_{spl} \right) T_M \Delta\theta \quad (1)$$

to the linear function

$$\Delta l = \left(r_{drum} + \frac{d}{2} + T_{spl} \right) T_M \Delta\theta \quad (2)$$

where d is the cable diameter and T_M is the transmission ratio from motor to drum.

Using a quick estimate for the IPAnema winch the motor accuracy causes an uncertainty in the final cable length of $\pm 4 \times 10^{-4}$ mm.

2.3 Rope Ovalisation

One phenomena which is characteristic of plastic fibre ropes is ovalisation. Ovalisation is essentially a yielding of the cable shape under increasing tensions resulting in a closer fit of the cable against the drum/pulley surface as depicted in Fig. 3. Feyrer [3] discusses this in detail for wire ropes, but it is more pronounced in plastic fibre ropes. An investigation by Michael and Vogel [6] into the ovalisation of plastic fibre ropes, where the ovalisation was measured using a laser scanner showed over 10 % decrease in diameter of the cable at cable forces of perhaps one tenth of the breaking strength. Results show a mostly linear relationship between tension and resulting ovalisation, but this only applies for the tension range investigated as ultimately the radius will not reduce below a minimum threshold. Simply put the ovalisation will cause less cable to be wound on the drum than a simple consideration of drum circumference would predict.

¹ Bosch Rexroth: MSK 050B-0600-NN-M2-UG1-RNNN.

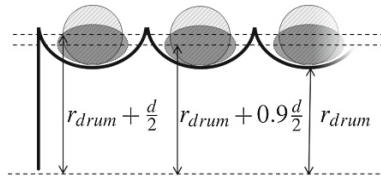


Fig. 3 Rope ovalisation on winch drum

Naturally there are many factors which effect this ovalisation. The shape of the groove plays an important role, as does the type of material used. It is also closely coupled with the natural thinning of the cable under tension, but adds an additional effect. For the measured ovalisation in [6] ultra high density polyethylene fibres were used, which is also the type used on the IPAnema winch. This enables a simple prediction of lack of winding for the IPAnema winch at on tenth of the breaking strength with the following assumptions: a drum radius r_{drum} of 47 mm and a cable diameter d of 6 mm.

As we neglect mechanical errors for a motor rotation 490.1705 radian as used in the experiments discussed in Sect. 3. The transmission ratio T_M as before and a T_{spl} of $-\frac{7}{2\pi}$. Resulting in a cable length change of 1,997.2 mm. Assuming a 10 % change in the effective radius as measured by [6] and depicted in Fig. 3, with the same assumptions the change is 1,985.0 mm. Constituting to a 0.6 % change. Depending on the ratio of diameter of the cable to the radius of the drum this results in a length difference of about 0.3–1.3 % (if we assume the recommended bending radii for fibre ropes are maintained). This is considerable as it constitutes to several millimeters per meter of wound rope, and with long distances the absolute error will increase.

There is of course a limit to the ovalisation factor which can be assumed to be asymptotic. The length can never go below an effective cable diameter of zero. For the IPAnema winch this would constitute a length change of roughly six percent (3/50). This is evidently not realistic, but a benchmark figure.

2.4 Rope Elongation During Winch Winding

Another effect that has been observed during the operation of the winch is that tension niveaus by which cable was wound onto the drum will remain on the drum until the cable is unwound again. Cable elasticity in cable robots has been analyzed [4], but not the effect on the winch winding. This can be described through a short thought experiment: If there was no friction between the drum, and the cable exhibited no creep, then any force exerted on the cable should elongate the cable along the entire drum. This does not happen, instead friction between the drum and cable increases with the angle upon which the cable is wrapped around the drum according to the famous capstan equation

$$\mathbf{F}_l = \mathbf{F}_h e^{\mu * \alpha}. \quad (3)$$

Here the holding force \mathbf{F}_h required to counter a loading tension in the cable \mathbf{F}_l is significantly lower by friction μ and the angle α . The question is when a loading force is being used to wind up a drum, and then the cable is released of this force: how much of the cable reverts to its unstretched state.

An experiment to test for this phenomenon would be to wind an elongated cable under tension onto a drum and measure the resultant contraction after the cable has been removed. If the contraction is similar to that of a free hanging cable of the same length then all effects on cable are modeled through the capstan equation. Elongation during winding would still have an effect on the accuracy and that would be a gradual increase in winding space as segments of the cable which experience less tension [due to Eq. (3)] would gradually pull back cable that has been wound onto the drum. However, observation of the operating winches of cable robots suggests that this is not the case.

2.5 Uneven Helix

Another effect which force can have on the an inaccuracy in the l_{lead} of Eq. (1). This can be caused by uneven settling of the rope on the drum. In the case of the IPAnema winch, there are grooves in order to guide the cable on the drum, but even these will not stop minute settling of the cable to form an uneven helix. It is more significant for cable drums without grooves which can be practical depending on the situation. While this factor may seem only appropriate for drum based winches, also linear winches can suffer from this effect. Here it would not be a helix, but individual pulleys on a linear winch will not be perfectly aligned between the two blocks creating a gradient which will result in a slightly different length error. Here too the effect of this error is very small compared with other effects such as ovalisation.

3 Experimental Results

In order to evaluate the ovalisation factors a small experiment was conducted. Here the IPAnema winch was used to hoist a series of weights. These weights kept the cable under tension by exerting a constant cable force \mathbf{F}_c . A 6 mm diameter ultra high density polyethylene fibre cable was used for this investigation. This has a breaking strength of 43,000 N. The distance was measured using a laser range meter.

When conducting the experiment several precautions were taken. In order to mitigate any lasting by factors such as creep and hysteresis effects the order of weights was randomized. The distance traveled for each weight was recorded

within a constant settling time interval. In order to maintain a constant cable force, accelerations were kept to a minimum and slow smooth motion was initiated. Since distance traveled was measured as relative points and the cable force was kept constant effects of elongation can be ignored.

Figure 4 shows the results of an experiment done on the ovalisation. The least squares fit was also plotted for reference, as discussed in the Sect. 2.3 the nature of the relationship has to be asymptotic. These results show a significant deviation from the expected especially in the initial winding capacity even at lower cable forces. Instead of the $\approx 1,990$ mm as in Eqs. (1) and (2) the winch only wound cable from 1,993–2,007 mm. One reason for this difference could be the elongated winding which was discussed previously.

The effect of ovalisation is in the same order of magnitude, whether you use Eq. (1) or Eq. (2). In fact the error due to ovalisation is much greater than the error obtained by the approximation, which is also an indicator that ovalisation has more of an effect than an uneven helix.

However, the results clearly show that there is an effect on winding capacity of a drum affecting accuracy. Indeed the order of magnitude by which it is affected is comparable to that of pulleys on cable robots [10], and of the cable elongation. However, instead of the predicted 0.6 % length difference at one tenth of the breaking strength, occurred already at somewhere close to 900 N instead, almost one fiftieth.

Further experiments using a block and pulley system to elongate the distance traveled by the cable gave less clear results. The tendency to wind less cable with increasing force was still observable, but the introduction of further points of contact on the pulleys over which the cable will also show ovalisation and increased friction rendered the results incompatible with those gained by the simple experiment.

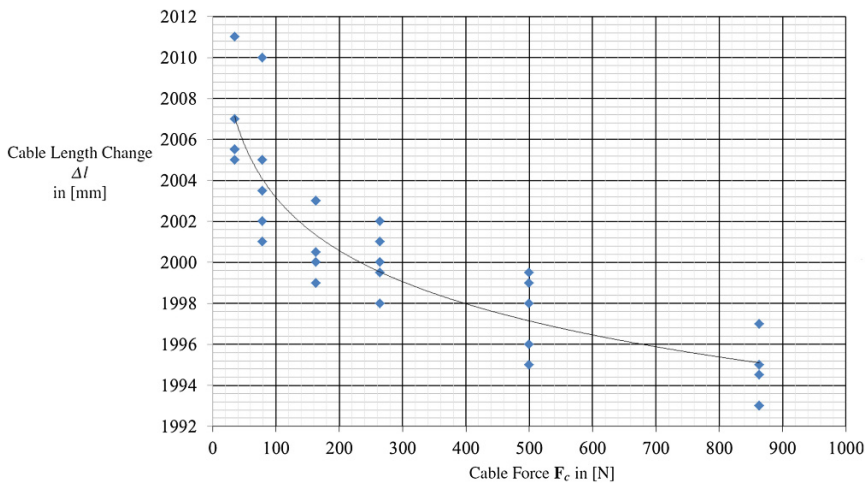


Fig. 4 Experimental results on ovalisation

4 Conclusions

An overview of different factors affecting the accuracy of the winches of cable-driven parallel robots has been given. Next to mechanical factors of the winch construction, ovalisation has been introduced. This phenomenon has been shown previously, but not in the context of winding accuracy of drum driven winches. Mechanical inaccuracies in the winch system and of the motor drive play an insignificant role when compared to the mechanical properties of the cable and the interaction in the winding process.

It was found that the ovalisation of the cable is a significant factor, but measured ovalisation does explain the complete difference in wound cable lengths. This was investigated by comparing results from ovalisation measurements to the winch winding properties under different forces.

This very clearly also shows the difficulty achieving high accuracy with cable robot systems. There are many factors which change the effective cable length under different conditions. The cable itself exhibits significant deformations under stresses of forces and temperature which are exacerbated by the winding mechanism. These effects also play part in wire ropes but are perhaps more significant in fibre ropes as here the elasticity and ovalisation are significantly higher.

It is necessary to further study the winch winding properties. The effect of elongation has yet to be validated experimentally and analyzed numerically to give a prediction on cable length.

Acknowledgments This work was supported by the FhG Internal Programs under Grant No. WISA 823 244.

References

1. Albus JS, Bostelman RV, Dagalakis NG (1992) The NIST ROBOCRANE. *J Res Nat Inst Stand Technol* 373–385
2. Bosch Rexroth AG (2006) Rexroth IndraDyn S Projekt Planning Manual: MSK Synchronous Motors, 5th edn. R91196289
3. Feyrer K (2007) Wire ropes: tension, endurance, reliability. Springer, ISBN 978-3-540-33831-4
4. Merlet JP (2009) Analysis of wire elasticity for wire-driven parallel robots. In: *Proceedings of EUROMES 08*, Springer, Netherlands, pp 471–478
5. Merlet JP (2013) Comparison of actuation schemes for wire-driven parallel robots. In: *New trends in mechanism and machine science*. Springer, Netherlands, pp 245–254
6. Michael M, Vogel W (2010) Ovalisierung von hochfesten Faserseilen in Rundrillen. In: *Z. Euroseil*, pp 57–59
7. Ottaviano E, Ceccarelli M, Paone A, Carbone G (2005) A low-cost easy operation 4-cable driven parallel manipulator. In: *Proceedings of the 2005 IEEE international conference on robotics and automation ICRA*, pp 4008–4013
8. Pott A et al (2012) IPAnema a family of cable-driven parallel robots for industrial applications. In: *Cable driven parallel robots*, Springer, pp 119–134

9. Riehl N, Gouttefarde M, Krut S, Baradat C, Pierrot F (2009) Effects of non-negligible cable mass on the static behavior of large workspace cable-driven parallel mechanisms. In: Proceedings of IEEE international conference on robotics and automation, Kobe, Japan, pp 2193–2198
10. Schmidt V, Pott A (2012) Implementing extended kinematics of a cable-driven parallel robot in real-time. In: Cable driven parallel robots, Springer, pp 287–298

Solving the Dynamic Equations of a 3-PRS Parallel Manipulator

M. Díaz-Rodríguez, R. Bautista-Quintero and J.A. Carretero

Abstract This paper presents and compares three approaches for solving the inverse dynamic model of a general 3-*PR*S parallel manipulator. The first method obtains the inverse dynamic model by describing the manipulator as three open kinematic chains. Then, the vector-loop closure constraints introduce the relationship between the dynamics of the open kinematic chains and the original closed loop chains. The second method exploits the characteristic of parallel manipulators such that the platform and the links are considered as subsystems. The third method is similar to the second method but uses a different formulation of the Jacobian matrix. This work provides some insight on some advantages and/or disadvantages on how to formulate the dynamic model of a lower mobility parallel manipulator, which can be considered in topic such as the optimal design, parameter identification, and model-based control.

Keywords Limited-DOF parallel manipulator · Inverse dynamics analysis · Jacobian formulation

M. Díaz-Rodríguez (✉)
Universidad de Los Andes, Mérida, Venezuela
e-mail: dmiguel@ula.ve

R. Bautista-Quintero
Instituto Tecnológico de Culiacán, Culiacán, Mexico
e-mail: rbautista@itculiacan.edu.mx

J.A. Carretero
University of New Brunswick, Fredericton, Canada
e-mail: juan.carretero@unb.ca

1 Introduction

Seminal research in Parallel Manipulators (PMs) described architectures of 6 Degrees of Freedom (DOF) in order to accomplish common industrial tasks. On the other hand, not all the applications require 6-DOF capabilities, thus, cost-effective PMs with less than 6 DOF (i.e., lower-mobility) have been proposed. One such architecture is the 3-PRS manipulator which has a platform and a fixed base connected through three identical set of links and joints (i.e., legs). Each leg has an actuated slider attached to the base by a prismatic joint (P), a coupler connected to the slider by a passive rotational joint (R) and to the platform by a passive spherical joint (S). The 3-PRS manipulator was first described in [3] for a telescope application, and then proposed as a machining centre [4] and for a medical application in [10]. The kinematics and workspace analysis of the manipulator have been extensively studied in [2, 3, 7, 12], to name a few. On the other hand, despite the fact that inverse dynamic modelling is essential for optimal design, parameter identification, and model-based control, few papers have focused on the dynamics modelling of the 3-PRS configuration.

Lagrangian formulations allowed to develop the inverse dynamics model of the 3-PRS manipulator [6]. The formulation uses the Lagrange multiplier to include the constraints forces that lead to a modelling approach not only intricate but also computationally complex. Li et al. [6] applied the Principle of Virtual Work (PVW), but they simplify the dynamics of the coupler link by dividing its mass into two portions located at its extremes. Tsai et al. [13] compute the inverse dynamic model along with the reaction forces through a special decomposition of the reaction forces at the joints that connect the leg with the platform. Reaction forces may be needed for structural design of a manipulator but its computation increases computational complexity which is unnecessary for parameter identification or model-based control. Staicu [11] analyzes and compares the power consumption of the 3-PRS vs. the 3-RPS configuration using the PVW with recursive modelling. The method obtains the Jacobian by differentiating the vector loop equation. Mata et al. [9] implement recursive velocity equations used in serial manipulator analysis to find the Jacobian for a 3-RPS manipulator.

This paper compares the computational number of operation of three formulations for inverse dynamic modelling of a 3-PRS. The first formulation applies the general solution of PMs dynamic modelling proposed in [5]. The second method considers the manipulator as a set of open kinematic chains and finds the Jacobian in joint space coordinates by taking into account the vector loop constraints at the split joints [9]. The third method relies on the modelling approach originally presented in [6]. Finally, the paper summarizes the complexity and the computational load of these three formulations.

Of particular interest in this paper are a comparison including advantages and disadvantages in the formulation of the dynamic model for low-mobility PMs which has not be performed to this date.

2 Development of the Dynamic Models

2.1 Dynamics Considering the Legs and Platform as Subsystems

The dynamic model of a 3-PRS can be obtained by splitting apart the manipulator at the spherical joints so that the moving platform is separated from the legs. The local joint coordinates systems \mathbf{q} can be used to develop the dynamic equations of each leg \mathbf{h}_i and the Cartesian coordinates \mathbf{x} for obtaining the dynamic equations of the platform \mathbf{f}_p . Then, the dynamic equations are combined and projected onto the active joint space as in [5]:

$$\boldsymbol{\tau} = \mathbf{J}_p^T \mathbf{f}_p + \sum_{i=1}^m \left(\frac{\delta \dot{q}_i}{\delta \dot{q}_a} \right)^T \mathbf{h}_i \quad (1)$$

where \mathbf{J}_p is the Jacobian projecting the task space coordinates (6 in the general case) to the n active joint coordinates while m is the number of joints for each leg. To develop the model in actuated joint space one has to project the passive joint variables to the active ones. That is:

$$\boldsymbol{\tau} = \mathbf{h}_i^a + \mathbf{J}_p^T \mathbf{f}_p + \mathbf{G}_I^T \mathbf{h}_i^p \quad (2)$$

where indices a and p stand for the active and passive joints, respectively, while \mathbf{G}_I is a $l \times n$ matrix mapping the dynamics from the passive to the active joints. Here, l represents the number of passive joint variables.

In Eq. (2), matrix \mathbf{G}_I can be obtained by considering the fact that the distance among adjacent joints at the platform is a constant length (due to the rigid body assumption). This length is calculated based on the norm of the vector obtained by subtracting the position of the adjacent joints. The partial derivatives of each equation with respect to the joints coordinates yields matrix \mathbf{G}_I .

Another approach to formulate the dynamic model is based on [5]. The method is based on mapping the dynamics equation of the passive joint onto the task space, and then, map them back to the active joint space so that:

$$\boldsymbol{\tau} = \mathbf{h}_i^a + \mathbf{J}_p^T [\mathbf{f}_p + \mathbf{G}_{II}^T \mathbf{h}_i^p] \quad (3)$$

where \mathbf{G}_{II} is a $l \times 6$ matrix that holds new definition that can be written as follow:

$$\mathbf{G}_{II}^T = \mathbf{J}_{v_i}^T \mathbf{J}_{q_i}^{-T} \quad (4)$$

where \mathbf{J}_{v_i} and $\mathbf{J}_{q_i}^{-T}$ can be obtained respectively from the direct Jacobian \mathbf{J}_x and the inverse Jacobian \mathbf{J}_q of the manipulator.

2.2 Dynamics Considering the Manipulator as Open Kinematic Chains

The 3-PRS can be split apart in $n - 1$ platform joints so that n open chain systems, in which the platform is attached to one of the legs, are obtained. Then, the constraints at the separated joints are included into the model by means of the Lagrange multipliers:

$$\boldsymbol{\tau} = \mathbf{h}_i + \mathbf{A}\boldsymbol{\lambda}_i \quad (5)$$

where \mathbf{A} is the Jacobian that can be obtained from the constraints forces at the separated joints. The linear velocity at the split joints can be computed through the Jacobian analysis of each leg. Then, the velocity obtained at the split joint through each leg are the same and can be used for computing the Jacobian. In this approach, recursive modelling of velocity analysis from serial manipulator analysis can be applied to each leg.

Once the Jacobian matrix is found, the Lagrange multiplier in Eq. (5) is eliminated by multiplying the matrix \mathbf{C} , so that, $\mathbf{C}\mathbf{A} = 0$. This can be done by the coordinated partitioning \mathbf{A} into the passive and the actuated joints. The following expression is obtained:

$$\boldsymbol{\tau} = \mathbf{h}^a + \mathbf{G}_{\text{III}}^T \mathbf{h}^p \quad (6)$$

where \mathbf{G}_{III} has dimensions $l \times n$ and can be computed as follows:

$$\mathbf{G}_{\text{III}} = \mathbf{A}_p^{-1} \mathbf{A}_a \quad (7)$$

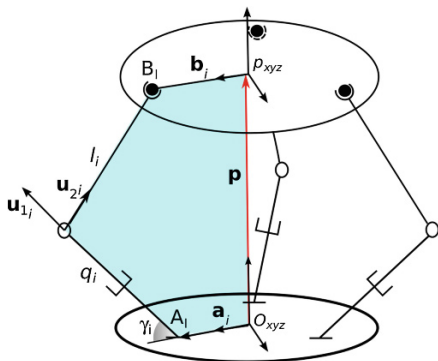
where subscripts p and a respectively refer to the passive and active variable terms in Jacobian \mathbf{A} .

3 Inverse Dynamics of the 3-PRS PM

Figure 1 shows a schematic representation of a 3-PRS PM. The manipulator is a lower mobility PM 3-DOF (less than 6-DOF). This manipulator holds the characteristic of zero torsion at its platform because the three spherical joints move in vertical planes intersecting at a common line [8]. In addition, the topology of its legs provides 2-DOF of angular rotation (2R) in two axes (A/B axis, rolling and pitching) and 1-DOF translation (1T) motion (heave) at the end effector.

For modelling purposes, a Cartesian coordinate frame is attached to point p at the moving platform while the global frame is attached to the point O at the base platform. The spherical joints at the platform are located to form an equilateral triangle at a distance g from the point p . The line of action of the prismatic joints

Fig. 1 3-PRS manipulator



intersect the base \$Oxy\$ plane forming also a equilateral triangle. The distance from \$O\$ to the intersection of the line of action of the prismatic joint and plane \$Oxy\$ is \$h\$.

The Denavit-Hartenberg (D-H) parameters listed in Table 1 are used for modelling purpose. The subscript \$i\$ identifies the leg's number.

In addition, the rotational matrix \${}^o\mathbf{R}_p\$ is described by three Euler angles \$\alpha\$, \$\beta\$ and \$\phi\$ as:

$${}^o\mathbf{R}_p = \begin{bmatrix} c_\alpha c_\beta & c_\alpha s_\beta s_\phi - s_\alpha c_\phi & c_\alpha s_\beta c_\phi + s_\alpha s_\phi \\ s_\alpha c_\beta & s_\alpha s_\beta s_\phi + c_\alpha c_\phi & s_\alpha s_\beta c_\phi - c_\alpha s_\phi \\ -s_\beta & c_\beta s_\phi & c_\beta c_\phi \end{bmatrix} \tag{8}$$

where \$c_*\$ and \$s_*\$ are the cosine and sine function respectively.

The position problem for the considered PM can be found in [3, 6, 9, 12]. The following subsection focus on the computation of the Jacobian matrix.

3.1 Jacobian Matrix for Model I

Matrices \$\mathbf{J}_p\$ and \$\mathbf{G}\$ for computing Eq. (2) are found following the approach presented in [6]. The vector loop equation of the \$i\$-th leg can be written as:

$$\mathbf{p} + \mathbf{b}_i = \mathbf{a}_i + q_i \mathbf{u}_{1i} + l_i \mathbf{u}_{2i} \tag{9}$$

Table 1 D-H Parameters for a 3-PRS PM

\$i\$	\$\theta_{i,1}\$	\$d_{i,1}\$	\$a_{i,1}\$	\$\alpha_{j,1}\$	\$\theta_{i,2}\$	\$d_{1,2}\$	\$a_{i,2}\$	\$\alpha_{i,2}\$
1	\$\pi/2\$	\$d_1\$	0	\$-\gamma_1\$	\$\theta_1\$	0	0	\$-\pi/2\$
2	\$\pi/2\$	\$d_2\$	0	\$-\gamma_2\$	\$\theta_2\$	0	0	\$-\pi/2\$
3	\$\pi/2\$	\$d_3\$	0	\$-\gamma_3\$	\$\theta_3\$	0	0	\$-\pi/2\$

where \mathbf{u}_{1i} and \mathbf{u}_{2i} are unit vectors, l_i is the distance between the rotational joint and the spherical joint, \mathbf{b}_i is the position vector from o to the centre of the spherical joint. Vector \mathbf{a}_i is the position vector between O and local frame of each leg. Differentiating Eq. (9) and after some algebraic manipulation the following equation can be obtained:

$$\mathbf{J}_q \dot{\mathbf{q}} = \mathbf{J}_x \dot{\mathbf{x}} \quad (10)$$

where

$$\mathbf{J}_q = \begin{bmatrix} \mathbf{u}_{21}^T \mathbf{u}_{11} & 0 & 0 \\ 0 & \mathbf{u}_{22}^T \mathbf{u}_{12} & 0 \\ 0 & 0 & \mathbf{u}_{23}^T \mathbf{u}_{13} \end{bmatrix} \quad \text{and} \quad \mathbf{J}_x = \begin{bmatrix} \mathbf{u}_{21}^T & (\mathbf{b}_1 \times \mathbf{u}_{21})^T \\ \mathbf{u}_{22}^T & (\mathbf{b}_2 \times \mathbf{u}_{22})^T \\ \mathbf{u}_{23}^T & (\mathbf{b}_3 \times \mathbf{u}_{23})^T \end{bmatrix}$$

Due to the constraints, the following set of equations hold:

$$\begin{aligned} x_p &= -hs_\alpha c_\beta \\ y_p &= -\frac{1}{2}h(c_\alpha c_\beta - s_\alpha s_\beta s_\phi - c_\alpha c_\phi) \\ \tan(\alpha) &= (s_\beta s_\phi)/(c_\phi + c_\beta) \end{aligned} \quad (11)$$

From the above equations, a $6 \times n$ constraint Jacobian mapping the dependent task space coordinates to the independent ones can be found such that:

$$[\dot{x}_p \ \dot{y}_p \ \dot{z}_p \ \dot{\phi} \ \dot{\beta} \ \dot{\alpha}]^T = \mathbf{J}_r [\dot{z}_p \ \dot{\phi} \ \dot{\beta}]^T \quad (12)$$

It is important to note that $\dot{\mathbf{x}} = [\dot{x}_p \ \dot{y}_p \ \dot{z}_p \ \omega_{p_x} \ \omega_{p_y} \ \omega_{p_z}]^T$. In order to apply Eq. (12), one has to find the angular velocity of the platform through the rate of change of the generalised coordinates $\dot{\mathbf{x}}_c = [\dot{\alpha} \ \dot{\beta} \ \dot{\phi}]^T$. Thus, the Jacobian can be obtained as:

$$\mathbf{J}_p = \mathbf{J}_r [\mathbf{J}_q^{-1} \mathbf{J}_x \mathbf{J}_r]^{-1} \quad (13)$$

Matrix $\mathbf{G}_{3 \times 3}$ is found by obtaining the partial derivatives of the following set of equations:

$$l_p^2 - \|\mathbf{a}_i + q_i \mathbf{u}_{1i} + l_i \mathbf{u}_{2i} - \mathbf{a}_{i+1} - q_{i+1} \mathbf{u}_{1i+1} - l_{i+1} \mathbf{u}_{2i+1}\| = 0 \quad (14)$$

with $i = 1, 2, 3$ and when $i = 3$, $i + 1 = 1$.

3.2 Jacobian Matrix for Model II

Another approach to compute matrices \mathbf{J}_p and \mathbf{G} is to consider that the spherical joints in each leg is constrained to move on a plane normal to the R joint. The Jacobian \mathbf{J}_p can be computed by finding the velocity of the point B_i with respect to the joint coordinates $\mathbf{J}_{q_i}\dot{\mathbf{q}}$ and also with respect to the Cartesian task space $\mathbf{J}_{v_i}\dot{\mathbf{x}}$. If both equations are written with respect to a coordinate system attached to the rotational joint, the component in the \mathbf{z}_{2_i} direction is equal to zero. Thus, \mathbf{J}_{v_i} is equal to \mathbf{J}_{x_i} but with its third row is eliminated. This third column of each leg gives the constraints relationship of the task space coordinates \mathbf{J}_r . The following equations can be used for computing the Jacobian:

$$\mathbf{J}_q^{-1}\mathbf{J}_x = \begin{bmatrix} \mathbf{J}_{q_1}^{-1}\mathbf{J}_{v_1} \\ \mathbf{J}_{q_2}^{-1}\mathbf{J}_{v_2} \\ \mathbf{J}_{q_3}^{-1}\mathbf{J}_{v_2} \end{bmatrix} \quad \mathbf{G}_{II}^T = \begin{bmatrix} \mathbf{J}_{v_1}^T\mathbf{J}_{q_1}^{-T}(:,2) & \mathbf{J}_{v_2}^T\mathbf{J}_{q_1}^{-T}(:,2) & \mathbf{J}_{v_3}^T\mathbf{J}_{q_3}^{-T}(:,2) \end{bmatrix} \quad (15)$$

where $\mathbf{A}(:,2)$ denotes the 2nd column of matrix \mathbf{A} .

3.3 Jacobian Matrix for Model III

The inverse dynamic is computed as a function of three open chains which are obtained after disassembling two spherical joints. The platform is attached to one of the legs, and the spherical joint is modelled as three intersecting revolute joints with their axis perpendicular to each other. Thus, one chain has a set of 5 D-H parameters, while the remaining legs have only sets of 2 variables. The Jacobian is computed by using well-known recursive modelling from serial manipulator analysis. The velocities at the cut joints have to be equal by computing it following each chain. Recursive formulation presented in [1] can be used to find the linear velocity of point B_j :

$$\mathbf{A}_i\dot{\mathbf{q}}_1 - \mathbf{A}_j\dot{\mathbf{q}}_j = 0 \quad (16)$$

where $n - 1$ equations are obtained by setting $i = 2 \dots 3$. The coordinate partitioning approach can be used in order to find the matrix \mathbf{G} . For the 3-PRS the following results are obtained:

$$\mathbf{X} = \begin{bmatrix} \mathbf{A}_1 & -\mathbf{A}_2 & \mathbf{0}_{3 \times 3} \\ \mathbf{A}_1 & \mathbf{0}_{3 \times 3} & -\mathbf{A}_3 \end{bmatrix} \dot{\mathbf{q}} = 0 \quad \mathbf{G}_{III} = \mathbf{X}_{dep}^{-1} \mathbf{X}_{ind} \quad (17)$$

Table 2 Computational effort for solving the inverse dynamic problem

Model Eq. (3)			Model Eq. (2)			Model Eq. (6)		
Term	×	±	Term	×	±	Term	×	±
\mathbf{h}^a	15	9	\mathbf{h}^a	15	9	\mathbf{h}^a	151	103
\mathbf{h}^p	24	22	\mathbf{h}^p	24	22	\mathbf{h}^p	694	461
\mathbf{f}_p	488	412	\mathbf{f}_p	488	412			
\mathbf{G}_{II}	51	24	\mathbf{G}_I	42	33	\mathbf{G}_{III}	300	255
$\mathbf{J}_q^{-1}\mathbf{J}_x$	54	25	$\mathbf{J}_q^{-1}\mathbf{J}_x$	66	35			
\mathbf{J}_r	50	25	\mathbf{J}_r	25	10			
\mathbf{J}_c	158	95	\mathbf{J}_c	146	90			
\mathbf{J}_p	304	198	\mathbf{J}_p	267	178			
Total	862	677	Total	813	675	Total	1,163	735

4 Results and Discussion

In order to compute the computational effort for computing Eqs. (2), (3) and (6), each term of the inverse dynamic model was found in closed form. A Computer Algebra Symbolic (CAS) program, such as Maple, was used for this purpose. The CAS program allowed to conduct the mathematical operation and then simplification of the equations through the use of its built-in function such as `simplify` and `combine, option=trig`. After obtaining the simplified equation, and in order to perform further simulations, Matlab code was developed by using the code generation capabilities of the software. The Matlab procedure with `optimize=tryhard` option of the package `CodeGeneration` was used to develop Matlab code.

The result of the computational effort for computing each of the terms is listed in Table 2 which shows that models in Eqs. (2) and (3), which are based on split the platform from the legs, have fewer number of operation than those of the model considering the platform attached to one of the legs. On the one hand, this fact is due to the inversion of a 6×6 matrix when finding the matrix \mathbf{G}_{III} . On the other hand, by having attached the platform in one the leg the projection of the platform generalised forces onto the actuated joints is cumbersome. It is important to note that the terms were found in closed form solution. A future work will included the comparison when Eq. (6) is computed recursively.

5 Conclusions

Three approaches were applied for developing the inverse dynamic model of a general 3-PRS parallel manipulator. Each term of the dynamic model was found in symbolic form allowing to compute the computational burden of the model. The

results showed that the approaches based on splitting the manipulator in two sub-systems (platform and legs) require fewer operations for computing the model than the obtained when using a joint coordinated system.

References

1. Angeles J (2002) Fundamentals of robotic mechanical systems. Springer, Berlin
2. Carretero JA, Nahon MA, Podhorodeski RP (2000) Workspace analysis and optimization of a novel 3-DOF parallel manipulator. *Int J Robot Autom* 14(4):178–188
3. Carretero JA, Podhorodeski RP, Gosselin CM (2000) Kinematic analysis and optimization of a new three degree-of-freedom spatial parallel manipulator. *ASME J Mech Des* 122(1):17–24
4. Fan KC, Wang H, Chang TH (2003) Sensitivity analysis of the 3-PRS parallel kinematic spindle platform of a serial-parallel machine tool. *Int J Mach Tools Manuf* 43(15):1561–1569
5. Khalil W, Ibrahim O (2007) General solution for the dynamic modeling of parallel robots. *J Intell Rob Syst* 49(1):19–37
6. Li YM, Xu QS (2004) Kinematics and inverse dynamics analysis for a general 3-PRS spatial parallel manipulator. *Robotica* 22(2):219–229
7. Li YM, Xu QS (2007) Kinematic analysis of a 3-PRS parallel manipulator. *Robot Comput-Integr Manuf* 23(4):395–408
8. Liu XJ, Bonev IA (2008) Orientation capability, error analysis, and dimensional optimization of two articulated tool heads with parallel kinematics. *J Manuf Sci Eng* 130(1):1–9
9. Mata V, Farhat N, Díaz-Rodríguez M, Valera A, Page A (2008) Dynamic parameters identification for parallel manipulator. In: Wu H (ed) *Parallel manipulators, towards new applications*. Tech Education and Publishing, Vienna, Austria, pp 21–44
10. Merlet JP (2001) Micro parallel robot MIPS for medical applications. In: *Proceedings of the 8th international conference on emerging technologies and factory automation (ETFA 2001)*, France, 15–18 Oct 2001
11. Staicu S (2012) Matrix modeling of inverse dynamics of spatial and planar parallel robots. *Multibody Sys Dyn* 27(2):239–265
12. Tsai MS, Shiau TN, Tsai YJ, Chang TH (2002) Direct kinematic analysis of a 3-PRS parallel manipulator. *Mech Mach Theory* 38(1):71–83
13. Tsai MS, Yuan WH (2010) Inverse dynamics analysis for a 3-PRS parallel mechanism based on a special decomposition of the reaction forces. *Mech Mach Theory* 45(11):1491–1508

Part VI
Dynamics of Machinery

Optimization of Textile Machines in Order to Increase Productivity

B. Corves, M. Hüsing, M. Schumacher and F. Schwarzfischer

Abstract Productivity is a quality criterion in the assessment of textile machines. Increasing the operating speed is a measure in order to increase productivity, but is often accompanied by unwanted vibrations. Due to noise radiation and degradation of the end product, these vibrations confine the increase of the operating speed. On the base of a chain stitch machine, the reasonable employ of mass balancing and power smoothing in order to decrease vibrations is stated. The reduced mass moment of inertia of the mechanism onto the drive shaft is employed to draw conclusions on the optimization potential of particular links. Using these methods, corrective measures are developed to enable a higher operating speed of the machine. A multi body model is generated in order to quantify the effects of the approach, showing good improvement in the vibrational behavior of the machine.

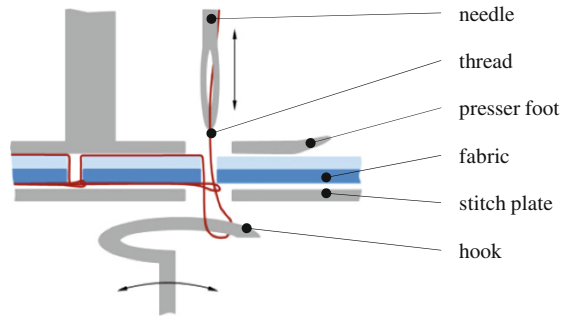
Keywords Textile machinery · Power smoothing · Reduced mass moment of inertia · Multi body system

1 Introduction

In the 21st century, textile industry banks on the mass production of cloth and other textiles. Modern textile machines are strongly characterized by their productivity. As productivity highly depends on the operating speed of the machines, increasing the velocity of the machine is a common procedure within the further development. Apart from the desired increase in productivity, this approach is often accompanied by unwanted vibrations, limiting the maximum speed of the machine due to noise radiation and degradation of the end product [2].

B. Corves (✉) · M. Hüsing · M. Schumacher · F. Schwarzfischer
Department of Mechanism Science and Dynamics of Machines, RWTH Aachen University,
Aachen, Germany
e-mail: corves@igm.rwth-aachen.de

Fig. 1 The chain stitch process



Based on an industrial case, a procedure on enabling a higher operating speed by minimizing vibrations is shown. The subject of the optimization process is a chain stitch machine, offering potential for improvement due to yet not optimized mechanisms and material selection. On demand of the producer of the machine, a complete redesign was not considered.

Figure 1 shows the chain stitch process: The fabric, positioned on the stitch plate, is held down by the presser foot.

At each stitch, the needle pulls a loop of thread through the fabric. The reversal motion of the thread is delayed to the motion of the needle because of inertia. While thread and needle split, a hook mechanism grabs the loop of thread before it can be pulled up along with the needle. Once the needle is withdrawn, the fabric moves forward and the process will be rerun [4]. Modern chain stitch machines are equipped with a needle support, holding up to several hundreds of needles.

Figure 2 shows the scheme of the mechanism that moves the needle support (5). It is a 6-bar Watt-II-Mechanism, containing two consecutive four-bar mechanisms. The first mechanism $A_0AB_1B_0$ is a crank-and-rocker mechanism with the crank 1. The second mechanism $B_0B_2CC_0$ generates a straight-line guiding movement of the point N. It is designed parallelogram-like, producing the needle-motion.

This paper presents the implementation of established methods [1, 3, 5, 6] in order to enhance the performance of the chain stitch machine. The focus is on the essential effects, neglecting further influences from bearings, process forces and others. As a first step, measured data of the vibrations of the machine was acquired. After data processing, a torsional vibration of the driving shaft was identified as the main effect impeding a higher operating speed of the machine. Furthermore, a movement of the entire machine in vertical direction was detected. Afterwards a simplified multi body model of the machine was built up in the software environment MSC.ADAMS. Proofing the assumptions, a verification of this model was carried out using the measured data. The next step consisted of calculating the reduced mass moment of inertia of the simplified mechanism with respect to the drive shaft. Specifying the influence of the parts of the mechanism, corrective measures could be developed in order to smooth the trend of the reduced mass inertia.

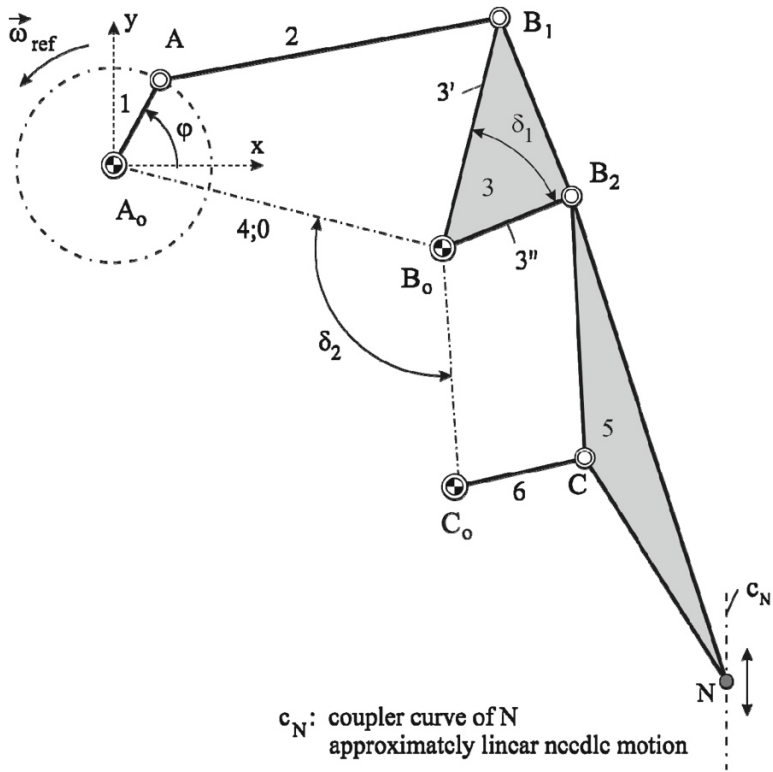


Fig. 2 Kinematic scheme of the needle support mechanism (not true to scale)

2 Materials and Methods

Considering data from conducted measures, the main effects that had to be taken into account were identified. To smooth the vibrations of the machine, mass balancing as well as power smoothing was considered. Furthermore, the reduced mass moment of inertia of the whole mechanism onto the drive shaft was considered in order to achieve information about the influence of particular links on the vibration of the machine and the drive shaft. Employing these methods improvement opportunities were derived, which were tested inside the multi body model.

2.1 Measured Data and Data Processing

To measure the movement of the entire machine, an optical coordinate-measuring device was utilized. The measured data enabled us to quantify the movement of the machine as well as to draw conclusions about the decisive directions of motions.

Furthermore, data from the electronic engine control was provided by the manufacturer of the motor, showing both angular velocity and torque characteristics.

2.2 Multi Body Model of the Textile Machine

To be able to quantify the results of mass balancing and power smoothing, a multi body model of the textile machine was built, Fig. 3.

Therefore the machine was suitably simplified. The machine frame was modeled as a rigid mass. It was connected to the ground by interlinking elements, holding the characteristics of the machine bearing. The mechanism itself was connected to the machine frame. The mechanism was modeled moving the needles up and down, neglecting ancillary units which were also driven by the motor. Assuming that the electronic control of the servomotor was able to provide a constant angular velocity of the shaft, a constant value was assigned to the shaft motion.

2.3 Mass Balancing

In order to reduce the vertical vibrations of the machine, mass balancing was taken into account. Figure 4 shows a crank-and-rocker mechanism with an additional counterweight m_a to balance the crank. For the case of a well-designed counterweight, its inertia forces about the joint A_0 balance the inertia forces (shaking forces) of the crank.

Balance masses on the oscillating links of the mechanism were not considered due to their impact on the reduced mass moment of inertia onto the drive shaft and therefore negative influence on the torsional vibrations of the shaft.

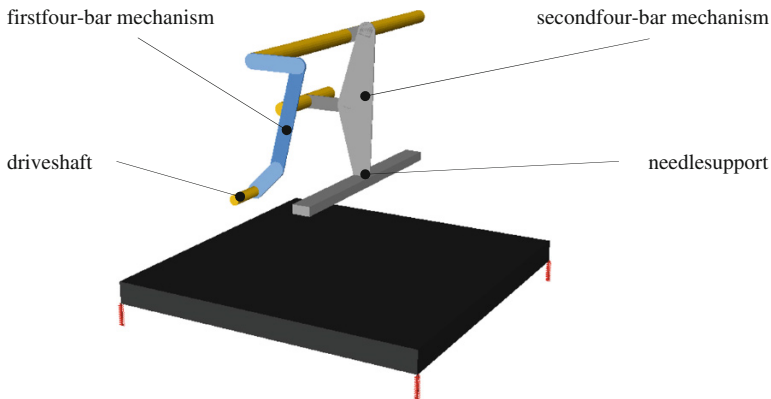


Fig. 3 Multi body model of the chain stitch machine

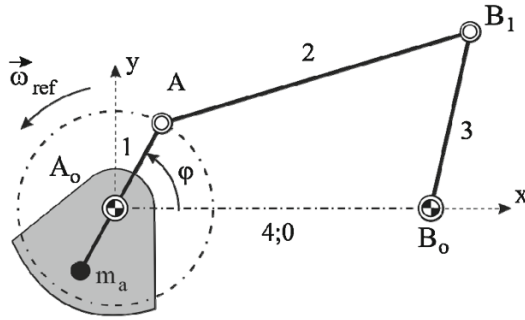


Fig. 4 Crank-and-rocker mechanism with counterweight to balance the crank

2.4 Power Smoothing

In order to determine the impact of the different links of the mechanism, their mass inertia is reduced onto the drive shaft which rotates at an angular velocity ω_{ref} . Figure 5 shows exemplarily the original as well as the equivalent system for the case of a crank-and-rocker mechanism. The trend of the reduced mass inertia of the equivalent system is represented.

Equating the kinetic energy of the reduced mechanism with the original system

$$E_{kin,red} = E_{kin}, \tag{1}$$

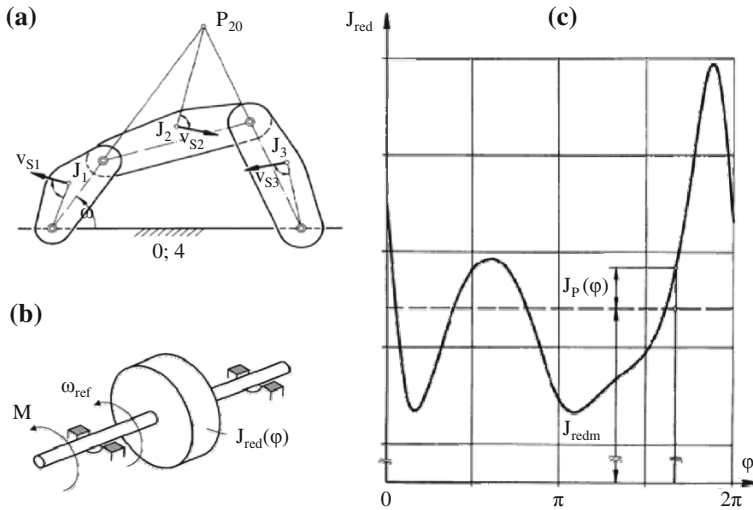


Fig. 5 Reduction of a four bar mechanism (a) onto the crank shaft, resulting in an equivalent system (b) with a reduced mass moment of inertia as a function of the crank shaft angle ϕ (c)

the reduced mass inertia follows as

$$J_{red}(\varphi) = \frac{1}{\omega_{ref}^2} \sum_i (m_i \cdot v_i^2 + J_i \cdot \omega_i^2). \quad (2)$$

where m_i is the mass, J_i is the mass moment of inertia and v_i and ω_i are the velocities of the link i . Considering the Euler-Lagrange equation

$$\frac{d}{dt} \left(\frac{\partial E_{kin}}{\partial \dot{\varphi}} \right) - \frac{\partial E_{kin}}{\partial \varphi} = M, \quad (3)$$

where E_{kin} denotes the kinetic energy of the system and M is the torque on the drive shaft (neglecting external forces and change of potential energy). It follows that

$$M = \frac{1}{2} \frac{dJ_{red}}{d\varphi} \cdot \omega_{ref}^2 + J_{red} \cdot \dot{\omega}_{ref}. \quad (4)$$

The influence of the particular links on the aggregate reduced mass moment of inertia allows comparing their impact on the torque and the torsional vibrations. Links having a strong influence on the mean value of the reduced mass inertia as well as these having a strong impact on the relative fluctuation can be identified.

3 Results

Following the procedure illustrated in Sect. 2, the mass inertias of the links were reduced onto the drive shaft. Figure 6 shows the reduced mass inertias of all parts of the mechanism as well as the reduced mass inertia of the complete mechanism.

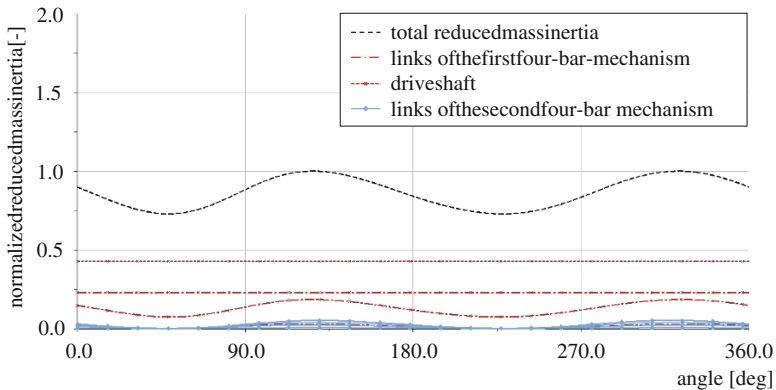


Fig. 6 Reduced mass inertia of the non-optimized mechanism

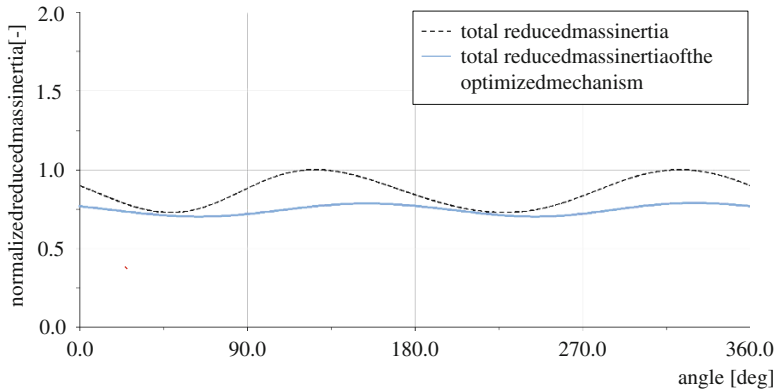


Fig. 7 Reduced mass inertia of the optimized mechanism

After identifying the parts having the most impact on the total reduced mass inertia as well as on its fluctuation, corrective measures were applied. The parts of the first four-bar-mechanism showed a big influence on the total reduced mass inertia. Therefore, these links were redesigned considering aspects of lightweight-design. The links of the second four-bar-mechanism revealed only a small influence on the total reduced mass inertia. Only the material of the needle support was subjected to a change in material. Due to the almost vertical oscillating movement of the needle support, this change in material also contributed to smooth the vertical vibration of the complete machine. In order to reduce the vertical vibration, a counterweight balancing the crank of the first four-bar-mechanism was designed.

Figure 7 shows the new total reduced mass inertia of the mechanism in comparison with the unbalanced mechanism. The mean value of the reduced mass inertia could be decreased by more than 18 percent. The relative fluctuation of the reduced mass inertia could be reduced by over 60 percent.

As a last step a flywheel was designed in order to decrease the relative fluctuation of the total reduced mass inertia. The flywheel was applied to the drive shaft. Before implementation, all corrective measures were applied in the multi body model. The simulation showed a significant decrease in both torsional and vertical vibrations, even for 90 % higher operating speeds. After the implementation of the corrective measures, the chain stitch machine was able to work at almost twice the initial operating speed, without exceeding the vibration amplitudes of the non-optimized machine at the default operating speed.

4 Conclusions

In this paper, the application of established methods of vibration reduction was shown on the base of a non-optimized textile machine. Due to an increase of operational speed, strong vibrations of the machine were detected. After processing

data provided by measurements, the focus was set on reducing the torsional vibrations concerning the drive shaft, generated by the mechanism of the machine, also having in mind the vertical vibrational movement of the whole machine. Reducing the mass inertia of the links of the mechanism onto the drive shaft, their impact on the absolute magnitude and the fluctuation of the reduced mass inertia could be quantified. Different parts were optimized and power smoothing was applied, designing a flywheel in order to smooth the trend of the required torque to drive the mechanism. The objective of reducing the vibrations of the machine was achieved.

References

1. Chaudhary H et al (2009) Dynamics and balancing of multibody systems. Lectures notes in applied and computational mechanics, vol 37
2. Demeulenaere B (2004) Dynamic balancing of reciprocating machinery with application to weaving machines. Ph.D. thesis, University of Leuven
3. Huesing M (2010) Maschinendynamik starrer systeme. Lecture, RWTH Aachen
4. Jones I et al (2013) Joining textiles: principles and application. Woodhead Publishing Series in Textiles, Cambridge
5. Uicker J et al (2011) Theory of machines and mechanisms. University Press, Oxford
6. Verschuure M (2009) Counterweight balancing of mechanisms using convex optimization techniques. University of Leuven, Germany

Motion Equation of Linkages with Changeable Close Loop

E. Gebel

Abstract It is known that the dynamical analysis of a linkage is usually carried out by Lagrange-Euler equation in the theory of mechanics and mechanism. This method is allowed to take into account effects connected with the inertia, Coriolis, centrifugal and gravitational forces. All of listed factors are especially important due to the intensive working conditions of the most of modern machinery. Due to the wide functionality of linkages and their reliability and durability, they are widely used. However, the complex scheme of a multi-lever linkage makes accurate solution of dynamical problem difficult. Using the homogeneous transformation in Denavit-Hartenberg notation leads to the compact matrix form of the dynamical model. The algorithm and programs for the studied linkage are based on the proposed model. An actuator of a lifting machine is used as illustrative example.

Keywords Linkages · Dynamics · Lagrange-Euler equation · Denavit-Hartenberg matrix transformations

1 Introduction

Most of modern machinery works under the intensive conditions (accelerated to the velocities and forces) therefore dynamics is the important problem for the investigation the reliability of the machine in terms of its strength, durability and precision operation [1]. Accounting dynamic phenomena in machineries is reduced the metal consumption, energy outlay, improving controllability and as a result increases their quality.

Mathematical model of dynamics with sufficient accuracy is described the process of the mechanism operation and is defined by the kinematical scheme,

E. Gebel (✉)
Omsk State Technical University, Omsk, Russia
e-mail: gebel_es@mail.ru

mechanical properties (for example inertia, elasticity and other) of its components, units and type and characteristics of the drive also.

Holonomic mechanical systems with retaining stationary links are linear conservative. We take into account the following assumption under dynamics description:

- all components of the mechanical system (elements of bearing constructions, links and so on) are rigid bodies i.e. without element elasticity;
- kinematical pairs and transmission gears are ideal i.e. no friction in them.

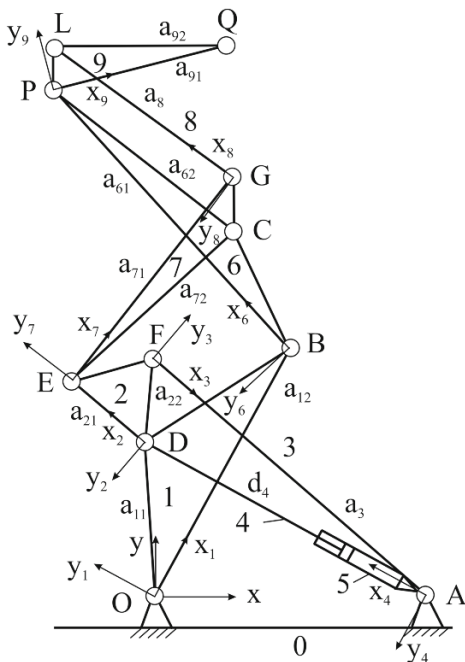
Such type of models is reflected the properties of many executive mechanisms with reasonable accuracy and widely used at analytical mechanics [2]. For example they are applied for determined constructive parameters and control laws that provides for the required quality of the mechanism working.

2 Dynamical Mathematical Model

Using the Euler-Lagrange equation for the moving equation of the linkages leads to nonlinear differential simultaneous equations of second order which reflect the effects related to the inertia, Coriolis, centrifugal and gravitational forces.

Plane linkage with changeable close loop [3] (Fig. 1) consists of eleven rotational and one translational kinematic pairs of fifth class. The input link AD is made

Fig. 1 Scheme of plane linkage with adjustable close loop



as a hydraulic cylinder, the movement of the rod leads to plane-parallel displacement of the output link PQL.

Initial data for dynamics are kinematic characteristics of the studied mechanism which have been found by matrix transformations Denavita-Hartenberg. The compact vector-matrix form of the equation of motion for a mechanism is convenient for analytical (numerical) investigation and implementation on a computer.

Differential equation Euler-Lagrange looks like:

$$\frac{d}{dt} \left(\frac{\partial L}{\partial \dot{q}_i} \right) - \frac{\partial L}{\partial q_i} = Q_i, \quad (1)$$

where $i = 1, \dots, 9$ —joint number; L —Lagrange function equals to the difference between the kinetic K and potential P energies of the mechanical system; q_i —generalized coordinates; \dot{q}_i —first derivative of the generalized coordinates by time; Q_i —generalized forces (or moments) created in i th joint at realization of the given motion i th link.

2.1 Kinetic Energy

In common case the kinematical energy of a mechanism depends on the masses and accelerations of its joints, the latest one are defined like a first derivative the joint velocities by time. Any point is described by homogeneous coordinates of radius vector r_i^j in coordinate system of i th link:

$$r_i^j = (x_i, y_i, z_i, 1)^T. \quad (2)$$

Symbol r_i denotes a radius vector of a point relative to the reference coordinate system connected with the base of the studied linkage (Fig. 1), $A_i^0 = A_1^0 \cdot A_2^1 \cdot \dots \cdot A_i^{i-1}$ is the matrix of homogeneous transformation in Denavita-Hartenberg notation. So the connection between the positions of a point into the local and the fixed coordinate systems describes the expression:

$$r_i = A_i^0 \cdot r_i^j, \quad (3)$$

By the assumptions the links of the considered mechanism are absolutely rigid bodies and any point with coordinates r_i^j has zero velocity into i th local coordinate system which is not inertial because of mechanism links are moved independently of acting forces due to accelerated motion of the references frame related to the i th link. Velocity of a point into the basic coordinate system xOy is determined by formula:

$$v_i^0 = v_i = dr_i^0/dt = d(A_i^0 \cdot r_i^i)/dt = \left[\sum (\partial A_i^0/\partial q_i) \dot{q}_i \right] r_i^i, \tag{4}$$

Note that r_i^i equals to zero because of the joint centers in the discussed mechanism coincide with origins of the local coordinate systems.

The derivative of the homogeneous transformation matrix A_i^0 by generalized coordinate q_i (for rotational and translational kinematic pairs) is calculated by the matrix H_i :

$$H_i^B = \begin{bmatrix} 0 & -1 & 0 & 0 \\ 1 & 0 & 0 & 0 \\ 0 & 0 & 0 & 0 \\ 0 & 0 & 0 & 0 \end{bmatrix}, \quad H_i^R = \begin{bmatrix} 0 & 0 & 0 & 0 \\ 0 & 0 & 0 & 0 \\ 0 & 0 & 0 & 1 \\ 0 & 0 & 0 & 0 \end{bmatrix}. \tag{5}$$

Thus, the result of the differentiation can be written as:

$$\partial A_i^{i-1}/\partial q_i = H_i \cdot A_i^{i-1} = \begin{cases} A_1^0 A_2^1 \dots A_{j-1}^{j-2} H_j A_j^{j-1} \dots A_i^{i-1}, & \text{if } j \leq i, \\ 0, & \text{if } j > i. \end{cases} \tag{6}$$

Expression (6) describes the displacement of the i th link points caused by the relative moving into the j th joint. If the partial derivative $\partial A_i^{i-1}/\partial q_i$ is denoted as U_{ij} Eq. (6) can be rearranged as following:

$$U_{ij} = \begin{cases} A_{j-1}^0 H_j A_j^{i-1}, & \text{if } j \leq i, \\ 0, & \text{if } j > i. \end{cases} \tag{7}$$

Matrix U_{ij} characterizes the velocity of the i th link relative to the basic coordinate system and does not depend on the mass distribution in this link. Analytical dependence (3) with this notation (7) will have the next form:

$$v_i^0 = \left[\sum U_{ij} \cdot \dot{q}_i \right] \cdot r_i^i. \tag{8}$$

In accordance with kinematic parameters described in the article [3] and analytical expression (7) for first rotational joint—rod OBD, the velocity of the joint D in the inertial coordinate system xOy caused by the displacement of the hydraulic cylinder rod AD will be equal to $U_{10} = \partial A_1^0/\partial q_1 = H_1 A_1^0$.

Similarly the dependences for the velocity of other mechanism links are developed as:

- the point E of the triangular link DEF: $U_{20} = A_1^0 H_1 A_2^1$;
- the point F of the rocker FA: $U_{30} = A_1^0 A_2^1 H_1 A_3^2$;
- the joint center P of the triangular link BPC: $U_{60} = A_{11}^0 H_1 A_6^1$;
- the point G of the triangular link ECG: $U_{70} = A_1^0 A_2^1 H_1 A_7^2$;

- joint centre L of the link GL: $U_{80} = A_1^0 A_2^1 A_7^2 H_1 A_8^7$;
- the point Q of the triangle link PLQ: $U_{90} = A_{11}^0 A_6^1 H_1 A_9^6$.

Analog velocity of the i th point relative to the basic coordinate system is obtained by substituting these expressions into the formula (8).

Kinetic energy dK_i of the mass element dm of the linkage mechanism i th link is determined as follows:

$$dK_i = 1/2(x_i^2 + y_i^2 + z_i^2)dm = 0.5 \cdot Tr\left(\dot{T}_i J_i T_i^T\right)dm, \tag{9}$$

where x_i, y_i, z_i —the centre of mass of the i th link coordinates into inertial coordinate system xOy; \dot{T}_i —first derivative of the resulting homogeneous transformation $T_i = A_1^0 \cdot A_2^1 \cdot \dots \cdot A_i^{i-1}$ by generalized coordinate; T —matrix transpose operation; Tr —trace of the matrix which are equaled to the sum of its diagonal elements;

$$J_i = \begin{bmatrix} J_{XX}^{(i)} & J_{XY}^{(i)} & J_{XZ}^{(i)} & m_i x_i^* \\ J_{YX}^{(i)} & J_{YY}^{(i)} & J_{YZ}^{(i)} & m_i y_i^* \\ J_{ZX}^{(i)} & J_{ZY}^{(i)} & J_{ZZ}^{(i)} & m_i z_i^* \\ m_i x_i^* & m_i y_i^* & m_i z_i^* & m_i \end{bmatrix} \text{---the inertia tensor of the } i\text{th link; } \tag{10}$$

here m_i —the mass of the i th moveable joint; x_i^*, y_i^*, z_i^* —coordinates of the centre of mass of i th link into local coordinate system; $J_{xx}^{(i)}, J_{yy}^{(i)}, J_{zz}^{(i)}$ —the axial inertia moment of the i th link relative to their own axes; $J_{XY}^{(i)}, J_{YX}^{(i)}, J_{ZY}^{(i)}, J_{XZ}^{(i)}, J_{YZ}^{(i)}, J_{XZ}^{(i)}$ —the centrifugal moments of inertia.

Substituting the velocity v_i expression (8) for the i th point of the moveable joint into formula (9) and adding the obtained analytical dependences for all links of the linkage mechanism the kinetic energy of the mechanical system can be written like a quadratic form of the numerical series:

$$\mathcal{K} = \sum \mathcal{K}_i = 0.5 \cdot \sum \sum \sum \left[Tr\left(U_{ip} J_i U_{ir}^T \dot{q}_p \dot{q}_r \right) \right] \tag{11}$$

The inertia tensor depends on the mass distribution into the i th joint of the investigated mechanism and does not depend on the position and velocity of links. Suppose that axis Oz of the inertial reference system xOy coincides with one of the main axes of the inertia tensor, the unit vectors of the other two axes Ox and Oy are collinear and co-directional with the unit vectors of the other two principal axes respectively.

In accordance with the analytic dependence (9) of the kinetic energy of kinematic link OBD of the planar linkage mechanism with adjustable close loop is defined as following:

$$K_1 = 0.5 \cdot \sum \text{Tr} \left(\dot{T}_1 J_1 \dot{T}_1^T \right) \dot{q}_1^2 = 0.5(2J_Z^5 + m_1 a_{10}^2) \dot{q}_1^2,$$

where $T_1 = U_{11} \cdot q_1$.

Similarly, we write the equations for the third, sixth, seventh, eighth and ninth movable joints of the considered linkages:

$$\begin{aligned} K_2 &= 0.5(2J_Z^5 + m_1 a_{12}^2) \dot{q}_1^2, & K_3 &= 0.5(2J_Z^3 + m_3 a_3^2) \dot{q}_1^2, \\ K_6 &= 0.5(2J_Z^6 + m_6 a_6^2) \dot{q}_1^2, & K_7 &= 0.5(2J_Z^7 + m_7 a_7^2) \dot{q}_1^2, \\ K_8 &= 0.5(2J_Z^8 + m_8 a_8^2) \dot{q}_1^2 & \text{and } K_9 &= 0.5(2J_Z^9 + m_9 a_9^2) \dot{q}_1^2 \end{aligned}$$

where $a_3 = a_{12} + a_{22}$, $a_6 = a_{11} + a_{61}$, $a_7 = a_{10} + a_{21} + a_{71}$, $a_8 = a_{10} + a_{21} + a_{71} + a_8$, $a_9 = a_{11} + a_{61} + a_{91}$.

Kinetic energy (11) of the mechanism equals to the algebraic sum of the expressions written for individual links:

$$K_M = \left(\begin{aligned} &J_z^1 + \frac{m_1 a_{10}^2}{2} + J_z^2 + \frac{m_2 a_{21}^2}{2} + J_z^3 + \frac{m_3 a_3^2}{2} + J_z^6 \\ &+ \frac{m_6 a_6^2}{2} + J_z^7 + \frac{m_7 a_7^2}{2} + J_z^8 + \frac{m_8 a_8^2}{2} + J_z^9 + \frac{m_9 a_9^2}{2} \end{aligned} \right) \dot{q}_1^2 \quad (12)$$

2.2 Potential Energy

The potential energy of the investigating object in a force field of the Earth is defined as:

$$\Pi_M = \sum \Pi_i = - \sum m_i \cdot G^T \cdot T_i \cdot R_i^* \quad (13)$$

where Π_i —potential energy of the i th link is calculated using formula:

$$\Pi_i = P_i \cdot y_i^*, \quad (14)$$

here P_i и y_i^* —weight and ordinate of the centre of mass of i th link in the inertial coordinate system xOy respectively.

The matrix form of expression (14) looks like:

$$\Pi_i = -m_i \cdot G^T \cdot T_i \cdot R_i^*, \quad (15)$$

where R_i^* —column matrix in which first three elements are Cartesian coordinates of the centre of gravity of the i th link connected up their own coordinate system; $G^T = (g_x, g_y, g_z, 0) = (0, -g, 0, 0)$ —row matrix describes the gravitational

acceleration in the basic coordinate system (g is a constant which equals to $9,8062 \text{ m/c}^2$).

According to formula (15) the potential energy expression of movable links $\Pi_1, \Pi_2, \Pi_3, \dots, \Pi_9$ of the linkages mechanism with changeable close loop is written down as:

$$\begin{aligned}\Pi_1 &= -m_1 \cdot G^T \cdot T_1 \cdot R_1^* = P_1 \cdot (y_1^* S_{10} - a_{10} C_{10}), \\ \Pi_2 &= -m_2 \cdot G^T \cdot T_2 \cdot R_2^* = P_2 (y_2^* S_{21+10} - a_{21} C_{21+10}), \\ \Pi_3 &= -m_3 \cdot G^T \cdot T_3 \cdot R_3^*, \quad \Pi_6 = -m_6 \cdot G^T \cdot T_6 \cdot R_6^*, \\ \Pi_7 &= -m_7 \cdot G^T \cdot T_7 \cdot R_7^*, \quad \Pi_8 = -m_8 \cdot G^T \cdot T_8 \cdot R_8^*, \\ \Pi_9 &= -m_9 \cdot G^T \cdot T_9 \cdot R_9^*\end{aligned}$$

2.3 Motion Equation

Using previous notations and obtained dependence (12) of the kinetic energy in the Lagrange equation (1) for a separate link in generalized form looks like:

$$\frac{d}{dt} \frac{\partial K}{\partial \dot{q}_i} - \frac{\partial K}{\partial q_i} = \sum_{i=1}^9 \sum_{j=1}^j \sum_{k=1}^i r \left(U_{ijk} J_i U_{ij}^T \right) \dot{q}_j \dot{q}_k + \sum_{i=j}^9 \sum_{j=1}^i r \left(U_{ij} J_i U_{ij}^T \right) \ddot{q}_j \quad (16)$$

The first partial derivative of the potential energy of i th joint by generalized coordinate calculated as following:

$$\frac{\partial \Pi}{\partial q_i} = - \sum_{i=1}^9 m_i G^T \frac{\partial T_i}{\partial q_i} R_i^* = - \sum_{i=1}^9 m_i G^T U_{ij} R_i^* \quad (17)$$

Substituting expressions (16) and (17) into right side of the Eq. (1) the resultant formula will be:

$$\begin{aligned}\sum_{i=1}^9 \sum_{j=1}^i Tr \left(U_{ikl} \cdot J_i \cdot U_{ij}^T \right) \ddot{q}_j + \sum_{i=1}^9 \sum_{j=1}^i \sum_{k=1}^j Tr \left(U_{ikl} \cdot J_i \cdot U_{ij}^T \right) \dot{q}_j \dot{q}_k - \\ - \sum_{i=1}^9 m_i G_j^T U_{ij}^i R_{ij}^* = Q_i.\end{aligned} \quad (18)$$

The generalized force acting in i th joint is determined by differential equation:

$$Q_i = \sum_{k=1}^9 D_{ik} \ddot{q}_k + \sum_{j=1}^9 \sum_{k=1}^9 h_{ijk} \dot{q}_j \dot{q}_k + c_i \quad (19)$$

or the matrix form of Eq. (19) will be:

$$Q(t) = D(q(t))\ddot{q}(t) + h(q(t), \dot{q}(t)) + c(q(t)), \tag{20}$$

where $Q(t)$ — n -dimensional column vector of generalized forces generated by actuators in the joints; $q(t)$ — n -dimensional column vector of the generalized coordinates; $\dot{q}(t)$ — n -dimensional column vector of the generalized speeds; $\ddot{q}(t)$ — n -dimensional column vector of the generalized accelerations; $D(q(t))$ —square symmetric matrix ($n \times n$), which elements are calculated from expression:

$$D_{ik} = \sum_{j=\max(i,k)}^9 Tr(U_{ij}J_iU_{ik}^T), \text{ where } (i = \overline{1,9}), \tag{21}$$

here $h(q(t), \dot{q}(t))$ — n -dimensional column vector of the Coriolis and centrifugal forces which elements are obtained as following:

$$h_i = \sum_{j=1}^9 \sum_{k=1}^9 h_{ijk}\dot{q}_j\dot{q}_k = \sum_{l=\max(i,j,k)}^9 Tr(U_{ijk}J_lU_{ij}^T), \tag{22}$$

where $c(q(t))$ — n -dimensional column vector of the gravitational forces with elements equal to:

$$c_i = \sum_{j=i}^9 (-m_iG^T U_{ij}R_j^*). \tag{23}$$

For example the analytical expression for the calculation the element D_{11} of the inertial matrix $D(q)$ (21) is obtained as following:

$$D_{11} = U_{11}J_1U_{11}^T = 2J_Z^5 + m_1a_{12}^2.$$

Expression h_1 of the vector (22) is written down using equality $h_{ik} = h_{ikj}$:

$$h_1 = \sum_{j=1}^9 \sum_{k=1}^9 h_{1jk} \cdot \dot{q}_j \cdot \dot{q}_k.$$

The parameter c_1 of first moveable link of the matrix (23) is calculated:

$$c_1 = - \left(\begin{aligned} & m_1G^T U_{11}R_1^* + m_2G^T U_{21}R_2^* + m_3G^T U_{31}R_3^* + m_6G^T U_{61}R_6^* \\ & + m_7G^T U_{71}R_7^* + m_8G^T U_{81}R_8^* + m_9G^T U_{91}R_9^* \end{aligned} \right).$$

Using analytical dependences $D_{jk}(q(t))$, $h_{ijk}(q(t), \dot{q}(t))$ and $c_i(q(t))$ the motion Eq. (1) of the investigated mechanism will be found as following:

$$\sum_{i=1}^9 \sum_{j=1}^i Tr(U_{ikl} \cdot J_i \cdot U_{ij}^T) \ddot{q}_j + \sum_{i=1}^9 \sum_{j=1}^i \sum_{k=1}^j Tr(U_{ikl} \cdot J_i \cdot U_{ij}^T) \dot{q}_j \dot{q}_k - \sum_{i=1}^9 m_i G_j^T U_{ij}^i R_{ij}^* = D(q(t)) \ddot{q}(t) + h(q(t), \dot{q}(t)) + c(q(t)).$$

3 Conclusions

Generally, the lifting machines are constructed by scissors lift lever system called Nuremberg scissors and a lifting cargo platform. The key disadvantages of that lifting systems are the following: limited lifting capacity; low stability at the highest position of the platform; low operation parameters and durability; structure complexity and high material capacity.

The proposed structure of the multi-lever plane mechanism with a changeable closed loop is increased lateral and longitudinal stiffness providing lifting action by only one hydraulic actuator.

The results of kinematical analysis [4] show that the operating platform moves within the vertical working area from 0.3 through 1.8 m. The parallel level motion of the platform has a negligible inclination in 2.51° and does not impact the operational capacity of the system. The estimated load capacity of the proposed mechanism is up to 200 kg. It can be folded for transportation and used for both internal and external construction work.

This paper describes a systematic methodology for the dynamical analysis of the linkages. The approach is based on the combination of the homogeneous transformations and Lagrange-Euler method that leads to the compact matrix form of the moving equation of the studied mechanism.

Result of the numerical experiment shows that the oscillations of the linkage are close to the single frequency so its amplitudes can be estimated by the first-level form of the link vibration. When the mechanism starts moving the amplitude of the output link oscillation is in order to $(2 \div 4) \times 10^{-3} l$, where l is a length of mechanism links.

Investigation of kinematic and dynamic characteristics of the multi-lever mechanism with changeable close loop allows finding the motion law which affect on the productivity, reliability and durability of a machinery [5]. This information is used for the design of the new technological process.

References

1. Dzholdasbekov Y (2001) A theory of mechanisms of high grades. Gylym, Almaty, p 427
2. Kolovsky MZ, Evgrafov AN, Semenov YA, Slousch AV (2000) Advanced theory of mechanisms and machines. Springer, Berlin, Heidelberg, p 394
3. Zhursenbaev BI, Sarbasov TA (2010) Innovation patent “Jack scaffold” № 22439, issued by the committee on intellectual property rights, ministry of justice of the Republic of Kazakhstan as of 25 Feb 2010
4. Gebel ES, Zhursenbaev BI, Solomin VY (2012) Numerical simulation of the lifting mechanism. Proceedings of 9th international conference on mathematical problems in engineering, aerospace and sciences: ICNPAA 2012, Vienna, Austria. pp 408–415
5. Gebel ES, Khomchenko VG (2013) Design linkage precise positioning: monograph, Publishing house OSTU, Omsk, p 138

Elastodynamic Analysis of the Sucker Rod Pumping System Mechanism

N. Dumitru, N. Craciunoiu, R. Malciu and N. Ploscaru

Abstract The paper aims to identify the dynamic response of the oil pumping unit system mechanism using the analytical method and the experimental method. By numerical processing of the developed mathematical models for longitudinal and transverse vibrations of the mechanism connecting rod and walking beam, the time variation diagrams of the linear elastic displacement were obtained in the Maple programming environment. In order to confirm the theoretical results but also for a complex analysis of the entire pumping system, there was determined the force acting upon the polished rod and there were compared the values obtained by calculus and the values experimentally determined for the angle of rotation of the walking beam. Permanent monitoring of the pumping rod mechanical stress and vibration acceleration might contribute to more efficient operation of oil deep extraction wells.

Keywords Beam pumping unit system · Walking beam · Polished rod · Acceleration of vibration

1 Introduction

Artificial pumping systems for deep extraction have a significant share in most countries with developed oil industry, both as wells number and as flow rate. This equipment transforms a rotary motion provided by prime mover in a reciprocating motion that is transferred as a vertical displacement to the down-hole pump by a set of rods, which provides mechanical energy to the fluid and allows its elevation to the surface. Since the 1990s, there were comprehensive studies such as, for example, [2, 1] or [6], regarding the structures subjected to transient loads using non-gradient method or non-linear analysis optimization. Many researchers turned

N. Dumitru (✉) · N. Craciunoiu · R. Malciu · N. Ploscaru
University of Craiova, Craiova, Romania
e-mail: nicolae_dtru@yahoo.com

their attention to identify also the loads and the boundary conditions, as shown in papers like [8], or to use numerical optimization methods, as shown in papers like [4]. In the 2000s, researches recorded an extension of the dynamic response optimization of multi-body flexible systems. In [5] the equivalent static load was calculated using the finite element method and introduced in the equation governing the dynamics of multi-body flexible systems. There were also presented applications of this method for dynamic response optimization. The purpose of our paper is to identify the dynamic response of a rod pumping unit system by developing methods of modeling, simulation and experimental testing. Therefore, a model of a rod pumping unit system was developed and there were determined the mathematical models for linear elastic longitudinal and transverse displacements of the connecting rod and walking beam as described in Sect. 2. Section 3 is devoted to numerical simulation of the developed model using ADAMS software.

2 Longitudinal and Transverse Vibration Analysis with Regard to the Constraint Forces Acting in the Joints

This paper aims to study the dynamic response of the oil pumping unit system mechanism using the analytical method and the experimental method. Using the analytical method, the mathematical models for longitudinal and transverse vibrations of the mechanism connecting rod and walking beam were developed. Structurally, the mechanism consists of two dyads. As a characteristic of this mechanism, it is noticed the presence of a flexible element (steel cable) that connects the walking beam and the pumping rod. Vibrations were studied theoretically for the connecting rod (2) and, the walking beam (3), and the influence of the pumping process dynamic parameters was experimentally determined.

- Mathematical models

The mathematical model of longitudinal and transverse vibrations of the links 2 and 3 considered linear-elastic straight beams (Fig. 1) were developed [7] and solved as follows.

From a preliminary rigid model kinematic analysis, the following kinematic parameters were known: $(x_A, y_A), (x_{O_2}, y_{O_2})$ —coordinates of the potential pairs of the dyad; $\vec{v}_A^E(t), \vec{v}_{O_2}^E(t)$ —the speed of the characteristic points A and O_2 with respect to the global marker (E); $\vec{a}_A^E(t), \vec{a}_{O_2}^E(t)$ —the acceleration of pairs A and O_2 with respect to the global marker (E); $\overset{E \rightarrow P'}{\omega}_2(t)$ —instantaneous absolute angular velocity of marker (P') with respect to the global marker (E); $\overset{E \rightarrow P''}{\omega}_3(t)$ —instantaneous absolute angular velocity of marker (P'') with respect to the global marker (E); $\overset{E \rightarrow P'}{\varepsilon}_2(t)$ —instantaneous absolute angular acceleration of marker (P') with respect to

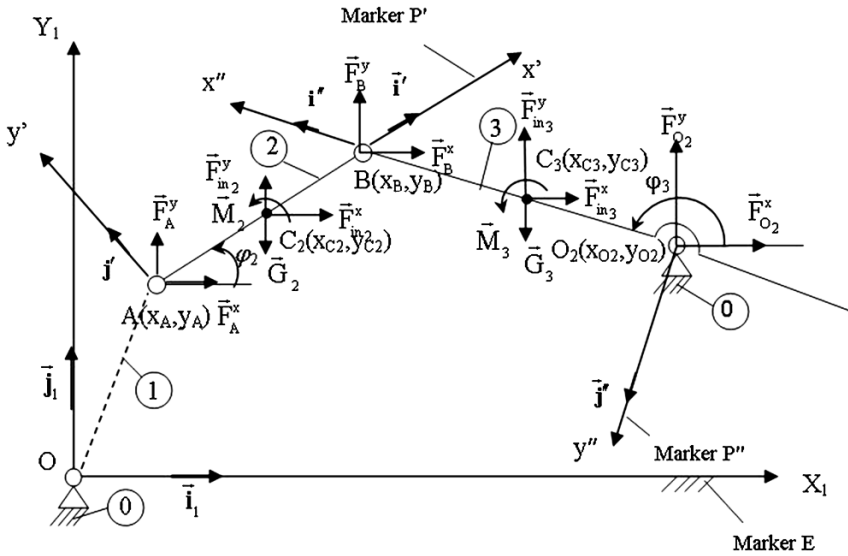


Fig. 1 Kinestatic model of the mechanism

the global marker (E); $\epsilon_3^{E \rightarrow P''}(t)$ —instantaneous absolute angular acceleration of marker (P'') with respect to the global marker (E); L_2, L_3 —the lengths of the dyad un-deformed links. It was considered that the forces and moments acting per unit length of the dyad links were zero, i.e.:

$$\begin{aligned} \bar{f}_2(x, t) = f_2'(x, t)\bar{i}' + f_2''(x, t)\bar{j}' = 0; \quad m_2(x, t) = 0 \\ \bar{f}_3(x, t) = f_3'(x, t)\bar{i}'' + f_3''(x, t)\bar{j}'' = 0; \quad m_3(x, t) = 0 \end{aligned} \tag{1}$$

The boundary conditions of the problem were considered as follows:

$$\begin{aligned} u_2'(0, t) = 0, u_2'(L_2, t) = 0, u_3'(0, t) = 0, u_3'(L_3, t) = 0; \\ \frac{\partial^2 u_2''(0, t)}{\partial x^2} = \frac{\partial^2 u_2''(L_2, t)}{\partial x^2} = 0; \quad \frac{\partial^2 u_3''(0, t)}{\partial x^2} = \frac{\partial^2 u_3''(L_3, t)}{\partial x^2} = 0 \end{aligned} \tag{2}$$

where: $\bar{u}_2(x, t) = u_2'(x, t)\bar{i}' + u_2''(x, t)\bar{j}'$ —the linear-elastic deformation of the link (2); $\bar{u}_3(x, t) = u_3'(x, t)\bar{i}'' + u_3''(x, t)\bar{j}''$ —the linear-elastic deformation of the link (3). The initial conditions of the problem were considered of the following form:

$$\bar{u}_2(x, 0) = \vec{0}, \quad \bar{u}_3(x, 0) = \vec{0}; \quad \frac{\partial \bar{u}_2(x, 0)}{\partial t} = \vec{0}, \quad \frac{\partial \bar{u}_3(x, 0)}{\partial t} = \vec{0}. \tag{3}$$

The vibrations mathematical model of a linear-elastic rectilinear kinematic element, with constant section, in a planar motion was deduced in [3] as a system of decoupled equations, having the form:

$$\begin{aligned}
 c^2 \frac{\partial^2 u_1}{\partial x^2} - \frac{\partial^2 u_1}{\partial t^2} + \omega^2 u_1 + \left(v_{O_2} \omega - a_{O_1} + \omega^2 x + \frac{f_1}{\rho} \right) &= 0; \\
 EI \frac{\partial^4 u_2}{\partial x^4} + \rho A \frac{\partial^2 u_2}{\partial t^2} + \omega^2 A \rho u_2 + (\rho A a_{O_2} + \rho A \omega v_{O_1} + \rho A \varepsilon x - f_2) &= 0
 \end{aligned}
 \tag{4}$$

where: E —the longitudinal modulus of elasticity; ρ —the linear specific mass of the link; $\vec{u}(x, t) = u_1(x, t)\vec{i} + u_2(x, t)\vec{j}$ —the linear-elastic displacement; $u_1(x, t)$ —the longitudinal displacement; $u_2(x, t)$ —the transverse displacement; $\vec{\omega}(t)$ —the angular velocity; $\vec{\varepsilon}(t)$ —the angular acceleration; A —the cross-sectional area of the link; I —the moment of inertia of beam cross-sectional geometry with respect to its neutral axis; $\vec{v}_O(t) = v_{O1}(t)\vec{i} + v_{O2}(t)\vec{j}$ —the speed of the origin O of the proper reference system; $\vec{a}_O(t) = a_{O1}(t)\vec{i} + a_{O2}(t)\vec{j}$ —the acceleration of the origin O of the proper reference system; $\vec{f}(x, t) = f_1(x, t)\vec{i} + f_2(x, t)\vec{j}$ —the external force per unit length of the link.

The longitudinal and transverse deformations of the dyad ABO₂ links were determined, considering them linear-elastic straight beams and taking into account the constraint forces (reactions) which occurred in the kinematic joints. There were determined first the constraint forces occurring in the kinematic joints of the dyad RRR considering it a rigid model. Besides the known data from the previous paragraph, there were also considered known the followings: the weights of the dyad links: $\vec{G}_2 = -G_2\vec{j}_1$, $\vec{G}_3 = -G_3\vec{j}_1$; the inertia forces and inertia torques acting on the dyad links; $\vec{F}_{in_2} = F_{in_2}^x\vec{i}_1 + F_{in_2}^y\vec{j}_1$; $\vec{M}_2 = M_2\vec{k}_1$; $\vec{F}_{in_3} = F_{in_3}^x\vec{i}_1 + F_{in_3}^y\vec{j}_1$; $\vec{M}_3 = M_3\vec{k}_1$; the coordinates of the dyad links center of mass C₂, respectively C₃, related to the marker (E). The constraint forces (reactions) occurring in the kinematic joints of dyad ABO₂ were determined using the methodology known in the specialty literature. By solving the dyad equilibrium equations system there were determined the following components: $F_A^x, F_A^y, F_B^x, F_B^y, F_{O_2}^x, F_{O_2}^y$. The forces acting per unit length of the dyad links were calculated as follows:

$$\begin{aligned}
 f_2(x, t) &= \frac{x}{L_2} \left\{ \left[\begin{array}{l} (F_A^x + F_B^x + F_{in_2}^x) \cos \varphi_2 + \\ (F_A^y + F_B^y + F_{in_2}^y - G_2) \sin \varphi_2 \end{array} \right] \vec{i} + \left[\begin{array}{l} (F_A^y + F_B^y + F_{in_2}^y - G_2) \cos \varphi_2 + \\ (-F_A^x - F_B^x - F_{in_2}^x) \sin \varphi_2 \end{array} \right] \vec{j} \right\}; \\
 f_3(x, t) &= \frac{x}{L_3} \left\{ \left[\begin{array}{l} (F_B^x - F_{O_2}^x - F_{in_3}^x) \cos(\pi - \varphi_3) + \\ (-F_B^y + F_{O_2}^y + F_{in_3}^y - G_3) \sin(\pi - \varphi_3) \end{array} \right] \vec{i}' + \left[\begin{array}{l} (F_B^y - F_{O_2}^y - F_{in_3}^y + G_3) \cos(\pi - \varphi_3) + \\ (F_B^x - F_{O_2}^x - F_{in_3}^x) \sin(\pi - \varphi_3) \end{array} \right] \vec{j}' \right\}
 \end{aligned}
 \tag{5}$$

The next notations were introduced:

$$\begin{aligned}
 R_2^x(x, t) &= \frac{x}{L_2} \left[\begin{array}{l} (F_A^x + F_B^x + F_{in_2}^x) \cos \varphi_2 + \\ (F_A^y + F_B^y + F_{in_2}^y - G_2) \sin \varphi_2 \end{array} \right]; R_2^y(x, t) = \frac{x}{L_2} \left[\begin{array}{l} (F_A^y + F_B^y + F_{in_2}^y - G_2) \cos \varphi_2 + \\ (-F_A^x - F_B^x - F_{in_2}^x) \sin \varphi_2 \end{array} \right]; \\
 R_3^x(x, t) &= \frac{x}{L_3} \left[\begin{array}{l} (F_B^x - F_{O_2}^x - F_{in_3}^x) \cos(\pi - \varphi_3) + \\ (-F_B^y + F_{O_2}^y + F_{in_3}^y - G_3) \sin(\pi - \varphi_3) \end{array} \right]; R_3^y(x, t) = \frac{x}{L_3} \left[\begin{array}{l} (F_B^y - F_{O_2}^y - F_{in_3}^y + G_3) \cos(\pi - \varphi_3) + \\ (F_B^x - F_{O_2}^x - F_{in_3}^x) \sin(\pi - \varphi_3) \end{array} \right].
 \end{aligned}
 \tag{6}$$

Using them, Eq. (5) became:

$$f_2(x, t) = R_2^x(x, t) \vec{i} + R_2^y(x, t) \vec{j}; f_3(x, t) = R_3^x(x, t) \vec{i}' + R_3^y(x, t) \vec{j}'. \tag{7}$$

Considering the constraint forces (reactions) from the kinematic joints of the dyad, the linear-elastic deformations components of the dyad links during the temporary motion sub-range $[t_k, t_{k+1}]$, $k = \overline{0, n}$, became:

- for the link 2:

$$\begin{aligned}
 u'_{2k}(x, t) &= \frac{2}{L_2} \sum_{n=1}^{\infty} \left\{ R_{2k}^{*x}(n) \cos \left(\sqrt{c^2 \alpha_n^2 - \dot{\varphi}_{2k}^2} \cdot t \right) + \frac{1}{\sqrt{c^2 \alpha_n^2 - \dot{\varphi}_{2k}^2}} \cdot \int_0^t \frac{R_{2k}^{*x}(n, \tau)}{\rho} \sin \left[\sqrt{c^2 \alpha_n^2 - \dot{\varphi}_{2k}^2} (t - \tau) \right] d\tau + \frac{2}{c^2 \alpha_n^2 - \dot{\varphi}_{2k}^2} \cdot \left[\frac{L_2}{\pi \cdot n} (1 - (-1)^{n+1}) (\dot{y}_{Ak} \dot{\varphi}_{2k} - \ddot{x}_{Ak}) + \frac{L_2^2}{\pi \cdot n} (-1)^{n+1} \dot{\varphi}_{2k}^2 \right] \sin^2 \left(\frac{\sqrt{c^2 \alpha_n^2 - \dot{\varphi}_{2k}^2}}{2} \cdot t \right) \right\} \sin(\alpha_n x); \\
 u''_{2k}(x, t) &= \frac{2}{\rho A_2 L_2} \sum_{n=1}^{\infty} \left\{ \rho A_2 R_{2k}^{*y}(n) \cos \left(\sqrt{\frac{EI_2 \alpha_n^4 + \rho A_2 \dot{\varphi}_{2k}^2}{\rho A_2}} \cdot t \right) + \sqrt{\frac{\rho A_2}{EI_2 \alpha_n^4 + \rho A_2 \dot{\varphi}_{2k}^2}} \cdot \int_0^t \left[-R_{2k}^{*y}(n, \tau) \sin \left(\sqrt{\frac{EI_2 \alpha_n^4 + \rho A_2 \dot{\varphi}_{2k}^2}{\rho A_2}} \cdot (t - \tau) \right) \right] \cdot d\tau - \frac{2 \rho A_2}{EI_2 \alpha_n^4 + \rho A_2 \dot{\varphi}_{2k}^2} \cdot [\rho A_2 \ddot{y}_{Ak} \cdot \frac{L_2}{\pi \cdot n} (1 + (-1)^{n+1}) + \rho A_2 \dot{x}_{Ak} \dot{\varphi}_{2k} \frac{L_2}{\pi \cdot n} (1 + (-1)^{n+1}) + \rho A_2 \ddot{\varphi}_{2k} (-1)^{n+1} \frac{L_2^2}{\pi \cdot n}] \cdot \sin^2 \left(\sqrt{\frac{EI_2 \alpha_n^4 + \rho A_2 \dot{\varphi}_{2k}^2}{\rho A_2}} \cdot t \right) \right\} \sin(\alpha_n x).
 \end{aligned}
 \tag{8}$$

- for the link 3:

$$\begin{aligned}
 u'_{3k}(x, t) &= \frac{2}{L_3} \sum_{n=1}^{\infty} \left\{ R_{3k}^{*x}(n) \cos\left(\sqrt{c^2\alpha_n^2 - \dot{\varphi}_{3k}^2} \cdot t\right) + \frac{1}{\sqrt{c^2\alpha_n^2 - \dot{\varphi}_{3k}^2}} \right. \\
 &\cdot \int_0^t \frac{R_{3k}^{*x}(n, \tau)}{\rho} \sin\left[\sqrt{c^2\alpha_n^2 - \dot{\varphi}_{3k}^2}(t - \tau)\right] d\tau + \frac{2}{c^2\alpha_n^2 - \dot{\varphi}_{3k}^2} \cdot \\
 &\cdot \left. \left[\frac{L_3^2}{\pi \cdot n} (-1)^{n+1} \dot{\varphi}_{3k}^2 \right] \sin^2\left(\frac{\sqrt{c^2\alpha_n^2 - \dot{\varphi}_{3k}^2}}{2} \cdot t\right) \right\} \sin(\alpha_n x); \tag{9} \\
 u''_{3k}(x, t) &= \frac{2}{\rho A_3 L_3} \sum_{n=1}^{\infty} \left\{ \rho A_3 R_{3k}^{*y}(n) \cos\left(\sqrt{\frac{EI_3\alpha_n^4 + \rho A_3 \dot{\varphi}_{3k}^2}{\rho A_3}} \cdot t\right) + \sqrt{\frac{\rho A_3}{EI_3\alpha_n^4 + \rho A_3 \dot{\varphi}_{3k}^2}} \right. \\
 &\cdot \int_0^t \left[-R_{3k}^{*y}(n, \tau) \sin\left(\sqrt{\frac{EI_3\alpha_n^4 + \rho A_3 \dot{\varphi}_{3k}^2}{\rho A_3}} \cdot (t - \tau)\right) \right] \cdot d\tau - \frac{2\rho A_3}{EI_3\alpha_n^4 + \rho A_3 \dot{\varphi}_{3k}^2} \cdot \\
 &\cdot \left. \left[\rho A_3 \ddot{\varphi}_{3k} (-1)^{n+1} \frac{L_3^2}{\pi \cdot n} \right] \cdot \sin^2\left(\sqrt{\frac{EI_3\alpha_n^4 + \rho A_3 \dot{\varphi}_{3k}^2}{\rho A_3}} \cdot t\right) \right\} \sin(\alpha_n x)
 \end{aligned}$$

where: $\alpha_n = \frac{\pi \cdot n}{L_2}$ for the link 2; $\alpha_n = \frac{\pi \cdot n}{L_3}$ for the link 3; $\dot{\varphi}_{2k} = \omega_{2k}$, $\dot{\varphi}_{3k} = \omega_{3k}$ — instantaneous absolute angular velocities of the dyad links; $\ddot{\varphi}_{2k} = \varepsilon_{2k}$, $\ddot{\varphi}_{3k} = \varepsilon_{3k}$ — instantaneous absolute angular accelerations of the dyad links. The following input data were considered: the length of the mechanism links, namely the crank, the connecting rod, the walking beam, steel cable and polished rod; the coordinates of the bearing center O_2 ; the wellbore coordinates; the masses of the mechanism component kinematic elements; the variation law of the crank angle: $\varphi(t) = 0.724 \cdot t$.

- Numerical processing

By numerical processing of the mathematical models presented above the time variation diagrams of the linear elastic displacements were obtained in the Maple

Fig. 2 The time variation diagram of the walking beam linear elastic longitudinal displacements

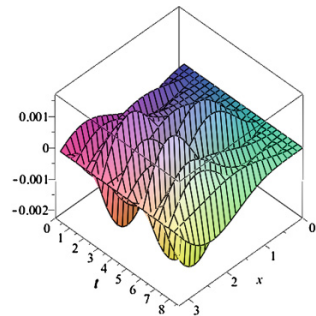
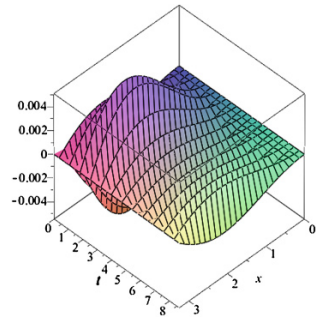


Fig. 3 The time variation diagram of the walking beam linear elastic transverse displacements



programming environment. For example, in Figs. 2 and 3 there are presented the time variation diagrams of the longitudinal and transverse linear elastic displacements of the walking beam.

3 Experimental Modeling and Virtual Prototyping in Dynamical Regime

Another way to identify the dynamic response of the mechanism is the dynamic analysis when kinematic elements are considered as rigid bodies, except the cable of steel connecting the walking beam and the pumping rod. It is a modal-dynamic analysis mainly focused on determining the time variation law of the moment from the driving joint. This problem will be treated and published separately, but some of the results obtained by modeling with ADAMS software are certified and shown here. The time variation law of the force acting upon the polished rod experimentally determined is presented in Fig. 4. The angular velocity variation law presented in Fig. 5 was determined by the dynamic analysis of the mechanism and it will be presented in detail in another paper. It has been experimentally determined the law of variation of the angle of rotation of the walking beam as seen in Fig. 6, law used to process mathematical models for analyzing the walking beam vibration.

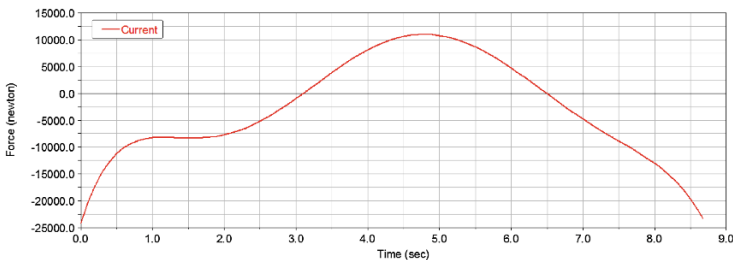


Fig. 4 The time variation law of the F_p force acting on the pumping rod

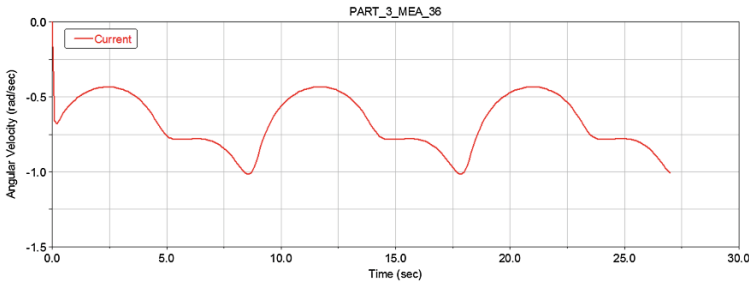


Fig. 5 The time variation law of the angular velocity of the motor joint

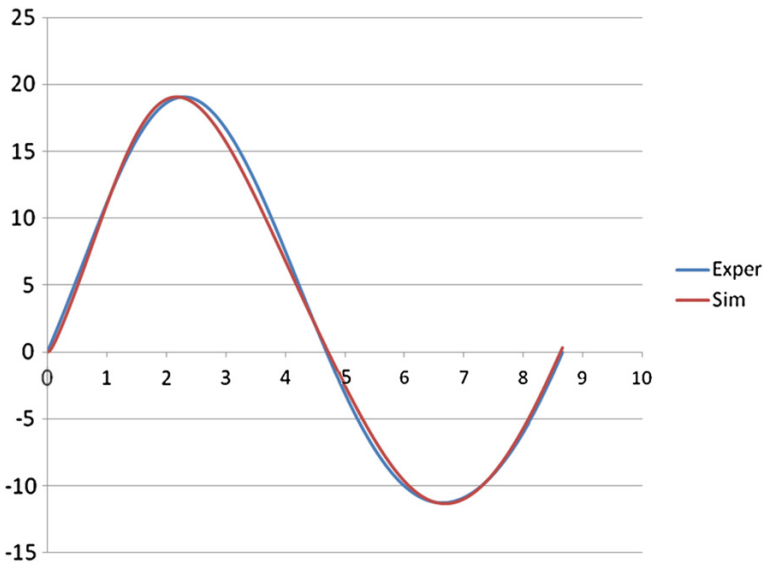


Fig. 6 Diagram of time variation of the walking beam angle of rotation given by the experiment and the one obtained by modeling and simulation in ADAMS

In Fig. 6 there are shown two diagrams in order to compare the variation of the angle of rotation of the walking beam given by the experiment and the one obtained by modeling and simulation in dynamic regime using ADAMS programming environment, for a full cycle of 8.67 s.

4 Conclusions

For the studied oil pumping unit system mechanism there were determined the mathematical models for linear elastic longitudinal and transverse displacements of the connecting rod 2—Eq. (8) and the walking beam 3—Eq. (9), on the motion

temporary sub-range $[t_k, t_{k+1}]$, $k = \overline{0, n}$, considering the constraint (reaction) forces acting in the joints. These mathematical models processing in MAPLE programming environment led to the time variation diagrams of longitudinal and transverse elastic deformation presented as example for the walking beam by Fig. 2 and, respectively, Fig. 3. The time variation diagrams for longitudinal and transverse elastic deformations were processed for the all length of the link but, considering the software flexibility, it might be obtained the time variation laws of the deformation for different points along the links length. Small values of deformations were justified by the high stiffness of each of the two kinematic elements (connecting rod 2 and walking beam 3). The force acting upon the polished rod was experimentally determined as presented by Fig. 4. The variation of the angle of rotation of the walking beam given by the experiment and the one obtained by modeling and simulation in dynamic regime using ADAMS programming environment were compared for a full cycle of operation (Fig 5).

References

1. Arora JS, Dutta A (1997) Explicit and implicit methods for design sensitivity analysis of nonlinear structures under dynamic loads. *Appl Mech Rev Trans ASME* 50:S11–S19
2. Bucher I (2002) Parametric optimization of structures under combined base motion direct forces and static loading. *J Vibr Acoust Trans ASME* 124:132–140
3. Buculei M (1981) Mouvements aleatoires des mecanismes plans a elements deformables. *Rev Roum Sci Techn Mec app* 26:2
4. Chahande AI, Arora JS (1993) Development of a multiplier method for dynamic response optimization problems. *Struct Optim* 6:69–78
5. Kang BS, Park GJ (2005) Optimization of flexible multibody dynamic systems using the equivalent static load method. *Am Inst Aeronaut Astronaut J* 43(4):846–852
6. Kim NH, Choi KK (2001) Design sensitivity analysis and optimization of nonlinear transient dynamics. *Mech Struct Mach* 29:351–371
7. Nanu G, Dumitru N (2001) *Mecanisme cu bare-teorie si aplicatii*. Ed. Universitaria, Craiova, Romania, ISBN 973-8043-49-2
8. Wang BT (2002) Prediction of impact and harmonic forces acting on arbitrary structures: theoretical formulation. *Mech Syst Sig Process* 16:935–953

Dimensioning the NC: Axes of a Radial Cam Grinding Machine

V. Crhák, P. Jirásko and M. Václavík

Abstract The computer program deals with the dimensioning of drives and optimizing structural nodes parameters of the radial cam grinder controlled with a three-axis control system. Source information for dimensioning drives is the radial cam contour and a number of structural and technological parameters, such as maximum spindle torque, grinding tool diameter, feed along the cam surface, etc. Conceptually, it is considered with mechanisms with constant gear between the working motion of NC axes and the servo motor (gearboxes and linear ball screws). The calculation results are performance characteristics for each servo motor and the optimized parameters of structural nodes. These parameters are driving torques (maximum, effective) and speed (maximum), constant gear ratios, pitch and diameters of ball screws, etc. It is also considered the positional deviation caused by the compliances of the gear mechanisms.

Keywords NC axis · Drive · Program · Design

1 Introduction

The issues of dimensioning and optimizing the NC axes of the control system of a radial cam working machine (in general, with milling and grinding technologies) are based on the productivity requirements of a particular type of a cam manufactured in series. The customer presents a request for the production of a specific radial cam with the desired productivity and geometric precision of its contour.

V. Crhák (✉) · P. Jirásko · M. Václavík
VÚTS, a.s., Liberec, Czech Republic
e-mail: vladislav.crhak@vuts.cz

P. Jirásko
e-mail: petr.jirasko@vuts.cz

M. Václavík
e-mail: miroslav.vaclavik@vuts.cz

There is designed the production technology of the cam contour (also with the possibility of milling as a roughing operation and a grinding as a finishing operation) and a design concept of NC axes kinematic chains [1]. There are established requirements for gearing mechanisms, the performance of the grinding spindle and there is left to choose the appropriate servo drives (actuators). On the basis of the above requirements, it is necessary to get an idea of the dynamic demands on all the elements of NC axes kinematic chains, including drives. For this purpose has been developed computing program for dimensioning and optimizing the design nodes (groups) and drives of those machine NC axes kinematic chains.

The NC axes system is based on two axes of translational movement (V , Z) and one axis of rotational movement (C). Interpolating axes are rotational C and translational V whereas C —axis is carried by V —axis [2]. The positioning Z —axis has a defined law of displacement which is independent on the cam contour; working motion of this axis is given by grinding technology.

There was designed a prototype of single-purpose machine *BRV-300 CNC radial cam grinder* [3] in VÚTS, a.s. in the Department of Mechatronics (company deals with research, development and manufacture of machinery and equipment for manufacturing). This machine was awarded with an honorable mention at the MSV 2012 (International Mechanical Engineering Trade Fair) in Brno (CZ), whose design concept of NC axes and drives are the subject of this paper.

2 Input Parameters

The basic input parameters (Fig. 1) are polar coordinates of the radial cam contour to be ground. This data is specified by the customer or is the result of the kinematic synthesis of a cam mechanism [4].

Another input is a system of four switches according to Fig. 1, defining tool rotation and the position of the ground contour. This contour can be realized by external or internal groove wall. Rotation of the tool is deduced from the front view to a clamped cam whereas *PLUS* sense is clockwise.

Input parameters for the computation of the dynamics of interpolating axes C and V are geometric (tool diameter), speed (tool feed), force (spindle torque), as well as mass parameters, gear ratios and parameters of components stiffness (gearboxes and linear transducers).

The last inputs are the parameters and displacement diagram of Z —axis.

3 Inputs and Corresponding Outputs

The rotation (C —axis) and translation (V , Z —axes) are regarded as working axes movements, which are involved in the ground contour of the radial cam (interpolation movement C and V , positioning motion Z). There is generally applied the following kinematic chain for all three axes:

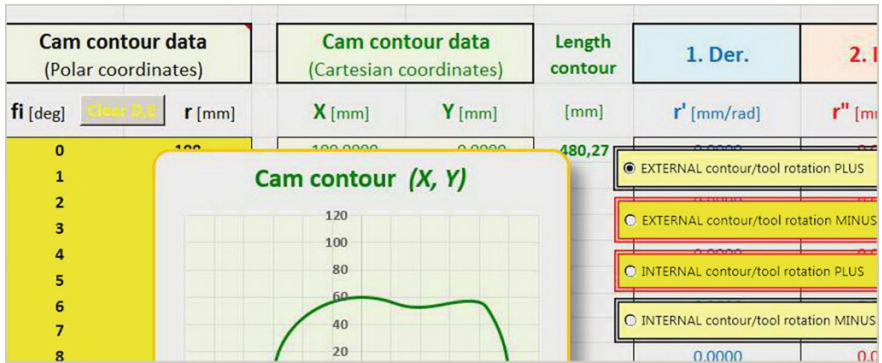


Fig. 1 Data of the ground radial cam contour

C—axis—between working motion and servomotor, there is an arbitrary rotational gear (e.g. planetary gearbox) with a constant gear ratio; V, Z—axes—between working motion and servomotor in the direction from the servomotor, there is an arbitrary rotational gear (e.g. planetary gearbox, toothed gearing or belt drive) with a constant gear ratio, followed by a rotary—linear gear (e.g. ball screw) with a constant gear ratio.

3.1 Tangential Working Force to the Worked Radial Cam Contour

Working force $F [N]$ is derived from the maximum torque of used tool spindle and tool diameter. This force is decomposed into rectangular components, which burden the axes C and V.

There are the following machining options: Internal and external contour; Down-feed and up-feed working based on the sense of tool rotation; Ascending and descending part of the radial cam contour (those parts are automatically evaluated by the program based on the sense of production data, derivations and options of switches according to Fig. 1)

3.2 Dynamics of C: Axis

The following is a listing of outputs according to Fig. 2:

C-axis dynamics—a press button of activating the function of solving the dynamics; $n_C [1/min]$ —Instantaneous speed of C—axis (speed of the workpiece) derived from the defined feed $f [mm/min]$; $M_{SerC} [Nm]$ —driving torque of the servomotor of C—axis under the action of dynamic inertia forces (also with the servomotor rotor) and external working forces; $EKM_C [Nm]$ —effective torque of

Note									[mm]/100
C-axis dynamics									4,46E-04
									EKM _C
C-axis dynamics with external forces (machining, loss), Torsion									
n _C	ω _C	ε _C	M _C	M _{PřeC}	M _{SerC}	n _{SerC}	gama _C	M _{DynSerC}	
[1/min]	[rad/sec]	[rad/sec ²]	[Nm]	[Nm]	[Nm]	[1/min]	[deg]	[Nm]	
1.91	0.2000	0.0000	34.00	1.61	1.61	47.7	2.56E-04	0.0000	

Fig. 2 Outputs of solving the dynamics of C—axis

the C—axis servomotor; n_{max_C} [1/min]—instantaneous maximum speed of the C—axis servomotor; $Max(Abs)$ [deg]—maximum torsion value of C—axis, which is illustratively transferred to the arc length of a 100 [mm] radius.

3.3 Dynamics of V: Axis

It follows the listing of outputs according to Fig. 3. *V-axis dynamics* is a press button of activating the function of solving the dynamics.

Outputs are the following variables, including functional outputs:

v_V [m/sec]—instantaneous speed of V—axis (i.e. instantaneous speed of the cam workpiece itself in direction of V—axis) derived from feed f [mm/min]; M_{SerV} [Nm]—driving moment of the servomotor of V—axis under the action of dynamic inertia (also with the servomotor rotor) and external working forces; EKM_V [Nm]—effective moment of the V—axis servomotor; n_{max_V} [1/min]—instantaneous

Note									PERR_V [mm]
V-axis dynamics									2,24E-03
									EKM _V
V-axis dynamics with external forces (machining, loss), Torsion									
v _V	a _V	F _{Vsuma}	M _{šrV}	M _{PřeV}	M _{SerV}	n _{SerV}	gama _V	M _{DynSerV}	
[m/sec]	[m/sec ²]	[N]	[Nm]	[Nm]	[Nm]	[1/min]	[rad]	[Nm]	
0.00	0.00	0.00	0.00	0.00	0.00	0.00	0.00E+00	0.0000	

Fig. 3 Dynamics of V—axis

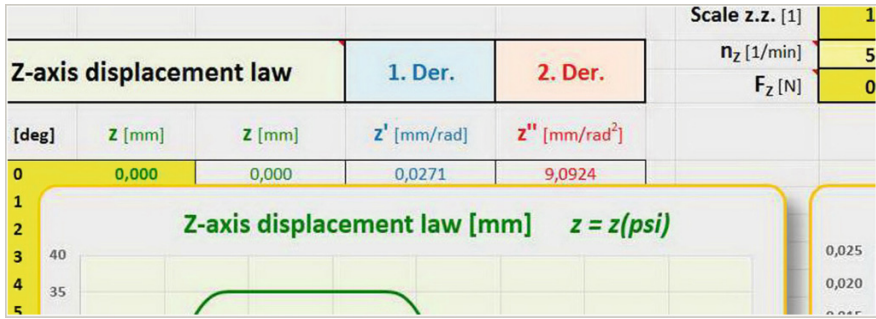


Fig. 4 Displacement diagram of positioning Z—axis

maximum speed of the V—axis servomotor; $Max(Abs) [deg]$ —maximum value of $gama_V$ torsion of V—axis, which is converted to a positioning error of V— $PERR_V [mm]$ coordinate.

3.4 Dynamics of Z: Axis

Definition of the displacement diagram of positioning Z—axis:

Z—axis motion (displacement law) is independent on the cam contour and is only related to grinding technology This axis makes the so-called oscillating movement (Fig. 4).

Scale z.z. [-] (input data)—a scale of displacement diagram. This parameter transforms displacement diagram including derivations; $n_z [1/min]$ (input data), it is a speed of the virtual shaft of Z—axis (*Master*); $F_z [N]$ (input data)—a specification of the anticipated machining force in Z—axis.

Outputs are similar to those in V—axis, therefore, we do not address them in the paper.

This program part can generally solve the kinematics and dynamics of general displacement law implemented by an electronic cam with a working sliding motion. The issues of implementing the displacement diagrams of electronic cams are dealt with in [1].

4 Basic Computing Relations

Only basic computing relations with usual generally specified units are mentioned.

Tangential machining force $F[N], M_k = F \frac{d}{2}$, where M_k is max. torque of tool spindle;

$$F = \frac{2M_k}{\left(\frac{d}{1000}\right)} = 2000 \frac{M_k}{d}; [N] = [Nm, mm] \quad (1)$$

Angle α [deg] as a normal angle of the machined radial cam contour;

$$\alpha = \arctg \frac{dr}{rd\varphi}; \frac{dr}{d\varphi} = r'; \alpha = \arctg \frac{r'}{r}; [rad] = \left[\frac{mm}{rad}, mm \right] \quad (2)$$

Tangential machining force F [N] decomposed into components F_C (C—axis) and F_V (V—axis). Generally, it is valid: $F_C = F \cos \alpha$; $F_V = F \sin \alpha$ [5].

Sense (signum) of forces F_C and F_V depends on the 1st derivation r' $\left[\frac{mm}{rad}\right]$, tool rotation (plus/minus) and the machined contour (external/internal), see the switches in Fig. 1.

4.1 Dynamics of C: Axis

The basic technological condition of the radial cams grinding is tool constant feed f $\left[\frac{mm}{min}\right]$ along the cam contour. Instantaneous angular velocity ω_C $\left[\frac{rad}{sec}\right]$ and angular acceleration ε_C $\left[\frac{rad}{sec^2}\right]$ on the given contour radius vector r [mm] result from feed f . Constant feed f condition also applies to V—axis.

$$\omega_C = \left(\frac{1}{60}\right) \frac{f}{r} \cos \left(\arctg \frac{r'}{r}\right); \left[\frac{rad}{sec}\right] = \left[\frac{mm}{min}, \frac{mm}{rad}, mm\right] \quad (3)$$

$$\varepsilon_C = -\left(\frac{1}{60}\right) \frac{f}{r} \sin \alpha \frac{\omega_C}{1 + \left(\frac{r'}{r}\right)^2} \frac{r''}{r}; \left[\frac{rad}{sec^2}\right] = \left[\frac{mm}{min}, \frac{mm}{rad}, \frac{mm}{rad^2}, \frac{rad}{sec}, mm\right] \quad (4)$$

Driving torque of the servomotor M_{SerC} [Nm] has to be distinguished from the driving torque usable on the servomotor shaft. M_{SerC} is involved in the dynamics of the own servomotor rotor (the same applies to V and Z—axes) [6].

$$M_{SerC} = \left(\frac{J_{Obr} + J_{Csuma}}{i_{PreC}^2} + J_{PreC} + J_{SerC} \right) \varepsilon_C i_{PreC} + \frac{F_C r}{1000 i_{PreC}} + M_{ZtrPreC} \quad (5)$$

4.2 Dynamics of V: Axis

Speed v_V $\left[\frac{m}{sec}\right]$;

$$v_V = \left(\frac{1}{60 \cdot 1000} \right) f \sin \alpha; \left[\frac{m}{sec} \right] = \left[\frac{mm}{min} \right] \quad (6)$$

Acceleration $a_V \left[\frac{m}{sec^2} \right];$

$$a_V = \left(\frac{1}{60 \cdot 1000} \right) f \cos \alpha \frac{\omega_C}{1 + \left(\frac{r'}{r} \right)^2} \frac{r''}{r}; \left[\frac{m}{sec^2} \right] = \left[\frac{mm}{min}, \frac{mm}{rad}, \frac{mm}{rad^2}, \frac{rad}{sec}, mm \right] \quad (7)$$

$$\text{optionally } a_V = \left(\frac{1}{1000} \right) (r'' \omega_C^2 + r' \varepsilon_C); \left[\frac{m}{sec^2} \right] = \left[\frac{mm}{rad^2}, \frac{rad}{sec}, \frac{mm}{rad}, \frac{rad}{sec^2} \right] \quad (8)$$

Driving torque of the servomotor $M_{SerV} [Nm];$

$$M_{SerV} = \left[\frac{m_V \left(\frac{H_V}{2\pi \cdot 1000} \right)^2}{i_{P r e V}^2} + \frac{J_{S r V}}{i_{P r e V}^2} + J_{P r e V} \right] \varepsilon_{SerV} + \frac{F_{Vsuma} \left(\frac{H_V}{2\pi \cdot 1000} \right)}{i_{P r e V}} + \quad (9)$$

4.3 Dynamics of Z: Axis

Basically, it is implementing the displacement diagram of electronic cam, thus $z = z(\psi_M) [mm]; \psi_M [deg]; \psi_M \in (0, 360); \psi_M$ is virtual shaft (*Master*).

Speed $v_Z \left[\frac{m}{sec} \right];$

$$v_Z = \left(\frac{1}{1000} \right) z' \omega_M; \left[\frac{m}{sec} \right] = \left[\frac{mm}{rad}, \frac{rad}{sec} \right] \quad (10)$$

Acceleration $a_Z \left[\frac{m}{sec^2} \right];$

$$a_Z = \left(\frac{1}{1000} \right) z'' \omega_M^2; \left[\frac{m}{sec^2} \right] = \left[\frac{mm}{rad^2}, \frac{rad}{sec} \right] \quad (11)$$

Other force values are analogous to V—axis.

5 Conclusions

Dimensioning the drives and optimizing all the used structural elements with their parameters in interaction is a complicated matter where the individual structural elements cannot be considered separately without mutual relations. In its particulars, the choice seems to be simple, but it must be realized that the optimum design

result of the kinematic chain of NC axes of a machine is a combination of many parameters and quantities.

Performance, speed and maximum torque of grinding spindle directly relate to used tool (diameter in relation to the spindle speed and cutting speed); the choice of conventional grinding with grinding wheel trueing or the use of wheels with CBN (cubic boron nitride, it is a type of cutting tool material offering a high hardness); tool feed rate along the ground contour; material and hardness of the ground cam contour and technology of grinding (roughing, finishing, the size of material removals in grinding cycles). Gear ratios of rotational constant gears (planetary gearboxes, worm gearboxes, toothed gears, belt gears) have connections with stiffness parameters and efficiency of gears, ball screw pitch; diameters and efficiency. An important part of the manufacturing accuracy is the choice of measuring system, which can be realized by direct or indirect measurement. Whole project is completed by the selection of an suitable servomotor.

The final choice of a servomotor must comply with the main catalog parameters: *maximum torque*, *effective torque* and *maximum instantaneous speed*.

There is a large number of structural nodes on the market (gearboxes, linear units) and it is necessary to match their combinations with drives and the selected technology of machining and to optimize them e.g. with this program.

To making the program have led demands on effective design of a single-purpose machine and fast price cost calculation based on known inputs submitted by the customer.

The main advantage is a reduction of the cost of creating a price quotation and the total costs reduction of machine production, which is designed with an emphasis on maximum utilization of sub-elements.

The program has no known disadvantages, because it is still being developed, so that any deficiencies are fixed immediately.

References

1. Jirásko P (2010) Methodology of electronic cam applications in drives of working links of mechanisms of processing machines, Dissertation, TU Liberec CZ
2. Jirásko P, Crhák V, Bureš P (2012) The conception of the control system of radial cam grinder, conference IFToMM 2012, ISBN 978-94-007-5124-8, p. 495
3. VÚTS, a.s. (2012) The BRV-300 CNC radial cam grinder. Project: FR-TI1/594—investigation of sophisticated methods for the design and development of single-purpose machines, components and peripheries of processing machines (2009–2013, MPO/FR), RIV/46709002: / 12:#0000509
4. Koloc Z, Václavík M (1993) Cam mechanisms. Elsevier
5. Marek J (2010) A kolektiv: konstrukce CNC obráběcích strojů, MM publishing 2010, ISBN 978-80-254-7980-3
6. Suk-Hwan Suh, Seong-Kyoon Kang, Dae-Hyuk Chung, Ian stroud: theory and design CNC systems, Springer, e-ISBN 978-1-84800-336-1

Efficiency Analysis of Shifted Spur Gear Transmissions

A. Diez-Ibarbia, A. Fernández del Rincón, M. Iglesias, A. De Juan, P. García and F. Viadero

Abstract A quasi-static analysis of a shifted spur gear transmission is presented in this work. With this study, the influence of the profile modifications and the dissipative effects on the efficiency is assessed. Among the dissipative effects, friction between teeth in presence of lubricant is studied in this work, because of its important effect on power losses in the operating conditions used. Friction forces have been implemented by means of a Coulomb's model with a variable friction coefficient (VFC). One VFC formulation have been developed derived from the well-known Niemann formulation and compared with a second one developed by Hai Xu. The final aim is to assess the impact on the efficiency of both the frictional effect and the profile shifting.

Keywords Efficiency · Power losses · Friction coefficient · Load sharing · Sliding velocity

1 Introduction

The sources of power losses in gear transmissions can be typically classified by their load dependency. Friction or rolling forces among gear teeth are classified as load-dependent losses, while the non load-dependent losses are due to the fluid motion involved (lubricant, refrigerant, air) [8, 11–13].

In this study less than 6.000 rpm speed is used, thus, only load-dependent losses are considered. Special attention is paid to the friction effect on the efficiency calculation, neglecting the rolling effects contribution due to its lesser impact in the study conditions [1, 7]. The friction effect has been studied through the use of different formulations of the Friction Coefficient (FC) [12].

A. Diez-Ibarbia · A. Fernández del Rincón · M. Iglesias · A. De Juan · P. García · F. Viadero (✉)
Mechanical Engineering Department, University of Cantabria, Santander, Spain
e-mail: fernando.viadero@unican.es

The aim of this study is to present and determine the influence of the friction and the shifting modifications on the energetic efficiency of this mechanical system. In this work, the shift factors of gears 1 and 2 are constrained to be equal in absolute value with opposite signs ($x_1 + x_2 = 0$ is fulfilled for every case).

To achieve this goal, the use of the load contact model (LCM) and the methodology of the efficiency calculation previously developed by the authors [3–6] is applied.

The model features have been extended in order to include the analysis of shifted gears as they are widely used in real transmission applications. Besides, it is foreseen that this modification may have an impact on the efficiency among other parameters, so, determining this impact is a question of great interest.

2 Efficiency Calculation

As it was presented in a previous work [3], an efficiency calculation methodology has been developed by the authors. The mechanical efficiency as the relationship between energy output and energy input for a given period of time is defined as.

$$\eta = \frac{P_{out}}{P_{in}} = \frac{P_{in} - P_{loss}}{P_{in}} \quad (1)$$

Regarding the efficiency calculation, it was stated that two different approaches can be done (numerical and analytical), depending on the friction coefficient and load sharing chosen in the calculation [3]. In this study the numerical approach is used because only variable friction coefficient formulation is considered.

Any friction coefficient (FC) and load sharing (LS) formulation could be used so as to obtain the efficiency. Previously to perform this calculation, the loading forces, the sliding velocity and the FC must be obtained for every pair of teeth in contact using a load contact model (LCM).

By means of calculating the power losses in mesh cycle, which is obtained by Eq. (2), the efficiency value could be calculated (Eq. 1).

$$P_{loss,inst} = \sum_{z=1}^N F_R(\theta) * V_s(\theta) = \sum_{z=1}^N \mu(\theta) * F_N(\theta) * V_s(\theta) \quad (2)$$

where N is the number of pairs of teeth in contact, μ is the friction coefficient, F_N is the normal load and V_S is the sliding velocity for each contact.

In the proposed model, instantaneous power losses are obtained using Eq. (3) because of the simplicity of the method, but the same results should be obtained with Eq. (2).

$$P_{loss,inst} = \sum_{z=1}^N (T_{in} * \omega_1 - T_{out} * \omega_2) \tag{3}$$

Defining the power losses along the mesh cycle as:

$$P_{loss} = \frac{\int_{-\frac{\theta_p}{2}}^{\frac{\theta_p}{2}} P_{loss,inst} d\theta}{\theta_p} \tag{4}$$

So as to calculate the efficiency, the power losses calculation is enough to define this value. But, in order to make an assessment of the value obtained, a parameter that comprehend all the effect of the parameters that are involved in the efficiency calculation is necessary. As it has been explained, efficiency mainly depends on sliding velocity, friction coefficient and load sharing. To facilitate the interpretation of the results, the instantaneous power loss factor (H_{vinst}) has been defined as.

$$H_{vinst} = \int_A^E \frac{\mu(\theta) * F_N(\theta) * V_s(\theta)}{F_{Nmax} * V} d\theta \tag{5}$$

3 Friction Coefficient Models

Friction coefficient plays an important role in the methodology with respect to the selection of the approach. In this study, the FC is obtained using two formulations: (i) a variation of Niemann’s proposal [2, 7, 9, 10] and (ii) according to Hai Xu et al. [12]:

Niemann variation FC is formulated as:

$$\mu_m = 0.048 * \left(\frac{F_{bt}}{V_{\Sigma C} * \rho_c} \right)^{0.2} * \eta_{oil}^{-0.05} * R_a^{0.25} * X_L \tag{6}$$

where F_{bt} is the normal applied load in the pitch point, ρ_c is the equivalent curvature radius in the pitch point, b is the gear width, η_{oil} is the oil density, R_a is the roughness, and parameters $V_{\Sigma C}$ and X_L are defined as:

$$V_{\Sigma C} = 2 * V_t * \sin(\alpha_{wr}) \text{ and } X_L = \frac{1}{\left(\frac{F_{bt}(\theta)}{b} \right)^d}; \quad d = 0.0651 \text{ for mineral oil}$$

Taking this formulation as starting point, the following variation of the original equation have been done arriving to obtain variable friction coefficient.

$$\mu(\theta) = 0.048 * \left(\frac{F_{br}(\theta)}{V_{\Sigma C} * \rho_c(\theta)} \right)^{0.2} * \eta_{oil}^{-0.05} * R_a^{0.25} * X_L * \tanh\left(\frac{V_s(\theta)}{v_o}\right) \quad (7)$$

The variation, designed as VFC2 [3], considers the variation in the normal applied load and in the equivalent curvature radius and includes an additional correction to avoid the singularity when the friction force changes its direction. This correction is based on the sigmoid function, where v_o is the sliding speed threshold.

The Hai Xu variable friction coefficient is obtained by means of regression analysis of empirical data:

$$\mu(\theta) = e^{f(SR, P_h, \eta_{oil}, R_a)} * P_h^{b_2} * |SR|^{b_3} * V_e^{b_6} * \eta_{oil}^{b_7} * \rho_c^{b_8} \quad (8)$$

where SR is the sliding to rolling ratio, P_h is the local pressure evaluated in GPa and V_e is the entraining velocity.

$$f(SR, P_h, \eta_{oil}, R_a) = b_1 + b_4 * |SR| * P_h * \log_{10}(\eta_{oil}) + b_5 * e^{-|SR| * P_h * \log_{10}(\eta_{oil})} + b_9 * e^{R_a} \quad (9)$$

In this study, 75 W 90 mineral oil is considered as lubricant and its dynamic viscosity is 10.6 mPa s at the working temperature of 100 °C. Besides, the roughness considered is 0.8 μm in both FC formulations.

4 Results and Discussion

A quasi-static comparison among the efficiency values obtained with each FC considered is done in this study. The working parameters used are presented in Table 1.

In order to distinguish the differences among the two FC formulations, the aforementioned normalized parameters involved in the calculation of efficiency are presented in Fig. 1. As it can be appreciated, the different FC approaches have a big impact on the H_{vinst} , but also cause a slight variation in LS curves.

The power losses during the double contact period are greater in the Hai Xu et al. formulation than in Niemann's. In order to assess the comparison among efficiency values obtained with each friction coefficient considered, these are presented in Fig. 2.

It can be noticed that there is a shift limit value for which the efficiency starts to decrease. The reason for this behavior is that the single contact takes place far from the pitch point region in which neither the sliding velocity nor the friction coefficient are not nearly to be null, turning this fact into a bigger power loss factor (Fig. 3).

Table 1 Operating conditions and pinion/gear parameters

Main parameters			
Number of the pinion teeth	18	Module	3
Number of the gear teeth	36	Face width	26.7 mm
Pressure angle	20°	Mean roughness	0.8 μm
<i>Operating conditions</i>		<i>Power (kW)</i>	<i>Torque (Nm)</i>
OC1	25	159	1,500
OC2	25	40	6,000
OC3	50	159	3,000
OC4	100	637	1,500
OC5	100	159	6,000

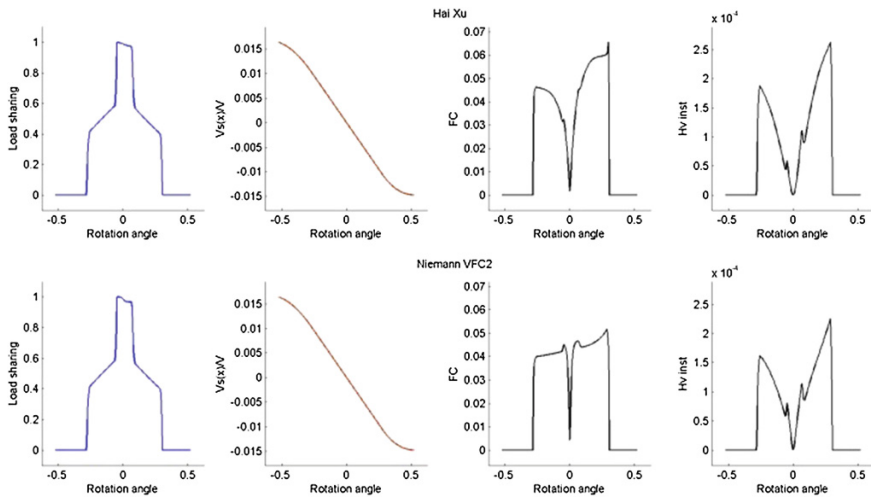


Fig. 1 Comparison between the two formulations. Load sharing, sliding velocity, friction coefficient and instantaneous power loss factor

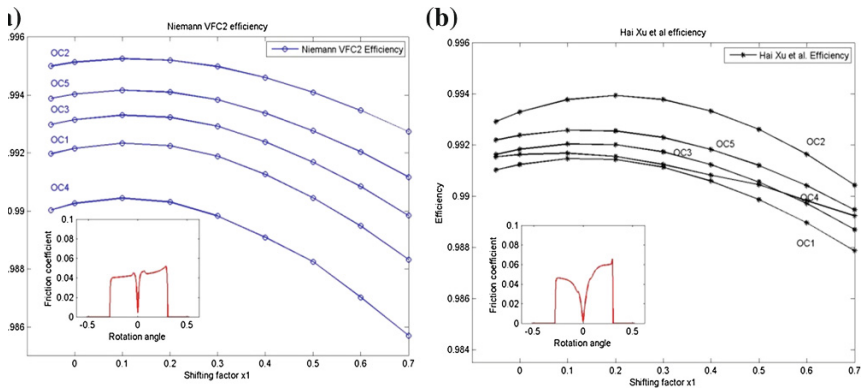


Fig. 2 Comparison of efficiency values using FC of **a** VFC2, **b** Hai Xu et al.

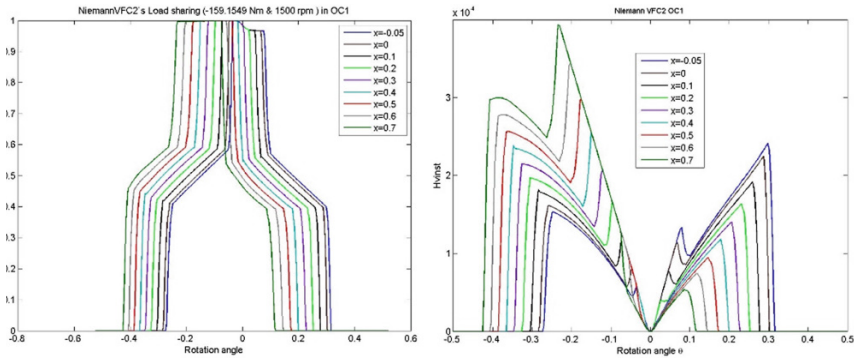


Fig. 3 Load sharing and instantaneous power loss factor for several shifting values in OC1

In Fig. 2 it can be also shown the comparison among operating conditions for each FC formulation, in order to determine the influence of the torque and the speed on the efficiency. Regarding to this, as a general rule, it can be noticed that the higher the torque is, the lower the efficiency value is and the lower the speed is, the lower the efficiency value is.

Moreover, a comparison among FC formulations also can be made, so as to determine how the shape and the parameters of the FC influence the efficiency value. The difference among the efficiency values obtained by using one formulation or another is considerable. As a matter of fact, it can be appreciated whereas with the Niemann formulation, efficiency values are mainly influenced by the torque effect (the higher the torque is, the lower the efficiency value is), with the Hai Xu et al. formulation, both the torque and the speed influence the efficiency value. So as to comprehend why there is this difference, the friction coefficient of both formulations are presented for all shifting cases in OC1 and OC4 (Figs. 4 and 5), assessing the factors that affects each FC formulation.

So as to clarify the comparison among FC formulations, the mean values for one meshing period are presented in Table 2, when there is not profile modification.

From Figs. 4 and 5, some facts related to the friction coefficient dependence can be inferred.

On one hand, the change in the behavior of the friction coefficient when the operating conditions vary can be analyzed. If only Niemann VFC2 is considered (Fig. 4), it can be appreciated that the value of this friction coefficient is highly dependent on the torque (from OC2 to OC4 almost double the FC mean value). That is why the higher is the applied torque, the higher is the value of the friction coefficient, whereas this dependence is not so clear in the Hai Xu et al. formulation. Assessing the Hai Xu et al. formulation (Fig. 5 and Table 2), it can be appreciated the same behavior but only when the contact takes place close to the pitch point region (one pair of teeth in contact). With respect to the FC dependence on the speed, during the double contact period, the lower the speed is, the greater the FC value is. As the

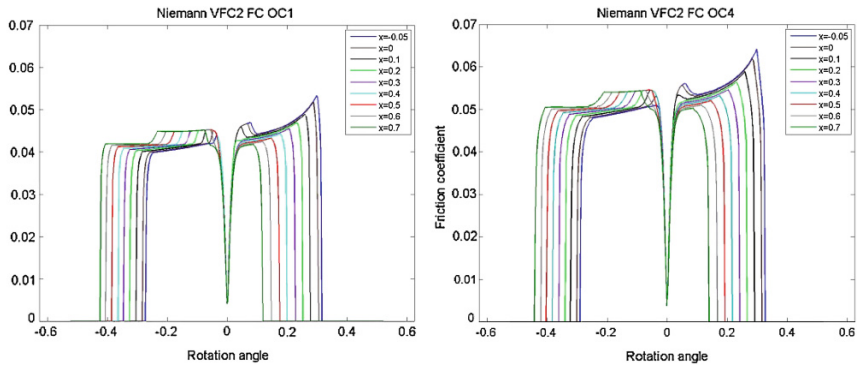


Fig. 4 Niemann VFC2 friction coefficient in OC1 and OC4

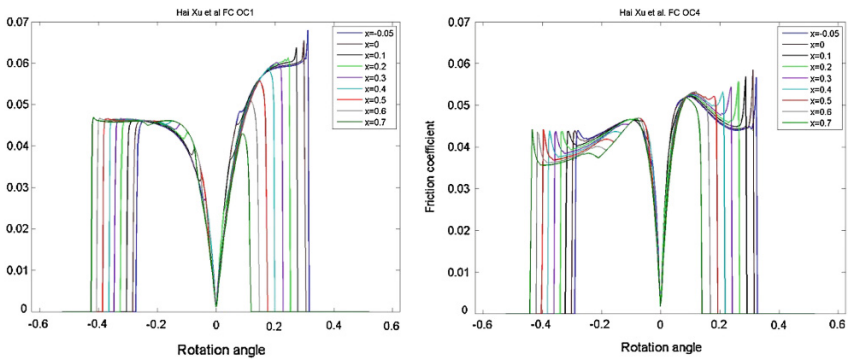


Fig. 5 Hai Xu et al. friction coefficient in OC1 and OC4

Table 2 Friction coefficients mean values and variations when there is not profile shifting

$x = 0$	OC1	OC2	OC3	OC4	OC5
Niemann VFC2	0.0440	0.0275	0.0374	0.0505	0.0329
Hai Xu	0.0421	0.0326	0.0410	0.0437	0.0382

main part of the power losses are during the double contact period (because the sliding velocity achieves its greatest value), in this formulation it can be settled that the speed dependence on the efficiency is stronger than the torque one.

On the other hand, the differences among the friction coefficients with the same operating conditions can be also analyzed. Regarding to this analysis, it can be noticed that only similar results are obtained with low speed and medium torque, being greater the Niemann VFC2 with high level of torque and vice versa with low level of torque.

5 Conclusions

In this study, an efficiency analysis of shifted spur gears has been done using the load contact model and the methodology of the efficiency calculation previously developed by the authors [3–6]. Special attention has been given to dissipative aspects in this kind of systems, specifically, to the friction effect in the calculation of the power losses. The friction, implemented by means of Coulomb model, has been modeled by the use of the Hai Xu formulation and variations of the Niemann formulation, with the aim of determining the influence of the friction on the energetic efficiency of the system.

It can be concluded that an efficiency decrease is obtained when a high shifting value is used (higher than 0.3).

Niemann formulation efficiency values are mainly influenced by the torque level (the higher the torque is, the lower the efficiency value), while the Hai Xu formulation efficiency values are mainly influenced by the speed (the lower the speed is, the lower the efficiency value is).

Only similar efficiency values among formulations are obtained when medium torque and low speed are considered. Hence, it can be concluded that the choice of the FC formulation is going to affect all the parameters involved on the simulation being a crucial aspect so as to obtain a good approximation of the real behavior of the system.

Acknowledgments The authors would like to acknowledge the COST ACTION TU 1105 for supporting this research.

References

1. Anderson NE, Loewenthal SH (1981) Effect of geometry and operating conditions on spur gear system power loss. *J Mech Des Trans ASME*. 103(4):151–159
2. Baglioni S, Cianetti F, Landi L (2012) Influence of the addendum modification on spur gear efficiency. *Mech Mach Theory* 49:216–233
3. Diez-Ibarbia A, Fernández del Rincón A, Iglesias M, Viadero F (2013) Efficiency analysis of shifted spur gears. In: Proceedings of the second conference MeTrApp, Bilbao
4. Fernandez del Rincon A, Viadero F, Iglesias M, de-Juan A, García P, Sancibrian R (2012) Effect of cracks and pitting defects on gear meshing. *Proc IMechE Part C J Mech Eng Sci* 226 (11):2805–2815
5. Fernandez Del Rincon A, Viadero F, Iglesias M, García P, De-Juan A, Sancibrian R (2013) A model for the study of meshing stiffness in spur gear transmissions. *Mech Mach Theory* 61:30–58
6. Fernández A, Iglesias M, de-Juan A, García P, Sancibrián R, Viadero F (2014) Gear transmission dynamic: effects of tooth profile deviations and support flexibility. *Appl Acoust* 77(0):138–149 (3)
7. Höhn BR (2010) Improvements on noise reduction and efficiency of gears. *Meccanica* 45 (3):425–437
8. Martin KF (1978) A review of friction predictions in gear teeth. *Wear* 49(2):201–238

9. Michaelis K, Höhn BR, Hinterstoiber M (2011) Influence factors on gearbox power loss. *Ind Lubr Tribol* 63(1):46–55
10. Ohlendorf H (1958) Verlustleistung und erwärmung von stirnrädern. Dissertation, TU München
11. Sánchez MB (2013) Modelo de cálculo resistente de engranajes cilíndricos de alto grado de recubrimiento. Dissertation, UNED
12. Xu H (2005) Development of a generalized mechanical efficiency prediction methodology for gear pairs. Dissertation, The Ohio State University
13. Yada T (1997) Review of gear efficiency equation and force treatment. *JSME Int J Ser C Dyn Control Rob Des Manuf* 40(1):1–8

Part VII
Dynamics of Multi-body Systems

A New Approach to Eliminate the Constraints Violation at the Position and Velocity Levels in Constrained Mechanical Multibody Systems

P. Flores

Abstract In this work, a general and comprehensive methodology to eliminate the constraints violation at the position and velocity levels is presented. This new approach is derived under the framework of multibody dynamics formulation. The basic idea of this methodology is to add corrective terms to the position and velocity vectors with the intent to satisfy the corresponding kinematic constraint equations. These corrective terms are evaluated as function of the Moore-Penrose generalized inverse of the Jacobian matrix and of the kinematic constraint equations. A planar four bar mechanism is used as a demonstrative example of application, which allows to show the effectiveness of presented method.

Keywords Constraints violation · Equations of motion · Multibody systems

1 Introduction

The equations of motion for constrained mechanical multibody systems are frequently formulated using the Newton-Euler's approach, which is augmented with the acceleration constraint equations. This formulation results in the establishment of a mixed set of differential and algebraic equations, which are solved in order to predict the dynamic behavior of general multibody systems. It is known that the standard resolution of the equations of motion is highly prone to constraints violation because the position and velocity constraint equations are not fulfilled.

The problem of modeling and simulating constrained mechanical systems has been widely studied over the last decades [1–4]. Recent review papers of interest on the formulation of mechanical multibody systems have been provided by Rahnejat [5], Eberhard and Schiehlen [6], Schiehlen [7] and Nikravesh [8]. The various methodologies to formulate constrained mechanical systems differ in the considered

P. Flores (✉)
University of Minho, Braga, Portugal
e-mail: pflores@dem.uminho.pt

principle, type of adopted coordinates, and the selected method for handling constraints in systems characterized by open and closed-chain topologies [9]. The solution of dynamic equations of motion for constrained multibody systems is often performed using Lagrange multipliers technique, which leads to a set of differential-algebraic equations. Except for simple mechanical systems, an analytical solution of the equations of motion cannot be found, and therefore, a numerical solution is required. In the standard Lagrange multipliers technique, the acceleration constraints are taken into account during the numerical solution of the equations of motion and, therefore, there is no violation of the acceleration constraints. In contrast, if the position and velocity constraints are not utilized in the process, violation of the position and velocity constraints will occur due to the numerical integration errors. Thus, special procedures have to be implemented to eliminate or at least minimize such violations [10, 11].

The methods to handle the problem of constraints violation for constrained mechanical systems fall into three main categories: (i) constraint stabilization methods; (ii) coordinate partitioning methods and (iii) direct correction formulations. The constraint stabilization approaches are probably the most popular due to their simplicity and easiness for computational implementation. Yet, their major drawback is the ambiguity in selecting the stabilization parameters, which ultimately can lead to failure simulations, even for systems that have valid solutions. The coordinate partitioning methods have the great merit of allowing the rigorous resolution of the constraint equations at the position, velocity and acceleration levels. Yet, they suffer from poor numerical efficiency due to the requirement for the iterative solution for dependent generalized coordinates in the Newton-Raphson method. Finally, the direct formulations have physical meaning, computational efficiency, but they can exhibit some numerical instability.

Thus, the main emphasis of this work is on the elimination of the constraints violation during the analysis of constrained mechanical multibody systems. Body coordinates formulation is used to describe the system components and the kinematic joints. The equations governing the kinematic and dynamic behavior of the general mechanical systems incorporate corrective terms that can be added to the position and velocity vectors in order to satisfy the corresponding constraint equations. These corrective terms are expressed in terms of the Jacobian matrix and kinematic constraint equations. The described methodology is embedded in the standard method to solve the equations of motion based on the Lagrange multipliers technique. The effectiveness of the presented methodology is shown through the analysis of a four bar mechanism. The outcomes, in terms of constraints violation and computational efficiency, are analyzed and compared with those obtained with the standard Lagrange multipliers method (SLM), Baumgarte stabilization method (BSM), penalty method (PM) the augmented Lagrangian formulation (ALF) and Coordinate Partitioning method (CPM).

2 Multibody Systems Formulation

In general, a multibody system contains mechanical components (bodies) that describe large translational and rotational motions and kinematic joints that impose constraints on the relative motion of the bodies. Forces that may act on the components of a multibody system can be the result of springs, dampers, actuators or external forces such as gravity. In order to analyze the kinematic and dynamic response of a constrained multibody system, it is first necessary to formulate the governing equations of motion. Thus, if the configuration of a constrained multibody system is described by n generalized coordinates, then a set of m independent algebraic kinematic (scleronomic) constraints Φ can be written as [2]

$$\Phi \equiv \Phi(\mathbf{q}) = \mathbf{0} \tag{1}$$

where \mathbf{q} is the array of generalized coordinates.

The first time derivative of Eq. (1) provides the velocity constraint equations as

$$\dot{\Phi} \equiv \mathbf{D}\mathbf{v} = \mathbf{0} \tag{2}$$

where \mathbf{D} denotes the system Jacobian matrix and \mathbf{v} is the array of generalized velocities. Differentiation of Eq. (2) with respect to time leads to acceleration constraint equations as

$$\ddot{\Phi} \equiv \mathbf{D}\dot{\mathbf{v}} + \dot{\mathbf{D}}\mathbf{v} = \mathbf{0} \tag{3}$$

in which $\dot{\mathbf{v}}$ is the array of generalized accelerations.

For a constrained mechanical multibody system, the Newton-Euler equations of motion are written as [9]

$$\mathbf{M}\dot{\mathbf{v}} = \mathbf{g} + \mathbf{D}^T\lambda \tag{4}$$

where \mathbf{M} is the global inertia matrix, \mathbf{g} is the vector of generalized forces, λ is an array of Lagrange multipliers, and $\mathbf{D}^T\lambda$ provides the array of reaction forces.

In the kinematic and analysis, a unique solution is obtained when the algebraic constraint equations at the acceleration level are considered simultaneously with the differential equations of motion together with a set of appropriate initial conditions on the coordinates and velocities. Therefore, appending Eqs. (3) to (4) yields the following equation that can be solved for the accelerations and Lagrange multipliers

$$\begin{bmatrix} \mathbf{M} & -\mathbf{D}^T \\ \mathbf{D} & \mathbf{0} \end{bmatrix} \begin{Bmatrix} \dot{\mathbf{v}} \\ \lambda \end{Bmatrix} = \begin{Bmatrix} \mathbf{g} \\ -\dot{\mathbf{D}}\mathbf{v} \end{Bmatrix} \tag{5}$$

This method of formulating the equations of motion is commonly referred to as the standard Lagrange multipliers method, and is hereafter designated by SLM [2].

Numerical integration of the equations of motion, in general, requires integrating velocities and accelerations at each time step to obtain coordinates and velocities at the next time step, i.e.,

$$\left\{ \begin{array}{c} \mathbf{v} \\ \dot{\mathbf{v}} \end{array} \right\} \rightarrow \int \rightarrow \left\{ \begin{array}{c} \mathbf{q} \\ \mathbf{v} \end{array} \right\} \quad (6)$$

It should be noted that depending on the choice of the coordinates and velocities for a body, particularly the rotational coordinates and velocities, the array of coordinates, \mathbf{q} , may not be directly the integral of \mathbf{v} . Obtaining \mathbf{q} from the integration of \mathbf{v} may require a prior transformation step. In addition, numerical errors due to the finite precision of the numerical methodologies leads to constraint violation at the coordinate and velocity levels; i.e., $\Phi \neq \mathbf{0}$ and $\dot{\Phi} \neq \mathbf{0}$. Therefore, special procedures, capable of eliminating the error in the constraints, or at least keeping such errors under control, must be implemented.

3 Methodology to Eliminate the Constraints Violation

The main purpose of this section is to present a general and comprehensive approach to deal with the elimination of the constraints violation at both position and velocity levels. For this purpose, let consider that Eqs. (1)–(5) are employed to model a multibody system and the integration process is performed according to Eq. (6). Due to numerical integration errors, in order not to violate the constraints at the coordinate level, the array of coordinates needs to be corrected as

$$\mathbf{q}^c = \mathbf{q}^u + \delta\mathbf{q} \quad (7)$$

where superscripts u and c denote uncorrected and corrected variables respectively, and $\delta\mathbf{q}$ represents the array of corrections to the coordinates. This means that the corrective term has to be added to vector \mathbf{q}^u in order to ensure that the constraint Eq. (1) are satisfied, that is

$$\Phi(\mathbf{q}^c) = \Phi(\mathbf{q}^u) + \delta\Phi = \mathbf{0} \quad (8)$$

The term $\delta\Phi$ in Eq. (8) can be understood as the variation of the constraint equations and can be expressed as [12]

$$\delta\Phi = \frac{\partial\Phi}{\partial\mathbf{q}_1} \delta\mathbf{q}_1 + \frac{\partial\Phi}{\partial\mathbf{q}_2} \delta\mathbf{q}_2 + \cdots + \frac{\partial\Phi}{\partial\mathbf{q}_n} \delta\mathbf{q}_n = \mathbf{D}\delta\mathbf{q} \quad (9)$$

Combining Eqs. (8) and (9) yields $\Phi(\mathbf{q}^u) + \mathbf{D}\delta\mathbf{q} = \mathbf{0}$, which ultimately leads to

$$\delta \mathbf{q} = -\mathbf{D}^{-1} \Phi(\mathbf{q}^u) \tag{10}$$

It must be noted that, in general, the Jacobian matrix, \mathbf{D} , is not square, therefore, \mathbf{D}^{-1} does not exist. However, the concept of Moore-Penrose generalized inverse matrix, \mathbf{D}^+ , can be employed as

$$\mathbf{D}^+ = \mathbf{D}^T(\mathbf{D}\mathbf{D}^T)^{-1} \tag{11}$$

such that $\mathbf{D}\mathbf{D}^+\mathbf{D} = \mathbf{D}$ and $\mathbf{D}^+\mathbf{D}\mathbf{D}^+ = \mathbf{D}^+$, and both $\mathbf{D}^+\mathbf{D}$ and $\mathbf{D}\mathbf{D}^+$ are symmetric matrices. Hence, it is possible to establish the following mathematical relation

$$\mathbf{D}^T(\mathbf{D}\mathbf{D}^T)^{-1} = \mathbf{D}^T(\mathbf{D}^+)^T\mathbf{D}^+ = (\mathbf{D}^+\mathbf{D})^T\mathbf{D}^+ = \mathbf{D}^+\mathbf{D}\mathbf{D}^+ = \mathbf{D}^+ \tag{12}$$

Thus, Eq. (10) can be rewritten in the following form

$$\delta \mathbf{q} = -\mathbf{D}^T(\mathbf{D}\mathbf{D}^T)^{-1} \Phi(\mathbf{q}^u) \tag{13}$$

Substituting Eq. (13) into Eq. (7) yields

$$\mathbf{q}^c = \mathbf{q}^u - \mathbf{D}^T(\mathbf{D}\mathbf{D}^T)^{-1} \Phi(\mathbf{q}^u) \tag{14}$$

This represents the corrected generalized coordinates in each time step. It should be noted that the kinematic constraints of Eq. (1) are nonlinear and, therefore Eq. (14) must be solved iteratively by an algorithm such as the Newton-Raphson.

In a similar manner, the array of velocities are corrected as

$$\mathbf{v}^c = \mathbf{v}^u + \delta \mathbf{v} \tag{15}$$

This corrected array of velocities should satisfy the velocity constraints of Eq. (2) as

$$\dot{\Phi}(\mathbf{q}^c, \mathbf{v}^c) = \dot{\Phi}(\mathbf{q}^c, \mathbf{v}^u) + \delta \dot{\Phi} = \mathbf{0} \tag{16}$$

The term $\delta \dot{\Phi}$ represents the variation of the velocity constraints expressed as

$$\delta \dot{\Phi} = \frac{\partial \dot{\Phi}}{\partial \mathbf{q}} \delta \mathbf{q} + \frac{\partial \dot{\Phi}}{\partial \dot{\mathbf{q}}} \delta \dot{\mathbf{q}} \tag{17}$$

Since the array of coordinates is already corrected, $\delta \mathbf{q} = \mathbf{0}$. Furthermore, the derivative of the velocity constraints with respect to vector of array of velocities is the Jacobian matrix \mathbf{D} . Consequently, Eq. (17) is simplified to

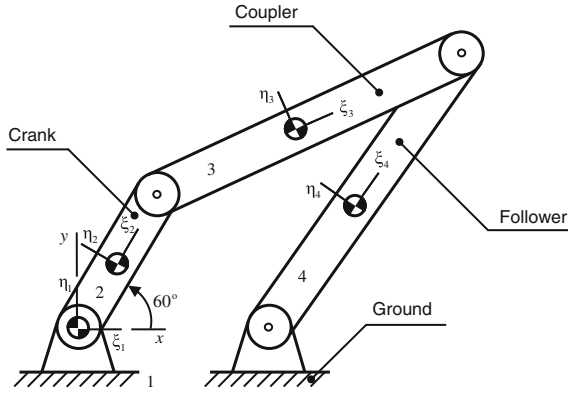


Fig. 1 Planar four bar mechanism

$$\delta \dot{\Phi} = \mathbf{D} \delta \mathbf{v} \tag{18}$$

Combining Eqs. (16) and (18) results in

$$\dot{\Phi}(\mathbf{q}^c, \mathbf{v}^u) + \mathbf{D} \delta \mathbf{v} = \mathbf{0} \tag{19}$$

This equation can be expressed as

$$\begin{aligned} \delta \mathbf{v} &= -\mathbf{D}^+ \dot{\Phi}(\mathbf{q}^c, \mathbf{v}^u) \\ &= -\mathbf{D}^T (\mathbf{D} \mathbf{D}^T)^{-1} \dot{\Phi}(\mathbf{q}^c, \mathbf{v}^u) \end{aligned} \tag{20}$$

Substitution of Eq. (20) into Eq. (15) yields

$$\mathbf{v}^c = \mathbf{v}^u - \mathbf{D}^T (\mathbf{D} \mathbf{D}^T)^{-1} \dot{\Phi}(\mathbf{q}^c, \mathbf{v}^u) \tag{21}$$

Equation (21) represents the corrected velocities in each integration time step.

4 Demonstrative Example of Application

An elementary planar four bar mechanism is utilized as a numerical example to demonstrate the effectiveness of the methodology proposed to eliminate the constraints violation, as it is shown in Fig. 1. The system is released from rest under the effect of gravity. The dimensional and inertia properties of each body together with the set of initial conditions necessary to carry out a dynamic analysis are listed in Table 1. Table 2 presents the parameters used for the different models, necessary to characterize the problem, and to solve the system dynamics. The values of the

Table 1 Governing properties for the planar four bar mechanism

Body	Length (m)	Mass (kg)	Moment of inertia (kg m ²)	x (m)	y (m)	ϕ (rad)	\dot{x} (m/s)	\dot{y} (m/s)	$\dot{\phi}$ (rad/s)
Ground	2.5	0.00	0.00	0.0000	0.0000	0.0000	0.0000	0.0000	0.0000
Crank	2.0	1.00	0.30	0.5000	0.8660	1.0472	0.0000	0.0000	0.0000
Coupler	4.0	2.25	2.00	2.8235	2.5535	0.4332	0.0000	0.0000	0.0000
Follower	4.0	2.20	1.35	3.5735	1.6875	1.0042	0.0000	0.0000	0.0000

Table 2 Parameters used for the dynamic simulations of the planar four bar mechanism

Final time of simulation	5.0 s	Penalty— α	1×10^7
Integrator algorithm	Euler	Penalty— ω	10
Baumgarte— α, β	5	Penalty— μ	1

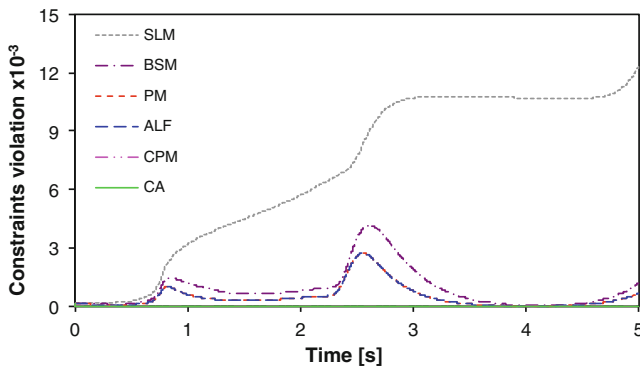


Fig. 2 Constraints violation ($\Phi^T \Phi$) of the planar four bar mechanism for the different methods

parameters used in this work are extracted from Ref. [9]. In order to keep the analysis simple, the crudest Euler integration method is considered.

Figure 2 shows the plots of the constraints violation ($\Phi^T \Phi$) of the four bar mechanism for different methods. It can be observed that when the standard Lagrange method (SLM) is used, the violation of constraints grows indefinitely with the time. This method can produce unacceptable results due to the numerical integration errors. However, when the standard Lagrange method incorporates the Baumgarte stabilization method (BSM), the response is slightly different. With the Baumgarte approach, the violation does not growth with time, instead it tends to stabilize or stay under control. The penalty method (PM) and augmented Lagrangian formulation (ALF) exhibit better behavior when compared to BSM. Finally, it can be observed that the coordinate partitioning method (CPM) and the corrective approach (CA) completely eliminate the violation of constraints. In general, the results plotted are in line with those published in [2, 9].

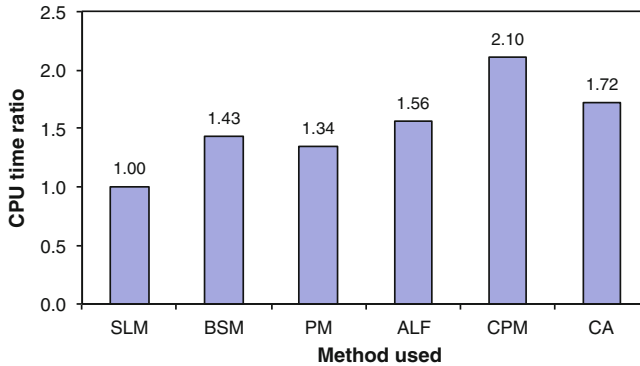


Fig. 3 Computation time ratio for the different methods

The efficiency of the different methods used to solve the dynamic equations of motion for the planar four bar mechanism are summarized in Fig. 3. In a broad sense, it can be stated that the standard Lagrange method is more efficient than Baumgarte stabilization approach. In turn, the penalty method exhibits better performance when compared with the standard Lagrange method, while the penalty method is about 22 % more efficient than the augmented Lagrangian formulation. It must be noted that, however, the behavior of the system can be affected by the values selected for the penalty parameters [9]. It should be mentioned that the coordinate partitioning method and the corrective approach are the less efficient due to the demand for the iterative solution for dependent generalized coordinates. This is the price to pay for the better accuracy of these methods.

5 Conclusions

An alternative approach to eliminate the violation of the kinematic constraint equations in the framework of multibody systems formulation was presented in this work. The basic idea of the described approach is to add corrective terms to the position and velocity vectors with the intent to satisfy the corresponding kinematic constraint equations. These corrective terms are evaluated as function of the Moore-Penrose generalized inverse of the Jacobian matrix and of the kinematic constraint equations. The accuracy and efficiency of the presented method was demonstrated through the modeling and analysis of a four bar mechanism. Furthermore, this method is independent of the integration algorithm used and it does not depend on the selection of any ambiguous penalty parameters.

References

1. Wittenburg J (1977) Dynamics of systems of rigid bodies. B.G. Teubner, Stuttgart, Germany
2. Nikravesh PE (1988) Computer-aided analysis of mechanical systems. Prentice Hall, Englewood Cliffs, New Jersey
3. Shabana AA (1989) Dynamics of multibody systems. Wiley, New York
4. Schiehlen W (1990) Multibody systems handbook. Springer, Berlin
5. Rahnejat H (2000) Multi-body dynamics: historical evolution and application. Proc Inst Mech Eng Part C J Mech Eng Sci 214:149–173
6. Eberhard P, Schiehlen W (2006) Computational dynamics of multibody systems: history, formalisms, and applications. J Comput Nonlinear Dyn 1:3–12
7. Schiehlen W (2007) Research trends in multibody system dynamics. Multibody SysDyn 18:3–13
8. Nikravesh PE (2008) Newtonian-based methodologies in multi-body dynamics. Proc Inst Mech Eng Part K J Multi-body Dyn 222:277–288
9. Jalón JG, Bayo E (1994) Kinematic and dynamic simulations of multibody systems: the real-time challenge. Springer, New York
10. Rosen A, Edelstein E (1997) Investigation of a new formulation of the Lagrange method for constrained dynamic systems. J Appl Mech 64:116–122
11. Blajer W (2002) Elimination of constraint violation and accuracy aspects in numerical simulation of multibody systems. Multibody Sys Dyn 7:265–284
12. Flores P (2011) A methodology for quantifying the position errors due to manufacturing and assemble tolerances. J Mech Eng 57(6):457–467

Vehicle Dynamic Simulation Using Robotic Techniques and Taking into Account a Tyre Model

B. Menkouz and M. Haddad

Abstract This work deals with the utilization of robotic inspired techniques in order to simulate vehicle dynamic. These techniques are based on Khalil-Klein-finger description for vehicle geometry and Newton-Euler formalism for movement equation generation. The technique is applied to a four-wheel model taking into account the suspension system. Obtained results are compared and validated with those obtained by vehicle dynamic simulation software Pc-Crash. This one is specialised on road accidents reconstruction.

Keywords Vehicle dynamic simulation · Multibody System · Modified Denavit and Hartenberg · Newton-Euler

1 Introduction

In order to improve its performances, a vehicle is subjected to different study's types. A study could aim for example on traction elements design, on suspension optimization or on fuel consumption.

Earlier a vehicle was made and subjected to experimental tests to be judged about its behaviour and was made again with necessary modifications. To obtain the final product, this step was repeated several times. This method is full of disadvantages because it presented essentially a lost of time and the product cost was very high.

Nowadays, computer science development allow to researchers and engineers to study, simulate and analyse the vehicle behaviour computationally. Indeed, this one

B. Menkouz (✉) · M. Haddad
Laboratoire Mécanique des Structures, École Militaire Polytechnique,
Bordj El Bahri, Algiers, Algeria
e-mail: b.menkouz@gmail.com

M. Haddad
e-mail: haddadmoussa2003@yahoo.fr

is now virtually made and the passage to the physical prototype is performed if a maximum of faults is eliminated and the functioning is optimised.

Analysing vehicle on machine is based on its variables calculation which are expressed with models that describe exactly the system and its elements behaviour. The most requested model is the dynamic behaviour one.

With engineering point of view, the study of vehicle dynamic is primordial for design, identifications, control and simulation actions. These are omnipresent in development, exploitation and modernisation different steps. Indeed, The major care of an automotive manufacturer is how to get a less expensive final product. In this case, a design software based on vehicle dynamic is indispensable. Moreover, an accurate estimation of inertial and road geometry parameters need a valid vehicle dynamic model (VDM). This one is also needed to control an unmanned ground vehicle (UGV) or for board electronic system for driver assistance on modern vehicle. A VDM is also useful for 3D simulation in order to reconstruct a road accident scenario or for driving simulators.

A VDM could be defined as a set of laws (models) which describe the interaction between the vehicle, the driver and the environment. These laws are usually presented as mathematical equations binding vehicle design parameters, driver orders and environment external solicitations.

In this paper, we use robotic techniques (RT) in order to elaborate a VDM. The approach used is explained within [1–3]. A vehicle could be considered as a tree MultiBody System (MBS) where the chassis is the base and tyres are terminal links [3]. Within [4–6] robotic techniques where used to establish a VDM but tyres were supposed rigid. However, in this work we take into account a principal characteristic of a deformable tyre, the slip angle, and use it as input to tyre contact model.

The application is performed on four wheels model with considering the suspension system. Results of developed model are compared and validated with those obtained by vehicle dynamic simulation software Pc-Crash [7]. This one is specialised on road accidents reconstruction.

2 Four-Wheeled Vehicle Modelled with Robotic Techniques

The vehicle is composed of a chassis, two front steerable wheels and two rear wheels. Every wheel is attached to the chassis via an independent suspension system with k_i spring stiffness and b_i damper coefficient. If we consider that wheels are in permanent contact relative to ground, then this and the vehicle form a tree closed loop (Fig. 1).

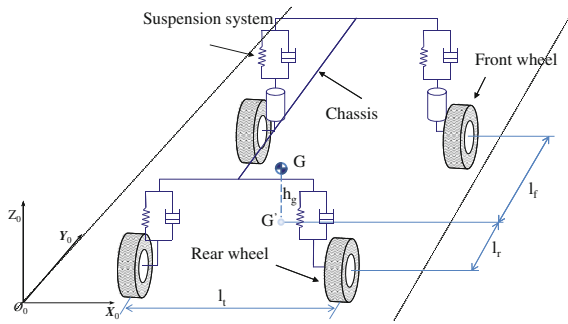


Fig. 1 Four wheel model as MBS

2.1 MDH Geometrical Description

In order to use the *Modified Denavit and Hartenberg* (MDH) method to describe the geometry of this structure, we introduce a spatial carrier between the ground (the reference link) and the chassis (the moving base). The carrier is defined as a sequence of three consecutive Prismatic joints and three consecutive Revolute joints. In addition, passive joints between ground and tyres are fictively cut and replaced by constraints equations developed later. The equivalent obtained tree structure is presented at (Fig. 2).

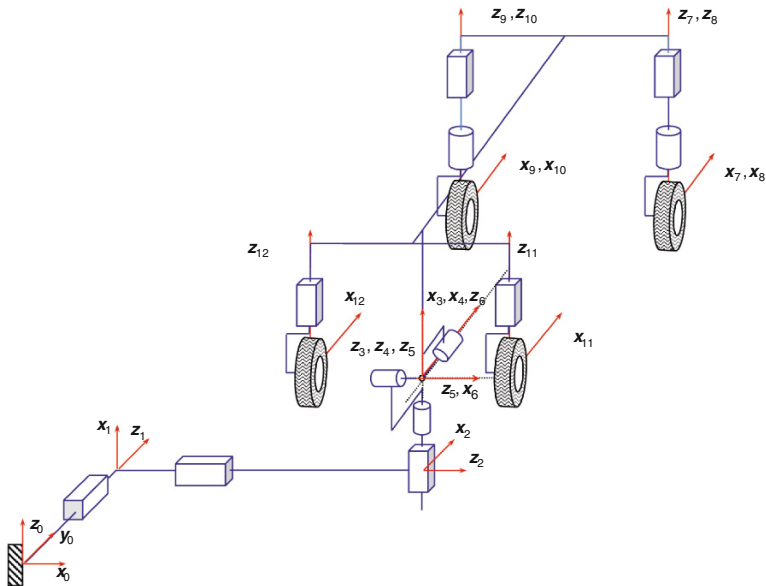


Fig. 2 MDH four-wheeled model geometric description

Table 1 MDH four-wheeled model parameters

j	a_j	σ_j	γ_j	b_j	α_j	d_j	θ_j	r_j
1	0	1	0	0	$-\pi/2$	0	$-\pi/2$	y
2	1	1	0	0	$-\pi/2$	0	$-\pi/2$	x
3	2	1	0	0	$-\pi/2$	0	0	z
4	3	0	0	0	0	0	φ	0
5	4	0	0	0	$\pi/2$	0	$\psi + \pi/2$	0
6	5	0	0	0	$\pi/2$	0	$\theta + \pi/2$	0
7	6	1	0	lf	$\pi/2$	ld	$\pi/2$	z_1
8	7	0	0	0	0	0	β_1	0
9	6	1	0	lf	$\pi/2$	$-ld$	$\pi/2$	z_2
10	9	0	0	0	0	0	β_2	0
11	6	1	0	$-lr$	$\pi/2$	ld	$\pi/2$	z_3
12	6	1	0	$-lr$	$\pi/2$	$-ld$	$\pi/2$	z_4

MDH parameters are listed on Table 1.

Where x , y and z are respectively longitudinal, lateral and vertical position of G . φ , ψ and θ are, respectively, yaw, pitch and roll angles. z_i is the vertical displacement of tyre i suspension system. β_1 and β_2 are front, right and left, steering angles. q is the joint variables and defined as:

$$q = (y, x, z, \varphi, \psi, \theta, z_1, \beta_1, z_2, \beta_2, z_3, z_4)^t \tag{1}$$

2.2 Constraints Equations

Thanks to suspension system, tyres are supposed on permanent contact with the ground. Cutting joints between tyres and ground is expressed by tyre center (C_i) position and velocity constraints equations.

2.2.1 Tyre Center Position Constraint

Tyre center position constraint is given by the following equation:

$$\overrightarrow{G'C_i} \cdot \overrightarrow{z_0} = 0 \tag{2}$$

where

$$\overrightarrow{G'C_i} = \overrightarrow{G'G} + \overrightarrow{GC_i} \tag{3}$$

$\overrightarrow{G\mathbb{G}}$, as seen on Fig. 1, is the vertical projection of G on the plane containing tyres centers C_i .

2.2.2 Tyre Center Velocity Constraint

The vertical velocity of tyre center relative to the ground is supposed equal to zero and is given by:

$$\overrightarrow{V_{tyre}^{ground}(C_i)} \cdot \overrightarrow{z_0} = 0 \tag{4}$$

This equation is then developed and written under this form:

$$J(q)\dot{q} = 0 \tag{5}$$

$J(q)$ is the Jacobean matrix. If we suppose that G has no vertical velocity ($\dot{z} = 0$) and with the these notes: $S = \sin(\cdot)$, $C = \cos(\cdot)$, $f = l_f C \psi S$, $g = l_r C \psi S \theta$ and $h = \frac{1}{2} l_t S \psi$, we obtain:

$$J = \begin{pmatrix} 0 & 0 & 0 & h+f & -l_f C \theta & \frac{1}{2} l_t & 1 & 0 & 0 & 0 & 0 & 0 \\ 0 & 0 & 0 & -h+f & -l_f C \theta & -\frac{1}{2} l_t & 0 & 0 & 1 & 0 & 0 & 0 \\ 0 & 0 & 0 & h-g & l_r C \theta & \frac{1}{2} l_t & 0 & 0 & 0 & 0 & 1 & 0 \\ 0 & 0 & 0 & -h-g & l_r C \theta & -\frac{1}{2} l_t & 0 & 0 & 0 & 0 & 0 & 1 \end{pmatrix} \tag{6}$$

J can be reduced to J_r , Eq. (7), by eliminating all nil column. Performing correspondent changes on \dot{q} we obtain his first reduced form \dot{q}_{r1} Eq. (8).

$$J_r = \begin{pmatrix} h+f & -l_f C \theta & \frac{1}{2} l_t & 1 & 0 & 0 & 0 \\ -h+f & -l_f C \theta & -\frac{1}{2} l_t & 0 & 1 & 0 & 0 \\ h-g & l_r C \theta & \frac{1}{2} l_t & 0 & 0 & 1 & 0 \\ -h-g & l_r C \theta & -\frac{1}{2} l_t & 0 & 0 & 0 & 1 \end{pmatrix} \tag{7}$$

$$\dot{q}_{r1} = (\dot{\phi}, \dot{\psi}, \dot{\theta}, \dot{z}_1, \dot{z}_2, \dot{z}_3, \dot{z}_4)^t \tag{8}$$

Substituting J and \dot{q} by J_r and \dot{q}_{r1} in Eq. (5), and performing derivation relative to time, we obtain the equation Eq. (9).

$$J_r(q)\ddot{q}_{r1} + \Phi(q, \dot{q}) = 0 \tag{9}$$

where

$$\Phi = \begin{pmatrix} \frac{1}{2} l_t A + l_f B & -l_f D \\ -\frac{1}{2} l_t A + l_f B & -l_f D \\ \frac{1}{2} l_t A - l_r B & l_r D \\ -\frac{1}{2} l_t A - l_r B & l_r D \end{pmatrix} \begin{pmatrix} \dot{\phi} \\ \dot{\psi} \end{pmatrix} \tag{10}$$

and $A = \dot{\psi} C \psi$, $B = \dot{\theta} C \psi C \theta - \dot{\psi} S \psi S \theta$ and $D = -\dot{\theta} C \theta$.

2.3 The Inverse Dynamic Model (IDM)

IDM is obtained if we write joint torques in terms of joints positions, velocities and accelerations, and also in terms of external forces and moments (F_e and M_e) applied on structure. If we suppose that all joints are passive, IDM is written then as:

$$\Gamma = \Gamma_{tr} + J^t \lambda + k_i q_i + b_i \dot{q}_i = 0 \quad (11)$$

Γ_{tr} vector of joints torques of equivalent tree structure. It is given by NE recursive algorithm Eq. (12). λ vector of Lagrange multipliers. They correspond to transmitted forces between cut joints. It can be easily demonstrated that λ_i (λ elements) correspond to forces developed by suspension systems to maintain tyres on ground.

$$\Gamma_{tr} = NE(q, \dot{q}, \ddot{q}, F_e, M_e) \quad (12)$$

In an other hand, Γ_{tr} can also be written as:

$$\Gamma_{tr} = A(q)\ddot{q} + H(q, \dot{q}) \quad (13)$$

$A(q)$ is inertia matrix and $H(q, \dot{q})$ vector containing Coriolis, centrifugal and gravity forces.

2.4 The Direct Dynamic Model (DDM)

The direct dynamic model gives joints accelerations expressed as function (fct) of joints position, velocity and torques and also external applied forces and moments. MDD is defined as:

$$\ddot{q} = fct(q, \dot{q}, \Gamma, F_e, M_e) \quad (14)$$

We will use the MDD to calculate a second reduced form of \ddot{q} , it is given by:

$$\ddot{q}_{r2} = (\ddot{y}, \ddot{x}, \ddot{\phi}, \ddot{\psi}, \ddot{\theta})^t \quad (15)$$

With this reduction adoption and using Eqs. 11 and 13 we can easily prove this equation:

$$\ddot{q}_{r2} = -A_r^{-1}(q)H_r(q, \dot{q}) \quad (16)$$

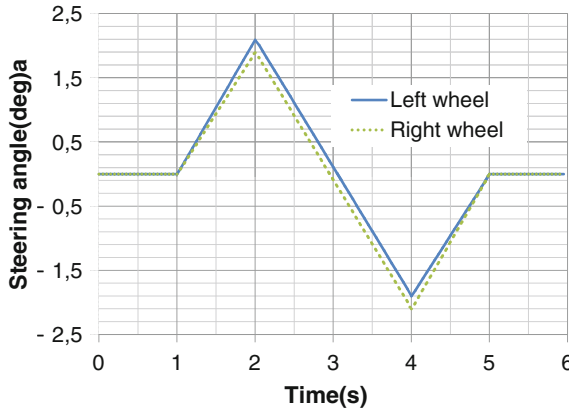


Fig. 3 Front wheels steering angles

A_r et H_r are reduced forms of A and H which can be calculated using the IDM. Indeed, we deduce from Eqs. 12 and 13 that $H = \Gamma_{tr}$ if $\ddot{q} = 0$ and that the i th column of A is equal to Γ_{tr} if: $\ddot{q} = u_i, \dot{q} = 0, g = 0, F_e = 0$ and $M_e = 0$ (g is the gravity and it appears in NE recursive algorithm).

Where u_i is the $(n \times 1)$ unit vector whose i th element is equal to 1, and the other elements are zeros. Iterating the procedure for $i = 1, \dots, n$ leads to the construction of the entire inertia matrix.

Note that \ddot{z}_i can be deduced from equation Eq. (9).

3 Simulation and Results

To validate the implemented model, we order to the vehicle to perform a lane change manoeuvre at a speed $V = 17$ m/s. Correspondent wheels steering angles are shown on Fig. 3.

On Table 2 are listed simulation parameters. Where m is the mass of the vehicle, I_x, I_y, I_z are vehicle inertia, l_f, l_r, l_t, h_g , are as seen on Fig. 1, μ is road-tyre friction coefficient, and k_i, b_i are suspension parameters.

Linear tyre model parameters adjusting are $\alpha_{max} = 10^\circ$ for adherence coefficient $\mu = 1$ [7].

On following figures are presented respectively normal and lateral forces applied on front wheels, vehicle roll angle and suspension vertical displacements. Obtained results are very satisfactory. However, we have to note that Pc-Crash doesn't allow visualizing suspension vertical displacements (Figs. 4, 5 and 6).

Table 2 Simulations parameters

Parameter	m	l_f	l_r	l_i	h_g	I_x	$I_y = I_z$	m
Value	807 kg	0.715 m	0.835 m	1.4 m	0.3 m	172.4 kgm ²	430 kgm ²	0.8
Parameter	$k_1 = k_2$	$k_3 = k_4$	$b_1 = b_2$	$b_3 = b_4$				
Value	15,245.5 N/m	13,054.5 N/m	1,682.7 Ns/m	1,440.8 Ns/m				

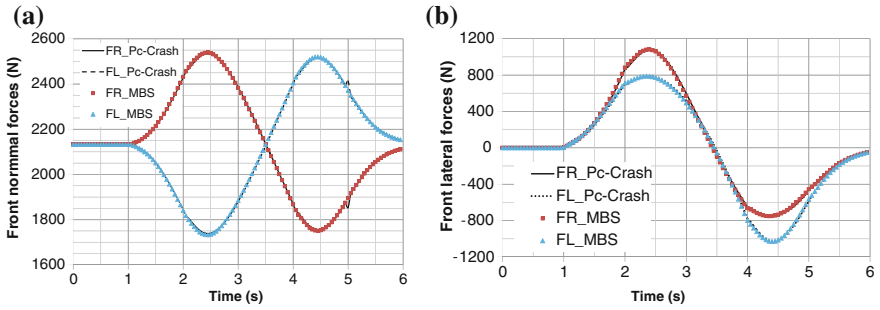


Fig. 4 Forces applied on front wheels: a normal forces, b lateral forces

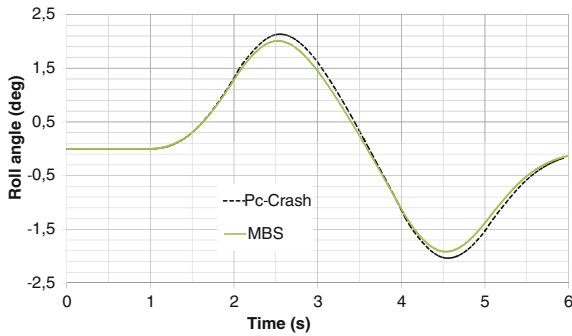


Fig. 5 Roll angle

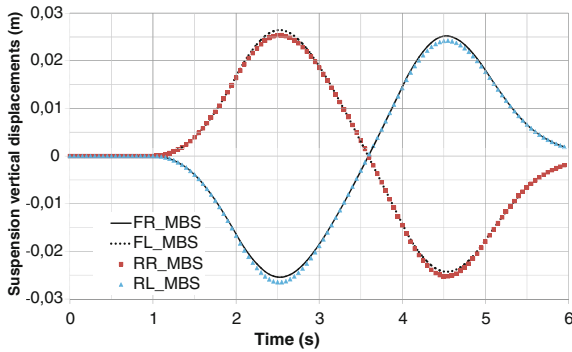


Fig. 6 Suspension systems vertical displacements

4 Conclusions

In this paper we used robotic techniques to simulate vehicle dynamics. These methods were applied on a four-wheeled model taking into account of suspension system. Tyre contact model used is linear one. Obtained results, which were satisfactory, were compared and validated with those of Pc-Crash software.

MBS based on robotic techniques developed models are open and extensible. Indeed, they permit to pass from a model complexity level to another one with minimum modifications.

References

1. Wisama K (2010) Dynamic modeling of robots using recursive Newton-Euler techniques, *ICINCO2010*, Portugal
2. Haddad M (2008) Exploitation optimale des plateformes mobiles et des manipulateurs mobiles à roues. Extensions de l'approche des profils aléatoires de trajectoires. Thèse de Doctorat, École Militaire Polytechnique, Algiers, Algeria
3. Venture G (2003) Identification des paramètres dynamiques d'une voiture, Thèse de Doctorat, Nantes, France
4. Menkouz B (2008) Modélisation dynamique des véhicules. Aide à la simulation des scénarios des accidents routiers, Mémoire d'ingénieur, École Militaire Polytechnique, Algiers, Algeria
5. Haddad M, Zennadi K (2010) Modèle dynamique des véhicules. Aide à la simulation des accidents de type dérapage, Actes des 7èmes Journées de Mécanique de l'École Militaire Polytechnique, Algiers, Algeria
6. Menkouz B (2012) Modélisation et simulation du comportement dynamique des véhicules. Prise en compte du modèle de comportement pneu-sol, Mémoire de magister, École Militaire Polytechnique, Algiers, Algeria
7. Steffan D (2006) PC-Crash program for vehicle accidents. Technical manual of Pc-Crash, Linz, Austria

An Advanced 3D Multi-body System Model for the Human Lumbar Spine

S. Sousa and J.C.P. Claro

Abstract A novel 3D multi-body system model of the human lumbar spine is presented, allowing the dynamic study of the all set but also to access mechanical demands, characteristics and performance under work of the individual intervertebral discs. An advanced FEM analysis was used for the most precise characterization of the disc 6 DOF mechanical behavior, in order to build up a tool capable of predicting and assist in the design of disc recovery strategies—namely in the development of replacement materials for the degenerated disc nucleus—as well as in the analysis of variations in the mechanical properties (disorders) at disc level or kinematic structure (e.g. interbody fusion, pedicle fixation, etc.), and its influence in the overall spine dynamics and at motion segments individual level. Preliminary results of the model, at different levels of its development, are presented.

Keywords Computer simulation · Multibody Systems · Biodynamics · Spine column

1 Introduction

Low back pain affects about 80 % of world's population, at some point of their life, been lumbar disc diseases and, among them, the degeneration of the disc's nucleus pulposus (NP) and consequent loss of internal pressure, one of the main causes [1]. Current treatments, if not just palliative, present multiple and severe side effects, which lead the research to look for reliable prosthetic solutions for partial or complete substitution of the nucleus, not only as a viable alternative but also, and

S. Sousa (✉) · J.C.P. Claro
University of Minho, Braga, Portugal
e-mail: sofia_sts@hotmail.com

J.C.P. Claro
e-mail: jcclaro@dem.uminho.pt

preferably, involving minimally invasive and lower traumatic techniques and shorter recovery time and ambulatory periods for the patients.

It's with this background that a '*in silico*' study of the working conditions of the intervertebral disc (IVD)—as part of a broader research project (*NPMimetic.com*)—was developed. In a first stage as a way to characterize and quantify the mechanical behavior of the IVD bio-system, through a Finite Elements Method (FEM) and, in a second phase, to analyze the IVD performance '*de per si*', as well as eventual influences in the global dynamics of the spinal system, using a Multi-Body System (MBS) analysis.

The option for the MBS model is justified by its considerably low computational demand, when compared to FEM for instance, but also for its versatility in the definition of complex dynamic loading conditions and ease of introducing eventual variations on the characteristics of specific components, allowing stable and reliable solutions in the dynamic analysis of a complex system, involving the IVD but also the main ligaments and facets acting on the mechanical stabilization of the spine. Other works can be referred in this field, such as Lengsfeld et al. [2] that used ADAMS[®] software to study the lumbar spine, Esat and Acar [3] that presented a multibody lumbar spine model implemented in Anybody Modeling System software and Monteiro et al. [4] that developed a specific code coupling a multibody system dynamic and a finite element model to study the cervical and lumbar spine.

With this model the objective is to provide data about IVD's 3D loading state for normal daily life activities, as well as in its full physiological range, allowing the analysis, quantification and systematization of its 'real' performance conditions, been in natural physiological situation or with a partial or total replacement of the NP by a prosthetic material. Subsequently, these data will be used as a feedback to the FEM model, allowing its detailed study at the nucleus/annulus level and the verification and possible re-engineering of the prosthetic material.

Besides the prediction of the effect of alterations in the mechanical characteristics of the NP due to an implant, this MBS tool is also able to predict the effects of other local alterations—such as those induced by a motion segment fusion, by surgical intervention, or due to degeneration/ageing phenomena, for instance—allowing the quantification of the (clinical well known) change on the loading pattern induced in the neighborhood levels of the spine.

Furthermore, it can also be useful in the design of mechanical devices for spine stabilization, namely in the most recent and yet in development partially mobile, mechanical driven, linkage systems.

2 Implementation

The MBS model, mainly intended for a forward analysis, implemented in a commercial software (WM-VisualNastran), has six rigid bodies representing the five lumbar vertebrae and the sacrum, interconnected through fifty non-linear Maxwell elements (spring/damper parallel sets) emulating the twenty main ligaments [5] and

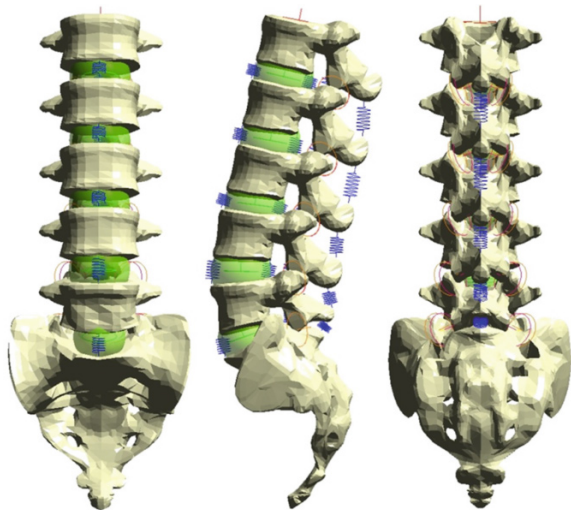
five IVDs, besides the five bilateral posterior spinous processes (currently defined as simple spatial constrains, with no specific surface contact law) in a complete lumbar set, as shown in Fig. 1.

For the mechanical characteristics of the IVD, data generated by an in-house advanced osmo-porous-hiper-viscoelastic FEM model, specifically developed within the “NP Mimetic” project [6, 7], were used in the prediction of the mechanical behavior in translation (T_x , T_y and T_z) and in rotation (R_x , R_y and R_z) along the three coordinated axis of the medial plane of the IVD. For the ligaments, published available data were used, giving a special attention to those that are more relevant for the stability and performance of the spine—namely the longitudinal anterior (ALL) and posterior (PLL), flavum (FL), interspinous (ISL) and supraspinous (SSL) ligaments—after a careful curation and selection [8–10]. Currently, Chazal results are implemented.

Figure 2 displays a left antero-posterior perspective detail of the kinematic model scheme, where the central cube represents the IVD, with its 6 DOF, the helical lines stand for the ligaments and the processes defined by direct contact between adjacent bodies.

Subsequently, a throughout sensitivity study of the motion segment geometric parameters (variation of average thickness, sagittal angle between end-plates and transverse section of IVD and annulus/nucleus ratio) on IVD’s behavior was carried out, and results parameterized and introduced in the force/torque versus elongation/rotation equations of the Maxwell elements, according to their different levels on the spine.

Fig. 1 Multi-body model of the human lumbar spine



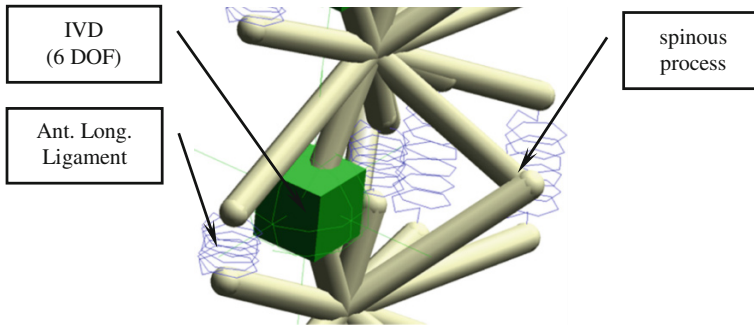
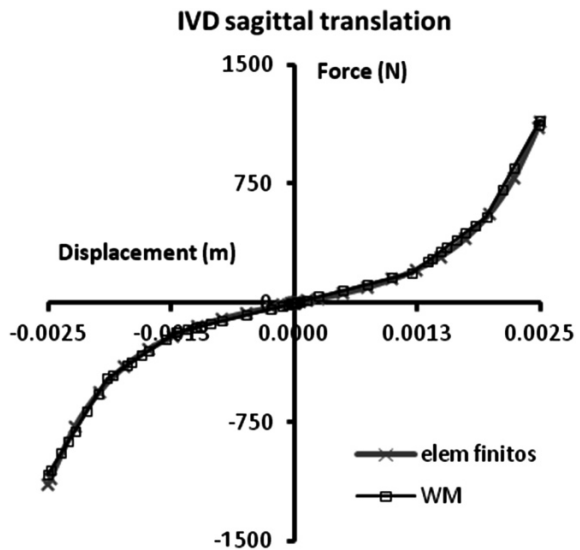


Fig. 2 Detail of the MBS joints on the motion segment

Fig. 3 Comparison between FEM analysis and Multibody model IVDs' force-displacement curves



3 Results

Preliminary results are presented, showing the potentialities of the model in the reproduction and quantification of different circumstances, in three different phases:

- (a) validation of the answer of each one of the components '*de per si*'—as illustrated in Figs. 3 and 4;
- (b) analysis of the correlation with others experimental works [11]—Fig. 5—and with the answer to daily-life, usual but complex composition of load cases and applied ratios, using external published data (e.g. Rolhmann [12] and Bergmann [13])

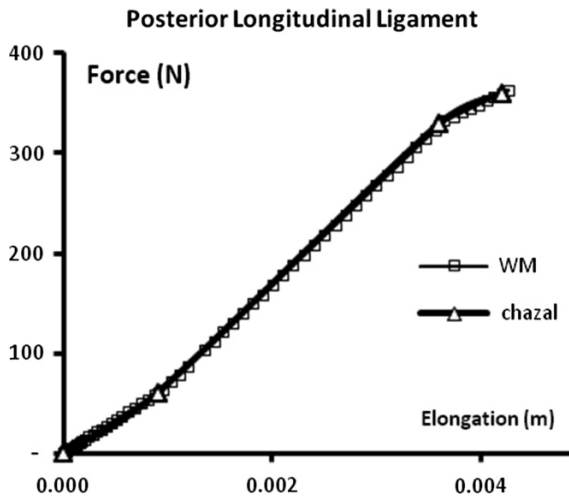


Fig. 4 Comparison between experimental data [8] and Multibody model ligaments' force-displacement curves

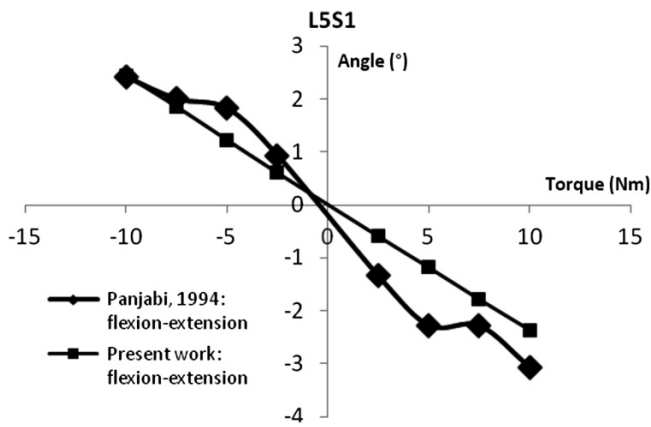


Fig. 5 Comparison between experimental data [11] and Multibody's IVD response

(c) study on the influence of critical parameters (namely of the functional characteristics of the IVD) and the virtualization of the 'fusion' of one motion segment, in the static and dynamic response of the other levels and of the all lumbar section—Figs. 6 and 7.

Fig. 6 Flexion: percentage increase in static load, for a L4-L5 interbody fusion

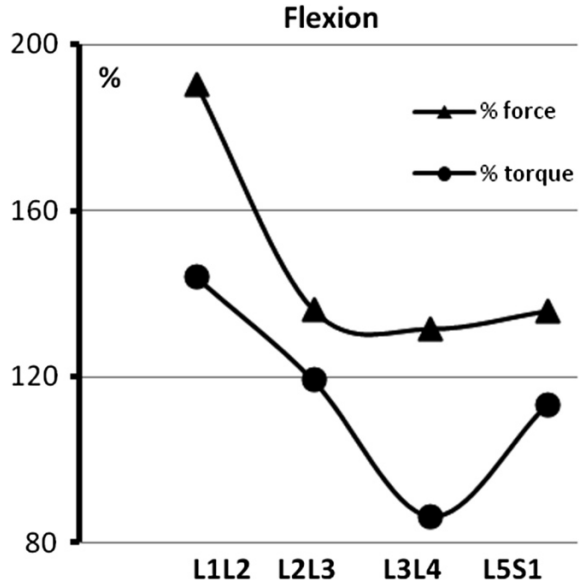
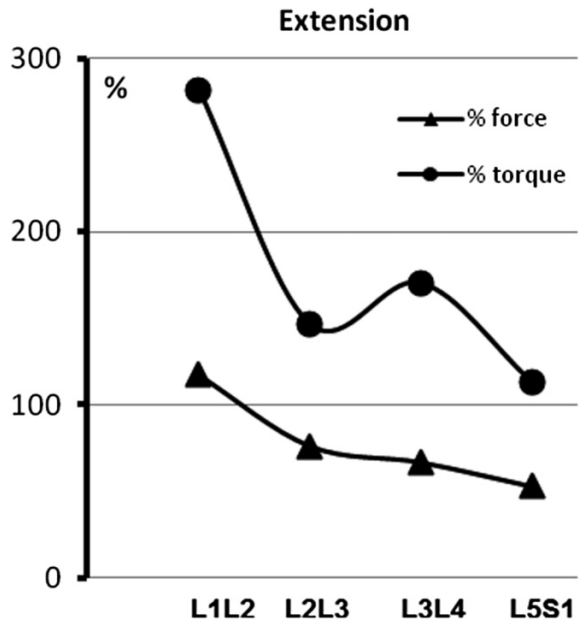


Fig. 7 Extension: percentage increase in static load, for a L4-L5 interbody fusion



4 Conclusions

The model is in a phase of tuning-up, to suit the needs of broader project's objectives—implying a post-processing of output data, via a FEM analysis, aiming the full mechanical design of the advanced prosthetic materials under developed for NP regeneration.

However it is presently fully validated, already shown to be a feasible and reliable, 'light' computer demanding tool, suitable for the study and analysis of several complex problems involving various clinical problematic of the lumbar spine, and the corresponding prediction and design of mechanical solutions.

Acknowledgments This work was performed within the European Project “NP Mimetic—Biomimetic Nano-Fibre Based Nucleus Pulposus Regeneration for the Treatment of Degenerative Disc Disease”, funded by the European Commission under FP7 (grant NMP-2009-SMALL-3-CP-FP 246351)

References

1. Kraemer J (2008) Intervertebral disk diseases: causes, diagnosis, treatment and prophylaxis. Thieme, Stuttgart
2. Lengsfeld M et al (2000) Lumbar spine curvature during office chair sitting, Germany. *Med Eng Phys* 22:665–669
3. Esat V, Acar M (2007) A Multi-body model of the whole human spine for whiplash investigations. In: 20th enhanced safety oh vehicles conference: innovations for safety: opportunities and challenges, Lyon
4. Monteiro N et al (2011) Structural analysis of the intervertebral discs adjacent to an interbody fusion using multibody dynamics and finite element cosimulation. *Multibody Syst Dyn* 25:245–270
5. Behrsin J, Briggs C (1988) Ligaments of the lumbar spine: a review. *Surg Radiol Anat* 10:211–219
6. Castro A et al (2013) The role of poroelasticity on the biomechanics of the intervertebral disc: a finite element study. In: 5th National Congress on Biomechanics, Espinho, Portugal
7. Castro A et al (2012) A poroelastic approach for an open source finite element model of the intervertebral disc. In: Proceedings of CMBBE2012 symposium
8. Chazal J et al (1985) Biomechanical properties of spinal ligaments and a histological study of the supraspinal ligament in traction. *J Biomech* 18(3):167–176
9. Neumann P et al (1992) Mechanical properties of the human lumbar anterior longitudinal ligament. *J Biomech* 25(10):1185–1194
10. Pintar FA et al (1992) Biomechanical properties of human lumbar spine ligaments. *J Biomech* 25:1351–1356
11. Panjabi M et al (1994) Mechanical behavior of the human lumbar and lumbosacral spine as shown by three-dimensional load-displacement curves. *New Haven J Bone Joint Surg* 76 (3):413–423
12. Rohlmann A et al (2007) An instrumented implant for vertebral body replacement that measures loads in the anterior spinal column. *Med Eng Phys* 29:580–585
13. Bergmann G (ed) (2008) Charite—Universitaetsmedizin Berlin “OrthoLoad”. Retrieved 06 Nov 2012, <http://www.orthoload.com>

Energy-Consistent Integration Scheme for Multi-body Systems with Dissipation

S. Conde Martín and J.C. García Orden

Abstract This work is concerned with the numerical solution of the evolution equations of thermo-mechanical systems, in such a way that the scheme itself satisfies the laws of thermodynamics. Within this framework, we present a novel integration scheme for the dynamics of viscoelastic continuum bodies in isothermal conditions. The proposed scheme intrinsically satisfies the laws of thermodynamics arising from the continuous. This approach enables us to address the inclusion of dissipation in bodies which is typically present in multi-body applications of interest. The resulting solutions are physically accurate since they preserve the fundamental physical properties of the model. Furthermore, the method gives an excellent performance with respect to robustness and stability. Proof for these claims as well as numerical examples that illustrate the performance of the novel scheme are provided.

Keywords Time integration · Structure preservation · Geometric integration · Thermodynamics · Viscoelasticity

1 Introduction

Preserving structure integrators have widely been developed for conservative (Hamiltonian) systems, being the most representative method the well-known energy-momentum due to Simó and Tarnow [1]. Recently, after the works of Romero [2], these ideas are being used in evolution system with irreversible processes, i.e. non-conservative, such as those with internal dissipation mechanisms (viscoelasticity, plasticity, damage). In this context, the structure meant to be pre-

S. Conde Martín (✉) · J.C. García Orden
Technical University of Madrid, Madrid, Spain
e-mail: sergio.conde@upm.es

J.C. García Orden
e-mail: juancarlos.garcia@upm.es

served is understood in the thermodynamical way, namely, the integrator must intrinsically satisfy the laws of thermodynamics as in conservative problems this one preserved the Hamiltonian.

Within this framework, we present a novel integration method for the dynamics of an isothermal viscoelastic continuum body. This method exactly preserves the continuum laws of thermodynamics intrinsically, plus equations symmetries. The resulting solutions are physically accurate since they preserve fundamental physical properties of the model. What is more, they show an excellent performance with respect to the method's robustness and stability.

The viscoelastic behaviour is modeled according to Holzapfel and Simó [3] (regardless of temperature). Such model is able to simulate large-strain deformations although the viscoelastic evolution equations are linear. Our approach is based on a double semidiscretisation, spatial (FE-based) and temporal, being on the latter one where we do our main contribution.

2 Problem Definition

2.1 Kinematics

An arbitrary point \mathbf{X} in the reference configuration \mathcal{B}_0 can be described at time t in the current configuration \mathcal{B}_t by using the nonlinear mapping φ , so that $\mathbf{x} = \varphi(\mathbf{X}, t)$. The deformation of a continuum can be described with the deformation gradient \mathbf{F} , which is given by the derivative of the vector \mathbf{x} with respect to the reference vector \mathbf{X} . Likewise, the linear momentum per unit reference volume \mathbf{p} is derived by taking temporal derivative of the mapping. Then, the deformation gradient, the right Cauchy-Green strain tensor \mathbf{C} and the linear momentum are defined by

$$\mathbf{F} := \frac{\partial \varphi}{\partial \mathbf{X}}, \quad \mathbf{C} := \mathbf{F}^T \mathbf{F}, \quad \mathbf{p} := \rho_0 \frac{\partial \varphi}{\partial t} \quad (1)$$

The assumption of the dilatational-deviatoric multiplicative split of the deformation gradient is considered. It is based on a modified deformation gradient tensor $\bar{\mathbf{F}} : \mathcal{B}_0 \times [0, T] \rightarrow \mathbb{R}^{d \times d}$, whose dilatational part vanishes, i.e. $\det \bar{\mathbf{F}} = 1$. Consequently, a modified Green-Lagrange tensor $\bar{\mathbf{C}} : \mathcal{B}_0 \times [0, T] \rightarrow \mathbb{R}^{d \times d}$ is defined, that is

$$\bar{\mathbf{F}} := J^{-\frac{1}{3}} \mathbf{F}, \quad \bar{\mathbf{C}} := J^{-\frac{2}{3}} \mathbf{C} \quad \text{with} \quad J := \det \mathbf{F} = \sqrt{\det \mathbf{C}}, \quad (2)$$

As internal variables for isotropic material behaviour we choose symmetric strain-like tensors $\bar{\Gamma}^\alpha : \mathcal{B}_0 \times [0, T] \rightarrow \mathbb{R}^{d \times d}$, where $\alpha \in [1, m]$ is the number of internal variables. These variables are responsible for mathematically modelling the

dissipative effects which take place in viscoelastic materials. The internal variables are history dependent but not measurable as the external variable \mathbf{F} .

2.2 Material Model: Viscoelasticity

Based on the concept of internal variables Holzapfel and Simó [3] proposed a material constitutive behavior governed by the Helmholtz free energy (regardless of temperature) per unit reference volume function $\Psi: \mathcal{B}_0 \times [0, T] \rightarrow \mathbb{R}$, as follows

$$\Psi(\mathbf{C}, \bar{\Gamma}^\alpha) = \Psi_{\text{vol}}^\infty(J) + \Psi_{\text{iso}}^\infty(\bar{\mathbf{C}}) + \sum_{\alpha=1}^m \left[\mu_\alpha \bar{\Gamma}^\alpha : \bar{\Gamma}^\alpha - 2 \frac{\partial \Psi_{\text{iso}}^\alpha(\bar{\mathbf{C}})}{\partial \bar{\mathbf{C}}} : \bar{\Gamma}^\alpha + \Psi_{\text{iso}}^\alpha(\bar{\mathbf{C}}) \right], \quad (3)$$

where $\Psi^\infty: \mathcal{B}_0 \times [0, T] \rightarrow \mathbb{R}$ represents an arbitrary smooth hyperelastic potential, $\mu_\alpha \in \mathbb{R}_+$ is a non-negative parameter and $\Psi^\alpha: \mathcal{B}_0 \times [0, T] \rightarrow \mathbb{R}$ is the hyperelastic potential of the material which characterizes the dissipation processes which is normally assumed to be a proportional part of Ψ^∞ [4],

$$\Psi^\alpha(\mathbf{C}) = \beta_\alpha \Psi^\infty(\mathbf{C}) \quad \text{with} \quad \beta_\alpha = \frac{2\mu_\alpha}{E^\infty} \quad \forall \alpha = 1, \dots, m, \quad (4)$$

E^∞ being the Young modulus which defines Ψ^∞ .

Accordingly, constitutive laws are derived for the symmetric Piola-Kirchhoff stress tensor $\mathbf{S}: \mathcal{B}_0 \times [0, T] \rightarrow \mathbb{R}^{d \times d}$ and the internal stress or non-equilibrium stress tensor associated to each α -dissipative process $\bar{\mathbf{Q}}^\alpha: \mathcal{B}_0 \times [0, T] \rightarrow \mathbb{R}^{d \times d}$

$$\mathbf{S} = 2 \frac{\partial \Psi(\mathbf{C}, \bar{\Gamma}^\alpha)}{\partial \mathbf{C}}, \quad \bar{\mathbf{Q}}^\alpha = - \frac{\partial \Psi(\mathbf{C}, \bar{\Gamma}^\alpha)}{\partial \bar{\Gamma}^\alpha}, \quad (5)$$

Finally, each α -dissipative process involves a long term viscoelastic evolution which defines the irreversible mechanism by which the energy is dissipated in the material. This process is characterized by the relaxation/retardation time $\tau_\alpha \in \mathbb{R}_+$ and determined by the following *dissipative evolution equations* for the internal strains, which are inspired by linear viscoelasticity and were proposed in [3]

$$\dot{\bar{\Gamma}}^\alpha = \frac{1}{\eta_\alpha} \bar{\mathbf{Q}}^\alpha \quad \text{in } \mathcal{B}_0 \times [0, T] \quad \text{with} \quad \eta_\alpha = 2\mu_\alpha \tau_\alpha \geq 0 \quad \forall \alpha = 1, \dots, m. \quad (6)$$

($\dot{\bullet}$) indicating time differentiation and η_α being a coefficient associated to the α -dissipative process.

2.3 Laws of Thermodynamics

This model is in accordance with the laws of thermodynamics. Thus, the Clausius-Planck inequality, for viscoelasticity in isothermal conditions, states that the internal rate of dissipation per reference volume must be non-negative for any particle of the body for all instants, that is

$$\dot{\mathcal{D}}_{\text{int}} = \frac{1}{2} \mathbf{S} : \dot{\mathbf{C}} - \dot{\Psi} = \sum_{\alpha=1}^m \mathbf{Q}^{\alpha} : \dot{\Gamma}^{\alpha} = \sum_{\alpha=1}^m \frac{1}{\eta_{\alpha}} \mathbf{Q}^{\alpha} : \mathbf{Q}^{\alpha} \geq 0. \quad (7)$$

Note that use has been made of evolution equations in 6 in order to demonstrate the non-negative rate of dissipation, proving the satisfaction of the laws of thermodynamics.

3 Weak Form of Initial-Boundary Value Problem

The weak form of the viscoelastic problem is given by the principle of virtual works

$$\langle \dot{\mathbf{p}}, \mathbf{w}_{\varphi} \rangle_{\mathcal{B}_0} + \langle \mathbf{F}\mathbf{S}, \frac{\partial \mathbf{w}_{\varphi}}{\partial \mathbf{X}} \rangle_{\mathcal{B}_0} - \langle \mathbf{b}_0, \mathbf{w}_{\varphi} \rangle_{\mathcal{B}_0} - \langle \bar{\mathbf{t}}, \mathbf{w}_{\varphi} \rangle_{\partial \mathcal{B}_0} = 0, \quad (8)$$

where $\mathbf{w}_{\varphi} \in \mathcal{V}$, \mathcal{V} being the infinite dimensional space containing all the variations of φ that fulfill the boundary conditions. The notation $\langle \bullet, \bullet \rangle_{\square} = \int_{\square} (\bullet)(\bullet) d\square$ stands for the inner product. In addition, \mathbf{b}_0 accounts for the external forces per unit reference volume and $\bar{\mathbf{t}}$ for tractions acting on the boundary.

The thermodynamic state of the viscoelastic body is fully described at a given instant by φ , the momentum per unit reference volume \mathbf{p} and internal variables $\bar{\Gamma}^{\alpha}$. All of them constitute the state variables of the system which, in what follow, we will collect in the vector \mathbf{z} that defines the infinite dimensional configuration space \mathcal{S} as

$$\mathcal{S} : \{ \mathbf{z} = [\varphi, \mathbf{p}, \bar{\Gamma}^{\alpha}] : \mathcal{B}_0 \rightarrow \mathbb{R}^d \times \mathbb{R}^d \times \mathbb{R}^{d \times d}, \det \left(\frac{\partial \varphi}{\partial \mathbf{X}} \right) > 0 \}. \quad (9)$$

4 Discretization: Energy-Consistent Scheme

The formulation of the energy-consistent scheme is ground on the use of the classical finite element method (FE) plus the use of *discrete derivative* operator [5], which is the key to obtaining energy-consistency.

4.1 Standard Galerkin FE Discretization

Consider a partition of the continuum \mathcal{B}_0 into a conforming, regular mesh of N_e finite elements, each denoted \mathcal{B}_e , connecting \mathcal{N} nodes, defining a discrete configuration \mathcal{B}_0^h . Then, the measurable variables are directly spatially discretized by using standard Galerkin isoparametric approach, with shape functions of the form $N^a: \mathcal{B}_0^h \rightarrow \mathbb{R}$,

$$\phi^h(\mathbf{X}, t) = \sum_{a=1}^{\mathcal{N}} N^a(\mathbf{X}) \mathbf{x}^a(t), \quad \mathbf{p}^h(\mathbf{X}, t) = \sum_{a=1}^{\mathcal{N}} N^a(\mathbf{X}) \mathbf{p}^a(t), \quad (10)$$

while the spatial discrete counterpart of the internal ones (non-measurable) is achieved by performing the time integration of the spatial counterpart of the evolution Eqs. 6. That is,

$$\dot{\bar{\Gamma}}^{\alpha,h} = \frac{1}{\eta_\alpha} \bar{\mathbf{Q}}^{\alpha,h} \text{ in } \mathcal{B}_0^h \times [0, T] \quad \forall \alpha = 1, \dots, m. \quad (11)$$

where hereafter the superscript h indicates spatial-approximated fields arising from the discretization given by 10.

4.2 Temporal Discretization: Discrete Derivative Operator

For the temporal discretization consider a partition of the time integration interval $[0, T]$ into N_t subintervals as $\mathcal{I}_{n+1} = [t_{n+1}, t_n]$ with $0 = t_0 \leq \dots \leq t_{N_t} = T$ and $\Delta t = |\mathcal{I}_{n+1}| = \text{constant}$, for the sake of simplicity, such that $\mathbf{z}_i(\mathbf{X}) \simeq \mathbf{z}(\mathbf{X}, t_i)$.

As said before, the key factor of the formulation proposed is the *discrete derivative operator* [5] which has two important properties: *directionality* and *consistency*

$$\langle Df(\mathbf{x}, \mathbf{y}), \mathbf{x} - \mathbf{y} \rangle_{\mathbf{U}} = f(\mathbf{x}) - f(\mathbf{y}), \quad (12)$$

$$Df(\mathbf{x}, \mathbf{y}) = Df\left(\frac{\mathbf{x} + \mathbf{y}}{2}\right) + \mathcal{O}(\|\mathbf{x} - \mathbf{y}\|^2). \quad (13)$$

\mathbf{x} and \mathbf{y} being any pair of variables pertaining to an inner product space. Note also that we have introduced the notation D for the discrete derivative operator while D for the standard derivative.

The first one holds the key to preserve discretely the evolution structure that the continuous system possesses while the second one ensures the second order accuracy.

4.3 Energy-Consistent Integration Scheme

Taking into account the above introduced discretizations, we proposed a monolithic second-order accurate energy-consistent integration scheme which reads

$$\begin{aligned}
 & \frac{\varphi_{n+1}^h - \varphi_n^h}{\Delta t} - \frac{1}{\rho_0} \mathbf{p}_{n+\frac{1}{2}}^h = \mathbf{0}, \\
 & \left\langle \frac{\mathbf{p}_{n+1}^h - \mathbf{p}_n^h}{\Delta t}, \mathbf{w}_\varphi^h \right\rangle_{\mathcal{B}_0^h} + \left\langle \mathbf{F}_{n+\frac{1}{2}}^h, \tilde{\mathbf{S}} \right\rangle_{\frac{\partial \mathbf{X}}{\partial \mathcal{B}_0^h}} - \langle \tilde{\mathbf{b}}_0, \mathbf{w}_\varphi^h \rangle_{\mathcal{B}_0^h} - \langle \tilde{\mathbf{t}}, \mathbf{w}_\varphi^h \rangle_{\partial \mathcal{B}_0^h} = \mathbf{0}, \\
 & \frac{\bar{\Gamma}_{n+1}^{\alpha,h} - \bar{\Gamma}_n^{\alpha,h}}{\Delta t} - \frac{1}{\eta_\alpha} \tilde{\mathbf{Q}}^\alpha = \mathbf{0} \quad \forall \alpha = 1, \dots, m, \\
 & \text{in } \mathcal{B}_0^h \times \mathcal{I}_{n+1} \text{ with } \mathbf{w}_\varphi^h = \sum_{a=1}^N N^a(\mathbf{X}) \mathbf{w}_\varphi^a \quad \text{and } (\bullet)_{n+\frac{1}{2}} = \frac{(\bullet)_{n+1} + (\bullet)_n}{2}.
 \end{aligned} \tag{14}$$

where $\tilde{\mathbf{b}}_0$ and $\tilde{\mathbf{t}}$ being second order approximations to the external forces per unit volume acting in the body and the external forces acting on its boundary, respectively.

In addition, $\tilde{\mathbf{S}}$ and $\tilde{\mathbf{Q}}^\alpha$ denote the discrete counterpart of the constitutive laws 5 which are obtained by the application of discrete derivative operator, that is

$$\left. \begin{aligned}
 \tilde{\mathbf{S}} &= 2D_C \Psi(\mathbf{C}_{n+1}^h, \mathbf{C}_n^h, \bar{\Gamma}_{n+1}^{\alpha,h}, \bar{\Gamma}_n^{\alpha,h}), \\
 \tilde{\mathbf{Q}}^\alpha &= -D_{\bar{\Gamma}^\alpha} \Psi(\mathbf{C}_{n+1}^h, \mathbf{C}_n^h, \bar{\Gamma}_{n+1}^{\alpha,h}, \bar{\Gamma}_n^{\alpha,h})
 \end{aligned} \right\} \text{in } \mathbf{B}_0^h \times \mathcal{I}_{n+1}. \tag{15}$$

For more details about its computation the reader is referred to [5].

Finally, it should be noted that this choice is the key ingredient for the scheme to be energy-consistent as it will be seen next.

4.4 Discrete Form of the Laws of Thermodynamics and Symmetries

By using the directionality property of the discrete derivative operator one may write the energy balance in any time interval \mathcal{I}_n as follows

$$\begin{aligned}
 E_{n+1}^h - E_n^h &= \langle DE(\mathbf{z}_{n+1}^h, \mathbf{z}_n^h), \mathbf{z}_{n+1}^h - \mathbf{z}_n^h \rangle_{\mathcal{I}} = \langle D_\varphi E(\mathbf{z}_{n+1}^h, \mathbf{z}_n^h), \varphi_{n+1}^h - \varphi_n^h \rangle_\varphi \\
 &+ \langle D_{\mathbf{p}} E(\mathbf{z}_{n+1}^h, \mathbf{z}_n^h), \mathbf{p}_{n+1}^h - \mathbf{p}_n^h \rangle_{\mathbf{p}} + \sum_{\alpha=1}^m \langle D_{\bar{\Gamma}^\alpha} E(\mathbf{z}_{n+1}^h, \mathbf{z}_n^h), \bar{\Gamma}_{n+1}^{\alpha,h} - \bar{\Gamma}_n^{\alpha,h} \rangle_{\bar{\Gamma}^\alpha}
 \end{aligned} \tag{16}$$

where E_i^h is the discrete total energy of the system, internal plus kinetic, expressed in terms of the discrete state vector \mathbf{z}_i^h . Further elaboration of the above expression, by using 14 together with the definition and properties of the discrete derivative operator, leads the energy balance to be

$$\begin{aligned}
 E_{n+1}^h - E_n^h &= \\
 &\left\langle \frac{\mathbf{P}_{n+1}^h - \mathbf{P}_n^h}{\Delta t}, \varphi_{n+1}^h - \varphi_n^h \right\rangle_{\mathcal{B}_0^h} + \left\langle \mathbf{F}_{n+\frac{1}{2}}^h \tilde{\mathbf{S}}, \frac{\partial(\varphi_{n+1}^h - \varphi_n^h)}{\partial \mathbf{X}} \right\rangle_{\mathcal{B}_0^h} - \Delta t \sum_{\alpha=1}^m \left\langle \frac{1}{\eta_\alpha}, \tilde{\mathbf{Q}}^\alpha : \tilde{\mathbf{Q}}^\alpha \right\rangle_{\mathcal{B}_0^h} \\
 &= \left\langle \tilde{\mathbf{b}}_0, \varphi_{n+1}^h - \varphi_n^h \right\rangle_{\mathcal{B}_0^h} + \left\langle \tilde{\mathbf{t}}, \varphi_{n+1}^h - \varphi_n^h \right\rangle_{\partial \mathcal{B}_0^h} - \Delta t \sum_{\alpha=1}^m \left\langle \frac{1}{\eta_\alpha}, \tilde{\mathbf{Q}}^\alpha : \tilde{\mathbf{Q}}^\alpha \right\rangle_{\mathcal{B}_0^h},
 \end{aligned}
 \tag{17}$$

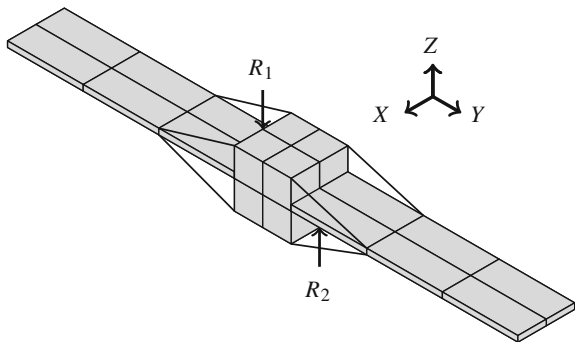
It can be easily concluded that the energy balance is unconditionally decreasing in every time step in absence of external forces, $\tilde{\mathbf{b}}_0 = \tilde{\mathbf{t}} = \mathbf{0}$. As a result, the proposed scheme is energy-consistent in the sense that it satisfies the laws of thermodynamics by construction.

The full demonstration can be found in a recent work published by the authors [6], as well as the proofs for the conservation of symmetries.

5 Numerical Example

Consider the maneuver of a satellite with flexible solar panels made of viscoelastic material, depicted Fig. 1. The body is a $1 \times 1 \times 1$ m cube with a mass of 500 kg, and each panel is 4 m long, 1 m wide and 0.1 m thick. Each panel is hinged to the satellite body by three smooth spherical joints and connected by four rigid elements, acting as stiffeners of the panels. The satellite body is equipped with two rockets R_1 and R_2 that provide the necessary thrust 18 to perform the maneuver, aimed to change of attitude of the satellite in 90.

Fig. 1 Satellite: mesh and boundary condition definition



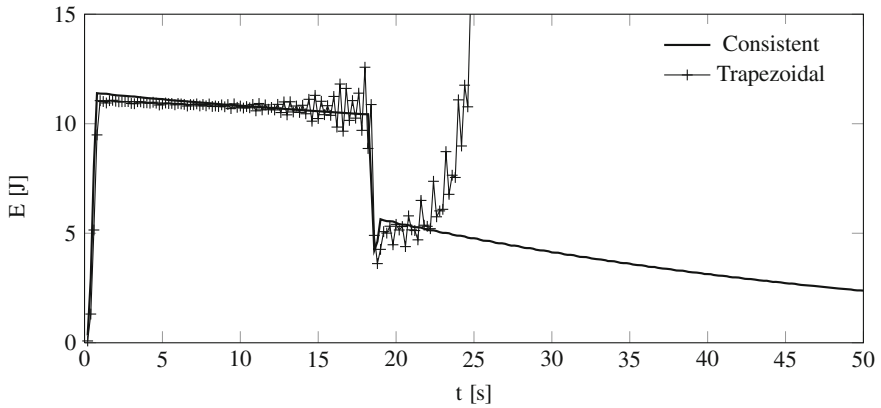


Fig. 2 Evolution of the total energy of the system, kinetic plus internal, obtained with the trapezoidal and consistent scheme. Only the consistent scheme provided a full solution which, in addition, is in accordance with the laws of thermodynamics

$$f_1(t) = -f_2(t) = \begin{cases} -200t & \text{for } t \leq 0.5 \text{ s} \\ 200(t - 1) & \text{for } 0.5 < t \leq 1 \text{ s} \\ 0 & \text{for } 1 < t \leq 18.2 \text{ s} \\ 200(t - 18.2) & \text{for } 18.2 < t \leq 18.7 \text{ s} \\ 200(18.7 - t) & \text{for } 18.7 < t \leq 19.2 \text{ s} \\ 0 & \text{for } t > 19.2 \text{ s} \end{cases} \quad (18)$$

The satellite body are modeled with a homogeneous Saint Venant-Kirchhoff material with density $\rho_{0,b} = 500 \text{ kg/m}^3$, a Young modulus $E_b = 1 \text{ GPa}$ and Poisson coefficient $\nu_b = 0.3$. The panels are modeled by the viscoelastic material 3 based on Neo-hookean hyperelasticity and only one internal variable, with $\nu_p = 0.4$, $E_p = 0.01 \text{ MPa}$, $\tau_p = 20 \text{ s}$, $\mu_p = 50.2 \text{ MPa}$ and $\rho_{0,p} = 100 \text{ kg/m}^3$.

We integrate this example for a time interval $[0,50] \text{ s}$ with a time step size $\Delta t = 0.2 \text{ s}$ using Trapezoidal, Midpoint and consistent methods.

Figure 2 depicts the evolution of the energy of the system obtained with each scheme. It clearly shows that the Trapezoidal scheme provides a non-physical evolution of the energy in the free-force phase of the motion, which eventually cause this method to collapse. Instead, the consistent method successes in simulating the whole time interval, enhancing the stability and robustness of the method and allowing to calculate long term simulations with the same time step as the one which makes Trapezoidal method explode.

6 Conclusions

We have addressed the development and implementation of an energy-consistent scheme for finite deformation viscoelasticity able to be employed in multi-body system. Our approach departs from classical procedures, extending the concepts involved in conserving integration schemes to the integration of dissipative problems. Essentially, it is only necessary to program different expressions for the residual vector and the tangent matrix derived from the use of the discrete derivative operator, which is the key to discretely satisfying the laws of thermodynamics and the symmetries.

The consistent scheme not only conserves angular and linear momentum, and the laws of thermodynamics, but considerably improves the stability and enables the use of larger time steps.

Acknowledgments Financial support for this research was provided by the Education Ministry of Spain under Project No. DPI 2012-36429. This support is gratefully acknowledged.

References

1. Simó JC, Tarnow N (1992) The discrete energy-momentum method. Conserving algorithm for nonlinear elastodynamics. *Zeitschrift für Angewandte Mathematik und Physik (ZAMP)*, 43 (5):757–792
2. Romero I (2010) Algorithms for coupled problems that preserve symmetries and the laws of thermodynamics Part I: Monolithic integrators and their application to finite strain thermoelasticity. *Comput Methods Appl Mech Eng* 199:1841–1858
3. Holzapfel GA, Simó JC (1996) A new viscoelastic constitutive model for continuous media at finite thermomechanical changes. *Int J Solids Struct* 33(20):3019–3034
4. Govindjee S, Simó JC (1992) Mullins effect and the strain amplitude dependence of the storage modulus. *Solids Struct* 29:1737–1751
5. González O (1996) Design and analysis of conserving integrators for nonlinear hamiltonian systems with symmetry. Ph.D. thesis, Stanford
6. Conde Martín S, García Orden JC, Romero I (2014) Energy-consistent time integration for nonlinear viscoelasticity. *Computational Mechanics*. doi:[10.1007/s00466-014-1000-x](https://doi.org/10.1007/s00466-014-1000-x)

Multi-objective Optimization of Mechanisms with Clearances in Revolute Joints

Z. Zhang, L. Xu, Y.Y. Tay, P. Flores and H. Lankarani

Abstract Despite extensive work on the evaluation of the dynamic performances of various mechanisms and multi-body mechanical systems with revolute joint clearances, limited work has been conducted in optimizing the performances of these systems. A multi-objective optimization technique is presented to examine and to quantify the effect of combined objective functions with several design variables on the response of the systems. In particular, a Kriging meta-model based on the Design-of-Experiment method is utilized to optimize the systems' performance. The reason for implementing this meta-model is to replace the computational intensive simulations with a more efficient mathematical model. In this study, a simple slider-crank mechanism with a revolute clearance joint at the slider pin is modeled, and its dynamic response is analyzed using the multi-body dynamic software, MSC ADAMS. The revolute joint clearance is modeled as a pin-in-hole dry contact utilizing the Hertzian contact force model with hysteresis damping. Response surfaces are generated on the prediction of the system's performances for three different objective functions and for different range of design variables. The objective functions are combined to develop a single response surface characterizing the dynamic responses of the system at different range of design variables in order to optimize its performance.

Z. Zhang (✉) · L. Xu · Y.Y. Tay · H. Lankarani
Wichita State University, Wichita, USA
e-mail: zxzhang1@wichita.edu

L. Xu
e-mail: lxxu3@wichita.edu

Y.Y. Tay
e-mail: yxtay1@wichita.edu

H. Lankarani
e-mail: hamid.lankarani@wichita.edu

P. Flores
University of Minho, Braga, Portugal
e-mail: pflores@dem.uminho.pt

Keywords Slider-crank mechanism · Revolute joint clearances · Multi-body dynamics · Design-of-experiment · Kriging meta-model

1 Introduction

Over the last two decades, a number of researchers have proposed various methodology on the influence of joint clearance in planar and spatial mechanical systems. It is known that joint clearance can degrade the performance of a system by introducing vibration, noise and wear. Dubowsky et al. [1] presented a performance study on joint clearance by developing a simple ring model to demonstrate the dynamic force amplification caused by the presence of joint clearance. Dubowsky and Moeing [2] extended the simple ring model by showing that excessive impact force developed at the joint can cause mechanical failure. The influence of clearance joint on the performance of a fourbar mechanism when subjected to various combinations of clearance joints was also investigated by Bengisu et al. [3].

Lankarani et al. [4] extended the work on contact-impact force by modifying the Hertz contact law to include a hysteresis damping function to account for the dissipation of impact energy. During the period of contact, the indentation depth, relative penetration velocity and non-linear force are readily available and are related to the contact force. Flores et al. [5] conducted extensive study using experimental and computer models to predict the dynamic response of a mechanical system with dry and lubricated revolute joints. In their study, the subjective measurements determined to be of influential to the performance of a mechanical system are clearance size, crank angular velocity and number of joints modeled as clearance joints. A general approach in analyzing the kinematics and dynamics of a mechanism with joint clearance using the continuous impact model assumption is presented by Furuhashi et al. [6]. By using the Lagrangian function, they analyzed the dynamic performance of the mechanism when subjected to multiple clearance joints and a comparative study was performed. A equation of motion equation is formulated by Wilson and Fawcett [7] by examining the influence of mechanisms with joint clearances.

In the recent decade, many researches have experimented with various methodology to optimize a mechanism in an attempt to obtain a optimal solution. With the advancement of computational power, researchers are beginning to harvest the benefits of computer models. In order to reduce computational complexity, the neural network, proposed by Erkaya and Uzmay [8] can be used to investigate the effects of joints with clearances and the kinematic transmission quality. Another alternative method in analyzing path generation problem is the generic algorithm-fuzzy logic method, which is proposed by Laribi et al. [9]. The genetic algorithm method is excellent in generating solutions to optimization problems [10]. However, the genetic algorithm do not scale well with system complexity and computational cost increases dramatically for huge model functions. Feng et al. [11]

proposed a method to control the distribution of inertia forces by optimizing the mass distribution of a mechanism with joint clearance.

The primary objective of this study is to conduct a multi-objective optimization, utilizing the Kriging meta-model, to demonstrate the influence of various design variables on the dynamic response of a mechanism with joint clearance. Examples of design variables that could be identified in this study are the clearance sizes, material/stiffness coefficient, links length ratio, etc. Due to the wide range of design variables, analyzing the effect of each variable using the simulation model or experimental method could be quite inefficient and expensive. Therefore, a methodology is presented to predict the dynamic performance of the mechanism at any desirable combination of design variables. First, the classic slider-crank mechanism is modeled using the design/analysis software, MSC ADAMS. Next, a Latin Hypercube Sampling (LHS) method determines the number of sampling points needed to form the basis for the Kriging model. Finally, a multi-objective analysis is performed to combine all the objective functions into a single response surface.

2 Multi-objective Optimization

This study focuses on optimizing the performance of mechanisms with revolute joint clearances with the more cost-effective Kriging meta-model. The multi-objective optimization can be performed on mechanisms with revolute joint clearances with different set of objective functions and design variables. For example, the optimization of a mechanism with joint clearances can be described as:

$$\mathbf{Objective\ functions} : \min \left\{ \underline{q}, \underline{\dot{q}}, \underline{\ddot{q}} \right\}_{\max}, \min \{F_N\}_{\max}, \min \{T\}_{\max}, \min \{P\}_{\max}$$

$$\mathbf{Design\ variables} : c, l_{ratio}, m_{ratio}, K_{stiff}, \mu$$

where \underline{q} , $\underline{\dot{q}}$ and $\underline{\ddot{q}}$ could be some kinematic responses from the system; F_N is the contact force generated at the clearance joints; T is the input torque requirement; P is the input power required, calculated as the product of input torque T , and the angular operating speed ω ; c is the clearance size; l_{ratio} could be some geometric length or length ratio for the different bodies in the system; m_{ratio} could be some mass or mass ratio for different bodies in the system; K_{stiff} is the stiffness coefficient of the bodies at the joint(s) where there is a clearance; and μ is the coefficient of friction at the clearance.

In computer simulation, such as the analysis of a slider-crank mechanism, the space-filling design is particularly suitable for deterministic design because the

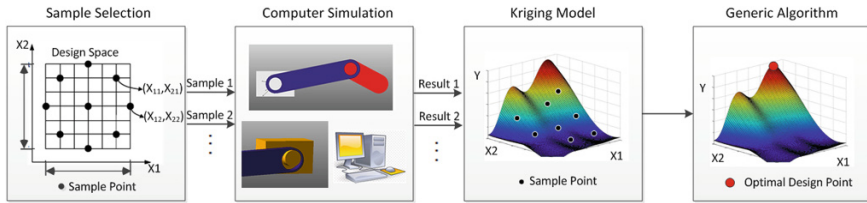


Fig. 1 Flowchart for implementation of system optimization using Kriging model

design points are generally spread out evenly and uniformly [12]. One of the space-filling design is the Latin Hypercube Sampling. This method not only reduces the number of simulation iterations, it also retains the proper orthogonality and proportionality of the sample. The Kriging model is a method of interpolation for integrating a given sample points to approximate the model parameters and to determine any desirable response of a new design point without the need to conduct simulation or experiment [13]. A detailed description and implementation of the Kriging model in optimizing mechanisms with joint clearances is presented by Zhang et al. [14].

Among many techniques used to capture the non-linearity of a mechanism are the artificial neural network and Kriging meta-model. The precision in Kriging model are usually far superior than the neural network method and the meta-model performs as good or better in optimization involving a large number of independent variables [15]. For a given set of design variables/parameters, a complete simulation cycle might required thousands or more integration steps, which is computational expensive and inefficient. This process of performing multiple simulations can be eliminated by optimizing this process using the Kriging model. The first part of this optimization work is to acquire initial design points using the LHS technique to serve as a basis to construct the surrogate Kriging model. Once several design points are obtained, the dynamic responses of the mechanism is evaluated using MSC ADAMS. Subsequently, a prediction model can be developed to predict the value of the objective functions over a range of design space. The implementation of the method is shown systematically in Fig. 1. Based on the polynomial curve of the Kriging model, the system can be optimized using a multi-objective optimization method.

3 Modeling Revolute Joints with Clearance

Joint clearance exists to allow some sort of tolerance due to imperfect in journals and bearings. A revolute joint with clearance is illustrated in Fig. 2, with the radii R_B and R_J for the journal and bearing respectively. As observed in Fig. 2, the indentation depth due to the contact/impact between the journal and bearing can be defined as:

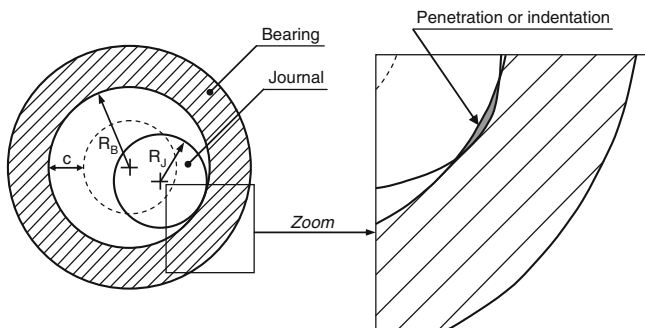


Fig. 2 Illustration of a revolute joint with clearance

$$\delta = e - c \quad (1)$$

where e is the magnitude of eccentricity and c is the radial clearance.

The radial clearance can be defined as the difference between the radius of the bearing and that of the journal:

$$c = R_B - R_J \quad (2)$$

A contact-impact force is developed when the journal is in contacts with the bearing's surface and the indentation depth will be greater than zero. A Hertzian-based contact force model with hysteresis damping, based on work by Lankarani and Nikravesh [4, 16] can be defined as:

$$F_N = K \delta^n \left[1 + \frac{3(1 - c_e^2) \dot{\delta}}{4 \dot{\delta}^{(-)}} \right] \quad (3)$$

where the c_e is the coefficient of restitution; $\dot{\delta}$ is the relative velocity at penetration and $\dot{\delta}^{(-)}$ is the initial velocity at impact, and the exponent n is the material contact coefficient. The material properties, and the contact surface of the journal and bearing is utilized to define the stiffness coefficient, K as:

$$K = \frac{4}{3(\sigma_B + \sigma_J)} \left[\frac{R_B R_J}{R_B - R_J} \right]^{\frac{1}{2}}, \quad \sigma_i = \frac{1 - \nu_k^2}{E_k} \quad (i = B, J) \quad (4)$$

where variables ν_k and E_k are the coefficient of Poisson and Young's modulus for the journal and bearing respectively.

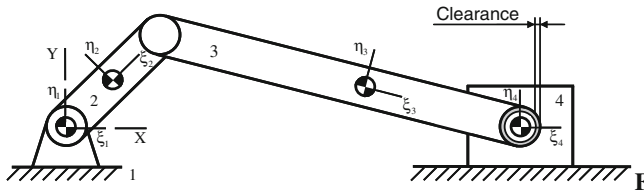


Fig. 3 Configuration of a simple slider-crank mechanism with joint clearance at the piston

Table 1 Geometric and mechanical properties of the slider-crank mechanism [17]

Link	Length (m)	Mass (kg)	Moment of inertia (kg.m ²)
2	0.05	0.30	0.00010
3	0.12	0.21	0.00025
4	0.06	0.14	0.00010

4 Illustrative Example of Modeling of a Slider-Crank Mechanism with Joint Clearance

This section presents the work on computational modeling and multi-objective optimization of a simple slider-crank mechanism with revolute clearance joint at the piston pin. This mechanism is modeled using the design and analysis software, MSC ADAMS and it comprises of four multi-body links that represent the crank (link 2), coupler (link 3), slider (link 4) and ground (link 1). The configuration of the mechanism clearing showing the clearance joint is illustrated in Fig. 3. Additionally, the mechanical and geometric properties are illustrated in Table 1 [17].

For the computer model, all links are modeled as rigid bodies. At initial simulation time, the journal's and bearing's centers coincide and the initial crank angle is set at zero degrees. In order to ensure accuracy in the modeling of the slider-crank mechanism with clearance joint, the slider's dynamic responses are validated with the experimental and numerical results by Flores et al. [18] and Koshyet et al. [19], and the results are found to be in good agreement. Therefore, the slider-crank mechanism developed in this study is fairly accurate in simulating the dynamic behavior of the system.

The dynamic response of the slider-crank mechanism with revolute joint clearance is further studied for the multi-objective optimization. The Kriging meta-model is developed in order to optimize and analyze the simulated results. The implementation of the Kriging model is illustrated previously in Fig. 1. The genetic algorithm technique is used to find the minimal contact force at the clearance, power consumption and slider's acceleration by controlling the appropriate values of the design variables. The LHS method is used to create a set of sample points and the validated slider-crank with joint clearance model is used to obtain the performances acquire from the sample points. Once sampling is performed, the absolute

Table 2 The design variables and objective function used for the development of the Kriging model

	Variables/functions	Range of variables
Design variables	1. c , radial clearance size (mm)	0.05–0.5
	2. K_{stiff} material/contact stiffness coefficient (N/m ^{1.5})	3.4E+009–1.7E+010
Objective functions	1. \ddot{x}_{slider} , slider acceleration (m/s ²)	
	2. F_N , contact force at joint clearance (N)	
	3. P , power consumption (W)	

maximum value obtained from the simulated results for the slider’s acceleration, contact force at joint clearance and power consumption is treated as the objective functions to form a basis for building the surrage Kriging model. By using this technique, the desirable quantitative values from the objective functions can be predicted without the need for iterative simulations.

Table 2 shows the design variables, namely, the radial clearance size and material/contact stiffness coefficient. Also illustrated in this table is the primary objective functions investigated such as the slider’s acceleration, contact force at the revolute joint clearance and power consumption of the system. The crank is K_{stiff} given a constant angular velocity of 5,000 rpm or 523.6 rad/s. A high crank angular velocity is defined to ensure that the effect of radial clearance size and contact stiffness is sensitive and visible in the system. Due to the high stiffness coefficient, a stiff integration method is utilized to increase the computational efficiency. A backward difference numerical formulation used in this study is the GSTIFF integration method and a small time step of 10⁻⁶ s is chosen for the variable integration time step. A generic radial clearance size of 0.05–0.5 mm is chosen to emulate a non-ideal revolute joint. The stiffness coefficient ranging from 3.4E+009 N/m^{1.5} to 1.7E+009 N/m^{1.5} is calculated based on the Young’s modulus of metal to be between 113 and 210 GPa and a typical Poission coefficient in the region of 0.23 and 0.3. The exponent n is set at 1.5, which corresponds to metal-to-metal contact.

Table 3 represents the sample points acquired from the LHS, the design variables inserted in the simulation model and the simulated objective functions. Using the Kriging study, the response surfaces for each objective functions are plotted as shown in Fig. 4. Following the development of the Kriging model, an 11th point is constructed to evaluate its accuracy. The clearance size and stiffness coefficient of the 11th point is 0.18 mm and 1.0E+010 N/m^{1.5}. Additionally, the absolute value for the slider’s acceleration is obtained from the Kriging model and computer model to quantify its accuracy. Based on the results sampled from the 11th point, the predicted acceleration from the meta-model is within 6 % of the actual value. This shows fairly reasonable prediction of the Kriging model.

Illustrated in Fig. 4a is the clearance joint contact force as the functions of clearance size and stiffness coefficient. In a similar manner, the slider’s acceleration and power consumption of the system are evaluated as shown in Fig. 4b, c. It can be

Table 3 Sample points acquire from LHS and the simulated results

Sample point	Clearance size (mm)	Stiffness (N/m ^{1.5})	Slider's acceleration (m/s ²)	Contact force (N)	Power (W)
1	0.50	9.4E+09	1.1E+05	1.5E+04	1.2E+05
2	0.45	3.4E+09	1.0E+05	1.4E+04	0.9E+05
3	0.05	1.5E+10	2.0E+04	2.7E+03	1.9E+04
4	0.30	1.1E+10	8.5E+04	1.2E+04	8.2E+04
5	0.15	1.2E+10	2.7E+04	3.7E+03	2.5E+04
6	0.35	6.4E+09	9.3E+04	1.3E+04	9.1E+04
7	0.25	1.7E+10	6.8E+04	9.6E+03	6.2E+04
8	0.10	7.9E+09	2.0E+04	2.8E+03	1.8E+04
9	0.20	4.9E+09	4.5E+04	6.3E+03	4.3E+04
10	0.40	1.4E+10	9.1E+04	1.3E+04	9.3E+04

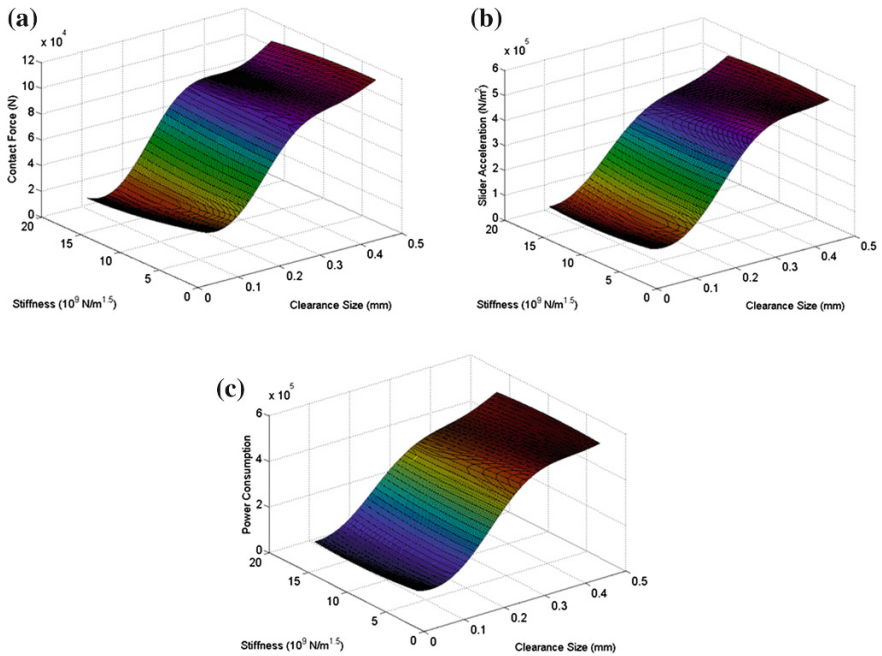


Fig. 4 Response surfaces acquired using the Kriging model for each objective functions: **a** joint contact force; **b** slider's acceleration; **c** power consumption of the system

observed that the objective functions are more sensitive to the change in clearance size than the stiffness coefficient in the range of parameters examined. The clearance size, slider's acceleration and power consumption grow monotonically with

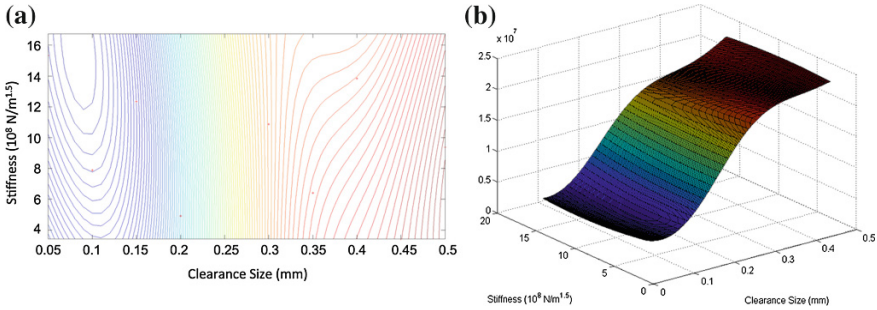


Fig. 5 Response contour and surface plots of multi-objective analysis **a** contour plot **b** surface plot

increasing clearance size. The rate of change in surface steepness gradually becomes smooth at higher clearance size. The optimal point can be identified to have a stiffness coefficient of $3.4E+009 \text{ N/m}^{1.5}$ and joint clearance of 0.05 mm. The response surfaces indicate that the lowest value in the range of design variables yield optimal response. However, the absolute optimal point can be further determined by using a wider range of design variables. Further examination of the slider-crank system with larger sample size on the design variables is produced in [14].

Once the Kriging model for each objective function has been determined, the multi-objective synthesis is realized by combining the objective functions to develop a multi-objective response surface. For the slider-crank mechanism example, the three objective functions are the slider’s acceleration (\ddot{x}_{slider}), joint clearance force (F_N), and power consumption (P) of the mechanical system. The weight factors are set at by assuming the contributions for all objective functions are identical. Thus, the multi-objective function \mathfrak{F} is:

$$\mathfrak{F} = \frac{1}{3}\ddot{x}_{slider} + \frac{1}{3}F_N + \frac{1}{3}P \tag{5}$$

Figure 5 represents the contour and response surface of multi-objective optimization respective derived using Eq. (5). The multi-objective plots yield similar results from the previous analysis, in which the response is highly sensitive to the change in clearance size rather than the stiffness coefficient. Using the meta-model and multi-objective analysis, it can be concluded that the performance of the slider-crank mechanism can be optimized by reducing the clearance size.

5 Conclusions

This research work was focused on developing a multi-objective optimization technique to examine and quantify the combined effect of various objective functions with several design variables on the dynamic responses of mechanisms with

joint clearances. This is accomplished by developing a surrogate Kriging meta-model to optimize the system's performance. This meta-model technique allows the prediction of the system's dynamic responses at various design points without the need for iterative computer simulations.

The goal of this study was achieved by using an illustrative study of a simple slider-crank mechanism with revolute joint clearance at the piston pin. The joint clearance at the piston pin was formulated based on the Hertzian contact force model and was modeled as a pin-in-hole dry contact. A Coulumb-type friction force was chosen in this study. For the mechanism studied, the dynamic responses predicted using the meta-model were found to be in good agreement with the experimental and simulated results reported in the literature. The global results obtained from the meta-model indicated that the objective functions were quite sensitive to the change in clearance size, but not to the stiffness coefficient, within the range considered. Next, the multi-objective synthesis was performed by defining identical weight factors for all the design functions and these objective functions were optimized simultaneously to form a single response surface plot. The multi-objective optimization indicated similar findings with the ones from the meta-model analysis. After applying the genetic algorithm scheme, it was found that the system can be optimized by using a small clearance size of 0.05 mm and a stiffness coefficient of 10^{10} N/m^{1.5}, within the range of design variables considered. The presented methodology can be utilized for the optimization of various mechanisms with joint clearances. Further studies may include examining the accuracy of the presented methodology with more complex mechanisms such as mechanisms with multiple joint clearances or mechanisms with a large number of objective functions and design variables.

References

1. Dubowsky S, Norris M, Aloni E, Tamir A (1984) An analytical and experimental study of the prediction of impacts in planar mechanical systems with clearances. *J Mech Transm Autom Des* 106(4):444–451
2. Dubowsky S, Moening M (1978) An experimental and analytical study of impact forces in elastic mechanical systems with clearances. *Mech Mach Theor* 13(4):451–465
3. Bengisu MT, Hidayetoglu T, Akay A (1986) A theoretical and experimental investigation of contact loss in the clearances of a four-bar mechanism. *J Mech Transm Autom Des ASME* 108:224–237
4. Lankarani HM, Nikravesh PE (1990) A contact force model with hysteresis damping for impact analysis of multibody systems. *J Mech Des* 112(3):369–376
5. Flores P, Lankarani HM (2010) Spatial rigid-multi-body systems with lubricated spherical clearance joints: modeling and simulation. *Nonlinear Dyn* 60(1–2):99–114
6. Furuhashi T, Morita N, Matsuura M (1978) Research on dynamics of four-bar linkage with clearances at turning pairs. *JSME bull*, 1st report, general theory of continuous contact model, pp 518–523
7. Wilson R, Fawcett JN (1974) Dynamics of slider-crank mechanism with clearance in the sliding bearing. *Mech Mach Theor* 9(1):6180

8. Erkaya S, Uzmay I (2008) A neural-genetic (NN-GA) approach for optimizing mechanisms having joints with clearance. *Multibody Sys Dyn* 20(1):69–83
9. Laribi MA, Mlika A, Romdhane L, Zeghloul S (2004) A combined genetic algorithm-fuzzy logic method (GA-FL) in mechanisms synthesis. *Mech Mach Theor* 39(7):717–735
10. Goldberg DE (1989) *Genetic algorithms in search, optimization and machine learning*, 1st edn. Addison-Wesley Professional
11. Feng B, Morita N, Torri T (2002) A new optimization method for dynamic design of planar linkage with clearances at joints—optimizing the mass distribution of links to reduce the change of joint forces. *J Mech Des* 124:68–73
12. Montgomery DC (2009) *Design and analysis of experiment*, 8th edn. Wiley, Singapore
13. Simpson TW (2001) Kriging models for global approximation in simulation-based multidisciplinary design optimization. *AIAA J* 39(12):2233–2241
14. Zhang Z, Xu L, Flores P, Lankarani HM (2013) A DOE- and Kriging-based model for studying the dynamics of multibody mechanical systems with revolute clearance joints. *ASME J Comput Nonlinear Dyn* 9:031013-1:13. doi:[10.1115/1.4026233](https://doi.org/10.1115/1.4026233)
15. Gomes MVC, Bogle ID, Biscaia EV Jr, Odlock D (2008) Using kriging models for real-time process optimisation. In: 18th European symposium on computer aided process
16. Lankarani HM, Nikravesh PE (1994) Continuous contact force models for impact analysis in multibody systems. *Nonlinear Dyn* 5(2):237–246
17. Flores P, Ambrosio J, Claro JCP, Lankarani HM (2007) Dynamic behavior of planar rigid multi-body systems including revolute joints with clearance. *Proc Inst Mech Eng Part K: J Multi-Body Dyn* 221(2):161–174
18. Flores P, Koshy CS, Lankarani HM, Ambrosio J, Claro JCP (2011) Numerical and experimental investigation on multibody systems with revolute clearance joints. *Nonlinear Dyn* 65(4):383–398
19. Koshy CS, Flores P, Lankarani HM (2013) Study of the effect of contact force models on the dynamic response of mechanical systems with dry clearance joints: computational and experimental approaches. *Nonlinear dynamics NODY-D-12-03975*, vol 73, pp 325–338. doi:[10.1007/s11071-013-0787-x](https://doi.org/10.1007/s11071-013-0787-x)

Biomechanical Experimental Data Curation: An Example for Main Lumbar Spine Ligaments Characterization for a MBS Spine Model

C. Lourenço and J.C.P. Claro

Abstract This work overviews an extensive analysis in the context of mechanical characterization of human biomaterials, carried out over a broad set of published experimental data. Focused on main lumbar spine ligaments, several test procedures are exhaustively analyzed, in order to identify possible causes for divergences that have been found in some results. Moreover, guidelines are proposed for data filtering and selection. The main objective of the task was to retrieve trustworthy inputs to a hybrid Finite Element Analysis/Multibody System dynamic simulation model of the human intervertebral disc, which can be used on the prediction of nucleus prosthetics working performance.

Keywords Biomechanics · Data curation · Experimental data · Spine ligaments

1 Introduction

The knowledge on mechanical and geometrical properties of spine ligaments is a key requirement to understand and model, with a minimum of fidelity, the normal operation of the column [1]. One of the most relevant characteristics of ligaments mechanical behavior is their force/elongation nonlinearity. Actually, ligaments are expected to allow small movements around their neutral position, without significant actuating or produced force and, simultaneously, to provide stability to the column, by a progressive increase in stiffness as motion amplitude increases and physiological limits are approached. This behavior was typified by Panjabi [2], who formulated the concepts of ‘neutral’ and ‘elastic’ working zones.

C. Lourenço (✉) · J.C.P. Claro
University of Minho, Braga, Portugal
e-mail: lourenco.carina@gmail.com

J.C.P. Claro
e-mail: jcclaro@dem.uminho.pt

A considerable number of published experimental studies on the subject can be found, but usually following different procedures, ranging from testing each ligament per se or the entire ‘functional spinal unit’ (FSU). On the other hand, the majority of the tests are performed *in vitro*, while *in vivo* tests are restricted to ligaments laying near the skin surface, as the supraspinous and the interspinous [3–8]. Besides, the majority of these works present force-displacement and/or stress-strain curves that are linear extrapolations—based on very few points or just on the final rupture conditions [7, 9–12]. As consequence, the crucial part of the viscoelastic behavior is vanished.

In normal daily activities, ligaments’ working condition fall in the zones where the most noticeable stress-strain ratio changes occur. Therefore, it is indispensable to rely upon experimental data, but also on a careful analysis of the experimental test protocols that are followed, in order to assure some reliability to the model.

Here, some of the most relevant experimental works on mechanical characterization of the lumbar spinal ligaments are analyzed, in order to detect incoherencies, point out possible explanations to these discrepancies, compare and find common aspects among some authors’ results and emphasize the most relevant factors to take into consideration during curation processes. These are the main guidelines for collecting information on biomaterials mechanical properties, to be introduced in an hybrid Finite Element Analysis/Multibody System (FEA/MBS) dynamic simulation model of the intervertebral disc, which is used for *in silico* performance prediction of *nucleus pulposus* prosthetic implants.

2 Analysis of Experimental Works and Criteria for Data Selection

Each ligament is mechanically characterized by the combination of three factors: force, elongation and stiffness, where the stiffness corresponds to the slope of the force-displacement/stress-strain curve as shown in Fig. 1 [13].

Fig. 1 Typical load-displacement curve of a ligament. Adapted from [1]

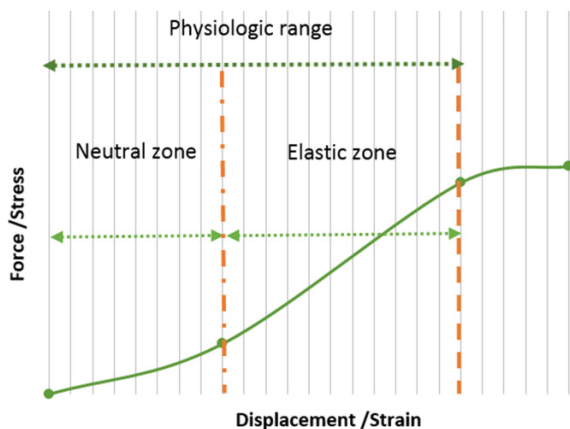
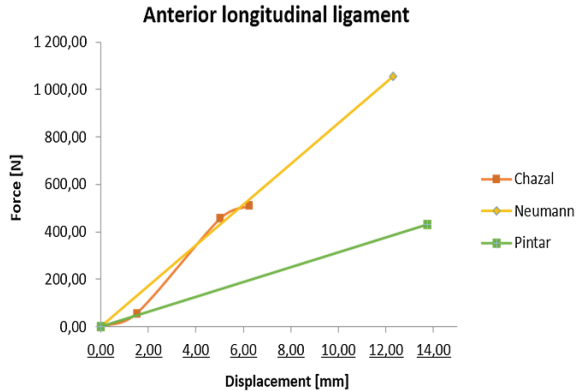


Fig. 2 Anterior longitudinal ligament force-displacement curves [9, 14, 15]



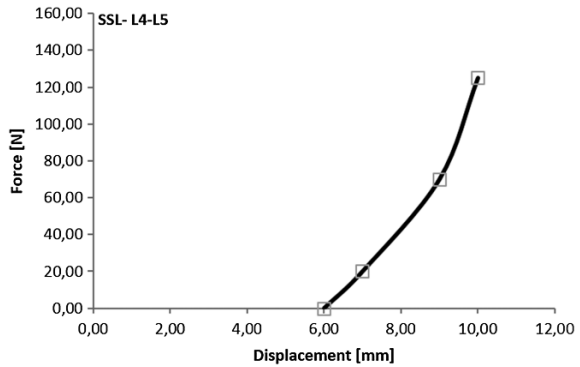
In a curation process of published data, a huge spread of results for the properties of the same ligament can be found (Fig. 2) [9, 14, 15]. This variability may be due to factors such as: dissimilarity in the age of specimens' donors, differences in test protocols, degeneration of specimens, storing, conditioning handling, or simply by test errors. These are just some of the possible factors, since the mechanical characteristics of a ligament are dependent on several variables, such as age, sex, weight, height, physical fitness and genetic influence [16].

2.1 Dumas et al. [6]

Tensile tests were carried out on 25 specimens with an average age of 66 years old, collected from 14 human lumbar columns between levels T11 and L5, not later than 24 h after death. A method of progressive dissection was used, i.e. starting with the motion segment (MS), the set without the disc was tested. Afterwards, each ligament was removed and the remaining of the MS was tested again, which lead to force-elongation curves for each one of the situations. During the tests the ligaments were covered with a commercial jelly, in order to maintain hydration. For pre-conditioning, the specimens were previously subjected to several loading cycles. The results are shown in Fig. 3.

Despite of a rigorous methodology for conservation of the ligaments and of having extensively characterized the samples, recording weight, sex, age and time interval since the death, some procedures could compromise the performance of the ligaments. For instance, the progressive dissection of the ligaments coupled to the preconditioning, may induce permanent deformations, probably due to the presence of micro ruptures in the fibers. Another disadvantage of the methodology is that, only supraspinous ligament was tested individually.

Fig. 3 Typical force-elongation curve obtained for one specimen (supraspinous ligament), according to [6]



2.2 Pintar et al. [9]

In situ tests for determination of the biomechanical properties of the lumbar ligament were performed using 132 bone-ligament-bone type samples taken from 38 cadavers. The average age of the tested specimens is 63 years old, and the tests were performed up to 48 h after death. The geometric studies were performed using a cryomicrotome technique. The force-elongation curves were obtained from normalized force-time and displacement-time curves. In order to reduce the number of curves, values were averaged for each tested ligament, according to their level in the column. Results are shown in Fig. 4, whereas Table 1 summarizes the tested parameters.

This paper presents a significant number of test samples, with different approaches, when compared with most of available studies, namely in what concerns to the relation established between each of the tested parameters and the column level.

However, other studies, such as [14, 17], sustain that there is no significant difference in the mechanical properties of the ligaments along the column's level.

Besides, although the authors ensure a “match” between age, geometrical and mechanical properties of the ligaments, the way results are presented avoids to clearly establish this relationship. Since, two distinct groups of samples were involved in this study, one to determinate geometrical characteristics of the ligaments and another to determinate de mechanical properties.

Moreover, as force-elongation curves were obtained by normalization of time dependent curves, their usual sigmoid shape was vanished, which means that an important part of the physiological behavior of the ligaments was lost. Finally, the reconstruction of stress-strain curves, based on the tabulated data, lead to linear graphs since only the values for the for the rupture point are provided.

These results may be suitable as an initial approach for simpler models, where ligaments can be modeled as linear springs, but not to complex models.

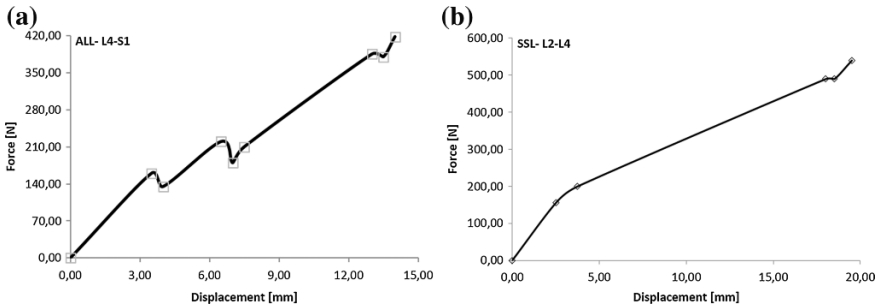


Fig. 4 Average biomechanical force-deformation curves, adapted from [9], derived for **a** Anterior longitudinal ligament; **b** Supraspinous ligament

Table 1 Biomechanical parameters of human lumbar ligaments

Parameter	Ligament	T12-L1	L1-L2	L2-L3	L3-L4	L4-L5	L5-S1
Stiffness (N mm ⁻¹)	ALL	32.9	32.4	20.8	39.5	40.5	13.2
	PLL	10.0	17.1	36.6	10.6	25.8	21.8
	LF	24.2	23.0	25.1	34.5	27.2	20.2
	ISL	12.1	10.0	9.6	18.1	8.7	16.3
	SSL	15.1	23.0	24.8	34.8	18.0	17.8
Stress at failure (MPa)	ALL	9.1	13.4	16.1	12.8	15.8	8.2
	PLL	7.2	11.5	28.4	12.2	20.6	19.7
	LF	13.2	2.5	1.3	2.9	2.9	4.1
	ISL	4.2	5.9	1.8	1.8	2.9	5.5
	SSL	4.0	15.5	9.9	2.6	12.7	14.0
Strain at failure (%)	ALL	31.9	44.0	49.0	32.8	44.7	28.1
	PLL	16.2	15.7	11.3	15.8	12.7	15.0
	LF	61.5	78.6	28.8	70.6	102.0	83.1
	ISL	59.4	119.7	51.5	96.5	87.4	52.9
	SSL	75.0	83.4	70.6	109.4	106.3	115.1

3 Experimental Data, Suitable for Modeling Purposes

3.1 Chazal et al. [14]

This work reports the results of tensile tests performed on 43 human samples, taken from 18 spines, 34 obtained from 12 fresh cadavers and tested within 24 h after death, and the remaining 9 selected from living humans and withdrawn through of surgical procedures. The average age of donors is 53 years. The samples were of the bone-ligament-bone type, to avoid damage to the ligaments by the clamping system of the test rig, and were tested immediately or within a few hours after dissection. In the latter case, the ligaments were immersed in a solution of water, alcohol and

Table 2 Detailed results for each of the ligaments, adapted from [15]

	Point A							Point B					Point C			
	Level	Years	Area (mm ²)	Length (mm)	Force (N)	Displac. (mm)	Stress (N/mm ²)	Strain (Δ/L)	Force (N)	Displac. (mm)	Stress (N/mm ²)	Strain (Δ/L)	Force (N)	Displac. (mm)	Stress (N/mm ²)	Strain (Δ/L)
ALL	L1-L2	70	44	11	40	1	0.9	0.09	450	5.2	10	0.47	500	6	11	0.55
	L3-L4	70	70	13	70	1.6	1	0.12	480	5.2	7	0.4	525	6	8	0.46
	L3-L4	75	74	12.5	30	1.2	0.4	0.09	390	4.5	5	0.36	440	5.4	6	0.43
	L4-L5	80	74	12.5	75	1.8	1.01	0.08	510	5.6	7	0.45	570	7.4	8	0.59
	L4-L5	63	66	12.5	60	2	0.9	0.16	450	4.4	7	0.35	520	6.5	8	0.52
PLL	L1-L2	50	20	11.5	30	0.8	1.5	0.07	360	3.6	18	0.31	390	5	19	0.43
	L2-L3	70	34	12.5	75	1.6	2.2	0.13	465	4.4	14	0.35	510	5.4	15	0.43
	L2-L3	70	34	12	45	0.8	1.32	0.06	360	2.6	10.5	0.21	420	3.2	12	0.26
	L2-L3	75	26	10.5	40	0.6	1.53	0.25	330	2.6	13	0.25	380	4.2	15	0.4
	L3-L4	80	21	10.5	40	0.8	1.9	0.07	210	2.6	10	0.25	240	4	12	0.38
LF	L3-L4	63	19	12.5	60	0.9	315	0.08	330	3.6	17	0.29	360	4.2	19	0.34
	L3-L4	60	39	19	75	1.6	1.92	0.08	315	3.8	8	0.2	340	4.8	9	0.25
ISL/SSL	L4-L5	60	47	11.5	60	1.6	1.27	0.14	270	3.4	10	0.3	300	4.4	12	0.38
	L4-L5	40	1	13	30	1.2	2.7	0.09	120	3	11	0.23	140	4.2	12	0.32

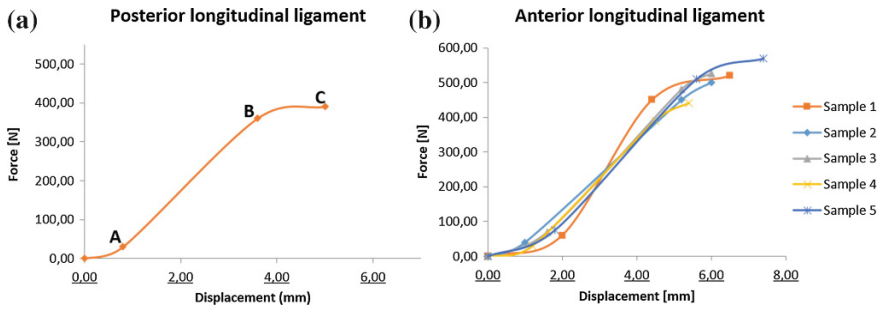


Fig. 5 **a** Force-displacement curve for PLL (points A, B and C). **b** Force-displacement curves for ALL (data retrieved from Table 2)

glycerin, to retain hydration [14, 18]. Specimens taken from living donors were tested within one hour after excision and, meanwhile, placed in Ringer's solution [7, 14, 18].

Since ligaments are composed of long and short fibers, and mechanical properties are directly dependent on their anatomical integrity, they were tested intact. Moreover, for the same reason, supra and interspinous ligaments were tested together in order to prevent possible damage, as they share part of the fibers' structure.

Test results, in spite of not providing the force-elongation curves record three points (A, B and C) that allow their extrapolation (Table 2). Although it is not the ideal solution, it provides a reasonable approximation, as shown in Fig. 5a for the highlighted sample in Table 2 (dashed box). Results show consistency between different samples for the same type of ligament (Fig. 5b), which is an indication of the accuracy and reliability of the performed tests.

In this study, besides the results of the tensile tests, geometric characteristics and other details of the samples are provided, such as age, gender of the donor and column level of the sample, allowing to establish relations among all these data. Thus, it becomes easier to analyze and compare results, as well as to gather possible causes for discrepancies. Although the average age of donors is higher than desirable, this is a problem common to most studies on spinal ligaments.

4 Conclusions

When collecting experimental data from literature, a thorough and careful analysis is indispensable to ensure that the chosen data suit the model purposes.

As a matter of fact, there is a reasonable number of published papers on experimental tests, retrieving mechanical properties of biomaterials. However, when examined closely, it turns out that some studies have information gaps, failures in procedures, or data inconsistencies that make much arguable their use in

a model that is expected to reproduce the in vivo behavior of a given bio-structure. Thus, when selecting this kind of data, there is a certain number of factors that must always be considered, such as, age, possible pathologies of the donors, handling and storage procedures of the samples (for instance, hydration status), and testing protocols.

Besides, when the objective is to use those experimental (real) data in computational models, namely in the case of the spinal ligaments, it is desirable to seek and choose results obtained from samples of the same or adjacent levels. Specifically, in the case of the lumbar spine, samples of the lowest levels (L3-L4, L4-L5) should be selected whenever possible, due to their working conditions of higher loads and greater mobility [19].

The major drawbacks of most of the studies are related to the high average age of the source specimens, but also to the fact that several works do not supply force-elongation curves, which is essential for the understanding, analysis and characterization of ligaments' behavior. Filling these gaps could be the starting point for investing in new experimental trials, taking advantage of the acquired knowledge and the technological advances to the development of rigorous test equipment, since the majority of the performed studies are from more than 20 years ago.

Acknowledgments This work was performed within the European Project “NP Mimetic—Biomimetic Nano-Fibre Based Nucleus Pulposus Regeneration for the Treatment of Degenerative Disc Disease”, funded by the European Commission under FP7 (grant NMP-2009-SMALL-3-CP-FP 246351)

References

1. White AA, Panjabi MM (1990) Clinical biomechanics of the spine, vol 2. Lippincott, Philadelphia
2. Panjabi MM (1992) The stabilizing system of the spine. Part II. Neutral zone and instability hypothesis. *J Spinal Disord Tech* 5(4):390–397
3. Adams MA, Hutton WC (1981) The relevance of torsion to the mechanical derangement of the lumbar spine. *Spine (Phila Pa 1976)* 6(3):241–248
4. Adams MA, Hutton WC (1982) Prolapsed intervertebral disc: a hyperflexion injury. *Spine (Phila Pa 1976)* 7(3):184–191
5. Agostoni E, Mognoni P, Torri G, Miserocchi G (1967) Forces deforming the rib cage. *Respir Physiol* 2(1):105–117
6. Dumas GA, Beaudoin L, Drouin G (1987) In situ mechanical behavior of posterior spinal ligaments in the lumbar region. An in vitro study. *J Biomech* 20(3):301–310
7. Myklebust JB, Pintar F, Yoganandan N, Cusick JF, Maiman D, Myers TJ, Sances A Jr (1988) Tensile strength of spinal ligaments. *Spine (Phila Pa 1976)* 13(5):528–531
8. Panjabi MM, Goel VK, Takata K (1982) Physiologic strains in the lumbar spinal ligaments: an in vitro biomechanical study. *Spine (Phila Pa 1976)* 7(3):192–203
9. Pintar FA, Yoganandan N, Myers T, Elhagediab A, Sances A Jr (1992) Biomechanical properties of human lumbar spine ligaments. *J Biomech* 25(11):1351–1356
10. Cyron BM, Hutton WC (1980) Articular tropism and stability of the lumbar spine. *Spine (Phila Pa 1976)* 5(2):168–172

11. Yahia LH, Audet J, Drouin G (1991) Rheological properties of the human lumbar spine ligaments. *J Biomed Eng* 13(5):399–406
12. Nachemson AL, Evans JH (1968) Some mechanical properties of the third human lumbar interlaminar ligament (ligamentum flavum). *J Biomech* 1(3):211–220
13. Bogduk N (1997) *Clinical anatomy of the lumbar spine and sacrum* 3rd edn, vol 128. PA: Churchill Livingstone, Philadelphia
14. Chazal J, Tanguy A, Bourges M, Gaurel G, Escande G, Guillot M, Vanneuville G (1985) Biomechanical properties of spinal ligaments and a histological study of the supraspinal ligament in traction. *J Biomech* 18(3):167–176
15. Neumann P, Keller TS, Ekström L, Perry L, Hansson TH, Spengler DM (1992) Mechanical properties of the human lumbar anterior longitudinal ligament. *J Biomech* 25(10):1185–1194
16. Zander T, Rohlmann A, Bergmann G (2004) Influence of ligament stiffness on the mechanical behavior of a functional spinal unit. *J Biomech* 37(7):1107–1111
17. Waters RL, Morris JM (1973) An in vitro study of normal and scoliotic interspinous ligaments. *J Biomech* 6(4):343–348
18. Tkaczuk H (1968) Tensile properties of human lumbar longitudinal ligaments
19. Heuer F, Schmidt H, Klezl Z, Claes L, Wilke H-J (2007) Stepwise reduction of functional spinal structures increase range of motion and change lordosis angle. *J Biomech* 40(2):271–280

A Three-Dimensional Multibody Model of the Human Ankle-Foot Complex

T.M. Malaquias, S.B. Gonçalves and M. Tavares da Silva

Abstract In this work, a three-dimensional foot and leg model is proposed, which combines six rigid bodies and five kinematic pairs to produce an articulated system of four segments (toes, mid-forefoot, rearfoot and leg) with thirteen independent degrees-of-freedom. The model is described using a multibody dynamics formulation with natural coordinates and estimated anthropometric parameters. A massless link is used to model the anatomical offset between the talocrural and talocalcaneal joints, avoiding the inclusion of a specific rigid body to model the talus bone. The reliability of the model was tested through its application to the study of the kinematic and dynamic patterns of the human gait. A male subject was analyzed and his data compared with literature, enabling to attest the consistency and realism of the proposed model.

Keywords Multi-segment foot model · Multibody dynamics · Kinematics · Kinetics · Gait analysis

1 Introduction

One of the major issues in the analysis of human movement is modelling the ankle-foot complex. It can be described as a multi-joint structure, which is responsible for supporting and propelling the body during locomotion. Therefore, a proper modeling of this apparatus is essential to understand its kinematics and dynamics, enabling also the study of possible dysfunctions that occur at this level.

T.M. Malaquias (✉) · S.B. Gonçalves · M.T. da Silva
IDMEC, Instituto Superior Técnico, Universidade de Lisboa, Lisbon, Portugal
e-mail: tiago.malaquias@tecnico.ulisboa.pt

S.B. Gonçalves
e-mail: sergio.goncalves@tecnico.ulisboa.pt

M.T. da Silva
e-mail: miguelsilva@tecnico.ulisboa.pt

Several foot models, with a variable number of rigid bodies and degrees of freedom (DOF), have been proposed whose topological complexity varies essentially with the goal of the study [7]. Mono and two-segmental foot models are recurrent in literature [1–3], presenting high computational efficiency, however they are inefficient to analyze all the singularities that occur at ankle–foot and tarsus level. More complex models, such as the three-segmental foot model purposed by Delp et al. [6] enable the understanding, with more reliability, of the dynamics of the normal and pathological foot. Other foot models with a higher number of segments have also been applied only in the kinematic analysis of the foot [7]. Despite allowing the perception of other DOFs, they are overly complex, restricting their application in full-body models and in dynamics simulations, which is one of the goals of the present model.

A novel approach to a three-dimensional (3D) three-segment foot model is presented in this work to simulate the ankle–foot complex. This model aims to be integrated in a broader whole-body biomechanical model for inverse and forward dynamics simulations of non-pathological and pathological human movements, with particular focus to clinical and academic gait studies.

2 Methods

2.1 Model

A 3D leg and foot model is proposed in which the four major anatomical segments of the targeted biological structure (leg, rearfoot, mid-forefoot and toes) are described with six rigid bodies whose relative motion is constrained by five kinematic pairs to produce an articulated mechanical system with thirteen DOFs. The model is described using a multibody dynamics formulation with natural coordinates implemented in the built-in software—*Apollo*, developed over the last years in IDMEC/IST [13]. Two rigid bodies are used to model the leg segment (tibia and fibula) and the remaining four to model the foot. The foot is divided in three distinct anatomical segments: (a) the rearfoot (RF) comprising the calcaneus bone and described by one rigid body; (b) the mid-forefoot (MFF) comprising the cuboid, navicular, cuneiforms and metatarsals bones and described by two rigid bodies; and (c) the toes (TO) comprising the phalangeal bones and described by one rigid body. As represented in Fig. 1, the four segments are interconnected by three revolute and two universal joints. The revolute joints are used to model the flexion-extension of the toes at the metatarsophalangeal joint, the internal rotation of the foot at the metatarsal level and the medial-lateral rotation of the leg. The universal joints are used to model the two rotations about the midtarsal joint and the two rotations about the talocalcaneal and talocrural joint (see Table 1).

The three segment structure adopted in this work steamed from laboratory practice of different daily movements, suggesting the idea that the motion of the

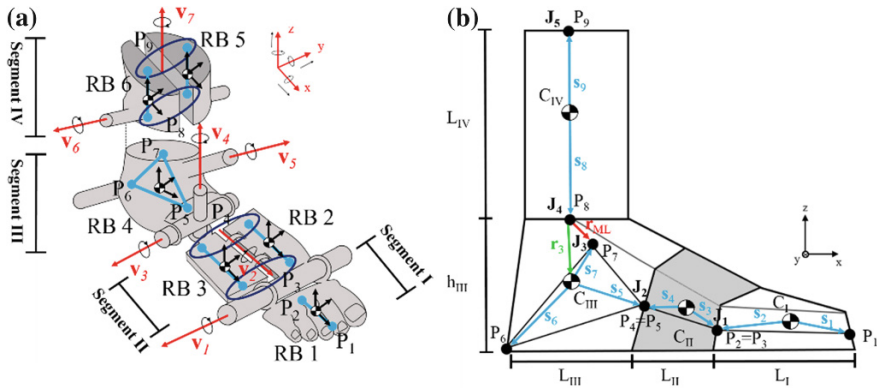


Fig. 1 a Schematic representation of the axes of rotation (v_i) and the DOFs of the model and the corresponding multibody formulation (left). b Position of the centers of mass (C_i) relative to joint coordinates (s_i) (cyan) (right)

Table 1 Foot model segments and joints and their respective description

Anatomic segment		Rigid body	Osteology
I	Toes	1	Phalanges I–V
II	Mid-forefoot	2 and 3	Navicular, cuboid, cuneiforms and metatarsus
III	Rearfoot	4	Calcaneus
IV	Leg	5 and 6	Tibia and Fibula
Arthrology		Joint type	DOF
J_1	Metatarsophalangeal	Revolute	Plantarflexion/Dorsiflexion
J_2	Midtarsal (Chopart’s joint)	Universal	Plantarflexion/Dorsiflexion
			Aduction/Abduction
J_3		Revolute	Internal rotation
$J_{4,1}$	Talocalcaneal	Universal (w/ massless link)	Inversion/Eversion
$J_{4,2}$	Talocrural		Plantarflexion/Dorsiflexion
J_5	Knee	Revolute	Medial/Lateral rotation

metatarsals due to movements at both midtarsal and tarsometatarsal joints should not be neglected. It follows that the insertion of a third segment between the toes and the rearfoot would increase the reliability of the model, since its inclusion enables the study of motions that happen at these joints, as well as it allows the analysis of the variations of the foot longitudinal arch.

It is important to note that the midtarsal and tarsometatarsal joints are responsible for different motions [14]. However, in this work the model will consider that the different degrees of freedom of each joint are concentrated in only one joint between the talus and the navicular and cuboid (the midtarsal joint). The choice of the midtarsal joint as opposed to the tarsometatarsal joint was based on a set of experimental trials, which showed that motions at this level are more significant.

Table 2 Vector coordinates on the local reference frame of the joint rotation axes for the right foot (\mathbf{v}_{i_rf} see Fig. 1a) (note that for the left foot: $v_{y_lf} = -v_{y_rf}$)

	v_{x_rf}	v_{y_rf}	v_{z_rf}		v_{x_rf}	v_{y_rf}	v_{z_rf}
v_1	$-\sin 18^\circ$	$-\cos 18^\circ$	0	v_5	$\cos 35.3^\circ \cdot \cos 19.8^\circ$	$\cos 35.3^\circ \cdot \sin 19.8^\circ$	$\sin 35.3^\circ$
v_2	1	0	0	v_6	$-\sin 6^\circ \cdot \cos 8^\circ$	$-\cos 6^\circ \cdot \cos 8^\circ$	$-\sin 8^\circ$
v_3	0	-1	0	v_7	0	0	1
v_4	0	0	1				

Another important aspect of the model is the inclusion of non-intersecting axes for the talocrural and the talocalcaneal joints, which respectively define the ankle plantar/dorsiflexion and the inversion/eversion rotation axes (see Fig. 1) [9]. The modelling of this joint complex is achieved by considering the talus as a massless link, i.e., as a virtual segment with no mass that is introduced to assure that the physiological distance existing between the two referred joints is preserved. This solution presents the advantage of solving the kinematic problem without increasing the dynamic complexity of the model, since both joints are defined using exclusively the following kinematic constraints: (a) a fixed length between the talocalcaneal (\mathbf{P}_7) and talocrural (\mathbf{P}_8) joints; (b) a fixed angle between the two non-intersecting axes of the talocalcaneal (\mathbf{v}_5) and talocrural (\mathbf{v}_6) joints; and (c) fixed angles between the massless link virtual segment ($\mathbf{r}_{ML} = \mathbf{P}_8 - \mathbf{P}_7$) and the talocalcaneal (\mathbf{v}_5) and talocrural (\mathbf{v}_6) rotation axes.

In forward dynamics simulations, the introduction of a massless link instead of a rigid body to model the talus bone avoids the increase of the integration time due to the inclusion of a small mass as reported by Anderson and Pandy [3]. Regarding the definition of the rotation axes of these joints, and for inverse dynamics analysis, Hicks [8] suggested the use of two anatomical landmarks for each joint as reference base to define these vectors. This suggestion is the one adopted in the acquisition protocol presented in Sect. 2.3. For forward dynamics simulations, the direction of these vectors as well as their application points is defined using tabled anthropometric data [3]. However, due to the differences between the local reference frames of both works, the vector coordinates of both axes (\mathbf{v}_5 and \mathbf{v}_6) had to be recalculated for the values presented in Table 2.

2.2 Anthropometry

The computation of the global mass matrix of the system requires the specification of a set of anthropometric parameters (mass, inertia, length and center of mass location) for each segment included in the model. Despite the diversity of three segment foot models reported in the literature, the corresponding anthropometric data is scarce or non-existent.

Table 3 Anthropometric data: length ($l_r = l_i/l_f$), height ($h_{r,f} = h_i/l_f$; $h_{r,fb} = h_i/h_{fb}$) mass (m_i) and radius of gyration (r_i)

Segment	l_r (%)	$h_{r,f}$ (%)	$h_{r,fb}$ (%)	m_r (%)	r_x (%)	r_y (%)	r_z (%)
I	27	–	–	0.289	30.29	30.29	42.84
II	33	–	–	0.676	39.81	41.18	43.70
III	40	28	–	1.014	21.94	34.21	34.28
IV	–	–	24	4.943	27.11	25.31	8.6

Table 4 Center of mass location relative to the proximal joint (s_i) and the relevant vectors defined to compute it (r_i) (see Fig. 1)

	P_1	P_F	s_x	s_y	s_z		P_1	P_F	s_x	s_y	s_z
s_1	CM ₁	P ₁	17.04	0.00	–6.85	s_6	CM ₃	P ₆	–24.60	0.00	–13.69
s_2	CM ₁	P ₂	–9.96	0.00	–6.85	s_7	CM ₃	P ₇	$r_{MLx} - 1.20$	r_{MLy}	$r_{MLz} + 14.31$
s_3	CM ₂	P ₃	18.15	0.00	–7.04	r_{ML}	P ₈	P ₇	Experimental Vector		
s_4	CM ₂	P ₄	–14.85	0.00	7.04	r_3	P ₈	CM ₃	1.20	0.00	–14.31
s_5	CM ₃	P ₅	15.40	0.00	–4.69						

Hence, the two segment foot model presented by Anderson and Pandy [3] was used as a reference to compute the anthropometric parameters required by the present model. Accordingly, the values of the mass, length and center of mass location of the toes (segment I) and hindfoot (segment II) of the reference model were normalized as a percentage of the total body mass (m_{fb}), height (l_{fb}) and foot length (l_f).

The hindfoot was split into rearfoot (segment III) and mid-forefoot (segment II) with the relative motion between the two newly created segments occurring at the level of the midtarsal joint, which is simulated as a combined action of a universal joint (J_2) and a revolute joint (J_3) (see Table 1). The segment corresponding to the toes was kept unchanged.

The calculation of the relevant anthropometric parameters required the introduction of some assumptions: (i) the center of mass location of segment II (CM_{II}) relative to the proximal joint (J_2 and J_3) was assumed to be 45 % of the distance between J_1 and J_2 ; (ii) the masses of segments II and III (m_{II} and m_{III}) relative to the mass of segment I (m_2) are respectively 40 and 60 % (see Table 3); (iii) the inertia of segment III was estimated from the inertia of segment II (see Eq. 1); and (iv) the mass and inertial characteristics of both models are equivalent when both are in the anatomical reference position. Having these assumptions in mind, the center of mass location of segment III (CM_{III}) is calculated in such a way that assumption (iv) is fulfilled. In Table 4, the centers of mass location (s_i) with respect to joints J_1 , J_2 and J_4 is presented. The computation of v_7 requires the definition of the massless link vector ($r_{ML} = P_8 - P_7$). Its definition can be obtained by estimating the location of the talocalcaneal (P_7) and talocrural (P_8) joints (see Sect. 2.3). Currently, the

authors are developing a new approach to compute this vector, based in anthropometric measurements and functional methods to be applied in forward dynamics analysis.

It is important to note that in an inverse dynamics analysis the length of each segment can be computed using the experimental data. However, if the goal is a forward dynamics simulation, the length of each segment has to be given as input. These values can be computed using the relative lengths presented in Table 3 and the value of the total foot length. In the present work the values: (a) male: 26.96 cm; (b) female: 24.38 cm were adopted (based on [12]).

The values of the inertia for all the segments were calculated from the data presented by Anderson and Pandy [3]. The vector of principal moments of inertia of segment III (\mathbf{I}_{III}) was calculated from the product of the principal inertia of segment II (\mathbf{I}_2) by an inertia scaling factor (ζ), as:

$$\mathbf{I}_{III} = \mathbf{I}_2 \zeta = \mathbf{I}_2 \frac{m_{III}}{m_2} \left(\frac{l_{III}}{l_2} \right)^2 \quad (1)$$

The correction factor formulation arrives from the general expression of the moment of inertia, which states that the moment of inertia is proportional to the product of the mass and the square of the length ($\mathbf{I} \propto m \cdot l^2$). The principal inertia of segment II (\mathbf{I}_{II}) was then computed using the Huygens–Steiner theorem and in such a way that assumption (iv) is fulfilled. Since the local reference frames of the proposed model and the one presented in [3] differ from a given angle around the vertical axis, the final inertia of each segment was adjusted to the new local reference frame recurring to Mohr’s circle. The products of inertia resulting from this adjustment are very small and, therefore, were neglected in this work. Finally, the inertia for each segment was expressed as a percentage of the radius of gyration of the segment normalized by its length (see Table 3).

A more detailed explanation of the methodology used to compute all the relevant anthropometric parameters can be obtained in [10].

2.3 Acquisition Protocol

An inverse dynamics analysis of the major kinematic and dynamic foot gait patterns was performed to attest the proposed model. The assessment of the model was achieved by acquiring the gait patterns of a male subject (23 years old, 87.0 kg and 1.87 m) with no history of gait disorders. The kinematic and dynamic data required for the validation of the model was experimentally acquired recurring to a Mocap system (14 IR Cameras Qualisys ProReflex MC1000 and 3 Force Plates AMTI OR 6-7-1000) in the Lisbon Biomechanics Lab. The acquisition frequencies were respectively settled at 100 Hz to the IR cameras and 1,000 Hz to the force plates. The volunteer was asked to walk continuously in his natural cadence. Ten valid

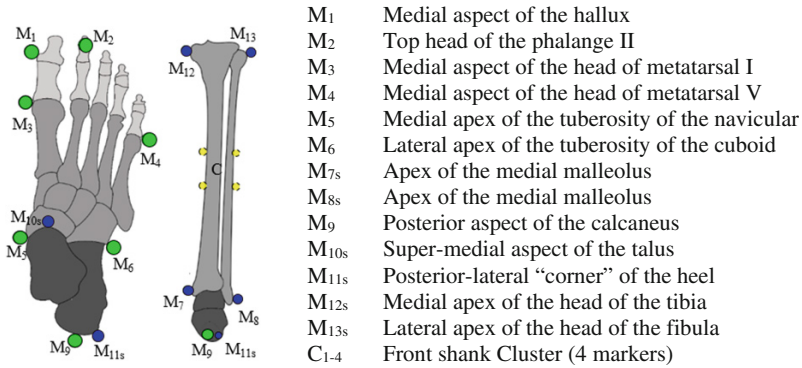


Fig. 2 Marker set protocol description (s refers to calibration markers)

trials were acquired for each foot, being chosen the best five to perform the intra-subject statistical analysis.

The differences on the proposed model require the definition of a new marker set protocol. Hence, the *Milwaukee Foot Model* protocol [11] was adapted to consider the specifications of the model addressed in this work (see Fig. 2). The marker set protocol considers seventeen markers (7 tracking/calibration, 4 tracking and 6 calibration markers), located in palpable anatomical landmarks. The markers M_{10s} and M_{11s} are used only as calibration markers and define the location (the midpoint of M_{10s} and M_{11s}) and rotation axis of the talocalcaneal joint as suggested by Hicks [8]. The midpoints of the markers M₃ and M₄, M₅ and M₆, M_{7s} and M_{8s} and M_{12s} and M_{13s} define respectively the metatarsophalangeal, midtarsal, talocrural and knee joints. The anterior location of the toes are computed using the *x* and *z* components of the marker M₁ and the *y* component of the marker M₂.

The suggested protocol was applied in the acquisition of the experimental data presented in this work. The kinematic and dynamic analysis was performed using a three-dimensional multibody dynamics analysis software—*Apollo* [13]. The statistical analysis was performed using software developed in *Matlab*.

3 Results and Discussion

The kinematic formulation presented in this work successfully allowed the definition of a three segment foot model, contemplating a fourth virtual segment to assist in the modelling of the talocrural and talocalcaneal joints. The results obtained for the angular displacement of these joints as well as for the metatarsophalangeal joint presented a set of patterns consistent with the ones observed in the literature. The same was observed for the dynamic results. Only a few works address the patterns of the midtarsal joint. Bruening et al. [4, 5] presented recently an analogous model obtaining results that are similar to the ones obtained in this work. In particular, the

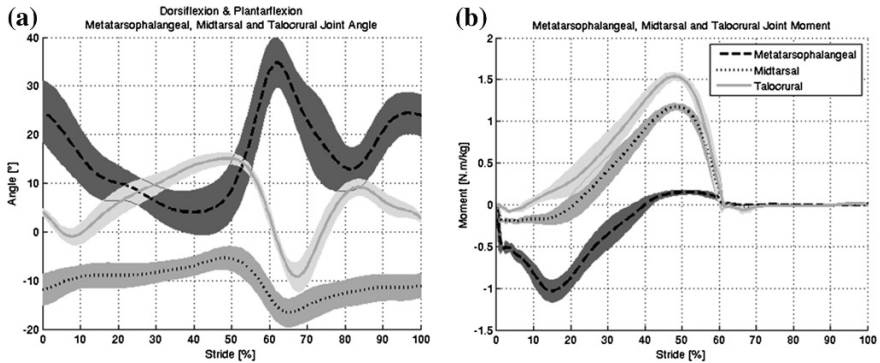


Fig. 3 **a** Joint angular displacement (*left*). **b** Moment of force (*right*)

analysis of the plantar/dorsiflexion enables the study of the spring like behavior of the longitudinal arch of the foot, which could be of particular interest in the study of neuropathologies and in the design of orthopaedic solutions. In this article, the results focused on the study of sagittal motions, however the model can also analyze all the DOFs presented in Table 1. The kinematic and dynamic patterns of all the DOFs can be consulted in [10] (Fig. 3).

4 Conclusions

The comparison of the outcome of the kinematic and dynamic analysis with other models in literature allowed the validation of the applicability and reliability of the model. Besides the study of the motion at the talocrural, talocalcaneal and metatarsophalangeal joints, the model allowed also the analysis of the variations in the longitudinal foot arch and the kinematics and dynamics of themidtarsal joint. This additional information could be of particular interest in the study of ankle-foot disorders. Moreover, the suggested acquisition protocol successfully enabled the computation of all the drivers required to guide the model, validating their applicability in both clinical and academic studies.

Acknowledgments The authors would like to thank *Fundação para a Ciência e Tecnologia* (FCT) for its support (SFRH/BD/51574/2011).

References

1. Ackermann M, van den Bogert AJ (2010) Optimality principles for model-based prediction of human gait. *J Biomech* 43:1055–1060
2. Ambrósio JA, Silva M (2005) A biomechanical multibody model with a detailed locomotion muscle apparatus. *Advances in computational multibody systems*, Springer, Netherlands, pp 155–184

3. Anderson FC, Pandy MG (1999) A dynamic optimization solution for vertical jumping in three dimensions. *Comput Methods Biomech Biomed Eng* 2:201–231
4. Bruening DA, Cooney KM, Buczek FL (2012) Analysis of a kinetic multi-segment foot model. Part I: model repeatability and kinematic validity. *Gait & Posture* 35:529–534
5. Bruening DA, Cooney KM, Buczek FL (2012) Analysis of a kinetic multi-segment foot model part II: kinetics and clinical implications. *Gait & Posture* 35:535–540
6. Delp SL, Loan JP, Hoy MG, Zajac FE, Topp EL, Rosen JM (1990) An interactive graphics-based model of the lower extremity to study orthopaedic surgical procedures. *IEEE Trans Biomed Eng* 37:757–767
7. Deschamps K, Staes F, Roosen P, Nobels F, Desloovere K, Bruyninckx H et al (2011) Body of evidence supporting the clinical use of 3D multisegment foot models: a systematic review. *Gait & Posture* 33:338–349
8. Hicks J (1953) The mechanics of the foot: I. The joints. *J Anat* 87:345
9. Isman RE, Inman VT (1969) Anthropometric studies of the human foot and ankle. San Francisco
10. Malaquias T (2013) Development of a three-dimensional multibody model of the human leg and foot for application to movement analysis. University of Lisbon, Instituto Superior Técnico
11. Myers KA, Wang M, Marks RM, Harris GF (2004) Validation of a multisegment foot and ankle kinematic model for pediatric gait. *IEEE Trans Neural Syst Rehabil Eng* 12:122–130
12. Parham KR, Gordon CC, Bensek CK (1985) Anthropometry of the foot and lower leg of US army soldiers. Fort Jackson, SC
13. Silva MT (2003) Human motion analysis using multibody dynamics and optimization tools. Instituto Superior Técnico, Universidade Técnica de Lisboa, (2003)
14. Williams LH, Peter L, Warwick R, Dyson M, Bannister E (1989) *Gray's anatomy*, 37th edn

Inverse Dynamics of 2-DOF Parallel Mechanism Used for Orientation

T. Itul, B. Gherman, D. Cocorean and D. Pisla

Abstract The paper presents the dynamic model of a 2-DOF orientation mechanism, where the Euler's second law has been used. The kinematics, workspace and singularities of the mechanism are also presented. The dynamic model is developed using the motion equations of the mobile platform. Simulations results using the mentioned model as well as a commercial simulation software are shown.

Keywords 2-DOF parallel mechanism · Orientation angles · Kinematics · Inverse dynamics

1 Introduction

Orientation mechanisms have found utility in the fields like medical robotics or where the use of radio antennas, satellite TV antennas, telescopes, cameras, solar panels, etc., are a necessity, providing not only a good precision, but also a high rigidity.

In [5], the authors present the dynamics of a 3-DOF parallel mechanism by using the Newton-Euler formalisms in two steps. First, the relations between the spherical joint reactions forces and the kinematic parameters of the mobile platform are determined, followed secondly by the determination of the generalized active torques. In [9], the dynamic model of a 3-DOF (degrees of freedom) parallel mech-

T. Itul (✉) · B. Gherman · D. Cocorean · D. Pisla
Technical University of Cluj-Napoca, Cluj-Napoca, Romania
e-mail: Tiberiu.Itul@mep.utcluj.ro

B. Gherman
e-mail: Bogdan.Gherman@mep.utcluj.ro

D. Cocorean
e-mail: Dragos.Cocorean@mep.utcluj.ro

D. Pisla
e-mail: Doina.Pisla@mep.utcluj.ro

anism used for orientation is presented. The dynamic model with and without friction is developed. Staicu in [11] and [12] developed the inverse kinematic and dynamic model of an orienting gear train mechanism using recursive matrix relations. The fundamental principle of virtual work has been used and it establishes a direct recursive determination of the variation in real-time of torques and powers of the actuators. The dynamic model of a 3-DOF serial-parallel mechanism is presented in [14]. The Newton-Euler approach has been used to calculate the actuation and reaction forces of the mechanism in [3] as well. The dynamic analysis of a macro-micro parallel manipulator has been studied in [13]. The manipulator architecture is a simplified planar version adopted from the structure of the Large Adaptive Reflector (LAR), the Canadian design of next-generation giant radio telescopes. The dynamic equation of motion of such a structure is obtained using the Newton-Euler formulation. Although the Lagrangian formalism has been reputed of being inefficient for closed-loop mechanisms, including parallel robots, Abdellatif decided to prove otherwise [1]. He considered open-loop subchains of the manipulator and derived their dynamics by the Lagrangian formalism and with respect to an own set of generalized coordinates and velocities. Miller and Clavel present the dynamic model of the world wide known parallel DELTA robot based on Lagrange equations, [8]. Itul and Pisla present a comparative study between different dynamical methods for 3-DOF parallel robots regarding certain parameters [4, 7]. In [2], Filho and Cabral developed the inverse dynamics for a Hexa architecture by using the Newton-Euler's formulation and calculating forces and moments during its operation. The paper also presents a general method to calculate the Jacobian matrix for parallel robots and to search for the singular positions for both direct and inverse kinematic.

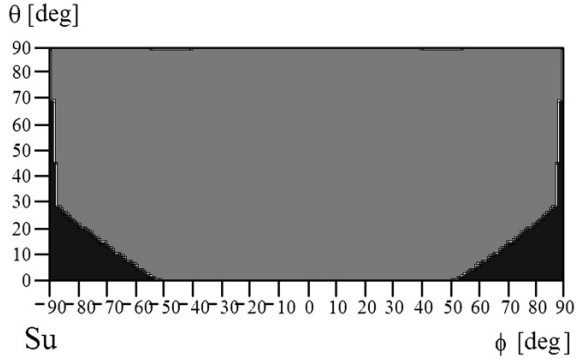
The current paper presents the dynamic model of a 2-DOF orientation mechanism, being organized as follows: Sect. 2 presents the kinematics and workspace of the parallel mechanism, Sect. 3 presents the inverse dynamics and some numerical results. A few conclusions are drawn at the end of the paper.

2 Kinematics and Workspace

The kinematic scheme of the parallel mechanism, named 2SPS- U_V is shown in Fig. 1 [6], the U-joint having the vertical axis fixed. The mechanism consist in a fixed base OB_1B_2 and a mobile platform OA_1A_2 connected through a main universal joint in O and two telescopic legs B_1A_1 , B_2A_2 ended with spherical joints. The fixed axis of the universal joint O is vertical. The mechanism's generalized coordinates are the telescopic legs lengths q_1 , q_2 and operational coordinates are the azimuth angle φ and elevation angle θ corresponding to the two axes of U joint.

In this case, the rotation matrix has the form:

Fig. 2 The reachable workspace of the 2SPS-U_v parallel mechanism (the grey area)



$$[J] = \begin{bmatrix} \bar{e}_1 \cdot \frac{\partial \bar{P}_1}{\partial \phi} & \bar{e}_1 \cdot \frac{\partial \bar{P}_1}{\partial \theta} \\ \bar{e}_2 \cdot \frac{\partial \bar{P}_2}{\partial \phi} & \bar{e}_2 \cdot \frac{\partial \bar{P}_2}{\partial \theta} \end{bmatrix}^{-1} = \begin{bmatrix} \bar{e}_1 \cdot (\bar{i}_0 \times \bar{P}_1) & \bar{e}_1 \cdot (\bar{j} \times \bar{P}_1) \\ \bar{e}_2 \cdot (\bar{i}_0 \times \bar{P}_2) & \bar{e}_2 \cdot (\bar{j} \times \bar{P}_2) \end{bmatrix}^{-1}; \tag{6}$$

$$\dot{X} = \begin{bmatrix} \dot{\phi} \\ \dot{\theta} \end{bmatrix}; \quad \dot{q} = \begin{bmatrix} \dot{q}_1 \\ \dot{q}_2 \end{bmatrix};$$

\bar{e}_1 and \bar{e}_2 are the legs unit vectors; \bar{i}_0 and \bar{j} are the OX and Oy axes unit vectors. Scalar components of angular velocity are:

$$\omega_x = \dot{\phi} \cdot \cos(\theta); \quad \omega_y = \dot{\theta}; \quad \omega_z = \dot{\phi} \cdot \sin(\theta) \tag{7}$$

In the ideal case the shape of workspace is a rectangle located in the $\phi\theta$ plane with the sides π and $\pi/2$. In real case, the workspace area and its shape are affected by the constraints due to: allowed spherical joints angles; actuated joints stroke; transmission angles; presence of singularities.

The upper spherical joints restraints could be avoided by replacing them with universal joints.

For the actuated joints and for transmission angles are imposed the conditions:

$$q_{\min} \leq q_i \leq q_{\max}; \quad \psi_i \geq 20^\circ; \quad i = 1, 2 \tag{8}$$

In order to avoid singularities, the reachable workspace can be determined imposing the condition:

$$Det[J]^{-1} < 0 \tag{9}$$

Following an optimization process concerning the workspace maximization, the following values for the geometric parameters of the mechanism have been established: $x_1 = x_2 = 0.20$ m; $y_1 = -y_2 = 0.25$ m; $Z_{B1} = Z_{B2} = -0.75$ m; $Y_{B1} = -Y_{B2} = 0.05$ m; $X_{B1} = X_{B2} = -0.9$ m; $q_{\min} = 1.0$ m; $q_{\max} = 1.5$ m. The constraints

(8) and (9) lead to the maximal workspace shown in Fig. 2. The reachable workspace area is 4.58 rad^2 .

3 Inverse Dynamics and Numerical Results

The target is to evaluate the generalized actuation forces Q_1 and Q_2 , using the hypothesis that friction forces are neglected, when the motion equations of the platform $\varphi = \varphi(t)$, $\theta = \theta(t)$ and the mass distribution of the mechanism components are known (Fig. 3).

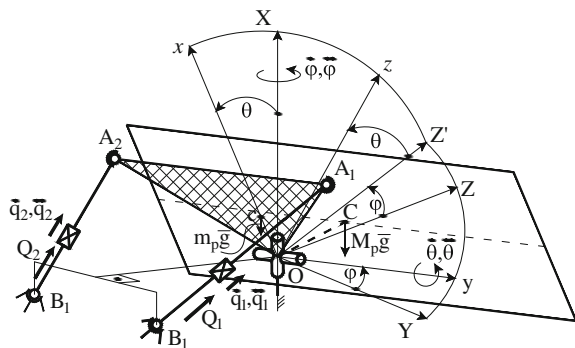
For this reason, the mobile platform is separated from the rest and Euler’s second law (principle of angular momentum) with respect to the fixed point O is used:

$$\begin{aligned} \dot{\vec{H}}_o &= \vec{M}_o; \\ \dot{\vec{H}}_o &= [I] \cdot \vec{\varepsilon} + \vec{\omega} \times [I] \cdot \vec{\omega}; \\ \vec{M}_o &= \vec{P}_1 \times Q_1^* \cdot \vec{e}_1 + \vec{P}_2 \times Q_2^* \cdot \vec{e}_2 \\ &\quad + \vec{r}_C \times M_p \vec{g} + \vec{r}_c \times m_p \vec{g} + \vec{M}_u \end{aligned} \tag{10}$$

where $[I]$ represents the inertia moments matrix; $\vec{\varepsilon}$ is the angular acceleration; $\vec{\omega}$ is the angular velocity, Q_1^* and Q_2^* are the forces with which the telescopic legs act upon the mobile platform; M_p is the mass of the manipulated homogenous panel, having the dimensions $L \times l$; m_p is the mass of the triangular homogenous mobile platform having the form of a isosceles triangle with the base $2y_1$ and the height x_1 ; $\vec{r}_C = [x_C \ 0 \ z_C]$ is the position vector of the mass center of the panel in the $Oxyz$ reference system; $\vec{r}_c = [x_c \ 0 \ 0]$ is the position vector of the mobile platform in the same reference system; \vec{M}_u is the torque taken by the U-joint.

After achieving the scalar product with the unit vectors \vec{i}_o and \vec{j} of the universal joint axes, using (10), the forces Q_1^* and Q_2^* are evaluated:

Fig. 3 The forces that act upon the 2SPS-U_V parallel mechanism



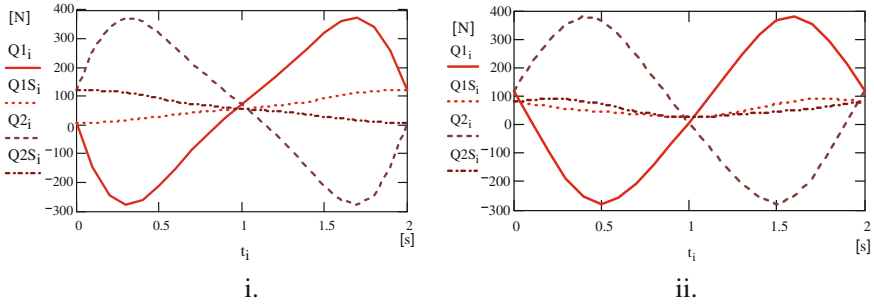


Fig. 4 The generalized forces variation in the case of a: **a** linear trajectory; **b** ellipse

$$\begin{bmatrix} Q_1^* \\ Q_2^* \end{bmatrix} = [J]^T \begin{bmatrix} ([I] \cdot \bar{e} + \hat{\omega} \times [I] \cdot \bar{\omega}) \cdot \bar{i}_o \\ ([I] \cdot \bar{e} + \hat{\omega} \times [I] \cdot \bar{\omega}) \cdot \bar{j} - (\bar{r}_C \times M_p \bar{g} + \bar{r}_c \times m_p \bar{g}) \cdot \bar{j} \end{bmatrix} \quad (11)$$

The actuation joints take upon both the weight ($m_t \cdot g$) and the inertia of the superior parts of the telescopic legs. The expressions of the generalized actuation forces are:

$$\begin{aligned} Q_1 &= Q_1^* + m_t \cdot \ddot{q}_1 - m_t \cdot \bar{g} \cdot \bar{e}_1; \\ Q_2 &= Q_2^* + m_t \cdot \ddot{q}_2 - m_t \cdot \bar{g} \cdot \bar{e}_2 \end{aligned} \quad (12)$$

For the mechanism, besides the constructive data coming from the optimization process, the following have also been considered: $M_p = 40$ kg, $L = 2$ m, $l = 1$ m, $m_p = 2$ kg, $m_t = 2$ kg, $x_c = 0.10$ m, $z_c = 0.05$ m, $x_c = 0.07$ m.

Two types of motions have been imposed to the mobile platform, in the plane of the operational coordinates: a linear (13a) and an elliptic motion (13b).

$$\begin{cases} \varphi = -\frac{\pi}{8} \cdot t^5 + 5 \cdot \frac{\pi}{8} \cdot t^4 - 5 \cdot \frac{\pi}{6} \cdot t^3 + \frac{\pi}{3}; \\ \theta = \frac{\pi}{4} \end{cases} \quad (13a)$$

$$\begin{cases} \varphi = \frac{\pi}{6} \cdot \sin(\pi \cdot t) \\ \theta = \frac{\pi}{4} + \frac{\pi}{12} \cdot \cos(\pi \cdot t) \end{cases} \quad (13b)$$

In Fig. 4, the variation diagrams of the generalized forces obtained using the motion equations (Q_{1i} and Q_{2i}) and in static conditions (Q_{1Si} and Q_{2Si}) are presented, for $t \in [0, 2s]$. The motions being symmetric, the diagonals of the two forces Q_1 and Q_2 are mirrored.

A trajectory similar to the one on (13a) has been simulated using the simulation package from Siemens NX, namely the RecurDYN solver [10]. In Fig. 5, simulations using the RecurDYN and the developed inverse dynamic model are presented, showing a very good correlation between the two and practically validating

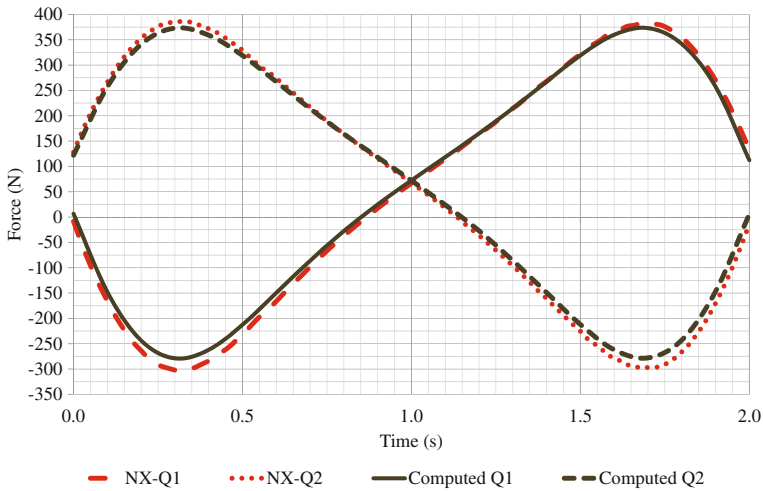


Fig. 5 Validation of the inverse dynamic model using the RecurDYN solver

Table 1 The λ and η ratios

T (s)	λ	η
2	3.05	2.49
4	1.456	0.623
8	1.086	0.156
16	1.014	0.039

the work presented in the paper. In Table 1, the following are computed: the ratio $\lambda = \frac{Q_{\max}}{QS_{\max}}$, between the total generalized maximum force and the static maximum force and the maximum ratio $\eta = \max\left(\frac{Q-QS}{QS}\right)$, between the dynamic and static forces, for the same trajectory and different motion periods $T = 2, 4, 8, 16$ s.

4 Conclusions

The paper presents the inverse dynamic model for a mechanism used for orientation. The Euler’s second law has been used, considering as main application the orientation of a panel whose dimensions and weight are known. Considering different motion periods for the same trajectory, the ratio Q_{\max}/QS_{\max} decreases, clearly indicating that in the case of manipulating large objects, for which the inertia moments become important, for a correct dimensioning of the actuation motors, a dynamic computation is necessary. The inverse dynamic model developed in the paper, has been validated using a commercial multi-body system simulation software.

Acknowledgments This paper was supported by the Project no. 173/2012, code PN-II-PCCA-2011-3.2-0414, entitled “Robotic assisted brachytherapy, an innovative approach of inoperable cancers—CHANCE” financed by UEFISCDI and the Scopes International Grant IZ74Z0-137361/1, Creative Alliance in Research and Education focused on Medical and Service Robotics-CARE-Robotics.

References

1. Abdellatif H, Heimann B (2009) Computational efficient inverse dynamics of 6-DOF fully parallel manipulators by using the Lagrangian formalism. *Mech Mach Theory* 44(1):192–207
2. Filho SCT, Cabral ELL (2006) Dynamics and Jacobian analysis of a parallel architecture robot: the Hexa. In: ABCM symposium series in mechatronics, vol 2, pp 166–173
3. Ibrahim O, Khalil W (2007) Kinematic and dynamic modeling of the 3-RPS parallel manipulator. In: 12th IFToMM World Congress, Besançon
4. Itul T, Pisla D (2003) Comparative study between D’Alembert principle and lagrange formulation for guiding in three points parallel robot dynamic analysis. In: Proceedings of 14th international conference on control systems and computer science, vol 1. Politehnica Press, Bucharest, pp 100–105
5. Itul T, Pisla D (2008) Dynamics of a 3-DOF parallel mechanism used for orientation applications. In: International conference on automation, quality and testing, robotics, vol 2, Cluj-Napoca, pp 398–403
6. Itul T et al (2014) Comparative study of two 2-DOF parallel mechanisms used for orientation. *Mech Mach Sci* 18:145–157
7. Itul T et al (2006) On the solution of inverse dynamics for 6-DOF robot with triangular platform. In: Proceedings of EUCOMES
8. Miller K, Clavel R (1992) The Lagrange-based model of DELTA-4 robot dynamics. *Robotersysteme* 8:49–54
9. Pisla D, Itul T (2009) The influence of motion mode and friction on the dynamics of a parallel robot used for orientation applications. In: Proceedings of EUCOMES 08, Cassino, pp 209–218
10. Siemens NX (2014) RecurDYN solver. http://www.plm.automation.siemens.com/en_us/
11. Staicu S, Zhang D (2008) A novel dynamic modelling approach for parallel mechanisms analysis. *Rob Comput-Integr Manuf* 24(1):167–172
12. Staicu S (2009) Dynamics of a 2-DOF orienting gear mechanism. *Rev Roumanie des Sci Tech* 54(1):67–77
13. Taghirad HD, Nahon MA (2012) Dynamic analysis of a macro–micro redundantly actuated parallel manipulator. *Adv Rob* 22(9):949–981
14. Wang K et al (2013) Dynamics analysis of a three-DOF planar serial–parallel mechanism for active dynamic balancing with respect to a given trajectory. *Int J Adv Rob Sys* 10:1–10

Wear Prediction of Ceramic-on-Ceramic Artificial Hip Joints

E. Askari, P. Flores, D. Dabirrahmani and R. Appleyard

Abstract Wear can influence the lifetime and performance of implants and has been found to be a key factor in primary failure of artificial hip joints. The present study aims to present a spatial multibody dynamic model to predict wear in ceramic-on-ceramic hip implants. The problem was formulated by developing a spatial multibody dynamic model of a hip prosthesis taking three-dimensional physiological loading and motion of the human body into account. Then, the Archard wear model was integrated into the dynamic calculation of the hip implant to predict wear. Additionally, geometries of the cup and head were updated throughout the simulation to generate a more realistic wear simulation. The results were validated against current literature. Finally it was illustrated that friction-induced vibration caused excessive wear of hip implant components.

Keywords Wear simulation · Ceramic-on-ceramic hip joint · Multibody systems

1 Introduction

Friction-induced vibration is an undesirable oscillation in artificial hip joints due to tribological interactions between the head and cup. These tribological interactions during the human daily activities can cause articulating surfaces of hip implants to

E. Askari (✉) · D. Dabirrahmani · R. Appleyard
Macquarie University, Sydney, Australia
e-mail: ehsanaskary@gmail.com

D. Dabirrahmani
e-mail: daneh.turner@mq.edu.au

R. Appleyard
e-mail: richard.appleyard@mq.edu.au

P. Flores
University of Minho, Braga, Portugal
e-mail: pflores@dem.uminho.pt

undergo wear. Moreover, vibration induced by friction can lead to excessive wear of the head and cup of hip implants [11]. Wear can influence the lifetime and performance of implants and has been found to be a key factor in primary failure of artificial hip joints [22].

The most commonly used artificial hip joint combination is a metal head within a plastic cup which is referred to a soft-on-hard couple. This combination is known to suffer from cup wear with the resultant plastic debris reported to induce osteolysis. Computing the wear profile of soft-on-hard bearing couples has been the subject of a number of studies [12, 15]. In an effort to reduce wear, hard-on-hard material combinations have been developed namely metal-on-metal (MoM) and ceramic-on-ceramic (CoC). However with hard-on-hard couples, wear occurs across both the head and cup surface [15]. Ceramic-on-Ceramic hip implants have been used increasingly since their introduction in the 1970s [6]. Ceramic bearings have the potential advantage of lower wear rates in total hip arthroplasty compared with metal-on-metal hip implants and soft-on-hard bearings [13]. Despite very low wear rates of ceramic bearings, it continues to be an important research topic because wear of artificial hip joints is a key issue leading to their primary failure even in CoC hip arthroplasties.

To evaluate implant wear computationally, Archard's wear model is the most commonly utilised method [15]. This wear model requires knowledge of the contact pressure, sliding distance of the contact point and tribological data such as the wear coefficient of the bearing materials. Implant head-cup contact properties can be numerically determined by means of the finite element method [9], boundary element method [22] and Hertz contact model [8].

The contact point between the head and cup follows a certain characteristic track during normal human gait, and this 'contact point track' is an important parameter to determine wear since any variation in the track shape can cause a huge variation in the wear rate [3]. Mattei et al. [17] used a theoretical contact point track, where the contact point was assumed to be located at the interface of the head and cup and along the line joining both the centres of the head and cup. Another study assumed that the centre of the femoral head was fixed and the motion of the femur was simulated by applying physiological rotations [12]. Furthermore, Saikko and Calonius [20] developed a computational method based on Euler angles to compute the slide tracks for the three-axis motion of the hip joint in walking and for two hip simulators.

Recently it was reported that, on top of the normal gross motion, the femoral head vibrates inside the cup with micron amplitude due to friction-induced vibration [4, 5]. This results in a change in the contact point trajectory in both micro and macro scales, which can affect the final wear profile. Mattei and Di Puccio [16] recently determined the changes of contact point trajectory due to friction and calculated its effect on wear prediction. However, their model did not include the vibration of the femoral head inside the cup and they reported that wear decreased as friction increased which cannot be justified physically. To the best of our knowledge, no one has investigated the effect of friction-induced vibration on both wear prediction and the corresponding wear map of artificial hip joints.

Thus, the influence of friction-induced vibration on wear simulation of ceramic-on-ceramic artificial hip joints is modelled and studied in the present investigation. Moreover, it is hypothesised that this undesirable oscillation can lead to excessive wear in artificial hip joints. For this purpose, a spatial multibody dynamic model is developed, which allows for the evaluation of both sliding distance and contact pressure in order to calculate the wear of hip implants. The friction-induced vibration and contact-impact events occurring between the head and cup surfaces are taken into consideration as external generalised forces in the governing equation of the motion. A friction-velocity relation and a Hertz contact model are employed to formulate tangential and normal contact forces, respectively. Three-dimensional physiological loading and motion of the human body are also taken into account. Nonlinear governing motion equations are solved, using adaptive Runge-Kutta-Fehlberg method and the geometry of worn bearing surfaces is updated during the wear simulation. Finally, the methodology is validated by comparing the wear prediction to current literature. Moreover, the influence of friction on wear predictions and the corresponding wear maps are studied.

2 Governing Motion Equations of Multibody Systems

It is well known that the equations of motion for a multibody dynamic system with holonomic constraints can be written as [19],

$$\mathbf{M}\ddot{\mathbf{q}} = \mathbf{g} + \mathbf{g}^{(c)} \quad (1)$$

$$\Phi(\mathbf{q}, t) = 0 \quad (2)$$

in which \mathbf{M} is the system mass matrix, \mathbf{q} generalized coordinates of the system, $\ddot{\mathbf{q}}$ the acceleration vector, and \mathbf{g} the generalized force vector containing all external forces and moments. The bodies in the multibody system are interconnected by joints imposing constraints on the bodies' relative motion. Expressing these conditions as algebraic equations in terms of a generalised coordinate and time, t , holonomic kinematic constraints defined in Eq. (2) are introduced. Moreover, $\mathbf{g}^{(c)}$ is the vector of constraint reaction equations, which can be rewritten by means of the Jacobian matrix of the constraint equations ($\Phi_{\mathbf{q}}$) and the vector of Lagrange multipliers (λ) as [19]

$$\mathbf{g}^{(c)} = -\Phi_{\mathbf{q}}^T \lambda \quad (3)$$

Substituting Eq. (3) in Eq. (1) yields,

$$\mathbf{M}\ddot{\mathbf{q}} + \Phi_{\mathbf{q}}^T \lambda = \mathbf{g} \quad (4)$$

Furthermore, differentiating Eq. (2) twice with respect to time, the constraint equation can be written as follows

$$\Phi_q \ddot{\mathbf{q}} = -(\Phi_q \dot{\mathbf{q}})_q \dot{\mathbf{q}} - 2\Phi_{q_r} \dot{\mathbf{q}} - \Phi_{tt} = \gamma \quad (5)$$

where γ is a vector function of velocity and position of the system as well as time. As a consequence, both Eqs. (4) and (5) yield a system of differential algebraic equations to be solved for $\ddot{\mathbf{q}}$ and λ , given by

$$\begin{bmatrix} \mathbf{M} & \Phi_q^T \\ \Phi_q & 0 \end{bmatrix} \begin{Bmatrix} \ddot{\mathbf{q}} \\ \lambda \end{Bmatrix} = \begin{Bmatrix} \mathbf{g} \\ \gamma \end{Bmatrix} \quad (6)$$

The Eq. (6) can be solved only if the coefficient matrix of Eq. (6) is non-singular. This can be achieved by having a positive definite mass matrix and the Jacobian matrix Φ_q full row rank [5].

Normal contact force and tangential friction force in the articulation surface between the femoral head and cup play important roles in multibody dynamics formulations. The contact between the femoral head and cup which are a sphere and a hemisphere can be modelled by a modified Hertz contact law proposed by Lankarani and Nikravesh [14], which is given by

$$\mathbf{F}^n = -K \delta^{\frac{3}{2}} \left(1 + \frac{3(1-c_e^2)}{4} \frac{\dot{\delta}}{\dot{\delta}^{(-)}} \right) \mathbf{n} \quad (7)$$

where $\dot{\delta}$ and $\dot{\delta}^{(-)}$ are the relative penetration velocity and the initial contact velocity, respectively, and c_e is the coefficient of restitution. The generalised stiffness parameter K depends on the geometry and physical properties of the contacting surfaces [10].

The tangential contact force can be evaluated as friction force from the modified Coulomb friction law

$$\mathbf{F}^t = -\mu(v_t) \|\mathbf{F}^n\| \mathbf{t} \quad (8)$$

where v_t represent the tangential velocity and μ denotes the friction coefficient that depends on the relative velocity between the head and cup.

3 Numerical Wear Models

Wear is the progressive loss of substance as a result of relative motion between surfaces. Although some typical features of the wear process are demonstrated experimentally and there are some simple models to compute wear, such as the

well-known Archard's wear methodology, no laws of wear exist. The Archard wear equation can be written as follow

$$I = \frac{V}{s} = \frac{KP}{H} \quad (9)$$

where the dimensionless constant K denotes the wear coefficient, V is volumetric wear, s sliding distance, P contact pressure and H is material hardness. Moreover, it is more preferable for engineering applications to utilise the ratio K/H , termed wear coefficient (k), dimensionally expressed as $\text{mm}^3/\text{Nm}^{-1}$. In addition to the volumetric wear model of Archard defined in Eq. (9), the Archard's depth wear equation as the linear wear rate can be written as follows

$$\frac{dh}{ds} = \frac{KP}{H} \quad (10)$$

in which P is contact pressure and h is depth wear.

A numerical solution for the wear depth, using Archard's wear model Eq. (10), may be obtained by the forward Euler integration algorithm to yield the following updating formula for wear depth

$$h_i = h_{i-1} + kP_i\Delta s_i \quad (11)$$

in which h_i refers to the wear depth at the i th step while h_{i-1} represents the wear depth at the previous step. The last term in Eq. (11) is the incremental wear depth which is a function of the contact pressure and the incremental sliding distance at the corresponding cycle.

4 Results and Discussion

The main objective of this study is to investigate the wear of CoC artificial hip joints with the following geometric properties: the femoral head radius equal to 14 mm and radial clearance of 50 μm . Material parameters of the bearing couples were defined according to Uddin and Zhang [23]. Al_2O_3 ceramic had a Young's modulus and Poisson ratio of 375 GPa and 0.3, respectively. The wear factor for CoC couples was assumed to be 0.2×10^{-8} [23]. In vivo three dimensional physiological loads and rotations were applied to the femoral head centre and nonlinear dynamic equations were solved numerically.

Table 1 lists the results from the current study and compares them with the available literature. It can be seen that linear and volumetric wear results obtained from the present work compare well with hip simulator and computational studies as well as clinical studies.

Table 1 Comparison of results with the available literature

	Method	Linear wear (μm)	Volumetric wear (mm^3)
Present study (very low friction)	Computation	2.18	0.16
Present study (friction)	Computation	0.10 mm (cup) 0.19 mm (head)	6.84
Dorlot [7], Mittelmeier and Heisel [18]	Clinical tests	2–5	–
Stewart et al. [21], Affatato et al. [2]	Hip simulator	–	0.10–1.02
Uddin and Zhang [23]	Computation	1.32	0.17
Affatato et al. [1]	Clinical tests	0.01–1.40 mm (head)	0.34–695

Trajectory and linear wear computation of the cup and femoral head for CoC hip implants are depicted in Fig. 1. The trajectories of the contact point between the cup and head conform to the worn path both in terms of location and shape. Moreover, the present study determined that wear increases as bearing surface friction increases. This conclusion is depicted in Fig. 1 where linear and volumetric wear of the friction model were around 50 times greater than the case with very low friction. This wear phenomenon can be justified by considering two physical reasons; (i) friction induced an increase in the overall trajectory of the contact point track and (ii) friction induced microscopic vibration of the femoral head within the cup (see Fig. 1). Consequently, the sliding distance increased significantly, which increased linear and volumetric wear.

5 Conclusions

A multibody dynamic approach was proposed to integrate the Archard's wear model into our spatial multibody dynamic formulation in order to predict linear and volumetric wear of CoC artificial hip joints. The gross movement and vibration of the femoral head inside the cup for both frictionless and frictional contact was modelled and wear determined. The alteration of hip implant couple geometries was also taken into account by updating the corresponding surface geometries as the simulation progressed. The present procedure for very low friction showed very promising results in comparison with the available literature. While previous hip simulators and computational studies have generally underestimated wear rates of artificial hip joints when compared to clinical results, the present article illustrated that friction-induced vibration increased the wear rate significantly. The increase in wear prediction of our model was a result of friction increasing the sliding distance of the femoral head across the cup in both the micro and macro sense, with a wide vibration band and greater overall range of movement of the contact point. The trajectory of the contact point conformed to the wear map on the cup and head surfaces.

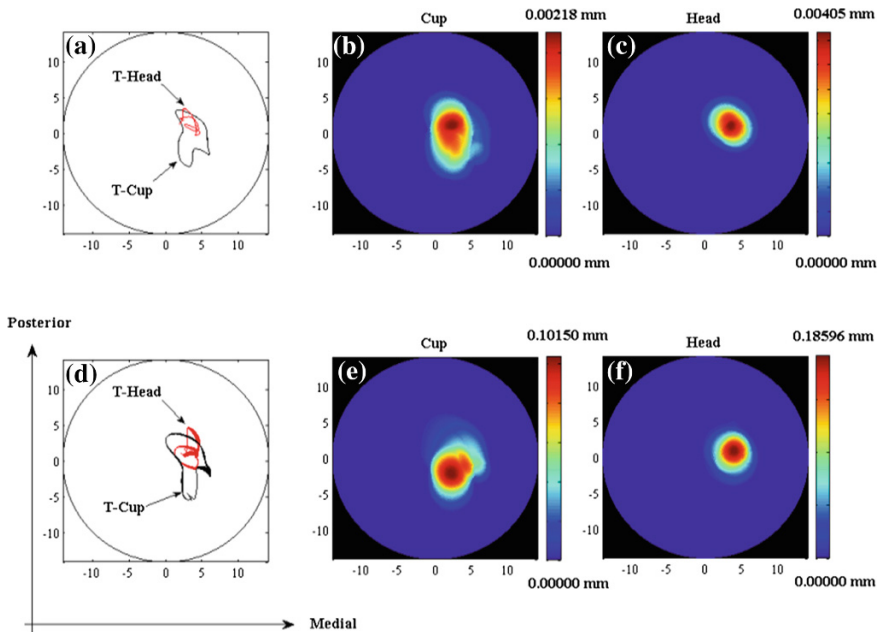


Fig. 1 Ceramic-on-ceramic (CoC) hip implant with three-dimensional physiological loading and motion of the human body assuming frictionless where volumetric wear = 0.163 mm^3 (top row) and frictional contact where volumetric wear = 6.975 mm^3 and $cf/cd = 0.1/0.065$ (bottom row): **a** and **d** Contact point trajectory on the head and cup, illustrated as *T-Head* and *T-Cup*, respectively; **b** and **e** Linear wear depth on the cup; **c** and **f** Linear wear depth on the head

Additionally, this study confirmed our hypothesis that friction-induced vibration is the cause of high wear rates observed clinically.

Acknowledgments The first author gratefully acknowledges Macquarie University for International Macquarie University Research Excellence Scholarship (iMQRES)—No. 2010017. The second author expresses his gratitude to the Portuguese Foundation for the Science and Technology under the research project BIOJOINTS (PTDC/EME-PME/099764/2008).

References

1. Affatato S, Traina F De Fine M, Carmignato S, Toni A (2012) Alumina-on-alumina hip implants: a Wear study of retrieved components. *J Bone Joint Surg* 94-B: 37–42
2. Affatato S, Bersaglia G, Foltran I, Emiliani D, Traina F, Toni A (2004) The influence of implant position on the wear of alumina-on-alumina studied in a hip simulator. *Wear* 400–405
3. Archard JF (1953) Contact and rubbing of flat surfaces. *J Appl Phys* 24:981–988
4. Askari E, Flores P, Dabirrahmani D, Appleyard R (2014) Nonlinear vibration and dynamics of ceramic on ceramic artificial hip joints: a spatial multibody modelling. *Nonlinear Dyn* 76:1365–1377

5. Askari E, Flores P, Dabirrahmani D, Appleyard R (2014) Study of the friction-induced vibration and contact mechanics of artificial hip joints. *Tribol Int* 70:1–10
6. Boutin P (1972) Arthroplastie totale de la hanche par prothèse en alumine frittée. Etude expérimentale et premières applications cliniques. *Revue Chirurgie Orthopedique* 58:229–2246
7. Dorlot JM (1992) Long-term effects of alumina components in total hip prostheses. *Clin Orthop Relat Res* 282:47–52
8. Flodin A, Andersson S (2001) A simplified model for wear prediction in helical gears. *Wear* 249:285–292
9. Hegadekatte V, Huber N, Kraft O (2005) Finite element based simulation of dry sliding wear. *Modell Simul Mater Sci Eng* 13:57–75
10. Hertz H (1881) Über die Berührung fester elastischer Körper. *J reine und angewandte Mathematik* 92:156–171
11. Ibrahim RA (1994) Friction-induced vibration, chatter, squeal, and chaos. Part I: Mechanics of contact and friction. *Appl Mech Rev* 47(7):209–226
12. Jourdan F, Samida A (2009) An implicit numerical method for wear modelling applied to a hip joint prosthesis problem. *Comput Methods Appl Mech Eng* 198:2209–2217
13. Lancaster JG, Dowson D, Isaac GH, Fisher J (1997) The wear of ultra-high molecular weight polyethylene sliding on metallic and ceramic counterfaces representative of current femoral surfaces in joint replacement. In: *Proceedings of the institution of mechanical engineers, Part H* 211, pp 17–24
14. Lankarani H, Nikravesh P (1990) A contact force model with hysteresis damping for impact analysis of multibody systems. *J Mech Des* 112:369–376
15. Liu F, Leslie I, Williams S, Fisher J, Jin Z (2008) Development of computational wear simulation of metal-on-metal hip resurfacing replacements. *J Biomech* 41:686–694
16. Mattei L, Di Puccio F (2013) Wear simulation of metal-on-metal hip replacements with frictional contact. *J Tribol* 135(2)
17. Mattei L, Di Puccio F, Ciulli E (2013) A comparative study of wear laws for soft-on-hard hip implants using a mathematical wear model. *Tribol Int* 63:66–77
18. Mittelmeier H, Heisel J (1992) Sixteen years' experience with ceramic hip prostheses. *Clin Orthop Relat Res* 282:64–72
19. Nikravesh PE (1988) *Computer-aided analysis of mechanical systems*. Prentice-Hall, Englewood Cliffs, NJ
20. Saikko V, Caloni O (2002) Slide track analysis of the relative motion between femoral head and acetabular cup in walking and hip simulator. *J Biomech* 35(4):455–464
21. Stewart T, Nevelos J, Tipper J, Insley G, Streicher R, Ingham E, Fisher J (2001) Long term simulator studies of alumina ceramic/ceramic hip joints with swing phase micro-separation; analysis of wear and wear debris generation. In: *Combined Orthopaedic Research Societies Meeting*, Rhodes, Greece
22. Teoh SH, Chan WH, Thampuran R (2002) An elasto-plastic finite element model for polyethylene wear in total hip arthroplasty. *J Biomech* 35(3):323–330
23. Uddin MS, Zhang LC (2013) Predicting the wear of hard-on-hard hip joint prostheses. *Wear* 301:192–200

Techniques for Geometrical Detection of Contact Within Multibody Systems

M. Machado, P. Flores and J. Ambrósio

Abstract Within a multibody dynamics algorithm, the occurrence of contact events is checked at each time integration step, being the contact forces computed, together with other existing forces, and then introduced into the Newton-Euler equations of motion as external generalized forces. In general, the evaluation of these contact forces relies on constitutive laws, which have to be selected according to the material's nature of the contacting bodies (from linear elastic to nonlinear dissipative models). Prior to the calculation of the contact forces, a geometrical detection of the contact is required. This is not a trivial task and it depends on two key factors: (i) mathematical representation of the contact geometries and, (ii) proximity queries and simulation parameters. In this work, an overview of the most used techniques for the geometrical detection of contact is presented, given a special attention to the application field of multibody system dynamics.

Keywords Contact detection · Contact geometry · Proximity query · Simulation parameters

1 Introduction

A contact mechanics problem can be analyzed by using either the finite element method (FEM) or the multibody system (MBS) dynamics. There is no doubt that the FEM is the most powerful and accurate method to solve contact problems. In turn, the MBS formulation is the most efficient approach for the dynamic analysis of

M. Machado (✉)

Institute of Mechanical Engineering and Industrial Management (INEGI), Porto, Portugal
e-mail: mmachado@inegi.up.pt

P. Flores

University of Minho, Braga, Portugal
e-mail: pflores@dem.uminho.pt

J. Ambrósio

IST, University of Lisbon, Lisbon, Portugal
e-mail: jorge@dem.ist.utl.pt

the gross motion of mechanical systems [5, 6]. Regardless of the method used to describe contact problems of the colliding bodies, it is necessary to model and analyze the contact process. This involves two main tasks: (i) geometrical detection of contact, and (ii) evaluation of contact forces (i.e., contact response). The former is a chief step in contact modeling of moving bodies, which deals with the definition of the contact geometries and the determination of when, where and which points are in contact. The efficiency and accuracy of this step strongly depend on the complexity and number of potential colliding bodies, as well as the kinematics of the contact parts [5, 6].

The evaluation of the contact forces can be performed by considering different approaches, and constitutive laws that take into account material properties of the contacting bodies, geometric characteristics of the impacting surfaces and, eventually, the impact velocity. These models are widely described in the literature and there are several review papers on this matter, focusing on the contact force analysis within multibody systems formulation [6, 10].

Regarding contact detection, there is not so many information, being most of the studies dedicated to the scope of computer graphics [3]. Thus, an overview of the paramount techniques for contact detection is presented in this work, given a special attention to the MBS dynamics application field [5].

From a mechanical viewpoint, contact detection is a two-step procedure that includes the identification of the coordinates of the potential contact points and the evaluation of the contact indentation. The contact detection process is often referred to as collision detection and the associated computational algorithms rely on several factors, which can be grouped in six classes: (i) mathematical representation of contact geometries, (ii) proximity queries, (iii) environmental simulation parameters, (iv) performance, (v) robustness, and (vi) ease of implementation and use [3]. Despite all these issues influence the modeling process of a MBS with contact, the first three are the ones that affect most the dynamic of the MBS. Hence, these three factors will be described throughout this work.

2 Mathematical Representation of Contact Geometries

The efficiency of a contact detection process relies upon the geometric representation of the contact surfaces that can be represented by means of polygonal or nonpolygonal models, as Fig. 1 illustrates [8]. Polygonal models are frequently applied to model complex shapes. Nonetheless, when the contact analysis method demands a continuous representation (as in the field of multibody dynamics), nonpolygonal models are used. The nonpolygonal models can be classified into three main groups, namely constructive solid geometry (CSG), implicit methods and parametric functions (Fig. 1).

The use of CSG models is easy and straightforward, but it is restricted because the CSG representations have to be described by a set of Boolean operations instead of a mathematical expression.

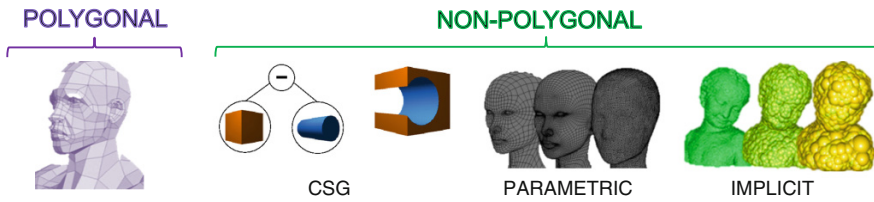


Fig. 1 Taxonomy of geometrical models [8]

Implicit function defines the location of the points belonging to surface. With this type of representation, the boundaries of an object are well defined as closed manifolds, and the evaluation whether a point belongs to the surface, or not, is an easy and trivial task [7, 8]. Nonetheless, the three Cartesian coordinates are not independent. This is a disadvantage of the implicit method because it does not allow for generating, in a systematic manner, a set of consecutive points located on a surface. Furthermore, efficient rendering and accurate modeling of sharp edges is usually a hard task whenever implicit representations are used.

Parametric representations are a set of equations that map one or two parameters into Euclidean space. One parameter is used to define a curve. To describe a parametric surface two parameters are demanded. With this approach, it is quite easy to generate a set of points belonging to a surface, because the Cartesian coordinates are explicit and independent functions of the parametric coordinates [4]. It is worth noting that parametric representations are generally non-unique, so the same quantities may be expressed by a number of different parameterizations. The major advantage of parametric representation is that it allows for the reduction of a 3-D problem to the 2-D domain, avoiding the use of complex and timing consuming numerical solutions. Parametric surfaces are easier to polygonalize and render as compared to the implicits. With the parametric method, it is possible to define different types of surfaces that can range from very simple geometries, such as spheres, to surfaces with a high-degree of complexity (e.g., NURBS). In short, the parametric method allows for efficient contact search algorithm for generating and representing arbitrary surfaces, which offers great flexibility, and precision for handling freeform shapes. It should be highlighted that the implicit and parametric approaches can exhibit complementary characteristics and it may be convenient to convert from one form to another or combined both representations in a hybrid surface model [7, 8].

3 Proximity Queries

The subject of contact detection is quite challenging and an actual problem in various areas such as, discrete element methods, robotic systems, MBS simulations, or video games engines and computer graphics. The diversity of application fields

Table 1 Five proximity queries (adapted from [7])

Query	Definition	Condition
Collision detection	Checks whether two objects overlap in space or their boundaries share at least one common point	$\text{col}(P, Q) = P \cap Q$
Separation distance	Length of the shortest line segment joining two sets of points	$d_{\text{sep}}(P, Q) = \min_{p \in P} \min_{q \in Q} p - q $
Spanning distance	Maximum deviation of one set from the other	$d_{\text{span}}(P, Q) = \max_{p \in P} \max_{q \in Q} p - q $
Hausdorff distance	Maximum distance between the points of two sets	$d_{\text{haus}}(P, Q) = \max_{p \in P} \min_{q \in Q} p - q $
Penetration depth	Minimum distance needed to translate one set to make it disjoint from the other	$d_{\text{pen}}(P, Q) = \min \mathbf{v} , \text{ such that } \min_{p \in P} \min_{q \in Q} \mathbf{p} - \mathbf{q} + \mathbf{v} > 0$

demands different specifications to deal with the contact detection problem and, hence, different proximity queries. The five most common and easily defined proximity measures are: (i) collision detection, (ii) minimum distance (also called separation distance), (iii) maximum distance (also referred as spanning distance), (iv) Hausdorff distance, and (v) penetration depth. Such queries are depicted in Table 1. Furthermore, there are queries applicable to dynamic scenarios, such as finding when the next contact between two moving bodies will occur (i.e., the estimated time of arrival or time of impact computation query) [3, 8]. In the context of MBS dynamics, the main proximity queries are the separation distance and the penetration depth. The former is utilized to check whenever contact occurs, and also to identify the set of contacting points (i.e., the contact manifold or the contact locus). In turn, the penetration depth query is applied in contact conditions to evaluate the contact indentation [14].

4 Environmental Simulation Parameters

The environmental simulation parameters have also effect on the contact detection process. An example of these parameters is the number of contacting objects in a system. A larger number of such objects may slow down significantly the performance of a contact detection algorithm, since the proximity queries have to be checked in every simulation step for each body. Thus, a contact detection method has to be applied according to the complexity of the contact scenario. There are two main categories of contact detection approaches: (i) the single-phase formulation and (ii) the broad-phase and narrow-phase methods.

4.1 Single-Phase Approach

Single-phase approach is recommended wherever the contact simulation only requires a small number of contact calculations in each simulation step, such as a MBS with a few contacting bodies that are located nearby. The solution of this type of problems usually relies on the common-normal concept, which states that two points are the potential contact points if the normal vectors at these points are collinear to each other and perpendicular with the tangential plane of contact. The unknown variables of such problem are the coordinates of the potential contact points, which are reached by an iterative process when a set of geometric constraints is fulfilled. These constraints express collinearity and orthogonality conditions between the vectors defining the contacting surfaces at the contact points, namely the normal, tangent, binormal and distance vectors. As a result, a system of nonlinear equations, obtained from equaling both normal vectors and from equaling the normal vector to the distance vector, is solved numerically. In general, there are two possible scenarios: (i) contact at a single point without indentation (Fig. 2a), and (ii) contact at multiple points with indentation (Fig. 2b). The contact is detected when the minimum distance is lesser than or equal to zero and positive when surfaces are apart [11].

4.2 Broad-Phase and Narrow-Phase Methods

The broad-phase and narrow-phase methods (also referred as n -body processing and pair processing, respectively) are used when it is intended to reduce the number of pairs tested and, thus, to speed up the computational simulation [3]. The broad-phase methods identifies smaller groups of objects that may be colliding and quickly excludes those that definitely are not, either because they are far away from each other, or because other features inherent to the system or the application (e.g., game rules). In contact mechanics, the broad-phase algorithms are generally utilized to check if the bodies are closely enough to be considered contact candidates [13]. In these cases narrow-phase methods are employed, which test with more accuracy

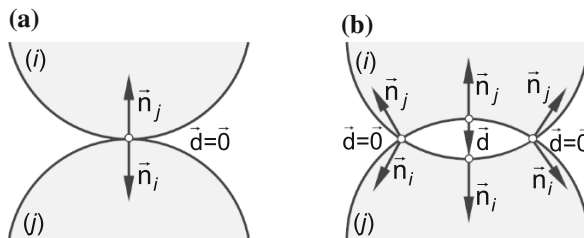


Fig. 2 Two possible contact scenarios: **a** Contact at a single point with-out indentation; **b** Contact at multiple points with indentation

the subgroup of possible contacting pairs pointed out by the broad-phase algorithms. Narrow-phase approaches usually report more detailed information that is afterwards used to compute indentation and contact forces.

Spatial data structures are usually applied to formulate broad-phase and narrow-phase algorithms. These structures fall into two classes: space partitioning and model partitioning. A space partitioning is a subdivision of space into convex regions called cells. Using such a structure, several pairs of bodies can be quickly excluded from intersection testing, as it is only necessary to test the pairs of bodies that share a cell. The most commonly used space partitioning structures are: voxel grids, octrees and k -d trees, and binary space partitioning (BSP) trees. Figure 3 illustrates how to generate a BSP tree [3, 14].

A model partitioning is often a better choice than space partitioning, because the model partitioning structures do not suffer from the problem of having multiple references to the same object. The basic strategy is to subdivide a set of objects into geometric coherent subsets and compute a bounding volume (BV) for each subset of objects. A BV of a model is a primitive shape that encloses the model and should have the following properties: (i) a BV should fit the model as tightly as possible in order to reduce the probability of a given object intersect the BV but not the model; (ii) overlap tests between BVs should be computationally cheap; (iii) a BV should be described using a relatively small amount of storage, which is preferably smaller than the storage used by the model; (iv) the cost of computing a BV for a given model should be low [14]. The most used BV are: bounding spheres, axis-aligned bounding boxes (AABBs), oriented bounding boxes (OBBs) and discrete-orientation polytopes (k -DOPs). These BV are illustrated in Fig. 4. Nonetheless, there are some authors that utilized quadric and superquadric representations as bounding volumes. These geometric descriptions demand a greater computation effort than the bounding spheres, but are more accurate as they fit the model tighter than spheres [9]. Some of libraries and software packages developed for computing proximity are based on bounding hierarchies, such as DEFORMCD, H-COLLIDE, IMPACT, OPCODE, PQP, RAPID and SOLID.

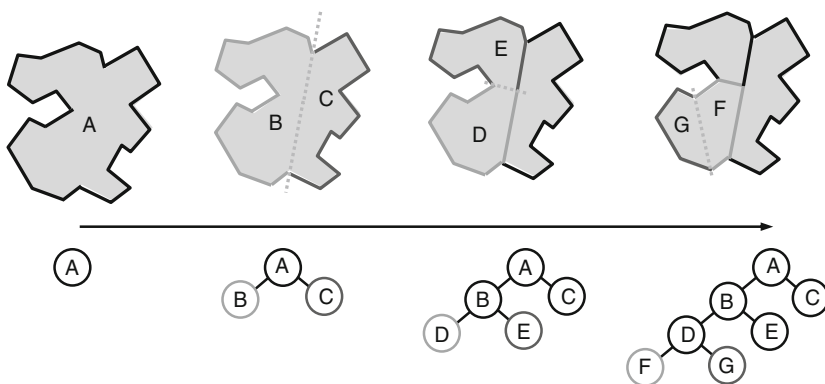


Fig. 3 Four steps to generate a BSP tree [14]

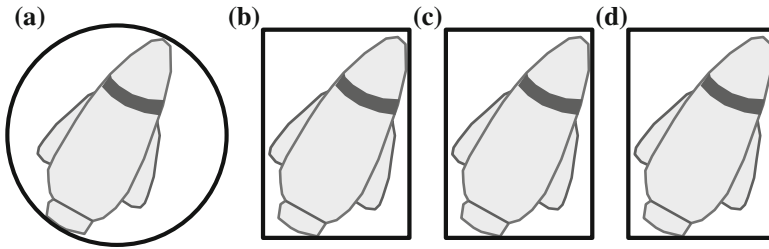


Fig. 4 Bounding volumes: **a** Sphere; **b** AABB; **c** OBB; **d** 8-DOP

With the intention to improve the computational efficiency of the contact algorithms, some researchers use graphical processing units (GPUs) for fast image-space-based intersection techniques or as a co-processor for accelerating mathematics or geometry calculations, because GPUs have inherently more raw processing power than the main CPUs [3]. In MBS dynamics, GPU-assisted algorithms have been used to perform large-scale simulations of ground vehicles running on sand, powder composites and granular material flow [12]. Other alternative method to speed up the CPU times of a contact simulation is to apply lookup table-based approaches, also named as surrogate contact models [1, 2].

5 Conclusions

The contact modeling in MBS can be divided in contact detection and contact response. The contact detection is a two-step process that includes the identification of the spatial coordinates of the potential contact points and the evaluation of the contact indentation. In turn, the contact response consists of computing the contact force based on the state variables of the system. The dynamic response of the MBS is obtained by simply including updated forces into the equations of motion.

The contact detection is a common problem to several areas. Thus, several software packages and computational methods devoted to this topic. In a broad sense, these algorithms rely on three key features: (i) geometric representation, (ii) proximity queries and (iii) environment simulation parameters. The geometric representation corresponds to the mathematical method used to define the geometry of the contact scenario and the colliding objects, which can be accomplished by using polygonal models or non-polygonal models, such as CSG approaches, implicit or parametric functions. In turn, a proximity query consists of a computation that produces information about the relative configuration or placement of objects. Some examples of proximity queries are: collision detection, minimum distance, maximum distance, Hausdorff distance, and penetration depth. Environmental simulation parameters affect also the contact detection process, such as the number of contacting bodies, which may slow down significantly the performance

of a contact detection algorithm. The single-phase approach is employed when the contact simulation only requires a small number of contact calculations in each simulation step (e.g. the common-normal concept). To speed up the simulation, advanced methods are used, which are classified as broad-phase and the narrow-phase approaches. The broad-phase methods identifies smaller groups of objects that may be colliding and quickly excludes those that definitely are not. Then, narrow-phase methods are employed, which ones test with more accuracy the subgroup of possible contacting pairs pointed out by the broad-phase algorithms.

In summary, there are several techniques for geometrical detection that can be used to solve contact problems within MBS. These formulations have inherently advantages and disadvantages for each particular scenario. None of the methods described above can a priori be considered to be superior compared to other for all applications. It is a fact that a specific contact problem within a MBS might be easier to describe by one technique, but this does not yield a general predominance of this formulation in all situations. Still, the presented overview is considered noteworthy and a useful guideline for future studies on contact modeling.

References

1. Bei Y, Fregly BJ (2004) Multibody dynamic simulation of knee contact mechanics. *Med Eng Phys* 26:777–789
2. Bozzone M et al (2011) A lookup table-based method for wheel–rail contact analysis. *Proc Inst Mech Eng Part K: J Multi-body Dyn* 225:127–138
3. Ericson C (2005) Real-time collision detection. Morgan Kaufmann Publishers, Burlington
4. Farin GE (1995) NURBS curves and surfaces: from projective geometry to practical use. AK Peters
5. Flores P, Ambrósio J (2010) On the contact detection for contact-impact analysis in multibody systems. *Multibody Sys Dyn* 24:103–122
6. Gilardi G, Sharf I (2002) Literature survey of contact dynamics modeling. *Mech Mach Theory* 37:1213–1239
7. Gottschalk S (2000) Collision queries using oriented bounding boxes. Ph.D. thesis (2000)
8. Lin M, Gottschalk S (1998) Collision detection between geometric models: a survey. In: *Proceedings of IMA conference on mathematics of surfaces*, Birmingham, UK, 602–608
9. Lopes DS et al (2011) A mathematical framework for rigid contact detection between quadric and superquadric surfaces. *Multibody Sys Dyn* 24:103–122
10. Machado M et al (2012) Compliant contact force models in multibody dynamics: evolution of the Hertz contact theory. *Mech Mach Theory* 53:99–121
11. Pombo J et al (2007) A new wheel-rail contact model for railway dynamics. *Veh Syst Dyn* 45:165–189
12. Tasora A, Anitescu M (2010) A convex complementary approach for simulating large granular flows. *J Comput Nonlinear Dyn*, 5, 031004, 7 p
13. Tasora A, Righettini P (2003) Sliding contact between freeform surfaces. *Multibody Sys Dyn* 10:239–262
14. van den Bergen GJA (2004) Collision detection in interactive 3D environments. Morgan Kaufmann, Burlington

On the Equivalence Between Forward and Inverse Dynamic Analysis of Human Motion Tasks

C. Quental, J. Folgado, J. Ambrósio and J. Monteiro

Abstract The vast majority of musculoskeletal models of the upper limb follow an inverse dynamic approach due to its efficiency. Yet, a forward dynamic approach is more powerful. The aim of this study is to develop a forward dynamic model of the upper limb and to investigate its ability to track prescribed motions. For that purpose, an inverse dynamic model is applied to estimate the muscle forces responsible for two experimentally acquired motions, which are then given as input to the forward dynamic model. In order to enhance numerical stability, a proportional-derivative controller is implemented in a feedback loop. The results show that the forward dynamic approach is able to successfully simulate the acquired motions without needing relevant control forces or torques.

Keywords Musculoskeletal model · Inverse dynamics · Forward dynamics · Proportional-derivative control · Muscle forces

1 Introduction

Knowledge regarding the mechanical behavior of the human body under different conditions can be quite helpful for clinical decisions in orthopedic and neurological problems. Since direct *in vivo* or *in vitro* measurements are difficult or even impossible to perform, researchers have focused on the development of accurate

C. Quental (✉) · J. Folgado · J. Ambrósio
LAETA, IDMEC, Instituto Superior Técnico, Universidade de Lisboa, Lisbon, Portugal
e-mail: cquental@dem.ist.utl.pt

J. Folgado
e-mail: jfolgado@dem.ist.utl.pt

J. Ambrósio
e-mail: jorge@dem.ist.utl.pt

J. Monteiro
Faculty of Medicine, Universidade de Lisboa, Lisbon, Portugal
e-mail: jac.monteiro@hsm-min-saude.pt

biomechanical models and numerical techniques to study the human body [3]. Regarding human motion, detailed musculoskeletal models have been used to investigate joint kinematics and ergonomics, and have often been coupled with muscle force estimation techniques to evaluate muscular action and joint reaction forces [7, 11].

Depending on the goals, musculoskeletal models are either applied following an inverse dynamic or a forward dynamic approach. From the computational point of view, the inverse dynamic approach is far more efficient, and thus is the most commonly applied procedure to estimate muscle and joint reaction forces [7, 11, 12]. Yet, forward dynamic simulations are particularly powerful as they allow for the identification of causal relationships between neural control inputs, muscle forces, and the task performance [9]. The aim of this paper is to develop a forward dynamic model of the upper limb and evaluate its performance regarding the simulation of upper limb tasks. For that purpose, the muscle forces of the upper limb are estimated, for experimentally acquired motions, using an inverse dynamic model of the upper limb, and are given as input to the forward dynamic model. In order to enhance the stability of the forward dynamic simulations, a proportional-derivative controller is also implemented to track the acquired motions.

2 Materials and Methods

The following section provides a brief description of the biomechanical model of the upper limb and of the inverse and forward dynamic procedures implemented.

2.1 *Biomechanical Model*

The biomechanical model of the upper limb is composed of 7 rigid bodies, namely the thorax, rib cage, clavicle, scapula, humerus, ulna, and radius. Considering the thorax and rib cage static, the relative motion of the remaining bodies is constrained by the sternoclavicular, acromioclavicular (AC), and glenohumeral (GH) joints, each modeled by a 3 degrees of freedom (d.o.f.) spherical joint; the scapulothoracic (ST) joint, modeled by two holonomic constraints that ensure the scapula to glide over the thorax; and the humeroulnar and radioulnar joints, each represented by 1 d. o.f. hinge joints. The skeletal system is actuated by 21 muscles, defined by 69 bundles using the obstacle set-method [5]. The muscle contraction dynamics is simulated by a Hill-type muscle model that includes an active contractile element and a passive element. For further detail regarding the numerical implementation of the biomechanical model, the reader is referred to the work of Quental et al. [11, 13].

2.2 Inverse Dynamic Analysis

Following the recommendations from the International Society of Biomechanics [18], an unloaded motion of abduction in the coronal plane, from 13° to 109°, and of anterior flexion in the sagittal plane, from 11° to 114°, were acquired at the Laboratory of Biomechanics of Lisbon (LBL) for a male subject (25 years, 179 cm, 75 kg). The dynamic tracking of the scapula was accomplished using the methodology proposed by Senk and Chèze [14], the axial rotation of the clavicle was estimated by minimizing the AC joint rotations [17], and the GH joint center was estimated using the algorithm of Gamage and Lasenby [4].

The optimization problem associated with the indeterminate muscle force sharing problem is formulated in terms of finding the muscle activations that lead to the minimization of an objective function, related to the muscle metabolic energy consumption [10]. Mathematically, it is formulated as follows:

$$\min J(t, \mathbf{a}) = \sum_{t=1}^n \sum_{i=1}^m c_1 \frac{V^i F_{CE}^i}{PCSA^i} + c_2 V^i a_t^i + c_3 V^i (a_t^i)^2$$

subject to,

$$(a) \mathbf{f}_t(\mathbf{a}) = \left(\Phi_{\mathbf{q}}^T \boldsymbol{\lambda} + (\mathbf{M}\ddot{\mathbf{q}} - \mathbf{g}) \right)_t = 0, \quad t = 1, \dots, n \quad (1)$$

$$(b) \mathbf{0} \leq \mathbf{a} \leq \mathbf{1}$$

$$(c) \left(\frac{\mathbf{f}_{GH}^T \boldsymbol{\tau}_{GHd}}{\mathbf{f}_{GH}^T \mathbf{n}_{GH}} \right)_t \leq th_d, \quad t = 1, \dots, n$$

$$(d) (\mathbf{f}_{ST}^T \mathbf{n}_{ST})_t > 0, \quad t = 1, \dots, n$$

where n is the total number of time frames, m is the number of muscle bundles, V^i is the volume of muscle i , F_{CE}^i is the active force of muscle i , $PCSA^i$ is the physiological cross-sectional area of muscle i , and a_t^i is the activation at the time frame t for muscle i . The variables c_1 , c_2 , and c_3 are weighting factors [10]. The constraints of the optimization problem are (a) the equations of motion, represented by $\mathbf{f}_t(\mathbf{a})$, in which $\Phi_{\mathbf{q}}$ is the Jacobian matrix of the constraint equations, $\boldsymbol{\lambda}$ is the Lagrange multipliers vector, \mathbf{M} is the mass matrix of the system, $\ddot{\mathbf{q}}$ is the acceleration vector, and \mathbf{g} is the generalized vector of external forces; (b) the bounds of the muscle activations \mathbf{a} ; (c) the stability of the GH joint [2], in which \mathbf{f}_{GH} represents the GH joint reaction force, \mathbf{n}_{GH} the normal to the glenoid plane, and $\boldsymbol{\tau}_{GH}$ the unitary vector in the glenoid plane describing the direction d with a stability threshold th_d ; and (d) the stability of the ST joint, for which the reaction force is denoted by \mathbf{f}_{ST} and the directional vector of compression between the scapula and thorax by \mathbf{n}_{ST} . A more detailed description of the numerical methods used to solve the redundant muscle force sharing problem is provided in [11].

2.3 Forward Dynamic Analysis

In a forward dynamic analysis, the acceleration vector of the mechanical system is assumed unknown, which means that there are only n_c equations for $n_c + n_l$ unknowns: the n_c elements of $\ddot{\mathbf{q}}$ and the n_l elements of λ . In order to have enough number of equations, the acceleration kinematic equations are appended to the equations of motion, leading to a system of differential algebraic equations of the form [1, 8]:

$$\begin{bmatrix} \mathbf{M} & \Phi_{\mathbf{q}}^T \\ \Phi_{\mathbf{q}} & \mathbf{0} \end{bmatrix} \begin{bmatrix} \ddot{\mathbf{q}} \\ \lambda \end{bmatrix} = \begin{bmatrix} \mathbf{g} \\ \gamma \end{bmatrix} \quad (2)$$

where γ is the right-hand side vector of the acceleration equations. Since Eq. (2) does not explicitly use the position and velocity constraint equations, the Baumgarte stabilization method is employed to keep any possible constraint violations under control. Accordingly, Eq. (2) is modified to:

$$\begin{bmatrix} \mathbf{M} & \Phi_{\mathbf{q}}^T \\ \Phi_{\mathbf{q}} & \mathbf{0} \end{bmatrix} \begin{bmatrix} \ddot{\mathbf{q}} \\ \lambda \end{bmatrix} = \begin{bmatrix} \mathbf{g} \\ \gamma - 2\alpha\dot{\Phi} - \beta^2\Phi \end{bmatrix} \quad (3)$$

where α and β are prescribed positive constants that represent the feedback control parameters for the velocity and position constraint equations, $\dot{\Phi}$ and Φ , respectively [6]. In this study, $\alpha = \beta = 5$ [8].

Starting from an initial condition \mathbf{q}_0 and $\dot{\mathbf{q}}_0$, Eq. (3) is solved for $\ddot{\mathbf{q}}$ and λ . Note that the biomechanical model is driven by the muscle forces, which are estimated from previously performed inverse dynamic analyses. Then, the velocities $\dot{\mathbf{q}}_t$ and accelerations $\ddot{\mathbf{q}}_t$ are integrated in order to obtain the new positions $\mathbf{q}_{t+\Delta t}$ and velocities $\dot{\mathbf{q}}_{t+\Delta t}$ for the next time step. This procedure is repeated until the kinematic behavior of the mechanical system is completely described for the selected period of analysis. Figure 1 summarizes the steps of the forward dynamic process.

2.3.1 Feedback Controller

In this study, a proportional-derivative (PD) controller is employed in a feedback loop to compensate the error between the desired trajectory of the biomechanical model and the actual one [15, 16]. Mathematically, the PD controller is described by:

$$\mathbf{g}_{control}(t) = \mathbf{k}_p(\mathbf{q}^{exp}(t) - \mathbf{q}(t)) + \mathbf{k}_v(\dot{\mathbf{q}}^{exp}(t) - \dot{\mathbf{q}}(t)) \quad (4)$$

where \mathbf{k}_p are the proportional gains, \mathbf{k}_v are the derivative gains, and $\mathbf{q}^{exp}(t)$ and $\dot{\mathbf{q}}^{exp}(t)$ are the desired position and velocity vectors, respectively, for the time t . The output $\mathbf{g}_{control}(t)$, which is introduced in Eq. (3) as an external force vector, represents the forces and torques necessary to counteract the deviation of the control

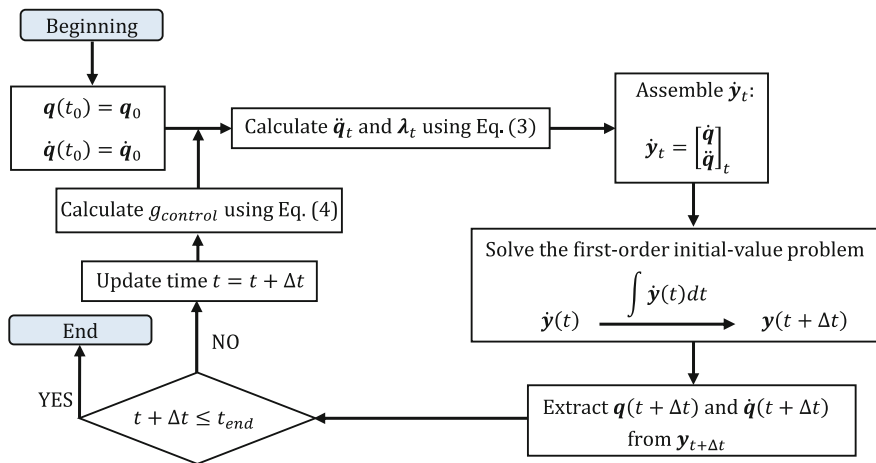


Fig. 1 Flowchart of the forward dynamic analysis

variables from the desired reference. The proportional gains were defined by a trial and error process, while the derivative gains were defined assuming that $\mathbf{k}_v = 2\sqrt{\mathbf{k}_p}$ [16].

Considering θ_{ξ}^i , θ_{η}^i , and θ_{ζ}^i the rotational d.o.f. of body i around, respectively, the x -, y -, and z -axis of its body-fixed reference frame, the degrees of freedom of the biomechanical system selected to be monitored and controlled were the $\theta_{\xi}^{clavicle}$, $\theta_{\eta}^{clavicle}$, $\theta_{\zeta}^{clavicle}$, $\theta_{\eta}^{scapula}$, $\theta_{\xi}^{scapula}$, $\theta_{\xi}^{humerus}$, $\theta_{\eta}^{humerus}$, $\theta_{\zeta}^{humerus}$, θ_{ξ}^{ulna} , θ_{ζ}^{ulna} , and θ_{η}^{radius} .

2.4 Forward Dynamic Simulation Evaluation

As a measure of the performance of the forward dynamic simulations, the root-mean-square error (*RMSE*), between the measured and simulated positions, is calculated. In particular, for each rigid body of the biomechanical model, the *RMSE* is calculated for the position of its center of mass (*RMSE_p*) and the orientation of its body-fixed reference frame (*RMSE_r*), as expressed in Eq. (5).

Table 1 Root-mean-square errors between the measured and simulated positions of the clavicle, scapula, humerus, ulna, and radius

RMSE	Abduction		Flexion	
	Translation (mm)	Rotation (°)	Translation (mm)	Rotation (°)
Clavicle	1.9e ⁻⁴	1.3e ⁻⁴	2.5e ⁻⁴	2.1e ⁻⁴
Scapula	3.8e ⁻⁴	1.3e ⁻⁴	5.1e ⁻⁴	9.2e ⁻⁵
Humerus	5.2e ⁻⁴	5.2e ⁻⁶	5.3e ⁻⁴	9.7e ⁻⁶
Ulna	5.2e ⁻⁴	1.9e ⁻⁵	5.2e ⁻⁴	3.5e ⁻⁶
Radius	7.9e ⁻⁴	4.5e ⁻⁴	8.7e ⁻⁴	3.3e ⁻⁴

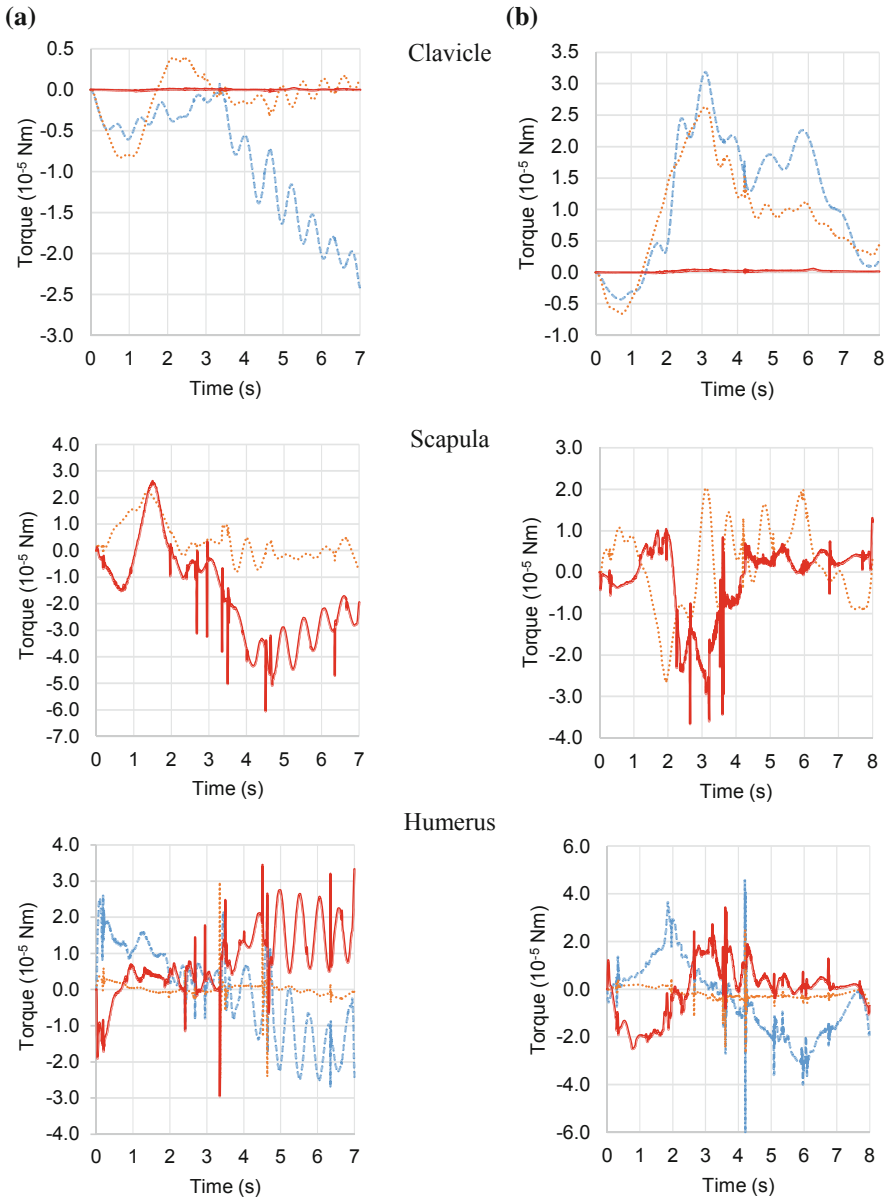


Fig. 2 Control torques applied to the clavicle, scapula, and humerus during the forward dynamic simulations of the **a** abduction and **b** anterior flexion motions. The torques color codes are θ_ξ (blue dashed), θ_η (orange dotted), θ_ζ (red solid).

$$\begin{aligned}
 RMSE_t &= \sqrt{\frac{\sum_{k=1}^n (x^{sim}(k) - x^{exp}(k))^2 + (y^{sim}(k) - y^{exp}(k))^2 + (z^{sim}(k) - z^{exp}(k))^2}{3n}} \\
 RMSE_r &= \sqrt{\frac{\sum_{k=1}^n (\theta_x^{sim}(k) - \theta_x^{exp}(k))^2 + (\theta_y^{sim}(k) - \theta_y^{exp}(k))^2 + (\theta_z^{sim}(k) - \theta_z^{exp}(k))^2}{3n}}
 \end{aligned}
 \tag{5}$$

3 Results

The forward dynamic procedure successfully simulated the motions of abduction in the coronal plane and anterior flexion in the sagittal plane, acquired at the LBL. The *RMSEs* estimated for the clavicle, scapula, humerus, ulna, and radius are quite small, as shown in Table 1.

In both motions, the torques applied to the biomechanical system by the feedback controller remained quite small throughout the analysis, as depicted in Fig. 2 for the clavicle, scapula, and humerus. Considering that the sole purpose of the feedback controller is to keep the inaccuracies resulting from the numerical integration procedure under control, such small torques provide further confidence in the forward dynamic model developed. Interestingly, even though the applied control torques are quite small, the forward dynamic procedure is unable to simulate the acquired motions if the feedback controller is removed. Note that small changes in the configuration of the biomechanical model, changes the direction of the applied forces, which further deviates the model from the desired configuration. Finally, in terms of computational cost, the forward dynamics procedure takes about 50 % more CPU time to run.

4 Conclusions

In this paper, a forward dynamic model of the upper limb was developed and its performance regarding the simulation of upper limb tasks was evaluated. For the sake of numerical stability, a proportional-derivative controller was also implemented in a feedback loop. Driven by the muscle forces, estimated for prescribed motions of abduction and anterior flexion using the inverse dynamic model of the upper limb described here, the forward dynamic model was able to simulate the desired motions. The small control torques and *RMSEs* obtained show that the muscle forces output from the inverse dynamic model are able to successfully drive the forward dynamic model.

References

1. De Jalón JG, Bayo E (1993) Kinematic and dynamic simulation of multibody systems: the real-time challenge. Springer, New York
2. Dickerson CR et al (2007) A mathematical musculoskeletal shoulder model for proactive ergonomic analysis. *Comput Methods Biomech Biomed Eng* 10(6):389–400
3. Favre P et al (2009) Numerical modelling of the shoulder for clinical applications. *Philos Trans A Math Phys Eng Sci* 367(1895):2095–2118
4. Gamage SS, Lasenby J (2002) New least squares solutions for estimating the average centre of rotation and the axis of rotation. *J Biomech* 35(1):87–93
5. Garner BA, Pandy MG (2000) The obstacle-set method for representing muscle paths in musculoskeletal models. *Comput Methods Biomech Biomed Eng* 3(1):1–30
6. Machado M et al (2012) Compliant contact force models in multibody dynamics: evolution of the Hertz contact theory. *Mech Mach Theory* 53:99–121
7. Nikooyan AA et al (2011) Development of a comprehensive musculoskeletal model of the shoulder and elbow. *Med Biol Eng Comput* 49(12):1425–1435
8. Nikravesh PE (1988) Computer-aided analysis of mechanical systems. Prentice Hall, Upper Saddle River
9. Neptune RR et al (2009) Forward dynamics simulations provide insight into muscle mechanical work during human locomotion. *Exerc Sport Sci Rev* 37(4):203–210
10. Praagman M et al (2006) The relationship between two different mechanical cost functions and muscle oxygen consumption. *J Biomech* 39(4):758–765
11. Quental C et al (2012) A multibody biomechanical model of the upper limb including the shoulder girdle. *Multibody Sys Dyn* 28(1–2):83–108
12. Quental C et al (2013) Multibody system of the upper limb including a reverse shoulder prosthesis. *J Biomech Eng* 135(11):111005
13. Quental C et al (2013) Critical analysis of musculoskeletal modelling complexity in multibody biomechanical models of the upper limb. *Comput Methods Biomech Biomed Eng* (in press)
14. Senk M, Chèze L (2010) A new method for motion capture of the scapula using an optoelectronic tracking device: a feasibility study. *Comput Methods Biomech Biomed Eng* 13(3):397–401
15. Seth A, Pandy MG (2007) A neuromusculoskeletal tracking method for estimating individual muscle forces in human movement. *J Biomech* 40(2):356–366
16. Thelen DG et al (2003) Generating dynamic simulations of movement using computed muscle control. *J Biomech* 36(3):321–328
17. Van der Helm FC, Pronk GM (1995) Three-dimensional recording and description of motions of the shoulder mechanism. *J Biomech Eng* 117(1):27–40
18. Wu G et al (2005) ISB recommendation on definitions of joint coordinate systems of various joints for the reporting of human joint motion—part II: shoulder, elbow, wrist, and hand. *J Biomech* 38(5):981–992

Railway Vehicle Modelling for the Vehicle-Track Interaction Compatibility Analysis

H. Magalhães, J. Ambrósio and J. Pombo

Abstract Railway vehicle homologation, with respect to running dynamics, is addressed via dedicated norms. The results required, such as, accelerations and/or wheel-rail contact forces, obtained from experimental tests or simulations, must be available. Multibody dynamics allows the modelling of railway vehicles and their representation in real operations conditions, being the realism of the multibody models greatly influenced by the modelling assumptions. In this paper, two alternative multibody models of the Light Rail Vehicle 2000 (LRV) are constructed and simulated in a realistic railway track scenarios. The vehicle-track interaction compatibility analysis consists of two stages: the use of the simplified method described in the norm “UIC 518—Testing and Approval of Railway Vehicles from the Point of View of their Dynamic Behaviour—Safety—Track Fatigue—Running Behaviour” for decision making; and, visualization inspection of the vehicle motion with respect to the track via dedicated tools for understanding the mechanisms involved.

Keywords Multibody models · Cylindrical joints with clearances · Railway dynamics · Vehicle approval · Wheel–rail contact

H. Magalhães (✉) · J. Ambrósio · J. Pombo
LAETA, IDMEC, Instituto Superior Tecnico, University of Lisbon, Lisbon, Portugal
e-mail: hugomagalhaes@ist.utl.pt

J. Ambrósio
e-mail: jorge@dem.ist.utl.pt

J. Pombo
LAETA, IDMEC, ISEL, Polytechnic Institute of Lisbon, Lisbon, Portugal
e-mail: jpombo@dem.ist.utl.pt

1 Introduction

The state-of-the-art in multibody system dynamics enables to modelling of mechanical systems of great complexity [3, 4, 6]. The dynamic response of the mechanical system, namely its motion and the forces associated, is the object of study. In the particular case of railway vehicles, the dynamic analysis intends to assess the running safely and the comfort perceived by the passengers [9]. This assessment depends, not only on the dynamic characteristics of the vehicle, but also on the track geometry. The analysis of the compatibility between the vehicle and the track is used in this work to address the different options available for vehicle modelling.

The vehicle is a mechanical system characterized by a group of bodies which are interconnected by joints and/or force elements. Usually the body structural deformation is neglected because only the large rigid body motions have impact in the vehicle dynamics. The joints defined as kinematic constraints define the relative motion between the bodies. The formulation of different kinematic joints used in vehicle modelling are available in reference [6, 8]. Of interest is the modelling of mechanical joints that are imperfect or for which significant wear exists. Recently, some formulations have been proposed [1, 4]. In many realistic mechanical joints, the relative motion between two bodies takes into account either the joint defects or considers them perfect. Regarding the force elements, there are passive elements, such as springs, hydraulic and friction dampers, and the active elements, for instances, the actuators of tilting systems [3]. Their numerical models, linear or nonlinear, vary with the nature of the element. The dynamic behaviour of the force element can be defined by analytical formulas, such as, the reaction force of the spring is defined by the product of the deformation with the stiffness, or by interpolating over an amount of representative points of their constitutive behaviour. This is an option to model a bump stop with a non-linear behaviour which is not possible with an analytical formula.

The interaction between the vehicle and the track is represented by an appropriate contact model [2]. The methodology used here to determine the contact forces follows three essential steps: first, the points of contact between wheels and rails are determined; secondly, the creepages, i.e., the relative velocities, are calculated at the points of contact; and, finally, the contact forces are determined [8]. Normal and tangential forces are generated in each contact wheel–rail. The Hertzian contact formulation is used to determine the normal forces. The tangential or creep forces can be determined using the formulation proposed by Polach [7].

The industry specifies a series of limit values on the forces that the vehicle can apply on the rails, the forces that the vehicle bogies or wheelsets can be subjected to and the accelerations on the bogies or wheelsets and on the carbody. These limit values are split into three categories: the *safety limit values* that ensure that the vehicle will not be in any risk of derailment, the *track loading limit values* that ensure that the track will not be damaged by the passage of the vehicle and the *comfort limit values* that ensure that the vehicle is comfortable enough to be used for passengers transportation. In this work, the Simplified Method presented in the

norm UIC 518 [9] is used. This method evaluates the *safety* and *the comfort limit values* based in the accelerations on the bogie, above of the outer wheelsets, and the accelerations measured in the carbody, on the pivots.

The interpretation of the spatial motion of the vehicle with respect to the track is difficult, if not impossible, without the use of dedicated visualization tools. After the dynamic analysis of a mechanical system, the SAGA Program is used for the visualization and animation of the system [5], which is modified to allow for the visualization of wheel–rail contact features. The clear identification of the wheel–rail contact points in the animation and the contact status are unique features of the graphical post-processing tool [5].

2 Multibody Approaches to Vehicle Modelling

A typical railway vehicle, from the multibody point of view, is composed by a carbody, where the passengers travel. The carbody is interconnected with the bogie frame by the secondary suspension and the bogie-carbody connection. The primary suspension interconnects the bogie frame to the wheelsets. Each suspension system and its modelling involve different levels of abstraction.

Each bogie of the LRV consists of one bogie frame, two wheelsets, four axleboxes and the mechanical elements that compose the primary suspension. At each extremity of the wheelset, one axlebox with roller bearings is assembled. Thus, the axlebox and the wheelsets are connected by a revolute joint. The mechanical elements which interconnect the axlebox and the bogie frame are the helicoidal springs and the guides as depicted in Fig. 1a. Three linear springs are used to model each helicoidal spring [3]. The guides are vertically assembled passing through the axleboxes. Due to the existence of clearance between the guide and the axlebox, the relative motion between the axlebox and the bogie is not perfectly axial. In this

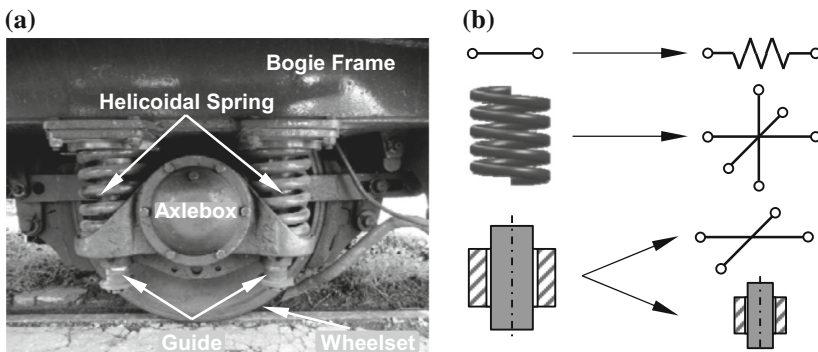


Fig. 1 a Primary suspension of the light rail vehicle 2000 (LRV); b Modelling of the helicoidal springs and the guides

case, only the transversal effects are relevant which is associated to the contact between the guides and the axlebox. To represent the guides two approaches are proposed. The first one is using two transversal force elements characterized by a linear stiffness. The second one and more realistic is using worn joints, namely, cylindrical joints with clearance.

Figure 2 presents the secondary suspension of the LRV, which involves on the carbody structure a skate and in the bogie side a conical roller. In turn, the roller seats in the top of two elastic elements, as depicted in Fig. 2a, which act as the stiffness of the secondary suspension. These components are vertically constrained and are responsible for the vertical forces that develop between the carbody and the bogie frame. To model this secondary suspension is used a long force element, as depicted in Fig. 2b, being the attaching point in the carbody placed in a realistic position. In this way, only the vertical forces can develop. In each side of the bogie is one skate-roller set, leading to the four sets in which carbody seats on the two bogies. Special emphasis is put in the low position of the attaching point in the bogie frame so that it does not compromise the realism of the model.

The traction forces between the bogie and the carbody is transmitted through the kingpin, presented in the bogie-carbody connection. Figure 3a presents the bogie-carbody connection of the LRV. There are two pivot shafts which are rigidly fixed to the carbody. Each pivot shaft is vertically assembled passing through the bogie frame. The pivot is concentric with a rubber ring assembled in the bogie frame. In this way, the horizontal traction forces, between the carbody and the bogie frame, are transmitted. As mentioned for the modelling of the guides, two alternative models are used to represent the kingpin, as shown in Fig. 3b. The first one implies the modelling of two transversal force elements characterized by a linear stiffness. In the second case, it is proposed to use a cylindrical joint with clearance.

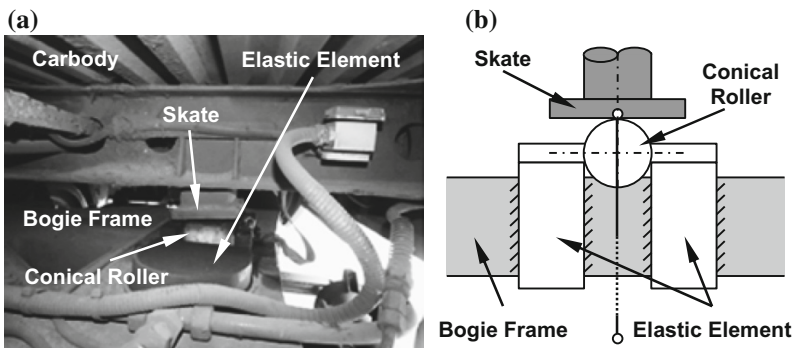


Fig. 2 a Secondary suspension of the LRV; b Modelling of the roller-skate

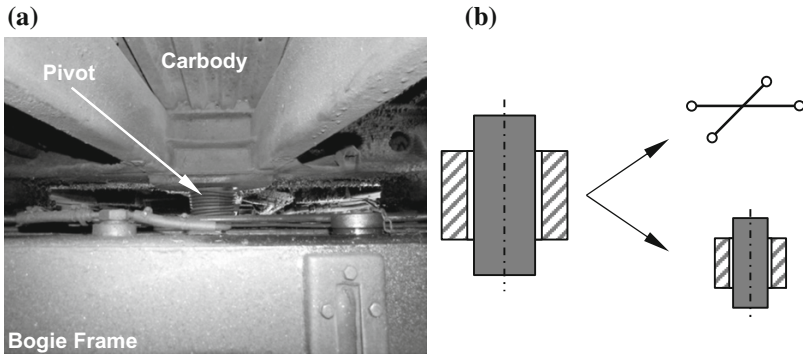


Fig. 3 a Bogie-carbody connection of the LRV; b Modelling of the kingpin

3 Vehicle Models

Figure 4 presents the bodies considered in the multibody model of the LRV. The green rectangle represents the carbody of the LRV, blue represent the bogie frame, yellow represent the axleboxes and the white ones are the wheelsets. Figure 4 also presents the mechanical elements which interconnect the bodies. In the left half of the model, the linear force elements are shown while in the right half, the joints, namely the revolute joint and the cylindrical joints with clearance, are presented. Regarding the force elements, each one is presented by a line with two coloured extremities. The colour of the extremity corresponds to the body to which the force element is connected. Each line represents one linear spring.

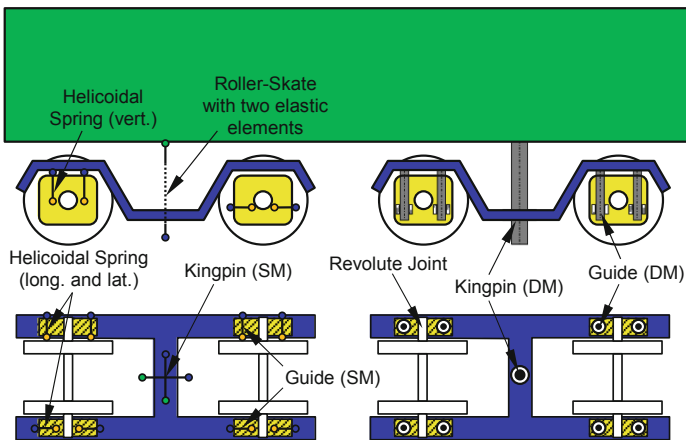


Fig. 4 Schematic representation of the modelling of the suspension elements

Two multibody models are defined as detailed (DM) and simple (SM) models. Their difference is the modelling of the guides and the kingpin, being cylindrical joints with clearances used in DM and linear force elements used in SM, as shown in Fig. 4. For the sake of conciseness the modelling data for the vehicle is not presented here. However, the interested reader can access Ref. [10] for details.

4 Case Studies

The LRV models are simulated in a realistic track model, based on a section of an existing railway network with, approximately, 3 km of extension. The DM and SM are tested at velocities of 40, 50 and 60 km/h. Simple drivers on the two wheelsets of the front bogie ensure that the vehicles run with constant speeds, which is required due to the slopes and the irregularities existing in this mountainous track.

The objective in this study is to assess the dynamic performance of the railway vehicle according to the norm UIC 518 [9] and, in the process, to identify the level of modelling that better fits such purpose. Table 1 present selected characteristic

Table 1 Characteristic values for the detailed model and for the simple model [9]

		Detailed Model						Simple Model					
		40 km/h		50 km/h		60 km/h		40 km/h		50 km/h		60 km/h	
		Straight	Curve	Straight	Curve	Straight	Curve	Straight	Curve	Straight	Curve	Straight	Curve
Running Safety	s^+ - bogie frame front wheelset	2.3	3.0	2.7	3.2	4.4	5.5	2.0	2.4	3.8	4.5	4.1	5.0
	s^+ - bogie frame rear wheelset	1.6	1.9	2.6	3.0	3.4	3.8	2.2	2.7	3.6	4.2	4.3	5.4
	s^* - front kingpin	1.7	1.9	2.5	2.9	3.5	3.9	2.4	2.3	5.4	5.3	4.4	5.0
	s^* - front kingpin	0.4	0.6	0.7	0.9	0.9	1.3	0.8	1.0	1.8	2.1	2.7	3.3
	s^* - rear kingpin	1.6	1.8	2.5	2.8	3.4	3.7	2.3	2.2	5.4	5.2	4.4	5.1
	s^* - rear kingpin	0.4	0.5	0.6	0.9	1.0	1.5	0.9	1.0	1.8	2.1	3.1	3.9
	Ride Characteristics	q^* - front kingpin	1.4	1.4	2.2	2.2	3.0	3.0	1.9	1.9	4.4	4.4	3.5
q^* - front kingpin		0.3	0.3	0.5	0.5	0.7	0.7	0.7	0.7	1.4	1.4	2.1	2.1
q^* - rear kingpin		1.4	1.4	2.1	2.1	2.9	2.9	1.9	1.9	4.4	4.4	3.6	3.6
q^* - rear kingpin		0.3	0.3	0.5	0.5	0.8	0.8	0.7	0.7	1.4	1.4	2.5	2.5
q^* - RMS front kingpin		1.0	1.0	1.6	1.6	2.3	2.3	1.1	1.1	2.3	2.3	2.4	2.4
q^* - RMS front kingpin		0.1	0.1	0.2	0.2	0.3	0.3	0.5	0.5	0.8	0.8	1.4	1.4
q^* - RMS rear kingpin		1.0	1.0	1.6	1.6	2.3	2.3	1.1	1.1	2.3	2.3	2.4	2.4
q^* - RMS rear kingpin		0.1	0.1	0.2	0.2	0.3	0.3	0.5	0.5	0.8	0.8	1.5	1.5

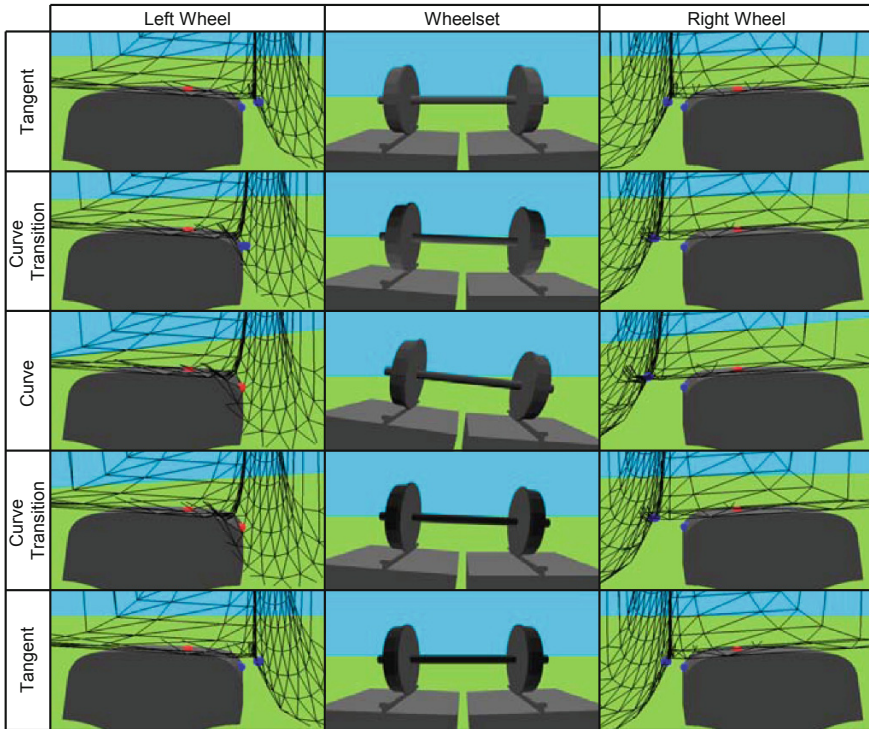


Fig. 5 Visualization of the left wheelset during the curve negotiation

values for both case studies measured in terms of accelerations of boggies, kingpin of the carbody to boggie connection and passenger locations. These results are obtained using SM [9]. The comparison between the values obtained and the accepted are thresholds highlighted using a colour codes: Red for the limit value exceeded; orange for values exceeding 75 % of the limit value; yellow for values exceeding 50 % of the limit value, green for values exceed 25 % of the limit value; and white indicate that the values are inferior to 25 % of the limit value.

In terms of running safety, the detailed model and the simple model present admissible values until 40 km/h. In terms of ride characteristics, both present inadmissible results. These results support the recommendation that the vehicle is not accepted for running in the railway under scrutiny. As presented in Table 1, the values associated with the lateral acceleration on the carbody constitute the principal problem of these models. This is justified by the high stiffness associated with the bogie-carbody connection.

These models can be compared qualitatively to understand the mechanism of wheel–rail contact that lead to the results. Figure 5 presents five frames of a wheelset negotiating a track which includes tangent, a curve transition and a curve section. These frames represent an example of a correct insertion of the vehicle on the track taking into account the contact between the wheels and the rails. The

correct insertion of the vehicle in the track depends on the suspension system and on the velocity. A large loss of contact between one wheel of the Detailed Model and the rail is identified during 4.1, 5.3 and 6.1 meters at 40, 50 and 60 km/h, respectively. In turn, for the same section of the track, the Simple Model does not present any contact loss. This qualitative analysis, not being used to form the decision on acceptance, shows the importance of the existence of some vehicle suspension compliance to accommodate for the track induced lateral perturbations.

5 Conclusions

The compatibility analysis proposed in this work involves two stages: post-processing of dynamic results as follows in the Simplified Method of the norm UIC 518 [9]; visualization of the vehicle response with respect to the track. From the post-processor, two conclusions are obtained. First, it is concluded that the lateral accelerations on the carbody are the responsible for the critical values that lead to vehicle non-acceptance. This is justified by the high constraint in bogie-carbody connection. Second, the Detailed Model presents better results. For a given section of the track, one wheel of the Detailed Model loses completely the contact during 4–6 m, approximately. This event is not verified in the case of the Simple Model for the same section of the track. This loss of contact is justified by the constraint imposed by the cylindrical joints with clearance presented in the primary suspension, which is softened by the spring model used in the simple vehicle model.

Acknowledgments The work reported was developed in SMARTRACK and WEARWHEEL projects funded by Foundation for Science and Technology.

References

1. Ambrósio J, Verissimo P (2009) Improved bushing models for general multibody systems and vehicle dynamics. *Multibody Sys Dyn* 22:341–365
2. Arnold M, Burgermeister B, Führer C, Hippmann G, Rill G (2011) Numerical methods in vehicle system dynamics: state of the art and current developments. *Veh Sys Dyn* 49 (7):1159–1207
3. Bruni S, Vinolas J, Mats B, Polach O, Stichel S (2011) Modelling of suspension components in a rail vehicle dynamics context. *Veh Sys Dyn* 49(7):1021–1072
4. Flores P, Ambrósio J, Claro J, Lankarani H (2008) Kinematics and dynamics of multibody systems with imperfect joints: models and case studies. Springer, Dordrecht
5. Milho J, Ambrósio J (1995) System animation for graphical analysis—SAGA User's Guide VS 1.0. Technical report IDMEC/CPM—95/029, Institute of Mechanical Engineering, Instituto Superior Técnico, Lisbon, Portugal
6. Nikravesh PE (1988) Computer-aided analysis of mechanical systems. Prentice-Hall, Englewood Cliffs
7. Polach O (1999) A fast wheel-rail forces calculation computer code. *Veh Sys Dyn Suppl* 33:728–739

8. Pombo J (2004) A multibody methodology for railway dynamics applications. PhD dissertation, Instituto Superior Técnico, Lisbon, Portugal
9. Fiche UIC 518 (2005) Testing and approval of railway vehicles from the point of view of their dynamic behaviour—safety—track fatigue—running behaviour
10. Magalhaes H (2013) Development of advanced computational models of railway vehicles. Master thesis, Instituto Superior Tecnico, University of Lisbon, Lisbon, Portugal

Validation of an Enhanced Cylindrical Contact Force Model Using Numerical and Analytical Approaches

C. Pereira, A. Ramalho and J. Ambrosio

Abstract A numerical study is conducted to evaluate the suitability of a new enhanced contact force model to describe contact between cylindrical bodies for very low clearances. An analytical comparison with the behaviour presented by the Johnson cylindrical contact force model is also conducted. Results demonstrate that the enhanced cylindrical model ensures the accuracy of the Johnson cylindrical model although with the simplicity of the Hertz contact model. Differences lower than 6 % separate the numerical results from those obtained with the enhanced model for the application domain analysed.

Keywords Contact mechanics · Contact dynamics · Cylindrical contact force models · Finite element models

1 Introduction

The slider crank mechanism is one of the most widely used mechanisms in mechanical applications to convert reciprocating to rotary motion or vice versa. The assembly of a piston, cylinder, connecting-rod and crankshaft is the classic form of the slider crank mechanism. Each of these individual parts required extensive tolerancing, both in design and manufacturing. In selecting limits of size for any application, the type of fit is determined first, based on the use or service required

C. Pereira (✉)

Polytechnic Institute of Coimbra, Coimbra, Portugal
e-mail: candida@isec.pt

A. Ramalho

University of Coimbra, Coimbra, Portugal
e-mail: amilcar.ramalho@dem.uc.pt

J. Ambrosio

Technical University of Lisbon, Lisbon, Portugal
e-mail: jorge@dem.ist.utl.pt

from the equipment being designed. Then the limits of size of the mating parts are established, to insure that the desired fit will be produced [1]. Regardless of the kind of fit that is used, relative motion exists with associated clearances. Thus, effective and accurate cylindrical contact models that describe the relationship between the deformation experienced by contacting cylindrical bodies and the applied contact force in real applications are required.

The purpose of this work is therefore to provide a deeper understanding on the suitability of the Johnson model and a new enhanced cylindrical contact force model to describe the conformal contact between cylindrical geometries whose contact conditions are associated with common examples of mechanical engineering practice [1, 2]. By applying a finite elements analysis, a numerical study is conducted using a deformable/deformable contact approach. In addition, a comparative assessment between the Johnson and the new enhanced model is also conducted.

2 Analytical Cylindrical Contact Force Models

The expressions that define most of the models available in the literature describing the contact involving cylindrical geometries include logarithmic functions. This means that each cylindrical contact model has a specific validity domain of application, which depends on the clearance value and the material properties. A comparative assessment of most of these models was recently presented by the authors [3]. From this study it was concluded that the cylindrical contact model presented by Johnson [4] is the one that best describes the contact between internal contacting cylinders, when compared with other cylindrical models. Therefore, it was chosen to validate a new enhanced cylindrical contact force model proposed by the authors. In the model suggested by Johnson, the total penetration, δ , of two deformable contacting cylinders of radius R_i and R_j made with materials with similar elastic modulus and Poisson coefficients—denoted by E and ν , respectively—and submitted to the action of a compressive load, F_n , is given by Eq. (1):

$$\delta = \frac{F_c}{\pi E^*} \left\{ \ln \left(\frac{4\pi E^* \Delta R}{F_c} \right) - 1 \right\} \quad (1)$$

In Eq. (1), F_n is expressed per unit of the axial length of the cylinder, E^* is the composite modulus, assuming materials with similar elastic modulus and Poisson ratios denoted by E and ν , respectively, and ΔR represents the difference between cylinders' radii, $(R_i - R_j)$, corresponding to the radial clearance between the two concentric cylindrical bodies. For each given penetration, Eq. (1) has to be solved iteratively to evaluate the contact force that fulfils it. When used in the framework of forward dynamic analysis, this procedure is not only computationally costly, but it also represents a numerical difficulty when running a computational code, especially if a greater number of contacting bodies is involved [3].

To overcome the drawbacks associated with the Johnson cylindrical contact force, an alternative model, without domain validity problems and defining the contact force as an explicit function of penetration, has been recently proposed by the authors. In this model the contact force is evaluated as described in [5]:

$$\delta = \left(\frac{F_c \Delta R}{(a \Delta R + b) E^*} \right)^{1/n} \quad (2)$$

where the constants assume the following values as a result of an optimization procedure: $a = 0.965$, $b = 0.0965$, $n = Y \Delta R^{-0.005}$, $Y = 1.5 [\ln(1000 \Delta R)]^{-0.15}$ if $\Delta R = [0.005, 0.34954]$ or $Y = 0.0151 \Delta R + 1.151$ if $\Delta R = [0.34954, 2.0]$ mm. The remaining quantities in Eq. (2) have the same meaning as described for Eq. (1).

3 Cylindrical Contact Modelling in Marc®

The internal contact between two concentric cylinders was modelled as a deformable/deformable contact, instead of rigid/deformable or rigid/rigid, because as rigid bodies they not suffer any type of deformations and so the stiffness of the contact is overestimated, in particular for small clearances, and real bodies are not absolutely rigid [6]. It was assumed that both internal and external cylinders have equal elastic properties, with a Young modulus of 2.07×10^{11} Pa and a Poisson ratio of 0.3. The load is applied in the center nodes of the axis of the internal cylinder and is defined as being increase linearly over time. Concerning boundary conditions, displacement and rotation constraints are applied corresponding to fixing the upper half of the outside boundary of the external cylinder. Figure 1 illustrates the mesh geometry, obtained using MARC® nonlinear finite element code, for a clearance value of 0.1 mm, and highlights how the contact is defined and the meshing of the finite element model. A very fine mesh is required for good accuracy, particularly in the contact area illustrated by area 1 in Fig. 1. The mesh of the remaining part of the bushing is coarser.

To show the dimensions of element size of the finite element model developed, in particular the contact elements size, area 1 is discretized in regions 2 and 3 as indicated in the right side of Fig. 1. These areas are defined only by their boundary elements to reduce computational costs. The contact definition is introduced in the CONTACT TABLE option described in Ref. [7]. The four-node plane stress isoparametric elements used to model the cylinders have sizes between 6.63 and 1.31 μm . The choice of this mesh results from a sensitivity analysis of the contact forces as a function of the element sizes, which indicates that further mesh refinements do not alter the results obtained. The total number of nodes and elements is 125,024 and 123,800, respectively.

The distributions of the contact stress, obtained for clearance values of 1 and 0.01 mm, are shown in Fig. 2. The parabolic shape symmetry of the contact stresses confirms that, for this level of clearances, the Hertz elastic contact theory remains valid [4].

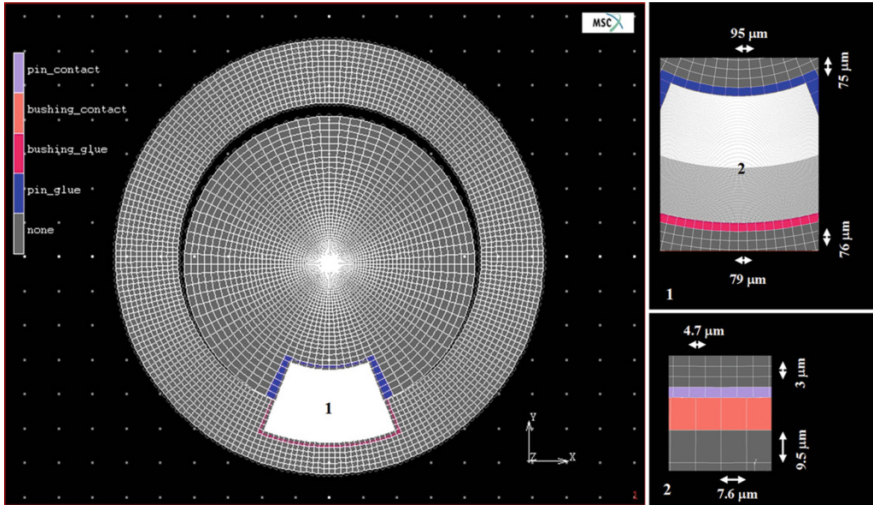


Fig. 1 Cylinders mesh in a deformable/deformable contact scenario using MARC®

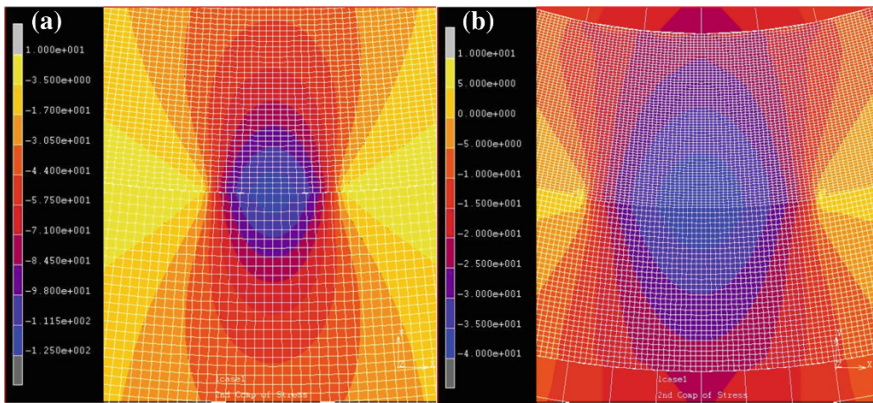


Fig. 2 Contact stress distributions on the cylinders for clearance values of a 1 mm and b 0.01 mm

4 Comparison Between Cylindrical Contact Approaches

Penetration values—measured at the internal cylinder center that is at a point far enough from the contact—obtained with the finite element model and those resulting from the application of the two analytical cylindrical contact models, for loads of 20, 40 and 100 N/mm, are evaluated. Figure 3 shows the relation between penetration and clearance for a load of 40 N/mm and clearances values in the range of 5 µm–1.5 mm. It must be noted that the same trend is observed for the loads of 20 and 100 N/mm, although not shown.

Fig. 3 Penetration depths obtained with the finite element (FEM), Johnson and the new enhanced contact models for a load of 40 N/mm

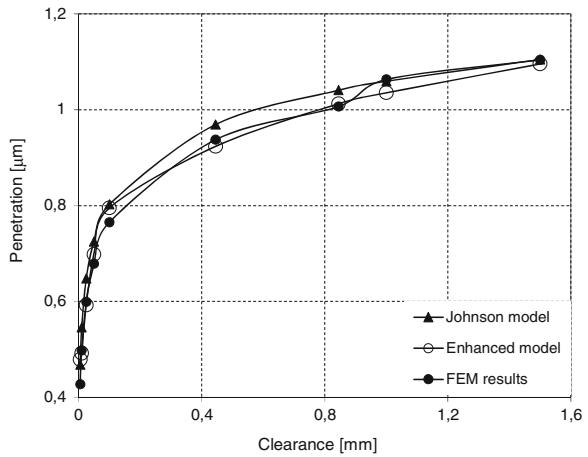


Table 1 Differences obtained with the finite element (FEM), Johnson (JM) and the new enhanced (EM) contact models for a load of 20 N/mm

Clearance (mm)	Diff FEM/JM (%)	Diff _{FEM/EM} (%)	Diff _{EM/JM} (%)
0.005	9	16	8
0.010	8	3	5
0.025	7	2	5
0.050	6	6	0
0.100	4	6	2
0.445	2	1	3
0.845	2	2	0
1.000	2	3	1
1.500	3	5	3

The differences obtained when numerical results are compared with those resulting from the application of the two analytical contact models for loads of 20, 40 and 100 N/mm, and for the range of clearances and loads under analysis, are presented in Tables 1, 2 and 3, respectively. These tables also summarize the differences between the penetrations obtained using the Johnson and the enhanced cylindrical models. The difference between each two models, $Diff_{a/b}$, is calculated through Eq. (3), where δ_a and δ_b are the penetrations obtained with numerical results, the Johnson and the Enhanced cylindrical models, respectively, for each combination of contact load and radial clearance.

$$Diff_{a/b} = \frac{\delta_a - \delta_b}{\delta_b} \tag{3}$$

Table 2 Differences obtained with the finite element (FEM), Johnson (JM) and the new enhanced (EM) contact models for a load of 40 N/mm

Clearance (mm)	Diff _{FEM/JM} (%)	Diff _{FEM/EM} (%)	Diff _{EM/JM} (%)
0.005	9	11	2
0.010	9	1	10
0.025	8	1	9
0.050	6	3	4
0.100	5	4	1
0.445	3	1	5
0.845	3	1	3
1.000	0	3	2
1.500	0	1	1

Table 3 Differences obtained with the finite element (FEM), Johnson (JM) and the new enhanced (EM) contact models for a load of 100 N/mm

Clearance (mm)	Diff _{FEM/JM} (%)	Diff _{FEM/EM} (%)	Diff _{EM/JM} (%)
0.005	10	10	1
0.010	9	4	13
0.025	10	2	11
0.050	9	3	6
0.100	8	5	3
0.445	5	1	6
0.845	5	0	5
1.000	5	1	5
1.500	3	1	4

From Tables 1, 2 and 3, it can be concluded that differences lower than 10 % separate the finite element results from the results presented by the Johnson model, even for very low clearance values. Differences lower than 5 % are obtained for clearance values higher than 0.445 mm; for lower clearance values, the difference increases up to 10 % with decreasing clearance values. The same trend is observed regardless of the load value considered. Based on the global set of numerical results, it can be concluded that a good agreement between numerical results and the Johnson model is found, for a suitably refined mesh, even for extremely low clearance values. Thus, it can be concluded that even for very small clearance/external radii ratios, the analytical solution proposed by Johnson, based on the Hertz pressure distribution, remains appropriate to describe the conformal contact between cylindrical geometries, even with very low clearance values. Additionally, it proves to be the model that best describes contact between cylindrical bodies,

when compared with other models available in the literature [3]. With this model, a maximum difference of less than 10 % is achieved, for the range of contact conditions herein analyzed, which does, however, contradict the results obtained by Sassi and Desvignes [8] and by Liu et al. [9].

Sassi and Desvignes [8] applied a seminumerical approach to study both non-conformal and conformal contact and concluded that the Hertz theory has limitations in the treatment of conformal contacts, because it overestimates the contact area and underestimates the maximum pressure at the contact center. In the present work it is shown that, if the deformable/deformable approach is used and if the comparison between numerical and analytical models is performed in terms of deformation at a point far enough from the contact, divergences lower than 10 % in relation to the model suggested by Johnson are obtained. Liu et al. [9] pointed out that, for contacting cylindrical geometries, the model proposed by Johnson when compared with the FEM results, is only effective in the condition that the clearance is large enough and the normal load is very small, i.e. for non-conformal contact conditions. However, the range of clearances and deformations analyzed by these authors are very different than those herein discussed.

Except for the lowest clearance value under analysis, a very good agreement, in general better than the observed for the model proposed by Johnson, is found between numerical results and the enhanced contact model. A noteworthy decreasing in the difference value for clearances higher than 0.445 mm is also observed, regardless of the load value applied. Differences lower than 6 % are obtained for the overall domains of clearance and load values, and lower than 5 % for clearances higher than 0.445 mm. The difference increases substantially, reaching a maximum of 16 %, when the lowest clearance and load values are considered.

Concerning the comparison between the model proposed by Johnson and the new enhanced contact model, a good agreement is also found. Even for low clearance values, a maximum difference below 10 % is found between the two analytical models, although a difference of 13 % is observed for the highest load value. This can be explained by the fact that the new model uses a single expression to describe the internal contact in a large application domain. Therefore, some inaccuracy can be expected, particularly for the smallest clearance values and for very low or very high loads.

5 Conclusions

In order to validate the use of an enhanced cylindrical contact force model to describe the interaction between cylindrical bodies in conditions of conformal contact, a numerical study using the finite element code MARC[®] is conducted and the results compared with those obtained using the analytical cylindrical contact force proposed by Johnson.

The results obtained with the finite elements, Johnson and Enhanced cylindrical contact force models show that, except for the lowest clearance, the enhanced cylindrical contact force model presents a better agreement with numerical results than that achieved with the Johnson model, since a maximum difference of 6 % is obtained. With the Johnson model, this difference reaches 10 % for the range of contact conditions herein analyzed. Differences lower than 13 % separate both analytical cylindrical models for the overall domain under analysis. Thus, it can be concluded that, even for low clearance values, the Johnson and Enhanced cylindrical contact force models provide results with good quality when compared with detailed finite element analysis. These models are therefore accurate enough to describe the conformal contact between bodies with cylindrical geometries.

Since the new enhanced cylindrical contact force model has both the accuracy of the Johnson cylindrical model and the simplicity of the Hertz contact model, because the contact force is described as an explicit function of penetration and thus inefficient iterative procedures are avoided, it is a very useful alternative to current cylindrical contact force models for modeling the contact between cylindrical geometries, especially for implementation in a computational program for dynamic impact.

References

1. Oberg E et al (2000) Machinery's handbook, 26th edn. Industrial Press, New York
2. BS EN ISO 286-1:2010 (2010) Geometrical product specifications (GPS)—ISO code system for tolerances on linear sizes. Part 1: basis of tolerances, deviations and fits
3. Pereira CM et al (2011) A critical overview of internal and external cylinder contact force models. *Nonlinear Dyn* 63(4):681–697
4. Johnson KL (1985) Contact mechanics. Cambridge University Press, Cambridge
5. Malça C et al (2012) An enhanced cylindrical contact force model for multibody dynamics applications. In: Proceedings of the EUROMECH colloquium 524—multibody system modelling, control and simulation for engineering design, Enschede, Netherlands, pp. 30–31
6. Pereira C et al (2011) Conformal cylindrical contact force model verification using a finite element analysis. In: Proceedings of the thirteenth international conference on civil, structural and environmental engineering computing. Civil-Comp Press, UK, paper 135
7. Marc (2000) MARC User Information. MARC Analysis Research Corporation. Palo Alto
8. Sassi M, Desvignes M (1998) A seminumerical method for three-dimensional frictionless contact problems. *Math Comput Modell* 28:413–425
9. Liu C-S et al (2007) The FEM analysis and approximate model for cylindrical joints with clearances. *Mech Mach Theory* 42:183–197

Human Gait Analyses Using Multibody Systems Formulation: Normal and Pathological Scenarios

P. Moreira, J. Peixoto, U. Lugrís, J. Cuadrado, P. Flores and P. Souto

Abstract The main goal of this work is to present planar biomechanical multibody model, suitable to be used in inverse dynamic analyses. The proposed approach is straightforward and computationally efficient for the study of different human gait scenarios e.g. normal and pathological. For this, a biomechanical model of the lower limb of the human body was considered. The model consists of three rigid bodies (thigh, calf and foot), corresponding to relevant anatomical segments of lower limb. The three bodies are connected by revolute joints and described by eight natural coordinates, which are the Cartesian coordinates of the basic points located at the joints (hip, knee, ankle, metatarsal-phalangeal). The anthropometric dimensions of the model correspond to those of a normal male of 1.77 m and 80.0 kg and a poliomyelitis (polio) patient of 1.78 m and 92 kg. The total biomechanical system encompasses 5 degrees-of-freedom: 2 degrees-of-freedom for hip trajectory, 1 degree-of-freedom for hip flexion-extension motion, 1 degree-of-freedom for knee flexion-extension and 1 degree-of-freedom for ankle plantarflexion-dorsiflexion. The developed model was applied to solve an inverse dynamics problem of human

P. Moreira (✉) · P. Flores
CT2M—Center for Mechanical and Material Technologies, University of Minho,
Braga, Portugal
e-mail: pfsmoreira@dem.uminho.pt

P. Flores
e-mail: pflores@dem.uminho.pt

J. Peixoto · P. Souto
Department of Textile Engineering, University of Minho, Braga, Portugal
e-mail: jjorge@det.uminho.pt

P. Souto
e-mail: souto@det.uminho.pt

U. Lugrís · J. Cuadrado
Laboratorio de Ingenieria Mecanica, Escuela Politecnica Superior, University of A Coruña,
A Coruña, Spain
e-mail: ulugris@udc.es

J. Cuadrado
e-mail: javicua@udc.es

motion. Therefore, the main objective of this study is to determine the joint kinematics, moments-of-force and reaction forces during an entire gait cycle.

Keywords Biomechanics · Human gait · Multibody dynamics · Matrix-R · Inverse dynamics

1 Introduction

Over the last years, there is a huge interest in analyze the normal and pathological human gait. Usually, it includes the motion tracking by means of an optical system, and the evaluation of ground reaction forces through force plates.

The obtained positions of a specific number of skin markers are applied to the calculation of corresponding velocities and accelerations histories, defining a computational biomechanical model. These data are filtered in order to remove the noise introduced by the motion capture system and differentiated to yield the histories of the coordinates at velocity and acceleration level. The equations of motion of the biomechanical model are solved using a forward or inverse dynamics problem. The obtained results could be extremely useful to support traditional medical diagnosis and therapy planning, such as anticipate the result of a surgery or to help in the optimization design of the prosthetic and orthotic devices [4, 5].

The analysis of human gait is a complex task, relies mostly on the use of the multibody formulations applied as kinematic and dynamic tools. The human body can, thus, be considered a multibody system, composed by rigid or flexible bodies and connected by kinematic joints [2, 6].

2 Methodologies

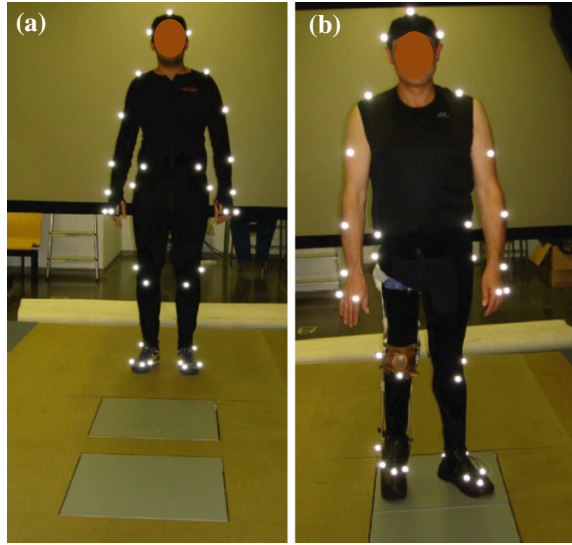
2.1 *Experimental Approach*

The experimental data utilized in this work was obtained in a human gait laboratory, Fig. 1. A normal adult male of age 26, mass 80 kg and height 177 cm and a polio patient male of age 43, mass 92 kg and height 178 cm have been dressed with a special suit with 37 reflective markers attached, as illustrated in Fig. 1. The polio patient was wearing a traditional KAFO orthosis on the right leg.

For the experimental procedure, the subjects walk on a walkway with two AMTI AccuGait force plates, located in such a way that each plate measures the ground reactions of one foot during the gait cycle. The motion is captured by an optical system composed by 12 Natural Point OptiTrack FLEX: V100 cameras (100 Hz).

The trajectories of the markers present noise associated with the motion capture. The Singular Spectrum Analysis (SSA) filter is applied to the marker's position,

Fig. 1 Experimental gait analysis procedure **a** Normal male; **b** Pathological male (polio)



which are then used to predict internal positions by means of simple algebraic relations [1]. The values of the positions at each instant of time are not kinematically consistent due to errors of the motion tracking. The kinematic consistency of the natural coordinates at position level is imposed, by means of the augmented Lagrangian minimization process expressed by:

$$\begin{aligned} (\mathbf{W} + \Phi_{\mathbf{q}}^T \alpha_p \Phi_{\mathbf{q}}) \Delta \mathbf{q}_{i+1} &= -\mathbf{W}(\mathbf{q}_i - \mathbf{q}^*) - \Phi_{\mathbf{q}}^T (\alpha_p \Phi + \lambda_i) \\ \lambda_{i+1} &= \lambda_i + \alpha_p \Phi; i = 1, 2, \dots \end{aligned} \quad (1)$$

where \mathbf{q}^* is the vector of inconsistent natural coordinates, $\Delta \mathbf{q}_{i+1} = \mathbf{q}_{i+1} - \mathbf{q}_i$, Φ is the corresponding Jacobian matrix, λ is the vector of Lagrange multipliers, α_p is the penalty factor, and \mathbf{W} is a weighting matrix that allows to assign different weights to the different coordinates according to their expected errors. Different weighting factors can be assigned to each natural coordinate, thus for example, the skin movement artifact on the thigh is larger than on the shank [1].

2.2 Computational Model

A 2D biomechanical model of the right leg of the human body was developed. The biomechanical model consists of three rigid bodies (thigh, calf and foot), corresponding to relevant anatomical segments of lower limb, Fig. 2. These three bodies are connected by revolute joints and described by eight natural coordinates, which

Fig. 2 Biomechanical model of lower limb

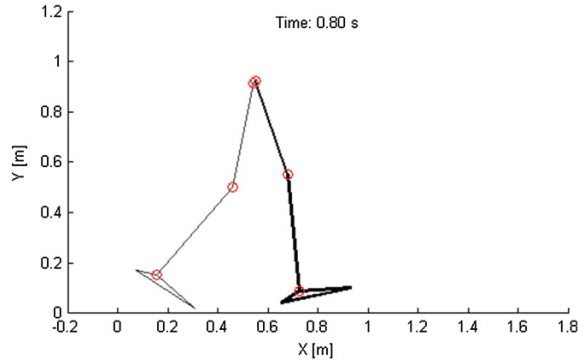


Table 1 Inertial properties of rigid bodies used in the biomechanical models

Body	Mass (kg)	Moment of inertia (kg.m ²)
<i>Normal male</i>		
Foot	0.77	0.0035
Calf	3.28	0.0490
Thigh	6.86	0.1238
<i>Pathological male</i>		
Foot	0.82	0.0016
Calf	4.00	0.0537
Thigh	9.28	0.1173

are the Cartesian coordinates of the basic points located at the human articulations (hip, knee, ankle, metatarsal-phalangeal).

The anthropometric data of the three anatomical segments and their corresponding bodies is listed in Table 1, and it is extracted from the data present in [7] and from the anthropometric dimensions measured directly from the subject. The biomechanical system encompasses 5-degrees-of-freedom: 2 degrees-of-freedom for hip trajectory, 1 degree-of-freedom for hip flexion-extension motion, 1 degree-of-freedom for knee flexion-extension and 1 degree-of-freedom for ankle plantar-flexion-dorsiflexion. The developed model was applied to solve an inverse dynamic problem of human motion. In this work, two distinct methodologies were adopted to perform the inverse dynamic analysis of human gait: the classical Newton-Euler equations and the multibody methodology based on the projection matrix-R.

2.3 Newton Euler Equations

The Newton-Euler formulation is considered here to study the dynamic behaviour of the biomechanical model described above. The present analysis closely follows

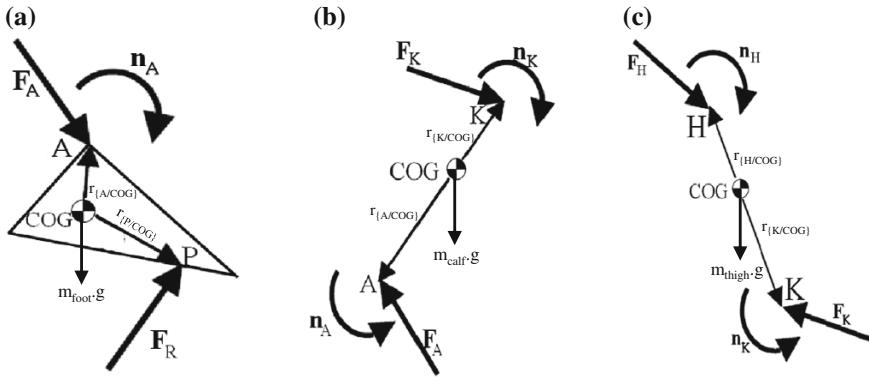


Fig. 3 Free-body diagram of rigid bodies; **a** Foot; **b** Calf; **c** Thigh [6]

the development done by Silva [6]. Thus, the dynamic equations of motion of a free rigid body can be expressed in the following form [6]:

$$\begin{cases} \sum \mathbf{F} + m\mathbf{a}_g = m\mathbf{a} \\ \sum \mathbf{n} = I\alpha \end{cases} \quad (2)$$

in which $\sum \mathbf{F}$ represents the external applied forces, m denotes the mass of the body, \mathbf{a} is the linear acceleration, \mathbf{a}_g is the gravitational acceleration. In a similar way, $\sum \mathbf{n}$ represents the sum of the external applied moments of force, I denotes the mass moment of inertia and α denotes the angular acceleration of the body. This procedure is repeated for all the rigid bodies that constitute the biomechanical model. Figure 3 includes the free body diagram of the foot, calf and thigh, which are represented in static balance of forces. For the particular case of the foot segment, the ground reaction force \mathbf{F}_R and its application point P are obtained by direct measurement in the force plate. Point A denotes the revolute joint between foot and calf, location of which is obtained as described in Sect. 2.1. The experimental data is utilized to calculate the linear and angular acceleration components, as well as, the angular velocity vector for the rigid body.

Analysing the diagram of Fig. 3a, it can be observed that for the case of the foot, the reaction force at ankle joint \mathbf{F}_A and the net moment-of-force \mathbf{n}_A needed to be calculated. These variables are obtained from the resolution of the dynamic equations of motion (2), written for the foot segment, yielding:

$$\begin{cases} \mathbf{F}_A = m(\mathbf{a} - \mathbf{a}_g) - \mathbf{F}_R \\ \mathbf{n}_A = I\alpha - (\mathbf{r}_{COG} - \mathbf{r}_P) \times \mathbf{F}_R - (\mathbf{r}_{COG} - \mathbf{r}_A) \times \mathbf{F}_A \end{cases} \quad (3)$$

The complete description of the Newton Euler methodology can be found in [6]. The procedure used to calculate the forces and moments on the calf (Fig. 3b) and thigh (Fig. 3c) is quite similar to the one used for the foot example.

2.4 Multibody Methodology Based on the Projection Matrix-R

The dynamics of a multibody system can be described by the constrained Lagrangian equations:

$$\begin{aligned} \mathbf{M}\ddot{\mathbf{q}} + \Phi_q^T \lambda &= \mathbf{Q} \\ \Phi &= \mathbf{0} \end{aligned} \quad (4)$$

where \mathbf{M} is the mass matrix, $\ddot{\mathbf{q}}$ is the accelerations vector, Φ is the constraints vector, Φ_q is the Jacobian matrix of the constraints, λ represents the Lagrange multipliers vector and \mathbf{Q} is the applied forces vector. Equation (4) represents a system of differential-algebraic equations [3, 6]. The purpose of the method based on the projection matrix-R is to obtain a system of ordinary differential equations with dimension n_i equal to the number of degrees of freedom, using a set \mathbf{z} of independent coordinates [3]. The following relation between velocities is established:

$$\dot{\mathbf{q}} = \mathbf{R}\mathbf{z} \quad (5)$$

where \mathbf{q} are all the n_d dependent variables and \mathbf{z} is a set of n_i independent variables. After differentiating the Eq. (5):

$$\ddot{\mathbf{q}} = \mathbf{R}\ddot{\mathbf{z}} + \dot{\mathbf{R}}\dot{\mathbf{z}} \quad (6)$$

Thus, substitution of Eq. (6) into Eq. (4) yields,

$$\mathbf{M}\mathbf{R}\ddot{\mathbf{z}} + \mathbf{M}\dot{\mathbf{R}}\dot{\mathbf{z}} + \Phi_q^T \lambda = \mathbf{Q} \quad (7)$$

Premultiplying by \mathbf{R}^T results,

$$\mathbf{R}^T \mathbf{M} \mathbf{R} \ddot{\mathbf{z}} = \mathbf{R}^T (\mathbf{Q} - \mathbf{M} \dot{\mathbf{R}} \dot{\mathbf{z}}) \quad (8)$$

In order to solve the inverse dynamics of human motion, a set of independent coordinates \mathbf{z} is calculated from the previous set of natural coordinates: the two Cartesian coordinates of hip joint, along with the hip, knee and ankle rotation angles. After that, the SSA filter is applied in order to reduce the noise introduced by the kinematic consistency imposed to the natural coordinates [1]. Once obtained the histories of the independent coordinates \mathbf{z} , and their derivatives, $\dot{\mathbf{z}}$ and $\ddot{\mathbf{z}}$, the inverse dynamics problem is solved using the velocity transformation formulation matrix-R [3], which provides the motor efforts required to generate motion. The motor efforts are obtained as an external force and moment-of-force acting on the hip and the corresponding internal joint torques. However, they are not the correct ground reaction force, moment-of-force and joint's moment-of-force. The external

force and moment-of-force must be applied at the foot contacting the ground, instead of hip. Thus, a simple linear relation can be established between the two sets of motor efforts. The relation is obtained by equating the vector of generalized forces due to the set of force and moment-of-forces applied at the hip and the vector of generalized forces due to the set of force and moment-of-forces applied at the foot [1, 6].

3 Results and Discussion

The original kinematic data obtained from the gait tracking process has some noise, which could lead to kinematic inconsistency and also could cause unacceptable errors in dynamic analysis. The raw and filtered kinematic data of a skin marker (right femoral epicondyle) for the normal male is presented in the plots of Fig. 4.

The presented methodologies has been used to study the biomechanical response of human motion considering different pathologies that induce irregular an unsafe gait patterns. Figure 5 shows the knee joint angles for the polio patient, during a entire gait cycle. It can be observed that the right knee angle does not exhibit any knee flexion movement (Fig. 5a). The orthosis locks the knee during the entire gait cycle. The left knee angle presents a normal pattern. This data is corroborated by the analysis of the center-of-pressure plots (Fig. 5b).

The methodology presented through this work is applied to the inverse dynamic analysis of human gait. The proposed biomechanical model is able to calculate not only the moments-of-force occurring in the joints, but also the joint reaction forces. The results concerning the hip Y reaction force and ankle moment-of-force occurring in the right leg is presented in the plots of Fig. 6.

From the analysis of the obtained results, it can be concluded that a good correlation is found between the two methodologies. As expected for the same input data, the multibody methodology based on the projection matrix-R, produces similar results to those obtained using the classical Newton Euler equations Fig. 6.

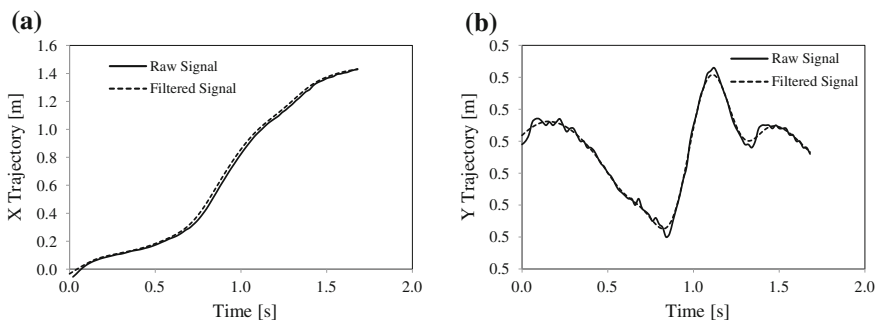


Fig. 4 Right femoral epicondyle skin marker trajectory (normal male); **a** X trajectory; **b** Y trajectory

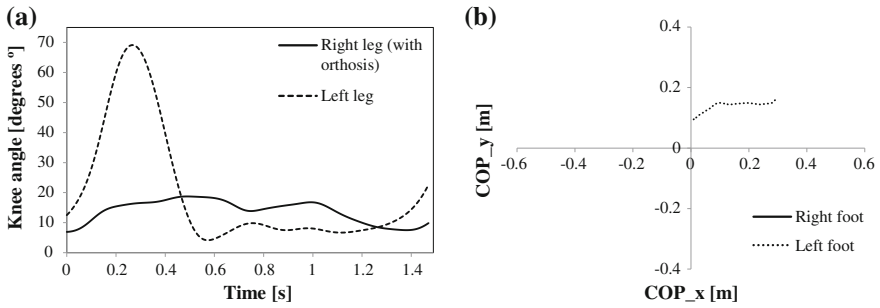


Fig. 5 **a** Knee joint angle during the entire gait cycle for the polio patient cop and **b** center-of-pressure curves (COP) during an entire gait cycle for the polio patient

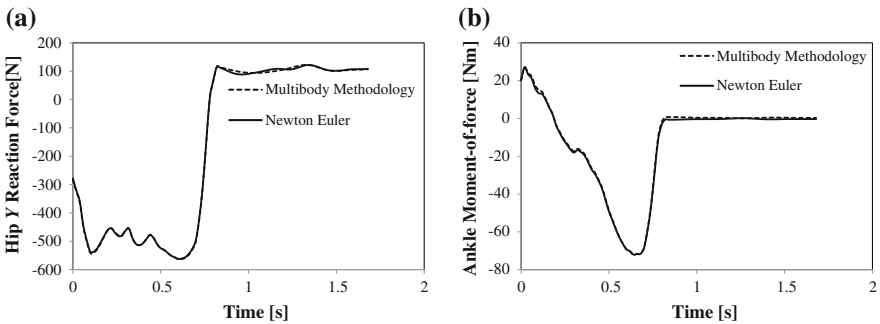


Fig. 6 Comparison of results for the hip Y reaction force **(a)** and ankle moment-of-force **(b)** using two distinct methodologies: multibody methodology based on matrix-R and classical Newton-Euler equations for the normal male

Acknowledgments The first author would like to thank the Portuguese Foundation for Science and Technology (FCT) for the PhD Grant SFRH/BD/64477/2009.

References

1. Alonso JF, Cuadrado J, Lugiés U, Pintado P (2010) A compact smoothing-differentiation and projection approach for the kinematic data consistency of biomechanical systems. *Multibody Sys Dyn* 24(1):67–80
2. Ambrósio J, Kecskemethy A (2007) Multibody dynamics of biomechanical models for human motion via optimization. In: Garcia Orden JC, Goicolea J, Cuadrado J (eds) *Multibody dynamics: computational methods and applications*. Springer, Dordrecht, pp 245–272
3. García de Jalón J, Bayo E (1994) *Kinematic and dynamic simulation of multibody systems—the real-time challenge*. Springer, New York
4. Moreira P, Ramôa P, Flores P (2013) Design of a new knee orthosis locking system. In: *ASME 2013 international mechanical engineering congress exposition, IMECE2013, San Diego*

5. Peixoto J, Flores P, Souto P (2012) Breathable impermeable and odourless lining for orthopaedic footwear application. In: Proceedings of ITCDC 2012 6th international textile, clouding and design conference, Dubrovnik, pp. 7–10
6. Silva MT (2003) Human motion analysis using multibody dynamics and optimization tools. PhD thesis, Instituto Superior Técnico, Lisboa
7. Vaughan CL, Davis BL, O'Connor JC (1992) Dynamics of human gait, 2nd edn. Kiboho, Cape Town

Numerical Simulation of a Granular Material Damper

T. Koga, T. Sato, A. Weller and K. Ono

Abstract We investigated the damping mechanism of a granular material damping system applied to vibration reduction in structures that have a small vibration displacement. We devised a computational model of the movement of the primary system and the individual granules and obtained those motions by numerical simulation. Based on the fundamental idea that the damping effect of a granular material damper is governed by the motion of the granules, we classified the granular material as “equivalent added mass” and “relative motion mass”, and considered the relation of those mass classes to the damping characteristics.

Keywords Damper · Granular materials · Forced vibration · Single degree of freedom system · Damping ratio

1 Introduction

A granular material damper is a damping element that consists of a container filled with a granular material placed on the mass part of the primary vibration system and which uses the motion of the granular material to produce a damping effect. The damping characteristics of a granular material damper are thus governed by the motion of the granular material, so we can understand those characteristics by analyzing the motion of the granular material.

T. Koga (✉)
Hitachi Ltd, Hitachi, Japan
e-mail: tomoko.koga.bf@hitachi.com

T. Sato · A. Weller · K. Ono
Tokyo Denki University, Tokyo, Japan
e-mail: taichi@mail.dendai.ac.jp

A. Weller
e-mail: alexis.w@satolab.n.dendai.ac.jp

K. Ono
e-mail: kazuhirono@satolab.n.dendai.ac.jp

Araki and Yokomichi et alia have applied a powder impact damper to vibration systems of a single degree of freedom and of multiple degrees of freedom and considered the damping effect due to the powder, which is understood as a single mass whose coefficient of restitution is zero [1]. Saeki et alia used the discrete element method to calculate the motion of individual granules to study the damping characteristics of granular materials [2]. Even though, in that research, the granular material is treated as a single mass the granules, in the other hand, are treated as individual masses and different analytical methods are applied, the movement of the granular material is large compared to the motion of the primary system. We can thus take the impact force of the granular material on the primary system as the basis of the damping mechanism. In addition to the work just cited, the effects of the size, quantity of the granules and the shape and number of the granular material containers on the damping characteristics have also been studied [3–5].

In general, previous researches have mostly assumed a large movement of the granular material. There is thus already considerable knowledge concerning the damping characteristics for the case in which granular material dampers are applied to structures that have large displacement amplitude.

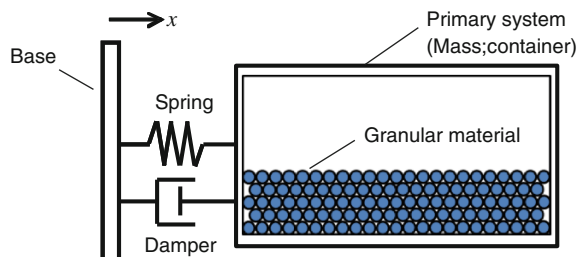
For cases in which the displacement amplitude of the primary system is small as the movement of the granular material is, it may be difficult to attribute the basic damping effect due to the collision of the granular material on the primary system. That is to say, it is not sufficiently clear what factors we need to focus on to realize a high degree of damping from a granular material damper in a structure for which the natural frequency is relatively high and the displacement amplitude is small.

In the work reported here, we investigated the damping mechanism of a granular material damper for a structure that has a small vibration displacement.

2 Structure of a Granular Material Damper

In our granular material damper model (Fig. 1), the primary vibration system (primary system) has 1° of freedom and consists of a spring constant, a damping coefficient, and a mass (container). In this model, the primary system can move only in the x direction. Granular material is arranged in the container. Furthermore, to simplify the movement of the granular material, we take the granule shape to be cylindrical.

Fig. 1 Model of damper with granular materials



3 Numerical Simulation of a Granular Material Damper

3.1 Computational Model of the Primary System and the Granular Material

In the computation model of the granular material damper (Fig. 2), we denote the mass of the primary system as M , the spring constant of the spring that supports the primary mass as K , and the damping coefficient as C . Given a forced displacement of the base (x_b) as input to model an external vibration, we obtain the horizontal displacement of the container (x_m), the horizontal and vertical displacement of the granular material ($z_h(i, j)$ and $z_v(i, j)$), and the angle of rotation, ($z_\theta(i, j)$). The subscripts i and j in the terms respectively indicate the row and column positions of an individual granule.

The granules all have the same mass (m_p) and radius (r). The contact between two granules and between a granule and the inner wall of the container are modeled as springs and dampers as shown in Fig. 3.

3.2 Equations of Motion for the Primary System and Granular Material

The model described in the previous section enables the equation of motion of the primary system to be represented as follows.

Fig. 2 Computation model for a granular material damper

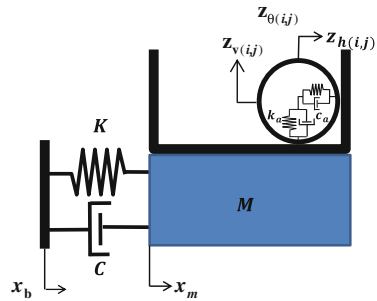
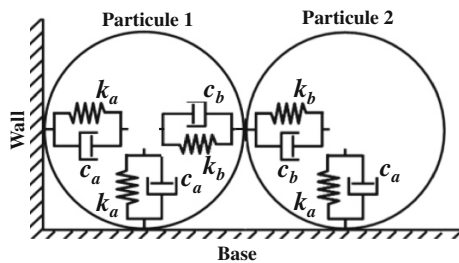


Fig. 3 Contact model for the granular material



$$\begin{aligned}
M\ddot{x}_m = & -K(x_m - x_b) - C(\dot{x}_m - \dot{x}_b) \\
& - \sum_{i=1}^p N_{L(i,1)} \left[k_a \{ r - (z_{h(i,1)} - x_m) \}^{\frac{3}{2}} + c_a (-\dot{z}_{h(i,1)} + \dot{x}_m) \right] \\
& + \sum_{i=1}^p N_{R(i,q)} \left[k_a \{ r - (x_m + l - z_{h(i,q)}) \}^{\frac{3}{2}} + c_a (-\dot{x}_m + \dot{z}_{h(i,q)}) \right] \\
& + \sum_{j=1}^q N_{B(1,j)} \operatorname{sgn}(\dot{z}_{h(1,j)} - \dot{x}_m - r\dot{z}_{\theta(1,j)}) \mu_a \left\{ k_a (r - z_{v(1,j)})^{\frac{3}{2}} + c_a (-\dot{z}_{v(1,j)}) \right\}
\end{aligned} \tag{1}$$

In the equation above, $N_{L(i,1)}$ is the constant for determining if there is a contact between the left wall and the cylinder in the i th row from the bottom of the first column; it has the value 1 if there is contact and 0 otherwise. $N_{R(i,q)}$ is the constant for determining if there is a contact between the right wall and the cylinder in the i th row from the bottom of column q . $N_{B(1,j)}$ is a constant for determining if there is a contact between the bottom row of granules with the bottom surface of the container (the primary system). The function sgn in the equation determines the direction of the force of friction; it takes the value 1 when the value within the parentheses is positive, -1 when the value is negative, and 0 when the value is zero. The term μ_a is the coefficient of friction between the granular material and the bottom surface of the primary system.

Because the contact of the granular material with the container walls or bottom is modeled as shown in Fig. 3, the spring constant k_a , k_b and the damping coefficient c_a , c_b are given by the equations according to the Hertz theory of contact.

The spring constant and damping coefficient are used to formulate equations of motion for multiple granules to obtain the horizontal, vertical and rotational displacements of individual granules. We used Intel Visual FORTRAN[®] to perform the computation on the basis of the equation of motion previously introduced. We used the Runge-Kutta method to solve the equation of motion.

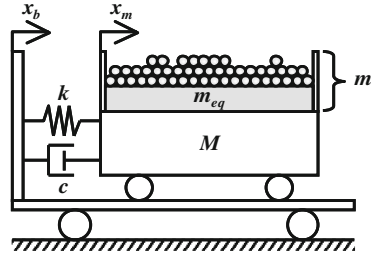
4 Deriving the Equivalent Added Mass, Relative Motion Mass of the Granular Material and Damping Ratio

4.1 Equivalent Added Mass and Relative Motion Mass

The damping effect of the granular material damper is obtained by the movement of the granular material. Therefore, as a step towards a deeper understanding of the mechanism of damping by granular material, we consider the motion of the granular material as broadly either ‘moving’ or ‘not moving’ relative to mass M .

We modeled a single degree of freedom vibration system that involves granular material as shown in Fig. 4. Granular material of total mass m is placed in a single

Fig. 4 Vibration model



degree of freedom vibration system (the primary system) that is excited in forced vibration by foundation motion. One part of the granular material moves together with the container of mass M and the other part moves relative to the container. In Fig. 4, the mass that moves together with the container is represented as a rectangular block that is implicitly attached to mass M and we refer to that mass here as the equivalent added mass m_{eq} . The remaining granular material mass ($m - m_{eq}$) is drawn as circles to represent individual granules that can move freely. We refer to that mass as the relative motion mass.

In Fig. 4, the displacement of the primary system excited in forced vibration by foundation motion is denoted as x_m , the displacement of the base is denoted as x_b , and the relative displacement of the two is denoted as x . Given

$$x = X\sin(\omega t - \phi) \tag{2}$$

$$x = x_m - x_b \tag{3}$$

we obtain the internal force f_i from the relative displacement x as follows.

$$f_i = c\dot{x} + kx \tag{4}$$

Because the equivalent added mass m_{eq} is attached to the mass of the primary system M , the internal force f_i is then expressed by the following equation.

$$f_i = -(M + m_{eq})\ddot{x}_m \tag{5}$$

Expressing the acceleration of the primary system \ddot{x}_m as

$$\ddot{x}_m = A_m\sin(\omega t - \phi - \theta) \tag{6}$$

$$\theta = \cos^{-1}\left(\frac{kX}{(M + m_{eq})A_m}\right) \tag{7}$$

f_i is given by Eq. 8.

$$f_i = -(M + m_{eq})A_m \sin \left(\omega t - \phi - \cos^{-1} \left(\frac{kX}{(M + m_{eq})A_m} \right) \right) \quad (8)$$

Expressing the relation of the internal force f_i and the relative displacement x as

$$\frac{(f_i - kx)^2}{(c\omega X)^2} + \left(\frac{x}{X} \right)^2 = 1 \quad (9)$$

the Lissajous pattern for $(f_i - kx)$ and x is an ellipse that has no inclination. Using that property, we define the equivalent added mass m_{eq} as the mass for which the inclination of the Lissajous pattern is zero.

4.2 Derivation of the Damping Ratio Using the Equivalent Added Mass

The work over one period of vibration (the energy loss within the system) is expressed as the area of the Lissajous pattern for the internal force and the displacement W_f .

$$W_f = \pi c \omega X^2 \quad (10)$$

In practice, the shape of the Lissajous pattern is not necessarily elliptical, but by regarding the area of the pattern to be equal to, the apparent damping coefficient C_{eq} and ζ can be obtained with Eqs. 11 and 12.

$$C_{eq} = \frac{W_f}{\pi \omega X^2} \quad (11)$$

$$\zeta = \frac{C_{eq}}{2\sqrt{(M + m_{eq})k}} \quad (12)$$

We obtain the area of the Lissajous pattern W_f from the computational results of Sect. 2, and obtain the damping ratio by the method described above. With those results, we discuss the forced vibration characteristics due to the granular material and the relation of the equivalent added mass to the relative motion mass.

5 Damping Characteristics of a Granular Material Damper for Various Total Masses of Material

We varied the total mass of the granular material in the container over the range from 1 to 7 kg and calculated the displacement and acceleration of the granular material and container for an acceleration of 1.0 m/s^2 applied to the base. We used the calculated results and the method described in Sect. 3 to obtain the equivalent added mass, the relative motion mass, and the damping ratio. The damping ratio and relative motion mass for various total masses are presented in Fig. 5.

In Fig. 5, up to a total mass of 5 kg, both the relative motion mass and the damping ratio increase. In that range, the relative motion mass is considered to increase the damping ratio by moving differently from the primary system. However, when the total mass of the granular material is 6 kg, the damping ratio increases further, even though the relative motion mass had been decreasing up to that point. Furthermore, when the total mass of the granular material is 7 kg, the relative motion mass again increases and the damping ratio decreases. We consider these results in light of the following additional inference.

The total mass of the granular material is plotted in relation to the relative motion mass and equivalent added mass in Fig. 6. The relative motion mass increase monotonically up to 5 kg, decrease somewhat in the range from 5 to 6 kg, and then increases again. The equivalent added mass, on the other hand, being the result of subtracting the relative motion mass from the total mass, is larger at the total masses of 6 and 7 kg total mass than at 5 kg.

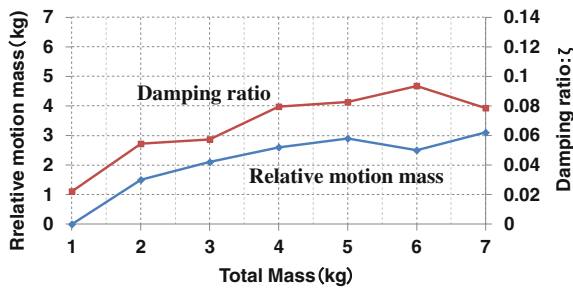
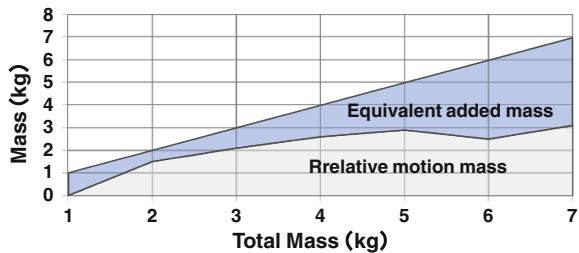


Fig. 5 Damping ratios and relative motion masses for various total granular material masses

Fig. 6 Relative motion mass and equivalent added mass



Comparing Figs. 6 and 5, we consider the relation of the relative motion mass and the equivalent added mass to the damping ratio. Because the relative motion mass increases up to the total mass of 5 kg, the damping characteristic is considered to improve. On the basis of that consideration, the behavior at the total mass of 6 kg cannot be explained. Specifically, even though the contribution of the relative motion mass to the damping ratio is decreasing at the total mass of 6 kg, the damping ratio is increasing.

We make the following inference concerning the behavior at the total mass of 6 kg. The relative motion mass is the mass of the granular material that is displaced relative to the primary system (“translation motion”). However, the motion of the granular material is not simply translation, but also includes rotation. The granular material follows the movement of the primary system (there is no relative motion mass), and even if there is rotational motion at that time, the rotation of the granules dissipates overall system energy and thus contributes to damping. That is to say, we can infer that parts of the equivalent added mass rotate when the total mass is 6 kg so that the damping ratio is larger than when the total mass is 5 kg.

6 Conclusions

We introduced the equivalent added mass and relative motion mass of granular materials as physical quantities to explain the damping mechanism of a granular material damper for cases in which the vibration amplitude is relatively small. We formulated a computational model for a granular material damper and calculate the motions of each part by numerical simulation. We confirmed the possibility of using the concepts of equivalent added mass and relative motion mass to distinguish damping mechanisms in a granular material damper.

References

1. Makino T, Nakahara K, Nakao S, Sato T (2003) Vibration control characteristics of structures that use granular material impact phenomena. *JSME Dyn Des Conf Proc* 685:1929–1934
2. Park J, Palumbo DL (2009) Damping of structural vibration using lightweight granular materials. *Exp Mech* 49(5):697–705
3. Saeki M (2002) Impact damping with granular materials in a horizontally vibrating system. *J Sound Vib* 251(1):153–161
4. Tanaka Y, Makino T, Sato N (2008) Study of particle size characteristics using a granular material damper. *JSME Kyushu Conf Proc* 61:193–194
5. Yokomichi I, Araki Y et al (1996) Impact damper with granular materials for multibody system. *J Press Vessel Technol* 118(1):95–103

Wagon Multibody Model and Its Real-Time Application

M. Spiriyagin, S.S.N. Ahmad, C. Cole, Y.Q. Sun and Tim McSweeney

Abstract Experimental railway research focused on the laboratory study of rail vehicle dynamics allows avoiding expensive field tests and reduces the cost of the development of new vehicles as well as making it simpler to improve design characteristics for existing vehicles. An example of such research is the investigation of the dynamic behaviour of a wagon suspension performed with the full-scale rail vehicle test rig in the CRE High Lab at Central Queensland University. Commonly, at the design stage of a test rig, it is necessary to estimate the working behaviour of different subsystems such as electrical, hydraulic, etc. It is possible to do this in two ways, either by means of the on-line or real-time simulation processes. The first process is adequate but it does not take into account all the nuances of the system configuration and does not allow testing of the equipment used in subsystems. Therefore, the optimal method is the usage of the real-time simulation process, which is also called hardware-in the-loop simulation. One of the major requirements of such an approach is the accurate representation of the behaviour of subsystems in the real-time mode. A real-time wagon model was developed based on the Gensys multibody simulation software version running under the Realtime Linux kernel open source software compiled and distributed by Open Source Automation Development Lab. In this paper, the authors focus on their simulation and verification methodology. All results obtained are presented and limitations are discussed. The discussion on real-time simulation methodology should help with

M. Spiriyagin (✉) · C. Cole · Y.Q. Sun · T. McSweeney
Central Queensland University, Brisbane, Australia
e-mail: m.spiriyagin@cqu.edu.au

C. Cole
e-mail: c.cole@cqu.edu.au

Y.Q. Sun
e-mail: y.q.sun@cqu.edu.au

T. McSweeney
e-mail: t.mcsweeney@cqu.edu.au

S.S.N. Ahmad
CRC for Rail Innovation, Central Queensland University, Brisbane, Australia
e-mail: ahmad@cqu.edu.au

the development and verification of rail vehicle test rig design at the early stages, leading to the reduction of design errors and related equipment failures.

Keywords Wagon · Test rig · Multibody model · Real-time simulation · Methodology

1 Introduction

The design stage of a railway vehicle usually uses a test rig in the laboratory to analyze in detail the dynamic behavior of different elements of the vehicle. An example of a suitable test rig for investigation of the dynamics of wagon suspension behavior is a full-scale test rig in CQU's CRE high lab [1].

The real-time simulation is useful in the design stage of any process where the controllers/actuators can be tested before making a full scale model [2]. The implementation of a real-time wagon model in the design stage is shown in Fig. 1. The hardware component of the test rig is usually installed with force or torque actuators in a laboratory [3]. The physical system is simulated in a specialized multibody simulation software.

A few real-time models of railway vehicles have been developed by using Matlab/Simulink [4, 5] and Gensys multibody simulation models [6]. The Matlab models inherently possess the complication of the difficulty in changing parameters which can be simplified by the use of multibody simulation software such as Gensys for rail vehicles [7].

In real-time simulation, the simulator solves model equations at discrete time-steps [2]. Hence, proper time-step selection is necessary to properly represent the system frequency. In a typical time step, the simulator executes the following set of tasks: (1) read input and generate outputs, (2) solve model equations, (3) exchange results with other simulation nodes, (4) wait for the start of the next step.

In this paper, a typical three-piece bogie wagon model (see Fig. 2) has been considered to show the possibility of reducing calculation time by simplifying some parameters such as track and contact models; friction elements, couplings and masses.

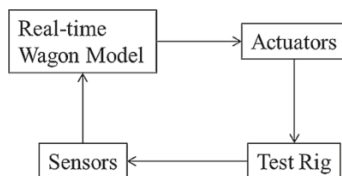


Fig. 1 Integration of real-time model in the design stage

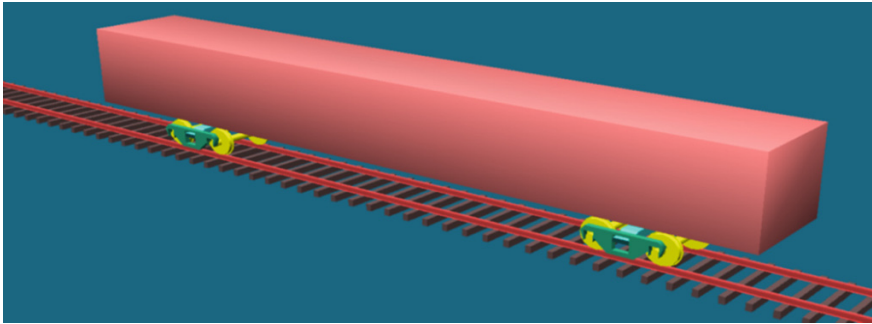


Fig. 2 Graphical representation of the real time model

2 Research Methodology

An approach has been taken to improve calculation time by reducing the degrees of freedom of different components of the model without compromising the output significantly. The full wagon model (FWM) and the suggested modifications of the model for real-time application are discussed in Sects. 2.1 and 2.2. All wagon models need to pass the wagon model acceptance procedure (WMAp) established in [8]. For brevity, in this paper only Stage 1 tests as per the WMAp have been performed. Examples of results delivered from some tests are shown in Figs. 3 and 4.

The calculation time has been determined by using a special routine inside the multibody software Gensys as per [6]. The total calculation time can be determined by using Eq. (1).

$$t_{out} = t_{sys} + t_{coupl} + t_{func} + t_{mass} + t_{constr} + t_{integ} + t_{ds} \tag{1}$$

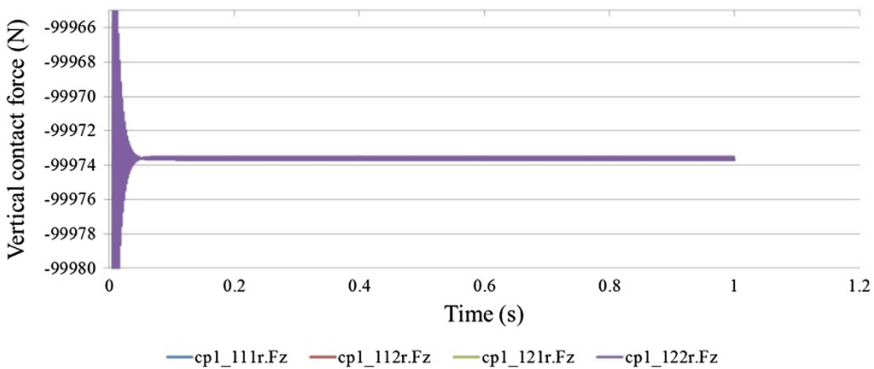


Fig. 3 Example of a numerical integrator stability check of the real time model for vertical wheel forces at the contact interface

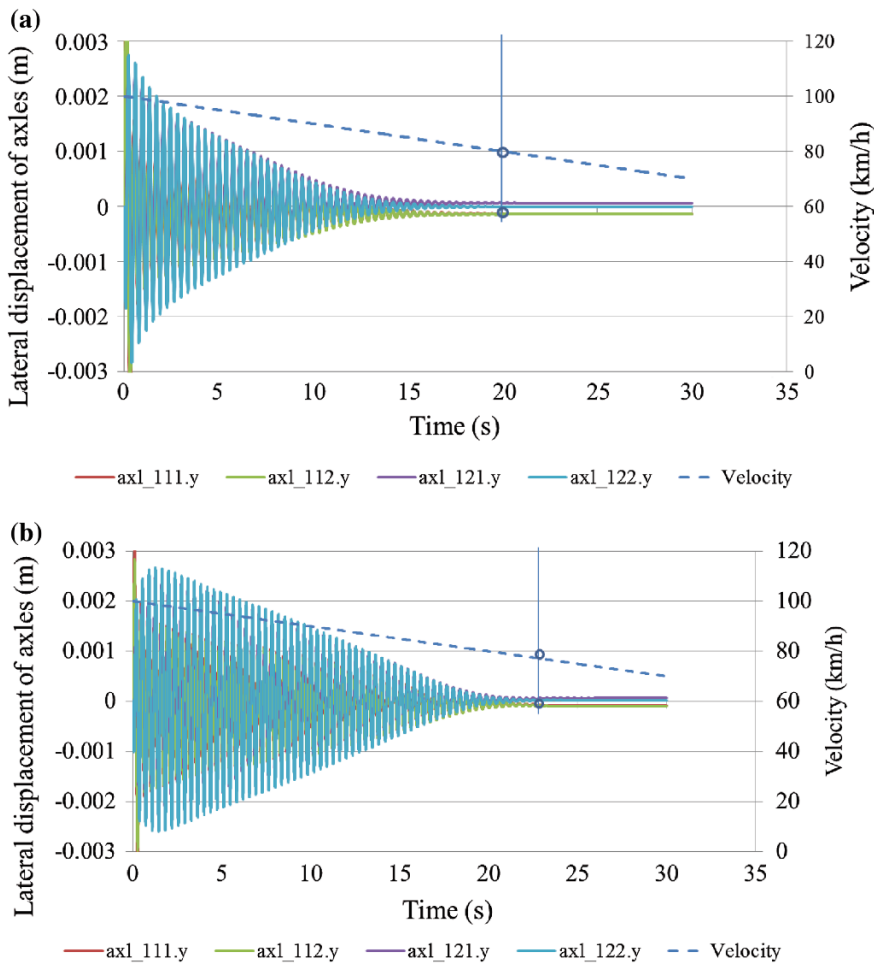


Fig. 4 Critical speed of (a) full wagon model and (b) RT wagon model [axle numbers denote position of wagon, bogie and axle respectively, example- axl_121 means wagon number 1, bogie number 2 and axle number 1 (first axle of second bogie of first wagon)]

where t_{sys} = the computational time spent on the position definition of local coordinate systems with reference to the global coordinate system, t_{coupl} = the computational time spent on commands for coupling elements (coupling elements are elements of various types that connect masses to each other), t_{func} = the computational time required for the calculation of defined functions in the model script, t_{mass} = the computational time spent on mass-commands (a mass-command creates an inertia in the model, e.g. car-body, bogie, wheelset, etc.), t_{cnstr} = the computational time spent on constraint commands, t_{integ} = the computational time required for calculation inside of the numerical integrator and t_{ds} = the computational time required for output data storage.

Table 1 Wagon parameters

Component	Mass (kg)	Mass moment of inertia (kg m ²)		
	m	I_{xx}	I_{yy}	I_{zz}
Wagon body				
Empty	7,735	6033.3	186516.63	192085.83
Bogie				
Wheelset	800	450	100	450
Sideframe	800	43	565	522
Bolster	1,000	347	43	363

2.1 Full Wagon Model Description

The typical three-piece bogie wagon considered here has a tare weight of 16 tonnes and gross weight of 80 tonnes. The distance between the two bogie centers is 14 m. The full wagon model consists of a wagon body, two bogie frames, two bolsters, 4 sideframes and 4 wheelsets. All bodies are considered as rigid masses with six degrees of freedom. The mass and moment of inertia parameters of the three-piece bogie wagon are presented in Table 1. The friction coefficient between wheels and rails has been chosen as 0.4. Wheel and rail profiles used are new ENS1002t32.5 wheel and UIC60i40 rail respectively. For demonstration purposes, simulation of an empty wagon on a straight ideal track has been considered in this paper.

2.2 Modifications of the Full Wagon Model for Real-Time Hardware-in-the-Loop Application

The full wagon model can be simplified in the following stages to obtain a model suitable for the real time application. A summary of modifications is presented in Table 2.

- Choice of numerical integrator

A list of potential numerical integrators for real time simulation in multibody software packages is available in [6]. The full wagon model requires a relatively time consuming integrator such as the Runge-Kutta method with step size controller and backsteps to meet tolerance ('heun_c' [9]) due to the presence of large numbers of friction elements and small masses inside the model. Considering the simplified model in case of a real time model the two step Runge-Kutta numerical integrator ('heun' [9]) has been chosen as it gives a relatively accurate result with less computational effort [3].

Table 2 Conversion of full wagon model (FWM) to real time model (RTM)

Component	FWM	RTM	Improvement in RTM
Integrator	Heun_c [9]	Heun [9]	backstepping is not required
Track geometry and irregularity	Separate function blocks for geometry and irregularity	In one function block	Reduced functions, storage
Graphical figures and associated post processing	Exist	Included for initial check, but in final version, this section was removed	Reduced functions, storage
Creep and creep forces	Creep force law function used to connect a wheelset to detailed track structure, requires less input but calculation time is high	Lookup table used, requires more input but calculation time is low as it uses pre-calculated wheel—rail geometry functions	Reduced functions
Saving variables for post processing	5 Files containing parameters of wagon body, axles, bolster, sideframe and bogie are inserted	Only required parameters were stored, to obtain the critical speed and vehicle stability; after acceptance of the model, all storage was removed	Functions, storage reduced
Primary suspension: longitudinal and lateral stops	Exist	Removed	Couplings, functions reduced
Limit values as per standard	Calculated	Avoided, after preliminary check of the model these calculations are not required for real time application	Functions, storage reduced

- Simplified contact and track model

The track model has been simplified by using a direct input of linear properties inside the model. In the full wagon model this is usually done by calling a file from the input library which may increase the time required for calculation. The contact subroutine of the full wagon model has been simplified by using a lookup table; the approach is discussed in [7]. This eliminates numerous mass, function and coupling elements of the FWM.

- Reduction of elements

In addition to simplifying subroutines, the stiffness and damping elements in all couplings can be replaced by fewer equivalent stiffness and damping elements. The friction elements require comparatively high times for simulation which can be modified or removed to reduce calculation time. As an example, the full wagon model uses 20 friction couplings, 16 of which are relevant to friction wedges. There is scope for reduction of calculation time if the wedges are replaced by an equivalent damping coefficient in the primary suspension.

- Reduction of storage and/or sending calculated results by network data

In full wagon analysis there is a need to estimate different sorts of data for vehicle tests. For real-time applications, it is common that the calculation in one time-step also involves data receive and sending processes [6]. Furthermore, in the real time modeling approach the output is directly used in the controller to execute a control mechanism, thus providing the potential for reducing the time needed for storage of data in comparison with a full model. In the real-time model, all data storage commands were deactivated to obtain a reduced calculation time.

3 Verification of the Real Time Model

The verification of the real time model with respect to the full wagon model has been done in two stages—vertical contact force test and critical speed.

- Vertical contact force test to check the stability of the real time model

The real time model has four axles only running on the track and representing the full mass of the wagon. This stage is very important; more detailed information can be found in [10]. The contact forces have been found to stabilize in a short time.

- Critical speed

The real time model was also tested for critical speed. The speed of the wagon was decreased from 100 km/h at a rate of 1 km/h per second to obtain the critical speed. The critical speed of the real time wagon was found to be about 77 km/h compared to about 80 km/h for the full wagon model. The wagon body was excited during the test of critical speed which also proves the stability of the real time model (Fig. 5).

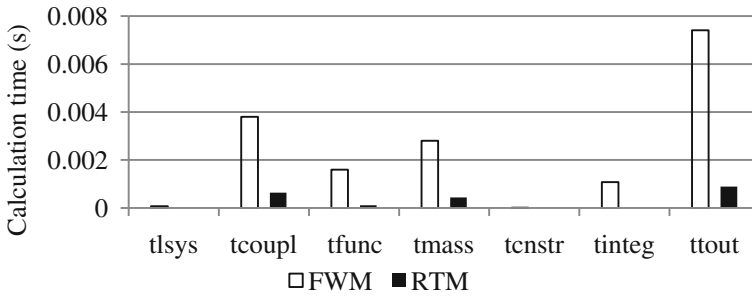


Fig. 5 Calculation time for different elements of the full wagon model and the real-time wagon model

4 Results

The total computational time for the full wagon model is about 7.4 ms while that of the real time model is significantly reduced to about 0.9 ms for 1 ms time step (Fig. 6). A further reduction of about 0.1 ms was obtained when all the storage variables were deactivated. The computer used to obtain the calculation times is equipped with an Intel[®] Core[™] i7-3770 CPU @ 3.40 GHz, RAM 8 Gb. It is also observed that couplings, functions, masses and integrators inside the models consume the most time for calculation. It follows that careful selection of couplings, functions, masses and integrators can reduce the total time for calculation.

A reduction in calculation time of 6.5 ms for 1 ms time step has been achieved by the strategies described in this paper. The coupling component has been found to be the most influential parameter in reducing the calculation time, providing about 48 % of the total reduction in calculation time (Fig. 6).

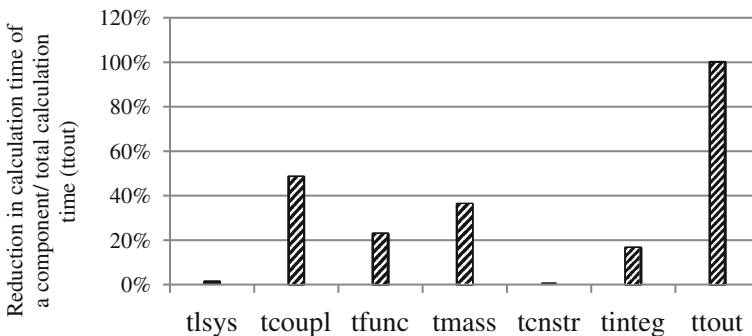


Fig. 6 Component wise reduction in calculation time

5 Discussion

The conversion of a full wagon model into a real time model requires exhaustive simulations with required operating conditions. A simple approach has been presented here with a view to reduce the calculation time while maintaining similar critical speed. A further time reduction can be achieved if a higher performance computer is used. A simple model with reduced coupler elements such as presented in [11] can also be utilized in the multibody simulation software to achieve a real time model.

Introduction of track irregularities and curved track will change the conversion parameters which will require further modification of the model to achieve similar outcomes of that of the full wagon model.

Reduction of calculation time in a simulation helps to add a hardware controller that can act based on the result obtained from the simulation. A time-step requirement for typical mechanical vehicle systems is between 1 and 10 ms [2]. However, a stiff system may require a smaller time-step. In case of a higher number of friction elements, even lower time-steps such as 100–500 μ s might be required. The RT model developed in this paper was stable at the time step of 1 ms which is sufficient for the vehicle dynamics test using a shaker test rig.

It can also be noted that the actuator used in the wagon shaker test rig at the CRE high lab requires an input signal every 0.1 s. This value is limited by characteristics of the actuators, which apply forces to the wagon body in the shaker test rig in order to replicate real operational conditions. Thus it is possible to integrate the RT model in the shaker test rig to test the actuator for different input conditions in a physical wagon system that may realistically occur.

6 Conclusion

A simplification procedure to convert a full wagon model into a suitable model for the purpose of real-time hardware-in-the-loop simulation has been proposed. The easiest way to convert the model is to use simplified numerical integrators, track and contact subroutine. Reduction of as many friction elements, couplings, functions and masses as possible also help in reducing calculation time. The use of specialized software for this purpose can reduce the complexity of changing parameters if required. The RT model developed here is capable of testing the actuator in the shaker test rig developed in the CRE lab. The proposed methodology can be used in other complex operations and track combinations such as track irregularities and track gradients to further improve the model for more versatile operational scenarios.

Acknowledgments The authors are grateful to the CRC for Rail Innovation (established and supported under the Australian Government's Cooperative Research Centres program) for the funding of this research. The authors acknowledge the support of the Centre for Railway

Engineering at Central Queensland University that has contributed to this project. The authors also acknowledge DESolver for use of the Gensys software in vehicle dynamics simulation undertaken for this study.

References

1. Cole C, McClanachan M, Simson S, Skerman D (2006) Evaluating the performance of 3-piece bogies on short defects and with unequal wheel diameters. In: Presented at the conference on railway engineering. Melbourne, Australia
2. Belanger J, Venne P, Paquin JN (2010) The what, where and why of real-time simulation . Available <http://www.opal-rt.com/technical-document/what-where-and-why-real-time-simulation>
3. Spiryagin M, Cole C, Sun YQ, McClanachan M, Spiryagin V, McSweeney T (eds) (2014) Advanced simulation methodologies. In: Design and simulation of rail vehicles. CRC Press, Boca Raton, pp 300–308
4. Maki Y, Shimomura T, Sasaki K (2009) Building a railway vehicle model for hardware-in-the-loop simulation. Q Rep RTRI 50:193–198
5. Umehara Y, Sasaki k, Watanabe N, Maki Y, Tezuka K (eds) (2008) A study of virtual running test of railway vehicle. In: 8th world congress on railway research. Seoul, South Korea
6. Spiryagin M, Sun YQ, Cole C, McSweeney T, Simson S, Persson I (2013) Development of a real-time bogie test rig model based on railway specialised multibody software. Veh Syst Dyn 51(2):236–250
7. Spiryagin M, Cole C, Sun YQ, McSweeney T (eds) (2013) Mechatronic real-time multibody model of bogie test rig. In: 23rd International symposium on dynamics of vehicles on roads and tracks (IAVSD). Qingdao, China
8. Spiryagin M, George A, Ahmad SSN, Rathakrishnan K, Sun YQ, Cole C (eds) (2012) Wagon model acceptance procedure using Australian standards. In: Conference on railway engineering. Brisbane, Australia
9. DESolver, users manual for program calc. Available http://www.gensys.se/doc_html/calc.html
10. Bosso N, Spiryagin M, Gugliotta A, Somà A (2013) Mechatronic modeling of real-time wheel-rail contact. Springer, Berlin
11. Harder RF (ed) (2001) Dynamic modeling and simulation of three-piece freight vehicle suspensions with nonlinear frictional behaviour using Adams/Rail. In: Proceedings of the 2001 IEEE/ASME joint railroad conference. Toronto, Canada, pp 185–191

Part VIII
Control Issues of Mechanical Systems

Experimental Validation of the Mechatronic Model of a Parallel Manipulator

O. Altuzarra, F.J. Campa, C. Roldan-Paraponiaris and Ch. Pinto

Abstract In this paper, a mechatronic model of a planar parallel manipulator is developed and experimentally validated. The model considers the dynamics of the actuators, as well as the PID control algorithm with position, velocity and current cascaded loops and their timing. As our main contributions, the dynamics of the manipulator have been solved using the principle of equivalent energy to split up the closed-loop mechanism, and the torque calculated is regarded as a disturbance on the actuators, avoiding solving the forward dynamic problem. Also, the dynamics of the actuators take into account the inertia and the friction parameters, which have been experimentally identified by means of a grey-box identification method. Several experiments have been carried out on a prototype, varying the motion profile, the velocity and acceleration, and the position control gain. The results show a reasonable correlation and provide the basis for further discussion.

Keywords Mechatronics · Parallel manipulators · Analytical mechanics

1 Introduction

Theoretically, parallel kinematic machines have advantages over the serial ones in terms of dynamic behavior precision and stiffness. However, the complex dynamics derived from the closed chain kinematics and the clearances between joints among other factors, make it difficult to put those capacities into practice. This causes a lack of precision and stiffness that in some fields cannot be accepted [5]. One of the tools for the improvement of these machines is the simulation as mentioned by [2].

In the present work, a mechatronic model of a parallel kinematic manipulator that integrates the dynamics of the manipulator, the actuator and the control has been developed and validated experimentally. First, the approach followed to model

O. Altuzarra (✉) · F.J. Campa · C. Roldan-Paraponiaris · Ch. Pinto
University of the Basque Country UPV/EHU, Leioa, Spain
e-mail: oscar.altuzarra@ehu.es

the dynamics of the manipulator is shown. Second, the dynamic model of the actuators is presented. Then, both dynamic models and the control have been integrated into a single mechatronic model of the machine. Finally, some experimental results performed on a real prototype are presented.

2 Dynamic Modelling of the Manipulator

An explicit set of differential equations describing the dynamics in terms of the actuation variables, the mass properties and the actuation forces, is necessary for the implementation of the control on real time applications. Such set is called explicit or detailed form since inertia, gravitational and Coriolis terms are obtained separately and in closed form. Lagrangian formalism is a method reported to be very efficient in open chain mechanisms, but a prohibitive task for parallel manipulators because of the kinematic constraints due to closed loops [3]. However, exploiting less known capacities of Analytical Mechanics, such as quasi-velocities, Boltzmann-Hamel equations and the principle of energy equivalence, it is possible to find the aforementioned dynamic equations with a good computational efficiency [1]. The latter approach will be used in this paper.

The horizontally planar two DOFs 5R parallel mechanism under study is a classical test bench to evaluate the performance of new methodologies on closed-loop mechanisms, Fig. 1. Kinematic analysis shows the interdependence of kinematic parameters, and the difficulty to express every variable of the mechanism explicitly in terms of the generalized coordinates $\mathbf{q}_a = [\theta_1, \theta_2]^T$.

For the dynamics, the mechanism will be split up into b open-chained subsystems where Lagrange equations can be applied more easily with their specific generalized coordinates \mathbf{q}_b . Using Euler's operator [4], dynamic equations are obtained as a function of the known Lagrangian function L_b and the unknown generalized forces τ_b :

$$\tau_b = \mathcal{E}(L_b) = \frac{d}{dt} \frac{\partial L_b}{\partial \dot{\mathbf{q}}_b} - \frac{\partial L_b}{\partial \mathbf{q}_b} \quad (1)$$

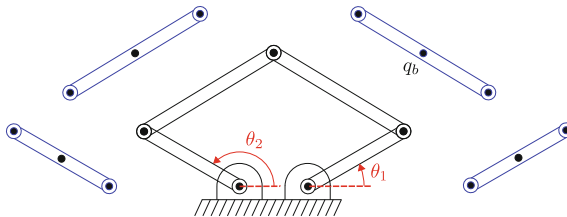


Fig. 1 Dynamic modelling of the 5R mechanism

The condition that individuals subsystems b move as they were part of the assembled mechanism a implies that \mathbf{q}_B , the set of all the generalized coordinates \mathbf{q}_b belonging to every subsystem b , is a function of the generalized coordinates \mathbf{q}_a . Furthermore, the virtual displacements are related by the Jacobian:

$$\delta \mathbf{q}_B = \frac{\partial \mathbf{q}_B}{\partial \mathbf{q}_a} \delta \mathbf{q}_a = \mathbf{J} \delta \mathbf{q}_a \quad (2)$$

Also, as the motion is identical, the virtual work done by the assembled system and the set of subsystems is the same:

$$\delta W_a = \delta W_B \quad (3)$$

$$\delta \mathbf{q}_a^T \tau_a = \delta \mathbf{q}_B^T \tau_B = \delta \mathbf{q}_a^T \mathbf{J}^T \tau_B \quad (4)$$

$$\tau_a = \mathbf{J}^T \tau_B = \sum_{b=1}^B \mathbf{J}_b^T \tau_b \quad (5)$$

We will define subsystems b as free bodies moving on the horizontal plane, being their local generalized coordinates $\mathbf{q}_b = [x_b, y_b, \phi_b]^T$ the position of the center of mass and the orientation of the body, Fig. 1. Upon application of Eq. (1) we get:

$$\tau_b = \mathcal{E}(L_b) = \begin{bmatrix} m_b & 0 & 0 \\ 0 & m_b & 0 \\ 0 & 0 & I_b \end{bmatrix} \ddot{\mathbf{q}}_b = \mathbf{M}_b \ddot{\mathbf{q}}_b \quad (6)$$

Using the kinematic relationship $\dot{\mathbf{q}}_b = \mathbf{J}_b \dot{\mathbf{q}}_a$ we obtain:

$$\tau_b = \mathbf{M}_b \mathbf{J}_b \ddot{\mathbf{q}}_a + \mathbf{M}_b \dot{\mathbf{J}}_b \dot{\mathbf{q}}_a \quad (7)$$

And the contribution of subsystem b to the mechanism's dynamics in terms of the actuation variables results in:

$$\tau_{a_b} = \mathbf{J}_b^T \tau_b = \mathbf{J}_b^T \mathbf{M}_b \mathbf{J}_b \ddot{\mathbf{q}}_a + \mathbf{J}_b^T \mathbf{M}_b \dot{\mathbf{J}}_b \dot{\mathbf{q}}_a \quad (8)$$

where the second term on the far right can be split into two, one depending on the squared generalized velocities and the other one \mathbf{c}_b depending on the product of generalized velocities:

$$\tau_{a_b} = \mathbf{I}_b \ddot{\mathbf{q}}_a + \mathbf{C}_b \dot{\mathbf{q}}_a^2 + \mathbf{c}_b \quad (9)$$

Finally, the addition of every part is performed using the principle of energy equivalence to get the explicit dynamics expression:

$$\tau_a = \mathbf{I}\ddot{\mathbf{q}}_a + \mathbf{C}\dot{\mathbf{q}}_a^2 + \mathbf{c} \quad (10)$$

where there is no gravitational term as every body is moving on a horizontal plane. Matrices \mathbf{I} , \mathbf{C} and \mathbf{c} are function only of the position of the mechanism.

3 Dynamic Model of the Actuation System

The actuation system used for the 5-R mechanism is composed of two identical actuators based on an Schneider BSH1401P AC motor coupled to a Neugart PLE-160 gearbox with a gear ratio of 40:1. An inertial model with 1 degree of freedom has been used, where θ represents the rotation of the motor measured at the encoder, τ is the torque of the motor generated by the supplied current and τ_f is the load torque caused by friction. Moreover, J represents the total inertia of the actuator, that is $J = J_m + J_g$.

Furthermore, the equation that represents the dynamic behavior of the actuator can be written as

$$\tau - \tau_f = J\ddot{\theta} \quad (11)$$

As for the friction, a non-linear model is used to represent its dynamics. This friction model only takes into account the viscous and the Coulomb friction effects as shown in Eq. (12), where c represents the viscous friction coefficient and F_c is the Coulomb friction torque, which has been represented as an hyperbolic tangent dependent on β and the motor speed.

$$\tau_f = c\dot{\theta} + F_c \cdot \tanh(\beta\dot{\theta}) \quad (12)$$

Friction parameters are unknown and system-specific, thus, a system identification method was used to identify them. The herein method employed consists in minimizing the least-square error between the experimental data and the model of the system by means of a pseudo-linear regression mathematical method, Eq. 13, where, $\hat{\tau}$ is the estimated torque, ρ is defined as the vector of unknown parameters, φ is the matrix containing the experimental data measured at t samples, and η is the vector containing the non-linear parameters, Eq. 14.

$$\hat{\tau}(t|\rho, \eta) = \rho^T \cdot \varphi(\tau, \eta) \quad (13)$$

$$\rho = \begin{Bmatrix} J \\ c \\ F \end{Bmatrix} \quad \varphi(t, \eta) = \begin{bmatrix} \ddot{\theta}(t) \\ \dot{\theta}(t) \\ \tanh(\beta\dot{\theta}(t)) \end{bmatrix} \quad \eta = \{\beta\} \quad (14)$$

Moreover, the function to be minimized is written as Eq. 15.

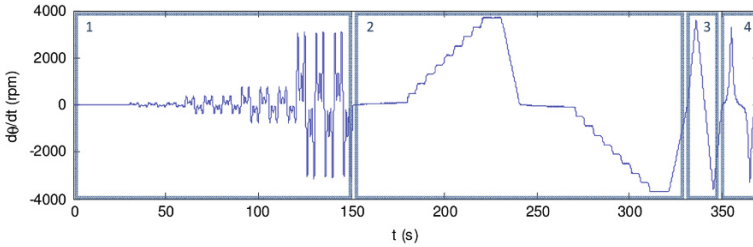


Fig. 2 Velocity multiprofile test signal

$$V_N(\rho, \eta) = \sum_{t=1}^N |\tau(t_i) - \rho^T \cdot \varphi(t_i, \eta)|^2 = \|\tau - \Phi(\eta)\rho\|^2 \tag{15}$$

This function can be separated by means of the pseudo-inverse of the matrix Φ (see [6] [7]), hence the problem is reduced to finding out the optimum value of η and then calculate the optimum values of the vector ρ as follows.

$$\hat{\rho}(\hat{\eta}) \equiv \Phi^+(\hat{\eta})\tau \tag{16}$$

In order to acquire representative experimental data, the planned motion has to excite all the phenomena described in the dynamic modeling [6]. To do so, the trajectory shown on Fig. 2 has been used. It consists of 1) a sum of sinusoids with frequencies 0.1, 0.3, 0.5 Hz and increasing amplitude from 10 rpm to 3,700 rpm, 2) two stages of ascending and descending velocity steps from 10 rpm to 3,700 rpm, 3) two stages with constant acceleration and deceleration, and 4) two stages of exponentially increasing and decreasing velocity. As a result of the identification procedure, the following parameters are obtained: $J = 13 \times 10^{-4}$ kg m², $c = 1.7 \times 10^{-3}$ N m s/rad, $F_c = 0.478$ N m and $\beta = 10.78$.

4 Mechatronic Model of the Manipulator

The motion control algorithm of the 5R manipulator is based on an axis-by-axis joint space control with a cascaded PID control of current, velocity and position. The velocity and current are controlled by the actuators drives with a cycle time of 250 and 62.5 μ s respectively, whereas the position control is performed with a cycle time of 20 ms by a software developed in Labview on a NI PXI platform. Position is measured by the encoder of the actuators, that is, an indirect method is used to measure the position of the end-effector.

In order to model the dynamic behavior of the whole system, the common approach is based on integrating the dynamics of the actuators and the robot as a single system. Instead, the approach here followed considers the manipulator as a

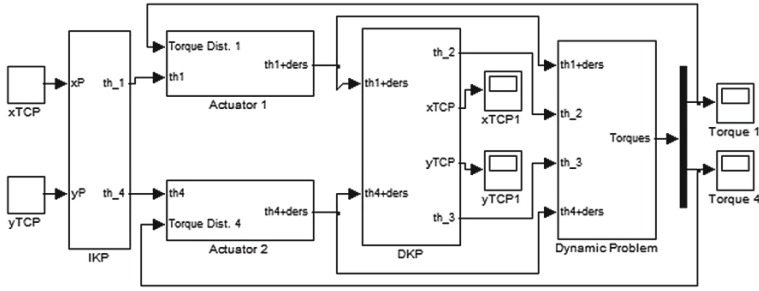


Fig. 3 Mechatronic model of the 5R manipulator

disturbance that the actuators must overcome to perform the commanded motion. The model of the system has been programmed in Matlab/Simulink as follows, see Fig. 3. First, the commanded path in the workspace is converted to the joint space solving the Inverse Kinematics Problem (IKP). Then, the joint space position commands enter both actuators models where the control loops have been programmed. The output of both models is the simulated angular position in the joints, which is fed into the Direct Kinematics Problem (DKP) to calculate the position of the end-effector in the workspace. The simulated angular position in the joints are also introduced into the Dynamic Problem of the 5R. The torques obtained are fed back into the actuators model as torque disturbances.

The model of the actuator dynamics and the control is shown in Fig. 4. First, there is an outer loop with a proportional action and a velocity feed-forward for the position control. The inner loop is for the motor velocity control, where a proportional-integral action has been taken. A low-pass filter is applied to the reference of both loops. The current loop is considered to be faster than the others and is replaced by the torque constant k_t of the motor. Two sources of disturbance are

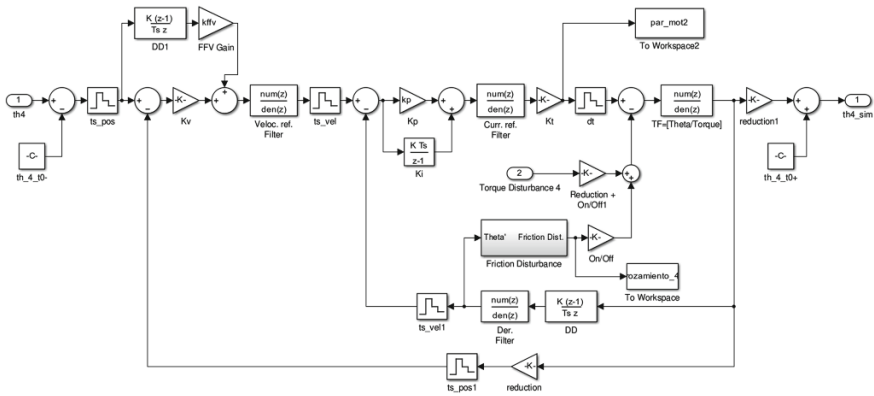


Fig. 4 Mechatronic model of the actuators

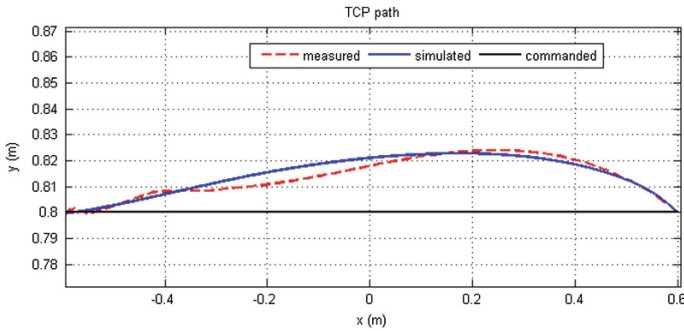


Fig. 5 Comparison of the programmed, experimental and simulated paths in a X displacement

considered, the torque disturbance from the mechanism and the friction torque identified for the actuator. The plant is the transfer function that represents the identified inertia of the actuator. Finally, the different timing of the loops has been taken into account.

5 Experimental Validation

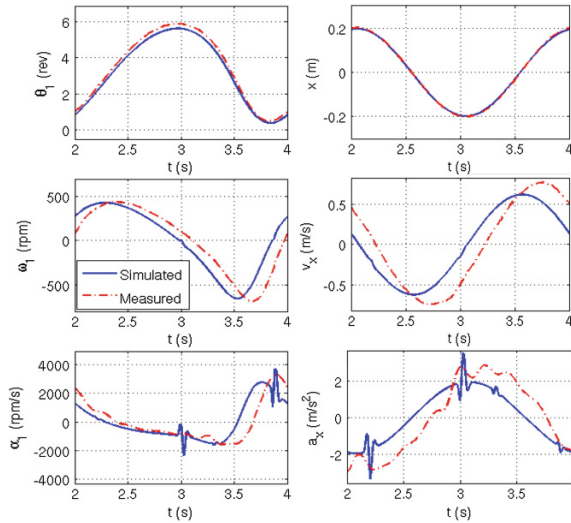
In order to validate the model developed, the programmed, performed and simulated paths of the end effector are compared. The performed path is calculated applying the DKP transformation to the angular positions measured at the encoders. The gains of the velocity loop are $k_p = 0.14 \text{ As/rad}$ and $k_i = 11.45 \text{ A/rad}$.

The first test is a displacement in X direction with a trapezoidal velocity profile. The path length is of 1.2 m, the feed speed is 1 m/s and the acceleration 1 m/s^2 . The gain tested in the position loop is $k_v = 3.541/\text{s}$, which is a low value. The result is shown in Fig. 5. It can be seen how the end effector path deviates from the programmed path up to 22 mm due to the low gain. That behavior is adequately predicted by the simulation.

The deviation of the simulated from the measured path is due to the complex and coupled dynamics between actuators, joints clearances and mechanism disturbances. Therefore, higher order dynamics are neglected which are shown in the measured signal.

The second test is a counterclockwise circular displacement, with a radius of 0.2 m and a constant feed speed of 0.628 m/s. The gain tested in the position loop is $k_v = 19.21/\text{s}$, which leads to lower error. Some results are shown in Fig. 6 (continuous line = simulation, discontinuous line = measured). Again, there is an agreement between the measured and the simulated magnitudes. In the acceleration plot in Fig. 6, the peaks observed are a result of the numerical derivative from the velocity signal when it is a near-zero value.

Fig. 6 Position, velocity and acceleration in the joint space and in the workspace



6 Conclusions

A mechatronic model of a 5R parallel machine that takes into account the dynamics of the manipulator, the actuator and the control has been developed. The dynamic modeling of the manipulator is based on analytical mechanics, which provide a reasonably efficient solution. The dynamics of the actuator has been modeled as a rigid body with friction, whose parameters have been identified experimentally. Also, a real prototype has been developed to validate the model. The tests results indicates that there is a reasonable agreement between the model and the real behavior of the machine.

Acknowledgements The authors of this paper wish to acknowledge the finance received from the Spanish Government via the Ministerio de Educacion y Ciencia (Project DPI2011-22955), the ERDF of the European Union, the Government of the Basque Country (Project GIC07/78, IT445-10), and the University of the Basque Country (Project EHUA13/30).

References

1. Abdellatif H, Heimann B (2009) Computational efficient inverse dynamics of 6-DOF fully parallel manipulators by using the Lagrangian formalism. *Mech Mach Theory* 44:192–207
2. Brecher C, Ostermann T, Friedrich D (2006) Control concept for PKM considering the mechanical coupling between actuators. In: Chemnitz parallel kinematics seminar, Chemnitz, Germany, pp 413–427
3. Ebert-Uphoff I, Kozak K (2002) Review of the role of Quasi-coordinates for the kinematic and dynamic modeling of parallel manipulators. In: Proceedings of the workshop on fundamental

- issues and future research directions for parallel mechanisms and manipulators, Quebec, pp 328–338
4. Lurie AI (2002) Analytical mechanics (series: foundations of engineering mechanics). Springer, Berlin
 5. Pritschow G (2002) Influence of the dynamic stiffness on the accuracy of PKM. In: Chemnitz parallel kinematic seminar, Chemnitz, Germany, pp 313–333
 6. Roldan C, Campa FJ, Altuzarra O, Amezua E (2013) Automatic identification of the inertia and friction of an electromechanical actuator. In: Proceedings of the second conference MeTrApp 2013 on new advances in mechanisms, transmissions and applications, Bilbao, Spain, pp 409–417
 7. Wernholt E, Gunnarsson S (2006) Nonlinear identification of a physically parameterized robot model. In: SYSID 2006, Newcastle, Australia

Preferable Operation Modes of a Wind Turbine with a Differential Planetary Gearbox

M. Dosaev, A. Holub and L. Klimina

Abstract The paper is devoted to studying behaviour of a small-scale wind turbine with a differential planetary gearbox. Control torque is applied to an external ring of a gearbox, a wind receiving element is rigidly joined with a carrier, and a rotor of an electrical generator is rigidly joined with a sun gear. The closed mathematical model of the mechanical system in question is constructed to find effective control strategies. This model takes into account aerodynamic load upon blades of the turbine as well as electromagnetic torque acting on the rotor of the generator. An operation mode of the mechanical system corresponds to a steady point of model equations. We performed parametrical analysis of the dynamical system, found the set of possible operation modes and suggested different control algorithms. Constructed control laws allow the mechanical system to approach a preferable operation mode from any initial conditions. We solved this control problem by piecewise constant control and linear feedback control. We discussed different purposes of control for the mechanical system in question.

Keywords Small-scale wind turbine · Differential planetary gearbox · Operation modes · Domain of attraction · Linear feedback control

1 Introduction

Differential planetary gearboxes (DPG) are widely used in modern industrial wind turbines. Practical demands encourage a lot of authors to search for hi-tech solutions of varied engineering problems [1, 2, 5–8]. Most of publications in this fruitful field are devoted to large scale industrial turbines connected to a grid. So the corresponding model possesses no parameters responsible for changing of the electrical load in the circuit.

M. Dosaev · A. Holub · L. Klimina (✉)
Lomonosov Moscow State University, Moscow, Russia
e-mail: klimina@imec.msu.ru

The situation with small-scale wind turbines connected to a local circuit is quite different. In this case any consumer can essentially change torque acting on the rotor of a generator of a turbine. Mathematical model of a small-scale wind turbine should take into account special parameters describing features of a generator and electrical load in a generator circuit. Moreover control approach for such turbines should depend on changeable conditions in a local circuit, otherwise control is not efficient.

There is a lack of complete dynamical models for small-scale wind turbines in modern wind turbine engineering, especially in research of control mechanisms. In the same time the ecologic and economic situation strongly forces engineers to develop autonomous green energy sources for individual consumers. Such wind energy systems are in demand for individual household, in country, in camping, in expeditions, for remote objects etc. The work [3] provided a unique full dynamical model of a small-scale wind turbine controlled by means of a DPG.

The present paper introduces smart control approaches based on the model [3] and directed to solve several common practical tasks. Designed control laws allow maintaining an operation mode with a needed value of an output power. Sometimes external conditions permit several regimes satisfying power requirement. The special control strategy is introduced for transfer to an operation mode which is preferable due to one of the following criteria: minimal power costs for control (the highest tip speed ratio of a turbine), most safety mode (in the case of strong wind), a balance between power costs and safety. We showed that a piecewise constant control torque is enough for first two criteria, but the third case is more complicated and can be guaranteed by a linear feedback control.

2 Statement of the Problem

Let's describe the mechanical model of a horizontal axis wind turbine (HAWT) equipped by a DPG, the model of external actions, and let's introduce a control problem to be solved.

2.1 Description of the Mechanical System

The mechanical system consists of a wind turbine, a DPG and a rotor of an electric generator. Generator is connected to a local electrical circuit with a changeable external resistance R .

The DPG includes two coaxes gears (Fig. 1) with different diameters: an external ring and a sun. Four small gears (planets) are rotating between these rings. Centers of planets are connected with a carrier.

O_z —axis of rotation of the turbine as well as of the carrier, the sun and the external ring. The turbine is rigidly joined with the carrier. The sun is rigidly joined

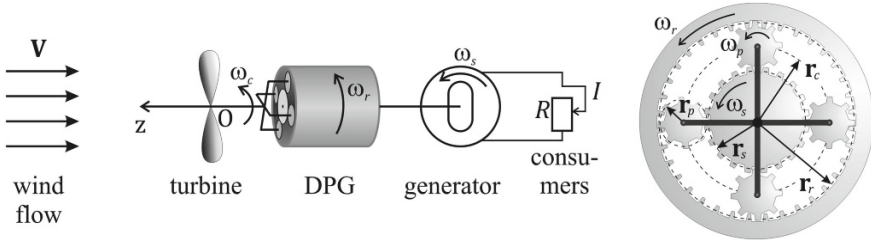


Fig. 1 A scheme of the wind power system; a scheme of the DPG

with the rotor of the generator. $\omega_c, \omega_s, \omega_r, \omega_p$ —angular speeds of the carrier, the sun, the external ring, each planet. r_c, r_s, r_r, r_p —radiuses of corresponding rings ($r_c = r_s + r_p, r_r = r_s + 2r_p$).

J_c, J_s, J_r, J_p —central moments of inertia of rigid bodies “turbine + carrier”, “sun + rotor”, the external ring, each planet. m_p —mass of each planet.

2.2 Model of External Forces

Assume that the turbine is under an aerodynamic action of an upcoming wind flow of a speed V , and the rotor of the generator is influenced by an electromagnetic field presenting between the rotor and the stator. Let’s use the following model (as in [7]) for corresponding torques (aerodynamic torque T_c , electromagnetic torque T_s) with respect to the axis of rotation:

$$T_c = 0.5\rho S b V^2 f(\lambda), \quad T_s = -c^2 \omega_s (R + r)^{-1}.$$

Here $\lambda = b\omega_c V^{-1}$ —tip speed ratio, $f(\lambda)$ —dimensionless aerodynamic torque; ρ —density of air, S —characteristic area of the turbine, b —radius of the turbine; c —coefficient of electromechanical interaction (responsible for conversion of mechanical energy into electrical energy), r —inner resistance of the generator.

A function $f(\lambda)$ is essentially nonlinear. Here we use experimental data obtained in the aerodynamic tunnel of the Institute of Mechanics of LMSU (for the HAWT with the diameter 1 m) to identify this function. The function shown in Fig. 2 approximates experimental points obtained for wind speed from 4 to 6.5 m/s. This function possesses principal properties corresponding to important features of an aerodynamic torque: it decreases for λ less than a certain value (e.g. $\lambda < \lambda_1$) as well as for λ larger than some another value (e.g. $\lambda > \lambda_2$); there is a significant interval of λ for which the function $f(\lambda)$ increases (e.g. $\lambda_1 < \lambda < \lambda_2$). Moreover, a typical aerodynamic function $f(\lambda)$ intersects zero only once. We chose a certain example of a function $f(\lambda)$ just for illustration. Further results are valid for a wide class of functions possessing properties listed above.

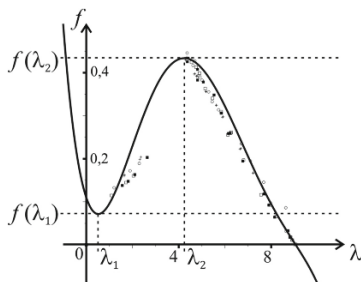


Fig. 2 Approximation of experimental points (for $V = 4 \div 6.5$ m/s) provides an example of a dimensionless aerodynamic torque $f(\lambda)$

2.3 Discussion of the Control Problem

Assume that control torque T_r is applied to an external ring of the gearbox. This torque can be used to reach and maintain a program operation mode of a HAWT. Assume that operation mode corresponds to a stable regime with steady rotation of the turbine as well as of the rotor of the generator. Suppose that a program value of angular speed of the rotor is given: $\omega_s = \omega_s^*$ (e.g. due to requirements of consumers). If external conditions allow several steady regimes with $\omega_s = \omega_s^*$, such regimes can be distinguished via the value of angular speed ω_c of the turbine.

There is a certain reasoning to suggest which of these regimes is the most preferable. For instance the regime with the largest value of ω_c provides the largest power gain; the regime with the lowest angular speed ω_c is the most safety (it is better to switch to this mode for too strong wind); a regime with a middle value of ω_c keeps balance between efficiency and safeness. Anyway one of available regimes should be chosen as preferable. The control law should be found that transfers the HAWT to the preferable operation mode (from any initial state) and supports this mode. Let's show how to solve this task using piecewise constant and linear feedback types of control torque.

3 Dynamical Equations of the Model

The mechanical system has two degrees of freedom (there is no slipping between elements of DPG). The dimensionless form of dynamical equations is as follows:

$$\begin{cases} \frac{d\lambda}{d\tau} = A_1 f(\lambda) - A_2 u - A_3 \mu; \\ \frac{d\mu}{d\tau} = B_1 f(\lambda) + B_2 u - B_3 \mu; \end{cases} \quad (1)$$

Here τ —dimensionless time, u —dimensionless control function; μ —dimensionless angular speed of the rotor of the generator:

$$\tau = Vt/b, \quad u = -\frac{r_r}{r_s \rho S b V^2} T_r, \quad \mu = \frac{c^2}{(R+r)\rho S b V^2} \omega_s;$$

$A_1, A_2, A_3, B_1, B_2, B_3$ —positive dimensionless constants:

$$\begin{aligned} A_1 &= \frac{r_s}{4r_c}(A_2 + A_3), \quad A_2 = \frac{r_c}{Jr_s} \rho S b^3 \left(\frac{r_r}{r_p} J_p + \frac{r_r r_p}{2r_s^2} J_s \right), \\ A_3 &= \frac{r_c}{Jr_s} \rho S b^3 \left(\frac{r_r}{r_p} J_p + \frac{r_p}{2r_r} J_r \right), \quad B_1 = \frac{1}{4J} \frac{c^2 b}{(R+r)V} \left(\frac{2r_c r_r}{r_s r_p} J_p + \frac{r_c r_p}{r_s r_r} J_r \right), \\ B_2 &= \frac{r_c}{Jr_s} \frac{c^2 b}{(R+r)V} \left(\frac{r_r r_p}{4r_c r_s} J_c + \frac{r_c r_r r_p}{r_s} m_p - \frac{r_c r_r}{r_s r_p} J_p \right), \quad B_3 = B_2 + \frac{4r_c}{r_s} B_1, \\ J &= \frac{r_p r_r}{4r_s^2} J_c J_s + \frac{r_p}{4r_r} J_c J_r + \frac{r_c^2 r_p}{r_s^2 r_r} J_s J_r + \frac{r_r}{r_p} J_c J_p + \frac{r_c^2 r_r}{r_s^2 r_p} J_s J_p + \frac{r_c^2}{r_r r_p} J_r J_p \\ &\quad + \frac{r_c^2 r_r}{r_s^2 r_p} J_s m_p r_p^2 + \frac{r_c^2}{r_r r_p} J_r m_p r_p^2 + \frac{4r_c^2 r_r}{r_p^3} J_p m_p r_p^2. \end{aligned}$$

4 Steady Solutions and Control Strategies

Each steady solution (λ^*, μ^*) of Eq. (1) satisfies following relations:

$$\begin{cases} u = af(\lambda^*), & \text{where } a = r_s/4r_c; \\ u = \mu^*. \end{cases} \tag{2}$$

In particular fixed points of a phase plane (λ, μ) can be located only on the curve $\mu = af(\lambda)$ (for any control).

Assume that control function has the following general form:

$$u = \mu^* + \alpha(\lambda - \lambda^*), \tag{3}$$

where (λ^*, μ^*) —program values, α —feedback control coefficient. Fixed points are intersections of the curve $\mu = af(\lambda)$ and the straight line given by Eq. (3).

Conditions of stability of a steady solution are as follows:

$$\begin{cases} -A_1 f'|_{\lambda^*} + B_3 + A_2 \alpha > 0; \\ -af'|_{\lambda^*} + \alpha > 0. \end{cases} \tag{4}$$

If $f'|_{\lambda^*} < 0$, then the corresponding fixed point is stable for $\alpha = 0$. So a constant control $u = \mu^*$ is enough to support a steady solution (λ^*, μ^*) for which $\lambda^* < \lambda_1$ or $\lambda^* > \lambda_2$. In a general case there can be one or three fixed points [given by Eq. (2)] for $u = \mu^*$: Fig. 3.

If $\mu^* > af(\lambda_2)$ or $\mu^* < af(\lambda_1)$ then control strategy is the most simple: constant control $u = \mu^*$ brings the system to the only steady point (Fig. 3a, c), and this point

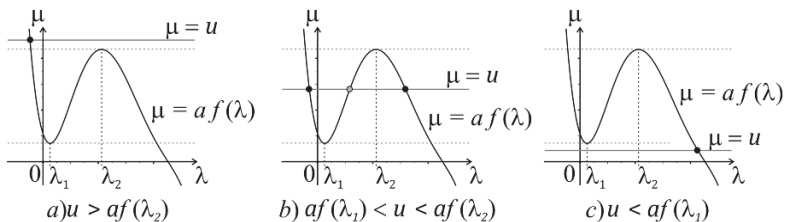


Fig. 3 Fixed points of Eq. (1) for the case of a constant control u

corresponds to a preferable operation mode (note that the Eq. (1) has no cycles on the phase plane if u is constant [4].

If $\lambda^* \in (-\infty, \lambda_1) \cup (\lambda_2, \infty)$ and $f(\lambda_1) < a^{-1}\mu^* < f(\lambda_2)$, then a constant control $u = \mu^*$ maintains a preferable fixed point, and piecewise constant control is needed to switch between two possible stable fixed points (Fig. 3b). Let's introduce a corresponding control strategy for the case when one would like to transfer to a fixed point with $\lambda^* > \lambda_2$ from any initial conditions:

- (1) Set $u = u_1 < af(\lambda_1)$ (for instance, let an external ring be free from a control: $u = 0$). Then the case shown in Fig. 3c takes place and the system comes to the only presenting fixed point for which tip speed ratio is large then λ_2 .
- (2) Switch u to the program value $u = \mu^*$. A point to which the system came on the previous step is lying in the domain of attraction of the preferable fixed point (λ^*, μ^*) , $\lambda^* > \lambda_2$. This feature of the domain of attraction is illustrated by Fig. 4 (arrows show directions of phase velocities).

The transfer of the dynamical system [Eq. (1)] to the fixed point (λ^*, μ^*) , where $\lambda^* < \lambda_1$, can be performed similarly.

The most complicated case is when one would like to stabilize a fixed point with $f'|\lambda^* > 0$. For this task piecewise constant control is not effective. Feedback coefficient α should be large enough to make left parts of both Eq. (4) be positive. Because $A_1A_2^{-1} > a$ [see notations to Eq. (1)], the following condition is very enough:

$$\alpha > A_1A_2^{-1} \max_{\lambda} (f') \tag{5}$$

If α satisfies Eq. (5), then the fixed point (λ^*, μ^*) of Eq. (1) is stable for $\lambda_1 < \lambda^* < \lambda_2$. Moreover for such α this fixed point represents the only solution of Eq. (2) (inclination of the line $\mu = u$ exceeds inclination of a tangent to a curve $\mu = af(\lambda)$ for any λ). In addition for such α the condition of the Bendixson criterion is fulfilled in the whole phase plane: so there are no any cycles. All this means that for u given by Eq. (3) with α satisfying Eq. (5) domain of attraction of a preferable steady point coincides with a whole phase plane. The proposed control problem is completely solved.

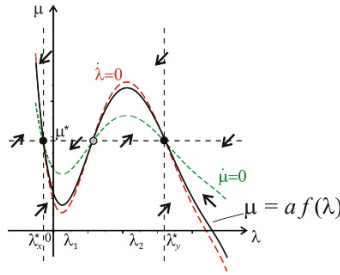


Fig. 4 All points lying on the curve $\mu=af(\lambda)$ to the right of the fixed point (λ_y^*,μ^*) belong to the domain of attraction of this fixed point

5 Discussion and Conclusions

The electromechanical model of a HAWT with a DPG is studied. The quasi-steady approach is applied for modeling of interaction between rigid body and medium. We combined this approach with experimental identification of an aerodynamic torque. Our experiments were performed for a certain range of wind speeds (Fig. 2). It should be noticed that aerodynamic function $f(\lambda)$ essentially changes if wind speed increases sufficiently. So, one has to make experimental reidentification of the function $f(\lambda)$ for another interval of wind speed.

We modeled electromechanical torque, which acts upon the rotor of the generator, as a linear function of angular speed of the rotor. There do exist types of generators with essentially nonlinear electromechanical torque. However such nonlinearity leads to additional power losses. So, linear type of interaction is preferable.

Special control strategies are proposed that allow reaching and stabilizing the preferable operation mode of the system. Corresponding control laws are represented by piecewise constant functions and linear feedback functions. Qualitative methods of the theory of differential equations are used for constructing control functions and confirming the efficiency of control laws. Finally we showed that the DPP is able to solve wide range of control tasks. Our approach opens new easy, safe and beneficial way in control of power conversion systems.

Acknowledgments The work is partially supported by RFBR: projects 12-01-00364, 14-08-01130.

References

1. Chen C-L et al (2013) System for optimal energy generation. In: Proceedings of 5th international conference on advanced power system automation and protection, APAP2013, Jeju, Korea, 28–31 Oct 2013 (CD-ROM). Korean Institute of Electrical Engineers Power Engineering Society, Seoul, 5 p

2. Chen Z et al (2009) A review of the state of the art of power electronics for wind turbines. *IEEE Trans Power Electron* 24(8):1859–1875
3. Dosaev M et al (2013) Power output estimation of steady regimes of a HAWT with differential gearbox. In: *Dynamical systems: applications*. Wydawnictwo Politechniki Lodzkiej, Lodz, pp 647–656
4. Klimina L, Holub A (2014) Regulation of operation modes of a wind energy system by means of a differential planetary gearbox. In: *Mechatronics, automation, control*, no. 4. “New Technologies” Publishing, Moscow, pp 24–32 (in Russian)
5. Müller H et al (2006) Grid compatibility of variable speed wind turbines with directly coupled synchronous generator and hydro-dynamically controlled gearbox. In: *Proceedings of sixth international workshop on large-scale integration of wind power and transmission networks for offshore wind farms*, 26–28 Oct 2006, Delft, NL, TU Delft, Delft, pp 307–315
6. Polinder H et al (2006) Comparison of direct-drive and geared generator concepts for wind turbines. *IEEE Trans Energy Convers* 21(3):725–733
7. Rossi C et al (2009) W-CVT continuously variable transmission for wind energy conversion system. <http://www.die.ing.unibo.it/pers/grandi/papers/PEMWA2009.pdf>
8. Tsai M-Ch, Huang Ch-Ch (2012) Development of a variable-inertia device with a magnetic planetary gearbox. *IEEE-ASME Trans Mechatron* 16(6):1120–1128

Hybrid Position/Force Control of a Cable-Driven Parallel Robot with Experimental Evaluation

Werner Kraus, Philipp Miermeister, Valentin Schmidt and Andreas Pott

Abstract For cable-driven parallel robots elastic cables are used to manipulate the end-effector in the workspace. In this paper we present a hybrid position/force control which allows for applying defined forces on the environment and simultaneous movement along the surface. We propose a synchronous control of the cable forces to ensure the stability of the end-effector during movement. The performance of the controller is experimentally presented regarding contact establishment and dynamic behaviour during a motion on the cable robot IPAnema 3.

Keywords Cable robot · Parallel robot · Force control · Redundant robot · Contact control

1 Introduction

Due to their huge workspace, high dynamics and lightweight structure, cable-driven parallel robots, in the following referred to as cable robots, received high interest in the past. In this paper, we present the design and experimental evaluation of a Cartesian force control for a cable robot. Processes like grinding and polishing demand an accurately controlled contact force to give reliable results. Force control allows also to compensate for deviations in the work piece geometry by keeping the tool constantly in contact with the surface. There exist simple mechanical solutions like air controlled cylinders which allow for a constant process force. The drawback is, that the system adds additional weight to the end-effector and the direction of the force is typically fixed with respect to the end-effector frame. The aim of the hybrid position and force control is to apply process forces in a programmable direction to a surface while the movement perpendicular to the force vector is position controlled. The theory behind this approach was already developed in the 80s [5].

W. Kraus (✉) · P. Miermeister · V. Schmidt · A. Pott
Fraunhofer Institute for Manufacturing Engineering and Automation IPA, Stuttgart, Germany
e-mail: Werner.Kraus@ipa.fhg.de

The contact problem was investigated for both serial [1, 5] and classical parallel robots [6]. The major concern regarding stability is the transient system properties when the end-effector comes in contact with the environment. In [2] this problem is solved by a state machine based approach using acceleration and brake controllers for bringing the robot into contact.

In addition to the known contact problem, we have to ensure, that the cables remain under tension. The state machine based approach presented in [2] is adapted for the cable robot. To keep the cables under tension, we introduce a decoupled cable force controller to tension the cables during the contact force control. For this, the cable force control presented in [3] is modified regarding the setpoint determination. A task coordinate system is established to realize the hybrid position and force control. The controller is implemented using a CNC and PLC on an industrial PC. To make the force control accessible by standard industrial machine interfaces new commands based on standardized G-Code are established.

This paper is organized as follows: The robot model including kinematic and the determination of cable force distributions are summarized in Chap. 2. The design and implementation of the Cartesian force controller is described in Chap. 3. Experimental results are presented and discussed in Chap. 4. Finally, conclusions and an outlook on future work is given in Chap. 5.

2 Robot Model

For completeness, we briefly review the robot model. The geometry of the robot is described by the proximal anchor points on the robot base \mathbf{A}_i and the distal anchor points on the end-effector \mathbf{B}_i . The index i denotes the cable number and m is the absolute number of cables. By applying a vector loop as shown in Fig. 1 the cable vector \mathbf{l}_i follows as

$$\mathbf{l}_i = \mathbf{a}_i - \mathbf{r} - \mathbf{R}\mathbf{b}_i, \quad (1)$$

while \mathbf{r} is the platform position vector and rotation matrix \mathbf{R} describes the orientation with respect to the base coordinate frame.

The structure equation with the structure matrix \mathbf{A}^T describes the force and torque equilibrium at the end-effector for a given cable force distribution \mathbf{f} and can be written as

$$\underbrace{\begin{bmatrix} \mathbf{u}_1 & \cdots & \mathbf{u}_m \\ \mathbf{b}_1 \times \mathbf{u}_1 & \cdots & \mathbf{b}_m \times \mathbf{u}_m \end{bmatrix}}_{\mathbf{A}^T(\mathbf{r}, \mathbf{R})} \underbrace{\begin{bmatrix} f_1 \\ \vdots \\ f_m \end{bmatrix}}_{\mathbf{f}} = - \underbrace{\begin{bmatrix} \mathbf{f}_p \\ \boldsymbol{\tau}_p \end{bmatrix}}_{\mathbf{w}}, \quad (2)$$

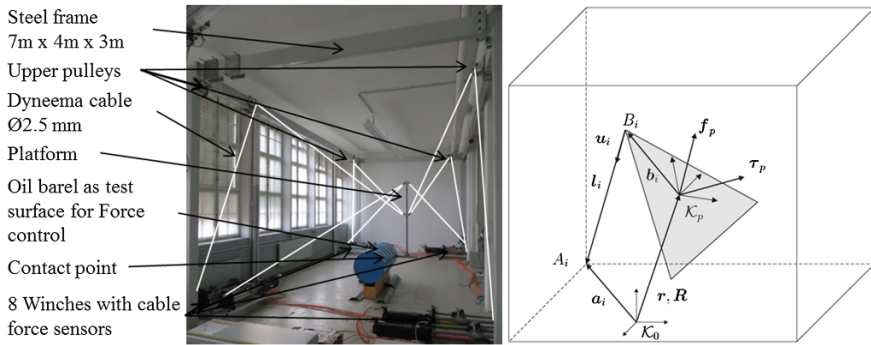


Fig. 1 Cable-driven parallel robot IPAnema 3: complete robot (*left*) and robot kinematic (*right*)

with $u_i = \frac{l_i}{\|l_i\|}$. The applied wrench w consists of external forces f_p and torques τ_p and also includes the weight of the platform.

To compute a force distribution f , which solves the structure Eq. (2) and is continuous along a trajectory, the closed-form solution presented in [4] is used. In this approach, a medium feasible force distribution $f_{med} = (f_{min} + f_{max})/2$ is introduced which is based on the minimum cable force f_{min} and maximum cable force f_{max} , respectively. With the Moore-Penrose matrix inverse A^{+T} the force distribution is obtained by

$$f = f_{med} - A^{+T}(w + A^T f_{med}). \tag{3}$$

This algorithm is applied for the setpoint generation for the cable force controller.

3 Controller Design and Implementation

3.1 Controller Design

The Cartesian force control targets on the control of the wrench in a given direction e.g. perpendicular to the surface of the environment. While using a cable robot for applying the contact force, additionally the cables have to be kept under tension. Especially for the simultaneous position controlled movement in the tangential plane this is important, as friction forces have to be overcome. To realize the hybrid Cartesian force control for a cable robot, the control problem is divided into three parts:

- The position control with CNC which sets the cable length $l_{set,CNC}$ to move the platform along a path

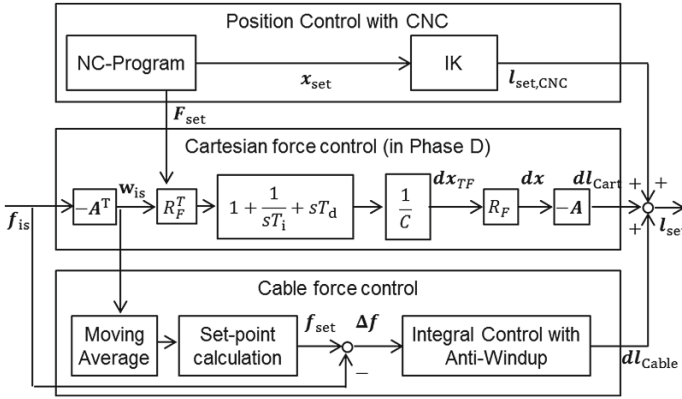


Fig. 2 Structure of the implementation with Cartesian and cable force controller

- The Cartesian force control which generates a change in cable length setpoint dl_{Cart} allowing to control the external platform wrench i.e. contact force using platform position control.
- The cable force control for keeping the cables under tension. For this, a feasible force distribution is calculated for the measured wrench. The controller output is the modification dl_{Cable} of the cable length setpoint.

The output of the three controllers are summed up by

$$l_{set} = l_{set,CNC} + dl_{Cart} + dl_{Cable}, \tag{4}$$

to the cable length setpoint l_{set} which is commanded to the servo drives. The control structure is visualized in Fig. 2. In the following, the Cartesian and cable force control are described in detail.

3.2 Cartesian Force Control

The Cartesian force control is based on an indirect force measurement over the cable force sensors. For the transformation from joint to Cartesian space, the structure matrix A^T describing the actual cable directions is used. The wrench w is derived by

$$w = -A^T f_{is}, \tag{5}$$

where f_{is} corresponds to the measured cable forces.

We introduce a task coordinate system \mathcal{K}_t which lies in the contact point and the z-axis coincides with the desired force direction. The transformation from world \mathcal{K}_0

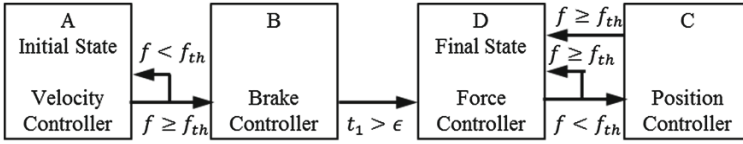


Fig. 3 Cartesian force control: State machine with transition conditions for the establishment of the contact

to task coordinate system \mathcal{K}_t is described by the rotation matrix \mathbf{R}_F . The desired force vector $\mathbf{F}_{set,0}$ is transformed by

$$\mathbf{F}_{set,t} = \mathbf{R}_F^T \mathbf{F}_{set,0}, \tag{6}$$

to the task coordinate system, where the z component represents the scalar desired force F_{set} . With the coordinate transformation the Cartesian force control can be designed as a one-dimensional controller.

The state machine is structured in four phases as illustrated in Fig. 3. In phase A, a velocity controller moves the platform in the direction of the surface with a maximal velocity v_{max} . The contact between the end-effector and the surface is detected when the threshold force F_{th} is exceeded. As the measured wrench is disturbed by measurement errors, we also observe the derivative of the force to identify the contact. Then, in phase B a brake controller slows down the end-effector. Next in phase D, the closed-loop force control is activated. A PID controller with a constant stiffness estimation C is applied. The parameters for the gain C , integrator reset time T_i and derivative time T_d were experimentally determined. When the robot loses the contact to the surface, this means the force is less than the threshold force, the state machine switches to Phase C and a position controller brings the end-effector again in contact.

3.3 Cable Force Control

Redundant cable robots have the property that the cables can be tensed against each other without exerting an external force. In the present control architecture, the external forces are controlled by the Cartesian force control. Therefore, the cable force control aims at the control of the internal tensions and has to be decoupled from the Cartesian force control. As the wrench is controlled by the Cartesian force control, we propose to use the measured wrench \mathbf{w}_{is} for the determination of the setpoint of the cable forces \mathbf{F}_{set} according to Eq. 3. This makes sure, the controlled cable force is compatible to the actual external forces and does not influence the motion of the end-effector. To avoid instabilities due to the synchronous control of the external wrench and the internal cable forces, a moving average of 2 s is applied

on the wrench to slow down the control loop. The control error in cable force $\Delta \mathbf{f}$ is established by

$$\Delta \mathbf{f} = \mathbf{f}_{\text{set}} - \mathbf{f}_{\text{is}}. \quad (7)$$

The integral control with anti-windup is realized according [3].

The cable force control is necessary to keep the cables under tension during the position controlled movement of the platform. During the contact establishment, the system properties and also the wrench changes abruptly. This leads to the destabilization of the contact controller. In this transient phase, the cable force controller also influences the external forces and additionally disturbs the contact controller. To avoid this problem, the cable force control is disabled during contact establishment. With this approach, we can eliminate additional sources of instabilities due to the internal cable force control. After contact establishment, the cable force control is enabled again.

3.4 Implementation

The control algorithms are implemented on the cable robot IPAnema 3 using eight cables and a straight line platform as shown in Fig. 1.

The robot control is realized on an industrial PC with Beckhoff TwinCAT 3.1 CNC at a cycle time of 1 ms. The field bus protocol is EtherCAT. For the force measurement each winch is equipped with a cable force sensor of type Tectis F2301 with a measurement range of $\pm 5,000$ N. The analog output signal of the force sensors is digitized in A/D-converters and sent via the field bus to the control. The cable type is LIROS D-Pro 01505-0250 based on Dyneema SK 75 fibre (Polyethylene) with a diameter of 2.5 mm.

The CNC executes the position control for a path programmed in G-code. Three additional axes were added to the CNC which are interpreted as desired force vector. This allows for the smooth interpolation of the force vector along a trajectory.

4 Experimental Evaluation

4.1 Contact Establishment

The course of the force during force control is shown in Fig. 4. The time derivative of the contact force $d(\mathbf{F}_{\text{is}})/dt$ is noisy, but clearly signals when the end-effector comes in contact.

One interesting point is the contact establishment under the condition of changing stiffness in the contact. For this, the Cartesian force control was applied

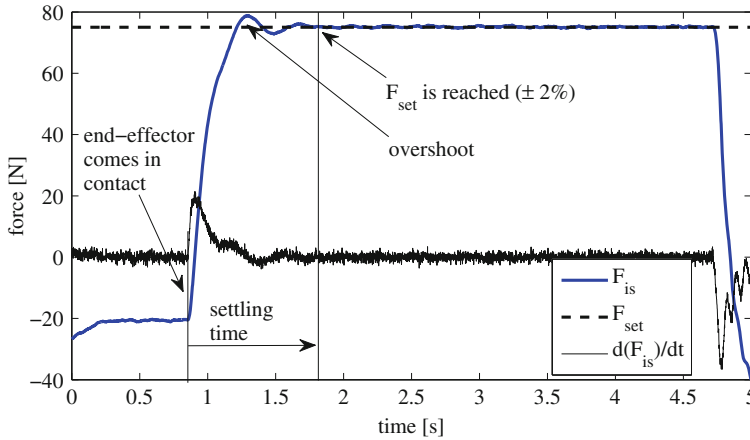
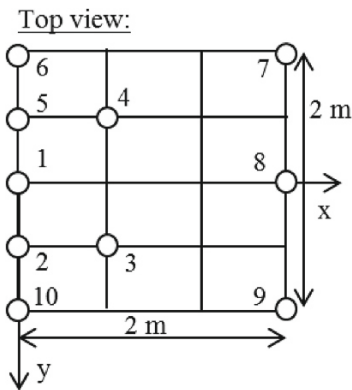


Fig. 4 Course of the force during contact establishment, force control and release



position	overshoot		settling time	
	mean [%]	σ [%]	mean [s]	σ [s]
1	9.357	1.171	0.781	0.191
2	8.698	0.840	1.378	0.242
3	5.692	0.351	0.981	0.093
4	4.299	0.927	0.866	0.138
5	8.573	0.486	0.977	0.081
6	8.329	0.461	1.035	0.019
7	18.106	2.227	0.804	0.156
8	15.024	2.857	0.742	0.209
9	5.100	0.353	0.889	0.010
10	3.910	0.067	3.517	0.413
average	8.709	-	1.197	-

Fig. 5 Experimental evaluation of the contact establishment at different positions and resulting overshoot and settling time

on the floor at ten different positions which are visualized in Fig. 5. Position 1 lies in the center of the workspace, whereas 7 and 9 are on the edge of robot’s footprint.

The evaluation criteria for the contact establishment are the overshoot and settling time. For the experiment the approaching velocity is 50 mm/s and the desired force amounts 75 N. The experimental results are presented in Table 5. We can observe a maximum overshoot of 18.2 % whereas the average lies at 8.7 %. The settling time is defined as the time from the first contact to the surface until the control error is smaller than 2 %. The mean settling time is in average 1.2 s.

The results show a compromise between an acceptable overshoot and a settling time. By changing the approaching velocity, this compromise can be influenced in favor of one evaluation criteria.

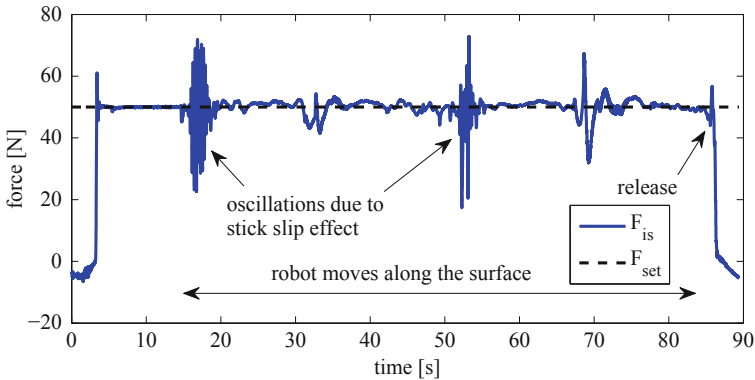


Fig. 6 Course of the force normal to the surface on the oil barrel

4.2 Following Behaviour

The following behaviour of the force control during a simultaneous motion of the end-effector was investigated on oil barrels. The test set-up is shown in Fig. 1. The test scenario is exemplary for a spherical surface which can be found at wings of airplanes or blades of wind turbines. The path along the oil barrel is programmed offline. In addition, we also programmed the desired force vector which is aligned to the normal vector of the surface.

The quantitative behaviour of the contact force along the surface is shown in Fig. 6. The desired force is 50 N. As the contact point of the end-effector to the oil barrel is eccentric, the stiffness is low and stick slip effects in the contact generate oscillations. The oscillation is relatively high, when the robot moves position controlled into a direction where it is not very stiff. Since the cables are tensed, these critical positions were overcome.

5 Conclusion

In this paper we proposed the implementation of a hybrid Cartesian force control. By using the measured wrench as input for the setpoint determination of cable forces we were able to tense the cables during the contact control. The experimental evaluation on the IPAnema 3 are promising. Further investigation could analyze a specific process by attaching a tool and running the process. Another interesting point is the online identification of the stiffness in the contact and how such knowledge can improve the control quality.

References

1. Albu-Schaffer A, Ott C, Frese U, Hirzinger G (2003) Cartesian impedance control of redundant robots: recent results with the DLR-light-weight-arms. In: International conference on robotics and automation (ICRA) vol 3, pp 3704–3709
2. Assuncao V, Schumacher W (2003) Hybrid force control for parallel manipulators. In: 11th mediterranean conference on control and automation (MED)
3. Kraus W, Schmidt V, Rajendra P, Pott A (2014) System identification and cable force control for a cable-driven parallel robot with industrial servo drives. In: International conference on robotics and automation (ICRA)
4. Pott A, Bruckmann T, Mikelsons L (2009) Closed-form force distribution for parallel wire robots. In: Proceedings of 5th international workshop on computational kinematics 2009, 6–8 May 2009. Springer, Duisburg, Germany, pp 25–34
5. Raibert MH, Craig JJ (1981) Hybrid position/force control of manipulators. *J Dyn Syst Measur Control* 103:126–133
6. Tang H, Yaol J, Cheng L, Zhao Y (2012) Hybrid force/position control investigation of parallel machine tool with redundant actuation. *Appl Mech Mater* 121–126

The Control System of a Parallel Robot for Brachytherapy

C. Vaida, D. Pisla, A. Szilaghyi, F. Covaciu, D. Cocorean and N. Plitea

Abstract Huge efforts have been made by the entire scientific community to provide better solutions aiming to improve survival and life expectancy in the fight against cancer. Such an approach is brachytherapy (BT), the targeted irradiation of tumors achieved by placing radioactive cell inside or very close to the tumor itself. The paper presents the control system of a parallel robot designed specifically for brachytherapy. The PARA-BRACHYROB modular structure is capable to target multiple organs in the thoracic-abdominal area under CT-Scan real-time monitoring providing an accurate tool for the delivery of the BT seeds at the defined locations. The control system is designed according to a specific protocol covering both therapeutic and safety issues.

Keywords Parallel robot · Brachytherapy · Design · Control

C. Vaida (✉) · D. Pisla · A. Szilaghyi · F. Covaciu · D. Cocorean · N. Plitea
Technical University of Cluj-Napoca, Memorandumului 28, 400114 Cluj-Napoca, Romania
e-mail: calin.vaida@mep.utcluj.ro

D. Pisla
e-mail: doina.pisla@mep.utcluj.ro

A. Szilaghyi
e-mail: andras.szilaghyi@mep.utcluj.ro

F. Covaciu
e-mail: florin.covaciu@mep.utcluj.ro

D. Cocorean
e-mail: dragos.cocorean@mep.utcluj.ro

N. Plitea
e-mail: nicolae.plitea@mep.utcluj.ro

1 Introduction

Cancer is the world's leading cause of death, followed by heart disease and stroke [15]. Brachytherapy is a form of radiotherapy where a radiation source is placed inside or near to the targeted area. Brachytherapy is commonly used as an effective treatment for cervical, prostate, breast, and skin cancer used also to treat tumors in many other body sites.

The prostate gland is one of the most commonly cancer affected male organs in developed countries, and numerous number of treatment options are available, depending on the patient's age, medical history and anatomy, as well as on the cancers stage [3]. The primary treatment options may include: active monitoring without treatment, radical prostatectomy, chemotherapy [7], external beam radiation therapy (EBRT), and more recently, less invasive treatments such as cryotherapy, high intensity focused ultrasound (HIFU) and internal radiation therapy, namely brachytherapy. The latter method has, in recent years, increased in popularity among patients with early stages of cancer due to its low morbidity, short hospitalization and relatively few side-effects [8]. There are some researches around the world focused on robotic assisted brachytherapy. Nikolai Hungr et al. [8] introduced a new 3D ultrasound robotic prostate brachytherapy system.

Gabor Fichtinger et al. in [4] presented a robotically assisted prostate brachytherapy system consisting of a TRUS unit, a spatially coregistered (registered in correlation with the TRUS unit) needle insertion robot, and a software tool, FDA approved, for the treatment planning and image-registered implant system. Zhang et al. in [16] introduced a 2-DOF needling and seed delivery serial device for the insertion of radioactive seeds in the prostate. Bassan et al. [1] built a 5-DOF two stage hybrid robotic system to perform 3D ultrasound guided percutaneous needle insertion surgery. The macro stage is responsible for the orientation of the needle with parallel mechanism and the micro stage for needle insertion and rotation. Jiang et al. [9] developed in a prototype and 3D model of a 5-DOF hybrid robot for prostate needle insertion surgery under continuous MRI guidance. The robot consists in three stages: the pitch/lift module, the yaw/horizontal module and the insertion module. Fischer et al. [5] introduced a 4-DOF hybrid robot for real-time control transperineal prostate needle orientation under MRI guidance and perform insertion motion manually.

The control system of medical robots is a key component of any complex device, all having as main characteristic the dependability with emphasis on safety. Depending of the motion type different control solutions can be adopted from dedicated PLCs, to industrial PCs or Field Programmable Gate Arrays (FPGA) [6]. Brachytherapy performed under CT-Scan requires even more safety protocols as the patient is left alone in the room with the robot (both placed on the CT-Scan mobile couch) and in case of any error, unwanted events might occur.

The vast majority of robotic systems for BT are designed especially for prostate cancer treatment [14] and the current progress and therapeutic indexes point out clearly the need of new robotic solutions capable of targeting other organs and more

important deeply located tumors which are impossible to reach manually. Based on these conclusions, the authors propose an innovative parallel robotic system, capable of positioning the brachytherapy needles, in various organs, in any part of the thoracic-abdominal area, working under real-time CT monitoring.

The paper is organized as follows: Sect. 2 presents the innovative parallel robot for brachytherapy entitled PARA-BRACHYROB continuing with its design in Sect. 2. Section 3 presents the control system of the robot and in Sect. 4 is illustrated the experimental model of the robot, followed by conclusions, future work and references.

2 PARA-BRACHYROB a Modular Parallel Robot for Brachytherapy

Analyzing the brachytherapy procedure, the robot task can be defined as follows: the robot should introduce, based on radiological data, rigid needles inside the patient body following a linear trajectory. Due to the varying distances, which can reach up to 250 mm inside the patient body, the proposed innovative robotic solution is a 5-DOF structure working as a two stage device: the needle positioning and orientation stage [12] and the needle insertion stage. Figure 1 presents the kinematic scheme of the PARA-BRACHYROB cylindrical 5-DOF parallel robot, which consists of two modules, the first one having 3-DOF, with 3 active joints, denoted with q_1, q_2, q_3 and a second one (CRU) with 3-DOF and two active joints, q_4, q_5 . The two modules have a total of 4 (four) active translational joints and one active rotational joint. A fixed coordinates system OXYZ is introduced along the active rotational joint (q_3), with the q_1 and q_2 moving along the Z axis. The second module is positioned on the X axis, at a distance d_{12} from the origin, with the active joints q_4 and q_5 moving along an axis parallel with the Z axis. The two modules are interconnected with two Cardan joints having the first rotation axis around the Z axis and the second one perpendicular to it, actuating the needle holder module. This module integrates an additional motor q_6 , which performs the second motion stage, namely the needle insertion. The use of one redundant motion enhances the overall robot behavior enabling better control for the needle position.

Based on Fig. 1 and using the geometrical parameters of the robot components the final equations of the inverse geometrical model are computed:

$$q_1 = l_1 + Z_E + (d_{ac} + 2 \cdot l_c) \cdot \cos(\theta) \tag{1}$$

$$q_2 = l_1 + Z_E + (d_{ac} + 2 \cdot l_c) \cdot \cos(\theta) + \sqrt{d_1^2 - (r_{A1} - b_1)^2} \tag{2}$$

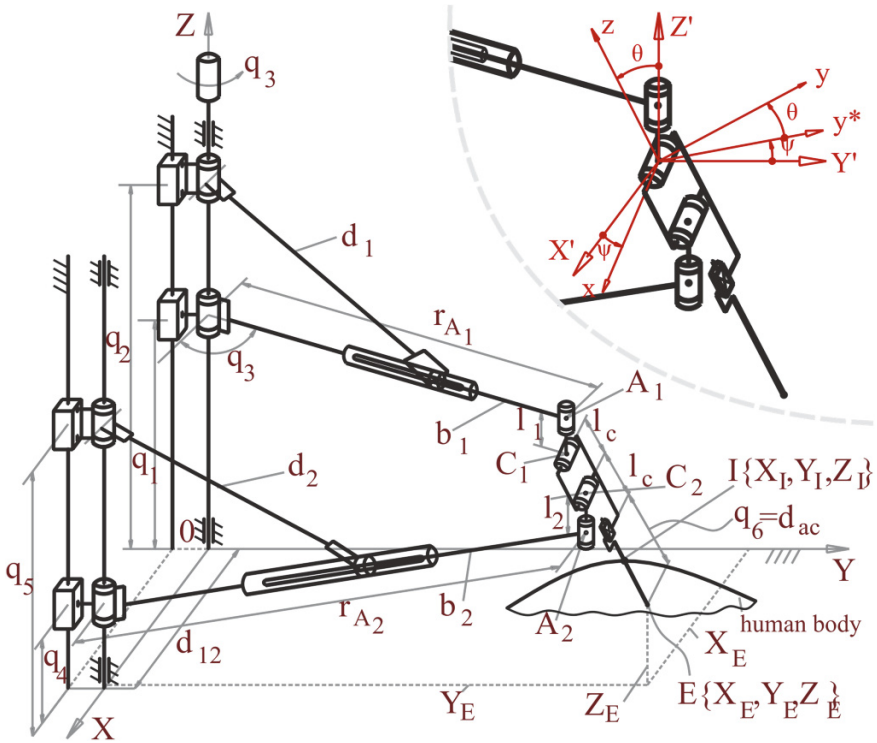


Fig. 1 Kinematic scheme of the PARA-BRACHYROB robot

$$q_3 = a \tan 2 \left(b_1 + \sqrt{d_1^2 - (q_2 - q_1)^2} \cdot \sin(q_3), b_1 + \sqrt{d_1^2 - (q_2 - q_1)^2} \cdot \cos(q_3) \right) \quad (3)$$

$$q_4 = l_2 + Z_E + (d_{ac} + 2 \cdot l_c) \cdot \cos(\theta) \quad (4)$$

$$q_5 = l_2 + Z_E + (d_{ac} + 2 \cdot l_c) \cdot \cos(\theta) + \sqrt{d_2^2 - (r_{A2} - b_2)^2} \quad (5)$$

$$q_6 = d_{ac} \quad (6)$$

The kinematic models [11] will be integrated in the control system of the robot, where every needle insertion task uses the two stage approach described before.

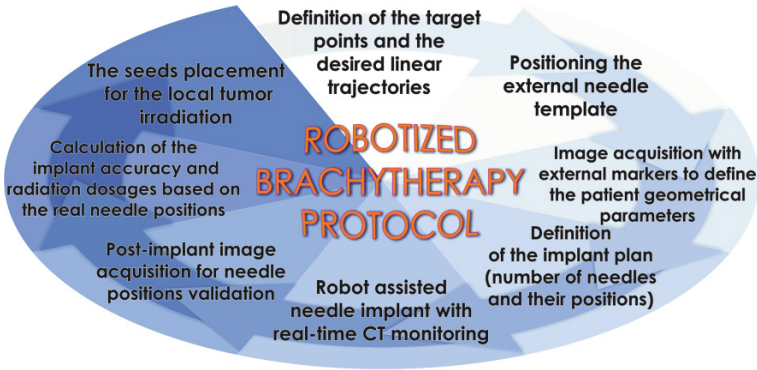


Fig. 2 Protocol defining the needle insertion in robotic brachytherapy

3 PARA-BRACHYROB Control System and User Interface

In many cases very tight protocols are defined to enable non-specialists (e.g. physicians) to use safely the robotic devices. For PARA-BRACHYROB a brachytherapy protocol has been defined in [13] and illustrated in Fig. 2.

A schematic representation of the PARA-BRACHYROB control and actuation system is presented in Fig. 3. The control system of the robot is structured on three levels. The first one, **the User level**, integrates a power panel – an industrial computer, with a touch screen display and the Windows XP Embedded operating system, through which the user can interact with the robot. The second is the **Command and Control level**, containing the PLC—the command and control unit, which based on

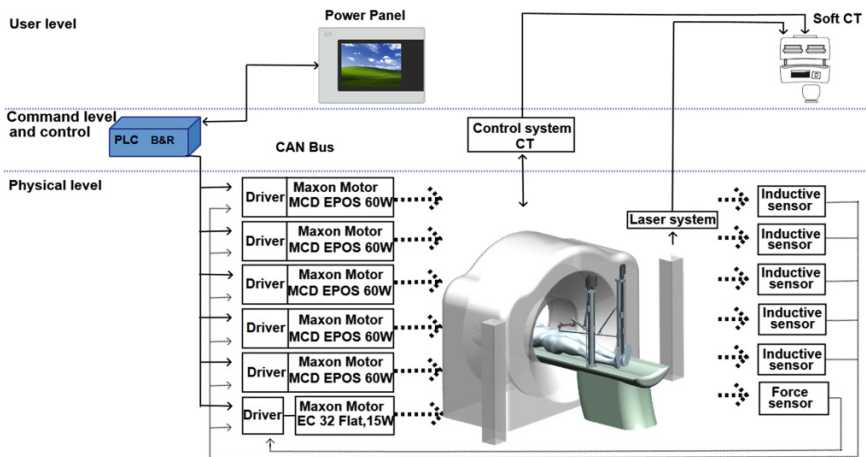


Fig. 3 PARA-BRACHYROB robot control and actuation system scheme

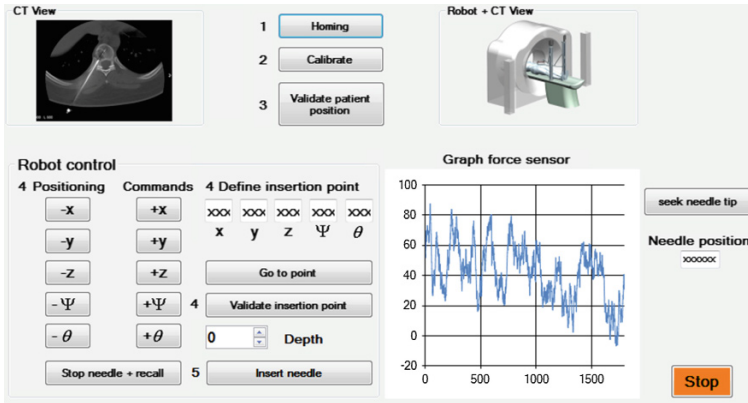


Fig. 4 Control system—user interface

the input data and using the implemented control algorithm generates the electrical signals, which via the CAN Bus are transmitted to the actuators. The third is the **Physical level** contains the mechanical structure of the “PARA-BRACHYROB” parallel robot, the inductive sensors - used as limit switching devices, connected directly to the motors and the needle insertion module. For the control system an integrated solution from BR-Automation [2] was adopted, while for the motors, compact solutions from Maxon [10] were selected. The needle insertion module integrates a force sensor which monitors the force along the needle axis to monitor and avoid any deformations, deviations or trajectory alterations.

The PARA-BRACHYROB user interface is presented in Fig. 4, showing the control window for the brachytherapy procedure. The commands numeric codes are used to show the execution order, as for safety reason the higher level controls will be available only after the successful completion of the previous ones. At the beginning of the procedure, the **Homing** button will achieve the initial setup of the robot by moving it into the Nest position. The next step achieved by **Calibration** will define the relative position between the robot and the CT Scan laser coordinates system. From this moment on, the robot will remain fixed during the entire medical procedure. The patient is positioned on the CT Scan mobile table and his position is also calibrated with respect to the CT-Scan laser system. One this action is completed, using the **Validate Patient Position** button will define the relationship between the robot coordinates system and the patient. In the fourth step, the actual needle insertion procedure is performed, as a two stage motion. Having as inputs, for each needle, the coordinates of the insertion point I (X_I, Y_I, Z_I) and target point E (X_E, Y_E, Z_E) the final needle orientation is easily computed:

$$\begin{aligned} \psi_{IE} &= \text{atan2}(Y_E - Y_I, X_E - X_I); \\ \theta_{IE} &= \text{atan2}\left(\sqrt{(Y_I - Y_E)^2 + (X_I - X_E)^2}, Z_I - Z_E\right); \end{aligned} \tag{7}$$

Having the coordinates of point I and the values for ψ and θ these values are saved in **Define Insertion Point**. Using the **Go to Point** command, the robot will position the needle tip at the given coordinates. The position is checked and if necessary small corrections are applied using the **Positioning Commands**. Once the needle is properly positioned and oriented the **Validate insertion point** is pressed, blocking all the robot actuators in their current positions. The second stage of the motion refers to the actual needle insertion achieved by the actuation of the needle insertion module. The needle insertion procedure is a sequential motion, which uses a predefined increment which depends on the tumor location. This increment can be determined automatically by the virtual environment software based on the critical areas where different internal structures are located very close to the needle path. Each step is performed using the **Insert Needle** command. During the motion the force sensor will display real-time values to automatically stopping the motion if abnormal values are registered. As the robot and the patient are both located on the mobile couch of the CT-Scan, the needle advance can be checked and validated by repeated scans of the interest area.

At any moment the robot can be stopped and during the needle insertion a command, **Stop Needle + Recall**, allows the quick retraction of the needle.

While the entire positioning and insertion procedure seems complicated and time consuming, it must be underlined that it avoids general anesthesia, open surgery and enables the local treatment of tumors which will lead to much better prognosis in both curative and palliative treatments for the patients. Furthermore, the procedure is minimally invasive being tolerated also by patients where only a palliative treatment can be applied.

The mechanical structure of the PARA-BRACHYROB parallel robot has been designed with respect to several criteria:

- The robot must have provide a sufficiently large workspace to cover any organs inside the thoracic and abdominal body areas (Fig. 5);

Fig. 5 The workspace of the robot, determined analytically



Acknowledgments This paper was supported by the Project no. 173/2012, code PN-II-PCCA-2011-3.2-0414, entitled “Robotic assisted brachytherapy, an innovative approach of in-operable cancers—CHANCE” financed by UEFISCDI and the Scopes International Grant IZ74Z0-137361/1, Creative Alliance in Research and Education focused on Medical and Service Robotics-CARE-Robotics.

References

1. Bassan H et al (2007) A novel manipulator for 3D ultrasound guided percutaneous needle insertion. In: IEEE international conference on robotics and automation, ISSN 1050-4729, pp 617–622
2. BR-Automation (2014) www.br-automation.com
3. Carpenter TJ, Forsythe K, Kao J, Stone NN, Stock RG (2011) Outcomes for patients with extraprostatic prostate cancer treated with trimodality therapy, including brachytherapy, external beam radiotherapy, and hormone therapy. *Brachytherapy* 10(4):261–268
4. Fichtinger G et al (2006) Robotically assisted prostate brachytherapy with transrectal ultrasound guidance - Phantom experiments. *Brachytherapy* 5(1):14–26
5. Fischer GS et al (2006) Design of a robot for transperineal prostate needle placement in MRI scanner. In: IEEE international conference on mechatronics, ISBN 0-7803-9712-6, pp 592–597
6. Franc M, Haze A (2013) A study on the FPGA implementation of the bilateral control algorithm towards haptic teleoperation. *Automatika* 54(1):49–61
7. Gerbaulet A, Pötter R, Mazon JJ, Meertens H, Limbergen EV (2002) The GEC ESTRO handbook of brachytherapy. ACCO, Leuven, Belgium, ISBN 90-804532-6
8. Hungr N et al (2012) 3D Ultrasound robotic prostate brachytherapy system with prostate motion tracking. *IEEE trans robotics* 28(6):1382–1397 (ISSN 1552-3098)
9. Jiang S et al (2012) Kinematic analysis of a 5-DOF hybrid-driven MR compatible robot for minimally invasive prostatic interventions. *Robotica* 30(7):1147–1156
10. Maxon motors Inc, www.maxonmotors.com (2014)
11. Pislá D et al (2014) Application oriented design and simulation of an innovative parallel robot for brachytherapy, accepted for proceedings of the ASME 2014 Int. Design Eng. Tech. conferences and computers and Inf. in Eng. Conf.—IDETC/CIE, New York, USA, 17–20 Aug 2014
12. Plitea N et al (2013) Parallel robot for brachytherapy with two kinematic guiding chains of the platform (the needle) type CYL-U, Patent pending, A/10006/2013
13. Plitea N et al (2014) Structural analysis and synthesis of parallel robots for brachytherapy. In: *New trends in medical and service robots, MMS 16*, Springer, Berlin, pp 191–204
14. Podder TK, Fichtinger G (2010) Robotic brachytherapy—overview of robotic brachytherapy approaches and synergistic applications, AAPM annual meeting, 19 July 2010
15. Rijo J, Ross H (2010) The global economic cost of cancer—American Cancer Society, Inc No. 005444 (2010)
16. Zhang YD et al (2006) Semi-automated needling and seed delivery device for prostate brachytherapy. In: IEEE/RSJ international conference on intelligent robots and systems, pp 1279-1284

Ambient Assisted Living Platform for Remote Monitoring of Bedridden People

F. Pereira, C. Barros, V. Carvalho, J. Machado, C.P. Leão, F. Soares, K. Bezerra and D. Matos

Abstract The aim of this paper is to present a platform for remote monitoring of bedridden people developed in the context of Ambient Assisted Living (AAL). This platform, Medical Care Terminal (MCT), includes the measurement of biomedical data (body temperature, galvanic skin resistance, electrocardiogram and electromyogram, level of oxygen, body position and breathing) as well environmental data (level of alcohol in the air, carbon monoxide level in the air, brightness and temperature). It presents three main issues, namely: it has a user-friendly interface; it is simple to use by a single elderly person; it can be adapted to the needs of a specific patient (custom-made solution), as the system can be configured in function of the measurements required for that specific patient (modular configuration). Finally, it is a low cost solution, affordable for low budget markets.

F. Pereira (✉) · C. Barros · V. Carvalho · C.P. Leão · F. Soares
R&D Centro ALGORITMI, School of Engineering, University of Minho, Guimarães,
Portugal
e-mail: filipe.as.pereira@gmail.com

C. Barros
e-mail: carla.barros@dps.uminho.pt

V. Carvalho
e-mail: vcarvalho@ipca.pt

C.P. Leão
e-mail: cpl@dps.uminho.pt

F. Soares
e-mail: fsoares@dei.uminho.pt

V. Carvalho · D. Matos
IPCA-EST, Barcelos, Portugal
e-mail: dmatos@ipca.pt

J. Machado · K. Bezerra · D. Matos
R&D CT2M Centre, School of Engineering, University of Minho, Guimarães, Portugal
e-mail: jmachado@dem.uminho.pt

K. Bezerra
e-mail: karolceli@gmail.com

Keywords Ambient assisted living (AAL) · Bedridden people · Physiological systems · Remote monitoring

1 Introduction

In the near future, the society, especially in European countries, will face a serious demographic change known as aging society.

As population's average age will drastically increase and, also, due to the characteristic diseases of industrialized countries, such as cardiovascular diseases, diabetes, sedentary way of life, stress, and others, the healthcare of bedridden people will be a serious issue to solve, in the next few years.

Concerning aging society problems, in the European context, EU27 population will continue to get older. In 2008, the share of 65 + population was over 17 %, being expected a rising to 30 % in 2060. In the case of 85 + population the shares will rise from 4 to 12 % [1]. Eurostat also estimates that from 2015 onwards, deaths outnumber births. These facts will imply important changes in social behavior, lifestyle and own identity of senior people. They will remain independent and capable to work for a longer time. However, an important drawback is that as the life expectancy increases, the prevalence of health impairments also increases, requiring an intensive support for their daily life tasks [2].

This scenario, termed as Ambient Assisted Living (AAL), provides important opportunities in the design and development of innovative mechatronic devices in order to facilitate the care of bedridden people, no matter if it comes from the effects of age or from accidents.

This paper presents an AAL platform for remote monitoring of bedridden people. It includes a platform for handling all incoming signals to allow the remote biomedical and environmental data monitoring. In order to achieve the proposed goal, the paper is organized as follows: Sect. 1 presents the context and motivation for this work; Sect. 2 presents the solution adopted for solving this issue: the development of a Medical Care Terminal and respective characteristics allowing dealing with the proposed problem; further, Sect. 3 demonstrates how the problem of data acquisition is handled; Sect. 4 proposes an architecture for the remote monitoring system and illustrates the implementation of some experiments; Sect. 5 details the implementation for the system; Sect. 6 describes the web interface developed for this system; and, finally, Sect. 7 presents some conclusions and the perspectives for future work.

2 Medical Care Terminal (MCT)

The Medical Care Terminal (MCT) is a concept based on telemedicine providing clinical healthcare at a distance [3]. The MCT's main goal is the remote monitoring of bedridden people providing comparable health outcomes to traditional in-person patient encounters. In this kind of monitoring, the sensors are used to capture and transmit biometric data and remote contact via video is used to continuous, real-time, monitoring [4].

The system is able to collect physiological data of the patient and it allows a remote medical interface, allowing medical instructions to prescribe to the patient, if convenient. This remote system helps to continuously monitor important physiological parameters, such as the body temperature (BT), the galvanic skin resistance (GSR), the electrocardiogram (ECG), the electromyogram (EMG), the blood oxygen level, the body position and the airflow during the breath. These parameters are tracked through sensors connected to the patient's body, and the data is sent to the physician or, e.g., to hospital's information systems. Some examples of application can be found elsewhere [4–8].

Almost all applications developed in this area are related to the acquisition of physiological signals. Most of which does not consider the monitoring of environmental variables. This is an important issue, since the indoor air quality has become a critical part of clinical environments management protocols for the wellbeing of patients, who may be the source of microbial spreading and are vulnerable to be infected [9]. The MCT's environment monitoring mainly concerns of physical (temperature and brightness) and chemical (level of alcohol and carbon monoxide in the air) measurements, ensuring the patient's comfort and a preventive disease strategy.

This AAL remote platform is composed by a local system for data acquisition, with wireless communication with a local computer, and by a system for handling all incoming signals for the final presentation of results on the remote computer, though an Internet connection. One of the great advantages of the MCT is the delivering of alert messages, by email, to the caregiver in case of any abnormality occurs.

3 Physiological and Environmental Data Acquisition

The MCT system is based on the e-Health Sensor Platform, designed by Cooking Hacks™ [10]. This kit includes the biomedical monitoring and the environmental data acquisition systems, and the remote connection platform.

The biomedical monitoring system supports some different sensors allowing the measurement of heart rate, blood oxygen (SpO₂), airflow (breathing), body temperature, blood glucose meter, galvanic skin response (GSR), blood pressure (sphygmomanometer) and the patient's position in bed (standing/sitting, supine,



Fig. 1 **a** The e-health sensor platform; **b** the MaxStream[®] XBee-PRO[™]

prone, left and right positions) [10]. All available sensors are presented in Fig. 1a connected to the e-Health platform.

The environmental data acquisition system is composed of four sensors, allowing the monitoring of the alcohol and the carbon monoxide levels in the air, the brightness and the environmental temperature. The air quality sensor presents an output value proportional to the air quality measured by the sensor. The carbon monoxide (CO) sensor is suitable for detecting concentrations of CO in air. The MQ-7 version can detect CO concentrations anywhere from 20 to 2,000 ppm. The light sensor comprises a LDR (light dependent resistor) to obtain the light intensity measurement. The temperature sensor monitors the environment temperature (°C).

The communication between the Arduino platform and the local computer is performed through XBee[™] Modules for the signals transmission [11]. Wireless transmission of sensor devices is performed via a Zigbee radio, specifically the MaxStream[®] XBee-PRO[™] (Fig. 1b).

Some physiological signals need to be acquired with high accuracy, because of the information that they give to the physiologist. Examples are the electrocardiogram (ECG) or the electromyogram (EMG), which are of great importance for the patient health monitoring. The Shimmer Research[™] Bio Starter Kit[®] has proved to be useful due to the high-quality signals acquisition. This wireless kit provides sensors' modules for ECG, EMG, and also for body acceleration measurement, which enables to detect the movement of human body in the three orthogonal axes (x, y, z) [12]. The use of each one of these sensor's modules are non-invasive, demanding the electrodes placing on the patient. The Shimmer unit allows the real-time data capture, streaming, storage and transmission to a computer by Bluetooth, which is a low cost and a robust connection with low power consumption [13].

4 System's Architecture

The MCT has high quality biomedical sensors that perform the analysis in real time, through an integrated system that enables operation of biomedical sensors. The general architecture proposed for the MCT is presented in Fig. 2.

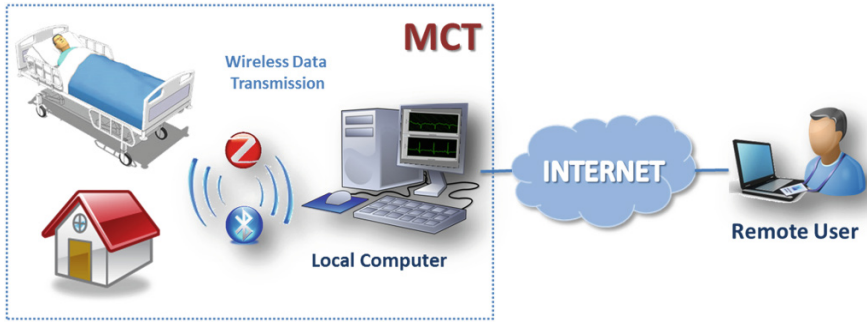


Fig. 2 General architecture proposed for the MCT system

As mentioned before, the e-Health platform and the Shimmer™ device capture physiological data through the electrodes/sensors placed on the human body. The local computer is connected to both devices via Zigbee and Bluetooth connections, respectively, allowing the control and the configuration of the devices as well as enabling the transfer of physiological data.

The remote users will access the platform through an interface available on an Internet browser. On the basis of this architecture, the users have access to the interface, where they can monitor the patients. The acquired data are then presented to user on the interface [14]. With the existence of a webcam, it is possible the online observation of the patient.

5 System Implementation

The implementation of the MCT system requires the development of web application capable of receiving the sensor's outcomes remotely. Both used equipment to acquire the biometric and environmental data were integrated in the system using the LabVIEW software. The Virtual Instrument Software Architecture (VISA), a standard for configuring, programming, and troubleshooting instrumentation systems, was used as a programming interface between the hardware and development environments, the LabVIEW, allowing the operation and control of all sensors.

The choice of the software and the programming language has influence on the final application's usability. The MCT web interface was developed also making use of the LabVIEW, since it has its own web server and an interesting tool—the Web Publishing Tool. Indeed, this tool allows the easily development of Remote Panels by the web publishing of the front panel (user interface) built. This feature allows the embedment of the application's front panel in a HTML document for the web page, enabling the web server. Thus, the user can view and remotely control the front panel from the web page, in real time. On the user-side, the LabVIEW web interface needs the installation of the LabVIEW Runtime plug-in. When the user accesses the webpage, this plug-in is loaded and a TCP (Transmission Control

Protocol) connection to the LabVIEW server is established. The TCP/IP is a robust Internet protocol that ensures the data transmission over the network [13]. The user can remotely interact with the physiological and environments data acquisition devices through the web browser.

6 Web Interface

The interface is organized in tabs layout. The tabs intend to be easily identified and accessible, referring to the signals to be acquired during patient monitoring. The “Home Page” tab is the MCT default page (Fig. 3).

The user can choose between two other tabs. The first provides the physiological data measurements, with the access to all biometric sensors. Figure 4 shows the “Biomedical Data” tab during an ECG acquisition. The use of Shimmer device demands its connection to the local computer, and the data streaming needs to be started by the remote user. These processes can be executed making use of the four buttons available in the ECG, EMG and accelerometer tabs (Fig. 4a). The other signals are acquired with no required user action.

The second tab corresponds to the environmental data acquisition, allowing the monitoring of the environmental variables profiles, room temperature, brightness and air quality. Figure 5 presents the room temperature control panel.

The interface contains a “Remote Monitoring” panel, flanking the main panel, which enables to verify the remote connection. This comprises a graph to show the sound’s amplitude and an image window to display the real time image acquired from the remote web camera, for the continuous observation of the patient.

From the web interface it is also possible to record the measured data in MS Excel allowing further analyses. In addition, if any result is abnormal, an email will

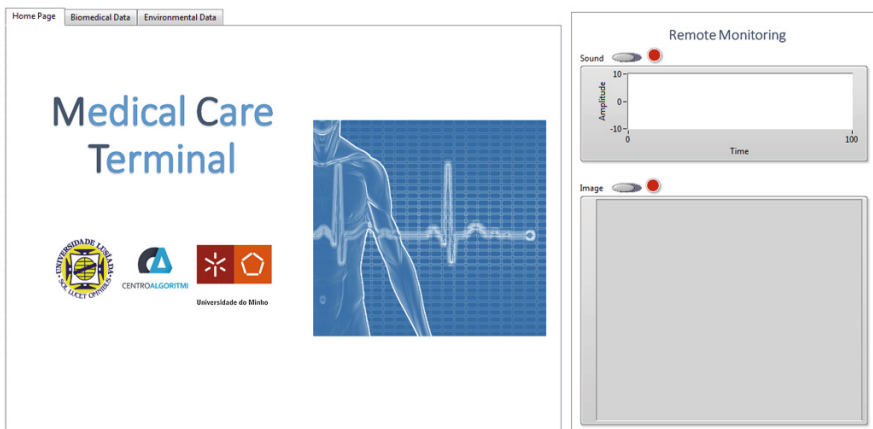


Fig. 3 The “welcome page” of the MCT web interface

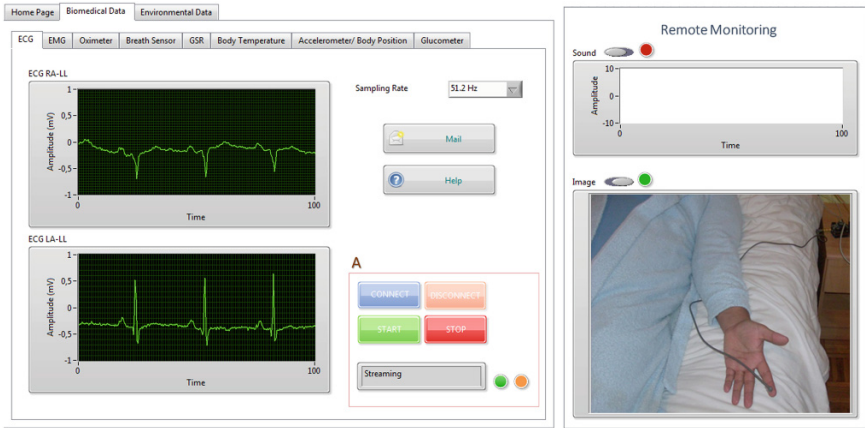


Fig. 4 The “biomedical data” tab, during ECG acquisition, with the display window



Fig. 5 The “environmental data” tab, with “room temperature” tab selected

be sent to the caregiver/remote user. All sensor panels contain information regarding each sensor, instructions to the way the electrodes should be placed, as well as the common values of measurement. This information is available in each panel by clicking the button “Help”. The web interface design has undergone several changes since its first version, improving the access of the important information for the effective remote patient monitoring. It is of great value that the caregiver/remote user accesses in a simple and easy way, in order to collect the important data to be analysed. Thus, the required help information, the buttons and the display windows were disposed in such a way that there is no entropy, facilitating the interaction of the user with the system.

7 Conclusions and Future Work

The work presented in this paper is part of a research project focused on the design and development of a mechatronic system to support bedridden persons.

The proposed system, Medical Care Terminal (MCT), provides the caregiver the ability to monitor, in real time, the patient as well as the environmental conditions. It also allows the possibility of remote communication under authentication. The system includes the measurement of biomedical data (body temperature, BP, GSR, ECG, EMG, level of oxygen, body position and breath airflow) as well environmental data (level of alcohol in the air, carbon monoxide level in the air, room brightness and temperature).

This system presents advantageous features, particularly, its user-friendly interface; its intuitiveness; to be a custom-made solution, by the modular configuration of parameters required; and to be an affordable solution. Future improvements in the MCT project include the addition of new functionalities, such as, applications for, e.g., smartphones or tablets. The work presented in this paper is still under development however the preliminary insights obtained are very encouraging.

Acknowledgments The authors are grateful to the Portuguese Foundation for Science and Technology (FCT) for funding through the R&D project FCOMP-01-0124-FEDER-022601 (reference FCT PTDC/CPE-PEC/122329/2010).

References

1. Giannakouris K (2008) Population and social conditions. Technical report 72/2008, Eurostat
2. Commission of the European Communities (2005). Green paper confronting demographic change: a new solidarity between the generations. Technical report COM 94 final (2005)
3. Perednia DA, Allen A (1995) Telemedicine technology and clinical applications. *J Am Med Assoc* 273(6):483–488
4. Verulkar SM, Limkar M (2012) Real time health monitoring using GPRS technology. *Int J Comput Sci Netw*
5. Bricon-Souf N et al (2005) A distributed coordination platform for home care: analysis, framework and prototupe. *Int J Med Inform* 74(10):809–825
6. Silva H et al (2011) AAL+: continuous institutional and home care through wireless biosignal monitoring systems. In: *Handbook of digital homecare: communications in medical and care compunetics*, vol 3. Springer, Berlin Heidelberg, pp 115–142
7. Vilas-Boas MC et al (2013) Monitoring of bedridden patients: development of a fall detection tool. In: *IEEE 3rd Portuguese meeting in bioengineering (ENBENG)*, 6p, Braga, Portugal, 20–23 Feb 2013 (ISBN: 978-1-4673-4859-1)
8. Gamasu R (2014) ECG based integrated mobile tele medicine system for emergency health tribulations. *Int J Biosci Biotechnol* 6(1):83–94
9. Yang CT et al (2014) Construction and application of an intelligent air quality monitoring system for healthcare environment. *J Med Syst* 38:1–10
10. *Cooking Hacks*, by Libelium: Available online via <http://www.cooking-hacks.com>. Accessed in Feb 2014

11. Huang M et al (2007) The wireless sensor network for home-care system using zigbee. In: 3rd international conference on intelligent information hiding and multimedia signal processing (IIHMSP), vol 1. pp 643, 646, 26–28 Nov 2007
12. Shimmer discovery in motion: Available online via <http://www.shimmersensing.com/>. Accessed in Feb 2014
13. Orduna P et al (2012) Using LabVIEW remote panel in remote laboratories: advantages and disadvantages. In: Global engineering education conference (EDUCON), 2012 IEEE, pp 1–7
14. Botia JA et al (2012) Ambient assisted living system for in-home monitoring of healthy independent elders. *Expert Syst Appl* 39:8136–8148

Part IX
Mechanisms for Biomechanics

Design and Simulation of Humanoid Spine

Daniele Cafolla and Ceccarelli Marco

Abstract Human spine is a complex structure with mechanism behaviour. The aim of this paper is to propose a mechanism simulating human spine with a serial linkage of spherical joints. The proposed joint unit mimics the combined structure of two connected vertebrae along with the intermediate intervertebral disc. In this paper design requirements are fully achieved. The proposed mechanism is very light, low-cost and easy to manufacture, functional and easy to use.

Keywords Design · Simulation · Human spine · Mechanics of spine

1 Introduction

Each spine is unique and reacts in a slightly different way, and the dynamics of the human spine are difficult to quantify. Therefore, in order to study the dynamics of a spine, it is necessary to develop a model of human spine that is general enough to encompass the possible variations in form and function, but specific enough to simulate realistically vertebrae under loading and stress. Owing to a spine, vertebrates have more flexible torsos than others beings. To understand, simulate and utilize the motion of vertebrate's torso, researchers have made many bio-vertebrate robots such as robotic dog, fish or snake, [5].

The robotic spine concept has been studied over the past years. These studies built humanoid robots with a flexible spine which would enhance the human-like movements of the robots and increase the range of movement of the robot's torso. These humanoid robots dealt with the movement of the whole spine, rather than the relative

D. Cafolla (✉) · C. Marco
LARM: Laboratory of Robotics and Mechatronics, DICEM; University of Cassino
and South Latium, Cassino, Italy
e-mail: cafolla@unicas.it

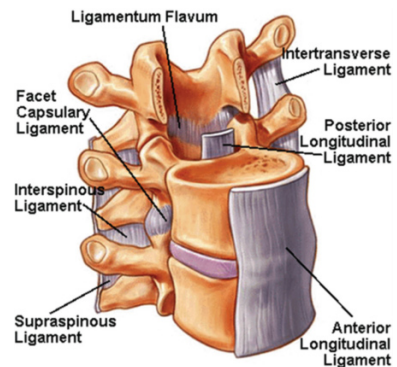
C. Marco
e-mail: ceccarelli@unicas.it

position and stiffness of a vertebra with respect to the adjacent ones, [8, 13, 14, 17]. They sufficiently accomplished flexible spine movements with less than the total number of vertebrae in a human spine. However, no research has yet been completed on the subject of developing a robotic spine with anatomically accurate vertebrae geometry and movements for tactile medical education and/or proficiency assessment, [10].

2 Human Spine

Human vertebral column is a complex structure and mechanism. It is made up of interconnected vertebrae by discs and ligaments. It consists of seven cervical, twelve thoracic, five lumbar, five sacral and five coccygeal vertebrae. The sacral and coccygeal vertebrae are usually fused. In the lateral plane, the normal spine exhibits physiologic cervical lordosis, thoracic kyphosis, and lumbar lordosis. Those shapes increase the flexibility and shock-absorbing capacity of the vertebral column, while maintaining the adequate stiffness and stability. Although a vertebra is not actually a rigid body, usually it can be considered to behave as such, because deformations within the vertebra are insignificant compared to the deformations of the connective tissue. Two adjacent vertebrae, ligaments, inter-vertebral disc and facets form a functional spinal unit, as a motion segment. It exhibits biomechanical characteristics similar to those of the entire spine. Each motion segment has six degree-of-freedom (DOF), and the whole spine can produce three movements: mainly flexion extension, lateral bending, and axial rotation. They can be simply summarized as the combinations of rotational and translational movements. In biological kinematics, motion of a spine is realized by a number of functional spinal units (FSU), as shown in Fig. 1. The motions in human spine are coupled, where translation or rotation along or about one single axis is consistently associated with translation or rotation along or about a second axis. Literature has shown these coupled motions clearly as in [15]. Biological material data remains one of the limiting factors for biomechanical modelling. Existing data are comprised mostly of

Fig. 1 A human-spine and FSU physiological organization, [16]



quasi-static force-displacement measurements with calculations of linear stiffness. Normal variance of biological tissues typically yields a standard deviation for stiffness values of at least 20 %. No matter how refined an element mesh might be, the accuracy of the model can never be better than 20 %, [16]. The coupled motion can lead to computation difficulties while modelling a complex structure like the human spine. Another fundamental issue related to our research is scoliosis. Scoliosis is defined as abnormal lateral curvature of the spine. It is usually considered as a three-dimensional deformity, because axial rotation will always accompany the lateral curvature. Most scoliotic curves will stabilize if not treated, but a few will progress. Mild scoliotic curves result in cosmetic deformities of the trunk. These can create psychological problems for the patients who have them. Severe scoliotic curves may alter balance and coordination, interfere with the function of internal organs, allow premature degeneration of the spinal column, and cause deterioration of neurological function, [15]. Thus, the correction of the deformity is required when the patient risks severe deformity. The purpose of this correction is to stabilize the spine until a solid fusion occurs in the treated area. Once the spine has been fused, it can once again perform its function without the aid of instruments. Hence, it is necessary to generate a general model that can represent these problems as related to the human spine. Many efforts have been made in the past. They can be categorized into different sub areas according to the researchers' interests as pointed out in [15].

3 The Attached Problem

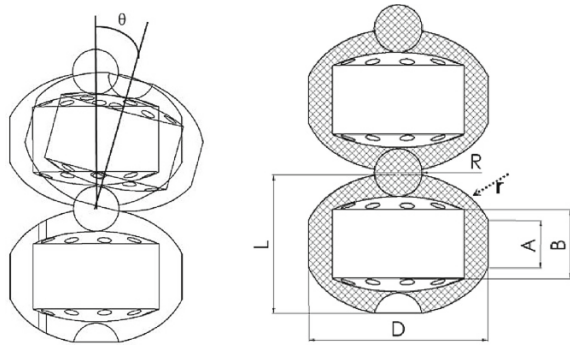
Biomechanical models that are employed for the spinal modelling can be divided into two classes: Computational models and Experimental models. The computational models can be used to provide insight into the mechanisms by which a particular motion occurs or can be used to investigate the complex dynamics of multi-linked segments during motion. Computational modelling can be classified into two categories: one includes the numerical models, which usually use finite element methods, the other includes the analytical models, where the geometry is simplified and requires few boundary conditions. The simplicity of analytical models normally leads to an intuitive understanding of human spine mechanisms. Detailed finite element discretisations of intervertebral discs can provide fine-scale stress and strain field approximations. These fields are obtained, at significant computational cost as reported in [1, 2, 11, 12, 19]. An alternative choice makes use of nonlinear multi-body dynamics formulations as in [3, 9]. In these formulations, the vertebral bodies are assumed to be rigid and interconnected by a collection of conventional mechanical joints. The advantages of this formulation include the fact that these models are relatively low dimensional, [3, 9]. There are some experimental studies of spinal motion that have been carried out to examine and characterize the physics of spinal motion. As advanced measurement technologies have become more and more common, experimental techniques and protocols have

likewise matured. A hybrid approach called EMG assisted optimization (EMGAO) was developed by using both optimization and an EMG assisted approach, lateral radiographs are employed to characterize spinal kinematics and frequency domain characterization of the spinal motion is studied, as mentioned in [7].

4 The Proposed Design Solution

Torsos of some bio-vertebrate robots adopt torsos without bio-spine structure, as the most advanced quadruped robots on Earth. In order to simulate the motion of a human spine, a manipulator system should satisfy not only on mobility property, reachable workspace and isotropic kinematical performance, but even for static and dynamic performance. A spine of human usually can work under two different modes: active mode and passive mode. Under active mode, muscles and ligaments control the motion of the spine following the person's will. Under passive mode, the spine passively moves under the outside load, as pointed out in [18]. Despite its incredible structure and functional abilities the spine is an unstable formation. Only under the coordinated forces that are generated by muscles the human trunk can maintain a particular posture and produce a specific movement. There are multiple muscle groups energizing the human spine and are grouped either by their proximity to the vertebrae as deep, intermediate, and superficial or by how many vertebrae they connect. The group that connects multiple vertebrae is called semispinalis spanning 4–6 vertebral joints. The latter group is the one responsible for the movement of the spine while the shorter ones are maintaining the spinal column's integrity, [4, 15, 20, 21]. The proposed mechanism is a serial linkage of special joints in analogy to the human spine in analogy to the human spine. Those joints are discs and steel spheres. In a manner similar to the human spine, each disc of these joints is actuated and the synchronised motion of the discs gives a uniform curvature to the manipulator. The proposed joint unit mimics the combined structure of two subsequent vertebrae along with the intermediate intervertebral disc. The role of a vertebrae is played by a disc with a curved surface on the upper and lower ends of it. The role of the spinal disc is assumed by a ball which is encapsulated in the disc so as to allow the disc to flex, bend, and twist, without falling out of the joint. The joint possess a homogeneous, spherically shaped working envelope. Because of the disc geometry, the hemispherical surface is reduced to a smaller but well-defined spherical section. This spherical section can be described by the angle θ , as the maximum angle that discs can revolve with respect to the main axis through the centre of the steel ball in. The angle θ can be calculated as a function of the dimensions of the joint, as shown in Fig. 2: where r is the curvature of the disc, L is the thickness of the disc, A is the finite width of flange, B is the high of the void surface, D is the effective diameter of the disc, r is the ball radius, and C is the contact surface between disc and ball.

Fig. 2 A scheme for a conceptual design of a two-vertebra system for simulation



5 Simulation Models and Results

A CAD design of a human vertebra has been elaborated as in Fig. 3a by using SolidWorks Environment. Then several units have been assembled to form a human spine, as in Fig. 3b. Starting from the vertebra sketch a disc was built using its dimensions to make it more human-like. The purpose of the design is to make it balanced, easy and cheap to build Fig. 4a the obtained design with to stacked disc to give an idea of the target to achieve. Nine modules were assembled together to simulate a scaled comparable human-like vertebrae of the Human Spine and test the behaviour, Fig. 4b. The integration of the ball is done by a proper opening on the top and bottom of the two curved surfaces of the disc. The assembled model has been tested through numerical simulation in SolidWorks environment. The body is assumed as composed of various modules made of POM (Polyoxymethylene), a commercial thermoplastic that has high stiffness, low friction and excellent dimensional stability. POM has a density of $\rho = 1.410\text{--}1.420 \text{ g/cm}^3$, tensile strength 70 N/mm^2 , modulus of elasticity in traction $3,000 \text{ N/mm}^2$. Other POM advantages are high abrasion resistance, high heat resistance, low water absorption. For the static FEM simulation the considered known data were used to compute how much tension must be developed by the erector spine with a moment arm of 6 cm from the L5-S1 to maintain the body in a lifting position with segment moment arms as specified, Fig. 5a. Segment weights shown in approximated for a 600 N ($\approx 61 \text{ kg}$) person. Several experiment have been carried out using IMU Sensors and positioning them on the spine while subjects were trying to maintaining their body in a lifting position.

The requested erector spine tension 1714 N as in [6] were fully verified with the carried out experiment. This force was applied in the model acting along the spine as a tension in the Y direction as the gravity. Next Step was applying a solid mesh to the model, Fig. 5b. The resultant forces of the simulation are shown in Table 1 and the resultant Torques are shown in Table 2.

The study results also show a good resistance to Stress using Von Mises method, shown in Fig. 6a, it has a Minimum of 25.168 N/m^2 and a maximum of 27.369 N/m^2 . The model has a minimum displacement, shown in Fig. 6b, which has a range

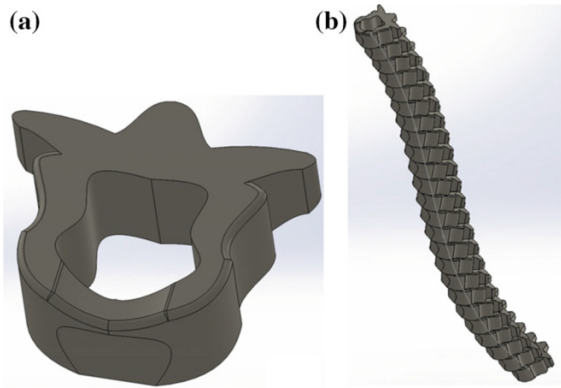


Fig. 3 A spine CAD model: a A vertebra. b A human spine

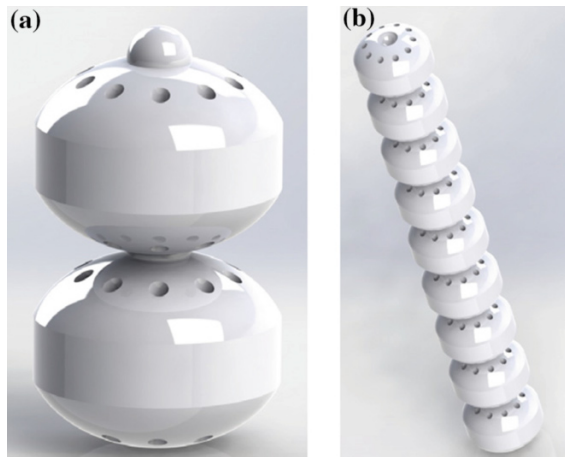


Fig. 4 3D Rendering: a Discs stack detail. b CAD model of the human Spine

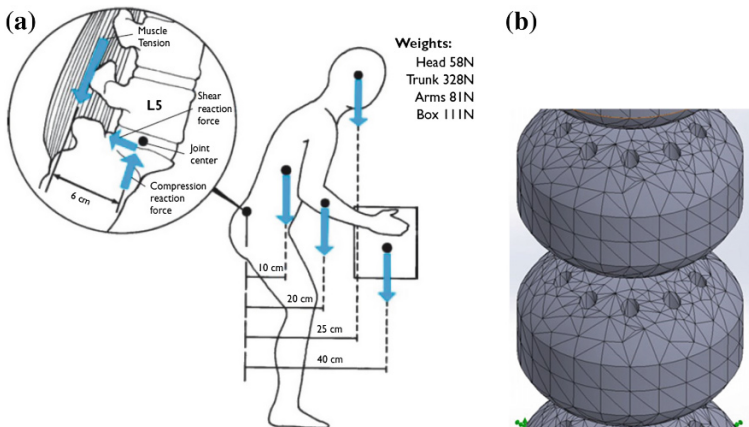


Fig. 5 FEM simulation procedure: a A scheme of a human body, [6]. b Prototype mesh

Table 1 Resultant forces

Units	Sum X	Sum Y	Sum Z	Resultant
N	4.220	1263.400	-0.135	1263.410

Table 2 Resultant torques

Units	Sum X	Sum Y	Sum Z	Resultant
Nm	0	0	0	0

between 0 and 5,958 mm. Finally the Strain Analysis, Fig. 6c shows that the chosen material is good for this application. The Strain results have a minimum of $7.768\text{e}-009$ and a maximum of 0.011. Knowing that the chosen structure and material are suitable for the attached problem, the posture of the prototype was compared to real human one, the results are shown in Fig. 7 proving that they are similar. A further model verification has been made by considering how much compressive stress is

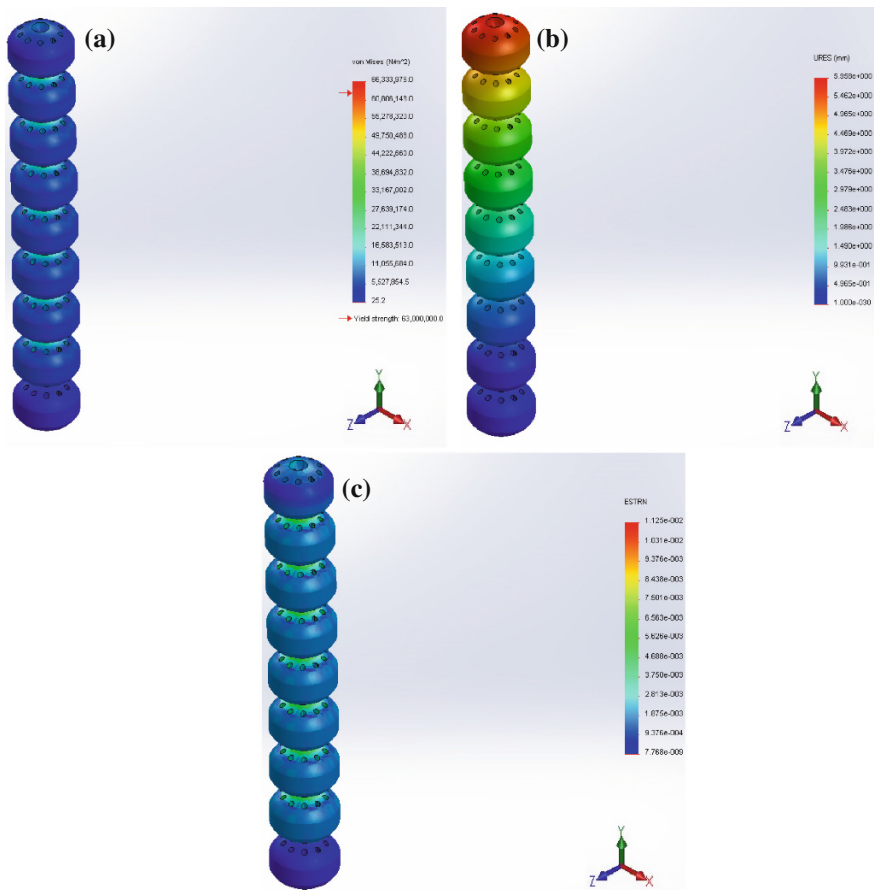


Fig. 6 FEM analysis results: **a** Von mises. **b** Displacement. **c** Strain

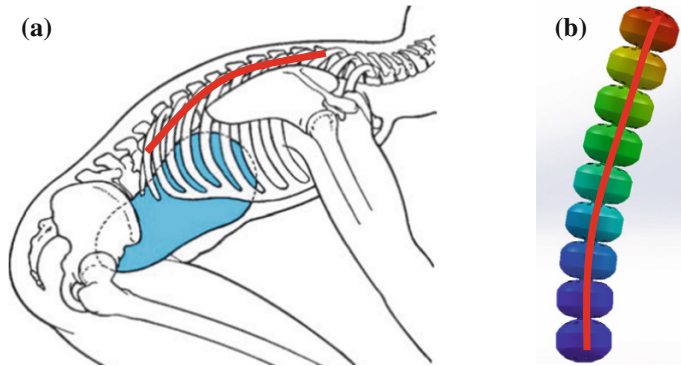


Fig. 7 Posture comparison: **a** Human posture [6]. **b** Prototype posture

present on the L1, L2 vertebral disc of a 625 N (≈ 64 kg) woman, given that approximately 45 % of body weight is supported by the disc in two cases: when she stands in anatomical position; when she stands erect holding a 222 N suitcase. Assuming that the disc is oriented horizontally and that its surface area is 20 cm^2 as mentioned in [6]. In the first case the calculated stress will be 14 N/cm^2 and in the second case the stress result will be 25.2 N/cm^2 . These calculated results on a human spine are similar to the stress results of the FEM shown simulation pointing out that the proposed model has a human-like behaviour.

6 Conclusions

Characteristics of a human spine including nearly isotropic kinematical performance, fast speed, available under both active and passive modes and reachable workspace, a proper structure was adopted. A CAD model has been designed in SolidWorks environment and tested SolidWorks Simulation FEM Analysis. The Simulation shows that the chosen mechanism behaviour suitably reproduce the natural movement of the human spine using the results obtained from the references and from experimental test. The designed prototype fully respects the design target; it is very light (166.46 g), low-cost and easy to manufacture (Derlin), functional and easy to use.

References

1. Belytschko TB, Andriacchi TP, Schultz AB, Galante JO (1973) Analog studies of forces in the human spine: computational techniques. *J Biomech* 6:361–371
2. Belytschko TB, Kulak RF, Schultz AB, Galante JO (1974) Finite element stress analysis of an intervertebral disc. *J Biomech* 7:277–285

3. Buckley MA, Johnson GR (1996) Computer simulation of the dynamics of a human arm and orthosis linkage mechanism. In: Institution of Mechanical Engineers, vol 211. Part H, pp 349–257
4. Ceccarelli M, Saltarello RC, Carbone G, Carvalho JCM (2011) Simulation of the lumbar spine as a multi-module parallel manipulator. *Appl Bionics Biomech* 8:363–374. doi:[10.3233/ABB-2011-0046](https://doi.org/10.3233/ABB-2011-0046)
5. Giuseppe CL, Lim HO (2003) Numerical and experimental estimation of stiffness performances for the humanoid robot Wabian-RV. In: IEEE/ASME international conference on advanced intelligent mechatronics (AIM)
6. Hall JS (2013) Basic biomechanics.: LAVOISIER S.A.S
7. Harvey SB, Hukins DWL (1998) Measurement of lumbar spinal flexion-extension kinematics from lateral radiograph: simulation of the effects of out-of-plane movement and errors in reference point placement. *Med Eng Phys* 20:403–409
8. Howell JN, Conatser RR, Williams RL, Burns J (2008) The virtual haptic back: a simulation for training in palpatory diagnosis. *BMC Med Edu* 8:14
9. Hurmuzlu Y, Basdogan C, Carollo JJ (1998) Presenting joint kinematics of human location using phase portraits and poincare maps. *J. Biomech* 27(12):1495–1499
10. Karadogan E, Williams RL (2012) Dynamics and control of the robotic lumbar spine (RLS). In: Proceedings of the ASME 2012 international design engineering technical conferences and mechanisms and robotics conference, Chicago, Illinois, USA, 2012, Paper #DETC2012-70250
11. Kulak RF, Belytschko TB, Schulz AB, Galante JO (1976) Nonlinear behaviour of the human, intervertebral disc under axial load. *J Biomech* 9:377–387
12. Kulak RF, Schulz AB, Belytschko TB, Galante O (1975) Biomechanical characteristics of vertebral motion segments and intervertebral discs. In: Symposium on the lumbar spine, orthopedic clinics of North America, vol 6(1), pp 121–133, Jan 1975
13. Mizuuchi I, Inaba M, Inoue H (2001) Flexible spine human-form robot-development and control of the posture of the spine. In: IEEE/RSJ international conference on intelligent robots and systems, Maui, Hawaii, USA
14. Mizuuchi I et al (2002) The design and control of the flexible spine of a fully tendondriven humanoid “Kenta”. In: IEEE/RSJ international conference on intelligent robots and systems, Lausanne, Switzerland
15. Nieto NJ, Vinciguerra A, Brach del Prever E, Ceccarelli M (1987) Estimate of torsional stiffness and shear moduli of human cervical spine discs. *Añales de Ingeniería Mecánica. Associazione Spagnola di Ingegneria Meccanica* 5(2):193–197
16. Oxalad TR, Lin R-M, Panjabi MM (1992) Three-dimensional mechanical properties of the thoracolumbar junction. *J Orthop Res* 10:573–580
17. Roos L, Guenter F, Guignard A, Billard AG (2006) Design of a biomimetic spine for the humanoid robot “Robota”. In: IEEE / RAS-EMBS international conference, Pisa, Italy
18. Rosfedt M, Ekstom L, Broman H, Hansson T (1998) Axial stiffness of human lumbar motion segments, force dependence. *J Mech* 31:503–509
19. Schulz AB, Belytschko TB, Andriacchi TP, Galante JO (1973) Analog studies of forces in the human spine: mechanical properties and motion segment behaviour. *J. Biomech* 6:373–383
20. White AA, Panjabi MM (1990) Clinical biomechanics of the spine. Lippincott Williams & Wilkins, Philadelphia, Pa, USA
21. Yoganandan N, Kumaresan S, Pintar FA (2001) Biomechanics of the cervical spine. Part 2. Cervical spine soft tissue responses and biomechanical modelling. *Clin Biomech* 16(1):1–27

Feet Compliance in Two Legged Locomotion

Magdalena Zurawska and Teresa Zielinska

Abstract The concept of compliant robotic foot is proposed and the method of postural equilibration analysis of two-legged robot with compliant feet is proposed. Trajectories of foot reaction force are obtained. Those trajectories are crucial for postural stability evaluation. Presented results are useful for robot motion synthesis and for a compliant feet design. Presented method was tested using simulations, results will be applied in the real robot.

Keywords Feet compliance · Human locomotion

1 Introduction

Current trends are aiming robots moving naturally (like the animals). Special attention is paid to humanoids imitating us, not only by their appearance, but also by their motion. To achieve it, not only the adequate shaping of the body and sophisticated control is needed, but also the proper foot-ground contact must be assured [1]. Character of such contact depends on the body parts movements and on the properties of mechanical structure including the feet. Recently walking robots with compliant elements are the focus of attention. In earlier designs the foot was usually made as one stiff module, in current designs more often the compliance is introduced. Biological world, where the compliance assures impact-less interaction with the environment, inspires the anthropomorphic feet design—Fig. 1a. Simplest way for achieving the compliance is to produce the whole foot from soft material [5] or to use the soft layer as the foot “sole”. In more complex designs the foot is

This work was partially supported by EMARO.

M. Zurawska (✉) · T. Zielinska

Faculty of Power and Aeronautical Engineering, Warsaw University of Technology, Ul. Nowowiejska 24, 00–665 Warsaw, Poland
e-mail: teresaz@meil.pw.edu.pl

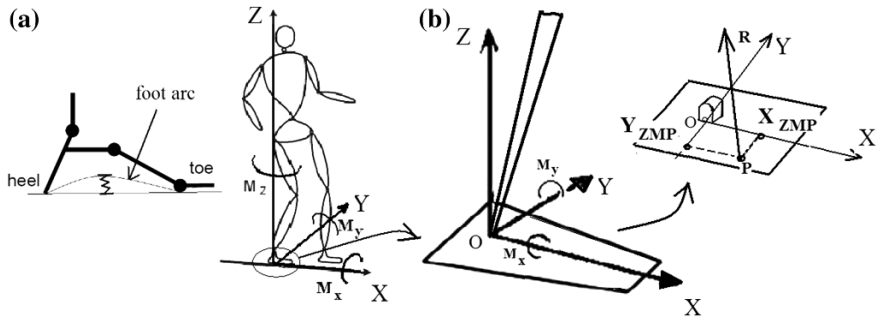


Fig. 1 Human foot arc acts like the spring (a), Zero Moment Point concept (b)

divided into segments connected by passive joints [6]. Before prototyping the key question must be answered if the invention improves the postural stabilization.

2 ZMP

Postural stability of bipedal locomotion in single support phase is commonly tested using Zero Moment Point (ZMP) criterion. This criterion states that the posture is stable during single support phase if M_x , M_y moments due to gravity and body inertial forces are equilibrated by the moment due to reaction force R —Fig. 1b. Neglecting the distance between the ground and the ankle joint and omitting some terms which are small in value but troublesome for calculation, the ZMP is expressed by well known formula [9]:

$$Y_{ZMP} = \frac{\sum_i [y_i(m_i \ddot{z}_i + m_i \cdot g)] - \sum_i (z_i \cdot m_i \ddot{y}_i)}{\sum_i (m_i \ddot{z}_i + m_i \cdot g)} \tag{1}$$

$$X_{ZMP} = \frac{\sum_i [x_i(m_i \ddot{z}_i + m_i \cdot g)] - \sum_i (z_i \cdot m_i \ddot{x}_i)}{\sum_i (m_i \ddot{z}_i + m_i \cdot g)} \tag{2}$$

m_i are the point masses of the body parts, x_i , y_i , z_i are the coordinates of those masses and appropriately \ddot{x}_i , \ddot{y}_i , \ddot{z}_i are their accelerations.

3 Problem Statement

The compliant contact between the ground and the human foot is obtained due to the work of the foot arc [4] and due to the positional adjustments in the ankle joint. In our works on compliant feet we started from simple structure with one vertical spring located near to the ankle joint—it made an equivalent of the foot arc.

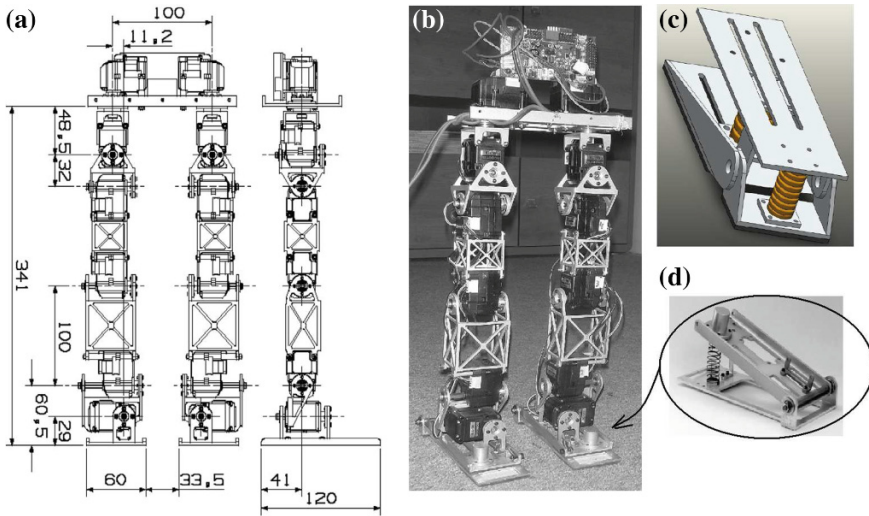


Fig. 2 Design drawing of two legged robot (a), prototype (b), enlarged view of its foot (c), presented in [7] experimentally tested structure imitating human foot compliance (d)

According to [7] it is well imitating the human leg compliance—Fig. 2d. Theoretical and experimental research confirmed that our solution supports well the postural stability. The *ZMP* trajectory was located nearer to the footprint center comparing to the foot without compliance [3]. Such design was used in our small biped (Fig. 2) moving using human gait pattern [10]. Despite of the advantages the system has some limitations, with one spring the foot absorbs well the touch-in impacts, however due to lack of the front compliance the take-off impulse (due to spring release) can not be achieved. Lateral compliance is also missing. In this work we are presenting the concept with expanded compliance. Four compliant elements are located in the four vertices of the foot frame. The rectangular foot is made of two stiff layers with the compliant elements between them. The elements consisting of spring and damper each are located in the vertices (Fig. 3). The gait stability is analyzed. The *ZMP* trajectories for the compliant foot and for traditional foot are compared.

4 Evaluation of *ZMP* Trajectories

Due to the acting force the compliant elements are compressed. Compression influences the body posture what is reflected by changes of the *ZMP* position. To obtain the compressions first the forces must be evaluated. Considered foot is the statically undetermined system—additional conditions must be introduced. In our case they result from the foot axial symmetry, the point *O* which is the ankle joint is

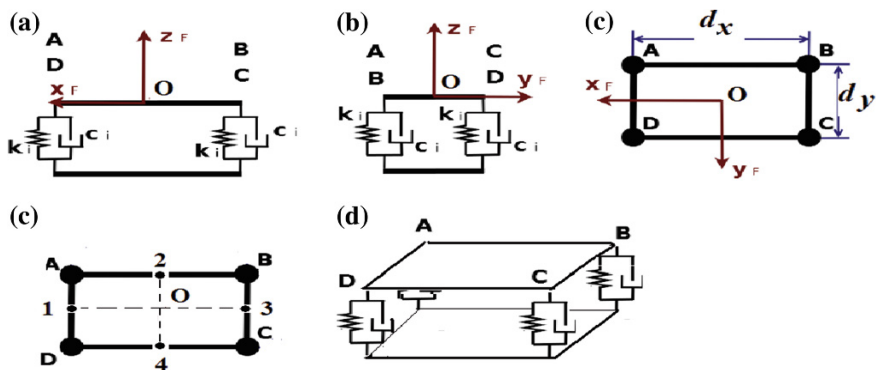


Fig. 3 Planar views of the foot, in XZ plane (side) (a), in XY plane (front, back) (b) XY plane (top) (c), top view with the points used in calculations (d), schematic view of the foot (e)

located symmetrically in the middle of the rectangular foot frame. For each of the 1, 2, 3, 4 points located symmetrically towards O equilibrium conditions result in: $F_1 = \frac{F}{d_x} \left(\frac{d_x}{2} \pm X_{zmp} \right)$, $F_2 = \frac{F}{d_y} \left(\frac{d_y}{2} \mp Y_{zmp} \right)$, $F_3 = \frac{F}{d_x} \left(\frac{d_x}{2} \mp X_{zmp} \right)$, $F_4 = \frac{F}{d_y} \left(\frac{d_y}{2} \pm Y_{zmp} \right)$, where X_{zmp} and Y_{zmp} are the ZMP coordinates where the reaction force is applied. F denotes vertical force exerted by the robot on the ground. Reaction forces in foot vertices A, B, C, D are equal to: $F_A = \frac{1}{2}(F_1 + F_2)$, $F_B = \frac{1}{2}(F_2 + F_3)$, $F_C = \frac{1}{2}(F_3 + F_4)$, $F_D = \frac{1}{2}(F_1 + F_4)$. Each of four spring-damper systems located in A, B, C, D is described by:

$$c_k \dot{z}_k + k_k z_k = F_k, \tag{3}$$

where: $k = A, B, C, D$, c_k —damping factor, k_k —spring stiffness, F_k —the part of force F applied to k -th system. Knowing the total force F developed by the robot on the ground and ZMP position, the forces F_i , $i = 1, 2, 3, 4$ and next the forces F_k , $k = A, B, C, D$ are evaluated. This allows to obtain the compression of compliant elements. Compression influences the robot posture what is considered when evaluating final position of the ZMP .

5 Results

Considered human body model is represented by the stick diagram in Fig. 4. The point masses, its localization and the segments lengths were defined using the anthropomorphic data for typical 50 centile man 1.75 m tall with 75 kg body mass. Foot size was $d_x = 0.27$ m, $d_y = 0.1$ m. Recorded by us human gait pattern for slow walk of such person was applied—Fig. 5. First the ZMP trajectory was evaluated together with force F . Next for each point of ZMP trajectory the forces F_i ($i = 1, 2, 3, 4$), the forces F_k , and finally the compressions were calculated.

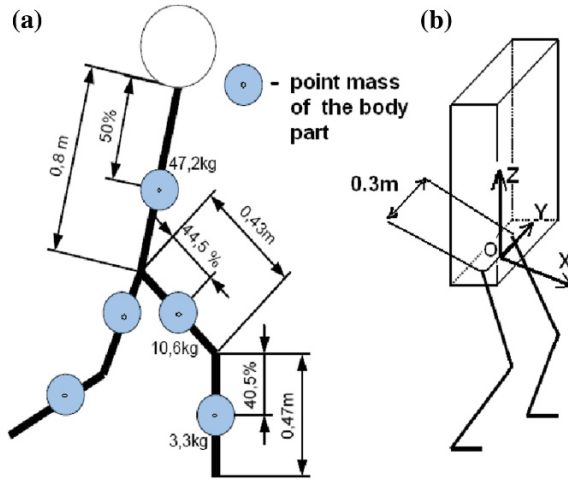


Fig. 4 Human body model

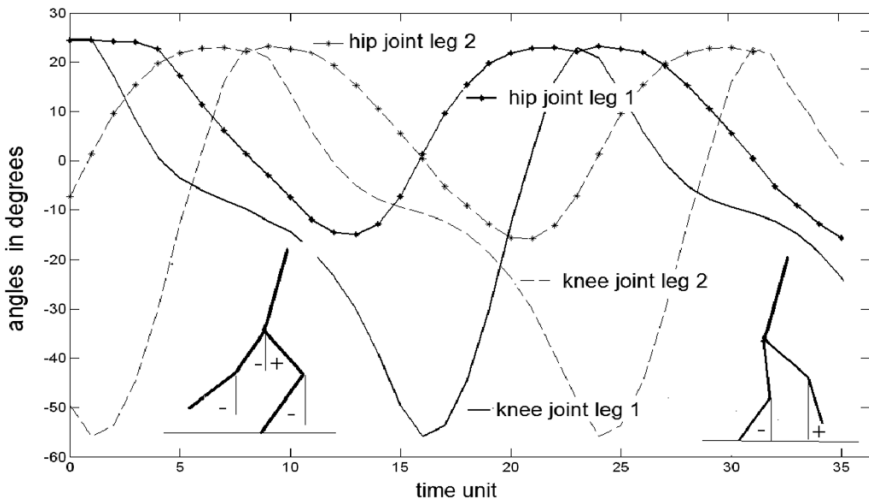


Fig. 5 Hip and knee angles in human walk; the angles are measured from the vertical lines crossing the joints, they are positive if the appropriate leg segment is in the front of such line (negative if it is opposite)

Taking into account the change of robot posture due to compressions the resultant ZMP was obtained. It was assumed that all compliant elements have equal parameters: $k_k = 150 \frac{\text{kN}}{\text{m}}$, $c_k = 70 \frac{\text{kg}}{\text{s}}$. Such values were selected assuming that no-loaded length of the springs is 0.06 m and that its maximum compression during walking should be no $>50\%$ of its free length. Figure 6 illustrates the ZMP trajectories for the

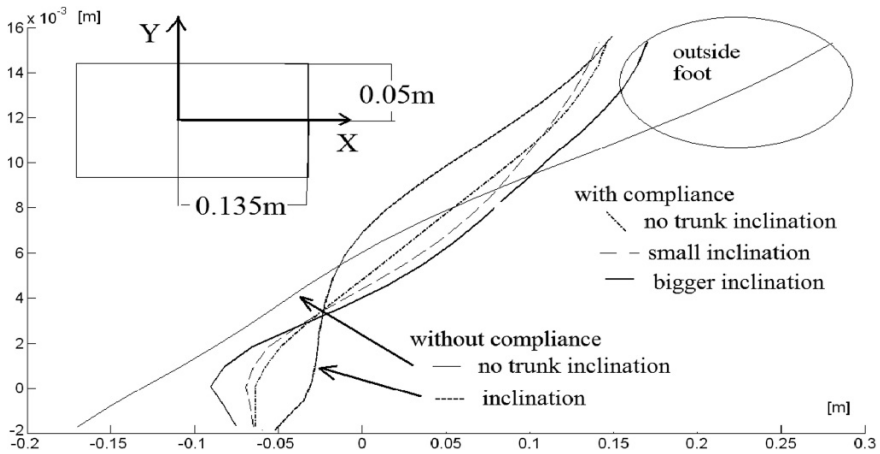


Fig. 6 ZMP trajectories

traditional foot and for the compliant foot. For the foot without compliance and without compensatory trunk inclinations the ZMP localization is exceeding the foot size. Noticing it we introduced compensatory movements of the upper body as it is a common practice in humanoids motion tuning [2]. The introduced upper body backward-forward sway was in range $\pm 8^\circ$. Such range matches the human motion properties. After modification the ZMP went into the foot-print, posture become stable. With the compliant foot and with the upper body sway (as above) the ZMP trajectory was shifted more to the rear of the foot-print during beginning of single

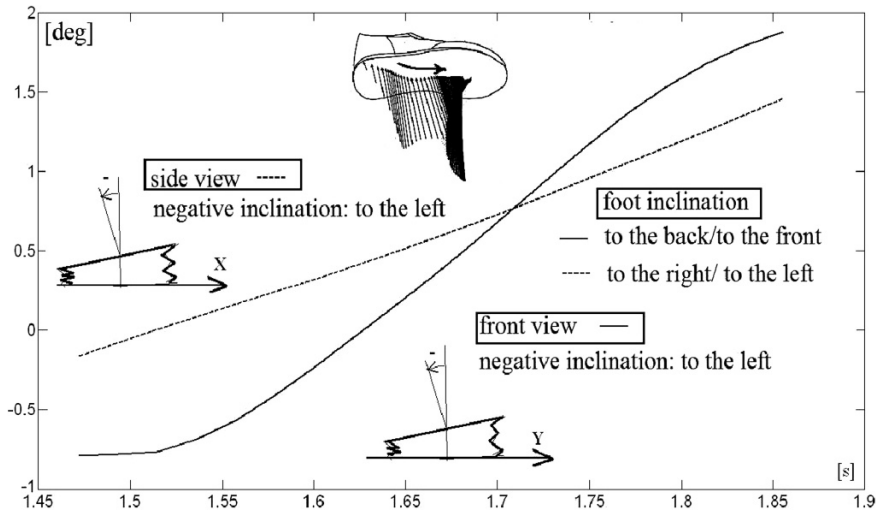


Fig. 7 The change of foot inclination during single support phase. In the upper part of this figure, for the comparison with the results shown in Fig. 6, the human reaction force is sketched

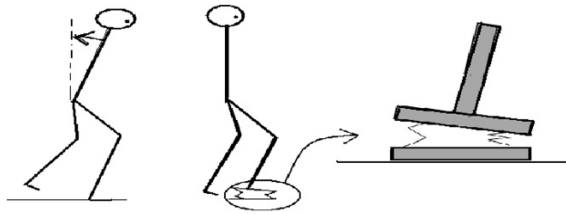


Fig. 8 Postural stability is obtained due to proper trunk positioning or due to the work of compliant feet

support comparing to the situation with traditional foot (and with upper body sway). By the end of single support the ZMP was shifted more to the front—see Fig. 6 thick solid line. The very end of support phase become unstable. When decreasing the trunk back-front inclination the ZMP trajectory shifts to the front by the beginning of the single support phase and to the back by its end. As it can be observed (Fig. 6) the trunk inclination is not needed, the ZMP trajectory stays within the foot-print. Figure 7 is showing that the inclination of the foot layer (due to compression) changes in range $< -0.16^\circ, 1.46^\circ >$ to side and in range $< -0.8^\circ, 1.9^\circ >$ to front-rear direction. It was also tested that the length to width proportion of the foot influences the ZMP trajectory as well. The above obtained results are showing that the adjustments of the robot postural stability by actively powered trunk inclinations are not needed when the compliant feet are applied (Fig. 8). The choice of compliant parameters together with the foot size must be carefully performed. The wrong choice can bring or no effect (too stiff elements) or can cause the problems with postural stabilization (too flexible elements).

6 Conclusions

Proposed compliant foot is not a very complex structure. Our final aim is to deliver the method for the design of small, lightweight autonomous bipeds. Such construction must be simple and with the light feet what is important for energy savings. The possible avoidance of trunk compensatory motions is also the advantage. It must be also noted that with more centered localization of ZMP trajectory the robot can comply with bigger external disturbances without losing the postural stability, therefore the proper adjustment of such trajectory is crucial for the gaits over undulating surfaces. Currently we are developing the prototype of small humanoid [8]. Presented method will be used for compliant feet design and for robot motion synthesis.

References

1. Bruneau O, Ben Oezdou F (1997) Compliant contact of walking robot feet. In: Proceedings of ECPD international conference on intelligent robotics, intelligent automation and active systems, pp 1–7
2. Bum-Joo Lee, Yong-Duk Kim, Jong-Hwan Kim (2005) Balance control of humanoid robot using its upper body; for HuroSot. In: Proceedings of 16th IFAC world congress, vol 17, pp 2087–2092
3. González de Alba A, Zielinska T (2012) Postural equilibrium criteria concerning feet properties for biped robots. *J Autom, Mobile Robot Intell Syst* 6(1):35–40
4. Hashimoto K, Takezaki Y, Hattori K, Kondo H, Takashima T, Lim HOO, Takanishi A (2010) A Study of function of foot's medial longitudinal arch using biped humanoid robot. In: 2010 IEEE/RSJ international conference on intelligent robots and systems, pp 2206–2211
5. Meyer F, Sprowitz A, Lungarella M, Berthouze L (2004) Simple and low-cost compliant leg-foot system. In: IEEE international conference on intelligent robots and systems, vol 1, pp 515–520
6. Sellaouti R, Stasse O, Kajita S, Yokoi K, Kheddar A (2006) Faster and smoother walking of humanoid HRP-2 with passive toe joints. In: IEEE international conference on intelligent robots and systems, pp 4909–4914
7. Song S, LaMontagna Ch, Collins S, Geyer H (2013) The effect of foot compliance encoded in the windlass mechanism on the energetics of human walking. In: 35th international conference on IEEE EMBS, pp 3179–3182
8. Szumowski M (2014) Project desing and prototype of humanidal robot. Warsaw University of Technology, Diploma work
9. Vukobratovic M, Borovac B (2004) Zero-moment point—35 years of its life. *Int J Humanoid Rob* 1(1):157–173
10. Zielinska T, Chew C-M, Kryczka P, Jargilo T (2009) Robot gait synthesis using the scheme of human motion skills development. *Mech Mach Theory* 44(3):541–558

Lab Experiences with LARM Clutched Arm for Assisting Disabled People

C. Copilusi, M. Kaur and M. Ceccarelli

Abstract Laboratory experiences are reported for an assistive manipulation task by using a prototype of LARM clutched arm. The design and operation of LARM clutched arm are revised to achieve a fairly simple use in an application for assisting disabled people in food feeding actions. Results show a suitable arm behavior and proper motion properties in lab tests with arm programming that have been performed mainly by student as user-oriented implementation.

Keywords Service robots · Experimental robotics · Robotic arms · Clutched systems · Assistive food feeding robot

1 Introduction

Nowadays there are many solutions which can help disabled people to walk, to feed, to carry objects or to fulfill different manipulation tasks. These solutions are represented by robotic systems or mechanical devices that are specially designed for these types of tasks. In a particular case, for human feeding process, there are several robotic systems available as those outlined in [1–8]. In general, these systems use a large number of actuators and their control units cannot be easily accessible to a disabled person.

The reported aim is to show how to adapt the LARM clutched arm for disabled human in the case of feeding process. This clutched arm has been used in research purposes in the LARM laboratory frame [9–12]. Path planning has been experienced as reported in [11] with numerical examples and test results, while validation

C. Copilusi (✉)
University of Craiova, Craiova, Romania
e-mail: cristache03@yahoo.co.uk

M. Kaur · M. Ceccarelli
University of Cassino and South Latium, Cassino, Italy
e-mail: ceccarelli@unicas.it

of its functioning for humanoid robot's arm is described in the experiment tests from [9]. In Gu et al. [10] ADAMS simulations have been computed to design and characterize the several operation modes of LARM clutched arm as reported in [11]. The design, operations and experimental validations on this arm are described in detail mainly in [12].

In this paper lab experiences are reported to check the feasibility of LARM clutched arm in user-oriented use for tasks in assisting disabled people. Lab tests were performed for assisting disabled people on feeding process by setting up different functionality modes. The obtained results can be considered as comparable with the motions for the feeding process by a healthy human subject.

2 LARM Clutched Arm

LARM clutched arm is a robotic arm with a single actuator from which the motion is transmitted to joints with the help of gears and electromagnetic clutches. These components make possible the arm's movement in a tridimensional space by using only one electric motor [9–12]. Because of a single actuator, LARM clutched arm can be controlled by no expert users in Robotics. Furthermore this arm is characterized by light weight structure, which ensures the safety when a collision occurs between the robotic arm and a human. The single actuator implies a low-cost design with respect to other traditional robotic arms. Other aspect of this arm is that the motor works only when there is a movement of the arm and there is no energy consumption when the arm stops with energy saving. The sizes of all components are supposed as those of human arm to give it an anthropomorphic design.

The arm has a parallelogram-based design for the limb part which makes it possible to drive the upper arm and forearm from the shoulder. The main idea is to use a proper clutch system to obtain three sub-motions from the source motion of a single motor as shown in Fig. 1, [12]. The shoulder is the main powered component and outputs three rotations (R_1 to R_3). Rotation axes R_1 and R_2 are orthogonal to each other, while the axes for R_2 and R_3 are coaxial.

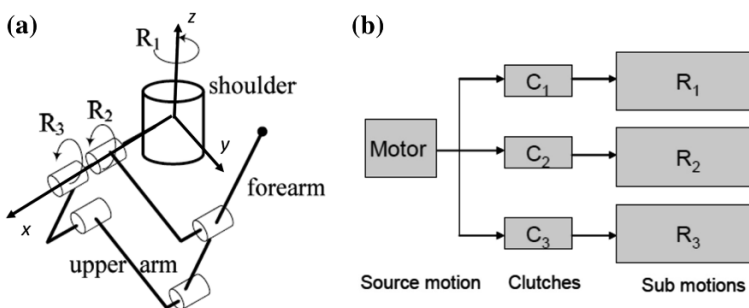


Fig. 1 A model of LARM clutched arm: **a** a design scheme; **b** a scheme for actuation

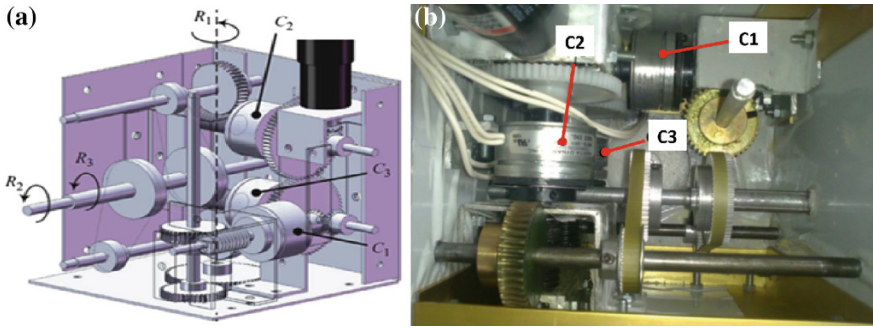


Fig. 2 The shoulder of LARM clutched arm: a a CAD model; b a built prototype in Cassino

Figure 2a shows a CAD model of the design of the LARM clutched arm. The output shaft for R_2 and R_3 is a double cylindrical shaft, within which the full cylinder gives outputs for the R_2 rotation. Coaxial to this shaft there is a hollow cylindrical shaft which outputs the R_3 rotation. The Fig. 2b shows a photo of the shoulder prototype of LARM clutched arm at LARM in Cassino.

Figure 2 shows how the gears and three electromagnetic clutches (marked as C_1 , C_2 and C_3) are combined in the shoulder to give three rotations. The motion of joints can be transmitted or stopped by changing the state of clutches. With three clutches there are eight possible modes for different combination of operation state. OP_0 is a stationary mode, i.e. there is no rotation during this operation mode; while OP_1 to OP_3 are single operation modes, with one rotation when one clutch is activated. OP_4 to OP_7 are multi-rotational operation modes, since during these operation modes there are more than one rotation when clutches are simultaneously activated. Figure 3 shows the photo of a prototype of LARM clutched arm at LARM in Cassino in a lab setup for tests. This arm can be attached to a wheel chair

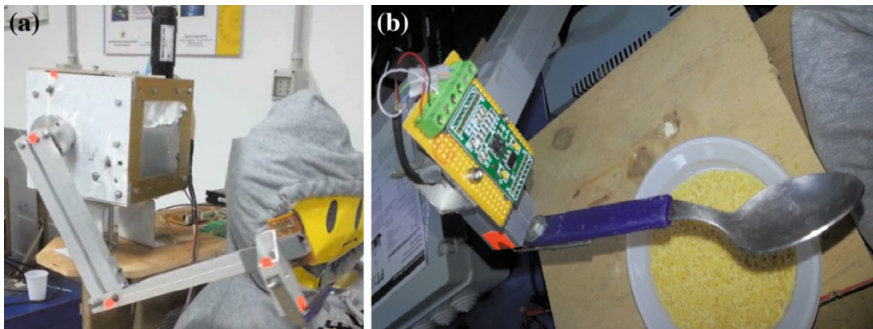


Fig. 3 A lab setup for tests: a the prototype of LARM clutched arm; b spoon end-effector with accelerometer

to help disabled persons for assistive movements like for example in food feeding. In this case a spoon can be attached perpendicularly to the forearm as an end part with the aim to perform the food feeding action.

3 Experimental Setup

In Fig. 4 the lab setup is summarized as using suitable accelerometer sensors (three-axis for maximum of ± 5 g) and data acquisition card to monitor the arm operation during tests. A clamp handling the spoon with a three directional accelerometer is used as an end-effector.

In the prototype three equal 24V DC frictional electromagnetic clutches are used from Inertia Dynamics products with maximum transmissible torque of 1.6 Nm. The control unit is composed of a PLC, a NI-PCI, and a servo amplifier. For a generic movement of LARM clutched arm, the CLANCONS program, that was elaborated especially in LabVIEW, sends the signal to the clutches that can be activated or deactivated by changing the current state. The motor's information that are acquired by the servo-amplifier are analogical and they are sent to the PCI through ACH14 and ACH15, where as the servo-amplifier on the base of this signal gives current to the motor through command +motor and -motor.

In order to control the arm operation, a GUI interface (Graphic User Interface) has been elaborated in LabVIEW as named CLACONS (CLutched Arm CONTROL System). It has two modes: Adjust mode and Control mode. The Adjust mode can be used to control the arm manually to bring it to a desired position; while Control mode can be used for automatic function of arm.

In order to compare the operation of food feeding that can be achieved by the LARM clutched arm with a similar human operation, an ultra-high speed equipment called CONTEMPLAS [13] has been used. The CONTEMPLAS Equipment is presented in Fig. 5 with an overview when it was used for a first motion analysis on a human subject to study human upper limb motion during feeding process. This equipment uses two ultra-high speed cameras which can track special markers with reflexive properties during motions. These markers are usually attached on joint

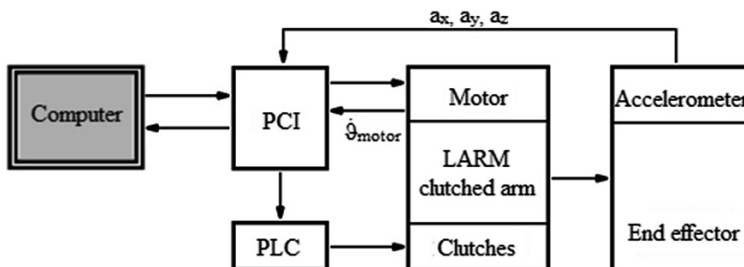


Fig. 4 The block diagram for the lab setup

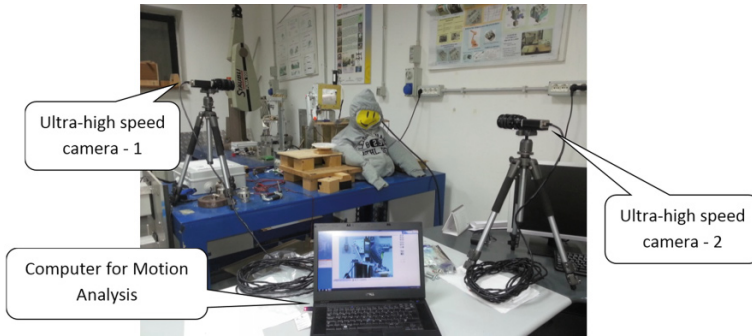


Fig. 5 Setup with ultra-high speed video analysis equipment (CONTEMPLAS) for experimental tests

centers of the interest mobile system are used by tracking and measuring certain entities of a moving system. In our case, the mobile system it is firstly represented by the human upper limb and then by the LARM Clutched Arm. The equipment is capable to track automatically desired trajectories or to analyze them after a video was recorded. A lab layout has been settled to perform tests, to check the feasibility and to characterize the performance characteristics of the proposed application, as shown in Figs. 3, 4 and 5.

4 Results of Lab Tests

A mannequin has been used in the lab tests as a disabled person for food feeding from a dish, Fig. 6. The trajectory for the arm movement during the food feeding action is planned in joint space as reported in Fig. 7, where θ_1 is angle which characterizes the shoulder movement, while θ_2 and θ_3 are the angles characterizing the arm and forearm’s movements, respectively. The trajectory in Fig. 7 is computed by double numerical integration from the acquired accelerations. In Fig. 7, point 1 represents the starting point for the motion of LARM clutched arm. Point no. 2 represents the location where the spoon is introduced inside the dish for food loading. The curve between points 2 and 3 represents the motion of the spoon that is loaded with food. The length of this curve is about 25 mm since the dish radius is equal to 200 mm. The curve between points 3 and 4 describes the motion when the spoon with food leaves the plate area and all the clutches are activated in a special combination. Another phase of this process is represented by the curve between points 4 and 5 when the loaded spoon lifts up to a proper position according to the mannequin size and space location. In this case the clutch C2 is activated. For the spoon displacement from point 5 to 6, the clutch C1 is activated, and the path between those points represents the distance from the dish position and mannequin. These motions can be interpreted by snapshots no 2 and 3 in Fig. 6. At this stage the

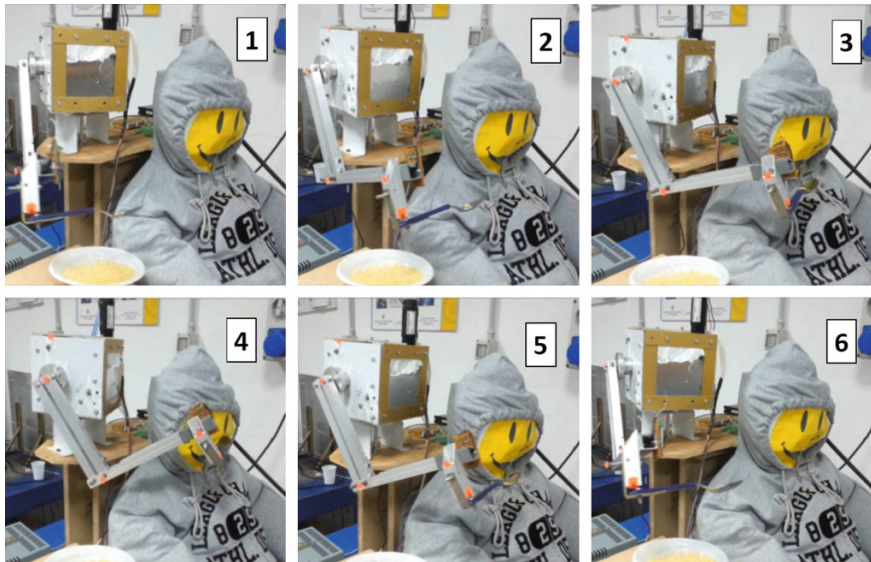


Fig. 6 A photographic sequence of arm's movement during a lab test

loaded spoon is located in the mannequin head area. For unloading the food from the spoon all the clutches are activated in a proper combination. Thus, another path is generated between points 6 and 7. Finally, the spoon is manipulated between points 7 and 8 by actuating clutch C2, and after this the spoon is retracted from the mannequin head area between points 8 and 9 when clutch C1 is activated. This path corresponds the snapshots no 4 and 5 in Fig. 6. These points are identified also in the acceleration diagram in Fig. 8 as acquired from the accelerometer. These values of acceleration look similar to the values of human arm's acceleration during the similar action of food feeding within a range of $4\text{--}8\text{ mm/s}^2$.

A video experimental analysis, by using CONTEMPLAS, as in Fig. 6, consists in attaching special markers on the joints of the shoulder, elbow and wrist joints, and tracking them during a feeding process when a human perform a motion with a spoon.

The measured motion characteristics of a healthy person are reported in Figs. 9 and 10 with a comparison with LARM clutched arm. The time history variation is almost the same time in both cases. In human elbow case the position of elbow position has a value of 1 m, but in the case of the LARM clutched arm this is larger and reaches a value of 1.8 m. This large value is due to the programmed path (as in Fig. 7) and the mannequin dimensional parameters vs. human subject (heights of the both cases are different). For wrist position (Fig. 9b), the time history is different but the obtained values are almost the same on both cases.

The obtained position for this joint has a value of 2 m. A reason for the different time history can be given by the missing joint between the equivalent wrist and hand. Arm motion has been monitored also through joint angles, Fig. 10. The

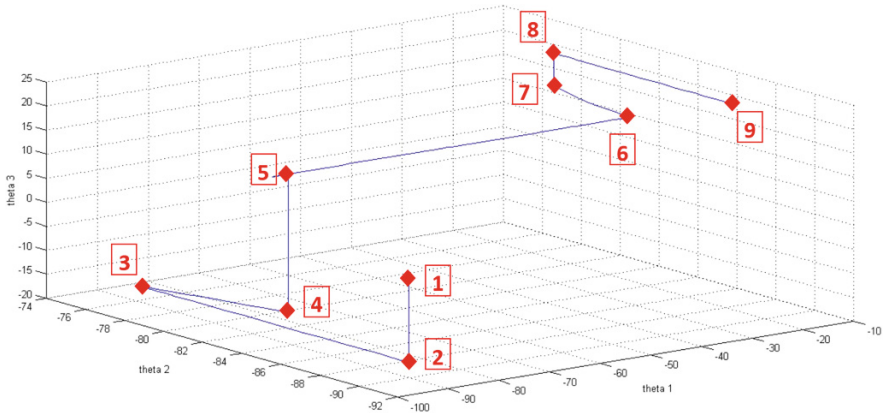


Fig. 7 The planned trajectory in joint space for arm feeding movement of the lab tests

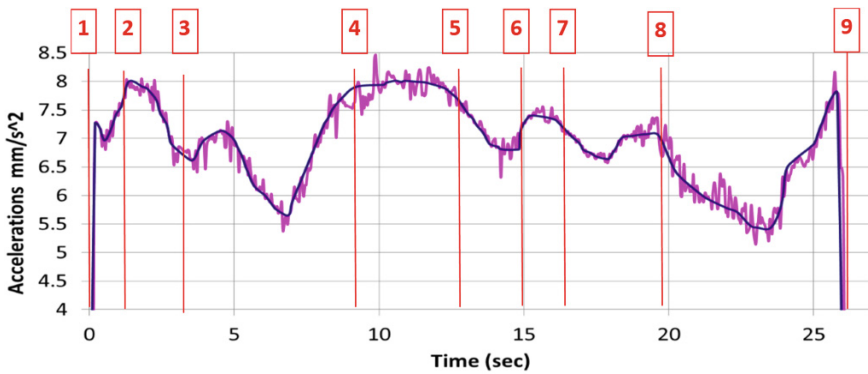


Fig. 8 Measured acceleration magnitude of LARM clutched arm end-point (*magenta line* is for acquired data and *black line* is for filtered data)

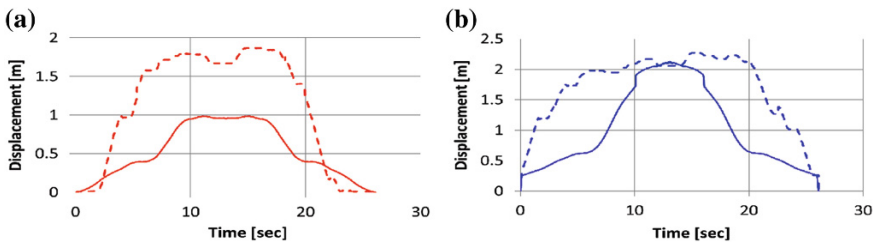


Fig. 9 Test results of arm end-point on a human subject (in *continuous line*) and LARM clutched arm (in *dotted line*): **a** elbow position; **b** wrist position

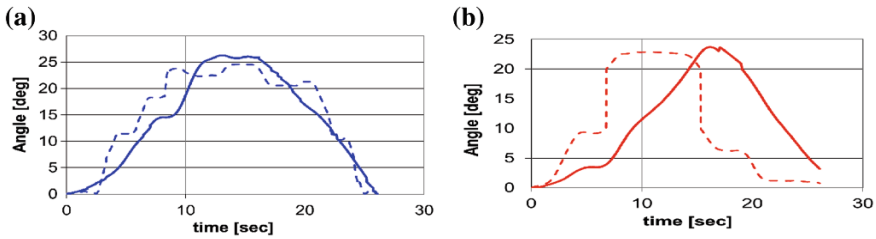


Fig. 10 Measured angles for the human arm (*continuous line*) and LARM arm (*dotted line*): **a** shoulder angle; **b** elbow angle

shoulder angular motion ranges is from 0 to 26° in case of a human subject, but in the case of LARM clutched arm this is from 0 to 24.95°, Fig. 10a. Another aspect is that the time history for LARM clutched arm is not smooth as in a human motion. This is due to the coupling combinations of the magnetic clutches the robotic structure. In case of elbow joint the angular amplitude in both cases are between 0 and 24°, Fig. 10b.

From the reported test results in accelerations and angles it is possible to consider acceptable the planned trajectory by using specific points and motion modes of the LARM clutched arm in the assistive manipulation for food feeding.

5 Conclusions

In this paper, the characteristics and functioning of an anthropomorphic clutched arm built at LARM, in Cassino (Italy) are analyzed through an experimental experience for assisting disable peoples in food feeding. This robotic arm has only one actuator from which the motion is transmitted to joints with the help of gears and electromagnetic clutches. The movement of this robotic arm has been successfully experienced as suitable for food feeding action because it behaves like a human arm during those tasks in terms of trajectory and acceleration.

Acknowledgments This work was partially supported by the grant number 45C/2014, awarded in the internal grant competition of the University of Craiova.

References

1. Soyama R, Ishii S, Fukase A (2003) The development of meal-assistance robot 'my spoon'. In: Proceeding of the 8th international conference on rehabilitation robotics, pp 88–91
2. Topping M (2002) An overview of the development of Handy 1, a rehabilitation robot to assist the severely disabled. *J Intell Robot Syst* 34:253–263 (Kluwer Academic Publishers)
3. NEATER, User Manual Instructions (2013)

4. Hermann R et al (1999) Powered feeding devices: an evaluation of three models. *Arch Phys Med Rehabil* 80:1237–1242
5. Guglielmelli E et al (2009) Self-feeding apparatus. US Patent 2009/0104004
6. Pourmohammadali H (2007) Design of a multiple-user intelligent feeding robot for elderly and disabled people. Master thesis, University of Waterloo, Ontario, Canada
7. Song W-K et al (2010) Design of novel feeding robot for Korean food. ICOST2010, LNCS 6159. In: Lee Y et al (eds) Springer, pp 152–159
8. Song WK, Kim J (2012) Novel assistive robot for self-feeding. *Robot Syst Appl Control Program J* 44–60
9. Ceccarelli M, Gu H (2011) Trajectory planning for a 1-dof clutched robotic arm. *Robotica* 29:745–756
10. Gu H, Ceccarelli M, Carbone G (2010) Design and simulation of a 1-dof anthropomorphic clutched arm for humanoid robots. *Int J Humanoid Rob* 7:157–182
11. Gu H, Ceccarelli M (2012) A multiobjective optimal path planning for a 1-DOF clutched ARM. *Mech Based Des Struct Mach* 40(1):109–121
12. Kaur M (2013) LARM clutched arm functionality and characteristics. Bachelor thesis, LARM Cassino University and South Lathium, Cassino
13. Ernst B, Helas S (2013) CONTEMPLAS-user manual

Design and Simulation of Walking Operation of a Cassino Biped Locomotor

Mingfeng Wang and Marco Ceccarelli

Abstract A mechanical design of a novel Cassino biped locomotor is presented through a dynamics walking simulation. The biped locomotor consists of two tripod leg mechanisms, whose 3-D model is elaborated in SolidWorks® environment. A planning of biped walking gait is performed with waist swinging. Dynamics simulation is carried out in MSC.ADAMS® environment, and results show that the proposed biped locomotor with proper input forces of linear actuators gives limited reaction forces between feet and ground, and has a practical and feasible walking ability on a flat ground.

Keywords Biped locomotors · Tripod leg mechanisms · Biped walking · Dynamics simulation

1 Introduction

Legged locomotion has a number of advantages as compared with conventional wheeled and crawler-type locomotion, such as higher mobility, better obstacle overcoming ability, active suspension and so on, especially when it operates in rough or unconstructed environment [1–3].

Biped locomotors, as a significant and hot topic, have attracted interests of many research communities in the past decade, and a lot of prototypes have been built in the laboratories and even for specific application tasks [2, 3]. In addition, compared with serial mechanisms, parallel mechanisms is well known for having better performances in terms of dynamic performance, accuracy, ratio of payload to own

M. Wang (✉) · M. Ceccarelli
Laboratory of Robotics and Mechatronics (LARM), DiCEM—University of Cassino
and South Latium, Cassino, FR, Italy
e-mail: wang@unicas.it

M. Ceccarelli
e-mail: ceccarelli@unicas.it

weight and has been widely studied both in industry and academia [4]. However, most of the existing biped locomotors are based on leg designs with human-like architectures by using serial chain solutions, such as ASIMO, NAO, HUBO, HRP-4 and so on, while WL-16 (Waseda Leg-No.16) is based on leg designs with Gough-Stewart parallel mechanisms and achieves world first dynamic biped walking by carrying an adult human [5]. Ota et al. [6] and Sugahara et al. [7] have also proposed to use Gough-Stewart parallel mechanisms for leg modules. Ceccarelli and Carbone [8] has investigated the possibility of using parallel manipulator mechanisms with less than six degrees of freedom for leg design as inspired from the human leg muscular system, and Pan and Gao [9] have presented a new kind of parallel leg hexapod walking robot when nuclear disaster happens. Nevertheless, the potentiality of parallel mechanisms for leg designs has not been fully investigated.

At Laboratory of Robotics and Mechatronics (LARM) in Cassino, a research line is devoted to a novel biped locomotor with leg designs of 3-DOF parallel mechanisms [10]. The architecture has been investigated for relevant applications [11, 12] for significant advantages of simpler structure and kinematics, larger workspace, and convenient control as compared with 6-DOF parallel mechanisms.

In this paper, the mechanical design problem of Cassino biped locomotor is presented with the aim to build a biped locomotor by using tripod leg mechanisms. A three dimensional (3-D) model is elaborated in SolidWorks[®] environment with low-cost easy-operation high-payload features. Based on a planning of biped walking gait with waist swinging, dynamics simulation of the designed model is carried out in MSC.ADAMS[®] environment in order to evaluate the operation performances of the proposed biped locomotor.

2 A Biped Locomotor with 2-Tripod Leg Mechanisms

A 3-D model of the proposed biped locomotor is designed in the SolidWorks[®] environment, as shown in Fig. 1a. The biped locomotor consists of two 3-DOF leg mechanisms and a waist. Two leg mechanisms are installed on the waist, and between the waist and feet are two tripod mechanisms of six identical linear actuators with U-joints at each end. The kinematic scheme of a 3-UPU parallel manipulator as a tripod mechanism is shown in Fig. 1b.

Furthermore, in order to improve the compactness of the proposed locomotor, the male parts of the lower U-joints are designed as the bottom part of the rod of each linear actuator, and the assembly of lower six U-joints are shown in Fig. 1a as a zoomed view. For each leg mechanism, the upper and lower three U-joints are installed in equilateral triangle arrangement with one ahead and the other two rear, as shown in Fig. 2, where each three inner revolute axes are installed pointing to the center of the triangle and the radiuses are r_a and r_b , respectively. To guarantee the feet possessing pure translational motion, the two U-joints in each limb are arranged with the two outer revolute joint axes parallel to each other and the two inner revolute joint axes also parallel to one another, as indicated in [10].

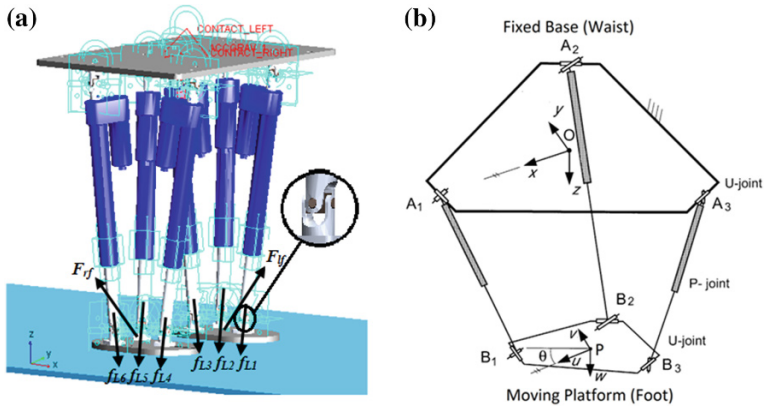


Fig. 1 A Cassino biped locomotor: a a 3-D model; b a kinematic scheme

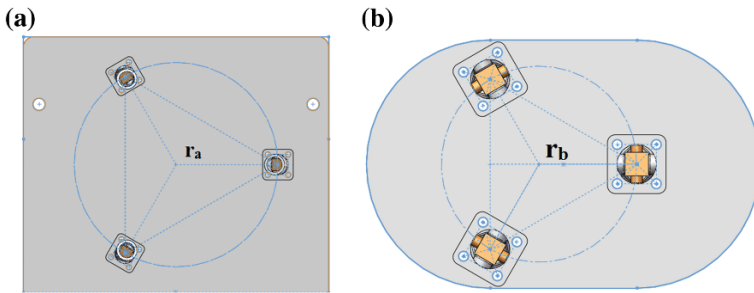


Fig. 2 A scheme of arrangement of U-joints: a on the waist; b on the feet

The main specifications of the model are listed in Tables 1 and 2, as referring to dimension parameters in Fig. 3. The distance between the upper U-joints and waist is equal to that between the lower ones and feet, noted as $D_{uw} = D_{uf}$; the distance between the two U-joints in each linear actuator, namely the length of limb, is indicated as L_i ($i = 1, 2, \dots, 6$) and the initial value of L_i is set as L_{i0} , which determines the initial height of the designed model; the stroke of three linear actuators is L_s , and the displacement of each linear actuator, ΔL_i , can be expressed as

Table 1 Main specifications of the 3-D model of the proposed biped locomotor in Fig. 1

Degrees of freedom	Weight	Dimension (L × W × H)	Step size	Step cycle
6 (3 per leg mechanism)	11 kg	500 × 300 × 502 mm	200 × 40 mm	1.5 s/step

Table 2 Dimension parameters for the model in Fig. 3 (in mm)

L	W	H	Hw	Lf	Wf	Hf	Duw	Duf	Li0
500	300	502	10	201.6	126.6	10	35	35	435

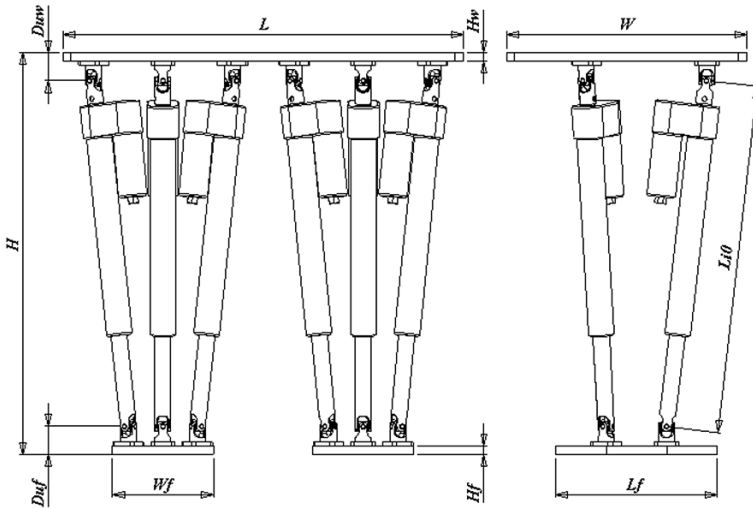


Fig. 3 Dimension parameters of the 3-D model in Fig. 1

Table 3 Mass values of components for the 3-D model in Fig. 3 (in kg)

m_W (waist)	m_F (foot)	m_{LT} (tube)	m_{LR} (rod)	m_{Leg} (leg)	Total mass
4.15	0.72	0.70	0.24	3.45	11.05

$$\Delta Li = Li - Li0 \tag{1}$$

The feasibility of the mechanical design is obtained by using light materials (like aluminium alloy) and commercial components (like universal joints and linear actuators) which are modeled properly in the proposed CAD design for simulation, as shown in Fig. 1a. In this model, the mass center is set in the geometry center of each element, and the calculated mass values of each component are listed in Table 3, where the mass value of each leg can be calculated by considering a limb of each tripod mechanism as a tube frame body and a sliding rod

$$m_{Leg} = 3(m_{LT} + m_{LR}) + m_F \tag{2}$$

3 A Planning of the Walking Gait with Waist Swinging

A planning of the biped walking gait is proposed as based on waist swinging, as shown in Fig. 4. The supporting foot contact with the ground is indicated with gray color, while the swinging foot in the air is indicated with white color, COG

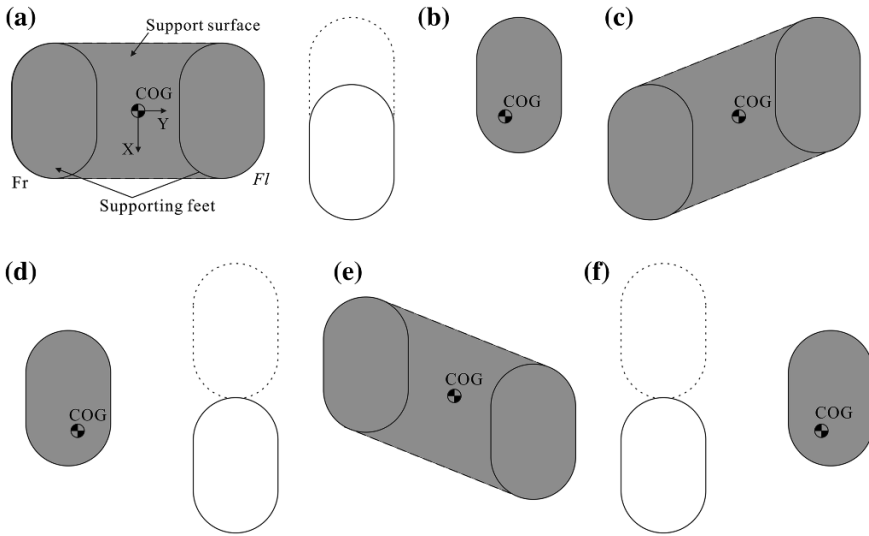


Fig. 4 A scheme for motion sequence of the biped walking gait in the horizontal plane: **a** start and end phase; **b** half step phase; **c–f** normal walking phases

indicates the vertical projection of gravity center of the locomotor on the horizontal plane, and the support surface that is formed by using the supporting feet areas is indicated with gray color. Fl and Fr represent the left and right feet, respectively and the size of a foot can be indicated by Lf and Rf , as shown in Fig. 4a.

In Fig. 4, the biped walking motion is shown as six different phases in as referring to double-support phases and single-support phases. The double-support phase means that both of the left and right feet are in contact with the ground as supporting feet, as shown in Fig. 4a, c, e, while the single-support phase means that either of the feet is swinging in the air, as shown in Fig. 4b, d, f.

Walking stability is an important issue for biped locomotors, since they can only provide one or two feet in contact with the ground. Since that zero moment point (ZMP) requires COG location inside the ground contact area, the COG is needed to be adjusted during the walking cycle so that a statically equilibrium can be ensured with proper foot size. The waist swinging, during the walking cycle, can be used for COG position adjustment purpose.

4 Dynamics Walking Simulation

A dynamics walking model is elaborated in MSC.ADAMS[®] environment as based on the proposed 3-D model in Fig. 1a, and the input motions for the six linear actuators are obtained as based on the kinematic analysis of prescribed human-like gait trajectory for a tripod leg mechanism [10], as shown in Fig. 5.

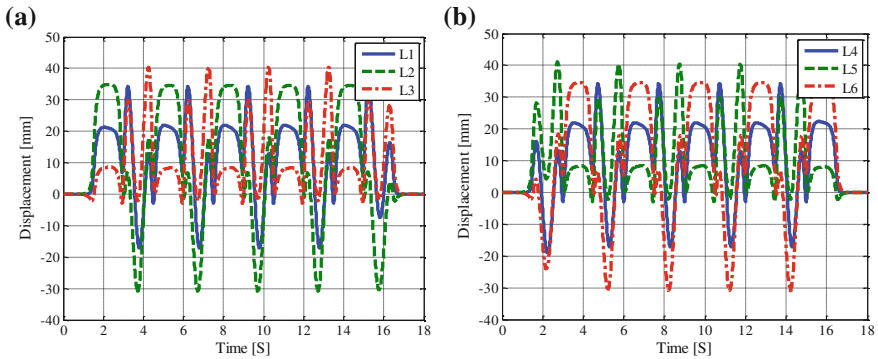


Fig. 5 Input displacements of six linear actuators: **a** for *left leg*; **b** for *right leg*

In Fig. 1a, the reference system for the measured characterization values is fixed on the ground which is a world frame. 3-D solid contacting constraints are added for simulating the contact behavior between the feet and ground. Friction is prescribed for ground contact by using a coulomb friction model. The input force of six linear actuators and the reaction forces between the feet and ground are indicated as f_{Li} ($i = 1, 2, \dots, 6$), and F_{lf} , F_{rf} , respectively. These characteristics are useful to evaluate the proposed tripod design for a practical feasible operation and optimal design purposes. Simulation time is prescribed in 18 s, including 10 full steps (1.5 s/step) of normal biped walking, 2 half steps (1.5 s/step) of start and end of biped walking, and simulation step size is computed as 0.1 s.

In Fig. 5, the input motions of six linear actuators in left and right leg mechanisms are obtained by using the Spline function in MSC.ADAMS[®] environment, and the displacements as function of time are at the rod of each linear actuator.

5 Simulation Results

Simulation results are obtained as shown in Figs. 6, 7 and 8. It is obvious that peaks of values occur during the start or end phases of biped walking for the change from statically stable phase to dynamically stable phase, so in this section, the analysis of simulation results is focused on the normal walking phases and these results are useful performance indexes for evaluating a practical feasible design solution for the biped locomotor.

In Fig. 6, the force curves of f_{L1} and f_{L4} , f_{L2} and f_{L6} , f_{L3} and f_{L5} are similar to each other with one step delay, respectively, which is coincident with the symmetry structure and the proposed planning of walking gait. In addition, during the normal walking, the peak values of forces f_{Li} ($i = 1, 2, \dots, 6$) are less than 215.30 N, 228.03 N, 305.27 N, 194.42 N, 327.32 N, 212.45 N, respectively, which are useful

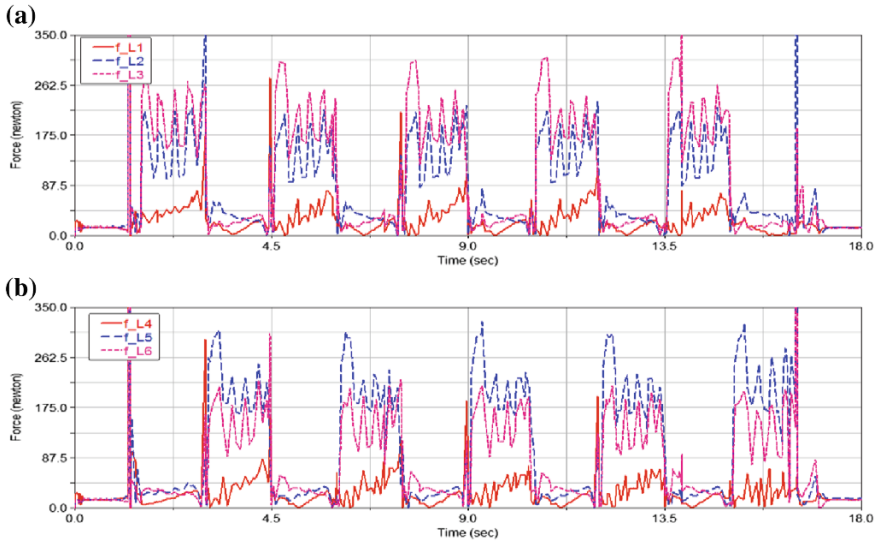


Fig. 6 Computed input actuation forces of the six linear actuators: **a** left leg; **b** right leg

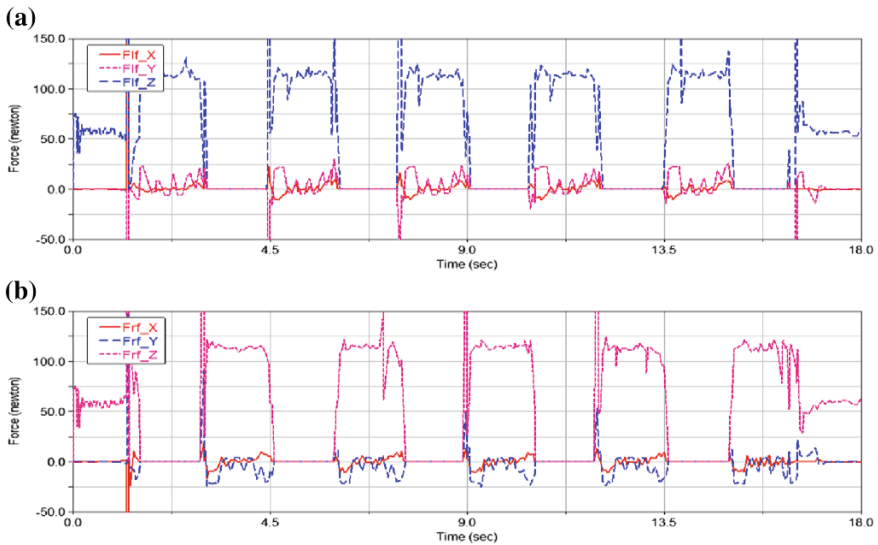


Fig. 7 Computed reaction forces between feet and ground: **a** left foot; **b** right foot

for selecting actuators with proper sizes and output power, also reasonable for the locomotor weight.

In Fig. 7, the Z-axis component of reaction forces is much larger than the other two axes components, and there is always a jump in each step, which is caused by

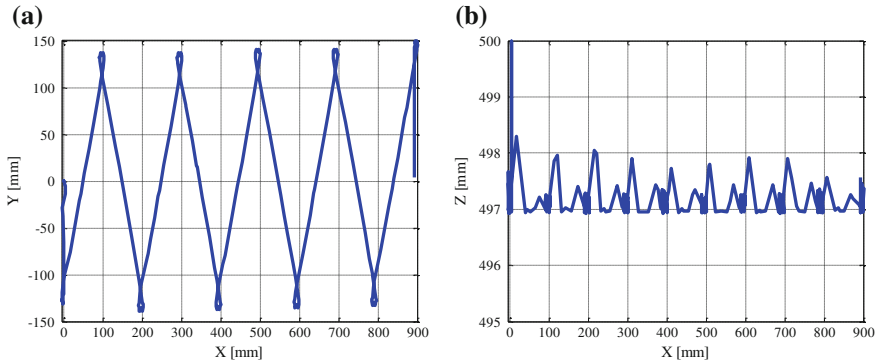


Fig. 8 Computed trajectory of the waist MC: **a** in O - XY plane; **b** in O - XZ plane

the corresponding foot landing on the ground as an impact. Particularly, the impact forces of start and end phases are much larger than those of the normal biped walking phases, because the biped locomotor changes from statically stable walking into dynamically stable walking at this moment.

In Fig. 8, the computed trajectory of waist MC is plotted in O - XY plane and O - XZ plane, where both of the maximum and minimum displacements are 131.16 and -138.78 mm, 496.71 and 498.05 mm. The circles, which occur in O - XY plane, are caused by a small slipping motion between the supporting foot and ground during swinging the other leg in the air.

6 Conclusions

A mechanical design of a novel Cassino biped locomotor with two tripod mechanisms has been presented through a dynamics walking simulation. A 3-D model has been elaborated in SolidWorks[®] environment for evaluating design performances and checking the operation feasibility. A planning of biped walking gait has been proposed by properly operating waist swinging. Dynamics simulation has been carried out in MSC.ADAMS[®] environment, and results show that the proposed biped locomotor with proper input forces of linear actuators gives limited reaction forces between feet and ground, and has a practical and feasible walking ability on a flat ground.

Acknowledgments The first author would like to acknowledge Chinese Scholarship Council (CSC) for supporting his PhD study and research at the Laboratory of Locomotrics and Mechatronics (LARM) in the University of Cassino and South Latium, Italy, for the years 2013–2015.

References

1. Pfeiffer F (2004) Technological aspects of walking. *Walking: biological and technological aspects*. Springer Wien, New York, pp 119–154
2. Siciliano B, Khatib O (2008) *Handbook of robotics*. Part G, legged robots. Springer, New York, pp 361–390
3. Carbone G, Ceccarelli M (2005) Legged locomotoric systems, cutting edge locomotorics. ARS Scientific Book, pp 553–576
4. Ceccarelli M (2004) *Fundamentals of mechanics of robotic manipulation*. Kluwer Academic Publishers, Dordrecht
5. Hashimoto H et al (2009) Biped landing pattern modification method and walking experiments in outdoor environment. *J Robot Mechatron* 20(5):775–784
6. Ota Y et al (1998) Research on a six-legged walking robot with parallel mechanism. In: *Proceedings of international conference on intelligent robots and systems*, Victoria, pp 241–248
7. Sugahara Y et al (2002) Design of a battery-powered multi-purpose bipedal locomotor with parallel mechanism. In: *Proceedings of international conference on intelligent robots and systems*, Lausanne, vol 3, pp 2658–2663
8. Ceccarelli M, Carbone G (2009) A new leg design with parallel mechanism architecture. In: *Proceedings of international conference on advanced intelligent mechatronics*, Singapore, pp 1447–1452
9. Pan Y, Gao F (2013) Payload capability analysis of a new kind of parallel leg hexapod walking robot. In: *Proceedings of international conference on advanced mechatronic systems (ICAMechS)*, Luoyang, pp 541–544
10. Wang MF, Ceccarelli M (2013) Design and simulation for kinematic characteristics of a tripod mechanism for biped locomotors. In: *Proceedings of international workshop on locomotorics in Alpe-Adria-Danube region (RAAD)*, Portorož, pp 124–131
11. Clavel R (1988) DELTA, a fast robot with parallel geometry. In: *Proceedings of the 18th international symposium on industrial robots*, Lausanne, pp 91–100
12. Joshi S, Tsai LW (2003) A comparison study of two 3-DOF parallel manipulators: one with three and the other with four supporting legs. *IEEE Trans Robot Autom* 19(2):200–209

Pneumatic Video Tactile Sensor for Laparoscopic Surgery

M. Dosaev, I. Goryacheva, F.-C. Su, C.-H. Yeh, M.-S. Ju,
M. Gubenko, A. Lyubicheva, A. Morozov and Yu Selyutskiy

Abstract The main purpose of the study is design of the innovative tool for determination of mechanical properties of soft biological tissues during minimally invasive surgical operations. This applied problem is closely related with fundamental problems of diagnostics of pathological conditions of soft biological tissues by means of the tactile sensor. In this paper, the contact interaction between the tactile sensor and the soft biological tissue is studied. The analysis of the stress-strain state of soft tissue is carried out using the solution of boundary value problem of contact mechanics. As a first approximation, the linear elastic model of biological tissue is used in formulation of the problem of contact interaction between biological tissues and the artificial tactile sensor. A method is proposed for determination of mechanical characteristics of the studied tissue basing on measurement of the air pressure in pneumatic chamber of the sensor and on processing of images of the contact area between the sensor head and the tissue. An approach is developed for measuring the axial displacement of the central point of the sensor head and using this information in the procedure of estimation of tissue properties, which extends the potential of the proposed method. The prototype of the miniature video pneumotactile sensor is constructed and tested. Results of these experiments are in good agreement with results of numerical simulations.

Keywords Biomechanics · Contact interaction · Videotactile sensor · Soft biological tissue

M. Dosaev (✉) · Y. Selyutskiy
Lomonosov Moscow State University, Moscow, Russia
e-mail: dosayev@imec.msu.ru

I. Goryacheva · M. Gubenko · A. Lyubicheva · A. Morozov
Institute for Problem in Mechanics of RAS, Moscow, Russia
e-mail: goryache@ipmnet.ru

F.-C. Su · C.-H. Yeh · M.-S. Ju
National Cheng Kung University, Tainan, Taiwan

1 Introduction

The fast-evolving branch of medicine—minimally invasive surgery surely needs in special tools that allow performing an express analysis and recognition of different interior tissues. One of directions of such instrument development is related to creating of so-called tactile sensors, which process the information about characteristics of the contact between elastic sensor head and soft biological tissue. For solving problems of pathology diagnostics of soft biological tissues it is advisable to construct mathematical models for such tissues and to describe its interaction with a sensor head. Soft tissues are considered in mathematical models as continuum. The main hypothesis of tactile diagnostics is in the fact that alteration of mechanical properties of soft tissues (such as elasticity, viscosity, relaxation and so on) accompany soft tissue pathologies. This means, in particular, that local inclusions (blood vessels, tumor, etc.) can be detected by changes of values of parameters of corresponding mathematical models.

First prototype of video tactile sensor was designed by joint Taiwanese-Russian team from National Cheng Kung University (Tainan) and Lomonosov Moscow State University in 2009 [1–4] and now is under patent application. The new method was proposed for noninvasive assessment of the functional state of soft biological tissues and diagnosing their pathologies. This method is based on measuring the radius of contact between sensor head and soft tissue under consideration. The diameter of sensor head was 16 mm.

Since during laparoscopic operation it is difficult to reach human body tissue for palpation and observation, it is reasonable to develop a tactile sensor combined with a laparoscopy to replace the physician finger and eyes. Due to the fact that laparoscopic instrument size is limited (diameter of standard trocar for laparoscopy is 10–12 mm) we decreased diameter of tool down to 10 mm. The goal of study is to design a new diagnostic system combining a laparoscopy with a miniaturized video tactile sensor. The new diagnostic hardware can be used for sensing properties of the pathological tissue for diagnostic purpose and minimally invasive surgery. To develop such diagnostic system it is necessary to find a solution of the fundamental problem of sensor contact interaction with inhomogeneous soft tissues and to develop algorithms for processing of images acquired from the micro video tactile sensor.

We considered the problem of identification of inhomogeneities in soft biological tissue as a special but important case of the general problem of the identification of inhomogeneities in solids. Its complexity follows from the need of the simultaneous determination of both the position and the shape of the inclusions in the biological tissue.

The study contains several stages: (1) developing a prototype of the miniature tactile sensor for determining mechanical characteristics of soft tissue, (2) mathematical modeling the contact interaction between sensitive sensor head and biological tissue, (3) performing validation tests using stiff and soft tissues samples.

2 Sensor Design

We considered several different modifications of sensor constructions. The following variant of sensor design was chosen after preliminary tests and calculations for prototype manufacturing. The sensor frame consists of metallic cylindrical tube with diameter 10 mm. This size satisfies a standard laparoscopic trocar dimension. A silicon transparent head is fixed on the edge of the tube. The head is a hollow spherical segment, which bounded the hermetic chamber inside the tube. Taiwanese team performed special selection of sensor head material aiming to providing needed transparency, minimal gas permeability and stiffness. A micro video camera equipped by focusing lenses, a light source, and an optical displacement sensor are located inside the chamber. The light source provides possibility of regulating illumination inside chamber for improving image obtained by video camera. Due to the fact that focusing lenses with diameter 1.5 mm are available at the time, we chose micro video camera with the same diameter. We additionally provided a possibility of controlled air supply inside the chamber. Ability to change the pressure inside the chamber allows us to change the stiffness of sensor head. Thus, it is possible to measure the characteristics of elasticity of various materials that have significantly different elasticity moduli.

3 Experiments

The prototype of video tactile sensor was fixed in tribometer UMT-3M. The experimental setup is shown in Fig. 1. The prototype consists of cylinder 3 fixed by one butt to load sensor of tribometer 1. Soft silicon spherical membrane 5 (the sensor head) is fixed on the other butt of cylinder 3. Optical proximity displacement sensor, micro video camera and light emitting diode are built-in inside the cylinder 3.

An excess air pressure inside the cylinder is guaranteed by reservoir with compressed air and flexible frame 6. The excess pressure is measured by sensitive air pressure sensor and controlled by pressure regulator.

During experiments the sensor head was indented into samples with different Young moduli. The built-in video camera was used for capturing the contact area between the transparent sensor head and sample. The displacement of the central point of the head was obtained by displacement sensor. At the same moment the tribometer provided displacement of cylinder and applied normal load.

The region of contact that occurs at the interface of the membrane material was determined by the well distinguishable glare on the surface of the silicon membrane bending.

Video camera was calibrated with the purpose to measure linear dimensions of objects in obtained images. The essence of the calibration consisted in getting synchronous optical image of the contact area by two cameras. The second camera was used as the external reference one. The indentation of a thin glass plate mounted on the external camera (Fig. 2) was carried out.

Fig. 1 Photo of experimental setup: 1—load sensor, 2—wires of video camera, displacement sensor, and light source; 3—cylindrical frame; 4—sample; 5—transparent sensor head; 6—flexible pipe for air supply

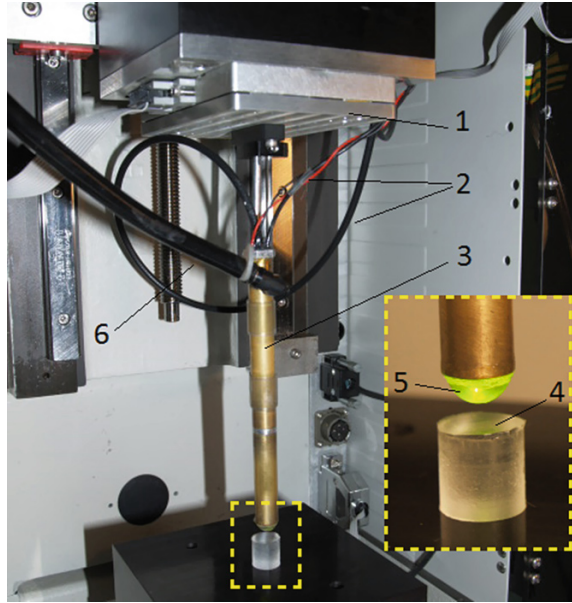


Fig. 2 Indentation of glass fixed on reference video camera

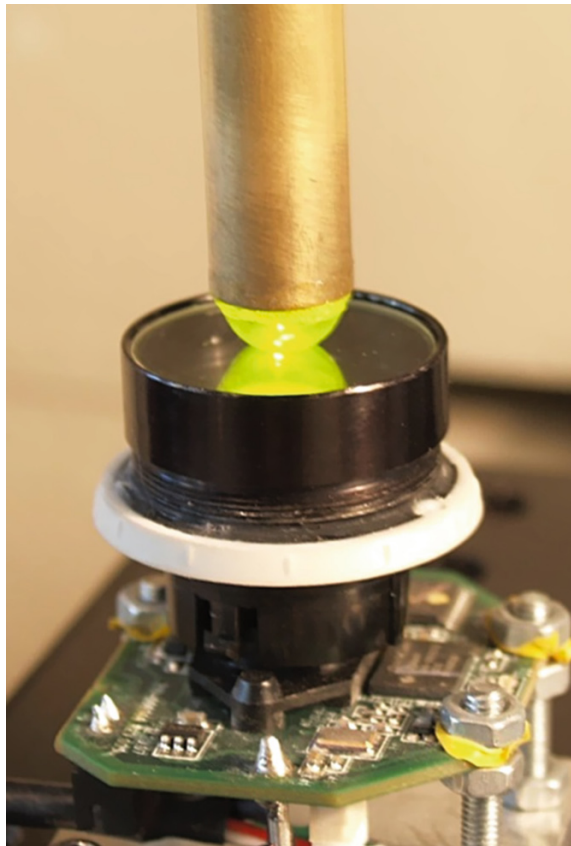
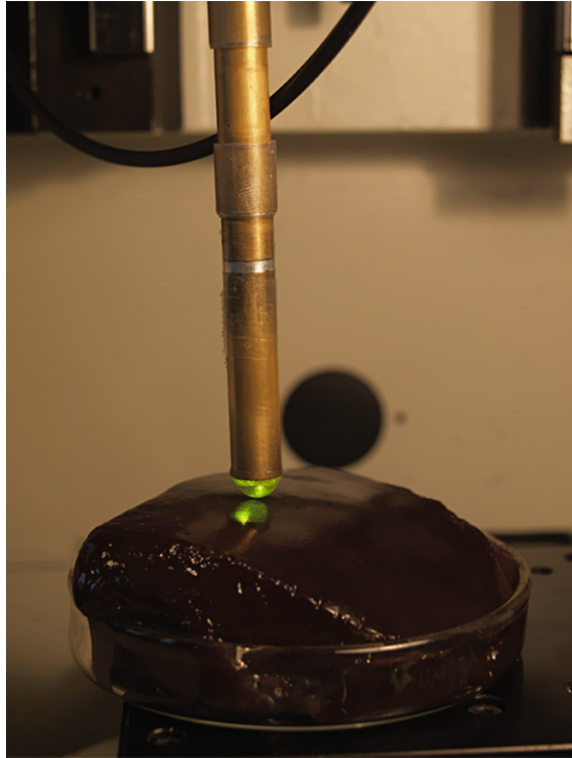


Fig. 3 Experiment with porcine liver



Alcohol was added to the contact zone for better identification of contact area in captured images. The contour of the liquid meniscus was well visible in images taken from both cameras. The comparison of the radius of the contact area obtained by external video camera with the radius obtained by built-in camera allowed us to determine the linear function between the length of the object image in pixels and linear size of the object itself in millimeters.

Series of experiments on indentation of sensor head were carried out into different subjects including rigid plane, silicon sample with known properties, and fresh porcine liver (Fig. 3).

Examples of experimental dependences of the radius of the contact area on the applied normal load are shown in Fig. 4.

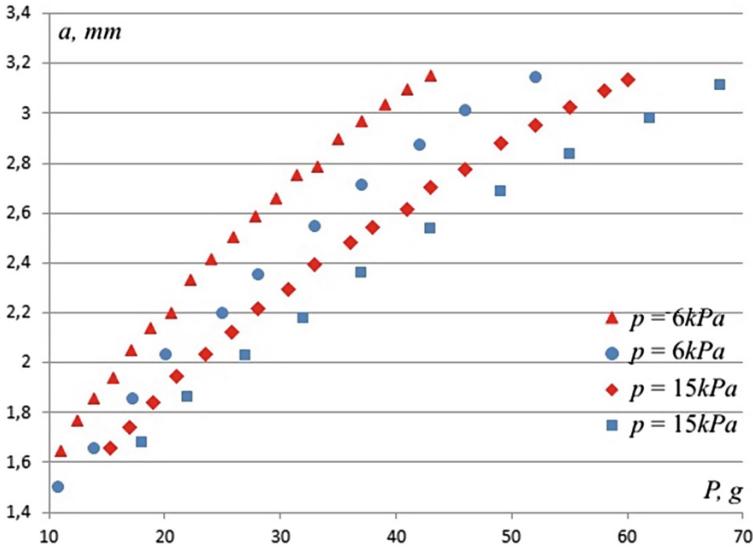


Fig. 4 Dependences of the radius a of the contact area on the applied normal load P under different interior air pressure p (blue points correspond to indentation into silicon sample, red points correspond to indentation into rigid plane)

4 Computer Modeling

We constructed the mathematical mechanical model of contact interaction between sensor head and soft tissue. The sensor head is modeled as a linear elastic semi-sphere with specified mechanical characteristics. Solving the contact problem we applied the finite element method. Geometrical and mechanical characteristics of proposed tactile sensor were taken to account during calculations. One can use many different linear and nonlinear models for soft tissue modeling. Nevertheless sometimes it is enough to evaluate simple medium model for phenomenological method of tissue diagnosis. For the start we modeled soft tissue by linear elastic cylindrical samples with plane surface.

The calculations were performed with MSC.MARC (Fig. 5) and ANSYS 14.0 Mechanical solver (Fig. 6). The model was quite simple; it is axisymmetric problem for linear elastic bodies. The problem was solved with geometrically nonlinear formulation, as the large strains were expected. Specified mesh consisted of higher order 2-D elements (PLANE183), 8-node or 6-node. Representative mesh size for the sensor head was about 0,06 mm. The amount of elements did not exceed fifteen thousand for all the models. Contact interaction was modeled using asymmetric augmented Lagrange method with sample as a target surface and sensor head as a contact surface.

The boundary conditions reproduced experimental conditions as close to as possible. The base of the investigating sample was fixed in normal direction,

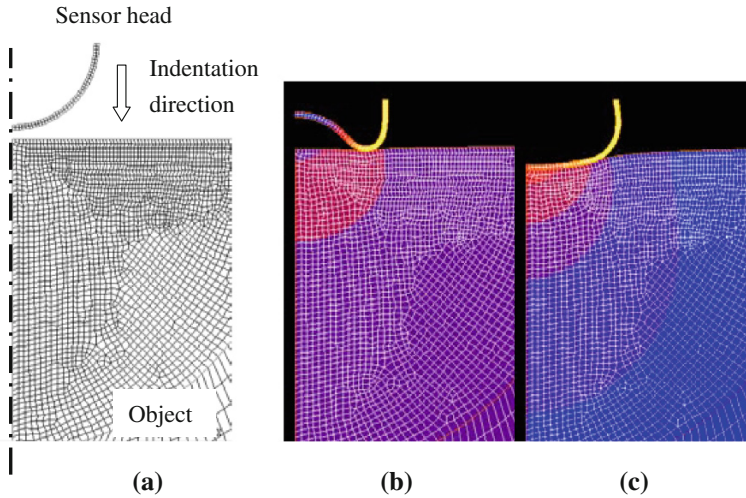


Fig. 5 Simulation of sensor head indentation into soft tissue: **a** before contact; **b** interior air pressure is equal to atmospheric pressure; **c** after increasing air pressure inside the sensor head

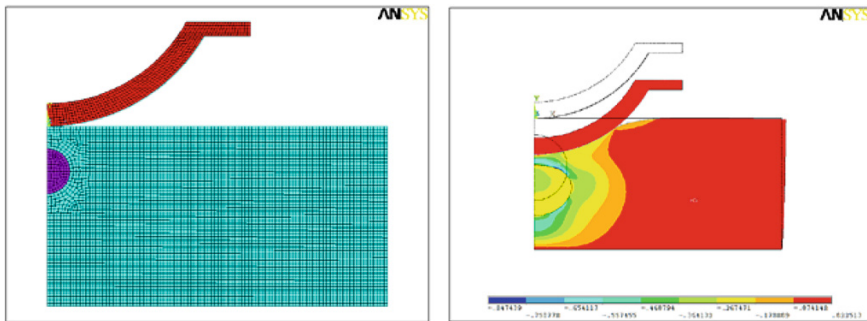


Fig. 6 FEM model of sensor head indentation into soft tissue containing inclusion

symmetry boundary conditions were set on the axis of symmetry. Loading conditions could be defined as normal displacements or as vertical force at the top of semisphere. Contact friction coefficient and sample’s material properties were varied from problem to problem (for hard plastic, silicone or tissue).

Numerical calculations were carried out for indentation of the sensor head into a soft tissue containing spherical inclusion. Mechanical characteristics of soft tissue were taken close to characteristics of porcine liver (given in Table 1).

The spatial problems are solved for both cases: when axes of symmetry of sensor head and inclusion coincide and when these axes do not coincide. The contact schema for tissue with inclusion and elastic deformations e_{yy} is presented at Fig. 6. In calculations we varied values of inclusion radius (0.5–2 mm), values of distance

Table 1 Mechanical characteristics taken for calculations

Subject	Young's modulus	Poisson's ratio
Sensor head	2.1 MPa	0.4
Soft tissue	2.5 kPa	0.499
Inclusion	5–15 kPa	0.499

between the top of inclusion and surface of tissue (0.5–1 mm), ratios of elastic moduli of soft tissues and inclusion, and coefficient of friction between sensor head and soft tissue (0.1–1).

5 Discussion and Conclusion

The interesting fact was observed in experiments and in calculations: if interior air pressure is small enough during indentation, then a central part of sensor head bends inwards. The contact area in this case has a hoop shape (Fig. 5b). Increasing the interior pressure one can reach its critical value when the contact area became to have a convex shape again (Fig. 5c).

Experimental dependences of the radius of the contact area on the applied normal load and on the axial displacement of central point of the sensor head are constructed. The character of obtained dependences (Fig. 4) indicates good perspectives for applying the method proposed in [1–4] for analysis of soft tissue mechanical characteristics using miniature video tactile sensor.

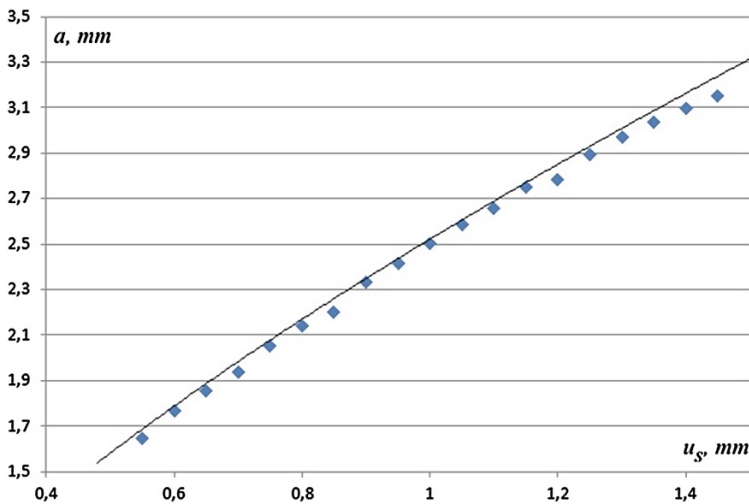


Fig. 7 Dependence of the radius a of the contact area on the axial displacement u_s of central point

Analysis of simulation results showed that the maximum pressure value increases significantly if the relative stiffness of inclusion increases. However, the radius of contact area changes slightly. The range of varying values was determined for which the method sensitivity allows to make a conclusion about presence of the inclusion. In particular, we showed that the value of maximal pressure in contact area can be an indicator of inclusion presence.

The comparison of calculated and experimental dependences of the radius of the contact area on the axial displacement of central point of the sensor head is represented in Fig. 7 for case when the sensor head contacted with the rigid plane. Good quantitative agreement between experimental and calculation data allows us to dress the mentioned above method by an additional technique for result control.

Acknowledgments The work was partially supported by Russian Foundation for Basic Research (project N 12-08-92005) and Taiwan National Science Council.

References

1. Goryacheva I et al (2010) The analysis of contact interaction between tactile sensor head and soft biological tissue. In: Proceedings of Taiwan-Russian bilateral symposium on problems in advanced mechanics, Moscow, MSU Publishing, pp 73–76
2. Goryacheva I et al (2010) Visual sensor approach for the determination of mechanical properties of soft biological tissues. In: Proceedings of the first IFToMM Asian conference on mechanism and machine science, Taipei
3. Yeh C-S et al (2010) Development of vision-based tactile sensor for palpation of pathological soft tissues. In: Lim CT, Goh JCH (eds) WCB 2010, IFMBE proceedings 31, pp 1270–1273
4. Yeh C-S et al (2014) Image-assisted method for estimating local stiffness of soft tissues and calibration of bias due to aqueous humor effect. *Sens Actuators A: Phys* 212:42–51. <http://dx.doi.org/10.1016/j.sna.2014.03.013>

Design of a New Medical Device for Aiding Clinical Diagnosis of Patellofemoral Disorders

A. Leal, R. Pereira, H. Pereira, P. Flores, F.S. Silva
and J. Espregueira-Mendes

Abstract The purpose of this work is presenting the development of a medical device to assist on the diagnosis of patellofemoral disorders. Patellofemoral joint is one of the most complex articulations of the human body with high functional and biomechanical requirements. Anatomical and physiological abnormalities of this articulation result in knee problems with high social incidence. Their proper diagnosis and consequent correction might prevent or delay the development of diseases like arthritis, decreasing their long-term negative impact in life-quality and health economy. Clinical history, physical examination and imaging studies should be complementary procedures in the diagnosis of patellofemoral disorders, but until now they cannot be performed simultaneously. Furthermore, non-objectivity, inaccuracy and limited reliability and reproducibility are often found among assessment methods. Since the majority of the patellofemoral cases are recurrently misdiagnosed, there is in fact an urgent need for standardizing the whole methodology. From concept to design development, with strong clinical meaningful sustainability, we believe this work may give great contributions on these issues.

Keywords Knee · Patellar instability · Physical examination · Medical devices · Biomedical engineering

A. Leal (✉) · P. Flores · F.S. Silva
University of Minho, Braga, Portugal
e-mail: aleal@dem.uminho.pt

A. Leal · R. Pereira · H. Pereira · J. Espregueira-Mendes
Clínica Espregueira-Mendes F.C. Porto Dragão Stadium—FIFA Medical Centre of Excellence, Porto, Portugal

1 Introduction

Most of the medical devices currently available derive from last century engineering scientific discoveries. The active cooperation of the respective scientific domains, health sciences and engineering, is taken as the key solution to solve daily clinical problems [1]. This correlation entirely fits our team interests, representing an appealing challenge to all the involved parts in the project. The extended knowledge and experience of the clinicians involved, sustained by literature review, allowed identifying one area where this kind of approach is essential: on the understanding of patellofemoral disorders.

In the clinical perception, the disorders related with the patellofemoral joint are among the most problematic pathological conditions of the knee. Nevertheless, they remain one of the most neglected and among the least understood, perhaps mainly because they share a common thread with and have impact on nearly all knee conditions. Thus their definition is covered by a dense ambiguity. Patellofemoral physiopathology is often misunderstood specially due to the high complexity of this articulation and its multifactorial etiology. These limitations on the etiopathogenic understanding compromises the diagnosis since it lacks in correlation between symptoms, physical assessment and radiological findings [1–3]. Moreover, the assessment methodology applied is barely rigorous, accurate or reliable. Low sensitivity and specificity, as well as poor-to-moderate inter/intra-observer reliability and validity are found for the clinical tests and outcome measures along with physical examination procedures to assess patellar instability [4]. However clinicians consider physical examination the core to understand the pathology, its function is then limited to a more qualitative than quantitative role within diagnosis. Due to this involving subjectivity, misdiagnosis is a recurrent reality for these cases. Consequently, the diagnostic errors can result in surgical strategies not addressing the specific critical problem or, in contrast, lead to unnecessary surgical interventions instead of applying conservative rehabilitation treatment. In conclusion, concerning the accomplishment of the most suitable treatment for each patient, a new objective, reproducible and reliable diagnostic methodology is plentiful claimed, in both the scopes of scientific literature and orthopedics clinical practice [1, 5].

Regarding the social viewpoint, patellofemoral disorders affect a variety of individuals and worryingly the highest incidence is found among one of the most active social sector, young adults, especially in women and sports [2, 6]. Besides epidemiology, a strong negative long term impact is originated by this kind of problems, for instance arthritis, which is per se a leading joint disease, major cause of disability and one of the most common predictors of health problems, in first-to-third world countries [6]. An ideal diagnosis would detect and allow to correct joint dysfunction, preventing or at least delaying disease progress, and therefore significantly saving the unestimated costs services that cartilage injuries treatment represents for national health, as well as the negative impact on the life quality and social domains.

On the scientific research perspective, studies focusing on the joint kinematics are common, yet present limitations on the dynamic articular evaluation and lack on biomechanical and clinical important aspects, such as on the understanding of the contribution of patellar ligamentous passive restraints on damage and repair, however several authors alert for the importance of this fact. Few developments have been addressing this topic, trying to create suitable systems for a better patellofemoral assessment. Even though they have not been widely disclosed nor reached the health market, if so their application would be limited, once they only quantify patellar lateral position, inclination or displacement, although few consider loading. Moreover, the majority of them are not able for use within imaging equipment, specifically computed axial tomography scan (CT-scan) or magnetic resonance imaging (MRI) devices, does not allowing the accurate examination of soft tissue structures and precise articular position [5].

2 Concept and Strategic Approach

Medical devices development requires an increased care and concern to assure users health and physical integrity. Therefore a plan was elaborated for this project development. From objectives and hypothesis to the unique value propositions, taking into account: origin problems and issues; required participants and partners, stakeholders and prospective customers; every detail had a rigorous planning [1].

Concretely describing what was aimed to develop, it is a medical device for accurate and direct quantification of patellar instability, along the diverse planes and axes of motion, for quantifying abnormal movement patterns of the patellofemoral joint. It should work inside imaging equipment, in particular CT-scan and MRI, i.e., it should be MR safe and MR compatible, in order to obtain at least one image of each translation, rotation or concomitantly combined movements patterns, which may be measured between two bony points with high precision.

Specifying some applications, this medical device may be useful for accurate and direct quantification of patellofemoral laxity. Static laxity is measured involving only one degree of freedom of the joint, whereas dynamic laxity consider the whole joint kinematics (patella stabilization, alignment and patella tracking in the femoral trochlea) i.e., abnormal movement patterns of this articulation. Additionally, the device enhances the visualization and measuring of bone morphometrics (e.g.: femur and its trochlear groove depth). It will be useful for evaluating instability of the patellofemoral joint such those resulting from ruptures of the soft tissues (such as the medial-patellofemoral ligament), which are inserted within the joint, contributing for passive stabilization.

The proposed device has to be integrated with a device previously developed in the scope of our research team: Porto-Knee Testing Device[®] (P-KTD[®]). P-KTD[®] is a knee laxity testing device for measurement of antero-posterior, postero-anterior

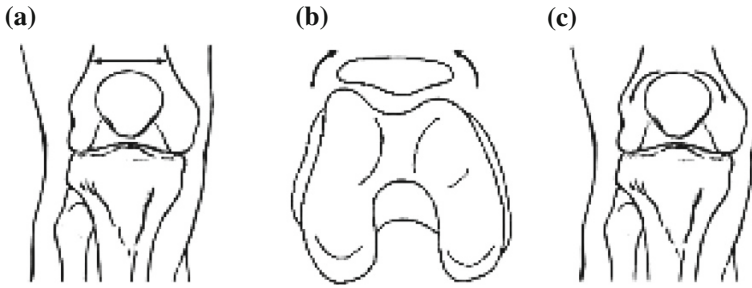


Fig. 1 Patellofemoral joint movements along different axes and planes: **a** medial-lateral translation; **b** medial-lateral tilt; **c** internal-external rotation

tibial translation and internal-external rotation, i.e. it has similar abilities but focused on the evaluation of knee ligaments, specifically the posterior and anterior cruciate ligaments [7]. At the moment, it is the most objective, accurate and complete tool applied in the clinical practice in this scope.

Prior desired functions could initially be identified based on the literature and were then well-defined by the clinical advisory board: patellar medial-lateral translations, patellar tilt and patellar internal-external rotation in the coronal plane—see Fig. 1. In order to complete the functional establishment around these priorities, several brainstormings took place between all the stakeholders.

From different groups of stakeholders (orthopaedists, physical therapists, mechanical and biomedical engineers, imaging technicians and prospective patients and costumers), a few specialists—key opinion leaders (KOL)—were selected for consulting. From clinical to technical perspectives, the KOL allowed the conceptual progression, defining main specifications and requirements.

Specifications list included categories such as apropos to structure, procedural parameters, function and handling, adaptability and comfort, security, costs and durability. On the other hand, an analysis was performed to understand the expectations, preferences and aversions involved. Users' needs and buyers requirements (respecting to ergonomics and economics, portability and ease of use, among others), as well as most important technical characteristics (like inter alia materials, forces amplitude and direction, values of pressure, positions and displacements to respect) were taken into account. A map of correlations, considering priorities and objective values of each parameter, was constructed, from which the core differential features of the device resulted to be [8]:

1. Compatibility with imaging equipments (specifically, MRI and CT-Scan);
2. Modular and complementary structure for linkage to P-KTD[®];
3. Anatomical shape structure/Ergonomics;
4. Adaptability to the widest range of ages.

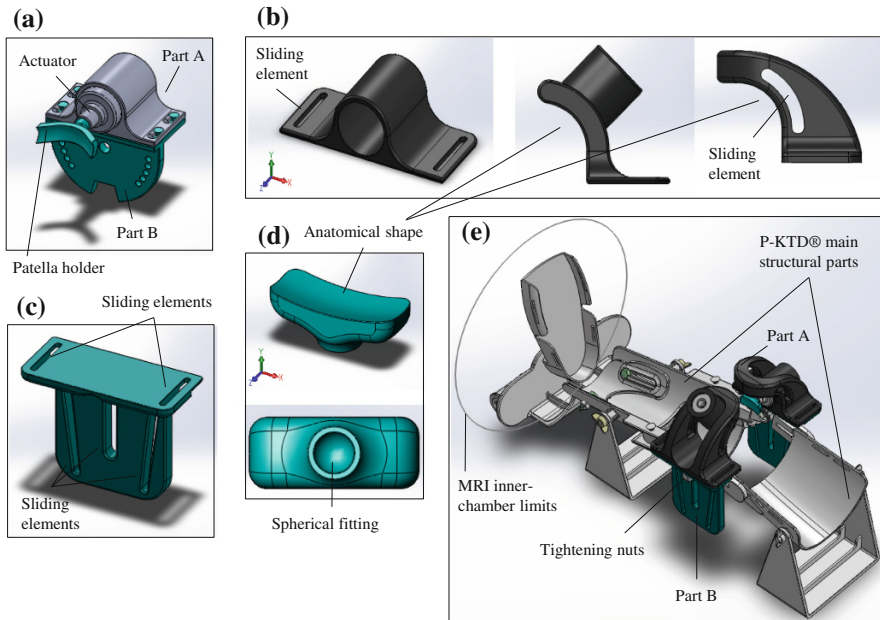


Fig. 2 Three-dimensional device design images: **a** primary design solution; **b** part A; **c** part B; **d** patella holder; **e** final design solution assembled with P-KTD[®]

3 Design and Development

The development of the three-dimensional (3D) design was strictly in line with the concept description and quality analysis of the Sect. 2, and developed within a SolidWorks[®] software environment.

Accordingly with the first feature appointed, non-ferromagnetic materials (preferably polymers, resins, composites, among others), i.e., non-detectable by magnetic fields, should be considered for device composition. Materials density and opacity are also considerable parameters, in order to avoid artefact effect on imaging. Moreover, the device should be able to be introduced (already considering the incorporation with the P-KTD[®]) inside the intern chamber of an MRI or CT-Scan equipment, respecting their standard dimensions.

Primary 3D solution for the device design is illustrated in Fig. 2a, essentially composed by parts A and B and a patella holder, fitted in the actuator.

In order to accomplish feature 2—considering the linkage to P-KTD[®] and its multiple conformations, which respect to each 10° of angular flexion of the human knee, from 0° to 50°—, a mechanism of transversal ribs was designed, with two points of fixture by tightening nuts (maintaining the same system as used with

P-KTD[®]), between part B and the main structural parts of P-KTD[®]—see Fig. 2c. Likewise this solution was thought to include the feature 4—which respects to the adaptability of the device to the widest range of ages, considering the variability of body dimensions—, once it allows to set up or down in the anterior-posterior axis, according to the height of the patella, variable with the patient dimensions, in each articular position of the P-KTD[®] and, consequently, each patient knee position. Due to the patients' variability on patella dimensions and on the exterior diameter of the knee zone, there is the need of adaptation also in terms of width—medial-lateral axis. This feature is possible through the design of two sliding ribs in the part A, on each side of the emboli structure, perpendicular to two respective ones in the part B, respectively, for an independent relative movement of both parts, fixing the desirable position by tightening nuts—see Fig. 2b.

To define a structure anatomically shaped—feature 3—patellofemoral joint anthropometrics understanding was required, mainly of the patella once it would be the body part in contact with the device along the exam. In average, patellar width (distance between the patellar medial and lateral facets extremities) and length (distance between the patellar apex and basis) are, respectively, 46 and 36 mm, whereas the patellar thickness is 17 mm (being the medial facet slightly thicker than the lateral one) [9]—see Fig. 2d. These dimensions have strongly influenced the design of the patella holders.

Figure 2b displays part A evolutionary design. The design of the emboli sliding and support structure, in part A is justified not just to address the feature 4, but also to enrich the versatility of the device, since with this emboli positions range, the force can be applied in multiple points and directions, consenting for several testing scenarios exploration (for instance, to test patellar tilt in different force direction amplitudes). Moreover, it took in account the feature 3, for its dimensions and centre point of design.

The actuators (see Fig. 2a) for moving or holding the patient's patella into position may work independently and alternatively from each other. It can be of any suitable kind, namely manually inflatable bags, spring-loaded elements or hydraulic means like emboli. The choice of actuators/mechanism of force application is respecting the feature 1. Actuators are linked to the patella holders through a spherical fitting (see Fig. 2d), with a limited motion course, according feature 3 and to accomplish feature 4. Finally, actuators release is a mandatory requirement in this device, in order to safe and accurately perform the test, preventing the application of excessive force onto the anatomical structures.

On Fig. 2e one can see all the parts assembled. The main structural side parts of P-KTD[®] may include multiple elements to ensure that the leg, thigh and foot lay and remain fixed against it, during the exam, like for instance belts, straps, girdles, fasteners, cuffs, or clamps, not represented in the figures. Device support and stability, on the horizontal plane, is provided by the flat bases of P-KTD[®], which are fastened to the side parts, alike the part B, through tightening nuts, or

alternatively clamps or ratchets. Also not represented in the figures, there are scales, included in the horizontal face of part A, to initially indicate the position of the patella, as well as to indicate the displacement, between each test step, plus in the emboli sliding structure, indicating the relative angle to patella position.

4 Physical Prototype Functional Evaluation

As result of the conceptual and designing development, a physical prototype was built and subject to functional evaluation. The sequence of tests performed is quite simple and easily suitable for incorporation in current MRI or CT-scan exam sequences, as long as the device is user friendly. The device is manually or automatically placed over the examination table of the MRI or CT-scan equipment, subsequently being positioned inside their inner chamber for imaging acquisition during the assessment. The acquisition is performed with and without pressure applied on the patella, through its lateral and medial edge, patella's basis and apex and anterior face (Fig. 3).

Through imaging findings visualization, the device measuring ability allow accurate measurements of translation and/or rotation, i.e. contemplates an empirical error comprised between, respectively, 1–2 mm or 1–2°, depending on the sharpness of the technician. Such tests could enable to increase either dynamic understanding of patellofemoral joint under pathologic conditions (correlated to patient complaints), either understanding its normal kinematics. Besides the measurements of abovementioned required translations and rotations (Fig. 1), the displacements the device promotes likely allow measuring the ability of motion restraining, by exposure of bone landmarks and soft tissues, as well as better distal femoral epiphyseal and patellar morphometric measurements, such as trochlear groove depth, crossing sign, lateral trochlear inclination, trochlear facet asymmetry. This way, the clinician will be able to evaluate the condition of the tissues that ideally resist dislocation and promote alignment of the anatomical structures of the joint. In

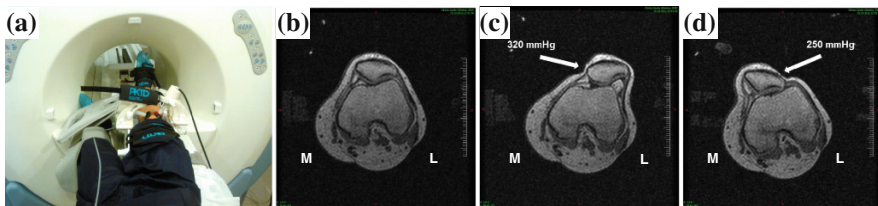


Fig. 3 Patellofemoral joint testing in MRI: **a** assembling scheme of physical prototype with patient; and axial view images for **b** patellar neutral position with no loading; **c** patellar lateral translation under loading; **d** patellar medial translation under loading

some cases, it is possible to measure accurately combined movements patterns, which besides configuring a dynamic feature to the device, can also be correlated to associated injuries (related to ligaments, cartilage or menisci) detected in the images. These findings can constitute important clinical information in the scope of diagnosis and follow-up, after conservative or surgical treatments.

Some flaws were detected throughout the functional evaluation, and appointed for correction, just to mention an example: in order to avoid the phenomenon of rebound during the patellar driving, the patella holder was coated with a shaped neoprene piece of tissue, for a better adherence to the skin, consequently allowing better patellar holding for rigour improvement. Technically, it significantly contributed to enhance the ergonomics of the device. Other evolutions followed similar process.

5 Concluding Remarks and Future Perspectives

The device developed in the scope of the present work intends not just to overcome all the drawbacks with state-of-art methods, but it represents a breakthrough innovative concept, which has been claimed on related scientific literature and clinical practice. The development of a medical device with such properties will ideally allow performing a rigorous and accurate physical examination of the patellofemoral joint, producing a reliable, feasible and reproducible diagnosis report. Clinical testing and validation will be the forthcoming work to develop. The identification of several clinical test scenarios is aimed, based on an extensive battery of tests performance. Thus, it may be a major scientific and technical, novel and unique solution for patellofemoral instability evaluation, from which objective criteria can arise for subsequent establishment of treatment standard algorithm. As consequence, it may configure the core information clinicians need for differential treatment screening, more appropriate treatment, avoidance of collateral effects, leading to a higher success rate in patients' recovery, an optimized resources managing and an improvement of services, patient's health and life quality.

Acknowledgments The first author expresses her gratitude to Fundação para a Ciência e a Tecnologia (FCT) for the PhD grant (SFRH/BDE/51821/2012).

References

1. Leal A, Pereira H, Silva FS, Flores P, Espregueira-Mendes J (2013) Clinical diagnosis of patellofemoral disorders: the role of bioengineering. In: Proceedings of 3rd Port. bioengineering meeting. IEEE
2. Zaffagnini S, Dejour D, Arendt EA (2010) Patellofemoral pain, instability, and arthritis: clinical presentation, imaging and treatment. Springer, Berlin
3. Fithian DC, Neyret P, Servien E (2008) Patellar instability: the Lyon experience. *Curr Orthop Pract* 19:328–338

4. Smith TO et al (2012) The intra- and inter-observer reliability of the physical examination methods used to assess patients with patellofemoral joint instability. *Knee* 19:404–410
5. Leal A et al (2014) Patellofemoral evaluation: do we need an objective kinematic approach. In: Gobbi A, Espregueira-mendes J, Nakamura N (eds) *Patellofemoral joint. State of the art in evaluation and management*. Springer, Berlin
6. Arendt E (2005) Anatomy and malalignment of the patellofemoral joint: its relation to patellofemoral arthrosis. *Clin Orthop Relat Res* 71–75
7. Espregueira-Mendes J et al (2012) Assessment of rotatory laxity in anterior cruciate ligament-deficient knees using magnetic resonance imaging with Porto-knee testing device. *Knee Surg Sports Traumatol Arthrosc* 20:671–678
8. Leal A (2013) Report on biomedical rehabilitation equipments: development of a device to assist on the diagnosis of the patellofemoral joint disorders
9. Baldwin JL, House CK (2005) Anatomic dimensions of the patella measured during total knee arthroplasty. *J Arthroplasty* 20:250–257

Lab Experiences with a Linkage Exoskeleton for Walking Assistance

I. Silva, M. Ceccarelli, C. Copilusi and P. Flores

Abstract Results of experimental tests are reported and discussed by using a linkage exoskeleton for walking assistance. The exoskeleton is actuated by a single actuator and has been designed with adjustable link mechanisms. Walking operation has been recorded with joint angles and trajectories that have been analyzed to be similar to human walking characteristics.

Keywords Rehabilitation · Exoskeleton's · Experimental mechanics · Walking

1 Introduction

The number of people with reduced mobility capacity increases every year as mainly caused by spinal cord injuries and strokes (causing hemiparesis) or due to an advanced age. Reduced mobility in individuals is a factor with great influence on quality of life and dependence of others in performing daily tasks [1]. Physical therapy treatments involving motor learning are required for help them regaining proper use of the impaired limbs. The most important element of this treatments is retraining motion coordination by performing well-focused and carefully-directed repetitive exercises [2]. Robotic systems for gait rehabilitation could promote the

I. Silva (✉) · P. Flores
University of Minho, Minho, Portugal
e-mail: ivommsilva@hotmail.com

P. Flores
e-mail: pflores@dem.uminho.pt

M. Ceccarelli
University of Cassino and South Latium, Cassino, Italy
e-mail: ceccarelli@unicas.it

C. Copilusi
University of Craiova, Craiova, Romania
e-mail: cristache03@yahoo.co.uk

training of patients by providing controlled assistance. Robotic rehabilitation devices may serve as a complement to the work of therapists allowing patients to receive proper treatment to obtain a better rehabilitation therapy. It provides a greater active involvement of patients in rehabilitation and the motivation of these is essential to facilitate and improve motion learning and exercise [3]. Robots used for gait rehabilitation can be divided into two categories as with active and passive solutions. In a passive device, the limbs of a patient must provide enough power so the movement can occur. Generally these devices are only composed by springs and links. The active devices must provide sufficient force to execute the movement of lower limbs, requiring proper controlled motors or actuators [4]. Several exoskeleton systems have been developed with distinct purposes. University of Tsukuba has developed some generations of Hybrid Assistive Limb (HAL) to physically support a user's daily activities [5]. Another example is BLEEX, Berkeley Lower Limb Exoskeleton that has been designed to augment the human lower limbs for load carrying over various terrains [6]. The LOKOMAT exoskeleton is one example of a treadmill gait trainer [7]. Moreover, other treadmill exoskeletons have been developed such as LOPES [8], ALEX [9] and LokoHelp [10]. In addition to treadmill gait trainers, other over-ground gait trainers have been developed such as RoboKnee [11], Nurse-Assisting Exoskeleton [12], NTU Exoskeleton [13], EXPOS [14] and Vanderbilt Exoskeleton [15].

The high costs, low portability, and size specificity are a disadvantage of some of these systems. In this paper, a set of tests are discussed as obtained with in a low-cost, light weight and size adjustable exoskeleton that has been designed for human rehabilitation.

A singly actuated exoskeleton's prototype [16] has been for this work. The ankle joint is not actuated which is a limitation of the system as in most of current exoskeletons. Thus, it is required a redesign of the exoskeleton's mechanism in order to achieve an optimal gait pattern (similar to human) including foot coordination. A series of experiments have been conducted on the exoskeleton prototype in order to test its functionalities and limitations for further developments. His gait pattern have been recorded by using CONTEMPLAS software for motion tracking. Joint angles and trajectories have been recorded for further analysis. Then, using the same equipment, one human subject has been tested for recording one gait cycle as reference walking data. The results between the exoskeleton and the human gait have been then compared and discussed.

2 A Linkage Exoskeleton

This work has been focused on a low-cost linkage exoskeleton with a simple construction, lightweight and easy adaption to the human leg anatomy. A leg exoskeleton that has been designed at LARM has been experienced with experimental tests [16]. The leg mechanism is composed by a Chebyshev linkage and a pantograph as shown in Fig. 1. This mechanism has 1 DOF and the link lengths can

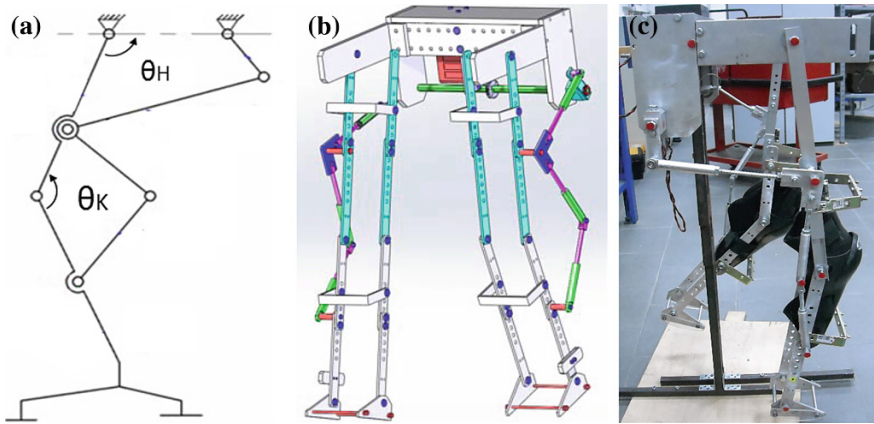


Fig. 1 The LARM exoskeleton: a a kinematic scheme; b a SolidWorks model; c a prototype

be sized to be better adjusted to the human leg anatomy. The mobility of knee and hip joint can be assisted with this exoskeleton, and the ankle joint has been neglected due to its small angular amplitude.

3 Experimental Setup

A first test has been conducted with one human individual (1.81 m, 72 kg) in a passive treadmill with 5° inclination. The lower left limb motion has been analyzed during one full gait cycle. Then, the exoskeleton has been tested “on air” by using a support structure as shown in Fig. 1c.

Colored markers have been attached to the joints of interest (points at hip, knee and ankle) in order to measure the angles between them and to follow their trajectories by using CONTEMPLAS system [17]. This image acquisition system is composed by two ultra-fast cameras and a specialized software, Fig. 2.

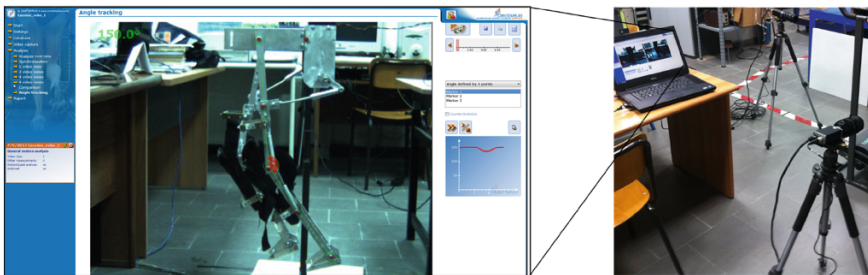


Fig. 2 A lab setup by using image tracking system CONTEMPLAS

4 Test Results

Tests have been worked out with a human to get walking data for reference and then the exoskeleton prototype has been tested to check its functionality with human-like walking characteristics. A human subject has taken 1.7 s to perform one gait cycle during a walking test. Figures 3 and 4 shows two snapshots of the both CONTEMPLAS modes for gait analysis that have been used in the tests.

During the gait, the knee and ankle joint have shown a variation of approximately 46° and 15° respectively as shown in Fig. 5. The passive inclined treadmill might have influenced results particularly on the ankle joint angles. The knee and ankle point trajectories have been also tracked as in Fig. 3b in order to characterize the walking functionality. Typical are the shape of the trajectories as eight-shaped path for knee point and a banana-shaped path for ankle point [18].

Fig. 3 Angle measuring results by using CONTEMPLAS system

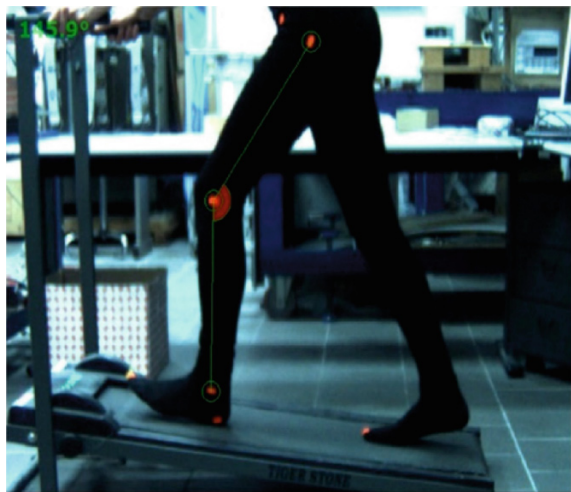
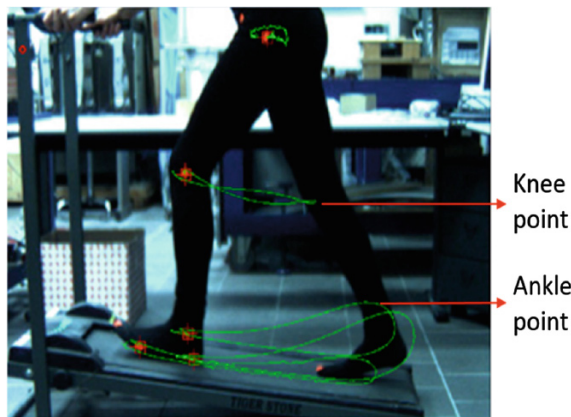


Fig. 4 Point trajectories results in leg structure during human walking by using CONTEMPLAS system



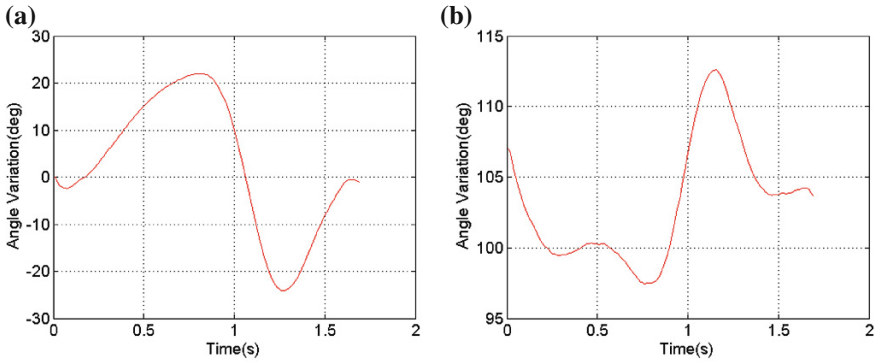


Fig. 5 Acquired angle variation during walking tests with human subject, Fig. 3, for: **a** knee joint; **b** ankle joint

The exoskeleton’s motion tests have been worked out with a gait cycle of 4.8 s, which is a time significantly longer than the previous experiment with human subject. Differences in the functioning of the left and right limb of the exoskeleton can be observed in the test results in Fig. 6.

The joints have presented an angle variation of 34.6° and 32.9° for the left and right hip respectively, and 14.5° and 27.4° for the left and right knee. Those differences between left and right limbs may indicate some defects in the mechanism that can be recognized as due compliance of joints and links, as well as small size differences. The point trajectories as shown in Fig. 6 have been analyzed and compared to the trajectories of the human walking in Fig. 3.

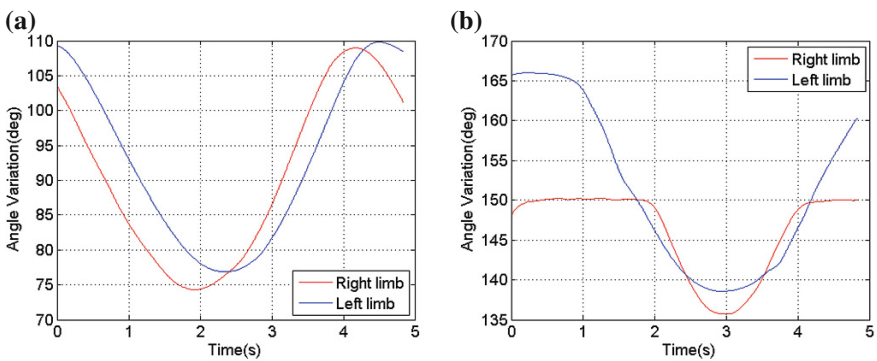


Fig. 6 Measured joint angles of the exoskeleton during walking test at: **a** hip joint; **b** knee joint

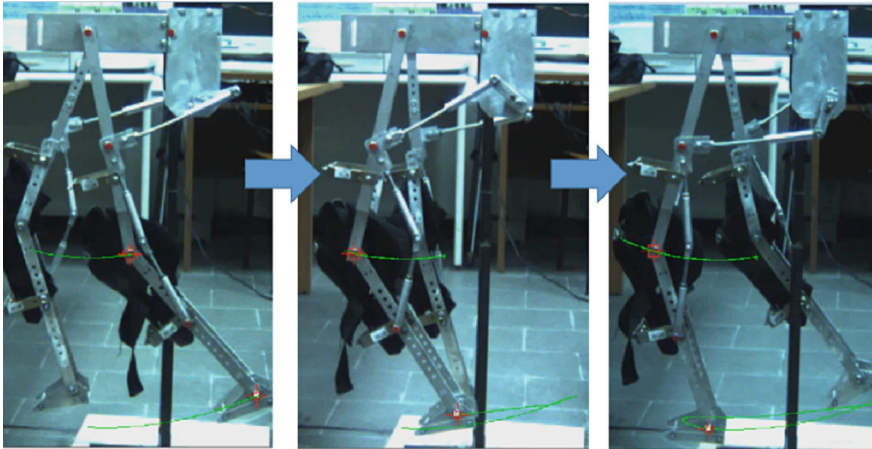


Fig. 7 A snapshot of measured trajectories of the exoskeleton’s joints during a walking test

It’s possible to observe that the exoskeleton has a smaller hip angle variation as resulting in a smaller step size. The trajectories of both human and exoskeleton’s knee and ankle points reveal a similar shape as shown in Fig. 7.

The exoskeleton’s trajectories have a smaller length than the human ones as shown in Fig. 8. This can be due as a consequence of having a smaller step size. The difference between the human and the exoskeleton’s paths can also be due the fact that the exoskeleton has been tested “on air” by neglecting the contact forces with the ground.

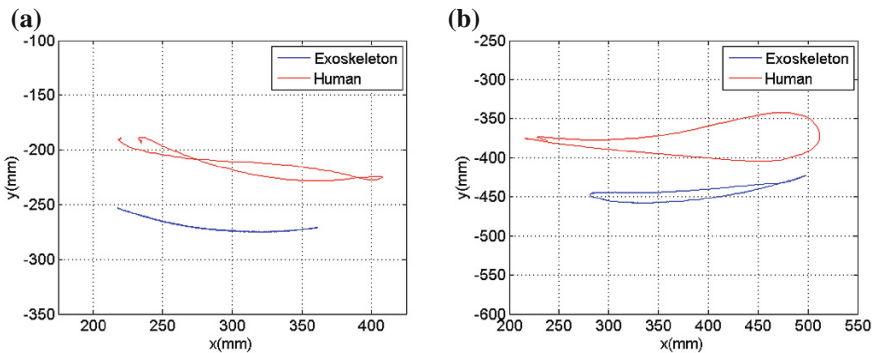


Fig. 8 Point trajectories comparison: a knee; b ankle

5 Conclusions

The tested exoskeleton's prototype is a preliminary solution in a design activity at LARM. Its gait pattern has revealed a behavior similar to the human gait regarding knee angles, and trajectories of ankle and knee points. Future work should involve the test of the exoskeleton's gait on the ground in order to compare experimental results.

References

1. Novandy B, Yoon J, Manurung M A (2009) Interaction control of a programmable footpad-type gait rehabilitation robot for active walking on various terrains. In: IEEE 11th international conference on rehabilitation robotics, pp 23–26
2. Banala SK, Kim SH, Agrawal SK, Scholz JP (2009) Robot assisted gait training with active leg exoskeleton (ALEX). *IEEE Trans Neural Syst Rehabil Eng* 17(1)
3. Cooper R, Dicianno BE, Brewer B, LoPresti E, Ding D, Simpson R, Grindle G, Wang H (2008) A perspective on intelligent devices and environments in medical rehabilitation. *Med Eng Phys* 30:1387–1398
4. Banala S, Agrawal S (2005) Gait rehabilitation with an active leg orthosis. In: Proceedings of international design engineering technical conferences and computers and information in engineering conference, pp 24–28
5. Kawamoto H, Lee S, Kanbe S, Sankai Y (2003) Power assist method for HAL-3 using EMGbased feedback controller. In: Proceedings of the IEEE international conference on systems, man, and cybernetics. pp. 1648–1653
6. Kazerouni H, Steger R (2006) The Berkeley lower extremity exoskeleton, *Transactions of the ASME. J Dyn Syst, Meas Control* 128:14–25
7. Low K-H, Yin Y-H (2007) An integrated lower exoskeleton system towards design of a portable active orthotic device. *Int J Robot Autom, USA, Jan* 22:32–42
8. Veneman JF, Kruidhof R, Hekman EEG, Ekkelenkamp R, Van Asseldonk EHF, van der Kooij H (2007) Design and evaluation of the LOPES exoskeleton robot for interactive gait rehabilitation. *IEEE Trans Neural Syst Rehabil Eng* 15(3):379–386
9. Banala SK, Kim SH, Agrawal SK, Scholz JP (2008) Robot assisted gait training with active leg exoskeleton (ALEX). *IEEE Trans Neural Syst Rehabil Eng* 17(1):2–8
10. Freivogel S, Mehrholz J, Husak-Sotomayor T, Schmalohr D (2008) Gait training with the newly developed 'LokoHelp'-system is feasible for non-ambulatory patients after stroke, spinal cord and brain injury. feasibility study, *Brain Inj* 22(7–8):625–632
11. Pratt JE, Krupp BT, Morse CJ, Collins SH (2004) The RoboKnee: an exoskeleton for enhancing strength and endurance during walking. In: Proceedings IEEE international conference on robotics and automation, New Orleans USA, pp 2430–2435
12. Yamamoto K, Ishii M, Hyodo K, Yoshimitsu T, Matsuo T (2003) Development of power assisting suit (miniaturization of supply system to realize wearable suit). *Jpn Soc Mech Eng Int J, Ser C* 46(3):923–930
13. Low KH, Liu X, Yu H (2005) Development of NTU wearable exoskeleton system for assistive technologies, *Mechatronics and Automation*. In: IEEE international conference, vol 2, pp 1099–1106
14. Kyoungchul K, Doyoung J (2006) Design and control of an exoskeleton for the elderly and patients. *IEEE/ASME Trans Mechatron* 11(4):428–432

15. Farris RJ, Quintero HA, Goldfarb M (2011) Preliminary evaluation of a powered lower limb orthosis to aid walking in paraplegic individuals. *IEEE Trans Neural Syst Rehabil Eng* 19 (6):652–659
16. Copilusi C, Ceccarelli M, Dumitru N, Carbone G (2013) Design and simulation of a leg exoskeleton linkage for a human rehabilitation system, SYROM 2013 Brasov. Springer, Dordrecht, pp 117–125
17. CONTEMPLAS (2010) Motion analysis equipment user manual
18. Marco Ceccarelli (2013) Problems and experiences on cable-based service robots for physiotherapy applications, new trends in medical and service robots. Springer, Dordrecht, pp 27–42

Characterization and Analysis of Data in Autistic Walk Pressure

L. Souza, S. Rosa, M. Carvalho and T. Torquato

Abstract Child autism is a disorder of premature start which predominantly affects three abilities: social interaction, communication/language and behavior. The consequences of this disorder are variable. Several theories have been created in an attempt to explain the characteristics present in people with autism, however the etiology remains unknown. This article proposes a new method to help identify Autism. The objective has its basis on stepping mechanic etiology to characterize as the stepping pressure dynamics of an autistic is bigger in certain areas of the foot. For that, we have used the Symbolic Dynamics methodology (SD) which will help symbolize the signal temporal series generated from the balls of the foot's pressures during the walking of patients with autism, so we shall visualize the dynamics of the activities of the stepping pressure. The methodology used in this work started with the obtaining of data from the Autistic Walk Pressure, followed by the symbolization of temporal series using the Symbolic Dynamics methodology which helped us to analyze and characterize the data. The results have shown that the distancing of the distribution indicates evidence of structure deterministic in the data, allowing to distinguish particular characteristics of Autism by its walking.

Keywords Child autism · Symbolic dynamic · Genetic algorithm

L. Souza (✉) · M. Carvalho
University of Brasília, Brasília, Brazil
e-mail: lynwoodfera@gmail.com

M. Carvalho
e-mail: molavom@gmail.com

S. Rosa
MIT Media Lab—Camera Culture, EUA, Brussels, Belgium
e-mail: suelia@unb.br

T. Torquato
Federal Institute of Goiás, Goiânia, Brazil
e-mail: thiane_marques@hotmail.com

1 Introduction

Child autism is a disorder of premature start which predominantly affects three abilities: social interaction, communication/language and behavior. Known as a human development disorder, autism is quite known, but it intrigues us all with its numerous and different characteristics, for example, an autistic child which has a completely ordinary appearance and at the same time an irregular personality, having several abilities in some areas, and at the same time with others quite strained.

The symptoms which can evidence autism are present from the beginning of life, and can be characterized before 3 years old. The individuals with such disease have a restricted lifestyle and repetitive behaviors, but their intelligence conditions may vary from mental retard to levels of extremely high intelligence, happening in special occasions of being considered geniuses, due to their great intelligence in specific situations.

Over the last decade, the rise in incidence of the autistic disorder have called the attention of worldwide health [2, 3]. In initial reports about the autistic disorder prevalence statistics in the end of 1970s, there was a consensus of 4 cases for every 10,000 children [7], but from 2000 on this number has reached worrying numbers, only in the United States, children demonstrably with autism were already 4 cases for 1,000 children [2], the “Center for Disease Control and Prevention”, in 2010, published an estimated prevalence of 1 for each 68 children in the world are diagnosed with autism.

The realization of child diagnosis is difficult, because its clinic manifestations appear to be multifaceted and heterogeneous [5]. There is a variation of clinic pictures which may be various according to their intellectual level, their age, symptoms, family dynamics, school routine, etc.

Parents start to clearly find out that their children are different from the others of the same age when they start to use the language, mainly due to the delay to start the verbal language, having the parents look for medical help. Parents can observe characteristics of child autism when they are around three months old, but the definitive diagnosis is, in general, found out from 3 years old on. Even the more concerned parents who notice the symptoms, take their children to a doctor no later than after 2 years old [6].

This distance between the first symptoms and the definitive diagnosis is a grave feature in the child’s quality of life. It would be important for parents to identify the initial symptoms and look for a professional doctor as early as possible [5]. The population’s unawareness about autism makes the parents’ understanding more difficult ahead of the symptoms their children present. If the doctor identifies autism in the beginning of life, it is possible to trace therapies which control the advancement of the syndrome.

Literature shows that children who began treatment during the period of 3 years of age have presented a high level in their development. The ones who develop

language skills before 5 years old have had bigger chances of adapting to regular school, substantially improved their linguistic and communication skills [6].

Furthermore, the sooner a diagnosis is established, the bigger the chances of an adequate development for the child. The improvement in their skills will be intimately connected to the time of finding autism, being indispensable for an improvement in the life of the child [5].

The diagnosis of this syndrome must be carried out by a professional with extreme clinic expertise, because there are no able laboratory examination to identify autism, therefore its diagnosis is basically found through the doctor's clinical assessment, observing the various symptoms presented by the patient.

Nevertheless, this research proposes a new method to help identify and treat this disorder which affects the life of thousands of children and, consequently, their family's lifestyle. As the diagnosis for detecting autism is done only through clinical assessment, there is a check-list to assess and eventually diagnose autism and for that we are proposing a new parameter which may help the professional in this diagnosis process.

The methodology we are proposing is carried out through collected data from the Pressure of the Autistic Walk (PAW), and having these data at hand we will apply the Symbolic Dynamics technique (SD) to analyze all existing dynamics in the collected data through PAW. With this methodology, it is possible to determine some particular characteristics present in children which may have this disorder.

2 Methodology

The PAW data of each individual come from capturing eight different electrodes which represent the complete walk, the data are stored by a microcontroller developed for this end [9].

For characterization and analysis of the PAW data, we have used the symbolization of experimental temporal series describe by [4]. The method consists of transforming the signals or temporal series into a sequence of symbols, based on an alphabet. For example, using a binary alphabet ($n = 2$), to each available measure in the data we have attributed the symbols "0" or "1", when the value of the measure is below or above a threshold data point, respectively, as shown in Fig. 1, for the case of a periodical temporal series (sinusoidal). After that, a sequence of symbols of " m " length is chosen, and the relative frequencies of all possible sequences of symbols of " m " dimension are calculated for the complete sequence obtained from the discretization of the experimental signals (see Table 1).

One can represent the " m " length by its decimal equivalent, for example, the sequence 011_2 (binary basis) by 3^{10} (decimal basis), with this, the statistics distribution of the symbolic sequences can be represented as a histogram, shown in Fig. 2, in which the horizontal axis corresponds to the symbolic sequences and the vertical axis the relative frequency of the sequences [4].

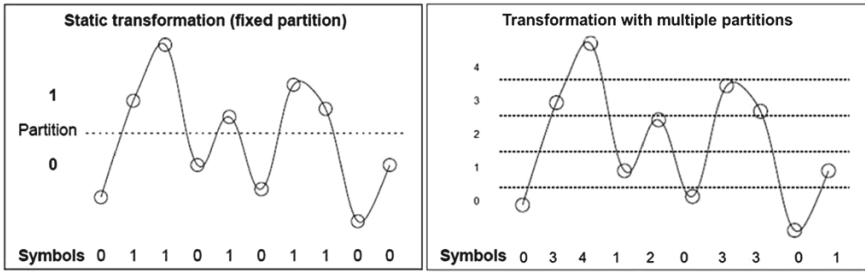
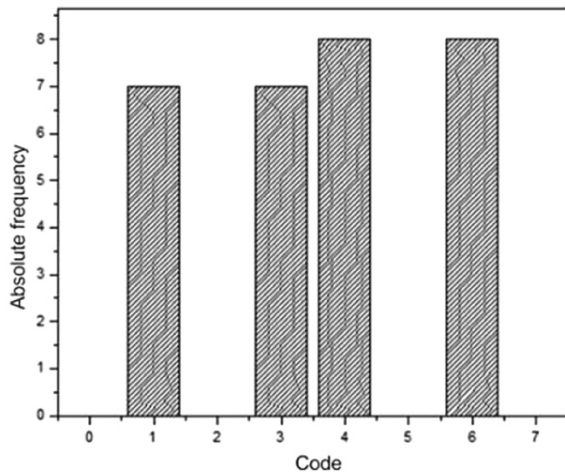


Fig. 1 Symbolization of the temporal series

Table 1 Frequency of the sequences obtained in Fig. 2

Sequence	Code	Frequency
000	0	0
001	1	7
010	2	0
011	3	7
100	4	8
101	5	0
110	6	8
111	7	0

Fig. 2 Distribution of absolute frequency for a periodical temporal series



For purely random data, all symbolic sequences of “ m ” length are equiprobable. Therefore, the distance from this behavior indicates the evidence of deterministic structure in the data.

In symbolization there are four parameters to be adjusted: Alphabet Size (AS), Word Size (WS), Window Size (WSz) e Window Step (WSt). AS defines how many symbols will be used for symbolizing the series, that is, we configure the quantity of existing partitions; WS is the amount of symbols which will form the word; WSz is the section of the signal which will be symbolized and WSt is the time interval between a temporal window position and the subsequent position during the symbolization of the signal [8].

Depending on the attributed values to the parameters, a distinction may not be possible between the signals after symbolization. To solve this type of problem we use an optimization to find the values for the parameters which best configure the symbolization, as an optimization tool we have used Genetic Algorithms, because they are a very indicated tool in the literature [1]. The objective is to find parameters which afford a better distinction between the signals of PAW.

As a function of activating the optimization, we have implemented Shannon’s Entropy [4], a statistic measure capable of finding degrees of uncertainty among the used values, thus, the lower the value of Shannon’s index the lower the degree of uncertainty, however, comparing signals of PAW with autism and PAW without autism, the larger the difference in the degree of uncertainty among them, the better the differentiation between the signals, consequently, the more adequate the parameters used for symbolizing the temporal series at that moment.

$$H_s(L) = - \frac{1}{\log N_{obs}} \sum_i p_{i,L} \log_{p_{i,L}} \tag{1}$$

Where N_{obs} is the total number of columns of the histogram with value different from zero and $P_{i,L}$ is the relative frequency of the values in each column of the histogram. For each generation of individuals created by the Genetic Algorithm, their entropy will be calculated, generating for each one their aptitude, thus we shall add the aptitudes of all individuals of demonstrably with autism and a non-autistic one, calculating the difference between them afterwards.

$$Dif = \left| \int i_n - \int i_a \right| \tag{2}$$

After this process the Genetic Algorith will find the population with bigger aptitude, which means that it will be the population which has a bigger difference between PAW. At the end of the optimization, the Genetic Algorithm will inform us of the parameter values used to symbolize the population which has obtained the biggest difference between the signals.

Table 2 Genetic operators used in the optimization

Genetic operators	Values
Chromosome size	8
Population size	50
Crossover rate	0.80
Mutation rate	0.90
Crossover points	2
Individuals in elitism	3
Number of generations	10
Type of selection	Rank
Type of optimization	Maximization

Table 3 Optimized parameter values in symbolizing the temporal series using the genetic algorithm

Parameters	Values
Word size	2
Alphabet size	3
Window size	5
Window step	3
Aptitude	858,542,685,245

3 Preliminary Results

As it is proposed in this project, we will symbolize the PAW signals of autistic and non-autistic people and through the symbolization of the temporal series we shall abstract clear characteristics which differentiate both signals.

In Symbolic Dynamics there are four configuration parameters, in which the values of these parameters can mean changes in the symbolization results. To start the optimization, the following values have been described in Table 2 for each genetic operator.

Through the cited methods, at the end of the optimization the Genetic Algorithm has generated the values with greater aptitude the parameters which have been used so that such individual could be found, are described in Table 3.

Configuring the symbolization with the parameters described in Table 3, we find the following results which relate all symbolization dynamics between both types of PAW signals (see Figs. 3 and 4):

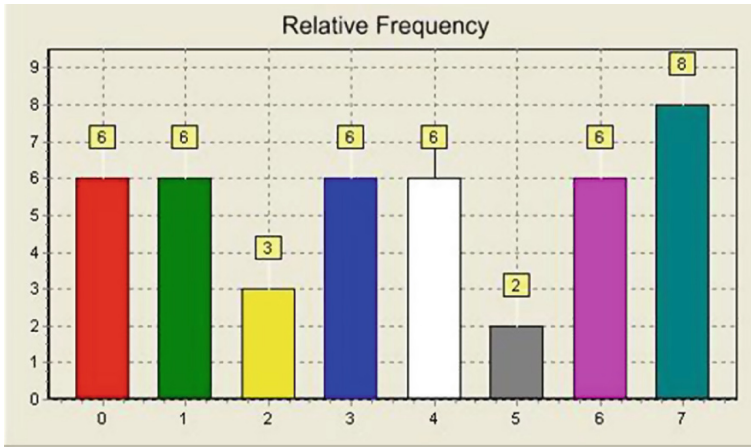


Fig. 3 Frequency of symbolization among all signals without autism

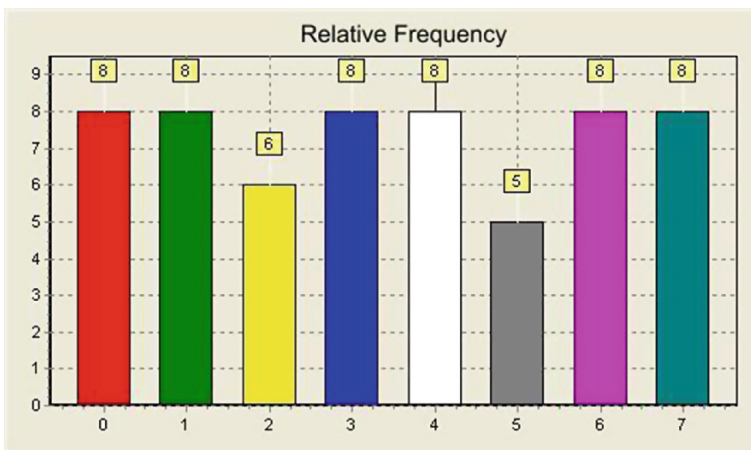


Fig. 4 Frequency of symbolization among all signals with autism

4 Conclusions

These are initial tests to characterize and analyze PAW signals applying the Symbolic Dynamics methodology. The capturing method of PAW signals developed by [9] has been a work which involved only the creation of the capture method of these signals, but it would be a big loss not to analyze these signals as a way to extract important information which can aid the diagnosis of this disorder which reaches more than 70 million people around the world, according to data from the UN in 2012.

The method choice for data analysis was inspired by the works of [4, 8], who applied the Symbolic Dynamics in periodical and bioelectric signals, obtaining great results with the method and being very efficient in applying in different types of signals.

The initial results according to Figs. 3 and 4 have been very encouraging, because by observing the values, we have detected that in individuals who have autism demonstrated bigger values than the signals of individuals without autism.

The application of SD to analysis and characterization of PAW data initially, have become very promising, being able to visually differentiate through histograms values which show deterministic characteristics, allowing for differentiation and later greater analysis, reaching better results.

References

1. Azevedo FM (1999) Algoritmos genéticos em redes neurais artificiais, V Escola de Redes Neurais, ITA. São José dos Campos – SP, 19 de Julho
2. Bertrand J, Mars A, Boyle C, Bove F, Yeargin-Allsopp M, Decoufle P (2001) prevalence of autism in United States population: the brick township, New Jersey, investigation. *Pediatrics* 108(5):1151–1161
3. Croen LA, Grether JK, Hoogstrate J, Selvin S (2002) The changing prevalence of autism in California. *J Autism Dev Disord* 32(3):207–215
4. Daw CS, Finney CE, Tracy ER (2003) A review of symbolic analysis of experimental data. *Rev Scientifics Instrum* 74:916–930
5. Moraes C (2011) Autismo infantil: Aspectos clínicos e epidemiológicos, *Revista Debates em Psiquiatria*. Rio de Janeiro. Ano 1:6–9
6. Robins D, Dumont-Mathieu L (2006) Early screening for autism spectrum disorders: update on the modified checklist for autism in toddlers and other measures. *Dev Behav Pediatr* 27(2)
7. Rutter M (1978) Diagnosis and definition of childhood autism. *J Autism Child Schizophr* 8:139–161
8. Souza L (2012) Caracterização e Detecção Automática de Eventos Epileptiformes em Sinais de Eletroencefalograma por Dinâmica Simbólica. Dissertação de Mestrado em Ciências Mecânicas, Universidade de Brasília, Distrito Federal
9. Ximenes M, Peron G (2013) Implementação e avaliação de uma palmilha de látex com sistema de sensores para investigação da distribuição de pressão plantar em indivíduos autistas. Dissertação de graduação em engenharia eletrônica, Universidade de Brasília, Campus Gama, DF, p 77

Physiological-Like Testing of the Dislocation Stability of Artificial Hip Joints

S. Herrmann, M. Kähler, R. Grawe, D. Kluess, C. Woernle
and R. Bader

Abstract Dislocation of total hip replacements (THR) is a major reason for revision procedures. Dislocations may be caused by a prior prosthetic or bony contact (impingement) or by dynamic forces leading to spontaneous separation. Contributing factors are, above all, implant position and design and soft tissue condition. In order to enable evaluation of THR stability under physiological and reproducible conditions within an experimental setup, a novel hardware-in-the-loop (HiL) joint simulator has been developed. A six-axes industrial robot with a 6-DOF force-torque sensor moves and loads real THR components in a closed control loop with a musculoskeletal multibody model. By HiL simulation of load cases with a high tendency to impingement and subsequent dislocation, contributing factors can be identified.

Keywords Artificial hip joint · Dislocation Stability

M. Kähler · R. Grawe · C. Woernle
Department of Mechanical Engineering and Marine Technology, University of Rostock,
Rostock, Germany
e-mail: michael.kaehler2@gmail.com

R. Grawe
e-mail: robert.grawe@uni-rostock.de

C. Woernle
e-mail: woernle@uni-rostock.de

S. Herrmann (✉) · D. Kluess · R. Bader
Department of Orthopedics, University Medicine Rostock, Rostock, Germany
e-mail: sven.herrmann@med.uni-rostock.de

D. Kluess
e-mail: daniel.kluess@med.uni-rostock.de

R. Bader
e-mail: rainer.bader@med.uni-rostock.de

1 Introduction

Dislocation of total hip replacements (THR), i.e. levering the prosthetic ball-head out of the acetabular cup, is a serious postoperative complication and a major reason for revision procedures. Mechanisms linked to the dislocation process involve prior prosthetic or bony contact (impingement), and spontaneous separation due to dynamic forces. In both cases, the soft tissue response during the dislocation process which may alter the force magnitude and direction acting on the hip joint is most important. While THR loading has been thoroughly explored for daily life activities [1], the dynamic load situation under worst-case scenarios like dislocation events is quite unknown. THR dislocation and the precise contribution of each influencing factor is not yet fully understood as *in vivo* measurements of manoeuvres inducing dislocation are not available.

In order to experimentally evaluate THR stability under physiological and reproducible conditions, a biomechanical approach based on hardware-in-the-loop (HiL) simulations has been developed [2, 3, 8]. The physical HiL test setup consists of a six-axes industrial robot that moves and loads a real endoprosthesis. The anatomical environment of the joint is extracted into a musculoskeletal model running in real-time that bidirectionally interacts with the robot (Fig. 1). The objective of the musculoskeletal model is to calculate physiological reaction forces/torques within the joint. The functional principle of HiL simulations for testing total hip and knee replacements has been successfully demonstrated [2, 3, 8].

In the present contribution, a modified formulation of the inverse dynamics redundancy problem compared to [8] is described that avoids computationally expensive calculations of explicit loop closure conditions. Further, results of dislocation scenarios are presented.

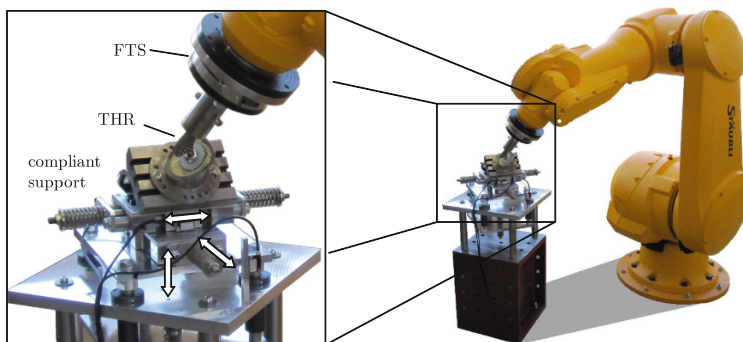


Fig. 1 Physical setup of the HiL joint simulator with a 6-DOF force-torque sensor (*FTS*) and a total hip replacement (*THR*)

2 Functional Principle of HiL Simulations for Testing THR

The functional principle of the HiL simulations for testing THR is based on complementary sets of free and constrained directions of the artificial joint [2, 3, 8]. For an artificial hip joint according to Fig. 2, the three rotations of the femur relative to the pelvis with rotation angles summarised in vector $\beta \in \mathbb{R}^3$ are free within the anatomical range of motion. The three translational movements of the femoral head center with coordinates summarised in vector $z \in \mathbb{R}^3$ are treated as constrained directions. For an actual time instant t , the multibody model delivers values of the rotation angles β in the free directions and of the reaction forces in the constrained directions, summarised in the vector $f^r \in \mathbb{R}^3$. Soft tissue forces comprising passive ligament and capsule forces and active muscle forces as well as gravitational and inertial forces are also taken into account. Both rotation angles β and reaction forces f^r are transferred to the robot controller. Hence, the robot rotates the femoral component into the position $\bar{\beta}$ and applies the reaction forces \bar{f}^r onto the endoprosthesis. In the case of ideal transmission of the magnitudes the robot values $\bar{\beta}$ and \bar{f}^r are identical with the corresponding values β and f^r of the model.

To close the HiL control loop the displacement components of the femoral head center $z \in \mathbb{R}^3$ are measured and fed back to the multibody model. Another loop is

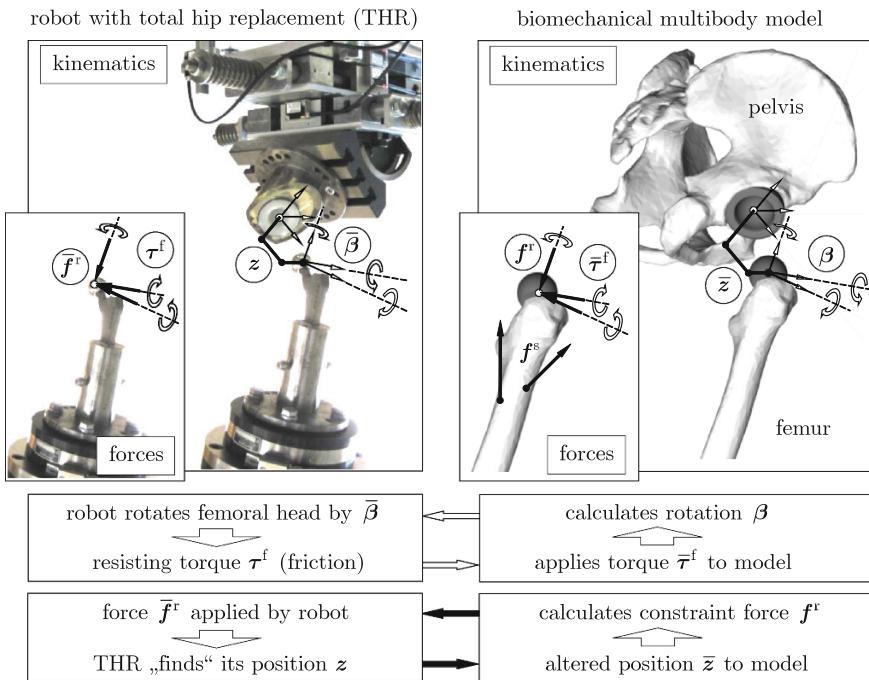


Fig. 2 Functional principle of the HiL joint simulator for testing THR [8]

closed by the resisting torque components $\tau^f \in \mathbb{R}^3$ along the unconstrained rotations $\bar{\beta}$, which are also measured and fed back to the multibody model. The resisting torques τ^f may be caused by friction forces in the THR. For ideal signal transmissions differences between τ^f , z and $\bar{\tau}^f$, \bar{z} , respectively, vanish.

The robot is able to apply the reaction force components \bar{f}^r if the endoprosthesis withstands these loads in the corresponding directions. Then no relative translational displacement occurs, thus $z = \mathbf{0}$. Otherwise, the femoral head is moved out of the acetabular cup by a displacement z indicating a dislocation event.

3 Musculoskeletal Model for THR Testing

Depending on the load case under consideration specific musculoskeletal models are built up. A human motion that is prone to dislocation of total hip replacements (THR) is a deep squat with both feet attached to the ground that are symmetrical with respect to the sagittal plane.

According to Fig. 3, the musculoskeletal model used for these investigations represents the right lower extremity of the human body.

3.1 Model Topology and Coordinates

The kinematic chain of the multibody model consists of the foot assumed to be ground-fixed, tibia and fibula modeled as one rigid body, femur, pelvis, and the

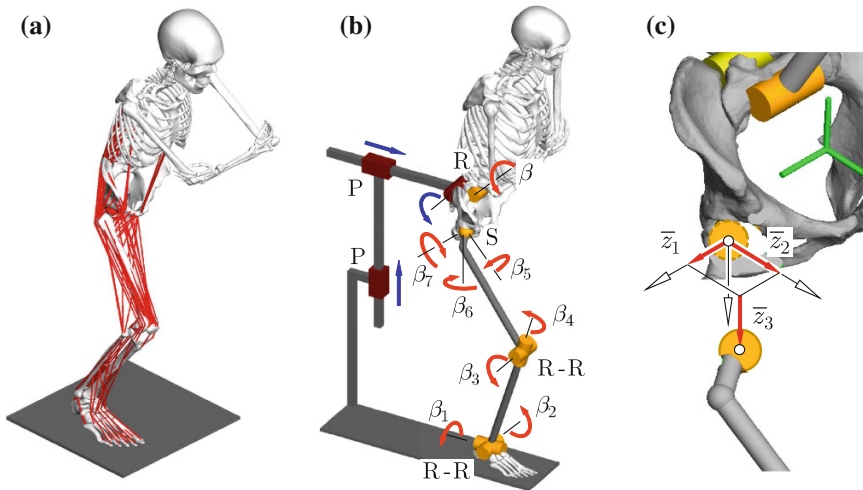


Fig. 3 Multibody model of the lower extremity for THR testing. **a** Musculoskeletal model. **b** Multibody topology (joints: *R*-revolute, *P*-prismatic, *S*-spherical). **c** Dislocation coordinates

upper body including head and arms summarized as one rigid body. Both ankle and knee joint are modelled by universal joints (U) with two rotational degrees of freedom each. The upper body is attached to the pelvis at the sacrum endplate centre by a revolute joint. The hip joint is modelled by a kinematic subchain consisting of three orthogonal prismatic joints and three revolute joints with co-intersecting axes being equivalent to a spherical joint (S). According to Fig. 3, the revolute joints (rotation angles $\beta_5, \beta_6, \beta_7$) enable the free hip joint motions: abduction/adduction, internal/external rotation, and flexion/extension. The coordinates of the prismatic joints are constrained by the measurements \bar{z} provided by the robot, see Fig. 2. The symmetry condition is achieved by means of a fictive planar joint in the sagittal plane, connecting the pelvis by two prismatic (P) and a revolute (R) joint with the ground. The constraint forces and torques of the planar joint represent the reaction forces between the modeled right lower extremity and its left counterpart that is not included in the model. With altogether eleven joint degrees of freedom and one kinematical loop, the overall degree of freedom of the model is $d = 5$.

The loop closure conditions are appropriately formulated by cutting the loop at the planar joint. The cut planar joint leads to three implicit loop closure constraints for the eight joint coordinates of the spanning tree $\beta = [\beta_1 \dots \beta_8]^T$ that read at the position and velocity levels (constraint Jacobian G), respectively,

$$g(\beta, \bar{z}) = \mathbf{0} \quad \text{and} \quad \dot{g} \equiv G(\beta, \bar{z}) \dot{\beta} = \mathbf{0} \quad \text{with} \quad G = \frac{\partial g}{\partial \beta} \in \mathbb{R}^{3,8}. \tag{1}$$

The constraints depend on the measured displacements \bar{z} in the constrained directions of the hip joint, see Fig. 2. In (1), the time derivative of \bar{z} is neglected as the dynamics of the displacements in the constrained directions is not physically based but governed by the force controller of the robot. This assumption is considered to be acceptable as long as the displacements \bar{z} are small.

3.2 Inverse Dynamics

The equations of motion of the multibody model shown in Fig. 3 are formulated in terms of the joint coordinates of the spanning tree $\beta \in \mathbb{R}^8$,

$$M(\beta, \bar{z}) \ddot{\beta} = \tau^c(\beta, \dot{\beta}, \bar{z}) + \tau^p(\beta, \dot{\beta}, \bar{z}) + \tau^f + \tau^m(\beta, \bar{z}, \alpha) + G^T(\beta)\lambda. \tag{2}$$

The mass matrix $M \in \mathbb{R}^{8,8}$ is obtained under the assumption that the soft tissue masses are added to the masses of the corresponding skeletal bodies. Dynamic wobbling of the muscle masses is neglected. The vector $\tau^c \in \mathbb{R}^8$ contains the torques of the centrifugal and gravity forces with respect to the joint axes, $\tau^f \in \mathbb{R}^8$ are the measured resisting torques fed back from the robot into the model according

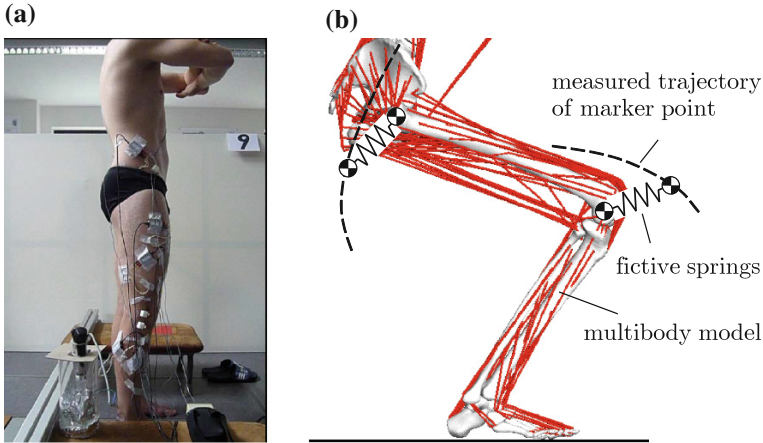


Fig. 4 Definition of physiological motions. **a** Motion capturing. **b** Transferring measured motion data onto the multibody model

to Fig. 2, $\tau^p \in \mathbb{R}^8$ are the torques due to passive soft tissue structures such as the hip capsule, and $\tau^m \in \mathbb{R}^8$ are the torques from the active muscle forces depending on muscle activation levels α , see (5). The term $\mathbf{G}^T \lambda$ includes the torques of the constraint forces at the cut planar joint that are expressed by means of the constraint Jacobian \mathbf{G} from (1) and vector $\lambda \in \mathbb{R}^3$ with the reaction force coordinates (Lagrange multipliers) of the planar joint.

Dislocation scenarios are analyzed for given human motions that are measured by a motion capture system. In order to transfer the measured motions onto the joint coordinates of the multibody model β , the sum of the squares of the distances between the measured marker points and the related points on the model are minimised, as qualitatively illustrated in Fig. 4 by coupling the related points by springs.

It is assumed that the position, velocity, and acceleration of primary joint coordinates $\beta(t)$ are known from these measurements. Further, the actual displacements in the constrained directions z are known from the measurements at the physical test setup. The inverse dynamics calculation yields the torques τ^m driving the overall system as well as the joint reaction force at the hip joint f^r to be applied to the endoprosthesis by the robot according to Fig. 2.

The equations of motion (2) provide eight linear equations for the eight muscle torques τ^m and the three reaction force coordinates λ (unit matrix \mathbf{I}),

$$\begin{bmatrix} \mathbf{I} & \mathbf{G}^T \end{bmatrix} \begin{bmatrix} \tau^m \\ \lambda \end{bmatrix} = \mathbf{b} \quad \text{with} \quad \mathbf{b} = \mathbf{J}^T (\mathbf{M} \ddot{\beta} - \tau^c - \tau^p - \bar{\tau}^f). \quad (3)$$

The solution of (3) with respect to τ^m and λ is not unique as the kinematic loop shown in Fig. 3 can be internally loaded by the active muscle torques τ^m without changing its position. A solution of this redundancy problem is obtained by

regarding (3) as an equality constraint for a static optimisation problem minimising a quadratic objective function with a diagonal weighting matrix Q [7],

$$Z(x) \equiv x^T Q x = \min_x \quad \text{with} \quad x = \begin{bmatrix} \tau^m \\ \lambda \end{bmatrix} \quad \text{subjected to (3)}. \tag{4}$$

The forces $f^m \in \mathbb{R}^{n_f}$ of n_f muscles taken into account are modelled in terms of their muscle activation levels α which are used to scale the isometric force of each muscle [4], hence

$$f^m = B(\beta, \bar{z}) C \alpha \tag{5}$$

where matrix $B \in \mathbb{R}^{n_f, n_f}$ summarizes the normalized force/torque directions of each muscle. The diagonal matrix $C \in \mathbb{R}^{n_f, n_f}$ contains the isometric muscle forces $C_i = A_i \sigma_i$ obtained from the physiological cross section area A_i times the physiological muscle stress σ_i . Up to $n_f = 70$ muscles were taken into account.

In the multibody system, the muscle forces f^m from (5) are projected onto the directions of the joint motions by means of a Jacobi matrix J ,

$$\tau^m = J^T(\beta, \bar{z}) B(\beta, \bar{z}) C \alpha. \tag{6}$$

For muscle torques τ^m given by the solution of (4), muscle activations α are calculated by solving a second quadratic optimisation problem with a positive definite weighting matrix P and a weighting vector p ,

$$\begin{aligned} Z_\alpha(x) &\equiv \alpha^T P \alpha + p^T \alpha \\ &= \min_\alpha \quad \text{with} \quad \alpha \quad \text{subjected to (6) and } 0 \leq \alpha_i \leq 1. \end{aligned} \tag{7}$$

Finally, the reaction forces f^r at the hip joint are calculated using the laws of momentum and moment of momentum of the bodies of the spanning tree with the reaction force coordinates obtained from (4) and the muscle forces from (5).

The simulation model has been built up in the multibody software SIMPACK. To parametrise the musculoskeletal model, osseous geometries were derived from a human male computed tomography dataset [6] using reconstructing techniques [5].

4 HiL Simulation Results

Calculated hip joint forces were previously validated against in vivo measurement data for normal squatting demonstrating good agreement between measured and computed forces both in magnitudes and patterns. The HiL simulation was then used to quantify THR stability under physiological conditions with respect to manoeuvres associated to posterior dislocation for which in vivo measurements are not available.

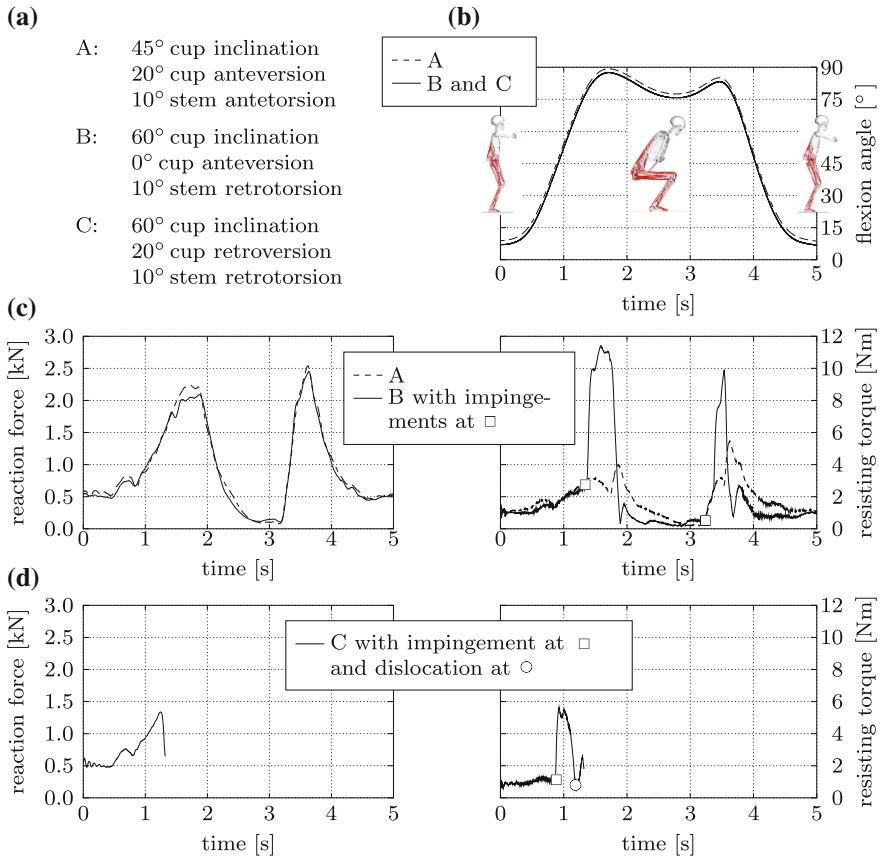


Fig. 5 Deep squat in combination with adduction. **a** Positions of implant components. **b** Flexion angle versus time. **c** Joint reaction force $|f^r|$ (left) and resisting torque $|\tau^r|$ (right) versus time for implant positions A and B. **d** Joint reaction force $|f^r|$ (left) and resisting torque $|\tau^r|$ (right) versus time for implant position C

Among the considered load cases, a deep squat in combination with adduction showed the highest tendency to impingement and dislocation. As an example, the influence of three implant positions according to Fig. 5a on the impingement behaviour is considered for this load case. The flexion angle shown in Fig. 5b is defined between the femur axis and the frontal pelvis plane, whereby pelvis inclination is taken into account. The absolute values of the joint reaction force $|f^r|$ and of the resisting torque $|\tau^r|$ are shown for implant positions A and B in Fig. 5c and for implant position C in Fig. 5d.

With implant position A with 45° cup inclination, 20° cup anteversion, and 20° stem antetorsion no impingements occurred. The resisting torque is roughly proportional to the joint force and caused by friction between the prosthesis components. Implant position B with the steeper 60° cup inclination in combination with

0° cup anteversion and 10° stem retrotorsion shows impingements at 78° flexion during squatting and rising up, respectively, that do not lead to dislocation, however. Most adverse among the three implant positions is C with an additional cup retroversion of 20° with impingement at 41, 5° flexion and complete posterior dislocation at 68° flexion.

5 Conclusion and Outlook

Robot-based HiL-simulation enables reproducible, physiological-like experimental testing of total hip endoprostheses giving visual insights into the process of impingement and dislocation events. By taking the fully musculoskeletal model into account, several influencing factors like soft tissue condition as well as movement and load parameters of the artificial hip joint can be systematically analysed in the future. Ongoing work also considers HiL simulation of knee endoprostheses.

Acknowledgments The authors would like to thank the Deutsche Forschungsgemeinschaft (BA 3347/3-1/2 and WO 452/8-1/2) for supporting the research work presented and Prof. Klaus Schittkowski for providing the FORTRAN subroutine to solve the quadratic optimisation problems.

References

1. Bergmann G, Deuretzbacher G, Heller M, Graichen F, Rohlmann A, Strauss J, Duda GN (2001) Hip contact forces and gait patterns from routine activities. *J Biomech* 34(7):859–871
2. Herrmann S, Kähler M, Souffrant R, Rachholz R, Zierath J, Kluess D, Mittelmeier W, Woernle C, Bader R (2012) HiL simulation in biomechanics: a new approach for testing total joint replacements. *Comput Methods Programs Biomed* 105:109–119
3. Herrmann S, Woernle C, Kähler M, Rachholz R, Souffrant R, Zierath J, Kluess D, Bader R (2012) HiL simulation for testing joint stability after total knee arthroplasty. *Multibody SysDyn* 28:55–67
4. Kaufman K, An KN, Litchy W, Chao E (1991) Physiological prediction of muscle forces. *Neuroscience* 40(3):781–804
5. Kluess D, Souffrant R, Mittelmeier W, Wree A, Schmitz KP, Bader R (2009) A convenient approach for finite-element-analyses of orthopaedic implants in bone contact: modeling and experimental validation. *Comput Methods Programs Biomed* 95(1):23–30
6. Spitzer V, Ackerman MJ, Scherzinger AL, Whitlock D (1996) The visible human male: a technical report. *J Am Med Inform Assoc* 3(2):118–130
7. Vaughan CL, Hay JG, Andrews JG (1982) Closed loop problems in biomechanics. Part II—an optimization approach. *J Biomech* 15(3):201–210
8. Woernle C, Kähler M, Rachholz R, Zierath J, Herrmann S, Souffrant R, Kluess D, Bader R (2013) Robot-based testing of total joint replacements. In: Gerstmayr J, Gatringer H (eds) *Multibody system dynamics, robotics and control*. Springer, Berlin

Experimental Bench Used to Test Human Elbow Endoprosthesis

D. Tarnita, D. Popa, C. Boborelu, N. Dumitru, D. Calafeteanu
and D.N. Tarnita

Abstract In this paper, the 3D virtual model and the prototype of an experimental bench designed and used to test endoprosthesis prototypes for elbow joint in flexion-extension and pronation-supination movements are presented. The experimental tests were carried out on a group of nine healthy subjects and on the corpse prosthetic elbow. Experimental data for flexion-extension movement cycles were acquired using SimiMotion video system. The data files and the flexion-extension angle diagrams are obtained for all the subjects and for the corpse prosthetic elbow. The command programs in C++ for the performance of experimental tests on the bench are elaborated. A comparative experimental study of flexion-extension movement for healthy elbows and for the prosthetic corpse elbow joint fixed on the experimental bench is presented.

Keywords Experimental bench · Human elbow joint · Flexion-extension · Elbow endoprosthesis

D. Tarnita (✉) · D. Popa · N. Dumitru · D.N. Tarnita
University of Craiova, Craiova, Romania
e-mail: tarnita.daniela@gmail.com

D. Popa
e-mail: popadragoslaurentiu@yahoo.com

N. Dumitru
e-mail: nicolae_dtru@yahoo.com

D.N. Tarnita
e-mail: dan_tarnita@yahoo.com

C. Boborelu · D. Calafeteanu
Emergency Hospital, Craiova, Romania
e-mail: boborelu.cristian@gmail.com

D. Calafeteanu
e-mail: danutcalafeteanu@yahoo.com

1 Introduction

Total elbow replacement is very important to rehabilitate the biomechanics of an affected elbow joint. Prosthetic design greatly influences average survival rates of total elbow replacement [15]. Hence it is very important to evaluate in vitro and to test new endoprosthesis prototypes they are implanted into patients. An extensive experimental validation of the mechanical behaviour of the whole bone composite model, compared to human specimens for different loading conditions [5]. In [6] cadaveric tibias and polyurethane foam as a testing bench to assess the pullout strength of different staple leg profiles are used. Synthetic tibias and femurs manufactured as a dummy to test the effect of radiographic alignment in knee arthroplasty are used. Kinematics measurement techniques are modern tools that offer the possibility of measuring the joints kinematics and the biomechanical response to diseases of the musculoskeletal system. The human joints movements data are collected with different acquisition systems, they are analyzed and are represented as temporal diagrams [3, 4, 9–13]. Hand goniometers or video system acquisition were formerly employed for measuring elbow kinematics [3, 4, 14]. In [4, 8] an electrogoniometer was used to illustrate the range of elbow motion required in performing normal activities of daily living and to evaluate patients with elbow and forearm problems. The electromagnetic motion tracking data was used and the first three-dimensional elbow kinematic was described in [12].

2 Experimental Device

The main purpose of this paper is to design and present the 3D model and the physical prototype of our experimental bench used to test elbow endoprosthesis at flexion-extension and pronation-supination movements. The experimental bench designed and carried out within the researches made by our team presents the advantage that it can be used for experimental testing of other joints and endoprosthesis (knee, ankle, radiocarpal joints, etc.), in their various positions. We consider its functionality represents an important advantage in the field of experimental testing of different known endoprosthesis, but, also, of new designed prototypes. In this study, a new elbow endoprosthesis prototype, type ball joint, designed by our team, is tested. The following criteria were taken into account: (1) to allow flexion and extension of forearm bones from horizontal, vertical or lopsided position; (2) to allow pronation-supination movements; (3) to allow the simulation of an actuation drawn upon human biological system.

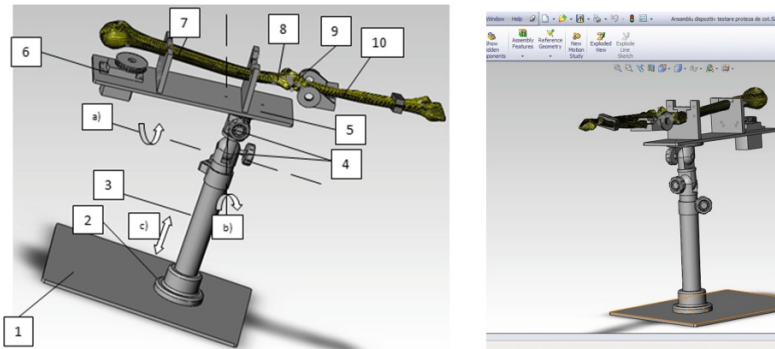


Fig. 1 3D virtual model of experimental bench assembly

2.1 Three Dimensional Virtual Model

The virtual model of the experimental bench assembly is realized using SolidWorks software [1, 2, 14] and it is presented in Fig. 1, where the components are pointed out: 1-base plate; 2-flange; 3-column; 4-maneuver wheels; 5-upper plate; 6-servomotor for the flexion-extension of forearm bones; 7-humerus; 8-elbow endoprosthesis; 9-guiding pulleys for driving cables; 10-radius and ulna.

Based on the virtual models elaborated for all the components and for bench assembly, the physical prototype of the experimental bench has been made of duralumin and stainless steel. From the point of view of the position occupied by humerus, radius, ulna and, implicitly, elbow endoprosthesis, in relation to the base plate 1, the following observations can be made: (1) the superstructure of the experimental bench (components 5–10) can glide after c) axis, the distance between base plate 1 and upper plate 5 being modified; (2) to test the functionality of elbow endoprosthesis 8, relative positions of bones in relation to base plate 1 are provided by rotating the superstructure of the experimental bench around the axes a) and b) by means of maneuver wheels 4.

2.2 Driving, Command and Control Systems

The driving system is inspired from the study of bone and muscular system of human upper limb. For actuation, two direct current servomotors mechanically coupled with transmissions through cables and pulleys were selected. The four-channel pulley 2 is mounted on servomotor 1(used for flexion-extension movements) and four steel cables which glide through the flexible cylindrical sheathings 5 are connected to the pulley. The driving cables can be stressed through the special screws 3 that are threaded in plate 6 which binds and supports the humerus. The servomotor 4, also connected with transmissions through cables and pulleys, has

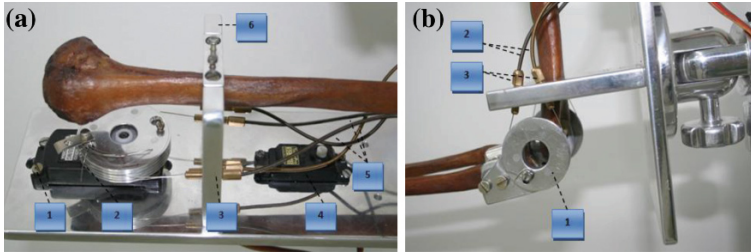


Fig. 2 a Electrical actuators used in the driving system; b Details on the transmissions through cables and pulleys (area of elbow joint)

the role of rotating the radius around the ulna in the pronation-supination movement (Fig. 2a). In Fig. 2b the transmission system through cables and pulleys in the area of elbow joint is presented.

It can be seen the double pulley 1, joint with the forearm bones, which mechanically connects four steel cables routed through flexible cylindrical shirts 2 strained by special screws 3.

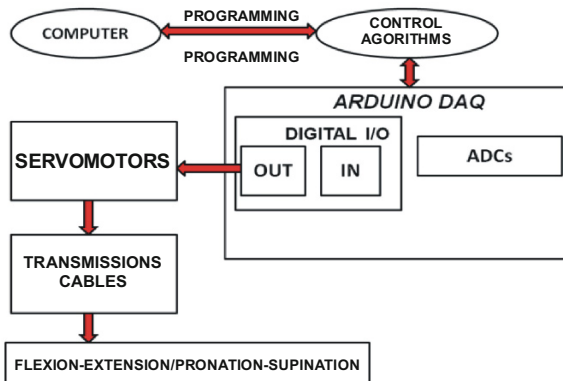
When driving servomotor axis is rotated clockwise, the upper driving cables are stressed and the flexion of forearm bones in relation to humerus is performed. When counterclockwise command is given to the servomotor axis, the lower driving cables which produce the extension of forearm bones in relation to fixed humerus will be stressed. The repetitive flexion-extension and pronation-supination movements are initiated by command and control system based on Arduino Duemilanove command board which is programmed in C++ [1, 2, 14].

The block diagram of command and control system is presented in Fig. 3.

Various positions of the joint in relation to base plate are presented in Fig. 4.

In Figs. 5 and 6 three frames of flexion-extension movement and, respectively, four frames of pronation-supination movement of the prosthetic corpse elbow on the experimental bench are presented.

Fig. 3 Block diagram of command and control system



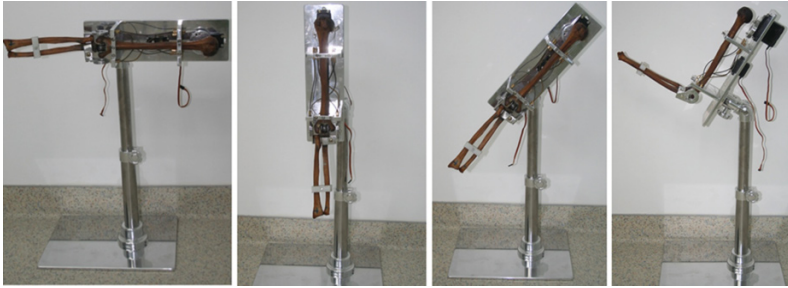


Fig. 4 Positions that can be taken by upper limb bones in relation to base plate

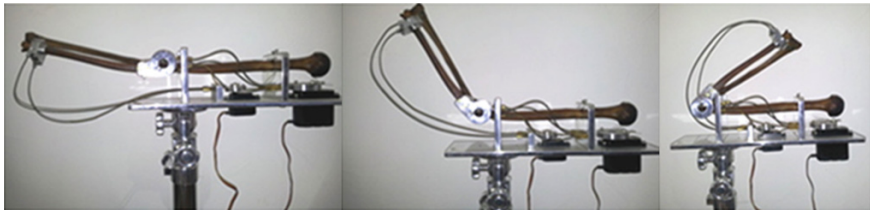


Fig. 5 Frames of flexion-extension movement

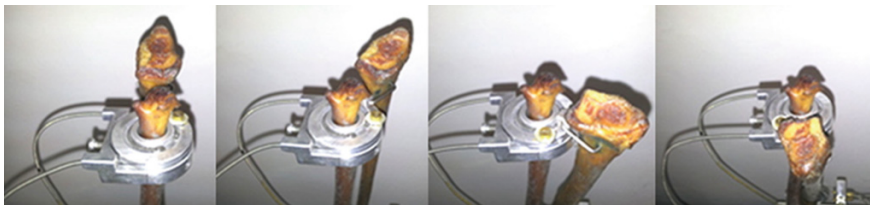


Fig. 6 Frames of pronation-supination movement

3 Method

In order to analyze the kinematics of human elbow flexion-extension movement, an optical motion analysis system was used, the SimiMotion data gathering system based on a video camera Sony DCR-SR 11 full HD [14]. The analysis procedure is based on attaching a series of markers on the system to be analyzed, the positioning of these markers practically representing the identification of the points of interest of the system studied, by SIMI software. The subjects were equipped with three markers attached to the right upper limb in 3 points: lateral edge of acromion-glenohumeral joint; external epicondyle of humerus; radial styloid-radiocarpal joint (Fig. 7).



Fig. 7 Three frames of the film processed with SimiMotion

By attaching the markers, the soft automatically generates the equivalent model of the studied system and follows their motion on each frame captured by the video camera, recording and analyzing simultaneously the positions of markers, serving to obtain the movement laws [14]. The angular amplitudes of human elbow flexion-extension were obtained for each subject from the report generated by the gathering system, as data files type .txt. All data files were processed in Excel and MATLAB environment and then assessed [13, 14]. Considering the natural biological variability of elbow mobility from one individual to another, 7 consecutive cycles were selected for each subject and for the test on the artificial bench and normalized by interpolation with Cubic splines functions, using MATLAB. The interpolated cycles were reported on the abscissa from 0 to 100 %. The average cycle was determined as the arithmetic mean of the movement cycles.

4 Results

The diagrams of the average cycles of the 9 subjects and of the final average cycle of flexion-extension angle for the entire group are presented in Fig. 8.

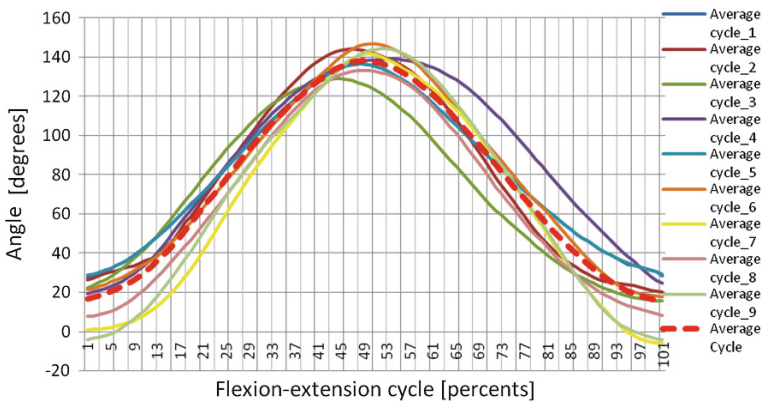


Fig. 8 Normalized diagrams of flexion-extension angles corresponding to average cycles of nine subjects and of the final average cycle

Table 1 Main statistical indicators for the nine subjects

Statistical indicators	Sub 1	Sub 2	Sub 3	Sub 4	Sub 5	Sub 6	Sub 7	Sub 8	Sub 9	Average cycle
Maximum	135.31	144.14	129.01	138.92	136.40	146.71	141.76	133.21	144.26	138.18
Amplitude	108.58	123.89	113.37	119.47	107.58	129.06	147.57	125.46	148.55	123.302
Average	80.02	78.59	72.11	82.47	81.12	79.60	68.34	68.25	69.45	76.03

The main statistical indicators of average cycles of each subject and of the average flexion-extension cycle of the entire experimental group are presented in Table 1.

By comparing the maximum values of the average flexion-extension cycles of human elbow joint corresponding to the 9 subjects, it can be seen this values varied between 133.21° and 146.71° and their average value is 138.968°, with a standard deviation of 6.033° in relation to the maximum value of the average cycle, which is equal to 138.18°. The two maximum values are very close, without significant differences. The minor differences prove a good repeatability of the performance of flexion-extension movement imposed for all the subjects.

In Fig. 9 the variation in time of cyclic flexion-extension angle [degrees] of the elbow joint with prosthesis on the experimental bench is presented. The maximum flexion-extension angle values varies for the seven consecutive cycles from 133.94° to 135.82° with an average value equal to 134.87°, very close of 134.68° which is the maximum value of the average cycle (standard deviation is 0.567°) (Table 2).

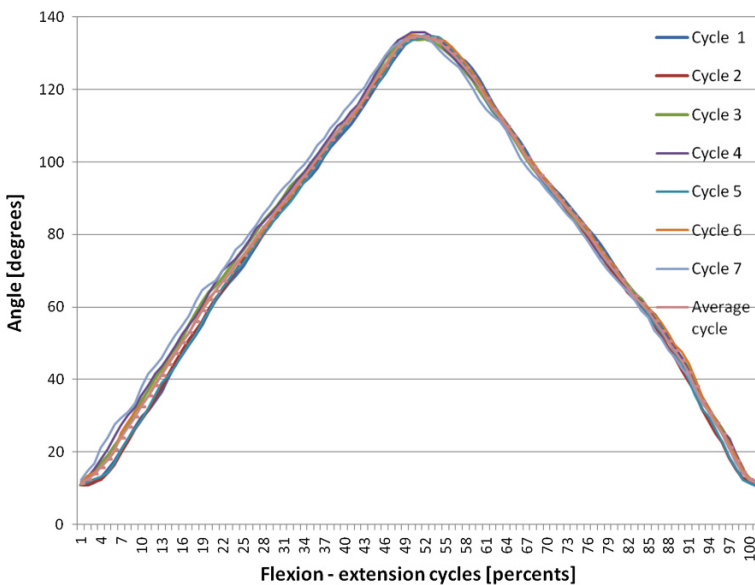


Fig. 9 Variation in time of flexion-extension angle of the elbow joint with prosthesis

Table 2 Main statistical indicators for seven consecutive cycles of prosthetic corpse elbow

Statistical indicators	Cycle 1	Cycle 2	Cycle 3	Cycle 4	Cycle 5	Cycle 6	Cycle 7	Average cycle
Maximum	134.81	134.67	133.94	135.82	134.69	135.14	134.98	134.68
Amplitude	123.95	123.81	122.95	125.26	124.11	123.44	122.99	123.33
Average	75.52	74.91	76.80	77.26	75.02	76.71	77.28	76.22

The maximum values of the medium elbow cycles for the nine subjects and for the seven cycles of corpse determined during the performed trials were compared and tested with an unpaired Student *t*-test, considering $\alpha = 0.05$. The *p*-values corresponding to these tests are calculated using ANOVA. The maximum flexion angles were not significantly different ($t_{\text{calc}} = 2.027 < t_{\text{cr}} = 2.14$ and $p = 0.077 > 0.05$). In a similar manner the average values for the nine subjects and for the seven cycles of corpse elbow were compared and we obtained the following results: ($t_{\text{calc}} = 2.01 < t_{\text{cr}} = 2.14$ and $p = 0.822 > 0.05$). In conclusion, the compared values are not significantly different.

5 Conclusions

The paper presents the 3D model and the physical prototype of our experimental bench used to test elbow endoprosthesis at flexion-extension and pronation-supination movements. A comparison based on the experimental data gathered for nine healthy subjects and for the elbow joint with prosthesis on the experimental bench is presented. The statistical analysis of flexion-extension angle during the flexion-extension movement has revealed insignificant differences between the maximum and average values of the prosthetic corpse joint on the experimental bench and of the healthy subjects group. The first conclusion is that the studied elbow prosthesis manages to re-establish the mobility for the elbow joint as close to the normal one. The second conclusion is that the proposed experimental bench designed and carried out allows the testing of the prosthetic corpse elbow and it also presents the advantage that it can be used for experimental testing of endoprosthesis joints (knee, ankle, joints, etc.), in their various positions.

References

1. Berceanu C et al (2010) Exteroceptive sensor system of a new developed artificial hand. *J Solid State Phenom Robot Aut Syst* 166–167:51–56
2. Berceanu C, Tarnita D (2012) Mechanical design and control issues of a dexterous robotic hand. *Adv Mater Res* 463–464:1268–1271

3. Boone DC, Azen SP (1979) Normal range of motion of joints in male subjects. *J Bone Joint Surg* 61-A:756–759
4. Chao EY, An KN, Askew LJ, Morrey BF (1980) Electrogoniometer for the measurement of human elbow joint rotation. *J Biomech Eng* 102(4):301–310
5. Cristofolini L, Viceconti M (2000) Mechanical validation of whole bone composite tibia model. *J Biomech* 33:279–288
6. Firoozhakhsh KK et al (1996) Staple leg profile influence on pullout strength: a biomechanical study. *Clin Orthop Relat Res* 331:300–307
7. Morrey BF, Askew LJ, Chao EY (1981) A biomechanical study of normal functional elbow motion. *J Bone Joint Surg* 63:872–877
8. Pislá D et al (2013) Kinematics and workspace modeling of a new hybrid robot used in minimally invasive surgery. *Robot Comput Integr Manuf* 29:463–474
9. Plitea N, Hesselbach J et al (2009) Dynamic analysis and design of a surgical parallel robot used in laparoscopy. *J VibroEng* 11:215–225
10. Richards JG (1999) The measurement of human motion: a comparison of commercially available systems. *Hum Mov Sci* 18:589–602
11. Tanaka S, An KN, Morrey BF (1998) Kinematics and laxity of ulnohumeral joint under varus-valgus stress. *J Musculoskel Res* 2:45–54
12. Tarnita D et al (2013) Experimental measurement of flexion-extension movement in normal and osteoarthritic human knee. *Rom J Morphol Embryol* 54(2):309–313
13. Tarnita D, Marghitu DB (2013) Analysis of a hand arm system. *Robot Comput Integr Manuf* 29(6):493–501
14. Verdonschot NJ et al (1993) Pre-clinical testing of hip prosthetic design: a comparison of finite element calculations and laboratory tests. *Proc Instn Mech Engrs* 207:149–154

A Dynamic Intramedullary Implant for Bone Fracture Repair

A. Dowd, B.J. Mac Donald, R. Lostado, W.T. McCartney and D. Comiskey

Abstract Intramedullary (IM) nails are commonly used in the fixation of long bone fractures such as fractures of the femur and tibia. They are commonly hollow, rigid rods made from 316L steel or titanium alloys. Static locked IM nails which ensure that both ends of the long bone do not move relative to each other have traditionally been used, however, recent research suggests that such rigid bone-nail constructs do not provide optimal conditions for bone healing. Dynamic fixation allows the bone fragments to move a prescribed distance relative to each other, thus causing micro-motions at the fracture site and stimulating healing via callus formation. This paper describes the development and proof of concept of a new dynamic IM nail, incorporating an internal mechanism which allows for a tailored micro-motion at the fracture site. In vitro bench testing using synthetic composite bones (Sawbones, USA) was carried out to compare the performance of the new device with standard IM nails under compression, four-point bending and torsional loads. It was found that the dynamic implant performed well in comparison the standard nail and provided the required micro motion at the fracture site.

Keywords Biomechanics · Intramedullary nail · Fracture fixation · Bone healing

A. Dowd · B.J. Mac Donald (✉) · D. Comiskey
Dublin City University, Dublin, Ireland
e-mail: bryan.macdonald@dcu.ie

R. Lostado
University of La Rioja, Logroño, Spain
e-mail: ruben.lostado@unirioja.es

W.T. McCartney
Marie-Louise Veterinary Hospital, Dublin, Ireland

1 Introduction

Intramedullary (IM) nails have been commonly used in orthopedic surgery to fix long bone (e.g. femur, tibia) fractures since the early twentieth century. They are commonly used where reduction of the bone fracture is difficult, immediate weight bearing is required and the fracture cannot be immobilized with a cast [1]. IM nails come in many forms; they have developed from solid rods to hollow devices with fluted edges to encourage revascularization of the medulla.

Static locked IM nails ensure that both ends of the long bone do not move relative to each other, while dynamic IM nails allow a prescribed amount of motion between the bone fragments. Inter-fragmentary strain (IFS) theory [2] describes how bone healing is optimal when micro-movements are encouraged at the fracture gap and a small gap is left between bone fragments in order to encourage callus formation. Locked IM nails are currently most commonly used, especially for comminuted (i.e. crushed) unstable femur fractures. Static locked nails generally result in bone fragments being compressed together thus preventing micro-movements and callus formation.

Perren [2] suggests that static fixation improves the fracture rate as the fracture appears healed relatively early in radiographs. Sarmiento et al. [3] argues that, although the fracture line remains in a dynamically fixated fracture, the bone is actually stronger than those where the fracture line disappears. Jargodzinski and Sarmiento [4] conclude that initial stability, followed by micro motion is desirable for fracture healing with callus formation and that micro-motion in the initial six weeks after fracture has desirable increases in bone density and stiffness.

This paper describes the design and validation of a new concept for a dynamic compression intramedullary nail. The principal objective of the new concept is to allow a prescribed motion at the fracture site to promote bone healing.

2 Design Process

2.1 Design Specification

In order to be compliant with current regulations and exist in tandem with current IM nail technology it is important that any design for a new IM nail consider the main aspects of current IM nailing technology and procedure.

The nail insertion technique should be similar to current methods to ensure that further surgical training is not required. It should allow compression of fragments and loads to be applied to the bone in order to promote faster bone healing. Bone fragments should only be permitted to move by a prescribed magnitude. Bone length must be reset: in order to prevent shortening of comminuted fractures and to encourage rapid bone healing the bone should return to its original position after compression. One of the most important aspects of the new design is to allow its stiffness to be varied in order to suit specific patient requirements.

In terms of mechanical design it is important that a minimal amount of components are used: the least possible number of foreign components should be inserted into the body and less components allows for easier assembly/adjustment. The IM nail and all its components must be constructed from biocompatible materials and must not corrode or degrade in vivo. The nail should be constructed from a rigid material that only allows prescribed motion in the required axial direction. The dynamic mechanism in the IM nail must be enclosed to prevent fragment migration in the case of component failure. Finally, the nail must be radio-opaque in order to allow for positioning during surgery and monitor healing post-surgery.

Any new IM nail designed for clinical use must comply with the relevant ISO standards [5–9].

2.2 Design Concepts

The key design feature of the new IM nail was to introduce a flexible region which would allow for dynamic behavior. Numerous initial concepts were generated. Synthetic bones [10] were used to assist in the design of the implant: a synthetic femur with a glass fiber and epoxy resin composite shell (cortical bone), rigid polyurethane foam core (cancellous bone) and intramedullary cavity was used in this case. In order to reduce variables it was decided to design a retrograde IM nail which is inserted through the knee end of the femur (as opposed to a antegrade design which would be inserted through the trochanter at the hip joint).

A number of initial concepts (Fig. 1) were rejected due to complexities in design or manufacture and, as the variation in stiffness would be difficult to predict and control. The mechanical integrity of the nail would be greatly compromised by these designs.

The final three concepts selected for detailed design are shown in Fig. 2. Figure 2a utilizes the material removal concept mentioned above but incorporates slits cut circumferentially into the nail. In order to prevent bowing these slits are cut from all sides in order to promote axial compression. Bone in-growth would potentially allow the implant to become stiffer over time. This could be counteracted by initially placing a biodegradable material in the slots—as the material degraded over time the

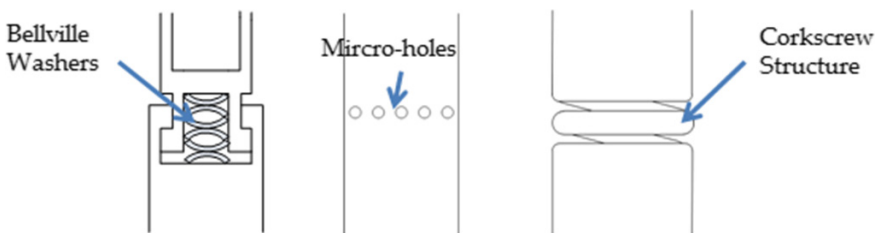


Fig. 1 Rejected initial concepts

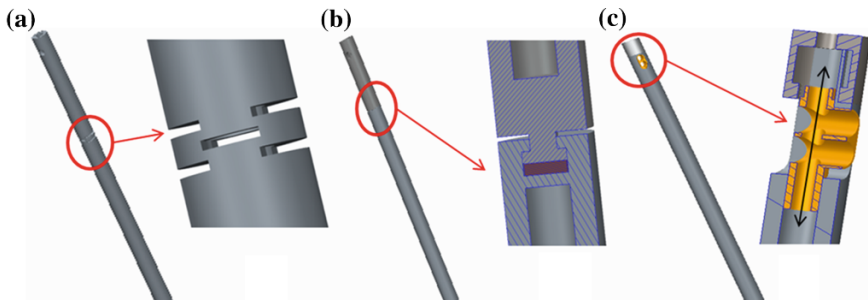


Fig. 2 Final three design concepts: **a** slotted nail, **b** rubber insert, **c** spring loaded insert

implant would become more flexible, thus giving a more flexible implant in the later stages of healing. This design has the advantage of having no extra components or mechanisms, however, this also results in the disadvantage that the stiffness of the nail cannot be tailored to suit patient requirements.

The concept shown in Fig. 2b allows for axial movement using a disc of an elastomeric material that can be compressed. The disc compresses under load and is reset as the load is removed. This design has the potential to allow discs of different stiffness to be inserted according to patient's requirements but it is likely that the elastic properties of the material would deteriorate over time due to the cyclic nature of the loading.

The concept shown in Fig. 2c incorporates a sliding insert in the nail which is returned to its original position by a compression spring. Springs are generally capable of being cyclically compressed without damage or significant changes in their properties so it is expected that this mechanism would survive the bone healing process. This design ensures that the nail is reset which allows micro-motion of the fragments to be continuously repeated until the bone is fully healed.

After conducting a matrix analysis which considered the strengths and weaknesses of each design, together with the limitations imposed by the manufacturing facilities available and feedback from orthopedic surgeons, it was determined that concept 2-C should be developed into a detailed design and validated using experimental tests. Table 1 shows a summarized version of the matrix analysis grid, where a zero to five weighting system was used, with 5 being the most desirable.

2.3 Detailed Design

The finalized design consisted of a spring and slider mechanism. The main advantages of this design are the simplicity of the mechanism and that the slider and spring allow the nail to be reset after loading. The axial motion of the sliding insert is limited by the pin and slot shown in Fig. 3. This allows a maximum of 2 mm motion in the axial direction. The cap shown in Fig. 3b is designed to a specific length to ensure

Table 1 Summary of matrix analysis

Attributes	Concept 1: slotted nail	Concept 2: rubber insert	Concept 3: spring loaded insert
Axial motion allowed	2	4	5
Tailored stiffness	0	3	3
Stiffness control	3	1	3
Torsional rigidity	1	1	3
Mechanical integrity	1	4	4
Biocompatibility	5	3	4
Ease of use	5	3	4
Reliability	5	2	3
Manufacturing complexity	1	3	3
Fit with available facilities	2	5	5
Feedback from surgeons	2	3	4
Total	22	32	41

that the screw holes are easy to locate using a screw guide. A small threaded pin is used to protrude into the slot to ensure that the sliding insert does not rotate relative to the screw prior to insertion. If rotation were to occur the holes would not be visible and screw insertion would be impossible. In the embodiment shown below the pin also functions as a mechanical stop to prevent excessive axial motion.

Figure 3b shows the compression of the spring due to the patient walking on the femur. As the leg impacts the ground force is transmitted through the distal femur and body weight is applied through the proximal femur into the screws shown in the figure. Once the load has been removed (e.g. during the gait cycle) the screws will return to their original position by the spring force assisted by the weight of the lower leg.

Two screws are used in order to aid with torsional stability and are necessary to prevent malrotation and migration of the nail. The end cap is inserted into the distal

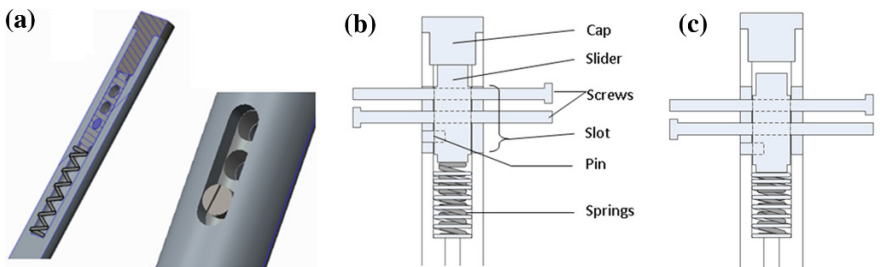
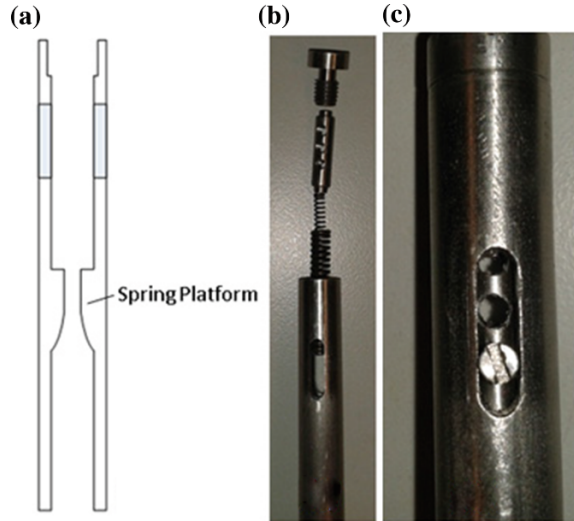


Fig. 3 Detail design: **a** overview, **b** slider mechanism in neutral position, **c** slider mechanism under compression

Fig. 4 **a** Detail of spring platform, **b** spring and slider mechanism, **c** assembled mechanism



end of the nail to prevent bone in-growth—this is a mandatory feature as it allows the nail to be removed and prevents biological tissue from growing inside the nail.

3 Experimental Verification

The nail concept was manufactured from 316L stainless steel. The slight curvature seen in most IM nails was neglected for the purposes of verification in order to reduce uncertainties in the experimental tests. Two compression springs were inserted into the nail as shown in Fig. 4b.

Four point bending tests, compression tests and torsion tests were carried out on four different specimens: (1) an intact synthetic femur, (2) a fractured synthetic femur fixed with a standard IM nail with one screw in the proximal end, (3) a fractured synthetic femur fixed with a standard IM nail with two screws in the proximal end and (4) a fractured synthetic femur fixed with the new dynamic IM nail concept (Fig. 5). Specialized jigs were designed to hold the femur in position for each test.

4 Results

Figure 5 shows the results obtained from the four point bending tests. A number of experiments were carried out for each test ($n = 3$) and the median result is presented in Fig. 5 to allow comparison between the different configurations. It is clear that the prototype is performing between the performance of a rigid standard nail construct (2 screws) and a relatively free standard nail construct (1 screw).

Fig. 5 Experimental tests: **a** four point bending, **b** compression, **c** torsion

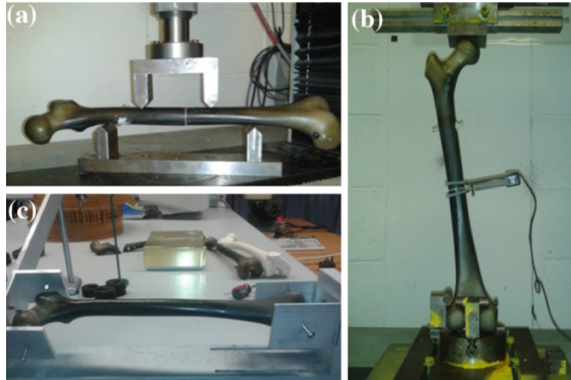


Table 2 Results from compression tests

Displacement (mm)				
Force (kN)	Intact bone	1 screw IM nail	2 screw IM nail	Concept
0	0	0	0	0
-0.02	0.0002	0.010	0.040	1.2
-0.04	0.0004	0.018	0.056	1.3
-0.06	0.0005	0.025	0.068	1.35
-0.08	0.0007	0.036	0.077	1.37
-0.1	0.0010	0.041	0.080	1.4

The results from the compression tests are shown in Table 2. It was difficult to satisfactorily display these results graphically as the displacement of the concept dynamic nail was an order of magnitude greater than the other configurations (Figs. 6 and 7).

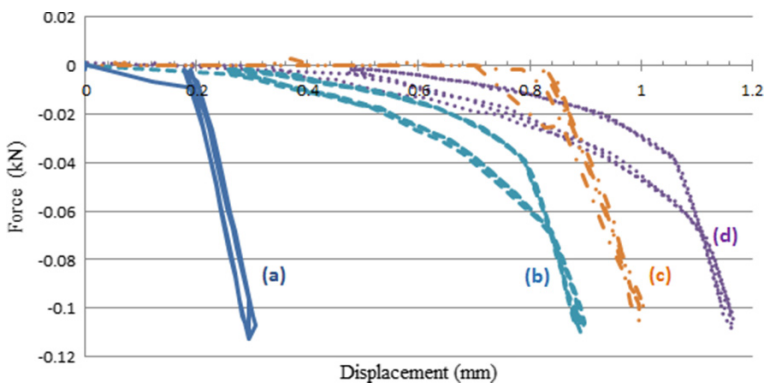


Fig. 6 Results from four point bending tests: **a** intact femur, **b** standard im nail (2 screws), **c** dynamic nail, **d** standard im nail (1 screw)

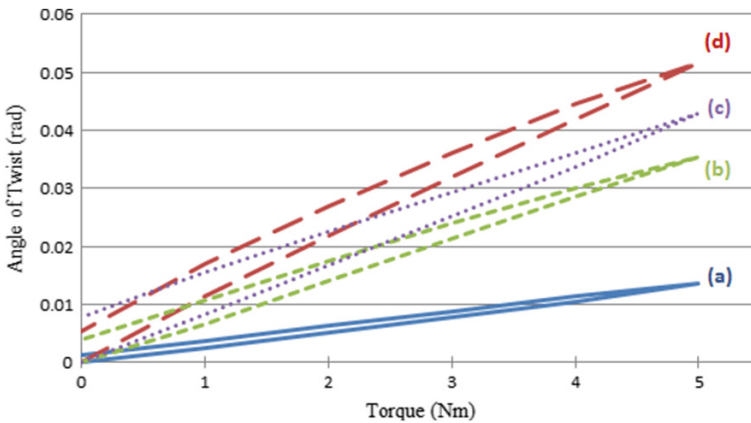


Fig. 7 Results from torsion tests: **a** intact femur, **b** standard im nail (2 screws), **c** standard im nail (1 screw), **d** dynamic nail

5 Conclusions

It is clear from the results that the new dynamic nail concept has comparable performance with the currently available alternatives under four point bending while still offering increased fracture gap movement under compression loading. The torsion test showed that the current design has quite poor torsional rigidity when compared to the alternatives. This appears to be due to unforeseen rotation at the proximal screws. Poor performance in torsion is a known problem with IM nails in general [11], however, it is not acceptable that the new design should be less torsionally rigid than the standard designs. Future work will investigate improving the torsional rigidity of the dynamic nail concept. The fact that the dynamic nail concept has comparable bending rigidity with current designs but allows significantly greater micro-motion at the fracture site is very encouraging.

References

1. Wagner M, Frigg R (2006) AO manual of fracture management: internal fixators, Thieme
2. Perren SM (2002) Evolution of the internal fixation of long bone fractures: the scientific basis of biological internal fixation: choosing a new balance between stability and biology. *J Bone Jt Surg—Br* 84:1093–1110
3. Sarmiento A, Schaeffer J, Beckerman L (1977) Fracture healing in rat femora as affected by functional weight bearing. *J Bone Jt Surg* 59(3):369–375
4. Jagodzinski M, Krettek C (2007) Effect of mechanical stability on fracture healing—an update. *Injury* 38(1):S3–S10
5. ISO 15142-1 (2003) Implants for surgery: metal intramedullary nailing systems
6. ISO 14602 (2010) Non-active surgical implants: implants for osteosynthesis

7. ISO 8319-1 (1996) Orthopaedic instruments: drive connections; part 1: keys for use with screws with hexagon socket heads
8. ISO 8319-2 (1966) Orthopaedic instruments: drive connections; part 2: screwdrivers for single slot head screws, screws with cruciate slot and cross-recessed head screws
9. ISO 8828 (1988) Implants for surgery: guidance on care and handling of orthopaedic implants
10. <http://www.sawbones.com/products/bio/composite.aspx>
11. Allen WC, Heiple KG, Burstein AH A fluted femoral intramedullary rod. Biomechanical analysis and preliminary clinical results. *J Bone Jt Surg, Am* 60(4):506–515

A Computational Benchmark for 2D Gait Analysis Problems

R. Pàmies-Vilà, J.M. Font-Llagunes, U. Lugrís, F.J. Alonso
and J. Cuadrado

Abstract The aim of this paper is to present a computational benchmark for gait analysis that has been developed in order to share real data captured in a biomechanics laboratory and the results of the inverse dynamic analysis. This work belongs to the library of computational multibody benchmark problems that the Technical Committee for Multibody Dynamics of the International Federation for the Promotion of Mechanism and Machine Science (IFTOMM) is developing. The work presents the kinematic and dynamic study of human motion by means of multibody system dynamics techniques. The subject selected to perform the experiments walks on a walkway that encloses two force plates. The motion is captured by 12 optical cameras that acquire the position of 37 passive markers. The inverse dynamic analysis (IDA) is carried out using a 12-segment 2D model with 14 degrees of freedom. Displacement signals are filtered using an algorithm based on Singular Spectrum Analysis (SSA) and the natural coordinates of the model are calculated using algebraic relations among the marker positions. Afterwards, a procedure ensures the kinematic consistency and the data processing continues with the approximation of the position histories using B-spline curves. The velocity and acceleration values are then obtained by analytical derivation. The double support indeterminacy is solved using the Corrected Force Plate (CFP) sharing method. The IDA provides the joint drive torques that the musculoskeletal system generates

R. Pàmies-Vilà (✉) · J.M. Font-Llagunes
Universitat Politècnica de Catalunya, Barcelona, Spain
e-mail: rosa.pamies@upc.edu

J.M. Font-Llagunes
e-mail: josep.m.font@upc.edu

U. Lugrís · J. Cuadrado
Universidad de La Coruña, A Coruña, Spain
e-mail: ulugris@udc.es

J. Cuadrado
e-mail: javicud@cdf.udc.es

F.J. Alonso
Universidad de Extremadura, Badajoz, Spain
e-mail: fjas@unex.es

during human locomotion from acquired kinematic data, foot-ground contact forces and estimated body segment parameters (BSP). All this information is available online in <http://iftomm-multibody.org/benchmark>. Therefore, it can be viewed by other researchers, which can submit their own results using the same input data and proposing new solutions.

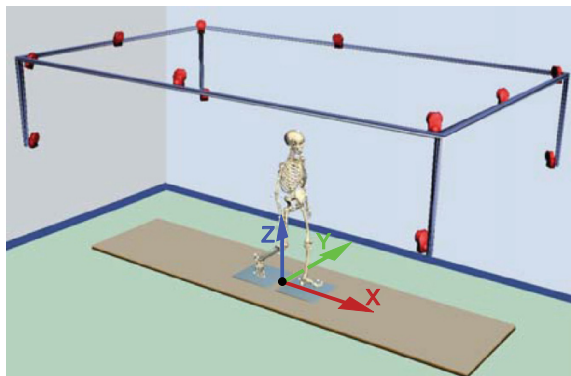
Keywords Gait analysis · Inverse dynamics · Benchmark · Biomechanics

1 Introduction

The 2D gait benchmark is presented as a tool for researchers to share the gait analysis experience and to discuss different methodologies in a comprehensive reference. The resource is intended to be a tool for facilitating collaboration and for discussing systematic treatment of gait analysis methods. This benchmark includes the kinematics of a full-body model and the reaction forces measured via two force-plate devices. The joint torques obtained via an Inverse Dynamic Analysis (IDA), that is, the torques developed by the musculoskeletal system during the movement, are also shared. This information is available in the library of computational benchmark problems, concretely inside the biomechanical models section, and more specifically in the musculoskeletal models folder (<http://iftomm-multibody.org/benchmark>).

The experiments take place in a laboratory that includes an optoelectronic system that captures the motion and two force plates for measuring the foot-ground contact wrenches (Fig. 1). The motion data is collected using twelve 100 Hz Optitrack FLEX:V100R2 cameras and the software which provides the 3D trajectories of the 37 passive markers attached to the human body. The foot-ground contact

Fig. 1 Gait analysis laboratory configuration



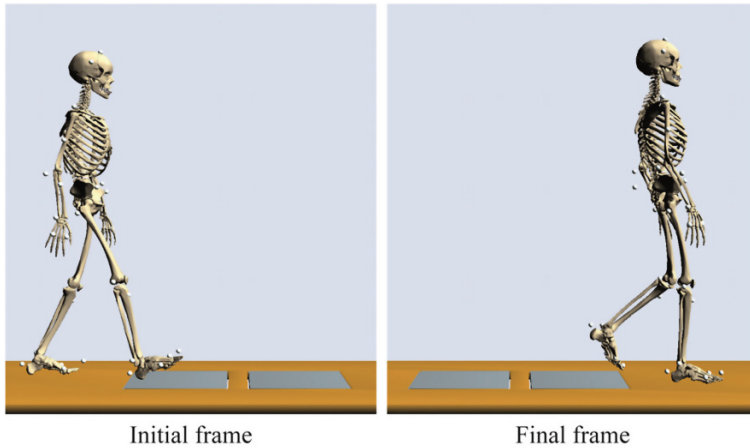


Fig. 2 Initial and final frame of the captured motion

wrenches are measured using two AMTI AccuGait force plates located on a walkway where the subject walks (also sampled at 100 Hz). Each force plate measures the ground reactions on one foot during the gait cycle.

Marker positions are expressed in the global coordinate system, which is defined using the axes $\{X, Y, Z\}$ (Fig. 1). Each force plate registers the ground reactions on one foot during the gait cycle, obtaining as a result one force (three components) and one moment about the centre of the plate (also three components). These force and moment components define the mentioned contact wrench at the plate centre.

The recorded motion contains more than one cycle (Fig. 2). It covers all instants with force plate information available. It starts at the heel strike of the right foot (0 % of gait cycle), includes also the next heel strike of the same foot (100 %) and finishes at the toe off of the left foot belonging to the next cycle (116 %).

2 Dynamics Modelling

2.1 Biomechanical Model

The human body is modelled as a multibody system formed by rigid bodies, an approach which has been widely used to analyse human gait. The subject selected to perform the experiments is a healthy adult male, 27 years old, mass 80 kg and height 1.75 m. Figure 3 shows the position of the 37 markers used, and Table 1 contains the anatomical points used to place the markers.

A text file containing the position history of each marker is available on the website. In a similar way, a text file containing the force plate measurements is also accessible.

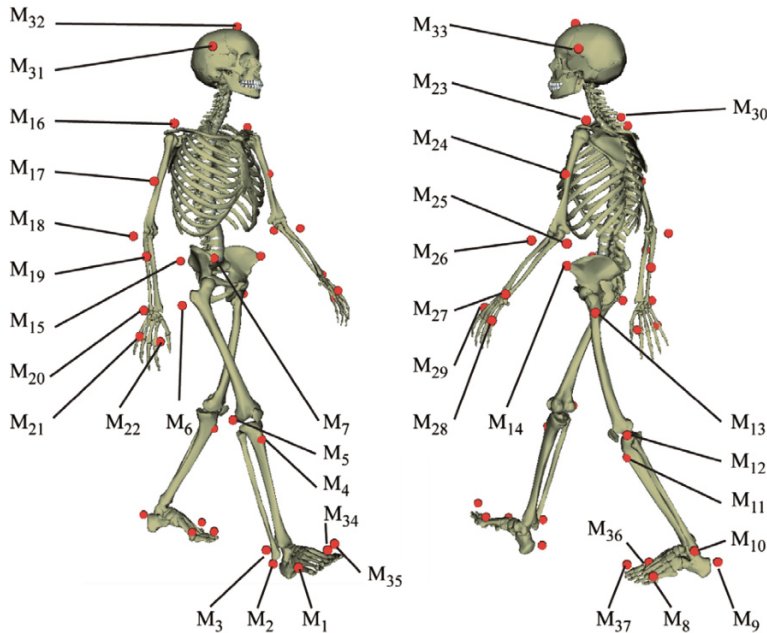


Fig. 3 View of the human skeleton with the considered motion capture marker protocol

The natural coordinates of a 3D model are calculated by means of simple algebraic relations among the filtered displacement signals [6].

The IDA is carried out using a 12-segment 2D model (Fig. 4a) with 14 degrees of freedom. X and Z components of the 3D joints are selected to obtain the planar coordinates $\tilde{\mathbf{q}}$ (Points P_i at Fig. 4b). In order to solve the violation of the kinematic constraints (due to skin motion, muscle deformation, and 2D simplification), a new set of coordinates \mathbf{q} is calculated by imposing the kinematic consistency at position level through a minimization problem, Eq. (1):

$$\min_{\mathbf{q}} V = \frac{1}{2} (\mathbf{q} - \tilde{\mathbf{q}})^T \mathbf{W} (\mathbf{q} - \tilde{\mathbf{q}}) \quad \text{s.t.} \quad \Phi(\mathbf{q}) = \mathbf{0} \quad (1)$$

where \mathbf{W} is a weighting diagonal matrix that allows assigning different weights to the coordinates. Higher weighting factors are associated to those coordinates with lower expected error. The minimization is only subjected to scleronomic constraints $\Phi(\mathbf{q}) = \mathbf{0}$, and \mathbf{q} includes only the end points of the segments. The process used to guarantee kinematic data consistency follows an augmented Lagrangian minimization process as described in [2].

From the kinematically consistent data set obtained above, a set of independent coordinates \mathbf{z} is calculated: the two Cartesian coordinates of the hip joint (P_4), and the relative orientation of each segment (see Fig. 4b, c).

Table 1 Placement of the set of markers used

No.	Placement	No.	Placement
M ₁	Right metatarsal head V	M ₈	Left metatarsal head V
M ₂	Right calcaneus	M ₉	Left calcaneus
M ₃	Right lateral malleolus	M ₁₀	Left lateral malleolus
M ₄	Right tibial tuberosity	M ₁₁	Left tibial tuberosity
M ₅	Right lateral femoral epicondyle	M ₁₂	Left lateral femoral epicondyle
M ₆	Right femoral greater trochanter	M ₁₃	Left femoral greater trochanter
M ₇	Right ASIS	M ₁₄	Left ASIS
M ₁₅	Sacrum		
M ₁₆	Right acromion in the shoulder girdle	M ₂₃	Left acromion in the shoulder girdle
M ₁₇	Right deltoid tuberosity	M ₂₄	Left deltoid tuberosity
M ₁₈	Right lateral humeral epicondyle	M ₂₅	Left lateral humeral epicondyle
M ₁₉	Middle of right forearm	M ₂₆	Middle of left forearm
M ₂₀	Right radial styloid in the wrist	M ₂₇	Left radial styloid in the wrist
M ₂₁	Right metacarpal head V	M ₂₈	Left metacarpal head V
M ₂₂	Right metacarpal head II	M ₂₉	Left metacarpal head II
M ₃₀	1st vertebra of the thoracic spine		
M ₃₁	Right side of the head	M ₃₃	Left side of the head
M ₃₂	Top of the head		
M ₃₄	Right metatarsal head I	M ₃₆	Left metatarsal head I
M ₃₅	Right distal phalange of the third toe	M ₃₇	Left distal phalange of the third toe

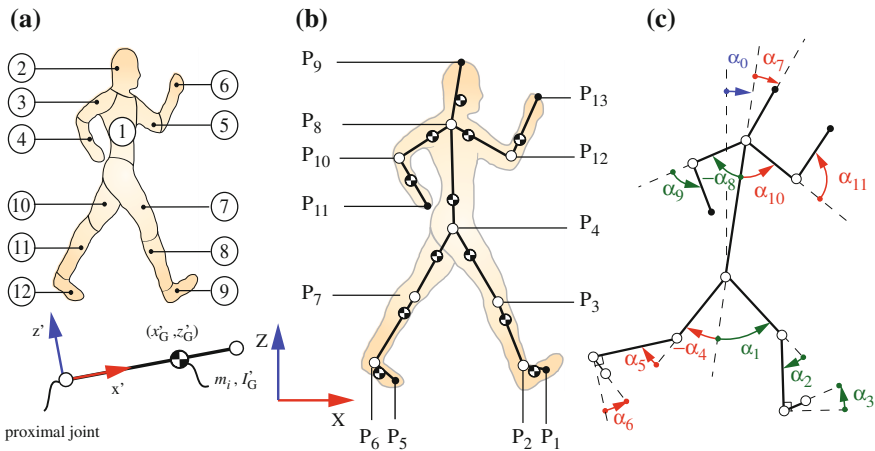


Fig. 4 Two-dimensional biomechanical model: **a** body numeration, **b** points used to define the configuration, **c** biomechanical angles

The obtained signals usually present low-amplitude high-frequency noise, which is amplified when numerical differentiation is used to calculate their corresponding velocities and accelerations. In this work, a filter based on Singular Spectrum Analysis (SSA) is applied to the displacement signals. The advantages of using this kind of filter are discussed in [1]. The algorithm decomposes the original signal into independent additive components with decreasing weights. This processing facilitates extracting the signal latent trend from the inherent random noise that the motion capture process introduces. Moreover, the algorithm only requires the selection of two parameters, namely, the window length (L) and the number of components to use for reconstruction (r). A way to overcome the uncertainty in the choice of L is to apply sequentially the SSA filter, as explained in [1]. When this sequential procedure is applied, the results are not very sensitive to the window length. In this work, the SSA filter is applied three consecutive times, the window length is fixed as $L = 10$ and the two main components of the decomposition are used in the signal reconstruction.

The data processing continues with the approximation of the position histories using B-spline curves and obtaining, by analytical derivation, the velocity and acceleration values: for each coordinate of the independent coordinate vector \mathbf{z} , and for a given tolerance, a B-spline form of the temporal function is calculated. The De Boor algorithm with a tolerance of 10^{-9} , which guarantees that the Root Mean Square Error (RMSE) between the original data and the new values is less than 0.001 %, is used [3]. The B-form function of the input data is obtained, and the velocities $\dot{\mathbf{z}}$ and the accelerations $\ddot{\mathbf{z}}$ can be obtained using analytical spline differentiation techniques. Consequently, the kinematic data set required to perform the IDA is completely known ($\mathbf{z}, \dot{\mathbf{z}}, \ddot{\mathbf{z}}$), and it is consistent with the rigid body assumption of the multibody system at position, velocity and acceleration levels. The resulting X and Z coordinates of the points P_1, P_2, \dots, P_{13} , and the biomechanical angles shown in Fig. 4c are also available on the website.

Finally, in order to complete the biomechanical model definition, the anthropometric parameters are needed. They are summarized in Table 2. It should be noted that the moment of inertia of the segments is referred to their centre of mass (COM).

2.2 Multibody Formulation

The equations of motion of the multibody system can be written as:

$$\begin{cases} \mathbf{M}\ddot{\mathbf{q}} + \Phi_{\mathbf{q}}^T \boldsymbol{\lambda} = \mathbf{Q} \\ \Phi(\mathbf{q}) = \mathbf{0} \end{cases} \quad (2)$$

Once the histories of the independent coordinates \mathbf{z} , and their time derivatives, $\dot{\mathbf{z}}$ and $\ddot{\mathbf{z}}$, have been obtained, the inverse dynamics problem is solved by means of the velocity transformation formulation known as matrix-R, which provides the

Table 2 Anthropometric data for the 2D model with twelve segments

No.	Name	Length	COM location		Mass m_i (kg)	Principal moment of inertia I'_G (10^{-2} kg · m ²)
		L_i (m)	x'_G (m)	z'_G (m)		
1	Trunk	0.498	0.230	0	37.801	44.448
2	Head	0.343	0.139	0.039	5.119	2.163
3	Right arm	0.311	0.146	0	1.922	1.190
4	Right forearm	0.376	0.171	0	2.299	0.974
5	Left arm	0.311	0.146	0	1.922	1.190
6	Left forearm	0.376	0.171	0	2.299	0.974
7	Right thigh	0.417	0.154	0	9.284	12.215
8	Right shank	0.422	0.170	0	4.008	5.153
9	Right hindfoot	0.143	0.037	-0.023	1.027	0.441
10	Left thigh	0.417	0.154	0	9.284	12.215
11	Left shank	0.422	0.170	0	4.008	5.153
12	Left hindfoot	0.143	0.037	-0.023	1.027	0.441

required actuation in the form of generalized forces associated to the independent coordinates \mathbf{z} [4]:

$$\mathbf{R}^T \mathbf{M} \mathbf{R} \ddot{\mathbf{z}} = \mathbf{R}^T (\mathbf{Q} - \mathbf{M} \mathbf{S} \mathbf{c}) \tag{3}$$

which can be rewritten as:

$$\mathbf{R}^T \mathbf{M} \mathbf{R} \ddot{\mathbf{z}} = \mathbf{R}^T (\hat{\mathbf{Q}} - \mathbf{M} \mathbf{S} \mathbf{c}) + \mathbf{Q}_m \tag{4}$$

being $\mathbf{R}^T \mathbf{Q} = \mathbf{R}^T \hat{\mathbf{Q}} + \mathbf{Q}_m$, where $\hat{\mathbf{Q}}$ are the known generalized forces associated to constant forces or forces that only depend on the system states (such as the gravitational forces), and \mathbf{Q}_m are the generalized forces associated to the independent coordinates, i.e., the unknowns of the inverse dynamics problem:

$$\mathbf{Q}_m = \mathbf{R}^T \mathbf{M} \mathbf{R} \ddot{\mathbf{z}} - \mathbf{R}^T (\hat{\mathbf{Q}} - \mathbf{M} \mathbf{S} \mathbf{c}) \tag{5}$$

Nevertheless, since the independent coordinates \mathbf{z} are the position of the hip and the absolute angles of all the bodies, the generalized forces \mathbf{Q}_m calculated via IDA do not correspond to the actual contact forces and the net joint motor torques. Therefore, in order to obtain the joint motor torques, the contact wrench must be expressed at its actual location, i.e., the contacting foot/feet (Fig. 5).

The procedure to obtain the actual forces and torques involves different steps as it is explained in [5]. During the single support phase, the problem is determined, so that, the resultant reaction can be translated to the contacting foot, and the actual joint torques can be recalculated properly equating their corresponding generalized

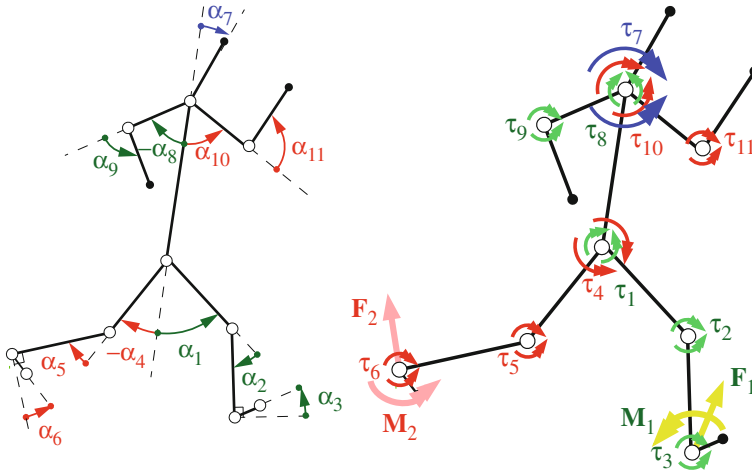


Fig. 5 Joint angles, external reactions and joint drive torques

forces to those obtained when the contact wrench acts on the hip joint. However, during the double support phase, how this wrench is shared between the two foot-ground contacts is unknown and a sharing criterion has to be used for estimating the amount of the total wrench assigned to each foot. This benchmark uses the Corrected Force Plate (CFP) method developed by the authors [5].

The obtained results are the inverse dynamic wrenches (see Fig. 5). They start at the toe off of one foot, include one double support, and finish at the heel strike of the other foot. The online results file contains the contact reactions at each foot (\mathbf{F}_1 , \mathbf{M}_1 , \mathbf{F}_2 , \mathbf{M}_2) and the joint torques (τ_1, \dots, τ_{11}). Note that the index of the joint torques τ_i is the same as the angle index α_i .

3 Conclusions

A computational benchmark for 2D gait analysis has been presented. A multibody methodology for the dynamic analysis of human motion has been implemented. The inverse dynamics problem is addressed with the aim of calculating the musculoskeletal forces developed at the anatomical joints of the human body while performing a prescribed movement. For this purpose, the CFP sharing method has been used.

In order to share all the results, the library tool provided by the Technical Committee for Multibody Dynamics of the International Federation for the Promotion of Mechanism and Machine Science (IFTtoMM) is used. All the input data and also the output results have been uploaded, so that researchers can compare the

obtained forces and torques using their own method for inverse dynamic analysis of gait. Moreover, the data can also be used to perform a forward dynamics simulation. Finally, visual information regarding the captured motion and the obtained 2D data is available on the website.

References

1. Alonso F, Del Castillo J, Pintado P (2005) Application of singular spectrum analysis to the smoothing of raw kinematic signals. *J Biomech* 38:1085–1092
2. Alonso F, Cuadrado J, Ligrís U, Pintado P (2010) A compact smoothing-differentiation and projection approach for the kinematic data consistency of biomechanical systems. *Multibody Sys Dyn* 24(1):67–80
3. De Boor C (1978) *A practical guide to spline*. Springer, New York
4. Garcia de Jalon J, Bayo E (1994) *Kinematic and dynamic simulation of multibody systems—the real-time challenge*. Springer, New York
5. Ligrís U, Carlin J, Luaces A, Cuadrado J (2013) Gait analysis system for spinal cord-injured subjects assisted by active orthoses and crutches. *J Multi-body Dyn* 227(4):363–374
6. Pàmies-Vilà R (2012) *Application of multibody dynamics techniques to the analysis of human gait*. PhD thesis, Universitat Politècnica de Catalunya. Available online: <http://www.tdx.cat/handle/10803/123774>

Development and Early Results of a New Concept of an Orthopedic Footwear Stirrup

J. Peixoto, B. Moura, P. Moreira, A.P. Souto and P. Flores

Abstract The development and early results of a new solution for an orthopedic footwear stirrup is presented throughout this work. In the sequel of this process, the most common biomedical orthotic solutions for low limbs are revisited. Subsequently, the conceptual design of a new solution of an orthopedic footwear stirrup is presented and discussed. This procedure starts with the identification and full characterization of the problem at hand. Then, several stirrup conceptual models are presented, analyzed and compared with the purpose to find the best solution for the stirrup. After this task, a computational analysis is performed in order to assess the dynamic response of the solution adopted. This task is carried out by utilizing a commercial software based on the finite element method. Finally, after the selection of the different materials and manufacturing processes, the functional physical prototype is built, incorporated and tested in an actual orthopedic footwear.

Keywords Foot stirrup · New design · Orthopedic footwear · Biomechanics

J. Peixoto (✉) · B. Moura · P. Moreira · A.P. Souto · P. Flores
University of Minho, Braga, Portugal
e-mail: jjorge@det.uminho.pt

B. Moura
e-mail: a37064@alunos.uminho.pt

P. Moreira
e-mail: pfsmoreira@dem.uminho.pt

A.P. Souto
e-mail: souto@det.uminho.pt

P. Flores
e-mail: pflores@dem.uminho.pt

1 Introduction

This paper reports on the investigation that is being undertaken at the University of Minho concerning the development of functional orthopedic footwear to be utilized in KAFO orthoses (acronym for Knee Ankle Foot Orthoses). It is well known that for people with severe lower-limb muscle weakness, the primary functions of a KAFO are to augment stability and to facilitate functional ambulation. Predominant diagnoses include spinal cord injury, poliomyelitis and certain other neuromuscular weaknesses [1, 2].

Over the last decades, several research works have been performed in the field of new materials and new production techniques, directly related to the orthopedic footwear [3]. However, the development on the footwear associated with orthoses did not have received significant attention, being the solutions available, in general, robustness and durability of the system's elements the only design variables. Important issues, such as the application of advanced materials to achieve functionality and give better aesthetic values are usually neglected. Several solutions like laminate lining, insole and foot stirrup are already implemented. Laminate lining with hydrophilic membranes finished with functional treatments have proved to be highly efficient because reduced or eliminated the bromhidrosis problem and improve waterproof property [3]. Additional and relevant aspects to take into account in orthopedic footwear are the toe puffs, counters and insoles, because these materials can give a very good contribution to reduce or even eliminate the humidity inside of footwear.

The main motivation for this research comes from current interest in developing new technical solutions that allows for the improvement of the life quality of people with physical handicap. In fact, over the last decades, the attention to design and analysis of technical aids for treatment and rehabilitation of people with mobility limitations has been growing a very significant manner [4, 5]. In particular, the scientific and technical domain of Biomechanics of Motion plays a crucial role, in the measure that it permits to quantify the kinematic and dynamic parameters associated with the human daily activities [6]. This study deals with the design and development of a new foot stirrup to be utilized in orthopedic footwear. This piece of work is part of a broader research project that has been developed at the Textile and Mechanical Departments of the University of Minho, main purpose of which is to develop new manufacturing process of orthopedic footwear. It has been recognized by users that the foot stirrups currently available are heavy, which causes high-energy consumption and unbalanced motion. Moreover, the convectional solutions exhibit particular zones of fracture due to their non-optimized geometry [7]. The main content of this work is on the computational performance of the conventional and a new foot stirrup. This desideratum is achieved by using the well-established finite element approach, especially in what concerns with the quantification of the level of stress that exists in the parts. The studies carried out within the scope of this investigation allow for the optimization of the new solution in terms of weight and geometry.

2 Human Gait Description

The main purpose of this section is present a brief description of the human gait. A non-pathological human walking can be established as the process of locomotion involving the use of the two legs, alternately, to provide support and propulsion, with at least one foot in contact with the ground at all instants [8]. Very often, the terms walking and gait are often used interchangeably but they differ slightly since the term walking refers to the locomotion process itself and the term gait refers to the manner or style of walking.

The human walking is a periodical motion and the gait cycle is defined as the time interval, which separates two successive occurrences of one of the repetitive events of walking. It is conventionally accepted that the gait cycle starts, and ends, with the initial contact of the right foot. During the gait cycle, seven major events can be identified, namely: (1) Initial contact or heel strike (HS); (2) Opposite toe off; (3) Heel rise; (4) Opposite initial contact; (5) Terminal contact or toe off (TO); (6) Feet adjacent; (7) Tibia vertical [9]. These seven events are illustrated in the animation sequence of Fig. 1. The gait cycle is divided in seven periods, which are grouped in two distinct phases: (1) stance and (2) swing phases. The stance phase, also called support phase or contact phase lasts from heel strike to toe off, while the swing phase lasts from toe off to heel strike.

In each gait cycle, there are also two period of double support, i.e., periods of time when both feet are in contact with the ground. The stance phase usually lasts about 60 % of the cycle, the swing phase about 40 % and each period of double support about 10 % [7]. It must be noticed that the terms heel strike and toe off can only be applied to the non-pathological gait. Initial and terminal contact are often used in the bibliography since in pathological gait the heel and the toes may not be the first and last part of the foot to touch and leave the ground, respectively.

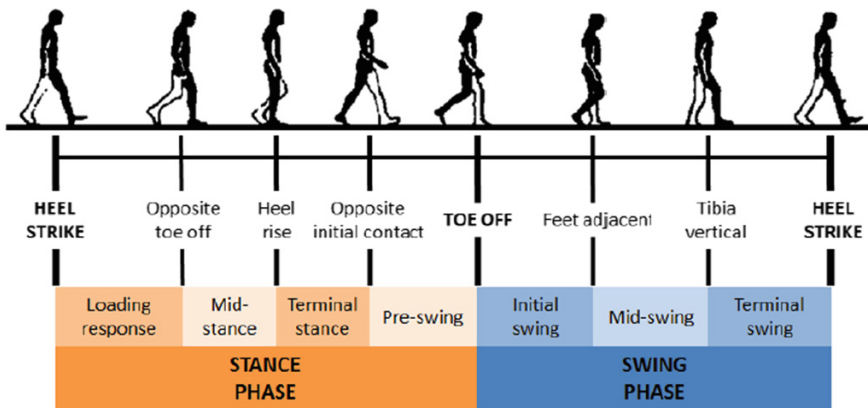


Fig. 1 Normal gait cycle by the *right leg* illustrating the major events and phases of gait [9]

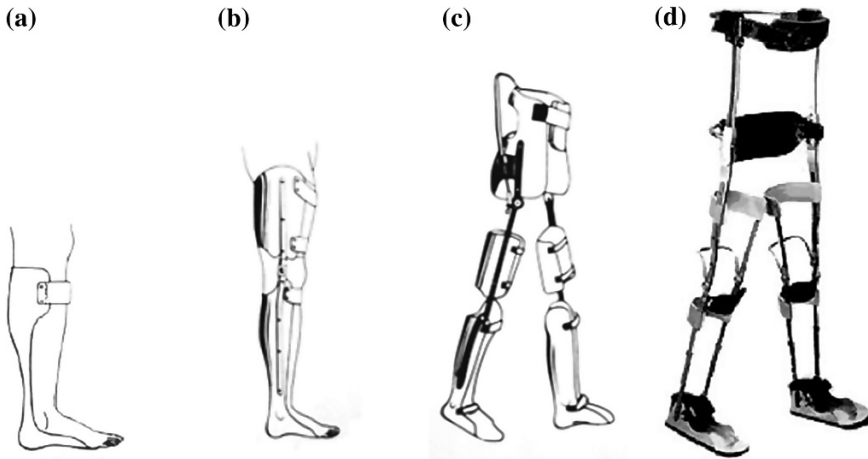


Fig. 2 Lower limb orthoses. a AFO, b KAFO, c HKAFO, d THKAFO [7, 11]

3 Human Gait Description

Orthoses are medical devices that support or correct the function of a limb or the torso [10]. They are also known as braces or caliper. In particular, a lower limb orthosis is an external device that is applied or attached to a lower limb. Its function is to control motion, provide support, reduce pain, correct flexible deformities or prevent the progression of fixed deformities. Orthoses are usually named according to their location in the human body. There are four major types of lower limb orthoses, namely: (1) Ankle-foot orthoses—AFO; (2) Knee-ankle-foot orthoses—KAFO; (3) Hip-knee-ankle-foot orthoses—HKAFO; (4) Trunk-hip-knee-ankle-foot orthoses—THKAFO [10]. Figure 2 shows these four types of orthoses.

4 Methodology

The general methodology followed in this work can be divided into three main phases, namely (1) study of the human gait cycle in order to characterize the dynamic loads developed during the different motion phases; (2) computational simulations of the conventional foot stirrup and proposed solution; (3) incorporation of a physical prototype in an actual orthopedic footwear.

In this work, the distribution of pressure developed on the patient's feet during gait is measured using pressure plates. The dynamic measurements were performed individually for each foot, where the subject has to walk on the plate according to the selected recording variant. In this study, the pressure measurements were

Table 1 Material characteristics of conventional foot stirrup stainless steel AISI 420

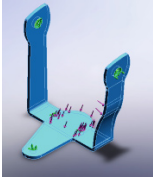
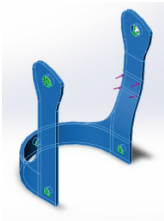
Conventional stirrup	Properties	
	Name	1.4021 (X20Cr13)
	Model type	Linear elastic isotropic
	Default failure criterion	Max von mises stress
	Yield strength	7.85e8 N/m ²
	Tensile strength	7.3e8 N/m ²
	Elastic modulus	1.9e11 N/m ²
	Poisson's ratio	0.28
	Mass density	7,800 kg/m ³

Table 2 Characteristics of material used in alternative foot stirrup aluminum 7075 T6

Alternative stirrup	Properties	
	Name	7075-T6 (SN)
	Model type	Linear elastic isotropic
	Default failure criterion	Max von mises stress
	Yield strength	5.05e8 N/m ²
	Tensile strength	5.7e8 N/m ²
	Elastic modulus	7.2e10 N/m ²
	Poisson's ratio	0.33
	Mass density	2,810 kg/m ³

performed using the footscan[®] 3D Gait Scientific 2 m system. Due to the footscan[®] 3D interface, the user has the possibility to synchronize his system with other measurement tools, namely force plates. The full characterization of the human gait for normal and pathological cases are performed with basis on the biomechanics of motion, which allows for the identification of the worst scenarios in terms of loads during human gait [3].

The conventional foot stirrup considered in the present work is made by stainless steel AISI 420 type, which was computationally simulated for different geometries. For this purpose, a commercial program that is based on the finite element approach is employed, which allows for the quantification of level of stresses for the different models considered. Table 1 presents the main characteristics and the geometry of conventional foot stirrup. The conventional geometry has angles of about 90°, making the foot stirrup quite susceptible to rupture. Another important factor is the material density. In this case, the foot stirrup weight represents 18 % of total weight of footwear.

The alternative geometry of the new foot stirrup eliminates the angles of 90° and uses a lighter material, as it is shown in Table 2. Thus, with this new geometry solution the fragile area now located on the holes.

Table 3 Static analysis with the Global Postural Position (GPS)

Number of samples	4.096
Time (s)	20.000
Total mass (kg)	91.386
Mass on left foot (kg)	59.787
Mass on right foot (kg)	31.599
Mass of the left foot on the 1st metatarsal (kg)	20.983
Mass of the left foot on the 5th metatarsal (kg)	39.794
Mass of the left foot on the calcaneus (kg)	0.990
Mass of the right foot on the 1st metatarsal (kg)	0.029
Mass of the right foot on the 5th metatarsal (kg)	6.981
Mass of the right foot on the calcaneus (kg)	24.589

5 Results and Discussion

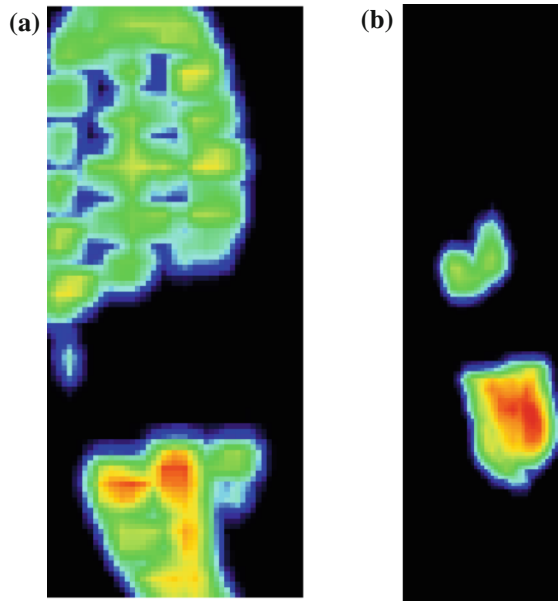
This section includes some of the earlier of this study. Firstly, two different devices, Lux Stabilometric footboard and Podata footboard, are used to carry out a stabilometric analysis. The Lux Stabilometric footboard has three load cells while the Podata footboard is provided with six cells (bipodalic), which can be adjusted in order to record the load under the 1st and 5th metatarsal and heel of each foot. Table 3 illustrates main parameters considered for the static analyses.

Figure 3 illustrates one atypical foot, as results of polio pathology. It is possible to verify that the force applied on the right calcaneus is equal to 24.589 kg, which represents 78 % of total weight on right leg. It is also possible to observe that the left leg of the user has a different forces distribution.

Figure 4 depicts the dynamic results associated with human gait for one foot normal and one foot with cavus foot pathology. These plots represent the gait of the user considered in the present study. The intensity of pressure increases from green to red colours. In the dynamic analysis it can be verified that the differences between right and left feet responses during the gait. It is also possible to observe the high pressure on right foot located in calcaneus zone.

Fig. 3 Cavus foot considered in the present work

Fig. 4 **a** Left/normal foot. **b** Right/cavus foot



The foot stirrup connects the orthoses and footwear, being a key element for KAFO orthoses. The user considered in the present study has 93 kg mass, which is equivalent to 912 N. Another important factor to analyze the forces applied by the user during his gait, is the pronation angle, which is equal to 20° in the present case. Initial contact with the ground during the stance phase occurs with the calcaneus. This contact area supports the entire body weight (912 N), which corresponds to the force applied when the foot is in the normal position. In this particular case, there is an excessive pronation that produces an extra force equal to 970 N that corresponds to ground reaction force. Considering this force applied on the conventional and presented stirrup models, a fatigue analysis was performed, being the results illustrated in Fig. 5.

Figure 5a shows the fatigue response for the conventional foot stirrup. The minimum number of cycles of critical area is approximately 1.62 million. Considering that user has one step away from 0.5 m and walk 3,000 m per day. In the present analysis, the Soderberg criterion is used because it provides a high level of safety. Figure 5b shows the fatigue results of new foot stirrup. The minimum number of cycles of critical area is approximately 425 thousand cycles. Considering that user has one step away from 0.5 m and run 3,000 m per day. Comparing this value with the conventional foot stirrup it can be observed that it is relatively low, because it is not considered the fixing system in the shoe.

In the present study, global results in terms of stresses when the von Mises criterion is considered, for both conventional and new solution foot stirrup. Although the value obtained for the new foot stirrup fatigue is lower than the conventional, the new solution presented a very reasonable durability, i.e. approximately 9 months. Once the

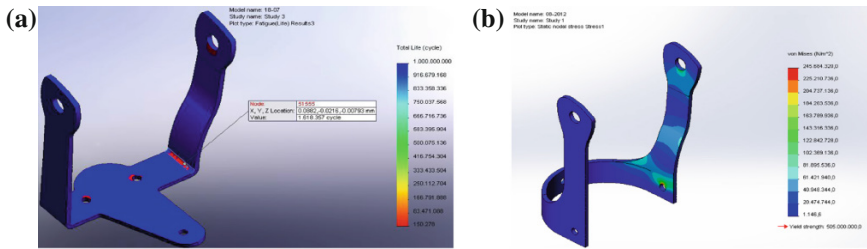


Fig. 5 a conventional stirrup performance. b Presented stirrup performance

new foot stirrup is 50 % lighter than the conventional one, this difference makes the gait be less painful to the user. From the obtained outcomes, it can be observed that the new solution performs better than the conventional one and it has been object of further investigation in the case of actual orthopedic footwear. Finally, the best proposed solution for the foot stirrup is introduced into actual orthopedic footwear with the purpose to test and validate its functionality in a real environment. The prototype was more effective in the elimination of fluids and nonexistence of odors during the test performed by the user.

6 Conclusions

The design and development of a new foot stirrup to be applied on functional orthopedic footwear has been presented in this work. In the sequel of this process computational simulations were performed to test and verify the new proposed solution. This work culminates in the manufacturing of a physical prototype to be included in actual orthopedic footwear. In general, based on the computational results, it can be said that the new solution is less prone to fatigue and rupture due to the new geometrical configuration, when compared with the conventional model. Further, the durability of the new solution is longer. This fact has been demonstrated from both computational and actual tests. Moreover, based on the user experience, it can be drawn that the new model manufactured with a new geometry is 25 % lighter and, consequently, reduces the fatigue during gait. In short, the new approach is appropriate and functional for daily activities.

References

1. Ceccarelli, Merrit JL, Yoshida MK (2000) Knee-ankle-foot orthoses, indications and practical applications of long leg braces. *Phys Med Rehabil State Art Rev* 14:395–422
2. Goldberg B, Hsu JD (eds) (1997) *Atlas of orthosis and assistive devices*, 3rd edn. Mosby, St. Louis

3. Peixoto J, Flores P, Souto AP Breathable impermeable and odourless lining for orthopaedic footwear application. In: Proceedings of ITC&DC 2012 6th international textile, clouding and design conference, Dubrovnik, Croacia, 7–10 Oct, pp 87–92
4. Moreira P, Ramôa P, Silva LF, Flores P (2011) On the biomechanical design of stance control knee ankle foot orthosis (SCKAFO). In: Proceedings of MUSME 2011, the international symposium on multibody systems and mechatronics Valencia, Spain, 25–28 Oct 2011, pp 305–322
5. Corraza S, Mundermann L, Chaudhri M, Demottio T, Cobelli C, Andriacchi P (2006) Motion capture system to study musculoskeletal biomechanics: visual hull computer vision and image understanding. *Anal Biomed Eng*
6. Meireles F, Machado M, Silva M, Flores P (2009) Dynamic modeling and analysis of human locomotion using multibody system methodologies. *Int J Comput Vision Biomech* 2 (2):199–206
7. Moura B (2011) Projeto e Desenvolvimento de Estribo para Calçado Ortopédico. MSc Dissertation, University of Minho, Portugal
8. Whittle M (2007) *Gait analysis: an introduction*. Butterworth-Heinemann Elsevier, Philadelphia
9. Winter DA (2009) *Biomechanics and motor control of human movement*. Wiley, New Jersey
10. Edelstein JE, Bruckner J (2002) *Orthotics: a comprehensive clinical approach*. Slack, New Jersey
11. Ferreira P, Development of a two-dimensional biomechanical multibody model for the analysis of the human gait with an ankle-foot orthoses. MSc Dissertation, University of Minho, Portugal

Dynamic Analysis of an Exoskeleton New Ankle Joint Mechanism

N. Dumitru, C. Copilusi, I. Geonea, D. Tarnita and I. Dumitrache

Abstract In this paper, a dynamic analysis is performed for a new ankle joint mechanism used on an exoskeleton structure. The designed exoskeleton structure will be used in human rehabilitation purposes. The aim of this research is to determine the connection forces through an inverse dynamic analysis in order to use these for numerical simulations of the proposed prototype. The obtained results validate the design techniques, which demonstrates the engineering feasibility of the proposed design.

Keywords Human locomotion · Walking rehabilitation · Dynamic analysis · Exoskeleton · Ankle joint

1 Introduction

Human locomotion dynamic analysis is a difficult approach due to the human locomotion system complexity. Nowadays a large variety of human walking rehabilitation systems are developed for improving the walking quality, minimizing the recovery process period and to gain access of disabled people for a better life.

N. Dumitru (✉) · C. Copilusi · I. Geonea · D. Tarnita · I. Dumitrache
University of Craiova, Craiova, Romania
e-mail: nicolae_dtru@yahoo.com

C. Copilusi
e-mail: cristache03@yahoo.co.uk

I. Geonea
e-mail: igeonea@yahoo.com

D. Tarnita
e-mail: tarnita.daniela@gmail.com

I. Dumitrache
e-mail: dumitrachesilviuionut@ymail.com

Existing solutions of human exoskeletons are currently used for walking with an anthropomorphic structure (human-like). These use three or more actuators for hip, knee and ankle joints. These exoskeleton types were used to obtain anthropomorphic legs structure and has the same degrees of freedom as human limbs [1–7]. However, there are some weaknesses: complex and expensive design and manufacturing, complex control systems by considering the actuators number and their position on an exoskeleton leg. In order to develop these types of rehabilitation systems are used modern techniques of design and calculus. These treat experimental kinematic and dynamic analyses. Through many researches as in [8–12], were performed different types of approaches for exoskeletons dynamic analyses.

On this research, a method for an inverse dynamic analysis will be applied in order to obtain the connection forces from the human ankle joint level during walking. The research starts by analysing the human gait on experimental way for obtaining the input data used on this analysis. On third part of this research, a kinematic scheme is proposed and this is useful for an inverse dynamic analysis. The research is continued by applying the Newton-Euler method completed with Lagrange multipliers on the proposed leg exoskeleton structure. The obtained results from numerical processing demonstrates the use of this method. At the end these results validate the inverse dynamic analysis and the feasibility of the new leg exoskeleton design.

2 Human Walking Experimental Analysis

By considering the research aim, one of the starting points regards the human law for ankle joint motion during walking. Faculty of Mechanics from University of Craiova, owns an equipment called CONTEMPLAS [13]. This equipment gives identification by using video sequences of special reflective markers that are placed on a mobile system through high-speed cameras. By using three reflective markers, these were attached on a human leg (M1 on tibia segment, M2-ankle joint centre, M3-metatarsian joints) as it shown in Fig. 1. Also this has a pressure platform in order to establish the reaction forces or pressures during the contact between foot and ground.

At the beginning of this experimental analysis, the anthropomorphic data regarding the chosen human subject where known as 1.70 m height, 58 kg as weight, femur size equal with 402 mm, shank size equal with 331 mm, and ankle-foot size 24 mm. The analysis procedure consists on monitoring the reflective markers position during gait. At the end of this analysis, the software equipment automatically give the desired results, and in particular the ankle joint trajectory during one gait as in Fig. 1. The time when human subject performs a single gait 100 (%) was 1.2 s.

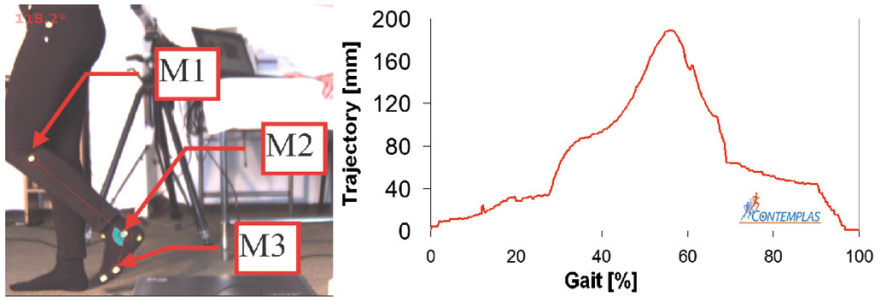


Fig. 1 Markers identification during walking tests and acquired trajectory for human ankle joint (millimetres) versus gait (%) during a test

3 Inverse Dynamic Analysis of a New Exoskeleton Ankle Joint Mechanism

The proposed exoskeleton structure is shown in Fig. 2. This consists from two mechanisms, one for knee joint actuation and other for ankle joint actuation.

The kinematic scheme of the proposed mechanism for driving the human ankle joint and foot is presented in Fig. 2a. The driving was designed in two ways, namely: a cam mechanism and a mechanism with linear actuator as it shown in Fig. 2a. Figure 2b illustrates a mechanism for driving the tibia (link 7 in Fig. 2a, b). The study of this mechanism is not the subject of this paper.

$$\Phi(\mathbf{q}, \mathbf{t}) = 0 \tag{1}$$

Equation (1) includes the kinematic constraint equations imposed by kinematic joints and driving constraints. The number of driving constraints is equal with the one of the system kinematic DOF. This is a situation when the mechanical system is kinematically determined. For this case, the Jacobian corresponding to Eq. (1) is a quadratic and nonsingular one.

The proposed dynamic analysis is based on Newton-Euler method completed with Lagrange multipliers [12]. This method has been applied on the mechanism from Fig. 2a. For this, the motion equations which defines the behaviour of a mobile mechanical systems on a dynamic mode can be written as

$$\begin{bmatrix} \mathbf{M} & \mathbf{J}_q^T \\ \mathbf{J}_q & 0 \end{bmatrix} \begin{bmatrix} \ddot{\mathbf{q}} \\ \boldsymbol{\lambda} \end{bmatrix} = \begin{bmatrix} \mathbf{Q}^A \\ \mathbf{a} \end{bmatrix} \tag{2}$$

where: \mathbf{M} —mass matrix; $\vec{\mathbf{q}}$ —vector of generalized coordinates; \mathbf{J}_q —Jacobian matrix corresponding to the “ \mathbf{q} ” generalized coordinates which satisfy the Eq. (1); $\boldsymbol{\lambda}$ —Lagrange multipliers vector; \mathbf{Q}^A —matrix of applied generalized forces.

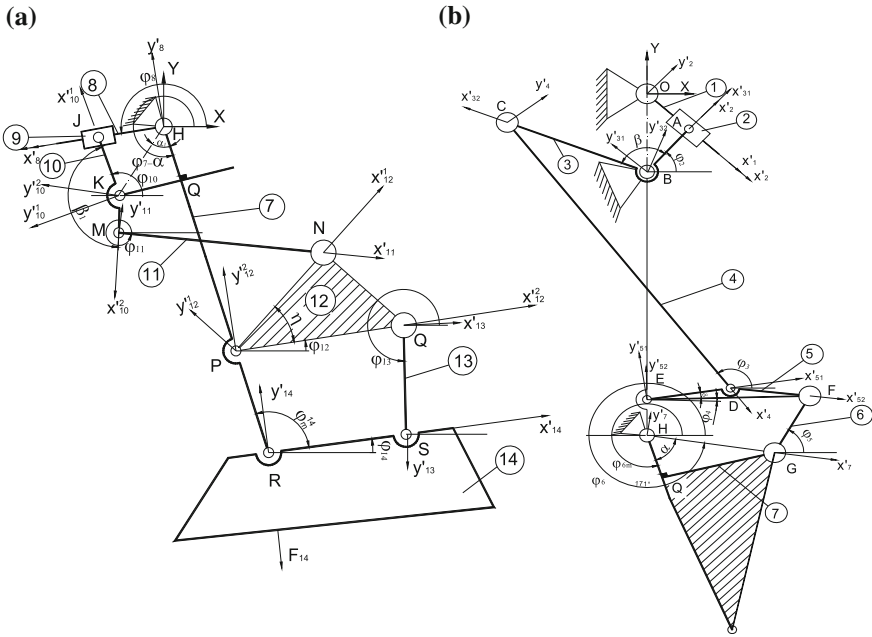


Fig. 2 Kinematic scheme of the proposed leg exoskeleton: **(a)** ankle joint mechanism; **(b)** partial leg exoskeleton without ankle joint mechanism

Differentiating Eq. (1) depending on time, we will obtain

$$\dot{\Phi} = \mathbf{J}_q \dot{\mathbf{q}} + \frac{\partial \Phi}{\partial \mathbf{t}} = 0 \tag{3}$$

$$\ddot{\Phi} = \mathbf{J}_q \ddot{\mathbf{q}} + 2\mathbf{J}_q \dot{\mathbf{q}} + (\mathbf{J}_q \dot{\mathbf{q}})_{\mathbf{q}} \cdot \dot{\mathbf{q}} + \frac{\partial^2 \Phi}{\partial \mathbf{t}^2} = 0 \tag{4}$$

We consider

$$\mathbf{a} = -2\mathbf{J}_q \cdot \dot{\mathbf{q}} - (\mathbf{J}_q \cdot \dot{\mathbf{q}})_{\mathbf{q}} \cdot \dot{\mathbf{q}} - \frac{\partial^2 \Phi}{\partial \mathbf{t}^2}; (\mathbf{J}_q \cdot \dot{\mathbf{q}})_{\mathbf{q}} = \frac{\partial}{\partial \mathbf{q}} (\mathbf{J}_q \cdot \dot{\mathbf{q}}) \tag{5}$$

Then we may write using Eq. (2)

$$\mathbf{M} \ddot{\mathbf{q}} + \mathbf{J}_q^T \lambda = \mathbf{Q}^A \tag{6}$$

$$\mathbf{J}_q \ddot{\mathbf{q}} = \mathbf{a} \tag{7}$$

Jacobian \mathbf{J}_q , is quadratic and nonsingular, so

$$\ddot{\mathbf{q}} = [\mathbf{J}_q]^{-1} \cdot \mathbf{a} \tag{8}$$

We determine the Lagrange multipliers using Eq. (6)

$$\lambda = [\mathbf{J}^{-1}] \cdot [\mathbf{Q}_a - \mathbf{M} \ddot{\mathbf{q}}] \tag{9}$$

The vector of generalized coordinates for an element “i” is

$$\mathbf{q}_i = [\mathbf{r}_i^T \quad \varphi_i]^T \tag{10}$$

In order to calculate the constraint forces in a kinematic pair “k” there are considered the reference frames \mathbf{R}'_i and \mathbf{R}'_j , rigidly attached to the element “i”, and “j”, respectively, the reference frames \mathbf{R}''_i and \mathbf{R}''_j , rigidly attached to the element “i” and “j”, centered in the kinematic joint “k”. The components of the constraint forces may be determined for each element using the relationships given by [14]. With the above equations and considering the scheme from Fig. 2a, the connection forces for each joint will be obtained. This can be done by creating an algorithm for computation with Maple software. For this, the following steps will be accomplished: the kinematic constraints Eq. (1) will be written; the Jacobian matrix will be identified from the mechanism kinematic analysis; mass matrices will be defined; \mathbf{Q}^A generalized forces vector will be also identified; the generalized coordinates vector will be defined and a proper equations system which control the mechanism kinematics will be created; the; Lagrange multipliers vector will be identified; computing the connection forces from each joint on dynamic mode.

With the aid of generalized coordinates laws and with the connection forces, properly established for each kinematic joint, a database will be created for a further research based on the mechanical system finite element analysis. This represents the final design phase in order to evaluate the behaviour on dynamic mode.

The connection force depending with the global reference system for a revolute joint as is described in [14] is given by

$$\begin{aligned} \mathbf{F}_i'' &= -[\mathbf{R}_{i' i''}] \cdot [\mathbf{A}_{oi}]^T \cdot \mathbf{J}_{ri}^{kT} \cdot \lambda^k \\ \mathbf{T}_i'' &= \left([\mathbf{S}_i^M]^T \cdot [\mathbf{P}_{oi}]^T \cdot \mathbf{J}_{ri}^{kT} - \mathbf{J}_{\varphi i}^{kT} \right) \cdot \lambda^k \end{aligned} \tag{11}$$

where: $\mathbf{R}_{i' i''}$, \mathbf{A}_{oi} represents coordinate transformation matrices and other terms are given by

$$\mathbf{P}_{oi} = \frac{d}{d\varphi_i} [\mathbf{A}_{oi}], \quad \mathbf{J}_{qi} = [\mathbf{J}_{ri}, \mathbf{J}_{\varphi i}]^T \tag{12}$$

4 Connection Forces Calculus for the Exoskeleton Ankle Joint Mechanism

Based on the above described method, the connection forces variation laws will be obtained for the proposed mechanism from Fig. 2a. For this, the kinematic constraints Eq. (1) can be written. The generalized coordinates, generalized speed and generalized acceleration vectors which corresponds to the mechanism kinematic configuration is given by

$$\mathbf{q} = \{\mathbf{x}_J, \mathbf{y}_J, \varphi_8, \varphi_{10}, \mathbf{x}_M, \mathbf{y}_M, \varphi_{11}, \varphi_{12}, \mathbf{x}_Q, \mathbf{y}_Q, \varphi_{13}, \varphi_{14}, \mathbf{x}_S, \mathbf{y}_S\}^T \quad (13)$$

$$\dot{\mathbf{q}} = \{\dot{\mathbf{x}}_J, \dot{\mathbf{y}}_J, \dot{\varphi}_8, \dot{\varphi}_{10}, \dot{\mathbf{x}}_M, \dot{\mathbf{y}}_M, \dot{\varphi}_{11}, \dot{\varphi}_{12}, \dot{\mathbf{x}}_Q, \dot{\mathbf{y}}_Q, \dot{\varphi}_{13}, \dot{\varphi}_{14}, \dot{\mathbf{x}}_S, \dot{\mathbf{y}}_S\}^T \quad (14)$$

$$\ddot{\mathbf{q}} = \{\ddot{\mathbf{x}}_J, \ddot{\mathbf{y}}_J, \ddot{\varphi}_8, \ddot{\varphi}_{10}, \ddot{\mathbf{x}}_M, \ddot{\mathbf{y}}_M, \ddot{\varphi}_{11}, \ddot{\varphi}_{12}, \ddot{\mathbf{x}}_Q, \ddot{\mathbf{y}}_Q, \ddot{\varphi}_{13}, \ddot{\varphi}_{14}, \ddot{\mathbf{x}}_S, \ddot{\mathbf{y}}_S\}^T \quad (15)$$

The motion Equations for Newton-Euler method completed with Lagrange multipliers are on the same form as the one from Eq. 2. The proper mass matrix in this case is the following

$$\mathbf{M} = \text{diag} \left(\mathbf{m}_8, \mathbf{m}_8, \frac{1}{3} \mathbf{m}_8 \mathbf{L}_8^2, \frac{1}{3} \mathbf{m}_{10} \mathbf{L}_{10}^2, \mathbf{m}_{10}, \mathbf{m}_{10}, \frac{1}{3} \mathbf{m}_{11} \mathbf{L}_{11}^2, \frac{1}{3} \mathbf{m}_{12} \mathbf{L}_{12}^2, \right. \\ \left. \mathbf{m}_{12}, \mathbf{m}_{12}, \frac{1}{3} \mathbf{m}_{13} \mathbf{L}_{13}^2, \frac{1}{3} \mathbf{m}_{14} \mathbf{L}_{14}^2, \mathbf{m}_{14}, \mathbf{m}_{14} \right) \quad (16)$$

The applied generalized forces vector is

$$\mathbf{Q}^\Lambda = [0, -\mathbf{m}_8 \mathbf{g}, 0, 0, 0, -\mathbf{m}_{10} \mathbf{g}, 0, 0, 0, -\mathbf{m}_{12} \mathbf{g}, 0, 0, \mathbf{F}_t^x, -\mathbf{m}_{14} \mathbf{g} + \mathbf{F}_t^y]^T \quad (17)$$

$$\mathbf{J}_q \cdot \ddot{\mathbf{q}} = \mathbf{a} = \begin{bmatrix} \ddot{\mathbf{S}}_8 \cos \varphi_8 - 2\dot{\mathbf{S}}_8 \dot{\varphi}_8 \sin \varphi_8 - \mathbf{S}_8 (\dot{\varphi}_8)^2 \cos \varphi_8 \\ \ddot{\mathbf{S}}_8 \sin \varphi_8 + 2\dot{\mathbf{S}}_8 \dot{\varphi}_8 \sin \varphi_8 - \mathbf{S}_8 (\dot{\varphi}_8)^2 \sin \varphi_8 \\ -\ddot{\mathbf{S}}_8 \cos \varphi_8 + 2\dot{\mathbf{S}}_8 \dot{\varphi}_8 \sin \varphi_8 + \mathbf{S}_8 (\dot{\varphi}_8)^2 \cos \varphi_8 - \mathbf{I}_{JK} (\dot{\varphi}_{10})^2 \cos \varphi_{10} \\ -\ddot{\mathbf{S}}_8 \sin \varphi_8 - 2\dot{\mathbf{S}}_8 \dot{\varphi}_8 \sin \varphi_8 + \mathbf{S}_8 (\dot{\varphi}_8)^2 \sin \varphi_8 - \mathbf{I}_{JK} (\dot{\varphi}_{10})^2 \sin \varphi_{10} \\ -(\dot{\varphi}_{10})^2 \mathbf{I}_{KM} \cos(\varphi_{10} + \beta_1) \\ -(\dot{\varphi}_{10})^2 \mathbf{I}_{KM} \sin(\varphi_{10} + \beta_1) \\ (\dot{\varphi}_{11})^2 \mathbf{I}_{MN} \cos \varphi_{11} - \ddot{\varphi}_7 \mathbf{I}_{HP} \sin(\varphi_7 - \alpha) - (\dot{\varphi}_7)^2 \mathbf{I}_{HP} \cos(\varphi_7 - \alpha) - (\dot{\varphi}_{12})^2 \mathbf{I}_{PN} \cos(\varphi_{12} + \eta) \\ (\dot{\varphi}_{11})^2 \mathbf{I}_{MN} \sin \varphi_{11} + \ddot{\varphi}_7 \mathbf{I}_{HP} \cos(\varphi_7 - \alpha) - (\dot{\varphi}_7)^2 \mathbf{I}_{HP} \sin(\varphi_7 - \alpha) - (\dot{\varphi}_{12})^2 \mathbf{I}_{PN} \sin(\varphi_{12} + \eta) \\ -\ddot{\varphi}_7 \mathbf{I}_{HP} \sin(\varphi_7 - \alpha) - (\dot{\varphi}_7)^2 \mathbf{I}_{HP} \cos(\varphi_7 - \alpha) - (\dot{\varphi}_{12})^2 \mathbf{I}_{PQ} \cos(\varphi_{12} + \eta) \\ \ddot{\varphi}_7 \mathbf{I}_{HP} \cos(\varphi_7 - \alpha) - (\dot{\varphi}_7)^2 \mathbf{I}_{HP} \sin(\varphi_7 - \alpha) - (\dot{\varphi}_{12})^2 \mathbf{I}_{PQ} \sin(\varphi_{12} + \eta) \\ (\dot{\varphi}_{13})^2 \mathbf{I}_{QS} \cos \varphi_{13} - \ddot{\varphi}_7 \mathbf{I}_{HR} \sin(\varphi_7 - \alpha) - (\dot{\varphi}_7)^2 \mathbf{I}_{HR} \cos(\varphi_7 - \alpha) - (\dot{\varphi}_{14})^2 \mathbf{I}_{RS} \cos \varphi_{14} \\ (\dot{\varphi}_{13})^2 \mathbf{I}_{QS} \sin \varphi_{13} + \ddot{\varphi}_7 \mathbf{I}_{HR} \cos(\varphi_7 - \alpha) - (\dot{\varphi}_7)^2 \mathbf{I}_{HR} \sin(\varphi_7 - \alpha) - (\dot{\varphi}_{14})^2 \mathbf{I}_{RS} \sin \varphi_{14} \\ -\ddot{\varphi}_7 \mathbf{I}_{HR} \sin(\varphi_7 - \alpha) - (\dot{\varphi}_7)^2 \mathbf{I}_{HR} \cos(\varphi_7 - \alpha) \\ \ddot{\varphi}_7 \mathbf{I}_{HR} \cos(\varphi_7 - \alpha) - (\dot{\varphi}_7)^2 \mathbf{I}_{HR} \sin(\varphi_7 - \alpha) \end{bmatrix} \quad (18)$$

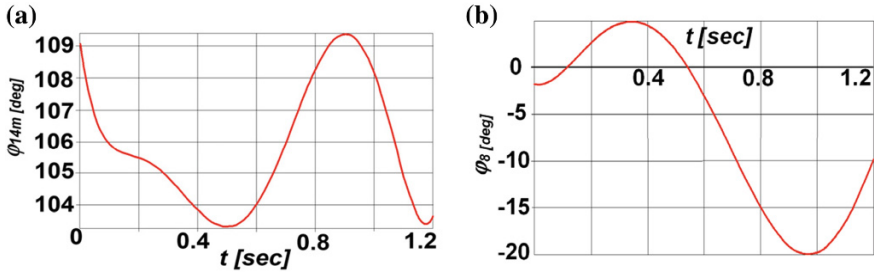


Fig. 3 Computed angle variation laws for the proposed mechanism: (a) ϕ_{14m} (degrees) equivalent to the ankle joint versus time (s); (b) ϕ_8 (degrees) computed angle variation law from the actuator no. 8 versus time (s)

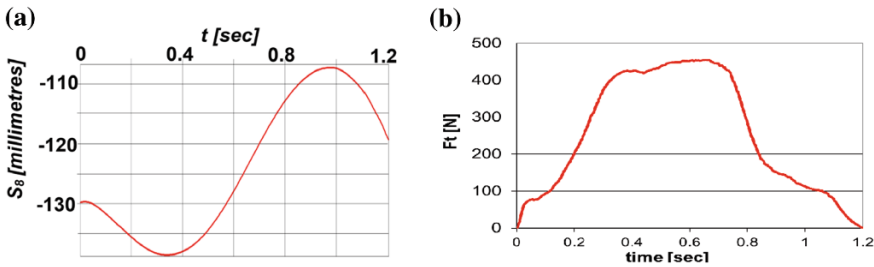


Fig. 4 Computed motion law (millimetres) for the S_8 linear actuator versus time (s)—(a) and the contact force (N) between foot and ground versus time (s)—(b)

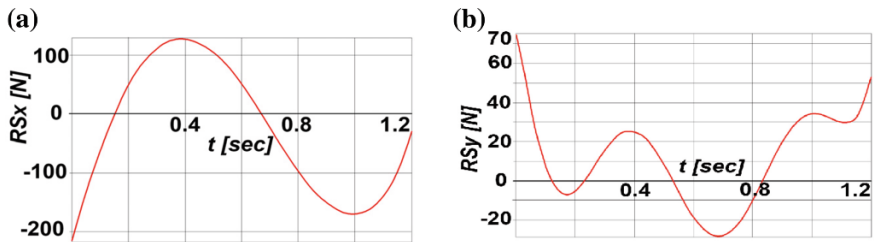


Fig. 5 Computed connection force components variation laws for ankle joint equivalent mechanism: (a) R_{Sx} (N) versus time (s); (b) R_{Sy} (N) versus time (s)

The input data for mathematical model processing are given by the dimensional elements, which corresponds with the human subject proposed for experimental analysis. A numerical processing was performed by creating a calculus algorithm with MAPLE software aid. The obtained results are shown on plots from Figs. 3, 4a and 5. In Fig. 3a is represented the ϕ_{14m} angle variation law on time, obtained from experimental analysis. Also were determined the kinematic parameters motion laws

depending on time and especially the linear actuator no 8 limits (S_8 actuating displacement). The computed value obtained through numerical simulations is 6 degrees for φ_{14m} , as is shown in Fig. 3a. Another result is given by the φ_8 computed angle variation law which has a value of 24 degrees as it shown on Fig. 3b. Also this algorithm permit to obtain the linear actuator total displacement which for the dynamic analysis of the proposed ankle joint mechanism has a value of 35 mm as it can be seen on Fig. 4. The final results and the most important ones are given by the connection forces components variation, which on horizontal plane has a maximum value of 300 N and on vertical plane the computed maximum value is 95 N, as it shown in Fig. 5.

5 Conclusions

The two kinematic schemes illustrated by Fig. 2a, b define a mechanism having the mobility M equal with 2 DOF, respectively one for driving the human ankle joint and other for knee. The kinematic chain is closed only by contact with the support surface. This contact was substituted by the reaction force F_t , experimentally determined. Through this research, a new ankle joint mechanism for a leg exoskeleton is validated by performing an inverse dynamic analysis. The obtained results from numerical processing confirm the application of the proposed method for this dynamic analysis, namely Newton Euler method completed with Lagrange multipliers. The developed research use modern design and computations techniques starting from experimental approaches and finalizing with results that are almost impossible to obtain on analytical ways. The connection forces can be used further as input data for virtual simulations, in order to complete the leg exoskeleton design.

References

1. Ceccarelli M, Carbone G, Ottaviano E, Lanni C (2009) Leg designs for walking machines at LARM in Cassino. In: ASI workshop on robotics for moon exploration, Rome
2. Copilusi C, Ceccarelli M, Carbone G, Margine A (2013) Mechanism of a leg exoskeleton for walking rehabilitation purposes. New advances in mechanisms, transmissions and applications. In: Proceedings of the 2nd conference MeTrApp, Ed. Springer, Berlin, pp 117–126
3. Copilusi C, Ceccarelli M, Dumitru N, Carbone G (2013) Design and simulation of a leg exoskeleton linkage for a human rehabilitation system. In: Proceedings of the 11th symposium on science of mechanism SYROM, Ed. Springer, Dordrecht, pp 107–114
4. Eiichirou T (2012) Development of a walking-assistance apparatus for neuro-rehabilitation. Appl Mech Mater 162:258–265
5. Katsuhiko I (2007) Reduced DOF type walking robot based on closed link mechanism, bioinspiration and robotics: walking and climbing robots. In: Maki K (ed) Habib ISBN 978-3-902613-15-8, 544, I-Tech, Austria

6. Liu J, Tan M, Zhao XG (2007) Legged robots—an overview. *Trans Inst Measur Control* 29 (2):185–202
7. Shieh WB (1996) Design and optimization of planar leg mechanisms featuring symmetrical. Foot-Points Paths, Thesis report, University of Maryland
8. Copilusi C (2009) Research regarding applied mechanical systems in medicine. PhD. thesis, Craiova
9. Faure F et al (1997) Dynamic analysis of human walking. *J Comput Graph Simul* 53–65
10. Rosen J et al (2005) The human arm kinematics and dynamics during daily activities—toward a 7 DOF upper limb powered exoskeleton. *J Adv Robot* 10:532–539
11. Low KH et al (2004) Development of a lower extremity exoskeleton—preliminary study for dynamic walking. *Control Autom Robot Vis* 3:2088–2093
12. Amirouche F (2004) Fundamentals of multibody dynamics. Birkhauser Prentice Hall, Englewood Cliffs
13. Ernst B, Helas S (2013) CONTEMPLAS-user manual
14. Dumitru N et al (2008) Mechanisms and mechanical transmissions. E.D. Prentice Hall, Bucharest

Part X
Novel Designs

Analysing of Flying Conditions of Aircrafts Using Artificial Neural Networks

Ş. Yıldırım and S. Erkaya

Abstract In spite of advanced technology, the commercial aircraft's accidents are increasing year by year. Therefore, it is very important to analyse and predict flying conditions of aircrafts such as time to destination, distance to destination with outside temperature, altitude, ground speed and head wind. In this work, experimental measurements are taken from the aircraft during flying. Neural network based predictors are also designed to analyse destination time and destination distance for secure travelling conditions of passengers. Two type neural networks are used as predictor, that is, Back Propagation Neural Network (BPNN) and Radial Bases Neural Network (RBNN). The results show that RBNN has superior performance to adapt the parameters of the aircraft.

Keywords Flying condition · Neural predictor · Radial basis neural network

1 Introduction

Modern aircrafts are required to fly in a wide envelope with regard to speed, altitude, wing loading weight configuration etc. Due to their powerful ability of modelling the system characteristics, artificial neural networks (ANNs) have been extensively studied in the area of flight industries such as nonlinear adaptive control etc. Nowadays, some investigations have been done by some researchers.

Singh et al. [1] have derived an adaptive control law for wing-rock control. A radial basis function neural network has been used for synthesizing the controller, and adaptation law has also been performed for adjusting the network parameters. Napolitano and Kincheloe [2] have proposed an on-line learning neural controller in

Ş. Yıldırım (✉) · S. Erkaya
University of Erciyes, Kayseri, Turkey
e-mail: sahin@erciyes.edu.tr

S. Erkaya
e-mail: serkaya@erciyes.edu.tr

the autopilot control laws of a modern high-performance aircraft. Balakrishnan and Biega [3] have presented a neural network architecture for the solution of an aircraft control. An action and critic network has been used to approximately solve the dynamic programming equations. By using a high-gain observer and radial basis function neural network, adaptive output feedback control have been proposed for nonlinear systems represented by input-output models [4]. Also, a nonlinear adaptive flight control system has been designed by backstepping [5] and neural network controller. Calise [6] has proposed an approach for incorporating a neural network with real-time learning capability in flight control architecture. Calise et al. [7–9] have extensively worked on the control and estimation of aircrafts and helicopters using neural network. Li et al. [10] have proposed an on-line learning neuro-control scheme based on a growing radial basis function network for a nonlinear aircraft controller design.

In this paper, prediction and estimation the travelling destination time and destination distance of aircrafts using artificial neural networks are studied. Two type neural networks are used as predictor, that is, back propagation neural network and radial basis neural network. Training and testing stages of all networks are performed on programming language.

2 Rigid Body Equation of Motion for Aircrafts

Before modifying the equation of motion, it is better and important to review the axis system. Figure 1a shows the body axis system fixed to the aircraft and the inertial axis system that is fixed to the earth. Schematic representation of an element of mass on an airplane is shown in Fig. 1b.

The rigid body equations of motion are obtained from Newton's second law. For many problems in airplane dynamics, an axis system fixed to the earth can be used

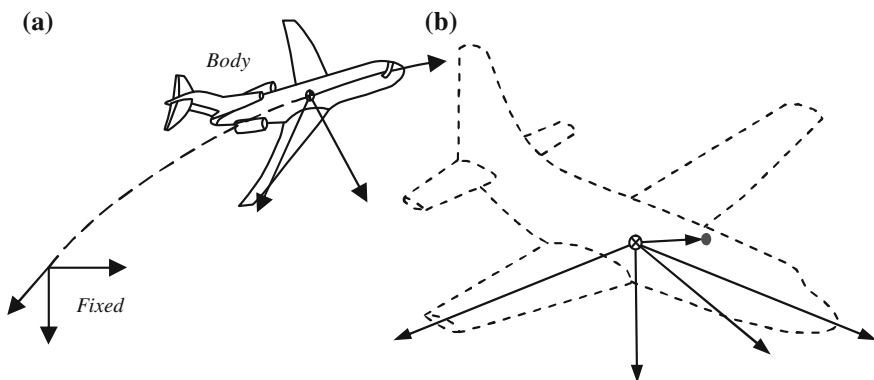


Fig. 1 a Body and inertial axis system. b An element of mass on an airplane

as an inertial reference frame. Newton's second law can be expressed in the following vector equations:

$$\sum \mathbf{F} = \frac{d}{dt}(m\mathbf{v}), \quad \sum \mathbf{M} = \frac{d}{dt}(\mathbf{H}) \quad (1)$$

The vector equations can be rewritten in scalar form and then consist of three force equations and three moment equations. The force equations can be expressed as follows:

$$F_x = d(mu)/dt \quad F_y = d(mv)/dt \quad F_z = d(mw)/dt \quad (2)$$

where F_x, F_y, F_z and u, v, w are the components of the force and velocity along the x, y and z axes, respectively. The force components are composed of contributions due to the aerodynamic, propulsive and gravitational forces acting on the airplane. The moment equations can be expressed in a similar manner.

$$L = dH_x/dt \quad M = dH_y/dt \quad N = dH_z/dt \quad (3)$$

where L, M, N and H_x, H_y, H_z are the components of the moment and moments of momentum along the $x, y,$ and z axes, respectively. If we let δm be an element of mass of the airplane, \mathbf{v} be the velocity of the elemental mass relative to an absolute or inertial frame, and $\delta \mathbf{F}$ be the resulting force acting on the elemental mass, then Newton's second law yields

$$\delta \mathbf{F} = \delta m(d\mathbf{v}/dt) \quad (4)$$

And the total external force acting on the airplane is found by summing all the elements of the airplane:

$$\sum \delta \mathbf{F} = \mathbf{F} \quad (5)$$

The velocity of the differential mass δm is

$$\mathbf{v} = \mathbf{v}_c + (d\mathbf{r}/dt) \quad (6)$$

where \mathbf{v}_c is the velocity of the center of mass of airplane and $d\mathbf{r}/dt$ is the velocity of the element relative to the center of mass. Substituting this expression for the velocity into Newton's second law yields

$$\sum \delta \mathbf{F} = \mathbf{F} = \frac{d}{dt} \sum \left(\mathbf{v}_c + \frac{d\mathbf{r}}{dt} \right) \delta m \quad (7)$$

If we assume that the mass of the vehicle is constant, (7) can be rewritten as

$$\mathbf{F} = m(d\mathbf{v}_c/dt) + \left(d^2 \sum \mathbf{r} \delta m / dt^2 \right) \quad (8)$$

Because \mathbf{r} is measured from the center of mass, the summation $\sum \mathbf{r} \delta m$ is equal to zero. The force equations then becomes

$$\mathbf{F} = m(d\mathbf{v}_c/dt) \quad (9)$$

which relates the external force on the airplane to the motion of the vehicle's center of mass. In a similar manner, we can develop the moment equation referred to a moving center of mass. For the differential element of mass, δm , the moment equation can be written as

$$\delta \mathbf{M} = d\delta \mathbf{H} / dt = d(\mathbf{r} \otimes \mathbf{v}) \delta m / dt \quad (10)$$

The velocity of the mass element can be expressed in terms of the velocity of the center of mass and the relative velocity of the mass element to the center of mass:

$$\mathbf{v} = \mathbf{v}_c + d\mathbf{r}/dt = \mathbf{v}_c + \omega \otimes \mathbf{r} \quad (11)$$

where ω is the angular velocity of the vehicle and \mathbf{r} is the position of the mass element measured from the center of mass. The total moment of momentum can be written as

$$\mathbf{H} = \sum \delta \mathbf{H} = \sum (\mathbf{r} \otimes \mathbf{v}_c) \delta m + \sum [\mathbf{r} \otimes (\omega \otimes \mathbf{r})] \delta m \quad (12)$$

The velocity \mathbf{v}_c is a constant with respect to the summation and can be taken outside the summation sign:

$$\mathbf{H} = \sum \mathbf{r} \delta m \otimes \mathbf{v}_c + \sum [\mathbf{r} \otimes (\omega \otimes \mathbf{r})] \delta m \quad (13)$$

The first term in (13) is zero because the term $\sum \mathbf{r} \delta m = 0$, as explained previously. If we express the angular velocity and position vector as

$$\boldsymbol{\omega} = p\mathbf{i} + q\mathbf{j} + r\mathbf{k}, \quad \mathbf{r} = x\mathbf{i} + y\mathbf{j} + z\mathbf{k} \quad (14)$$

then after expanding (13), \mathbf{H} can be written as

$$\mathbf{H} = (p\mathbf{i} + q\mathbf{j} + r\mathbf{k}) \sum (x^2 + y^2 + z^2) \delta m - \sum (x\mathbf{i} + y\mathbf{j} + z\mathbf{k})(px + qy + rz) \delta m \quad (15)$$

The scalar components of H are

$$\begin{aligned}
 H_x &= p \sum (y^2 + z^2) \delta m - q \sum xy \delta m - r \sum xz \delta m \\
 H_y &= -p \sum xy \delta m + q \sum (x^2 + z^2) \delta m - r \sum yz \delta m \\
 H_z &= -p \sum xz \delta m - q \sum yz \delta m + r \sum (x^2 + y^2) \delta m
 \end{aligned}
 \tag{16}$$

The summations in these equations are the mass moment and products of inertia of the airplane and are defined as follows:

$$\begin{aligned}
 I_x &= \iiint (y^2 + z^2) \delta m, & I_y &= \iiint (x^2 + z^2) \delta m, & I_z &= \iiint (x^2 + y^2) \delta m \\
 I_{xy} &= \iiint xy \delta m, & I_{xz} &= \iiint xz \delta m, & I_{yz} &= \iiint yz \delta m
 \end{aligned}
 \tag{17}$$

The terms I_x , I_y and I_z are the mass moments of inertia of the body about the x , y and z axes, respectively. The terms with the mixed indexes are called the products of inertia. Both the moments and products of inertia depend on the shape of the body and the manner in which its mass is distributed. The larger the moments of inertia, the greater will be the resistance to rotation. The scalar equations for the moment of momentum follow:

$$H_x = pI_x - qI_{xy} - rI_{xz}, \quad H_y = -pI_{xy} + qI_y - rI_{yz}, \quad H_z = -pI_{xz} - qI_{yz} + rI_z
 \tag{18}$$

If the reference frame is not rotating, then as the airplane rotates the moments and products of inertia will vary with time. To avoid this difficulty we will fix the axis system to the aircraft (body axis system). Now we must determine the derivatives of the vectors \mathbf{v} and \mathbf{H} referred to the rotating body frame of reference. It can be shown that the derivative of an arbitrary vector \mathbf{A} referred to a rotating body frame having an angular velocity $\boldsymbol{\omega}$ can be represented by the following vector identity:

$$\left. \frac{d\mathbf{A}}{dt} \right|_I = \left. \frac{d\mathbf{A}}{dt} \right|_B + \boldsymbol{\omega} \otimes \mathbf{A}
 \tag{19}$$

where the subscripts I and B refer to the inertial and body fixed frames of reference. Applying this identity to the equations derived earlier yields

$$\mathbf{F} = m \left. \frac{d\mathbf{v}_c}{dt} \right|_B + m(\boldsymbol{\omega} \otimes \mathbf{v}), \quad \mathbf{M} = \left. \frac{d\mathbf{H}}{dt} \right|_B + \boldsymbol{\omega} \otimes \mathbf{H}
 \tag{20}$$

The scalar equations are

$$\begin{aligned} F_x &= m(\dot{u} + qw - rv) & F_y &= m(\dot{v} + ru - pw) & F_z &= m(\dot{w} + pv - qu) \\ L &= \dot{H}_x + qH_z - rH_y & M &= \dot{H}_y + rH_x - pH_z & N &= \dot{H}_z + pH_y - qH_x \end{aligned} \quad (21)$$

The components of the force and moment acting on the airplane are composed of aerodynamic, gravitational, and propulsive contributions. By proper positioning of the body axis system, one can make the products of inertia $I_{yz} = I_{xy} = 0$. To do this we are assuming that the xz plane is a plane of symmetry of the airplane. With this assumption, the moment equations can be written as

$$\begin{aligned} L &= I_x \dot{p} - I_{xz} \dot{r} + qr(I_z - I_y) - I_{xz}pq, & M &= I_y \dot{q} + rp(I_x - I_z) + I_{xz}(p^2 - r^2) \\ N &= -I_{xz} \dot{p} + I_z \dot{r} + pq(I_y - I_x) + I_{xz}qr \end{aligned} \quad (22)$$

The earliest successful airplanes were generally flown without the aid of aircraft instruments. The pilots of these early vehicles were preoccupied primarily with manoeuvring and controlling their sometimes temperamental aircraft. The control of an airplane's altitude is very important for safe operation. Pilots use an altimeter to maintain adequate vertical spacing between their aircrafts and other airplanes operating in the same area and to establish sufficient distance between their airplane and the ground. The measurement of angle of attack is important for cruise control and stall warning. Several devices can be used to measure the angle of attack of an airplane, two of which are the vane and pressure-sensor type indicator. The pivot vane sensor is a mass-balanced wind vane that is free to align itself with the oncoming flow. In this study, experimental characteristics obtained from Boeing type airplane during a flying are outlined in Table 1.

3 Neural Networks

3.1 Back Propagation Neural Network (BPNN)

BPNN is the most prevalent of the supervised learning models of ANN. BPNN uses the gradient steepest descent method to correct the weight of the interconnective neuron. BPNN easily solves the interaction of processing elements by adding hidden layers. Network structure consists of an input layer with four linear neurons, a hidden layer with ten nonlinear neurons and an output layer with two linear neurons. Sigmoid activation function is used in the nonlinear neurons. In the learning process of BPNN, the interconnection weights are adjusted using an error convergence technique to obtain a desired output for a given input. In general, the error at the output layer in the BPNN model propagates backward to the input layer through the hidden layer in the network to obtain the final desired output. The gradient descent method is utilized to calculate the weight of the network and

Table 1 Flying characteristics of a boeing type airplane

Time to destination (t _{TTD} [min])	Outside temperature (T _{OT} [°C])	Altitude (H [m])	Distance to destination (X [km])	Ground speed (V _{GS} [km/h])	Head wind (V _{HW} [km/h])
57.00	-55.00	9,753	484.00	678	127.0
54.00	-55.00	9,753	448.00	678	128.0
52.00	-55.00	9,753	418.00	633	150.0
49.00	-55.00	9,753	400.00	633	150.0
47.00	-55.00	9,753	370.00	633	148.0
45.00	-55.00	9,783	351.00	640	148.0
42.00	-55.00	9,753	324.00	638	144.0
41.00	-55.00	9,783	307.00	638	144.0
38.00	-55.00	9,753	277.00	640	138.0
36.00	-55.00	9,753	261.00	646	137.0
32.00	-55.00	9,753	231.00	653	131.0
31.00	-55.00	9,753	214.00	655	128.0
27.00	-55.00	9,753	185.00	655	125.0
25.00	-58.00	9,753	168.00	683	116.0
22.00	-51.00	9,144	138.00	675	109.0
20.00	-44.00	8,220	116.00	650	101.0
18.00	-37.00	7,315	98.00	646	90.00
16.00	-34.00	7,010	81.00	635	94.00
15.00	-27.00	6,096	64.00	592	85.00
13.00	-21.00	5,054	50.00	574	53.00
12.00	-15.00	4,347	35.00	520	38.00
10.00	-10.00	3,780	20.00	540	38.00

adjusts the weight of interconnections to minimize the output error. The error function at the output neuron is defined as

$$E = \frac{1}{2} \sum_k (T_k - A_k)^2 \quad (23)$$

in which T_k and A_k represent the actual and predicted values of output neuron, respectively, and k is the output neuron. The gradient descent algorithm adapts the weights according to the gradient error, which is given by

$$\Delta W_{ij} = -\eta \times (\partial E / \partial W_{ij}) \quad (24)$$

where η is the learning rate and the general form of the $\partial E/\partial W_{ij}$ term is expressed by the following form:

$$\partial E/\partial W_{ij} = -\delta_j^n \cdot A_i^{n-1} \quad (25)$$

Finally, the value of weight of the interconnective neuron can be expressed as follows:

$$W_{ij}^m = W_{ij}^{m-1} + \Delta W_{ij}^m = W_{ij}^{m-1} + \eta \cdot \delta_j^n \cdot A_i^{n-1} \quad (26)$$

To accelerate the convergence of the error in the learning procedure, Momentum term has been proposed with the momentum gain, α , in (26).

$$W_{ij}^m = W_{ij}^{m-1} + \eta \cdot \delta_j^n \cdot A_i^{n-1} + \alpha \cdot \Delta W_{ij}^{m-1} \quad (27)$$

in which the value for α is between 0 and 1.

3.2 Radial Basis Neural Network (RBNN)

Radial Basis Neural Network (RBNN) is feedforward and has only one hidden layer. RBNN structure is good at modelling nonlinear data and can be trained in one stage rather than using an iterative process as in multi layer perception neural network and also learn the given application quickly. They are useful in solving problems where the input data are corrupted with additive noise. The transformation functions used are based on a Gaussian distribution. If the error of the network is minimized appropriately, it will produce outputs that sum to unity, which will represent a probability for the outputs. RBNN structure has an input layer, a hidden layer of radial units and an output layer of linear units as given in Fig. 2. The RBNN model is mathematically represented as follows:

$$f(x) = \sum_{i=1}^n w_i \phi(\|x - x_i\|) + \sum_{j=1}^m c_j p_j(x) \quad (28)$$

where n is the number of sampling points, x is the vector of input variables, x_i is the center of basis function ϕ , w_i is the unknown weighting coefficient, m is the total number of terms in the polynomial and c_j is the corresponding coefficient. Therefore, an RBNN is actually a linear combination of n basis functions with weighted coefficients. In this study is used Gaussian basis function as follows:

$$\varphi(t) = e^{-ct^2}, \quad 0 < c \leq 1 \quad (29)$$

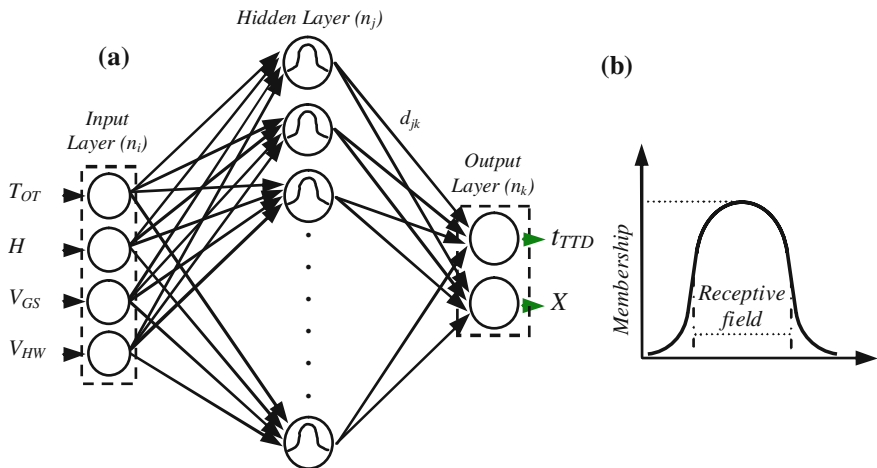


Fig. 2 Structure of RBF neural network (a), non-linear Gaussian transfer function (b)

4 Experimental and Simulation Approaches

In order to realize airplane destination time and distance, an experimental data set of the Boeing type airplane is employed. Training and testing stages of the network structures are performed on programming language. After the training of network is performed, the weights are saved and used to specify the network accuracy in predicting the destination time and distance. Time to destination and distance to destination for experimental and two type neural models are given in Tables 2 and 3, respectively.

Table 2 Destination times for experimental and neural model simulations

Time to destination (t_{TTD} [min])					
Experimental	BPNN	RBNN	Experimental	BPNN	RBNN
57.00	57.17	57.00	31.00	30.62	31.00
54.00	53.80	54.00	27.00	27.28	27.00
52.00	50.52	51.99	25.00	25.22	25.00
49.00	50.52	49.00	22.00	21.88	22.00
47.00	47.10	47.00	20.00	19.91	20.00
45.00	44.94	45.00	18.00	17.92	18.00
42.00	42.08	42.00	16.00	16.14	16.00
41.00	40.77	41.00	15.00	14.90	15.00
38.00	37.44	38.00	13.00	13.09	13.00
36.00	36.30	36.00	12.00	11.87	12.00
32.00	32.49	32.00	10.00	10.00	9.99

Table 3 Destination distances for experimental and neural model simulations

Distance to destination (X [km])					
Experimental	BPNN	RBNN	Experimental	BPNN	RBNN
484.00	482.96	484.00	214.00	212.93	214.00
448.00	449.24	448.00	185.00	183.19	185.00
418.00	408.12	417.99	168.00	165.89	168.00
400.00	408.12	400.00	138.00	138.84	138.00
370.00	372.21	370.00	116.00	116.99	116.00
351.00	351.43	351.00	98.00	98.80	98.00
324.00	321.27	324.00	81.00	79.64	81.00
307.00	308.69	307.00	64.00	64.95	64.00
277.00	275.94	277.00	50.00	48.27	50.00
261.00	265.33	261.00	35.00	37.04	35.00
231.00	229.79	231.00	20.00	19.91	20.00

As shown in tables, BPNN structure exhibits a certain deviation from the experimental result for each time. Contrary to BPNN, RBNN structure has good convergence ability. There is an exact matching to all experimental results except for three data in tables. Both the destination time and the destination distance are considered together, RBNN structure is evaluated as a predictor for the current study.

5 Conclusion and Discussion

In this paper, the flying conditions of an airplane are examined by using two types of neural networks. The properties of airplane are analysed and how those properties vary with altitude. For the comparison of flight test data and calibrating aircraft instrument, two types of neural network structures are used as predictors. The basic concepts behind several basic flight instruments are discussed. These are played an important role in flight test measurements of airplane performance, stability and control. The improvements offered by this new neural network analysis technology can be used to reduce the workload of the flight crew and improve the flight safety for the next generation of airplane design.

References

1. Singh SN, Yim W, Wells WR (1995) Direct adaptive and neural control of wing-rock motion of slender delta wings. *J Guid Control Dyn* 18(1):25–30
2. Napolitano MR, Kincheloe M (1995) On-Line learning neural-network controllers for autopilot systems. *J Guid Control Dyn* 33(6):1008–1015

3. Balakrishnan SN, Biega V (1996) Adaptive-critic-based neural networks for aircraft optimal control. *J Guid Control Dyn* 19(4):893–898
4. Khalil HK (1996) Adaptive output feedback control of nonlinear systems represented by input–output feedback. *IEEE Trans Autom Control* 41(2):177–188
5. Lee T, Kim Y (2001) Nonlinear adaptive flight control using backstepping and neural networks controller. *J Guid Control Dyn* 24(4):675–682
6. Calise AJ (1996) Neural networks in nonlinear aircraft flight control. *IEEE Aerosp Electron Syst Mag* 11(7):5–10
7. Calise AJ, Hovakimyan N, Idan M (2001) Adaptive output feedback control of nonlinear systems using neural networks. *Automatica* 37(8):1201–1211
8. McFarland MB, Calise AJ (2000) Adaptive nonlinear control of agile antiair missiles using neural networks. *IEEE Trans Control Syst Technol* 8(5):749–756
9. Hovakimyan N, Nardi F, Calise AJ (2002) Adaptive output feedback control of uncertain nonlinear systems using single-hidden-layer neural networks. *IEEE Trans Neural Netw* 13(6):1420–1431
10. Li Y, Sundararajan N, Saratchandran P (2001) Neuro-controller design for nonlinear fighter aircraft maneuver using fully tuned RBF networks. *Automatica* 37:1293–1301

Digital-Based Engineering Tools for Tailored Design of Medical Implants

R. Neto, T. Marques, M. Marta, N. Leal, M. Couto and M. Machado

Abstract With the advances in medicine and surgical treatments and the increase of computational tools and technical aids for supporting surgery, preoperative planning has become even more important and required. This technology relies upon digital tools and helps the clinicians to select the implant, to define its exact location and to establish a task outline for the surgery. Using these computational methods, it is also possible to design medical implants targeting a specific patient or clinical scenario. In this work, a three-step methodology for preoperative planning and design patient-specific implants is presented, namely (i) data acquisition and 3-D reconstruction, (ii) 3-D modelling and (iii) implant design. Two distinct case-studies are considered. The former consisted of a triple fracture of the distal femur, being the second case-study related to a maxillofacial deformity due to cancer removal surgery. For sake of pre-validation of the implant design, plastic prototypes were fabricated by using SL-stereolithography techniques. A tailored design of an implant leads to an enhancement on its biofunctionality, as this novel implant properly fits the extant medical need. Furthermore, the implant customization

R. Neto (✉) · T. Marques · N. Leal · M. Couto · M. Machado
INEGI—Instituto de Engenharia Mecânica e Gestão Industrial, Porto, Portugal
e-mail: rneto@inegi.up.pt

T. Marques
e-mail: tiagomr.marques@gmail.com

N. Leal
e-mail: nunoleal.pt@gmail.com

M. Couto
e-mail: mcouto@inegi.up.pt

M. Machado
e-mail: mmachado@inegi.up.pt

R. Neto · T. Marques · N. Leal · M. Couto · M. Machado
FEUP—Faculdade de Engenharia da Universidade do Porto, Porto, Portugal

M. Marta
Centro Hospitalar de São João, Porto, Portugal
e-mail: miguelmarta@yahoo.com

allows for its correct placement, promoting its fixation and longevity. In cases of osteosynthesis, a personalised design avoids the need of deforming the plates during surgery to fit patient's anatomy.

Keywords Preoperative planning · Image segmentation · 3-D reconstruction · Novel design · Computer modelling · Patient-specific implants · SL-stereolithography

1 Introduction

Preoperative planning offers many benefits for patient, surgeon and remaining members of the surgical team, avoiding delays and misunderstandings. The exercise of thinking throughout the sequential steps of the surgical intervention (i.e. preoperative planning) allows for predicting possible problems and to develop contingency plans for achieving a successful outcome [2]. With the development of imaging and computer technologies, the preoperative planning has become even more present in hospitals and clinical practices. Typically, an orthopaedic surgery of a trauma clinical case is preceded by a 3-D reconstruction of the patient's anatomy based on CT scans and a preoperative planning [3]. In some cases, additive manufacturing-based technologies (e.g. SL-stereolithography) complements the preoperative planning by combining virtual training with surgical training using physical models [1, 4, 5].

In a broad sense, an orthopaedic surgery involves the implantation of a medical device. These implants can present a standard geometry or a tailored design. Implant customization represents a suitable solution to achieve positive results in patient comfort and adequate strength distribution by designing the implant to fit a patient's anatomy. Also, the use of patient-specific implants increases the longevity of the implant leading to a deferment or suspension of the surgical revision intervention. The development of an implant with a tailored design is even more important in patients who require orthopaedic reconstruction as a consequence of bone loss (e.g. osteosarcoma [5]) or defect (e.g. trauma [4]). This demand motivates the present study. Thus, a general framework for preoperative planning and tailored design of medical implants is outlined based on digital methods. Two distinct case-studies are considered as demonstrative examples of application.

2 Methods

In this section, a three-step methodology for preoperative planning and tailored design of medical implants is presented, namely (i) data acquisition and 3-D reconstruction, (ii) 3-D modelling and (iii) implant design.

2.1 Data Acquisition and 3-D Reconstruction

Medical imaging techniques (e.g. MRI—Magnetic Resonance Imaging or CT—Computed tomography) are used to acquire patient’s personalized data, which is usually delivered on DICOM file format. Then, a digital software is used for 3-D virtual reconstruction of patient’s anatomy. For this task, MIMICS software (Materialise NV, Leuven, Belgium) is considered. The first step of 3-D virtual reconstruction comprises to import and correctly orient the DICOM image-set. A filter (e.g. discrete Gaussian filter) should be applied to reduce CT noise and artifacts. The next step is the image segmentation, which consists of combining the thresholding tool with the region growing option. Firstly, for the threshold, based on the image grayscale intensities, an interval of histogram level ranges is set to isolate the bone tissue. The region growing feature eliminates noise and separate structures that are not connected. The segmented masks can be edited (edit mask—draw, erase, local thresholding; multiple slice edit; 3-D edit mask; Boolean operations; etc.) in order to correct connections between different bones and isolate bone surfaces. After image segmentation, the 3-D anatomical model is calculated and a virtual reconstruction of the model is accomplished.

Figure 1 illustrates the final result of a segmentation process in MIMICS interface described above. As showed, the software provides three sectional views of the segmented masks (coronal, axial and sagittal) and also, the resultant 3-D model of patient’s anatomy (Fig. 1, lower right corner). At this point, the 3-D virtual model is able to be analysed by the surgeon, who decides if there is any area that need further studies. Then, the STL model is imported to the software of the SL-stereolithography equipment (Viper™ SLA® System, 3D Systems® Corporation, Rock Hill—SC) and an epoxy model of the patient’s anatomy is prototyped.

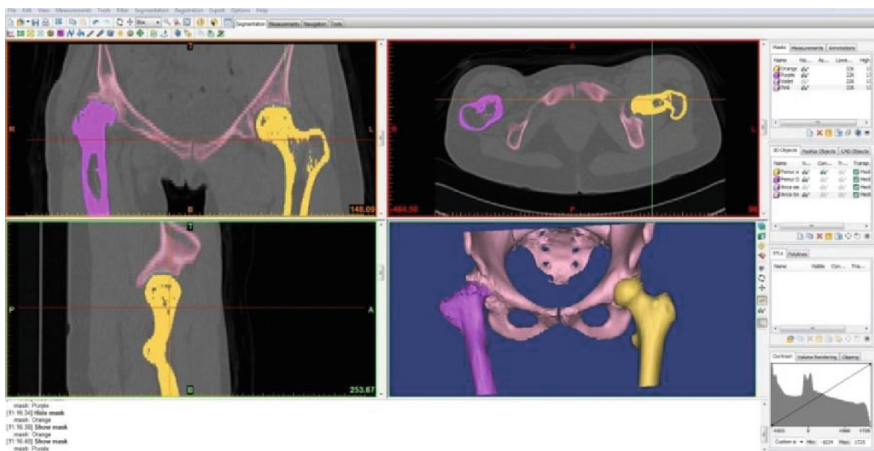


Fig. 1 MIMICS 16.0 interface: 3-D hip reconstruction

2.2 3-D Modelling

The 3-D modelling task entails two main steps, an evaluation of the 3-D virtual model and a 3-D manipulation and measuring. Within 3-matic 8.0 software (Materialise NV, Leuven, Belgium), Fix Wizard tool is used to examine and repair the 3-D virtual model in terms of inverted normals, bad edges (such as bad contours, near bad edges and planar holes), possible noise shells, and overlapping/intersecting triangles. Whenever a bone fracture exists, the anatomical position of the bones needed to be verified and realigned (Fig. 2). Afterwards, to determinate the exact dimensions and contours demanded for a proper fitting between the implant and patient's anatomy, a 3-D measuring is performed. In a broad sense, the 3-D modelling task has a fundamental role in the preoperative planning, since it provides an even more realistic view of the patient's anatomy and detailed data with relevance for the clinical guidelines of the planned surgery.

2.3 Implant Design

This task comprises the design project of the customized implant and it can be performed in a STL-editor (e.g. 3-matic). Prior to the implant design, the internal structure of the bony tissue, which will surround the implant, is analysed to identify the anatomical regions/points that are more appropriate for cuttings and placement of fixation systems. Furthermore, for sake of manufacturing or other purposes, some modelling adjustments of the implant design can be carried out.

For pre-validation purposes, implant 3-D models are prototyped by using SL-stereolithography techniques. After a careful examination, whenever geometrical imperfections are reported, one of the following actions has to be taken: (i) edit the geometry of the implant to eliminate the detected imperfections; (ii) restart the whole process of implant design. Thus, the implant design is an iterative process that stops with the validation of the implant geometry. The pre-operative planning is concluded when the implant is correctly positioned at the patient bone.

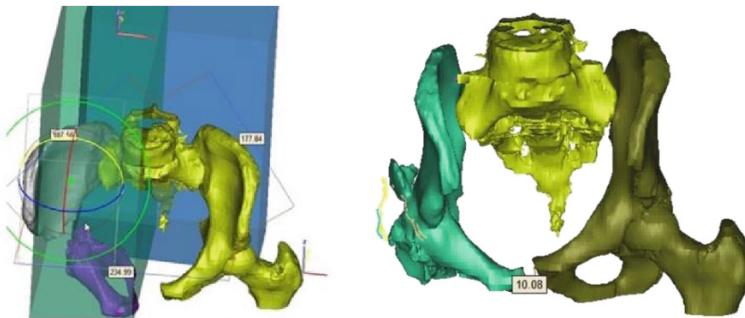


Fig. 2 3-D manipulation for the alignment of sacroiliac joint

At this point, the orthopaedic surgeon has a digital model of a patient-specific implant, which can be produced by additive manufacturing-based technologies, as well as a preoperative plan with relevant data for the clinical intervention (such as anatomical distances and the positioning of the implant and the fixation systems).

3 Demonstrative Examples of Application

3.1 Case-Study 1: Femur Fracture

This case-study consisted of a 46 years old female with a triple fracture of the distal femur, resultant of a trauma accident. CT scans (Brilliance CT 16-slice, Philips Healthcare, Best, Netherlands) are acquired providing specific data of patient's anatomy and trauma defects. The DICOM image-set comprises a total of 75 slices with 1.9 mm increment and pixel size of 0.487 mm. Using MIMICS 16.0 the DICOM image segmentation is conducted and a 3-D virtual model of patient's anatomy is accomplished. This provides a visualization of the fractures, i.e. a detailed analysis of the shape and positioning of bone fragments (Fig. 3a).

In the next step, using 3-matic 8.0 software, several operations of 3-D manipulation (such as rotate, move, etc.) were carried out in order to correct the position of the bones, to reduce the fractures and to ensure a correct placement and alignment of bones and its multiple fragments. Figure 3b shows the result of this process.

In order to stabilize the fractures and to keep the bone fragments aligned and in a correct position, a tailored system of implants was developed, namely a surgical plate and a set of screws. The designed plate is based on the Locking Compression Plate (LCP) commercialized by SYNTHES[®] (Synthes GmbH, Oberdorf, Switzerland) (Fig. 4a). This plate has a combination of locking and compression holes (Combi holes). These holes allow the surgeon to choose between conventional plating techniques, locked plating techniques, or a combination of both. Afterwards,

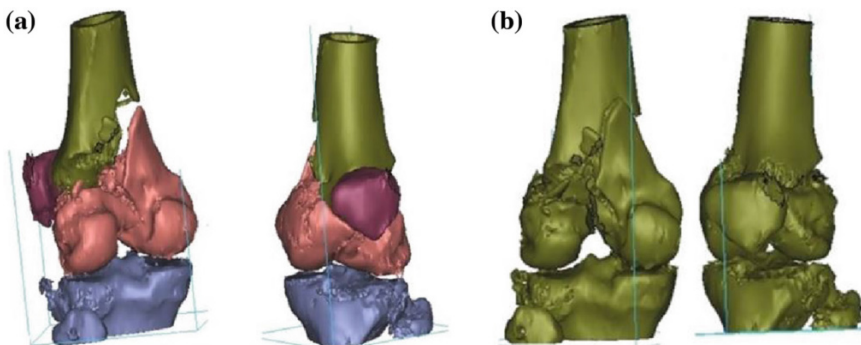


Fig. 3 a 3-D model after image segmentation; b 3-D model after 3-D manipulation in 3-matic 8.0 (fracture reduction and correct placement/alignment of bone segments)

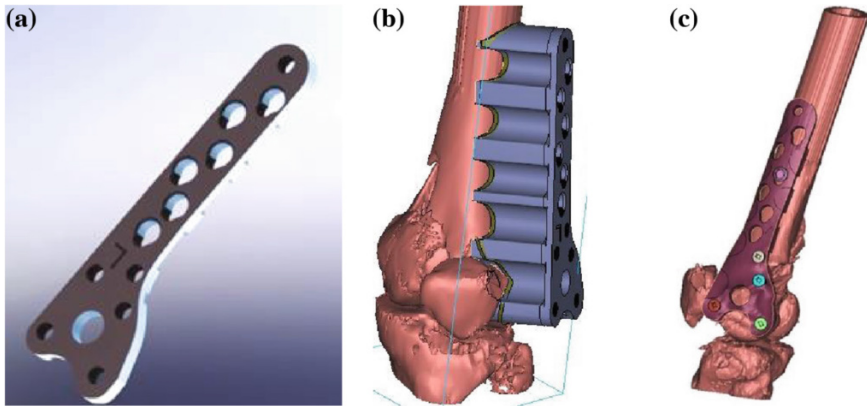


Fig. 4 **a** SYNTHES[®] locking compression plate. Implant design in 3-matic; **b** implant projection onto patient's anatomy; **c** tailored implant system—plate and locking screws

the CAD model of the surgical plate was projected onto patient's anatomy (Fig. 4b) to ensure an appropriate adjustment of the implant to patient. Within this process, some modelling operations were executed, such as surface fitting, trimming and smoothing. Following, the screws are introduced in order to lock the surgical plate in an anatomical position that will guarantee a correct alignment of the bones fragments and a stabilization of the fractures (Fig. 4c).

Due to the complexity of this case-study (with multiple fractures in the same bone), a pre-validation of the designed implant system is required. Therefore an epoxy model is fabricated by means of SL-stereolithography as Fig. 5 illustrates.

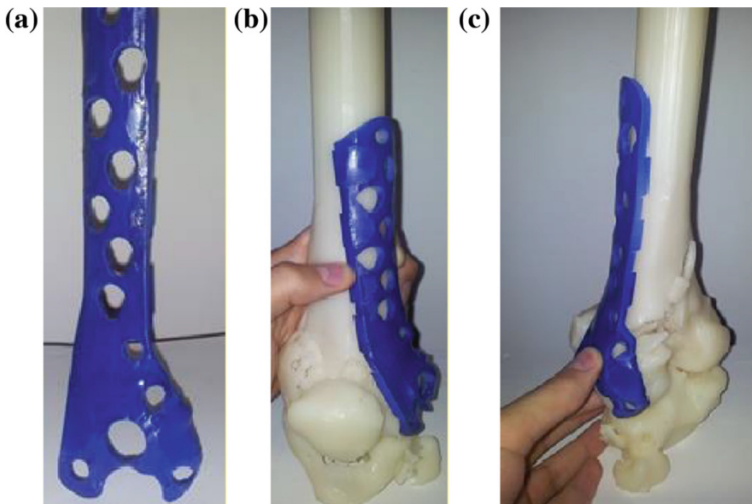


Fig. 5 Prototyped models for pre-validation: **a** plate; **b** anterior view; **c** posterior view

3.2 Case-Study 2: Maxillofacial Deformity

The case-study 2 reports a 68 years old female subject with a maxillofacial deformation resulting from cancer removal. CT scans (Toshiba Aquilion, Toshiba Medical Systems, Japan) are acquired to obtain fundamental information about the deformation and surrounding anatomical structures. The DICOM image-set comprises a total of 215 slices with 1 mm slice thickness and pixel size of 0.351 mm. Similarly to case-study 1, using this CT data, image segmentation process is conducted and a 3-D virtual reconstruction of the patient’s cranium is built. By analysing the model, an absence of part of the zygomatic and superior maxilla bone is observed (Fig. 6a). The 3-D manipulation step is skipped as there are no bone fragments to be repositioned. For sake of comprehension of the patient’s anatomy and malformation, the model is prototyped using SL-stereolithography (Fig. 7a).

Aiming to correct the internal and external appearance/function of the facial bony structure, a customized implant is developed. Within 3-matic 8.0, the reconstruction is performed by means of mirror modelling tools, in which the bone surface profile without defect is mimicked, using the middle sagittal plane as symmetry reference, to fill the missing bone area. An alignment is carried out in order to adapt the position of the mirrored section in the defected area. Finally, due

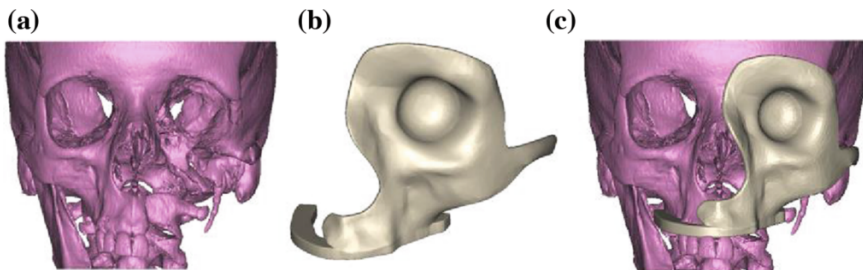


Fig. 6 3-D virtual models: **a** cranium; **b** prosthesis; **c** cranium and prosthesis

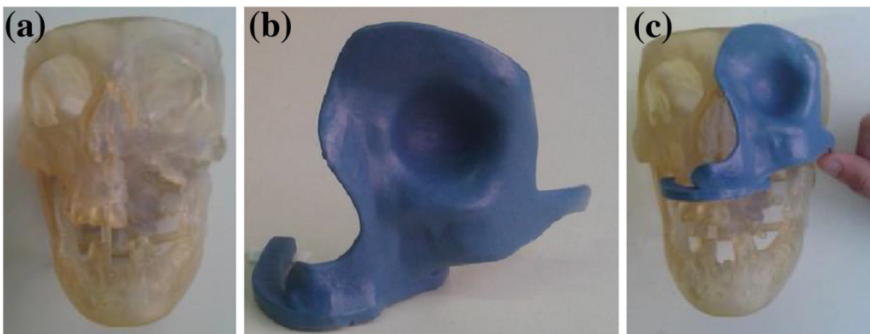


Fig. 7 3-D model plastic models: **a** cranium; **b** prosthesis; **c** cranium and prosthesis

to the importance of the maxilla in the chewing process, a bracket is added to the prosthesis design for supporting a future dental reconstruction (Figs. 6b and 7b).

Taking into account the bone density distribution in the surroundings of the defected area, as well as the prosthesis structural stability, the anatomical points more favourable to support the implant fixation are determined. SL-stereolithography is used for pre-validation of the implant design (Fig. 7).

4 Conclusions

The use of patient-specific implants promotes a correct placement and fixation of the implant and ensure its longevity. Combining digital methods with preoperative planning, a framework for tailored design of medical implants is presented. This approach entails three main tasks: (i) data acquisition and 3-D reconstruction; (ii) 3-D modelling; (iii) implant design. In a broad sense, the proposed methodology offers a set of advantages for orthopaedic surgeons, such as (i) the 3-D visualization of the injured area; (ii) the 3-D measuring and manipulation of bone fragments; (iii) the possibility of testing distinct treatments, i.e. different system of implants and surgical cuts; (iv) the 3-D visualization of the final result.

Within this work, two case-studies are presented resulting in two customized implants. It is important to mention that the project of new implant designs requires a pre-analysis of the internal bony structure to assure the static stability and structural support of the orthopaedic device. In both cases, the developed prosthetic models were prototyped using SL-stereolithography in order to proceed with its fabrication by investment casting in a biocompatible titanium alloy.

As future work, a topology optimization based on finite element methodologies is pointed out. This analysis could be an added value for the presented approach as it may lead to more lightweight products without compromising the structural stability of the prosthesis. Also, investigations on methods for automatizing the design procedure of customized implants are suggested as upcoming developments.

The advantages of the sophisticated design techniques used within the process of implant customization are widely recognised. However, due to its higher time and cost production, the medical community is still regularly using implants with a standard design. Thus, the goal of this work is to reverse this trend by improving and optimizing the process of implant customization in order to ensure high precision, cost-effectiveness and longevity to the orthopaedic implants.

Acknowledgments Authors gratefully acknowledge funding of project Tooling EDGE (Proj.13856) and project SAECTN-PII&DT/1/2011 co-financed by Programa Operacional Regional do Norte (ON.2—O Novo Norte), under Quadro de Referência Estratégico Nacional (QREN), through Fundo Europeu de Desenvolvimento Regional (FEDER).

References

1. Deshmukh TR et al (2012) A novel rapid prototyping and finite element method-based development of the patient-specific temporomandibular joint implant. *Comput Methods Biomech Biomed Eng* 15:363–370
2. Hak DJ et al (2010) Preoperative planning in orthopedic trauma: benefits and contemporary uses. *Orthopedics* 33(8):581–584
3. Lantada AD, Morgado PL (2012) Rapid prototyping for biomedical engineering: current capabilities and challenges. *Ann Rev Biomed Eng* 14:73–96
4. Suero EM et al (2010) Use of a virtual 3D software for planning of tibial plateau fracture reconstruction. *Injury* 41:589–591
5. Sun SP et al (2009) Full-scale 3D preoperative planning system for calcaneal osteotomy with a multimedia system. *J Foot Ankle Surg* 48:528–539

Synthesis of PR/RP-Chain Based Compliant Mechanisms: Design of Applications Exploiting Fibre Reinforced Material Characteristics

U. Hanke, E.-C. Lovasz, M. Zichner, N. Modler, A. Comsa and K.-H. Modler

Abstract Compliant mechanisms have several advantages, especially smaller number of elements and therefore less movable joints. The flexural members furthermore allow an integration of special functions like balancing or locking. To take advantage of compliant elements in applications a robust synthesis tool is needed. This demand fulfills a geometrical approach (Ehlig et al. in *Mechanisms, transmissions and applications*. Springer, Heidelberg, 2013, [1]) concentrating on solving guidance tasks by RR-chain (one link with two rotational joints (**R**)) based compliant linkages with maximum design freedom within the installation space. This step-by-step synthesis procedure is extended to PR (one link with one frame fixed prismatic joint (**P**) and one moving rotational joint (**R**))/RP (one link with one frame fixed rotational joint (**R**) and one moving prismatic joint (**P**))-chain based compliant linkages. The necessary analysis of the compliant beam element can be done by numerical analysis as well as through experiments and the elastic similitude. The synthesis method is presented and discussed by using an application for a cup holder mechanism made of fibre reinforced material and comparing this results to the result given in (Ehlig et al. in *Mechanisms, transmissions and applications*. Springer, Heidelberg, 2013, [1]).

Keywords Compliant mechanisms · Large deflections · Synthesis

1 Introduction

Classical linkage structures need additional elements (i.e. springs) for balancing or locking, which gives rise to the structure complexity. These features can be directly implemented by using compliant linkages. This function integration used in a

U. Hanke (✉) · M. Zichner · N. Modler · A. Comsa · K.-H. Modler
TU Dresden, Dresden, Germany
e-mail: uwe.hanke@tu-dresden.de

E.-C. Lovasz
Politehnica University Timișoara, Timișoara, Romania
e-mail: erwin.lovasz@upt.ro

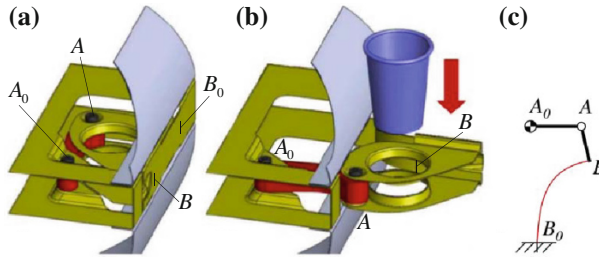


Fig. 1 Compliant cup holder mechanism [1]: **a** closed position, **b** open position, **c** kinematic scheme

compliant cup holder mechanism [1] lead to a simple two part assembly (RR-chain coupled to a beam element, see Fig. 1). The integrated compliant section allows the implementation of locking, so that additional springs are not required. The applied geometric based synthesis method, allows a direct use in the design process providing maximum design freedom regarding position and size of the mechanism.

This paper will extend the advances of this geometrical method to RP- and PR-chains and discuss differences to the RR-chain based linkages.

2 Synthesis

2.1 Synthesis Method

The compliant beam section B_0B of the mechanisms shown in Fig. 1c is integrated in the guidance link AB and acts like a spring element. For the synthesis model the large deflections of this beam section are introduced by a force/moment load, defined through the coupled joint pair. This can be a RR-, PR- or RP-joint pair. Its direct implementation into a graphical synthesis method is problematic. By using the elastic similitude of the beam a graphical implementation is possible. The result is a synthesis method with two serial coupled synthesis steps [1]:

- synthesis of the RR/PR/RP-chain and
- analysis and similarity transformation of the compliant beam element.

The synthesis of the RR/PR/RP-chain define the load configuration of the beam element. For the kinematic solution of the beam element two parameter can be used to define the load case. These parameter are direct coupled to the scaling and orientation of the beam element.

Table 1 Synthesis of the RP- and PR-chain

Step	PR-chain	RP-chain
1	Set moving joint A_1^{ab}	Set rotatory ground joint A_0^{bf}
2	Draw line a_1 defined by joint A_1^{ab} and pole P_{12}^{af}	Draw line f_1 defined by joint A_0^{bf} and pole P_{12}^{af}
3	Draw line f_1 defined by $P_{12}^{af}, \alpha_{12}^{af}$ and line a_1	Draw line a_1 defined by $P_{12}^{af}, \alpha_{12}^{af}$ and line f_1
4	Draw line b_1 defined by $A_1^{ab}, \alpha_{12}^{ab} = \alpha_{12}^{af}$ and line a_1	Draw line b_1 defined by $A_0^{bf}, \alpha_{12}^{bf} = \alpha_{12}^{af}$ and line f_1
5	The direction of translation of the prismatic pair ab is perpendicular to line b_1	The direction of translation of the prismatic pair bf is perpendicular to line b_1

2.2 Graphical 2-Pose Synthesis of PR- and RP-Chains

RR-, PR- and RP-chains are link systems with three links a, b, f . The further example will deal with f as frame link, a as guidance link and b as intermediate link. The graphical algorithm solving the two pose task is the construction of the relative pole triangle, for a given vertex of this triangle. In the case of a RR-chain three parameter can be arbitrarily chosen. The triangle of the PR- and RP-chain degenerate to a triangle with two parallel sides and one vertex at infinity. Therefore the synthesis of this special chains reduces to two parameters.

By introducing the rules referring to the Appendix the two pose synthesis of the PR- and RP-chain can be done by the synthesis steps listed in Table 1 referring Fig. 2.

The scheme in Fig. 2 is statically balanced in position 1, when the force action line of the between link a and f is equal to link line b_1 . This fact is of fundamental

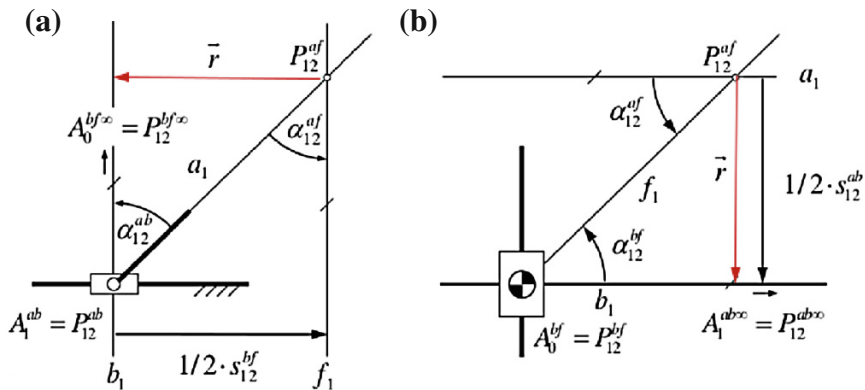


Fig. 2 Two pose synthesis of the: **a** PR-chain, **b** RP-chain

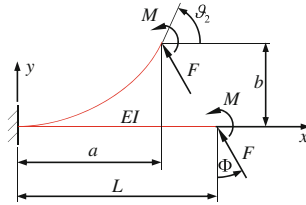


Fig. 3 Deflection of a cantilevered compliant beam under external load [1]

importance for the implementation of the compliant beam element. The shortest distance to b_1 measured from P_{12}^{af} is given by vector \vec{r} .

2.3 Similitude of the Compliant Beam Element

The deflection of the compliant beam depends on its material parameters (Young’s modulus E , cross section and resulting moment of inertia I), its length L and the load conditions. An initially undeflected beam loaded with a moment M_0 and a force F at the beam end is shown in Fig. 3. The force F is acting at an angle Φ .

The mathematical description of large-deflection behavior of cantilevered beams is subject to several scientific publications. The following statements and equations are based upon the considerations of Howell [2].

The Bernoulli-Euler equation is the vital element when dealing with large-deflection analysis. It says that the curvature κ can be written as

$$\kappa = \frac{d\vartheta}{ds} = \frac{d^2y/dx^2}{[1 + (dy/dx)^2]^{3/2}} = \frac{M}{EI}. \tag{1}$$

For a single moment end load ($F = 0$) the moment along the beam is constant and so is the curvature [2, 3]. For a single force end load ($M_0 = 0$) the internal moment can be written as $M = F \cos \Phi(a - x) + F \sin \Phi(b - y)$ and has to be substituted into Eq. (1). After performing a number of mathematical transformations and with $\kappa(s = L) = 0$ as well as $\vartheta(s = L) = \vartheta_2$ the equation results in

$$L = \sqrt{\frac{EI}{2F}} \int_{\vartheta_1=0}^{\vartheta_2} \frac{d\vartheta}{\sqrt{\cos \Phi(\sin \vartheta_2 - \sin \vartheta) - \sin \Phi(\cos \vartheta_2 - \cos \vartheta)}}. \tag{2}$$

A mixture of both moment and force load is equivalent to a single force load acting at a distance m (see Fig. 4) to the beam end. In this case the boundary condition for the curvature at the beam end is $\kappa(s = L) = mF/(EI)$. The solution of

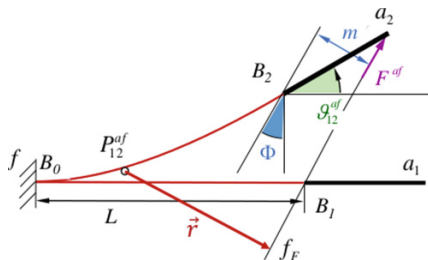


Fig. 4 Pole of a cantilevered compliant beam under external load

the differential Eq. (2) can be found in different ways [2, 4] and leads to the location B_2 for the angle ϑ_2 of the beam end for the compliant beam element.

The idea behind the synthesis is using the similitude theory [5, 6] to implement a precalculated beam element. The scaling affect the section modulus as well as the beam length. Using $I = L^4 I_L$ (I_L to the beam length normalised section modulus) in Eq. (2) the elastic similitude of the beam element is defined by the Hooke-number:

$$Ho = \frac{EL^2}{F}. \tag{3}$$

Scaling a model beam exemplarily with beam length L_M and a special load case to its double size L_S (same load case and model scale $M = L_S/L_M = 2$), the similiar bending behavior will occur by a constant Hooke-number $Ho_S/Ho_M = 1$. Using the same material $E_M = E_S$ similarity is given by a 4 times decreased force load ($F_M/F_S = 4$). Varying the section modulus independently, we have to use the modified Hooke-number

$$mHo = \frac{EI}{FL^2}. \tag{4}$$

The two positions of a undeflected and the deflected beam end define the pole of rotation P_{12}^{af} . This pole is coupled to the load conditions of the beam. This load conditions are defined by two parameters: the load direction Φ and the distance m , defining the moment introduced at the beam end. These parameter define the line f_F of action of the force F^{af} . The shortest distance between the pole P_{12}^{af} and f_F is given by the vector \vec{r} . This vector is used to find the dimensions of the compliant beam element by using a similarity transformation to scale and orient the beam according to the derived PR/RP-chain. The elastic similitude makes no difference if the deflections are calculated or found by experiment. In this case the use of a compliant tool kit [7] is a fast and easy way to get to reliable solutions. In this special case the implementation is done by use of the MATLAB programming environment. The geometric algorithms are based object oriented programming with three

Table 2 Task and solution parameter

	a_1	a_2	P^{af}_{12}	PR: A_1^{ab}	PR: A_2^{ab}	B_0	B_1	B_2
					RP: A_0^{bf}			
x	0.0	20.0	10.0	-30.0	50.0	-46.2	113.5	30.0
y	10.0	10.0	20.0	-20.0	-20.0	-0.0	-0.0	123.5
φ	0.0	90.0						

objects: points, lines and circles with their related methods and the beam is implemented by solving the elliptic integral (2).

3 Application

The described synthesis will be used to derive a cup holder mechanism as we can find in mobile vehicles [8]. This special application is feature implemented in luxury cars to fix a cup during driving. The location of this feature has to be in reaching distance to the driver. While not using this the cup holder shouldn't be visible hiding behind the board. The aim is the reduction of parts via integration of all locking functions within the compliance of the mechanism structure and discuss practical differences to the RR-chain based mechanism shown in [1].

The synthesis task is a two pose task referring to [1] (see Table 2). In the initial position a_1 the cupholder should be hiding behind the front board. The second position a_2 offers a panel with a circular hole to place the cup. When the holder is not in use the frontend should flush with the surface of the board. All joints should be located behind the board.

The derived PRB-linkage (Prismatic joint, Rotatory joint and compliant Beam element) given in Fig. 5a) is characterised by a small distance of the moving joint

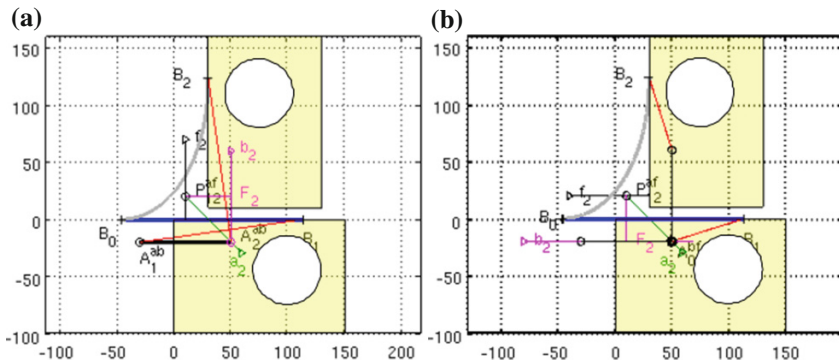


Fig. 5 Task solution for compliant: **a** PRB-linkage, **b** RPB-linkage

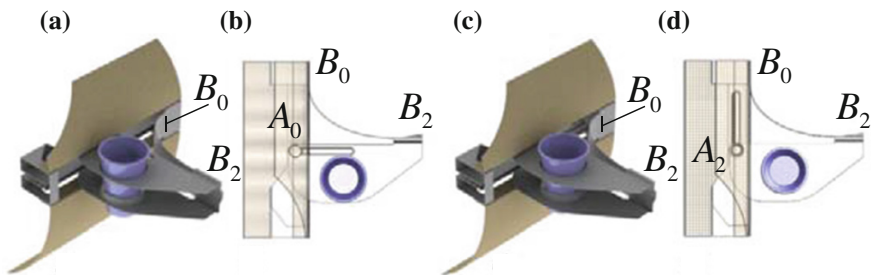


Fig. 6 Cup holder linkage: **a** PRB-linkage model, **b** PRB-linkage transparent top view, **c** RPB-linkage model, **d** RPB-linkage transparent top view

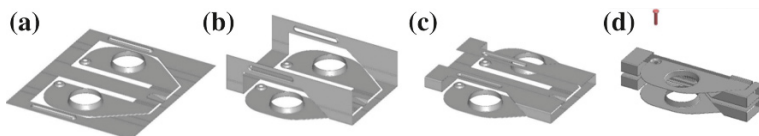


Fig. 7 Processing and assembly of a PRB-linkage: **a** preform, **b** 1 folding step, **c** second folding step, **d** bolt assembly

A^{ab} to the front end of the board. The beam element is relatively large, compared to the RR-chain solution given in [1]. Extending this distance will enlarge the beam and therefore lead to difficulties in the linkage design and its stability. Thermo-plastic fibre reinforced material (FRM) enable the adjustment their mechanical

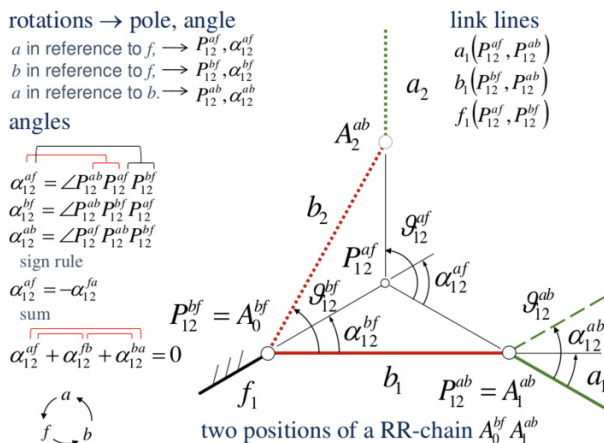


Fig. 8 Rules and nomenclature for the graphical synthesis demonstrated at a two pose RR-chain example

properties. Material with high strength, coupled with a low Young modulus E is extremely qualified for the use in compliant structures. A very compact design shown in Fig. 6 is possible.

The use of thermoplastic matrix material enables a easy post processing by thermobending. Using preprocessed FRM preforms (see Fig. 7a), the final processing in manufacturing this linkage is a three step folding processes (see Fig. 7b–d) with the final assembly of one bolt.

As seen in Figs. 5b and 6c, d the RPB-linkage is similar to the discussed PRB-linkage. Differences between these solutions are in design and kinematic behavior. Both linkages are less complex than the RR-chain based solution given in [1]. Instead of two bolts and one link arm, the PRB/RPB-linkage only use one bolt to complete the linkage.

4 Conclusions

Two parameters defining the PR/RP-chain and one the size of the beam element, give three free parameter that allow the geometrical synthesis for PR/RP-chain based mechanisms with a compliant beam element. Finally, it has been shown that the extension of the synthesis scheme given in [1] to PR/RP-chain based compliant linkages is possible. These structures are less complex and characterised by a simplified design.

Acknowledgments The authors would like to express their gratitude towards the Deutsche Forschungsgemeinschaft (DFG), which supports this research within the scope of the subproject D2 of the Collaborative Research Centre SFB 639 “Textile-Reinforced Composite Components in Function-Integrating Multi-Material Design for Complex Lightweight Applications”.

A.1 5 Appendix

Using graphical synthesis methods it is useful to name links with small letters and joints/poles as big letters. Motions are defined by link positions and the reference link from where this movement is measured. Handling definite positions we have to deal with link pairs and position pairs. Therefore all kinematic symbols are marked with indices P_{12}^{af} (af : link index $\rightarrow a$ moves in reference to b ; 12 pose index \rightarrow position 1 moves to position 2). This nomenclature leads to the rules given in Fig. 8.

References

1. Ehlig J, Hanke U, Lovasz E-C, Zichner M, Modler K-H (2013) Geometrical synthesis approach for compliant mechanisms—design of applications exploiting fibre reinforced material characteristics. *Mechanisms, Transmissions and Applications*, x-x, Springer, Dordrecht, Heidelberg, New York, London
2. Howell L (2001) *Compliant mechanisms*. Wiley-Interscience, New Jersey
3. Modler N et al (2013) Optimization of a test bench for testing compliant elements under shear-force-free bending load. *Procedia Mater Sci* 2:130–136
4. Venanzi S, Giesen P, Parenti-Castelli V (2005) A novel technique for position analysis of planar compliant mechanisms. *Mech Mach Theory* 40:1224–1239
5. Kerle H (2006) Zur Entwicklung von Baureihen für Getriebe und von belastbaren Getriebemodellen auf der Grundlage der Ähnlichkeitsmechanik. *Bewegungstechnik VDI-Getriebetagung 2006, VDI-Berichte 1966, VDI-Verlag, Düsseldorf*
6. Weber M (1930) Das Allgemeine Ähnlichkeitsprinzip der Physik und sein Zusammenhang mit der Dimensionslehre und der Modellwissenschaft. *Jahrbuch der Schiffbautechnischen Gesellschaft*, 31. Bd., Kap. XIV, S. 274–354, Springer, Berlin
7. Limaey P, Ramu G, Pamulapati S, Ananthasuresh GK (2012) A compliant mechanism kit with flexible beams and connectors along with analysis and optimal synthesis procedures. *Mech Mach Theory* 49:21–39
8. Barej M, Hüsing M, Corves B (2001) Teaching Mechanism theory—from hands-on analysis to virtual modeling. *Mech Mach Sci* 7:703–710 (Springer, Dordrecht, Heidelberg, New York, London)

Computer and Physical Simulation of Space Mirror Deployment

V.I. Bujakas

Abstract The new kinematic scheme for large petal-type space mirror package and deployment is considered. To check the approach the computer and physical models of multibody transformable structure were developed and studied. Results of simulation are presented in the paper.

Keywords Large space mirror · Kinematics of deployment · Computer and physical simulation

1 Introduction

Large solid deployable mirrors, intended for operation at mm, sub mm, IR and optical wavelengths are currently being developed within a number of programs and space projects [1–4, 7]. The classic design of petal type deployable reflector was proposed by Dornier Corporation during “FIRST” space project development (“FIRST”—far infrared space telescope) [5]. The similar design later was used for 10 m antenna of «Radioastron» space telescope and operates at cm wavelengths [6]. Within this design a petal type reflector is a transformable structure and contains a central mirror and a set of petals. In folded state the petals are disposed in vertical position above the central mirror. In open state the petals and the central mirror form large parabolic reflector. Stages of petal type mirror deployment are presented in Figs. 1, 2.

From kinematic point of view each petal is connected with central mirror by cylindrical hinge and rotates around the axis of the hinge during deployment. It has been shown that there exist such directions of axes of the hinges under which synchronous rotation of the petals leads to the disclosure of the mirror without

V.I. Bujakas (✉)

P. N. Lebedev Physical Institute of Russian Academy of Science, Moscow, Russia
e-mail: bujakas@yandex.ru

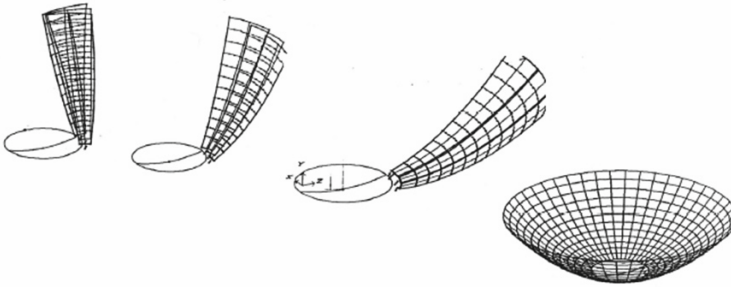


Fig. 1 The geometry of deployment

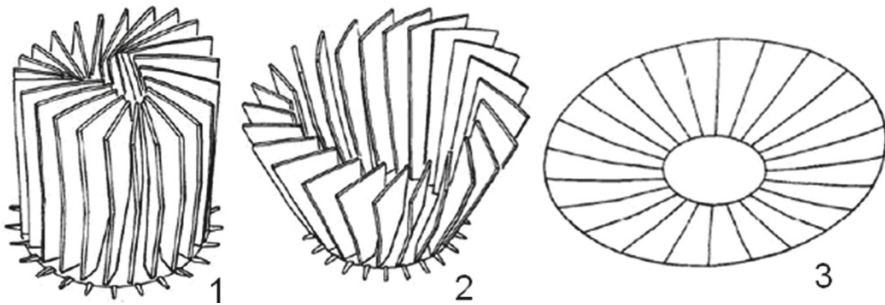


Fig. 2 Petal type mirror opening

cling. Synchronous rotation of the petals carried actuators, which are located on the back side of the central mirror.

However, there are drawbacks that limit the use of this kinematic scheme to create large deployable mirrors for short waves.

Main lacks of the design are as follows:

- after deployment the petals are not tied together by outer loop of the mirror, therefore the rigidity of open reflector is not very high (the geometric rigidity of closed shell did not used),
- errors in setting the position axes of cylindrical hinges and inaccuracies of petals opening distort the shape of the mirror surface, the value of which increases from the axis of rotation to the periphery of the mirror; however this part of mirror makes a decisive contribution to the effective area of the reflector and for short wave mirror must be made very precise. Therefore attempts were made, unfortunately unsuccessful, to tie the adjacent petals together via locks along outer loop of the mirror after deployment.

However ties fulfilled after deployment:

- produce uncontrolled disturbance of reflective surface and
- leads to a statically indeterminate, strained constructions of disclosed mirror, what is extremely undesirably for precision reflectors.

2 New Kinematics for Mirror Deployment

To overcome these shortcomings another version of petal type mirror deployment kinematics was proposed and developed [7]. We propose to retain the link between adjacent petals during all deployment process. To implement this approach, it is necessary first of all to abandon the cylindrical hinges connecting the petals with central mirror, replacing them with links that provide a greater degree of freedom of the petals. We considered a structure in which each petal is connected to a central mirror by two cylindrical hinges (Fig. 3).

Moreover the vertex of the petal is connected to the edge of the adjacent petal with connections that introduce to the structure two kinematic constraints (Fig. 5). Miniature linear actuators are used for deployment. During the opening the actuator moves the vertex of the petal along the outer edge of the adjacent petal (Figs. 4, 5).

The structure contains n petals and central mirror. Let
 N —total number of solid elements in the structure

$$N = n + 1,$$

S_1 —the number of kinematic constraints introduced by links between petals

$$S_1 = 2n,$$

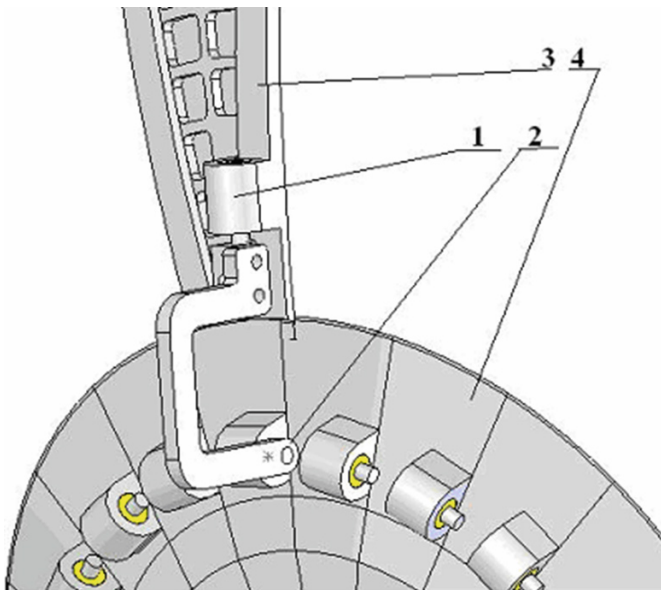


Fig. 3 Links between petal and central mirror. 1, 2 cylindrical hinges, 3 petal, 4 central mirror

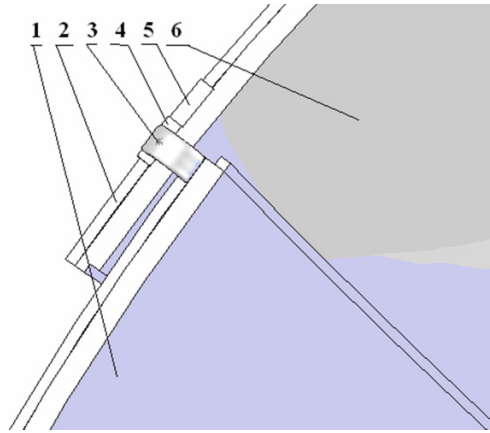


Fig. 4 Links between petals. 1, 6 petals, 2 guide, 3 rod, 4 slider, 5 linear actuator

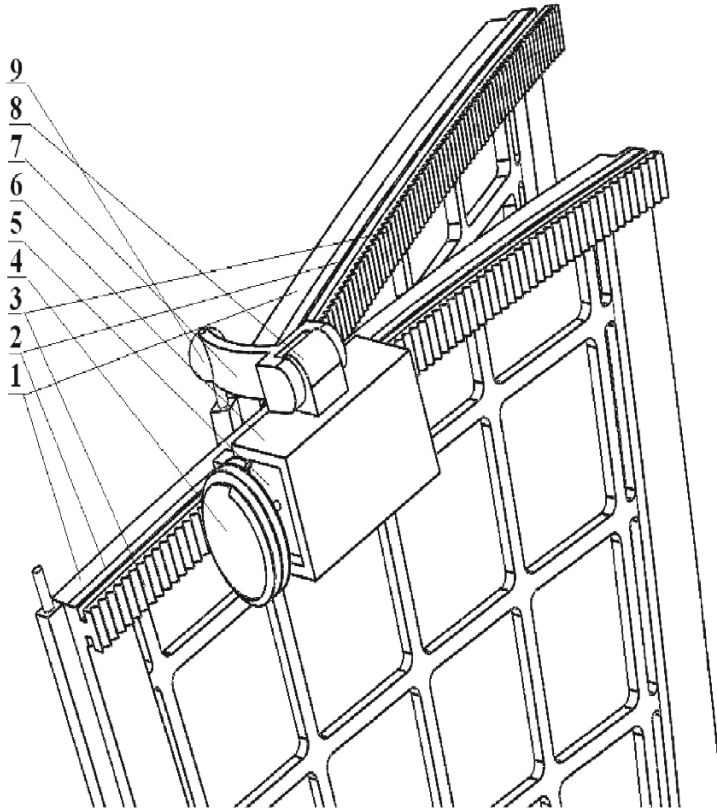


Fig. 5 Computer model of deployment mechanism. 1 petals, 2 guide, 3 worm rail, 4 screw, 5 motor, 6 holder of the motor (slider), 7 rod, 8 cylindrical hinge, 9 spherical hinge

S_2 —the number of kinematic constraints introduced by the links between the petals and central mirror

$$S_2 = 4n,$$

S —total number of kinematic constraints in the structure

$$S = S_1 + S_2 = 6n.$$

Thus Maxwell condition (necessary condition of statically determinacy)

$$S = 6N - 6$$

in the design is fulfilled. Direct calculations and computer model examination shows that the structure remains statically and kinematically determinate *indeed* in each moment of deployment, if positions of cylindrical hinges are correctly chosen. Therefore the structure remains stress free in each moment of deployment and is not requires precise synchronization for actuators operation during opening.

3 Computer Simulation

To check the approach the computer model within Solid Work package was made and studied. Some details of simulation are shown in Figs. 6, 7.

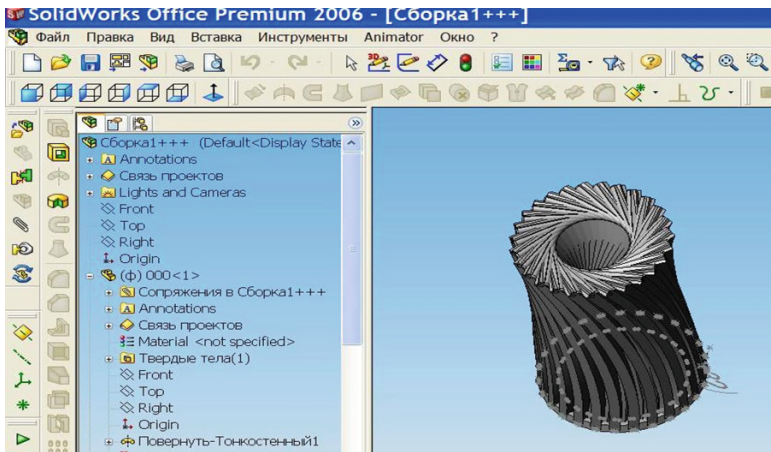


Fig. 6 Computer model of deployable reflector in closed state

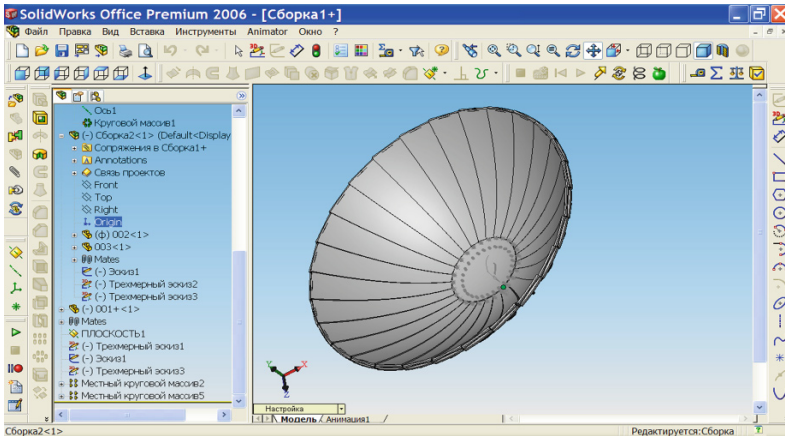


Fig. 7 Computer model of deployable reflector in open state

4 Physical Simulation

On the base of computer model the physical deployable model was fabricate. Main elements of physical model—petals and central mirror—were made by 3D printing technology. Some details of simulation are shown in Figs. 8, 9, 10, 11.

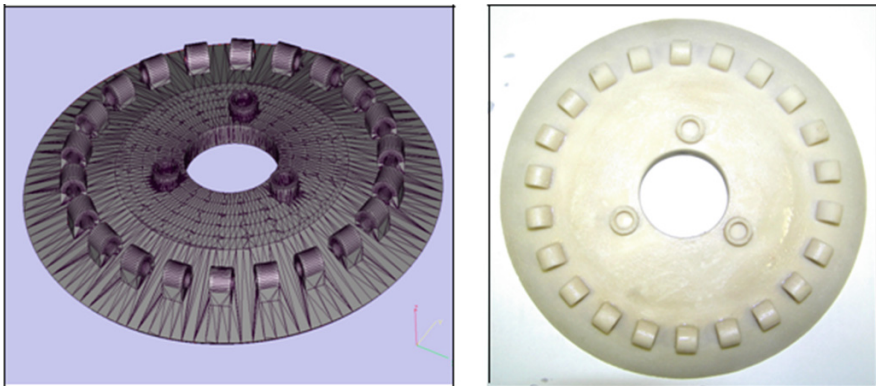


Fig. 8 Computer and physical models of central mirror

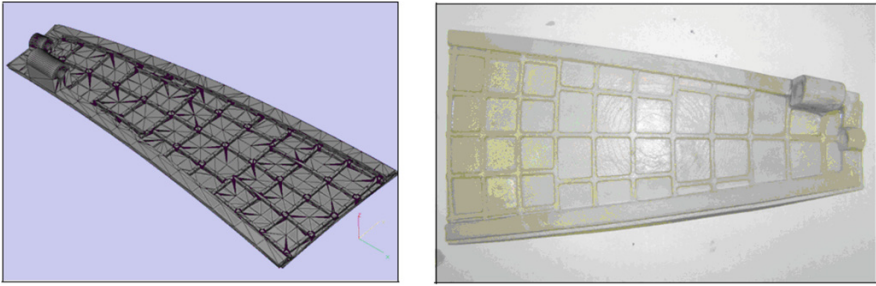


Fig. 9 Computer and physical models of petal

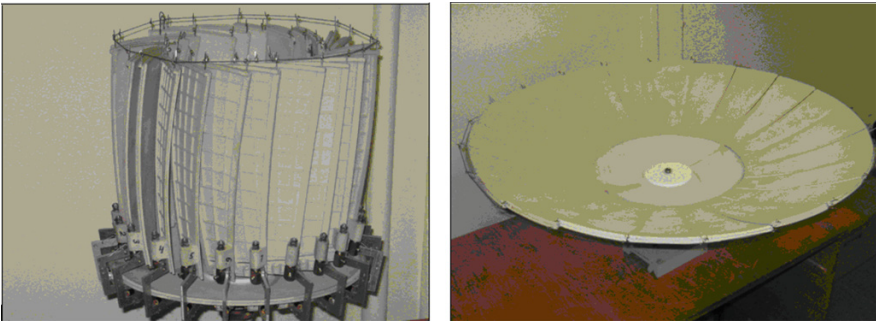


Fig. 10 Physical model of deployable reflector in closed and open state

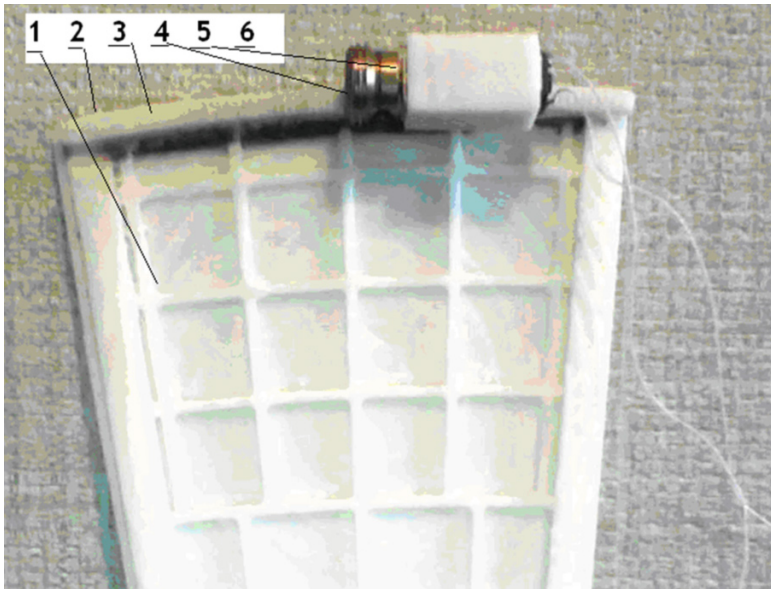


Fig. 11 Physical model of the deployment mechanism, made using 3D printing technology. 1 petal, 2 guide, 3 worm rail printed together with petal as a whole, 4 screw, 5 motor, 6 holder of the motor (slider)

5 Conclusions

To increase surface accuracy and rigidity of large deployable space mirror a new kinematic scheme for petal-type mirror package and deployment was proposed and developed. Computer and physical models of deployable reflector were made and studied. Simulation confirmed the feasibility of the proposed technical solution. Results may be useful for advanced space projects development.

References

1. <http://safir.jpl.nasa.gov/whatIs.shtml>
2. <http://www.asc.rssi.ru/millimetron>
3. <http://www.jwst.nasa.gov>
4. Arkhipov MY, Baryshev AM, Kardashev NS et al (2008) Deployable antennas for space radio telescope: radioastron and millimetron missions. In: Proceedings of the 30th ESA antenna workshop. Noordwijk, Netherlands
5. Bujakas VI (2013) Deployable antenna. Patent of Russian Federation No. 126199, 2013
6. Dornier, FIRST Technology study: Multisurface control mechanism for a de-ployable antenna. Final report. Dornier Report RP-FA-D003, 1987
7. Kardashev NS, Bujakas VI et al (2007) The millimetron project. In: Radioastronomical tools and techniques, Cambridge, UK

Permeability Evaluation of Flow Behaviors Within Perfusion Bioreactors

D. Freitas, H.A. Almeida and P.J. Bártolo

Abstract Tissue engineering aims to produce artificial tissue in order to create or repair damaged tissue. It is evident that scaffolds are of extreme importance, because they will be the support structure of the new tissue. This new tissue is cultivated *in vitro* in a bioreactor in which is placed the scaffold. In order to control the cell culture process inside of a bioreactor, it is essential to know the fluid flow inside the scaffold for an adequate exchange of nutrients and metabolic waste. A novel multifunctional bioreactor with a perfusion system module comprised of three different inlet and outlet membranes is being developed. This research work will evaluate the permeability of the scaffold under the three different inlet and outlet diffusion membranes of the culture chamber.

Keywords Bioreactor design · Flow behavior · Permeability · Scaffold · Numerical simulation

1 Introduction

Scaffold-based strategies represent the most promising approach of Tissue Engineering. Scaffold is the initial tridimensional biomechanical support for cell colonization, migration, growth and differentiation [1]. Tridimensional scaffolds used in

D. Freitas (✉) · H.A. Almeida · P.J. Bártolo
Centre for Rapid and Sustainable Product Development, Polytechnic Institute of Leiria,
Leiria, Portugal
e-mail: dino.freitas@ipleiria.pt

H.A. Almeida
e-mail: henrique.almeida@ipleiria.pt

P.J. Bártolo
Institute of Biotechnology, School of Mechanical, Civil and Aerospace Engineering,
University of Manchester, Manchester, UK
e-mail: paulojorge.dasilvabartolo@manchester.ac.uk

conjunction with living cells and biologically active molecules demonstrated promising results for tissue/organ repair and/or regeneration [2–4].

An ideal scaffold must satisfy some requirements, it should be biocompatible and biodegradable at a proper degradation rate matching the regeneration rate of the host tissue. It also should enable the diffusion of cell nutrients and oxygen and the establishment of a suitable mechanical and biological environment for the cells to secrete their own extracellular matrices in an organized way. Architecturally, the porosity, pore size and shape and pore interconnectivity are very important, playing an important role in promoting cellular migration, cellular bridging, vascularisation and new tissue ingrowth. Depending on the application, the optimal porosity and pore size diverge. Scaffolds must provide sufficient mechanical strength and stiffness to firstly maintain its structural stability during manipulation/implantation process, and later to provide structural support and allow transmission of regeneration enhancing forces to the host tissue site, withstanding the stresses in this environment. It may result in consequential reabsorption of native tissue, if there is not an appropriate stiffness and material strength at the site of implantation. A biomimetic scaffold should also be bioactive. It must be able to recruit cells from the surrounding native tissue, supplying a dynamic transmission of chemical, biological and mechanical signals [1–8].

Bioreactors are closed culture environment devices in which biological and or biomechanical processes develop under controlled conditions. The variables that are controlled include temperature, pH, gas concentration, media flow rate, shear stress, hydrodynamics and mechanical forces. These devices can be used for the expansion of cells for transplantation, to growth 3D tissues prior to implantation or as organ support devices [9].

Recent research has shown that the best fluid diffusion within the scaffolds is obtained through the use of perfusion bioreactors, in which the fluid media is forced through the scaffold pore network [10–14]. An additional, and critical, advantage of culture in a flow perfusion bioreactor is flow-induced mechanical stimulation of the cells within the scaffold, improving cell proliferation and differentiation [15]. In order to optimize the fluid flow behaviour within perfusion bioreactors, a novel system comprised of three different inlet and outlet membranes is being developed. This research work will evaluate the permeability of the scaffold under the three different inlet and outlet membranes of the bioreactor's culture chamber. Permeability is defined as the scaffold's capacity in allowing the flow of the culture media.

2 Perfusion Bioreactor Design

To perform the design optimization of the bioreactor, a cell culture chamber of the perfusion bioreactor with different configurations, with and without a scaffold in the center of the chamber, was modelled using a parametric CAD software (Solidworks from Dassault Systems). Perfusion bioreactors comprise dynamic pistons in order to

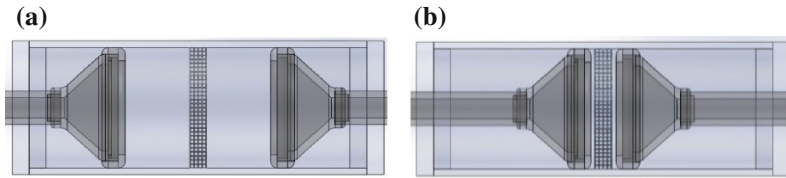


Fig. 1 Model of the perfusion bioreactor with the piston in the **a** open and **b** closed position

force the fluid flow within the chamber. Figure 1 illustrates the two positions of the pistons.

As mentioned before, this novel system contains three different inlet and outlet membrane configurations. Melchels et al. [16] determined the influence of the scaffold's geometry on the distribution of the cell seeding upon the scaffold. In order to have a homogenous cell distribution, a functionally graded geometric scaffold was modelled. In the case of regular geometric scaffolds, one needs to modify the fluid flow in order to obtain a homogenous cell distribution.

Figure 2 illustrates the fluid volumes used in the Computational Fluid Dynamic simulations (Ansys from Ansys, Inc.), comprising the three inlet and outlet membrane configurations. The three membrane configurations are encompassed of forcing the fluid flow in three specific directions, namely outwards from the center to the wall of the culture chamber (Fig. 2a), parallel to the chamber's axis (Fig. 2b), and inwards to the center of the chamber (Fig. 2c). The simulations were performed taking into account the fluid and velocity parameters as listed in Table 1. The meshed models were composed in average of 3,336,502 tetrahedron elements in the open position and 4,062,559 in the closed position, with an average element size of 0.820 mm (open) and 0.823 mm (closed).

After performing the numerical simulations, velocity plots on the scaffold's surface were obtained in order to define the correct fluid's velocity on the scaffold in order to determine the scaffold's permeability. Figure 3 illustrates the velocity plots based on the three membrane configurations and piston positions.

Fig. 2 Forced fluid flow **a** outwards to the wall of the chamber, **b** parallel to the chamber's axis, and **c** inwards to the center of the chamber

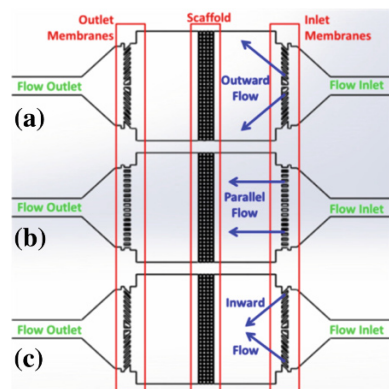


Table 1 Fluid characteristics of the culture media used in the CFD analysis

Parameter	Value
Density	1,030 kg/m ³
Dynamic viscosity	0.0025 Pa/s
Temperature	37 °C
Flow velocity (inlet and outlet)	0.2 m/s

In order to simplify the next set of numerical calculations, the scaffold was divided into 8 equal parts as illustrated in Fig. 4. The simulations were performed taking into account the fluid parameters as listed previously. The meshed model was composed of 38,866 tetrahedron elements with an average element size of 0.632 mm. The outlet was defined with zero pressure while three different regions of velocity were defined according to the previous results from the velocity plots.

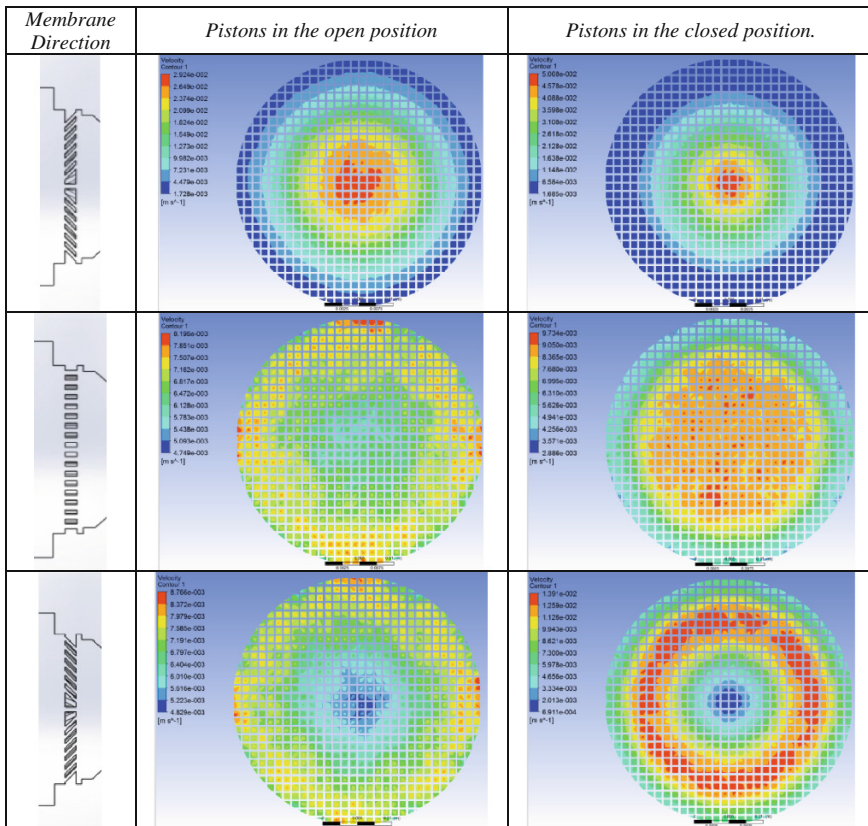


Fig. 3 Velocity plots of the three membrane configurations with the piston in the open and closed position

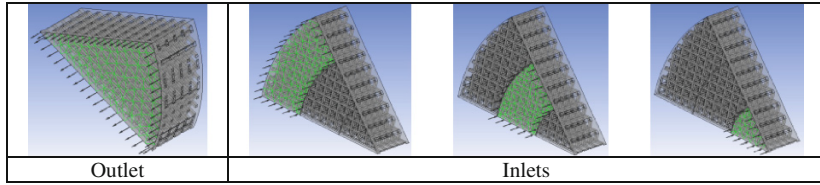


Fig. 4 Illustration of 1/8th of the scaffold and its inlet and outlet

3 Darcy’s Law

As the aim of this work is to study the permeability of porous scaffolds, a method based on Darcy’s Law seems to be an adequate approach. Darcy’s law is a phenomenologically derived constitutive equation that describes the flow of a fluid through a porous medium [17].

Darcy’s law is a simple proportional relationship between the instantaneous discharge rate through a porous medium, the viscosity of the fluid and the pressure drop over a given distance [17]:

$$Q = \frac{-kA (P_b - P_a)}{\mu L} \tag{1}$$

The total discharge, Q (units of volume per time, e.g., m^3/s) is equal to the product of the permeability of the medium, k (m^2), the cross-sectional area to flow, A (units of area, e.g., m^2), and the pressure drop ($P_b - P_a$), all divided by the viscosity, μ ($Pa \cdot s$) and the length over which the pressure drop is taking place (m). The negative sign is needed because fluid flows from high pressure to low pressure. If the change in pressure is negative (where $P_a > P_b$), then the flow will be in the positive ‘x’ direction. Dividing both sides of the equation by the area and using more general notation leads to the following equation [17]:

$$q = \frac{-k}{\mu} \nabla P \tag{2}$$

where q is the flux (discharge per unit area, with units of length per time, m/s) and ∇P is the pressure gradient vector (Pa/m). This value of flux, often referred to as the Darcy flux, is not the velocity which the water traveling through the pores is experiencing. The pore velocity (v) is related to the Darcy flux (q) by the porosity (n). The flux is divided by porosity to account for the fact that only a fraction of the total formation volume is available for flow. The pore velocity is the velocity a conservative tracer would experience if carried by the fluid through the formation [17]:

$$v = \frac{q}{n} \tag{3}$$

4 Scaffold Permeability

The second set of numerical simulations for the calculation of the scaffold’s permeability allowed obtaining both the total discharge Q (units of volume per time, e. g., m^3/s) and the pressure drop ($P_b - P_a$). Since the viscosity μ ($Pa \cdot s$) and the length over which the pressure drop is taking place (m), is already known, Eq. 2 was then applied in order to determine the scaffold’s permeability.

It is possible to observe the influence of the direction of the diffusion membrane within the culture chamber (Fig. 5). As the diffusion of the fluid is forced from the outer to the inner direction, the scaffold’s permeability tends to decrease. Figure 3 illustrates the velocity plots felt on the scaffold, based on the type of membrane configuration and the distance from the membrane. Some of the scaffolds present a more homogeneous inlet velocity distribution, while others present a more uneven distribution. This particular issue, not only influences the scaffold’s permeability, but influences the stimulation upon the cells regarding their proliferation and differentiation.

Figure 6 illustrates the influence of the proximity of the perfusion piston upon the scaffold. In the closed position, the fluid flow is forced and more concentrated in particular sections of the scaffold, increasing a more uneven inlet velocity distribution, decreasing the scaffold’s permeability. It is possible to conclude, as the inlet velocity upon the scaffold tends to a more homogenous distribution, the scaffold’s permeability tends to be higher.

Fig. 5 Influence of the membrane’s direction regarding the fluid flow

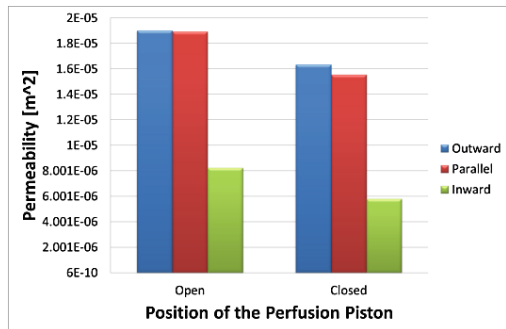
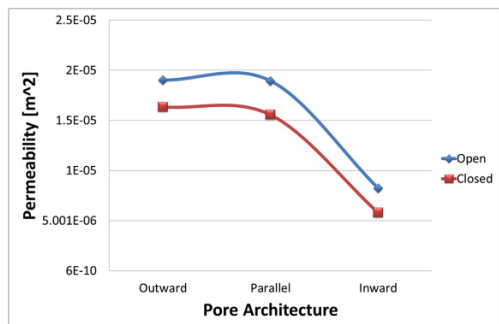


Fig. 6 Influence of the proximity of the perfusion piston



5 Conclusions

Tissue engineering aims to produce artificial tissue in order to create or repair damaged tissue. It is evident that scaffolds are of extreme importance, because they will be the support structure of the new tissue. This new tissue is cultivated *in vitro* in a bioreactor in which is placed the scaffold. In order to control the cell culture process inside of a bioreactor, it is essential to know the fluid flow inside the scaffold for an adequate exchange of nutrients and metabolic waste. A novel multifunctional bioreactor with a perfusion system module comprised of three different inlet and outlet membranes is being developed. This research work evaluates the permeability of the scaffold under the three different inlet and outlet membranes of the bioreactor chamber.

Results show that the scaffold's permeability is strongly influenced on the direction of the forced fluid flow, as well as the proximity of the perfusion piston. A more homogenous velocity distribution upon the scaffold, allows higher permeability. Therefore, it is possible to observe that current numerical tools play a critical role in the design and definition of the optimal design parameters for bioreactors.

Acknowledgments The authors acknowledge the support of the Strategic Project (PEST-OE/EME/UI4044/2013) funded by the Portuguese Foundation for Science and Technology. Authors also acknowledge the support of the European Commission through the Marie Curie Project "International Research Exchange for Biomedical Devices De-sign and Prototyping" "IREBID".

References

1. Bártolo P, Kruth J, Silva J, Levy G, Malshe A, Rajurkar K, Mitsuishi M, Ciurana J, Leu M (2012) Biomedical production of implants by additive electro-chemical and physical processes. *CIRP Ann Manuf Technol* 61:635–655
2. Liu Y, Lim J, Teoh S (2013) Review: development of clinically relevant scaffolds for vascularised bone tissue engineering. *Biotechnol Adv.* <http://dx.doi.org/10.1016/j.biotechadv.2012.10.003> (in press)
3. Almeida H, Bártolo P (2010) Virtual topological optimisation of scaffolds for rapid prototyping. *Med Eng Phys* 32:775–782
4. Reichert J, Cipitria A, Devakara E, Saifzadeh S, Krishnakanth P, Berner A, Woodruff M, Schell H, Mehta M, Schuetz M, Duda G, Hutmacher D (2012) A tissue engineering solution for segmental defect regeneration in load-bearing long bones. *Sci Transl Med* 4:1–10
5. Bao T, Franco R, Lee B (2012) Preparation and characterization of a novel 3D scaffold from poly(e-caprolactone)/biphasic calcium phosphate hybrid composite microspheres adhesion. *Biochem Eng J* 64:76–83
6. Reichert J, Wullschleger M, Cipitria A, Lienau J, Cheng T, Schütz M, Duda G, Nöth U, Eulert J, Hutmacher D (2011) Custom-made composite scaffolds for segmental defect repair in long bones. *Int Orthop (SICOT)* 35:1229–1236
7. Almeida H, Bártolo P (2013) Numerical simulation of polymeric extruded scaffolds under compression. *Procedia CIRP* 5:236–241

8. Porter J, Ruckh T, Popat K (2009) Bone tissue engineering: a review in bone biomimetics and drug delivery strategies. *Biotechnol Prog* 25(6):1539–1559
9. Martin I, Wendt D, Heberer M (2004) The role of bioreactors in tissue engineering. *Trends Biotechnol* 22(2):80–86
10. Cartmell SH, Porter BD, Garcia AJ, Guldborg RE (2003) Effects of medium perfusion rate on cell-seeded three-dimensional bone constructs in vitro. *Tissue Eng* 9:1197–1203
11. Freyria AM, Yang Y, Chajra H, Rousseau CF, Ronziere MC, Herbage D, El Haj AJ (2005) Optimization of dynamic culture conditions: effects on biosynthetic activities of chondrocytes grown in collagen sponges. *Tissue Eng* 11:674–684
12. Goldstein AS, Juarez TM, Helmke CD, Gustin MC, Mikos AG (2001) Effect of convection on osteoblastic cell growth and function in biodegradable polymer foam scaffolds. *Biomaterials* 22:1279–1288
13. Sikavitsas VI, Bancroft GN, Mikos AG (2002) Formation of threedimensional cell/polymer constructs for bone tissue engineering in a spinner flask and a rotating wall vessel bioreactor. *J Biomed Mater Res* 62:136–148
14. Wendt D, Stroebel S, Jakob M, John GT, Martin I (2006) Uniform tissues engineered by seeding and culturing cells in 3D scaffolds under perfusion at defined oxygen tensions. *Biorheology* 43:481–488
15. Jaasma MJ, Plunkett NA, O'Brien FJ (2008) Design and validation of a dynamic flow perfusion bioreactor for use with compliant tissue engineering scaffolds. *J Biotechnol* 133:490–496
16. Melchels FP, Tonnarelli B, Olivares AL, Martin I, Lacroix D, Feijen J, Wendt DJ, Grijpma DW (2011) The influence of the scaffold design on the distribution of adhering cells after perfusion cell seeding. *Biomaterials* 32(11):2878–2884
17. Dias MR, Fernandes PR, Guedes JM, Hollister SJ (2012) Permeability analysis of scaffolds for bone tissue engineering. *J Biomech* 45:938–944

Part XI
Mechanical Transmissions

Load Sharing and Contact Stress Calculation of High Contact Ratio Internal Spur Gears

M. Pleguezuelos, J.I. Pedrero and M.B. Sánchez

Abstract This paper presents a model of load sharing for high contact ratio internal spur gears, which takes into account the changing rigidity of the pair of teeth along the path of contact. It has been obtained from the minimum elastic potential energy criterion, resulting in a non-uniform load distribution among several tooth-pairs in simultaneous contact. This model has been used for the calculation of the determinant load conditions for pitting calculations, providing the theoretical values of the pitting nominal stresses. As no proposals of load sharing for this kind of internal spur gear transmissions can be found in literature, the proposed model can be used for strength calculations which may be suitable for standardization purposes.

Keywords Spur gears · Internal gears · Load distribution · Surface durability

1 Introduction

Load sharing among couples of teeth in simultaneous contact is not even due to the changing rigidity of the tooth pair along the path of contact [1–5].

In previous works [6], the authors developed a load distribution model for external teeth, from the minimum elastic potential criterion. The elastic potential of a pair of teeth was calculated and expressed as a function of the contact point and the normal load. The load sharing among several spur tooth-pairs in simultaneous contact was obtained by solving the variational problem of minimize the total potential (equal to the addition of the potential of each pair at its respective contact

M. Pleguezuelos (✉) · J.I. Pedrero · M.B. Sánchez
UNED, Madrid, Spain
e-mail: mpleguezuelos@ind.uned.es

J.I. Pedrero
e-mail: jpedrero@ind.uned.es

M.B. Sánchez
e-mail: msanchez@ind.uned.es

point) regarding the restriction of the total load to be equal to the sum of the load at each pair. From this model, the location of the points of critical stress and the determinant load conditions were obtained for bending and pitting calculations, providing accurate theoretical values of the nominal stresses [7, 8].

From the same hypotheses, models of load distribution have been also developed for non-standard tooth height gears [8], high transverse contact ratio (HTCR) external gears [10], and standard internal gears [11]. In all the cases, calculation methods for the nominal bending and contact stresses were developed [12–15].

In this work, a similar load distribution model is developed for high contact ratio spur gear transmissions with external tooth-pinion and internal tooth-wheel. This model and the Hertz equation have been used to determine the critical load conditions and the value of the critical contact stress. As the model of load distribution corresponds more accurately with the real operating conditions, results may be suitable for standardization purposes.

2 Load Distribution for Internal HTCR Spur Gears

The models presented in [6–15] are based on the assumption that the load distribution along the line of contact provides a minimum elastic potential, considering all the pairs of teeth in simultaneous contact. In this section the model for internal gears will be briefly presented.

The elastic potential energy of a spur tooth U is equal to the sum of the bending component U_x , the compressive component U_n and the shear component U_s :

$$U = U_x + U_n + U_s \quad (1)$$

All the components can be computed from the equations of the theory of elasticity and the geometry of the tooth. Of course U depends on the load point, which may be defined from its radius r_c , or its profile parameter ξ_c , defined as:

$$\xi_c = \frac{z}{2\pi} \sqrt{\frac{r_c^2}{r_b^2} - 1} \quad (2)$$

where z is the number of teeth and r_b the base radius. The potential of a pair of teeth in contact U_p will be the sum of the potential of the external pinion and the internal wheel. The last one can be also expressed as a function of the profile parameter ξ of the pinion since the difference of the curvature radii of both transverse profiles at their respective contact points is constant along the path of contact. The constant value of this difference is equal to the distance between the tangency points of the operating pressure line and both base circles of pinion and wheel, so that:

$$\zeta_w - \zeta = \lambda = \frac{z_2 - z_1}{2\pi} \tan \alpha'_t \tag{3}$$

where α'_t is the operating transverse pressure angle, λ the distance between both tangency points divided by the pinion base radius and the pinion angular pitch, and subscripts 1 and 2 denote the pinion and the wheel, respectively, except for the ζ parameter of the contact point in which w denotes the wheel and no subscript denotes the pinion. According to the linear theory of elasticity equations, all the components of the spur tooth-pair potential are proportional to the squared load F^2 and inversely proportional to the face width b ; consequently if we define the unitary potential of the tooth pair u_p as the potential for unitary load and face width, we have:

$$U_p(\zeta) = \frac{F^2}{b} u_p(\zeta) \tag{4}$$

The unitary potential of a pair of teeth can be computed from the geometry of pinion and wheel teeth, by numerical techniques of integration. If there are several (n) pairs of teeth in simultaneous contact, the total elastic potential U_T will be:

$$U_T = \sum_{i=1}^n U_{pi}(\zeta_i) = \frac{1}{b} \sum_{i=1}^n F_i^2 u_i(\zeta_i) = U_T(\zeta_1) \tag{5}$$

which can be expressed as a function of the ζ parameter of the first pair ζ_1 , because it can be checked that:

$$\zeta_{i+1} = \zeta_i + 1 \tag{6}$$

Summarizing, we have a variational problem which can be enunciated as follows: find the values of F_i which minimize the function:

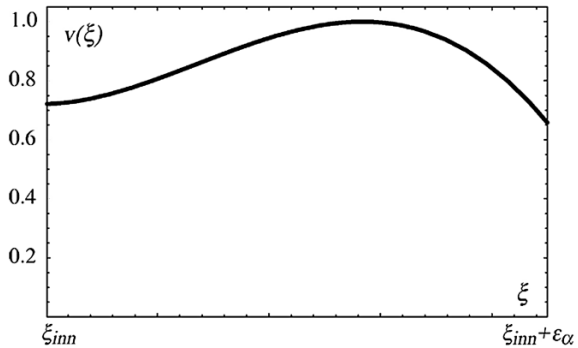
$$U_T = \frac{1}{b} \sum_{i=1}^n F_i^2 u_i(\zeta_i) \tag{7}$$

regarding the restriction:

$$\sum_{i=1}^n F_i = F = \frac{P}{\omega_1 r_{b1}} \tag{8}$$

where P is the transmitted power and ω_1 the pinion rotational velocity. The problem can be solved by means of the Lagrange's method, yielding the result:

Fig. 1 Inverse unitary potential $v(\xi)$



$$F_i(\xi_1) = \frac{\frac{1}{u_i}}{\sum_{j=1}^n \frac{1}{u_j}} F = \frac{v_i}{\sum_{j=1}^n v_j} F \tag{9}$$

in which $v(\xi) = u^{-1}(\xi)$ is the inverse unitary potential, which has been represented in Fig. 1 [values of the y-axis have been normalized to do $v_{\max} = 1$, since the absolute values of $v(\xi)$ have no influence on the load sharing, as seen in Eq. (9)]. According to this, the load sharing ratio $R(\xi)$ (or the fraction of the load supported by the considered pair of teeth) would be:

$$R_i(\xi_1) = \frac{F_i}{F} = \frac{v_i}{\sum_{j=1}^n v_j} \tag{10}$$

and the load per unit of length f , for spur internal gears, can be expressed as:

$$f(\xi) = \frac{F}{b} R(\xi) \tag{11}$$

The variation of the load sharing ratio along the path of contact for spur internal gears is represented in Fig. 2 (left), for transverse contact ratio ϵ_α between 1 and 2. Of course, $R(\xi) = 1$ along the interval of single pair tooth contact. Ordinates of singular points (0.35, 0.60, 0.65 and 0.40) are valid with, very small variations, for any pair of teeth [7], so these values can be used for calculations. Similarly, Fig. 2 (right) represents the load sharing ratio for high contact ratio spur internal gears, with ϵ_α between 2 and 3. A study similar to one presented in [11] but considering internal spur gears with contact ratio between 2 and 2.2 reveals that ordinates of singular points (0.25, 0.30, 0.40, 0.55, 0.40, 0.40, 0.60, 0.45, 0.35 and 0.30) keep also quite constant values. In this case variability is a little higher than that for ϵ_α smaller than 2, but always inside narrow intervals, around ± 0.03 .

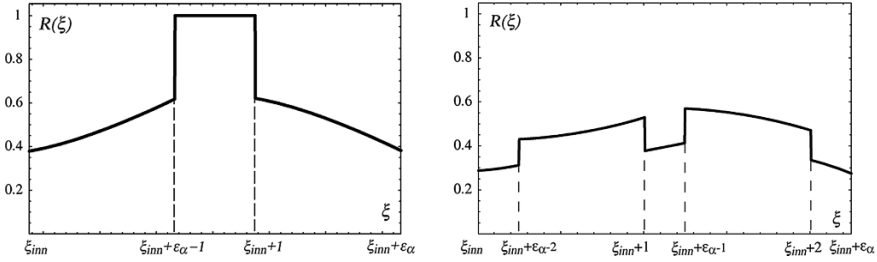


Fig. 2 Load sharing ratio $R(\xi)$: (left) standard contact ratio; (right) high contact ratio

3 Contact Stress Analysis

According to the gear calculation Standards [16, 17], the Hertz's equation can be used for the estimation of the contact stress at the surface of spur gears, as:

$$\sigma_H = Z_E \sqrt{\frac{f(\xi)}{\rho(\xi)}} \tag{12}$$

where Z_E is the elasticity factor (according to ISO 6336—2 [12]) and $\rho(\xi)$ the relative curvature radius of transverse profiles of pinion and wheel, at contact point ξ . Z_E depends on the modulus of elasticity E and the Poisson's ratio μ of the materials of each gear:

$$Z_E = \left[\pi \left(\frac{1 - \mu_1^2}{E_1} + \frac{1 - \mu_2^2}{E_2} \right) \right] \tag{13}$$

The relative curvature radius is:

$$\frac{1}{\rho(\xi)} = \frac{1}{\rho_{t1}(\xi)} - \frac{1}{\rho_{t2}(\xi)} \tag{14}$$

where the curvature radii of pinion and wheel transverse profiles are:

$$\begin{aligned} \rho_{t1}(\xi) &= \frac{\pi m \cos \alpha_t}{\cos \beta} \xi \\ \rho_{t2}(\xi) &= \frac{\pi m \cos \alpha_t}{\cos \beta} \xi_2 = \frac{\pi m \cos \alpha_t}{\cos \beta} (\lambda + \xi) \end{aligned} \tag{15}$$

m being the normal module, α_t the transverse pressure angle and β the helix angle. Replacing expressions of $\rho_{t1}(\xi)$ and $\rho_{t2}(\xi)$ in expression of $1/\rho(\xi)$, we have:

$$\frac{1}{\rho(\xi)} = \frac{\cos \beta}{\pi m \cos \alpha_t} \frac{\lambda}{\xi(\lambda + \xi)} \tag{16}$$

The problem is to find the absolute maximum of function $f(\zeta)/\rho(\zeta)$ inside the interval of contact $\zeta_{inn} \leq \zeta \leq \zeta_{inn} + \varepsilon_\alpha$.

According to the Hertz's equation, the contact stress for spur internal gear teeth can be expressed as:

$$\sigma_H = Z_E \sqrt{\frac{F}{b} R(\zeta) \frac{1}{\rho(\zeta)}} \tag{17}$$

The derivative of the function $1/\rho(\zeta)$ is negative for $\zeta > 0$, and consequently the function $1/\rho(\zeta)$ decreases with ζ along the complete interval of contact $[\zeta_{inn}, \zeta_{inn} + \varepsilon_\alpha]$. Then, according to Fig. 2 (right), the critical load conditions will necessarily be one of the following:

- (i) contact at the inner point of contact, with $\zeta = \zeta_{inn}$ and $R = 0.25$,
- (ii) contact at the inner point of two pair tooth contact, with $\zeta = \zeta_{inn} + \varepsilon_\alpha - 2$ and $R = 0.30$,
- (iii) contact at the outer point of the inner interval of two pair tooth contact, with $\zeta = \zeta_{inn} + 1$ and $R = 0.55$,
- (iv) contact at the inner point of the outer interval of two pair tooth contact, with $\zeta = \zeta_{inn} + \varepsilon_\alpha - 1$ and $R = 0.60$.

Accordingly, the critical contact stress can be computed from:

$$\sigma_H = Z_E \sqrt{\frac{F}{b} \max\left(\frac{0.25}{\rho(\zeta_{inn})}, \frac{0.30}{\rho(\zeta_{inn} + \varepsilon_\alpha - 2)}, \frac{0.55}{\rho(\zeta_{inn} + 1)}, \frac{0.60}{\rho(\zeta_{inn} + \varepsilon_\alpha - 1)}\right)} \tag{18}$$

In principle, any of the above mentioned load conditions could be the critical ones, however it is not usual to find them at conditions (iii) or (iv), because the relative curvature radius of the profiles decreases very quickly for typical values of the tooth number on pinion. Figure 3 represents the typical aspect of the evolution of the contact stress along the path of contact, for internal HTCR spur-gear transmissions, for both possibilities, (i) and (ii).

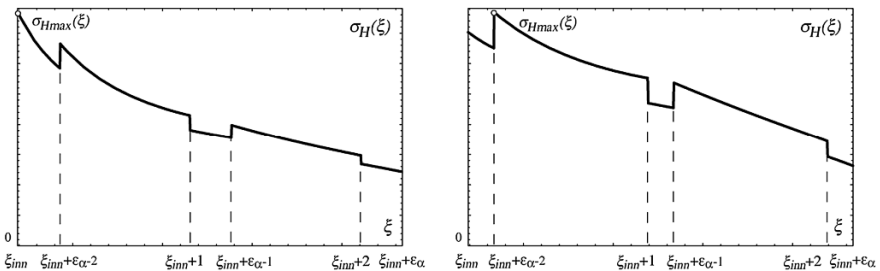


Fig. 3 Evolution of the contact stress: (left) condition (i); (right) condition (ii)

4 Conclusions

A model of load sharing among couples of teeth in simultaneous contact has been developed for high contact ratio internal spur gears. It has been obtained from the minimum elastic potential energy criterion, to account the changing rigidity of the couple of teeth along the path of contact, and has been applied to the calculation of the determinant load conditions and the critical contact stress.

The main conclusions can be summarized as follows: the critical load conditions will necessarily be located: (i) at the inner point of contact ($\xi = \xi_{inn}$), with the tooth loaded with the 25 % of the load ($R = 0.25$); or (ii) at the inner point of two pair tooth contact ($\xi = \xi_{inn} + \varepsilon_\alpha - 2$), with the tooth loaded with the 30 % of the load ($R = 0.30$); or (iii) at the outer point of the inner interval of two pair tooth contact ($\xi = \xi_{inn} + 1$), with the tooth loaded with the 55 % of the load ($R = 0.55$); or (iv) at the inner point of the outer interval of two pair tooth contact ($\xi = \xi_{inn} + \varepsilon_\alpha - 1$), with the tooth loaded with the 60 % of the load ($R = 0.60$).

Though any of the above mentioned load conditions could be the critical ones, the critical contact stress is usually located at the inner point of contact or at the inner point of two pair tooth contact—corresponding to conditions (i) and (ii)—because the relative curvature radius at the other two points is much smaller. However, for high values of ξ_{inn} , the profile parameter of the inner point of contact, the determinant load conditions may be given by conditions (iii) or (iv).

As no proposals for strength calculations of high contact ratio spur internal gears have been developed in the past, the proposed model of load sharing may be suitable for new developments of bending and pitting calculation methods, even for standardization purposes.

Acknowledgments Thanks are expressed to the Spanish Council for Scientific and Technological Research for the support of the project DPI2011–27661, “Advanced models for strength calculations and dynamic analysis of non-conventional cylindrical gears”.

References

1. Hayashi K (1963) Load distribution on the contact line of helical gear teeth. JSME Bull 22
2. Winter H, Placzek T (1991) Load distribution and topological flank modification of helical and double helical gears. Euro J Mech Eng 36
3. Boerner J (1996) Very efficient calculation of the load distribution on external gear sets—the method and applications of the program LVR. In: Proceedings VII ASME International Power Transmission and Gearing Conference, San Diego, CA
4. Guillbault R, Gosselin C, Cloutier L (2005) Express model for load sharing and stress analysis in helical gears. J Mech Des 127
5. Chen Z, Shao Y (2013) Mesh stiffness of an internal spur gear pair with ring gear rim deformation. Mech Mach Theory 69
6. Pedrero JI et al (2010) Load distribution model along the line of contact for involute external gears. Mech Mach Theory 45

7. Pedrero JI, Pleguezuelos M, Muñoz M (2011) Critical stress and load conditions for pitting calculations of spur and helical gear teeth. *Mech Mach Theory* 46
8. Sánchez MB, Pedrero JI, Pleguezuelos M (2013) Critical stress and load conditions for bending calculations of involute spur and helical gears. *Int J Fatigue* 48
9. Pedrero JI, Sánchez MB, Pleguezuelos M (2012) Load sharing model for non-standard involute spur gears. *Series: New Trends in Mechanism Science*. Springer, Berlin
10. Sánchez MB, Pleguezuelos M, Pedrero JI (2013) Enhanced model of load distribution along the line of contact for non-standard involute external gears. *Meccanica* 48
11. Pedrero JI, Pleguezuelos M, Aguiriano S (2007) Load distribution model for involute internal gear sets. In: *Proceedings X ASME International Power Transmission and Gearing Conference*, Las Vegas, NV
12. Pedrero JI, Vallejo II, Pleguezuelos M (2007) Calculation of tooth bending strength and surface durability of high transverse contact ratio spur and helical gear drives. *J Mech Des* 129
13. Pedrero JI, Pleguezuelos M, Muñoz M (2011) Contact stress calculation of undercut spur and helical gear teeth. *Mech Mach Theory* 46
14. Sánchez MB, Pedrero JI, Pleguezuelos M (2013) Contact stress calculation of high transverse contact ratio spur and helical gear teeth. *Mech Mach Theory* 64
15. Sánchez MB, Pleguezuelos M, Pedrero JI (2014) Tooth-root stress calculation of high transverse contact ratio spur and helical gears. *Meccanica* 49
16. ISO Standard 6336-2:2006 (2006) Calculation of load capacity of spur and helical gears—Part 2: calculation of surface durability (pitting). International Organization for Standardization, Geneva, Switzerland
17. AGMA Standard 2001-D04 (2004) Fundamental rating factors and calculation methods for involute spur and helical gear teeth. American Gear Manufacturers Association, Alexandria, VA

Calculation of Load Capacity of Cylindrical Gears: Review of Different Approaches and Calculation Tools

S.M.O. Tavares and P.M.S.T. de Castro

Abstract Gear design has been subjected to extensive standardization by different organizations with slight differences or different approaches taking into account the multiple aspects of the gear strength. In 1996 the International Organization for Standardization started publishing the ISO 6336 standard for calculation of load capacity of cylindrical spur and helical gears, which is composed of several parts that were not simultaneously made available. This article analyses the calculation of form and stress corrections factors (Y_F and Y_S) proposed in different sources, including the two versions of the ISO 6336 Part 3 standard (1996 and 2006). The 2006 version withdrew one of the methods for the bending strength calculations, the method C, which allows the calculation of the bending strength based on parameters obtained in published charts for the most common gear rack geometries; the 2006 method requires computational codes that should be implemented or acquired by the designers in order to solve some of the equations iteratively. The use of the earlier approach is however still of interest given the availability of charts for Y_F and Y_S determination based on load applied at the tooth tip. This paper discusses a MATLAB code for Y_F and Y_S calculation presenting an enhanced determination of the contact ratio factor Y_e .

Keywords ISO 6336 • Contact ratio factor • Load capacity of gears • Form factor • Spur and helical gears • Stress correction factor

S.M.O. Tavares (✉)
Instituto de Engenharia Mecânica e Gestão Industrial—INEGI, Oporto, Portugal
e-mail: sergio.tavares@fe.up.pt

P.M.S.T. de Castro
Faculdade de Engenharia da Universidade do Porto—FEUP, Porto, Portugal
e-mail: ptcastro@fe.up.pt

1 Introduction

The calculation of load capacity of spur and helical gears is nowadays commonly made according to ISO 6336 standards, [1]. The implications of the evolution of these standards since their appearance in 1996 will be discussed in this article, considering the major differences and limitations from the designer point of view and focused on the teeth bending strength calculations.

The procedures for gear design depend on many different factors, some of them of an empirical/experimental nature as fatigue material properties to be considered, whereas other aspects are readily amenable to computational algorithms, as for example the choice of the optimum addendum modification values x_1 and x_2 , so that values of maximum specific sliding in the pinion and wheel are made equal. ISO 6336 standards provide an integrated framework for the calculation of load capacity of spur and helical gears. The load capacity at the tooth root is determined based on the tooth root stress (σ_F), which may be determined as:

$$\sigma_F = \sigma_{F0} \cdot K_A \cdot K_V \cdot K_{F\beta} \cdot K_{F\alpha} \quad (1)$$

where σ_{F0} is the nominal tooth root stress, K_A is the application load factor which takes into account fluctuations of the applied torque, K_V is the dynamic factor, which takes into account the internal dynamic effects, $K_{F\beta}$ is the face load factor, which takes into account the uneven distribution of load over the facewidth of the teeth and $K_{F\alpha}$ is the transverse load factor that takes into account the uneven load distribution in the transverse direction. This nominal tooth root stress (σ_{F0}) may be determined by different methods. The last one proposed by ISO 6336-3 in 2006, is calculated as:

$$\sigma_{F0} = \frac{F_t}{b \cdot m_n} Y_F \cdot Y_S \cdot Y_\beta \cdot Y_B \cdot Y_{DT} \quad (2)$$

where F_t is the nominal tangential load applied in the tooth, b is the facewidth, m_n is the nominal module, Y_F is the form factor, Y_S is the stress correction factor, Y_β is the helix angle factor, Y_B is the rim thickness factor and Y_{DT} is the deep tooth factor. This procedure depends on many different factors, some of them clearly of an empirical nature. An aspect where rigorous analysis is required is the determination of form and stress correction factors in the calculation of bending strength (Y_F and Y_S respectively).

2 Tooth Root Stress

Interest for bending strength starts with the Lewis approach where the tooth is considered loaded at the tip and a parabola of equal bending strength is used to determine the thickness S_{Fn} (normal chordal dimension). This evolved, within ISO,

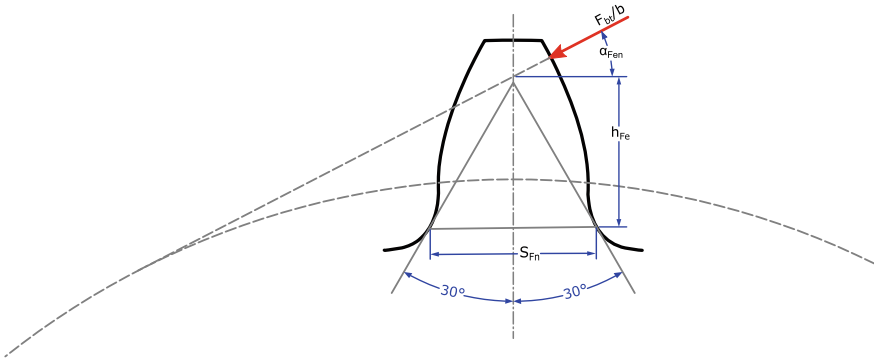


Fig. 1 Major variables for nominal tooth root stress estimation

to the use of straight lines making a 30° angle to the tooth bisecting line, Fig. 1. After lengthy work, [2], throughout which standards as AFNOR E23-015 (1982) appeared [3], ISO published the 1996 version of 6336 Part 3 including the so called B and C approaches for Y_F and Y_S calculation. The B approach is similar in the 1996 and 2006 versions, however in the latter it also takes into account the rim thickness and the deep tooth effects. The C approach estimates the nominal tooth root stress as:

$$\sigma_{F0} = \frac{F_t}{b \cdot m_n} Y_{Fa} \cdot Y_{Sa} \cdot Y_\varepsilon \cdot Y_\beta \tag{3}$$

where Y_{Fa} and Y_{Sa} are the form and stress correction factors, respectively, however, considering the load applied at the tooth tip. Y_ε is the contact ratio factor and Y_β is the helix angle factor. Therefore, these two approaches differ mainly as regards the assumption for loading location: it is external gear tooth tip loading for approach C (Y_{Fa} and Y_{Sa}), and loading at the outer point of single pair external gear tooth contact for method B (Y_F and Y_S). The implication of the difference between B and C is, of course, the need for an additional parameter, Y_ε , when using approach C. Y_ε , a value less than 1 that is a function of the contact ratio ε , corrects the over-conservative calculation based on a load applied at the tooth tip, leading to the relevant value for outer point of single pair external gear tooth contact. The estimation of the contact ratio factor has been adjusted along the time. Henriot in [4], proposes that this factor may be estimated as:

$$Y_\varepsilon = \frac{1}{\varepsilon} \tag{4}$$

However, Dufailly [5] and ISO 6336-3 1996, propose that this factor should be determined as:

$$Y_\varepsilon = 0.25 + \frac{0.75}{\varepsilon} \quad (5)$$

Theoretically, it should be $Y_{Fa} \times Y_{Sa} \times Y_\varepsilon = Y_F \times Y_S$; using the procedures of ISO 6336 Part 3, 1996, this is approximately the case, as shown e.g. by Dufailly [5]. The 2006 version of 6336 Part 3 no longer mentions method C.

If method B gives the direct answer to the problem, why bother?

The reason is simple and related to the use of standards by practitioners and Mechanical Engineering students. It just happens that while method C is based on general graphs that anyone interested can use to obtain Y_{Fa} and Y_{Sa} for a particular gear without difficulty, leaving for a later moment the consideration of the mating gear through the very simple calculation of Y_ε , method B is only accessible via a computer calculation taking into account from the very beginning the calculation carried out for the gear pair. This means that either the interested person has got calculating software (KISSsoft, GWJ, Dontyne, etc.) or the task of using method B can be daunting. By comparison, the use of method C is rather straightforward, since it is based on graphs provided for in standards (e.g. AFNOR [3]; ISO 6336 Part 3, 1996), or textbooks as Dufailly [5], Haberhauer and Bodenstein [6] and Linke [7].

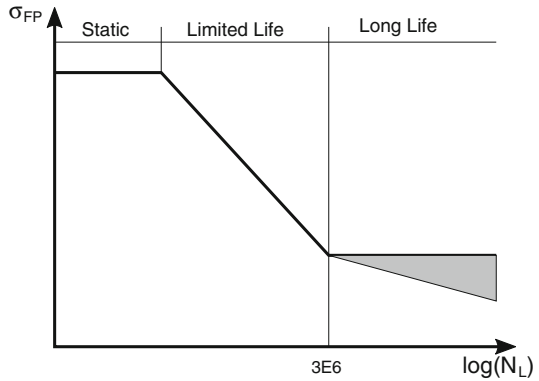
3 Permissible Bending Stress

Gear teeth are subjected to dynamic loads ranging from zero to a maximum value at the point defined in Fig. 1, therefore the permissible bending stress is determined from materials fatigue tests using gears as specimens in order to take into account the different effects of the teeth geometry. The calculation of this permissible bending stress is done by empirical formulas obtained from comparison of the stresses in gear teeth of different dimensions with experimental results. The method B of ISO 6336-2006 proposes that the permissible bending stress (σ_{FP}) is:

$$\sigma_{FP} = \frac{\sigma_{FG}}{S_{F_{\min}}} = \frac{\sigma_{F_{\lim}} \cdot Y_{ST} \cdot Y_{NT}}{S_{F_{\min}}} \cdot Y_{\delta_{relT}} \cdot Y_{R_{relT}} \cdot Y_X \quad (6)$$

where σ_{FG} is the tooth root stress limit, $S_{F_{\min}}$ is the minimum required safety factor for tooth root stress $\sigma_{F_{\lim}}$ is the nominal bending stress number from reference test gears, Y_{ST} is the stress correction factor, Y_{NT} is the life factor for tooth root stress, relevant to the dimensions of the reference test gear, $Y_{\delta_{relT}}$ is the relative notch sensitivity factor, $Y_{R_{relT}}$ is the relative surface factor and Y_X is the size factor relevant to tooth root strength. The life factor, Y_{NT} , takes into account different characteristics of the gears including the number of load cycles, materials, heat and surface treatments, failure criteria, residual stress, among others. This factor is usually higher than 1 for a limited life lower than $3E6$ cycles, Fig. 2.

Fig. 2 Typical plot of permissible bending stress versus number of load cycles



4 Results

In the present work, algorithms with B and C approaches were developed in MATLAB that can be used in the first steps of gear design. Figures 3, 4 and 5 illustrate some results that may be obtained with the algorithms developed in the present work. This type of plots can be found in the literature for the approach C, considering the Y_{Fa} , Y_{Sa} factors and the product $Y_{Fa} \times Y_{Sa}$.

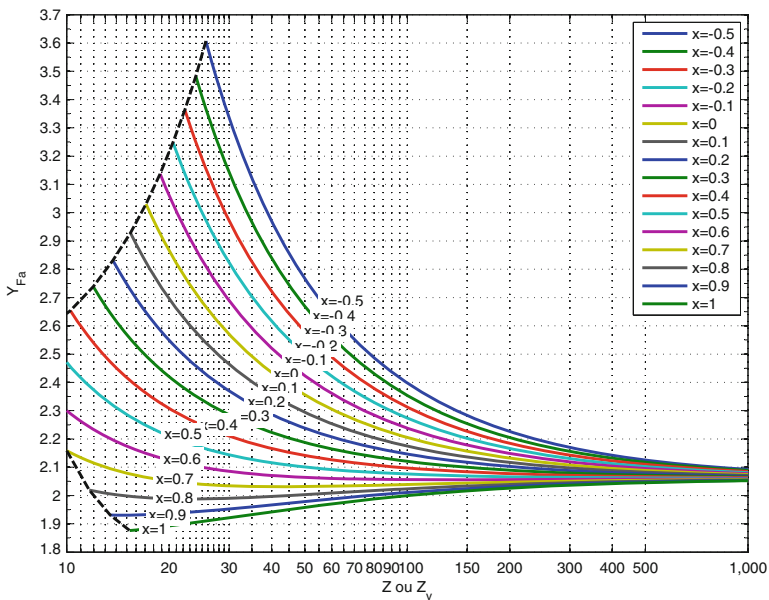


Fig. 3 Form factor, Y_{Fa} , for a gear produced with a rack with $\alpha = 20^\circ$, $h_{fp}/m_n = 1.25$ and $\rho_{fp}/m_n = 0.3$

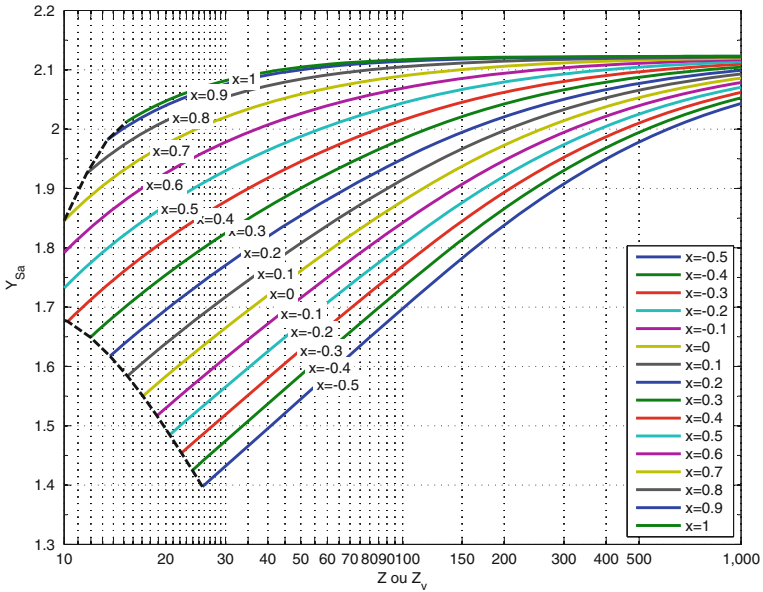


Fig. 4 Stress correction factor, Y_{Sa} , for a gear produced with a rack with $\alpha = 20^\circ$, $h_{fp}/m_n = 1.25$ and $\rho_{fp}/m_n = 0.3$

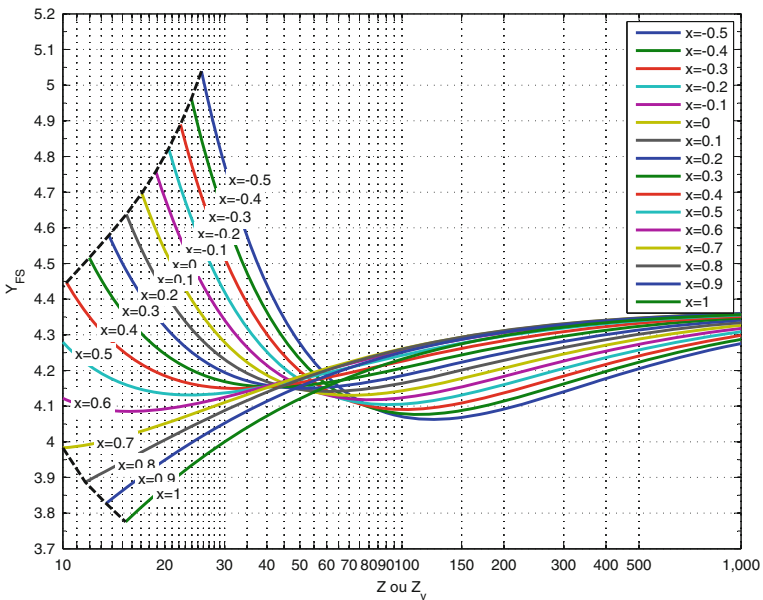


Fig. 5 Tip factor, Y_{FS} , for a gear produced with a rack with $\alpha = 20^\circ$, $h_{fp}/m_n = 1.25$ and $\rho_{fp}/m_n = 0.3$

Figure 6 shows the differences between the contact ratio factors calculated considering the formulation initially proposed by Henriot, Eq. 4 and the formulation presented in ISO Standard 6336 in 1996, Eq. 5, for different pinions and gear ratios. The results show significant differences, more than 15 %, a trend stabilizing with increasing the gear ratios.

Figure 7 shows a comparison of contact ratio factors estimated using the method B, the method C and the formulation proposed by Henriot. In the case of method B, for comparison proposes the equivalent contact ratio factor is estimated considering the following relation:

$$Y_\varepsilon = \frac{Y_F \cdot Y_S}{Y_{Fa} \cdot Y_{Sa}} \tag{7}$$

where Y_F and Y_S are calculated for the first point for outer point of single pair external gear tooth contact. It is concluded that this approach gives values between the other two methods and based on the assumptions considered it is expected that this approach gives more accurate values.

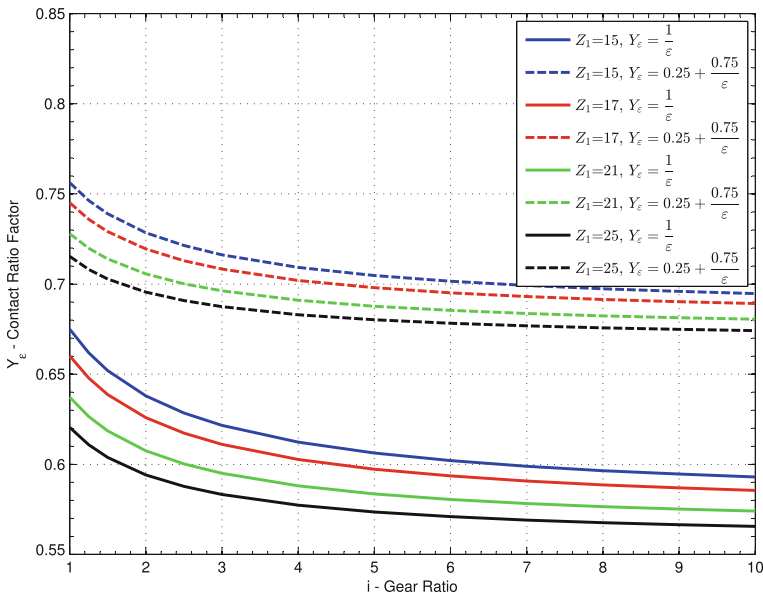


Fig. 6 Contact ratio factor differences between Henriot formulation, [4], and ISO 6336-3 1996 Method C

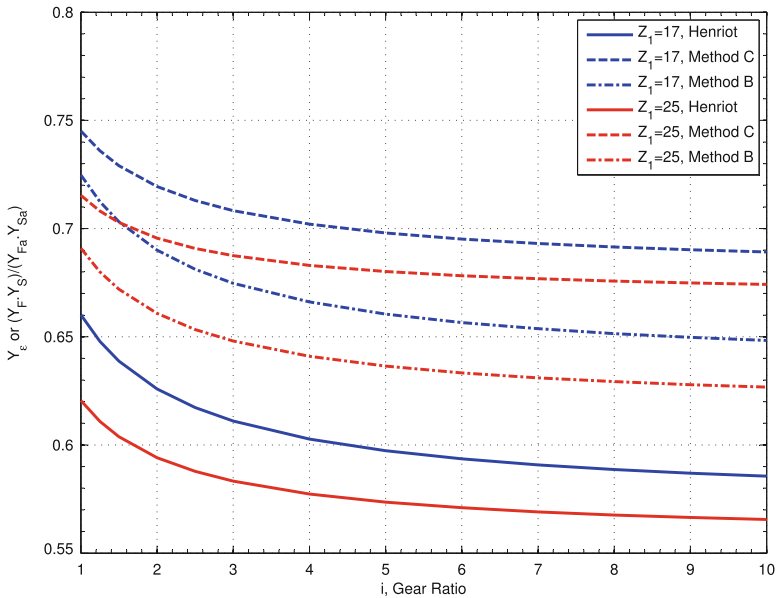


Fig. 7 Contact ratio factor differences between Henriot [4], and ISO 6336-3 Method B (calculated as $(Y_F \times Y_S)/(Y_{Fa} \times Y_{Sa})$) and method C

5 Conclusions

Multiple alternatives are found in the literature for cylindrical gear design. Considering the International Organization for Standardization standards, the previous availability of graphical solutions (ISO 6336 Part 3, 1996), was discontinued in the last version (ISO 6336 Part 3, 2006) where algorithms that cannot be easily solved manually are the only option offered. This leads to the generalized use of professional software in design offices of companies, and requires a change in the way the gear load capacity design is taught in engineering schools. The major changes in the different approaches are related with the gear point that promotes the maximum stress at the teeth root. In ISO 6336-3 1996 this aspect was considered by the contact ratio factor calculation (approach C), however the last version of the international standard proposes that the tooth root stress should be calculated in the first point for outer point of single pair external gear tooth contact (B). A comparison of the different approaches is presented in this work, showing that the earlier approach (B) may provide accurate results with an enhanced calculation of Y_{ϵ} , as made possible with the MATLAB code developed for the present work.

References

1. ISO 6336, Parts 1–6 (except 4, not yet published); various dates
2. IET—Institut de l’Engrenage et des Transmissions, cours special CACIA; VIII Méthode de calcul de la capacité de charge des engrenages à la rupture et à la pression superficielle. 13–17 Oct 1997
3. AFNOR, E23-015 (1982) Engrenages: détermination de la capacité de charge des engrenages cylindriques extérieurs de mécanique générale
4. Henriot (1968) Traité théorique et pratique des engrenages, Tome 1: Théorie et Technologie; 4e. éd., Dunod, Paris, pp 321–327
5. Dufailly J (1998) Calcul de la capacité de charge des engrenages cylindriques de transmission de puissance: présentation et analyse des méthodes ISO 6336. Paris, Ellipses
6. Haberhauer H, Bodenstern F (2007) Maschinenelemente: Gestaltung, Berechnung. Springer, Anwendung
7. Linke H (2010) Stirradverzahnung: Berechnung, Werkstoffe. Hanser, Fertigung

Load Distribution in Spur Gears Including the Effects of Friction

Pedro M.T. Marques, Ramiro C. Martins and Jorge H.O. Seabra

Abstract Friction losses between meshing gear teeth are amongst the most influential loss sources in a gearbox at nominal or near nominal operating conditions. Gear friction losses are influenced by speed, load and coefficient of friction. These factors and their variation along the path of contact must be taken into account in order to obtain accurate power loss predictions. Understanding how the power loss develops along the path of contact certainly helps in the development of more efficient and reliable gear designs. The aim of this work is then to introduce a formulation to calculate the load distribution along the path of contact taking into account elastic effects and friction.

Keywords Gears · Load distribution · Friction · Power loss · Efficiency

1 Introduction

The classical models of gear efficiency, Eq. (1), [1, 2] usually consider an average coefficient of friction along the path of contact (μ_{avg}), an input power (P_{in}) and a gear loss factor that depends on gear geometry and load (Hv) [1]. Some authors [1, 3] already presented some formulas based on empirical studies that aim to provide an average and constant coefficient of friction along the path of contact. Equation (1) is used to calculate the average power loss, ($PVZP$).

$$PVZP = P_{in} \cdot \mu_{avg} \cdot Hv, \quad (1)$$

P.M.T. Marques (✉) · R.C. Martins
INEGI, Universidade do Porto, Campus FEUP, Rua Dr. Roberto Frias 400, 4200-465 Porto,
Portugal
e-mail: pmarques@inegi.up.pt

J.H.O. Seabra
FEUP, Universidade do Porto, Rua Dr. Roberto Frias s/n, 4200-465 Porto, Portugal

where

$$H_v = \frac{1}{p_{bt}} \int_0^b \int_A^E \frac{F_N(x, y)}{F_{bt}} \cdot \frac{S(x, y)}{v_{tb}} dx dy \quad (2)$$

Taking the average of the power loss to have a rough idea of how much power a gear dissipates during operation, but understanding how the power loss develops along the path of contact is fundamental to design more reliable and more efficient gears. Having a correct load distribution is a fundamental step to understand the development of the power loss along the path of contact.

Some models using a non-uniform coefficient of friction were already published [4, 5]. Xu [6] introduced coefficient of friction formula that accounts for the different conditions along the path of contact. Velez et al. [7] who did no a priori assumption in load distribution also presented a model to calculate the average power loss generated by a meshing gear pair.

Equation (3) can be used to calculate how the power loss develops along the path of contact. In Eq. (3) b is the gear width, $F(x, y)$ is the force per unit of length, $S(x, y)$ the sliding velocity and $\mu(x, y)$ the coefficient of friction.

$$PVZP(x) = \int_0^b [F(x, y) \cdot S(x, y) \cdot \mu(x, y)] dy \quad (3)$$

This work deals with the procedure to calculate $F(x, y)$ considering elastic effects and a varying coefficient of friction.

2 Formulation of the Problem

The geometry of the gear teeth is quite complex, therefore, the usage of numerical methods to study the load distribution along the path of contact is viewed as a possibility. In this approach the dynamic effects will be disregarded, it will also be assumed that the deformation of the teeth is so small that the alteration of the geometry due to the deformations is not significant.

2.1 Load Distribution Model

In a frictionless world, the integral of the force per unit of length that acts normal to the contacting tooth surfaces along the lines of contact multiplied by the cosine of the base helix angle (β_b) and the base radius (r_b) must be such that the result is the torque (M) transmitted by the driven gear.

Consider that at any instant, the torque (M) that is transmitted by the driven gear is constant.

Consider now, several unit forces regularly distributed over the tooth flank in such a way that at the contact lines some of these unit forces are in the plane of action and perpendicular to the contact lines. Using finite element codes it is possible to extract the displacements in the points of interest for unit forces sequentially applied over each contact point. This process must be repeated for the driven and driving gears. The results will be given in terms of vectors of displacement for each Cartesian coordinate. The vector formed by the components of the displacement must be projected over the vector of the unit force correspondent to the point where the displacement is being evaluated at. This is simply the dot product between the displacement vector and the correspondent unit force vector.

Let the flexibility coefficient represented by a_{ij} be defined as the displacement in i due to a unit force applied in j . Due to the linear nature of this kind of problems, the displacement in i due to any force F_j is given by Eq. (4).

$$\delta_{ij} = a_{ij}F_j \tag{4}$$

The displacement in i due to a combination of loads in other points j can be calculated by superposition of effects, Eq. (5).

$$\delta_i = \sum_{j=1}^n \delta_{ij} = \sum_{j=1}^n a_{ij}F_j \tag{5}$$

The contribution of force F_i to the potential energy of the system can be computed using Eq. (6).

$$V_i = \frac{1}{2}F_i\delta_i \tag{6}$$

The elastic potential energy stored in the teeth of the driving gear, 1, or driven gear, 2, in the meshing gear pair, k , in a certain position along the path of contact is given by Eq. (7).

$$V_k^{1,2} = \frac{1}{2} \sum_{i=1}^n F_{ik} \left(\sum_{j=1}^n a_{ijk}^{1,2} F_{jk} \right) \tag{7}$$

The elastic potential energy stored in the meshing teeth of the gear is then given by Eq. (8).

$$V = \sum_{k=1}^m \left[\frac{1}{2} \sum_{i=1}^n F_{ik} \left(\sum_{j=1}^n a_{ijk}^1 F_{jk} \right) + \frac{1}{2} \sum_{i=1}^n F_{ik} \left(\sum_{j=1}^n a_{ijk}^2 F_{jk} \right) \right] \tag{8}$$

The sum of the forces acting in the flanks of the driving gear must balance the torque that is imposed to the driving gear. Equation (9) is the mathematical expression of this balance.

$$\sum_{k=1}^m \sum_{j=1}^n F_{jk} - \frac{M}{r_b \cdot \cos(\beta_b)} = 0 \tag{9}$$

Equation (9) assumes that there are no dissipative forces acting during the meshing process, which is not true. Equation (9) can be modified to take into account the dissipative effects through a constant coefficient of friction (μ), Eq. (10). Where r_b is the base radius of the driven gear and r_c is the distance measured perpendicularly to the contact line up to the intersection with the line of the plane of action that touches the base cylinder of the driving gear.

$$\sum_{k=1}^m \sum_{j=1}^n \left(F_{jk} \cdot \left(1 - \mu_{jk} \cdot \frac{S_{jk}}{|S_{jk}|} \cdot \frac{r_c}{r_b} \right) \right) - \frac{M}{r_b \cdot \cos(\beta_b)} = 0 \tag{10}$$

Combining Eqs. (8) and (10) the constrained expression for the elastic potential energy acting in the system results in Eq. (11). Note the *Lagrange* multiplier, λ , imposing the force balance through Eq. (10).

$$\begin{aligned} I(F_{11}, \dots, F_{nm}, \lambda) = & \sum_{k=1}^m \left[\frac{1}{2} \sum_{i=1}^n F_{ik} \left(\sum_{j=1}^n a_{ijk}^1 F_{jk} \right) + \frac{1}{2} \sum_{i=1}^n F_{ik} \left(\sum_{j=1}^n a_{ijk}^2 F_{jk} \right) \right] \\ & + \lambda \cdot \left[\sum_{k=1}^m \sum_{j=1}^n \left(F_{jk} \cdot \left(1 - \mu_{jk} \cdot \frac{S_{jk}}{|S_{jk}|} \cdot \frac{r_c}{r_b} \right) \right) - \frac{M}{r_b \cdot \cos(\beta_b)} \right] \end{aligned} \tag{11}$$

Consider that:

$$[a] = [a^1 + a^2] \tag{12}$$

Therefore:

$$\begin{aligned} I(F_{11}, \dots, F_{nm}, \lambda) = & \sum_{k=1}^m \left[\frac{1}{2} \sum_{i=1}^n F_{ik} \left(\sum_{j=1}^n a_{ijk} F_{jk} \right) \right] \\ & + \lambda \cdot \left[\sum_{k=1}^m \sum_{j=1}^n \left(F_{jk} \cdot \left(1 - \mu_{jk} \cdot \frac{S_{jk}}{|S_{jk}|} \cdot \frac{r_c}{r_b} \right) \right) - \frac{M}{r_b \cdot \cos(\beta_b)} \right] \end{aligned} \tag{13}$$

The way that the load distributes over the teeth in a certain mesh instant is the one that minimizes the total energy of the system, Eq. (13). The minimum of a function is the point where the gradient becomes zero. The simultaneous system of Eq. (14) allows the calculation of the minimum.

$$\begin{cases} \frac{\partial I(F_{11}, \dots, F_{nm}, \lambda)}{\partial F_{11}} = 0 \\ \vdots \\ \frac{\partial I(F_{11}, \dots, F_{nm}, \lambda)}{\partial F_{nm}} = 0 \\ \frac{\partial I(F_{11}, \dots, F_{nm}, \lambda)}{\partial \lambda} = 0 \end{cases} \tag{14}$$

Expanding Eq. (14) the simultaneous (15) is obtained.

$$\begin{cases} \frac{1}{2} \left[\sum_{i=1}^n F_{i1} (a_{i11} + a_{1i1}) \right] + \lambda \cdot \left[\sum_{j=1}^n \left(1 - \mu_{jk} \cdot \frac{S_{11}}{|S_{11}|} \cdot \frac{r_c}{r_b} \right) \right] = 0 \\ \vdots \\ \frac{1}{2} \left[\sum_{i=1}^n F_{im} (a_{im} + a_{nim}) \right] + \lambda \cdot \left[\sum_{j=1}^n \left(1 - \mu_{jk} \cdot \frac{S_{nm}}{|S_{nm}|} \cdot \frac{r_c}{r_b} \right) \right] = 0 \\ \sum_{k=1}^m \sum_{j=1}^n \left(F_{jk} \cdot \left(1 - \mu_{jk} \cdot \frac{S_{jk}}{|S_{jk}|} \cdot \frac{r_c}{r_b} \right) \right) - \frac{M}{r_b \cdot \cos(\beta_b)} = 0 \end{cases} \tag{15}$$

Substituting $C = r_b \cdot \cos(\beta_b)$ and $L_{jk} = 1 - \mu_{jk} \frac{S_{jk}}{|S_{jk}|} \cdot \frac{r_c}{r_b}$, Eq. (15) is written in matrix form according to (16).

$$\frac{1}{2} \begin{bmatrix} 2a_{11} & \dots & a_{1n1} + a_{n11} & 0 & \dots & 0 & 0 & \dots & 0 & 2L_{11} \\ \vdots & a_{ij1} + a_{ji1} & \vdots & \vdots & 0 & \vdots & \vdots & 0 & \vdots & \vdots \\ a_{n1} + a_{1n1} & \dots & 2a_{nn1} & 0 & \dots & 0 & 0 & \dots & 0 & 2L_{n1} \\ 0 & \dots & 0 & 2a_{11k} & \dots & a_{1nk} + a_{n1k} & 0 & \dots & 0 & 2L_{1k} \\ \vdots & 0 & \vdots & \vdots & a_{ijk} + a_{jik} & \vdots & \vdots & 0 & \vdots & \vdots \\ 0 & \dots & 0 & a_{1nk} + a_{n1k} & \dots & 2a_{nmk} & 0 & \dots & 0 & 2L_{nk} \\ 0 & \dots & 0 & 0 & \dots & 0 & 2a_{11m} & \dots & a_{1nm} + a_{n1m} & 2L_{1m} \\ \vdots & 0 & \vdots & \vdots & 0 & \vdots & \vdots & a_{ijm} + a_{jim} & \vdots & \vdots \\ 0 & \dots & 0 & 0 & \dots & 0 & a_{1nm} + a_{n1m} & \dots & 2a_{nnm} & 2L_{nm} \\ 2L_{11} & \dots & 2L_{n1} & 2L_{1k} & \dots & 2L_{1k} & 2L_{1m} & \dots & 2L_{nm} & 0 \end{bmatrix} \begin{bmatrix} F_{11} \\ \vdots \\ F_{n1} \\ F_{1k} \\ \vdots \\ F_{nk} \\ F_{1m} \\ \vdots \\ F_{nm} \\ \lambda \end{bmatrix} - \begin{bmatrix} 0 \\ \vdots \\ 0 \\ \vdots \\ 0 \\ \vdots \\ 0 \\ \vdots \\ 0 \\ M/C \end{bmatrix} = \begin{bmatrix} 0 \\ \vdots \\ 0 \\ \vdots \\ 0 \\ \vdots \\ 0 \\ \vdots \\ 0 \\ 0 \end{bmatrix} \tag{16}$$

The solution of this linear simultaneous system of equations will lead to the determination of number of forces which are not only in the plane of action but also perpendicular to the lines of contact. These forces can be viewed as the result of the

integral of a line load over a small length, which can then be divided by the local line length to obtain the load per unit of length in a particular location. Since, the dynamic effects were disregarded, solving the simultaneous (16) for a fixed number of points along the path of contact allows to obtain the load distribution. The *Lagrange* multiplier is an indication of the displacement.

The formulation that was presented in this section is valid for both helical and spur gears.

2.2 Coefficient of Friction

Xu [6] proposed a coefficient of friction based on results obtained with an EHL model (numerical results) that was validated with experimental traction curves. After validation, the model was ran $\approx 10,000$ times for different operating conditions. Then Xu fitted the results using a custom function, Eq. (17).

$$\mu^{Hai} = e^{f(SR, P_h, v_0, S)} P_h^{b2} |SR|^{b3} V_e^{b6} \mu_0^{b7} R^{b8} \tag{17}$$

$$f(SR, P_h, v_0, S) = b_1 + b_4 |SR| P_h \log_{10}(v_0) + b_5 e^{-|SR| P_h \log_{10}(v_0)} + b_9 e^S \tag{18}$$

Table 1 shows the coefficients b_1 to b_9 that go in Eqs. (17) and (18).

The coefficient of friction formula proposed by Xu [6] depends on the load distribution and the load distribution also depends on this same coefficient of friction. Therefore an iterative procedure is needed in order to obtain the solution for the load distribution using this coefficient of friction formulation. An initial solution for the load distribution is obtained with a constant $\mu = 0.05$ (standard value), then μ^{Xu} is recalculated with the previously calculated μ and so on until the solution converges.

3 Implementation and Results

Table 2 shows the simulation conditions and gear parameters.

Figure 1 shows the load distribution for a C14 spur gear at FZG load stage K11. These results indicate that there is a clear influence of the elastic effects and friction forces in the load distribution.

Table 1 Coefficients for the EHL based formula, [6]

b_1	-8.916465	b_2	1.03303	b_3	1.036077
b_4	-0.354068	b_5	2.812084	b_6	-0.100601
b_7	0.752755	b_8	-0.390958	b_9	0.620305

Table 2 Simulation conditions and gear parameters

Gears	Operating conditions (Gear 1)	Lubricant
$z_1 = 24, x_1 = 0.1715; z_2 = 16, x_2 = 0.1817$	$n = 200\text{rpm}$	PAO ISO VG 320
$\alpha = 20^\circ, m_n = 4.5\text{mm}, a = 91.5\text{mm}, b = 14\text{mm}$	$M = 477.8\text{Nm}$	$T = 80^\circ\text{C}$

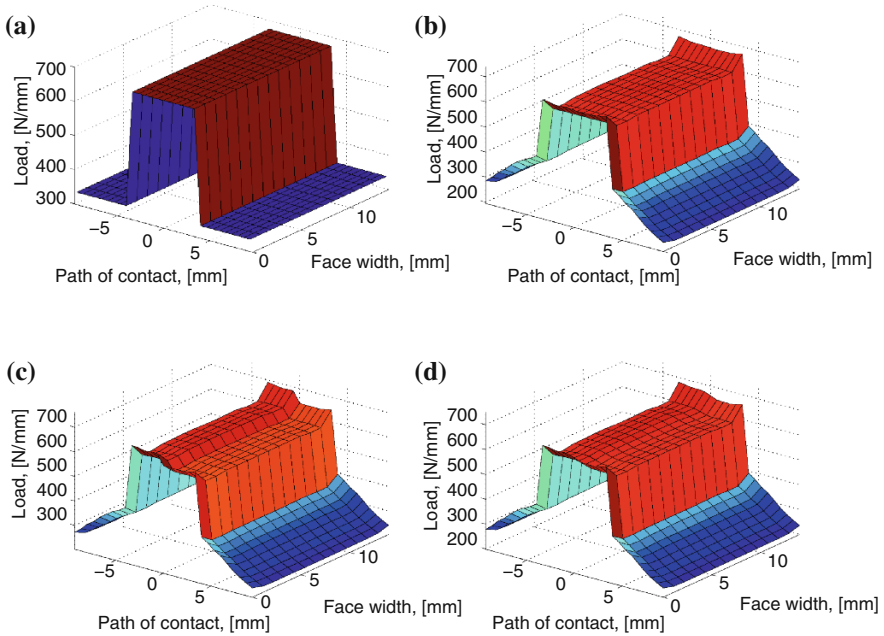


Fig. 1 Load distribution in a C14 spur gear considering tooth bending and three different coefficient of friction approaches. **a** $\mu = 0.00$ and no elasticity. **b** $\mu = 0.00$ and elasticity. **c** $\mu = 0.05$ and elasticity. **d** μ varies at each point according to Fig. 2a and elasticity

Figure 1a was obtained considering that load per unit of length is the force that acts perpendicular to a mesh of a single tooth pair divided by the (transmitted torque divided by the base radius and the base helix angle) the sum of the lengths of the contacting lines.

When the meshing process goes through the pitch point the sliding velocity changes sign, Fig. 2b, which justifies the step that is visible in Fig. 1c. If a variable coefficient of friction is used, Fig. 1d, this step is smoothed out because μ^{Xu} vanishes as it gets closer to the pitch point, Fig. 2a.

These results also show that the varying friction force along the path of contact is a potential source of dynamic excitation, which could be further investigated.

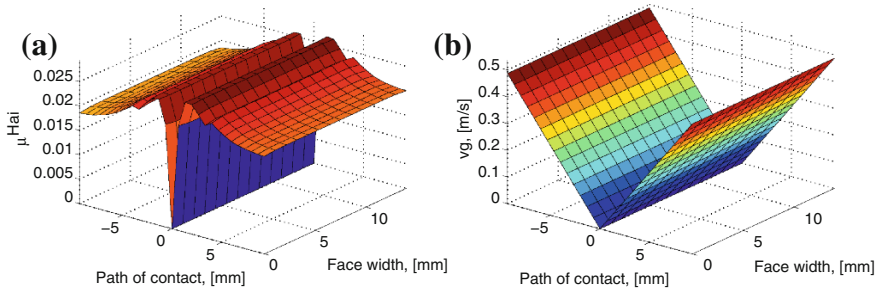
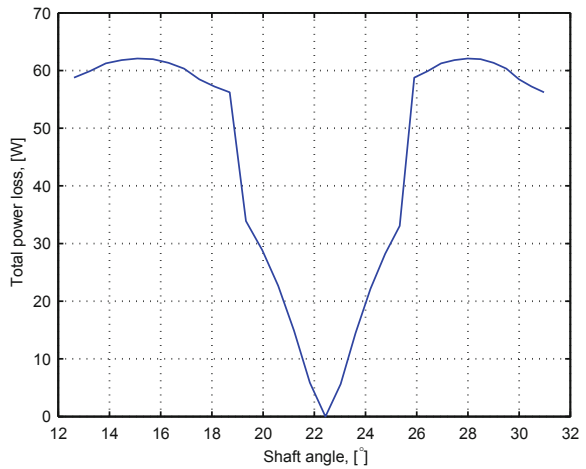


Fig. 2 Coefficient of friction (μ^{Hai}) and absolute value of the sliding velocity ($|S|$). **a** μ^{Hai} calculated according to Eq. (17). **b** Sliding velocity, (μ^{Hai})

Applying Eq. (3) for a meshing gear pair and summing the power loss generated by each pair of teeth in contact at a certain instant it is possible to obtain the total power loss varying with the angle of rotation, Fig. 3.

Figure 3 was obtained considering the load distribution from Fig. 1d and the coefficient of friction and sliding velocity from Fig. 2.

Fig. 3 Total power loss along the path of contact



4 Conclusions

The simulation results show that there is an influence of the friction forces in the load distribution along the path of contact. Considering a constant coefficient of friction in a load distribution formulation along the path of contact is not optimal because it will lead to exaggerated variations (step like) of load near the pitch point. Researchers interested in studying the friction forces as a potential source of dynamic excitation, may use a varying coefficient of friction instead of a constant one.

The average power loss, Eq. (1), predictions also benefit from a correct load distribution because, Eq. (2), will be more correctly evaluated. It should be noted that there are analytical formulas to calculate the gear loss factor, but these generally have some kind of assumption restricting their application to some cases, which sometimes results in significant deviations from the correct result. Since the formulation that was presented is valid for both spur and helical gears, the gear loss factor can now be more correctly evaluated using Eq. (2), considering the load distribution calculated according to the methodology that was proposed.

The model that was presented may also be useful to study the contact stress between meshing helical or spur gears.

Acknowledgements The authors of this work would like to acknowledge the national funds provided by FCT—Fundação para a Ciência e a Tecnologia within the project EXL/EMS-PRO/0103/2012.

References

1. Höhn BR, Michaelis K, Hinterstoiber M (2009) Optimization of gearbox efficiency. *Goriva i maziva* 48(4):462–480
2. Marques PM, Fernandes CM, Martins RC, Seabra JH (2014) Efficiency of a gearbox lubricated with wind turbine gear oils. *Tribol Int* 71(0):7–16 (2014). doi:<http://dx.doi.org/10.1016/j.triboint.2013.10.017>
3. Höhn BR, Michaelis K, Vollmer T (1996) Thermal rating of gear drives: balance between power loss and heat dissipation. AGMA technical paper
4. Benedict GH, Kelley BW (1961) Instantaneous coefficients of gear tooth friction. *ASLE Trans* 4(1):59–70. doi:[10.1080/05698196108972420](https://doi.org/10.1080/05698196108972420)
5. Diab Y, Ville F, Velez P (2006) Prediction of power losses due to tooth friction in gears. *Tribol Trans* 49(2):260–270. doi:[10.1080/05698190600614874](https://doi.org/10.1080/05698190600614874)
6. Hai X (2005) Development of a generalized mechanical efficiency prediction methodology for gear pairs. Ph.D. thesis, The Ohio State University (2005)
7. Velez P, Ville F (1996) An analytical approach to tooth friction losses in spur and helical gears—influence of profile modifications. *J Mech Des, Trans ASME* 131(10), 1010081–10100810. Cited By (since 1996) 11

Influence of Gear Loss Factor on the Power Loss Prediction

Carlos M.C.G. Fernandes, Pedro M.T. Marques, Ramiro C. Martins and Jorge H.O. Seabra

Abstract It is very important to properly calculate the gear loss factor in order to predict the gears power loss. A gear loss factor calculated considering the load distribution along the path of contact was implemented. Several gear loss factors were considered in the study. Some gear loss factors don't correlate with experimental results, putting in evidence the importance of a correct value of gear loss factor.

Keywords Power loss · Gears · Loss factor · FZG

Notations and Units

H_V	Gear loss factor [/]
P_{IN}	Input power of the gearbox [W]
P_{VZP}	Load dependent power loss of meshing gears [W]
P_{VZ0}	Load independent power loss of meshing gears [W]
P_{VL}	Rolling bearings power loss [W]
P_{VD}	Seals power loss [W]
μ	Coefficient of friction of meshing gears [/]
μ_{EXP}	Coefficient of friction of meshing gears determined experimentally [/]
μ_{Author}	Coefficient of friction of meshing gears determined experimentally with author gear loss factor [/]
$\mu_{Ohlendorf}$	Coefficient of friction of meshing gears determined experimentally with Ohlendorf gear loss factor [/]
μ_{mZ}	Coefficient of friction of meshing gears Schlenk [/]
ε_α	Transverse contact ratio [/]

C.M.C.G. Fernandes (✉) · P.M.T. Marques · R.C. Martins
INEGI, Universidade do Porto, Campus FEUP, Rua Dr. Roberto Frias 400,
4200-465 Porto, Portugal
e-mail: cfernandes@inegi.up.pt

J.H.O. Seabra
Universidade do Porto, porto, Portugal

1 Introduction

According to Hohn et al. [7] the power loss in a gearbox consists of gear, bearing, seals and auxiliary losses. Gear and bearing losses can be separated in no-load and load losses. No-load losses occur with the rotation of mechanical components, even without torque transmission. No-load losses are mainly related to lubricant viscosity and density as well as immersion depth of the components on a sump lubricated gearbox, but it also depends on operating conditions and internal design of the gearbox casing. No-load rolling bearing losses depend on type and size, arrangement, lubricant viscosity and immersion depth.

Load dependent losses occur in the contact of the power transmitting components. Load losses depended on the transmitted torque, coefficient of friction and sliding velocity in the contact areas of the components. Load dependent rolling bearing losses also depend on type and size, rolling and sliding conditions and lubricant type [1].

Power loss generated by gears is the main important cause of power loss in a gearbox. This work show the influence of the calculation of the gear loss factor, dependent on the geometry of the gear, in the prediction of the power loss.

2 Load Power Loss in Meshing Gears

Ohlendorf [11] introduced an approach for the load dependent losses of spur gears. The power loss generated between gear tooth contact can be calculated according to Eq. (1),

$$P_{VZP} = P_{IN} H_V \mu_{mZ} \quad (1)$$

where H_V represents the gear loss factor which is the main focus of this work.

This formula assumes that the coefficient of friction (μ_{mZ}) is constant along the path of contact. In fact this is a simplification of the problem.

3 Gear Loss Factor

Equation (1) can be used to calculate the average power loss between gear teeth, given the correct gear loss factor H_V . Despite considering β_b the equation initially proposed by Ohlendorf [11] is mostly valid for spur gears.

$$H_V^{ohl} = (1 + u) \frac{\pi}{z_1 \cos \beta_b} (1 - \varepsilon_x + \varepsilon_1^2 + \varepsilon_2^2) \tag{2}$$

Niemann and Winter [10] also proposed a gear loss factor that is shown in Eq. (3).

$$H_V^{Nie} = (1 + u) \frac{\pi}{z_1 \cos \beta_b} \varepsilon_x \left(\frac{1}{\varepsilon_x} - 1 + (2k_0^2 + 2k_0 + 1) \varepsilon_x \right) \tag{3}$$

Buckingham [2] also introduced a formula (4) for the efficiency of a meshing gear pair. A gear loss factor (Eq. 4) can also be derived from this approach.

$$H_V^{Buc} = (1 + u) \frac{\pi}{z_1 \cos \beta_b} \varepsilon_x (2k_0^2 - 2k_0 + 1) \tag{4}$$

Velex et al. which did no a priori assumption on tooth load distribution by using generalized displacements, in order to calculate the efficiency of a meshing gear pair, obtained a closed form solution for the efficiency of a meshing gear pair (constant coefficient of friction was assumed). It turns out that the equation suggested by Buckingham (4) is an approximation of the one suggested by Velex et al. [13] when $\mu \ll 1$.

$$\rho = 1 - \mu \cdot (1 + u) \cdot \frac{\pi}{z_1} \cdot \frac{1}{\cos \beta_b} \cdot \varepsilon_x \cdot A(\mu) \tag{5}$$

with

$$A(\mu) = \frac{2k_0^2 - 2k_0 + 1}{1 - \mu \cdot \left(\frac{\tan \alpha_t \cdot (2k_0 - 1) - \frac{\pi}{z_1} \varepsilon_x \cdot (2k_0^2 - 2k_0 + 1)}{\cos \beta_b} \right)} \tag{6}$$

where

$$k_0 = \frac{z_1}{2\pi \cdot \varepsilon_x \cdot u} \left(\left(\left(\frac{ra_2}{rp_2} \right)^2 \frac{1}{\cos \alpha_t^2} - 1 \right)^{\frac{1}{2}} - \tan \alpha_t \right) \tag{7}$$

Considering that the load distribution can be calculated just considering that the load per unit of length can be calculated according to Eq. (8) and that the coefficient is constant along the path of contact, the gear loss factor can be obtained by application of Eq. (9).

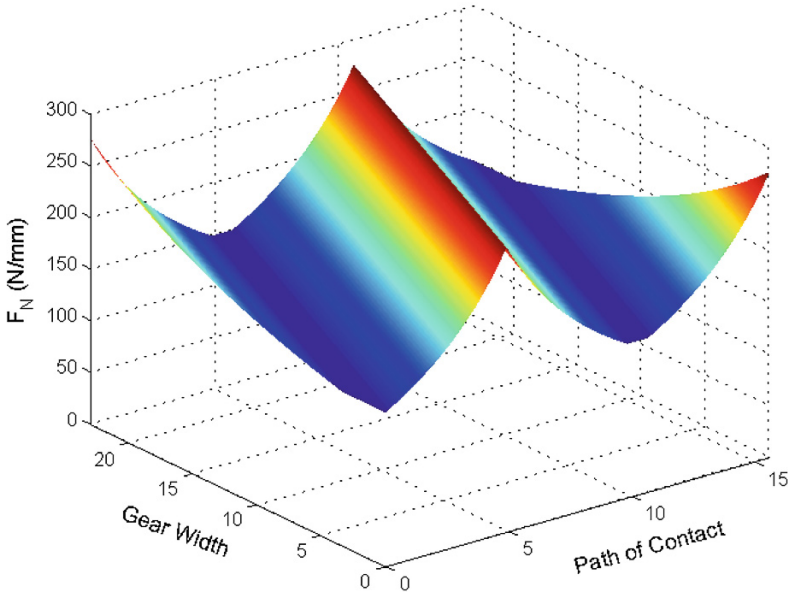


Fig. 1 Load distribution of a helical gear with an applied torque of 320 Nm

Equation (8) describes the load distribution along the path of contact, (if the elastic effects are disregarded, see Fig. 1). The l^i is the length of contact line over a single meshing teeth.

$$F_N(x, y) = F_n \cdot \frac{l^i(x)}{\sum_{i=1}^n l^i(x)} \tag{8}$$

$$H_V^{num} = \frac{1}{p_b} \int_0^b \int_A^E \frac{F_N(x, y)}{F_b} \cdot \frac{V_g(x, y)}{V_b} dx dy \tag{9}$$

4 Average Coefficient of Friction

Several authors [3, 4, 8, 9, 11, 12] have introduced different formulas to calculate the average coefficient of friction between gear teeth for different gear geometries. Due to the complexity of the problem, these equations are usually based in experimental results, and naturally, the results yielded by these models vary for the same operating conditions. In this work, instead of calculating the coefficient of

friction yielded by these formulations, a value is calculated from the experimental results and then compared to the models.

Assuming a correct calculation of P_{VZ0} , P_{VL} and P_{VD} the power loss generated by the meshing gears can be calculated according to Eq. (10).

$$P_{VZP} = P_V^{exp} - (P_{VZ0} + P_{VL} + P_{VD}) \tag{10}$$

Considering the power loss generated by the gears in the gearbox (Eq. 10) an average coefficient of friction (μ_{avg}) for all gear meshes in the gearbox can be calculated. μ_{avg} can be calculated according to different approaches (assuming almost the same COF for all gear meshes):

1. From Ohlendorf’s approach:

$$\mu_{avg} = \frac{P_{VZP}}{\sum_{i=1}^{n_{mesh}} P_a^i \cdot H_V^i} \tag{11}$$

H_V^i is the gear loss factor which can assume various forms, depending on the formulation that is used. Three H_V were defined according to Eqs. (2) H_V^{Ohl} , (9) H_V^{num} , (3) H_V^{Nie} , (4) H_V^{Buc} .

2. Considering the average power loss generated between gear teeth along the path of contact, μ_{avg} can be obtained solving Eq. (12) to find μ_{avg} .

$$P_{VZP} = \sum_{i=1}^{n_{mesh}} P_{in}^i \cdot \mu_{avg} \cdot (1 + u^i) \frac{\pi}{z_1^i \cdot \cos \beta_b^i} \varepsilon_x^i \Lambda^i(\mu_{avg}) \tag{12}$$

The coefficients of friction extracted from the gear mesh power loss obtained with Eq. (10) will be dependant of the formulation that is used to calculate the gear loss factor. In order to decide which gear loss factor formulation is better suited for the authors study, this factor was calculated for eight different gear geometries, in which, spur, helical and low loss gears are included. The gear loss factor was also calculated based on the results obtained with the commercial software *KissSoft* which accounts for elastic effects. Figure 2 shows the comparison between the different gear geometries as a function of the k_0 (7) parameter. There are clearly two groups of results that diverge at a certain point. The H501 and H951 geometries were previously tested for power loss in an FZG test rig [5]. Changing from H501 to H951 resulted in a dramatic power loss reduction, which was attributed to the H951 gear geometry (everything but the gear geometry was kept the same). These experimental results suggest that the gear loss factor of the H951 must be lower than that of the H501. The trends shown by the gear loss factors obtained with *KissSoft*, the author’s method and Ohlendorf are in accordance with the experimental observations [5]. The gear loss factors obtained with Eq. (9) are close to

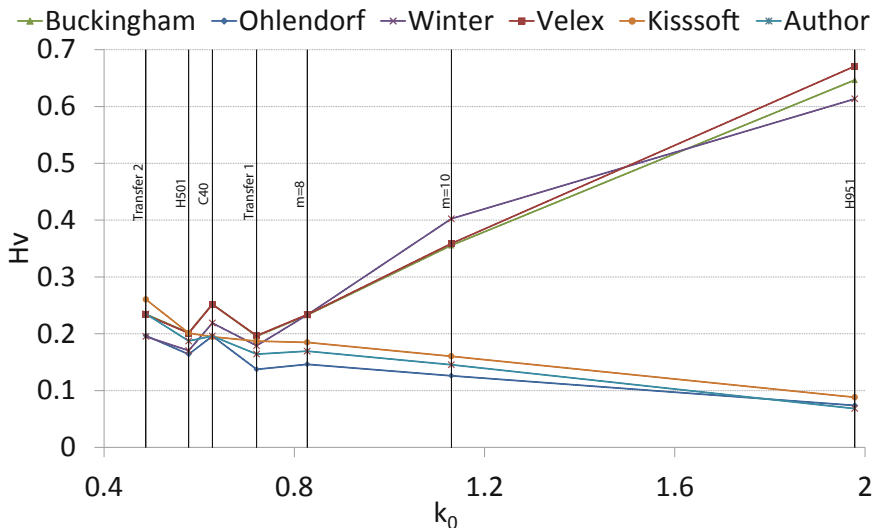


Fig. 2 Gear loss factor comparison with different formulas

those obtained with the ones derived from the *KissSoft* computations. Aiming for simplicity and fast computing the gear loss factor was calculated using Eq. (9).

5 Validation with Experimental Results

In order to validate the gear loss factor of the author, the coefficient of friction of Schlenk, presented in Eq. (13), was used. The lubricant parameter (XL) was previously determined with a spur gear geometry for different base oils [6]. Alternatively, experimental results presented in [5] were used to calculate an experimental coefficient of friction according Eq. (14).

$$\mu_{Schlenk} = \mu_{mZ} = 0.048 \cdot \left(\frac{F_{bt}/b}{v_{\Sigma C} \cdot \rho_{redC}} \right)^{0.2} \cdot \eta^{-0.05} \cdot Ra^{0.25} \cdot X_L \quad (13)$$

$$\mu_{EXP} = \frac{P_{VZF}^{EXP}}{P_{IN} H_V^{num}} \quad (14)$$

In the Fig. 3 is presented the experimental coefficient of friction calculated with author gear loss factor as well as the Ohlendorf gear loss factor. The Schlenk coefficient of friction was also presented. The results suggest that the gear loss factor presented by the author in Eq. (9) follow the trend of coefficient of friction suggested by Schlenk where the lubricant parameter was previously determined [6].

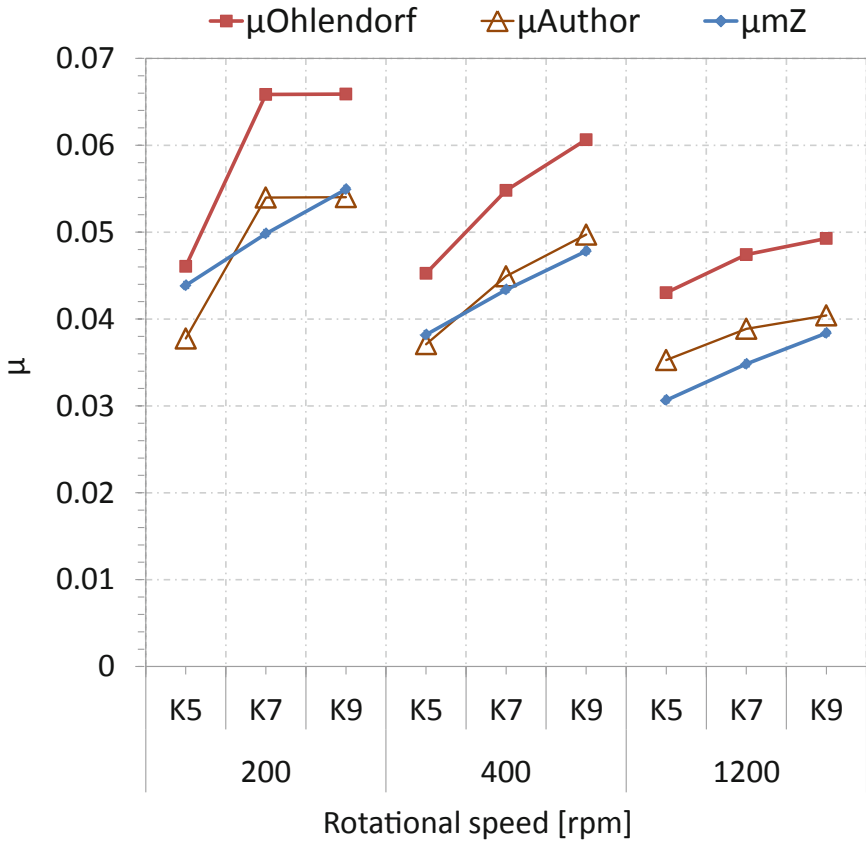


Fig. 3 Correlation between the experimental coefficient of friction calculated with author’s gear loss factor and Schlenk coefficient of friction

6 Conclusions

The gear loss factor H_V calculated with the method presented by the author, even without consider elastic effects of the gears, is reliable to predict the actual power loss of gears as proven with experimental results. This study clearly shows the importance of a correct evaluation of the gear loss factor in the prediction of the power loss generated in meshing gears.

Acknowledgements Fundação para a Ciência e a Tecnologia—FCT for the financial support given through the project “Modelização e ensaio da perda de potência e do desgaste em engrenagens helicoidais. Influência do material e da geometria da engrenagem”, with research contract EXCL/EMS-PRO/0103/2012.

References

1. SKF General Catalogue 6000 EN. SKF (Nov 2005)
2. Buckingham E (1949) Analytical mechanics of gears. Dover books for engineers. McGraw-Hill Book Co, New York. URL <http://books.google.pt/books?id=lThSAAAAAAAJ>
3. Doleschel A (2002) Wirkungsgradtest, vergleichende beurteilung des einflusses von schmierstoffen auf den wirkungsgrad bei zahnradgetrieben. FVA Forschungsvorhaben Nr. 345, FVA Forschungsheft Nr. 664
4. Eiselt H (1966) Beitrag zur experimentellen und rechnerischen bestimmung der fresstragfähigkeit von zahnradgetrieben unter berücksichtigung der zahnflankenreibung. Ph. D. thesis, TH Dresden
5. Fernandes C, Martins R, Seabra J (2013) Torque loss of spur and helical fzg gears lubricated with wind turbine gear oils. In: International Conference on Gears. Escuela Superior de Ciencias Experimentales y Tecnología, Campus de Móstoles de la Universidad Rey Juan Carlos, Madrid, Spain (2013)
6. Fernandes CM, Martins RC, Seabra JH (2013) Torque loss of type {C40} {FZG} gears lubricated with wind turbine gear oils. Tribology International 70. doi:<http://dx.doi.org/10.1016/j.triboint.2013.10.003>. URL <http://www.sciencedirect.com/science/article/pii/S0301679X13003381>
7. Höhn BR, Michaelis K, Hinterstoißer M (2009) Optimization of gearbox efficiency. goriva i maziva 48(4):462–480
8. Michaelis K (1987) Die integraltemperatur zur beurteilung der fresstragfähigkeit von stirnrädern. Ph.D. thesis, TU München
9. Naruse C, Haizuka S, Nemoto R, Kurokawa K (1986) Studies on frictional loss, temperature rise and limiting load for scoring of spur gear. Bull JSME 29(248):600–608. doi:[10.1299/jsme1958.29.600](https://doi.org/10.1299/jsme1958.29.600). URL <http://ci.nii.ac.jp/naid/110002358505/en/>
10. Niemann G, Winter H (1989) Maschinenelemente: Band 2: Getriebe allgemein, Zahnradgetriebe—Grundlagen, Stirnradgetriebe. Maschinenelemente/Gustav Niemann. Springer. URL <http://books.google.pt/books?id=FEiAr9K1rJsC>
11. Ohlendorf H (1958) Verlustleistung und Erwärmung von Stirnrädern. Ph.D. thesis, TU München
12. Schlenk L (1994) Untersuchungen zur Fresstragfähigkeit von Grozahnradern. Ph.D. thesis, TU München
13. Vexel P, Ville F (2009) An analytical approach to tooth friction losses in spur and helical gears—influence of profile modifications. J Mech Des Trans ASME 131(10):1010081–10100810

Hydraulic Hose as an Instability Reducer for a Flexible Shaft Composed by Universal Joints

V.H. Carneiro and J. Meireles

Abstract There are currently diverse options to execute the mechanical transmission of rotary movement. However, there may be advantageous to combine some individual features of some of them. For instance, the case of two shafts placed in a distant and non-collinear situation. A possible solution is a mechanism that combines the characteristics of a universal joint and a flexible shaft. Such mechanism could be obtained by placing universal joints in series, although this kind of mechanism would be instable. The objective of this paper is to analyze the possibility of using a hydraulic hose to reduce that instability and equally distribute the transmission angle in the suggested mechanism. It is shown that this may be viable, with some limitations, and may be an interesting opportunity for further development.

Keywords Flexible shaft · Instability · Universal joint · Hydraulic hose

1 Introduction

The selection of mechanical transmissions is a common process in machinery project. Their ability to guide mechanical movement, from a defined spatial coordinate to a different one, is an essential feature to solve many practical problems. Thus, there is a constant need to develop new ways to perform this task. A specific case of the application of mechanical transmissions is in the transfer of rotary and torque between two shafts, which by themselves have non collinear and angular axes. Some solutions allow this transmission, although many depend on the vectorial distance between the driving and driven shafts and the value of the angle of

V.H. Carneiro (✉) · J. Meireles
University of Minho, Braga, Portugal
e-mail: a53996@alunos.uminho.pt

J. Meireles
e-mail: meireles@dem.uminho.pt

their axes. Frequently, there is a close relationship between the workspace of a transmission and its geometrical parameters [1].

Currently, there are certain technologies that allow the reduction of the dependency between the distance and angle of transmission, like the case of flexible shafts (see for example [2, 3]). This kind of mechanism is composed by wires, spiraled tightly around a central wire. Layers of wire spirals are wound in opposite directions to each other and will not twist open if turned [4]. They are an efficient way that allows the transmission of rotary movement and torque between shafts with large values of distance and misalignments. However, they are frequently used in situations that require low values of dynamic torque. Additionally, there is an exponential decay of allowable torque when the angle of transmission increases. Thus, it can be inferred that it would be useful to find a solution that allows an angular distant transmission without an elevated loss of power.

A solution to this problem, the one suggested in this paper, is the design of a mechanism that combines a universal joint with the flexible shaft. One way of obtaining such mechanism would be the connection, in series, of several universal joints. Universal joints are used to transfer torque and angular motion between two intersecting axles [5] and are widely applied due to their low cost, high reliability and economic maintenance [6] in the automotive and machine tool industry [7]. The proposed mechanism would resemble Fig. 1.

Due to the characteristics of this kind of joint, even if the drive shaft presents constant torque and rotational speed, the driven shaft experiences fluctuating rotational speed, bending moments and torque. These are sources of potential parametric, forced and flutter type instabilities [5]. The kinematical consequences of this fact can be remedied, considering that the bodies are rigid, by using two universal joints in series [8]. However, for more than two joints placed in series, this is not viable. The simple application of a torque effort to the mechanism shown in Fig. 1, would lead to instability, erratic behavior and ruin of such mechanism. This way, it is mandatory to find a solution to control and to lower the instability.

This objective is precisely the focus of this paper. The use of a hydraulic hose as a medium to suppress the instabilities in the universal joints placed in series and to distribute uniformly the transmission angle between them. The way of analyzing that hypothesis is the execution of motion simulation on the referred mechanism

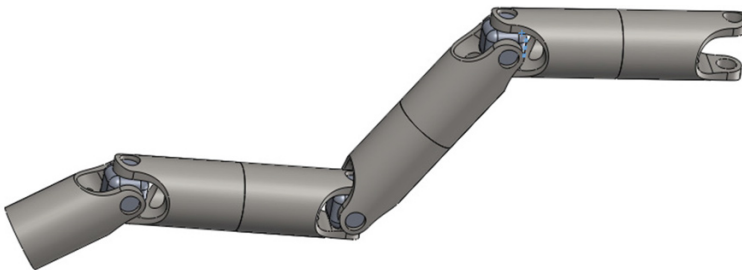


Fig. 1 Flexible shaft composed by universal joints

with and without the restraint of a hydraulic hose. Finally it is concluded that the use of the hydraulic hose may be a promising approach to develop such new type of flexible shafts.

2 Methodology

In order to study the use of a hydraulic hose as a way to control the instability of a flexible shaft composed by universal joints placed in series, there were executed motion simulations in two mechanisms. To build such mechanisms, there was a need to determine the geometric characteristics of the universal joints, the hydraulic hose, the motion simulations and the results comparison conditions. These matters are explored in the following section.

2.1 Component modeling

The universal joints (Fig. 2a) were modeled in accordance to the dimensions presented in Fig. 2b. The contacts in yoke's of each universal joint were modeled to have only one degree of freedom (rotation) with no friction.

The mechanisms were built by placing ten universal joints in series, composing a flexible shaft with a length of 940 mm. The contact of the universal joints was placed in the extremities and defined as rigid. Each universal joint was positioned with a 9° angle, thus the mechanisms presented an angle of 90° (Fig. 3).

The difference between the modeled mechanisms (Fig. 4a, b) is the adoption of a hydraulic hose (Fig. 4c), to reduce the system instability in one of them (Fig. 4b). Generally, this hose are composed by reinforced composite layers wound with reinforced fibers, rubber layers and polyethylene coating [9]. Their mechanical strength comes from the reinforcing fibers, as the rubber serves as a sealant [10]. The modeling of the hose was achieved by a rigid hollow tube curved in a 596.2 mm radius and an internal diameter of 33 mm. This assures that there is no initial interference between the universal joints and the hose.

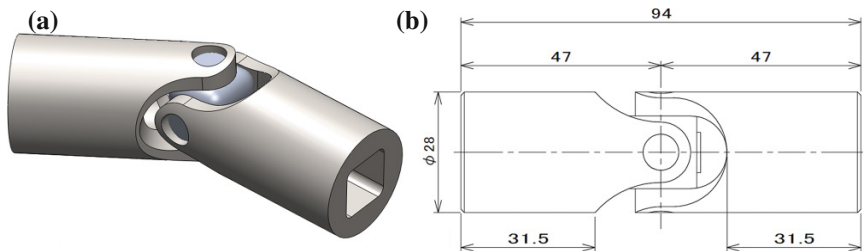
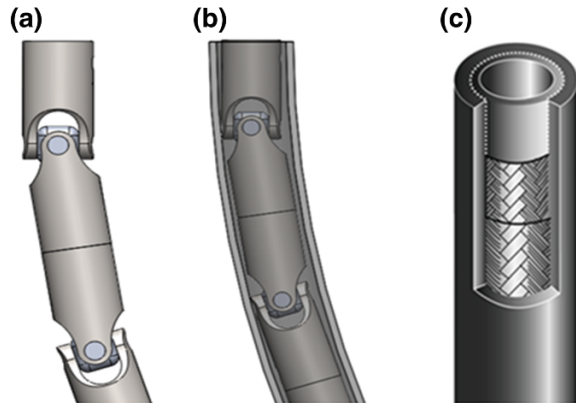


Fig. 2 Universal joint: **a** modeling; **b** dimensions



Fig. 3 Basic flexible shaft executing a 90° transmission

Fig. 4 Flexible shaft without (a) and with (b) hydraulic hose; individual hydraulic hose (c)



2.2 Motion Simulation

The motion simulation in the mechanisms was executed applying a constant rotary movement of 60 rpm by a virtual motor in one of the extremities (Fig. 5). It was defined that both extremities of the mechanisms would only be able to rotate in the plane of its cross section, thus no translation was allowed.

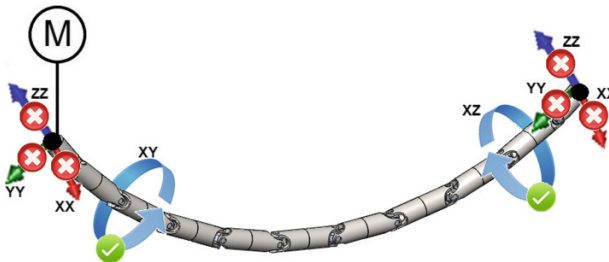


Fig. 5 Constraints on the motion simulation

Table 1 Characteristics of the materials and contacts

Material	Body	Type of material	Type of interaction
	Universal joints	Steel	Greasy
	Hydraulic hose	Rubber	
Friction	Type	Velocity (v)	Friction coefficient (μ)
	Static	0.10 mm/s	0.08
	Dynamic	10.16 mm/s	0.05
Elastic properties	Stiffness (k)	2,856 N/mm	
	Exponent (e)	1.1	
	Maximum damping (c _{max})	0.49 N	
	Penetration (d _{max})	0.1 mm	

Besides the established constraints, it was necessary to define the contact characteristics between the universal joints and the hydraulic hose (Table 1). The interaction was solved using the impact equation (Eq. 1):

$$F_n = k \times g^e + f(g, 0, 0, d_{max}, c_{max}) \times \frac{dg}{dt} \tag{1}$$

The force of impact is represented by F_n , k is the rigidity of the contact, e is the stiffening spring exponent of the system, g is the instant value of penetration, c_{max} is the maximum value of damping and d_{max} is the maximum value of penetration used by the software solver while applying c_{max} . As for the function $f(g, 0, 0, d_{max}, c_{max})$, it is used by the software to solve the instant force of collision. The solver used to perform, describes the location and orientations of all bodies in the mechanical system, considering the relationships and contacts between them.

2.3 Result Comparison Criterion

In order to compare the results, there was defined a methodology. As the objective was to determine if it is advantageous to use a hydraulic hose to reduce instability, the adopted comparison criterion was the measurement of the instant eccentricity in three universal joints of the mechanisms (Fig. 6). This was achieved by monitoring the linear displacement on the XX and YY axis and calculate their vectorial addition.

3 Results and Discussion

The execution of motion simulations in the referred mechanisms (with and without the hydraulic hose) allowed the determination of the instantaneous eccentricity in three of the universal joints and consequently to determine if there was a reduction of the instability while transmitting rotary movement.

Fig. 6 Monitored universal joints

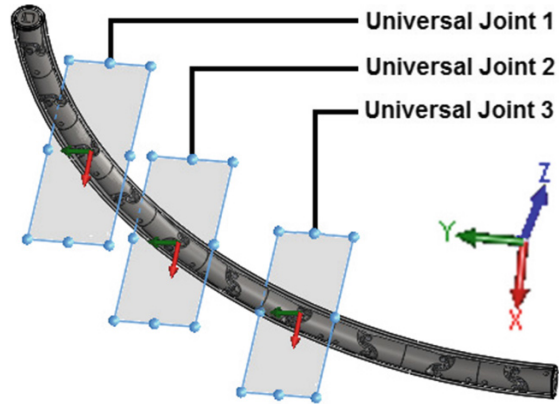
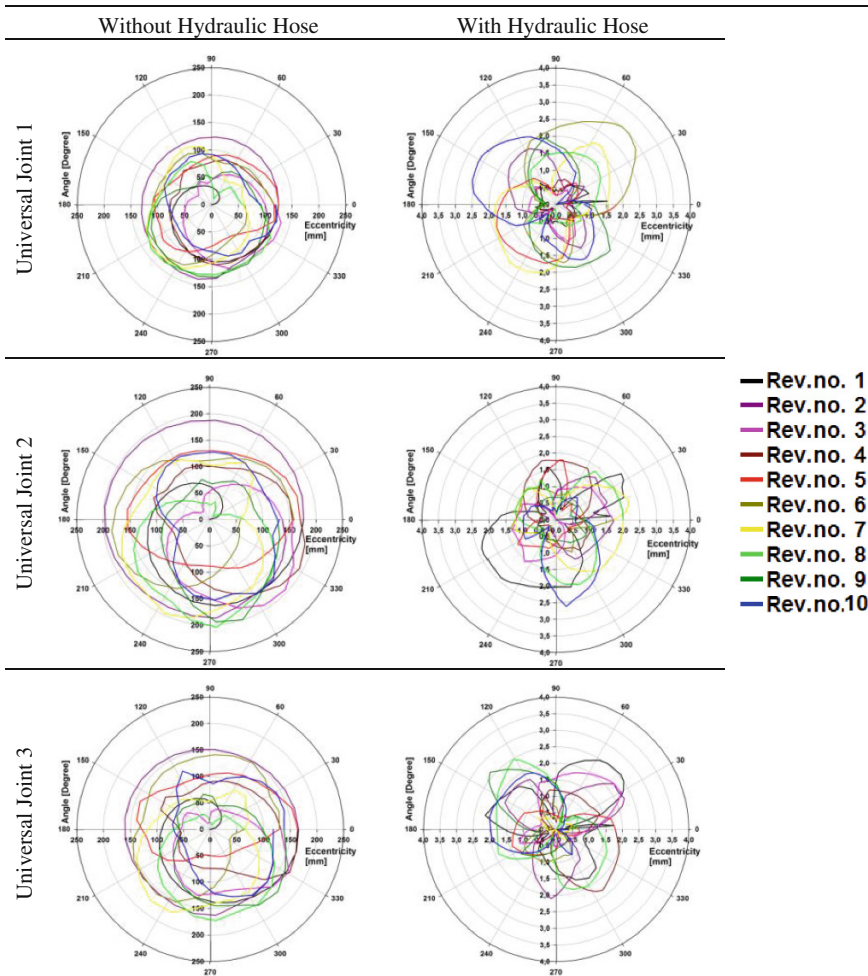


Table 2 Mechanism eccentricity in each revolution

No. of Revolutions	Without Hydraulic Hose	With Hydraulic Hose
0 [Initial]		
2		
4		
6		
8		
10		

Table 3 Eccentricity values of each mechanism per revolution



When the universal joints are placed in series without the restriction of the hydraulic hose, except in their extremities which allow rotation but not translation, there is extreme instability (Table 2). Additionally, there is an immediate loss of the angle balance in each universal joint. This instability is hazardous to the movement transmission and to the mechanism itself. It leads to loss of efficiency, reduction of the life and eventually to its ruin. It can also be visualized, in Table 2, that the use of the hydraulic hose retains this instability by distributing the transmission angle uniformly.

Interpreting Table 3, it can be confirmed that the use of a hydraulic hose is a possible solution to distribute uniformly the transmission angle and reduce the mechanism instability. The maximum eccentricity on the unrestrained solution reached values near 204 mm. However, for the retaining hydraulic hose, this value is nearly seventy times smaller, has the value of this solution is near 3 mm.

Additionally, it can be observed that the instability of the system is more significant in the middle of the mechanism, for the unrestrained mechanism. In the mechanism with the hydraulic hose, it tends to be more stable in the middle and more unstable near the extremities. This can be an advantage for the viability of the solution, given that in a real situation, the extremities of mechanism will be fixed to other mechanisms that can support the overall small instable tendencies.

4 Conclusions

The focus of this paper was the study of a hydraulic hose as a way to reduce the instability of a mechanism composed by universal joints placed in series to transmit rotary movement in angular and non-collinear situation.

In order to obtain conclusions on this solution, there were executed motion simulations in two similar mechanisms whose main difference was their insertion or non insertion, in the referred hydraulic hose. Afterwards, their eccentricity was measured while applying a rotary movement on one extremity of the mechanisms.

The collected data, namely the values of eccentricity and the visualization of the behavior of the mechanisms, determines that the use of a hydraulic hose may be a possible solution as mean to reduce the instability and balance the transmission angle between the universal joints. However, it must be taken in account that this is merely a motion study, whose objective was to determine if the exploration of the hydraulic hose is a possible solution to be further developed. There have not been taken in account the thermal and mechanical stresses generated by the friction and contacts. This will certainly change the mechanical properties of the components and the dynamic behavior of the system.

Considering these facts, the presented study is relevant as a validation for future research in this area, showing a possible path for the elaboration of universal joints in the design of a flexible shaft.

References

1. Zhang G et al (2014) Study of the workspace of a class of universal joints. *Mech Mach Theory* 73:244–258
2. Liebing R (2012) Flexible shaft arrangement—Patent US 2012-0264523 A1
3. Staniszewski W et al (2013) Intermodulation-resistant flexible shaft having electrically insulating coated wires—Patent US20130217509 A1
4. Guido G, Boehm M (2013) Flexible options with flexible shafts. *Transm Eng* 40–42

5. Mazzei AJ Jr et al (1999) Dynamic stability of a rotating shaft driven through a universal joint. *J Sound Vib* 222(1):19–47
6. Lu JW et al (2013) Dynamic analysis of cross shaft type universal joint with clearance. *J Mech Sci Technol* 27(11):3201–3205
7. Grossman K, Kauschinger B (2012) Eccentric universal joints for parallel kinematic machine tools. *Prod Eng Res Dev* 6:521–529
8. Bulut G, Parlar Z (2011) Dynamic stability of a shaft system connected through a Hooke's joint. *Mech Mach Theory* 46:1689–1695
9. Zhou WD et al (2013) Finite element analysis of high-pressure hose for radial horizontal wells in coalbed methane extraction. *J Coal Sci Eng* 19(2):182–186
10. Bregman PC et al (1993) Strength and stiffness of a flexible high-pressure spiral hose. *Acta Mech* 97:185–204

Propulsion Architectures Using Mechanical Energy Storage

Madhusudan Raghavan

Abstract Alternative propulsion architecture systems are described, and evaluated from the standpoint of efficiency and potential for use as mechanical energy storage systems in automobiles. We study air hybrids and describe modelling and simulation results along with experimental data from a test-bed to assess round-trip efficiencies of such storage systems. This is followed by an assessment of hydraulic hybrids and flywheel hybrids. These systems are sized for comparable applications. Simulations are then used to objectively compare losses in these systems and to estimate operating round-trip efficiencies in energy storage applications.

Keywords Hybrid propulsion · Mechanical · Flywheel · Hydraulic · Compressed air

1 Introduction

Hybrid propulsion systems offer improved fuel economy over conventional powertrains by recuperating kinetic energy via regenerative braking, storing the energy in on-board storage systems, using this energy when appropriate to offset accessory loads and to supplement driveline torque thereby reducing engine fuel consumption. Most light-duty hybrid vehicles to date have relied on electrical systems to accomplish powertrain hybridization via the addition of onboard electric motors and batteries. In the electrified powertrain literature, Robinette and Powell [1], describe the use of GM's 12 V start/stop system to turn the engine off and on during periods of vehicle idle. Hawkins et al. [2] describe GM's eAssist powertrain, which delivers approximately three times the peak electric boost and regenerative braking capability of GM's first generation 36 V Belted Alternator Starter.

GM's Two-Mode Hybrid system, produced for transit buses, with three planetary gear sets coaxially aligned, is described by Schmidt [3]. Grewe et al. [4],

M. Raghavan (✉)
General Motors R&D, Warren, USA
e-mail: madhu.raghavan@gm.com

describe the GM Two-Mode Hybrid system, adapted for full-size trucks and full-utility SUVs. This system integrates two electromechanical power-split operating modes with four fixed gear ratios and provides significant fuel savings. Miller et al. [5] describe GM’s Voltec 4ET50 multi-mode electric transaxle, which introduces a unique two-motor EV driving mode that allows both the driving motor and the generator to simultaneously provide tractive effort while reducing electric motor speeds and the total associated electric motor losses.

In the present work, we explore non-electrical approaches to hybridization. We describe air hybrids, flywheel hybrids and hydraulic hybrids and arrive at comparative estimates of their efficiencies using a combination of modeling, simulation and experimental testing.

2 Air Hybrid System Concept

The air hybrid system that we studied, is shown in Fig. 1. It was developed as part of a mechanical hybrid test-bed by our research partners, (Prof. James Schmiedeler and his team) at the University of Notre Dame [6]. It is comprised of a compressor-expander connected to the drivetrain through an infinitely variable transmission (IVT). The compressor-expander facilitates bi-directional energy exchange with the air tank over a range of pressures, while the Infinitely Variable Transmission (IVT) enables changes in power demand by changing the gear ratio. To keep things

Fig. 1 Air hybrid architecture test-bed

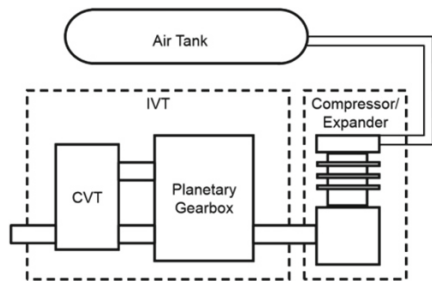
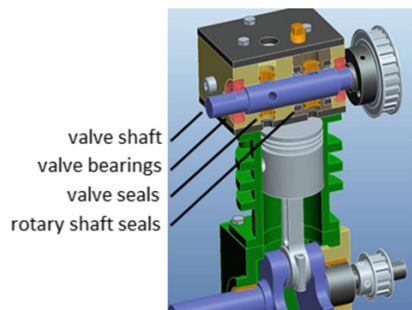


Fig. 2 Compressor-expander



simple, the team created a compressor-expander (Fig. 2) that can operate at a range of pressures.

When tank pressures are higher or lower than the design pressure, the compression and expansion events are less than ideal. Therefore the team inserted check valves in the system architecture to prevent over-compression and over-expansion and to broaden the regime of efficient operation of the system. Also a novel rotary valve system consisting of a cylindrical valve shaft with ports cut transversely through it was constructed.

The team also created a system model that comprehends valve flow dynamics, mass flow rates, check valve positions and their rates of change, etc. Additionally piston work and thermal conduction were also calculated to enable the formulation of expressions describing the rate of energy change of the system in terms of work done, heat lost, and enthalpy. Additionally rates of change of temperature and pressure were also formulated in terms of system parameters. Combining this thermodynamic model with a friction and kinematics model for the compressor allowed the prediction of compressor torque. The model results were then compared with results from an experimental test-bed of the cylinder and tank.

2.1 Experimental Setup

The basic experimental setup, consists of a high current power supply, a custom high power voltage regulator, a brushed DC motor, a servo drive, a single board computer, the compressor/expander, and the air tank. The IVT functionality was simulated by using the DC motor to set the speed of the system. The experimental pneumatic system is built around an off-the-shelf compressor, the Champion B1, which has a single cylinder, cast iron block, and a total swept volume of 145.2 cc. The valve port dimensions correspond to a design pressure of 200 kPa.

The pressure and temperature of the tank are monitored directly using a pressure sensor and a 15 mm temperature probe that extends into the tank. As expected, peak efficiency in compression mode occurs near the 200 kPa design pressure and tapers off at high pressures due to blow-back and other non-ideal behavior. At higher pressures and power levels, friction has a minimal effect on the overall efficiency, but at lower pressures, the difference between the efficiency surfaces with and without friction is very large.

The highest fixed speed round-trip efficiency (RTE) recorded on the experimental system is 8.5 %. Higher efficiencies are possible, with perhaps the best case RTE on the order of 16 % for the bench-top design. The main factors leading to efficiency loss are friction, insufficient valving, and thermal losses in the uninsulated tank. Despite these deficiencies in the current prototype, the matched simulation model for the compressor/expander (Fig. 3) shows that the concept could potentially offer higher efficiency with a relatively simple design. The most likely scenario, involving improved valving, reduced friction, and an insulated/heated tank could potentially reach an RTE efficiency of 47 %.

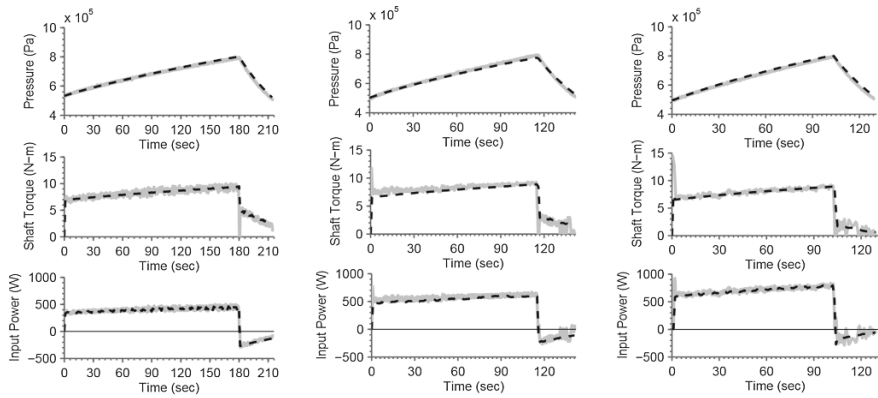


Fig. 3 Charge/discharge cycle at 500, 700, and 900 rpm. *Gray Expt., Dotted Modeling*

3 Flywheel and Hydraulic Energy Storage

The research described in this section was executed by our partners at the Ohio State University, Center for Automotive Research (Prof. Giorgio Rizzoni and his team) [7]. The components of the flywheel and hydraulic energy storage systems were sized to have the same power and energy capacity (~ 30 kW, ~ 150 kJ). The efficiency data for the components (e.g., clutch, CVT) were obtained from literature and datasheets. For this example, the platform was a 2009 mid-sized rear wheel drive SUV (1,900 kg mass, 0.357 m tire radius, 2.77:1 final drive ratio). The flywheel and hydraulic systems were connected in parallel to the vehicle driveshaft (see Fig. 4) and sized for a US06 driving schedule. Based on this, the key design specifications were: (a) vehicle deceleration = 1.5 m/s^2 , initial vehicle speed = 18 m/s (40 mph), final vehicle speed = 0 m/s, energy available = 300 kJ.

3.1 Flywheel Energy Storage System Design

The system design constraints were as shown in Table 1. A preliminary value of the inertia of the flywheel can be calculated starting from the equation of the mechanical energy:

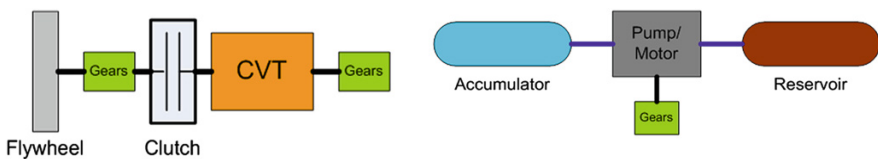


Fig. 4 Flywheel and hydraulic energy storage architectures

Table 1 Flywheel system design constraints

Design constraints	
Maximum flywheel speed	2100 rad/s (20,000 rpm)
Maximum CVT ratio	2.2:1
Minimum CVT ratio	0.4:1
Maximum clutch torque	300 Nm
Maximum CVT torque	300 Nm

$$I_{fly} = \frac{2 * E_{fly}}{(\omega_{fly,max}^2 - \omega_{fly,min}^2)} \tag{1}$$

where E_{fly} is the flywheel kinetic energy, I_{fly} is the flywheel inertia, $\omega_{fly,max}$ and $\omega_{fly,min}$ are the maximum and minimum flywheel speeds, respectively. For this case, with a minimum flywheel speed of 10,000 rpm and a desired energy of 300 kJ, the required inertia is 0.18 kgm². In the ideal case, all energy from the deceleration of the vehicle is absorbed by the flywheel. By knowing the CVT ratio and the vehicle speed, the flywheel speed can be calculated based upon the actual value of the CVT ratio and the values of the gear ratio of all the intermediate gears between the flywheel and the driveshaft [7]. Using simple optimization techniques it was determined that the optimum gearing for $g_{CVT} * g_{fly}$ is 20.5 (g_{CVT} is the CVT to driveshaft gearing, g_{fly} is the flywheel to CVT gearing.) For this example, we will assume $g_{CVT} = 4$ and $g_{fly} = 5.1$ ($g_{CVT} * g_{fly} = 20.4$). For the case where maximum flywheel speed is reached, knowing the gear ratios and maximum CVT ratio, the minimum vehicle speed for the flywheel to be connected can be determined according to the following expression:

$$V_{veh} = \frac{\omega_{fly} * r_w}{g_{CVT} * g_{fly} * g_{FD} * N_{CVT}} \tag{2}$$

where V_{veh} is the vehicle speed, r_w is the drive wheel ratio, g_{FD} is the final drive ratio, and N_{CVT} is the CVT ratio. For this case, the minimum velocity is 6.0 m/s. Table 2 summarizes the design parameter for the flywheel system.

Table 2 Flywheel storage system design parameters

Design parameters	
Flywheel inertia	0.18 kg m ²
CVT to driveshaft ratio	4:1
Flywheel to CVT ratio	5.1:1
Maximum flywheel speed	20,000 rpm
Minimum flywheel speed	10,000 rpm

3.2 Hydraulic Energy Storage System Design

The design constraints and steps for system design are a maximum accumulator pressure of 350 bar and an accumulator pressure ratio limitation of 4:1. The maximum energy for a range of accumulator sizes can be calculated for a range of pre-charge pressures. The smallest accumulator that satisfies the energy target was chosen in order to minimize size and weight penalties. Based on a simple optimization exercise [7], the commonly available 30 L accumulator size was selected. The gearing between the pump and driveshaft determines the speed range at which the pump can be operated. Based on initial vehicle speed for a typical braking event and maximum pump speed, gearing can be calculated.

$$g_{pump} = \frac{\omega_{pump,max} * r_w}{V_{veh} * g_{FD}} \quad (3)$$

g_{pump} is the gear ratio between pump and driveshaft, ω_{pump} is the pump speed. For the conditions given above and a conservative maximum pump speed of 2,500 rpm (262 rad/s), the gearing between the pump and vehicle is 1.9:1. The desired pump torque for a given condition is given by the following equation:

$$T_{pump,des} = \frac{M_{eff} * \frac{dV_{veh}}{dt} * r_w}{g_{FD} * g_{pump}} \quad (4)$$

M_{eff} is the effective vehicle mass. For the conditions given, the desired torque is 193 Nm. Knowing the desired torque, the necessary pump displacement required to provide this torque can be calculated:

$$D_{max,pump} = \frac{T_{pump,avail}}{\Delta P_{pump}} \quad (5)$$

The displacement necessary to deliver 193 Nm of torque is 110 cc/rev. Since a pump of this size and weight (~51 kg) is not feasible to be housed on a mid-sized SUV, a smaller pump with a displacement of 75 cc/rev, weighing 30 kg was selected for use. This pump is capable of providing 131 N with a delta pressure of 110 bar.

3.3 System Performance

The above mechanical and hydraulic storage system designs were compared in simulation, with the vehicle assumed to start from an initial velocity of 12 m/s with a net amount of energy of 75 kJ available for recovery (all losses subtracted a priori). The energy of 75 kJ is close to the weighted mean value for the net energy available during a braking event for the FTP cycle. Efficiencies were calculated as:

$$\begin{aligned}
 n_{one-way} &= \frac{\text{Maximum Stored Energy} - \text{Initial Stored Energy}}{\text{Initial Vehicle Energy} - \text{Minimum vehicle Energy}} \\
 n_{two-way} &= \frac{\text{Final Vehicle Energy} + \text{Net } \Delta \text{ in Stored Energy}}{\text{Initial Vehicle Energy}}
 \end{aligned}
 \tag{6}$$

3.3.1 Flywheel System

Figure 5 shows the results for the flywheel energy storage system. The flywheel starts at 10,000 rpm. At $t = 25$ s, a positive torque is commanded from the energy storage system. Initially, the clutch is slipped until lockup can occur, at which point the CVT ratio begins to vary until minimum flywheel speed is reached. At that point the flywheel energy storage system has exhausted its energy supply and would be decoupled from the drivetrain. Over a range of simulation conditions, the flywheel system showed a weighted mean round-trip efficiency of 59.7 %.

It is worth observing that, due to the energy losses that occur during the process, the final vehicle speed at the end of the acceleration phase is lower than the initial value. The end flywheel speed is also slightly less due to dynamic effects in the CVT controller, but still near the desired minimum speed of 10,000 rpm. Selecting gearing that allows for energy recovery at higher speeds leads to increasing clutch slippage at low speeds before the system can be completely coupled. These two factors lead to the low efficiency of the system design to accommodate the maximum values.

3.3.2 Hydraulic Energy Storage System

Figure 6 shows the results for the hydraulic energy storage system. Over a range of simulation conditions the hydraulic system showed a weighted mean round-trip efficiency of 47.7 %.

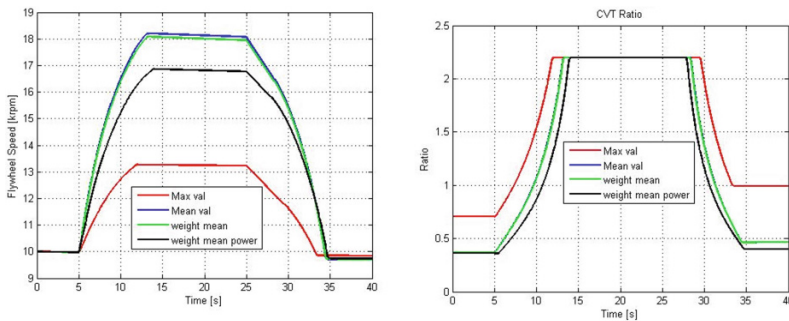


Fig. 5 Flywheel speeds and hybrid CVT ratio

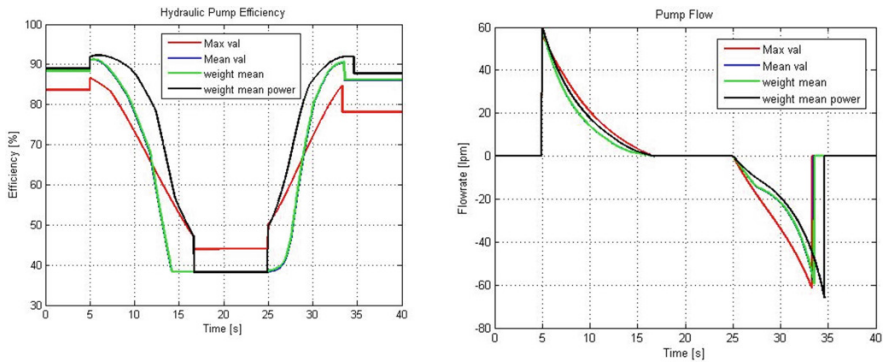


Fig. 6 Hydraulic pump efficiencies and flows

4 Conclusions

Mechanical energy storage systems were examined from the standpoint of establishing round-trip efficiencies for compressed air, flywheel, and hydraulic hybrid energy storage architectures. Our conclusions (subject to our assumptions which were constrained by available materials and components) are:

- air-storage systems showed a round-trip efficiency of approximately 10 % in practice, with the potential to go as high as 47 % with suitable valving, and thermal management
- flywheel storage systems showed a round-trip efficiency of approximately 60 %
- hydraulic storage systems showed a round-trip efficiency of approximately 48 %
- mechanical storage systems increase vehicle mass by approximately 4–5 %; this effect results in a 2–3 % increase in fuel consumption.

References

1. Robinette D, Powell M (2011) Optimizing 12 V start-stop for conventional powertrains. SAE 2011-01-0699
2. Hawkins S, Billotto F, Cottrell D, Houtman A, Poulos S, Rademacher R, Van Maanen K, Wilson D (2012) Development of general motors' eAssist powertrain. SAE Int J Altern Powertrains 1(1):308–323
3. Schmidt M (1999) Two-mode, compound-split electromechanical vehicular transmission. U.S. patent 5,931,757, 3 Aug 1999
4. Grewe T, Conlon B, Holmes A (2007) Defining the general motors 2-mode hybrid transmission. SAE 2007-01-0273
5. Miller M, Holmes A, Conlon B, Savagian P (2011) The GM Voltec 4ET50 multi-mode electric transaxle. SAE 2011-01-0887

6. Brown T, Atluri P, Schmiedeler JP (2014) Design of high speed rotary valves for pneumatic applications. *J Mech Des, Trans ASME* 136(1):015001
7. Francfort J, Carlson R (2012) Vehicle mass impact on vehicle losses and fuel economy. Paper # VSS 074, DOE annual merit review conference, 16 May 2012, Washington D.C

Part XII
Linkages and Manipulators

Closed-Chain Principal Vector Linkages

V. van der Wijk

Abstract For high-speed robotics dynamic balance is an important property for low base vibrations and short cycle times. To consider dynamic balance in the beginning of the design process of a manipulator, mechanism solutions can be synthesized from principal vector linkages, which are fundamental kinematic architectures with inherent force balance. In this paper it is shown how a closed-chain principal vector linkage can be analyzed as an open-chain principal vector linkage by modeling one element in a closed chain with two real and two virtual equivalent masses. The results are validated with a dynamic simulation.

Keywords Dynamic balance • Closed chain • Principal vector linkage • Equivalent masses

1 Introduction

The design of multi degree-of-freedom (DoF) mechanisms or manipulators that are dynamically balanced (i.e. shaking force balanced and shaking moment balanced) is increasingly important for high-speed applications such as pick and place tasks. With dynamic balance base vibrations are eliminated which helps, among others, to improve accuracy and to reduce cycle times [3, 7].

To obtain dynamically balanced mechanisms that are profitable in practice, it is important to consider dynamic balance in the beginning of the design process instead of aiming at balancing a mechanism after its kinematic synthesis with techniques as shown in [1, 2, 9]. This can be achieved by synthesis of balanced mechanisms from principal vector linkages, which are inherently force-balanced

V. van der Wijk (✉)

Faculty of Engineering Technology, Laboratory of Mechanical Automation and Mechatronics, University of Twente, Enschede, The Netherlands
e-mail: v.vanderwijk@utwente.nl

linkage architectures [5, 6] from which also moment balance solutions can be derived [4].

While principal vector linkages that are based on open kinematic chains have been investigated in detail [6], a principal vector linkage of a closed kinematic chain was only presented briefly [5]. The aim of this paper is to investigate in detail the design of a closed-chain principal vector linkage. Therefore a new way to model a general element in a closed chain mass-equivalently—with two real and two virtual equivalent masses—is presented. These equivalent masses can be included in the analysis of the mechanism without the modeled element, which is an open-chain principal vector linkage. This approach is shown for a principal vector linkage of a closed chain of four elements and the results are verified with a dynamic simulation.

2 Analysis of a Closed-Chain Principal Vector Linkage

In Fig. 1 a closed-chain principal vector linkage of the four principal elements A_0A_1 , A_1A_2 , A_2A_3 , and A_3A_0 and the principal vector links P_1B_1 , P_2B_1 , P_2B_2 , P_3B_2 , B_1S , and B_2S is shown. All elements have a general CoM and the linkage is designed such that the common CoM of all elements is in joint S for all motion of the mechanism. The design of the principal vector links is determined with the principal dimensions a_1 , a_{21} , a_{23} , and a_3 , which depend on the locations of the principal points P_1 , P_2 , and P_3 in their elements.

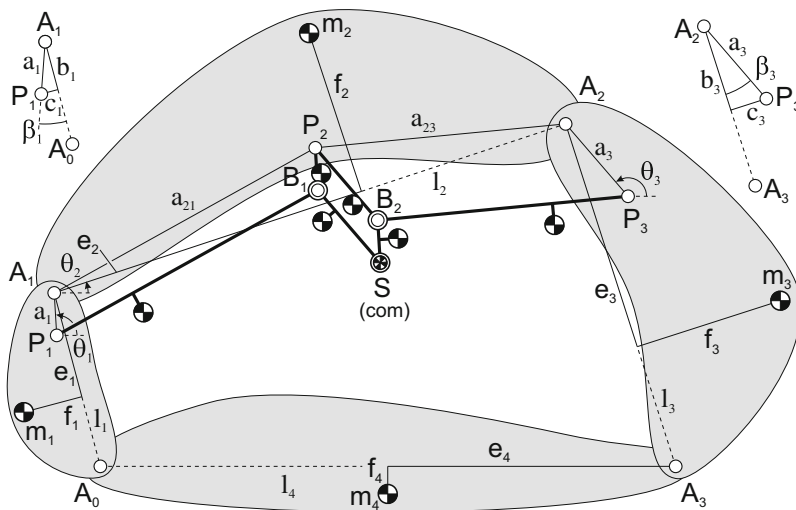


Fig. 1 Closed-chain principal vector linkage of the four principal elements A_0A_1 , A_1A_2 , A_2A_3 , and A_0A_3 . All elements have a general CoM of which the common CoM is in joint S for all motion

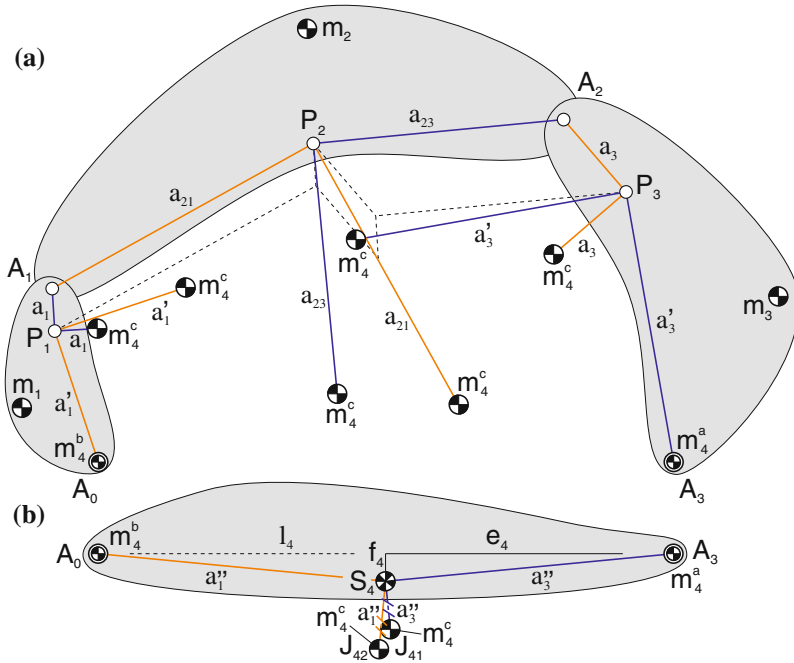


Fig. 2 a Mass equivalent principal open chain with the projection of the equivalent masses m_4^a , m_4^b , and m_4^c (the principal vector links are not shown). b Mass equivalent model of element A_0A_3 with real equivalent masses m_4^a and m_4^b in joints A_3 and A_0 , respectively, and a virtual equivalent mass in both J_{41} and J_{42} where S_4 is the common CoM of the four equivalent masses

When element A_0A_3 is eliminated, the remaining mechanism is an open-chain principal vector linkage of three principal elements in series, of which the analysis is shown in [6]. It will be shown that a closed-chain principal vector linkage can be analyzed similarly where the eliminated element is considered with equivalent masses that are projected onto the open-chain principal vector linkage.

Element A_0A_3 can be modeled mass equivalently as shown in Fig. 2b with an equivalent mass $m_4^a = m_4(1 - e_4/l_4)$ in A_3 , an equivalent mass $m_4^b = m_4e_4/l_4$ in A_0 , and an equivalent mass $m_4^c = m_4f_4/l_4$ in both J_{41} and J_{42} , which are at a distance a_3'' and a_1'' from S_4 , respectively, as illustrated. The CoM of the four equivalent masses is in S_4 , which is the location of the CoM of A_0A_3 in Fig. 1. Since the sum of m_4^a and m_4^b equals the real mass m_4 of the element, m_4^a and m_4^b will be referred to as real equivalent masses, and m_4^c , which does not represent the real mass of the element, will be referred to as a virtual equivalent mass.

Figure 2a shows the projection of the equivalent masses on the open-chain principal vector linkage. The result will be named the mass equivalent principal open chain (MEPC). The real equivalent masses m_4^a and m_4^b are located in the joints A_3 and A_0 , respectively, while the virtual equivalent mass m_4^c is located twice in each principal element about the principal points P_1 , P_2 , and P_3 . Their locations are

determined by distances $a'_1, a_1, a_{21}, a_{23}, a_3,$ and a'_3 from the principal points in the directions equal to the direction of the virtual equivalent mass in the mass equivalent model in Fig. 2b.

For analysis of the MEPC in Fig. 2a as an open-chain principal vector linkage, the virtual equivalent masses have the property that they act as a real mass for rotational motion of the element onto which they are projected while they are massless for translational motion of their element. In other words, a virtual equivalent mass has linear momentum only when the element onto which it is projected rotates while for translational motion of the element its linear momentum is zero.

As in [6], an open-chain principal vector linkage can be analyzed by investigating the linear momentum of each relative DoF individually. Figure 3a shows the relative motion of DoF 1 of the MEPC in Fig. 2a where elements A_1A_2 and A_2A_3 solely translate and element A_0A_1 solely rotates about P_1 . This means that the virtual masses in A_1A_2 and A_2A_3 are zero, while the virtual masses in A_0A_1 act as a real mass. The linear momentum of this motion can be represented with the Equivalent Linear Momentum System (ELMS) in Fig. 4a, which has equal linear momentum for rotation about P_1 . Similarly, Fig. 3b shows the relative motion of DoF 2 where elements A_0A_1 and A_2A_3 solely translate and element A_1A_2 solely rotates about P_2 . This means that the virtual masses in A_0A_1 and A_2A_3 are zero, while the virtual masses in A_1A_2 act as a real mass. The linear momentum of this motion can be represented with the ELMS in Fig. 5, which has equal linear momentum for rotation about P_2 . Figure 3c shows the relative motion of DoF 3 where elements A_0A_1 and A_1A_2 solely translate and element A_2A_3 solely rotates about P_3 . This means that the virtual masses in A_0A_1 and A_1A_2 are zero, while the virtual masses in A_2A_3 act as a real mass. The linear momentum of this motion can be represented with the ELMS in Fig. 4b, which has equal linear momentum for rotation about P_3 .

The force balance conditions, i.e. the conditions for the principal vector linkage for which the common CoM is in S , can be derived from the linear momentum of each DoF which has to be constant. The linear momentum of DoF 1 can be written from the ELMS in Fig. 4a rotating about P_1 with respect to reference frame x_1y_1 , which has the x_1 -axis aligned with line A_0A_1 , as

$$\frac{\bar{L}_1}{\dot{\theta}_1} = \mu_{11} \begin{bmatrix} c_1 \\ b_1 - l_1 \end{bmatrix} + \mu_{12} \begin{bmatrix} c_1 - f_1 \\ b_1 - e_1 \end{bmatrix} + v_{12} \begin{bmatrix} l_1 \\ 0 \end{bmatrix} + \mu_{13} \begin{bmatrix} c_1 \\ b_1 \end{bmatrix} - v_{13} \begin{bmatrix} -b_1 \\ c_1 \end{bmatrix} = \begin{bmatrix} 0 \\ 0 \end{bmatrix} \tag{1}$$

with $\mu_{11} = m_4^b, \mu_{12} = m_1, \mu_{13} = m_2 + m_3 + m_{31} + m_{32} + m_4^a + m_{12}p_{12}/a_1 + m_{13}p_{13}/a_1, v_{12} = m_4^c,$ and $v_{13} = m_{12}q_{12}/a_1 + m_{13}q_{13}/a_1$ and where b_1 and c_1 define P_1 as illustrated in Fig. 1. The linear momentum of DoF 2 can be written from the ELMS in Fig. 5 rotating about P_2 with respect to reference frame x_2y_2 , which has the x_2 -axis aligned with line A_1A_2 , as

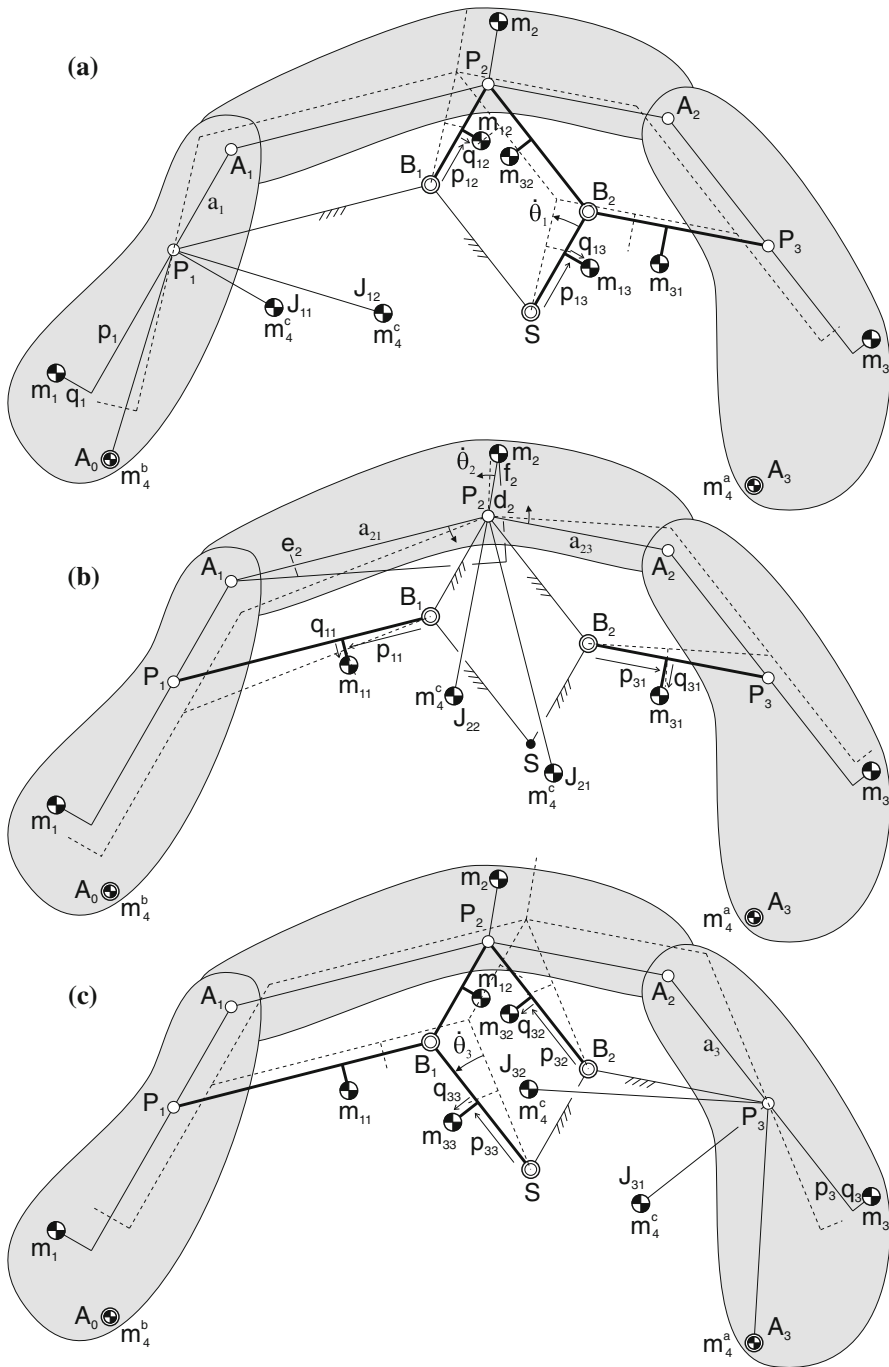


Fig. 3 Individual motions of (a) DoF 1; (b) DoF 2; and (c) DoF 3

Table 1 Parameters of the principal vector linkage in Fig. 1 for simulation

(m)	(kg)	(m)	(m)	(m)
$l_1 = 1.0$	$m_1 = 2.10$	$e_1 = 0.69$	$f_1 = 0.21$	$a_1 = 0.2206$
$l_2 = 3.0$	$m_2 = 3.00$	$e_2 = 1.80$	$f_2 = 0.93$	$b_1 = 0.2161$
$l_3 = 2.0$	$m_3 = 2.20$	$e_3 = 1.30$	$f_3 = 0.84$	$c_1 = 0.0439$
$l_4 = 3.2$	$m_4 = 1.10$	$e_4 = 1.312$	$f_4 = 0.10$	$a_{21} = 1.6838$
	$m_{11} = 0.20$	$p_{11} = 1.00$	$q_{11} = 0.20$	$a_{23} = 1.3770$
	$m_{12} = 0.10$	$p_{12} = 0.12$	$q_{12} = 0.09$	$b_{21} = 1.6565$
	$m_{13} = 0.11$	$p_{13} = 0.10$	$q_{13} = 0.10$	$c_2 = 0.3018$
	$m_{31} = 0.20$	$p_{31} = 0.85$	$q_{31} = 0.20$	$a_3 = 0.5140$
	$m_{32} = 0.105$	$p_{32} = 0.25$	$q_{32} = 0.08$	$b_3 = 0.4734$
	$m_{33} = 0.09$	$p_{33} = 0.27$	$q_{33} = 0.10$	$c_3 = 0.2004$

with $\mu_{31} = m_1 + m_2 + m_{11} + m_{12} + m_4^b + m_{32}p_{32}/a_3 + m_{33}p_{33}/a_3$, $\mu_{32} = m_3$, $\mu_{33} = m_4^a$, $v_{31} = m_{32}q_{32}/a_3 + m_{33}q_{33}/a_3$, and $v_{32} = m_4^c$ and where b_3 and c_3 define P_3 as illustrated in Fig. 1. From these linear momentum equations the six force balance conditions of the closed-chain principal vector linkage in Fig. 1 are obtained as:

$$\begin{aligned}
 &(\mu_{11} + \mu_{12} + \mu_{13})c_1 + v_{13}b_1 - \mu_{12}f_1 + v_{12}l_1 = 0 \\
 &(\mu_{11} + \mu_{12} + \mu_{13})b_1 - v_{13}c_1 - \mu_{12}e_1 - \mu_{11}l_1 = 0 \\
 &(\mu_{21} + \mu_{22} + \mu_{23})c_2 + (v_{21} - v_{23})b_{21} - \mu_{22}f_2 + v_{23}l_2 = 0 \\
 &-(\mu_{21} + \mu_{22} + \mu_{23})b_{21} + (v_{21} - v_{23})c_2 + \mu_{22}e_2 + \mu_{23}l_2 = 0 \\
 &(\mu_{31} + \mu_{32} + \mu_{33})c_3 + v_{31}b_3 - \mu_{32}f_3 + v_{32}l_3 = 0 \\
 &-(\mu_{31} + \mu_{32} + \mu_{33})b_3 + v_{31}c_3 + \mu_{32}e_3 + \mu_{33}l_3 = 0
 \end{aligned} \tag{4}$$

3 Dynamic Simulation

To validate the results, a dynamic model of the principal vector linkage in Fig. 1, where the only connection with the base is a pivot in S , was made in Spacar¹ with the parameters in Table 1. The parameters in the first four columns were chosen with which the parameters in the last column were calculated from Eq. 4. For the simulation time of 0.5 s a torque $\tau_1 = 50 \cos(4\pi t)$ was applied to element SB_1 and a torque $\tau_2 = -\tau_1$ was applied to element SB_2 . The dynamics were solved with solver ODE45 (Dormand-Prince) with a maximal step size of 0.0001s and with a relative tolerance of $1e^{-12}m$. The reaction forces in the pivot with the base were recorded and are displayed in Fig. 6. These shaking forces are expected to be zero for force balance and show an error which is about the computation accuracy.

¹ <http://www.spacar.nl/>.

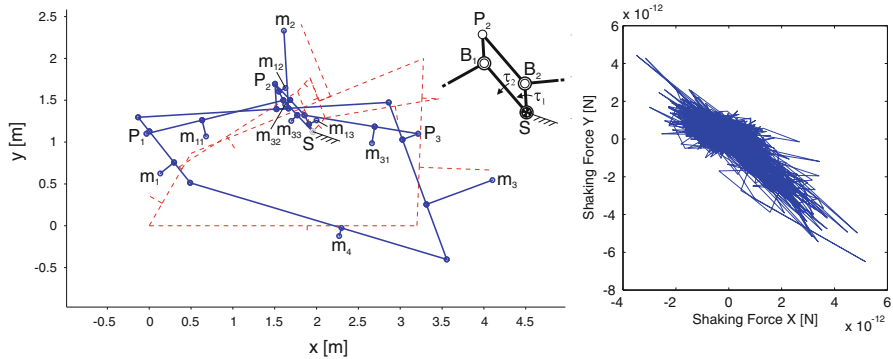


Fig. 6 The resulting shaking forces in pivot S show that the mechanism is force balanced about S

4 Discussion and Conclusion

This paper showed how a principal vector linkage of a closed chain of principal elements can be designed. A mass equivalent model of a general element in a closed chain with two real and two virtual equivalent masses was presented with which a closed-chain principal vector linkage was analyzed as an open-chain principal vector linkage. This mass equivalent model can be applied also for general dynamic modeling of mechanisms with closed kinematic chains. With the virtual equivalent masses the limitations of mass equivalent models with solely real equivalent masses in the joints as in [10] can be omitted and elements with generally located CoM can be considered in any kind of closed kinematic chain.

From the linear momentum equations of each relative DoF the force balance conditions were obtained with which the location of the principal point in each principal element was calculated. The ELMS of each relative DoF can be regarded also a reduced mass model where, for force balance, the principal point is also the common CoM in each model. Therefore the principal points are comparable with ‘barycenters’ as in [8]. How to derive the moment balance conditions of a closed-chain principal vector linkage is still an open issue. Then the presented mass equivalent model has to be inertia equivalent too. The simulated motion in Fig. 6 is moment balanced since the sum of the torques on the base equals zero.

References

1. Arakelian VG, Smith MR (2005) Shaking force and shaking moment balancing of mechanisms: A historical review with new examples. *Mech Des* 127:334–339
2. Arakelian VH, Smith MR (2005) Erratum: shaking force and shaking moment balancing of mechanisms: a historical review with new examples. *Mech Des* 127:1035
3. Lowen GG, Berkof RS (1968) Survey of investigations into the balancing of linkages. *Mechanisms* 3:221–231

4. Van der Wijk V (2013) Shaking-moment balancing of mechanisms with principal vectors and momentum. *J Front Mech Eng* 8(1):10–16
5. Van der Wijk V, Herder JL (2012) Inherently balanced 4R four-bar based linkages. In: Lenarčič J, Husty M (eds) Latest advances in robot kinematics. In: Proceedings of the IFToMM 13th international symposium on advances in robot kinematics. Springer, Berlin, pp 309–316, ISBN 978-94-007-4619-0
6. Van der Wijk V, Herder JL (2012) Synthesis method for linkages with center of mass at invariant link point—pantograph based mechanisms. *Mech Mach Theor* 48:15–28
7. Van der Wijk V, Krut S, Pierrot F, Herder JL (2013) Design and experimental evaluation of a dynamically balanced redundant planar 4-RRR parallel manipulator. *Int J Robot Res* 32(6):744–759
8. Wittenburg J (1977) Dynamics of systems of rigid bodies. B.G. Teubner, Stuttgart
9. Wu Y, Gosselin CM (2005) Design of reactionless 3-DOF and 6-DOF parallel manipulators using parallelepiped mechanisms. *IEEE Trans Rob* 21(5):821–833
10. Wu Y, Gosselin CM (2007) On the dynamic balancing of multi-dof parallel mechanisms with multiple legs. *Mech Des* 129:234–238

Design of a Low-Cost Manipulator Arm for Industrial Fields

E. Soriano, H. Rubio, C. Castejón and J.C. García-Prada

Abstract This study aims to build a manipulator arm defined by its universality, mobility, modularity, compatibility and economy. We develop an important part of both the basic and detail engineering required for the manufacture of a robotic arm. We propose some peculiarities in the design which differentiate it from other existing designs—namely, we use only linear pneumatic actuators in order to reduce production costs and to have a simple design for installation, starting and maintenance. To develop the design, last generation CAD–CAE software tools are used. These tools are employed for mechanical design and modelling as well as for dynamic simulation, mechanism analyses and the design and simulation of the pneumatic scheme. We define a complete design process and discuss applications designed for the manipulator arm. Once the basic specifications of the design are defined, we discuss the experimental prototype that was built. Based on that prototype, the design was refined until reaching its final version. We then developed a manipulator arm driven by pneumatic actuators.

Keywords Manipulator arm · Industrial robot · Pneumatic equipment · Kinematic model of planar link mechanism · Force control

1 Introduction

Nowadays, small- and medium-sized enterprises are subject to continuous changes and ever-increasing customer requests for the shortest delivery time, the best quality and the lowest product price. Companies are faced with unstable demands regarding the type and quantity of their products. Due to these demands, frequent

E. Soriano (✉) · H. Rubio · C. Castejón · J.C. García-Prada
Carlos III University of Madrid, Madrid, Spain
e-mail: esoriano@ing.uc3m.es

changes in the function and layout of work equipment are required. Problems with the adaptability of work equipment frequently occur. The adaptability of work equipment with regards to flexibility and responsiveness is defined by the equipment's universality, mobility, modularity, compatibility and economy [1]. Flexibility and cost are the main parameters governing the commercialisation of industrial robots, and the high expense of robot arms is an important factor blocking their commercialisation; an alternative approach is to employ low-cost manipulators that can be operated remotely. Such manipulators may be equipped with low-cost arms with open-loop control since many production actions do not require high speed or high precision. In addition to avoiding expensive feedback control systems, these manipulator arms need to be constructed from standard industrial components [2].

A manipulator arm is a type of (usually) programmable mechanical arm with functions similar to a human arm. Manipulator arms may be part of a more complex mechanism or be, itself, a complete mechanism. Parts of manipulator arms are interconnected by joints which allow either rotational movement, as a translational motion, or linear displacement.

Standard ISO 8373:1994 defines an industrial robot as a manipulator that is programmable in three or more axes: multipurpose, automatically controlled and reprogrammable. Within this definition, we find different types of industrial robots such as cartesian robots, cylindrical robots, spherical robots, SCARA robots, articulated robots and parallel robots.

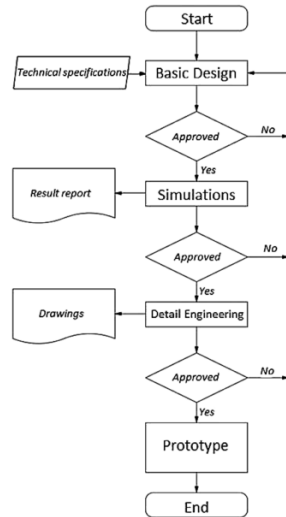
Recently, some pneumatic robot arms have been developed that can grasp objects without force sensors or feedback control [5, 6].

The articulated industrial robot is also called an industrial robotic arm or, simply, a manipulator arm. It is the most widely used type of robot in industrial applications, so there are many designs of robot arms [3, 4]. However, in our design, we introduce some particular characteristics that differentiate it from the rest. We use only linear pneumatic actuators in order to reduce production costs and to have a simple design for installation, starting and low-level maintenance.

2 Design Process

As shown in Fig. 1, we first defined the basic technical specifications required to start the design, which was based on data obtained from previous designs and features of the pneumatic system. Once the simulation results were satisfactory, we proceeded to the detail engineering stage and proposed drawings for manufacture and assembly. Finally, we tested the operation of the prototype in various applications.

Fig. 1 Design sequence



3 Manipulator Arm Design

One method of moving a manipulator arm is called articulated geometry. Robots with articulated geometry are broken into sections by joints. There might, for example, be base rotation, elevation and reach. There are several different articulated geometries for any given number of degrees of freedom. Our proposed manipulator arm consists of a pneumatic hand and pneumatic wrist.

We propose some peculiarities in the design which differentiate it from other existing designs. We use only linear pneumatic actuators, in order to make a low-cost design. Pneumatic actuators are widely used due to its simplicity, few break-downs and simple reparation. We avoid using complicated pieces made from cast iron or requiring high cost of tooling, how is the case of parts made by stamping. These pieces raises the costs for small series manufacture, the design is intended to be produced for special applications, performing relatively simple tasks. We make a simple and economical design without complex control system in order to reduce cost of both production and maintenance, we aim to minimize the cycle cost product life.

The manipulator arm is designed by using a planar ten-link mechanism and rotation about its central axis, as shown in Fig. 2.

Note that the planar ten-link mechanism can be considered as the superposition of three four-link mechanisms, so we take into account the assembly’s movement when we apply motion to one actuator and keep two others fixed.

Technical specifications for the low-cost manipulator arm are summarized in Table 1.

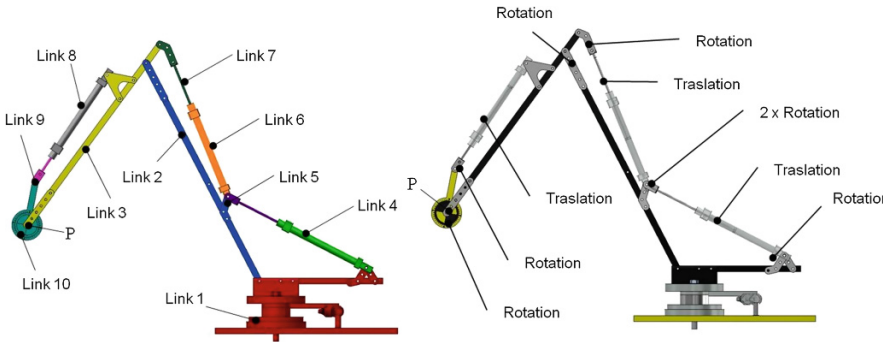


Fig. 2 Planar ten-link mechanism

Table 1 Technical specifications

Payload (N)	Robot mounting	Controllers	Protection	Weight (N)	Power (W)	Maximum speed (°/s)		
						X	Y	Z
50	Any angle	Pneumatic	IP67	260	400	450	450	720

We use only linear pneumatic actuators, which limits us in work range and some performance characteristics such as maximum speed. However, on the other hand, we obtain the lowest cost.

3.1 Mechanical Analysis

As shown in Fig. 2, point P will not have translational motion due to actuator 3 (link 8). This actuator will have no function in positioning point P and only provides rotational movement to link 9, which serves to position the robot gripper at the required angle. Also, we considered that actuator 1 (link 4) and actuator 2 (link 6) are used to position point P in space, placing it in the horizontal and vertical coordinates, while actuator 3 provides an angle to point P. Therefore, to calculate the position of point P, we will not take actuator 3 into account. Figure 3 shows the mechanism’s limit trajectory. We positioned one actuator into one of its extreme positions—either fully extended or fully retracted—which varies the position of the other actuator between those two limits. Thus, we obtain a region within which are all possible position points.

To analyse the problem, we have assigned a relative velocity between links 3 and 4, the pneumatic actuators. As shown in Fig. 4, we determinate the velocity of point a. From the velocity of point a, we obtain the velocity of point b as belonging to the same link. So, we know the speed of one point on each link and determine the rest.

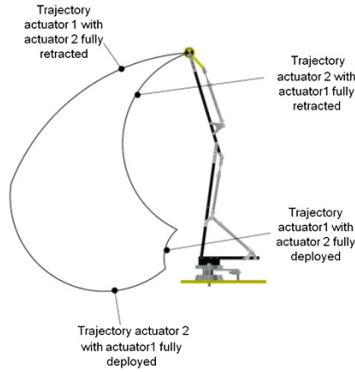


Fig. 3 Mechanism limit trajectory

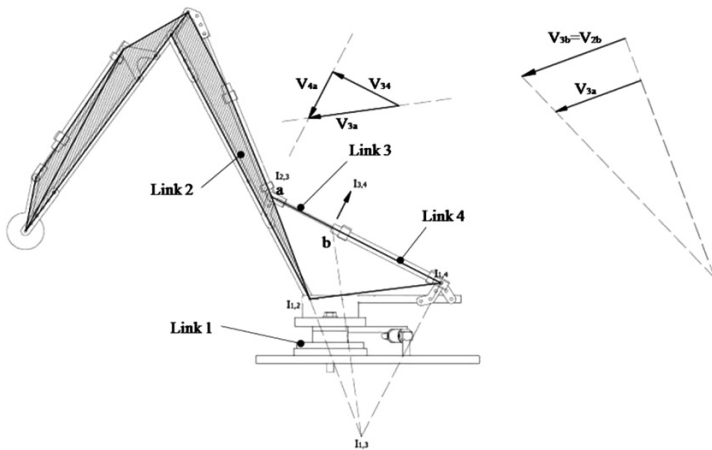


Fig. 4 Kinematic analysis with motion in actuator 1

After performing several simulations, we have observed that speed is not a determinant in calculating the actuators' necessary force because the inertia forces that are due to accelerations are not comparable to the static forces that are required to balance the system.

To perform the dynamic analysis, we applied a load of 50 N (aprox. 5 kg) in order to simulate the load at which the system is subjected. It was observed that, for the initial design, the force required in actuator 2 for maintaining trajectory was very high and impossible to reach with commercial pneumatic actuators. Therefore, we decided to make the following changes:

1. The length of link 2 with respect to link 1 of our initial design was very small, so we decided to implement a higher ratio of lengths. This forced us to separate the joint position of the fixed link to get the stroke length of actuator 1 (Fig. 5a).

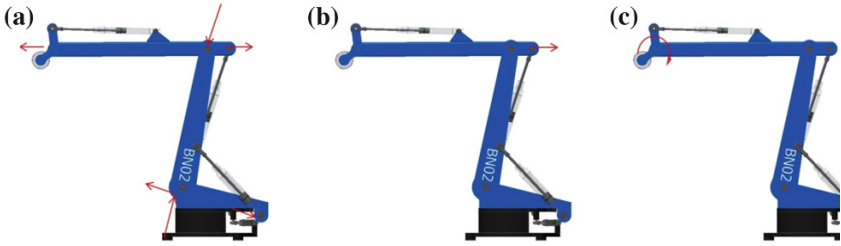


Fig. 5 Design evolution

2. We increased the distance between the joint connecting links 1 and 2 and the joint connecting link 2 to actuator 2 in order to increase the torque which makes cylinder 2 rotate link 2 (Fig. 5b).
3. We shifted cylinder 3 out of link 3's plane and also increased its stroke in order to get more rotation angle on the manipulator arm's wrist which, in the initial design, was extremely limited (Fig. 5c).

As shown in Fig. 6, we observed significant improvement in reducing peak forces in actuator 2 (which was the goal of this design)—reducing them below the required strength in actuator 1. Also, there are certain positions within the workspace that the mechanism will fail to reach with a limit pressure of 10 bar and a 5 kg load. In this case, it is necessary to define a lower burden in these work areas.

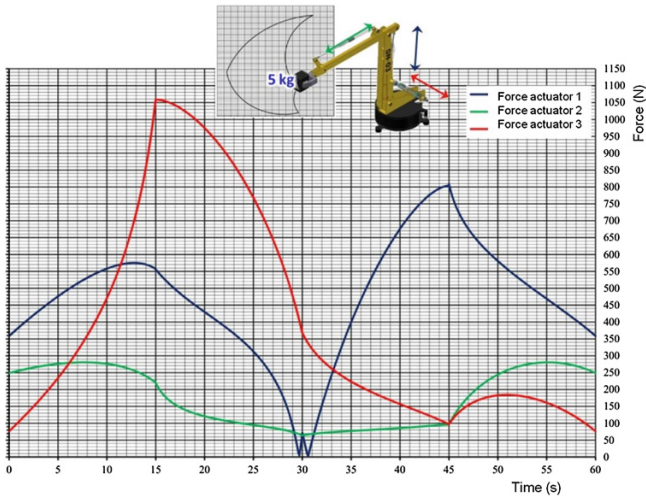


Fig. 6 Actuators required force

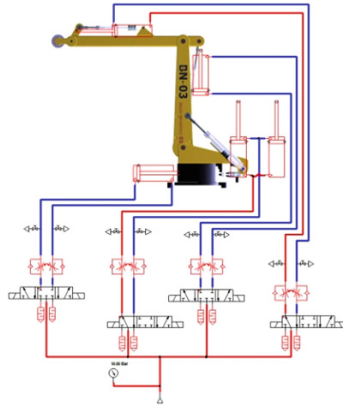


Fig. 7 Manipulator arm pneumatic scheme

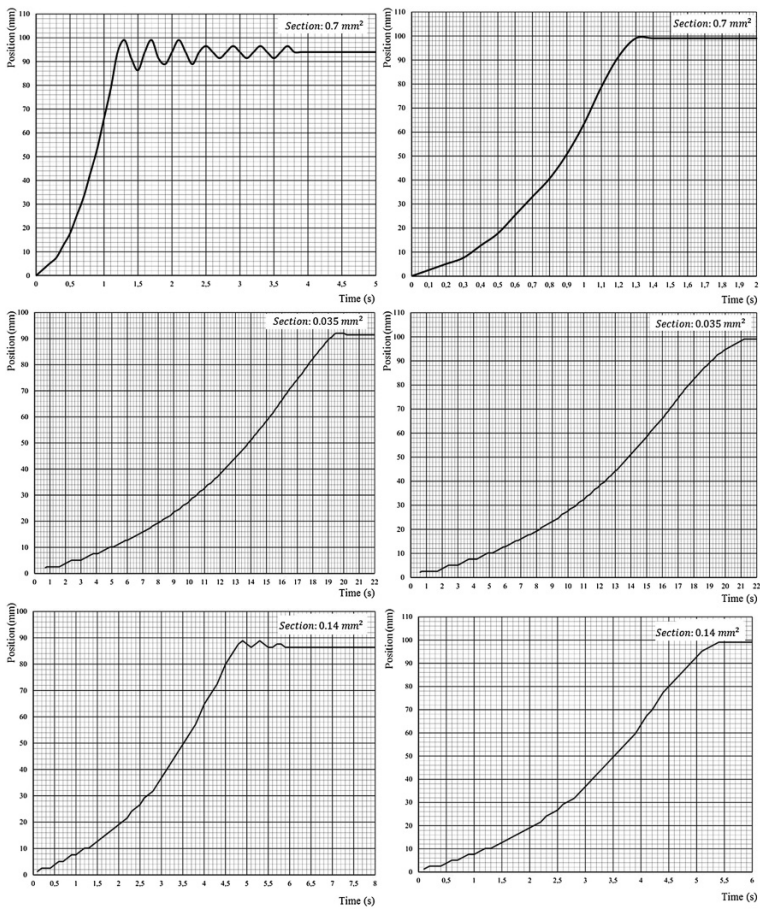
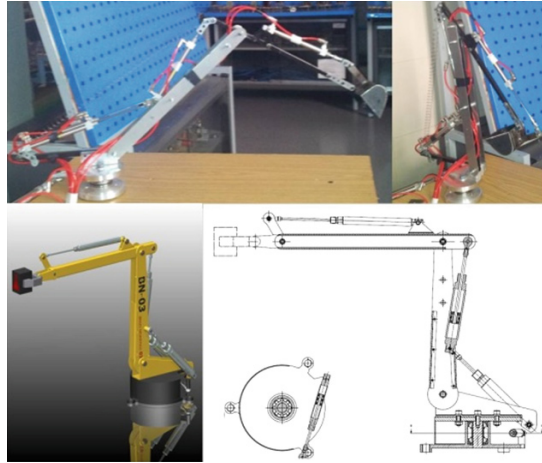


Fig. 8 Vibration and filling time

Fig. 9 Experimental prototype



3.2 *Pneumatic Design and Analysis*

In this section, we present the pneumatic circuit of our manipulator arm. The pressure is limited to a maximum of 10 bar, which is standard in the industry. Diagrams show the connections between valves, actuators and other devices; we use the symbols according to standard ISO 1219-1 (Fig. 7).

We observed a fluctuation in air pressure during the actuators' starts and stops, which in turn produces mechanical vibrations during the actuator rod's movements. This problem was solved by limiting the flow of air entering the cylinders by flow control valves. We performed several tests with different regulations in these valves in order to choose the best compromise solution for our application, as shown in Fig. 8. Decreasing the flow reduces vibrations but also reduces the system's speed.

4 Conclusions

We design a functional and economical manipulator arm using only linear pneumatic actuators; the final design fully meets this objective. To achieve this objective, we propose a design process and delineation of tasks taking into account the defined operational requirements. Using CAD/CAE tools, we perform kinematic and dynamic analyses based on the principles of the Theory of Machines and Mechanisms. Finally, we develop and test a straightforward pneumatic scheme to control the manipulator arm (Fig. 9).

References

1. Berlec T, Kušar J, Rihar L, Starbek M (2013) Selecting the most adaptable work equipment, *Strojniški vestnik. J Mech Eng* 59(6):400–408
2. Ko HK, Kim KH (2012) Design evolution of an actuation system for manipulator upper arm based on TRIZ. *J Adv Mech Des Syst Manuf* 6(1):131–139
3. Ko HK, Cho CH, Kim KH (2011) Rotational device for robot and robot arm using the same. Korean Patent Application 10-2011-0009594
4. Ko HK, Cho CH, Kim KH (2010) Design of an economic service robot hand based on biomimetics and TRIZ. *Trans Korea Soc Mech Eng Ser A* 34(11):1741–1747
5. Maeda S, Tsujiuchi N, Koizumi T, Sugiura M, Kojima H (2012) Development and control of a pneumatic robot arm for industrial fields. *Int J Adv Rob Syst* 9(59):1–7
6. Tsujiuchi N, Koizumi T, Nishino S, Komatsubara H, Kudawara T, Hirano M (2008) Development of pneumatic robot hand and construction of master-slave system. *J Syst Des Dyn* 2:1306–1315

Part XIII
Micro-mechanisms

A New Pseudo-Rigid-Body Model of Compliant Mechanisms Considering Axial Deflection of Flexural Beams

Yue-Qing Yu, Peng Zhou and Qi-Ping Xu

Abstract Based on pseudo-rigid-body model (PRBM), a new model is proposed considering the effect of axial deflection of flexural beam in compliant mechanisms. The axial and lateral deflections of flexural beam are modeled using three rigid links joined by one prismatic (P) pair with a linear spring and one revolute (R) pair with a torsion spring, respectively. The flexural beam subjected to an end force load is simulated by the PR PRBM with two degree-of-freedom. The optimal characteristic parameters of the PR PRBM are determined. The advantage of the new model is illustrated compared with the 1R (one revolute pair) and 2R (two revolute pairs) PRBM.

Keywords Compliant mechanism · Flexural beam · pseudo-rigid-body model · Axial deflection

1 Introduction

Compliant mechanisms gain their motion and function from the elastic deformation of component itself while conventional mechanisms achieve the transmission or transformation of motion, force and energy via kinematic pairs [1]. Compared with the rigid-body mechanisms, the advantages of compliant mechanisms can be considered in two categories, i.e., cost reduction (part-count reduction, reduced assembly time, and simplified manufacturing processes) and increased performance (increased precision, increased reliability, reduced wear, reduced weight, and reduced maintenance) [2]. As a new branch of modern mechanisms and machinery equipment, compliant mechanisms have a wide range of applications in the mechanical design, especially in the micro-electro-mechanical-system (MEMS) and micro-mechanisms. Therefore, it is of great importance to study the compliant

Y.-Q. Yu (✉) · P. Zhou · Q.-P. Xu
Beijing University of Technology, Beijing, China
e-mail: yqyu@bjut.edu.cn

mechanisms and a lot of achievements have been made on the structural and kinematic analysis of compliant mechanisms.

Midha and Howell [3] discussed the concept of compliant mechanisms and the relevant issues involved. The definition of segment was introduced and the connection types among segments of compliant component were obtained. Ananthasuresh et al. [4] presented a compliant notion clearly. The section was divided into several segments according to the structurally kinematic characteristics or the various material and cross-sectional characteristics. In Ref. [5], a method to determine the degree of freedom of compliant mechanisms was presented based on the segments and connection types among segments. With the geometrical nonlinear caused by the deformation of component, the kinematic analysis of compliant mechanisms is complicated.

In order to simplify the analysis and design of compliant mechanisms, Howell and Midha proposed a pseudo-rigid-body model (PRBM) [1] to simulate the deflection of flexible members using rigid-body components that have equivalent force-deflection characteristics. The theory of rigid body mechanisms can be applied in this way to investigate the compliant mechanisms. This work played an important role in the study of compliant mechanisms. In Ref. [6], the 1R PRBM of cantilever beam with end-force load was established to obtain the path of beam end by two rigid links joined with a revolute pair (1R) and a torsion spring. A loop-closure theory for the analysis and synthesis of compliant mechanisms was presented later [7]. The parameters of 1R PRBM for compliant mechanisms are different with the various loads and the accuracy is not high enough. Saxena and Kramer [8] modified the PRBM by introducing two linear springs to restrain the change of characteristic radius factor for different load modes. Furthermore, Su proposed a 3R PRBM [9] that is made of four rigid links joined by three revolute pairs (3R) and three torsion springs. Because the stiffness coefficients were considered synthetically during the optimization process of characteristic radius factor, this model had load independence which is critical for the applications where loads vary significantly. In order to simplify the optimization process, a 2R (two revolute pairs) PRBM [10] was developed based on the parametric approximation for the angular deflection of beam end. The optimal characteristic radius factors and stiffness coefficients were obtained in this model. The numerical results indicated that the 2R PRBM can provide a higher accuracy than the 1R PRBM and simplify the iterative process of the 3R PRBM.

However, the 1R, 2R and 3R pseudo-rigid-models contain revolute joints and can simulate the bending deformation of a flexural beam only, they are not useful to describe the axial deformation of the flexible beam. The axial deflection plays an important role in a large deflection beam. Therefore, a further investigation on the simulation accuracy of pseudo-rigid-body models is needed.

A new pseudo-rigid-body model (PRBM) with two degree of freedom is proposed in this paper. The axial deformation of a flexural beam is described by one rigid link with a prismatic (P) pair and a linear spring, and the lateral deflection of the beam is simulated by one rigid link with a revolute (R) joint and a torsion spring. Firstly, the PR PRBM of a flexural beam with end force load is developed.

The characteristic parameters of the PR PRBM are determined then. A numerical comparison among the 1R, 2R and PR pseudo-rigid-body models is presented as following to shows the advantage of the new model in simulating the large deflection beams of compliant mechanisms. Finally, some conclusions are made.

2 PR Pseudo-Rigid-Body Model

A flexural cantilever beam with an end force load is shown in Fig. 1a. θ_0 is the deflection angle of the flexural beam, a and b are the horizontal and vertical coordinates of the tip point of the beam, respectively. l is undeflected length of a flexural beam, and ϕ is the angle between the force direction and the horizontal direction. In order to simulate the axial and lateral deformations of the flexural beam with an end force, a PR pseudo-rigid-body model (PR PRBM) is proposed here, as shown in Fig. 1b. It consists of three rigid links joined by one Prismatic (P) pair with a linear spring and one Revolute (R) pair with a torsion spring. In this way, the axial deformation of the flexural beam can be described by the fixed and translating rigid links joined by the prismatic pair with a linear spring, and the main lateral deflection of the beam can be simulated by the sliding and rotating links joined by the pin joint with a torsion spring.

The length of each rigid link in the PR PRBM is presented as $\gamma_i l (i = 0, 1)$, and γ_i is called the characteristic radius factor, satisfying $\gamma_0 + \gamma_1 = 1$. $\Delta\gamma_0$ is the variable characteristic factor and $\Delta\gamma_0 l$ indicates the axial displacement of the prismatic pair. K_Θ and K_L are the torsion spring stiffness coefficient and linear spring stiffness coefficient, respectively. These five factors and coefficients are the key characteristic parameters of the PR PRBM and they can be determined as follows.

Firstly, the kinematic equations of the PR PRBM for the large deflection beam with an end force are established. The slope angle of the PR PRBM can be presented as Θ , ϕ is the angle between the force direction and the horizontal line,

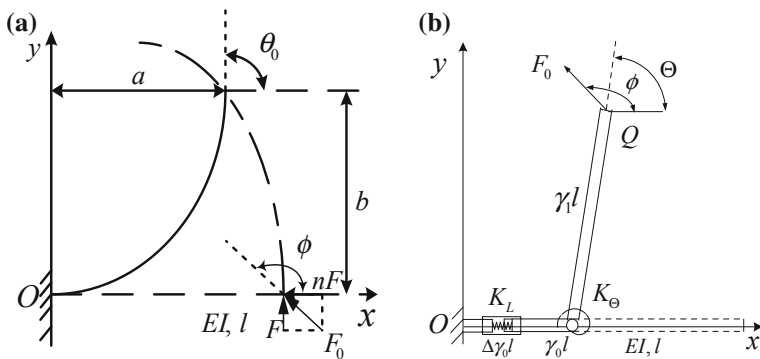


Fig. 1 a Flexural beam subjected to an end force. b PR pseudo-rigid-body model

shown in Fig. 1b. The tip point $Q = (Q_x, Q_y)^T = (a/l, b/l)^T$ of the flexural beam can be obtained from Elliptic Integrals [1] and that of the PR PRBM in Fig. 1b can be written as:

$$\begin{cases} Q_x = \gamma_0 + \Delta\gamma_0 + \gamma_1 \cos \Theta \\ Q_y = \gamma_1 \sin \Theta \end{cases} \quad (1)$$

So, the following relationship can be derived from the above equation:

$$\begin{cases} \Theta = \sin^{-1} \left(\frac{Q_y}{\gamma_1} \right) \\ \Delta\gamma_0 = Q_x - \gamma_1 \cos \Theta + \gamma_1 - 1 \end{cases} \quad (2)$$

The slope angle of the PR PRBM is Θ , and θ_0 is the deflection angle of the beam. Here, a factor C_θ (parametric angle coefficient) is introduced to rectify the existing error between the above two angles which can be approximately expressed as a linear relationship as follows [1]:

$$\Theta = C_\theta \theta_0 \quad (0 < C_\theta \leq 1) \quad (3)$$

The characteristic radius factors of the PR PRBM can be obtained via parametric approximation method, satisfying the constraints:

$$f(\Theta) = \left| \frac{\frac{\Theta}{C_\theta} - \theta_0}{\theta_0} \right| \leq \left| \left(\frac{\frac{\Theta}{C_\theta} - \theta_0}{\theta_0} \right)_{\max} \right| \quad (4)$$

The process to determine the characteristic radius factor of the PR PRBM can be presented in an optimization procedure and the flow chart is shown in Fig. 2.

When $n = 1.5$, the force load angle ϕ is equivalent to 146.3° , γ_0 , γ_1 , C_θ can be obtained as follows:

$$\gamma_0 = 0.1791, \quad \gamma_1 = 0.8281, \quad C_\theta = 0.7915$$

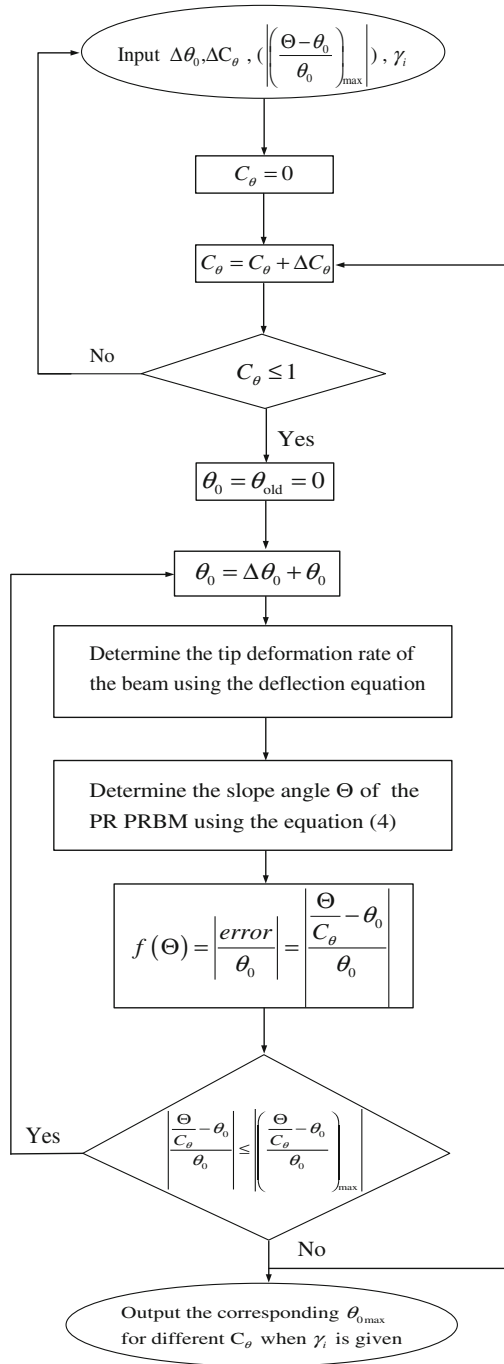
Using Least Square Polynomial Fitting Method [11], the variable characteristic factor $\Delta\gamma_0$ in Eq. (2) can be simplified as the following equation:

$$\Delta\gamma_0 = -0.0493\Theta^5 + 0.1711\Theta^4 - 0.2158\Theta^3 + 0.0891\Theta^2 - 0.0275\Theta \quad (5)$$

And the result in this case can be obtained as follows:

$$\Delta\gamma_0 = -0.1871$$

Fig. 2 Optimization flow chart of characteristic radius factors



Secondly, for a given force load F_0 exerted at end of the PR PRBM, and the torque and lateral force at the pivot are:

$$\begin{cases} T = F_x l(-\gamma_1 \sin \Theta) + F_y l(\gamma_1 \cos \Theta) \\ F_x = -K \Delta \gamma_0 l \end{cases} \tag{6}$$

where

$$F_x = F_0 \cos \phi, F_y = F_0 \sin \phi \tag{7}$$

presenting the horizontal and vertical force, respectively. From Eq.(6), we can have:

$$\begin{bmatrix} \Theta & 0 \\ 0 & -\Delta \gamma_0 l \end{bmatrix} \begin{bmatrix} K_1 \\ K \end{bmatrix} = \begin{bmatrix} -\gamma_1 \sin \Theta & \gamma_1 \cos \Theta & 0 \\ 0 & 0 & 1 \end{bmatrix} \begin{bmatrix} F_x l \\ F_y l \\ F_x \end{bmatrix} \tag{8}$$

where K, K_1 can be expressed by the nondimensionalized torsion spring stiffness coefficient K_Θ and the spring stiffness coefficient K_L as follows:

$$\begin{bmatrix} K_1 \\ K \end{bmatrix} = \begin{bmatrix} \frac{EI}{l} & 0 \\ 0 & \frac{EI}{l^3} \end{bmatrix} \begin{bmatrix} K_\Theta \\ K_L \end{bmatrix} \tag{9}$$

And so

$$\begin{bmatrix} K_\Theta \\ K_L \end{bmatrix} = \begin{bmatrix} \frac{-\gamma_1 \sin \Theta F_x l^2}{\Theta EI} + \frac{\gamma_1 \cos \Theta F_y l^2}{\Theta EI} \\ -\frac{F_x l^2}{\Delta \gamma_0 EI} \end{bmatrix} \tag{10}$$

Using the dimensionless force index $\alpha^2 = \frac{F_0 l^2}{EI}$ [1], we have

$$\begin{cases} K_\Theta = \frac{\alpha^2 \gamma_1 (-\sin \Theta \cos \phi + \cos \Theta \sin \phi)}{\Theta} \\ K_L = -\frac{\alpha^2 \cos \phi}{\Delta \gamma_0} \end{cases} \tag{11}$$

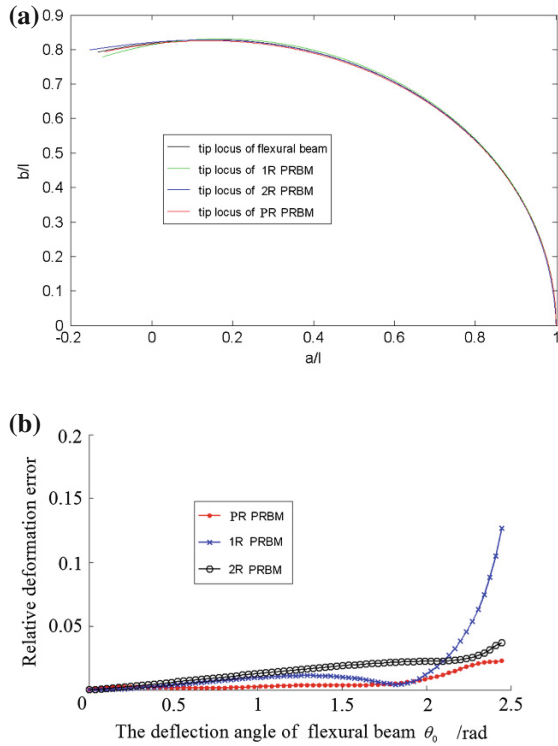
Applying Linear Regression [12], the spring stiffness coefficients of the PR PRBM can be obtained as follows.

$$K_\Theta = 1.31, K_L = 29.2124.$$

3 Numerical Results

In order to test the simulating accuracy of the PR PRBM, the tip locus of the PR PRBM, compared with 1R, 2R PRBM and the flexural beam are shown in Fig. 3a. It can be seen from the figure that the three PRBM models can mainly follow the tip locus of the flexural beam in a small deformation condition. However, for a large

Fig. 3 Simulation results.
a Tip locus of flexural beam and PRBMs **b** Tip error of flexural beam and PRBMs



deflection, the curve of 1R PRBM deviates a lot from the locus of flexural beam. This is because the 1R model has one degree-of-freedom only and so its simulation accuracy is low. The 2R PRBM has two degree-of-freedom and it has a higher simulation precision than the 1R PRBM. The PR PRBM which has also two degree-of-freedom improves further the tracing accuracy by using the prismatic pair to describe the axial deformation of the flexural beam. This result shows further the important role of the prismatic pair in the pseudo-rigid-body model and the superiority of PR PRBM in increasing the simulation precision for the large deflection of the flexural beam.

The relative error of the three pseudo-rigid-body models can be shown in Fig. 3b. The maximum errors of the 1R, 2R and PR model are 12.2, 3.72 and 2.73 %, respectively. It can be seen from the figures that the minimum relative deformation error is in the PR PRBM while the maximum one is in the 1R PRBM. The behaviors of the 2R PRBM are between them. These results agree well to the conclusions obtained above.

It can be summarized now from the above numerical results that the PR and 2R PRBM with two degree-of-freedom have higher simulation precision than the 1R PRBM with one degree-of-freedom in tracking the tip locus of flexural beam. Obviously, the increase of degree-of-freedom can improve the simulation precision

of the tip locus of the flexible beam. For the same condition of degree-of-freedom, the PR PRBM with a prismatic pair shows better behavior than the 2R PRBM with pin joints only. Therefore, the axial deformation of flexural beam can be simulated well by the prismatic pair and linear spring and the simulation precision can be improved using the PR PRBM.

4 Conclusions

The effects of lateral and axial deflection of flexural beam have been fully considered and a new PR pseudo-rigid-body model has been developed in this study. The PR PRBM has advantage in increasing the simulation precision compared with the 1R and 2R PRBM. The axial deformation plays a significant role in the large deflection of flexural beam subjected to end force load and it can be represented well by the prismatic pair and linear spring of the PR PRBM. The deformation characteristics of large deflection links in compliant mechanisms can be well described by the PR PRBM. Therefore, the new model developed in this paper has theoretical significance and application value in the analysis and design of compliant mechanisms.

Acknowledgments This work is supported by the National Natural Science Foundation of China (Grant No. 51175006).

References

1. Howell LL (2001) Compliant mechanisms. Wiley, Hoboken
2. Tuttle SB (1967) Mechanisms for engineering design. Wiley, Hoboken
3. Midha A, Howell LL (1994) On the nomenclature, classification, and abstractions of compliant mechanisms. *ASME Trans J Mech Des* 116:270–279
4. Ananthasuresh GK, Kota S (1995) Designing compliant mechanisms. *Mech Eng* 117:93–96
5. Ananthasuresh GK, Howell LL (1996) Case studies and a note on the degrees-of-freedom in compliant mechanisms. *ASME Trans J Mech Des* 118:1–12
6. Howell LL, Midha A (1995) Parametric deflection approximations for end loaded large deflection beams in compliant mechanisms. *ASME Trans J Mech Des* 117:156–165
7. Howell LL, Midha A (1996) A loop-closure theory for the analysis and synthesis of compliant mechanisms. *ASME Trans J Mech Des* 118:121–125
8. Saxena A, Kramer SN (1998) A simple and accurate method for determining large deflections in compliant mechanisms subjected to end forces and moments. *ASME Trans J Mech Des* 120:392–400
9. Su H (2009) A pseudo-rigid-body 3R model for determining large deflection of cantilever beams subjects to tip loads. *ASME Trans J Mech Robot* 1:021008
10. Yu YQ, Feng ZL, Xu QP (2012) A pseudo-rigid-body 2R model of flexural beam in compliant mechanisms. *Mech Mach Theor* 55:18–33
11. Xue G (2009) Numerical analysis. CRC Press, Boca Raton
12. Weisberg S (2005) Applied linear regression, 3rd edn. Wiley Interscience, Hoboken

An Internal Gyroscopic Micro-Mechanism for Development of Lateral Deviation of a Projectile

C.M. Umstead, Y.Y. Tay and H.M. Lankarani

Abstract The lateral control of a projectile for impacting a non-stationary target is of interest in many applications. Changing the flight trajectory can be achieved using the internal moving parts of the projectile. In this study, three small internal swing masses introduced to the projectile are controlled, and the masses are attached at the end of a massless rod. A mathematical model for the internal gyroscopic rotating disks of this mechanism and its trajectory path is developed. For this mechanism, the equations of motion are developed and solved numerically to simulate the trajectory of the projectile. The projectile is shown to move cyclically about the axis of rotation and deviate from its axis in a relatively even slope. A parametric study is conducted on actuating each mass in sequence or changing the weight of the mass to examine and evaluate the flight trajectory of the projectile. The results from this study show that the projectile could move in a lateral direction in a controlled manner by altering the mass mechanism in a predefined manner. This application may hold merit for controlling the re-entry flight trajectory of air vehicles.

Keywords Flight trajectory · Gyroscopic effect · Projectiles · Spatial mechanisms

1 Introduction

Early studies of ballistics control were done by means of changing the initial physical conditions of the projectiles. With the advances in technology, a number of studies have been conducted in active control of the projectile during spatial flight.

C.M. Umstead (✉) · Y.Y. Tay · H.M. Lankarani
Wichita State University, Wichita, USA
e-mail: cumstead@gmail.com

Y.Y. Tay
e-mail: yxtay1@wichita.edu

H.M. Lankarani
e-mail: hamid.lankarani@wichita.edu

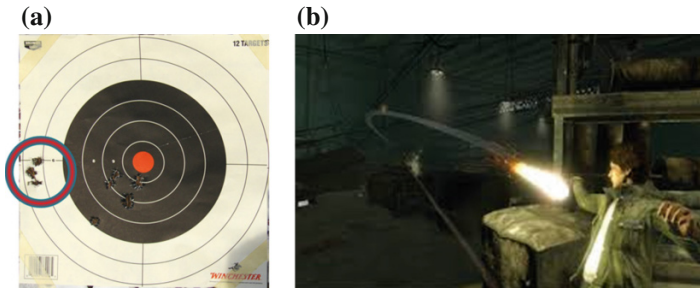


Fig. 1 **a** bullet deviation due to wind; **b** curving the path of a bullet from movie film *Wanted*, courtesy of Universal Picture

The flight control of a simple bullet in the lateral direction stems from observations of the bullets deviation from the desired target due to the influence of wind, shown in Fig. 1a. The film industry has utilized this concept to some exaggeration of this lateral deviation, as shown in Fig. 1b.

The idea of a single internal rotating mass is explored in 0. Several other researchers have explored different means of controlling the trajectory of an object. It is known that the control of a missile can be accomplished externally by fins or by control systems during mid-flight. Internally, the motion of the projectile can be controlled using translating and rotating masses located within the body. The concept of a translating mass is that a weight is constrained in a linear cavity within the projective. The mass then slides within the cavity, creating a change in the center of gravity and introduce gyroscopic forces to the projectile. Another method of translating mass concept is to attach masses to a rod of constant length and the rod rotates about the major axis of the projectile 0. With the use of several of these rods, the center of gravity and angle of attack can be altered to change the flight path of the projectile.

The concept of translating mass in altering path trajectory of an object was explored by several investigators. It is shown that the trajectory of a projectile can be altered due to moving mass from the dynamic coupling between two bodies 0. As the mass of a body is offset from the center of gravity, the trajectory of the body can deviate from a parabolic arc trajectory. Additionally, an offset mass in a body can increase the control authority of a body during the initial flight 0. Bryne et al. 0 analyzed the effect of altering the center of gravity of a body on the change in angle of attack and the flight path of an object. They concluded that while the effectiveness of this method can be increased by utilizing two or more masses to reduce the drastic movement of the body. As the projectile descends, the internal gyroscopic force created by the mass mechanism forces the projectile to change trajectory direction and direct the projectile to a desired point of impact.

The primary objective of this study is to examine and quantify the effect of gyroscopic forces produced by internal rotating disks micro-mechanism of a projectile in influencing the flight trajectory. This is achieved by developing the equations of motion of the system describing the dynamic behavior of the

projectile, and numerically solving them using MATLAB. A parametric study is conducted, and the variables identified in this parametric study are the weight of the masses, initial position of the masses and relative angular rotation of each mass, confined in the cavity of the projectile.

2 Methodology

Mathematical models for the projectile with different arrangements of rotating disks are developed and their corresponding equations of motion are solved numerically using the MATLAB computer program. The concept projectile model, considered as a bullet, with three rotating weights is investigated. The controllable input variables of this numerical model are the initial linear and angular velocity, and acceleration of the projectile. In flight, the gyroscopic force produced by the rotating disk mechanism controls the trajectory of the projectile.

The motion of the projectile and a single rotating disk are described by Frost et al. [1, 2] as:

$$m_d \vec{a}_d = \vec{F}_R + \vec{W}_d \tag{1}$$

$$m_p \vec{a}_p = -\vec{F}_R + \vec{W}_p + \vec{F}_A \tag{2}$$

where m_p and m_d are the mass of the projectile and disk; \vec{a}_d and \vec{a}_p are the accelerations of the disk and projectile; \vec{W}_d and \vec{W}_p are the weight of the disk and projectile; \vec{F}_R is the constraint force coupling the projectile and disk; and \vec{F}_A is the aerodynamic force acting on the projectile.

The equations of motion of the projectile and a single rotating disk combined can be described by combining Eqs. (1) and (2) as Eq. (3) which describes the motion of a single rotating mass mechanism, and it is expanded and used in this parametric study to analyze the trajectory of the projectile with three rotating mass mechanism.

$$m_p \vec{a}_p + m_d \vec{a}_d = \vec{W}_d + \vec{W}_p + \vec{F}_A \tag{3}$$

In this parametric study, the numerical model of the basic projectile is a simple cone shaped cylinder, 20 mm in diameter. It is assumed that the most influential force acting on the projectile during flight is gravitational force and air resistance. The projectile in spatial motion is considered to have 6° of freedom. It is known that the trajectory path of a projectile without the influence of gyroscopic force produced by the disk mechanism is parabolic in shape [2, 3]. The trajectory of the basic parabolic arc of a traditional projectile can be formulated as:

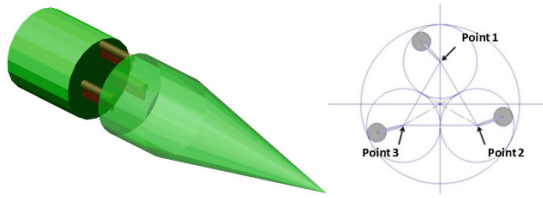


Fig. 2 Illustration of projectile with mass mechanisms and its rotational points

$$\vec{F}_{drag} + \vec{F}_{gravity} = m\vec{a} \tag{4}$$

$$\vec{F}_{drag} = -\frac{1}{2} \rho |\vec{v}|^2 C_d A \vec{v} \tag{5}$$

$$\vec{F}_{gravity} = [0 \quad \sin(\theta)g \quad \cos(\theta)g]^T \tag{6}$$

where ρ is the density of the air; C_d is the drag coefficient; A is the cross sectional area; and θ is the angle of the major axis relative to direction of gravity; \vec{v} is the velocity vector; g is the gravitational force.

The concept of the new projectile model with mass mechanism is illustrated in Fig. 2. The methodology is to incorporate three weights that could be rotated about the major axis of the projectile. The concept is that when the masses are rotated, the gyroscopic force generated from the mass mechanism will cause the projectile to deviate from its initial parabolic trajectory. By altering the use of three masses, the direction of the deviation can be controlled in the lateral direction. As previously mentioned, the parameters for this model are segment length, weight of each mass, and the initial angular velocity of each masses.

It can be shown that the rotation points are at the edge of an equilateral triangle centered form around the major axis of the projectile. Letting r be the maximum length of the rotation mass; $2r$ is one of the legs of the equilateral triangle. And the position of the rotation points are $(0, \frac{2\sqrt{3}}{3}r)$, $(-r, -\frac{\sqrt{3}}{3}r)$, and $(r, -\frac{\sqrt{3}}{3}r)$ respectively, with the origin located in the center of the triangle. The minimum radius for the projectile, R , in terms of r , is shown in Eq. (7).

$$R = \left(\frac{2\sqrt{3}}{3} + 1\right)r \approx 2.155r \tag{7}$$

The equation for motion of the projectile can be derived from examining various studies [1, 3, 4]. The force of the mass, denoted as \vec{F}_{mass} , can be described in Eq. (8). By combining Eqs. (4) and (5) into Eq. (8), the overall force equation from the system can be defined as Eq. (9):

$$\vec{F}_{mass} = m_d(\vec{a}_p + \vec{\alpha}_p \times \vec{r}_p + \vec{\omega}_p \times (\vec{\omega}_p \times \vec{r}_p) + \vec{\alpha}_d \times \vec{r}_{CD} + \vec{\omega}_d \times (\vec{\omega}_d \times \vec{r})) \quad (8)$$

$$m_p(\vec{a}_p + \vec{\omega}_p \times \vec{v}_p) + \sum_{i=1}^n (m_{d_i}(\vec{a}_p + \vec{\alpha}_p \times \vec{r}_{PC,i} + \vec{\omega}_p \times (\vec{\omega}_p \times \vec{r}_{p,i}) + \vec{\alpha}_{d,i} \times \vec{r}_i + \vec{\omega}_{d,i} \times (\vec{\omega}_{d,i} \times \vec{r}_i)) = \left(m_p + \sum_{i=1}^n m_{d_i} \right) * \vec{g} - \frac{1}{8} * C_d * \rho * |\vec{v}_p|^2 \pi d^2 \vec{v} \quad (9)$$

where \vec{r}_p is the vector radius of the projectile relative to the world's origin; \vec{r}_i is the vector radius of each masses relative to the projectile; $\vec{\omega}_p$ and \vec{v}_p are the angular and linear velocities of the projectile; $\vec{\omega}_d$ and \vec{v}_d are the angular and linear velocities of the disk; $\vec{\alpha}_p$ and $\vec{\alpha}_d$ are the angular velocities of the disk and projectile.

Torque is created by the offset of the rotation point from the major axis. The rotation point is denoted by \vec{p} . The angular acceleration can be found by using $\vec{\tau} = I\vec{\alpha}$, and the angular velocity of the project can then be determined 0. This rotation of the projectile changes the angle of the rod of the rotating disk and the location of the point of rotation with respect to the ground and subsequently the direction of force that is created by the disk on the projectile.

$$\vec{\tau} = \sum_{i=1}^3 \vec{p} \times \vec{F}_{mass_i} \quad (10)$$

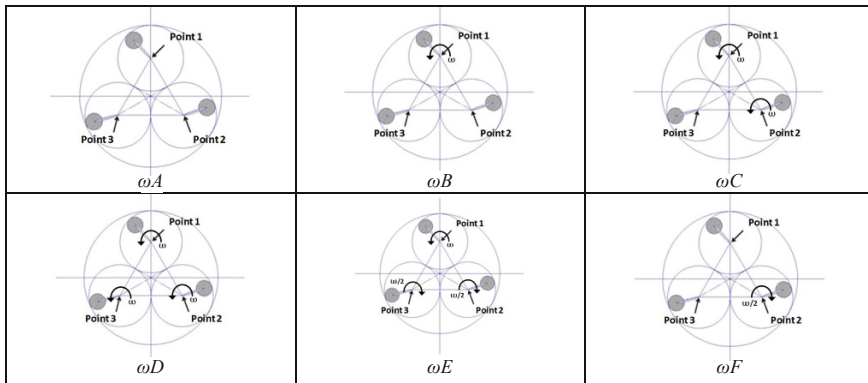
The polar moment of inertia about the major axis is estimated by treating the main body of the projectile like a solid cylinder and the masses as points, as shown in Eq. (11).

$$I = \frac{1}{2} m_p R^2 + \sum_{i=1}^3 m_{d_i} |\vec{r}_i + p_i|^2 \quad (11)$$

where R is the radius of the projectile and p_i is the point of rotation of each rods. With the moment of inertia and torque, the angular velocity of the projectile was found along with the subsequent changes in the location of rotation points and arms. The program MATLAB is used to solve the preceding equations to obtain the kinematics of the projectile and rotating disks mechanism. The equations of motion are numerically solved using the Runge-Kutta ODE45, mathematical solver with adjustable step-size.

A parametric study is conducted to examine the effect of different variables on the internal deviation of the projectile. The parametric variables considered are the weight of the masses, the angular velocity of the masses and the initial position of the masses. The parametric arrangement used in this study is shown in Table 1. First, the phase or initial position of the masses is set according to the parameter being examined. The configurations and initial positions of the masses are then

Table 1 Configurations and diagrams of cross-sectional view of rotating mass projectile mechanism, phase 1



altered in a sequential manner. The angular velocities of the masses were changed to reflect a given scenario represented by ω_i , where i is a letter between A and F to differentiate the configurations of the projectile model. The weights of the masses are categorized into three conditions, namely, *mass condition 1, 2 and 3*. For case study ωA , no rotations are assigned to the mass mechanism. For case studies ωB , angular velocity of 167 rpm is assigned to the top mass, and angular velocity of the same magnitude and direction are assigned to the remaining masses in sequential order for ωC and ωD . For ωE , two of the three masses are rotated in the opposite direction of the rotation of the projectile. Lastly, only one mass is rotated at the opposite direction for case study ωF . It is also clearly shown that the phase angles between the masses are identical for all case studies. To increase clarity, the phase angles shown in Table 1 are denoted as *phase 1*. The design parameters and function, and its characteristics used in this study are described in Table 2.

Table 2 Design parameters and functions for the analysis of projectile with mass mechanism

Design Parameters	Variables and range of variables	
	1. Position of masses	Phase 1 and Phase 2
2. Weight of masses (kg)	0.001, 0.05 0.10	
3. Initial angular rotation of masses (rpm)	-83.3 and 167.0	
4. Rotation direction of masses	Clockwise and counter-clockwise	
Functions	1. Deviation of trajectory (mm)	

3 Parametric Results and Discussions

A mathematical projectile model is developed to examine the gyroscopic effect of a projectile when masses are confined inside the projectile in a controlled arrangement. The parametric study involves examining the influence of predefined variables on the lateral trajectory path of a projectile. The variables of interests are the arrangement of masses, the weight of masses and the initial kinematic configurations of the masses. Figures 3, 4 and 5 illustrate the deviation of the projectile with masses.

From the numerical results for *mass condition 1, phase 1*, as shown in Fig. 3, the arrangement of ωD is shown to introduce the greatest deviation of 39 mm. As expected, the deviation for ωA produced the least deviation due to the non-existence of gyroscopic force. For *mass condition 2, phase 2*, the weights of the masses are increased from 0.01 to 0.05 kg and the numerical results is illustrated in Fig. 4. The extra weight has significant effects on the lateral trajectory of the projectile. Similar to findings from *condition 1, phase 1*, the greatest deflection occurred for ωD configuration, where the masses are rotated in the same direction as the projectile.

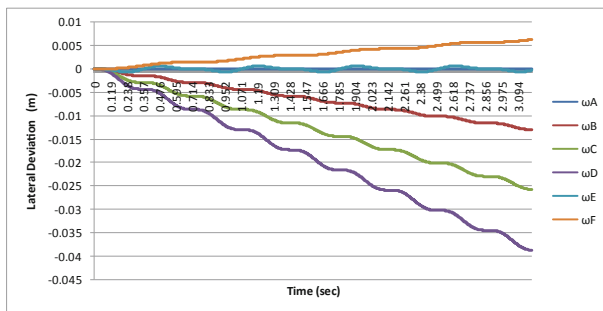


Fig. 3 Lateral deviation of projectile flight path for *mass condition 1, phase 1*

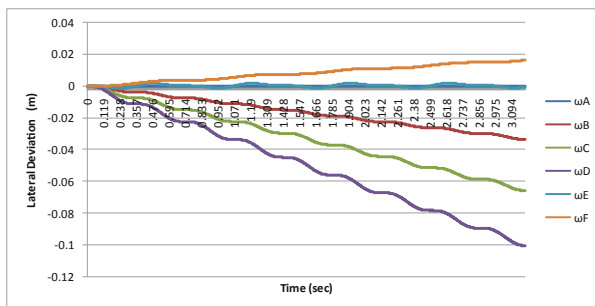


Fig. 4 Lateral deviation of projectile flight path for *mass condition 2, phase 1*

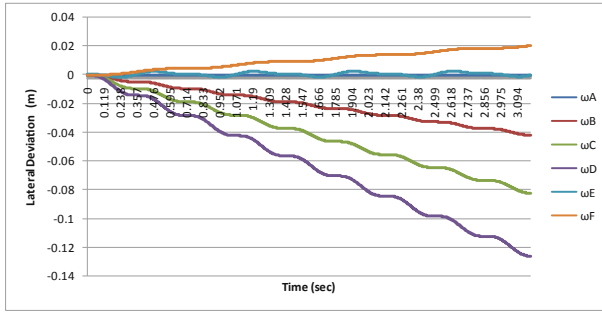


Fig. 5 Lateral deviation of projectile flight path for mass condition 3, phase 1

On the other hand, the increment in the path deviation of the projectile is not as much by incrementing the weight of the masses from 0.05 to 0.1 kg. Figure 5 depicts the numerical results for mass condition 3, phase 1. It is shown that the maximum path deviation for condition 3 when compared to condition 2 is only increased by approximately 20%. Hence, it is conclusive that the deviation of the projectile is not analogous to the increase in weight of the masses.

In this study, the influence of phase change or the arrangement of masses within the cavity of the projectile is also presented. The initial phase of the masses is changed by rotating the masses to some predefined locations as illustrated in Fig. 6. The new phase change, denoted as phase 2, of the masses is subjected to similar parametric study of the previous study. The shape or the deviation path, except for its magnitude values, for the phase 2 is quite similar to that of the previous numerical study. As such, the maximum flight deviation is used to present findings for the new phase change. The maximum deviation for all mass conditions for the phase 2, case 1 and phase 2, case 2 are shown in Fig. 6a, b. Similarly, the phase change on the deviation of the projectile is highly influential by increasing the weight of masses from 0.01 to 0.05 kg. The maximum deviation is also achieved in

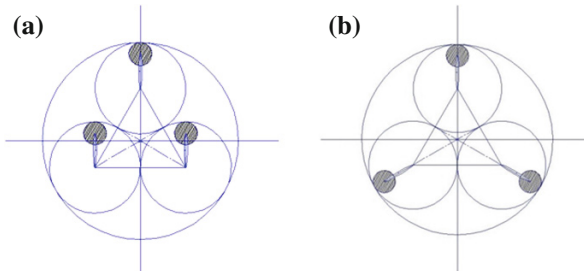


Fig. 6 Phase 2 configurations of disks mechanism: a case 1: masses pointing upwards; b case 2: masses evenly spaced

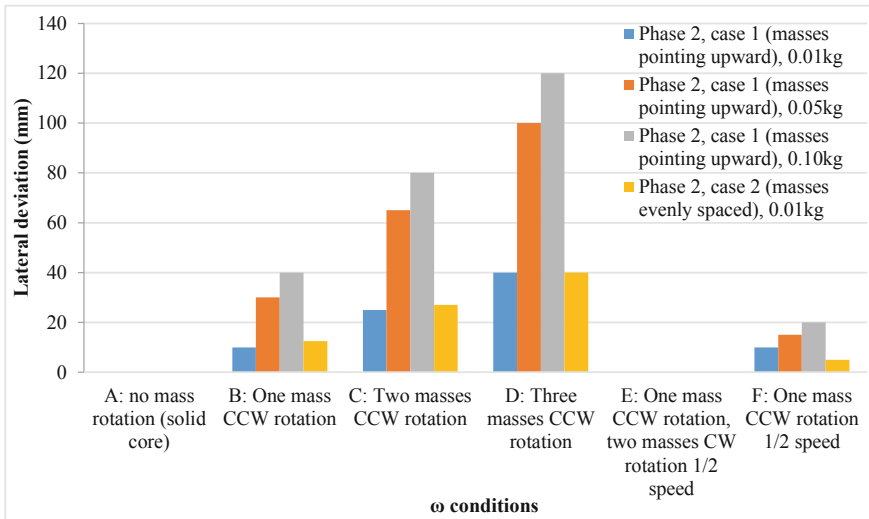


Fig. 7 Maximum lateral deviation of projectile with disk mechanism for *phase 2—case 1* and *case 2*

ωD condition, which correlates to approximately 120 mm of deviation. For ωD condition in both cases, the numerical results shown that it only needed 0.05 kg of masses to achieve the maximum deviation of 120 mm for *phase 1*, and to achieve similar deviation target, *phase 2, case 1* needed twice as much weight. Hence, the arrangement and configurations of masses in *phase 1* is more influential to the change in flight trajectory than that of *phase 2*. In addition to that, the numerical results shown that the lateral deviation from *phase 2, case 2* is comparable to that of *phase 2, case 1* for ωA to ωE conditions, but less effective for ωF condition (Fig. 7).

4 Conclusions

The objective of this study was to analyze and quantify the influence of gyroscopic forces due to the presence of three initial rotating micro-mechanism of a projectile on its flight trajectory. To accomplish this study, three masses were considered and mounted at the end of the massless rods. The massless rods, which were also mounted onto a disk, were constrained and confined in the main body of the projectile. The equations of motion of a projectile in flight were developed and numerically solved. In the parametric study, the configuration of the masses, weight of the masses and initial angular rotation of the masses were considered. In general, the numerical results shown that gyroscopic forces produced by the masses can introduce deviation to the course of the projectile. The maximum deviation of

projectile of slightly more than 120 mm can be accomplished by using the *phase 1, mass condition 1* and ωD condition, where the masses are rotated in the same direction as the projectile.

Some of the improvement to this methodology is to introduce a flight control system to perform a real-time correction for minor deviation of a projectile. In this study, the masses were positioned in a planar mode in the body of the projectile, the effect of positioning the masses in spatial configurations required additional study. Overlap, this application may hold merits for application for mechanisms that require minor trajectory adjustment for reaching some non-stationary targets.

References

1. Frost G, Costello M (2003) Stability and control of a projectile with an internal rotating disk. In: AIAA atmospheric flight mechanics conference and exhibit, Austin, Texas
2. Frost G, Costello M (2004) Linear theory of a rotating internal part projectile configuration in atmospheric flight. *J Guid Control Dyn* 27(5):898–905
3. Ollerenshaw D, Costello M (2008) Simplified projectile swerve solution for general control inputs. *J Guid Control Dyn* 31(5):1259–1265
4. Hainz LC, Costello M (2005) Modified projectile linear theory for rapid trajectory prediction. *J Guid Control Dyn* 28(5):1006–1014

An Approach to the Characterization of Flexure Hinges for the Purpose of Optimizing the Design of a Micromanipulator

D. Schoenen, I. Ivanov and B. Corves

Abstract A crucial factor for estimating the performance of a flexure hinge based micromanipulator requires knowledge of stiffness or compliance matrices. These can be determined by using an analytical method, the finite element method (FEM) or an experimental method. Hence, a generalization and a FEM enhancement of the analytical method for calculating the compliance or stiffness matrix of flexure hinges are suggested. For an experimental validation of the approach a test stand is necessary. This test stand permits testing of bending and torsional characteristics of flexure hinge specimen.

Keywords Flexure hinges · Micro manipulator · Validation test stand · Notch-joint · Compliance

1 Introduction

Conventional joints allow translational and/or rotational degrees of freedom by form or force closure theoretically without stiffness in the direction of movement and with infinite stiffness in the other, so-called parasitic directions. In contrast to these, flexure hinges gain their movability due to their own compliance and therefore have certain stiffness in all directions [1].

Among various types of flexure hinges, notch-joints are the most common [2]. There are different notch profiles to increase compliance in one or more directions [3]. Even though notch-joints are designable with two or three rotational degrees of freedom (DoF), those with only one DoF are preferably to be used, both in planar and spatial applications (cf. Fig. 1).

D. Schoenen (✉) · I. Ivanov · B. Corves
Department of Mechanism Theory and Dynamics of Machines (IGM), RWTH Aachen University, Aachen, Germany
e-mail: schoenen@rwth-aachen.de

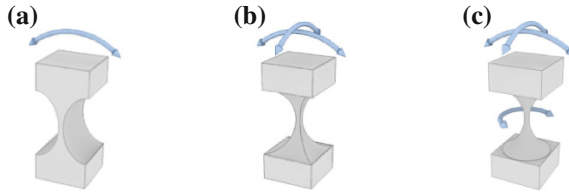


Fig. 1 Degrees of freedom and design of notch-joints 1DoF (a) 2DoF (b) and 3DoF (c)

Notch-joints have many advantages like free from backlash, frictionless and high potential for miniaturization. The disadvantages on the other hand are parasitic effects, motion deviation, and limited range of motion [4]. The stiffness- or compliance values need to be known to assess the operating characteristics. These values are necessary, because the stiffness or compliance matrix includes information about the desired and unwanted degrees of freedom, the motion accuracy and the range of motion [5].

The compliance matrix C defines a linear elastic context $\delta = C \cdot \Lambda$ between the deformation vector δ and the load vector Λ in Eq. (1). Figure 2 shows a notch-joint that is cantilevered and subjected to forces (F_i) and torques (T_i) on the other side. The resulting translational and rotational deformations (u_i, θ_i) can be determined by either analytical methods, the finite element methods (FEM) or experimental methods. These methods can be used to calculate the compliance matrix C and thus indirectly the stiffness matrix $K = C^{-1}$ of the notch-joint.

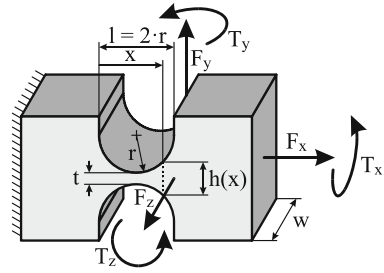
$$\begin{pmatrix} u_x \\ u_y \\ u_z \\ \theta_x \\ \theta_y \\ \theta_z \end{pmatrix} = \begin{pmatrix} C_{u_x;F_x} & 0 & 0 & 0 & 0 & 0 \\ 0 & C_{u_y;F_y} & 0 & 0 & 0 & C_{u_y;T_z} \\ 0 & 0 & C_{u_z;F_z} & 0 & C_{u_z;T_y} & 0 \\ 0 & 0 & 0 & C_{\theta_x;T_x} & 0 & 0 \\ 0 & 0 & C_{\theta_y;F_z} & 0 & C_{\theta_y;T_y} & 0 \\ 0 & C_{\theta_z;F_y} & 0 & 0 & 0 & C_{\theta_z;T_z} \end{pmatrix} \begin{pmatrix} F_x \\ F_y \\ F_z \\ T_x \\ T_y \\ T_z \end{pmatrix} \quad (1)$$

2 Generalization of the Analytical Method

The theory of the strength of materials provides a simple and rapid analytical method for calculating the compliance matrix of notch-joints. Because of this, there are already many approaches to describe the real operating behavior of notch-joints (first approach in [6]). In numerous previous publications set of formulas for a selected notch-joint was derived or optimized, whereas in this paper a general approach to the problem will be pursued.

Based on Castigliano’s second theorem (The first partial derivative of the strain energy U in a linear elastic structure with respect to the generalized force Q_i equals

Fig. 2 Notch-joint with right-elliptical cut-out



the generalized displacement q_i in the direction of Q_i [7]) the common elements of the compliance matrix C of notch-joints are determined [8] (cf. Eqs. (2–13).

Traction and Pressure along x-Axis:

$$U = \frac{1}{2} \int_0^l \frac{F_x^2(x)}{E \cdot A(x)} dx \text{ implies } \left. \frac{\partial U}{\partial F_x} \right|_{F_x=1N} = C_{u_x;F_x} = \frac{1}{E \cdot w} \int_0^l \frac{dx}{h(x)} \quad (2)$$

Deflection about z-Axis:

$$U = \frac{1}{2} \int_0^l \frac{T_z^2(x)}{E \cdot I_z(x)} dx + \frac{1}{2} \int_0^l \frac{K \cdot F_y^2(x)}{G \cdot A(x)} dx \quad (3)$$

$$\left. \frac{\partial U}{\partial T_z} \right|_{T_z=1Nm, F_y=0} = C_{\theta_z;T_z} = \frac{12}{E \cdot w} \int_0^l \frac{dx}{h^3(x)} \quad (4)$$

$$\begin{aligned} \left. \frac{\partial U}{\partial F_y} \right|_{T_z=0, F_y=1N} &= C_{u_y;F_y} \\ &= \frac{12 \cdot I^2}{E \cdot w} \int_0^l \frac{dx}{h^3(x)} - \frac{24 \cdot I}{E \cdot w} \int_0^l \frac{x}{h^3(x)} dx + \frac{12}{E \cdot w} \int_0^l \frac{x^2}{h^3(x)} dx + \frac{k}{G \cdot w} \int_0^l \frac{dx}{h(x)} \end{aligned} \quad (5)$$

$$\left. \frac{\partial U}{\partial T_z} \right|_{T_z=0, F_y=1N} = C_{\theta_z;F_y} = \frac{12 \cdot I}{E \cdot w} \int_0^l \frac{dx}{h^3(x)} - \frac{12}{E \cdot w} \int_0^l \frac{x}{h^3(x)} dx \quad (6)$$

$$\left. \frac{\partial U}{\partial F_y} \right|_{T_z=1Nm, F_y=0} = C_{u_y;T_z} = \frac{12 \cdot I}{E \cdot w} \int_0^l \frac{dx}{h^3(x)} - \frac{12}{E \cdot w} \int_0^l \frac{x}{h^3(x)} dx \quad (7)$$

Deflection about y-Axis:

$$U = \frac{1}{2} \int_0^l \frac{T_y^2(x)}{E \cdot I_y(x)} dx + \frac{1}{2} \int_0^l \frac{K \cdot F_z^2(x)}{G \cdot A(x)} dx \quad (8)$$

$$\left. \frac{\partial U}{\partial T_z} \right|_{T_y=1Nm, F_z=0} = C_{\theta_z; T_y} = \frac{12}{E \cdot w} \int_0^l \frac{dx}{h^3(x)} \quad (9)$$

$$\begin{aligned} \left. \frac{\partial U}{\partial F_z} \right|_{T_z=0, F_y=1N} &= C_{u_z; F_z} \\ &= \frac{12 \cdot I^2}{E \cdot w} \int_0^l \frac{dx}{h^3(x)} - \frac{24 \cdot I}{E \cdot w} \int_0^l \frac{x}{h(x)} dx + \frac{12}{E \cdot w^3} \int_0^l \frac{x^2}{h(x)} dx + \frac{k}{G \cdot w} \int_0^l \frac{dx}{h(x)} \end{aligned} \quad (10)$$

$$\left. \frac{\partial U}{\partial T_y} \right|_{T_z=0, F_z=1N} = C_{\theta_y; F_z} = \frac{12}{E \cdot w^3} \int_0^l \frac{x}{h(x)} dx - \frac{12 \cdot I}{E \cdot w^3} \int_0^l \frac{dx}{h(x)} \quad (11)$$

$$\left. \frac{\partial U}{\partial F_z} \right|_{T_y=1Nm, F_z=0} = C_{u_z; T_y} = \frac{12}{E \cdot w^3} \int_0^l \frac{x}{h(x)} dx - \frac{12 \cdot I}{E \cdot w^3} \int_0^l \frac{dx}{h(x)} \quad (12)$$

In the above equations $A(x) = w \cdot h(x)$ describes the cross-sectional area. If the shear effect is not negligible, the shear shape factor k is 1.2 (for rectangles) [7]. $I_z(x) = w \cdot h^3(x)/12$ and $I_y(x) = w^3 \cdot h(x)/12$ are the moments of inertia about the z - and y -axis. E is the Young's Modulus and G is the Modulus of Rigidity. In the above equations the notch-joint is fully described with a constant length l and width w and a variable height $h(x)$. The variable height $h(x)$ can be mathematically formulated for selected notch-joints for example a right-circular profile as $h(x) = 2r + t - 2\sqrt{r^2 - (x - r)^2}$ (cf. Fig. 2).

Such an approach is realized with mathematical software like MATLAB, because the problem of integrating several functions $h(x)$ can be solved numerically instead of an analytical approach. Accordingly, a program for the efficient calculation of the compliance and stiffness matrix of user-modified notch-joint profiles has been developed with a graphical user interface where the compliance and stiffness matrixes are shown for chosen notch profiles and given parameters of geometry and material. It serves as a foundation for higher modules, in which the operating characteristics of a micromanipulator can be investigated by compliance and stiffness calculation of serial and parallel kinematic structures [9].

3 Extension of the Analytical Method with FEM

Based on the second theorem of Castigliano the general torsion of the compliance matrix of notch-joints can also be determined using Eq. (13).

$$U = \frac{1}{2} \int_0^l \frac{T_x^2(x)}{G \cdot I_x(x)} dx \text{ implies } \left. \frac{\partial U}{\partial T_x} \right|_{T_x=1Nm} = C_{\theta_x-T_x} = \frac{1}{G} \int_0^l \frac{dx}{I_x(x)} \quad (13)$$

$I_x(x)$ is the moment of Inertia in case of a torsion about the x-Axis and results from various approximation formulas such as [10]

$$I_x(x) = w \cdot h^3(x) \cdot \left[0.333 - 0.21 \cdot \frac{h(x)}{w} \cdot \left(1 - \frac{h^4(x)}{12 \cdot w^4} \right) \right] \quad (14)$$

which is used in [8]. These approximation formulas lead to a very high torsional compliance, which is not detectable due to the lack of warping torsion in notch-joints (cf. Table 1).

Reliable results for all elements of the compliance matrix (including torsion) can be achieved with the help of FEM (such as in [11]). Modelling a large variety of similar notch-joints within the FEM-software is a very complex process. To work around the problem of “modelling by hand” a script oriented solution has been used. An approach like this allows a comprehensive characterization of notch-joints based on the results of previous studies [12]. The focus here is on circular and elliptical notch-joint profiles, as special cases of a general elliptical notch profile [13] (Fig. 3b). An analysis is conducted, in which the geometry parameters are varied and their effects on the operating behavior are taken into account. The results show that corresponding circular and elliptical notch-joints have similar properties. Furthermore, the properties of the circular notch-joints are nearly linear in contrast to those of the elliptical notch-joints. Thus these properties can be formulated mathematically by using low degree polynomials [14] (cf. Fig. 3a).

Table 1 Torsional compliance of right circular notch-joint (w = 16 mm, r = 2 mm)

Web thickness		0.2	0.3	0.4	0.5	0.6	(mm)
$\frac{E \cdot \theta}{M_z}$	Analytic	17.4379	6.3187	3.0732	1.7563	1.1115	$\left(\frac{10^9 \text{ rad}}{\text{m}^3}\right)$
	FEM	0.1675	0.0968	0.0663	0.0498	0.0395	

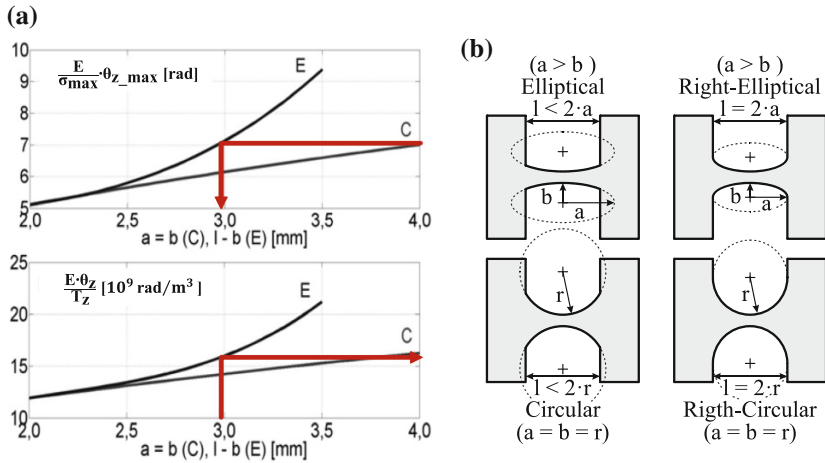


Fig. 3 Comparisons of circular and elliptical notch-joints with reference to bending compliance (top) or motion range (bottom) (a) and different notch-profiles (b)

4 Experiment

For experimental validation of the method described above, a test stand has been constructed on which the bending and torsional compliance of the tested notch-joints could be examined. The bending compliance (about the z-axis) causes the desired rotary degree of freedom and the torsional compliance (about the x-axis) causes the “most” unwanted parasitic motion [14]. The test stand consists of the frame and the plate. In each of them one end of the tested notch-joint-specimen is clamped. The plate contains the force sensors and also serves as a lever arm through which the notch-joint is subjected to load and deformed. Micrometer screws are attached onto the frame and generate the stroke which corresponds to a bending- or torsional-deformation of the notch-joint. The subsequent bending- or torsional-stress is indicated by a voltage, which is measured by the force sensor (cf. Fig. 4).

The profile of the tested notch-joints is circular. The geometry parameters are as follows: $w = 16$ mm, $l = 4$ mm, $t = 0.4$ mm, $r = 3$ mm. Despite the tight manufacturing tolerances achieved by eroding, the influence of the deviation in the hinge thickness on the bending- and torsional compliance cannot be neglected (Fig. 5).

After the quality inspection using scanning electron microscopy two tested notch-joints with the same width ($w = 15.952$ mm) and maximum difference in minimum hinge thickness ($t_1 = 401.7$ μ m, $t_2 = 408.5$ μ m) are selected for the comparative analysis. In addition to the experimental results, the corresponding analytical and FEM results are presented in Tables 2, 3.

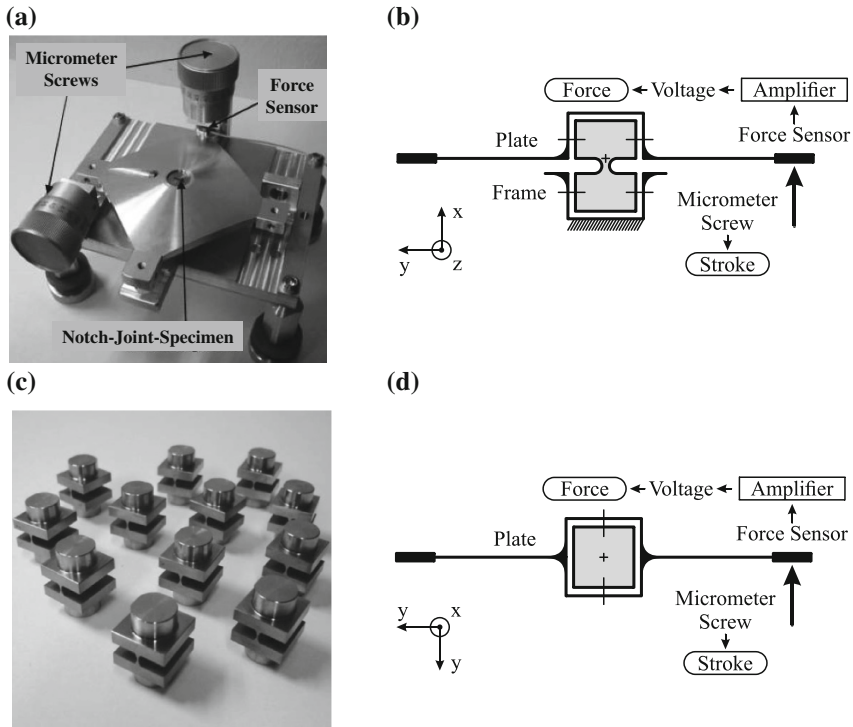


Fig. 4 Test stand (a) and schematic representation of setup for estimating the bending compliance (b) and torsional compliance (d) of the test specimen (circular notch joints) (c)

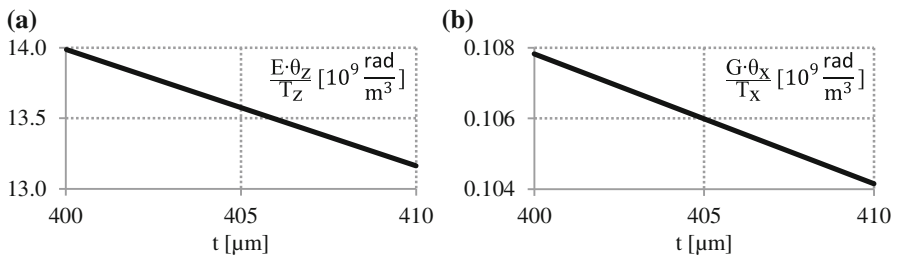


Fig. 5 The effect of deviation in the hinge thickness of circular notch-joints (based on FEM: $w = 15.95$ mm, $l = 4$ mm, $r = 3$ mm). **a** Bending compliance. **b** Torsional compliance

Table 2 Bending compliance of tested notch-joints ($w = 15.95$ mm, $l = 4$ mm, $r = 3$ mm)

Web thickness (μm)	Test $\frac{\theta_z}{M_z} \left(\frac{\text{rad}}{\text{Nm}} \right)$	FEM $\frac{E \cdot \theta_z}{M_z} \left(\frac{10^9 \text{ rad}}{\text{m}^3} \right)$	Analytic $\frac{E \cdot \theta_z}{M_z} \left(\frac{10^9 \text{ rad}}{\text{m}^3} \right)$
401.7	0.1462	13.8485	14.6849
408.5	0.1359	13.2871	14.0749

Table 3 Torsional compliance of tested notch-joints ($w = 15.95$ mm, $l = 4$ mm, $r = 3$ mm)

Web thickness	Test	FEM	Analytic
(μm)	$\frac{\theta_x}{M_x} \left(\frac{\text{rad}}{\text{Nm}} \right)$	$\frac{G \cdot \theta_x}{M_x} \left(\frac{10^9 \text{ rad}}{\text{m}^3} \right)$	$\frac{G \cdot \theta_x}{M_x} \left(\frac{10^9 \text{ rad}}{\text{m}^3} \right)$
401.7	0.002972	0.1072	—
408.5	0.002899	0.1047	—

5 Conclusions

The experimental results show that an increasing minimum hinge thickness in the tested notch-joints logically leads to a reduction of the bending and torsion compliances; bending: 7.5 %, torsion: 2.5 %. These results are in a good conformity with the FEM results; bending: 4.1 %, torsion 2.3 %. While comparing the compliance, the results of FEM using Young's Modulus $E \approx 95 \dots 100$ GPa also show good conformity. The material of the tested notch-joints-specimen is Ti-6Al-4 V. The Young's Modulus of this material is $E \approx 110$ GPa [15]. The real value of E for the semi-finished part before and after finishing is unknown. Therefore, an experimental verification of the Young's Modulus of the notch-joints is necessary to evaluate the methods for calculating compliance matrices of notch-joints. Only with a reliable and accurate value of the elastic modulus is required to discuss measurement errors, and to examine correlations between the analytical method, the finite element method and the experimental method.

Acknowledgments The authors are grateful to Univ.-Prof. Dr. rer. nat. J. Mayer and the Facility for Electron Microscopy, RWTH Aachen for the conduct of measurements on the test specimen. This collaboration has resulted in a joint research project funded by the German Grant Authority DFG, which also includes the Laboratory for Machine Tools and Production Engineering of RWTH Aachen University.

References

1. Christen G, Kunz H, Pfefferkorn H (1997) Stoffschlüssige Gelenke für nachgiebige Mechanismen. Kolloquium Getriebetechnik, Warnemünde, pp 59–68
2. Raatz A (2006) Stoffschlüssige Gelenke aus pseudo-elastischen Formgedächtnislegierungen in Parallelrobotern. Dissertation, TU Braunschweig
3. Linß S, Erbe T, Zentner L (2011) On polynomial flexure hinges for increased deflection and an approach for simplified manufacturing. In: 13th World congress in mechanism and machine science, 2011, A11_512
4. Howell LL (2001) Compliant mechanisms. Wiley, Hoboken
5. Smith ST (2000) Flexures, elements of elastic mechanisms. Gordon and Breach, UK
6. Paros JM, Weisbord L (1965) How to design flexure hinges. Machine design 37:151–156
7. Ugural AC, Fenster SK (2003) Advanced strength and applied elasticity. Pearson Education, Upper Saddle River
8. Lobontiu N (2003) Compliant mechanisms, design of flexure hinges. CRC Press, Boca Raton

9. Ivanov I, Corves B (2012) Stiffness oriented design of flexure hinge based parallel manipulators. In: 2th International conference on microactuators and micromechanisms, Durgapur (India), (in press)
10. Young WC (1989) Roark's formulas for stress and strain. McGraw-Hill, New York
11. Zhang S, Fasse ED (2001) A finite-element-based method to determine the spatial stiffness properties of a notch hinge. Mech Des 123:141–147
12. Linß S, Zentner L (2011) Gestaltung von Festkörpergelenken für den gezielten Einsatz in ebenen nachgiebigen Mechanismen. 9. Kolloquium Getriebetechnik, Chemnitz, S. 291–311
13. Chen G, Shao X, Huang X (2008) A new generalized model for elliptical arc flexure hinges. Sci Instr 79:095103
14. Ivanov I, Corves B (2012) Characterization of flexure hinges using the script oriented programming within a FEM software application. In: Mechanism and machine science vol 3, Springer, Berlin, pp 225–233
15. DIN 17851 (1990) Titanlegierungen. Beuth

Part XIV
Teaching Methods

Machine and Mechanism Design at UMinho: Research-Teaching Interaction

M. Lima, E. Seabra and L.F. Silva

Abstract The Multiweave project involved the design of a prototype machine with several mechanisms, namely gear trains and various conjugate cams with oscillating roller followers. For this design phase the research team integrated postgraduate student work. In order to evaluate the quality of the manufactured cam profiles as well as the accuracy of the follower's displacement, an experimental work has been designed. This study, which was carried out within a final year Mechanical Engineering student's group project, was of great importance in the development of the prototype machine to produce multidirectional woven fabrics, which was the main objective of the Multiweave project. The whole set-up is presented with the experimental details and the results are analysed and discussed. This measurement system is based on a laser triangulation sensor Micro-Epsilon ILD 1302-50 to measure with no contact and high resolution. The obtained results were compared with the expected theoretical values and it could be concluded that, in general, the experimental results adjust very well to the theoretical ones. However it was possible to conclude about the existence of some differences due to clearances in joints, geometric differences in the kinematic chain and manufacturing defects on the follower in terms of irregularities and surface roughness as well as some manufacturing imperfections of the cam surface.

Keywords Multiweave · Multiaxial fabric · Cam mechanisms · Laser measurements

M. Lima (✉) · E. Seabra · L.F. Silva
University of Minho, Braga, Portugal
e-mail: mlima@dem.uminho.pt

E. Seabra
e-mail: eseaba@dem.uminho.pt

L.F. Silva
e-mail: lffsilva@dem.uminho.pt

1 Introduction

In the Multiweave project a prototype weaving machine to produce a multidirectional woven fabric was investigated, designed and manufactured [1–3]. This is an innovative textile structure designed to compensate the usual anisotropic properties of conventional biaxial fabrics, being of great importance for technical applications such as in the reinforcement of special composite materials requiring improved mechanical properties for high technology applications. Figure 1 is an example of such fabrics made from high tenacity polyester and carbon fibres and the Multiweave prototype is partially shown in Fig. 2. The concept of the machine contains several mechanisms such as for the movements of the reed, heddle and weft insertion, all in perfect synchronization and achieved by means of conjugate cam mechanisms.

2 Cams Design and Manufacturing

The proper design of cam mechanisms is usually one of the most important and difficult steps in machine design. In the case of Multiweave and following the practice of the industry, conjugate cams were recommended [4]. Spring return is not acceptable for two main reasons: it would considerably increase the already high

Fig. 1 Multiweave fabric sample

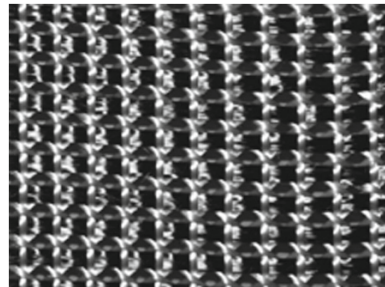


Fig. 2 Multiweave prototype

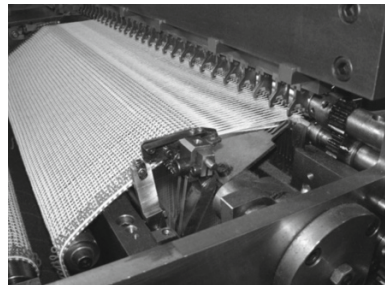
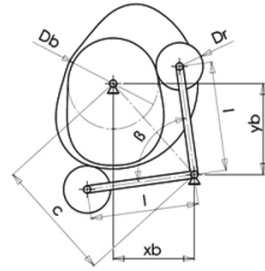


Fig. 3 Conjugate cams geometric model



torque required in the cam shaft and, in the case of failure to follow the cam profile, it would result in unacceptable collisions with catastrophic results. The work was therefore concerned with the process of designing and manufacturing such mechanisms. A model of a conjugate cam with oscillating roller follower is shown in Fig. 3 where the basic design parameters are represented, namely,

- D_b Cam base diameter
- D_r Roller diameter
- c Distance from cam axis to follower pivot
- l Follower arms length
- β Follower arms angle
- x_b, y_b Coordinates of follower pivot from cam axis

For the modelling a program was created in MATLAB[®] environment which is capable of computing single or conjugate cams with oscillating or translating roller followers and contains equations for 10 different methods. In our case, modified sine method has been used [4]. Furthermore it allows inputting an unlimited number of sections for rising, dwell and return. The final part, after completing the design with the help of CAD software is obtained in a CNC machine.

As an example, the conjugate cams of the weft insertion mechanism were obtained as represented in Fig. 4. The complete 3D SolidWorks[®] design of one of the two conjugate cams is represented in Fig. 5, after adding several elements such as a large centre hole for reduced mass and 4 fixing holes.

Fig. 4 Cam profiles and pitch curves as obtained from MATLAB

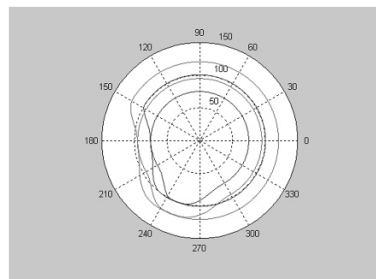
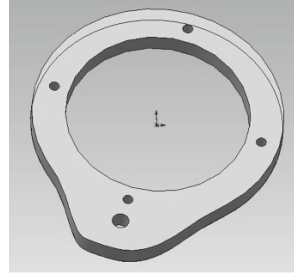


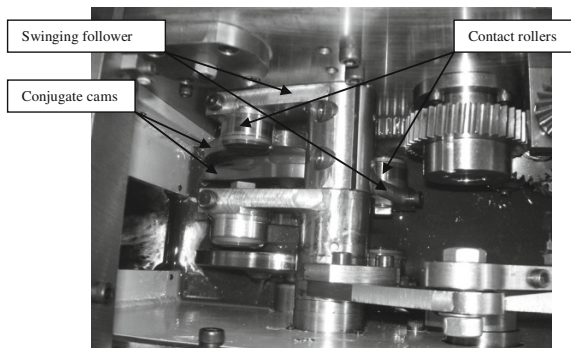
Fig. 5 3D design of one cam

One of the cam boxes of the prototype, with two sets of conjugate cams can be seen in Fig. 6, partially immersed in the lubrication oil. Also clearly visible are the swinging followers with two arms and the respective contact rollers.

The mechanism of the weft insertion can be seen in Fig. 7a, b, where conjugate cams with oscillating roller follower move a four bar linkage to drive a gear train to act upon the final pinion and flexible rack mechanism.

3 Students Project Work

Part of a final year students project, an experimental work was planned and carried out in order to analyse the kinematics of the weft insertion cam mechanisms in situ and to confirm the predictions of the theoretical model as well as to verify any deviations, possibly due to manufacturing errors, assembling problems and play in joints. This work involved the development of a measurement system based on a laser triangulation sensor to measure, with no contact and high resolution, the followers' oscillating displacements of the conjugate cams represented in the cam box of Fig. 6. A laser sensor Micro-Epsilon ILD 1302-50 [5, 6], with a resolution of 10 μm has been used involving two measurements: the follower displacement and the cams profiles. Very low speed was used in order to minimise vibrations. Figure 8

Fig. 6 Conjugate cams in cam box

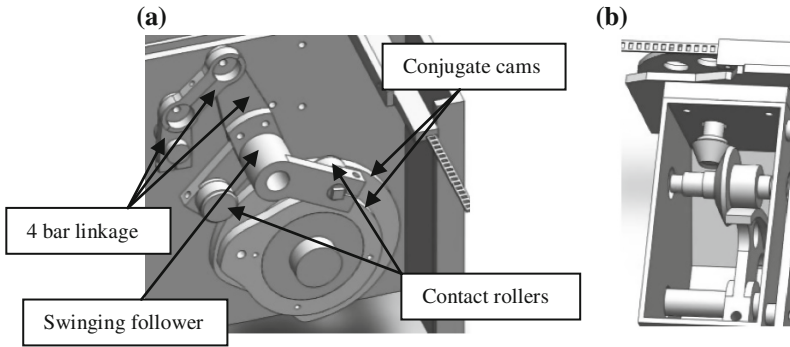
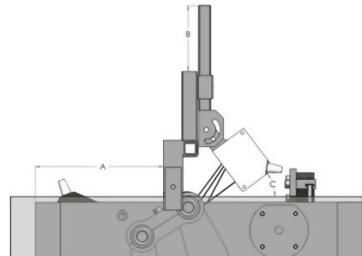


Fig. 7 Details of the weft insertion mechanism. **a** Conjugate cams and 4 bar linkage, **b** Transmission to flexible rack

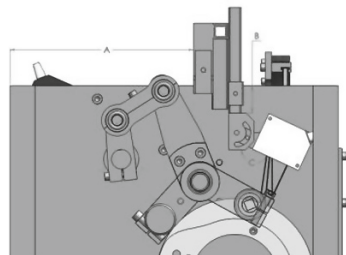
Fig. 8 Measurement of follower position



represents the geometry when measuring the follower position ($A = 143.7$ mm, $B = 92.4$ mm, $C = 43.1^\circ$) and Fig. 9 when measuring the cams profiles ($A = 234.3$ mm, $B = 37.9$ mm, $C = 163.1^\circ$).

To accomplish this experimental work, a PC-based commercial data acquisition hardware has been used together with a software specifically developed for this purpose using the LabVIEW[®] platform from National Instruments.

Fig. 9 Measurement of cams profiles



4 Results and Discussion

Figure 10 represents the experimental data versus the theoretical values for the cam follower displacement, as obtained with the set-up shown in Fig. 8. It can be concluded that, in general, the experimental results follow the theoretical values for the modified sine equation. However, looking at the results with more detail, there are some visible differences between the experimental and theoretical values, as shown in Fig. 11.

These visible differences in the follower movements (rise and return), happened, approximately, between 0° and 90°, which can be linked to measuring errors due to the curvature of the follower’s surface and consequently, perpendicularity loss

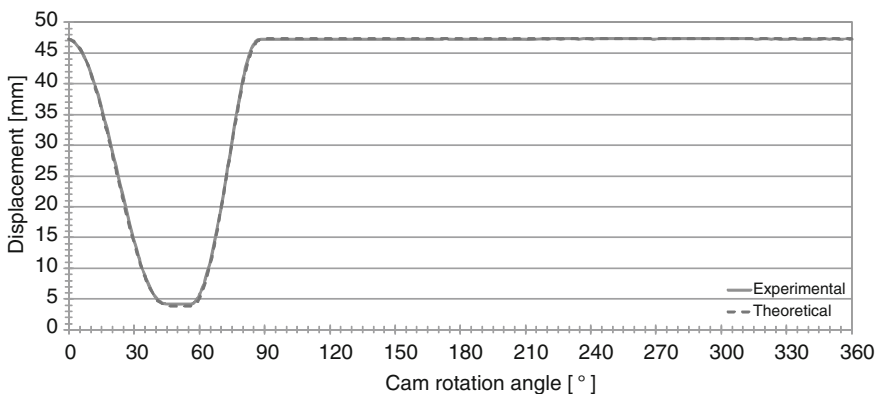


Fig. 10 Experimental data versus theoretical values for the cam follower displacement

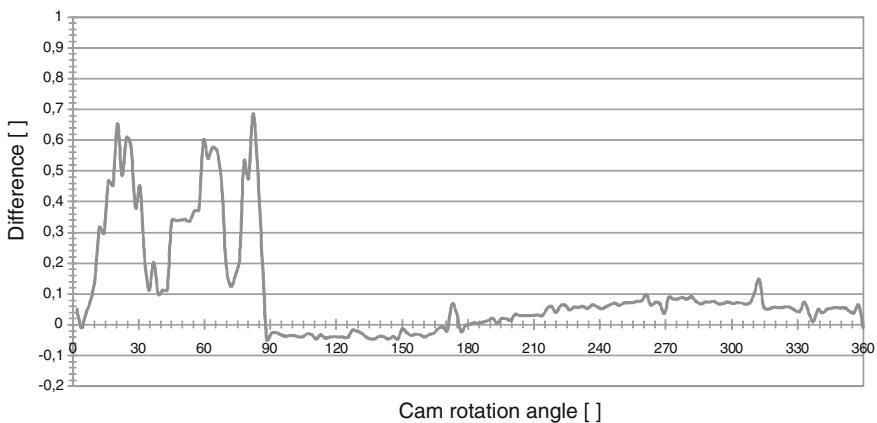


Fig. 11 Differences between experimental and theoretical values for the cam follower displacement of Fig. 10

between the laser beam and the measured surface, existence of clearances in joints and differences between designed and real cam profiles, originating a different follower displacement.

It can also be observed that, approximately between 0° and 90° the experimental data are greater than the expected theoretical values, which may be due to existent clearances in joints and geometric differences in the kinematic chain, besides the ones existing in the follower shaft.

On the other hand, it is also visible the occurrence of a peak in the beginning of the follower's return movement, approximately between 55° and 60° , that can be related once again to existent clearances in joints, manufacturing defects on the follower surface (in terms of irregularities and surface roughness), and to other manufacturing imperfections of the cam surface.

Finally, between 90° and 360° , it can be also observed two types of problems: the first one, which is related to a sinusoidal variation of the differences (approximately with the same width), can be induced by the noise, surface roughness, measuring interferences; and, the second one, due to a quick ascent followed by a descent movement (curve with two concavities, first negative and then positive), which was probably created by a cam off-centred or by a manufacturing defect.

Figures 12 and 13 respectively present the experimental data versus the theoretical values for the rise and return displacement of the cam profiles, as obtained by the set-up shown in Fig. 9. Globally, it can be concluded that, in both cases, the experimental results follow the theoretical values. However, as it is highlighted in detail in Figs. 14 and 15, there are some observable differences between the experimental and theoretical values.

These observable differences in the cams profiles (rise and return), occurred, approximately, between the rotation angles of 0° and 90° . This could have been derived from the measuring errors due to the cams curvatures, cams off-centred, and designed cams profiles different from the real cams profiles, originating different follower's displacements.

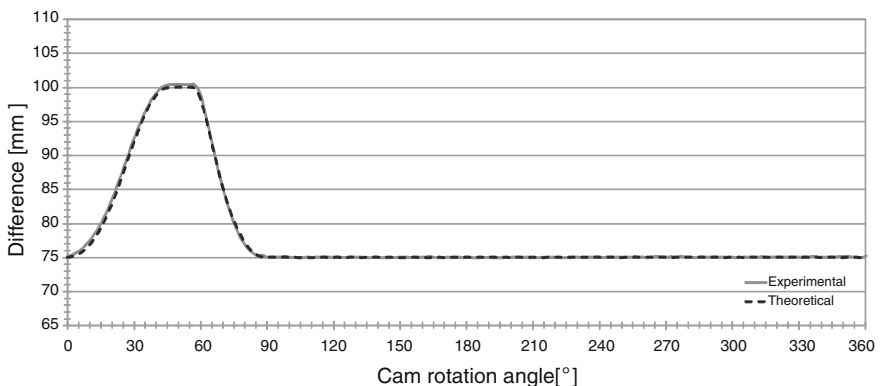


Fig. 12 Experimental data versus theoretical values for the rising cam profile

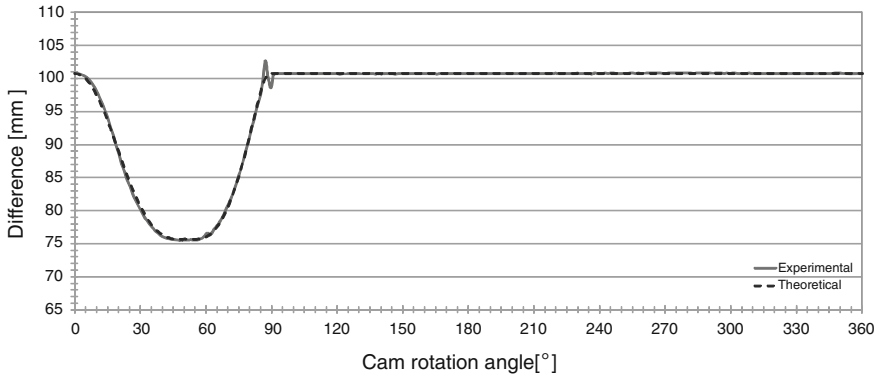


Fig. 13 Experimental data versus theoretical values for the return cam profile

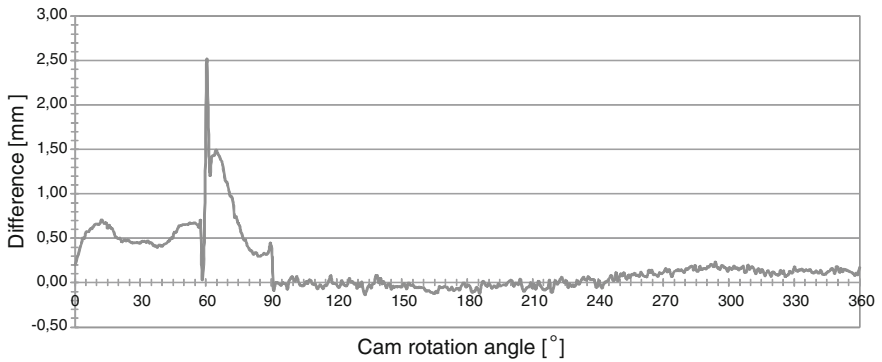


Fig. 14 Differences between experimental and theoretical values for the rising cam profile

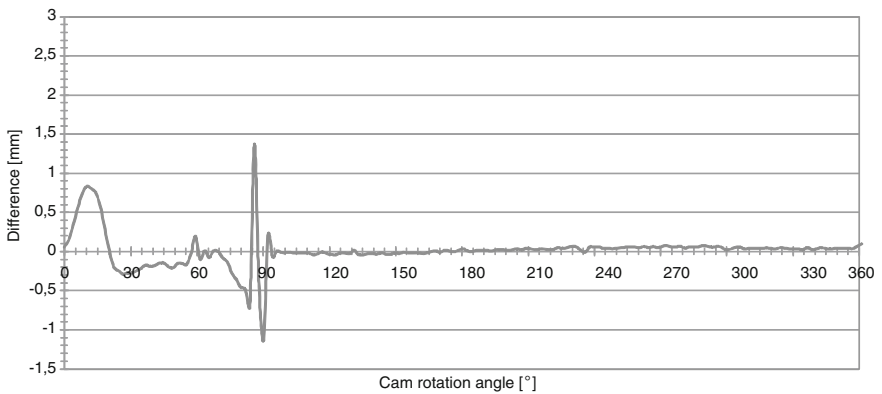


Fig. 15 Differences between experimental and theoretical values for the return cam profile

It can also be observed in the rising cam, approximately between 45° and 55° , that the experimental data are greater than the expected theoretical values, while for the return cam the opposite occurs. As in previous cases, it can be due to cams off-centred and manufacture defects in the cams profiles.

It is also possible to observe the clear occurrence of two peaks: one in the rising cam at the beginning of the follower's return movement (around 60°), and another in the return cam at the ending of the follower's rising movement (around 87°). Once again these peaks can be related to some manufacturing defects on the cams surfaces, where it is possible to confirm (at naked eye) local irregularities.

Finally, it can also be observed, between the rotation angles of 90° and 360° , two types of problems, which, for the authors, are of the same nature of those described in the analysis carried out for the cam follower displacement.

Due to the main errors identified in the follower movement and in the cams profiles, and their consistency (occurring in the same angular positions), it is possible to conclude that the acquisition system designed and developed specifically for this purpose (based on a laser triangulation sensor) proved to be very appropriate to measure, with no contact and with high resolution, the follower oscillating movements (rise and return) of conjugate cams. On the other hand, based on the angles of the detected cam position errors, it allowed the evaluation of the errors magnitude in the cams and follower. According to the computed results, it was also possible to conclude that the magnitude of the obtained differences between the theoretical values and experimental data are similar for the follower and cams.

5 Conclusions

The interaction between teaching and research has been achieved with success. In the design phase the research team integrated postgraduate student work. Later an experimental study was carried out within a final year Mechanical Engineering student's group project to evaluate the conformity of various mechanisms.

As a result, conjugate cams could be obtained using a MATLAB[®] based program which allowed a very fast design process. The designer can quickly obtain and compare several different designs, and, on the basis of the analysis of the kinematics characteristics, optimize the mechanism. The result can easily be exported to a CAD tool to create the complete 3D design of the cams. The final CAD file is directly used as a source data for the CNC manufacturing.

An investigation was carried out to evaluate the quality of the manufactured cam profiles as well as the accuracy of the follower displacement. An experimental work was designed and carried out based on a measurement system using a laser triangulation sensor Micro-Epsilon ILD 1302-50 to measure with no contact and high resolution. The obtained results were compared with the expected theoretical values. It could be concluded that, in general, the experimental readings follow the theoretical values but with some visible differences between the measured results and the expected theoretical values which could be explained by the clearances in

joints, geometric differences in the kinematic chain and manufacturing defects on the follower surface in terms of irregularities and surface roughness as well as some manufacturing imperfections of the cam surface. This study has been of great importance to improve the quality of the manufactured mechanisms and to the development of the Multiweave prototype.

References

1. Lima M et al (2007) MULTIWEAVE—multiaxial weaving: from concept to prototype. In: AUTEX 2007 international conference, 7th annual textile conference by Autex, From emerging innovations to global business, 26–28 June 2007, Tampere, Finland, ISBN 978-952-15-1794-5
2. Lima M et al (2007) MULTIWEAVE—Prototype weaving machine for multiaxial technical fabrics. In: ALTEX 2007 conference proceedings, CD ROM, ALTEX 2007, 20–22nd Sept 2007, Roubaix, France
3. Lima M et al (2009) MULTIWEAVE—prototype weaving machine for multiaxial technical fabrics. *Indian J Fibre Text Res* 34:59–63
4. Lima M, Zabka P (2010) Design and analysis of conjugate cam mechanisms for a special weaving machine application. In: 2nd international conference on innovations, recent trends and challenges in mechatronics, mechanical engineering and new high-tech products development —MECAHITECH'10, Bucharest, Romania, 23–24 Sep 2010
5. Micro-Epsilon (2011) ILD 1302. <http://www.micro-epsilon.com/index.html>. As visited on 29 July 2011
6. Micro-Epsilon (2011) optoNCDT-1302. http://www.cdiweb.com/datasheets/micro_epsilon/dax-optoNCDT-1302-en.pdf. As visited on 29 July 2011

Computer Aided, Task-Based Kinematic Design of Linkages: A New Lecture for Engineering Students

K. Abdul-Sater, T.C. Lueth and F. Irlinger

Abstract This paper presents the topics, methods and objectives of a new lecture on CAD-integrated kinematic design of linkages for master students. The contents enable students in mechanical engineering to analyze and synthesize structures kinematically using advanced software tools such as numerical and algebraic computation software as well as 3D solid modeler. The structures range from 1-DOF mechanisms up to multi-DOF serial and parallel linkages. Using a generalized nomenclature and vector-matrix-based formulation of the geometry and kinematics of the systems, students are enabled to design both planar and spatial structures. The major objective is to provide the techniques and foundations for task specific synthesis and analysis of linkages with a strong focus on practical applications, which is demonstrated in an example design session in this paper.

Keywords Computer aided linkage design · Task specific design · Analysis and synthesis

1 Introduction

The lecture presented in this paper enables master students to analyze and synthesize different *task specific* linkages kinematically in a computer aided design process. The structures students shall be able to create range from serial to parallel mechanisms both planar and spatial and may lie behind mechanical and mecha-

K. Abdul-Sater (✉) · T.C. Lueth · F. Irlinger

Institute of Micro Technology and Medical Device Technology, Faculty of Mechanical Engineering, Technische Universität München, 85748 Garching, Germany
e-mail: kassim.abdul-sater@tum.de

T.C. Lueth
e-mail: tim.lueth@tum.de

F. Irlinger
e-mail: irlinger@tum.de

tronic devices in different applications. Examples of such applications may require a single motion path of specific parts and are for instance car door guidance, retractable tops of sports cars or transformable furniture. Furthermore, also tasks are considered which require a task specific workspace. Examples of this case are e.g., laparoscopic orientation tasks of medical devices, pick-and-place or welding tasks.

The lecture starts with a review of basic mathematical tools such as linear algebra, vector calculus and nonlinear equations. Based on this, kinematics foundations (see Sect. 2) are introduced, which are then followed by the synthesis section (Sect. 3), representing the biggest part of the lecture. In order to enable students to design feasible structures, another section on different kinematic analysis techniques is provided. A particular feature of the lecture is that the introduction of any kinematics calculations always parallels a discussion on practical applications as well as the implementation using 3D-CAD or calculation software tools such as Matlab, Mathematica or Maple. Thereby, the goal is to teach a *creative kinematic design process*, which may directly fade to a virtual product development process. An efficient way to combine a CAD-system and a calculation tool is introduced in order to show how to partially automate computations or to evaluate variations of parameters. This is based on the approach of ‘*CAD-integrated kinematic design using externally connected solver-code*’, which, however, is not part of this paper (for details see [1]). We also wish to mention that, due to space limitations, we had to restrict ourselves here to three sources of the numerous excellent literature on the kinematic theory.

2 Nomenclature and Mathematical Modeling

The kinematics part starts by introducing coordinate frames $B_1 \dots B_m$, corresponding to the number of links $K_1 \dots K_m$, in order to measure the motion of a linkage with respect to a fixed world frame W . The frames allow us to introduce the elements of the group of rotations $SO(3)$ as matrices ${}^W\mathbf{R}_{B_j}$, assembled from the unit vectors of a frame B_j . The nomenclature is inspired from a notation used in [4], Sect. 1, where the left superscript indicates that coordinates are measured in W . If a particular linkage configuration i should be addressed (in particular for synthesis) another right superscript is added: ${}^W\mathbf{R}_{B_j}^i$. Based on this, the *composition of coordinate rotations* is introduced in order to demonstrate the construction of general spatial orientations, where finally the composition of *longitude, latitude and roll angles* is shown, suitable to define spherical orientation tasks (see e.g., [3]).

Translation vectors are denoted as ${}^W\mathbf{t}_{B_j}$, which point from the origin of W to that of B_j and are measured in W . Using these entities the *displacement equation* is derived, which describes a configuration i of points X in a rigid link:

$${}^W \mathbf{x}^i = {}^W \mathbf{R}_{Bj}^i {}^{Bj} \mathbf{x} + {}^W \mathbf{t}_{Bj}^i, \quad i = 1, \dots, n \quad (1)$$

By adding a fourth vector component normalized to 1, the *homogeneous representation* of the displacement equation is obtained:

$${}^W \mathbf{x}^i = \begin{pmatrix} {}^W \mathbf{R}_{Bj}^i & {}^W \mathbf{t}_{Bj}^i \\ 0^T & 1 \end{pmatrix}^{Bj} \mathbf{x} = {}^W \mathbf{T}_{Bj}^i \mathbf{x}. \text{ Using this notation then } ({}^W \mathbf{T}_{Bj}^i)^{-1} = {}^{Bj} \mathbf{T}_W^i$$

(*inverse of a displacement*) and ${}^W \mathbf{T}_{B2}^i = {}^W \mathbf{T}_{B1}^{i B1} \mathbf{T}_{B2}^i$ (*composition of displacements*) are introduced. However, in what follows the focus is on performing vector calculations in W , which are introduced by deriving the *relative displacements*, denoted as $\mathbf{T}_{Bj}^{kl} = {}^W \mathbf{T}_{Bj}^l ({}^W \mathbf{T}_{Bj}^k)^{-1}$, which only consist of coordinates measured in W . For this reason the simplified notation \mathbf{T}_{Bj}^{kl} only contains information on the frame Bj . \mathbf{T}_{Bj}^{kl} represents the transformation of Bj from a configuration k to l and its parameters are obtained by solving (1) at $i = k$ for ${}^{Bj} \mathbf{x}$ and re-substituting into (1) at $i = l$. This yields the relative displacement equation:

$$\mathbf{x}^l = \mathbf{R}_{Bj}^{kl} \mathbf{x}^k + \mathbf{t}_{Bj}^{kl} \quad (2)$$

For planar motion one has $\mathbf{R} \in SO(2)$, $t \in \mathbb{R}^2$ and hence T is an element of the motion group $SE(2)$ and it is shown how 2×1 -vectors x can be used to describe the location of revolute joints (R joints) of planar structures, while the orientation of hinges is not of interest. For $\mathbf{t} = 0$ and $\mathbf{R} \in SO(3)$ the spherical motion is obtained and students learn that in this case the orientation of R joints of spherical structures can be described by 3×1 coordinate vectors \mathbf{x} . For the general spatial case one has $\mathbf{R} \in SO(3)$, $\mathbf{t} \in \mathbb{R}^3$ and hence $\mathbf{T} \in SE(3)$ and it is shown how 3×1 -vectors \mathbf{x} may then be used to describe the center points of spherical (S) or universal (T) joints.

3 Kinematic Finite Position Synthesis

Based on the kinematics foundations the lecture introduces into the kinematic dimensional synthesis, which represents the biggest part of the lecture. Among other approaches such as optimization-based techniques the *algebraic finite position synthesis (FPS) theory* is selected, and [3] is the fundamental reference for the synthesis contents of our lecture. FPS is selected because it has grown into a well-developed theory with numerous robust algebraic solution techniques for a variety of basic linkage building blocks, also known as dyads. This allows it to design serial as well as parallel linkages with task specific DOF and kinematic dimensions. Even though it is clear that following this approach one can only design a linkage for a finite set of poses corresponding to the number of dimensional parameters in a linkage, we believe that FPS provides the best way to understand the fundamental nature of kinematic synthesis and also to learn an efficient formulation of kinematic

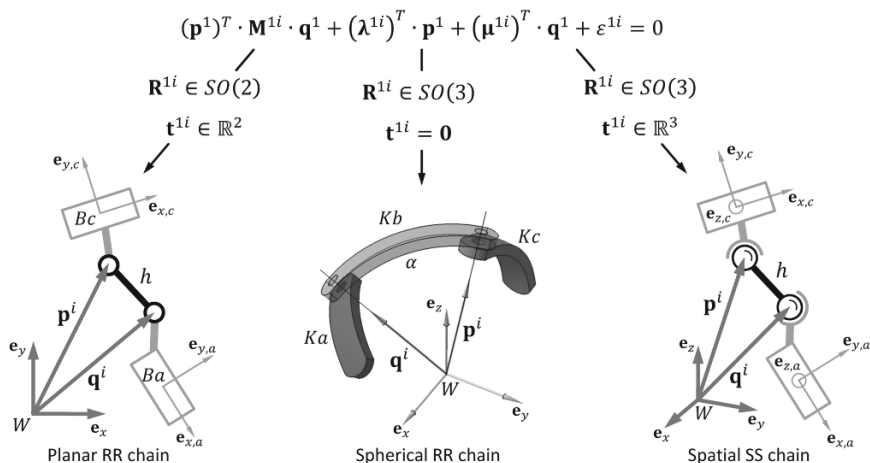


Fig. 1 Teaching strategy for kinematic finite position synthesis: the synthesis of planar and spherical RR chains and spatial SS chains by using one single design equation

design problems in general. Once understood the basic issues and formulations, students on the one hand can create surprisingly new linkage solutions for a given task using 3D CAD-systems in combination with computational tools (see Sect. 5). On the other hand, optimization-based synthesis can still be applied using the efficient formulations and valid initial guesses obtained from the algebraic solutions.

The particular feature of the synthesis section of our lecture is, that a unified notation is used to formulate the design problem for the *planar and spherical RR dyad* as well as the *spatial SS dyad*. This yields one single synthesis or design equation which includes each of these chains (see Fig. 1). For the planar RR and spatial SS chain these synthesis equations are based on the well-known constrained equation describing the constant distance h among the R or S joints in each configuration i of the chain: $(\mathbf{p}^i - \mathbf{q}^i)^T (\mathbf{p}^i - \mathbf{q}^i) = h^2, \quad i = 1, \dots, n$. Herein \mathbf{p} and \mathbf{q} are vectors measured in W , which point from the origin of W to the center points of the joints. In the case of planar RR chains one has 2×1 -vectors, for spatial SS chains one has general 3×1 -vectors. Subtracting the first equation from the remaining ones eliminates the parameter h and substituting relative displacements $\mathbf{q}^i = \mathbf{R}_{Ba}^{1i} \mathbf{q}^1 + \mathbf{t}_{Ba}^{1i}$ and $\mathbf{p}^i = \mathbf{R}_{Bc}^{1i} \mathbf{p}^1 + \mathbf{t}_{Bc}^{1i}$ using Eq. (2) allows it to describe \mathbf{p}^i and \mathbf{q}^i in terms of $\mathbf{p}^1, \mathbf{q}^1$ and the movement of the frames Ba and Bc . From these frames students see that the constrained-based synthesis approach cannot be used to synthesize joints among consecutive links. The movement of Ba and Bc will be pre-defined for synthesis and after some rearranging of the constraint equation the set of bilinear scalar design equations is obtained:

$$(\mathbf{p}^1)^T \mathbf{M}^{li} \mathbf{q}^1 + (\lambda^{li})^T \mathbf{p}^1 + (\mu^{li})^T \mathbf{q}^1 + \varepsilon^{li} = 0, \quad i = 2, \dots, n, \quad (3)$$

where $\mathbf{M}^{li} = \mathbf{E} - (\mathbf{R}_{Bc}^{li})^T \mathbf{R}_{Ba}^{li}$, $(\lambda^{li})^T = (\mathbf{t}_{Bc}^{li} - \mathbf{t}_{Ba}^{li})^T \mathbf{R}_{Bc}^{li}$, $(\mu^{li})^T = (\mathbf{t}_{Ba}^{li} - \mathbf{t}_{Bc}^{li})^T \mathbf{R}_{Ba}^{li}$ and $\varepsilon^{li} = \frac{1}{2}(\mathbf{t}_{Bc}^{li})^T \mathbf{t}_{Bc}^{li} - (\mathbf{t}_{Ba}^{li})^T \mathbf{t}_{Bc}^{li} + \frac{1}{2}(\mathbf{t}_{Ba}^{li})^T \mathbf{t}_{Ba}^{li}$. Techniques to solve Eq. (3) for $n = 2$, $n = 3$ and $n = 4$ pre-defined task poses of Ba and Bc are then discussed.

For the planar RR chain and $n = 4$ there are four unknown parameters $\mathbf{q}^1 = (x_q^1, y_q^1)^T$ and $\mathbf{p}^1 = (x_p^1, y_p^1)^T$ in three equations. However, the bilinear structure does not allow a direct solution for the unknowns but requires the introduction of an *algebraic elimination procedure*. This yields two algebraic curves of order three in the coordinates of \mathbf{p}^1 and \mathbf{q}^1 , which are generalized versions of the well-known *center point* and *circle point curve* of a planar RR chain with one fixed pivot. For five pre-defined task poses only an outlook is provided because we aim to provide some free design parameters often needed to address given space requirements in kinematic design problems in practice. Implementation of the problem is then discussed using the calculation software and students learn how to study variations of the parameters of the problem in the 3D-CAD tool. Then the simple planar RR chain with one fixed pivot is used to introduce into the synthesis procedures of planar parallel mechanisms. Here the approach of combining different solutions of RR synthesis is described. On the one hand design procedures for classical 1-DOF structures such as *4R and 7R linkages for guidance and function generation tasks* are discussed. On the other hand the use of the RR synthesis approach for the design of *task specific serial 3R Structures* is motivated by considering one of the frames Ba or Bc performing rotational motion about a fixed pre-defined revolute joint.

The design of spatial SS chains is also restricted to $n = 4$ pre-defined task poses for the same reason mentioned before. Compared to the planar case, it is shown that one can either select \mathbf{q}^1 or \mathbf{p}^1 and then solve the three synthesis equations directly for \mathbf{p}^1 or \mathbf{q}^1 . As an application a synthesis procedure for a *spatial RSSR function generation linkage* is provided and its implementation in CAD is discussed.

The synthesis equations of a spherical RR chain originate from a constrained equation, describing the constant angle α among the R joints in each configuration (see Fig. 1): $(\mathbf{p}^i)^T \mathbf{q}^i = |\mathbf{p}^i| |\mathbf{q}^i| \cos \alpha, \quad i = 1, \dots, n$. However, manipulating this analogue to the previous cases students learn that the spherical synthesis problem takes the simple form: $(\mathbf{p}^1)^T \mathbf{M}^{li} \mathbf{q}^1 = 0, i = 2, \dots, n$. Even though here one has three dimensional (unknown) vectors $\mathbf{q}^1 = (x_q^1, y_q^1, z_q^1)^T$ and $\mathbf{p}^1 = (x_p^1, y_p^1, z_p^1)^T$ the spherical RR synthesis problem is homogeneous in character, which means that only four of the six unknowns are independent. The students are already familiar with homogeneous coordinates from the kinematics foundations section (Sect. 2), which allows it to derive the solution procedures for $n = 2, n = 3$ and $n = 4$ pre-defined task orientations analogue to the solution of the planar RR synthesis problem. Compared to the planar case, for $n = 4$ we end up with generalized

versions of the well-known *center-axis* and *circling-axis cones* and these conic surfaces of order three are studied using the calculation tools as well as the CAD system. Beside combining different solutions of the RR synthesis for *spherical 1-DOF structures (4Rs)* it is also shown here how to use the general synthesis equation for the design of *spherical task specific serial 3Rs and parallel 5Rs* (see Sect. 5).

While dyad-based synthesis enables the students to solve up to four-position tasks, dyads do not allow it to constrain consecutive links. For this reason another method is provided, which is based on the *pole of a planar displacement*, which allows it to determine a revolute joint among two consecutive links that perform planar motion. The method is derived by considering the coupling among two consecutive frames Ba and Bb , introduced by a R joint q . The coupling is described by two relative displacement equations, that relate two linkage configurations 1 and 2: $\mathbf{q}^2 = \mathbf{R}_{Ba}^{12}\mathbf{q}^1 + \mathbf{t}_{Ba}^{12}$ and $\mathbf{q}^2 = \mathbf{R}_{Bb}^{12}\mathbf{q}^1 + \mathbf{t}_{Bb}^{12}$. Solving these equations for \mathbf{q}^1 yields an equation that has the structure of the equation of the pole of a displacement (see e.g., [3]):

$$\mathbf{q}^1 = (\mathbf{E} - (\mathbf{R}_{Ba}^{12})^T \mathbf{R}_{Bb}^{12})^{-1} (\mathbf{R}_{Ba}^{12})^T (\mathbf{t}_{Bb}^{12} - \mathbf{t}_{Ba}^{12}) \quad (4)$$

Considering a complete linkage, this approach can be used to design a planar structure, so that it can be assembled in two pre-defined configurations, defined by two poses of each link that make up the structure.

4 Kinematic Linkage Analysis

In order to enable students to design feasible task specific structures also a linkage analysis section is required. Here, some fundamental results for *kinematic position and velocity analysis* of serial but also parallel mechanisms were selected, which were found in [2] or [3]. The different topics are always discussed in connection to implementation into a numerical calculation tool. For serial chains the widely used *Denavit-Hartenberg convention* is introduced to derive the kinematics equations of a spatial general chain. This alternating composition of homogeneous transforms about the z - and the x -axis of coordinate frames is used to define a certain spatial pose of an end-effector frame B : ${}^W\mathbf{T}_B = {}^W\mathbf{T}_{1,z}^1 \mathbf{T}_{2,x}^2 \mathbf{T}_{3,z}^3 \dots \mathbf{T}_{B,z}$. Based on this, adoptions of the general formulation are discussed in order to describe planar and spherical chains.

The kinematics equations allow the introduction of the *forward and inverse kinematics position problem* of serial linkages. Here the differences of these problems are discussed and an overview on the difficulties of inverse kinematics is provided. The nonlinearity of this problem is discussed and we provide specific solution approaches for a set of different serial topologies, such as the TRS-chain, often met in industrial applications. In addition solution procedures for planar and

spherical RR and 3R chains are derived to provide an ‘inverse analysis counterpart’ to the synthesis section.

By straight forward differentiation of the Denavit-Hartenberg formalism with respect to time the *velocity inverse kinematics problem* is introduced, which is demonstrated for a general spatial 6R serial chain. The key discussion is about *tangent operators* (derived as $\mathbf{S} = \dot{\mathbf{T}}(\mathbf{T})^{-1}$), which allow it to introduce the *twist 6-vector representation for velocities*. Students learn that these 6-vectors can be used to define the *Plücker line coordinates* of the axes of the spatial 6R by considering zero-pitch twists. This allows it to introduce the twist representation of the velocity inverse kinematics of the general spatial 6R chain:

$$s = \begin{pmatrix} {}^W w_B \\ {}^W \mathbf{t}_B \times {}^W w_B + {}^W \dot{\mathbf{t}}_B \end{pmatrix} = \begin{pmatrix} {}^W r_1 & \dots & {}^W r_6 \\ {}^W \mathbf{t}_1 \times {}^W r_1 & \dots & {}^W \mathbf{t}_6 \times {}^W r_6 \end{pmatrix} \begin{pmatrix} \dot{q}_1 \\ \vdots \\ \dot{q}_6 \end{pmatrix}. \quad (5)$$

The twist \hat{s} represents the absolute velocity of the end effector frame B . An axis i has the Plücker coordinate vector ${}^W \hat{\mathbf{I}}_i = ({}^W \mathbf{r}_i, {}^W \mathbf{t}_i \times {}^W \mathbf{r}_i)$, measured in W , and a corresponding joint rate \dot{q}_i . The 6×6 -matrix in Eq. (5) is a version of the *Jacobian of a spatial serial chain* and the solution of (5) for $\dot{q}_1, \dots, \dot{q}_6$ solves the velocity inverse kinematics problem. Students benefit from this representation, because they learn that *singularities of a serial structure* can be seen as linear dependent joint axes.

Based on the kinematics equations of serial linkages students then learn how to apply the composition of displacements to planar and spherical closed loop linkages, in order to derive the *loop equations*. This topic is introduced by deriving vector loop equations of the planar and spherical 4R and 5R, which are then used to derive the *standard form of a constraint equation* for a single loop. This takes the well-known form $a(\phi) \cos \psi + b(\phi) \sin \psi = c(\phi)$, where ϕ and ψ are input and output joint parameters of the loop. This is solved for the unknown ψ using the well-known *tangent-half-angle solution approach*

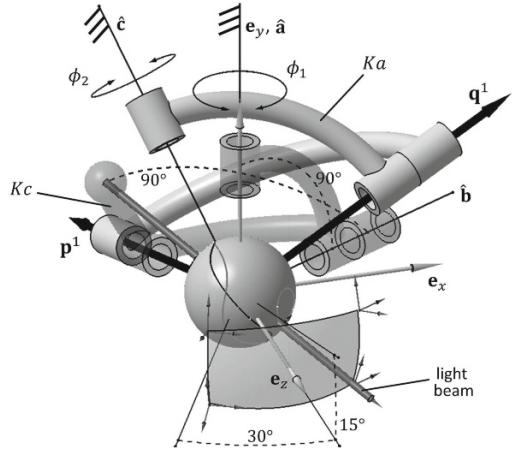
$$\psi(\phi) = 2 \arctan \left(\frac{b \pm \sqrt{a^2 + b^2 - c^2}}{a + c} \right). \quad (6)$$

Applicability of (6) for multiloop planar linkages and an *outlook on numerical solutions of loop equations using the Newton-Raphson algorithm* is provided.

5 Example Design Session

As an example of the possible linkage designs students may find using the techniques provided in our lecture we present a concrete kinematic design session for a spherical orientation task. However, due to space limitations we restrict ourselves to

Fig. 2 A spherical 5R linkage, designed to enable an orientable light beam of a car



the synthesis part. A subsequent analysis may include a study on transmission properties, a singularity analysis or inverse kinematics calculations of the linkage designed here. The goal is to design a novel advanced front-lighting system, which enables an orientable light beam of a car. The guidance task of the headlight, which provides the beam, requires an independent orientation along a range of $\pm 30^\circ$ longitude angles and a range of $\pm 15^\circ$ latitude angles while preserving a roll angle equal to zero. Combining this orientation data yields four task orientations which are represented as four frames (Fig. 2), spanning a quadrilateral ‘workspace area’ of the beam (note that the headlight is not shown Fig. 2). The different longitude angles are measured from the z -axis of a fixed world frame W , while latitude angles are measured from the xz -plane of this frame.

In order to orient the beam a special spherical RR chain is defined, whose axes \hat{a} and \hat{b} enclose an angle of 90° and which has its fixed axis \hat{a} coinciding with the y -axis of W . Next, the light source is considered being attached to the end link of the RR chain such that the beam encloses an angle equal to 90° with the moving axis \hat{b} . In defining so, a guiding chain is obtained, which enables the desired independent orientation along the longitude and latitude.

We are interested in a parallel kinematic device because given space limitations require that actuators need to be placed at the fixed base. One of these actuators may hence be defined at axis \hat{a} , providing the driving angle ϕ_1 . To obtain a task specific parallel device, the RR chain is extended into a 2-DOF 5R closed loop by synthesizing a spherical 3R chain for the four previously defined task orientations. Here the design equation $(\mathbf{p}^1)^T \mathbf{M}^{li} \mathbf{q}^1 = 0$ where $\mathbf{M}^{li} = \mathbf{E} - (\mathbf{R}_{Bc}^{li})^T \mathbf{R}_{Ba}^{li}$ and $i = 2, 3, 4$ from Sect. 3 is used and the frame Ba or link Ka is considered to perform rotational motion about the fixed axis \hat{c} . The location of \hat{c} is chosen with respect to the given space requirements and it provides the second actuated axis with the other driving angle ϕ_2 . After defining four arbitrary values for this angle and using the pre-defined angles $\pm 30^\circ$ and $\pm 15^\circ$ of the frame Bc the rotation matrices \mathbf{R}_{Ba}^{li} and \mathbf{R}_{Bc}^{li}

can be assembled. The algebraic solution procedure of the design equations then yields the conic surfaces containing all valid directions \mathbf{q}^1 and \mathbf{p}^1 . Figure 2 shows intersection curves of these surfaces with a sphere where a valid \mathbf{q}^1 and \mathbf{p}^1 was selected to obtain the desired task specific 5R.

6 Conclusion

The lecture for engineering students presented in this paper provides numerous kinematic analysis and synthesis techniques towards a computer aided, task-based design of linkages and enables students to select task specific structures for planar, spherical and spatial motion tasks. Consequently the finite position synthesis of planar, spherical and spatial linkage building blocks is provided, which are used to assemble complete linkages. To obtain feasible designs or to regard given requirements of a task underspecified synthesis procedures are discussed, which allow it to produce more linkage solutions. E.g., for the spherical 5R from Sect. 5 one may select different \mathbf{q}^1 and \mathbf{p}^1 at the conic surfaces to obtain different transmission properties, higher compactness, etc. However, one may also state the three synthesis equations as a function of further free design parameters $\{\phi_2^1, \phi_2^2, \phi_2^3, \phi_2^4, x_c, y_c\}$. Each parameter configuration will then yield different conic surfaces and will hence yield different 5Rs, whose kinematic properties can be evaluated.

References

1. Abdul-Sater K, Irlinger F, Lueth TC (2012) CAD-Integrierte Auslegung Ebener Gelenkgetriebe. In: VDI BERICHTE 2175, conference, Bewegungstechnik, pp 225–242
2. Angeles A (1997) Fundamentals of robotic mechanical systems—theory, methods and algorithms., Springer mechanical engineering seriesSpringer, Berlin
3. McCarthy JM, Soh GS (2010) Geometric design of linkages, 2nd edn., Springer interdisciplinary applied mathematicsSpringer, New York
4. Waldron K, Schmiedeler J (2008) Springer handbook of robotics. in: Siciliano B, Kathib O (eds) Springer, Berlin, Heidelberg, New York

Part XV
History of Mechanism Science

A.N. Krylov: The Pioneer of Photographic Non-invasive Measurement Methods in Russian Science

Andrei Vukolov and Alexander Golovin

Abstract The life of famous Russian Soviet naval architect and mathematician acad. A.N. Krylov occupies an especial place in history of Russian Navy. The brilliant scientist, one of the most significant naval artillery theorists, he was also very thorough experimentalist. His colossal archive appears as one of the most fully documented and systematized personal scientific libraries in Russia. However, there is the aspect of Krylov's legacy that has weak presentation in actual modern literature. It is his interest to non-invasive measurement methods with usage of photographic techniques that were being part of everyday life in the beginning of twentieth century. In this paper detailed description of photographic ship pitching recording method developed by Krylov would be presented.

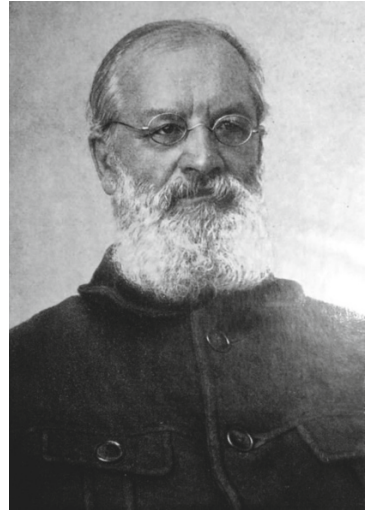
Keywords A.N. Krylov · Photographic · Non-invasive measurement · Ship pitching · Oscillogram

1 The Period of Theoretical Development

From 1900 to 1908 A.N. Krylov (Fig. 1) was a chief of Practice (cyr. “*Opytovij*”) Pool. From February, 1902 to January, 1904 he was active carrying investigations of survivability and insubmersibility of ironclad ships. Research of artillery direction systems behaviour in case of pitching was part of these investigations. Through the era of supersized artillery the volley-produced oscillations transferred significant perturbation to the ship. In that case the correction of projectile trajectories was necessary. Especially, combination of factors (e. a. large shooting distance, necessity of synchronous measurement for large and small values, high perturbation

A. Vukolov (✉) · A. Golovin
Bauman Moscow State Technical University, Moscow, Russia
e-mail: twdragon@bmstu.ru

A. Golovin
e-mail: aalgol@mail.ru

Fig. 1 A.N. Krylov

velocity, low temporal density of measurements) required to develop the special complex measurement principles and methods. Krylov successfully developed the original photography-based method.

There are no direct references about new non-invasive measurement method development in Krylov's legacy before 1905 [1]. Over against this, in his memories dating back to 1902–1904 he focused on congestion with research, e. a. optimal design of armored cruisers and outreach activity. The following citation is from Krylov's memoir book "My Memories" [2].

31 of March, 1904 the ironclad ship "Petropavlovsk", being under flag of vice-admiral Makaroff, hit a mine barrage and detonation of mines or powder magazines was occurred. The ironclad ship sank, admiral Makaroff died.
 Rumors which done about that accident were predicted by me...
 ... I did a report on the session...
 ... that report was printed entirely...
 I continued, supervising the Pool, except current work over model testing to do (...) a number of another works...
 ... to produce experiments with gunboat "Uraletz" using my proposed method for ship pitching influence definition to sharpshooting.¹

Krylov dates the ending of above citation himself by July of 1905. Later (in 1906–1908) the gunboat "Uraletz" was mentioned due to experiments with devices for photographic ship pitching recording [3]. Thereby, there are every reasons to presume that fundamentals of the new method were fully developed and ready to apply in experiment near summer 1905. However, there are no references in Krylov's legacy to such development. The first publication of results had obtained using the method [4] is dated to December, 1908. There are some conceivably

¹ Translation by A. Vukolov.

earlier papers [5] in Archive of USSR Academy of Science not dated by author (approximate dating due to protocols of Special Council [6] of Academy of Science). Most likely, the beginning of development of the photographic pitching recording method can be dated to period from May 1904 to March 1905. Krylov also had visited Italy at that period; thereat he could learn theory of photography and photogrammetric methods [2]. He assigned development of idea and base theory to French engineer Huet [7] with reference to “Mémorial du Génie Maritime”, 1874.²

2 Method of Photographic Recording of Ship Pitching. Theory and Realization

The method had been proposed by Krylov practically turns the photo camera to analog oscilloscope with direct values conversion. On Fig. 2 camera is installed on the ship with optical axis oriented perpendicular to lengthwise keel plane (rolling mode) or to lengthwise axis (plunging mode). The sighting point of a camera must be positioned to skyline.

Resulting photograph registers the viewable (by brightness) boundary between sky and water (Fig. 3a). When pitch angle value is θ (Fig. 2) then the boundary on photograph become displaced by:

$$HH_1 = OH \cdot \tan(\theta) = f \cdot \tan(\theta) = HN \quad (1)$$

where OH_1 is length of ray path from refraction point to focal plane; f —focal length of the lens, HN —vertical ort (trace length) on Fig. 3a. Timebase for recording is obtained using following decision. There is the slot diaphragm near focal plane. The paper tape coated with photosensitive material driven by the slit with known speed using clockwork. Resulting oscillogram looks like Fig. 3b.

As we can see in [7], Krylov developed the special camera for ship pitching recording. This camera, its drawings and full technical description aren't preserved before present day. The camera contained electromagnetic shot marker (Fig. 4), which connected to cannon shutter releasing button. Marker consists of shutter N which is released when cannon fires by electric signal. Shutter is driven by pre-pressurized spring and provide timings near 1/100 s. Releasing of the shutter is implemented by electromagnet which still working when cannon shutter releasing button is not pressed. The oscillogram with shot mark given on Fig. 5.

² It was occasionally impossible to allocate original publication.

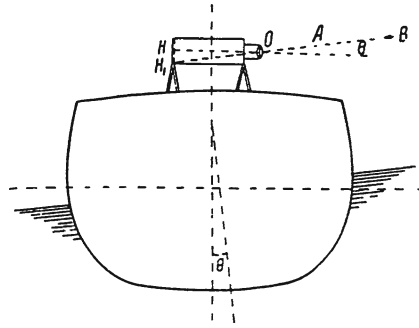


Fig. 2 Camera installation

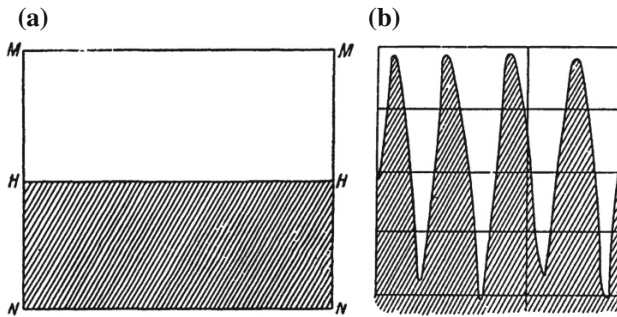


Fig. 3 Registration

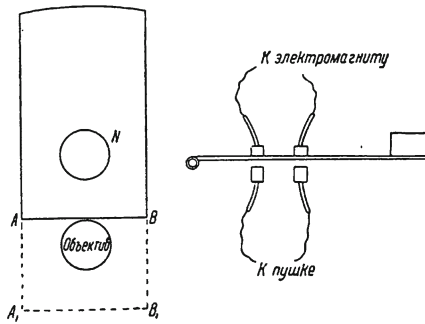


Fig. 4 Shot marker (original sketch)

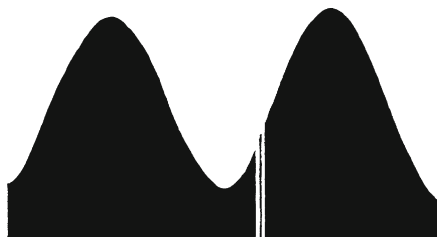


Fig. 5 Oscillogram with shot mark (facsimile from original tape)

3 Practical Application

The first proved document that contained a reference to practical application of the photographic ship pitching recording method is “Uraletz” gunboat workbook [8]. This document contains, inter alia, the references to [5] and original oscillogram³ (145-mm negative photographic paper tape more than 5 m length). Also it contains table of parameters that was used for scaling for given set of lenses (Table 1). When scales were determined, we could use the oscillogram to calculate deviations and influence of shots on pitching. There is unclassified document in Krylov’s personal archive, which contains table of deviations obtained by photographic method. Conceivably, the page (Fig. 6) is an extension of [5], but the information had not verified till present. The results obtained in 1907 were included into [4] and into unpublished work “The Influence of Pitching to Shooting Accuracy” [9].

And yet, the main practical application of photographic ship pitching recording method have been found in February, 1913 when carried out large research with Fram tanks. Tank system was being prepared to install on battle cruisers “Izmail” and “Kinburn” which are under construction that time, and it also being prepared to commit into project of ship family “Gangut”. A.N. Krylov stayed then in general-lieutenant rank, was appointed as chairman of Special Marine Commission which tasked to test tank system in Atlantic Ocean.

The test had performed [10] on chartered 98-m steamship “Meteor” of 4,300 displacement tons. It was equipped with Fram tanks, and immediately before experiment, the team retrofitted it with photogoniometers, gyroscopic pitching recorders designed by Fram and Petrovac, photographic oscilloscope designed by Krylov. Photographic chemicals and materials, laboratory equipment components for film treatment and fixation were also loaded aboard. In one of empty storerooms the darkroom laboratory with semi-automatic film treatment was developed under guidance of prof. N.A. Smirnov [2]. Time saved for us an equipment arrangement schema which implies original solution with sophisticated reservation of recording devices (Fig. 7). For example, photographic oscilloscopes and gyroscopic recorders

³ 1907, October 17. Pitching oscillogram (rolling mode). Photographic negative tape. St. Petersburg branch of Archive of Russian Academy of Science, fund 759, inv. 1, #98/12.

Table 1 Scaling parameters for different lenses (from [7])

Focal length (mm)	Ort length (mm)	Pitching angle	Scale (mm/rad)
250 (Zeiss lens)	10	2°29'	230.72
350 (Zeiss lens)	10	1.63°	351.51
600 (DeRogée lens)	10	0.95°	603.11
900 (DeRogée lens)	10	0.64°	895.25

Fig. 6 Experimental protocol with results of measurements made on photographs (original typescript)

- 45 -

Т А Б Л И Ц А 7-ая Сер. по транспорту.
 5-го Октября 1907 года. 1-ая серия.
 Доклады 26 кадетского КЛАСА БОИВАН
 Препод: = 45; = 37. " По способностям "

№	№	Координаты точки по-прежнему	Координаты точки по-новому	Окращения	№
пункта	пункта	в км	в ми	в ми	пункта
59	1	61,5 + 9,0	84,5 + 12,3 - 16,3	+14,2	205,7 201,6
60	2	51,0 - 3,0	70,0 - 4,1 - 30,8	- 2,2	948,4 4,8
61	3	55,0 - 7,5	75,5 - 10,3 - 20,3	- 8,4	640,1 70,5
62	4	79,5 + 7,5	109,0 + 10,3 + 8,2	+12,2	37,2 148,8
63	5	86,5 - 4,2	119,0 - 5,8 + 18,2	- 3,9	301,2 15,2
64	6	83,5 - 5,5	105,0 - 7,5 + 4,3	- 5,6	17,5 31,4
65	7	76,0 - 23,7	104,3 - 32,6 + 3,5	-30,7	12,3 942,5
66	8	41,0 - 10,0	66,3 - 13,7 - 44,5	-11,8	1980,2 139,2
67	9	98,5 + 8,5	185,0 + 11,7 + 34,2	+13,6	1189,5 185,0
68	10	108,5 + 15,0	149,0 + 20,6 + 48,2	+22,5	2223,2 492,8
		1007,5	+54,9		7455,5 2221,9
			-14,0		
			-19,1		
		= 100,8		=	775,6 = 27,5
			= -1,9	=	223,2 = 14,9

Высоты п. 67 и 68 были приотрешены:

(1, 2, 3 on Fig. 7) are placed at point where pitching is most noticeable—on uppermost deck near wireless house.

Krylov mentioned his photographic oscilloscope [10] as primary device for calibration of other ones. Apparently, simplicity of photographic pitching recording method in theory and realization brings it to leadership in terms of accuracy and reliability, further given that gyroscopic technology level was slightly low that time, in spite of highest standards of measurement devices design and production.

In [10] Krylov described the registration process⁴:

Tanks testing performs as following. The ship laid on course at odds wave. It was laying on that course for 10 min with dry tanks and then for 10 min with full tanks. Besides, all devices were recording the rolling pitch value, and moreover, Petrovac device and one of photographic devices were recording plunging pitch (Fig. 8).⁵ After that the ship changed

⁴ Citation translated by A. Vukolov.

⁵ This figure is also presented in original book [2].

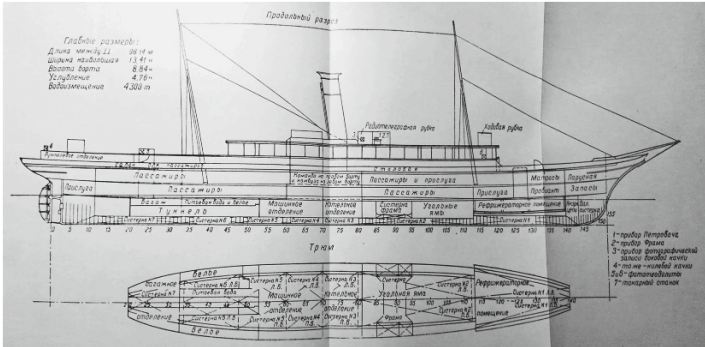


Fig. 7 Equipment arrangement schema (original facsimile). 1 Petrovac recorder, 2 fram recorder, 3 photographic oscilloscope (rolling mode), 4 photographic oscilloscope (pludging mode), 5, 6 photogoniometers, 7 heavy machinery (lathe)

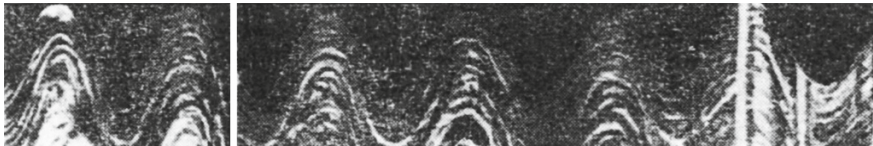


Fig. 8 Sample of pitching oscillogram from “Meteor”

course by 45°, e. a., to the right and again it was laying on that course for 10 min with dry tanks and then for 10 min with full tanks. After change the course again on 45° to the right, and so on until the ship had laid on course at odds wave finally.

...

On evening of the same day all data was treated as follows:

1. Copies are made for all records of roll pitching obtained with each device
2. Records of pludge pitching obtained with Petrovac device and photographic device also were copied
3. All measured roll pitching amplitudes obtained with gyroscopic devices, and the most characteristic ones compared with photographic oscillograms to control precision of gyroscopic devices
4. Results of amplitude measurement for each course were collected into separate work-sheet to determine average and maximal amplitudes...

⁵ This figure is also presented in original book [2].

4 Conclusions

As we can see above, the experimental method of photographic pitching recording and its practical realization, which Krylov proposed, had successfully tested for reliability. In addition, Krylov's memories [2, 7] contain mentions about the foreign engineers acquainted with equipment and results, namely the crew of Italian battleship "Dante Alighieri" meeting which had taken place near Madeira island at 7–8 of March, 1913. However, there are no verified testimonials about that the photographic pitching recording was used anytime further outside Russia as basin of experimental research. Apparently, the complexity of experiment associated with usage of chemicals and darkroom laboratory, was too high that time. Thus A. N. Krylov can be mentioned as one of pioneers in Russian science who started to use photographic non-invasive measurements as primary techniques.

Other mentions of photographic non-invasive measurements in Krylov's memoirs located after 1917. As pointed in "Notes about Works of acad. A.N. Krylov" which are presented in USSR Academy of Science between 1918–1940, he returned in theme near 1920. It was mostly unfinished works dedicated to distant recording of artillery shell trajectory and explosion using photogoniometers. Subsequently before invention of digital photography, the photographic non-invasive measurement techniques occupied in Russian science a narrow niche in sphere of sophisticated experiments on stationary machinery (e. a. bubble chambers and emulsion trackers) where experiment is strongly more complex than photographic treatment process.

Acknowledgments This work is dedicated, In Memoriam, to Alexander Alexandrovich Golovin. The scientist. The mentor. The friend. Sad that I had to finish preparation of this work without him. Would like to thank prof. Olga Egorova for her participation and attention to Russian text. Deepest appreciations to staff of Russian branch of Archive of Russian Academy of Science and especially to expert Anna Abaydulova for their help in our work with Krylov's documents.

References

1. Smirnov VI (ed) Handwritten Legacy of Academician Alexey Nikolaevich Krylov (in Russian), Works of USSR Academy of Science, vol 23. "Nauka". Leningrad branch, Leningrad
2. Krylov AN (1984) My memories (in Russian). "Sudostroenie", Leningrad
3. Krylov AN (1907) Memorandum to F. D. Remesnikov about the end of work upon installation of photoraphic pitching recording devices on "Uraletz" gunboat and about necessity of exchanging the artificial pitching by natural in swell at open space (in Russian). In: Fund 759, inv. 1, #98/2, pp 33–34. St. Petersburg branch of Archive of Russian Academy of Science
4. Krylov AN (1908) About experimental shootings on pitching from "Uraletz" gunboat in 1907. Report of colonel Krylov. With 4 appendices (in Russian). In: Fund 759, inv. 1, #98/1, pp 1–46. St. Petersburg branch of Archive of Russian Academy of Science
5. Krylov AN (1906) About photographic recording of ship pitching. The Report for Marine Technical Committee. Litography (in Russian). In: Fund 759, inv. 1, #98 (special request

- needed for actual seat allocation). St. Petersburg branch of Archive of Russian Academy of Science
6. The report about scientific works of A. N. Krylov. An appendix to protocol of II session of Special Council. Official works (in Russian). In: Protocols of Academy of Science Special Council, Chap 29, c 355, p 45 (1916)
 7. Krylov AN (1951) Collected Works of acad. A. N. Krylov, vol XI. Ship pitching, chap. About Photographic Recording of Ship Pitching (in Russian), pp 261–264. USSR Academy of Science Publishing House, Moscow, Leningrad
 8. Krylov AN (1907) “Uraletz” workbook (in Russian). In: Fund 759, inv. 1, #98/5, pp 1–29. St. Petersburg branch of Archive of Russian Academy of Science
 9. Krylov AN (1908) The influence of ship pitching to shooting accuracy (in Russian). In: Fund 759, inv. 1, #98/10, pp 27–28. St. Petersburg branch of Archive of Russian Academy of Science
 10. Krylov AN (1951) Collected Works of acad. A. N. Krylov, vol XI. Ship pitching, chap. Testing of Fram tanks on “Meteor” steamship (in Russian), pp 273–285. USSR Academy of Science Publishing House, Moscow, Leningrad

Animation of Historical Patents

U. Döring, C. Brandt-Salloum, V. Henkel and T. Brix

Abstract The Geheimes Staatsarchiv Preußischer Kulturbesitz Berlin is an archive with thousands of patents from the 19th century. The documents include patent texts and figures as well as the comments of the reviewers. The paper is about first common activities of the archive and the Ilmenau University of Technology to make the documents available to a broad public. Aside of the digital reproduction and presentation of texts and images the activities focus on remodeling the technical devices and animate the models with WebGL in web browsers. In the created interactive animations different functional and constructive aspects can be explained to the viewers. The original content as well as the derived content like videos and interactive animations is finally made available in the DMG-Lib portal. The paper describes the used workflow and experiences as well as selected examples.

Keywords Historical patents · CAD · Interactive animation · Webgl · Knowledge preservation

1 Introduction

There are still a lot of documents spread all over the world full of content which is very interesting with respect to technological as well as historical aspects. Mostly those documents are in libraries and archives, but they may also be in other

U. Döring (✉) · V. Henkel · T. Brix
Ilmenau University of Technology, Ilmenau, Germany
e-mail: ulf.doering@tu-ilmenau.de

V. Henkel
e-mail: veit.henkel@tu-ilmenau.de

T. Brix
e-mail: torsten.brix@tu-ilmenau.de

C. Brandt-Salloum
Geheimes Staatsarchiv Preußischer Kulturbesitz, Berlin, Germany
e-mail: Christiane.Brandt-Salloum@gsta.spk-berlin.de

institutional or private ownership. Sometimes the owners even do not know about the value of the content for other persons and institutions. With the current digitization offensive it is possible to make a part of the documents available to a broad public and also to preserve it—at least in its digital form. Nevertheless the amount of documents and the possibilities to find them have to be improved in the next years and decades. It will cost a huge effort to make most of the documents online findable especially with respect to following observations:

- The location of the contents is not trivial, because owners often don't know which treasures they have—may be because of a leak of metadata or because of an ignorance of the value for others.
- A good digital reproduction is still cost intensive and budgets of cultural institutions like libraries, archives and museums as well as company archives etc. is very low compared to the necessary financial allocation.
- Digitization and online presentation are only the first step to make the contents available to a broad public. It is very important to supply sufficient tools for finding as well as understanding the content. This implies at least text recognition as far as the documents include textual content.
- Aside formal metadata especially technical metadata will help users to find the content they are looking for, but the extraction of technical information from texts and images is mostly cost intensive.
- Non-textual search like image based search may be very effective when the images are extracted from documents and enriched with describing texts to allow a preselection of relevant images.
- Sometimes technical comments or alternative representations of the content are needed to make the intention of the author understandable to the readers. The creation of derived/alternative representations will often be the most valuable enrichment but also the most cost intensive one.

In 2012 the Geheimes Staatsarchiv Preußischer Kulturbesitz Berlin (GStA PK, [1]) started to plan an exhibition to make a part of its extensive techno-historical documents available to a broader public. The focus of the exhibition is on historic patents in the context of the Prussian patent system. Because of the technical content of the documents which describes mainly machines and devices the archive looked for a partner with comprehensive experiences in the analysis and user oriented representation of mechanisms and machines. The Ilmenau University of technology (IUT) as one of the main supporters of the Digital Mechanism and Gear Library (DMG-Lib) [2] proved to be this partner.

2 Workflow

In preparation for the exhibition both partners selected patents with interesting content. The broadness of the examples and the attractiveness as well as the technical feasibility served as criteria for the selection. Finally 15 patents were

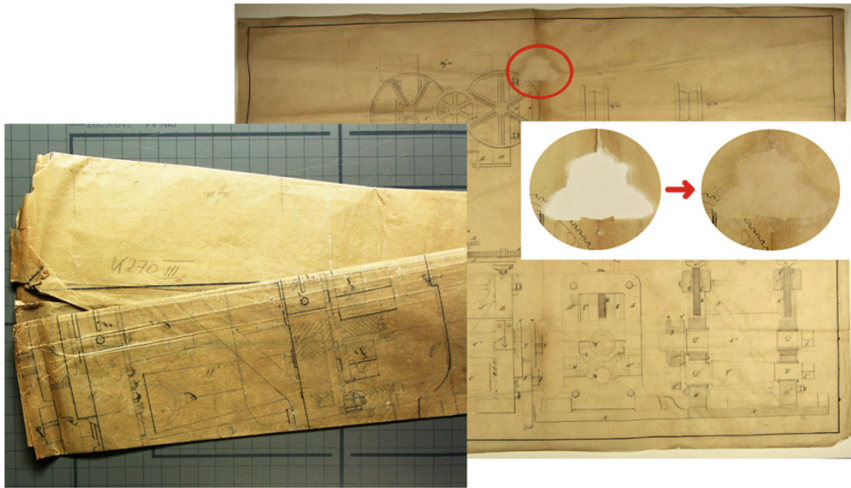


Fig. 1 Folded and unfolded drawing of patent K270 with marked patch [7]

selected for further processing in the workflow. The patents in the archive are named by a letter (derived from the name of the inventor) and a serial number.

2.1 Restoration

Because of the problematic condition of most of the documents it was necessary to start the workflow with a restoration step. Figure 1 shows as an example a folded as well as the unfolded and repaired drawing for patent K270 (Alfred Krupp: “Nahtloser Radreifen”).

2.2 Digitization

After restoration and flattening the documents were digitized. For the analysis of the drawings it is very important to see also the finest lines or even drawing marks like compass points. Therefore the scans were produced with at least 300 dpi. Some of the handwritten texts were transliterated to support a faster analysis.

2.3 Analysis of Operation and Construction

The analysis of the patents concerning the mode of operation as well as the proposed construction includes reading texts, clarification of historical terms, finding the relationship between drawings and texts and sometimes also investigations over

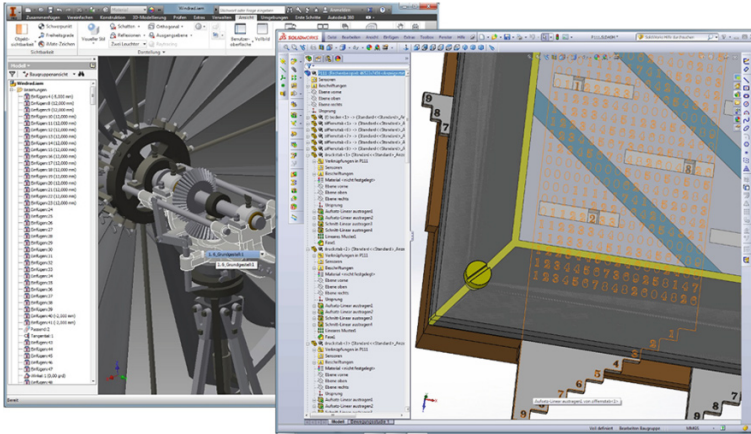


Fig. 2 Creation of models for patents H38 and P111 in different programs

the historical background. Drawings are usually the most useful source of information. Nevertheless the figures are in general more sketches (with the focus on the main ideas of the patent) than construction drawings (with all the details important for modeling/manufacturing). Often the creators of the drawings simplified details or left them out. A missing of dimensional accuracy is also a common problem. Thus during the analysis of the patents plausible solutions must be found in case of incomplete or inconsistent information. Functional prototypes of the patents would have simplified the analysis dramatically, but those models were damaged over the time or finally destroyed during World War II (see [3]).

2.4 Initial Modeling

For the initial creation of the 3D-models different CAD programs and Blender could be used (see Fig. 2). All tested programs were powerful enough to solve the modeling tasks. Depending on the detailedness of the models the modeling step can be very time consuming. In some cases consistency were only found during the modeling step. Then plausible constructive solutions were used in the model. The modeling itself was usually started by placing the scanned figures in an auxiliary plane. That allows easy access to the sketched shapes, dimensions, positions of axes etc.

2.5 Integration of the Models in WebGL

The 3D-CAD-models shall be usable for as many people as possible. Therefore the models were converted into data that is displayable in most of the present-days web browsers. In the web browsers a JavaScript program uses the WebGL-interface of

the graphics hardware for fast rendering of the 3D-models. Even mobile devices support WebGL more and more. This gives new possibilities for user interaction in exhibitions, books etc. especially in connection with supplying links to interactive models via QR-codes.

From a technical point of view the CAD-data is reduced to the surfaces of the models consisting of point positions and triangles. Assembling constraints or restrictions in the movement of parts are not transferred. The CAD-models are saved in STL- or OBJ-format. Optionally the powerful open source program Blender is used to reduce the complexity of the models and to generate smaller OBJ-files. These files are the input for a Java program which generates files with JavaScript data structures. The JavaScript program in the web browser of a user includes the files and uses the data to render the models. The main advantage of the presentation via a program is that the view of the model can be adapted to the needs of the presentation, e.g. the cameras position and zoom can be changed or parts can be made transparent, highlighted or completely hidden.

The main work in this workflow step is the definition of the different visualization/interaction aspects with all the information about visibility and movability of the single parts of the model. See Sect. 3 for examples.

2.6 Online Presentation

For the online presentation of the documents and also for long time preservation the DMG-Lib web portal is used. Here the documents are collected, connected with metadata, linked and indexed to make them browsable and searchable.

Each document gets an unique DMG-Lib identifier and URL which can be used to reference them in publications, on web pages or posters, e.g. by QR-codes. Via an OAI-interface the documents are integrated in Europeana.

3 Description of Selected Models

The set of models covers a wide range of inventions, e.g. a wind mill, a calculation machine, a tool, a bottle top or even a barrel washing machine. For a deeper understanding of the work some of the animated patents are discussed in more detail in this section.

3.1 Door Lock by Gaul (G26)

In 1844 Johann Peter Gaul submitted a description of a door lock to the Prussian Patent Office, see Fig. 3. At this time Gaul was a locksmith and inventor living in

Fig. 3 Illustrations of Gauls door lock from 1844 (patent G26)

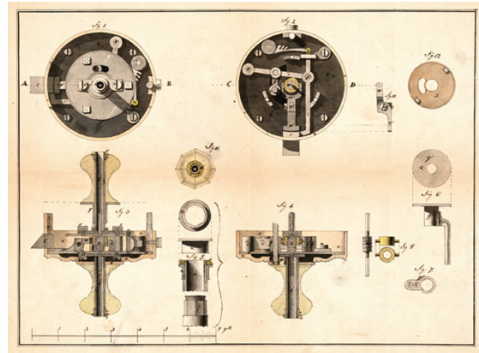
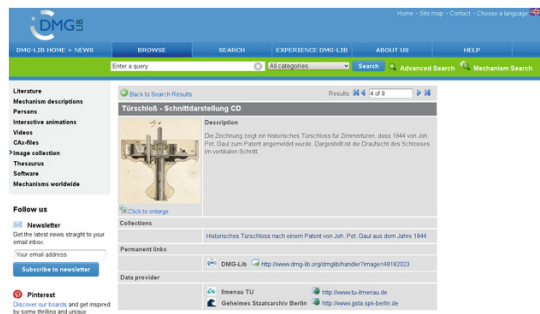


Fig. 4 One of the figures of Gauls door lock with its metadata in DMG-Lib



Erkelenz, Germany. The available documents for this patent cover 2 pages of description and 1 page with figures by Gaul as well as an expert opinion given by the referee Brix and his co-referees Nottebohm and Frank (Fig. 4).

For the interactive animation 3 aspects were defined:

- a view of all parts of the lock as assembly,
- the locking operation and
- the catching operation (see Fig. 5).

The hiding of most parts for the locking and catching aspects is essential for an easy understanding of these operation modes. The connection between textual descriptions and the shown parts can be explored by the users via clicks in a part list and according highlighting in the model.

In addition to the 3 aspects described above, an introduction sequence was designed which shows the connection of the original drawings of the lock and the CAD-model by cross-fading. The introduction shows also examples of the possible interactions to encourage users to interact with the model. The sequence looks like a video but it is in fact also an animation which is rendered on-the-fly with WebGL. Nevertheless a video was generated as a derivative. The video is used in the exhibition for a video projection and like the other digital items it is also supplied in DMG-Lib, see [4].

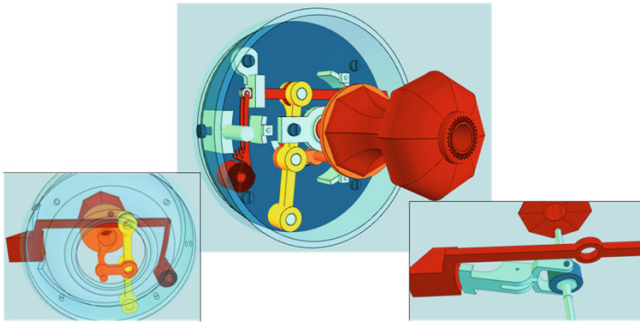


Fig. 5 Different aspects for the interactive animation of the patent G26

3.2 Machine Regulators by Siemens (S410)

The collection of the GStA PK also includes patents of famous inventors. In 1845 Werner and Wilhelm Siemens described on 4 textual pages and 3 drawing pages different variants of machine regulators. The expert opinion was given by referee Nottebohm and his co-referees Wedding and Brix. Further information can be found in [5] where the Siemens brothers explained their patent in more detail.

Figure 6 shows some of the drawings as well as details of the created models. The details cover 4 approaches to compare (and then control) the difference of 2 rotational velocities.

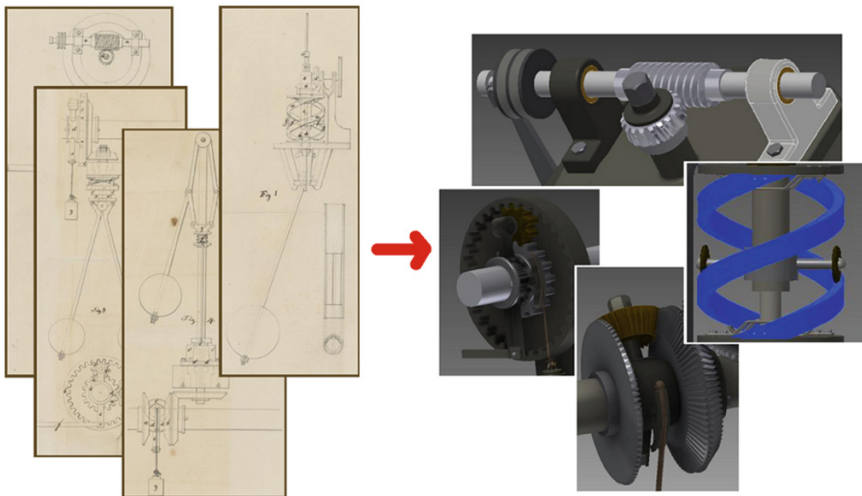


Fig. 6 Different aspects for the interactive animation of the patent S410

4 Conclusions

With the media station for the exhibition (online accessible at [6]) GStA PK and the DMG-Lib team of IUT made a first step to open the extensive treasure of GStA PK documents concerning mechanical devices and machines to the public in a modern way. As shown in the paper a workflow was established which could be used for the generation and publication of further high quality digital content. The variety of formats (texts, images, videos, interactive animations, CAD-data) and of covered research areas make the supplied content valuable for engineers, students, teachers, historians but also for laymen interested in technics. The publication via DMG-Lib as well as Europeana is essential for long term preservation as well as findability.

It is questionable if some of the old patents are reused in the patent system directly, e.g. to prove prior art, but the general process of collecting and animating models from paper based sources or of converting existing CAD data to interactive formats allows the construction of databases in which people can gather ideas very effectively. A large variety of previously understood solution principles and constructive solutions is essential for their imagination. Therefore the usage of those interactive models may mainly focus on teaching and self-studies. Nevertheless there also will be cases where engineers are looking for particular solutions and find them in interactive models but from a statistical point of view it is much more probable that a textual search in a database will return hits in text documents.

Acknowledgments The partners want to thank the Stiftung Preußischer Kulturbesitz for funding their work.

References

1. Website of the Geheimes Staatsarchiv Preußischer Kulturbesitz Berlin: <http://www.gsta.spk-berlin.de>
2. Website of the Digital Mechanism and Gear Library: <http://www.dmg-lib.org>
3. Geheimes Staatsarchiv Preußischer Kulturbesitz: Klosterstrasse 36. Sammeln, Ausstellen, Patentieren. Zu den Anfängen Preußens als Industriestaat. (2014) ISBN 978-3-923579-19-8
4. Döring U (2014) Introduction video for the interactive animation of Gauls door lock. Available via DMG-Lib. <http://www.dmg-lib.org/dmglib/handler?video=6991053>
5. Siemens W, Siemens W (1845) Siemens' Differenz-Regulator für Dampfmaschinen und Wasserwerke. In: Polytechnisches J (edited by Dingler JG), Band 98, Nr. XX, pp 81–89. Available via Dingler-Online. <http://dingler.culture.hu-berlin.de/article/pj098/ar098020>
6. Website with online access to the media station designed for the exhibition “Klosterstraße 36—Sammeln, Ausstellen, Patentieren—Zu den Anfängen Preußens als Industriestaat”: http://www.dmg-lib.org/dmglib/main/webGL/GSTA_KStr36/mediaStation/modelSelect.html
7. Peters H (2013) Fotodokumentation zur Restaurierung der Zeichnungen auf Transparentpapier, Geh. Staatsarchiv PK

Part XVI
Industrial and Non-industrial
Applications

Dynamic Modeling and Analysis of an Industrial Cutting File Machine

E. Seabra, Luís F. Silva and P. Flores

Abstract A multibody model of an industrial cutting file machine for dynamic analysis is presented in this work. One of the main subassembly systems of the machine is a cam-follower mechanism that is used to promote the motion of the tool (chisel). Thus, the Newton-Euler formulation for multibody systems is considered here to model and analyse this cam-follower mechanism. For this purpose, polynomial functions are used to describe cam profile, being the chisel defined as flat surface. The motion of the chisel is controlled by gravity and a translational spring element. The contact events that take place between the cam and follower surfaces are modelled using both penalty formulation and nonsmooth approach. The parameters studied and discussed throughout this work are the chisel displacement and velocity, as well as the dynamic spring load. Finally, an industrial cutting-file machine is utilized to obtain experimental data.

Keywords Multibody dynamics · Cutting file machine · Computational and experimental analysis

1 Introduction

The first metallic file tool was found in Crete, Greece, [1]. This file was manually produced using a chisel, which was impacted against a base body, producing the cutting edge files, since that, this process is denominated as cutting, or simply, cut [2]. Since the old years the experience has been demonstrated that the most efficient

E. Seabra (✉) · L.F. Silva · P. Flores
University of Minho, Braga, Portugal
e-mail: eseabra@dem.uminho.pt

L.F. Silva
e-mail: lffsilva@dem.uminho.pt

P. Flores
e-mail: pflores@dem.uminho.pt

way to produce files is based on this principle, that is, the base body is plastically conformed due to the chisel impact [3]. This principle was also illustrated in some of the most well known Leonard da Vinci drawings [4]. Black [5] is among the few authors who used the machining technology to produce files, nevertheless, without any relevant success, namely in what concerns to the cutting file performance. The first mechanical machine designed and constructed to produce files by cutting edges process was due to Frenchman Chopitel [2]. However, it was only at the end of nineteenth century that the industrial and massive files production was a reality, which starts the production in 1850 [6].

In a simple manner, the mechanical filing operation is made by employing tools (files) with multiple edges located in a plane or curved surface, which acts as cutting elements to remove, by plucking out material from the work piece. These cutting edges are the most relevant aspect on the performance of that mechanical operation. The experience demonstrates that the most efficient process to obtain the file cutting edges is by plastic deformation originated by the impact of the cutting tool (chisel), which has a reciprocate motion. The operating rate of the chisel can reach 200 Hz and causes a plastic deformation on the file body, with the shape of sharp edges. It must be mentioned that this operation does not involve plucking chip and, therefore, the whole moved material, as a consequence of the chisel movement is transferred to the top and to the front creating some wrinkling that originates an irregular appearance of the tooth cutting edges. It must be said that in this process, there are a preservation of the total volume of material.

The present investigation was developed under a protocol celebrated between the University of Minho and international enterprise Bahco Öbergue, which incorporates the company Snap-on, from USA. This collaborative project aims at transforming the old-approach, purely manual and totally dependent on the operator sensitivity, into a new and automatic file production system. Thus, this new methodology allows for the automatic adjustment of the control parameters of the files edges production, in order to produce files with better quality. It should be highlighted that this type of research work has not been studied yet in the thematic literature. In this work, a computational and experimental study of the cam follower mechanism of an industrial cutting file machine is presented and discussed. The Newton–Euler equations of motion are considered to simulate the dynamic behavior of the multibody system that compound the cutting file machine. In addition, the machine was instrumented in order to obtain the main kinematic and dynamic parameters that control the cutting file process.

2 Description of the Cutting File Machine

This research work has been developed based on an industrial machine-tool, OBJEKT 77563, supplied by Bahco Öbergue Company. Figure 1 depicts the overall view and the schematic representation of this machine-tool. The file teeth are produced by impact of the cutting beater (system composed by follower,

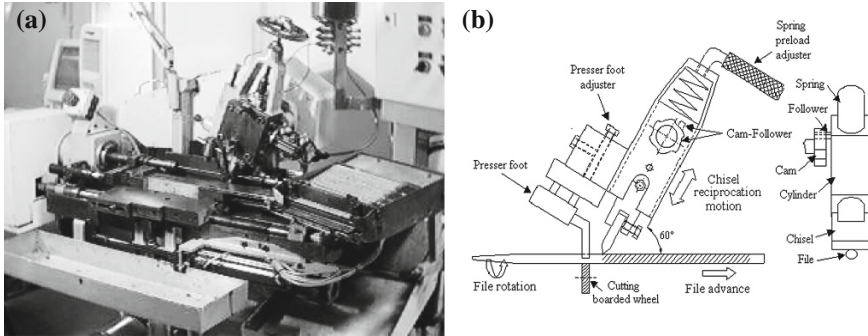


Fig. 1 a Cutting file machine, b Schematic representation of the mechanical system

cylinder and chisel), with a reciprocate movement. To generate this movement, the cutting bench has a wheel with six rebounds (cam) whose rotation forces the pin to move up. This will lift up the cylinder, to which the chisel is attached, which immediately falls down, when reaching the up-dead-point, impelled by the spring and its own weight. Thus, the impact energy of the chisel depends on the relationship between the spring force and the maximum distance between the chisel and the file (adjusted by a presser foot). The chisel describes a reciprocating motion that always reaches the same up dead point (maximum distance between the chisel and the file), while the pin, rigidly attached with the cylinder, which moves the chisel, which always passes by the tops of cam. On the other hand, the down dead point of the chisel is variable, and depends on the impact energy absorbed by the file body. The chisel impact energy depends on the relationship of the regulations of the spring pre-load and on the maximum distance between the chisel and file. During the file manufacture, in order to obtain a tooth with the appropriate geometry (depth of the penetration), it is required, not only the impact energy should be adequately adjusted, but also the maximum distance between the chisel and the file resulting from the regulation of the presser foot should have a value that allows the chisel to pass above the last produced tooth.

When the machine operates correctly, the kinetic energy produced during the descending chisel movement is totally absorbed by the base body of the file. For that purpose, the presser foot must be adjusted in order to prevent impacts between cam and pin during the descent of the chisel movement. It means that the pin should never collide with cam. When this situation does not happen, as consequence of incorrect positioning of the presser foot, it can be observed that the cutting operation produces a hard and increasing noise. The noise is due to the impact of the pin on the cam, and strongly depends on the spring force. This clash is undesirable for two main reasons; firstly, because it accelerates the cam and follower wear, and secondly, because it decreases the kinetic energy available for the cutting operation, since part of the energy is be absorbed by that impact. Hence, the file quality is significantly penalized.

3 Cam Follower Mechanism Characterization

Figure 2b schematically illustrates the experimental data relative to the follower displacement diagram corresponding to a sixth part of the cam angle rotation, since the cam has six rebounds and the cam-follower motion repeats itself six times in each complete cam rotation. In Fig. 2b, point A represents the maximum follower displacement, point B defines the instant of impact between the follower and file body, point C corresponds to the minimum follower displacement, that is, the maximum penetration/deformation of the body file, and finally, point D represents the re-contact between the cam and follower after the rebound effect [7].

Observing Fig. 2b, it is evident that the follower motion can be divided into two main phases, namely, the fall and the rise movements. In turn, these two phases can be analyzed into two different parts. Starting from maximum follower elevation, point A, the follower motion can be described and summarized by the following steps:

1. Fall #1—from point A to point B: the follower motion is influenced by three main factors, the gravity effect, the spring action and friction phenomenon that exists between the follower and guide. At point A, the follower is pushed down by preloaded spring and gravity action;
2. Fall #2—from point B to point C: point B represents the initial instant of impact between the follower (chisel) and the file body. The maximum penetration depth, which corresponds to the edge height, is represented by the distance between points B and C. Point C corresponds to the end of follower fall motion;
3. Rise #1—from point C to point D: this phase represents the rebound effect caused by the accumulated energy during the contact-impact process between the follower and file body. In this process, there is no contact between the follower and cam due to rebound effect and cam speed;

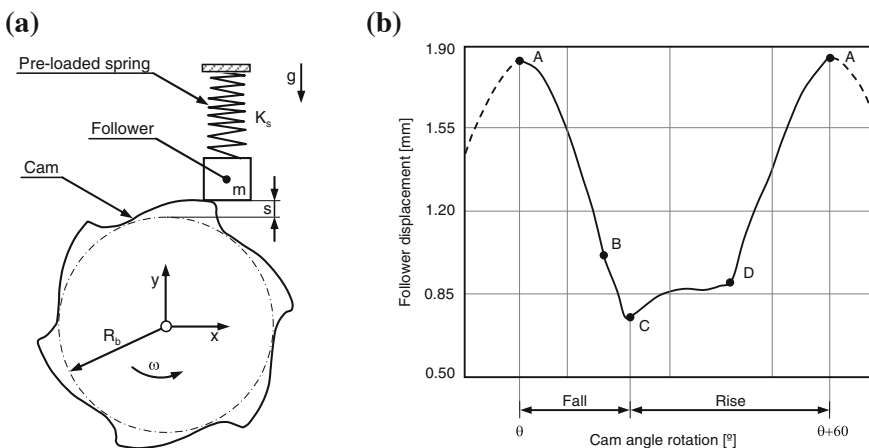


Fig. 2 a Kinematic configuration of the cam follower system; b Follower displacement

4. Rise #2—from point *D* to point *A*: the follower is in permanent contact with the cam surface, hence, the follower is rising and the spring is preloading in this process.

By knowing the cam follower mechanism completely defined, a graphical method was used to determine the displacement curve of the follower. This graphical procedure was based on the mechanism inversion principle, where in the relative motion between mechanism members is independent on the fixed member. In this procedure, the cam is treated as the fixed member and the follower is drawn tangent in the positions that it would take relative to the cam. Each successive follower position was then used to draw the displacement diagram.

The displacement diagram was the starting point for the analysis of the cam follower mechanism. Due to the need of high accuracy, the analytical methods are preferred to the graphical methods. Graphical methods have inherent accuracy limitations and should, therefore, be used only for low speed cams. However, the graphical construction provides a clear geometrical visualization of the formation process involved, based on the principle of inversion, while the analytical method makes this visualization difficult because everything is buried under its algebraic complexity. For better accuracy the cam cycle may be broken up into more divisions and/or the scale of the drawing may be increased. In the present study the cam was divided into 360 equal parts. Sometimes the basic cam’s profile curves can be inadequate on some occasions, especially in high-speed applications. A good overview on these subjects can be found in some classic references [8]. So, an alternative versatile way to specify the motion is to use a polynomial function. The displacement equation can be written as

$$s = C_0 + C_1\theta + C_2\theta^2 + C_3\theta^3 + C_4\theta^4 + \dots + C_n\theta^n \tag{1}$$

where *s* and *θ* are the follower displacement and the cam angle, respectively. The coefficients *C*₀, *C*₁, *C*₂, *C*₃, ... are chosen so that *s* and certain its derivatives satisfy the prescribed boundary conditions of the motion event. The best approximation for the polynomial function that expresses the follower displacement is a sixth degree polynomial, which can be written as

$$s = 2.793 - 44.873\theta + 258.802\theta^2 - 665.096\theta^3 + 896.635\theta^4 - 607.253\theta^5 + 161.998\theta^6 \tag{2}$$

This polynomial function was obtained by employing a mathematical tool dedicated for this purpose and the resulting correlation coefficient is equal to 0.999.

4 Results and Discussion

With the purpose to demonstrate the correlation between theoretical and experimental results, the main results for the standard machine operating conditions are presented and discussed in this section. The standard conditions in which the industrial machine operates are cutting file frequency equal to 187 Hz, distance between chisel and file equal to 0.6 mm and preload spring force equal to 335 N. Figure 3 shows the follower displacement and velocity for these conditions. The results are relative to a full cam rotation. Observing Fig. 3 it is evident the impressive correlation between the data obtain experimentally and with numerical simulation.

The influence of the chisel frequency is presented in what follows. For that purpose, several tests were performed using the fixed values for the distance between chisel and file and for the preload force spring, being the chisel frequency the only variable. After performing these tests, the files quality produced were verified. Table 1 shows the resulting data for the tests carried out.

Figure 4a shows the results with at low cutting frequency, that is, 38 Hz. It is evident that in this case, a continuous spring load during the follower rise and the dissipation of the elastic energy in the follower fall take place. Furthermore, it can be verified that a rebound happens immediately after the chisel penetration occurs. This fact is due to the kinetic energy that was not dissipated in the plastic deformation of the file. It was visible that the follower/chisel motion, counteracted by the spring, suffered a change of the direction, being the follower/chisel “stays stopped” (dwell) until occurs the cam contact. Figure 4b shows results obtained for tests performed at 150 Hz. Analyzing the force waveforms shown in the Fig. 4a, b, it can

Fig. 3 Theoretical and experimental results for the follower motion, when machine-operating conditions are frequency of 187 Hz, chisel-file distance equal to 0.6 mm and preload force spring of 335 N

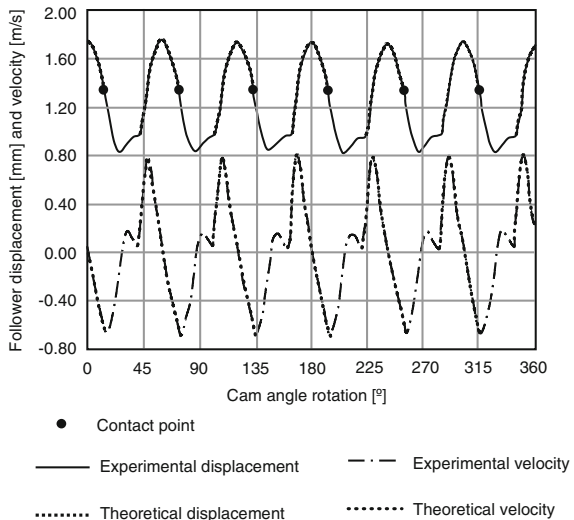


Table 1 Results for different cutting file frequencies

Cutting frequency (Hz)	Distance chisel-file (mm)	Preload force spring (N)	Average penetration (mm)	File quality obtained
38	0.6	335	–	Bad
75	0.6	335	–	Bad
112	0.6	335	–	Bad
150	0.6	335	–	Bad
187	0.6	335	0.407	Good
213	0.6	335	0.497	Good

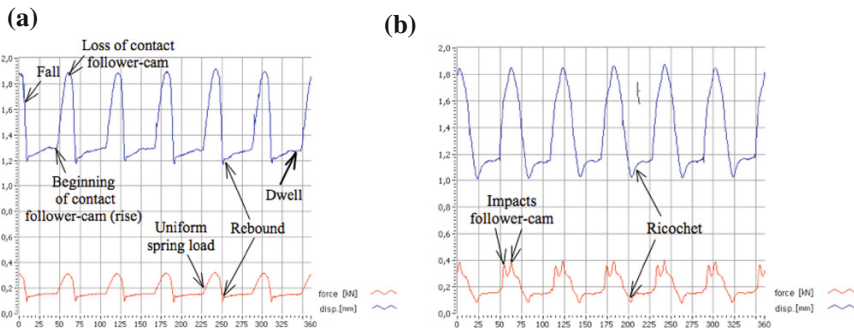


Fig. 4 **a** Waveforms of spring force and chisel displacement with a frequency of 38 Hz, distance of 0.6 mm and preload of 335 N (xx axis—degrees); **b** Waveforms of spring force and chisel displacement with a frequency of 150 Hz, distance of 0.6 mm and preload of 335 N (xx axis—degrees)

be concluded that the increase of cutting frequency produces impacts between cam and follower during the rising motion.

In order to study the influence of the distance between chisel and file on the quality of the files produced, several tests were performed using the fixed values for chisel cutting frequency and spring preload. Table 2 presents the results of those tests. From the data obtained, it can be concluded that the files produced with quality are those in which the values of distance chisel-file falls in the interval from 0.6 to 0.7 mm. It was also observed that when the distance is below 0.6 mm the destruction of the tooth previously made occurs. This fact is due to insufficient distance that does not allowed the chisel passing above the last produced tooth. On the other hand, when the distance is greater than 0.7 mm it was observed that the penetration of the chisel in the file was interrupted by the cam action, generating high impacts that originate anomalous vibrations in the machine, as well as files without quality.

The spring preload is an essential parameter to automatically control the cutting file machine. In fact, in files production, the spring preload is the only changed in order to maintain the chisel penetration into the quality interval. Thus, in this

Table 2 Results for different chisel-file distances

Cutting frequency (Hz)	Distance chisel-file (mm)	Preload force spring (N)	Average penetration (mm)	File quality obtained
187	0.4	335	–	Bad
187	0.5	335	–	Bad
187	0.6	335	0.407	Good
187	0.7	335	0.493	Good
187	0.8	335	0.572	Bad

Table 3 Results for different chisel-file distances

Cutting frequency (Hz)	Distance chisel-file (mm)	Preload force spring (N)	Average penetration (mm)	File quality obtained
187	0.6	315	0.376	Good
187	0.6	335	0.407	Good
187	0.6	355	0.485	Good
187	0.6	365	0.505	Good
187	0.6	375	0.568	Bad
187	0.6	385	0.635	Bad

section, the influence of the spring load on the file quality production is presented. In the tests performed, the distance between the chisel and file and the cutting file frequency are considered to be constant during the tests performed. Table 3 presents the results concerning to them tests.

5 Conclusions

In this work, a computational and experimental study of the cam follower mechanism of a cutting file machine was performed. The Newton-Euler equations of motion were used to simulate the dynamic behavior of the cutting file machine. In addition, the machine was instrumented in order to obtain the main kinematic and dynamic parameters that control the cutting file process. The correlation between computational and experimental is very good. The distance chisel-file of 0.6 mm is the most appropriate because it allows to produce teeth with quality using a larger interval of spring preload, being more easy to carry out the adjustment of the machine regulations. Finally it should be mentioned that the machine operation parameters that allows to obtain a quality file correspond to a cutting frequency of 187 Hz, a distance chisel-file of 0.6 mm and a spring preload from 315 to 365 N.

References

1. Fiteira T (1983) História das limas. Empresa de limas União Tomé Fêiteira, Portugal
2. Nicholson (1995) The guide to files and filing. Cooper Industries Inc., USA
3. Turner H (1862) The manufacture of the files and the material from which they are made with remarks on machine-cut files and unions, 2nd edn. Members of the Sheffield Mechanics Institution, UK
4. Ceccarelli M (1998) Mechanism schemes in teaching: a historical overview. *J Mech Des* 120:533–541
5. Black JB (1979) Workshop processes, practices, and materials. In: Arnold E (ed), UK
6. Öbergue (2001) Manual de acolhimento, Recursos humanos. Öbergue Ferramentas, Portugal
7. Flores P, Leine R, Glocker C (2012) Application of the nonsmooth dynamics approach to model and analysis of the contact-impact events in cam-follower systems. *Nonlinear Dyn* 69 (4):2117–2133
8. Erdman AG, Sandor GN (1997) Mechanism Design—analysis and synthesis, Third edn, vol I. Prentice Hall, New Jersey

An Overview of Industrial Communication Networks

M. Silva, F. Pereira, F. Soares, C.P. Leão, J. Machado
and V. Carvalho

Abstract This paper presents an overview on the industrial communication networks and protocols developed to monitor and control industrial processes. The most common protocols (Profibus, DeviceNet, Ethernet TCP-IP, AS-Interface, RS485, RS232, Host Link and FINS) are described and compared. These protocols and also different industrial networks can be tested using a dedicate Automation Platform, Remote Industrial Automation Protocol (PAIR). Different real-world case studies, selective solder industrial unit and other laboratorial prototypes are being designed to be used as demonstration of practical exercises.

Keywords Automation · Communication protocols · Industrial communication networks · Remote access

1 Introduction

It is well known the importance of automation and process control in industry. The frequency with which new challenges and requirements appear has induced the development of industrial automation area.

Currently, automated systems cannot be seen as “islands”, closed in themselves, but must permit interconnection, communication and monitoring between various modules.

The industrial communication networks massive development achieved in the last decade was often due to the diversity of teams working on new solutions. New

M. Silva (✉) · F. Pereira · F. Soares · C.P. Leão · V. Carvalho
R&D Centro Algoritmi, Engineering School, University of Minho, Guimarães, Portugal
e-mail: mario.jd.silva@sapo.pt

J. Machado
R&D CT2M, Engineering School, University of Minho, Guimarães, Portugal

V. Carvalho
IPCA-EST, Barcelos, Portugal

systems emerge, built over different concepts. As examples from these solutions, it may be appointed Profibus, DeviceNet, Ethernet TCP-IP, AS-Interface, RS485 and RS232 protocols [1–7].

With this problematic in mind, the authors developed several studies aiming to understand and teach the operation of these protocols to allow the communication between them. Thus, an Industrial Network Platform for monitoring and control of automated systems was designed and assembled, implementing several networks, each one with its own specific communication protocol [1, 2, 4]. Additionally, studies to remotely access, monitor and control the assembled network were also developed [3]. However, besides the obtained results were very satisfactory at that time, there is still space to improve the work done.

In order to better identify and propose solutions, this paper considers the following structure: Sect. 2 presents the Industrial Communication Networks, Sect. 3 shows the PAIR, Remote Industrial Automation Platform, and finally, Sect. 4, the Conclusion and Future Work.

2 Industrial Communication Networks

In previous works, Costa et al. [1–4] worked on industrial communication networks theme and its importance to automation and control systems. In a first step, the main characteristics of industrial communication networks and protocols were studied, in particular, Profibus, DeviceNet, Ethernet TCP-IP, AS-Interface, RS485 and RS232 protocols, which are presented in the following sub-sections. This study revealed itself of utmost importance since, when a communication network is to be chosen, it is necessary to consider if each protocol's characteristics is suitable to the system's requirements.

2.1 *Ethernet TCP-IP*

The well-known Ethernet TCP-IP protocol provides communication speeds up to 1 Gbps. It allows a low cost installation and its systems are flexible, as it can be seen either as a local network protocol, either as an industrial protocol. Using Ethernet TCP-IP it is possible to remotely access a network, favoring data sharing and the access to the several devices that compose the network. This is also possible in industrial networks, since the Programmable Logic Controllers (PLCs) have incorporated this technology.

Being an OSI Model based protocol, Ethernet TCP-IP implements the following layers: physical layer, data link, network, transport and application [8–10].

For communications from 100 Mbps or 1 Gbps, data physical transmission may use thin coaxial cable, twisted pair cable or fiber-optic cable. Instead of fiber-optic cable, communications of 10 Mbps use thick coaxial cable [1, 2, 9].

Data communication is supported by Medium Access Control (MAC) protocol and may be established as Simplex, Half-Duplex or Full-Duplex mode. In the later two cases, line communication's management is made by Carrier Sense Multiple Access/Collision Detection (CSMA/CD). Nevertheless, in large networks, collisions are common [1, 2, 9].

2.2 Profibus

Profibus protocol is characterized by being an open system, which may be used to assemble networks with sensors, actuators and controllers. With this protocol it is possible to use equipments from different manufacturers without many configuration problems.

With its physical data transmission being made over RS-485 protocol, this protocol shows characteristics such as asynchronous transmission non-return to zero (NRZ), baudrate from 9.6 kBit/s to 12 Mbit/s (selected according to the intended distance, which may range between 1,200 and 100 m, respectively), it uses a twisted pair cable with shield, it allows connection of 32 stations per segment (up to 127 stations). It is also possible to expand the extent of this network through the use of repeaters.

Another important feature of this protocol, due to its bus topology, is the simplicity of connection or equipment removal, not interfering with the functioning of other devices once, when the Profibus network is configured, a common transmission rate is established.

Currently, Profibus protocol may be found in three configurations: Profibus-Decentralized Periphery (DP), Profibus-Fieldbus Message Specification (FMS) and Profibus Process Automation (PA) [1, 2, 5].

2.3 DeviceNet

Based on the Controller Area Network (CAN) protocol, DeviceNet is widely used in industrial communication systems because it has reduced the implementation costs.

Another strong point of DeviceNet lies in its guidance for communications between low-level devices such as sensors and actuators. Being an open protocol also facilitates the integration of devices from different manufacturers and may include up to 64 nodes, with masters and slaves.

Depending on the length of the bus, this technology enables transmissions between 125 kbps, to distances of 500 m, and 500 kbps for distances of 100 m. Since it uses the CSMA/CD protocol, each node can access the bus whenever the latter is free [1, 2, 6].

2.4 AS-Interface

As the previously described protocols, AS-Interface (AS-I) is also an open protocol, facilitating compatibility between systems from different manufacturers. One of the strengths of this protocol lies in its low cost of implementation, requiring only a cable with two wires either to communication and power. Consequently, it facilitates the expansion of the systems. The AS-Interface is widely used as a sub-system for more complex buses, such as Profibus or Profinet, for example.

Physically, these networks can range from 100 m (adding repeaters it is possible to expand the system up to 300 m) and transmission speeds of 167 kbps. With a tree topology type (it is also possible bus and star topologies), 31 slaves can be attached to the master. Each slave can be coupled to 4 sensors and 4 actuators, at a maximum of 124 sensors and 124 actuators in the network.

In this protocol, the communication is made directly between the master system, which sends requests and the slave which provides the answer to the applications, as the following sequence: master makes request, the master waits, slave answers, slave waits [1, 2, 7].

2.5 RS485

Also known as EIA485, this protocol features for allowing networks with a maximum of 32 nodes. Sending information is based on the concept of sending packets between the Master and Slaves. Communication speed varies from 10 Mbps to 12 m extensions and 100 kbps for maximum distance of 1,333 m.

Despite its similarities with Profibus, RS485 shows communication difficulties when connecting devices from different manufacturers, due the lack of protocols created to rule communications over RS485 [1, 2].

2.6 RS232

In the RS232 protocol, also known as EIA232, the characters are sent asynchronously, bit by bit, being needed to send 2 additional bits per 8 bits character.

This protocol is widely used for communication between PLCs and PC, particularly for PLC programming. This characteristic was also very used on these studies, almost any time that programming a PLC was needed.

The main limitation of this protocol compared with those presented earlier, is to just be able to connect a device to each port [1, 2].

3 PAIR, Remote Industrial Automation Platform

PAIR, Remote Industrial Automation Platform (the acronym stands for Portuguese name), studies and assembles a monitoring and control system using Programmable Logic Controllers (PLCs). Once the PLC's manufacturer was Omron[®], Host Link [11] and Factory Interface Network Service (FINS) [12], both owned by the referred company, were analyzed. In order to better understand the characteristics of Host Link and FINS protocols, several tests were developed in a Modular Production System didactic kit, presented in the following sub-sections.

3.1 Host Link Protocol

This protocol allows communication via serial inputs/outputs of the CPU (Central Processor Unit) memory allocated for each control unit. With Host Link it is possible to read, write and change the CPU operating mode of each unit, from a personal computer. The maximum number of devices that may be connected with this protocol is 32 units and the maximum number of Words is 30 per message. Sending Host Link protocol frames can be done via RS232 port or via RS485.

The main limitation of this protocol lies in the impossibility of establishing communication with PLCs of a subnet as the Host Link only works with a direct connection between PC and PLC or PLC several bus connected to a PC [6, 11].

3.2 FINS Protocol

FINS is a network protocol used by Omron[®] for sending commands via RS232, Ethernet and other communications equipment used by the company.

In addition to resolving the limitation in access to PLCs configured on subnets, the FINS protocol is also characterized by being able to receive 269 Words and send 270 Words, and can still be used in Ethernet communications. The FINS protocol provides different frames for different modes of communication.

The Omron FINS protocol can be used through a program to transfer data and perform other services with remote PLC connected on an Ethernet network or via serial communication [6, 7, 12].

The Host Link and FINS protocols also differ in the format of the frames used, with the Host Link's frames being smaller, as can be seen in Table 1.

The Host Link protocol is advantageous in small networks with PLC configured in parallel given the smaller size of the frames used and the consequent ease of configuration. For more complex networks, especially with sub-networks, the FINS protocol is more appropriate, also allowing other communication skills [6].

Table 1 Command frame for writing

Action	Protocol	Frame
Writing	Hostlink	@00WR000A0001000237*
	FINS	@00FAF000000000102B0000A0000020001000200*
Reading	Host Link	@00WR0045*
	FINS	@00FA00400000000102000040*

3.3 PAIR Network Architecture

Following previous works [1, 3], PAIR implements a range of communication networks that use the protocols described above. PAIR network architecture is presented in Fig. 1.

The DeviceNet protocol is implemented for exchanging information between PLCs, connection to the security devices and control of inputs and outputs. The RS485 protocol connects two PLCs with different sensors. The Profibus was used to connect an inverter and an input/outputs control device. The RS232 protocol was used in the connection between a PLC and a reader of 2D/3D codes. At last, the Ethernet protocol allows the connection between PLCs, a control device of inputs and outputs and a vision system. It is responsible for allowing remote access to several networks implemented.

In addition to the aforesaid protocols, it was also used the Mechatrolink protocol for controlling a servomotor. With a transmission rate of 10 Mbps, this protocol has a high performance in terms of speed and high precision motion control [1].

Once implemented and tested each of these networks, the goal was to achieve communication between them, which was successfully achieved. This factor may prove to be quite important since in an industrial environment are often adopted solutions from different manufacturers and with different technologies.

Moreover, the communication between different networks also reveals important, improving remote network access and respective monitoring with all the inherent advantages [3].

However, the use of closed protocols, such as Host Link and FINS protocol, can cause barriers to communication with manufacturers not compatible with Omron protocol systems. The remote programming of the controller itself also was only possible with the aid of CX-Programmer (also owned by Omron).

3.4 Case-Study Prototypes

Different real-world prototypes were designed and developed: a small-scale house where alarm intrusion, entrance door opening/close, indoor lightning and attic temperature control were implemented; a two tank water level control, among others. Also, a kit that recreates a selective industrial welding machine is now being

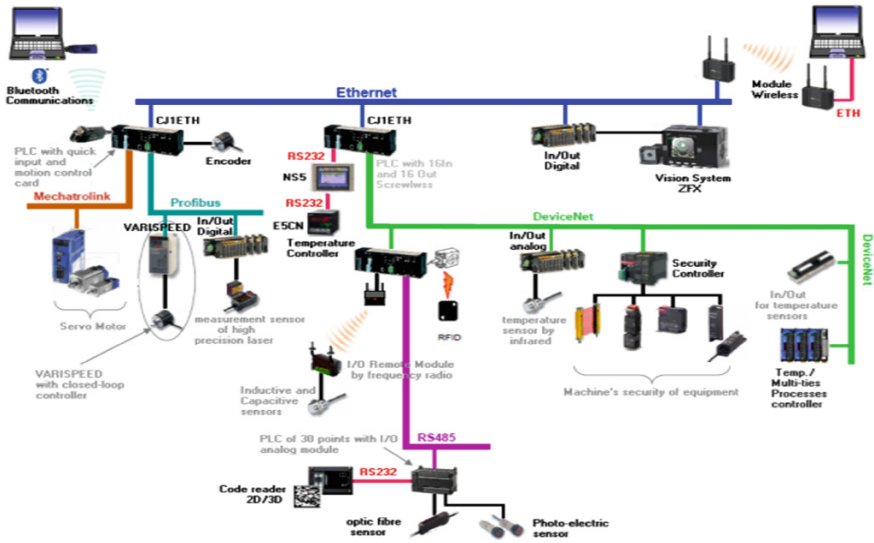


Fig. 1 PAIR network architecture

designed. In this kit it will also be necessary to monitor parameters such as the temperature, the oxygen, the amount of devices within the machine and which protocol should be applied to each one.

4 Conclusion and Future Work

The authors' research group has developed several studies in the field of industrial communication networks, for control and monitoring of processes.

For industry, to know which protocols are best suited to their needs and to be able to have a centralized management of their networks may represent a huge advantage over traditional systems. For companies with multiple branches, physically remote, this possibility can unveil also very advantageous in economic terms.

Despite the advantages in using the described Host Link and FINS protocols, as they are both owned by Omron®, their use may also set up limitations. So, the next step to implement will be a remote access and monitoring of network controllers only with open protocols, facilitating communication between PLCs of different manufacturers.

On the other hand, and despite having been studied, the AS-Interface protocol is not yet implemented in PAIR, so it will also be important to add a structure that refers to this protocol.

A review of these works proved to be very interesting as new needs arose to solve, thus showing the way forward for the next work.

Acknowledgments The authors of this paper are grateful to national funds by FCT—Fundação para a Ciência e Tecnologia in the scope of the project: PEst-OE/EEI/UI0319/2014.

References

1. Leão CP, Soares F, Machado J, Seabra E, Rodrigues H (2011) Design and development of a Industrial Network Laboratory. *Int J Emerg Technol Learn (iJET)* 6:21–26
2. Costa J, Carvalho N, Leão CP, Soares FO, Machado J (2010) Industrial network platform for monitoring and control of automated manufacturing systems. In: *Proceedings of IFAC 2010 - IFAC workshop on intelligent manufacturing systems*, Lisboa, Portugal, pp 168–173
3. Costa J, Carvalho N, Soares FO, Leão CP, Machado J (2010) Remote access to e-labs. In: *Proceedings of CONTROLO 2010—9th Portuguese conference on automatic control*, Coimbra, Portugal, pp 10–11
4. Costa J, Carvalho N, Soares FO, Leão CP, Machado J (2009) The FINS protocol for complex industrial applications: a case study. In: *Proceedings of ICINCO 2009—International conference on informatics in control*, Milan, Italy, 5 pp
5. <http://www.profibus.com/technology/profibus/>. Accessed on 3 Feb 2014
6. <http://www.odva.org/default.aspx?tabid=66>. Accessed on 3 Feb 2014
7. <http://www.as-interface.net/knowledge-base>. Accessed on 3 Feb 2014
8. Kurose JF, Ross KW (2010) *Computer networking: a top-down approach*, 5th ed. Pearson-Addison Wesley, Boston
9. Tanenbaum AS (2003) *Computer networks*, 4th edn. Pearson Education International, Upper Saddle River
10. Tang A, Scoggins S (1992) *Open networking with OSI*. Prentice Hall, Englewood Cliffs
11. Omron (2014) Serial communications boards and serial communications units. <http://downloads.industrial.omron.eu/.../W336-E1-10+CS-CJ-Series+OperManual.pdf>. Accessed on 6 Feb 2014
12. http://paginas.fe.up.pt/~pfs/recursos/plcs/omron/cs1/eth_manual/sec5.pdf. Accessed on 6 Feb 2014

Rapid Development of Control Algorithms and Interfaces for Remote Monitoring of Robotic Arm Through Internet of Things (IoT)

M. Murar and S. Brad

Abstract Time to market of a good is extremely critical and harvesting ideas and transforming them into products or services without using rapid development tools have small chances to succeed competition. Therefore, the goal of the paperwork and experimental project is to provide an overview upon how available rapid development tools and solutions can be employed for building remote connection, monitoring and control functionalities in a robotic cell towards connecting it to Internet of Things (IoT). Within the first part several important concepts like IoT, cloud computing and smart sensors and actuators are briefly presented. In the second part the architecture of the experimental design is proposed and resources are presented. The third part presents details about the experimental test bench, a simplified control logic diagram and the interface build on an IoT platform. In the last part conclusions are presented.

Keywords Internet of things · Rapid prototyping · Smart equipment · Robotics · Embedded designs

1 Introduction

The goal of this paperwork is to design and experiment affordable technologies for remote connecting, monitoring and control of a robot kinematic axis via Internet of Things (IoT). This is intended by using rapid prototyping tools in order to provide a broad overview of their advantages.

M. Murar (✉) · S. Brad
Technical University of Cluj-Napoca, Cluj-Napoca, Romania
e-mail: mircea.murar@muri.utcluj.ro

S. Brad
e-mail: stelian.brad@staff.utcluj.ro

Therefore within this chapter some of the concepts, methods and services used to achieve paper's goal are presented: Internet of Things, cloud computing, smart sensors and actuators.

1.1 Internet of Things

Even though not explicitly named so, in 1926, Nikola Tesla in an interview with Colliers magazine gave birth to an idea of what this day is more or less known as Internet of Things [8, 16].

Several definitions and opinions of what Internet of Things (IoT) is can be distinguished. Starting with the concept proposed by Kevin Ashton [1, 5, 7] up to a close synergy between the real world and the digital world whereas physical objects (sensors, actuators and even more complex devices) enhanced with distributed intelligence or at least with a unique identifier are seamlessly interconnected in order to be monitor and controlled by the IoT services and applications towards achieving specific goals [4, 6, 16, 18, 19, 21].

Things can be real world objects or virtual products which are identifiable and have the capabilities to “allow them to sense, actuate, identity, interact, interface and communicate” [16]. Thereby, things are active participants in any kind of business, information and social processes where they are enabled to interact and communicate among themselves by exchanging information they gathered.

Services and applications are the mainly composed out of the software products and the hardware infrastructure required to query, change and manage things state and the information associated with them together with linking them to the IoT with respect to security, functionality and privacy issues [5, 14, 20].

Estimated to reach a number of 50 billion connected devices by 2020, IoT will have a major impact upon all society related activities [17, 18]. Its advantages and disadvantages are explicitly presented within several researches [3, 20, 21].

1.2 Cloud Computing

Cloud terminology refers to an “elastic execution environment of resources involving multiple stakeholders and providing a metered service at multiple granularities for a specified level of quality” [9].

Even though not specifically related to IoT, cloud computing is considered as a major enabler for IoT. Cloud environment can offer valuable support for development of IoT since is designed to manage large, dynamic and distributed data sets. It is also enhanced with virtualization technologies, data and stream processing together with the required support to develop applications and services [10, 13]. Even more, cloud providers have tailored their cloud services to allow quick development of Internet of Things applications and prototypes by providing user

friendly and easy to use development dashboards for custom or branded hardware platforms. Cloud computing could provide IoT with required infrastructure to allow people and things to be connected: anytime, anyplace, with anything and anyone regardless the network and service used [20].

1.3 Smart Sensors and Actuators

IPSO Alliance defines smart objects as smart computers controlling a sensor or actuator with communication capabilities which are embedded into everyday equipment, therefore enabling a wide range of applications in all areas of society [15].

Figure 1, presents a generic smart sensor and/or actuator architecture, tested by authors in several experiments [2, 11, 12], which can be considered a *thing* since it presents, up to a level, the properties of a thing as previously defined.

2 Proposed Solution Architecture

The architecture of the experimental testing bench is built around an *mbed* development hardware as presented in Fig. 2. The *mbed* is used as a gateway to provide connectivity, control and monitoring functionalities between the electro-mechanical system with its smart sensors and actuators and the end-user application, used for monitor and control, running on a cloud platform which provides support for deploying IoT applications.

The goal of the proposed architecture is to provide a demonstrator for quick development of control algorithms and IoT connectivity for robotic systems applications using branded and custom embedded systems by employing rapid prototyping development environments. The following units were used:

- *IoT cloud* provider, for connecting things to an online platform having a suite of several built-in services for data feed and management, allowing therefore

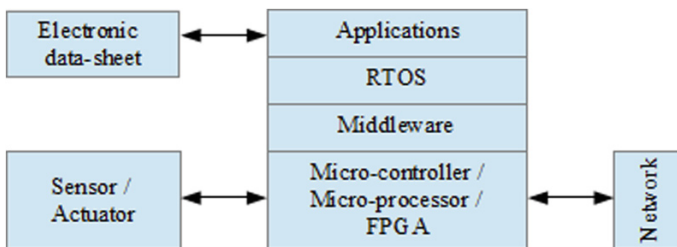


Fig. 1 Generic architecture of smart sensor/actuator

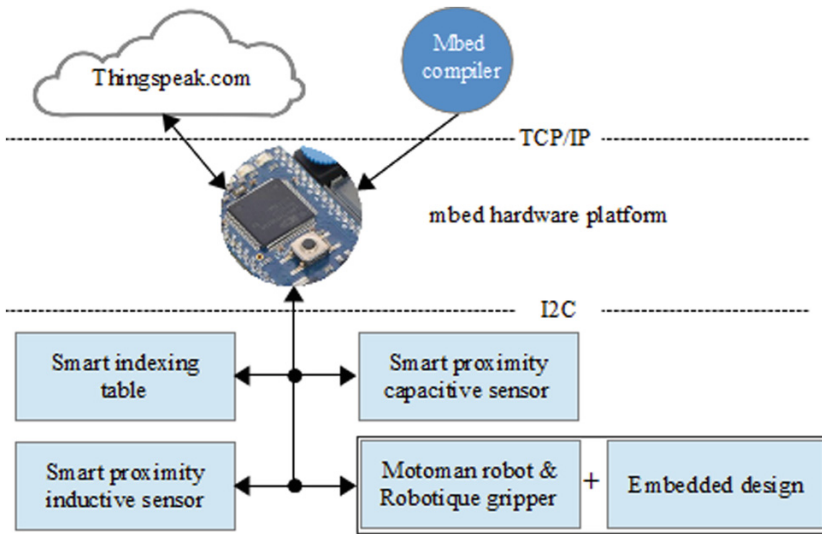


Fig. 2 Architecture of the experimental test bench

custom development of user specific applications. For this task the open-source development environment provided by Thingspeak.com was used.

- *Mbed* hardware and software platforms with its resources for rapid prototyping of embedded designs algorithms or software applications.
- *Smart sensors and actuators*, each sensor and actuator connected to a custom made embedded design for boosting their performances and provide the support for different applications.
- A *Motoman industrial robot (SDA10D)*, with seven axes of motion per arm is used to perform the task required to pick and place a metallic part.

3 Experimental Testing

The major parts of the experiment are the user-interface build on the *Thingspeak* platform, as presented in Fig. 3, which reads, writes and manage data through the *mbed* hardware platform (1) from the following equipment, as presented in Fig. 4: Motoman robotic arm (2), Robotiq™ gripper (3), indexing Table (4), proximity sensors (5), embedded design for one of the proximity sensors (6).

The *Thingspeak API* consists of mainly two parts: the visual interface and the process engine which is used for data management and as an interface to process equipment. The visual interface is a layout where the developer can add custom designed plugins built using HTML and CSS and dynamically managed using JQuery and Javascript, Fig. 3. The *Thingspeak* process engine is based on writing or

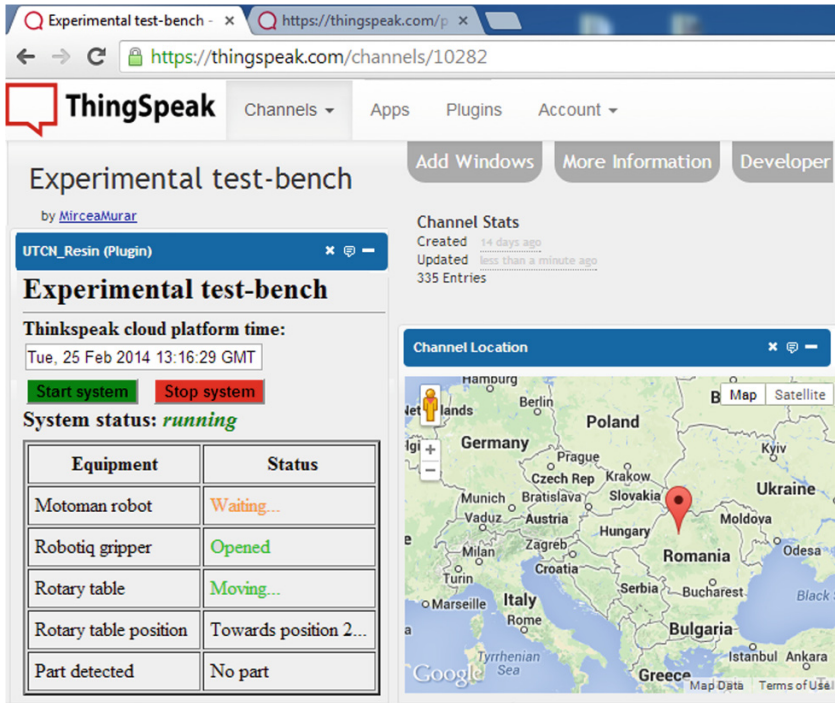


Fig. 3 Thingspeak interface (this figure was edited to fit page constraints)

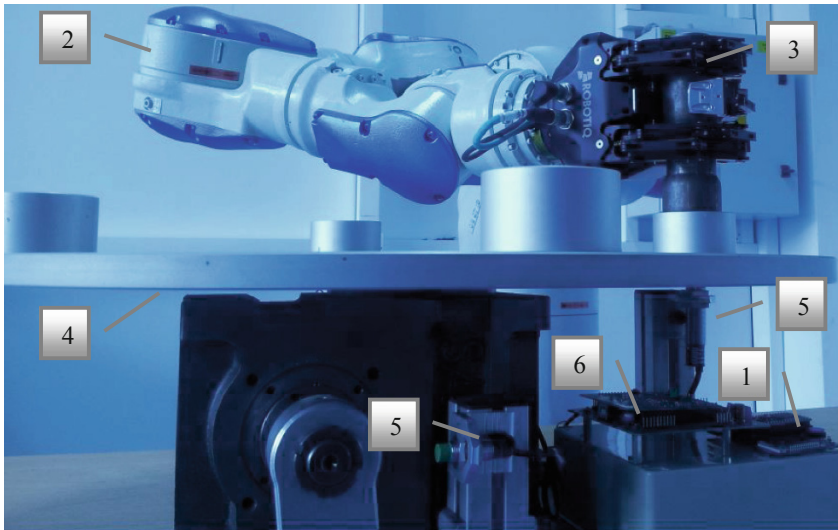


Fig. 4 Experimental testing bench (this figure was edited to fit page constraints)

Table 1 Content of HTTP requests

HTTP request	Thingspeak url	API key	Fields values
POST	http://api.thingspeak.com/update	Write key	“field1 = 21.5”
GET	http://api.thingspeak.com/channels/Channel_ID/feeds/last	Read key	–

reading data to a *channel*. Each channel has eight data fields which can be accessed by HTTP requests using uniquely generated API keys. Javascript and JQuery are used to scan for new data written to channel fields and process it in order to provide a meaningfully representation of received data. Also the above mentioned web programming languages are used to prepare data based on user actions on the visual interface which is to be read used to control process equipment.

The *mbed* hardware platform, NXP LPC1768, and an application board with an Ethernet shield together with the online compiler, software packages, libraries and resources were used to orchestrate the software algorithm used for managing the connection with the *Thingspeak* in order to update or read data by using HTTP requests. Based on its computational power the hardware platform is used to monitor, gather, preprocess and control the smart equipment involved within this experiment. To update or read from a channel feeds the content of a HTTP POST or GET requests triggered by the *mbed* software application should be as presented in Table 1.

Smart equipment embedded systems are based on Atmel ATmega32U4 micro-controllers running at 8 MHz with the required electronic circuitry to read data from sensors, drive the rotary table and trigger robot predefined jobs. The custom designed software for achieving the desired functionality was created in C/C++ using Atmel Studio 6. The output of proximity sensors is connected to an input of the assigned embedded design through a voltage level shifter to match the 5 V logic of the Atmel microcontroller. Output of the proximity sensors goes logic high if a capacitive or inductive part is detected, therefore, reading the input the developed software knows if a part is detected and reports its status when asked by the *mbed* hardware platform. Controlling the indexing table is achieved by toggling a microcontroller output which drives a relay that is connected in series with the coil of a 230Vac 9A contactor used to power the motor of the indexing table.

Each smart equipment has a software assigned unique I2C ID or address in order to be controlled by the I2C master (*mbed*) by reading and sending data to and from the *mbed* hardware platform over the I2C communication protocol.

Using INFORM III, Motoman specific robot programming language, the following robot routines were previously defined and gathered within a robot job: read and write robot digital inputs and outputs, open /close gripper, move the robot to pick and drop positions.

The software application of the embedded system associated with the robot controller is checking the I2C communication protocol for commands or requests

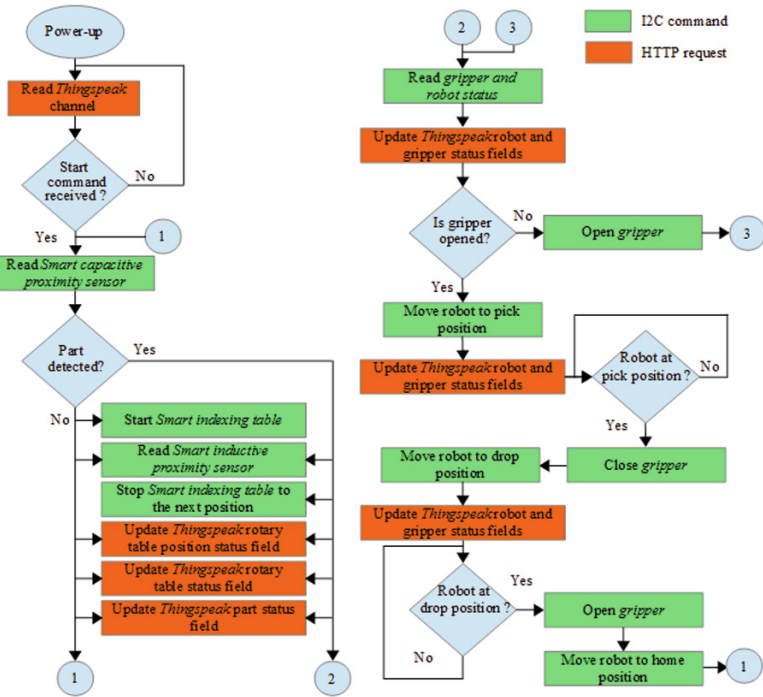


Fig. 5 mbed platform control logic (this figure was edited to fit page constraints)

sent by the *mbed* hardware platform. Each command is processed and specific digital inputs on the robot side are turned on. A robot procedure reads and decodes the signification of the active inputs and triggers one of the above mentioned routines. Robot digital outputs are updated in accordance with robot status and read and reported by the embedded design by the embedded design when a request is received from the *mbed* hardware platform.

Figure 5, presents a simplified logic diagram of the software application deployed within the *mbed* hardware platform.

4 Conclusions

Even if not fully built using rapid development tools since several custom made embedded designs with their software were used together with the robot software built on manufacturer proprietary programming language, the employed ones (*mbed* and *Thingspeak*) were capable to provide required functionality to reach the goal of this experimental application. The time required to build the experimental testing bench was significantly reduced by using the proposed rapid development tools. Replacing custom embedded designs with *mbed* hardware platform will result to a better development time, still additional hardware will be required.

Why connecting an electro-mechanical system to IoT? In the coming years everything will be connected to a network. This global network will bring advantages by providing enhance control upon things, achieving advanced monitoring features, data logging, distributed intelligence, reduce costs, product lifecycle management, preventive maintenance and many others, all of them achievable within a short time period by the advantages brought of using IoT. This paper work presents a method of how to connect, control and monitor equipment through IoT.

References

1. Ashton K (2009) That 'internet of things' thing. *RFiD J* 22:97–114
2. Brad S, Murar M (2013) Novel architecture of intelligent axes for fast integration into reconfigurable robot manipulators: a step towards sustainable manufacturing. *Ro J Tech Sci: Appl Mech* 58:107–128
3. Butala P, Vrabic R, Oosthuizen G (2013) Distributed manufacturing systems and the internet of things: a case study. Stellenbosch, South Africa
4. EU FP7 Project CASAGRAS (2009) CASAGRAS final report: RFID and the inclusive model for the internet of things
5. Goetz T (2011) Harnessing the power of feedback loops. *Wired Magazine*
6. Haller S (2009) Internet of things. In: *An integral part of the future internet, future internet assembly conference*
7. Haller S (2010) The things in the internet of things. In: *Internet of things conference, Tokyo, Japan*
8. Kennedy JB (1926) When woman is boss: an interview with Nikola Tesla. *Colliers*
9. Lutz S, Keith J, Burkhard N-L (2010) The future of cloud computing. In: *Opportunities for European cloud computing beyond 2010, Brussels*
10. Müller S (2010) The future of cloud computing. In: *Current offerings, barriers and challenges, Brussels*
11. Murar M, Brad S (2013) Control architecture for plug-and-play intelligent axes within fast reconfigurable manufacturing equipments. In: *CIRP design conference on smart product engineering, Springer, Bochum, pp 159–168*
12. Murar M, Brad S (2012) Providing configurability and plug-and-play capability to simple sensors: a step towards smart sensors for smart factories. *Appl Mech Mater* 162:597–606
13. Nosbusch K (2013) Industrial IoT in action, keynote sessions at internet of things world forum. Barcelona, Spain
14. Revell S (2013) Internet of things (IoT) and machine to machine communications (M2M) challenges and opportunities. Final paper, London, UK
15. Santucci G (2010) The internet of things: between the revolution of the internet and metamorphosis of objects
16. Smith IG et al (2012) *The internet of things 2012 New Horizons*. Halifax, UK
17. Soderbery R (2013) The internet of things: so what are we going to do about it? Keynote sessions at Internet of Things World Forum, Barcelona, Spain
18. Sundmaeker H, Guillemin P et al (2010) *Vision and challenges for realizing the internet of things*. Publications Office of the European Union, Luxembourg
19. Vermesan O et al (2009) *The internet of things—strategic research roadmap, cluster of European Research Projects on the internet of things, CERP-IoT*
20. Vermesan O, Friess P et al (2011) *Internet of things strategic research roadmap*
21. Vermesan O, Friess P (2013) *Internet of things—converging technologies for smart environments and integrated ecosystems*. River Publishers, Alborg

Numerical Simulation of Impact Loading on Open-Cell Aluminum Foams

P. Moreira, J.P. Mendonça and N. Peixinho

Abstract The main goal of this work is to present numerical results on the behavior of aluminum metal foams in impact scenarios. One type of metal foam with uniform-size cell structures with spherical voids is taken into account in this work. The uniform-size cell configurations are closely compact and present only one type of voids (large voids). Metal foams with different spherical voids dimensions were analyzed in order to investigate their influence on the mechanical properties of these structures using explicit finite element method (FEM). Results for force-deformation curves, specific stiffness and yield strength were obtained and discussed.

Keywords Open-cell aluminum foams · Mechanical properties · Impact behavior · Finite element analysis · Ansys[®] LS-DYNA

1 Introduction

During the last decades metallic foams have been used as a new type of engineering material in different application fields, such as automotive [3] and aerospace [4, 11, 16]. These metal materials possess important mechanical properties, including high rigidity, low density and large capability to absorb impact energy. There are other metal based cellular materials, such as metal hollow spheres and honeycombs that have excellent potential characteristics as blast and impact energy absorbers due to

P. Moreira (✉) · J.P. Mendonça · N. Peixinho
CT2M—Center for Mechanical and Material Technologies, University of Minho, Braga,
Portugal

e-mail: pfsmoreira@dem.uminho.pt

J.P. Mendonça
e-mail: jpmas@dem.uminho.pt

N. Peixinho
e-mail: peixinho@dem.uminho.pt

their ability to deform over a long stroke at an almost constant load [7]. Sandwich structures also represent another very important field for application of cellular foams. Sandwich structures typically consist of two thin and stiff composite face sheets bonded to a relatively thick light-weight core. The metallic cellular foams are used as core materials in sandwich structures [6].

Due to the previous enumerate mechanical properties, the use of metallic foams in impact related parts has been increasingly used in order to increase safety, particularly in the automotive and aerospace industry [12].

Metal foams are based on aluminum or nickel, but there are methods for foaming magnesium, zinc, copper, bronze, titanium, steel and gold. These materials are widely used due to their excellent stiffness-to weight capacity and damping capacity. The main obstacle has been the incapability for many industry manufacturers to distribute the materials/voids at the cell level [6].

The mechanical behavior of metallic foams is influenced by the cell structure, density and material properties of the foam material. The correct application of these metallic foams in the modern industry requires a detailed characterization of their deformation behavior, when subjected to different impact loads and different geometries. The size and shape of the cells influences their mechanical properties, namely in what concerns with the solid distribution in the porous structure [8].

The successful use of finite element package software's allows for analyses of complex structures and the efficiency and accuracy of the applied material models could be evaluated. Numerical and experimental simulations of aluminum foam deformation were carried out by several authors.

Rizov [15] investigated elastic-plastic behavior of closed cell cellular foams subjected to point and line loads both experimentally and numerically. The numerical simulation was carried out using ABAQUS.

Lee et al. [9] investigated the compressive behavior of open-cell aluminum alloy foam and stainless steel woven textile core materials at three different deformation rate regimes. Quasi-static experimental compressive tests were performed.

The mechanical properties of open-cell aluminum foams with dual-size cellular structure were studied experimentally and numerically by Kou et al. [8]. Uniform cell metal foams have a spherical shape and are closely compact. The cellular structure has a face-centered cubic arrangement. Dual-size foams have fillers composing a secondary link that is disposed in voids existing in uniform foam. The effect of dual-size cellular structure optimization on the mechanical properties of open-cell foams was investigated using finite element analysis (ABAQUS). The internal structure was modeled by an idealized unit cell extracted a real foam material, also called repeating unit or representative volume element (RVE).

Rajendran et al. [14] carried out numerical simulations using ANSYS/LS-DYNA for closed cell aluminium foam undergoing axial impact due to free fall of a drop hammer. Quasi-static axial crushing tests carried out on foams of three different densities were applied to derive the material properties. The simulation was validated with experimental results.

Guo et al. [2] studied experimentally and numerically the dynamic three-point bending behavior of double cylindrical tubes filled with closed-cell aluminum foam

core. The numerical simulation of the bending behavior was also executed with the explicit finite element method.

Rajaneesh et al. [13] reported numerical results of low velocity impact on open-face sandwich plates with an impactor of 2.65 kg mass hitting with 6.7 m/s velocity. The numerical simulation was done using 3D finite element models in LS-DYNA. The sandwich plates possessed a core made of commercial aluminum alloy foam (Alporas) with faceplates made of either ductile aluminum or brittle carbon fiber reinforced plastic. Numerically predicted contact force versus time, energy absorbed versus time along with the failure modes are compared with the experimental measurements and observations.

Cho et al. [1] performed impact tests with drop weights on closed-cell aluminum foam and the experimental results are compared with the simulation results. The finite element software, ABAQUS was used for the impact analysis. The low velocity impact damage behavior of aluminum foam was studied by comparing the numerical analysis and experimental result data. The numerically estimated damages, impact load history, and dissipated energy for penetration were compared with results of the experiments.

Jing et al. [5, 6] investigated numerically the dynamic response, energy absorption capability, and deformation and failure of clamped aluminum face-sheet cylindrical sandwich shells with closed-cell aluminum foam cores by impacting the shells at central area with metallic foam projectiles. Typical deformation modes and deflection response of sandwich shells, obtained from the experimental tests, were employed to validate the numerical simulation.

Pinto et al. [12] presented experimental results on the behavior of aluminum alloy metal foams with controlled pore morphology in compression. Two types of metal foams were analyzed, having uniform cell structure and with a dual-size cell arrangement seeking optimized mechanical properties. Results for stiffness and energy absorption were obtained and compared on weight efficiency basis.

Li et al. [10] performed finite element simulations in order to investigate the dynamic responses of metallic sandwich spherical shells with graded aluminum foam cores under inner blast loading. The deformation of spherical shells, the energy absorption of each core layer, and the propagation characteristic of stress waves in the foam core layers were analyzed, discussed and compared with experimental data.

However, experimental or computational investigations on the dynamic responses of open cell aluminum foams have yet to be reported. Therefore, the present work addresses this gap in the literature by exploring the aforementioned topic. Thus, in the context of this work, a numerical simulation on the impact response of open-cell metal foams with different spherical voids dimensions is presented and discussed.

2 Numerical Model

The idealized structures of open-cell metallic foams considered in this work were designed using Solidworks[®] CAD software (Dassault Systmes Solidworks Corp., Waltham, MA). The geometrical models consist in cylindrical specimens with 40 mm height and 16 mm diameter (Fig. 1) [12]. These models were selected for dynamic impact tests. One type of uniform size (US) open-cell aluminum foam with three different spherical voids dimension were studied: a single spherical open-cell with 4 mm (Fig. 1a), 5 mm (Fig. 1b) and 6 mm (Fig. 1c) diameter.

The procedure on the impact numerical simulations of rigid impactor on the aluminum foam is represented in Fig. 2. The impactor with a mass of 1 kg hits the different foams (US4, US5 and US6) with a velocity of 8 m/s. The aluminum foams have a mass of 2.1127 g (US4), 3.1394 g (US5) and 3.4813 g (US6). In this work, the same isotropic aluminium considered by [8] was used to simulate each foam subjected to impact. The impactor is made from structural steel. Table 1 summarizes the properties of the foam material with a bilinear isotropic hardening.

The finite element analyses were performed using the explicit solver LS-DYNA from the ANSYS[®] 14.0 Workbench (ANSYS Inc., Canonsburg, PA). The entire model (impactor + foam) comprises 204802 nodes and 643321 elements for the US4 foam, 166682 nodes and 598818 elements for the US5 foam, 121258 nodes and 443113 elements for the US6 foam. A tetrahedron element was used in all models instead of hexahedron, due to the geometric complexity of the different foams. The relevant center and span angle center, belonging to sizing meshing parameters, were set to fine option.

Regarding the boundary conditions, a fixed support was imposed on the bottom surface of the aluminum foam Fig. 2. Rigid impactor was projected vertically

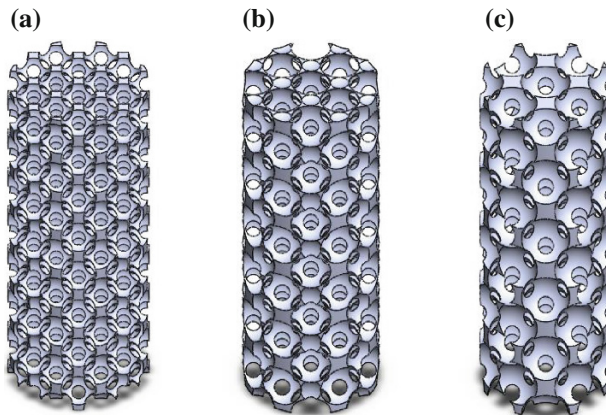


Fig. 1 Uniform size (US) open-cell aluminum foam with three different spherical voids dimensions: **a** US4 US4 open cell aluminum foam ($d = 4$ mm); **b** US5 US5 open cell aluminum foam ($d = 5$ mm); **c** US6 US6 open cell aluminum foam ($d = 6$ mm)

Fig. 2 Finite element model of the rigid impactor hitting the aluminum foam US4

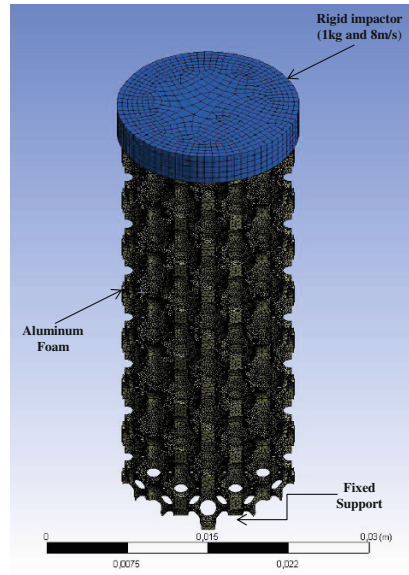


Table 1 Material properties

Physical property	Value
Density (kg m^{-3})	2,770
Young's modulus (Pa)	7.00E+10
Poisson's ratio	0.33
Bulk modulus (Pa)	6.86E+10
Shear modulus (Pa)	2.63E+10
Yield strength (Pa)	1.50E+8

against the top surface of the aluminum foam with a velocity of 8 m/s. The reaction force at the bottom of the impactor is a function of mass and impact acceleration. The Von Mises stress on the top surface of the foam was obtained by dividing the reaction force by the area of cross section of the foam. The yield strength is the maximum Von Mises verified during the impact scenario.

3 Results and Discussion

The simulation results presented and discussed in this section include: Impact force versus directional deformation (Fig. 3), yield strength σ^* (Fig. 4) and specific stiffness K^* (Fig. 5) of each foam. The simulation time is 90 μs .

Fig. 3 Impact force versus directional deformation (vertical)

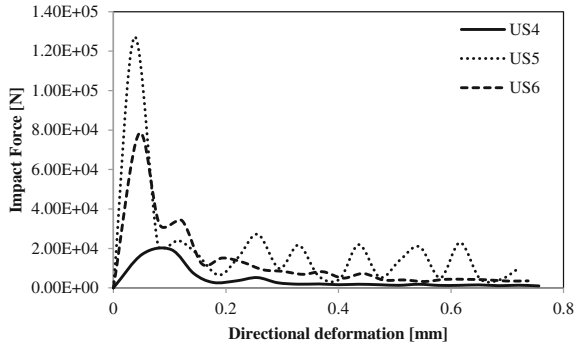


Fig. 4 Yield strength, σ^*

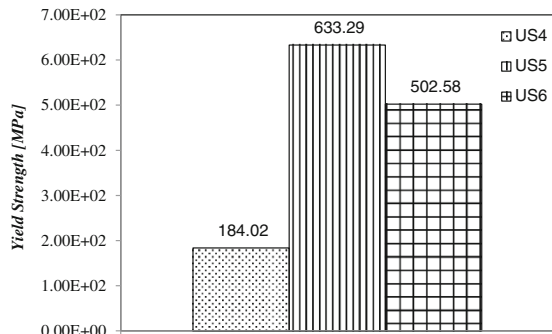
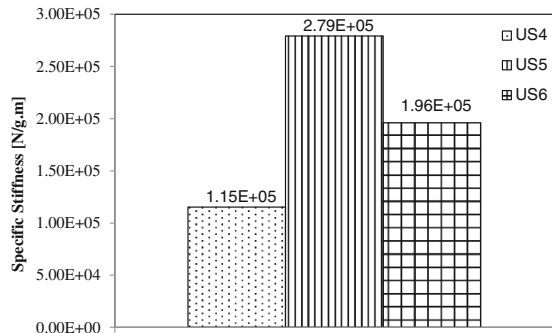


Fig. 5 Specific stiffness, K^*



From the analysis of Fig. 3, it can be concluded that the force - deformation curve of uniform aluminum foam US5 is much higher when compared with aluminum foams US4 and US6, specially during the first impact event. The aluminum foam US4 possesses the lowest force—deformation curve. It can also be observed that the deformation verified on the aluminum foam US4 is slightly higher, when compared with US5 and US6 aluminum foams. In Fig. 3 is evident that the different spherical voids dimensions influenced the foam response to dynamic conditions.

The yield strengths σ^* (Fig. 4) of aluminum foams US5 and US6 are 3 and 4 times approximately higher when compared to aluminum foam US4. The same behavior is verified when the specific stiffness's K^* are analysed (Fig. 5). The specific stiffness and yield strength of the uniform-size cellular structures are highly improved by introducing larger spherical voids.

4 Conclusions

The present work demonstrated that the finite element analyses are of paramount importance to study the influence of different spherical voids dimensions on the mechanical response of open cell metal foams. Within this study it was concluded that the geometric void shape significantly affect the dynamic impact behavior of metal foams.

One type of uniform size (US) open-cell aluminum foam with three different spherical voids dimension were studied: a single spherical open-cell with 4 mm (US4), 5 mm (US5) and 6 mm (US6) diameter. The force—deformation curve of uniform aluminum foam US5 is much higher when compared with aluminum foams US4 and US6, specially during the first impact event. The deformation verified on the aluminum foam US4 is slightly higher, when compared with US5 and US6 aluminum foams. The specific stiffness and yield strength of the uniform-size cellular structures are highly improved by introducing larger spherical voids.

The computational time required to perform the explicit finite element analysis simulations, for the US4, US5 and US6 foams were 13, 14 and 8 h, respectively.

Acknowledgements The authors would like to thank the Portuguese Foundation for Science and Technology (FCT) for the support given through project Development of advanced parts for impact energy absorption using carbon nanotubes as metallic foam reinforcement with functionally graded properties (PTDC/EME-PME/115668/2009).

References

1. Cho JU, Hong SJ, Lee SK, Cho C (2012) Impact fracture behavior at the material of aluminum foam. *Mater Sci Eng A* 539:250–258. doi:10.1016/j.msea.2012.01.091. URL <http://linkinghub.elsevier.com/retrieve/pii/S092150931200127X>
2. Guo L, Yu J (2011) Dynamic bending response of double cylindrical tubes filled with aluminum foam. *Int J Impact Eng* 38(2–3):85–94. doi:10.1016/j.ijimpeng.2010.10.004. URL <http://linkinghub.elsevier.com/retrieve/pii/S0734743X10001508>
3. Han MS, Bang SO, Cho JU, Lee S, Cho C (2013) Experimental study on the impact characteristics of a sandwich composite with an aluminum foam core. *Int J Automot Technol* 14(1):61–66. doi:10.1007/s12239
4. Hanssen A, Girard Y, Olovsson L, Berstad T, Langseth M (2006) A numerical model for bird strike of aluminium foam-based sandwich panels. *Int J Impact Eng* 32(7):1127–1144. doi:10.

- 1016/j.ijmpeng.2004.09.004. URL <http://linkinghub.elsevier.com/retrieve/pii/S0734743X0402015>
5. Jing L, Wang Z, Zhao L (2013) Dynamic response of cylindrical sandwich shells with metallic foam cores under blast loading Numerical simulations. *Compos Struct* 99:213–223. doi:10.1016/j.compstruct.2012.12.013. URL <http://linkinghub.elsevier.com/retrieve/pii/S0263822312006319>
 6. Jing L, Xi C, Wang Z, Zhao L (2013) Energy absorption and failure mechanism of metallic cylindrical sandwich shells under impact loading. *Mater Des* 52:470–480. doi:10.1016/j.matdes.2013.05.090. URL <http://linkinghub.elsevier.com/retrieve/pii/S0261306913005220>
 7. Karagiozova D, Langdon G, Nurick G (2012) Propagation of compaction waves in metal foams exhibiting strain hardening. *Int J Solids Struct* 49(19–20):2763–2777. doi:10.1016/j.ijsolstr.2012.03.012. URL <http://linkinghub.elsevier.com/retrieve/pii/S0020768312001047>
 8. Kou D, Li J, Yu J, Cheng H (2008) Mechanical behavior of open-cell metallic foams with dual-size cellular structure. *Scripta Materialia* 59(5):483–486. doi:10.1016/j.scriptamat.2008.04.022. URL <http://linkinghub.elsevier.com/retrieve/pii/S1359646208002935>
 9. Lee S, Barthelat F, Moldovan N, Espinosa HD, Wadley HN (2006) Deformation rate effects on failure modes of open-cell Al foams and textile cellular materials. *Int J Solids Struct* 43(1):53–73. doi:10.1016/j.ijsolstr.2005.06.101. URL <http://linkinghub.elsevier.com/retrieve/pii/S0020768305004269>
 10. Li S, Wang Z, Wu G, Zhao L, Li X (2014) Dynamic response of sandwich spherical shell with graded metallic foam cores subjected to blast loading. *Compos Part A Appl Sci Manuf* 56:262–271. doi:10.1016/j.compositesa.2013.10.019. URL <http://linkinghub.elsevier.com/retrieve/pii/S1359835X13002947>
 11. Ma ZT, Jia B, Pang BJ (2007) Behavior of aluminum foams under hypervelocity impact: validation of numerical simulation. *Adv Eng Mater* 9(10):888–891. doi:10.1002/adem.200700115. URL <http://doi.wiley.com/10.1002/adem.200700115>
 12. Pinto P, Peixinho N, Silva F, Soares D (2014) Compressive properties and energy absorption of aluminum foams with modified cellular geometry. *J Mater Process Technol* 214(3):571–577. doi:10.1016/j.jmatprotec.2013.11.011. URL <http://linkinghub.elsevier.com/retrieve/pii/S0924013613003385>
 13. Rajaneesh A, Sridhar I, Rajendran S (2012) Impact modeling of foam cored sandwich plates with ductile or brittle faceplates. *Compos Struct* 94(5):1745–1754. doi:10.1016/j.compstruct.2011.12.021. URL <http://linkinghub.elsevier.com/retrieve/pii/S0263822311004892>
 14. Rajendran R, Moorthi A, Basu S (2009) Numerical simulation of drop weight impact behaviour of closed cell aluminium foam. *Mater Des* 30(8):2823–2830. doi:10.1016/j.matdes.2009.01.026. URL <http://linkinghub.elsevier.com/retrieve/pii/S0261306909000223>
 15. Rizov VI (2006) Elasticplastic response of structural foams subjected to localized static loads. *Mater Des* 27(10):947–954. doi:10.1016/j.matdes.2005.02.013. URL <http://linkinghub.elsevier.com/retrieve/pii/S0261306905000713>
 16. Zhang X, Jia G, Huang H (2011) Numerical investigation of aluminum foam shield based on fractal theory and node-separation FEM. *Chin J Aeronaut* 24(6):734–740. doi:10.1016/S1000-9361(11)60086-1. URL <http://linkinghub.elsevier.com/retrieve/pii/S1000936111600861>

Combining the Finite Element Method and Response Surface Methodology for Adjustment of Contact Stress Ratios in Tapered Roller Bearings

R. Lostado, R. Escribano, R. Fernandez Martinez
and B.J. Mac Donald

Abstract This paper shows a methodology for adjusting the top-bottom contact stress ratio belonging to the outer raceway by combining the loads acting on the bearing by means the finite element method (FEM) and response surface methodology (RSM). A three-dimensional Finite Element (FE) model considering the material properties and geometry of a real tapered roller bearing was built. Subsequently, a design of experiments (DoE) study varying the input loads (preload, radial load, axial load and torque) was implemented. These input loads generated thought DoE were simulated in the FE model, and the contact stresses belonging to the outer raceway were obtained. A quadratic regression model for predicting the ratio between the contact stresses was formulated, and using the RSM method, a combination of input loads were found for adjusting a specific top-bottom contact stress ratio.

Keywords Double-row tapered roller bearing • Finite elements method (FEM) • Response surface methodology (RSM)

R. Lostado (✉) · R. Escribano
University of La Rioja, Logroño, Spain
e-mail: ruben.lostado@unirioja.es

R. Escribano
e-mail: ruben.escribanogarcia@gmail.com

R. Fernandez Martinez
University of Basque Country UPV/EHU, Bilbao, Spain
e-mail: roberto.fernandezm@ehu.es

B.J. Mac Donald
Dublin City University, Dublin, Ireland
e-mail: bryan.macdonald@dcu.ie

1 Introduction

Double-row tapered roller bearings are mechanical devices designed to support high axial, radial and moment loads. Due to this combination of loads, the bearing is subjected to high contact stresses, and for this reason it is very important to know both magnitudes and distribution of stresses in the outer raceway. These contact stress values and distributions are usually obtained through analytical methods and numerical methods such as the FEM. Analytical methods have the disadvantage of having to depreciate certain boundary conditions to solve the problem. FEM, conversely, can handle more realistic boundary conditions but generally this results in a high computational cost. Likewise, FE models require high mesh densities in order to obtain realistic results in the calculation of contact stresses [1]. Some authors have validated their FE models using forces and displacements to avoid the influence of mesh size in the contact stresses calculation [2, 3]. Moreover, Response Surface Methodology (RSM) is a method widely used for modelling and optimizing mechanical devices. This method uses the input variables and their responses in order to obtain the best response through identifying the combination of input variables [4]. In this case, both analytical and FE methods were used to determine the ratio between the contacts stresses belonging to the top and to the bottom on the outer raceway. A comparison of these two methods was carried out, and using the RMS method, a combination of input loads were found for adjusting a specific top-bottom contact stress ratio. In this case, the study was focused on a tapered roller bearing with a bore diameter of 78 mm; Outer diameter of 130 mm and longitude of the bearing of 90 mm.

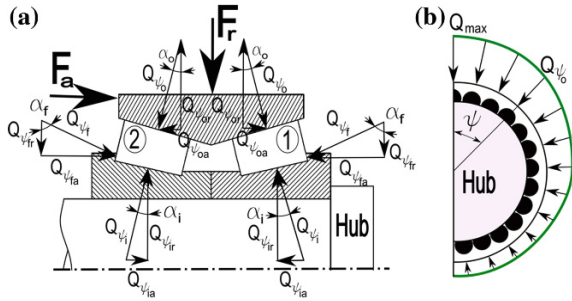
2 Calculation of the Contact Pressure Distribution

The calculation of contact stress distribution in double-row tapered roller bearing through analytical methods requires an assumption of no slack in the assembly while the value of the preload is reduced. This situation actually requires that the bearing only acts on the radial and axial forces, neglecting the preload and torque. Figure 1a shows the distribution of loads on the bearing. Likewise, this combination of loads produced a distribution of contact pressures in the outer raceway as shown in Fig. 1b.

2.1 Contact Stress Calculation Using the Analytical Method

The maximum normal load that each raceway can support is related to the maximum total strain (ϵ) that each raceway can undergo (See Eq. (1)), being the

Fig. 1 Loads applied over the tapered roller bearing (a) and contact stress distribution (b)



subscripts 1 and 2 belonging to the columns of the rollers and n the load-deflection exponent.

$$\frac{Q_{max2}}{Q_{max1}} = \left(\frac{\varepsilon_2}{\varepsilon_1}\right)^n \tag{1}$$

Likewise, considering the static condition in the bearing, the radial and axial loads (F_a and F_r) on each raceway could be calculated according to:

$$F_r = F_{r1} + F_{r2} \tag{2}$$

$$F_a = F_{a1} - F_{a2} \tag{3}$$

Also, F_r and F_a can be expressed according to Eqs. (4) and (5) for the first row of rollers as:

$$F_r = Z \cdot Q_{max1} \cdot J_r \cdot \cos \alpha \tag{4}$$

$$F_a = Z \cdot Q_{max1} \cdot J_a \cdot \cos \alpha \tag{5}$$

where the J_a and J_r are the integral function introduced in [5] and Z is the number of rollers. Table 1 shows the relation between the variables included in these equations.

Likewise, the distribution of loads on each roller is carried out according to Eqs. (6) and (7), being ψ the angular position of the rollers.

Table 1 Results from compression tests line contact

ε_1	ε_1	$\frac{F_r \cdot \tan \alpha}{F_a}$	J_r	J_a	$\frac{Q_{max2}}{Q_{max1}}$	$\frac{F_{r2}}{F_{r1}}$
0.5	9.5	∞	0.4906	0	1	1
...
0.9	0.1	0.6343	0.2741	0.4321	0.089	0.043
1.0	0	0.2523	0.2523	0.4817	0	0

$$Q_{\psi_1} = Q_{\max_1} \left[1 - \frac{1}{2\varepsilon_1} (1 - \cos \psi) \right]^{1,11} \tag{6}$$

$$Q_{\psi_2} = Q_{\max_2} \left[1 - \frac{1}{2\varepsilon_2} (1 - \cos \psi) \right]^{1,11} \tag{7}$$

The normal contact pressure σ_{ψ_1} between the outer raceway and the rollers is obtained from the width of the contact area (b_o) and the radii of curvature ($\sum \rho_o$) according to Eqs. (8) and (9).

$$\sum \rho_o = \frac{1}{D_m} \left[\frac{2}{1 + \gamma_o} \right] \tag{8}$$

$$\gamma_o = \frac{D_m \cdot \cos \alpha_o}{d_m} \tag{9}$$

where D_m and d_m are respectively, the mean diameter and bearing pitch diameter according to Fig. 2a. The width b_o of the contact area is calculated according to Eq. (10), and the value of contact pressure according to Eq. (11).

$$b_o = 3.35 \times 10^{-3} \left(\frac{Q_{\psi_1}}{l_t \cdot \sum \rho_o} \right)^{1/2} \tag{10}$$

$$\sigma_{\psi_1} = \frac{2 \cdot Q_{\psi_1}}{\pi \cdot l_t \cdot b_o} \tag{11}$$

And finally, the ratio is calculated according to Eq. (12)

$$\text{Ratio (S)} = \frac{\sigma_{1\text{Bottom}}}{\sigma_{1\text{Top}}} \cdot 100 \tag{12}$$

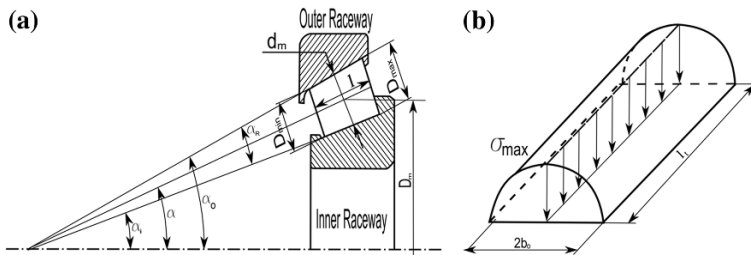


Fig. 2 Main dimensions of the tapered roller bearing (a) and theoretical contact stress distribution (b)

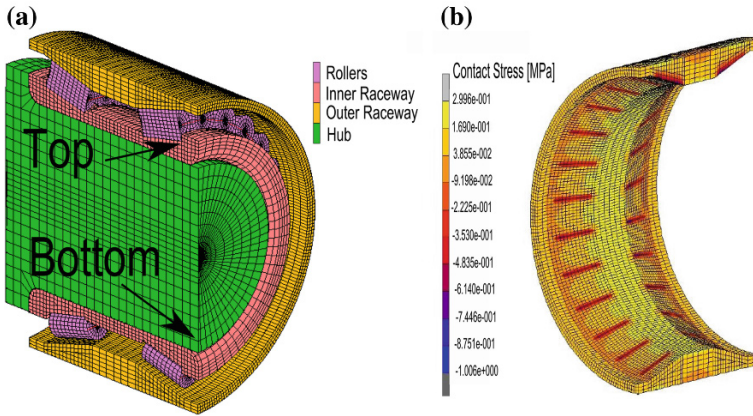


Fig. 3 FE model configuration (a) and contact stress distribution on the outer raceway (b)

2.2 Contact Stress Calculation Using FEM

In this case, the FE model uses a symmetry condition for modelling only one half of the double-row bearing (See Fig. 1) and was developed using Abaqus © software. One end of the axle was fixed to the ground while in the opposite end was assembled the bearing. A linear elastic material was used for modelling the raceways and rollers (Young’s modulus, $E = 20$ GPa, Poisson’s ratio, $\nu = 0.29$) [3] and 8-node elements with linear shape functions were considered. The coefficient of friction between the rollers and the outer raceway was taken as 0.001 [6], and the stick-slip model were considered for modelling the contact between rollers and raceways (Fig. 3).

3 Response Surface Methodology (RSM)

The RMS in a method that tries to find the relationships between input variables and response variables (output variables) thought a model, as well as to find an optimal response. RMS was focused originally for modelling numerical experiments and for reduces the number of them. Basically, RSM is a group of mathematical techniques by means of a low-degree polynomial function (Eq. 13).

$$y = f(x_1, x_2, x_3, \dots, x_k) + e \tag{13}$$

where y is an experiment response, and $(x_1, x_2, x_3, \dots, x_k)$ is the vector of inputs, e the error and f is the function defined as the cross-products of a polynomial with degree one or two. Also, design of experiments (DoE) [7] is a tool used for reduce the number of experiments at the same time the degree of accuracy of the model

Table 2 Input loads and levels thought central composite design (CCD)

Input	Notation	Magnitude	Levels		
			-1	0	+1
Preload	P	N	60,000	80,000	100,000
Load	L	N	8,000	9,000	10,000
Axial load	A	N	-200	0	200
Torque	T	N·mm	-10,0000	0	100,000

obtained is sufficient. Many researchers have developed methods for improve DoE but all methods involves the construction of a design matrix (inputs) and the measuring of the inputs and outputs of the experiment [8–10]. In this case, a set of experiments were implemented for analyse the influence of the inputs with the output using DoE. In this case, the input parameters were radial load (L), preload (P), axial load (A) and torque (T); and the output was the contact stress ratio (S). The design matrix was made by central composite design (CCD) which is useful to get quadratic models for the responses without use a complete three-level experiment (Table 2).

4 Results

Table 3 shows the experiment matrix generated using four inputs and three levels and their corresponding ratio calculated thought FE and theoretical model. From this table is possible to appreciate that the ratio obtained thought theoretical models assumed is close to zero for all cases. This is mainly due to the fact that in the theoretical model torque and preload are neglected.

4.1 Regression Model

Quadratic regression was used for modelling the relationship between the inputs and the contact stress ratio. Likewise, analysis of variance (ANOVA) was carry out using Design-Expert® v7 package [11], and the regression model obtained for modelling the contact stress ratio is shown in Eq (13).

Table 3 Process parameters and their limits

Run	Preload	Radial load	Axial load	Torque	Ratio FE (%)	Ratio Theor. (%)
1	10,000	100,000	-200	-100,000	24.7	≈ 0
2	10,000	100,000	-200	100,000	23.2	≈ 0
...
24	9,000	100,000	200	0	19.9	≈ 0
25	9,000	60,000	200	0	32.1	≈ 0

Table 4 Correlation, errors and significance

Regression	Corr	MAE normalized	RMSE normalized	Significance
Ratio	0.985	3.2	4.2	<0.0001

$$\begin{aligned}
 S = & -0.796 + 0.2062 \cdot P + 3.43 \cdot 10^{-2} \cdot L - 2 \cdot 10^{-4} \cdot A + 7.2 \cdot 10^{-3} \cdot P^2 \\
 & - 6.7 \cdot 10^{-3} \cdot P \cdot L + 1.02 \cdot 10^{-5} \cdot P \cdot A - 7 \cdot 10^{-8} \cdot P \cdot T - 5 \cdot 10^{-4} \cdot L^2 \quad (13) \\
 & + 3.13 \cdot 10^{-6} \cdot L \cdot A + 3 \cdot 10^{-8} \cdot L \cdot T + 1.7 \cdot 10^{-7} \cdot A^2
 \end{aligned}$$

Table 4 summarizes the correlations, errors and significances of the quadratic regression models. Also, Fig. 4a shows a good agreement between the actual (from FEM) and predicted (from Eq. 13) contact stress ratio.

4.2 Optimizing the Contact Stress Distribution

The optimization of the tapered roller bearing consisted of maximizing the top-bottom contact stress ratio when the value of the Radial Load was the maximum for any value of Axial Load and Torque. Figure 4b shows the best preload at different work conditions (Axial and Torque) and the corresponding top-bottom contact stress ratio obtained. The results show that the value of the contact stress ratio was

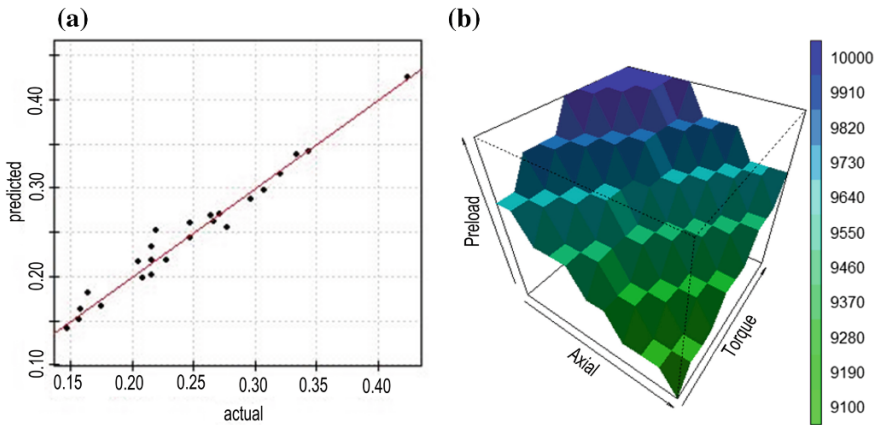


Fig. 4 Actual and predicted contact stress ratio (a) and *top-bottom* contact stress ratio maximization (b)

70 % when the preload had values between 9,100 and 10,000 N for any value of axial load and torque.

5 Conclusions

A methodology to obtain the maximum top-bottom contact stress ratio in a double-row tapered roller bearing combining the finite element method (FEM) and response surface methodology (RSM) has been presented in this work. The first step consisted of building a FE model to get the contact stresses in the outer raceway at different work conditions. Subsequently, a design of experiments (DoE) study was implemented in order to reduce the number of FE simulations and obtain the most representative combinations of inputs. A quadratic regression model using the input parameters and the results of the FE models was obtained via Response surface methodology (RSM). Using ANOVA techniques, an appropriate significance, errors and correlation of the quadratic model showed an agreement with the FE results. The paper concludes by showing an optimization process maximizing contact stress by varying preload when the values of the radial load are maximum for any torque and axial load values.

References

1. Feng Q, Prinja NK (2001) Benchmark tests for finite element modelling of contact, gapping and sliding, NAFEMS Report R0081
2. Laniado E et al (2010) Study of sliding between rollers and races in a roller bearing with a numerical model for mechanical event simulations. *Tribol Int* 43:2175–2182
3. Demirhan N, Kanber B (2008) Stress and displacement distributions on cylindrical roller bearing rings using FEM. *Mech Based Des Struct Mach* 36:86–102
4. Myers RH, Anderson-Cook CM (2009) Response surface methodology: process and product optimization using designed experiments. Wiley, Hoboken
5. Lundberg G, Sjövall H (1958) Stress and deformation in elastic contacts. Pub. 4, Institute of Theory of Elasticity and Strength of Materials, Chalmers Institute Technology, Gothenburg
6. Reusner H (1988) The logarithmic roller profile-the key to superior performance of cylindrical and taper roller bearings. *Ball Bearing J* 230:2–10
7. Fisher RA (1935) *The design of experiments* (8th ed., 1966) New York, Hafner Press
8. Box GE, Behnken DW (1960) Some new three level designs for the study of quantitative variables. *Technometrics* 2:455–475
9. Myers RH (1971) *Response surface methodology*. Allyn and Bacon, Boston
10. Taguchi G (1986) *Introduction to quality engineering: designing quality into product and processes*. Tokyo, Asian Productivity Organisation
11. Design-Expert Software, Version 7, user's guide, technical manual. Minneapolis (MN): Stat-Ease Inc. (2005)

Author Index

A

Abásolo, M., 53
Abdul-Sater, K., 891
Adouane, L., 157
Ahmad, S. S. N., 523
Almeida, H. A., 761
Alonso, F. J., 689
Altuzarra, O., 535
Alves, Pedro, 121
Ambrósio, J., 471, 479, 487, 497
Appleyard, R., 463
Araújo, A., 243
Arrouk, K. A., 43
Askari, E., 463
Avilés, R., 53

B

Bader, R., 659
Bağdadioglu, B., 175
Bai, Shaoping, 3
Barros, C., 573
Bártolo, P. J., 761
Bautista-Quintero, R., 325
Benoit, Romain, 69
Bento, David, 261
Bezerra, K., 573
Boborelu, C., 669
Borchard, J. -H., 81
Bouzgarrou, B. C., 43, 211
Brad, S., 941
Brandt-Salloum, C., 913
Braune, R., 139
Brito, F. P., 221
Brix, T., 913
Bujakas, V. I., 753
de Bustos, Fernández. I., 53

C

Cabrera, J. A., 299
Cafolla, Daniele, 585
Calafeteanu, D., 669
Campa, F. J., 535
Carneiro, V. H., 807
Caro, Stéphane, 21
Carretero, J. A., 325
Carvalho, M., 651
Carvalho, V., 573, 933
Castejón, C., 839
Castillo, J. J., 299
de Castro, P. M. S. T., 779
Ceccarelli, M., 603, 613, 643
Chen, Y., 269
Claro, J. C. P., 243, 405, 435
Cocorean, D., 455, 563
Cole, C., 523
Comiskey, D., 679
Comsa, A., 743
Conde Martín, S., 413
Copilusi, C., 603, 643, 709
Correia, P., 287
Corves, B., 139, 337, 869
Costa, T., 221
Couto, M., 733
Covaciu, F., 563
Craciunoiu, N., 355
Crhák, V., 365
Cruz, Francisco, 121
Cuadrado, J., 505, 689

D

Dabirrahmani, D., 463
Delanoue, Nicolas, 69
Díaz-Rodríguez, M., 325

Dierßen, F., 81
 Diez-Ibarbia, A., 373
 Ding, H. F., 91
 Döring, U., 913
 Doroftei, I., 157
 Dosaev, M., 545, 623
 Dowd, A., 679
 Dumitrache, I., 709
 Dumitru, N., 147, 355, 669, 709
 Erkaya, S., 307, 721
 Escribano, R., 957
 Espregueira-Mendes, J., 633

F

Fauroux, J. C., 157, 211
 Fernandes, Carlos M. C. G., 799
 Fernández del Rincón, A., 373
 Fernandez Martinez, R., 957
 Flores, P., 121, 129, 385, 423, 463, 471,
 505, 633, 643, 699, 923
 Folgado, J., 479
 Font-Llagunes, J. M., 689
 Freitas, D., 761

G

García Orden, J. C., 413
 García, P., 373
 García-Prada, J. C., 839
 Gebel, E., 345
 Geonea, I., 147, 709
 Gherman, B., 455
 Glazunov, V., 203
 Gogu, G., 43
 Golovin, Alexander, 903
 Gonçalves, S. B., 445
 Goryacheva, I., 623
 Grawe, R., 659
 Gruescu, C. M., 111
 Gubenko, M., 623
 Guo, Xiaoning, 195
 Gürcü, F., 167

H

Haddad, M., 395
 Hajžman, M., 233
 Hanke, U., 743
 Henkel, V., 913
 Herrmann, S., 659
 Hichri, B., 157

Holub, A., 545
 Hüsing, M., 139, 337

I

Iglesias, M., 373
 Irlinger, F., 891
 Itul, T., 455
 Ivanov, I., 869

J

Jaimez, M., 299
 Jirásko, P., 365
 Ju, M.-S., 623
 de Juan, A., 373

K

Kähler, M., 659
 Kahrs, L. A., 81
 Kaur, M., 603
 Kecskeméthy, A., 91
 Kiper, G., 167, 175
 Klimina, L., 545
 Klodowski, A., 99
 Kluess, D., 659
 Koga, T., 515
 Korkmaz, K., 167
 Kotlarski, J., 81
 Kozyrev, A., 203
 Kraus, Werner, 553
 Krid, M., 211

L

Lagrange, Sébastien, 69
 Lankarani, H. M., 423, 859
 Leal, A., 633
 Leal, N., 733
 Leão, C. P., 573, 933
 Lima, M., 881
 Lima, Rui, 261
 Lin, Dongliang, 13
 Liu, Z.-H., 269
 Liu, Zhijun, 13
 Lostado, R., 679, 957
 Lourenço, C., 435
 Lovasz, E.-C., 111, 743
 Lueth, T. C., 891
 Lugris, U., 505, 689
 Lyubicheva, A., 623

M

Mac Donald, B. J., 679, 957
 Machado, J., 573, 933
 Machado, M., 471, 733
 Magalhães, H., 487
 Malaquias, T. M., 445
 Malciu, R., 355
 Mall, Alexander, 315
 Marco, Ceccarelli, 585
 Mărgineanu, D., 111
 Marina, V. García, 53
 Marques, H. M. C., 129
 Marques, Pedro M. T., 789, 799
 Marques, T., 733
 Marta, M., 733
 Martins, J., 221
 Martins, Ramiro C., 789, 799
 Matos, D., 573
 McCartney, W. T., 679
 McSweeney, Tim, 523
 Meireles, J., 807
 Mencek, H., 277
 Mendonça, J. P., 949
 Menkouz, B., 395
 Merlet, J.-P., 31
 Mezouar, Y., 157
 Miermeister, Philipp, 553
 Modler, K.-H., 111, 743
 Modler, N., 743
 Moldovan, C. E., 111
 Monteiro, J., 479
 Moreira, P., 505, 699, 949
 Morozov, A., 623
 Moura, B., 699
 Murar, M., 941

N

Neto, R., 733
 Nurahmi, Latifah, 21

O

Oliveira, R. F., 129
 Ondrášek, J., 185
 Ono, K., 515
 Ortmaier, T., 81

P

Pàmies-Vilà, R., 689
 Pedrero, J. I., 771
 Peixinho, N., 243, 251, 287, 949

Peixoto, J., 505, 699
 Pereira, C., 497
 Pereira, F., 573, 933
 Pereira, H., 633
 Pereira, R., 633
 Perju, D., 111
 Pinho, A., 243
 Pinho, Diana, 261
 Pinto, Ch., 535
 Pinto, J., 221
 Pisla, D., 455, 563
 Pleguezuelos, M., 771
 Plitea, N., 563
 Ploscaru, N., 355
 Polach, P., 233
 Pombo, J., 487
 Pop, C., 111
 Popa, D., 669
 Pott, Andreas, 315, 553

Q

Quental, C., 479

R

Racilă, L., 147
 Raghavan, Madhusudan, 817
 Ramalho, A., 497
 Ribeiro, João., 261
 Roldan-Paraponiaris, C., 535
 Rosa, S., 651
 Rubio, H., 839
 Rull, Aleix, 61

S

Sánchez, M. B., 771
 Sato, T., 515
 Schmidt, Valentin, 315, 553
 Schoenen, D., 869
 Schumacher, M., 337
 Schwarzfischer, F., 337
 Seabra, E., 881, 923
 Seabra, Jorge H. O., 789,
 799
 Selyutskiy, Yu, 623
 Silva, F. S., 633
 Silva, I., 643
 Silva, Luís. F., 121, 881, 923
 da Silva, M. Tavares, 445
 Silva, M., 933
 Simón, A., 299

Simroth, F., 91
 Soares, F., 573, 933
 Soriano, E., 839
 Sousa, S., 405
 Souto, A. P., 505, 699
 Souza, L., 651
 Söylemez, E., 167
 Soylu, R., 277
 Spiriyagin, M., 523
 Su, F.-C., 623
 Sui, Pengju, 195
 Sun, Y. Q., 523
 Szilaghyi, A., 563

T

Tarnita, D. N., 669
 Tarnita, D., 669, 709
 Tavares, S. M. O., 779
 Tay, Y. Y., 423, 859
 Teixeira, J. C., 129
 Teixeira, S. F., 129
 Thomas, Federico, 61
 Torquato, T., 651

U

Umstead, C. M., 859
 Ungureanu, A., 147

V

Václavík, M., 365
 Vaida, C., 563
 van der Wijk, V., 829
 Vaz, Mário, 261

Viadero, F., 373
 Vidal, F., 299
 Vukolov, Andrei, 903

W

Wang, Hengli, 195
 Wang, Mingfeng, 613
 Weller, A., 515
 Wenger, Philippe, 21, 69
 Woernle, C., 659

X

Xie, J., 269
 Xu, L., 423
 Xu, Qi-Ping, 851

Y

Yan, Jianye, 13
 Yao, Ligang, 13, 195
 Yeh, C.-H., 623
 Yıldırım, Ş., 723
 Yu, Yue-Qing, 851

Z

Zeng, Shilong, 195
 Zhang, Z., 423
 Zhao, H., 269
 Zhou, Peng, 851
 Zichner, M., 743
 Zielinska, Teresa, 595
 Zurawska, Magdalena, 595